

Talanta

The International Journal of Pure and Applied Analytical Chemistry

Aims & Scope

Talanta provides a forum for the publication of original research papers, preliminary communications, and reviews in all branches of pure and applied analytical chemistry. Analytical data should be submitted only if they are clearly related to new analytical measurements. Original research papers on fundamental studies and novel sensor and instrumentation development are especially encouraged. Novel or improved applications in areas such as clinical chemistry, environmental analysis, geochemistry, and materials science and engineering are welcome. Methods should be validated by comparison with a standard method or analysis of a certified reference material, and relevant literature should be cited. Since classical spectrophotometric measurements and applications, solvent extraction, titrimetry, chemometrics, etc. are well established, studies in such areas should demonstrate a unique and substantial advantage over presently known systems. New reagents or systems should demonstrate clear advantage, and their presentation should be comprehensive rather than generating a series of similar papers for several analytes. Modifications of reagents should demonstrate significant improvements. Solvent extraction methods in particular, but others as well, should focus on the use of non-hazardous material substitutes and the minimization of waste generation. But obvious application of known chemistries or methods to established techniques are discouraged. Application of classical analytical approaches to relatively sample matrices having no major interferences, such as pharmaceutical preparations or reconstituted samples, are discouraged unless considerable improvements over other methods in the literature are demonstrated. Papers dealing with analytical data such as stability constants, pK_a values, etc. should be published in more specific journals, unless novel analytical methodology is demonstrated, or important analytical data are provided which could be useful in the development of analytical procedures.

Editors-in-Chief

Professor G.D. Christian, University of Washington, Department of Chemistry, 36 Bagely Hall, P.O. Box 351700, Seattle, WA 98195-1700, U.S.A.

Professor J.-M. Kauffmann, Université Libre de Bruxelles, Institut de Pharmacie, Campus de la Plaine, C.P. 205/6, Boulevard du Triomphe, B-1050 Bruxelles, Belgium

Associate Editors

Professor J.-H. Wang, Research Center for Analytical Sciences, Northeastern University, Box 332, Shenyang 110004, China

Professor J.L. Burguera, Los Andes University, IVAQUIM, Faculty of Sciences, P.O. Box 542, 5101-A Mérida, Venezuela.

Assistant Editors

Dr R.E. Synovec, Department of Chemistry, University of Washington, Box 351700, Seattle, WA 98195-1700, U.S.A.

Professor J.-C. Vire, Université Libre de Bruxelles, Institut de Pharmacie, Campus de la Plaine, C.P. 205/6, Boulevard du Triomphe, B-1050 Bruxelles, Belgium

Talanta

R. Apak (Istanbul, Turkey)
E. Bakker (Auburn, AL, U.S.A.)
D. Barceló (Barcelona, Spain)
B. Birch (Luton, UK)
K. S. Booksh (Tempe, AZ, U.S.A.)
J.-L. Capelo-Martinez (Caparica, Portugal)
Z. Cai (Kowloon, Hong Kong)
O. Chailapakul (Thailand)
S. Cosnier (Grenoble, France)
D. Diamond (Dublin, Ireland)
W. Frenzel (Berlin, Germany)
A.G. Gonzales (Seville, Spain)
P. de B. Harrington (OH, U.S.A.)

A. Ho (Hsin-chu, Taiwan)
P. Hubert (Liège, Belgium)
J. Kalivas (Pocatella, ID, U.S.A.)
B. Karlberg (Stockholm, Sweden)
J.-M. Lin (Beijing, China)
Y. Lin (Richland, WA, U.S.A.)
M.D. Luque de Caastro (Cordoba, Spain)
I.D. McKelvie (Victoria, Australia)
S. Motomizu (Okayama, Japan)
J.-M. Pingarron (Madrid, Spain)
E. Pretsch (Zürich, Switzerland)
W. Schuhmann (Bochum, Germany)
M. Shamsipur (Kermanshah, Iran)

M. Silva (Porto Alegre, Brazil)
P. Solich (Hradec Králové, Czech Republic)
K. Suzuki (Yokohama, Japan)
D.G. Themelis (Thessaloniki, Greece)
D.L. Tsalev (Sofia, Bulgaria)
B. Walczak (Katowice, Poland)
J. Wang (Tempe, AZ, U.S.A.)
J.D. Winefordner (Gainesville, U.S.A.)
Xiu-Ping Yan (Tianjin, China)
E.A.G. Zagatto (Piracicaba, SP, Brazil)
X. Zhang (China)



Development of an optical ammonia sensor based on polyaniline/epoxy resin (SU-8) composite

A. Airoudj^{a,b}, D. Debarnot^{a,*}, B. Bêche^c, F. Poncin-Epaillard^a

^a Laboratoire Polymères, Colloïdes, Interfaces, UMR 6120, Université du Maine, Avenue Olivier Messiaen, 72085 Le Mans, France

^b Laboratoire d'Acoustique de l'Université du Maine, UMR-CNRS 6613, Avenue Olivier Messiaen, 72085 Le Mans, France

^c Laboratoire PALMS-GMCM, UMR-CNRS 6627-6626, Institut de Physique de Rennes, 35042 Rennes, France

ARTICLE INFO

Article history:

Received 3 April 2008

Received in revised form

22 September 2008

Accepted 29 September 2008

Available online 14 October 2008

Keywords:

Ammonia sensor

Polymer sensitive layer

Optical transducer

Absorption variation measurement

ABSTRACT

Polyaniline (PANI)/glycidyl ether of bisphenol A (SU-8) composite film is elaborated in order to detect ammonia gas. These composite films are characterized by ultraviolet–visible (UV–vis) spectroscopy, Fourier transformed infrared (FTIR) spectroscopy and scanning electron microscopy (SEM). The sensitivity to ammonia is measured by optical absorption changes. The ammonia sensing properties of PANI/SU-8 composite films are studied, and then are compared to pure PANI films elaborated by chemical way. Experimental results show that the PANI/SU-8 optical sensor has simultaneously a rapid response to ammonia gas and regenerates easily, that is advantageous compared to pure PANI films.

© 2008 Elsevier B.V. All rights reserved.

1. Introduction

Electroconducting polymeric materials are of great interest for a large number of applications [1–3] due to their easy processing and relatively low cost compared to other materials such as inorganic ones. They can be used as promising materials for different types of chemical sensors (with electrical, optical or piezoelectrical transductions) because of their sensitivity at room temperature and their selectivity for specific chemical agents. The sensing ability of electroconducting polymers is based on modulation of their doping level during redox or acid–base interactions with some gases. This effect results in an immediate alteration of the conductivity and the optical absorbance.

Polyaniline (PANI) is one of the most promising conducting polymers because of its easy synthesis either through chemical or electrochemical methods and its selectivity to ammonia [4–6]. PANI shows electrical and optical property variations, when it is in contact with oxidant–reductor chemicals. In particular, the interaction between the conductive form of PANI – emeraldine salt (ES) – and the ammonia gas results in a decrease of the polaron density inside the band gap of the polymer according to the mechanism proposed in Fig. 1 [6–8]. Indeed, a lot of

articles describe electrical and optical sensors for NH₃ detection with PANI as sensitive layer [3,7–21]. Nonetheless, the poor solubility and mechanical properties of PANI imply difficulties in its practical use. In order to overcome these disadvantages, several methods have been developed [22–33]. One of them consists to elaborate conductive polymer composites. PANI/polymer composite has attracted considerable attention because even at very low PANI concentration, conducting composites with good mechanical properties and chemical stability can be obtained [29–31]. PANI composite can be prepared by chemical or electrochemical polymerization of aniline in a solution of the polymeric matrix. PANI can also be mixed with other polymers in the melt state. Different polymers can be used, such as polymethyl methacrylate (PMMA) [25,29,30], polyvinyl chloride [30], polystyrene [32], and epoxy resin [33]. For gas detection application, to our knowledge, only one study presents optical sensors based on PANI composite coatings using PMMA as matrix [25]. These gas sensors show slow recovery time and regeneration difficulty. On the other hand, the lack of description of optical gas sensors based on the polyaniline composite gives us the opportunity to develop a new optical sensor which will present simultaneously high sensitivity, fast optical response and short recovery time. To improve the characteristics of PANI sensors, we explored an epoxy resin as polymer matrix to elaborate conducting PANI composite. The epoxy-based polymer, which commercial name is SU-8, widely used as negative photoresist has also been studied for micro-electro-optical-mechanical sys-

* Corresponding author. Tel.: +33 2 43 83 39 82; fax: +33 2 43 83 35 58.
E-mail address: Dominique.Debarnot@univ-lemans.fr (D. Debarnot).

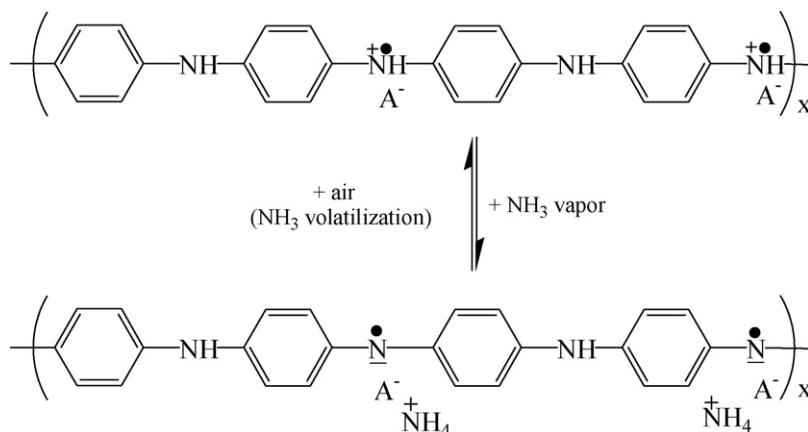


Fig. 1. Mechanism of the interaction of NH_3 with polyemeraldine salt. In this study, A^- is Cl^- .

tem (MEOMS) applications [34–37]. It is thermally stable, has good mechanical properties and good control of the film thickness [36]. The PANI/SU-8 composite films were characterized by UV–vis, FTIR spectroscopies and SEM. The performances of this PANI composite film as ammonia optical sensor have been evaluated by absorption spectroscopy and compared to pure PANI film.

2. Experimental

2.1. Reagents and materials

Aniline (99.8%, Aldrich), ammonium persulfate ($(\text{NH}_4)_2\text{S}_2\text{O}_8$, Aldrich), hydrochloric acid 37% (HCl, Aldrich), and hydroxide ammonium (NH_4OH , Aldrich) were used as the monomer, the oxidant, the dopant and the de-dopant, respectively. N-methyl-2-pyrrolidone (NMP, Aldrich) was used as solvent of PANI. Epoxy resin (glycidyl ether of bisphenol A (SU-8 2002), MicroChem, USA) was used as received as the polymer matrix.

2.2. Preparation of PANI/epoxy resin (SU-8) composites

PANI was prepared according to the method described by Stejskal et al. [38]. 1 mL of aniline monomer was dissolved in 100 mL of 1 M HCl aqueous solution. A solution of 0.56 g $(\text{NH}_4)_2\text{S}_2\text{O}_8$ in 10 mL of 1 M HCl aqueous solution was added into the monomer solution under continuous stirring. The reaction mixture was then stirred continuously at room temperature for 1 h. The dark green precipitate was collected by filtration under reduced pressure. The product was then treated with 1 M HCl aqueous solution containing 1 mL of aniline for 1 h and then dried under vacuum at room temperature to finally obtain the powder of doped polyaniline. In order to obtain the emeraldine base form (PANI-EB), the final powder was treated with 0.1 M NH_4OH for 2 h. After filtering and drying under vacuum for 48 h, the blue powder of the EB form was obtained.

The PANI-EB (0.6 g) was dissolved in 20 mL of NMP solvent to form PANI-EB solution with concentration of 3 or 10 wt.%. Depending on the desired concentration of PANI-EB in the matrix of epoxy resin, certain amount of epoxy resin was mixed with the PANI-EB solution under stirring for 24 h at room temperature. The concentration of PANI-EB (in weight percent in the composite) was defined as the ratio of the weight of PANI-EB to the total weight of PANI-EB and epoxy resin matrix (SU-8) in the solution. The resulting solution was spin-coated onto cleaned glass substrate to form film of PANI-EB/epoxy resin (SU-8). The thickness of the film was about 1 μm .

In order to obtain the PANI-ES/epoxy resin (PANI/SU-8) conducting films, the PANI-EB/SU-8 films were exposed to an atmosphere of saturated HCl (37%) vapor for 1 min. After few seconds of HCl exposure, the color of the film changed from blue to green due to the doping process.

2.3. Preparation of pure polyaniline films

PANI films were prepared following the method described in [39,40] with a slight modification. 1 mL of aniline monomer was added drop wise into 100 mL of 1 M HCl aqueous solution under stirring at room temperature. Then, cleaned glass substrate was immersed in the monomer solution. After the yellow drops of aniline dissolved completely in the acidic solution, 5 mL of 0.1 M $(\text{NH}_4)_2\text{S}_2\text{O}_8$ aqueous solution was added into the monomer solution to initiate the polymerization of the aniline monomer. Polymerization began immediately with an evident color alteration after 3–5 min, indicating polymer formation. The thickness of the green film deposited onto glass substrate depends on polymerization time and varied between 50 and 130 nm. The PANI-coated glass substrate was then thoroughly washed with 0.1 M HCl aqueous solution, and immersed into another aniline solution (1 mL aniline dissolved in 100 mL of 1 M HCl) for 30 min. This step is necessary to completely convert the polypyrroline form into the polyemeraldine salt (conducting form). Finally, the thin film was dried in air at room temperature.

2.4. Absorption spectra measurements and sensing system

The optical sensor consisted of PANI or PANI composite gas sensing film deposited onto glass substrate as described above, and placed into the measuring chamber.

The optical ammonia gas sensing system is shown in Fig. 2. It consists of a Carry 100 spectrophotometer in which the sealed measuring chamber has been inserted, a gas dilution system with flowmeters and a computer for data collection and analysis. The light source was a tungsten halogen lamp powered with a 12 V dc. The monochromator allowed selecting the working wavelength. The photodetector was used for signal detection. The spectrometer system was connected at a Compaq Prosignia 320 desktop computer. Windows-based Carry software was used for data acquisition and analysis. At the beginning of the experiment, the zero point of spectrometer was carried out without the PANI sensor.

Nitrogen gas (99.99%, Air Liquide) was used as dilution gas. The flows of ammonia and nitrogen gases were precisely con-

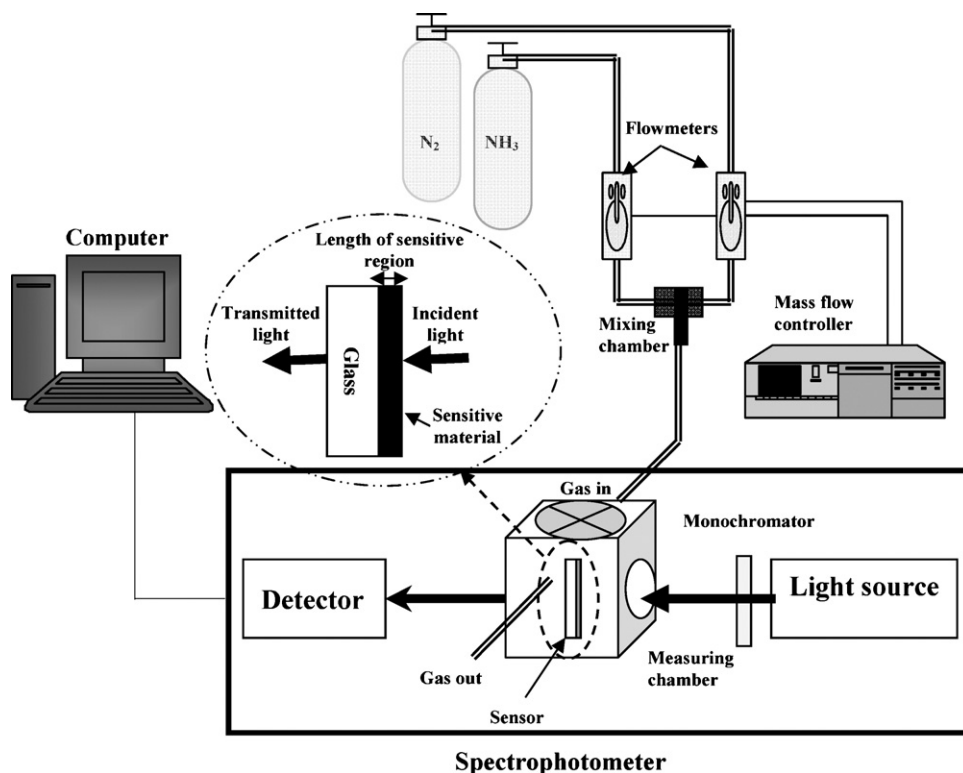


Fig. 2. Experimental set-up of ammonia gas sensing based on absorption variation measurement.

trolled by two flowmeters, which were plugged in a mass flow controller (MFC). A stream of nitrogen gas containing ammonia was passed through the polyaniline gas sensor and spectroscopic measurements were performed. The concentration of NH_3 gas in the measuring chamber was varied by mixing different flows of NH_3 gas and 500 sccm of N_2 gas. The concentration of NH_3 (ppm) was defined as the ratio of the flow rate of NH_3 gas to the total flow rate of NH_3 and N_2 gases. In this work, the ammonia concentration varied between 92 and 4618 ppm. The ammonia concentrations lower than 92 ppm were not measured due to experimental set-up limitation. After inserting the PANI sensor inside the measuring chamber, a certain amount of dried ammonia gas, diluted in nitrogen gas, was introduced into the measuring chamber. The interaction between NH_3 gas and the PANI film leads to optical absorbance variation of PANI. When the optical absorbance variation tends to a constant value depending on time, the NH_3 gas introduction was turned off and stream of pure N_2 gas was passed through the sensor to purge completely the NH_3 molecules in the measuring chamber and to regenerate the polyaniline sensor.

Sensitivity (S) was calculated as $(A - A_0)/A_0$ ratio, where A_0 is the initial optical absorbance of the sensor under N_2 and A the absorbance of the sensor when exposed to ammonia gas. The wavelength of the light source used in the experiment was fixed at 632 nm. All experiments were performed at room temperature.

Finally, a pure spin-coated SU-8 film (1 μm of thickness) was placed in the measuring chamber. The injection of NH_3 into the chamber did not lead to any change of the optical absorption, indicating that there is no interaction between NH_3 gas and the epoxy resin.

2.5. Thickness measurement

The thickness of pure polyaniline and polyaniline composite has been measured thanks to a Veeco profilometer (Dektak 8 model).

The thickness values are the average of at least five measurements taken at different locations of the polymer film.

2.6. FTIR analysis

FTIR measurements were performed on a Brüker IFS 66 spectrometer in transmission mode using a DTGS detector over the range 400–4000 cm^{-1} with a 2 cm^{-1} resolution averaged over 200 scans. All spectra were baseline-corrected. For FTIR analyses, polymer film was deposited directly onto KBr pellet.

2.7. Scanning electron microscopy (SEM)

The morphology of pure PANI and PANI composite films was observed using a JEOL microscope (JSM-5400) operating with an electron voltage of 5–20 kV. Each sample was fixed on the sample holder and a thin gold layer was deposited onto its surface in order to improve image resolution.

3. Results

3.1. Characterization of PANI/SU-8 films

3.1.1. Physico-chemical characterizations

The UV–vis spectra of pure epoxy resin (SU-8) film, PANI-EB/SU-8 (with PANI concentrations of 3 and 10 wt.%) and PANI-ES 10 wt.%/SU-8 composites are shown in Fig. 3. The UV–vis spectrum of SU-8 film shows only two absorption bands around 280 and 310 nm corresponding, respectively, to the absorption of the $\text{C}=\text{C}$ groups and to the $\pi-\pi^*$ transition of the benzene cycles. The spectrum shows also that the SU-8 film is totally transparent in the region of 350–900 nm. However, the UV–vis spectra of PANI-EB/SU-8 composite films show two new absorption bands due to PANI emeraldine base form [21,25]. The first absorption band with

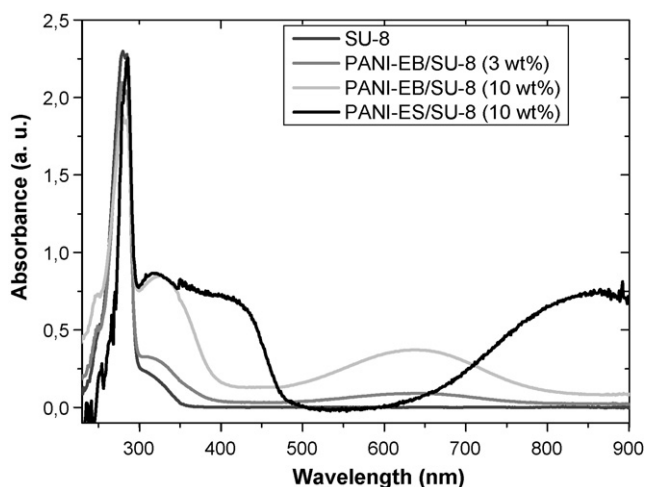


Fig. 3. UV-vis spectra of epoxy resin (SU-8), PANI-EB/SU-8 and PANI-ES 10 wt.%/SU-8 composite films.

maximum at ca. 325 nm is associated to π - π^* transition of the conjugated ring systems and the second band (at 640 nm) is assigned to the quinoid excitonic transition. The intensity of these absorption bands increases with increasing the concentration of PANI-EB in the epoxy resin matrix from 3 to 10 wt.%. The absorption peak of the resin at 310 nm is probably masked by the absorption band of the PANI.

The doping of PANI-EB is necessary to obtain the conducting form of PANI (PANI-ES) containing cation-radicals $\text{NH}^{+\bullet}$ (polarons). Indeed, polarons constitute the adsorption sites for NH_3 . The UV-vis spectrum of PANI-ES/SU-8 film (Fig. 3) shows an absorption band at 325 nm associated to π - π^* transition of the conjugated ring system and two new absorption bands at ~410 nm and between 820 and 900 nm, assigned to polaron band transition [25,41]. The appearance of these bands is the proof that the doping process was efficient.

The FTIR spectra of pure SU-8 epoxy resin, PANI doped with HCl (PANI-ES), and PANI-ES/SU-8 composite are shown in Fig. 4. In Fig. 4(a), the broad bands at ca. 2800–3000, 3100 and 3490 cm^{-1} represent aliphatic C–H stretching, aromatic C–H stretching and O–H vibrations, respectively. The presence of peaks at 915 and 832 cm^{-1} can be assigned to the epoxide and phenyl ring modes,

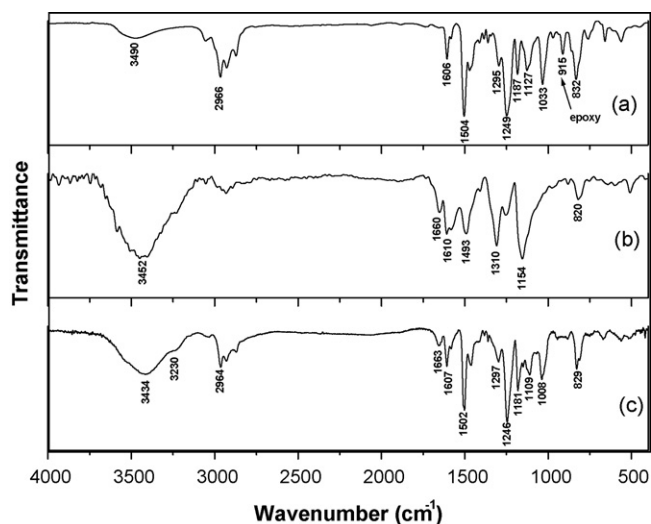


Fig. 4. FTIR spectra of SU-8 (a), PANI-ES (b) and PANI-ES/SU-8 composite films (c).

respectively. Besides, the SU-8 polymer shows C=C aromatic ring stretch at 1606 and 1504 cm^{-1} , the stretch modes of C–O groups at 1249 cm^{-1} , and of C–C groups at 1033 cm^{-1} . The peaks at 1120–1190 cm^{-1} can be attributed to the phenyl in-plane bending modes. These results are in accordance with other investigations [42–44]. All characteristic bands of PANI-ES form of polyaniline (Fig. 4(b)) were observed at: 3452, 1660, 1610, 1493, 1310, 1145 and 820 cm^{-1} . They are assigned to its main characteristic bonds of, respectively, N–H stretching, quinoid ring stretching, benzenoid ring stretching, C–N stretching, C–H aromatic in-plane and out-plane bending [7,45–53]. The FTIR spectrum of PANI-ES composite film, presented in Fig. 4(c), shows the disappearance of the infrared absorption peak of the epoxide ring mode at 915 cm^{-1} . The disappearance of this peak can be explained by reaction between PANI and SU-8 matrix. On the other hand, the spectrum clearly shows the presence of N–H stretching band at 3434 cm^{-1} of PANI. The other peaks of PANI are probably masked by the SU-8 epoxy resin bands. Indeed, all characteristic bands (except that of epoxy band) of SU-8 matrix were observed.

3.1.2. Morphology of PANI/SU-8 film

The SEM images of pure PANI film and PANI/epoxy resin composite film are shown in Fig. 5. These pictures clearly show that the pure PANI and PANI composite films have different surface morphologies. The pure PANI film appears to be dense (Fig. 5(a and b)), only small PANI clusters can be seen at the surface. The size of these clusters depends on the deposition time. It was found that for low deposition time, the film surface is smoother. Indeed, the surface of PANI deposited during 9 min (Fig. 5(a)) is smoother than that of PANI deposited during 13 min (Fig. 5(b)). Previous studies on the deposition time have shown the same results [20]. Fig. 5(c) and (d) shows the PANI/SU-8 surface morphology with a magnification of 600 and 3000, respectively. The PANI/SU-8 composite film shows a granular surface morphology with grain size of about 2 μm in diameter. The SEM images also show that the PANI/SU-8 composite seems to be a porous structure, suitable for gas detection.

3.2. Sensing properties

3.2.1. NH_3 sensing properties of pure PANI film

The sensing properties of pure PANI sensor were studied, in order to compare with those of PANI/SU-8 composite. Fig. 6(a) shows the optical response at 632 nm of the pure PANI film exposed to different concentrations of ammonia from 92 to 4618 ppm. When the absorbance variation due to the interaction of NH_3 molecules with PANI film tends to a constant value with time, the NH_3 gas is turned off, then starts the regeneration of PANI film in nitrogen stream at room temperature. The absorbance of the sensor is found to increase when exposed to ammonia gas. When the equilibrium between the adsorbed ammonia at the PANI surface and gas phase is obtained, no more variation of the absorbance is observed. Finally, when the injection of ammonia is turned off, the ammonia molecule desorption begins to restore the equilibrium of the concentrations and as a result, the absorbance of the sensor decreases. The regeneration of the sensor corresponding to NH_3 desorption is slowly reversible. The slow reversibility is more evident when the sensor is exposed to the first NH_3 concentration. Indeed, after exposition to 92 ppm of NH_3 , the absorbance decreases of about 60% after 15 min of regeneration whereas after exposition to 4618 ppm, the regeneration decreases of about 75% after 15 min in nitrogen stream. The same behavior has been observed for a PANI thin film optical sensor [25]. In the literature, in order to completely regenerate the sensor, a thermal method was proposed [3]. But, as reported in [10], the sensitivity of PANI decreases as a consequence of elevating temperature. The PANI can also be fully regenerated by

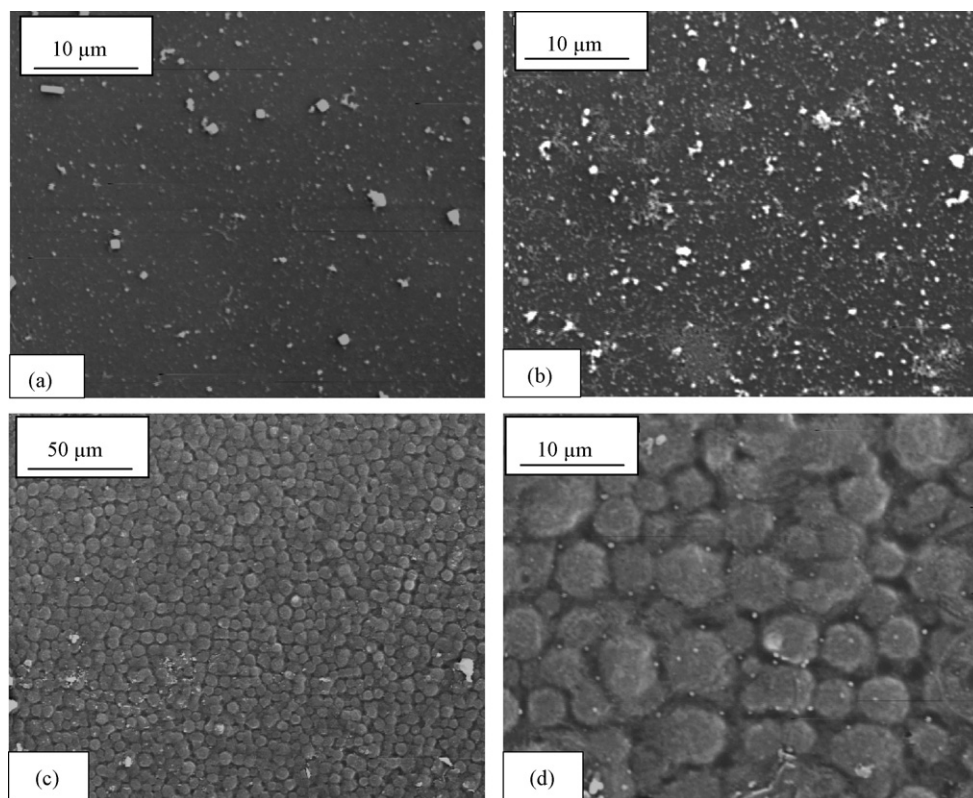


Fig. 5. SEM illustrations of surface morphologies of PANI deposited during 9 min (a), 13 min (b), and (c and d) PANI-ES (3 wt.%) / SU-8 composite.

treating with a dilute hydrochloric acid solution at room temperature [9].

On the other hand, the response time of the sensor (calculated at 90% of the absorbance variation) is around 1 min at 4618 ppm. Moreover, this sensor has a detection limit lower than 92 ppm, which is the experimental limit due to the dilution system.

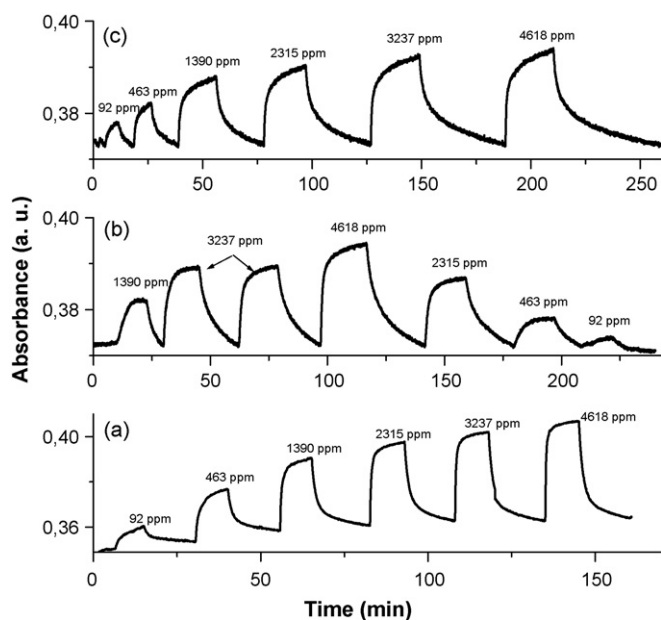


Fig. 6. Optical absorbance variations of sensors exposed to different concentrations of NH_3 (a) pure PANI; film thickness: 200 nm, (b) PANI/SU-8 composite; PANI concentration: 3 wt.%, film thickness: 1 μm and (c) PANI/SU-8 composite; PANI concentration: 10 wt.%, film thickness: 1 μm .

In Fig. 7, the sensitivity of the sensor as a function of ammonia concentration is illustrated. The sensitivity increases with increasing ammonia concentration and approaches a plateau value at high concentrations. The non-linear behavior of the response to ammonia gas was also observed for several PANI ammonia sensors [9,25]. This behavior can be explained by the gas diffusion phenomenon in the material.

Since the absorbance variation is controlled by the ammonia diffusion into the film, the relationship between absorbance and ammonia concentration (N) can be expressed by the following equation [9]:

$$A = A_0 \exp[(\alpha N)^{\gamma}] \quad (1)$$

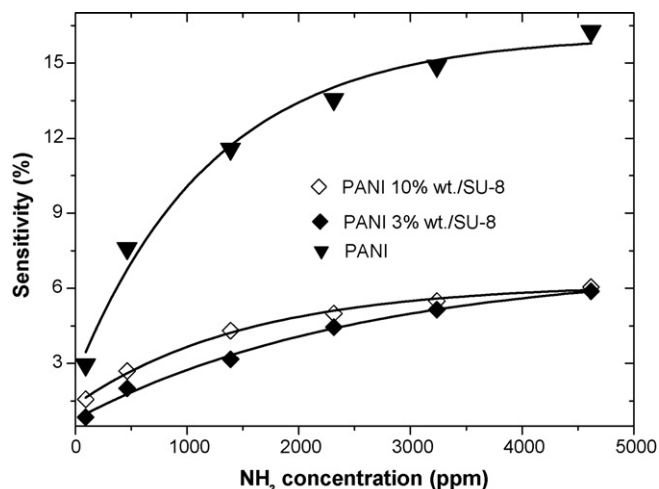


Fig. 7. Sensor sensitivity as a function of ammonia concentration.

where, A is the absorbance at ammonia concentration equals to N , A_0 is the initial absorbance at $N = 0$ ppm, α and γ are constants.

Then, the calibration curve, corresponding to $\log(A/A_0)$ in function of $\log N$, is linear between 463 and 4618 ppm of NH_3 with a linear regression coefficient of 0.99.

3.2.2. NH_3 sensing properties of PANI/SU-8 film

Fig. 6(b) and (c) illustrates the optical response of PANI/SU-8 films, either with 3 or 10 wt.% of PANI, respectively, exposed to different concentrations of NH_3 (92–4618 ppm). These sensors show a rapid and complete desorption of the NH_3 molecules from the PANI/SU-8 composite whatever the ammonia gas concentration is. However, the recovery time seems to increase with the increase of ammonia concentration. For example, the recovery times of the PANI 3 wt.%/SU-8 sensor are about 2 and 17 min after exposition to 92 and 4618 ppm of NH_3 , respectively. Moreover, the recovery time increases with the increase of PANI concentration in the polymer matrix. Indeed, the recovery time of the PANI 10 wt.%/SU-8 sensor is about 25 min after exposition to 4618 ppm of NH_3 .

Concerning the response time, the response to ammonia gas is fast. The response time increases with the content of PANI in SU-8 matrix. For example, at 4618 ppm, the PANI 3 wt.%/SU-8 sensor has a response time of 1 min and the PANI 10 wt.%/SU-8 sensor a response time of 3 min. On the other hand, the detection limit of these sensors is also lower than 92 ppm.

In Fig. 7 the sensitivity of the sensor as a function of ammonia concentration is also given for 3 and 10 wt.% PANI concentrations, respectively. The sensitivity of PANI/SU-8 sensors increases with increasing the NH_3 concentration as in the case of pure PANI sensor. The sensitivity approaches a plateau value at high concentrations. The non-linear behavior sensing response with ammonia gas was also observed for these sensors. Moreover, the sensitivity increases with increasing PANI concentration in the matrix. Indeed, the sensitivity of PANI 10 wt.%/SU-8 is 1.5 and 6% at 92 and 4618 ppm, respectively, while PANI 3 wt.%/SU-8 sensor has a sensitivity of 0.8 and 5% after exposition to 92 and 4618 ppm, respectively.

The repeatability of the PANI/SU-8 sensor responses is shown in Fig. 8. The sensor presents a good repeatability and reversibility, fast response to the ammonia gas and fast regeneration time at room temperature. These results show that SU-8 epoxy resin is suitable as polymer matrix for polyaniline composite gas sensors.

The calibration curve, calculated from Eq. (1) for PANI 3 wt.%/SU-8 sensor, presents a linear range from 92 to 4618 ppm of NH_3 with a linear regression coefficient of 0.99.

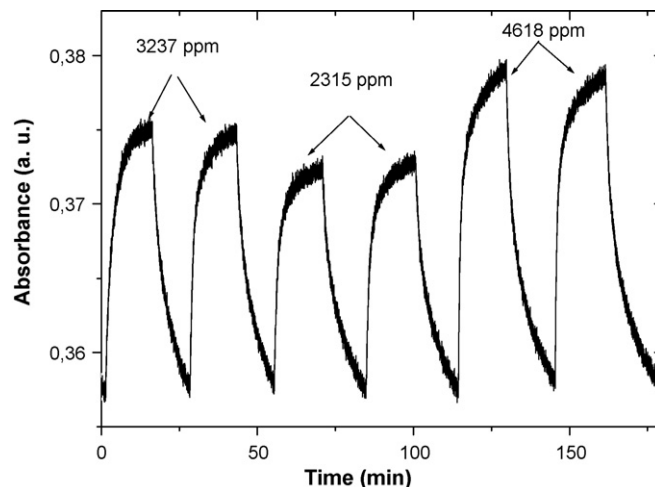


Fig. 8. Repeatability of the PANI/SU-8 composite sensor response. (PANI concentration: 3 wt.%, film thickness: 1 μm).

Finally, the selectivity of the sensor was studied with different gases (acetone, ethanol, methanol and HCl). The sensor has shown very small absorbance changes when exposed to these different gases. Then, the sensor sensitivity to these gases is negligible compared to that of NH_3 .

4. Discussion

The results can be summarized as follows: (1) the PANI/SU-8 composite is sensitive to ammonia, (2) pure epoxy resin (SU-8) film is not sensitive to ammonia, (3) the sensor based on PANI/SU-8 is rapidly and totally regenerated at room temperature, (4) the sensor based on pure polyaniline has a long regeneration time, (5) the response times of the PANI 3 wt.%/SU-8 sensor and the pure PANI sensor are in the same range, (6) the sensitivity of the pure PANI sensor is better than that of the PANI/SU-8 sensor and (7) the response of the sensors is logarithmic linear with ammonia concentration.

In order to compare the performances of the different sensors developed in this work, we have presented their figures of merit, which present the sensitivity of the sensor as a function of the response time or total regeneration time (recovery time) (Fig. 9). The metrological parameters (sensitivity, response time, regeneration time) of the sensors are determined for different ammonia

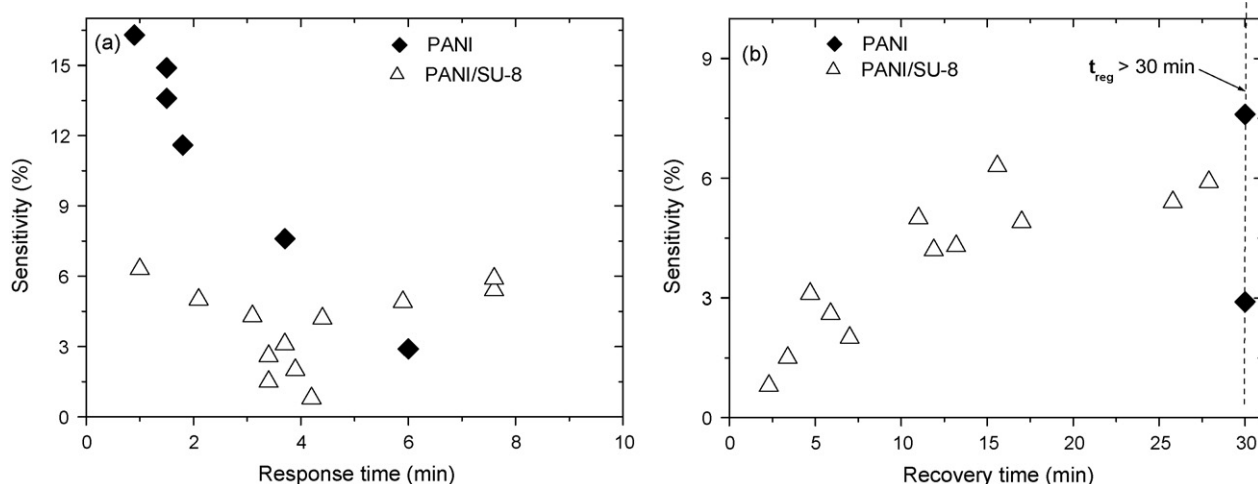


Fig. 9. Figures of merit for the different optical ammonia sensors.

concentrations and different polyaniline concentrations inside the polymer matrix. The dash line in the inset of Fig. 9(b) indicates that the regeneration time of the sensor is higher than 30 min.

The optical sensor based on pure PANI sensitive layer is simultaneous very sensitive to ammonia gas and has a fast response time (Fig. 9(a)), but its total regeneration time is higher than 30 min whatever NH_3 concentration is (Fig. 9(b)). The lower sensitivity of PANI/SU-8 films, compared to pure PANI films, can be due to the low concentration of adsorption sites (polarons) in the composite. In addition, the pure PANI film was deposited onto the two faces of the substrate, explaining also the higher sensitivity of pure PANI sensor. However, the better response time of PANI/SU-8 is as low as the better response time of pure PANI film. In addition, the NH_3 desorption from the PANI/SU-8 composite is faster than from pure PANI film (Fig. 9(b)). Moreover, the PANI/SU-8 sensor is simultaneous sensitive to the ammonia gas and fast regenerated in nitrogen gas at room temperature compared with pure PANI sensors. The increase in the sensitivity of the sensors seems to increase the total regeneration time. Indeed, the total regeneration time of the pure PANI layer (i.e. the most sensitive to ammonia gas) is higher than the total regeneration time of the PANI/SU-8 composite. The sensitivity of the sensor is the direct result of absorbed NH_3 molecule quantity by the sensitive layer. Thus, the capacity for absorption with respect to the NH_3 molecules increases the sensitivity of the layer, then increasing the necessary time to the desorption of the adsorbed species.

The sensing differences between pure PANI and PANI/SU-8 sensitive materials may also result from differences in their morphologies, which is supported by examination of SEM images (Fig. 5). For pure polyaniline films, the SEM images (Fig. 5(a) and (b)) show a very dense and smooth surface on which there are some granules. The SEM images of PANI 3 wt.%/SU-8 surfaces (Fig. 5(c) and (d)) show a uniform granular morphology (grain size of about 2 μm in diameter) and then a porous structure. The granular and porous structure of PANI/SU-8 composite seems to contribute to the short response time, short recovery time and good reversibility of PANI/epoxy resin sensor. The gas diffusion occurs more easily in porous structures, and the reaction between gas molecules and polarons occurs then easily. Moreover, in the PANI/SU-8 structure, the insulating host polymer leads to a lower quantity of absorbed ammonia than for pure PANI leading then to faster recovery of ammonia gas from the sensor. We also think that the better characteristics of PANI/SU-8 composite films as NH_3 detecting elements are attributed to their higher chemical stability compared to pure PANI films.

5. Conclusion

In this study, the optical ammonia gas sensor based on PANI/epoxy resin (SU-8) composite film was prepared by a solution casting method. The composite film has been characterized by UV–vis spectroscopy, FTIR and SEM measurements. The SEM images have shown that PANI/SU-8 film has a granular morphology and a porous structure. The film presents significant absorbance variations upon exposure to ammonia gas at room temperature. It was found that this sensor is sensitive, stable, fast in response and easy to regenerate at room temperature. The sensitivity of the composite sensor increases with increasing the PANI content. Then, SU-8 epoxy resin is suitable as a polymer matrix for polyaniline-based composite gas sensors. A very low concentration of PANI in the SU-8 matrix can render the composite sensitive to low ammonia gas concentration. The advantages of this composite sensor compared to the pure PANI sensor are its fast regeneration associated with improved mechanical properties and chemical stability.

Acknowledgement

The authors want to thank CER Micro-Cap-Ouest for financial support.

References

- [1] P.N. Bartlett, P.R. Birkin, *Synth. Met.* 61 (1993) 15.
- [2] J.A. Osaheni, S.A. Jenekhe, H. Vanherzeele, J.S. Meth, Y. Sun, A.G. MacDiarmid, *J. Phys. Chem.* 96 (1992) 2830.
- [3] A.L. Kukla, Y.M. Shirshov, S.A. Piletsky, *Sens. Actuators B* 37 (1996) 135.
- [4] Y. Cao, P. Smith, A.J. Heeger, *Synth. Met.* 48 (1992) 91.
- [5] A.A. Pud, *Synth. Met.* 66 (1994) 1.
- [6] D. Nicolas-Debarnot, F. Poncin-Epaillard, *Anal. Chim. Acta* 475 (2003) 1.
- [7] V.V. Chabukswar, S. Pethkar, A.A. Athawale, *Sens. Actuators B* 77 (2001) 657.
- [8] Z. Jin, Y. Su, Y. Duan, *Sens. Actuators B* 72 (2001) 75.
- [9] M.A. El-Sherif, J. Yuan, A. MacDiarmid, *J. Intel. Mater. Syst. Struct.* 11 (2000) 407.
- [10] M. Hirata, L. Sun, *Sens. Actuators B* 40 (1994) 159.
- [11] K. Xu, L. Zhu, J. Li, H. Tang, *Electrochim. Acta* 52 (2006) 723.
- [12] V. Dixit, J.C. Tewari, B.S. Sharma, *Sens. Actuators B* 120 (2006) 96.
- [13] J.-S. Kim, S.-O. Sohn, J.-S. Huh, *Sens. Actuators B* 108 (2005) 409.
- [14] Y. Andreu, S. de Marcos, J.R. Castillo, J. Galban, *Talanta* 65 (2005) 1045.
- [15] Y.-S. Lee, B.-S. Joo, N.-J. Choi, J.-O. Lim, J.-S. Huh, D.-D. Lee, *Sens. Actuators B* 93 (2003) 148.
- [16] J. Gao, J.-M. Sansinena, H.-L. Wang, *Synth. Met.* 135–136 (2003) 809.
- [17] S. Christie, E. Scorsone, K. Persaud, F. Kvasnik, *Sens. Actuators B* 90 (2003) 163.
- [18] D. Xie, Y. Jiang, W. Pan, D. Li, Z. Wu, Y. Li, *Sens. Actuators B* 81 (2002) 158.
- [19] P.T. Sotomayor, I.M. Raimundo, A.J.G. Zarbin, J.J.R. Rohwedder, G.O. Neto, O.L. Alves, *Sens. Actuators B* 74 (2001) 157.
- [20] J. Yuan, M.A. El-Sherif, A.G. MacDiarmid, W.E. Jones Jr., *SPIE Proc.* 4205 (2001) 170.
- [21] S.K. Dhawan, D. Kumar, M.K. Ram, S. Chandra, D.C. Trivedi, *Sens. Actuators B* 40 (1997) 99.
- [22] N.E. Agbor, M.C. Petty, A.P. Monkman, *Sens. Actuators B* 28 (1995) 173.
- [23] Q.M. Jia, J.B. Li, L.F. Wang, J.W. Zhu, M. Zheng, *Mater. Sci. Eng. A* 448 (2007) 356.
- [24] A. Riede, J. Stejskal, M. Helmstedt, *Synth. Met.* 121 (2001) 1365.
- [25] M.E. Nicho, M. Trejo, A. Garcia-Valenzuela, J.M. Saniger, J. Palacios, H. Hu, *Sens. Actuators B* 76 (2001) 18.
- [26] A.B. Kaiser, C.-J. Liu, P.W. Gilberd, B. Chapman, N.T. Kemp, B. Wessling, A.C. Partridge, W.T. Smith, J.S. Shapiro, *Synth. Met.* 84 (1997) 699.
- [27] M. Reghu, C.O. Yoon, C.Y. Yang, D. Moses, A.J. Heeger, Y. Cao, *Macromolecules* 26 (1993) 7245.
- [28] S.A. Chen, W.G. Fang, *Macromolecules* 24 (1991) 1242.
- [29] J.L. Cadenas, H. Hu, *Sol. Energy Mater. Sol. Cells* 55 (1998) 105.
- [30] M. Wan, M. Li, J. Li, Z. Liu, *Thin Solid Films* 259 (1995) 188.
- [31] T. Thanpichai, A. Sirivat, A.M. Jamieson, R. Rujiravanit, *Carbohydr. Polym.* 64 (2006) 560.
- [32] M. Matsuguchi, A. Okamoto, Y. Sakai, *Sens. Actuators B* 94 (2003) 46.
- [33] X. Yang, T. Zhao, Y. Yu, Y. Wei, *Synth. Met.* 142 (2004) 57.
- [34] N. Pelletier, B. Bêche, E. Gaviot, L. Camberlein, N. Grossard, F. Polet, J. Zyss, *IEEE Sens. J.* 6 (2006) 565.
- [35] B. Bêche, N. Pelletier, E. Gaviot, J. Zyss, *Opt. Commun.* 230 (2004) 91.
- [36] J.S. Kim, J.W. Kang, J.J. Kim, *Jpn. J. Appl. Phys.* 42 (2003) 1277.
- [37] J. Zhang, K.L. Tan, H.Q. Gong, *Polym. Test.* 20 (2001) 693.
- [38] J. Stejskal, I. Sapurina, J. Prokes, J. Zemek, *Synth. Met.* 105 (1999) 195.
- [39] W. Zheng, Y. Min, A.G. MacDiarmid, M. Angelopoulos, Y.-H. Liao, A.J. Epstein, *Synth. Met.* 84 (1997) 63.
- [40] I. Sapurina, A. Riede, J. Stejskal, *Synth. Met.* 123 (2001) 503.
- [41] P.L.B. Araujo, E.S. Araujo, R.F.S. Santos, A.P.L. Pacheco, *Microelectron. J.* 36 (2005) 1055.
- [42] T.L. Tan, D. Wong, P. Lee, R.S. Rawat, S. Springham, A. Patran, *Thin Solid Films* 504 (2006) 113.
- [43] D. Wong, T.L. Tan, P. Lee, R.S. Rawat, A. Patran, *Microelectron. Eng.* 83 (2006) 1912.
- [44] M. Joshi, N. Kale, R. Lal, V. Ramgopal Rao, S. Mukherji, *Biosens. Bioelectron.* 22 (11) (2007) 2429.
- [45] A.L. Schimid, L.M. Lira, S.I. Cordoba de Torresi, *Electrochim. Acta* 47 (2002) 2005.
- [46] M.I. Boyer, S. Quillard, G. Louarn, G. Froyer, S. Lefrant, *J. Phys. Chem. B* 104 (2000) 8952.
- [47] M. Trchova, J. Stejskal, J. Prokes, *Synth. Met.* 101 (1999) 840.
- [48] M.-I. Boyer, S. Quillard, E. Rebout, G. Louarn, J.P. Buisson, A. Monkman, S. Lefrant, *J. Phys. Chem. B* 102 (1998) 7382.
- [49] X. Jing, Y. Wang, D. Wu, J. Qiang, *Ultrason. Sonochem.* 14 (2007) 75.
- [50] A.A. Athawale, S.V. Bhagwat, P.P. Katre, *Sens. Actuators B* 114 (2006) 263.
- [51] M. Trchova, I. Sapurina, J. Prokes, J. Stejskal, *Synth. Met.* 135–136 (2003) 305.
- [52] X.-R. Zeng, T.-M. Ko, *Polymer* 39 (5) (1997) 1187.
- [53] A. Gök, F. Göde, B.E. Türkkan, *Mater. Sci. Eng. B* 133 (2006) 20.



In situ continuous derivatization/pre-concentration of carbonyl compounds with 2,4-dinitrophenylhydrazine in aqueous samples by solid-phase extraction Application to liquid chromatography determination of aldehydes

Clara-Eugenia Baños, Manuel Silva *

Department of Analytical Chemistry, Marie-Curie Building (Annex), Campus of Rabanales, University of Córdoba, E-14071 Córdoba, Spain

ARTICLE INFO

Article history:

Received 30 April 2008

Received in revised form

19 September 2008

Accepted 29 September 2008

Available online 14 October 2008

Keywords:

In situ derivatization

Solid-phase extraction

2,4-Dinitrophenylhydrazine

Carbonyl compounds

Low-molecular mass aldehydes

Liquid chromatography

Water samples

ABSTRACT

A rapid and straightforward continuous solid-phase extraction system has been developed for in situ derivatization and pre-concentration of carbonyl compounds in aqueous samples. Initially 2,4-dinitrophenylhydrazine, the derivatizing agent, was adsorbed on a C₁₈ mini-column and then 15-ml of sample were continuously aspirated into the flow system, where the derivatization and pre-concentration of the analytes (low-molecular mass aldehydes) were performed simultaneously. Following elution, 20 µl of the extract were injected into a LC–DAD system, in which hydrazones were successfully separated in 12 min on a RP-C₁₈ column using a linear gradient mobile phase of acetonitrile–water of 60–100% acetonitrile for 8 min, flowing at 0.5 ml/min. The whole analytical process can be accomplished within ca. 35 min. Under optimum conditions, limits of detection were obtained between 0.3 and 1.0 µg/l and RSDs (inter-day precision) from 1.2 to 4.6%. Finally, some applications on water samples are presented with recoveries ranged from 95.8 to 99.4%.

© 2008 Elsevier B.V. All rights reserved.

1. Introduction

Carbonyl compounds are acknowledged to be harmful organic pollutants that exist naturally in the atmosphere as a result of different phenomena such as photochemical oxidation of hydrocarbons, combustion of fossil fuels by motor vehicles and industrial activities, among others [1–3]. Many works have been carried out for the determination of carbonyl compounds in gaseous (air) samples by chromatographic techniques [4–12]; on the contrary, interest in the analysis of carbonyl compounds in water samples as pollutants has increased significantly in recent years because human beings are every day more exposed to contaminated waters. The dissolution of carbonyl compounds in ground waters after their deposition from the atmosphere by the rain and the formation of low-molecular mass aldehydes in drinking waters as disinfection by-products (DBPs) [13–16] are two currently significant contamination sources. Because of the impact on human health and the environmental importance of these compounds, simple, rapid and

sensitive analytical methods are required for their routine determination.

The direct determination of carbonyl compounds in aqueous matrices is complicated because of their high polarity, reactivity and volatility which impose the need for their derivatization prior their detection by chromatographic techniques. A variety of derivatizing reagents have been used for this purpose, being hydrazine-based reagents the most widespread choice [17]. Thus, the most frequently used method for the determination of carbonyl compounds in aqueous samples involves derivatization with an acidic solution of 2,4-dinitrophenylhydrazine (DNPH) to form the corresponding hydrazones followed by LC separation and ultraviolet (UV) detection [18–22] or mass spectrometry (MS) [12,15,23–25]. A typical procedure, as the one recommended by the EPA Method 8315A [22], involves the batch DNPH derivatization of the carbonyl compounds (at least 1 h at room temperature is recommended for aldehydes), the extraction of the hydrazones by solid-phase extraction (SPE) with C₁₈ cartridges, the elution with acetonitrile (ca. 10 ml) and the chromatographic analysis [22,24]. In some cases, to increase the pre-concentration factor, the eluate is evaporated to dryness and the residue dissolved in an acetonitrile:water mixture [24]. These methods provide good results and are relatively easy to carry out, but they involve

* Corresponding author. Tel.: +34 957 212099.

E-mail address: qa1sirom@uco.es (M. Silva).

an extensive work-up, consume materials, and solvents for the derivatization and the subsequent isolation of the hydrazones formed by using SPE. In these methods there are mainly two shortcomings, namely: low selectivity since other hydrophobic compounds of water could be also retained on C_{18} and the excess of DNPH interferes with the adsorption of the hydrazones (recoveries were not always high). In order to improve the DNPH-procedures a recent approach for the determination of aldehydes has been reported based on the combination of derivatization and polymer monolith microextraction (PMME) [26,27]. Two methodologies have been developed, the first based on DNPH derivatization before PMME has been proposed for the LC determination of some low-molecular mass aldehydes in saliva samples [26] and the second related to the *in situ* derivatization on the monolith has been applied to the determination of hexanal and heptanal in plasma [27]. Although the PMME technique reduces drastically the consumption of solvents and reagents, it has two significant drawbacks: the polymer monolith is not commercial and therefore it must be synthesized in the laboratory and the method has been only applied to sample volume of 1 ml because it uses a syringe infusion pump for delivering the sample solution. Despite the widespread use of solid-phase microextraction (SPME) for the analysis of organic compounds from aqueous samples, to our knowledge no reference has been found for the determination of carbonyl compounds by SPME using DNPH as derivatizing reagent. The restricted use of DNPH can be ascribed to its long reaction time and strongly acidic pH condition for the *in fibre* derivatization and the thermal decomposition of DNPH-carbonyl compounds. In this context, SPME is usually used in conjunction to GC for the determination of carbonyl compounds after their derivatization with *o*-(2,3,4,5,6-penta-fluorobenzyl)-hydroxylamine [28–33].

The aim of this study is to develop a rapid and sensitive method for the simultaneous DNPH-derivatization and pre-concentration of carbonyl compounds in aqueous samples by using a straightforward continuous SPE system. A C_{18} mini-column impregnated with DNPH and inserted in a simple flow manifold is used for *in situ* derivatization and pre-concentration of low-molecular mass (C_1 – C_6) aldehydes, which have been selected as model analytes. This new approach is expected to be a better alternative to the reported DNPH methods for the determination of carbonyl compounds in aqueous samples, which require batch derivatization of the analytes and SPE extraction and pre-concentration of the DNPH-derivatives on C_{18} cartridges. In fact, lower consumption of solvents as well as reagents and shorter analysis time with high sensitivity (pre-concentration factors up to 150) can be achieved by using the proposed method. Moreover, LC with UV detection was used in this work for the separation and determination of the DNPH-derivatives, but also it can be extrapolated to other chromatographic alternatives such as LC–MS and other carbonyl compounds.

2. Experimental

2.1. Standards and reagents

All chemicals and solvents used were of analytical-reagent and chromatographic grade, respectively, and milli-Q water was used throughout. Formaldehyde (37% (w/v) solution in water), acetaldehyde ($\geq 99.5\%$ purity) and hexanal ($\geq 98\%$ purity) were purchased from Sigma (Sigma-Aldrich Química, Madrid, Spain), whereas propanal ($\geq 96\%$ purity), butanal ($\geq 99\%$ purity) and pentanal ($\geq 97\%$ purity), were acquired from Fluka (Sigma-Aldrich Química). Standard solutions containing 1000 $\mu\text{g}/\text{ml}$ of each aldehyde were prepared in chromatographic grade methanol (Romil

Chemicals, Cambridge, UK), and then stored at 4°C in a refrigerator. Stock working mixture solutions were made by appropriate dilution of the corresponding standard solutions with milli-Q water. A 6.0×10^{-2} mol/l DNPH ($\geq 99\%$ purity, Fluka) stock solution was made by dissolving 594.4 mg of the derivatizing reagent in 50 ml of concentrated hydrochloric acid:water:acetonitrile solution (2:5:1) which was then stored in a freezer. A 1.5×10^{-3} mol/l (0.3 mg/ml) DNPH solution was prepared by appropriate dilution of the stock solution with milli-Q water. Silica RP sorbent with octadecyl functional groups (C_{18} , particle size 50 μm) was purchased from Sigma. Other solvents and chemicals were purchased from Romil Chemicals and Merck, respectively.

2.2. Apparatus

The LC system consisted of a Microsorb-MV 100-5 C_{18} 150 mm \times 4.6 mm (5 μm) column (Varian, Palo Alto, CA, USA), a Varian 230 multisolute pump, a Rheodyne Model 7215 injector (Cotati, CA, USA) fitted with a 20- μl injection loop and a Varian 335 PDA detector. Hydrazones were chromatographically separated by using a linear gradient mobile phase of acetonitrile–water of 60–100% acetonitrile circulated at 0.5 ml/min for 0–8 min, with the detection wavelength set at 360 nm. Under these conditions, all hydrazones were eluted within about 12 min. Retention times, peak heights and peak areas were provided by a 6.41 Varian Star Chromatography Workstation interfaced to a PC compatible computer.

SPE manifolds consisted of a Gilson Minipuls-3 peristaltic pump (Middleton, WI, USA) fitted with poly(vinyl chloride) tubes, two Rheodyne 5041 injection valves (Cotati, CA, USA), PTFE tubing of 0.5 mm I.D. for coils and laboratory-made mini-columns packed with 100 mg C_{18} sorbent material (Sigma). The mini-columns were made from PTFE capillaries of 3 mm I.D. and their ends capped by fitting 30 mm \times 0.5 mm I.D. PTFE tubing into a 10 mm \times 1 mm I.D. PTFE tube, which facilitated insertion into the continuous system. The mini-column was sealed at both ends with small plugs of glass wool to prevent material losses.

2.3. Derivatization/pre-concentration SPE procedures

Schematic diagrams of the SPE manifolds used for derivatization and pre-concentration of carbonyl compounds are depicted in Fig. 1. In both SPE systems, sorbent mini-columns were initially treated with acetonitrile (1.0 ml at 0.5 ml/min) and with milli-Q water (1.0 ml at 0.5 ml/min); after each working day, they were flushed with acetonitrile and milli-Q water in a similar way.

2.3.1. Method A: SPE *in situ* derivatization/pre-concentration

After conditioning, the SPE mini-column was loaded with 2.0 ml of a 1.5×10^{-3} mol/l DNPH solution (0.6 mg of DNPH) at 0.5 ml/min. Then a volume of 15 ml of standard solution or drinking water sample with a concentration between 1.0 and 200 $\mu\text{g}/\text{l}$ of aldehyde adjusted at pH ca. 3.0 with diluted hydrochloric acid was continuously introduced into the system at 1.0 ml/min. It is noteworthy that the sample was placed in a 15 ml PTFE vial that was tightly sealed and immersed in an ice bath in order to prevent possible evaporation losses. The aldehydes were *in situ* derivatized with DNPH on the C_{18} mini-column (100 mg), located in the loop of IV_1 , the sample matrix being sent to waste. Simultaneously, the loop of IV_2 was filled with the eluent (acetonitrile). Prior to elution, by switching IV_1 , residual aqueous solution inside the column and the connectors were flushed by passing an air stream through the carrier line of IV_2 at 0.5 ml/min for 2 min. In the elution step, IV_2 was switched and 100 μl of the eluent were injected into an air stream and passed through the column to elute the hydrazones. The extract

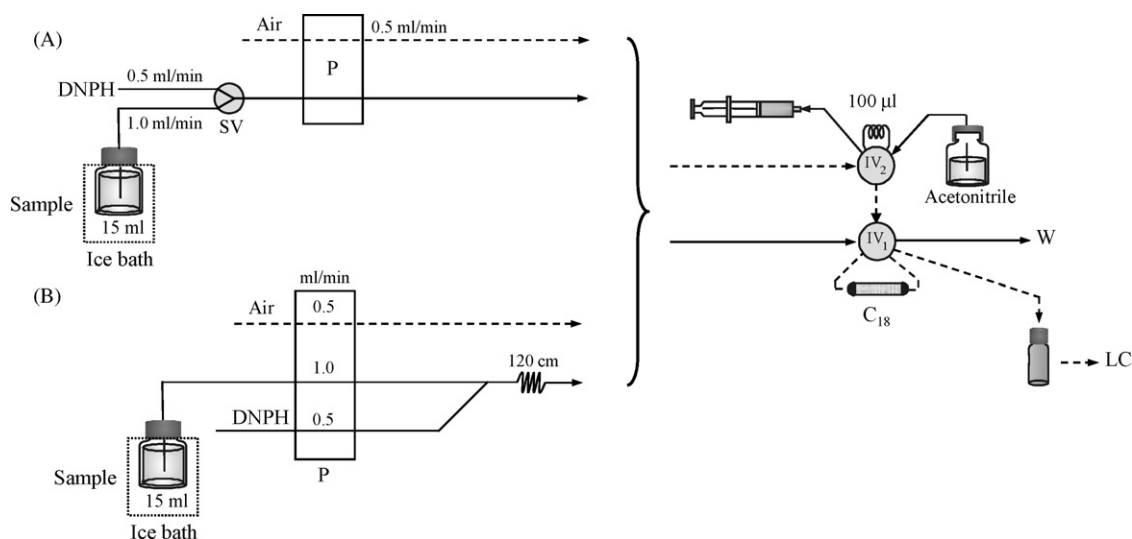


Fig. 1. Continuous-flow manifolds used for derivatization and pre-concentration (solid lines) and elution (dashed lines) of carbonyl compounds with DNPH. (A) SPE in situ derivatization/pre-concentration and (B) continuous derivatization and SPE pre-concentration. IV, injection valve; SV, selection valve; P, peristaltic pump; W, waste; LC, liquid chromatograph with DAD detection.

was collected in an Eppendorf vial and 20- μ l aliquot injected into the LC.

2.3.2. Method B: Continuous derivatization and SPE pre-concentration

Volumes of 15 ml of standard water samples containing between 7.5 and 1500 ng of low-molecular mass aldehydes adjusted at pH 2.0 with diluted hydrochloric acid were fed into the system and merged with the derivatizing reagent (1.5×10^{-3} mol/l DNPH). Hydrazones were formed in the reaction coil (120 cm long) and retained on the SPE mini-column (100 mg of C_{18}) located in the loop of the pre-concentration valve (IV_1) while the sample matrix was sent to waste. After pre-concentration, an air stream was passed through the mini-column at 0.5 ml/min for 2 min in order to remove residual aqueous phase from the mini-column and connections. Simultaneously, the loop of the elution valve (IV_2) was filled with 100 μ l of acetonitrile (eluent). In the elution step, IV_2 was switched and 100 μ l of the eluent were injected into an air stream and passed through the mini-column to elute the hydrazones, and the extract was collected in an Eppendorf vial and finally 20- μ l of the extract was injected into the LC.

3. Results and discussion

The aim of this work is to develop a continuous SPE system for the in situ derivatization/pre-concentration of carbonyl compounds by using DNPH as derivatizing agent (see Fig. 1A); however, it can be of interest to compare its features with those provided by a conventional flow manifold based on the continuous derivatization of analytes before SPE pre-concentration (see Fig. 1B), because excess of DNPH and reaction time are higher than in the in situ procedure. Formaldehyde, acetaldehyde, propanal, butanal, pentanal and hexanal were the carbonyl compounds selected for testing these approaches. A C_{18} mini-column was used because, as stated above, this sorbent has been widely used in the reported methods for the pre-concentration of the hydrazones after derivatization of the aldehydes with DNPH; the retained hydrazones were eluted with 100 μ l of acetonitrile. These SPE systems were assembled in order to obtain highly sensitive, accurate and reproducible results, with minimum sample handling and maximum throughput.

3.1. Development of the SPE systems

The sample pH is an important variable because it can influence both the derivatization of the aldehydes with DNPH and the interaction of the hydrazones with the C_{18} sorbent. Its influence on both methods was examined by using 10 ml volumes of a mixture of standard solutions of aldehydes that were adjusted to pH values from ca. 1.0 to 6.0 with hydrochloric acid. As can be seen in Fig. 2A and B, the dependencies found were different; thus, for in situ derivatization (Method A, Fig. 2A) a maximum was observed at pH ca. 3.0 for all aldehydes, whereas for continuous derivatization (Method B, Fig. 2B), the analytical signal was practically independent on the pH over the range studied (a slight increase was detected at pH smaller than 3.0). This difference can be ascribed to the fact that the DNPH solution was prepared in a hydrochloric acid medium, which provided a pH value of ca. 1.0 (see Section 2.1). As consequence, in the Method B variations of the sample pH over the range assayed do not significantly affect the pH of the mixture of the sample and DNPH solutions in the reaction coil, whereas in the in situ derivatization approach (Method A) the effect of this variable is more pronounced since the derivatization pH is closely related to that of the sample solution because DNPH was previously loaded on the SPE mini-column. In both cases, the decrease in the analytical signal at higher pH values can be ascribed to the full deprotonation of the hydrazine group of the DNPH ($pK_a = 2.2$) which probably hinders acid catalyzed derivatization of aldehydes to form the corresponding hydrazones. From these results a sample pH value of 3.0 and 2.0 was selected as optimal for Methods A and B, respectively, which were adjusted with hydrochloric acid.

The effect of DNPH is another significant variable to be studied in both approaches. In Method A, initial experiments were conducted to establish the influence of the volume of the DNPH solution and its flow rate by always loading a fixed amount of the derivatizing agent. Experimental results lead us to conclude that optimal conditions consisted of passing 2.0 ml of the DNPH solution through the SPE mini-column at a rate of 0.5 ml/min, resulting in the loading time of 4 min. In these conditions, the amount of DNPH was studied in the range of 0.2–0.8 mg. As it can be seen in Fig. 2C, maximum analytical signals were obtained for DNPH amounts of ca. 0.6 mg for all aldehydes and afterwards they remained practically

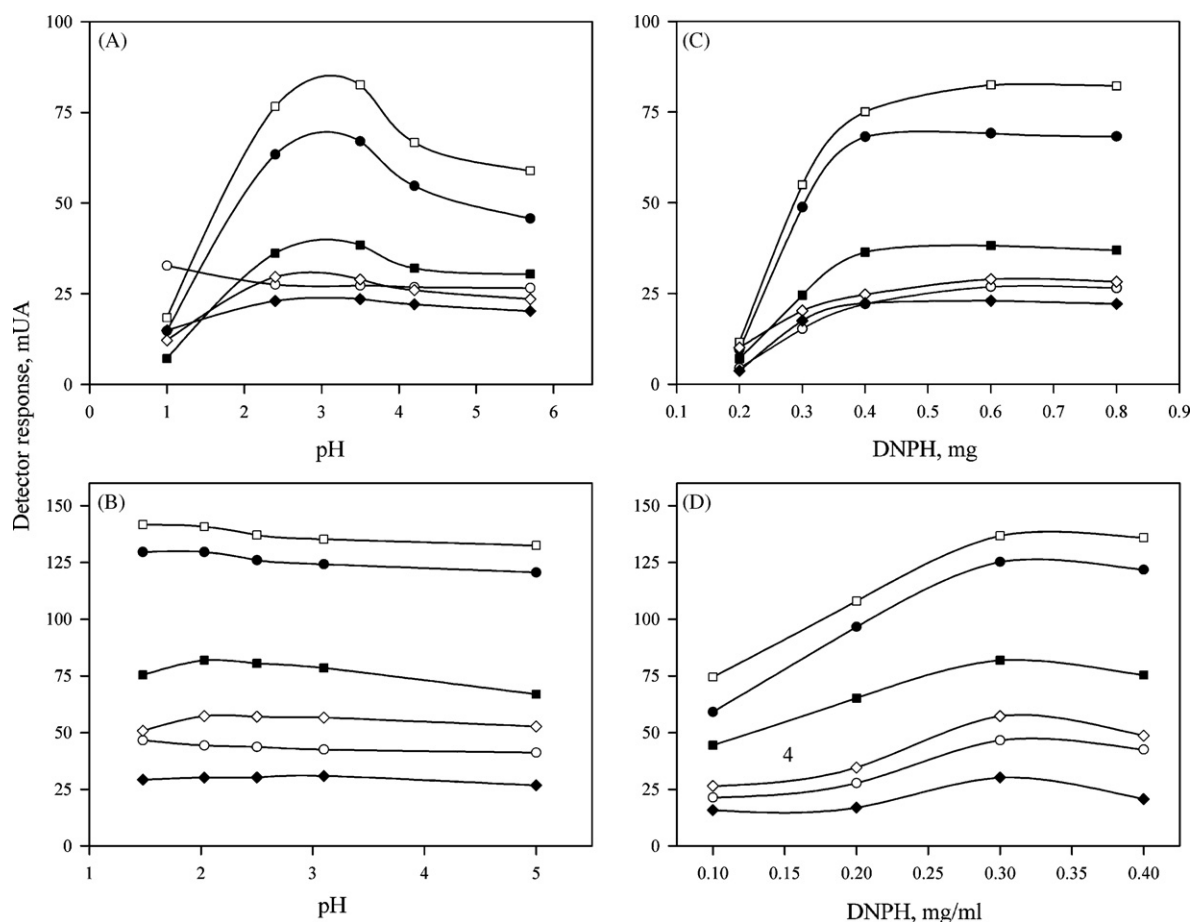


Fig. 2. Effect of the pH and DNPH on the derivatization and pre-concentration of low-molecular mass aldehydes. Method A: (A and C) and Method B: (B and D). Formaldehyde (○), acetaldehyde (●), propanal (□), butanal (■), pentanal (◇) and hexanal (◆) at 25 μ g/l. Sample volume, 10 ml. Other conditions as described in Section 2.

constant. This amount of DNPH was selected as optimal, which provided a DNPH to aldehydes molar ratio higher than 350 (concretely from ca. 350 to 1200 for formaldehyde to hexanal, respectively), which is sufficient for their quantitative derivatization. This excess of DNPH is higher than the one used in other reported applications of the DNPH method for aqueous samples, but based on the batch derivatization of carbonyl compounds [23]. This higher excess of DNPH and the inherent kinetic character of the proposed continuous flow method are probably the causes for the decrease in the derivatization time, without detriment in the analytical sensitivity, compared to the reported batch derivatization methods [15,22–25].

In Method B, the concentration of DNPH and its flow rate were studied over the range 0.1–0.4 mg/ml and 0.1–1.0 ml/min, respectively. As can be seen in Fig. 2D, the signal increased when the concentration of DNPH increased to ca. 0.3 mg/ml and then decreased slightly; this concentration was selected as optimal. Regarding DNPH flow rate, the maximum analytical signal was achieved at values over 0.2 ml/min, and so 0.5 ml/min was chosen as optimum for further experiments. In these selected experimental conditions, and for a sample volume of 10 ml, the Method B consumes 1.5 mg of DNPH per sample whereas the Method A requires only 0.6 mg of DNPH per analysis. The decrease in the analytical signal at DNPH concentrations higher than optimal in Method B can be ascribed to the possible interference of excess DNPH on the adsorption of hydrazones, which was practically negligible in Method A because DNPH had been previously adsorbed on the SPE mini-column.

From the results in Fig. 2, it is clear that Method B provides a slightly higher sensitivity for the determination of the low-molecular mass aldehydes, which can be ascribed to both kinetic and thermodynamic aspects. In fact, Method B was more sensitive due to its higher derivatization time and excess of DNPH because in Method A only 60% of the DNPH loaded on the SPE mini-column is adsorbed for the further derivatization of aldehydes. In this context, the length of the reaction coil was also optimized in Method B; the range studied was between 50 and 150 cm, and the signal remained constant above 120 cm (selected value).

Organic solvents of variable polarity (methanol, acetonitrile and 2-propanol) were tested as eluents. Thus, after derivatization and pre-concentration of the aldehydes, the hydrazones retained were eluted with 150 μ l of each solvent (propelled by an air stream as depicted in Fig. 1) and then analysed in the chromatograph. Acetonitrile was found to be the best eluent; the analytical signals were 1.6 or 5.6 times higher than those obtained with methanol and 2-propanol, respectively. The effect of the eluent volume was studied between 50 and 200 μ l by using loops of variable length in the injection valve (IV₂ in Fig. 1). Obviously, as the volume eluent increased, desorption was more efficient (but hydrazones were also more diluted). An injected volume of 100 μ l was chosen as optimal as a compromise between these opposing effects. A second injection with the same eluent volume revealed the absence of carry-over; thus, complete elution of hydrazones was obtained with one injection of 100 μ l of acetonitrile.

The influence of the flow-rate of the air stream (the carrier of the eluent volume) was examined between 0.5 and 2.0 ml/min. No

significant effect was observed, so 0.5 ml/min was selected for further experiments. Other SPE variables studied were the amount of C_{18} sorbent and the sample and eluent flow-rates, which were examined over the range 50–200 mg and 0.5–2.0 ml/min, respectively. Based on the results obtained, the following conditions were selected: sorbent amount: 100 mg; sample flow rate = 1.0 ml/min; eluent flow rate = 0.5 ml/min.

Finally, the maximum sample volume that the SPE system could handle to achieve low limits of detection (LODs) for the aldehydes was determined. For this purpose, variable volumes (5–20 ml) of aqueous standards containing the same amount of each compound were adjusted to the working pH and propelled to the continuous SPE system at a flow-rate of 1.0 ml/min. Based on the results, loss of efficiency for the derivatization and pre-concentration of aldehydes was not observed up to 15 ml, although in Method A, a slight decrease in the chromatographic signals, about 15%, was observed with respect to those achieved for 10 ml. In any case, a sample volume of 15 ml was selected for further experiments, which provided a pre-concentration factor of 150 for aldehydes that allows their detection in water samples below $\mu\text{g/l}$ levels.

3.2. Chromatographic determination of aldehydes and application to water samples

Under optimum conditions, analytical curves were obtained for both methods using 15-ml of aqueous samples containing variable amounts of aldehydes and by plotting peak height against analyte concentration. Table 1 gives the equations for the standard curves and other analytical figures of merit such as LODs, defined as the minimum analyte concentration providing a chromatographic signal three times higher than peak-to-peak noise, the precision expressed as the relative standard derivation (RSD) and obtained by analyzing six samples per run of 15-ml of aqueous samples spiked with 10 $\mu\text{g/l}$ of each aldehyde on three different days (inter-day precision), $n = 18$. As can be seen, Method B is slightly more sensitive although less precise due to the possible interference caused by the excess DNPH on the adsorption of hydrazones. From these results, Method A was finally selected because it offers higher robustness and the sufficient sensitivity for the determination of these carbonyl compounds in aqueous samples.

At this point, it may be interesting to compare the analytical features of the approach proposed for the simultaneous in situ DNPH derivatization/pre-concentration of carbonyl compounds, concretely low-molecular mass aldehydes, from aqueous samples with recent reported alternatives and also its significance on the sensitivity achieved by the subsequent chromatographic method.

In general, current methods are related to the pre-concentration of the corresponding DNPH-derivatives on a C_{18} sorbent by using classical SPE cartridges [22,23], on a C_{18} mini-column installed at the sample injection LC valve instead of a sample loop [18], and on a polymer monolith such as it is done in the PMME technique [26] after batch derivatization; in all cases, higher derivatization times than in the in situ derivatization approach proposed in this work are required (at least 1 h). The only reference on the simultaneous in situ derivatization/pre-concentration of aldehydes with DNPH from aqueous samples has been recently reported by Feng and co-workers [27], which is based on the PMME technique. Although in this case the derivatization times are similar, the PMME method requires the previous synthesis of the polymer monolith and many steps to perform the whole analytical process, which affect the precision of the method, RSD ca. 7%. The approach proposed in this work provides higher pre-concentration factor than the PMME one, 150 versus 20, and therefore the ensuing LC–DAD method has a similar sensitivity to other reported alternatives even based on MS detection [15,23–25]. By comparing with the EPA Method 8315A [22], which also uses DAD as detection system, the proposed method provides better sensitivity for the determination of the aldehydes studied in this work: LODs ranged from 0.3 to 1.0 $\mu\text{g/l}$ were achieved by the proposed method whereas for the EPA Method 8315A they ranged from 6.2 to 43.7 $\mu\text{g/l}$. The LODs achieved at the sub- $\mu\text{g/l}$ level are suitable for the determination of the aldehydes in water samples, as is the case of DBPs in drinking waters, in which their typical levels ranged from 5 to 20 $\mu\text{g/l}$ [16]. With respect to the selectivity, the inherent kinetic character of the proposed continuous flow method and the use of a high molar ratio of DNPH to carbonyl compounds can provide an increase in the selectivity when compared to the methods based on the batch derivatization [15,22–25].

In order to evaluate the usefulness of the method developed, it was applied to the determination of low-molecular mass aldehydes in waters, such as drinking, mineral and stream water samples. First, non-spiked 15.0 ml aliquots of the water samples were analysed and only acetaldehyde was detected in the stream water sample at a concentration of $3.3 \pm 0.1 \mu\text{g/l}$. Moreover, in order to assess possible matrix effects, concentrations of aldehydes between 5 and 20 $\mu\text{g/l}$ were spiked in all samples and the corresponding percentages of recovery determined. No matrix effect was observed in the determination of these aldehydes in this kind of water samples: the percentages of recovery ranged from 95.8 to 99.4%. Last, Fig. 3 shows the chromatograms obtained in the analysis of the stream water sample as well as the one obtained from a negative drinking water spiked with 10 $\mu\text{g/l}$ of each aldehyde.

Table 1
Characteristic parameters of the calibration graphs and analytical figures of merit for the determination of low-molecular mass aldehydes.

Aldehyde	Linear range ^a ($\mu\text{g/l}$)	Regression equation ^b	r	LOD ($\mu\text{g/l}$)	RSD (%)
Method A					
Formaldehyde	3.5–200	$H = 2.9 \pm 0.3 + (1.36 \pm 0.04) \times C$	0.9979	1.0	4.6
Acetaldehyde	1.0–200	$H = 1.5 \pm 0.4 + (3.53 \pm 0.03) \times C$	0.9993	0.3	1.5
Propanal	1.0–200	$H = 1.9 \pm 0.6 + (4.22 \pm 0.05) \times C$	0.9991	0.3	1.2
Butanal	2.0–200	$H = 1.7 \pm 0.4 + (1.95 \pm 0.02) \times C$	0.9990	0.6	2.7
Pentanal	3.5–200	$H = 1.9 \pm 0.6 + (1.48 \pm 0.01) \times C$	0.9992	1.0	3.1
Hexanal	3.5–200	$H = 2.4 \pm 0.9 + (1.17 \pm 0.02) \times C$	0.9985	1.0	4.2
Method B					
Formaldehyde	2.0–100	$H = -0.5 \pm 4.1 + (2.8 \pm 0.2) \times C$	0.9945	0.6	12.5
Acetaldehyde	0.5–100	$H = 2.7 \pm 0.9 + (7.5 \pm 0.1) \times C$	0.9989	0.1	8.8
Propanal	0.5–100	$H = -2.3 \pm 3.7 + (8.3 \pm 0.4) \times C$	0.9976	0.1	8.4
Butanal	1.0–100	$H = -0.5 \pm 3.3 + (4.6 \pm 0.2) \times C$	0.9984	0.3	11.6
Pentanal	1.5–100	$H = 5.2 \pm 2.3 + (3.3 \pm 0.1) \times C$	0.9985	0.4	10.1
Hexanal	2.5–100	$H = 2.4 \pm 5.9 + (1.8 \pm 0.1) \times C$	0.9924	0.7	16.5

^a Sample volume, 15 ml.

^b H, peak height (in mV); C, analyte concentration (in $\mu\text{g/l}$).

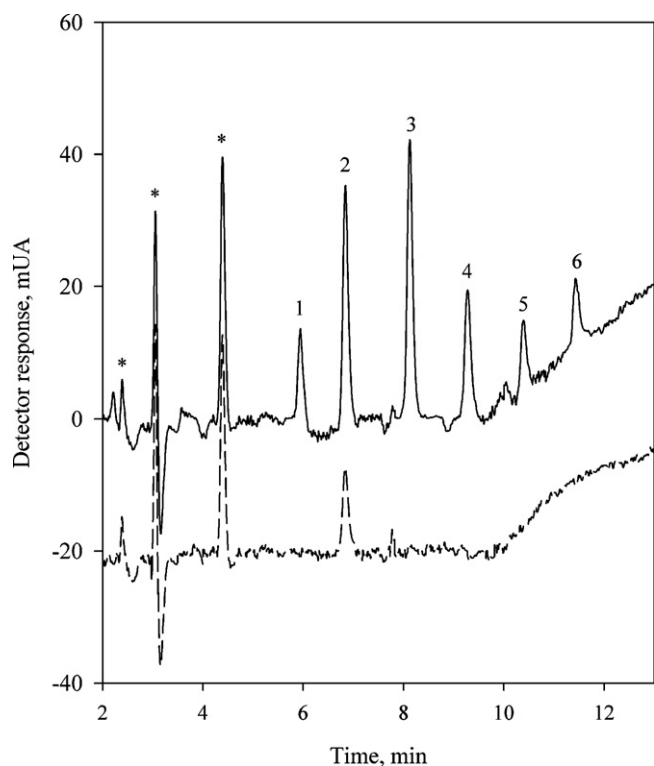


Fig. 3. Chromatograms for a drinking water spiked with 10 $\mu\text{g/l}$ of each aldehyde (solid line) and stream water sample (dashed line) after SPE in situ derivatization/pre-concentration. Peak assignment: 1, formaldehyde; 2, acetaldehyde; 3, propanal; 4, butanal; 5, pentanal; 6, hexanal; and *, unreacted DNPH. For other conditions see Section 2.

Acknowledgments

The authors gratefully acknowledge the subsidy provided by the Spanish Inter-Ministerial Commission of Science and Technology of

the Ministry of Education and Science under the CTQ2007-63962. FEDER also provided additional funding.

References

- [1] T.E. Graedel, *Atmospheric Chemical Compounds: Sources, Occurrence and Biosay*, Academic Press, Orlando, FL, 1986.
- [2] S.D. Piccot, J.J. Watson, J.W. Jones, *J. Geophys. Res.* 97 (1992) 9897.
- [3] H. Sakugawa, I.R. Kaplan, *Atmos. Environ.* 27B (1993) 203.
- [4] K.H. Kim, *J. Sep. Sci.* 30 (2007) 2708.
- [5] Y.G. Chi, Y.L. Feng, S. Wen, H.X. Lu, Z.Q. Yu, W.B. Zhang, G.Y. Sheng, J.M. Fu, *Talanta* 72 (2007) 539.
- [6] J.S. Herrington, Z.H. Fan, P.J. Li, J. Zhang, *Environ. Sci. Technol.* 41 (2007) 580.
- [7] T.L. Wang, H.W. Tong, X.Y. Yan, L.Q. Sheng, J. Yang, S.M. Liu, *Chromatographia* 62 (2005) 631.
- [8] S.M. van-Leeuwen, L. Hendriksen, U. Karst, *J. Chromatogr. A* 1058 (2004) 107.
- [9] S. Brombacher, M. Oehme, C. Dye, *Anal. Bioanal. Chem.* 372 (2002) 622.
- [10] J. Herrington, L. Zhang, D. Whitaker, L. Sheldon, J.F.J. Zhang, *J. Environ. Monit.* 7 (2005) 969.
- [11] E.A. Pereira, E. Carrillo, M.F.M. Tavares, *J. Chromatogr. A* 979 (2002) 409.
- [12] J. Zhang, L. Zhang, Z. Fan, V. Ilacqua, *Environ. Sci. Technol.* 34 (2000) 2601.
- [13] S.D. Richardson, A.D. Thruston Jr., T.V. Caughran, P.H. Chen, T.W. Collette, T.L. Floyd, K.M. Schenck, B.W. Lykins Jr., G.R. Sun, G. Majetich, *Environ. Sci. Technol.* 33 (1999) 3368.
- [14] S.D. Richardson, A.D. Thruston Jr., T.V. Caughran, P.H. Chen, T.W. Collette, K.M. Schenck, B.W. Lykins Jr., C. Rav-Acha, V. Glezer, *Air Soil Pollut.* 123 (2000) 95.
- [15] S.D. Richardson, *J. Environ. Monit.* 4 (2002) 1.
- [16] Y.F. Xie, *Am. Lab.* 32 (2000) 50, 52.
- [17] M. Vogel, A. Büldt, U. Karst, *Fresenius J. Anal. Chem.* 366 (2000) 781.
- [18] K. Takeda, S. Katoh, N. Nakatani, H. Sakugawa, *Anal. Sci.* 22 (2006) 1509.
- [19] A. Stafiej, K. Pyrzynska, A. Ranz, E. Lankmayr, *J. Biochem. Biophys. Methods* 69 (2006) 15.
- [20] E. Koivusalmi, E. Haatainen, A. Root, *Anal. Chem.* 71 (1999) 86.
- [21] E. Grosjean, P.G. Green, D. Grosjean, *Anal. Chem.* 71 (1999) 1851.
- [22] U.S. Environmental Protection Agency, *Method 8315A*, Cincinnati, OH, 1996.
- [23] C. Zwiener, F.H. Frimmel, *Anal. Bioanal. Chem.* 378 (2004) 862.
- [24] C. Zwiener, F.H. Frimmel, *Anal. Bioanal. Chem.* 372 (2002) 615.
- [25] S.D. Richardson, T.V. Caughran, T. Poiger, Y. Guo, F.G. Crumley, *Ozone Sci. Eng.* 22 (2000) 653.
- [26] H.J. Zhang, J.F. Huang, H. Wang, Y.Q. Feng, *Anal. Chim. Acta* 565 (2006) 129.
- [27] H.J. Zhang, J.F. Huang, B. Lin, Y.Q. Feng, *J. Chromatogr. A* 1160 (2007) 114.
- [28] E.E. Stashenko, J.R. Martínez, *Trends Anal. Chem.* 23 (2004) 553.
- [29] Q. Wang, J. O'Reilly, J. Pawliszyn, *J. Chromatogr. A* 1071 (2005) 147.
- [30] C.H. Deng, N. Li, X.M. Zhang, *J. Chromatogr. B* 813 (2004) 47.
- [31] C.H. Deng, X.M. Zhang, *Rapid Commun. Mass Spectrom.* 18 (2004) 1715.
- [32] P. Vesely, L. Lusk, G. Basarova, J. Seabrooks, D. Ryder, *J. Agric. Food Chem.* 51 (2003) 6941.
- [33] S.W. Tsai, C.M. Chang, *J. Chromatogr. A* 1015 (2003) 143.



Short communication

Preliminary evaluation of monolithic column high-performance liquid chromatography with tris(2,2'-bipyridyl)ruthenium(II) chemiluminescence detection for the determination of quetiapine in human body fluids

Sara A. Bellomarino^a, Allyson J. Brown^a, Xavier A. Conlan^{a,b}, Neil W. Barnett^{a,*}

^a School of Life and Environmental Sciences, Deakin University, Geelong, Victoria 3217, Australia

^b Institute for Technology Research and Innovation, Deakin University, Geelong, Victoria 3217, Australia

ARTICLE INFO

Article history:

Received 18 September 2008

Received in revised form 15 October 2008

Accepted 15 October 2008

Available online 1 November 2008

Keywords:

Quetiapine

Metabolites

Serum

Urine

Tris(2,2'-bipyridyl)ruthenium(II)

chemiluminescence

Monolithic HPLC

ABSTRACT

High-performance liquid chromatography (HPLC) with tris(2,2'-bipyridyl)ruthenium(II) chemiluminescence detection methodology is reported for the determination of the atypical antipsychotic drug quetiapine and the observation of its major active and inactive metabolites in human urine and serum. The method uses a monolithic chromatographic column allowing high flow rates of 3 mL min^{-1} enabling rapid quantification. Flow injection analysis (FIA) with tris(2,2'-bipyridyl)ruthenium(II) chemiluminescence detection and HPLC time of flight mass spectrometry (TOF-MS) were used for the determination of quetiapine in a pharmaceutical preparation to establish its suitability as a calibration standard. The limit of detection achieved with FIA was $2 \times 10^{-11} \text{ mol L}^{-1}$ in simple aqueous solution. The limits of detection achieved with HPLC were 7×10^{-8} and $2 \times 10^{-10} \text{ mol L}^{-1}$ in urine and serum, respectively. The calibration range for FIA was between 5×10^{-9} and $1 \times 10^{-6} \text{ mol L}^{-1}$. The calibration ranges for HPLC were between 1×10^{-7} – 1×10^{-4} and 1×10^{-8} – $1 \times 10^{-4} \text{ mol L}^{-1}$ in urine and serum, respectively. The quetiapine concentrations in patient samples were found to be $3 \times 10^{-6} \text{ mol L}^{-1}$ in urine and $7 \times 10^{-7} \text{ mol L}^{-1}$ in serum. Without the need for preconcentration, the HPLC detection limits compared favourably with those in previously published methodologies. The metabolites were identified using HPLC-TOF-MS.

© 2008 Elsevier B.V. All rights reserved.

1. Introduction

Quetiapine (see Fig. 1) is a relatively new atypical antipsychotic drug with a dibenzoethiazepine structure similar to clozapine [1]. The escalation in administration of quetiapine has led to an increased demand for therapeutic drug monitoring and metabolic investigations [2–4]. There have been reported advantages of therapeutic monitoring to avoid intoxication, non-response or non-compliance [2,4–6]. Quetiapine has been determined using a variety of techniques [1,3,4,6–10] and these have been summarised in Table 1. Several metabolites [1] (see Fig. 1) have also been identified certain in biological samples. However, many of these approaches lacked the necessary sensitivity for the determination of the quetiapine in human serum and or urine without preconcentration or analyte spiking [3,5–12]. The analytical utility of tris(2,2'-bipyridyl)ruthenium(II) chemiluminescence detection in conjunction with high-performance liquid chromatography (HPLC), flow analysis and capillary electrophoresis for an extensive

range of analytes has been well documented [13,14]. To the best of our knowledge, this paper presents for the first time the direct determination of quetiapine in human body fluids using monolithic column HPLC with tris(2,2'-bipyridyl)ruthenium(II) chemiluminescence detection. Furthermore, three metabolites of quetiapine were also detected with this instrumentation and their identity confirmed using electrospray ionisation time of flight mass spectrometry (ESI-TOF-MS).

2. Experimental

2.1. Instrumentation

2.1.1. FIA

The flow injection analysis manifold used is described in Fig. 2. The instrument consisted of a Gilson Miniplus 3 peristaltic pump from John Morris Scientific (Balwyn, Vic., Australia), bridged PVC tubing and 0.8 mm i.d. PTFE manifold tubing from DKSH (Caboolture, Qld., Australia) and a Valco six-port injection valve from SGE (Ringwood, Vic., Australia) with a $50 \mu\text{L}$ sample loop. The tris(2,2'-bipyridyl)ruthenium(II) solution was oxidised with lead dioxide to generate the reagent, which was injected manually into

* Corresponding author. Tel.: +61 3 5227 1409.

E-mail address: barnie@deakin.edu.au (N.W. Barnett).

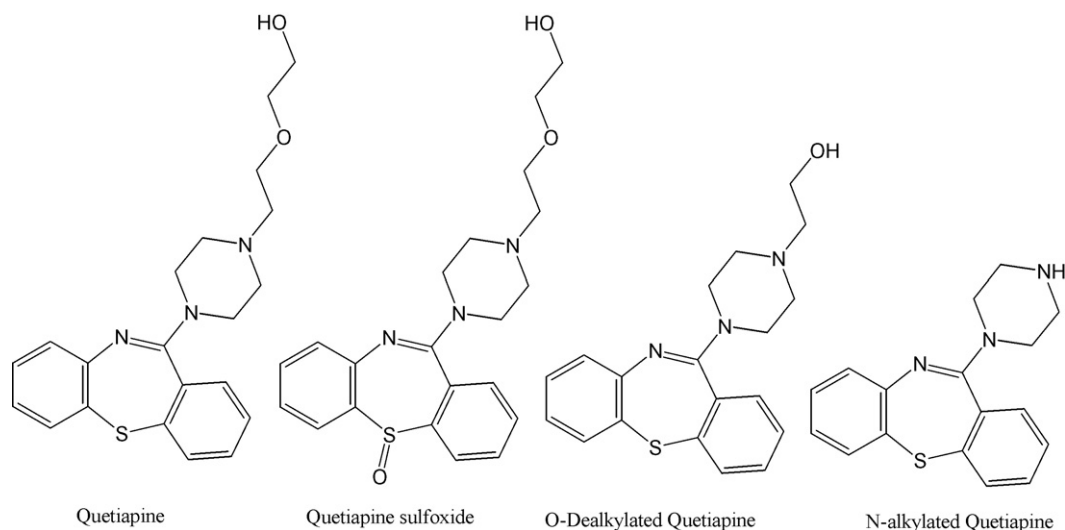


Fig. 1. The structures of quetiapine and three metabolites [1].

Table 1
Previous work on quetiapine.

Technique	Linear calibration range (M)	LOD (M)	Reference
HPLC-electrochemical detection-preconcentration	2.8×10^{-9} – 5.7×10^{-7}	ns	[12]
HPLC-UV-solid phase extraction	4.5×10^{-9} – 4.5×10^{-7}	1.7×10^{-9}	[4]
HPLC-UV-solid phase extraction	5.0×10^{-10} – 5.6×10^{-1}	1.0×10^{-10}	[9]
Capillary zone electrophoresis-UV	5.6×10^{-6} – 5.6×10^{-5}	1.7×10^{-7}	[14]
HPLC-MS/ESI-solid phase extraction	1.1×10^{-8} – 2.2×10^{-3}	3.4×10^{-10}	[13]
Voltammetry	4.0×10^{-6} – 2.0×10^{-4}	4.0×10^{-8}	[16]
HPLC-UV-solid phase extraction	2.8×10^{-7} – 4.5×10^{-7}	9.0×10^{-10}	[5]
HPLC-UV	2.2×10^{-8} – 4.1×10^{-7}	ns	[3]
HPLC-MS/MS-solid phase extraction	1.1×10^{-9} – 4.3×10^{-7}	3.3×10^{-10}	[7]
HPLC-MS/MS	5.6×10^{-11} – 5.6×10^{-9}	1.1×10^{-12}	[17]
HPLC-UV-solid phase extraction	1.6×10^{-7} – 8.4×10^{-7}	5.6×10^{-10}	[11]

ns = not stated.

a 0.05 M H_2SO_4 carrier stream. This was then merged with the sample stream at a 0.8 i.d. T-piece, immediately prior to entering a coiled PFTE flow-cell positioned flush against an Electron Tubes Model 9828SB photomultiplier tube (PMT) purchased from ETP (Ermington, NSW, Australia) at a total flow rate of 2.8 mL min^{-1} . The PMT was operated at 1000 V provided by an Electron Tubes Model PM20D power supply and Electron Tubes Model C611 voltage divider from ETP. The flow-cell and PMT were enclosed in a light-tight housing. The output from the PMT was converted by a Thorn-EMI Model A1 transimpedance amplifier purchased from ETP, recorded with a Type 3066 chart recorder from Yokogawa Hokushin Electric (Tokyo, Japan) and peak height was measured manually.

2.1.2. HPLC

The HPLC instrumentation consisted of a Hewlett–Packard 1100 series liquid chromatograph equipped with a quaternary pump, sol-

vent degasser, diode-array detector (DAD) and autosampler from Agilent Technologies (Forest Hill, Vic., Australia). The HPLC was fitted with a Chromolith Performance RP-18e 100 mm \times 4.6 mm column, a 5 mm monolithic guard column from Merck (Kilsyth, Vic., Australia). The chemiluminescence detector (as described above for FIA) was configured by replacing the carrier line in the 0.8 mm i.d. T-piece with the outlet line from the DAD (254 nm). Thus the column eluent traveled sequentially through both detectors, before merging with the chemiluminescence reagent which was propelled at a flow rate of 3 mL min^{-1} . Control of the HPLC pump, DAD, and data acquisition from the chemiluminescence detector was achieved using Hewlett Packard Chemstation Software (Agilent Technologies). Urine samples and serum samples were analysed by injecting 20 and 100 μL , respectively, and separated at a flow rate of 3 mL min^{-1} . Solvent composition of 15% methanol in an aqueous solution of trifluoroacetic acid (0.1%, v/v) was increased to 35% methanol over 7 min which was then raised to 100% methanol for a further 3 min.

2.1.3. Mass spectrometry

A 6210 MS/TOF mass spectrometer Agilent Technologies (Forest Hill, Vic., Australia) was used to identify the primary metabolites. The instrument was operated under the following conditions: drying gas, nitrogen (7 mL min^{-1} , 350°C); nebuliser gas, nitrogen (16 psi); capillary voltage, 4.0 kV; vaporizer temperature, 350°C ; and cone voltage, 60 V. Solvent composition of 15% (v/v) methanol in an aqueous solution of trifluoroacetic acid (0.1%, v/v) was increased to 35% (v/v) methanol over 21 min which was then

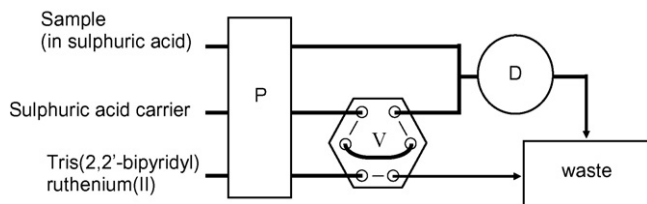


Fig. 2. Schematic of the FIA manifold used in this study (P = pump, V = injection valve, D = detector).

Table 2

Analytical figures of merit for quetiapine using FIA and HPLC with tris(2,2'-bipyridyl)ruthenium(II) chemiluminescence detection, where y is equal to the logarithm of the peak height for FIA and peak area for HPLC, and x is equal to the logarithm of the molarity of the quetiapine.

Instrumental method	Injection volume (μL)	Calibration function	Calibration range (mol L^{-1})	LOD (mol L^{-1})	R^2	RSD (%)
FIA	50	$y = 6 \times 10^{10}x + 6793$	$5 \times 10^{-9} - 1 \times 10^{-6}$	2×10^{-11}	0.99894	2.02
HPLC	20	$y = 6 \times 10^9x + 8867$	$1 \times 10^{-7} - 1 \times 10^{-4}$	7×10^{-8}	0.99923	2.07
HPLC	100	$y = 4 \times 10^{10}x + 30641$	$1 \times 10^{-8} - 1 \times 10^{-4}$	2×10^{-10}	0.99741	2.07

raised to 100% (v/v) methanol for a further 9 min at a flow rate of 1 mL min^{-1} .

2.2. Reagents

All solutions were prepared with deionised water (Millipore, MilliQ Water System, USA). HPLC-grade acetonitrile and methanol were obtained from BDH (Poole, UK). All mobile phases and samples were filtered through a $0.45 \mu\text{m}$ nylon membrane filter. Solutions of tris(2,2'-bipyridyl)ruthenium(II) ($1 \times 10^{-3} \text{ M}$, Strem, USA) were prepared in 0.05 M sulfuric acid. Stock solutions of quetiapine ($1 \times 10^{-3} \text{ M}$) were prepared by dissolving the appropriate amount of crushed Seroquel® (Astra Zeneca) tablets in 0.05 M sulfuric acid prior to ultrasonication for 30 min.

2.3. Patient samples

All patient data was removed prior to analysis and storage to comply with the privacy legislation for this pilot study. Blood and urine samples were collected in the morning by a medical professional approximately 12 h after last intake of Seroquel® (50 mg). The blood was collected in a vacutainer without an anticoagulant and then left to clot for 30 min at room temperature before being centrifuged at 2500 rpm for 15 min and the resultant serum collected. The serum and urine samples were stored at -80°C , prior to thawing for analysis. Samples were vortexed for 30 s and then centrifuged for 5 min before filtering through a $0.45 \mu\text{m}$ nylon membrane filter. Control urine samples were provided by a healthy volunteer and subjected to the same protocol.

3. Results and discussion

3.1. Analysis of Seroquel®

Due to the unavailability of an analytical standard for quetiapine, the pharmaceutical Seroquel® was used based on the dosage declared by the manufacturer. This approach was previously employed by Davies et al. [9] and Pucci et al. [15]. Standard solutions of Seroquel® were made up as described in Section 2.2. Subsequently, FIA with tris(2,2'-bipyridyl)ruthenium(II) chemiluminescence was used to obtain preliminary calibration functions and analytical figures of merit for quetiapine (see Table 2).

When analysed with HPLC, coupled to the same chemiluminescence detection system as used for FIA, the standard solutions of Seroquel® exhibited a single chromatographic peak at 5.80 min. This was later identified by HPLC-ESI-TOF-MS to be that of quetiapine. Thus clearly demonstrating that neither the FIA nor the HPLC with tris(2,2'-bipyridyl)ruthenium(II) chemiluminescence detection recorded a measurable response from the presence of any excipients in the pharmaceutical preparation. Accordingly, this FIA methodology with its low limits of detection and rapid sample throughput offers superior analytical performance for the quality assurance of Seroquel® formulations compared with earlier studies [15,16].

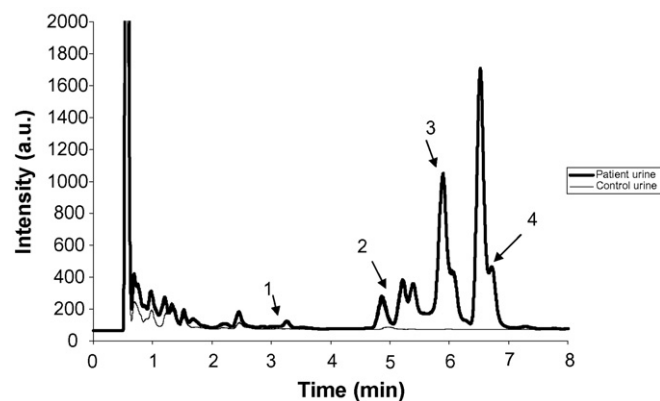


Fig. 3. Chromatogram of control and patient urine samples. The identified components are 1, O-dealkylated quetiapine; 2, N-alkylated quetiapine; 3, quetiapine; and 4, quetiapine sulfoxide.

3.2. Urine and serum analyses

Using the HPLC parameters described in Section 2.1.2 and similar standard solutions as those for FIA, calibration functions for quetiapine were obtained using two injection volumes and the resultant analytical figures of merit are shown in Table 2. These results revealed an extended calibration range compared to other methodologies reported for this analyte [4–6,8–10]. While the limits of detection achieved using HPLC were inferior compared to that attained with FIA, this was to be expected as the solvent mixtures, particularly the presence of methanol, do not provide an optimal chemical environment for the generation of tris(2,2'-bipyridyl)ruthenium(II) chemiluminescence [13,14]. While the detectability was adequate for the direct determination quetiapine in the two body fluids, the relative instability of the samples (at room temperature) and lack of analytical standards precluded the optimisation of the separation and as shown in Figs. 3 and 4 it

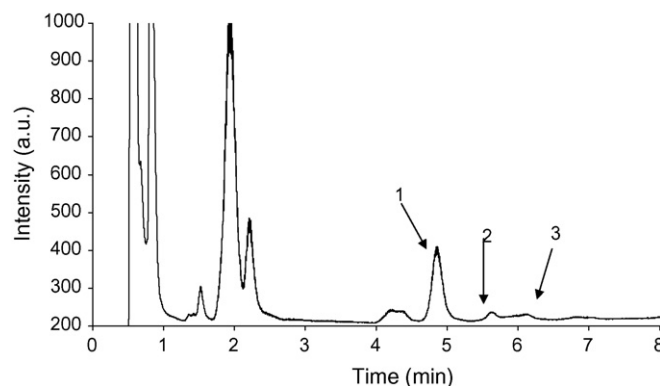


Fig. 4. Chromatogram of patient serum with identified components: 1, N-alkylated quetiapine; 2, quetiapine; 3, quetiapine sulfoxide.

is only good enough to estimate the quetiapine concentration and observe the presence of its metabolites.

The patients' urine sample was analysed using the above conditions with 20 μ L injection volume and compared with a control. The resulting chromatograms in Fig. 3 show that the chemiluminescence detection afforded analytically useful responses for quetiapine and its metabolites [3,8,17,18], the identity of three of which was later confirmed by HPLC-ESI-TOF-MS. The retention time for quetiapine was established (5.80 min) by spiking both urine samples and its concentration was determined to be 3×10^{-6} M using an external calibration. Similar methodology was applied to a serum sample with a 100 μ L injection volume (see Fig. 3) and the quetiapine concentration was found to be 7×10^{-7} M. It should also be noted that the serum sample was collected from a patient who had ingested only 50 mg of Seroquel[®], which was considered to be a relatively low dose given that the therapeutic range is between 150 and 750 mg/day [2,9,10,15,19–21].

The considerable differences in analyte concentrations found in the urine and serum samples is consistent with quetiapine having a biological half-life of approximately 5–8 h due to extensive metabolism after oral administration and excretion through urine and faeces [4,15,20,22]. The bioavailability of quetiapine is driven by the liver through sulfoxidation forming the major but inactive sulfoxide metabolite, and via lesser metabolic pathways, N- and O-dealkylation metabolites [22]. Furthermore, the extent and rate of quetiapine metabolism can vary greatly between individuals, due to patient compliance and the activities of drug metabolising enzymes [4].

The use of the monolithic column negated the need for extensive sample preparation due to its bimodal pore design, making it resistant to blocking [26]. The monoliths also permitted the use of relatively high-flow rates (3 mL min⁻¹) at low back-pressures, which afforded compatibility with the kinetics of the chemiluminescence detection and enabled rapid separation. The minimal sample preparation removed the need to match extraction and preconcentration solvents with HPLC gradients, which is often a problem with such sample pretreatment protocols [3].

4. Conclusion

Monolithic HPLC separations with tris(2,2'-bipyridyl) ruthenium(II) chemiluminescence detection were used for the estimation of quetiapine concentrations and the observation of its major metabolites (confirmed with mass spectrometry) in human urine and serum. The samples required only minimal sample preparation and no preconcentration step and the limits of detection were comparable to mass spectrometry (see Table 1). Given the availability of a complete set of analytical standards

and access to suitable patient samples, our preliminary evaluation of this technology could be refined and validated. This approach could be utilised for the rapid monitoring of quetiapine and its active and inactive metabolites thus facilitating a dose correction to be made on an individual patient basis. Such corrections are commonly required in order to account for the interactions of other drugs that may increase [23,24] or decrease [12,25] the metabolism of quetiapine.

The FIA methodology has the potential to be utilised for quality assurance of Seroquel[®] formulations.

References

- [1] C.L. DeVane, C.B. Nemeroff, Clin. Pharmacokinet. 40 (2001) 509.
- [2] M.A. Raggi, Curr. Med. Chem. 9 (2002) 1397.
- [3] J. Hasselstrom, K. Linnet, J. Chromatogr. B 798 (2003) 9.
- [4] J. Sache, J. Köller, S. Härtter, C. Hiemke, J. Chromatogr. B 830 (2006) 342.
- [5] M.A. Saracino, L. Mercolini, G. Flotta, L.J. Albers, R. Merli, M.A. Raggi, J. Chromatogr. B 843 (2006) 227.
- [6] L. Mercolini, M. Grillo, C. Bartoletti, G. Boncompagni, M.A. Raggi, Anal. Bioanal. Chem. 388 (2007) 235.
- [7] K.Y. Li, Z.N. Cheng, X. Li, X.L. Bai, B.K. Zhang, F. Wang, H.D. Li, Acta Pharmacol. Sin. 25 (2004) 110.
- [8] B. Barrett, M. Holcapek, J. Huclová, V. Borek-Dohalský, P. Fejt, B. Nemec, I. Jelínek, J. Pharmaceut. Biomed. Anal. 44 (2007) 498.
- [9] P.C. Davies, J. Wong, O. Gefvert, J. Pharmaceut. Biomed. Anal. 20 (1999) 271.
- [10] R. Mandrioli, S. Fanali, A. Ferranti, M.A. Raggi, J. Pharmaceut. Biomed. Anal. 30 (2002) 969.
- [11] K.Y. Li, Y.G. Zhou, H.Y. Ren, F. Wang, B.K. Zhang, H.D. Li, J. Chromatogr. B 850 (2007) 581.
- [12] J. Li, X. Li, Z.N. Cheng, B.K. Zhang, W.X. Peng, H.D. Li, Eur. J. Clin. Pharmacol. 60 (2005) 791.
- [13] N.W. Barnett, B.J. Hindson, S.W. Lewis, Anal. Chim. Acta 362 (1998) 131.
- [14] B.A. Gorman, P.S. Francis, N.W. Barnett, Analyst 131 (2006) 616.
- [15] V. Pucci, R. Mandrioli, A. Ferranti, S. Furlanetto, M.A. Raggi, J. Pharmaceut. Biomed. Anal. 32 (2003) 1037.
- [16] S.A. Ozkan, B. Dogan, B. Uslu, Microchim. Acta 153 (2006) 27.
- [17] Z. Zhou, X. Li, K. Li, Z. Xie, Z. Cheng, W. Peng, F. Wang, R. Zhu, H. Li, J. Chromatogr. B 802 (2004) 257.
- [18] H. Kircherr, W.N. Kühn-Velten, J. Chromatogr. B 843 (2006) 100.
- [19] F. Bochner, J. Allardice, D. Ames, J. Condon, G. Johnson, N. Keks, A. Mant, J. McEncroe, J. McGrath, P. Mitchell, J. Robinson, M. Sawyer, J. Tiller, J. White, Therapeutic Guidelines: Psychotropic, Therapeutic Guidelines Ltd., Melbourne, Australia, 2000.
- [20] AstraZeneca, in: Product Information, 2006, 1 pp <http://www1.astrazeneca-us.com/pi/Seroquel.pdf>.
- [21] S. Kasper, F. Müller-Spahn, Expert Opin. Pharmacother. 1 (2000) 783.
- [22] E. Spina, J. de Leon, Basic Clin. Pharma. Toxicol. 100 (2007) 4.
- [23] S.W. Grimm, N.M. Richtand, H.R. Winter, K.R. Stams, S.B. Reece, Br. J. Clin. Pharmacol. 61 (2005) 58.
- [24] Y.W.J. Wong, C. Yeh, P.T. Thyrum, J. Clin. Psychopharmacol. 21 (2001) 89.
- [25] W. Aichhorn, J. Marksteiner, T. Walch, G. Zernig, A. Saria, G. Kemmler, Int. Clin. Psychopharmacol. 21 (2006) 81.
- [26] Merck, Product Information (2008) 1 http://www.merck-chemicals.com/is-bin/INTERSHOP.enfinity/WFS/Merck-International-Site/en_US/-/USD/ViewProductDetail-Attachments?CatalogCategoryID=&ProductUID=8PSb.s10S-fQAAAEWPREW4z71&PortalCatalogUID=Uc6b.s1LfzAAAEW6tYfVhTI&-SelectedDocumentType=Bro#ankerBrochures.



High-resolution surface plasmon resonance sensors based on a dove prism

Olivier R. Bolduc, Ludovic S. Live, Jean-François Masson*

Département de Chimie, Université de Montréal, C.P. 6128 Succ. Centre-Ville, Montréal, Qc, Canada H3C 3J7

ARTICLE INFO

Article history:

Received 15 July 2008

Received in revised form

29 September 2008

Accepted 1 October 2008

Available online 17 October 2008

Keywords:

Portable SPR biosensor

Biosensing

Self-assembled monolayer (SAM)

Antibiotic resistance

ABSTRACT

Wavelength interrogation surface plasmon resonance (SPR) spectroscopy using a dove prism combines a simple and inexpensive optical design with high-resolution refractive index monitoring and biosensing. A BK7 dove prism inverts an optical image with a total internal reflection angle of 72.8° , an angle active in SPR. Hence, a unique system can accomplish SPR biosensing using wavelength interrogation and also perform SPR imaging. This optical configuration advantageously uses a single axis optical path between each optical component, simplifying the optical design of SPR instruments without compromise of the analytical performance. Fluidics were also incorporated to the instrument design for efficient sample delivery. The SPR instrument is characterized in terms of refractive index (RI) sensitivity, RI resolution, reproducibility, and application for monitoring low concentration biological events. Data analysis methodologies are compared for improved resolution of the measured response. Raw data analyzed using a minimum hunting procedure results in RI resolution in the 10^{-6} range, while pre-treating data with singular value decomposition improves the resolution by one order of magnitude. Depending on the spectrophotometer employed, the RI range accessible can be easily tuned; examples with a 550–850 nm and a 550–1100 nm spectrophotometers are shown and results respectively in RI ranges of 1.32–1.39 RIU and 1.32–1.42 RIU. Monitoring of μM concentration of β -lactamase is performed using the wavelength interrogation configuration of the biosensor. Finally, a SPR image of a surface with a water droplet (volume = 500 nL) was obtained using the dove prism SPR with a band pass filter and a CCD camera. SPR using a dove prism configuration combines advantages of portable SPR instruments, SPR imagers and research-grade SPR instruments in a unique platform.

© 2008 Elsevier B.V. All rights reserved.

1. Introduction

Surface plasmon resonance (SPR) sensing has become a widely utilized technique for the measurement of biomolecular interactions [1,2], quantification of proteins [3,4], and measurements of DNA [5]. Excellent reviews of the instrumentation [6], the technique [7] and recent advances in SPR spectroscopy [8] provide a general overview of SPR-based sensors. Briefly, the SPR phenomenon relies on the optical excitation of a charge-density oscillation existing at the interface of a thin metallic film and a dielectric. To achieve resonance conditions, the light must be in total internal reflection at a wavelength – angle couple matching the wavevector of the surface plasmon (SP). Therefore, multiple optical configurations can possibly excite the SP. The Kretschmann configuration of a SPR instrument couples light using attenuated total reflection (ATR) at a glass|Au interface. The most popular configuration uses monochromatic light to interrogate the angle in resonance with the SP [7]. Many commercially successful instruments are based on this opti-

cal configuration. Thus, in spite of the popularity of these types of SPR instruments, there is still a necessity to develop a SPR instrument combining high resolution of the SPR response, such as in the angular interrogation configuration, with the advantages of an inexpensive [9,10] and portable instrument [11,12]. Hence, a versatile and cost-effective technology could be implemented in many laboratories and yet, achieve low detection limits SPR sensing.

SPR instruments based on different configurations have been investigated as alternatives for the angle interrogation configuration. Among them, a SPR instrument using fiber optics as the sensing element is a cost-effective alternative to research-grade instrument, they are portable [13] and can be adapted to various applications such as salinity sensor [14], biosensor for wound healing [15], biosensor for cardiac markers [16,17] and biosensor for staphylococcal enterotoxin B [18]. Sensitivity of fiber optic SPR can be improved using near infrared excitation of a micro-prism located at the tip of the fiber optic [19]. However, the resolution achieved with this technique is limited by the numerical aperture (NA) of the optical fiber required to perform SPR on a fiber optic. A large numerical aperture (NA = 0.39) fiber is necessary to propagate the SPR-active angle – wavelength couples. However, due to a large number of angle – wavelength couples propagating in the

* Corresponding author. Tel.: +1 514 343 7342; fax: +1 514 343 7586.
E-mail address: jf.masson@umontreal.ca (J.-F. Masson).

fiber optics and entering in resonance with the SPR surface, the SPR spectrum broadens resulting in a limited resolution with this configuration. To minimize this effect, low numerical aperture fiber optic (NA = 0.12) can be modified with a micro-prism at the distal end to improve the SPR spectrum [20] and increase the accessible range of refractive index of the sensor [21]. Using this configuration, the resolution is limited to approx. 1.4×10^{-6} RIU. Further decrease of the numerical aperture of the fiber optic is necessary to achieve a resolution similar to the angle interrogation configuration (approx. 5×10^{-7} RIU). However, current manufacturing techniques do not allow such low numerical aperture.

An alternative to the angle interrogation SPR or using optical fiber uses a multi-wavelength excitation. This configuration combines elements of the angle interrogation SPR and fiber optic SPR instrument. In a multi-wavelength excitation scheme, collimated white light from an excitation optical fiber is reflected at a single angle and is analyzed with a spectrophotometer using a collection optical fiber [22,23]. Among other factors, the SPR resolution with multi-wavelength SPR is mainly limited, by the width of the SPR band. In addition, the spectral range of the spectrophotometer, which is a function of the grating density, will delimit the working range in refractive index of the SPR sensor. The recent advent of miniature spectrophotometer with a narrow spectral range and high-density diode arrays potentially enables the measurement of the refractive index with high resolution with a small footprint SPR instrument. These spectrophotometers allow the acquisition of a large number of data points around the SPR band, contributing to reduce the noise of the measurement and thereby improving the resolution of the SPR measurement. In the case of the angle interrogation configuration, the resolution depends on scanning the incident angle (slow measurement and complex mechanical setup) or by focusing the incident light beam at the glass|Au interface onto a linear array photodiode (precise alignment and lengthy optical path for high resolution). Hence, the angle interrogation configuration is not suitable for portability and for an inexpensive design of the SPR instrument. A current drawback limiting the use of multi-wavelength SPR instrument is the precise alignment of the optics at the angle of excitation [23] or the manufacture of a small sensing element [22]. The use of a dove prism is advantageous to circumvent these drawbacks. The dove prism inverts the image of a collimated light beam impinging parallel to the long edge of the dove prism. The total internal reflection angle of propagation in a BK7 dove prism is 72.8° , which is active in SPR with an excitation wavelength between 600 nm and 1000 nm depending on the refractive index of the solution. Hence, a single axis optical path is required to construct the SPR imaging instrument, greatly simplifying the optical setup without loss of spatial or optical resolution. The sensing element is simply composed of a glass slide coated with Au, onto which fluidics can be mounted for efficient sample delivery. This configuration combines the advantages of a portable, inexpensive SPR instrument with the high-resolution advantage of biosensing with the angle interrogation configuration SPR instrument.

Increasingly, the need of multiplex arrays is arising for simultaneous multi-analyte detection. Spatially resolved SPR measurements provide a technology for monitoring local changes of refractive index on a surface [24,25]. Thus, the detection of biomolecular interactions for multiple systems/replicates is possible on a spatially resolved sensing array [26]. SPR imaging, also called SPR microscopy, has been applied for high-throughput analyses of biomolecular binding event [1]. The SPR imaging methodology has been recently optimized with the improvement of the resolution [27], optical coupling [28] and protein array formation [29]. However, no SPR measurement possesses the dual

capability of measuring the conventional SPR response and the SPR image of a surface. The use of a dove prism SPR configuration can perform both conventional and SPR imaging techniques with a unique instrumental template.

Here, a SPR instrument is demonstrated based on the optical setup using a dove prism coupled with fiber optics and a miniature spectrophotometer. Although the dove prism SPR configuration is suitable for the development of a portable SPR instrument, this article presents the characterization in a laboratory of a SPR instruments based on this configuration. Characterization of the dynamic range, the sensitivity, refractive index resolution, the reproducibility and biosensing for β -lactamase are reported in this article. Among the multiple data analysis strategies previously developed to improve resolution of the SPR signal [30–33], the minimum hunting (polynomial fit) and the algorithm $(a - b)/(a + b)$ are investigated to maximize resolution of the SPR response. Spectral denoising is also performed using singular value decomposition (SVD) of the spectra to improve the signal to noise ratio and increase the resolution of the measured SPR response. Two configurations are presented: (1) using a collection fiber optic with a miniature spectrophotometer for multi-wavelength SPR and (2) using a bandpass filter and an imaging camera to perform SPR imaging. An image of water droplets on a Au surface of the SPR sensor demonstrates the SPR imaging configuration.

2. Experimental

2.1. SPR sensor

Glass slides of $3'' \times 1''$ were cleaned using piranha solution (70% H_2SO_4 :30% H_2O_2) at 80°C for 90 min. *Caution, piranha solution is highly corrosive!* The glass slides were then thoroughly rinsed with 18 M Ω water. Thereafter, the glass slides were further cleaned in an ultrasound bath with a 5:1:1 solution of H_2O : H_2O_2 : NH_4OH for 60 min. The glass slides were thoroughly rinsed with 18 M Ω water and stored in 18 M Ω water until use. The slides were air-dried undisturbed prior to metallization. Then, a 5-nm-thick adhesion layer of Cr followed with a 48 nm Au film were deposited to manufacture the SPR sensor.

2.2. SPR instrument

The SPR instrument was constructed based on a combination of wavelength interrogation fiber optic SPR and total internal reflection in a dove prism (Fig. 1). The broadband light from a halogen lamp was focused in a 200- μm -diameter fiber optic (excitation fiber optic). Light exiting the excitation fiber optic is collimated to a diameter of about 3 mm using a SMA collimating lens, passed through a sheet polarizer, the dove prism (BK7) with the SPR sensor contacted using refractive index matching oil (RI = 1.5150), and collected with another fiber optic (200- μm diameter) using an inverted SMA collimating lens. All these optical components were aligned in a single optical axis. The light exiting the collection fiber entered a miniature spectrophotometer. Depending on the RI range desired, a short-range spectrophotometer (550–850 nm) covers from 1.33 RIU to 1.39 RIU or a longer spectral range was obtained from a 550 nm to 1100 nm spectrophotometer which covers from 1.33 RIU to 1.42 RIU. If the imaging configuration was used, the collection fiber optic was removed and replaced with a band pass filter (620 ± 10 nm). The collimated light exiting the band pass filter was analyzed using a CCD camera (Andor technology). A 50:50 beam splitter can be mounted between the dove prism and the band pass filter for wavelength interrogation and imaging on a single platform.

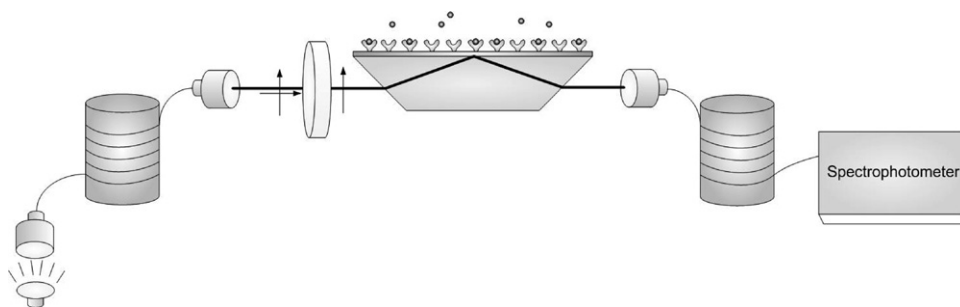


Fig. 1. Schematic representation of a SPR instrument using a dove prism. A single axis optical path between the excitation fiber and the collection fiber results in a small-footprint instrument.

A fluidic cell and syringe pump were constructed in-house. The fluidic cell made of Teflon has a spade-shaped channel of 0.5-mm deep. The housing was designed to hold the dove prism, the SPR sensor and the fluidic cell in close contact. The dual channel syringe pump was designed for sample flow rates between $8.3 \mu\text{L s}^{-1}$ and $108 \mu\text{L s}^{-1}$. A flow rate of $16 \mu\text{L s}^{-1}$ was typically used.

2.3. Calibration of the SPR sensor

Sucrose solutions with concentrations ranging from 0% w/w to 50% w/w were prepared in water to cover between 1.33 RIU and 1.42 RIU. Thereafter, the solutions were successively exposed to the SPR sensors using the syringe pump and the flow cell. Data analysis was performed using two methodologies: minimum hunting [31] and a $(a - b)/(a + b)$ algorithm around the minimum reflectance of the SPR spectrum [33]. SVD of the SPR spectra and reconstruction of the SPR spectra using the first three components was performed to optimize signal to noise. With both data analysis methodologies, an ordinary linear least squares (OLLSS) regression model was used to calibrate the SPR sensor.

2.4. Detection of β -lactamase

A monolayer of the N-hydroxysuccinimide ester of the 16-mercaptohexadecanoic acid (NHS-MHA) was formed by contact of the bare Au surface with a 5 mM solution of NHS-MHA overnight. NHS-MHA was prepared according a previously published procedure [16]. Following a thorough rinse of the NHS-MHA monolayer with ethanol and thereafter with PBS, the sensor was reacted with anti- β -lactamase (QED Bioscience Inc.) prepared at $37 \mu\text{g/mL}$ in refrigerated PBS pH 7.4. The reaction was carried overnight in a 4°C environment to minimize antibody degradation. Thereafter,

the samples were rinsed with PBS and reacted for 10 min in a 1 M aqueous solution of ethanolamine hydrochloride adjusted at a pH of 8.5 with 10 M NaOH. The slides were stored in PBS at 4°C for at least 60 min prior to use.

A solution at 700 nM of β -lactamase was prepared in PBS at 4°C by the dilution of a stock solution. This solution was kept at 4°C until 20 min prior to use, which was then equilibrated at room temperature for the analyses. These following measurements were performed without the use of a flow cell. A sensor with the β -lactamase specific monolayer was mounted on the SPR instrument and room temperature PBS was placed on the sensor for 10 min, in order to stabilize the sensor. A spectral reference (s-polarized light) was acquired immediately before the real-time measurement started. PBS was measured for 5 min to acquire the baseline response and was thereafter replaced with the β -lactamase solution for 20 min. Finally, the sensor was placed again in PBS for 5 min verifying the reversibility of the binding between the anti- β -lactamase and β -lactamase.

3. Results and discussion

3.1. SPR based on a dove prism

A SPR instrument using a dove prism allows a compact and a single axis optical path between an excitation fiber optic and a collection fiber optic (Fig. 1). With collimated incident light impinging on the prism, a single angle of 72.8° propagates in total internal reflection through a BK7 prism. At this angle, the surface plasmon on a 48-nm Au film is excited at a wavelength of approx. 610 nm with aqueous solutions (Fig. 2). With this experimental configuration, the instrument must combine multi-wavelength excitation with a spectrophotometer to observe the SPR spectrum.

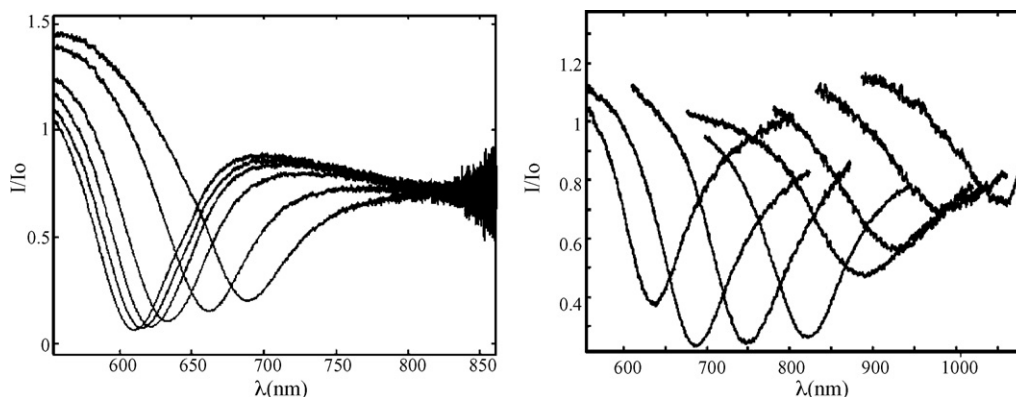


Fig. 2. SPR spectra are shown for the sucrose solutions with refractive index varying between 1.33 RIU and 1.36 RIU (short spectral range configuration of spectrophotometer) on the left and between 1.33 RIU and 1.42 RIU in the long spectral range configuration of spectrophotometer.

To accomplish this, fiber optic for light delivery and a miniature spectrophotometer result in a small footprint instrument, of 17 cm length \times 6.5 cm width \times 17 cm height for the optical components. The SPR instrument consists of a broadband halogen light source, an excitation fiber (vis-NIR fiber optic of 200 μ m diameter) with a collimating lens terminating the fiber, a polarizer, a dove prism, and a collection fiber identical to the excitation fiber. The active SPR area on the sensor is <1 cm², which can be tunable with the presence of an iris between the excitation fiber and the prism. The collected light is analyzed with a miniature spectrophotometer, the wavelength ranges from 550 nm to 850 nm for a short range of accessible refractive index (1.32–1.39 RIU) or with a wavelength range from 550 nm to 1100 nm, for a broader range of refractive index accessible to the SPR sensor (1.32–1.42 RIU). The multi-wavelength SPR instruments have the advantage of simultaneous acquisition of a complete wavelength scan of the SPR spectrum, allowing for fast acquisition of the SPR spectra. The data reported here are acquired at a rate of 50 Hz, the accumulation of 50 spectra composed one data point (1 s time resolution). In comparison, an instrument interrogating the SPR angle by moving the excitation beam cannot achieve such temporal resolution. Otherwise, focusing a beam on the SPR prism requires a lengthy optical path to achieve optimal spectral resolution. Hence, using the dove prism configuration, it is possible to achieve a compact design without compromising the spectral and temporal resolution. The alignment of the optical components is also much simpler compared to a SPR instrument interrogating multiple angles simultaneously. The dove prism simply requires the alignment of the optical components in a single axis, while light must be focused with a precise set of angles with a SPR instrument using the angle interrogation configuration.

A tunable spectral range is beneficial for different applications. Some applications require high-spectral resolution for monitoring the SPR response of low concentration of an analyte with high resolution (i.e. biosensor for a low protein concentration), while other application require a large spectral range to monitor changes in refractive index from bulk composition of the solution. With a multi-wavelength SPR configuration, the spectral range of the SPR instrument depends on the grating utilized in the spectrophotometer. Hence, a grating with a higher groove density will result in a larger spectral resolution, but a smaller refractive index range accessible to the instrument. In a first configuration presented here, a spectrophotometer with a spectral range between 550 nm and 850 nm analyzes the light exiting the SPR instrument. This spectrophotometer results in a refractive index range of the SPR instrument between 1.33 RIU and 1.39 RIU (Fig. 2), which is adequate for most applications with aqueous solutions, such as biosensing. The noise observed on the spectra at wavelengths >750 nm is due to the use of a narrow spectral range LED, emitting between 550 nm and 700 nm. A high power LED (Philips lumiled) is advantageous, resulting in short integration time (20 ms) for a single acquisition, such that multiple acquisitions are accumulated to compose a single spectrum with a reduced noise on the signal. Hence, kinetic data can be obtained at a fast acquisition rate, with a low noise on the measured spectra. In another configuration presented here, the SPR spectra are shown using a spectrophotometer sensitive between 550 nm and 1100 nm (Fig. 2). This longer spectral range is accessible using a halogen lamp and it results in measurable SPR response for solutions comprised between 1.33 RIU and 1.42 RIU. Thus, the range of refractive index accessible to the SPR instrument is tunable with different spectrophotometers. This instrumental configuration results in a single template applicable to different experiments.

The SPR sensor is calibrated to determine the sensitivity for refractive index within the biological realm of refractive indices. The measurement of the SPR response from solutions of varying

refractive index calibrates the SPR sensor for bulk refractive index changes. Fig. 2 shows the SPR spectra for both spectrophotometer configurations with sucrose solutions of increasing concentration, thus of increasing refractive index. A refractometer with an accuracy of 1×10^{-5} RIU accurately measures the refractive index of the sucrose solutions. Sucrose solutions are an appropriate model for refractive index calibration, as sucrose does not interact with the Au surface of SPR sensors [31]. Hence, the response measured with the SPR sensor results uniquely from the refractive index of bulk solution and no contribution is observed from the accumulation of molecules at the surface. Thereby, the sensitivity with the SPR using the dove prism was measured at 1765 ± 100 nm/RIU. A calibration curve for SPR sensors is non-linear for large refractive index changes, as the refractive index sensitivity increases for solutions of higher refractive index. Therefore, the sensitivity reported here, is only valid for the biologically relevant range of refractive indices between 1.33 RIU and 1.35 RIU. The error reported here is for two standard deviations on the regression, calculated using OLLSs regression.

3.2. Data analysis methodologies

SPR sensors respond to refractive index with a shift of the wavelength at which the SPR phenomena occur. Therefore, the data processing methodology used for the determination of the refractive index change must be accurate and sensitive to small changes of spectral position, rather than the intensity as in most spectroscopic applications. Moreover, the noise of the measured response must also be minimized. It is common to use a minimum finding algorithm by mathematically fitting a second-order polynomial to the SPR spectra and determining the minimum from the zero of the derivative of the second-order polynomial (Fig. 3). Otherwise, an algorithm calculating the difference between the intensity of the branches around a set wavelength (λ_0), divided by the sum of the intensity for both branches results in a measurement of the position of the SPR response (Fig. 3). Hence, the algorithm $(a-b)/(a+b)$, where a is the sum of the branch for $\lambda < \lambda_0$, while b is the sum of the branch for $\lambda > \lambda_0$, is sensitive to minute changes of the position of the SPR response. The dynamic range of the algorithm is limited to a SPR shift of less than the width of the peak at half height. Otherwise, the algorithm becomes insensitive to further displacement of the SPR peak. This algorithm is applied to

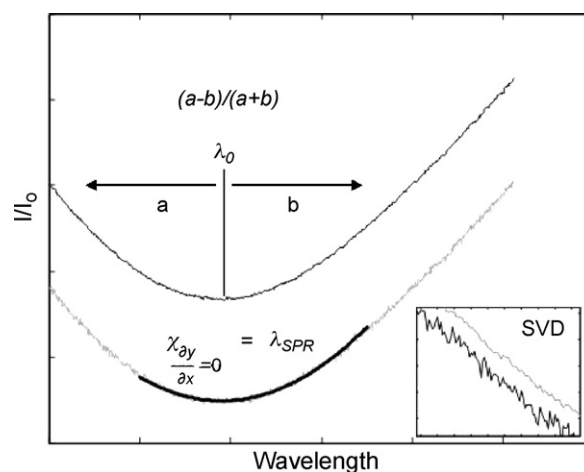


Fig. 3. Data analysis of SPR spectra using minimum hunting (λ_{SPR}) and with the $(a-b)/(a+b)$ algorithm. Singular value decomposition (SVD) and reconstitution with the first few components containing the chemical information is used to reduce the noise on the spectra.

accurately measure the topography with an atomic force microscope. In order to decrease the noise on the SPR spectra, a singular value decomposition of the SPR spectra into its principal components, followed by the reconstitution of the spectrum with the first three components containing the chemical information reduces the noise. In this case, the reconstitution of the SPR spectra with the first three principal components results in no loss of chemical information.

A flow cell was designed to deliver the samples to the SPR sensor using a syringe pump. The syringe pump has variable flow rate between 0.5 mL/min (8.3 μ L/s) to 6.5 mL/min (108 μ L/s). The results presented thereafter were obtained at 16 μ L/s. To measure the reproducibility of the SPR measurement, the SPR sensor is consecutively exposed for 5 min to 18 M Ω water and then for another 5 min to PBS, for a total of four cycles (Fig. 4). The SPR response is reproducible at a wavelength shift of 2.470 ± 0.011 nm between PBS (RI = 1.33498 at 20.00 °C) and water (RI = 1.33316 at 20.00 °C) using the minimum hunting data analysis. Singular value decomposition of the raw SPR spectra and reconstituting of the SPR spectra with the first three components results in a wavelength shift of 2.482 ± 0.021 nm. The errors reported are for two standard deviations on the mean SPR response. Thus, it is observed that denoising SPR spectra with singular value decomposition and reconstituting with the first three components do not alter the SPR response. Using the algorithm $(a-b)/(a+b)$ and singular value decomposition denoising yields a response of 0.0257 ± 0.0002 (unitless). The reproducibility of the flow cell is better than 1% variation ($n=4$) with each data analysis methodologies.

A significant decrease of the noise on the SPR response is observed from denoising the raw SPR spectra with singular value

Table 1

Comparison of data analysis methodologies for flow cell stability and β -lactamase biosensing.

	Minimum hunting	$(a-b)/(a+b)$
<i>Refractive index resolution</i>		
Raw data	3×10^{-6} RIU	9×10^{-7} RIU
SVD	1×10^{-6} RIU	1.5×10^{-7} RIU
<i>β-Lactamase response (700 nM)</i>		
Raw data	0.17 ± 0.03 nm	$6.4 \pm 0.8 \times 10^{-4}$
SVD	0.127 ± 0.005 nm	$4.05 \pm 0.15 \times 10^{-4}$

decomposition. A further decrease of the noise observed on the SPR spectra is observed for data processing using the $(a-b)/(a+b)$ algorithm. The continuous measurement of the SPR response for a water sample with the flow cell is used to calculate the resolution for each data analysis methodologies (Table 1). Two standard deviations on the mean measurement of the SPR response during a 2-min exposure to water at a flow rate of 16 μ L/s and dividing this value by the sensitivity calculates the resolution. Using minimum hunting without singular value decomposition, the resolution on the refractive index measured is 3×10^{-6} RIU. Singular value decomposition denoising the raw spectrum improves the resolution to 1×10^{-6} RIU. Therefore, an improvement by a factor of 3 of the resolution is observed for denoising the data using singular value decomposition with minimum hunting. In comparison, the algorithm $(a-b)/(a+b)$ significantly improves the resolution compared to the minimum hunting algorithm. A resolution of 9×10^{-7} RIU and 1.5×10^{-7} RIU is respectively observed for data processing using $(a-b)/(a+b)$ without denoising and with singular value decomposition denoising.

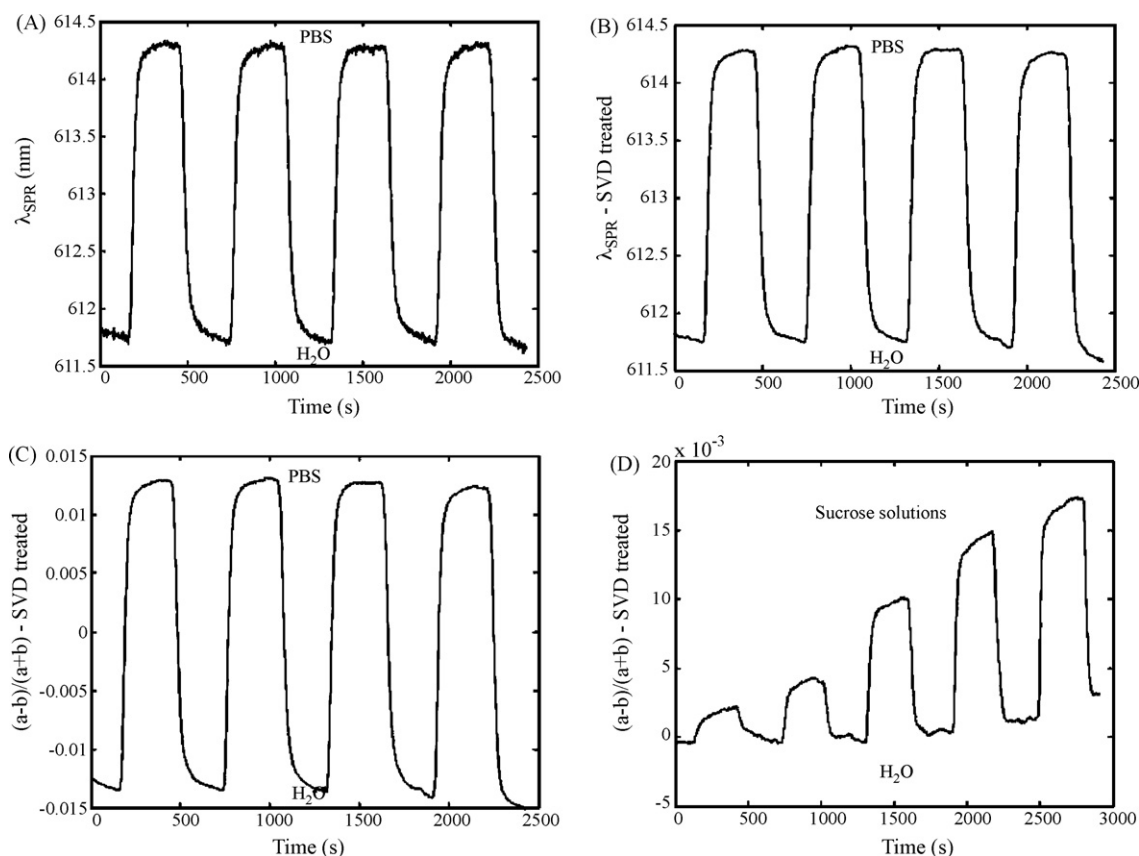


Fig. 4. Repeated measurement of phosphate saline buffer (PBS, 1.33498 RIU) and water (1.33287 RIU): (A) raw data processed with minimum hunting procedure, (B) singular value decomposition of the SPR spectra followed by the minimum hunting procedure, (C) singular value decomposition followed by the $(a-b)/(a+b)$ algorithm, and (D) calibration curve for sucrose solutions (RI ranges between 1.333 RIU and 1.334 RIU), data processed using singular value decomposition followed by the $(a-b)/(a+b)$ algorithm.

Therefore, a greater improvement is observed by denoising the data prior to processing with $(a-b)/(a+b)$ than with denoising prior to the minimum hunting algorithm. This greater improvement on the resolution observed for denoising $(a-b)/(a+b)$ may be due to the methodology of data processing. The main factor limiting the resolution for the minimum hunting procedure is the accuracy of the polynomial fit of the SPR minimum. The random noise on the SPR spectra does not alter significantly the shape of the spectra. Thus, the fit of the second-order polynomial for minimum hunting is only slightly improved by denoising. For the $(a-b)/(a+b)$ algorithm, the resolution is mainly limited by the random noise on the measurement. In this case, the reduction of the noise from random fluctuations on the spectrum significantly impacts the resolution of the SPR response. This results in a greater reduction of the noise and it improves significantly the resolution of the SPR instrument. The resolution in the 10^{-7} RIU range reported here rivals with the best SPR instruments and is adequate for high-resolution SPR biosensing. The resolution were respectively reported for angular interrogation SPR at 5×10^{-7} RIU [7], at 1.4×10^{-6} RIU for fiber optic SPR [13], at approx. 10^{-5} RIU for wavelength interrogation SPR [7,22], and at 5×10^{-5} RIU for intensity measurement SPR (SPR imaging) [7]. The significantly improved resolution obtained with the dove prism SPR instrument compared to other wavelength interrogation instrument is due to the data processing methodology and to a single angle excitation of the SPR phenomena. Some wavelength interrogation techniques do not impinge the SPR sensor at a unique angle. This results in a broader SPR spectrum and it decreases the resolution of other multi-wavelength SPR instruments.

To exhibit the potential to measure solutions with a small refractive index difference, a calibration curve was constructed for sucrose solutions with a refractive index between 1.333 and 1.334 (Fig. 4). Therefore, the difference in refractive index between each sucrose solutions is $<2 \times 10^{-4}$ RIU. As observed, the signal to noise ratio on the SPR response does not approach the limit of detection. The SPR signal measured with $(a-b)/(a+b)$ shows a linear response to refractive index, due to the short range of the calibration curve. The non-linearity of the SPR calibration is significant for refractive index calibration spanning over differences of >0.02 RIU. The sensitivity to refractive index was measured at 12.5 RIU^{-1} with the $(a-b)/(a+b)$ algorithm. The response measured with this data processing algorithm is unitless.

3.3. β -Lactamase biosensing

The SPR instrument was characterized for biosensing with a model biological system. A bioassay for β -lactamase was performed with the immobilization of anti- β -lactamase on a monolayer of N-hydroxysuccinimide ester of NHS-MHA. Immobilization of antibodies to a NHS-MHA monolayer has been demonstrated to maximize sensitivity in a direct bioassay format [34]. β -Lactamase is an appropriate biological model system due to its role in the resistance to traditional antibiotics, a commonly occurring problem in patients. The presence of β -lactamase is one of the most common factors in antibiotic resistance [35]. However, the detection technique for antibiotics resistance still relies on standard microbiological methodologies, increasing the time required to perform the assay and the throughput of the assay for antibiotics resis-

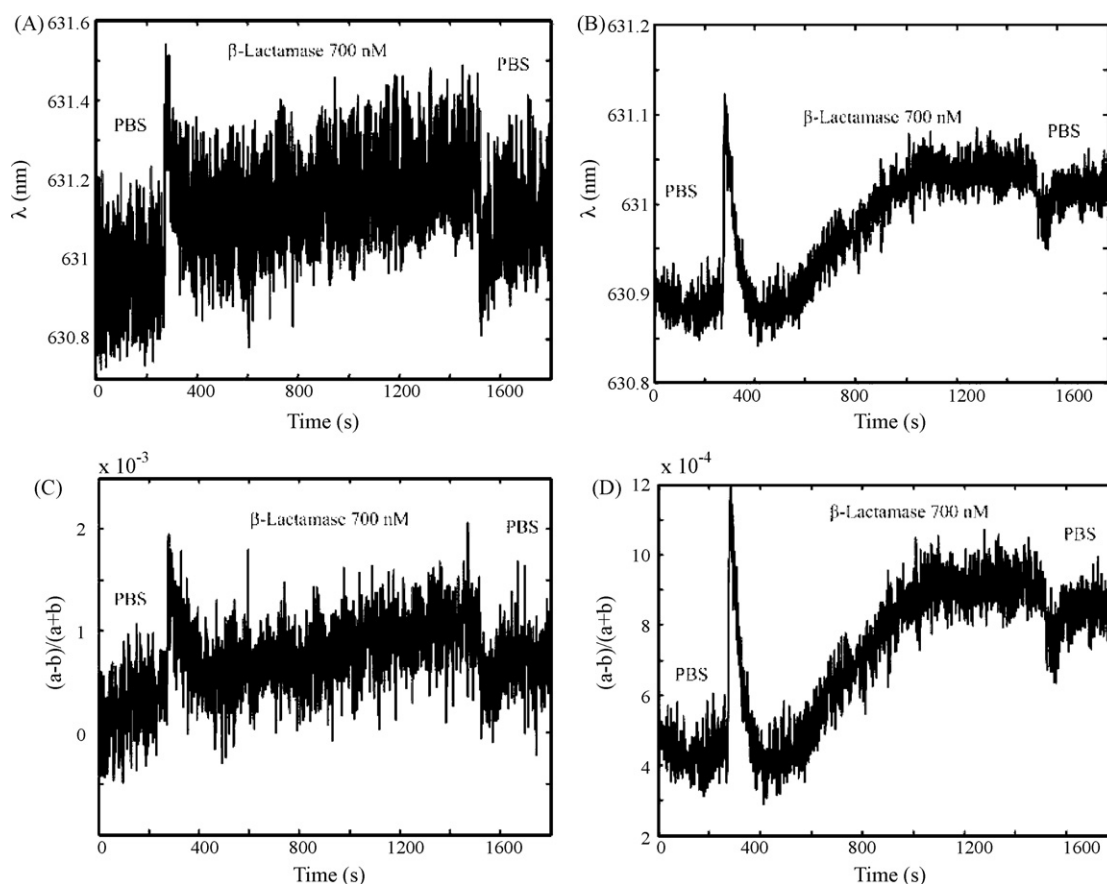


Fig. 5. Measurement of β -lactamase in PBS at μM levels using the dove prism SPR: (A) minimum hunting algorithm (relative error = 21%), (B) minimum hunting algorithm with singular value decomposition (relative error = 3.9%) and (C) $(a-b)/(a+b)$ algorithm (relative error = 13%) and (D) $(a-b)/(a+b)$ algorithm with singular value decomposition (relative error = 3.7%).

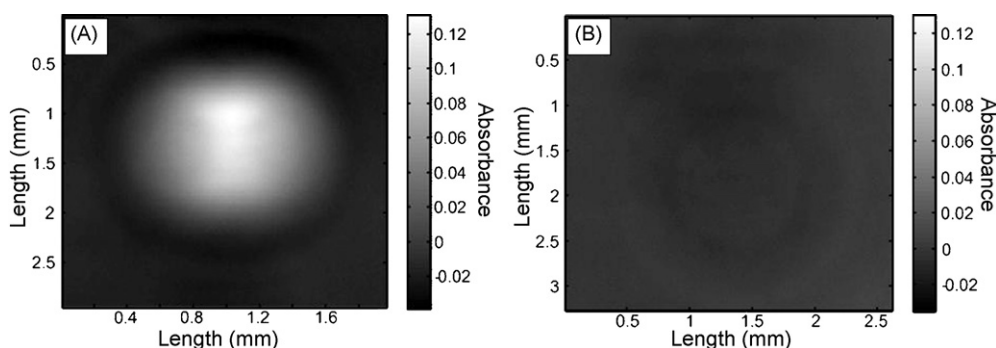


Fig. 6. (A) SPR image of a water droplet on a Au film and (B) total internal reflection image of a water droplet on a glass slide.

tance. Hence, detection of β -lactamase using SPR biosensors would offer improved methodology to quantify β -lactamase compared to actual detection techniques [36].

The detection of β -lactamase was performed in a PBS solution at μM concentration (Fig. 5). β -Lactamase was measured without the flow cell, in a diffusion limited regime. Each methodology investigated was used to process data in a comparative study. A significant improvement of the noise level is observed in the response of the β -lactamase biosensor depending of the data analysis methodology. The binding event of β -lactamase is visually indistinguishable from background noise using the minimum hunting procedure. The change of the SPR response between the PBS measured after β -lactamase binding and from the baseline prior to binding of β -lactamase is 0.17 ± 0.03 nm. The error represents two standard deviations on the mean and a relative error of 21%. Denoising data with singular value decomposition significantly improves the signal to noise ratio. The β -lactamase binding curve is clearly observed following denoising of the SPR spectra analyzed with minimum hunting. The change of the SPR response is then 0.127 ± 0.005 nm, resulting in a significantly reduced relative error at 3.9%. The algorithm $(a-b)/(a+b)$ reduces the noise level on the binding curve of β -lactamase compared to the minimum hunting procedure. The response measured is $6.4 \pm 0.8 \times 10^{-4}$ (unitless) with $(a-b)/(a+b)$. Hence, the relative error is 13%, significantly reduced compared to the minimum hunting procedure. However, this is still too large to observe the binding curve for β -lactamase. Denoising the data with singular value decomposition and analysis with $(a-b)/(a+b)$ reduces the noise to a level equivalent to minimum hunting. The response measured for β -lactamase binding is $4.05 \pm 0.15 \times 10^{-4}$ (unitless). Hence, denoising the SPR spectra also improves the signal to noise of the binding curve with $(a-b)/(a+b)$ and result in a relative error of 3.7%. Measurement of a dynamic process results in a similar relative error between minimum hunting and the $(a-b)/(a+b)$ algorithms. Therefore, it is noted that SVD accounts for the majority of the %R.S.D. improvement for the binding curve of β -lactamase.

3.4. SPR imaging

SPR imaging increases in popularity due to the multiplex array format allowing for the analysis of multiple molecules simultaneously in a single sample. The SPR instrument based on the dove prism can be readily modified to an imaging configuration with the replacement of the collection fiber – spectrophotometer with a bandpass filter and an imaging camera. Thus, a 620 ± 10 nm bandpass filter was mounted between the dove prism and an imaging CCD camera. The collimated light entering the dove prism is inverted through the prism with retention of spatial information. Hence, an image of the SPR surface can be obtained with this con-

figuration of the instrument. As an example, the SPR image of an individual water droplet on the Au surface of the SPR sensor was acquired with this configuration of the SPR instrument (Fig. 6). The image represents an area of approx. 1 cm^2 . The spatial resolution of the image could be improved using telescopic lenses on the collection side to magnify the image on the surface. The absorbance measured for the droplet is 0.12 with SPR imaging. Absorption by water would not account for the feature observed on the SPR image, as confirmed by the absence of an image of a water droplet acquired in identical conditions on a glass slide. Denoising the raw data with singular value decomposition can significantly reduce the noise on the SPR image. In this case, the reconstitution of the SPR image required the use of the first five components to avoid loss of chemical information. With typical SPR spectra (Figs. 2 and 3), the first three components adequately reconstitute the spectra without loss of chemical information. However, a SPR image requires a larger number of components to adequately reconstitute the image.

4. Conclusions

A versatile SPR instrument was designed to perform biosensing with the wavelength interrogation and imaging configurations. The SPR instrument combines low cost and off-the-shelf optical components with high resolution of the measured response. Depending on the data analysis methodology employed to process raw SPR spectra, the resolution varies between 3×10^{-6} RIU and 1.5×10^{-7} RIU. Fitting a second-order polynomial to the SPR spectra results in a resolution lower than using the $(a-b)/(a+b)$ algorithm. Denoising the data with singular value decomposition and reconstitution with the components containing the chemical information improves the resolution by approx. one order of magnitude. Therefore, the combination of $(a-b)/(a+b)$ and denoising with singular value decomposition increases the resolution. Depending on the spectrophotometer employed, the refractive index accessible ranges from 1.33 RIU to 1.39 RIU with a 550–850 nm spectrophotometer and from 1.33 RIU to 1.42 RIU with a 550–1100 nm spectrophotometer. The measurement of repeated injection of PBS is demonstrated with a custom-built flow cell resulting in a reproducibility of the measurement of <1% with the dove prism SPR instrument. A β -lactamase sensor was constructed with anti- β -lactamase immobilized on a NHS-MHA monolayer. Detection of a μM concentration of β -lactamase was performed in saline solution. Finally, the SPR instrument was modified to measure the SPR image of water droplets. It could be ultimately envisioned to locate a beam splitter between the dove prism and collection optics to select on a single platform either the conventional SPR spectroscopy or the SPR imager. Hence, the SPR instrument has the versatility of accomplishing traditional and imaging SPR measurements with high resolution using a single instrumental template.

Acknowledgements

The authors thank Martin Lambert, Louis Beaumont and Yves Teasdale for technical support with construction of elements from the SPR instrument. Financial support was provided by the Université de Montréal, the Fonds Québécois de la Recherche sur la Nature et les Technologies (FQRNT) and the Canadian Foundation for Innovation (CFI).

References

- [1] C.T. Campbell, G. Kim, *Biomaterials* 28 (2007) 2380.
- [2] R.J. Green, R.A. Frazier, K.M. Shakesheff, M.C. Davies, C.J. Roberts, S.J.B. Tendler, *Biomaterials* 21 (2000) 1823.
- [3] W.M. Mullett, E.P.C. Lai, J.M. Yeung, *Methods* 22 (2000) 77.
- [4] J.S. Yuk, K.S. Ha, *Exp. Mol. Med.* 37 (2005) 1.
- [5] J.M. Brockman, B.P. Nelson, R.M. Corn, *Annu. Rev. Phys. Chem.* 51 (2000) 41.
- [6] J. Homola, *Anal. Bioanal. Chem.* 377 (2003) 528.
- [7] J. Homola, S.S. Yee, G. Gauglitz, *Sensor Actuat. B-Chem.* 54 (1999) 3.
- [8] K.S. Phillips, Q. Cheng, *Anal. Bioanal. Chem.* 387 (2007) 1831.
- [9] B.K. Lavine, D.J. Westover, L. Oxenford, N. Midankar, N. Kaval, *Microchem. J.* 86 (2007) 147.
- [10] G. Neuert, S. Kufer, M. Benoit, H.E. Gaub, *Rev. Sci. Instrum.* 76 (2005).
- [11] A. Hemmi, T. Imato, Y. Aoki, M. Sato, N. Soh, Y. Asano, C. Akasaka, S. Okutani, S. Ohkubo, N. Kaneki, K. Shimada, T. Eguchi, T. Oinuma, *Sensor Actuat. B-Chem.* 108 (2005) 893.
- [12] A.N. Naimushin, S.D. Soelberg, D.U. Bartholomew, J.L. Elkind, C.E. Furlong, *Sensor Actuat. B-Chem.* 96 (2003) 253.
- [13] T. Akimoto, S. Wada, I. Karube, *Anal. Chim. Acta* 610 (2008) 119.
- [14] D.J. Gentleman, K.S. Booksh, *Talanta* 68 (2006) 504.
- [15] T.M. Battaglia, J.F. Masson, M.R. Sierks, S.P. Beaudoin, J. Rogers, K.N. Foster, G.A. Holloway, K.S. Booksh, *Anal. Chem.* 77 (2005) 7016.
- [16] J.F. Masson, T.M. Battaglia, P. Khairallah, S. Beaudoin, K.S. Booksh, *Anal. Chem.* 79 (2007) 612.
- [17] J.F. Masson, L. Obando, S. Beaudoin, K. Booksh, *Talanta* 62 (2004) 865.
- [18] R. Slavik, J. Homola, E. Brynda, *Biosens. Bioelectron.* 17 (2002) 591.
- [19] J.F. Masson, Y.C. Kim, L.A. Obando, W. Peng, K.S. Booksh, *Appl. Spectrosc.* 60 (2006) 1241.
- [20] Y.C. Kim, J.F. Masson, K.S. Booksh, *Talanta* 67 (2005) 908.
- [21] Y.C. Kim, S. Banerji, J.F. Masson, W. Peng, K.S. Booksh, *Analyst* 130 (2005) 838.
- [22] I. Stemmler, A. Brecht, G. Gauglitz, *Sensor Actuat. B-Chem.* 54 (1999) 98.
- [23] X.J. Zhao, Z. Wang, Y. Mu, H.Q. Zhang, Q.H. Jin, *Lab. Robot. Automat.* 12 (2000) 104.
- [24] S.D. Evans, H. Allinson, N. Boden, T.M. Flynn, J.R. Henderson, *J. Phys. Chem. B* 101 (1997) 2143.
- [25] C.E. Jordan, R.M. Corn, *Anal. Chem.* 69 (1997) 1449.
- [26] C.E.H. Berger, T.A.M. Beumer, R.P.H. Kooyman, J. Greve, *Anal. Chem.* 70 (1998) 703.
- [27] J.B. Beusink, A.M.C. Lokate, G.A.J. Besselink, G.J.M. Pruijn, R.B.M. Schasfoort, *Biosens. Bioelectron.* 23 (2008) 839.
- [28] B.K. Singh, A.C. Hillier, *Anal. Chem.* 78 (2006) 2009.
- [29] G. Klenkar, R. Valiokas, I. Lundstrom, A. Tinazli, R. Tampe, J. Piehler, B. Liedberg, *Anal. Chem.* 78 (2006) 3643.
- [30] T.M. Chinowsky, L.S. Jung, S.S. Yee, *Sensor Actuat. B-Chem.* 54 (1999) 89.
- [31] D.J. Gentleman, L.A. Obando, J.F. Masson, J.R. Holloway, K.S. Booksh, *Anal. Chim. Acta* 515 (2004) 291.
- [32] K. Johansen, R. Stalberg, I. Lundstrom, B. Liedberg, *Meas. Sci. Technol.* 11 (2000) 1630.
- [33] N.J. Tao, S. Boussaad, W.L. Huang, R.A. Arechabaleta, J. D'Agnese, *Rev. Sci. Instrum.* 70 (1999) 4656.
- [34] J.F. Masson, T.M. Battaglia, J. Cramer, S. Beaudoin, M. Sierks, K.S. Booksh, *Anal. Bioanal. Chem.* 386 (2006) 1951.
- [35] D.M. Livermore, *Clin. Microbiol. Rev.* 8 (1995) 557.
- [36] R.H. Yolken, W.T. Hughes, P.J. Stoppa, *J. Pediatr.* 97 (1980) 715.



Bioaerosols chemometric characterization by laser-induced fluorescence: Air sample analysis

Susana Cabredo^{a,*}, Alejandro Parra^a, Cecilia Sáenz^a, Jesús Anzano^b

^a Chemistry Department (Analytical Chemistry Area), University of La Rioja, C/ Madre de Dios 51, 26006 Logroño (La Rioja), Spain

^b Laser Laboratory, Analytical Chemistry Department, Faculty of Sciences, University of Zaragoza, C/ Pedro Cerbuna 12 (Edif. D), 50009 Zaragoza, Spain

ARTICLE INFO

Article history:

Received 24 July 2008

Accepted 17 October 2008

Available online 31 October 2008

Keywords:

Bioaerosol

Laser-induced fluorescence

Air analysis

Linear discriminant analysis

ABSTRACT

A laser-induced fluorescence (LIF) system was optimized using a solution of *Micrococcus luteus* in ethanol/water 50% (v/v) to obtain spectra in the gas phase of 46 bioaerosols. Experimental designs such as Plackett–Burman and factorial design were applied. The fluorescence spectra were treated chemometrically by principal component analysis, linear discriminant analysis and hierarchical cluster analysis to classify the microorganisms according to family, morphology and gram. The best results were obtained using LDA. The method was applied to air samples and the LIF results allowed to characterize bioaerosols reliability. The robustness of the technique was demonstrated by the identification of many bacteria.

© 2008 Elsevier B.V. All rights reserved.

1. Introduction

The increasing importance of aerosols, taking into consideration both environmental processes and the use of aerosol technologies, has generated great interest in aerosol characterization [1]. Different classical techniques have been applied successfully to the chemical characterization of aerosols [2–5]. The simple presence of fluorescence can be used to differentiate between biological and non-biological particles and individual particle spectra can give information more detail [6]. LIF was described in a previous paper for obtaining bacteria spectra in the liquid phase and a small bacteria fluorescence spectra collection was presented [7].

Other attractive laser techniques for on-line and in situ detection of aerosols have been developed: matrix-assisted laser desorption/ionization (MALDI) for individual airborne biomolecule containing particles detected and characterized in real-time [8]; time of flight mass spectrometry (MALDI TOF-MS) [9–10]; laser imaging detection and ranging (LIDAR) [11]; laser-induced breakdown spectrometry (LIBS) [12–14], including a comparison between LIBS and TOF-MS [15] (flow cytometry (FCM) [16,17] and surface-enhanced Raman spectroscopy (SERS) [18]).

Applications in the detection of pathogens in hospitals [19], in the degradation of biological weapon agents in the environment and in bioterrorism response are other important applications of bioaerosol analysis [20].

Real-time continuous monitoring of airborne microorganisms is becoming increasingly important. Evaluation using ultraviolet aerodynamic particle sizer spectrometers (UV-APS), sometimes called fluorescent aerodynamic particle sizer (FLAPS) for real-time continuous monitoring of bioaerosols, was applied in two types of aerosols: bacterial (e.g. *Bacillus subtilis* spores or vegetative cells, and *Pseudomonas fluorescens*); non-bacterial (e.g. NaCl, latex, peptone water, and nutrient agar/broth) [21]. Counting efficiency of the fluorescent particles was shown to depend on particle concentration with the upper limit of detection of the UV-APS [22] approximately 6×10^7 particles/m³. UV-APS was used to measure size distribution and concentration of biological and total particles inside the swine housing and at several outdoor locations [23]. In this line, simultaneous light scattering and intrinsic fluorescence measurements for bioaerosol detection enabled a substantially enhanced view of the discrimination of biological aerosols [24]. Ho et al. [25] showed that FLAPS technology permits measurement of fluorescence signals from single particles in an aerosol.

These references show the need for suitable methodology for classifying bioaerosols. The experimental designs applied in this study were the Plackett–Burman design and the 2^k factorial design using central composite design. The chemometric techniques used for the classification of data were principal component analysis, linear discriminant analysis and hierarchical cluster analysis [26,27].

In this study, we optimized the measurement system, using the experimental design, first the Plackett–Burman design and then factorial analysis. Once the system had been optimized, several bacteria fluorescence spectra were obtained, such as *Escherichia*

* Corresponding author. Tel.: +34 941 299 625.

E-mail address: susana.cabredo@unirioja.es (S. Cabredo).

coli, *Lactobacillus hilgardii*, *Micrococcus luteus*, *Staphylococcus epidermidis*, etc.

2. Experimental

2.1. Materials

The experimental setup (except the bioaerosol generator) developed for this study is schematically shown in a previous paper [7].

2.2. Instrumentation

Excimer laser $\lambda = 351$ nm (Lambda-Physik, Model Compex201), Coherent Lambda Physik GmbH, Hans-Böckler-Straße 12, D-37079 Göttingen, Germany. Dye laser $\lambda = 569$ –608 nm (Lambda-Physik, Model ScanMate2). Aerosol generator, Topas Aerosol generator ATM225, Topas GmbH, Wilischstr. 1, D-01279 Dresden, Germany. Monochromator, Bentham Instruments, Mod. TM300, 3 gratings: 2400 lines/mm, 1200 lines/mm, 600 lines/mm, Bentham Instruments Ltd., 2 Boulton Road, Reading, Berkshire RG2 0NH, UK. CCD detector, Andor Technologies DV401-UV. MARCONI CCD30-11 256×1024 pixels $26 \mu\text{m}^2$ 7 Millennium Way, Springvale Business Park, Belfast BT12 7AL, Northern Ireland. Luminometer from PerkinElmer Model LS50. Dekati Impactor (Dekati Ltd., Finland).

2.3. Laser spectroscopy material

Frequency doubler (Lambda-Physik), SHG-Crystal BBOI (295–220 nm), Coherent Lambda Physik GmbH, Hans-Böckler-Straße 12, D-37079 Göttingen, Germany. Two mirrors to collect disperse fluorescent radiation. Newport, reference 10D10AL2, 1791 Deere Avenue, Irvine, CA 92606, USA. Lens to focalize fluorescent radiation before monochromator, Newport, reference SBX022. Two microscope lens to focalize answer signal, $3.2^\circ/0.06^\circ$ ∞ –A and $10^\circ/0.20^\circ$ ∞ –A, Carl Zeiss Jena GmbH, Carl-Zeiss-Promenade 10, 07745 Jena. Cut-off filters, reference 35-5321-000, Coherent and reference 117303 Schott glass.

2.4. Chemicals

Dye, Rodamina 6G, Radiant Dyes Laser Accessories GMBH, Friedrichstrasse 58, 42929 Wermelskirchen, Germany. Ethanol, methanol and cetone, Panreac, Barcelona, Spain. Ultrapure water from Milli-Q, Millipore, Bedford, USA.

2.5. Biologicals

Bacteria from Spanish Collection of Types Cultures (CECT) and Area of Biochemistry and Molecular Biology of University of La Rioja, Spain. *Acetobacter pasteurianus*, C-658, IS-289; *B. subtilis*, var. *Niger*, CECT-38, C-262, C263; *Enterococcus avium*, Z-382; *Enterococcus faecalis*, Z-363, Z-397; *Enterococcus faecium*, Z-2, Z-187, Z-229, Z-357, Z-415; *Enterococcus hirae*, Z-314, Z-331, Z-362; *E. coli* Co-15, Co-32, C-408; *Gluconobacter oxydans*, C-657, I-40; *L. hilgardii*, J-81; *Lactobacillus fermentum*, C-533; *Lactobacillus plantarum*, J-21, J-34, J-39, J-61, J-63, J-71, J-73; *Lactococcus lactis*, C-144, C-534; *Leuconostoc mesenteroides*, J-47; *M. luteus*, C-157; *Oenococcus oeni*, IS-18; *Pediococcus acidilactici*, IS-111; *Pediococcus pentosaceus*, C-711, J-27, R-7; *Staphylococcus aureus*, Sa-2, Sa-28; *S. epidermidis*, Sa-46, Sa-41, Sa-8; *Staphylococcus simulans*, Sa-17.

2.6. Softwares

CCD software: Andor Technology, named Andor MCD, vers. 2.62 I2C, 7 Millennium Way, Springvale Business Park, Belfast, BT12 7AL, Northern Ireland. ORIGIN 6.0, OriginLab Corporation, One Roundhouse Plaza, Suite 303, Northampton, MA 01060, USA. STAT-GRAPHICS, version Plus 4.0; Manugistics, Inc., Rockville, MA, USA. SPSS 12.0, SPSS Inc., Chicago, IL, USA.

2.7. Samples

The air samples were obtained from the Chemistry Building of the University of La Rioja using a Dekati impactor with Petri dishes containing Brain Heart Infusion broth (BHI); seven samples were taken using this system and three samples by natural impact. All samples were incubated for 24 h, then 26 colonies were selected and carried to ethanol/water solution (50%) using a sterilized platinum handle. Finally, these solutions were analyzed by the proposed method.

2.8. Procedure

The experimental procedure to obtain the fluorescence spectra of bioaerosols in the gas phase was as follows. *M. luteus* culture from *M. luteus* C-157 bacterium was used. The bacterium was cultured in agar-TSI for 24 h in a 37°C oven, and then solved in a 50% (v/v) ethanol–water mixture. The solution was about 9×10^8 colony-forming units per millilitre (cfu/mL) and was used to calibrate the system. The solution was placed in an aerosol generator working at 300 L/h, previously prepared with 50% ethanol–water solution, and when the laser system was OK, aerosol generator was switched on.

A laser excimer was used at approximately 24 mJ, with a 10 Hz replate; laser radiation across the dye laser and frequency doubler (dye was Rhodamine 6G) and final laser radiation were 290 nm, 10 Hz and $300 \mu\text{J/pulse}$. This radiation strikes the bacterial aerosol and fluorescence radiation is collected with a lens and across two filters (-295 nm and $+540$ nm), it crosses a monochromator with a 600 lines/mm grating, and is measured with a CCD at 10°C . CCD software was used to measure this fluorescence with 300 accumulations at 0.5 s per accumulation. The results were saved using the CCD software and the spectra treated with Origin software.

3. Results and discussion

3.1. Previous studies

In a previous study [7], the spectra of certain bacteria were obtained in liquid phase using LIF. However, when working with bioaerosols instead of liquid samples, the measurement system had to be redesigned and different variables considered. In this case, the selected variables were: type of solvent, bacteria concentration (cfu/mL), aerosol volume, monochromator slit, number of accumulations, exposure time, CCD temperature, laser energy, laser frequency, filters, mirrors and lens.

Bearing in mind this prior experience and the consulted bibliography, the above-mentioned variables were defined before proceeding with chemometric optimization.

The tested solvents were water, water–ethanol (50%), water–methanol (50%) and acetone. No signal was obtained with water and acetone; however similar results were obtained with the two mixtures, so water–ethanol (50%) was selected. The concentration of bacteria corresponded to McFarland patterns, between 2 and 5. The flow of aerosol was limited to between

Table 1
Variables used for the chemometric study.

1	2	3	4	5	6	7	8	9	10
Bacteria	Bac	Morphology	Family/order	Gram	1	2	3	4	331.824 nm
<i>Bacillus subtilis</i> CECT38	BS	<i>bacillus</i>	Spore-type bacillus	+	1	1	1	1	8165.177
<i>B. subtilis</i> C262	BS	<i>bacillus</i>	Spore-type bacillus	+	1	1	1	1	2987.659
<i>B. subtilis</i> C263	BS	<i>bacillus</i>	Spore-type bacillus	+	1	1	1	1	4362.283
<i>Enterococcus faecalis</i> Z397	EF	<i>coccus</i>	Enterococcus	+	2	2	2	1	6017.780
<i>Enterococcus faecium</i> Z415	EFA	<i>coccus</i>	Enterococcus	+	3	2	2	1	6784.515
<i>E. faecium</i> Z187	EFA	<i>coccus</i>	Enterococcus	+	3	2	2	1	3273.992
<i>E. faecium</i> Z2	EFA	<i>coccus</i>	Enterococcus	+	3	2	2	1	2158.737
<i>E. faecium</i> Z229	EFA	<i>coccus</i>	Enterococcus	+	3	2	2	1	9416.179
<i>Escherichia coli</i> Co15	EC	<i>bacillus</i>	Enterobacteria	–	4	1	4	2	4967.539
<i>Lactobacillus hilgardii</i> J81	LH	<i>bacillus</i>	Lactic bacteria	+	5	1	4	1	7536.789
<i>Lactobacillus plantarum</i> J39	LP	<i>bacillus</i>	Lactic bacteria	+	6	1	4	1	5755.976
<i>L. plantarum</i> J21	LP	<i>bacillus</i>	Lactic bacteria	+	6	1	4	1	5432.108
<i>L. plantarum</i> J61	LP	<i>bacillus</i>	Lactic bacteria	+	6	1	4	1	1375.808
<i>L. plantarum</i> J63	LP	<i>bacillus</i>	Lactic bacteria	+	6	1	4	1	715.056
<i>Lactococcus lactis</i> C144	LL	<i>bacillus</i>	Lactic bacteria	+	7	1	4	1	5560.184
<i>Leuconostoc mesenteroides</i> J47	LM	<i>coccus</i>	Lactic bacteria	+	8	2	4	1	4661.333
<i>Micrococcus luteus</i> C157	ML	<i>coccus</i>	Staphylococcus	+	9	2	5	1	4242.548
<i>Oenococcus oeni</i> IS18	OO	<i>coccusbacillus</i>	Lactic bacteria	+	10	3	4	1	4009.219
<i>Pediococcus pentosaceus</i> R7	PP	<i>coccus</i>	Lactic bacteria	+	11	2	4	1	5852.257
<i>Staphylococcus epidermidis</i> Sa41	SE	<i>coccus</i>	Staphylococcus	+	12	2	5	1	3504.366
<i>Enterococcus hirae</i> Z314	EH	<i>coccus</i>	Enterococcus	+	15	2	2	1	3885.559
<i>E. hirae</i> Z331	EH	<i>coccus</i>	Enterococcus	+	15	2	2	1	6925.606
<i>Acetobacter pasteurianus</i> IS289	AP	<i>bacillus</i>	Acetic bacteria	–	13	1	6	2	5383.991
<i>A. pasteurianus</i> C658	AP	<i>bacillus</i>	Acetic bacteria	–	13	1	6	2	947.844
<i>Enterococcus avium</i> Z382	EA	<i>coccus</i>	Enterococcus	+	14	2	2	1	4556.340
<i>E. coli</i> Co15	EC	<i>bacillus</i>	Enterobacteria	–	4	1	3	2	5145.026
<i>E. coli</i> Co32	EC	<i>bacillus</i>	Enterobacteria	–	4	1	3	2	3775.709
<i>E. coli</i> C408	EC	<i>bacillus</i>	Enterobacteria	–	4	1	3	2	5725.794
<i>E. faecalis</i> Z363	EF	<i>coccus</i>	Enterococcus	+	2	2	2	1	12285.43
<i>E. faecium</i> Z357	EFA	<i>coccus</i>	Enterococcus	+	3	2	2	1	3768.973
<i>E. hirae</i> Z362	EH	<i>coccus</i>	Enterococcus	+	15	2	2	1	6499.992
<i>Gluconobacter oxydans</i> 140	GO	<i>bacillus</i>	Acetic bacteria	–	16	1	6	2	6255.509
<i>G. oxydans</i> C657	GO	<i>bacillus</i>	Acetic bacteria	–	16	1	6	2	599.447
<i>Staphylococcus aureus</i> Sa28	SA	<i>coccus</i>	Staphylococcus	+	17	2	5	1	2920.472
<i>S. aureus</i> Sa2	SA	<i>coccus</i>	Staphylococcus	+	17	2	5	1	2415.954
<i>S. epidermidis</i> Sa46	SE	<i>coccus</i>	Staphylococcus	+	12	2	5	1	3096.449
<i>S. epidermidis</i> Sa8	SE	<i>coccus</i>	Staphylococcus	+	12	2	5	1	1446.684
<i>Staphylococcus simulans</i> Sa17	SS	<i>coccus</i>	Staphylococcus	+	18	2	5	1	1187.259
<i>Pediococcus acidilactici</i> IS111	PA	<i>coccus</i>	Lactic bacteria	+	20	2	4	1	1495.380
<i>P. pentosaceus</i> J27	PP	<i>coccus</i>	Lactic bacteria	+	11	2	4	1	2029.947
<i>L. plantarum</i> J34	LP	<i>bacillus</i>	Lactic bacteria	+	6	1	4	1	1784.243
<i>Lactobacillus fermentum</i> C533	LF	<i>bacillus</i>	Lactic bacteria	+	19	1	4	1	2112.879
<i>L. lactis</i> C534	LL	<i>bacillus</i>	Lactic bacteria	+	7	1	4	1	1924.685
<i>P. pentosaceus</i> C711	PP	<i>coccus</i>	Lactic bacteria	+	11	2	4	1	2893.541
<i>L. plantarum</i> J71	LP	<i>bacillus</i>	Lactic bacteria	+	6	1	4	1	3529.694
<i>L. plantarum</i> J73	LP	<i>bacillus</i>	Lactic bacteria	+	6	1	4	1	7270.688

200 and 300 L/h, the maximum permitted by the equipment. The monochromator slit was adjusted to between 0.85 and 1 cm. The larger the number of accumulations, better the spectrum, although this increased analysis time and therefore 200 and 300 accumulations were selected. Exposure time referred to the time the CCD was gathering data and was limited to between 0.1 and 0.5 s. Contradictory results seemed to be obtained when studying CCD temperature, since a better spectrum was obtained at 10 °C than at a lower temperature. The temperature interval was between –10 °C and 10 °C. The energy and frequency of the excimer laser was modified between 24 and 40 mJ, and between 1 and 10 Hz, respectively. The filters (two cut-off filters, +540 and –295 nm), mirrors and lens variables referred to the presence or absence of these optical elements for gathering fluorescent radiation.

3.2. Optimization

To optimize all the variables mentioned previously, a chemometric study was performed to consider the possible interactions between variables. The Statgraphics program was used. The Plackett–Burman experiment was designed first and its variables

and levels are as follow: filters (0 and 2), mirrors (0 and 2), lens (Newport and microscope), laser energy (24 and 40 mJ), frequency (1 and 10 Hz), aerosol flow (200 and 300 L/h), CCD temperature (–10 °C and 10 °C), number of accumulations (200 and 300), exposition time (0.1 and 0.3 s), slit (0.85 and 1 cm) and bacteria concentration (McFarland 2 and 5).

Four responses were used to design the experiments: Resp 1 (area) corresponded to the fluorescence spectrum area calculated using the Origin program; Resp 2 (number of peaks) was the number of peaks in the fluorescence spectrum; Resp 3 (quality of peaks), the degree of definition of the peaks, scored between 1 and 10, according to our personal appreciation; and Resp 4 (overall quality) corresponded to spectrum quality, also scored between 1 and 10.

The results showed that the most significant variables were: CCD temperature, number of accumulations, exposure time and slit opening. Next, a factorial 2⁴ design was selected with a central point and two replicas, giving a total of 51 experiments, which were performed at random.

After optimization, a dessicator coupled to the aerosol generator was purchased, which eliminated 60% of the solvent. The

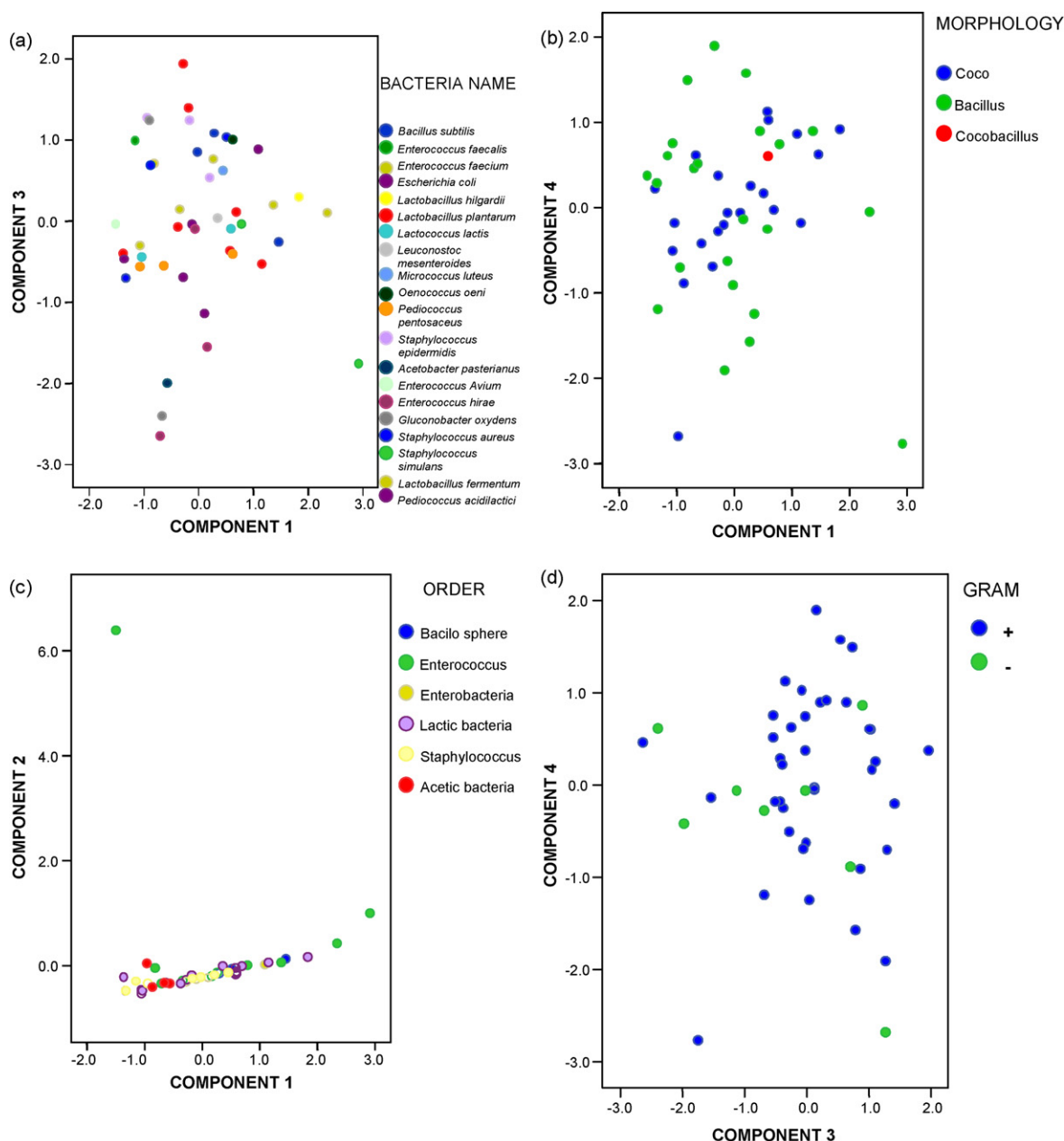


Fig. 1. Projections of the objects on the plot defined by two principal components: (a) PC1 vs PC3 according to bacteria name, (b) PC1 vs PC4 according to morphology, (c) PC1 vs PC2 according to order and (d) PC3 vs PC4 according to gram.

fluorescence spectra improved, despite having to work at 240 L/h instead of 300.

The final optimization results are: two cut-off filters (+540 and –295 nm), no mirrors, a Newport lens, 100 μ J/pulse as laser final energy, 10 Hz, 300 L/h as flow aerosol, 10 °C as CCD temperature, 300 accumulations, 0.5 s as exposition time and 0.85 cm as slit monochromator.

3.3. Bioaerosol fluorescence spectra

The optimized system was used to obtain the fluorescence spectra of the different standard bioaerosols. In all cases, a blank and three replicates of each bioaerosol were performed: *A. pasteurianus*, C-658, IS-289; *B. subtilis*, var. *Niger*, CECT-38, C-262, C263; *E. avium*, Z-382; *E. faecalis*, Z-363, Z-397; *E. faecium*, Z-2, Z-187, Z-229, Z-357, Z-415; *E. hirae*, Z-314, Z-331, Z-362; *E. coli* Co-15, Co-32, C-408; *G.*

oxydens, C-657, I-40; *L. hilgardii*, J-81; *L. fermentum*, C-533; *L. plantarum*, J-21, J-34, J-39, J-61, J-63, J-71, J-73; *L. lactis*, C-144, C-534; *L. mesenteroides*, J-47; *M. luteus*, C-157; *O. oeni*, IS-18; *P. acidilactici*, IS-111; *P. pentosaceus*, C-711, J-27, R-7; *S. aureus*, Sa-2, Sa-28; *S. epidermidis*, Sa-46, Sa-41, Sa-8; *S. simulans*, Sa-17.

The data obtained were exported to Origin, where they were adapted for comparison purposes, before being introduced in the SPSS program together with the known information for the bacteria. Table 1 shows the variables used. Column 1: name; column 2: initials; column 3: morphology; column 4: order or family; column 5: gram; columns 6–9: numerical encoding of the information in columns 2–5; columns 10–462: intensity of fluorescence at each wavelength.

The aim was to determine whether these bacteria could be classified by Name, Morphology, Family or Gram using their respective fluorescence spectra.

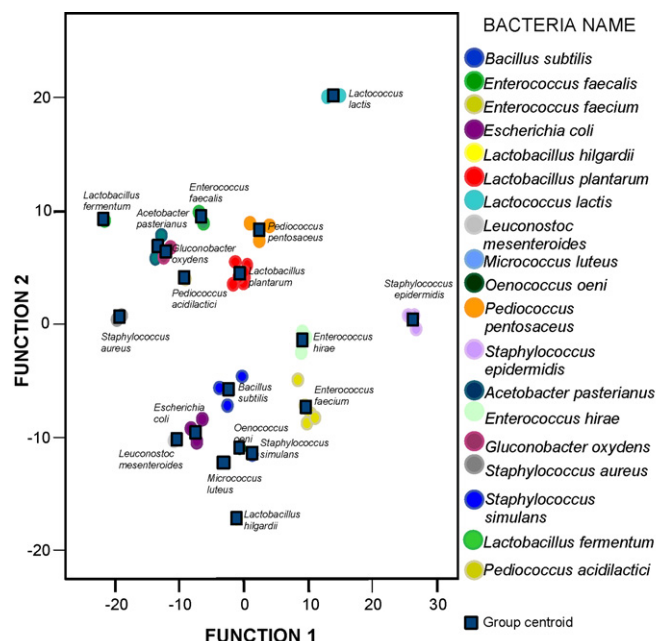


Fig. 2. Plot of the samples on the plane defined by the two first canonical discriminant functions according to the name of the bacteria.

3.4. Chemometric tools

After introducing the data from the above-mentioned table in the SPSS program, three chemometric tools were tested: principal component analysis (PCA), hierarchical cluster analysis (HCA) and linear discriminant analysis (LDA).

3.4.1. Principal component analysis

PCA was employed with each classification, i.e. name, morphology, family and gram parameter of the bacteria. During the analysis, four principal components were obtained (they accounted for 98.417% of the variance). The other components were not con-

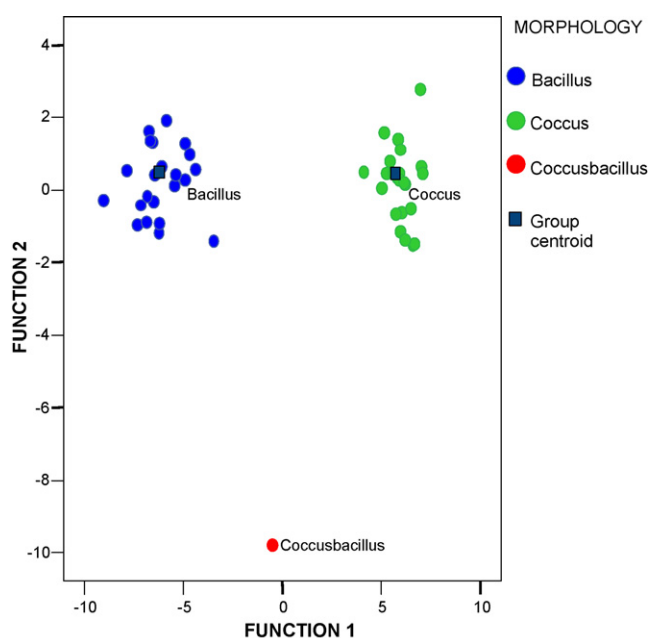


Fig. 3. Plot of the samples on the plane defined by the two first canonical discriminant functions according to morphology.

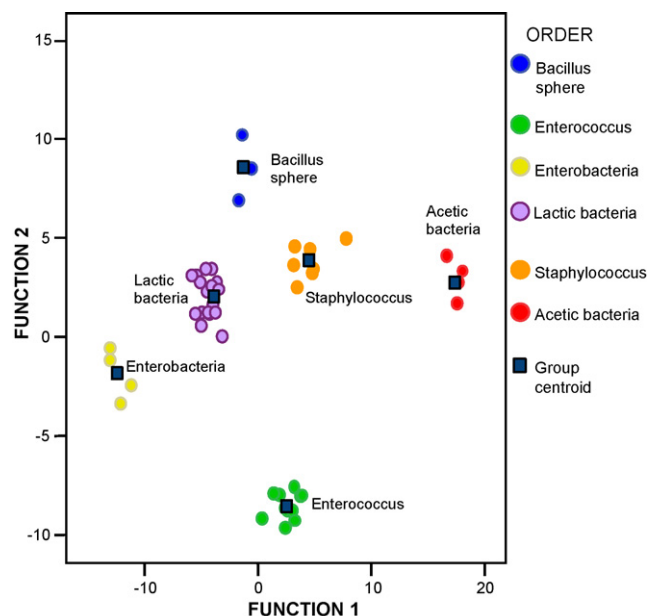


Fig. 4. Plot of the samples on the plane defined by the two first canonical discriminant functions according to family.

sidered. The scores were calculated from the principal components equations obtained.

All the possible graphic representations were made among the different components for all the classification parameters. Fig. 1 shows some examples of the projections of the objects of the plane defined by several pairs of principal components: (1a) name of the bacteria; (1b) morphology of the bacteria; (1c) family of the bacteria; (1d) gram.

As can be observed, the classification was incorrect because the points on the graphs were not grouped according to the encoded values, but rather mixed with one another. Therefore, the PCA cannot be used to classify these bacteria by name, morphology, family or gram.

3.4.2. Hierarchical cluster analysis

A hierarchical cluster analysis was performed in order to determine whether the objects of the data set could be divided in two groups. Based on the obtained results, the classification was incorrect in all cases. Therefore, HCA demonstrates that the selected variables have not sufficient explanatory power to differentiate the samples.

3.4.3. Linear discriminant analysis

As it is known, this technique is a widespread parametric method where objects are classified into either of a number of defined classes. The corresponding discriminant functions were calculated and, in all cases, the graphical representation of the samples in the plane defined by the first two discriminant functions was drawn.

Fig. 2 shows the classification according to the Name of the bacteria. Bacterium 14 – *E. avium* – was eliminated. Although there was a certain degree of grouping, it can be seen that the classification was not altogether correct.

Fig. 3 shows the classification according to morphology. Clearly, three differentiated groups were formed; hence, the classification was correct.

Fig. 4 shows the classification by family. Six well-differentiated groups were observed, indicating that this technique was appropriate for classifying the bacteria according to their family.

As regards the classification of bacteria by gram, no graph can be shown because there was only one discriminant function. The

classification results were as follow: of the 46 samples studied, 38 were classified as gram + and 8 as gram –, coinciding 100% with the true identity.

The conclusion that can be drawn from the results obtained by LDA is that a correct classification of bacteria was obtained by morphology, family and gram, but not by name.

3.5. Air samples

Air samples were taken at 10 locations in the Chemistry Building of the University of La Rioja. The samples were obtained by either natural impact or instrumental impact (Dekati Impactor) on Petri dishes with BHI as culture medium. Three samples were obtained by natural impact (3 h, 4 h and 24 h) and seven samples using the impactor (30 min or 1 h). Once the samples had been gathered, these dishes were cultured for 24 h and then 26 colonies were selected in total (one was discarded because it was a yeast). These colonies were isolated, cultured once again, and finally analyzed using bioaerosol generation-LIF.

The fluorescence spectra intensity values were introduced in the SPSS-LDA and very good results were obtained. When classifying by morphology, the program achieved a 100% classification in 23 of the 25 samples; it classified one sample as bacillus (94.76%) and another as coccus (77.57%). By family, the program classified correctly 22 of the 25 samples; in one case, it classified one sample as acetic bacterium (79.25%) and as lactic bacterium (20.75%); in other case, identified the sample as *Staphylococcus* (98.86%) and another sample as spore-type bacillus (78.51%), as *Staphylococcus* (16.92%) and as lactic bacteria (4.57%). Finally, as regards the classification by gram, the classification was correct in all cases except one, which the program classified as gram (95.97%).

To conclude we may say that the proposed model (bioaerosol fluorescence spectra by LIF and LDA) is very adequate for determining the form, family and gram of bacteria in airborne samples.

Acknowledgments

Government of Spain, Ministerio de Educación y Ciencia (project REN2002-01439/CLI), University of La Rioja (projects API-02/07,

API-03/07, API-04/05), Government of La Rioja (project ANGI 2001/36). Special thanks to Dra. Carmen Torres research group from the University of La Rioja. This work has not been possible without the advices and the collaboration of Professors Jim Winefordner, Ben Smith and Nico Omenetto from the University of Florida (Gainesville, FL, USA).

References

- [1] R.E. Clement, P.W. Yang, C.J. Koester, Anal. Chem. 73 (2001) 2761.
- [2] H. Chuang, P. Macuch, M.B. Tabacco, Anal. Chem. 73 (2001) 462.
- [3] D.N. Stratis-Cullum, G.D. Griffin, J. Mobley, A.A. Vass, T. Vo-Dinh, Anal. Chem. 75 (2003) 275.
- [4] J.W. Chan, A.P. Esposito, C.E. Talley, C.W. Hollars, S.M. Lane, T. Huser, Anal. Chem. 76 (2004) 599.
- [5] M.T. McBride, D. Masquelier, B.J. Hindson, A.J. Makarewicz, S. Brown, K. Burris, T. Metz, R.G. Langlois, K.W. Tsang, R. Bryan, D.A. Anderson, K.S. Venkateswaran, F.P. Milanovich, B.W. Colston Jr., Anal. Chem. 75 (2003) 5293.
- [6] R.G. Pinnick, S.C. Hill, Y.L. Pan, R.K. Chang, Atmos. Environ. 38 (2004) 1657.
- [7] S. Cabredo, A. Parra, J. Anzano, J. Fluoresc. 17 (2007) 171.
- [8] S.N. Jackson, K.K. Murray, Anal. Chem. 74 (2002) 4841.
- [9] S.C. Russel, G. Czerwieniec, C. Lebrilla, P. Steele, V. Riot, K. Coffee, M. Frank, E.E. Gard, Anal. Chem. 77 (2005) 4734.
- [10] A.L. Van Wuijckhuijse, M.A. Stowers, W.A. Kleefman, B.L.M. van Baar, Ch.E. Kientz, J.C.M. Marijnissen, Aerosol Sci. 36 (2005) 677.
- [11] F. Immler, D. Engelbart, O. Schrems, Atmos. Chem. Phys. 5 (2005) 345.
- [12] H.L. Xu, G. Mejean, W. Liu, Y. Kamali, J.F. Daigle, A. Azarm, P.T. Simard, P. Mathieu, G. Roy, J.R. Simard, S.L. Chin, Appl. Phys. B-Lasers Opt. 87 (2007) 151.
- [13] M. Baudelet, L. Guyon, J. Yu, J.P. Wolf, T. Amodeo, E. Frejafon, P. Laloi, J. Appl. Phys. 99 (2006), Art. No. 084701.
- [14] M. Baudelet, L. Guyon, J. Yu, J.P. Wolf, T. Amodeo, E. Frejafon, P. Laloi, Appl. Phys. Lett. 88 (2006) (Art. No. 063901).
- [15] D.C.S. Beddows, H.H. Telle, Spectrochim. Acta Part B 60 (2005) 1040.
- [16] P.S. Chen, C.S. Li, J. Environ. Monit. 7 (2005) 950.
- [17] P.S. Chen, C.S. Li, Aerosol Sci. Technol. 39 (2005) 231.
- [18] R.K. Chang, Y.L. Pan, Faraday Discuss. 137 (2008) 9.
- [19] P.A. Rusin, S.L. Maxwell, J.P. Brooks, C.P. Gerba, I.L. Pepper, Environ. Sci. Technol. 37 (2003) 4027.
- [20] A.L. Stuart, D.A. Wilkening, Environ. Sci. Technol. 39 (2005) 2736.
- [21] P.P. Hairston, J. Ho, F.R. Quant, J. Aerosol Sci. 28 (1997) 471.
- [22] V. Agranovski, Z. Ristovski, M. Hargreaves, P.J. Blackall, L. Morawska, Aerosol Sci. 34 (2003) 301.
- [23] V. Agranovski, Z. Ristovski, P. Blackall, L. Morawska, J. Aerosol Sci. 31 (2000) S739.
- [24] J.E. Barton, E. Hirst, P.H. Kaye, J.M. Clark, J. Aerosol Sci. 31 (2000) S967.
- [25] J. Ho, M. Spence, P. Hairston, Aerobiologia 15 (1999) 281.
- [26] E. Morgan, Chemometrics: Experimental Design, John Wiley & Sons, 1997.
- [27] B.F.J. Manly, Multivariate Statistical Methods, a Primer, 2nd ed., Chapman & Hall, 1998.



Determination of soluble ions and elements in ambient air suspended particulate matter: Inter-technique comparison of XRF, IC and ICP for sample-by-sample quality control

S. Canepari^{a,*}, C. Perrino^b, M.L. Astolfi^a, M. Catrambone^b, D. Perret^a

^a Chemistry Department, University of Rome "La Sapienza", P.le Aldo Moro, 5, 00185 Rome, Italy

^b C.N.R. Institute of Atmospheric Pollution, Via Salaria km. 29,300, 00015 Monterotondo St., Rome, Italy

ARTICLE INFO

Article history:

Received 31 January 2008

Received in revised form 15 October 2008

Accepted 17 October 2008

Available online 31 October 2008

Keywords:

Particulate matter

Quality control

Inter-technique comparison

Chemical characterization

Chemical fractionation analysis

ABSTRACT

In this paper, we describe a validation procedure for chemical fractionation analysis of elements (Al, As, Ba, Ca, Cd, Cr, Cu, Fe, K, Mg, Mn, Na, Ni, Pb, S, Sb, Si, Sr, Ti and V) and soluble ions (Cl^- , NO_3^- , SO_4^{2-} , Na^+ , NH_4^+ , Mg^{2+} , Ca^{2+}) in suspended particulate matter (PM). The procedure applies three distinct measurement techniques (XRF, IC and ICP-OES) to the analysis of individual samples. The techniques used generate different outputs at different stages in the procedure. This makes it possible to identify the contributions of specific parameters to measurement uncertainty. On this basis, we propose a scheme for controlling the analytical quality of data from individual samples in which inter-technique comparisons is used in the same way many analytical methods use surrogates. We apply this scheme to about 310 samples of PM_{10} and $\text{PM}_{2.5}$ identifying and assessing the main factors contributing to measurement uncertainty. This procedure successfully resolved a number of difficulties frequently encountered during the analysis of PM, including lack of appropriate reference materials and the low reliability of alternative techniques of quality control. The results demonstrate the critical importance of sample treatment prior to destructive analysis by IC and ICP.

© 2008 Elsevier B.V. All rights reserved.

1. Introduction

To evaluate and reduce the health and environmental effects of suspended particulate matter (PM), it is vitally important to know its chemical composition and the way it varies in time and in space. To achieve this, we need providing data which is as reliable and complete as possible. However, the analytical techniques most frequently used to monitor PM require expensive and time-consuming procedures to collect, process and analyze samples. There is thus a strongly felt need for novel analytical methods that can provide as much detail on the chemical composition of individual samples as possible, while at the same time guaranteeing high quality results.

In recent years, there has been much interest in chemical fractionation analysis, a technique in which a sequence of solvent extractions is used to identify the elements present in the sample [1–6]. Chemical fractionation is already widely used in the analysis of soil and sediments and is potentially an effective way of determining the detailed chemical composition of PM – thereby helping to identify individual sources of emission [7–9]. Data quality is thus

of vital importance—especially if we use the data for testing provisional models or for source apportionment [10–12]. However, the procedures applied during successive phases of leaching involve significant manipulation of samples and this can affect the reliability of the results [13,14]. It should be added that in the case of PM it is usual to have only a single, very small sample (of the order of 1 mg of dust). Furthermore, it is often impossible to repeat the analysis and in many cases sample concentrations are close to the quantification limits. To make matters worse, commercial reference materials differ in significant ways from field samples [15,16], making it impossible to rigorously assess the quality of analytical results. The typical chemical matrix for PM is strongly inhomogeneous. As a result, it is not possible to reproduce the full range of possible reactions within the sample and with the filtration membrane. This means that frequently used quality control techniques such as testing the percentage of added surrogate material recovered from different phases are inappropriate for this kind of analysis.

In previous work [15–17] we optimized and validated a chemical fractionation procedure for the identification of elements present in samples of PM. This method analyzes individual samples with successive solvent extractions. This makes it possible to successfully measure the soluble ionic fraction and the majority of elements

* Corresponding author. Tel.: +39 0649913742; fax: +39 064451751.

E-mail address: silvia.canepari@uniroma1.it (S. Canepari).

present in the sample. The application of this procedure proved to be a valuable approach to achieve meaningful characterization of the elemental composition of individual samples. A very significant enhancement of the selectivity towards different emission sources is obtained when chemical fractionated data are considered instead of total element content [18–20], particularly useful to identify the contribution of the natural events (i.e. sea salt and mineral dust events) to urban PM concentration [20] and of resuspended road dust—one of the main factors underlying increased concentrations of elements in urban areas [18,19].

However the results for Al, Cr and Si – important for the assessment of natural contributions to PM – were not sufficiently accurate. Recently [21] we have examined the possibility of avoiding this difficulty through a non-destructive analysis with XRF, before the solvent extraction stage. In the work reported here, we validate a complete three-step analytical procedure using certified reference materials and pairs of equivalent field samples. We go on to describe the design and application of a procedure for the analysis of samples of PM_{2.5} and PM₁₀. The scheme uses inter-technique comparisons to identify the main sources of measurement uncertainty and to ensure the quality of data for each individual sample.

2. Experimental

2.1. Reagents

Our experiments used the following reagents: de-ionized H₂O (MilliQ), HNO₃ (65%, RPE, Carlo Erba, Rome, Italy), H₂O₂ (30%, Suprapur, Pa Merck), glacial CH₃COOH (Carlo Erba), CH₃COOK (Pa Sigma), Ion Chromatography (IC) and Inductively Coupled Plasma (ICP) standards (Pa Merck).

2.2. Sampling procedure

The samples used for the validation of the procedure came from the Montelibretti monitoring station, located 30 km NE of Rome, on the outskirts of the city. Each samples was collected over 48 h, in the period between September and October 2005.

Twin filters were collected using the HYDRA Dual Sampler (FAI Instruments, Fontenuova – Rome, Italy), an automatic system for sequential sampling with two independent channels. The instrument was configured with a single PM_{2.5} head, compliant with the EN 12341 standard. Incoming air, with a flow rate of 2.3 m³/h, was divided between the two channels, thus creating two equivalent samples. Filtering was carried out by using 47 mm Teflon® filtering membranes (Teflon, Pall Life Sciences, Mi, Italy) with 1 µm pore size.

Inter-technique comparisons were based on 310 samples of PM₁₀ and PM_{2.5}, collected in the period January–March, 2005, in the framework of the “Fine Particles” project, funded by the Lazio regional government. The samples came from the traffic station of Montezemolo, sited in the center of the city of Rome and from the urban background station of Villa Ada, sited inside a park, about 200 m from the nearest street. The choice of these sites guaranteed a good level of data variability—essential for the correct estimation of confidence intervals. The amount of collected sample ranged from 0.53 to 4.87 mg, with a mean value of 2.05 mg. Filtered samples were conserved in Analyslide Petri dishes (Pall Life Sciences, Mi, Italy) at 5 °C. All analyses were performed within 30 days of sample collection.

2.3. Analytical procedure

The analytical procedure is summarized in Fig. 1. Below we provide additional details on the individual steps in the

process—necessary for a full understanding of the results described later in this paper.

2.3.1. XRF analysis

We used XRF to measure the total content of Al, Ca, Cr, Cu, Fe, K, Mg, Mn, Na, S, Si, Zn and Cl in our samples (output 1). Sampled filters were placed in steel sample holders. All analyses were performed using ED-XRF mod. X-Lab 2000 (Spectro, Robecco sul Naviglio - Mi, Italy).

For XRF calibration, the data from the original factory calibration were for some elements (Mn, Cu, Zn, K, Cr) one order of magnitude higher than the concentrations in real PM samples. For this reason it was necessary to include additional low concentration data. Since reference materials on this matrix are not available, a practical possibility is to create an operative database for XRF calibration determining the elements by using a different, reliable analytical technique, such as ICP. Twenty environmental PM₁₀ and PM_{2.5} samples collected on a Teflon® matrix, were selected and added to the original calibration database. In order to obtain a complete digestion of Al and Si, these samples were mineralized using HF, applying the procedure described in Bettinelli et al. [22]. In spite of the small differences observed in the XRF response when moving from PM₁₀ to PM_{2.5} and from traffic to rural samples, the results of this calibration were satisfactory, with Pearson coefficients ranging from 0.999 (Si, Zn, Mg) to 0.994 (Al, S).

2.3.2. Ultrasound-assisted extraction

Before extraction, the poly-methylpentene ring supporting the Teflon® filters was removed using a stainless steel scalpel (Swann-Morton, Sheffield, UK). The filters were placed in polyethylene tubes. 5.0 mL of 0.01 M CH₃COOH/CH₃COOK buffer at pH 4.5 (extracting solution) were added to each tube. The tubes were then exposed to ultrasonic irradiation (28/34 kHz, 80/180 W) for 15 min. A home-made rotating device guaranteed that all samples were exposed to the same dose of ultrasound. 1.0 mL of the solution extracted in this way was subjected to chromatographic analysis for non-volatile, soluble anions and cations (outputs 2 and 3).

2.3.3. IC analysis

The 1 mL portion of extract solution was diluted with ultrapure H₂O, creating 5 mL of final solution. For anion analysis, the final solution was further diluted to a ratio of 1:10; cation analysis used a dilution ratio of 1:20. Where required for effective IC detection within the range of linear calibration (0.01–15 mg/L for anions; 0.01–10 mg/L for cations, 0.005–0.75 mg/L for NH₄⁺) higher dilution ratios were also used. For cations we performed a five-point matrix-matched calibration on a weekly basis; for anions, a one-point calibration every day.

Cations (Na⁺, Ca²⁺, Mg²⁺ and NH₄⁺ – output 1) were determined using a DX-100 Dionex with a Dionex ION PAC CS12A-4 mm column, a ION PAC CG12A-4 mm pre-column, a CSRS-ULTRA-4 mm suppressor and a 25 µL loop. As an eluent, we used 20 mM methanesulphonic acid (CH₄O₃S) (isocratic) introduced at a rate of 1.2 mL/min.

Anions (NO₃⁻, SO₄²⁻, Cl⁻ – output 2) were determined using a DX-100 Dionex with a Dionex AS14-4 mm column, an AG14-4 mm pre-column, an ASRS-ULTRA 4 mm suppressor and a 25 µL loop. The eluent was 2.7 mM Na₂CO₃/1.0 mM NaHCO₃ (isocratic) introduced at a rate of 1.2 mL/min.

2.3.4. Filtration A

The remaining (4 mL) extract was filtered on a cellulose nitrate filter (Millipore, 0.45 µm pore size, previously washed with 20 mL

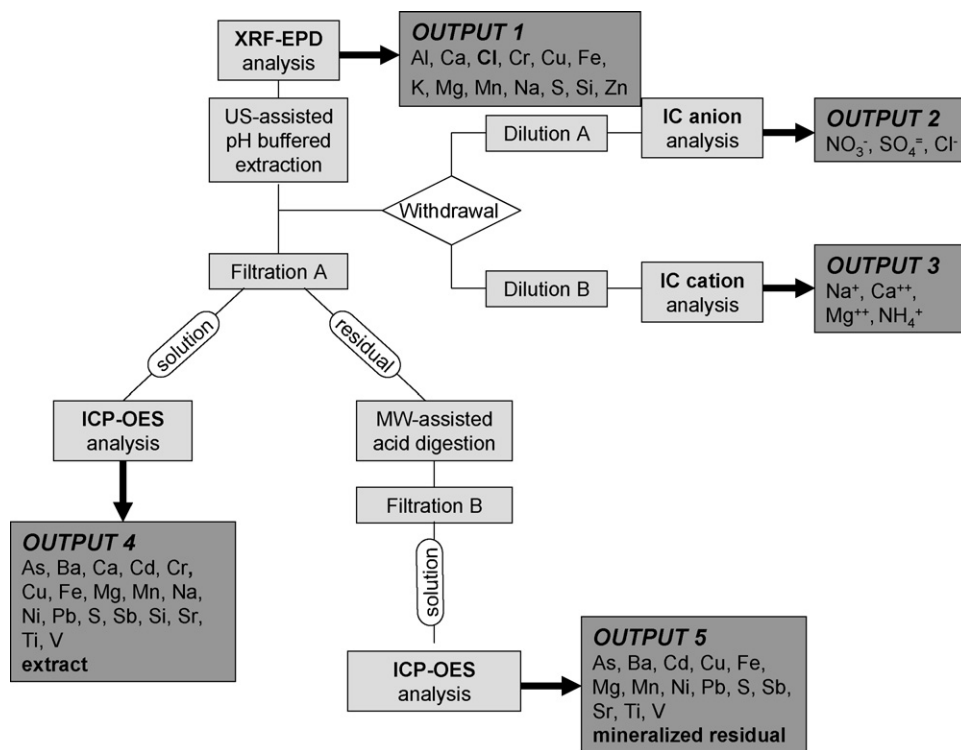


Fig. 1. The analytical procedure: a block diagram.

of extracting solution) and filled up to 10 mL with de-ionized water. The filtered solution was analyzed using ICP-OES (output 4). The residual solid was acid digested.

2.3.5. Microwave-assisted acid digestion and Filtration B

The residual solid on the sample filters was transferred to PTFE vessels. Four milliliters of 65% HNO₃ and 2 mL of 30% H₂O₂ were added to each vessel. The vessels were placed in a microwave (MW) oven (Milestone Ethos Touch Control with HPR 1000/6S rotor) and digested using a two-step temperature-time program. In the first step, the temperature was linearly increased to 180 °C in 8 min with a maximum power of 650 W. In the second step, the temperature was kept at 180 °C for 15 min. The solutions obtained were filtered on Millipore nitrate cellulose (NC) filters, previously treated with HNO₃ 10% (w/w) for 24 h, and filled with ultrapure H₂O to 10 mL. The mineralized residue fraction was analyzed using ICP-OES (output 5). The choice of digestion conditions and the procedures for cleaning the vessels are described elsewhere [15,16]. Note that the acid digestion with HNO₃/H₂O₂, which allows a good recovery of most elements [15], leads to incomplete recovery for some elements, such as Al and Si and Cr. However, the choice of this mixture, used also in the reference method EN 14902 (2005) [23] was made as the repeatability of results and the limits of detection of most elements are better with this mixture than the ones obtained when HF was added [17].

2.3.6. ICP-OES analysis

In this step, we determined As, Ba, Ca, Cd, Cr, Cu, Fe, Mg, Mn, Na, Ni, Pb, S, Sb, Si, Sr, Ti, and V in the extract fractions (output 4) and As, Ba, Cd, Cu, Fe, Mg, Mn, Ni, Pb, S, Sb, Sr, Ti, V in the mineralized residual fractions (output 5). Na is completely soluble in the extractant solution and Ca, Cr and Si were not determined in the mineralized residual fraction because of the poor quality of analytical results. However, Ca, Cr and Si total content were determined by XRF, so that

the solubility distribution of these elements can be obtained by difference. The analysis was performed with a simultaneous ICP-OES analyzer (Axial Varian ICP/VISTA MPX) with an ultrasonic nebulizer (U 5000 AT⁺, Cetac Technologies Inc.). The operating parameters have already been described elsewhere [15]. Standard solutions for daily six-point calibration were matrix-matched by preparation in 0.01 M CH₃COOH/CH₃COOK solution (pH 4.5) or HNO₃ 10% (w/w). To control nebulizer efficiency, an internal standard (yttrium 100 µg/L – wavelength 371.030 nm) was used.

2.4. Control charts

Instrument drift and calibration errors were monitored using appropriate control charts.

For the IC and ICP analyses, we prepared four standard matrix-matched 1 L solutions which were used respectively for the analysis of cations, anions, and elements in both the extracted and the mineralized residual fraction. For each parameter, we used 20 repeated measures to estimate mean values (m) and standard deviations from the mean (s). The solutions were then divided into 10 mL aliquots, and stored at –18 °C. Every 10 samples, we analyzed one of the stored aliquots. We then plotted the results for each parameter on our control charts, using a range of $m \pm 3s$. Percentage coefficients of variation (CV%) lay in the range 1–3% for the ICP-OES analyses and 0.5–2% for the IC analyses. To obtain percentage coefficients of variation for the XRF analysis, we took 20 readings for NIST 2783 Standard Reference Material, removing the filter and returning it to the sample holder after each reading. This procedure yielded CV% in the range of 2–10%. The same reference material was used for the control charts. In this case, we took one measurement every 20 samples. To check for drift in the source, we analyzed the capsule of source material once every 100 samples, using a multi-channel analyzer (MCA).

3. Results and discussion

3.1. Validation of the analytical procedure

Given the lack of appropriate reference materials, it is very difficult to validate analytical methods for PM. No commercially available CRM was suitable for the application of our complete procedure. As a result, it was difficult to compare calculated recovery and repeatability values for CRMs with those from real samples. As far as concerns the IC analysis (outputs 2 and 3) and the ICP-OES analysis (outputs 4 and 5), we have reported recovery values for reference material (NIST 1648) elsewhere [15,16]. For the XRF analysis (output 1), we compared recovery values with those for NIST 2783 Standard Reference Material. This material consists of urban particulate collected on a polycarbonate filter and certified for Al, Ca, Cr, Cu, Fe, K, Mg, Mn, Na, Pb, Ti, V, Zn. Reference values are also available for S and Si.

In the majority of cases, percentage recovery values ($R\%$ in Table 1) were significantly different from 100%. This was presumably due mostly to XRF calibration, which constitutes one of the weaker steps in the overall PM chemical characterization procedure. In order to obtain reliable results for PM samples, in fact, XRF calibration must be carried out on the same filter material used for PM sampling, that is, in our case, on Teflon® filters (see Section 2.3.1). An unpleasant consequence of this procedure is the defective percentage recovery values of NIST Reference Material.

Limits of quantification (LOQ) were calculated using the IUPAC procedure. XRF values were computed using the relation:

$$\text{LOQ} = \frac{10 \times \sqrt{\text{Background}} \times C_i}{N_i}$$

where C_i represents sample concentration (near LOD) and N_i is the net pulse count.

For all other analytes we chose the highest value between the instrumental LOQs, calculated using the regression curve, and the LOQs calculated from values for blanks [24,25]. These last were obtained by applying the complete analytical procedure to 10 blank filters. LOQ was calculated applying the expression $\text{LOQ} = \bar{m}_b + 10s_b$, where \bar{m}_b and s_b represent respectively the mean value for blanks and its standard deviation. We used instrumental LOQ value only for As, the sole element for which this procedure yielded higher value than that obtained with blanks.

To assess the repeatability of the complete method, we applied the procedure defined in UNI EN14902 [23], using 20 pairs of equivalent real samples, analyzed in random order. Relative repeatability, r_{rel} , of the set of filters pairs A and B, was calculated as follows:

$$\bar{X} = \frac{\sum_{i=1}^{20} (m_{iA} + m_{iB})}{40}; \quad r = \sqrt{\frac{\sum_{i=1}^{20} (m_{iA} - m_{iB})^2}{40}}; \quad r_{\text{rel}} = \frac{r}{\bar{X}} \times 100$$

where m_{iA} and m_{iB} are the masses of the analyte measured on the i th pair of filters A and B. To confirm, the repeatability of our method, we also calculated coefficient of linear regression (R^2) between results from the A and the B filters. This procedure enabled us to assess the robustness of our results with respect to the environmental variability of real samples. Values below the LOQ were excluded from the calculation. Table 1, summarizes the results.

Table 1 shows that for most of the analytes, repeatability values were satisfactory, also considering the high environmental variability of their concentrations. In agreement to this, Pearson coefficients are in most cases of the order of 0.99 and always higher than 0.9, with the sole exception of As in the mineralized residual fraction (0.854). In general, as expected, repeatability was worse when amounts of analyte in samples were close to the LOQ.

Calculations of repeatability for XRF measures on pairs of real samples gave values comparable to those for CRM and are, in most cases (Al, Ca, Cr, K, Mg, Na, S, Si), lower than 5%. This suggests that the repeatability of the sampling procedure plays a negligible role.

In the ICP analysis, r_{rel} values are higher than XRF ones, according to the longer sample manipulation. Anyway, they are lower than 10% for all the measured analytes, with the exception of As in both output 4 and 5 (respectively 10.5% and 19.4%), for Na and Si in output 4 (respectively 10.1% and 11.3%) and for Ni in output 5 (10.7%). We also calculated the repeatability of total concentration, computed by summing the amount of analyte in the extracted fractions (output 4) to the amount in mineralized residues (output 5). Despite to the uncertainty propagation, repeatability of the total concentrations are better than those of the extracted and mineralized residual fractions, with r_{rel} values ranging from 3.1% (Ba) to 9.5% (As) and R^2 ranging from 0.939 (Mg) to 0.999 (Ba). This result suggests that sample handling only has a small effect on repeatability but that efficiency of extraction plays a non-negligible role. With our current experimental method, the extraction takes place in an ultrasonic bath with no temperature control. This makes it one of the most delicate phases in the sequential extraction process [26] and suggests that better standardization will be needed in the future.

In the described procedure, several parameters can be measured by more than one analytical technique. This made it possible to make inter-technique comparisons. In particular it was possible to determine the total content of Mg, Mn, S, Fe and Cu both with XRF (output 1) or by summing the results for the extracted and the residual fraction with ICP-OES (output 4 + output 5). Similarly, concentrations of several ions (SO_4^{2-} , Mg^{2+} , Ca^{2+} , Na^+) could be determined both with IC (outputs 2 and 3) and with ICP-OES (output 4). Finally, given that Na and Cl, are present almost exclusively in the form of ions in soluble chemical species, XRF results for these elements could be compared directly with results for the extracted fraction (output 2 for Na and output 3 for Cl).

3.2. Identification and assessment of operational contributions to repeatability

Individual contributions to measurement uncertainties, are directly correlated with the analytical techniques on which the measurements are based (XRF, IC – anions, IC – cations, ICP-OES), the way these techniques are applied and the various operations involved in sample preparation (ultrasound extraction, filtration, dilutions, digestion with acids) [27]. Uncertainties due to instruments – such as those determined by calibration and drift – can be easily controlled using internal standards and control charts. However, the fact that we cannot apply the complete method to certified materials makes it very hard to determine the contribution of sample handling and other operational details to measurement uncertainties. One possibility is to use inter-technique comparisons for this purpose. As can be seen in Fig. 2, different operations affect different steps in the analytical procedure with different effects on the outputs from measurement instruments. Each output can be considered as a kind of “sample” taken while the analytical procedure is still in progress. Once we have measurements for a single analyte from at least two different technique, we can use it as tracer for operational contributes to uncertainty introduced during the application of the analytical procedure. For example: (i) we can use the comparison between output 3 and output 4 to isolate the separate contributions of Filtration A and sample dilution prior to the IC analysis; (ii) the only factors affecting the comparison between output 1 and output 2 are filter handling and the operations required for ultrasound extraction; (iii) the comparison between output 1 and the sum of outputs 4 and 5 reflects the com-

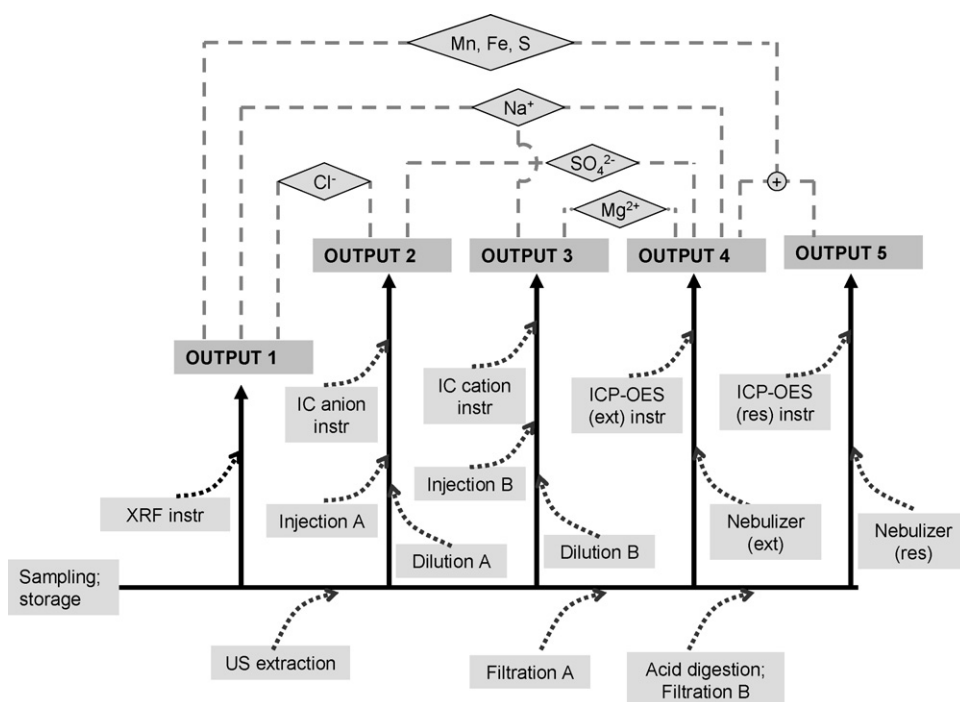


Fig. 2. Sources of uncertainty and tracer analytes. The match or lack of match between results from different instruments, for different tracers (shown on the top) depends on specific sources of measurement uncertainty. Dashed grey lines show comparisons between outputs. Dotted lines connect sources of uncertainty to the outputs they affect.

plete set of factors affecting measurement uncertainty. In sum, we can use inter-technique comparisons in the same way many analytical methods use surrogates. The technique provides us with a way of routinely identifying, assessing and monitoring different factors contributing to measurement uncertainty.

For each tracer, we began by calculating the coefficient of linear regression between the data from the techniques we were comparing (Table 2). Values for the Pearson coefficient (R^2) were >0.99 for all comparisons with the exception of the ICP-XRF comparison for Fe ($R^2=$) and Mg ($R^2=$) and of the IC-XRF comparison for Na ($R^2=0.976$) and Cl ($R^2=0.989$). Regarding Fe and Mg, this result is probably due to the lower repeatability of XRF (Fe) and ICP (Mg and Fe) measurements with respect to the other tracers one (see r_{rel} in Table 1). For Na and Cl, it is very likely that the observed discrepancy was due to sample contamination in the first part of the proce-

dure (before Filtration A), as suggested also by the high R^2 value (0.996) obtained when Na is used for IC-ICP comparison. It should also be observed that in all comparisons involving XRF, the slope and intercept of the regression line deviated significantly from theoretical expected values. This is more evidence of the critical role of calibration in the XRF technique.

In any case, inter-technique comparisons are only possible when instrumental repeatability is high enough to ensure the comparison will be sensitive to operational errors. This makes it necessary to identify mean relative deviations for all possible inter-technique comparisons and to define optimal conditions of use for each tracer. For the purposes of this assessment, we decided to transform the values from inter-technique comparisons so as to make them independent of systematic differences in the calibration of different instruments. For this correction, we used the linear regression val-

Table 2
Threshold values (QL), number of valid data (N°), mean percentage deviations ($\delta\%$) and linear regression parameters for inter-technique comparisons with different candidate tracers. Range in the last column is referred to the environmental variability of the whole set of samples (310).

	N°	QL (μg)	$\delta\%$	R^2	Slope	Intercept (μg)	Range (μg)
ICP (output 4 + output 5) vs. XRF (output 1)							
Cu	226	1.4	7.1	0.994	1.118	−0.33	0.6–7.1
Mn	261	0.16	6.2	0.996	0.852	0.03	0.1–2.7
S	310	–	4.9	0.998	1.178	0.08	10–122
Fe	156	28	12.1	0.938	0.865	0.04	3.0–77
Mg	174	2.9	10.4	0.956	1.192	0.06	0.7–11
IC cations (output 2) vs. ICP (output 4)							
Na ⁺	290	5.2	5.1	0.996	0.961	0.44	4.3–65
Mg ²⁺	255	1.0	5.5	0.997	0.974	−0.07	0.6–9.8
Ca ²⁺	263	11	4.0	0.996	1.05	0.78	7.1–92
IC anions (output 3) vs. ICP (output 4)							
SO ₄ ^{2−}	310	–	2.8	0.997	0.985	0.23	23–306
XRF (output 1) vs. IC cations (output 2)							
Na	263	5.1	10.2	0.976	1.254	−1.1	4.3–65
XRF (output 1) vs. IC anions (output 3)							
Cl	275	4.0	8.6	0.989	0.88	−1.2	3.3–86

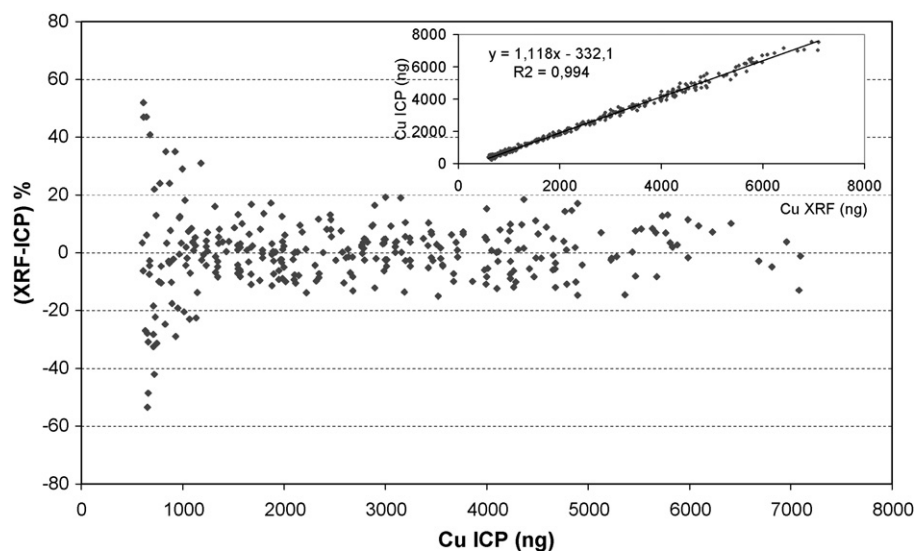


Fig. 3. Percentage deviations ($\delta_i\%$) between measurements of Cu with XRF (output 1) and ICP (output 4 + output 5).

ues reported in Table 2 and recalculated the values obtained from one of the two techniques so as to obtain a regression equation with intercept of zero and slope of 1.

For each sample, and for each pair of techniques, we went on to calculate percentage deviations $\delta_i\%$, using the expression:

$$\delta_i\% = (m'_{i,A} - m_{i,B}) / (m'_{i,A} + m_{i,B}) \times 200$$

where $m'_{i,A}$ is the corrected mass of tracer measured in the i th sample, using technique A, and $m_{i,B}$ is the mass of tracer measured with technique B.

Given we had no way of artificially creating samples with different concentrations of tracer, we applied inter-technique comparisons to 310 real samples of PM₁₀ (196 samples) and PM_{2.5} (114 samples), collected from different sites. We found, as expected, that for nearly all tracers, the $\delta_i\%$ values were higher when the amount of tracer in the sample was relatively small (see Fig. 3). The only exceptions were cases where the amount of tracer was significantly higher than the LOQ for both of the techniques in the comparison. This finding enabled us to determine a threshold value (QL in Table 2), above which $\delta_i\%$ s were independent of the amount of tracer and normally distributed. To confirm this finding, we used the Dixon and Grubbs outlier tests to detect and discard anomalous data, and applied the Shapiro-Wilk test for normality [28].

Table 2 provides mean $\delta_i\%$ s ($\delta\%$) for each tracer and for each inter-technique comparison and shows the considered number of samples (N°), where the amount of tracer was higher than QL. Values of $\delta\%$, N° and QL for Fe and Mg confirm that measurements of this two elements are not sufficiently reliable to be used as quality tracers. On the contrary, it can be seen that the quantity of S collected on filters was always much higher than QL. As a result, S is a very effective tracer, both in the ICP-XRF comparison (total S content), and in the comparison between IC (anions) and ICP (SO_4^{2-} soluble ion). All the other elements are mainly present in coarse particulate [29–31]. As a result, the amount of these elements in samples of PM_{2.5} is often below QL. By contrast, the amounts present in PM₁₀ is high enough to allow completely reliable comparisons.

To gain more detailed insights into the way different steps in the analysis contribute to measurement uncertainty, we examined correlations between comparison results for different tracers. The approach used is depicted in Fig. 4. This shows percentage deviation

values for a small set of data. We observe that in the XRF-ICP comparisons the patterns of $\delta_i\%$ for Cu, Mn and S are practically identical (Fig. 4c). This suggests the presence of one (or more) predominant sources of measurement uncertainty with the same effect on all three tracers. It should be noted that the ICP values used in the calculation represent the sum of the extracted and residue fractions (outputs 4 + 5), and that while S is present mainly in the extracted fraction, Cu and Mn are present in both (see the last column of Table 1). Some sources of uncertainty such as microwave acid digestion only affect the residue fraction (output 5) (Fig. 2). On the other hand, filtration of the extract fraction (Filtration A) obviously has different effects on the extract and residue fractions. In brief, these sources of uncertainty have different effects on the deviations in our tracers and cannot be the main factors determining the trends we observed.

The other inter-technique comparisons provide us with additional information. In particular the deviations in the comparison between XRF (output 1) and IC (anions) (output 3) (Fig. 4d) are very similar to those we observe for Cu, Mn and S in Fig. 4a. By contrast, the deviations measured in the comparisons between IC (outputs 2 and 3) and ICP (output 4) (Fig. 4a and b) are smaller and display very different trends. It thus appears that the main factors affecting measurement uncertainty exert their effects in the initial stages of the analytical procedure. Between XRF analysis and Ultrasound-Assisted Extraction the sample filter is taken out of the XRF sample holder and the polymethylpentene ring is manually removed with a scalpel. Although these operations are performed with great care, they can still lead to loss of sample material. What is more, validation with certified materials cannot control for these losses. The NIST 2783 used for validation of the XRF analysis comes on filters with no supporting ring, and is not suitable for the destructive analyses we use in the later stages of our procedure. The NIST 1648 used to validate our extraction methods does not come on a filter. We observe that the Teflon® filters used in our study are one of the most popular choices for this kind of work—mainly because analytical values for blank filters of this kind are especially low. The fact that the error we found is due to an unavoidable loss of sample material, casts doubt on the accuracy of other kinds of destructive analysis that use the same kind of filter. We note that similar problems may arise during the division of filter samples into portions—a procedure often applied during the chemical characterization of PM.

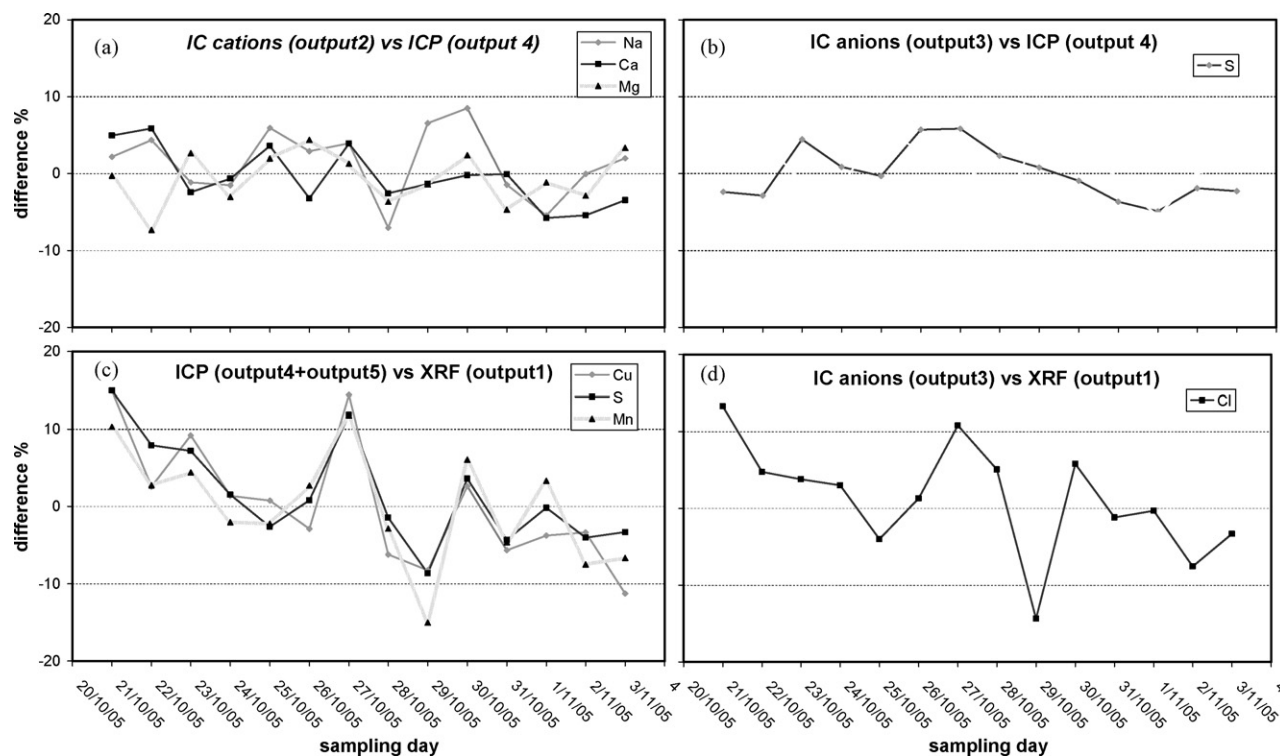


Fig. 4. Patterns of selected tracer percentage deviation values.

3.3. Process control

Procedures based on inter-technique comparisons, such as the scheme we have just described, can also be used to identify the role of operational errors in routine applications. They thus provide an effective form of process control. To apply them in this way, all we need to do is define the confidence intervals for inter-technique deviations (in our case $\pm\delta\%$ and $\pm 2\delta\%$, for the $\delta\%$ values shown in Table 2). We then select those values where deviations are independent of tracer quantities (value > QL), and plot them on the control chart. Where errors are detected, we can use the scheme proposed earlier to identify the nature of the error.

It is obvious that, in some cases, the identification of specific operational errors, affecting all measurements from a specific instrument, would allow us to recover data which would otherwise be lost.

4. Conclusions

We validated and applied to real PM₁₀ and PM_{2.5} samples a procedure for a meaningful inorganic characterization (inorganic ions, crystal, major and trace elements, elemental solubility) on a single filter. The procedure avails of XRF, IC and ICP measurements and some parameters can be analyzed by more than one of these techniques. This allowed us to propose a scheme for analytical quality control based on inter-techniques comparison. Some analytes (Cu, Mn and S total concentration; Ca²⁺, Mg²⁺, Na⁺, Cl⁻, NO₃⁻ and SO₄²⁻ soluble ions) were selected as “quality tracers” and the scheme described in this paper allowed us to use them for the identification and evaluation of some operative contributions to uncertainty in PM composition measurements. The relevance of the contributions can be traced on individual samples. These contributions could have hardly been detected with the conventional tools for data quality control, as they refer to phases of the procedure which are not applicable to reference materials. In par-

ticular, it has been shown that handlings of the sampled filters, such as removal of the supporting ring or division into portions, may give operational contributions to uncertainty higher than those related to solvent extraction and acid digestion treatment. Other critical aspects of the procedure, which should be subjected to further optimization in the future, are extraction efficiency and XRF calibration.

It is worth noting that this scheme for uncertainty sources traceability can be applied to any analytical procedure involving the use of more multi-parametric techniques, provided that some of the analytes are measured by more techniques, at different steps of the procedure. These requirements are quite common in elemental chemical fractionation procedures applied to PM, where the joined use of non-destructive and destructive techniques allows a beneficial increase in the number of analyzed parameters.

Acknowledgements

This study has been carried out in the framework of the “Polveri Fini project”, financed by the Lazio Region, and of the European Network of Excellence ACCENT (Atmospheric Composition Change). The Authors are also indebted to S. Della Torre, E. Rantica, T. Sargolini, E. Marconi, M.L. Marzo and L. Bottacci for their valuable technical contribution.

References

- [1] M.R. Heal, L.R. Hibbs, R.M. Agius, I.J. Beverland, Atmos. Environ. 39 (2005) 1417–1430.
- [2] K. Lehmann, A. Massling, A. Tilgner, S. Mertes, D. Galgon, A. Wiedensohler, Atmos. Environ. 39 (2005) 4257–4266.
- [3] S.-C. Hsu, F.-J. Lin, W.-L. Jeng, Atmos. Environ. 39 (2005) 3989–4001.
- [4] A.R. Baker, T.D. Jickells, M. Witt, K.L. Linge, Mar. Chem. 98 (2006) 43–58.
- [5] S. Qureshi, V.A. Dutkiewicz, A.R. Khan, K. Swami, K.X. Yang, L. Husain, J.J. Schwab, K.L. Demerjian, Atmos. Environ. 40 (2005) 238–251.
- [6] A.J. Fernández Espinosa, M. Ternero Rodríguez, Anal. Bioanal. Chem. 379 (2004) 684–699.

- [7] V.A. Dutkiewicz, S. Qureshi, L. Husain, J.J. Schwab, K.L. Demerjian, *Atmos. Environ.* 40 (2006) 347–359.
- [8] M.S. Al-Masri, K. Al-Kharfan, K. Al-Shamali, *Atmos. Environ.* 40 (2006) 753–761.
- [9] S.L. Quiterio, C.R. Sousa, G. Arbilla, V. Escaleira, *Atmos. Environ.* 39 (2005) 3503–3512.
- [10] M. Sillanpää, S. Saarikoski, R. Hillamo, A. Pennanen, U. Makkonen, Z. Spolnik, R. Van Grieken, T. Koskentalo, R.O. Salonen, *Sci. Total Environ.* 350 (2005) 119–135.
- [11] G. Güllü, İ. Ölmez, G. Tunce, J. Radioanal. Nucl. Chem. 259 (1) (2004) 163–171.
- [12] X. Querol, A. Alastuey, S. Rodriguez, F. Plana, C.R. Ruiz, N. Cots, G. Massagué, O. Puig, *Atmos. Environ.* 35 (2001) 6407–6419.
- [13] C.M. Davidson, P.C.S. Ferreira, A.M. Ure, *Fresenius J. Anal. Chem.* 363 (1999) 446–451.
- [14] M. Pueyo, G. Rauret, D. Luck, M. Yli-Halla, H. Muntau, P. Quevauviller, J.F. López-Sánchez, *J. Environ. Monit.* 3 (2001) 243–250.
- [15] S. Canepari, E. Cardarelli, A. Pietrodangelo, A. Giuliano, *Talanta* 69 (2006) 581–587.
- [16] S. Canepari, E. Cardarelli, A. Pietrodangelo, M. Strincone, *Talanta* 69 (2006) 588–595.
- [17] P. Bruno, S. Canepari, E. Cardarelli, C. Del Cavaliere, S. Ghighi, *Ann. Chim. (Rome)* 90 (2000) 645–654.
- [18] S. Canepari, C. Perrino, F. Olivieri, M.L. Astolfi, *Atmos. Environ.* 42 (2008) 8161–8175.
- [19] S. Canepari, A. Pietrodangelo, C. Perrino, M.L. Astolfi, M.L. Marzo, *Atmos. Environ.* (2008), doi:10.1016/j.atmosenv.2008.09.059.
- [20] C. Perrino, S. Canepari, M. Catrambone, S. Della Torre, E. Rantica, T. Sargolini, *Atmos. Environ.* (2008), doi:10.1016/j.atmosenv.2008.06.035.
- [21] M.L. Astolfi, S. Canepari, M. Catrambone, C. Perrino, A. Pietrodangelo, *Environ. Chem. Lett.* 3 (2006) 186–191.
- [22] M. Bettinelli, G.M. Beone, S. Spezia, C. Baffi, *Anal. Chim. Acta* 424 (2000) 289–296.
- [23] CEN, UNI EN 14902:2005:E, Ambient air quality – Standard method for the measurement of Pb, Cd, As and Ni in the PM₁₀ fraction of suspended particulate matter (2005).
- [24] M. Thompson, S.L.R. Ellison, R. Wood, *Pure Appl. Chem.* 74 (5) (2002) 835–855.
- [25] L.A. Currie, *Pure Appl. Chem.* 67 (10) (1995) 1699–1723.
- [26] S. Canepari, E. Cardarelli, S. Ghighi, L. Scimonelli, *Talanta* 66 (2005) 1122–1130.
- [27] A. Williams, S.L.R. Ellison, M. Roeslein (Eds.), EURACHEM/CITAC Guide Quantifying Uncertainty in Analytical Measurement, 2nd ed. (English) (2000), ISBN 0-948926-1595, available from LCC Limited, Teddington, London, or at Eurachem Secretariat, <http://www.eurachem.org/>.
- [28] EPA/600/R-96/084, Guidance for data quality assessment. Practical Methods for Data Analysis, EPA QA/G-9 QA97 Version 1998.
- [29] T.A. Pakkanen, V.-M. Kerminen, K. Loukkola, R.E. Hillamo, P. Aarnio, T. Koskentalo, W. Maenhaut, *Atmos. Environ.* 37 (2003) 1673–1690.
- [30] T.A. Pakkanen, K. Loukkola, C.H. Korhonen, M. Aurela, T. Makela, R.E. Hillamo, P. Aarnio, T. Koskentalo, A. Kousa, W. Maenhaut, *Atmos. Environ.* 35 (2001) 5381–5391.
- [31] M.L. Astolfi, S. Canepari, E. Cardarelli, S. Ghighi, *Ann. Chim. (Rome)* 96 (2006) 183–194.



H₂S sensing properties of nanocrystalline Sr₂Fe_{0.6}Ni_{0.4}MoO₆ thick film prepared by sol–gel citrate method

G.N. Chaudhari^{a,*}, N.N. Gedam^a, S.V. Jagtap^a, S.V. Manorama^b

^a Nano Technology Research Laboratory, Department of Chemistry, Shri Shivaji Science College, Amravati 444602, Maharashtra, India

^b Nanomaterials Laboratory, Indian Institute of Chemical Technology, Hyderabad 500007, India

ARTICLE INFO

Article history:

Received 8 July 2008

Received in revised form

30 September 2008

Accepted 1 October 2008

Available online 14 October 2008

Keywords:

Double perovskite structure

Gas response

Selectivity

H₂S gas

ABSTRACT

Nanocrystalline Sr₂FeMoO₆ (SFMO) belonging to the group of double perovskite oxides, was prepared by the sol–gel citrate method. The structural and microstructural characterization has been carried out with the help of X-ray diffraction (XRD) and transmission electron microscopy (TEM), respectively. XRD of Sr₂Fe_{1-x}Ni_xMoO₆ (SFNMO) shows the formation of solid solution with average grain size of about 40 nm. A comparative study of gas sensing behaviour of Sr₂FeMoO₆ and Sr₂Fe_{1-x}Ni_xMoO₆ with reducing gases like hydrogen sulfide (H₂S), liquid petroleum gas (LPG), hydrogen (H₂), ethanol (C₂H₅OH) and carbon monoxide (CO) were also discussed. The sensitivity is calculated by measuring the change the resistance of the sensor material in the presence of gas. Among the different composition of x ($x=0.2, 0.3, 0.4, 0.5$), Sr₂Fe_{0.6}Ni_{0.4}MoO₆ ($x=0.4$) shows better response to H₂S gas at 260 °C. Incorporation of palladium (Pd) improves the gas response, selectivity, response time and reduced the operating temperature from 260 to 220 °C for H₂S gas.

© 2008 Elsevier B.V. All rights reserved.

1. Introduction

Gases are the key measurands in many industrial or domestic activities. In the last decade, the specific demand for gas detection and monitoring has emerged particularly as the awareness of the need to protect the environment has grown.

Hydrogen sulfide (H₂S) is one of the typical bad smelling odors which is frequently generated from sewage, a dump or the human mouth. H₂S is a colorless toxic, flammable and bad smelling gas. With these properties, H₂S has become a recent target of rather extensive research on solid-state sensors.

One of the most interesting and sensitive sensors studied is the semiconductor metal oxide gas sensor. Recently, some composite oxides such as spinel AB₂O₄ [1] and perovskite ABO₃ [2] were found to be more attractive for their better selectivity and/or sensitivity to H₂S gas. In particular, the perovskite structure was established to be a promising material in detecting reducing gases. It is well known that a number of perovskite oxides (ABO₃) were used as gas sensor materials because of their stability in thermal and chemical atmospheres. So over the last decade, the perovskite oxide materials have created and promoted interest in gas sensors.

Modified Sr₂Fe_xNi_{1-x}MoO₆ a well-known member of the double perovskite family of oxides, has been studied due to its important

properties like crystalline structure, transport and magnetic properties [3]. Similarly Sr₂FeMoO₆ (SFMO) has been studied due to its magnetic properties [4]. Although much progress has been made on applications related to other areas for SFMO. As per our knowledge, the gas sensing properties of SFMO have not been explored for any gas.

In this paper, we report for the first time H₂S gas sensing phenomena observed in SFMO thick film prepared by sol–gel citrate method. The sensitivity of the SFMO based sensor to H₂S has been studied by measuring the resistance of the sensor material in air and then in H₂S environment. It has been observed that there is an increase in gas response when exposed to H₂S than other reducing gases like liquid petroleum gas (LPG), hydrogen (H₂), carbon monoxide (CO) and ethanol (C₂H₅OH). We have also tried to improve the response to H₂S gas by modifying the surface of Sr₂FeMoO₆ with Sr₂Fe_{1-x}Ni_xMoO₆ (SFNMO). The effect of partially substituted Ni²⁺ ions for Fe³⁺ sites of SFMO on gas response is also described. This sensor material is often modified by additive or dopant—e.g. noble metal such as Pd in order to improve the performance.

2. Experimental

Nanocrystalline SFNMO powder was synthesized by using sol–gel citrate method. The stoichiometric ratio of Ni(NO₃)₃·6H₂O, Fe(NO₃)₃·9H₂O, Sr(NO₃)₂, (NH₄)₆Mo₇O₂₄·4H₂O and citric acid monohydrate [C₆H₈O₇·H₂O] were weighed and dissolved in ethy-

* Corresponding author.

E-mail addresses: cgnroa@yahoo.com, nano.d@rediffmail.com (G.N. Chaudhari).

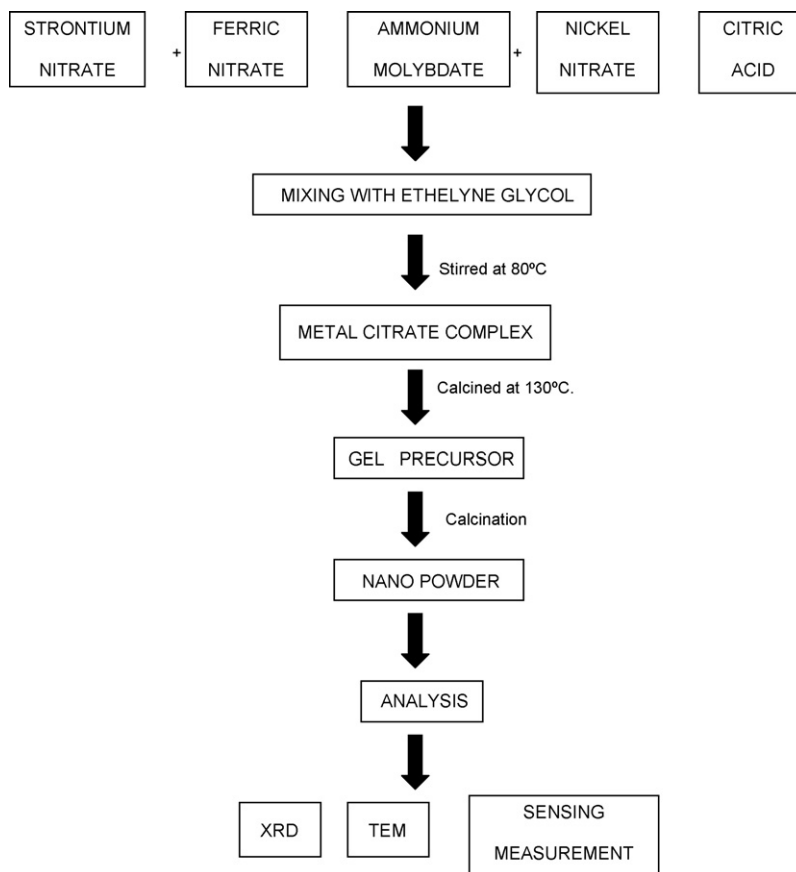


Fig. 1. Flowchart of synthesized SFNMO powder.

lene glycol at 80 °C. A transparent solution was obtained after 2 h. This solution was then heated at 130 °C for 12 h in a pressure vessel to form the gel precursor. The prepared product was subjected to 3 h heat treatment at 350 °C in a muffle furnace and then milled to a fine powder. The obtained powder was then calcined at 650 °C for 6 h. Fig. 1 shows the flowchart of synthesized nanocrystalline powder.

Incorporation of palladium (Pd) in the SFNMO was performed by the impregnation technique as follows:

Aqueous solution of PdCl_2 was impregnated followed by drying over night at 110 °C in an oven followed by calcination at 600 °C for 2 h. Subsequently, the above compound was ground into a fine powder and mixed with 2% polyvinyl alcohol (PVA) as a binder and 5% ethanol as a solvent to obtain a paste. The resulting paste was coated onto the alumina tube substrates provided with platinum wire electrodes for electrical contacts. After coating, the element was sintered at 700 °C for 2 h in a vertical furnace.

The gas sensitivity (S) was defined as: $S = (R_a - R_g)/R_a = \Delta R/R_a$; where, R_a and R_g are the resistance of sensor in air and the test gas, respectively. The sensor was examined under different reducing gases such as H_2S , LPG, H_2 , CO and ethanol whose concentration was fixed at 1000 ppm in air.

The crystal structure of the film was determined by X-ray diffraction (XRD) using a Siemens D5000 diffractometer with monochromatic $\text{CuK}\alpha$ radiation. The surface morphology of the synthesized powder was observed through a Hitachi-800 transmission electron microscope (TEM). The crystallite sizes of powders were calculated according to Scherrer's equation,

$$d = \frac{k\lambda}{\beta \cos \theta}$$

where, k is 0.9, λ is X-ray wavelength, β is full width at half-maximum in radians and θ is the diffraction peak position.

3. Results and discussion

The resulting SFNMO, annealed at 650 °C for 6 h, was examined by powder X-ray diffraction analysis in Fig. 2. Results agree very well with the XRD pattern reported in the literature [4]. The XRD pattern shows double perovskite with tetragonal structure. The SFNMO

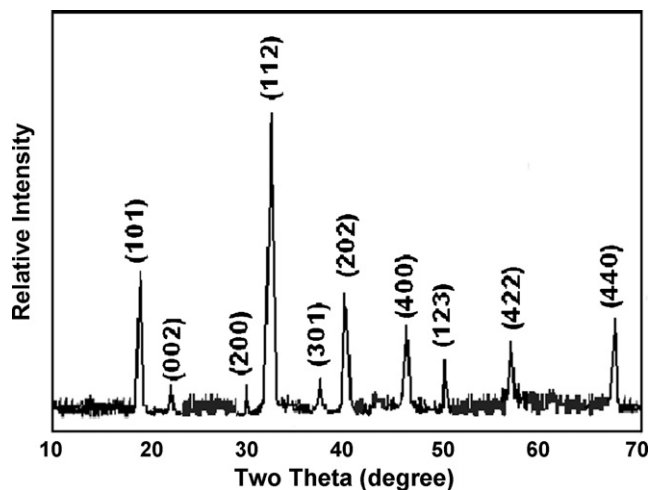


Fig. 2. XRD pattern of SFNMO, calcined at 650 °C for 6 h.

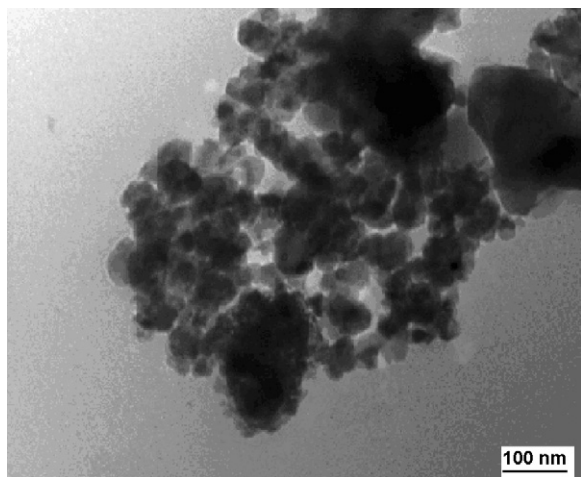


Fig. 3. TEM image of SFNMO, calcined at 650 °C.

had an average crystallite size of 40 nm calculated using Scherrer's equation applied to the XRD data. It should be noted that no nickel containing phase was detected due to formation of solid solution.

Fig. 3 shows the powder distribution obtained from TEM image. It can be seen that the particles have nanometer-scale morphology at a relatively low calcination temperature and are well dispersed from each other. The particle size is estimated to be between 35 and 45 nm for SFNMO.

When the material is exposed to reducing gases, the changes in resistance for the semiconductor-based sensors is mainly caused by the reaction between the reducing gases and the bound oxygen species adsorbed on the surface of the semiconductor, which changed with the operating temperature [5]. The gas response which is thermally activated depends on the operating temperature is presented in Fig. 4 which shows the response of SFMO sensor to H₂S, LPG, H₂, CO and ethanol. The gas response was measured as a function of operating temperature. SFMO senses all reducing gases but the response for H₂S gas at 310 °C is 0.45, which is much higher as compared to other reducing gases.

The gas sensing mechanism belongs to the surface-controlled type. The gas sensitivity is a function of grain size, surface state, oxygen adsorption and lattice defects. Normally, the smaller the grain size is, the higher is its gas sensing property [6]. Besides, in order to improve selectivity for particular application, surface modification

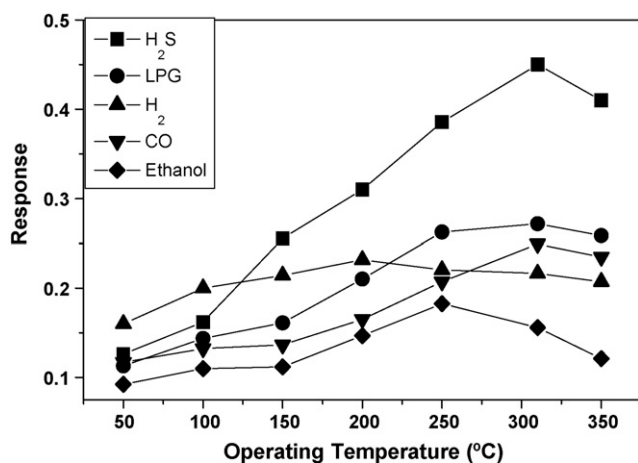


Fig. 4. Response as a function of operating temperature for undoped SFMO for H₂S, LPG, H₂, CO and ethanol.

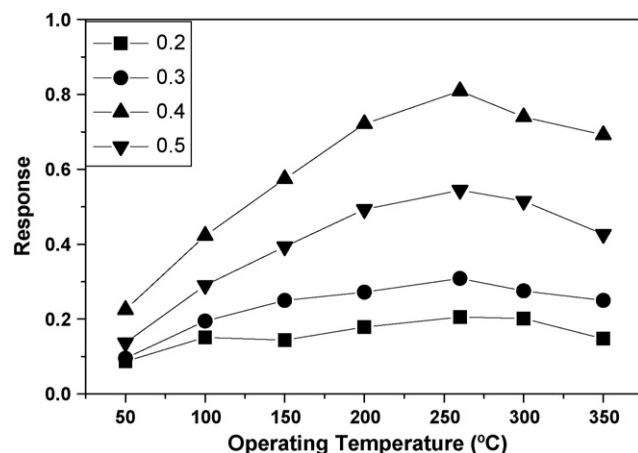


Fig. 5. Response as a function of operating temperature for different amount of Ni (A) 0.2, (B) 0.3, (C) 0.4 and (D) 0.5.

by proper choice of additives or dopants to the base materials are often used. The doping is generally based on the selection of most effective catalysts, which modulate specific chemical reaction on the semiconductor sensor surface.

The gas response of the Sr₂Fe_{1-x}Ni_xMoO₆ was markedly promoted by partial replacement of Fe ion by Ni ion. Fig. 5 shows the response as a function of operating temperature for Sr₂Fe_{1-x}Ni_xMoO₆ with different amount of 'x' (x = 0.2, 0.3, 0.4 and 0.5). The response to H₂S gas improves with increasing amount of Ni. The best response, in case of Sr₂Fe_{0.6}Ni_{0.4}MoO₆ (x = 0.4) may be because of more available sites for the oxygen to be adsorbed and in turn to oxidize the test gas. The decrease in response may be due to the insufficient number of sites available on the surface. The partial replacement results in a decrease of grain size and hence in an increase of surface area. Since small grains have relatively large grain boundary areas, the adsorption of H₂S molecules is relatively high. Fig. 6 shows the gas response of SFNMO as a function of different reducing gases. It is seen that sensor responds with very high sensitivity selectively to H₂S compared to the other test gases. Figure indicates the high response of SFNMO sensor to H₂S gas as compared to LPG, H₂, CO and ethanol at an operating temperature of 260 °C. Ni incorporation results in a decrease in operating temperature by 50 °C. The lower operating temperature is probably due to its larger surface area and high surface activity, which results in stronger interaction between the test gases and the mate-

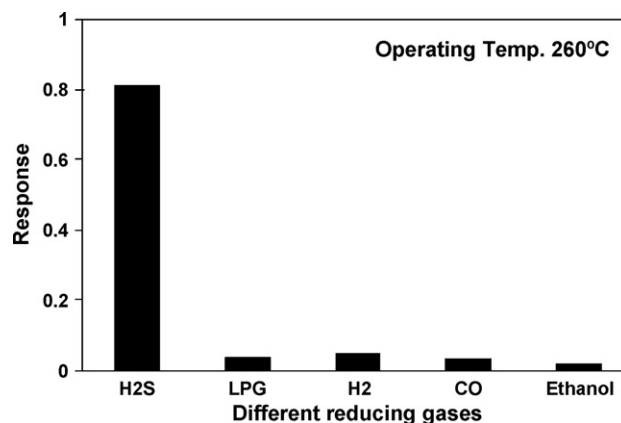


Fig. 6. Response of SFNMO versus different reducing gases at an operating temperature 260 °C.

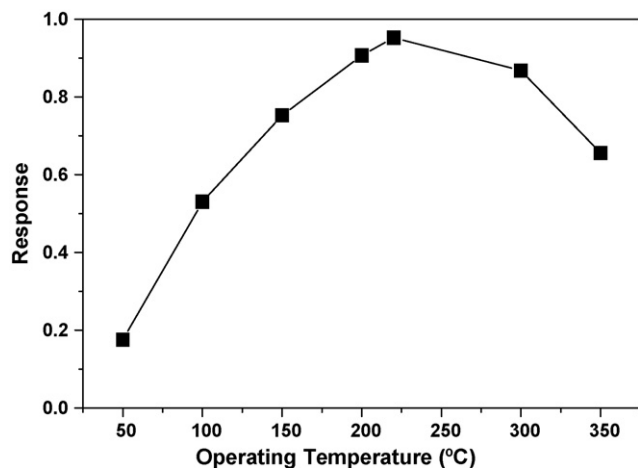


Fig. 7. Effect of Pd doping on SFNMO on the response to H₂S gas.

rial surface. Compared with SFMO, SFNMO showed better response to H₂S. The reason may be that the partial replacement of Fe ions by Ni ions is advantageous to adsorption and oxidation for H₂S. It is evident from the figure that the sensor was highly selective to H₂S gas against CO, LPG, H₂ and ethanol gases. The high selectivity to H₂S gas can be attributed to the surface modification by Ni over Sr₂Fe_{0.6}Ni_{0.4}MoO₆ film.

Noble metal such as Pd was added to SFNMO to improve the response and reduced the operating temperature. Fig. 7 shows the response of 0.5 wt% Pd doped SFNMO as a function of operating temperature for H₂S gas. We observed that sensor reaches its maximum value of response at 220 °C. The reduction in temperature, i.e. from 260 to 220 °C is considered to be very beneficial from the sensor point of view.

In general, the response of gas sensor increases as the concentration of sensing gas is increased. Fig. 8 shows response as a function of amount of gas (in ppm) for 0.5 wt% Pd doped SFNMO, at an operating temperature 220 °C. Figure shows that response of 0.5 wt% Pd doped SFNMO sensor exhibits good dependence on H₂S concentration up to about 100 ppm and further reaches to saturation level. As seen from figure, the response initially increased slowly with increasing concentration and then linearly as the gas concentration increased.

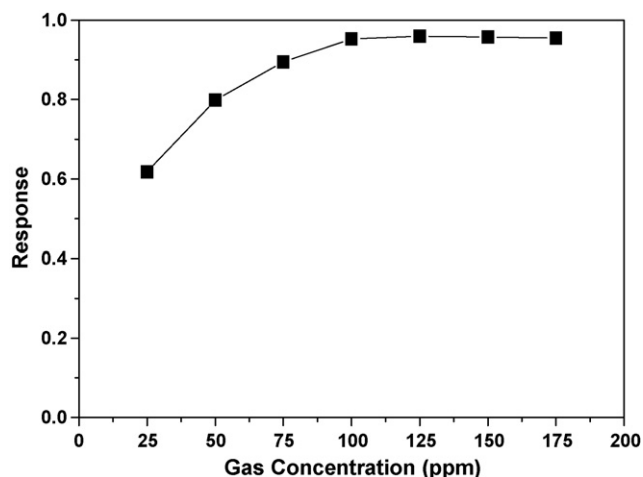


Fig. 8. Variation in response for SFNMO gas sensor as a function of gas concentration for H₂S in ppm.

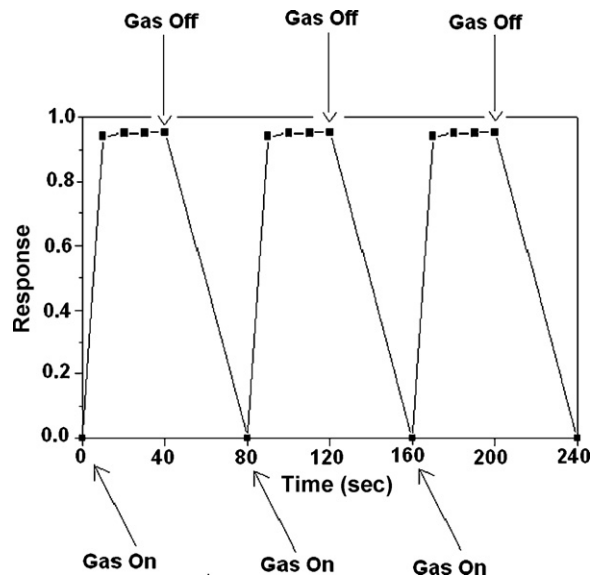
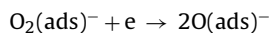
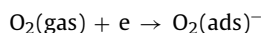


Fig. 9. Response characteristics of SFNMO at 220 °C.

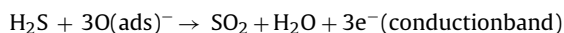
The response and recovery times were used to characterize the sensor performance. The response time defines the time taken for the sensor to reach 90% of the saturation value after contact the test gas with the surface of the sensor; the recovery time is the time of the resistance recovery to the initial level after the removal of the test gas from the environment. Fig. 9 shows the response and recovery time for H₂S gas at an operating temperature of 220 °C. The response and recovery levels were attained at ~20 and ~45 s, respectively, for 0.5 wt% Pd doped SFNMO.

4. Gas sensing mechanism

It is well known that the sensing mechanism of the oxide materials is surface controlled in which the grain size, surface states and oxygen adsorption play an important role [7]. The larger surface area generally provides more adsorption–desorption sites and thus the higher sensitivity. The H₂S sensing mechanism is based on the change in resistance of SFNMO thick film, which is controlled by H₂S vapor species and the amount of the chemisorbed oxygen on the surface. It is known that atmospheric oxygen molecules are adsorbed on the surface of semiconductor oxides in the form of O₂[−], O[−] or O^{2−}. The SFNMO film interacts with oxygen by transferring the electrons from the conduction band to adsorbed oxygen atoms. The reaction may be explained by the following reactions:



When reducing gas molecules like H₂S reacts with negatively charged oxygen adsorbates, the trapped electrons are given back to the conduction band of SFNMO. The reaction of H₂S gas may takes place by following way:



The energy released during decomposition of adsorbed H₂S molecules would be sufficient for electrons to jump up into the conduction band of SFNMO. An increase in operating temperature surely increases the thermal energy so as to stimulate the oxidation of H₂S. The reducing gas donates electrons to SFNMO, which results

increase in the electron concentration of the film. As a consequence, change in the resistance of SFNMO film is observed. This is the reason why the gas response increases with operating temperature. However, the response decreases at higher operating temperatures, as the oxygen adsorbates are desorbed from the surface of the sensor [8].

5. Conclusion

Double perovskite $\text{Sr}_2\text{Fe}_{0.6}\text{Ni}_{0.4}\text{MoO}_6$ with tetragonal structure was prepared by sol–gel citrate method. $\text{Sr}_2\text{Fe}_{0.6}\text{Ni}_{0.4}\text{MoO}_6$ shows response and selectivity for H_2S gas at an operating temperature of 260°C . XRD of $\text{Sr}_2\text{Fe}_{0.6}\text{Ni}_{0.4}\text{MoO}_6$ calcined at 650°C for 6 h showed good crystalline quality and TEM was utilized to observe the microstructure of the particles with a grain size of about 35–45 nm. Incorporation of 0.5 wt% Pd in $\text{Sr}_2\text{Fe}_{0.6}\text{Ni}_{0.4}\text{MoO}_6$ improves the gas response, response time and reduced the operating temperature for H_2S gas.

Acknowledgement

This work was financially supported by the Major Research Project sanctioned by University Grants Commission (UGC), New Delhi, India.

References

- [1] Y.-L. Liu, H. Wang, Y. Yang, Z.-M. Liu, H.-F. Yang, G.-L. Shen, R.Q. Yu, *Sensors and Actuators, B* 102 (2004) 148.
- [2] G.H. Jain, L.A. Patil, M.S. Wagh, D.R. Patil, S.A. Patil, D.P. Amalnerkar, *Sensors and Actuators, B* 117 (2006) 159.
- [3] M.L. Craus, L. Bilteanu, C. Neculita, M. Lozovan, *Optoelectronics and Advanced Materials* 8 (2006) 1720.
- [4] G. Aldica, C. Plapcianu, P. Badica, C. Valsangiacom, B. Popescu, *Optoelectronics and Advanced Materials* 8 (2006) 461.
- [5] H. Ohnishi, H. Sasaki, T. Matsumoto, M. Ippommatsu, *Sensors and Actuators, B* 14 (1993) 677.
- [6] J. Xu, Q. Pan, Y. Shun, Z. Tian, *Sensors and Actuators, B* 66 (2000) 277.
- [7] A. Rothschild, Y. Komen, *Journal of Applied Physics* 95 (2004) 6374.
- [8] J. Mizsei, *Sensors and Actuators, B* 23 (1995) 173.



Lipoic acid–palladium complex interaction with DNA, voltammetric and AFM characterization

Oana Corduneanu^a, Ana-Maria Chiorcea-Paquim^a, Merrill Garnett^b, Ana Maria Oliveira-Brett^{a,*}

^a Departamento de Química, Faculdade de Ciências e Tecnologia, Universidade de Coimbra, 3004-535 Coimbra, Portugal

^b Garnett McKeen Laboratory, Inc., 7 Shirley Street, Bohemia, NY 11716, USA

ARTICLE INFO

Article history:

Received 29 July 2008

Received in revised form 8 October 2008

Accepted 17 October 2008

Available online 6 November 2008

Keywords:

Lipoic acid

Lipoic acid–palladium complex

Poly-MVATM

Voltammetry

AFM

ABSTRACT

The mechanism of interaction of lipoic acid–palladium complex (LAPd) with double-stranded DNA (dsDNA), as well as the adsorption process and the redox behaviour of LAPd, of its ligand lipoic acid (LA), and of the LAPd-containing dietary supplement, Poly-MVATM, were studied using atomic force microscopy (AFM) and voltammetry at highly oriented pyrolytic graphite (HOPG) and glassy carbon electrodes. In the presence of small concentrations of LAPd molecules, the dsDNA molecules appeared less knotted and bended, and more extended on the HOPG surface, when compared with the dsDNA molecules adsorbed from the same dsDNA solution concentration. The voltammetric results demonstrated the interaction of both LAPd and Poly-MVATM with dsDNA, but no oxidative damage caused to dsDNA was detected. AFM images revealed different adsorption patterns and degree of surface coverage and correlation with the structure, the concentration of the solution, the applied potential, and the voltammetric behaviour of the LA, LAPd and Poly-MVATM was observed. The application of a negative potential caused the dissociation of the LAPd complex and Pd(0) nanoparticle deposition, whereas the application of a positive potential induced the oxidation of the LAPd complex and the formation of a mixed layer of LA and palladium oxides.

© 2008 Elsevier B.V. All rights reserved.

1. Introduction

The lipoic acid–palladium complex (LAPd) was originally designed as a non-toxic chemotherapeutic agent, in a prescription version called DNA Reductase, and consists of a palladium bonded to both end-groups of a lipoic acid (LA), the two sulfurs of the thiolane ring and the carboxyl of the pentanoic chain in a 1:1 ratio, Scheme 1 [1,2]. This arrangement is unique in that it allows the molecule to be both water and lipid soluble. The presence of the free radical scavenger, LA [3,4], and the addition of an alternative energy source, palladium [2,5,6], led to consider that LAPd can be used in the treatment of various cancers [2,7,8].

The LA, ligand in the LAPd complex, is a well established antioxidant that may act as a buffer in cancer therapy [9] where the drugs used are known promoters of oxidative stress, or in therapy of diseases associated with oxidative stress [10–13], either directly as a free radical scavenger [14–16] or indirectly due to its synergistic action with other antioxidants [17].

The LAPd-containing liquid dietary supplement, Poly-MVATM, is based on a LAPd polymer that exists as a trimer of lipoic acid–palladium complex joined to thiamine [1]. Besides the LAPd

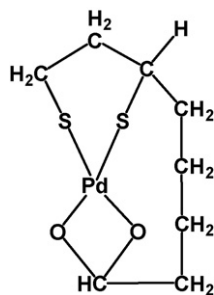
core unit, Poly-MVATM also contains free LA [18], minerals (molybdenum, rhodium, ruthenium), vitamins (B1, B2, B12) and amino acids (N-acetyl cysteine and formyl methionine). LAPd in Poly-MVATM was shown to regulate ischemic cell death and may be a potent neuroprotective agent for victims of transient ischemic attack, cardiac arrest, anesthetic accidents, or drowning [19]. Toxicological studies showed no accumulation in or damage to any tissues, and the median lethal dose, LD₅₀, in mice is greater than 5000 mg kg^{−1} (the highest dosage tested) [19–21]. The Ames test confirmed that the complex is free of mutagenicity [22].

Voltammetric methods have been used for the characterization of LA and palladium(II) containing solutions, at a glassy carbon electrode (GCE) [18,23]. The same methods were employed for the determination LA in two dietary supplements, Poly-MVATM and Solgar Alpha-Lipoic Acid [18]. Atomic force microscopy (AFM) was used to investigate the surface topography of highly oriented pyrolytic graphite (HOPG) electrodes modified with electrodeposited palladium nanoparticles and nanowires [23].

In the present paper, the mechanism of interaction of LAPd with double-stranded DNA (dsDNA) was studied voltammetrically and morphologically evaluated by magnetic AC mode (MAC Mode) AFM. For this purpose, a systematic study of the adsorption process and the redox behaviour of LAPd, of the ligand LA and of the LAPd-containing Poly-MVATM was carried out at two carbon electrodes, HOPG and GCE. The results revealed important correlations

* Corresponding author. Tel.: +351 239 835295; fax: +351 239 835295.

E-mail address: brett@ci.uc.pt (A.M. Oliveira-Brett).



Scheme 1. Proposed structure of LAPd.

between the different adsorption patterns, conformational changes and the voltammetric behaviour of LAPd and dsDNA upon interaction.

2. Experimental

2.1. Materials and reagents

Solutions of 10 mM LAPd and 13 mg mL⁻¹ Poly-MVATM (of proprietary blend as marketed, containing 40 mM LAPd) were from Garnett McKeen Laboratory, Inc. and were used without further purification. Solutions of different concentrations of either LAPd or Poly-MVATM were freshly prepared before each experiment by dilution of the appropriate quantity in supporting electrolyte. DL- α -lipoic acid (LA) was purchased from Sigma–Aldrich. A stock solution of 100 mM LA was prepared in ethanol/water 1:1 and kept at 4 °C. Calf thymus dsDNA and all the other reagents were Merck analytical grade. A stock solution of 300 μ g mL⁻¹ dsDNA was prepared in deionized water and kept at 4 °C.

The solutions were then diluted to the desired concentration by mixing buffer supporting electrolyte. All solutions were prepared using analytical grade reagents and purified water from a Millipore Milli-Q system (conductivity $\leq 0.1 \mu$ S cm⁻¹). The supporting electrolyte solutions were 0.1 M acetate buffer pH 4.5 and 0.1 M phosphate buffer pH 7.0. Nitrogen saturated solutions were obtained by bubbling high purity N₂ for a minimum of 10 min through the solution and a continuous flow of pure gas was maintained over the solution during the voltammetric experiments.

Microvolumes were measured using EP-10 and EP-100 Plus Motorized Microliter Pippettes (Rainin Instrument Co. Inc., Woburn, USA). The pH measurements were carried out with a Crison microPH 2001 pH-meter with an Ingold combined glass electrode. All experiments were done at room temperature (25 \pm 1 °C).

2.2. Atomic force microscopy

HOPG grade ZYB of 15 mm \times 15 mm \times 2 mm dimensions, from Advanced Ceramics Co., was used as a substrate in the AFM study. The HOPG was freshly cleaved with adhesive tape prior to each experiment and imaged by MAC Mode AFM in order to establish its cleanliness.

AFM was performed with a PicoSPM controlled by a MAC Mode module and interfaced with a PicoScan controller from Agilent Technologies, Tempe, AZ (formally Molecular Imaging). A CS AFM S scanner, with a scan range 6 μ m in x - y and 2 μ m in z , and silicon type II MAClevers of 225 μ m length, 2.8 N m⁻¹ spring constants, 60–90 kHz resonant frequencies in air, from Agilent Technologies, were used. All images (256 samples line⁻¹ \times 256 lines) were topographical and were taken in air at room temperature, by MAC Mode, with scan rates of 0.8–2.0 lines s⁻¹. When necessary, the

AFM images were processed by flattening in order to remove the background slope and the contrast and brightness were adjusted.

Section analyses were performed with PicoScan software version 5.3.1, Agilent Technologies and with Origin version 6.0 from Microcal Software, Inc., USA. The mean values of the heights and standard deviations were calculated with Origin version 6.0 from Microcal Software, Inc., USA.

2.3. Voltammetric parameters and electrochemical cells

The voltammetric experiments were performed using an Autolab running with GPES 4.9 software, Eco-Chemie, Utrecht, The Netherlands. Cyclic voltammograms (CVs) were recorded at scan rate of 50 mV s⁻¹. The differential pulse voltammetry (DPV) conditions were: pulse amplitude 50 mV, pulse width 70 ms, step potential 2 mV and scan rate of 5 mV s⁻¹. Measurements were carried out in a 0.5 mL one-compartment electrochemical cell using a glassy carbon electrode (GCE) ($d = 1.5$ mm), with a Pt wire counter electrode, and a Ag/AgCl (3 M KCl) electrode as reference.

The GCE was polished using diamond spray (particle size 1 μ m) before every electrochemical experiment. After polishing, the electrode was rinsed thoroughly with Milli-Q water then it was sonicated for 1 min in an ultrasound bath and again rinsed with water. After this mechanical treatment, the GCE was placed in buffer electrolyte and various CVs were recorded at $V = 100$ mV s⁻¹ until a steady state baseline voltammogram was obtained. This procedure ensured very reproducible experimental results.

Electrochemical deposition of LAPd on the HOPG electrode surface was performed in a one-compartment Teflon cell of approximately 12.5 mm internal diameter, holding the HOPG working electrode on the bottom of the cell. The Pt wire counter and the Ag/AgCl reference electrodes were placed in the cell dipping approximately 5 mm into the solution.

2.4. Sample preparation

The adsorption of LA, LAPd and Poly-MVATM onto HOPG and GCE and the dsDNA interaction with LAPd and Poly-MVATM were studied by MAC mode AFM in air and voltammetric methods, using the procedures described below. For all modified HOPG and GCEs the excess of solution was removed with Millipore Milli-Q water and the electrodes dried in a sterile atmosphere prior to AFM and voltammetric measurements.

2.4.1. Procedure 1 – LA, LAPd, Poly-MVATM and control dsDNA modified HOPG

The spontaneous adsorption of control dsDNA, from 5 μ g mL⁻¹ or 10 μ g mL⁻¹ dsDNA, and different concentrations of LA, LAPd and Poly-MVATM solutions was performed depositing 200 μ L samples of the desired solutions onto freshly cleaved HOPG surfaces and incubating for 3 min.

2.4.2. Procedure 2 – electrodeposited LAPd modified HOPG

The electrodeposition of LAPd was performed from concentrations of 0.1 mM LAPd in 0.1 M phosphate buffer solutions pH 7.0, by applying -1.0 V or $+1.2$ V vs. Ag/AgCl (3 M KCl), during 30 min.

2.4.3. Procedure 3 – electrodeposited LAPd and Poly-MVATM modified GCE

The electrodeposition was performed from 1 mM LAPd or 1.3 mg mL⁻¹ Poly-MVATM (containing 4 mM LAPd) in 0.1 M phosphate buffer pH 7.0, by continuous cycling (10 CVs) or by applying one of the potentials: -1.00 V or $+1.20$ V vs. Ag/AgCl (3 M KCl), during 30 min.

2.4.4. Procedure 4 – layer by layer dsDNA–LAPd modified HOPG

A volume of 200 μL from a 5 μM LAPd in 0.1 M phosphate buffer solution pH 7.0 was deposited for 3 min on a control dsDNA-modified HOPG electrode, *Procedure 1* (5 $\mu\text{g mL}^{-1}$ dsDNA).

2.4.5. Procedure 5 – layer by layer LAPd–dsDNA modified HOPG

A volume of 200 μL from a 5 $\mu\text{g mL}^{-1}$ dsDNA in 0.1 M phosphate buffer solution pH 7.0 was deposited for 3 min on a LAPd-modified HOPG electrode obtained using either 1 μM or 0.1 μM LAPd solutions, *Procedure 1*.

2.4.6. Procedure 6 – dsDNA–LAPd and dsDNA–Poly-MVATM modified HOPG

For the preparation of dsDNA–LAPd modified HOPG, 5 $\mu\text{g mL}^{-1}$ dsDNA were incubated with 5 μM LAPd or 0.1 μM LAPd, in 0.1 M phosphate buffer pH 7.0, at room temperature, during 24 h. For the preparation of dsDNA–Poly-MVATM modified HOPG, 10 $\mu\text{g mL}^{-1}$ dsDNA were incubated with 3.3 $\mu\text{g mL}^{-1}$ Poly-MVATM (containing 10 μM LAPd), in 0.1 M phosphate buffer pH 7.0, at room temperature, during 24 h. In order to prepare the dsDNA–LAPd and dsDNA–Poly-MVATM modified HOPG, 200 μL samples of the respective incubated solution were placed onto the freshly cleaved HOPG for 3 min.

2.4.7. Procedure 7 – control dsDNA, dsDNA–LAPd and dsDNA–Poly-MVATM modified GCE

The control dsDNA modified GCE was obtained by depositing a volume of 5 μL of 50 $\mu\text{g mL}^{-1}$ dsDNA in 0.1 M acetate buffer solution pH 4.5 onto the GCE for 10 min. The dsDNA–LAPd and dsDNA–Poly-MVATM modified GCE were obtained by incubating the control dsDNA modified GCE for 3, 5 and 10 min with 1.0 mM LAPd or 1.3 mg mL^{-1} Poly-MVATM (containing 4 mM LAPd) in 0.1 M phosphate buffer pH 7.0.

2.4.8. Procedure 8 – control dsDNA and dsDNA–LAPd modified GCE

The control dsDNA modified GCE was prepared from a 30 $\mu\text{g mL}^{-1}$ dsDNA in 0.1 M acetate buffer solution pH 4.5. The dsDNA–LAPd modified GCE was prepared from an incubated solution containing 30 $\mu\text{g mL}^{-1}$ dsDNA and 1 mM LAPd in 0.1 M phosphate buffer pH 7.0 at room temperature, during 48 h. The control dsDNA modified GCE and the dsDNA–LAPd modified GCE were prepared depositing 3 drops of 5 μL each on the GCE and dried under a flow of pure N_2 gas. The modified GCE was then placed in the electrochemical cell where the voltammograms were always recorded in 0.1 M acetate buffer pH 4.5.

3. Results and discussion

The adsorption process and the redox behaviour of LA, LAPd and Poly-MVATM were studied first using AFM and voltammetry and the results obtained are essential to explain the lipoic acid–palladium complex interactions with dsDNA. The investigation of the interaction of dsDNA with LAPd and Poly-MVATM will be based on different morphological and voltammetric modifications.

3.1. Adsorption process and redox behaviour of LA, LAPd and Poly-MVATM

3.1.1. AFM characterization of adsorbed LA, LAPd and Poly-MVATM

The adsorption process of the LA, LAPd and Poly-MVATM, was first investigated by AFM, using the procedures from Section 2.4. As described below, the topographical images clearly showed the capacity of LA, LAPd and Poly-MVATM to interact and adsorb spontaneously on carbon electrode surfaces, forming

different morphological films depending on solution concentration.

In all the AFM experiments the HOPG was used as working electrode, as its atomically flat terraces permit the correct evaluation of the morphological features of the adsorbed molecules and films. As a comparison, the GC surface has a root-mean-square (r.m.s.) roughness of 2.10 nm while the HOPG surface has a r.m.s. roughness of less than 0.06 nm, for a 1000 nm \times 1000 nm surface area. Furthermore, the experiments using GCE and HOPG electrodes showed similar electrochemical behaviour.

3.1.1.1. Spontaneous adsorption of LA onto HOPG. The LA molecule is the ligand in the LAPd complex and has a disulfide-containing base, a short alkyl chain with four CH_2 units, and a carboxyl termination [18]. The spontaneous adsorption of LA onto HOPG (Fig. 1A–D) was performed using the *Procedure 1*. AFM images in air of the LA modified HOPG, obtained from a solution of 400 μM LA, showed an approximately 0.5 nm height thin LA film (Fig. 1A) that corresponds to a monolayer formed by hydrophobic interactions between LA alkyl chains and the hydrophobic HOPG surface. Also the LA molecules have the tendency to form 0.8–5.0 nm height spherical aggregates which are uniformly distributed within the LA monolayer.

Using a higher concentration of 40 mM LA, two morphologically different LA layers were observed (Fig. 1B), with 1.5 ± 0.2 nm difference in height between the layers. The internal structure of those two LA layers was revealed in the higher magnification AFM images presented in Fig. 1C and D, which have the scan centres marked as white crosses in Fig. 1B. The first layer (Fig. 1C) was a thin multilayer of LA molecules, which covered completely the HOPG electrode, showed no pores and with large spherical aggregates of 1.0–6.0 nm height embedded into its structure. The second LA layer (Fig. 1D) was a thick and smooth multilayer, with only a few narrow indentations, of 0.8–1.8 nm depth, that were not sufficiently deep to reach the HOPG substrate underneath.

3.1.1.2. Spontaneous adsorption of LAPd onto HOPG. The LAPd modified HOPG electrode was obtained by spontaneous adsorption during 3 min, from different concentrations of LAPd, using the method described in *Procedure 1*. AFM images of the LAPd modified HOPG obtained from a low concentration of 0.1 μM LAPd solution showed large aggregates of 0.9 ± 0.2 nm height (Fig. 2A). LAPd presents a large three-dimensional structure, with the palladium in the centre of the complex, covalently coordinated with both oxygens of the LA carbonyl and one or more sulphur atoms (Scheme 1) [2]. The approximately 0.9 nm height of the LAPd aggregates is related with the deposition of a monolayer of molecules on the HOPG surface.

AFM images of adsorption from a 1 μM LAPd solution (Fig. 2B) showed looped filaments of 1.4 ± 0.1 nm height, as a result of the aggregation of the small LAPd molecules, and large portions of uncovered HOPG. AFM images of adsorption from a 10 μM LAPd solution (Fig. 2C) and 50 μM LAPd solutions (data not shown) showed similar results: a less compact LAPd film with larger pores of 1.6 ± 0.3 nm depth. The height of the LAPd films constantly increased with increasing the LAPd solution concentration, due to the formation of LAPd multilayers. Inside the LAPd film small aggregated molecules were observed.

AFM images of the LAPd modified HOPG obtained from a 100 μM LAPd solution (Fig. 2D) showed the formation of a thick uniform film, covering the electrode completely. Small indentations into the LAPd film were observed with the measured depth 0.7 ± 0.1 nm, not sufficiently deep to reach the HOPG. AFM images of LAPd modified HOPG surfaces obtained by spontaneous adsorption during 30 min

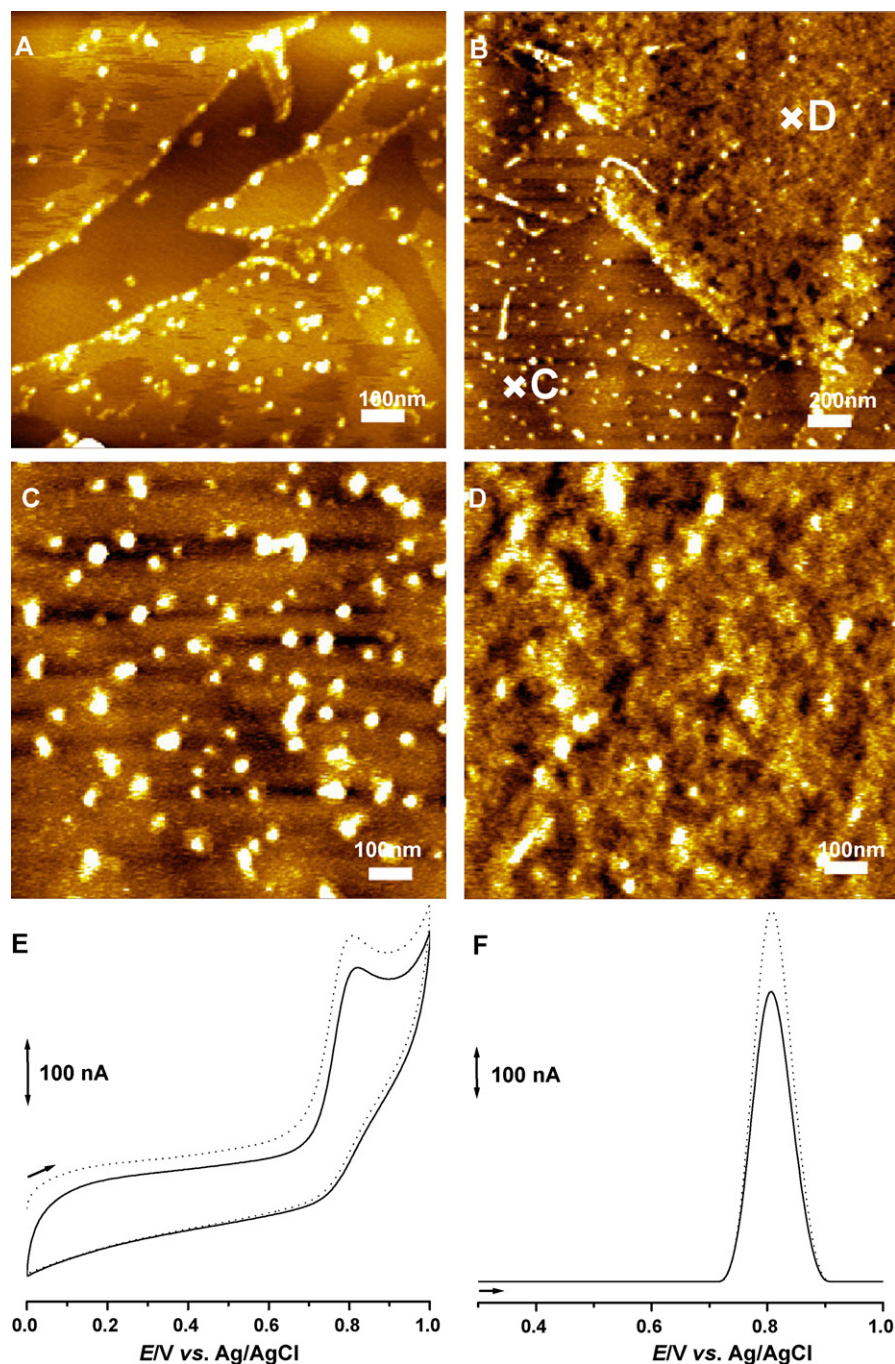


Fig. 1. AFM images of LA modified HOPG (*Procedure 1*) from: (A) 400 μ M and (B–D) 40 mM LA. (C and D) higher magnification images with the scan centres marked as white crosses in image (B). (E) CVs and (F) DPVs in 100 μ M LA in 0.1 M phosphate buffer pH 7.0, (•••) first and (—) 2nd scan. See Section 2 for details.

from the same solution concentration also led to a complete coverage of the HOPG.

3.1.1.3. Adsorption of LAPd under an applied potential. Electrodeposited LAPd modified HOPG surfaces were achieved by applying the potentials of -1.0 V or $+1.2$ V, during 30 min, in 0.1 mM LAPd, as described in *Procedure 2*. Negative and positive applied potentials have different effect on the adsorption and electrochemical behaviour of LAPd molecules onto HOPG (Fig. 3A and B).

AFM images of LAPd electrodeposited on HOPG at $E_{\text{dep}} = -1.00$ V showed small nanoparticles, with irregular shape and dimensions of approximately 3–7 nm height, randomly dispersed into a com-

plex, 1.4 ± 0.2 nm height, two-dimensional network spread over the HOPG terraces (Fig. 3A).

AFM studies performed in palladium(II) containing solutions demonstrated that at $E_{\text{dep}} = -1.00$ V, Pd(0) nanoparticles and nanowires were electrodeposited on the surface of HOPG [23]. Therefore, the application of a high negative potential caused the dissociation of the LAPd complex and Pd(0) deposition as nanoparticles, that were embedded into the observed network film formed by a mixture of LA and LAPd molecules (Fig. 3A). The network has many pores, the dark regions in the image, leading to exposed HOPG surface at the bottom of the pores and presents a minor surface coverage when compared with the LAPd multilayer films

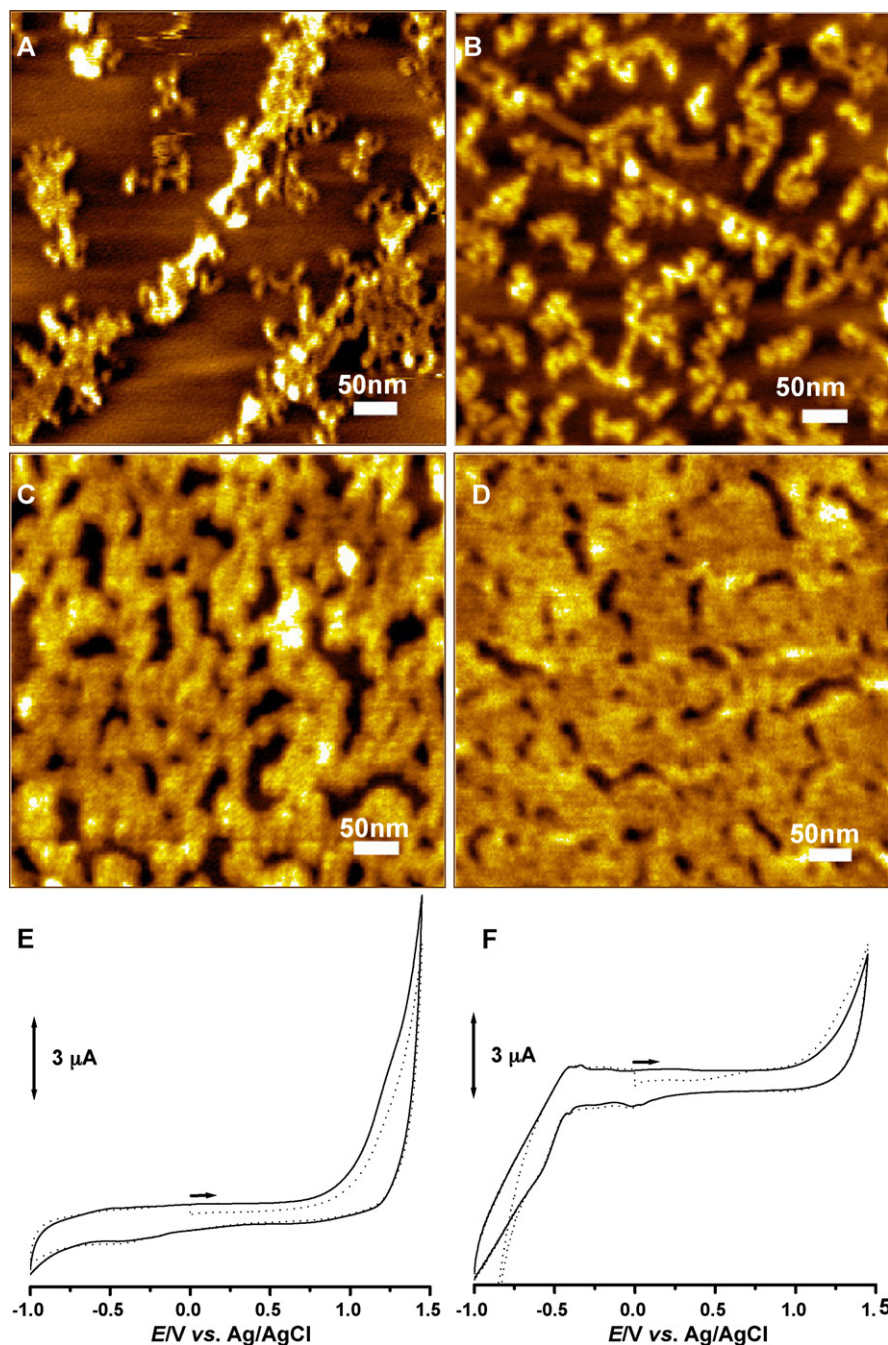


Fig. 2. (A–D) AFM images of LAPd modified HOPG (*Procedure 1*) from: (A) 0.1 μM, (B) 1 μM, (C) 10 μM and (D) 100 μM LAPd. (E, F) CVs in: (E) 1 mM LAPd in 0.1 M phosphate buffer pH 7.0, (•••) 1st and (—) 10th scan, (F) 0.1 M acetate buffer pH 4.5 (*Procedure 3*) after 10 CV scans in 1 mM LAPd, (•••) 1st and (—) 3rd scan. See Section 2 for details.

spontaneously adsorbed onto HOPG from the same solution concentration.

AFM images of LAPd electrodeposited at $E_{\text{dep}} = +1.2$ V showed a two-dimensional film (Fig. 3B) with a very compact morphology formed by small densely packed globular aggregates. The film presents both narrow pores as well as large ones that revealed uncovered HOPG, allowing the measurement of the film thickness of 2.7 ± 0.3 nm. The application of a positive potential induced the oxidation of the LAPd complex and the formation of a mixed multilayer of palladium oxides, LA and LAPd onto HOPG.

3.1.1.4. Spontaneous adsorption of Poly-MVATM onto HOPG. The Poly-MVATM modified HOPG was achieved by spontaneous adsorption

during 3 min as described in *Procedure 1*. AFM images of adsorption from $3.3 \mu\text{g mL}^{-1}$ Poly-MVATM (containing 10 μM LAPd) showed only a few molecules on the HOPG surface, assembled as small spherical 1.2 ± 0.3 nm height aggregates (Fig. 4A). For higher concentrations of $33 \mu\text{g mL}^{-1}$ Poly-MVATM (containing 100 μM LAPd), a uniform but incomplete film was observed, with the molecules forming thick globular filaments of 1.6 ± 0.4 nm height (Fig. 4B).

3.1.1.5. Comparison between LA, LAPd and Poly-MVATM spontaneous adsorption. The topography of the LAPd modified HOPG suggests that LAPd adsorbs strongly onto HOPG surface even at a very low concentration of 0.1 μM LAPd (Fig. 2A), when compared with LA molecules that only form incomplete monolayer films at 400 μM

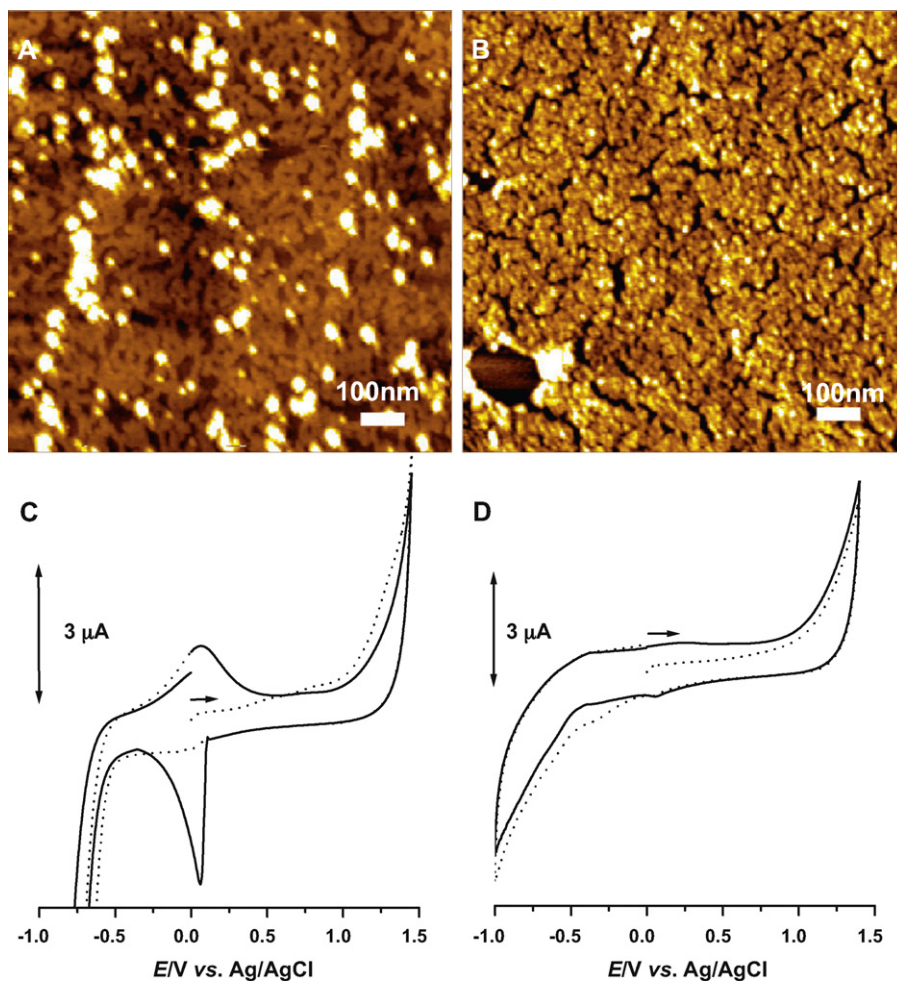


Fig. 3. (A and B) AFM images of electrodeposited LAPd modified HOPG (Procedure 2) from 100 μM LAPd: (A) -1.0 V and (B) $+1.2\text{ V}$. (C, D) CVs in 0.1 M acetate buffer pH 4.5 (Procedure 3) after 30 min electrodeposition in 1 mM LAPd: (C) -1.00 V , (D) $+1.20\text{ V}$, (•••) 1st and (—) 2nd scan. See Section 2 for details.

LA (Fig. 1A). The LAPd greater adsorption onto HOPG is due to the presence of palladium into the LA structure (Scheme 1), which facilitates the interaction with the HOPG substrate. Indeed, complementary AFM studies showed that palladium(II) presents spontaneous adsorption onto the HOPG electrode from either PdSO_4 or PdCl_2 solutions.

In the case of Poly-MVATM modified HOPG, and for the corresponding concentration of LAPd in solution (10 μM or 100 μM LAPd), a decreased surface coverage was observed (Fig. 4A and B), in comparison with the LAPd modified HOPG (Fig. 2C and D). The Poly-MVATM active ingredient is a LAPd polymer that exists as a trimer of LAPd joined to thiamine [1,2]. Consequently, in Poly-MVATM, palladium is more hidden into the complex polymeric structure, decreasing the possibility of direct LAPd interaction with the carbon electrode surface, which explains the lower adsorption of the Poly-MVATM.

3.1.2. Voltammetric characterization of LAPd and Poly-MVATM

3.1.2.1. Redox behaviour of LA, LAPd and Poly-MVATM. The redox behaviour of LA was investigated by CV and DPV at GCE in 100 μM LA in 0.1 M phosphate buffer pH 7.0, and one anodic irreversible peak occurred at $E_{\text{pa}} = +0.80\text{ V}$ (Fig. 1E and F) that was identified as the α -lipoic acid oxidation to β -lipoic acid [18].

Next, the voltammetric behaviour of LAPd at GCE was investigated by CV in 1 mM LAPd in 0.1 M phosphate buffer pH 7.0, N_2 saturated solution (Fig. 2) starting scanning at $E_i = 0.00\text{ V}$, in

the positive direction, between the potential limits of $E_1 = +1.40\text{ V}$ and $E_2 = -1.00\text{ V}$. Upon extensive cycling in the solution, an anodic peak at $E_{\text{pa}} = +1.20\text{ V}$ and a cathodic peak at $E_{\text{pc}} = -0.40\text{ V}$ (Fig. 2E) appeared. After 10 CV scans, the GCE was rinsed and transferred to 0.1 M acetate buffer pH 4.5 only. The voltammogram showed clearly a more complex redox behaviour at this pH (Fig. 2F) in agreement with the electrochemical behaviour of electrodeposited palladium nanostructures onto GCE [23].

The voltammetric behaviour of Poly-MVATM at GCE was studied by CV in 1.3 mg mL^{-1} of Poly-MVATM (containing 4 mM LAPd) in 0.1 M phosphate buffer pH 7.0. The CV experiments showed three oxidation peaks in the first scan (data not shown), which did not increase upon continuous cycling (10 CV scans) in the same solution. When the GCE was transferred to 0.1 M acetate buffer pH 4.5, the voltammogram showed in the first CV scan only one oxidation peak. Using DPV, scanning from $E_i = 0.0\text{ V}$ to $E_1 = +1.40\text{ V}$, a better assessment of the oxidation processes of Poly-MVATM and the comparison with the LAPd oxidation results (Fig. 5) was possible.

The DPV recorded in 1 mM LAPd in 0.1 M phosphate buffer pH 7.0 solution showed a well defined oxidation peak, $E_{\text{pa}} = +1.11\text{ V}$, while in the case of 1.3 mg mL^{-1} Poly-MVATM (4 mM LAPd) in 0.1 M phosphate buffer pH 7.0 solution, similarly to the CVs three oxidation peaks occurred at $E_{\text{pa}} = +0.57\text{ V}$, $+0.85\text{ V}$ and $+1.30\text{ V}$ (Fig. 5A).

After 3 min spontaneous adsorption directly from the stock solutions of LAPd (10 mM), Poly-MVATM (13 mg mL^{-1} , containing 40 mM LAPd), and 1 mM PdCl_2 on GCE surface, the electrode was

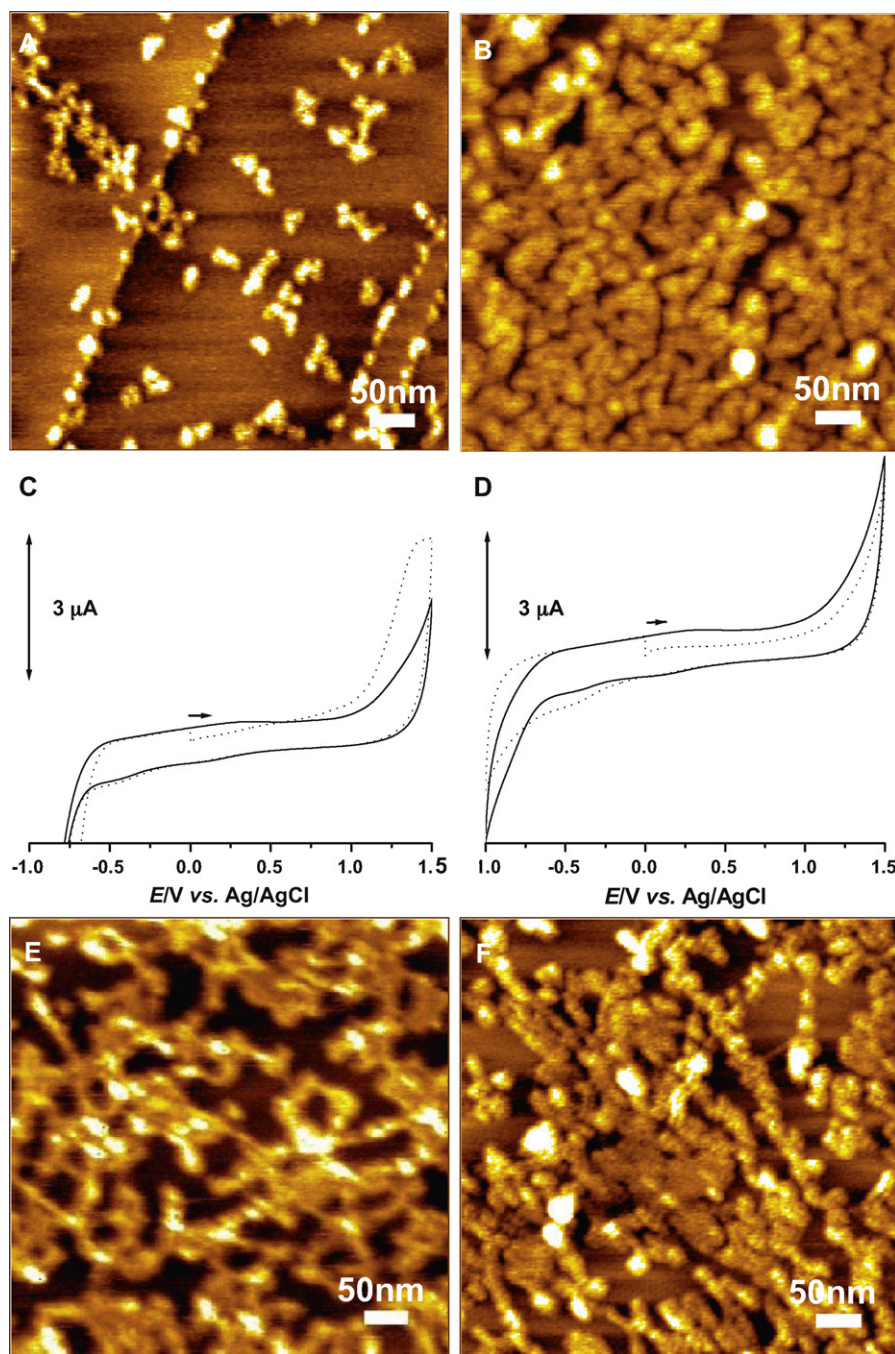


Fig. 4. (A, B, E, F) AFM images of (A and B) Poly-MVATM modified HOPG (Procedure 1) from: (A) 3.3 $\mu\text{g mL}^{-1}$ and (B) 33 $\mu\text{g mL}^{-1}$ Poly-MVATM, (E) control dsDNA modified HOPG (Procedure 1) from 10 $\mu\text{g mL}^{-1}$ dsDNA and (F) dsDNA–Poly-MVATM modified HOPG (Procedure 6). (C and D) CVs in 0.1 M acetate buffer pH 4.5 (Procedure 3) after 30 min electrodeposition in 1.3 mg mL^{-1} Poly-MVATM: (C) -1.00 V and (D) $+1.20\text{ V}$, (•••) 1st and (—) 3rd scan. See Section 2 for details.

transferred to 0.1 M acetate buffer pH 4.5 and DPVs (Fig. 5B) were recorded. The palladium characteristic voltammetric behaviour [23], seen in the voltammograms of Fig. 2E, was also observed after transferring the GCE to buffer (Figs. 2F and 5B). The voltammetry of the LAPd complex at the GCE and the AFM results are in agreement with the proposed LAPd structure (Scheme 1) that palladium incorporated into LA facilitates the interaction with the carbon substrates. The results obtained by DPV after spontaneous adsorption from either PdCl_2 or the LAPd solution (Fig. 5B) show the characteristic peak for palladium oxide formation during the voltammetric scan, $E_{\text{pa}} = +1.15\text{ V}$ in 0.1 M acetate buffer pH 4.5.

In the case of Poly-MVATM, the results showed that while three successive oxidation processes occur when the voltammogram was recorded in the Poly-MVATM containing solution (Fig. 5A), when the GCE was transferred to buffer an oxidation peak occurring at $E_{\text{pa}} = +1.10\text{ V}$ appeared, which is not related with the palladium oxide formation. The anodic peak at $E_{\text{pa}} = +0.85\text{ V}$ corresponds to the free LA present in Poly-MVATM, confirmed by standard addition of LA [18]. The differences in the oxidation potential between the standard LA (Fig. 1E and F) and LA in Poly-MVATM (Fig. 5A) are small and due to a matrix effect. The oxidation processes at $E_{\text{pa}} = +0.57\text{ V}$ is related to the oxidation

of other components present in the complex matrix of the Poly-MVATM.

3.1.2.2. Electrodeposition of LAPd and Poly-MVATM. Electrodeposition of LAPd and Poly-MVATM on GCE was carried out by applying the potentials $E_{\text{dep}} = -1.0$ V or $E_{\text{dep}} = +1.2$ V, during 30 min, *Procedure 3*, in 1 mM LAPd or 1.3 mg mL⁻¹ Poly-MVATM (containing 4 mM LAPd) in 0.1 M phosphate buffer pH 7.0.

A very complex redox behaviour, with various charge transfer reactions occurring at positive and negative potentials was observed in the CVs recorded in buffer (Fig. 3C) after electrodeposition at $E_{\text{dep}} = -1.0$ V in a 1 mM LAPd solution. The shape of the voltammetric wave changed upon cycling, in the subsequent scans a large anodic peak at $E_p = +0.06$ V and, after reversing the scan direction, a sharp cathodic peak at $E_{\text{pa}} = +0.05$ V, were found. After electrodeposition at $E_{\text{dep}} = +1.20$ V from 1 mM LAPd solution, the CVs obtained in 0.1 M acetate buffer pH 4.5 showed only small reduction peaks, at $E_{\text{pc}} = +0.06$ V and $E_{\text{pc}} = -0.30$ V, which improved slightly in the subsequent scans (Fig. 3D).

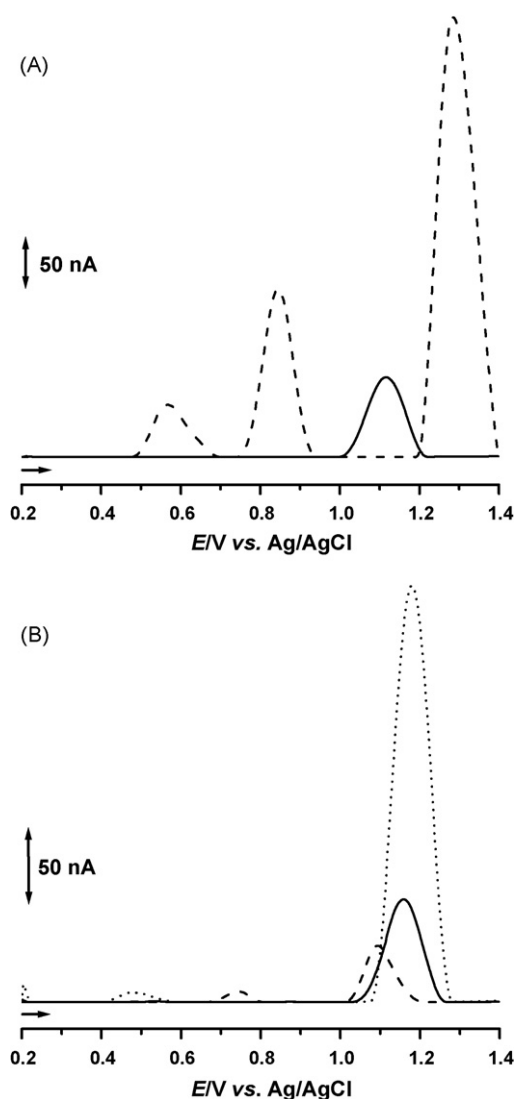


Fig. 5. DPVs in: (A) (—) 1 mM LAPd and (---) 1.3 mg mL⁻¹ Poly-MVATM (4 mM LAPd) in 0.1 M phosphate buffer pH 7.0. (B) 0.1 M acetate buffer pH 4.5 after 3 min spontaneous adsorption from: (—) 10 mM LAPd, (---) 13 mg mL⁻¹ Poly-MVATM (40 mM LAPd) and (●●●) 1 mM PdCl₂. See Section 2 for details.

Voltammetric studies performed in palladium containing solutions [23] showed that palladium is electrodeposited on GCE as Pd(0), after applying a negative potential, or palladium oxides, after applying a positive potential. Applying the potential of $E_{\text{dep}} = -1.00$ V ensured that more palladium could be removed from the LAPd complex and deposited at GCE as Pd(0), than in the case of continuous cycling (Fig. 5A and B) the voltammograms showing the characteristic palladium electrochemical behaviour [23], i.e. oxide formation and their reduction at positive potentials and hydrogen incorporation at negative potentials (Fig. 3C). Electrodeposition at $E_{\text{dep}} = +1.20$ V was also performed in order to confirm that palladium could be removed from the LAPd complex and deposited as palladium oxides. The peaks obtained in buffer only, although smaller than in the case of $E_{\text{dep}} = -1.00$ V electrodeposition, improved in the subsequent recorded scans, corresponding to reduction of the palladium oxides deposited on GCE to Pd(0) (Fig. 3D).

Whereas after the electrodeposition performed in the solution of 1.3 mg mL⁻¹ Poly-MVATM at $E_{\text{dep}} = -1.00$ V, the CVs showed in buffer an oxidation peak, $E_{\text{pa}} = +1.37$ V (Fig. 4C) after electrodeposition at $E_{\text{dep}} = +1.20$ V from the same the Poly-MVATM solution no peaks were observed (Fig. 4D). This means that the voltammetric behaviour of Poly-MVATM (Fig. 6) cannot be associated with the known electrochemistry of palladium (Fig. 3C and D); although a charge transfer reaction was observed in the first voltammogram, no other peaks could be detected in the following scans.

3.2. Interaction of dsDNA with LAPd and Poly-MVATM

3.2.1. AFM characterization of dsDNA–LAPd and dsDNA–Poly-MVATM interaction

The mechanism of interaction of LAPd and Poly-MVATM with dsDNA was investigated and characterized by AFM. The films on HOPG were prepared depositing layer by layer dsDNA–LAPd (*Procedure 4*) and LAPd–dsDNA (*Procedure 5*), and from incubated solutions of dsDNA–LAPd and dsDNA–Poly-MVATM (*Procedure 6*).

In order to have the dsDNA control adsorption pattern, AFM was employed to study spontaneous adsorption of dsDNA from solutions of 5 μ g mL⁻¹ and 10 μ g mL⁻¹ dsDNA, as described in *Procedure 1*. The AFM topographical images in air of the dsDNA film obtained from 5 μ g mL⁻¹ dsDNA showed coiled dsDNA molecules of 1.5 ± 0.6 nm height (Fig. 6A), while from 10 μ g mL⁻¹ dsDNA showed a thin network of 1.1 ± 0.2 nm height (Fig. 4E).

The layer by layer dsDNA–LAPd modified HOPG, *Procedure 4* (Fig. 6B), was obtained by LAPd spontaneous adsorption from a solution of 5 μ M LAPd onto the control dsDNA modified HOPG obtained from 5 μ g mL⁻¹ dsDNA (Fig. 6A). The AFM images showed small aggregates of molecules, as well as looped filaments with portions of linear dsDNA. The measured thickness of the dsDNA–LAPd film was of 1.3 ± 0.4 nm.

The layer by layer LAPd–dsDNA modified HOPG surfaces, *Procedure 5* (Fig. 6C and D), were obtained by dsDNA spontaneous adsorption from a solution of 5 μ g mL⁻¹ dsDNA onto a LAPd modified HOPG prepared from LAPd solutions of 0.1 μ M (Fig. 2A) or 1 μ M (Fig. 2B). The AFM images of the LAPd–dsDNA modified HOPG (0.1 μ M LAPd) (Fig. 6C) showed a loosely packed film of 1.6 ± 0.3 nm height and spherical aggregates, up to 5 nm height, adsorbed on the HOPG areas uncovered by the LAPd–dsDNA. The AFM images of the LAPd–dsDNA modified HOPG (1 μ M LAPd) (Fig. 6D) showed a non-compact, granular film of 1.4 ± 0.2 nm height, and unknotted extended dsDNA molecules could be imaged inside the LAPd–dsDNA film. The measured thickness of the layer by layer dsDNA–LAPd and LAPd–dsDNA films presented heights consistent with both the height of the coiled dsDNA molecules and LAPd films, leading to inconclusive results concerning the LAPd

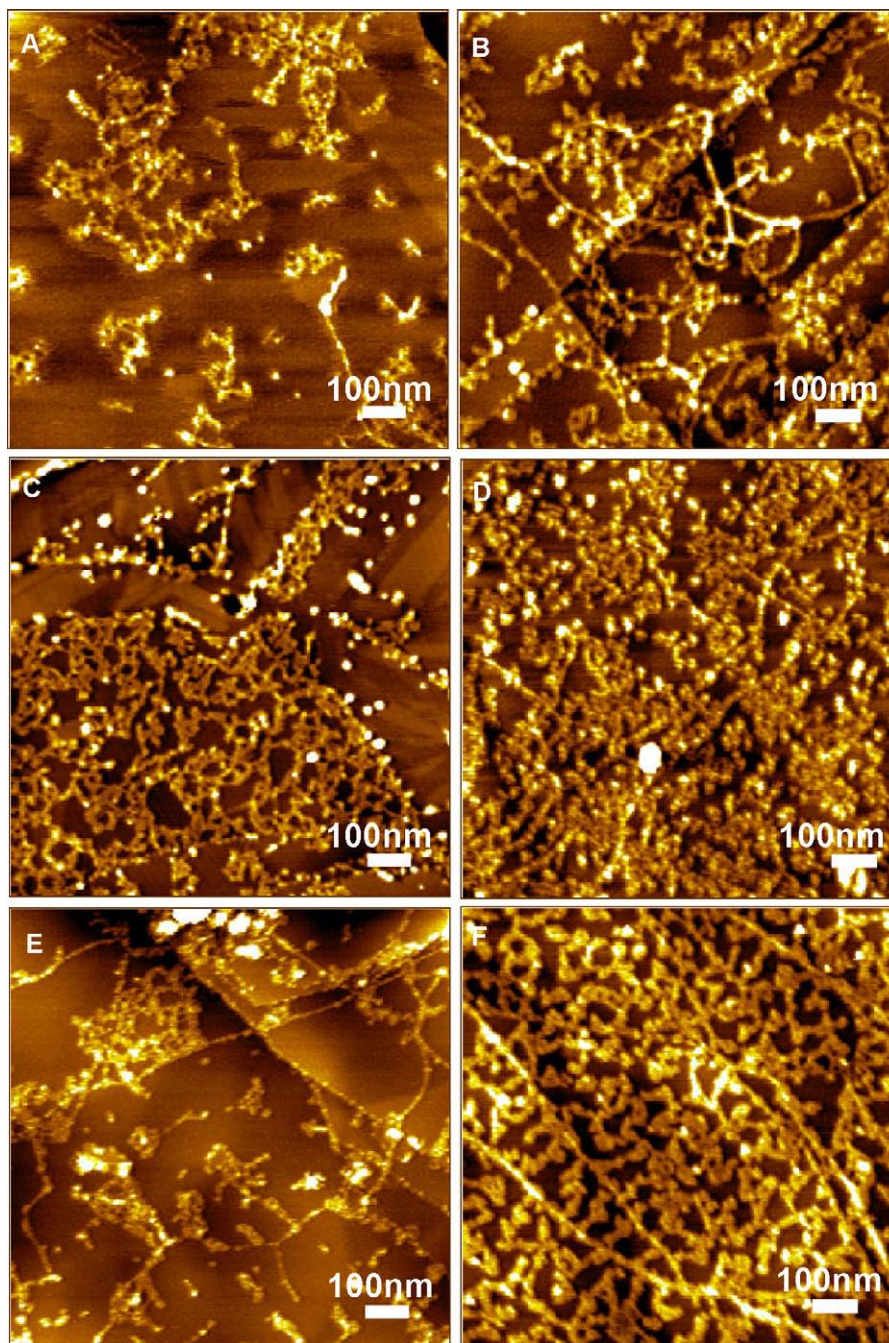


Fig. 6. AFM images of: (A) control dsDNA modified HOPG (*Procedure 1*) from $5 \mu\text{g mL}^{-1}$ dsDNA, (B) dsDNA–LAPd modified HOPG (*Procedure 4*). (C and D) LAPd–dsDNA modified HOPG (*Procedure 5*): (C) $0.1 \mu\text{M}$ and (D) $1.0 \mu\text{M}$ LAPd. (E and F) dsDNA–LAPd modified HOPG (*Procedure 6*): (E) $0.1 \mu\text{M}$ and (F) $5.0 \mu\text{M}$ LAPd. See Section 2 for details.

interaction with dsDNA. Therefore the LAPd interaction with dsDNA in solution was also AFM morphologically evaluated.

The HOPG electrode was modified by a dsDNA–LAPd film obtained by spontaneous adsorption during 3 min from incubated solutions of $5 \mu\text{g mL}^{-1}$ dsDNA with $0.1 \mu\text{M}$ or $5 \mu\text{M}$ LAPd, as described in the *Procedure 6*. AFM images of dsDNA–LAPd modified HOPG, from $0.1 \mu\text{M}$ LAPd, showed the HOPG surface covered by small aggregates, a few twisted molecules, as well as a high number of unknotted extended dsDNA molecules of $1.2 \pm 0.2 \text{ nm}$ height (Fig. 6E). Using $5 \mu\text{M}$ LAPd, the AFM images showed the formation of a network with thick filaments of $1.7 \pm 0.2 \text{ nm}$ height, and a number of dsDNA molecules arranged near the step edges of the HOPG were also observed inside the network film (Fig. 6F).

In conclusion, in the presence of lower concentration of LAPd the dsDNA molecules appeared less tangled and bended, and more extended on the HOPG surface (Fig. 6B–F), when compared with the dsDNA molecules adsorbed from the control dsDNA solution of the same concentration (Fig. 6A).

For the AFM morphological evaluation of the Poly-MVATM interaction with dsDNA in solution, the HOPG electrode was modified by a dsDNA–Poly-MVATM film obtained by spontaneous adsorption during 3 min from incubated solutions of $10 \mu\text{g mL}^{-1}$ dsDNA with $3.3 \mu\text{g mL}^{-1}$ Poly-MVATM (containing $10 \mu\text{M}$ LAPd), as described in the *Procedure 6*. AFM images showed a layer formed by tight loops and areas of the HOPG that were not covered at all (Fig. 4F). The dsDNA–Poly-MVATM film was composed by aggregates of

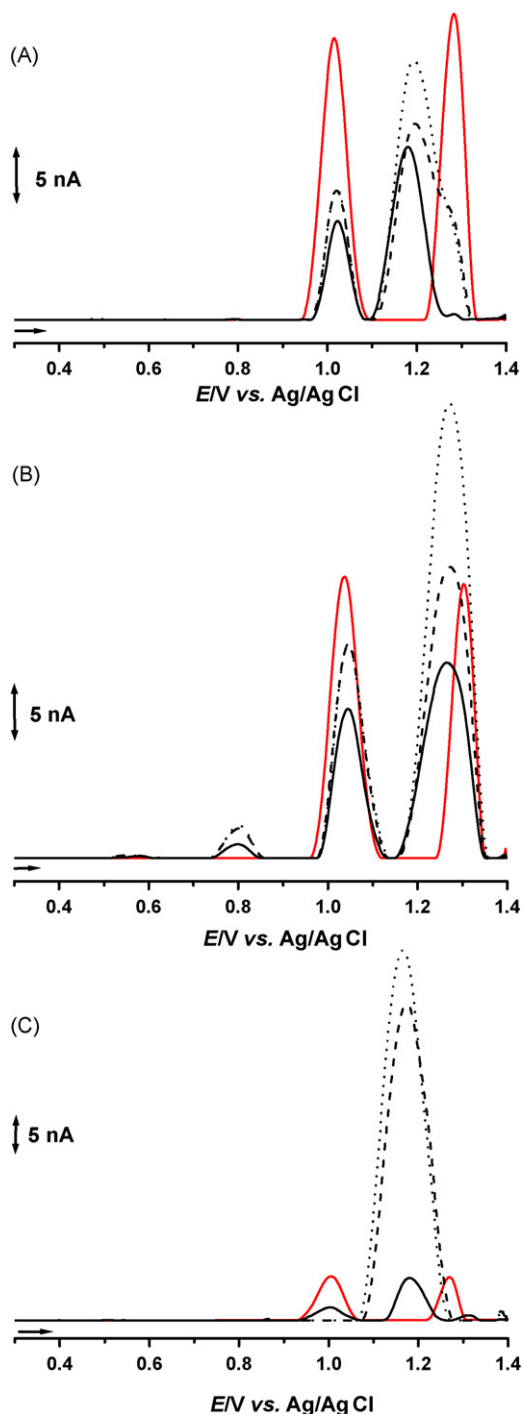


Fig. 7. DPVs in 0.1 M acetate buffer pH 4.5: (A–B) Procedure 7: (—) control dsDNA modified GCE, (A) dsDNA–LAPd modified GCE and (B) dsDNA–Poly-MVATM modified GCE, incubation time (—) 3, (---) 5, and (····) 10 min. (C) Procedure 8: (—) control dsDNA modified GCE and dsDNA–LAPd modified GCE (—) 1st, (---) 2nd and (····) 3rd scan. See Section 2 for details.

molecules of 1.8 ± 0.3 nm height, larger than the expected height of the dsDNA, which suggest a complex interaction of the dsDNA with the various molecules existent in the Poly-MVATM solution.

3.2.2. Voltammetric characterization of dsDNA–LAPd and dsDNA–Poly-MVATM interaction

The dsDNA interaction with LAPd and Poly-MVATM was studied in order to investigate the palladium complex action in inducing

double helix deconformation, hydrogen bonding cleavage and/or oxidative damage to DNA bases. The interaction was followed by DPV, and the observed changes of the purine bases' oxidation peak currents, desoxyguanosine (dGuo), $E_{pa} = +1.03$ V, and desoxyadenosine (dAdo), $E_{pa} = +1.30$ V, were compared with the results obtained for a dsDNA control solution. The occurrence of the guanine or/and adenine oxidation product peaks, the biomarkers 8-oxoguanine and 2,8-dihydroxyadenine, at $E_{pa} \sim +0.45$ V in 0.1 M acetate buffer pH 4.5, is an indication of oxidative damage caused to DNA [24,25].

The GCE was modified with a thin-layer of dsDNA, Procedure 7, and then incubated for different periods of time with either 1 mM LAPd or 1.3 mg mL⁻¹ Poly-MVATM (4 mM LAPd) in 0.1 M phosphate buffer pH 7.0. The DPV recorded in 0.1 M acetate buffer pH 4.5 showed changes in the peak currents corresponding to the oxidation of dGuo and dAdo, respectively, when compared with the results obtained for the dsDNA control solution (Fig. 7). However, other oxidation processes were also detected, the peak at $E_{pa} = +1.18$ V in the case of dsDNA–LAPd incubation (Fig. 7A) and oxidation peaks at $E_{pa} = +0.55$ V, $E_{pa} = +0.80$ V and $E_{pa} = +1.27$ V in the case of dsDNA–Poly-MVATM incubation (Fig. 7B) and all increased with increasing incubation times.

In another experiment, the interaction of LAPd with dsDNA was studied at GCE after 48 h incubation time, Procedure 8. The DPVs recorded in acetate buffer showed very small dGuo and dAdo peak currents, compared with the dsDNA control solution, and a large oxidation peak which rapidly increases in the following DPV scans, $E_{pa} = +1.18$ V, corresponding to the joint deposition of palladium oxides that hinders the DNA oxidation processes (Fig. 7C). The voltammetric results led to the conclusion that modification of the dsDNA structure occurs upon interaction with LAPd, recognized through the decrease of the dGuo and dAdo oxidation peaks (Fig. 7A and C). Moreover, no oxidative damage to dsDNA was detected, as no oxidation peaks corresponding to DNA oxidative damage were noted in the DPVs recorded either after short (10 min) or long (48 h) incubation times.

The interaction of dsDNA with Poly-MVATM (Fig. 7B) was found to be difficult to assess when compared to the interaction of dsDNA with LAPd, due to the other redox active compounds existent in the Poly-MVATM matrix. However, as no oxidation peaks of 8-oxoguanine or 2,8-dihydroxyadenine were observed in the DPV scans, it was concluded that there was no oxidative damage caused to dsDNA by Poly-MVATM.

4. Conclusions

The interaction of dsDNA with LAPd and Poly-MVATM was studied at room temperature, using AFM and voltammetry, showing that the interaction with either caused no oxidative damage to dsDNA. The interaction of dsDNA with low concentrations of the LAPd complex lead to less knotted and bended, and more extended dsDNA molecules on the HOPG surface, when compared with control dsDNA adsorbed on the HOPG.

The adsorption process and the redox behaviour of LA, LAPd and Poly-MVATM presents characteristic adsorption patterns and degree of HOPG surface coverage, depending on the chemical structures, the dimensions, the solution concentration and the applied potential. The LAPd molecules interact and adsorb strongly on HOPG, in comparison with LA, probably due to the incorporation of palladium into the ligand structure.

By applying high negative or high positive potentials, the stability of both the LAPd complex and the LAPd-containing Poly-MVATM solution was tested. The voltammetric and AFM results show that while in the case of LAPd complex palladium removal is still possible, in the Poly-MVATM solution the same is not achieved,

most likely due to palladium being sequestered within the LAPd polymer joined to thiamine.

Acknowledgements

Financial support from Fundação para a Ciência e Tecnologia (FCT), Post-Doctoral Grant SFRH/BPD/27087/2006 (A.-M. Chiorcea-Paquim), Ph.D. Grant SFRH/BD/18914/2004 (O. Corduneanu), POCI 2010 (co-financed by the European Community Fund FEDER), and CEMUC® (Research Unit 285), is gratefully acknowledged.

References

- [1] M. Garnett, J. Inorg. Biochem. 59 (1995) 231.
- [2] M. Garnett, U.S. Patent No. 5,776,973, 1998.
- [3] H.S. El-Abhar, M. Shaalan, M. Barakat, E.S. El-Denshary, J. Pineal Res. 33 (2002) 87.
- [4] K. Yamamoto, T. Ishikawa, T. Sakabe, T. Taguchi, S. Kawai, M. Marsala, NeuroReport 9 (1998) 1655.
- [5] J.W. Phillis, M.H. O'Regan, Int. Rev. Neurobiol. 51 (2002) 377.
- [6] R.M. Sapolsky, J. Neurosci. 6 (1986) 2240.
- [7] M. Garnett, U.S. Patent No. 5,463,093, 1995.
- [8] M. Garnett, U.S. Patent No. 5,679,697, 1997.
- [9] C. Prahalathan, E. Selvakumar, P. Varalakshmi, Clin. Chim. Acta. 360 (2005) 160.
- [10] V. Morelli, R.J. Zoorob, Am. Fam. Phys. 62 (2000) 1051.
- [11] K. Hager, A. Marahrens, M. Kenkies, P. Riederer, G. Munch, Arch. Gerontol. Geriatr. 32 (2001) 275.
- [12] M. Morini, L. Roccatagliata, R. Dell'Eva, E. Pedemonte, R. Furlan, S. Minghelli, D. Giunti, U. Pfeffer, M. Marchese, D. Noonan, et al., J. Neuroimmunol. 148 (2004) 146.
- [13] V. Yadav, G. Marracci, J. Lovera, et al., Mult. Scler. 11 (2005) 159.
- [14] G.Ph. Biewenga, J. de Jong, A. Bast, Arch. Biochem. Biophys. 312 (1994) 114.
- [15] C. Della Croce, G. Bronzetti, M. Cini, L. Caltavuturo, G. Poi, Toxicol. In Vitro 17 (2003) 753.
- [16] M. Trujillo, L. Folkes, S. Bartesaghi, B. Kalyanaraman, P. Wardman, R. Radi, Free Rad. Biol. Med. 39 (2005) 279.
- [17] G.Ph. Biewenga, G.R.M.M. Haenen, A. Bast, Gen. Pharm. 29 (1997) 315.
- [18] O. Corduneanu, M. Garnett, A.M. Oliveira Brett, Anal. Lett. 40 (2007) 1763.
- [19] F.J. Antonawich, S.M. Fiore, L.M. Welickya, Experim. Neurol. 189 (2004) 10.
- [20] Pharmakon USA, Acute Oral Toxicity Study in Mice (14 day) with Synthetic Reductase, 1, Calvert Laboratories, Inc., Olyphant, PA, 1995.
- [21] Pharmakon USA, Acute Intravenous Toxicity Study in Mice with Synthetic Reductase, 1, Calvert Laboratories, Inc., Olyphant, PA, 1995.
- [22] Pharmakon USA, Ames/Salmonella Plate Incorporation Assay on Synthetic DNA Reductase, 1, Calvert Laboratories, Inc., Olyphant, PA, 1995.
- [23] V.C. Diclescu, A.M. Chiorcea-Paquim, O. Corduneanu, A.M. Oliveira-Brett, J. Solid State Electrochem. 11 (2007) 887.
- [24] A.M. Oliveira-Brett, J.A.P. Piedade, S.H.P. Serrano, Electroanalysis 12 (2000) 969.
- [25] V.C. Diclescu, J.A.P. Piedade, A.M. Oliveira-Brett, Bioelectrochemistry 70 (2007) 141.



Thermally induced electrode protection against biofouling

Heiko Duwensee^{a,b}, Terannie Vázquez-Alvarez^b, Gerd-Uwe Flechsig^{a,*}, Joseph Wang^{c,*}

^a Department of Chemistry, University of Rostock, Dr.-Lorenz-Weg 1, 18051 Rostock, Germany

^b Department of Chemistry and Biochemistry, Biodesign Institute, Arizona State University, Tempe, AZ 85287-5801, USA

^c Department of Nanoengineering, University of California San Diego, La Jolla, CA 92093, USA

ARTICLE INFO

Article history:

Received 15 July 2008

Received in revised form 2 October 2008

Accepted 6 October 2008

Available online 17 October 2008

Keywords:

Heated electrode
Platinum wire electrode
Electrode fouling
Dopamine
Gelatin
Electrode conditioning

ABSTRACT

This paper demonstrates that a combined thermal and electrochemical conditioning step can greatly minimize electrode blocking. We detected 50 ppm dopamine after a blocking step in 1000 ppm gelatine solution. Only a treatment of the electrode at -1.5 V and 61.5°C can reveal the voltammetric dopamine signals to 82%. The increase of the peak separation of the cyclic voltammograms obtained in 50 ppm dopamine is limited to 14%, whereas negative polarization (-1.5 V) alone leads to a 31% increase compared to 109% upon thermal and 105% without any conditioning. The positive effects can be addressed to an enforced reductive degradation and accelerated removal of the blocking agents. Also the formation of hydrogen bubbles might play a significant role. Thermo-electrochemical treatment holds great promise for electrochemical sensors and detectors which are applied for long-term monitoring of samples that contain blocking matrices.

© 2008 Elsevier B.V. All rights reserved.

1. Introduction

So called “electrode fouling” is a major hindrance for the practical application of electrochemical sensors at remote or hidden places. Such blocking of the electrode surface can occur in different ways. Real samples often come with a complex matrix that already contains blocking substances. The latter can also be produced by the electrode process itself such as oxidation of the analyte or certain matrix components. Such build-up of an inhibition layer often leads to severe suppressions and distortions of the current signals, along with irreproducible data.

One approach to minimize fouling is the use of alternate electrode materials like carbon nanotubes [1–3], anodically pretreated carbon fiber microelectrodes [4] or boron-doped diamond, which combine attractive electrochemical properties (stability and sensitivity) [5,6] and high resistance to deactivation via fouling [7] or dissolved oxygen [8]. Glassy carbon electrodes modified with single and multiwall carbon nanotubes show a decrease in the over-voltage for NADH detection along with minimal surface fouling during amperometric detection [2,9]. A chemical reversibility of the NADH oxidation reaction was achieved by modification of the electrode surface with poly(1,2-diaminobenzene) conducting nan-

otube coatings [10]. Baranski applied a hot micro-disk electrode for the determination of aniline, which is known to produce fouling effects and proposed to use electrode heating for cleaning [11]. In 2005 we proposed to heat the electrode during the voltammetric and amperometric detection of NADH in order to prevent electrode blocking due to oxidation products of the analyte [12]. Electrically heated electrodes have been successfully applied for the analysis of a variety of substances including dissolved oxygen [13] heavy metals [14,15], nucleic acids, carbon hydrates [16,17], and organic compounds [18,19]. Chen et al. reported about electroluminescence measurements at directly heated wire [20–22] and carbon paste electrodes [23–25]. Another interesting approach of Chen et al. is directly heated graphite electrodes and their application for the determination of trace riboflavin [26,27]. The temperature rise can also be achieved by means of microwaves [28–31]. Electrochemistry at elevated temperature has been reviewed [32,33].

Here, we present an effective pretreatment procedure which allows to measure trace amounts of dopamine following a blocking by high level of surface-active materials. High gelatin concentrations are used to illustrate the efficiency of pretreatment process.

2. Experimental

2.1. Reagents

All solutions were prepared using deionized water (PURELAB system, $R \geq 18.2\text{ M}\Omega\text{ cm}$). Square wave voltammetric and cyclic

* Corresponding authors. Tel.: +49 381 4986470; fax: +49 381 4986461.
E-mail addresses: gerd-uwe.flechsig@uni-rostock.de (G.-U. Flechsig),
josephwang@ucsd.edu (J. Wang).

voltammetric measurements were carried out in 100 mM phosphate buffer solution containing 50 ppm of dopamine vs. an Ag/AgCl (3 M KCl) reference electrode from CH Instruments Inc. (Austin, TX, USA) and a platinum counter electrode at a constant 24 °C bulk solution temperature. Dopamine hydrochloride, gelatin, potassium ferrocyanide, potassium ferricyanide and potassium chloride were purchased from Sigma–Aldrich (St. Louis, MO, USA). A pH 7.04 phosphate buffer (PB) was prepared using sodium phosphate (dibasic and monobasic), purchased from EMD (Gibbstown, NJ, USA). NaOH was used to adjust the buffer pH. Stock solutions of dopamine ($1 \times 10^4 \mu\text{g/ml}$) and gelatin ($1 \times 10^3 \mu\text{g/ml}$) in buffer were prepared daily.

2.2. Construction of the electrode

The used platinum wire electrode consisted of two 5-mm long pieces of platinum wires (50 μm in diameter) which were soldered carefully to both sides of a double printed circuit board (20 mm \times 20 mm) which had a gap of 10 mm \times 5 mm between the two copper contacts. Before the measurements the soldering contacts and the copper input leads were isolated using a mixture of paraffin/polyethylene and cleaned by glowing in air by applying a current. The construction of the used electrode has been described in detail previously [15].

2.3. Apparatus and procedures

2.3.1. Square wave voltammetry and cyclic voltammetry

All square wave voltammetric and cyclic voltammetric measurements were carried out with a PalmSens potentiostat (Ivium Technologies, Eindhoven, The Netherlands). These measurements were performed using a three-electrode measuring system containing a platinum wire electrode as working electrode (described above), a platinum wire as counter electrode and an Ag/AgCl (3 M KCl) reference electrode (CH Instruments Inc., Austin, TX, USA). In case of the cyclic voltammetry the measurements were started at -0.2 V with a step potential of 5 mV, and the second vertex potential was 0.5 V, the scan rate was 100 mV/s. Always the fifth scan was considered and is shown in Figs. 1 and 2(B).

The square wave voltammetry measurements were performed from +0 to +0.8 V with a step potential of 1 mV and pulses of 25 mV at 10 Hz.

2.3.2. Temperature calibration

We performed a temperature calibration using 1 mM equimolar ferro-/ferricyanide in 20 mM potassium chloride by open circuit potentiometry with a μ -Autolab (Ecochemie, Utrecht, and The Netherlands). In these measurements we applied an alternating heating current with a frequency of 100 kHz which was delivered by a heating system that has been described previously [34,35].

Using the well known temperature coefficient for this redox couple (-1.56 mV/K) it is possible to calculate the electrode temperature from the measured potentials for each applied current. This procedure has also been described in more detail previously [13,14].

2.3.3. Passivation/cleaning and measuring procedure

To induce passivation of the electrode with gelatin, the electrode was dipped into a quiescent phosphate buffer solution 0.1 M (pH 7.04) containing 1000 ppm gelatin. After 5 min the electrode was removed, rinsed carefully with water and dipped into a phosphate buffer solution containing 50 ppm dopamine for the voltammetric measurements. To clean the electrode thermally (60 s at 61.5 °C), electrochemically (60 s, potential: -1.5 V), or electrochemically and thermally (60 s, potential: -1.5 V at 61.5 °C), a 60 s conditioning step has been performed immediately before the measurement.

3. Results and discussion

Fig. 1 displays the effect of three different conditioning procedures upon the cyclic voltammograms for 50 ppm dopamine. In all cases we initially performed a measurement on the clean electrode, followed by dipping it in a 1000 ppm gelatin solution for 5 min and repeating the voltammetric scan. In Fig. 1A we applied no cleaning step after the gelatin passivation. Fig. 1B depicts the cleaning effect of electrochemical conditioning at -1.5 V for 60 s. Although the original response could not be obtained, the dopamine signal is considerably better than without any conditioning. Thermal conditioning yields no improvement after the passivation (Fig. 1C). On the contrary, the signal of dopamine seemed even worse than without any cleaning. Only a combined thermo-electrochemical conditioning step of -1.5 V and 61.5 °C for 60 s leads to almost complete recovering of the dopamine signal as has been demonstrated in Fig. 1D. The improved resistance for fouling (vs. electrochemical activation alone) is more profound for a series of prolonged runs and exposures to gelatin (see additional data below).

Fig. 2 exhibits square wave and cyclic voltammetric curves of a series of repetitive cycles involving measurements of 50 ppm dopamine, a 5 min dipping in a 1000 ppm gelatin solution, and 60 s thermo-electrochemical conditioning steps at -1.5 V and 61.5 °C. Three cycles after 1, 4, and 7 cycles are displayed. The results of the full series of 12 cycles using thermal, electrochemical, and thermo-electrochemical cleaning procedures are depicted in Fig. 3. This series demonstrates the applicability of the new thermo-electrochemical cleaning procedure for long-term measurements. Only a combined 60 s conditioning at -1.5 V and 61.5 °C leads to a stable signal even after 12 repetitive passivation/cleaning cycles (Fig. 3d). Electrochemical conditioning alone is not sufficient for long-term measurements. Although after a few cycles a significant recovering of the dopamine signal is still observed (refer also to Fig. 1), a dramatic current suppression is observed after the fourth

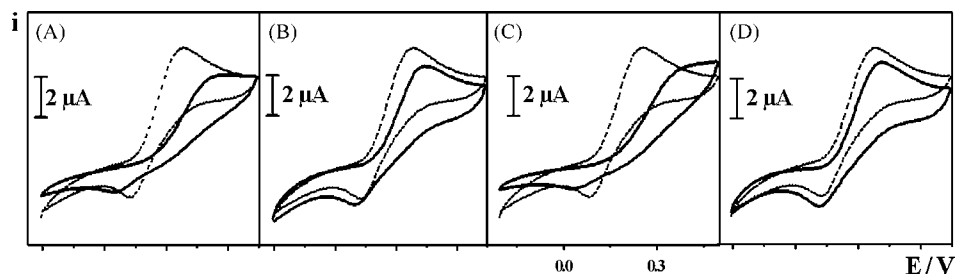


Fig. 1. Effect of different treatments: cyclic voltammetric response for 50 ppm dopamine in 100 mM phosphate buffer (pH 7.04) for a freshly cleaned platinum electrode (dotted line in all graphs). Before each of the other measurements the electrodes was dipped into a 1000 ppm gelatin solution for 5 min, rinsed and then dipped back in PB containing 50 ppm dopamine. Solid lines present the signal without any pretreatment (A), after an electrochemical pretreatment (60 s, potential: -1.5 V) (B), after a thermal pretreatment (60 s, at 61.5 °C) (C) and after a combination (thermal and electrochemical) pretreatment (60 s, potential: -1.5 V at 61.5 °C) (D).

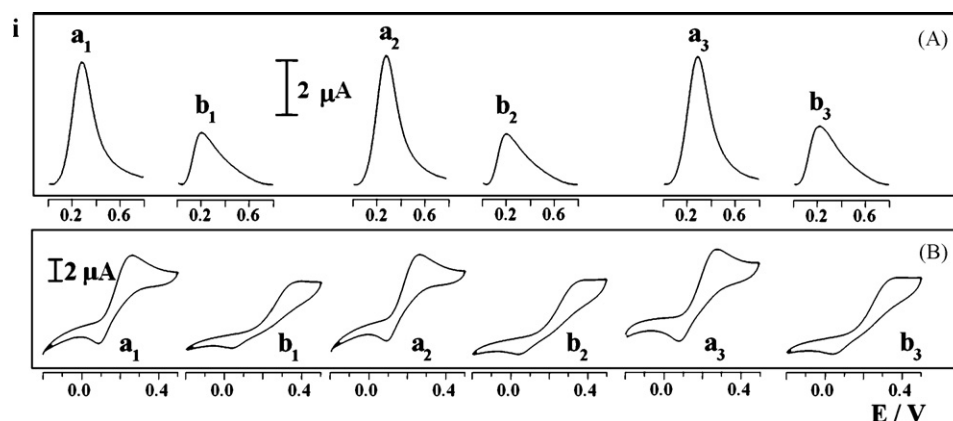


Fig. 2. Square wave voltammetry (A) and cyclic voltammetry (B) passivation and activation part of a series of 12 repetitive measurements (Ref. to Fig. 3). Out of these series the first (a_1 , b_1), fourth (a_2 , b_2) and seventh (a_3 , b_3) measurements are presented. Between each measurement the electrode was dipped in 1000 ppm gelatin solution for about 5 min, rinsed and then dipped back in PBS containing 50 ppm dopamine. Measurements (b_n) have been conducted without any pretreatment. Measurements (a_n) have been conducted after the electrode was electrochemically and thermally pretreated (60 s at -1.5 and 61.5°C).

cycle (Fig. 3b). Interestingly, the performance of a thermal treatment without polarization (Fig. 3c) is even slightly worse compared to measurements without any intermediate activation (Fig. 3a).

We observed a virulent gas bubble formation during the negative polarization (-1.5 V). These bubbles have been much smaller, if the electrode was simultaneously heated to 61.5°C . At room temperature, the bubbles tended to grow and to stick on the electrode for a long time. We suppose the following effects of polarization and heating. The strongly negative potential together with the formed hydrogen *in statu nascendi* leads at first to reductive degradation of blocking substances at the electrode surface. Secondly, the formed hydrogen bubbles loosen blocking films and particles mechanically as they are formed beneath. Thirdly, the elevated temperature accelerates degradation reactions at the low potential and due to the formed hydrogen *in statu nascendi*. Fourthly, the micro-stirring effect around the heated electrode causes a strong mass transport and hence, removal of the potentially passivating compounds. Fifthly, adsorption of any compound at a solid surface is diminished with increasing temperature. The finding that only a combined thermo-electrochemical treatment yields a long-term anti-blocking effect means that reduction at negative potentials

Table 1

Anodic (E_{ap}) and cathodic (E_{cp}) cyclic voltammetric peak potentials, and peak separation ΔE_p observed in a 0.1 M phosphate buffer (pH 7.04) containing 50 ppm dopamine depending upon their respective conditioning parameters (all potentials were measured vs. Ag/AgCl (3 M KCl) reference electrode).

Electrode treatment	E_{ap}	E_{cp}	ΔE_p
Freshly glow electrode	0.259	0.084	0.175
Passivation in 1000 ppm gelatine without conditioning	0.389	0.029	0.360
Passivation and thermal conditioning at 61.5°C for 60 s	0.394	0.029	0.365
Passivation and electrochemical conditioning at -1.5 V for 60 s	0.294	0.064	0.230
Passivation and thermal-electrochemical conditioning at 61.5°C and -1.5 V for 60 s	0.279	0.079	0.200

plays a crucial role and is dramatically enhanced by means of electrode heating (Fig. 3).

The positive effect of the new cleaning procedure is furthermore confirmed by the peak potentials of the cyclic voltammetric dopamine signals. Table 1 shows peak potentials and peak separations at the different cleaning conditions. Whereas the thermo-electrochemical treatment leads to a peak separation that is only slightly increased (by 25 mV), the electrochemical conditioning shows considerably higher increase in peak separation (55 mV) and hence, irreversibility due to the blocking gelatin film. The peak separations increase observed upon thermal (190 mV) or without any conditioning (185 mV) are dramatically worse.

4. Conclusions

The blocking effect of a 1000 ppm gelatin matrix component during the determination of 50 ppm dopamine can be dramatically reduced by means of a combined thermal and electrochemical conditioning step by means of a directly heated platinum wire electrode. The voltammetric dopamine signal can be maintained at ca. 82% of the initial value. A conventional electrochemical treatment alone yields only a limited cleaning effect for a few repetitive measurements. In long repetitive scan series the signal drops to ca. 39%. The blocking effect of 1000 ppm gelatin causes an immediate signal drop down to 29% of the initial value. Besides the peak currents also the peak separations can widely be stabilized by the new thermo-electrochemical conditioning; however, also the electrochemical conditioning preserves a relatively low peak separation.

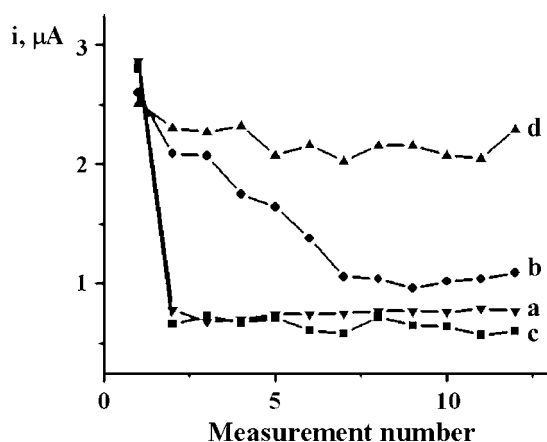


Fig. 3. Stability plots from 12 repetitive SWV measurements for 50 ppm dopamine in 100 mM phosphate buffer solution. Between each measurement the electrode was dipped in 1000 ppm gelatin solution for about 5 min, rinsed and then dipped back in PBS containing 50 ppm dopamine. Some measurements were taken out without any pretreatment (a), after electrochemical pretreatment (60 s, potential -1.5 V) (b), after thermal pretreatment (60 s, at 61.5°C) (c) and after combined thermal and electrochemical pretreatment (60 s, potential: -1.5 V at 61.5°C) (d).

The positive effects can be addressed to an enforced reductive degradation and accelerated removal of the blocking agents. Also the formation of hydrogen bubbles might play a significant role.

Thermo-electrochemical treatment holds great promise for unmodified electrochemical sensors and detectors which are applied for long-term monitoring of samples that contain blocking matrices. The improved resistance to surfactant interferences thus makes the new protocol very attractive for many direct electroanalytical applications in harsh environments, and obviates the need for protective membranes.

Acknowledgements

The research was granted by National Science Foundation (grant number CHE 0506529) and Deutsche Forschungsgemeinschaft (DFG; FL 384/2-3), H.D. was supported by Deutscher Akademischer Austausch Dienst (DAAD) and T.V. was supported by Louis Stokes AMP Bridges to the Doctorate Fellowship.

References

- [1] J. Wang, R.P. Deo, P. Poulin, M. Mangey, J. Am. Chem. Soc. 125 (2003) 14706.
- [2] J. Wang, M. Musameh, Anal. Chem. 75 (2003) 2075.
- [3] S.L. Lawrence, R.P. Deo, J. Wang, Electroanalysis 17 (2005) 65.
- [4] W.G. Kuhr, V.L. Barrett Michelle, R. Gagnon, P. Hopper, P. Pantano, Anal. Chem. 65 (1993) 617.
- [5] S. Jolley, M. Koppang, T. Jackson, G.M. Swain, Anal. Chem. 69 (1997) 4099–4107.
- [6] J. Xu, G.M. Swain, Anal. Chem. 70 (1998) 1502.
- [7] L.-F. Li, D. Totir, B. Miller, G. Chottiner, A. Argoitia, J.C. Angus, D.A. Scherson, J. Am. Chem. Soc. 119 (1997) 7875.
- [8] T. Yano, D.A. Tryk, K. Hashimoto, A.J. Fujishima, J. Electrochem. Soc. 145 (1998) 1870.
- [9] M. Musameh, J. Wang, A. Merkoci, Y. Lin, J. Electrochem. Commun. 4 (2002) 743.
- [10] F. Valentini, A. Salis, A. Curulli, G. Palleschi, Anal. Chem. 76 (2004) 3244.
- [11] A.S. Baranski, Anal. Chem. 74 (2002) 1294.
- [12] C. Lau, G.-U. Flechsig, P. Gründler, J. Wang, Anal. Chim. Acta 554 (2005) 74.
- [13] T. Zerihun, P. Gründler, J. Electroanal. Chem. 404 (1996) 243.
- [14] T. Zerihun, P. Gründler, J. Electroanal. Chem. 415 (1996) 85.
- [15] P. Gründler, G.-U. Flechsig, Electrochim. Acta 43 (1998) 3451.
- [16] C. Lau, S. Reiter, W. Schuhmann, P. Gründler, Anal. Bioanal. Chem. 379 (2004) 255.
- [17] C. Lau, S. Borgmann, M. Maciejewska, B. Ngounou, P. Gründler, W. Schuhmann, Biosens. Bioelectron. 22 (2007) 3014.
- [18] T. Zerihun, P. Gründler, J. Electroanal. Chem. 441 (1998) 57.
- [19] F. Wachholz, K. Biala, M. Piekarz, G.-U. Flechsig, Electrochem. Commun. 9 (2007) 2346.
- [20] Z.Y. Lin, J.J. Sun, J.H. Chen, L. Guo, G.N. Chen, Anal. Chim. Acta 564 (2006) 226.
- [21] Z.Y. Lin, J.J. Sun, J.H. Chen, L. Guo, G.N. Chen, Electrochem. Commun. 9 (2007) 269.
- [22] Z. Lin, J. Sun, J. Chen, L. Guo, G. Chen, Electrochim. Acta 53 (2007) 1708.
- [23] Z.Y. Lin, J.J. Sun, J.H. Chen, L. Guo, Y.T. Chen, G.N. Chen, Anal. Chem. 80 (2008) 2826.
- [24] Y.T. Chen, Z.Y. Lin, J.J. Sun, G.N. Chen, Electrophoresis 28 (2007) 3250.
- [25] Y. Chen, Z. Lin, J. Chen, J. Sun, L. Zhang, G. Chen, J. Chromatogr. A 1172 (2007) 84.
- [26] J.J. Sun, L. Guo, D.F. Zhang, W.H. Yin, G.N. Chen, Electrochem. Commun. 9 (2007) 283.
- [27] S.H. Wu, J.J. Sun, Z.B. Lin, A.H. Wu, Y.M. Zeng, L. Guo, D.F. Zhang, H.M. Dai, G.N. Chen, Electroanalysis 19 (2007) 2251.
- [28] U.K. Sur, F. Marken, R.G. Compton, B.A. Coles, New J. Chem. 28 (2004) 1544.
- [29] U.K. Sur, F. Marken, R. Seager, J.S. Foord, A. Chatterjee, B.A. Coles, R.G. Compton, Electroanalysis 17 (2005) 385.
- [30] M.A. Ghanem, R.G. Compton, B.A. Coles, E. Psillakis, M.A. Kulandainathan, F. Marken, Electrochim. Acta 53 (2007) 1092.
- [31] S. Förster, F.-M. Matysik, M.A. Ghanem, F. Marken, Analyst 131 (2006) 1210.
- [32] G.G. Wildgoose, D. Giovanelli, N.S. Lawrence, R.G. Compton, Electroanalysis 16 (2004) 421.
- [33] P. Gründler, G.-U. Flechsig, Microchim. Acta 154 (2006) 175.
- [34] F. Wachholz, J. Gimsa, H. Duwensee, H. Grabow, P. Gründler, G.-U. Flechsig, Electroanalysis 19 (2007) 535.
- [35] www.hot-wire-electrochemistry.de.



Classification of edible vegetable oils using square wave voltammetry with multivariate data analysis

Francisco Fernandes Gambarra-Neto^a, Glimaldo Marino^a, Mário César Ugulino Araújo^{a,*}, Roberto Kawakami Harrop Galvão^b, Márcio José Coelho Pontes^a, Everaldo Paulo de Medeiros^c, Renato Sousa Lima^a

^a Universidade Federal da Paraíba, Departamento de Química, João Pessoa, PB, Brazil

^b Instituto Tecnológico de Aeronáutica, Divisão de Engenharia Eletrônica, São José dos Campos, SP, Brazil

^c Embrapa, Centro Nacional de Pesquisa de Algodão, Campina Grande, PB, Brazil

ARTICLE INFO

Article history:

Received 8 May 2008

Received in revised form

29 September 2008

Accepted 1 October 2008

Available online 14 October 2008

Keywords:

Vegetable oil

Square wave voltammetry

Soft Independent Modelling of Class

Analogy

Linear Discriminant Analysis

Successive Projections Algorithm

ABSTRACT

This paper proposes a simple and non-expensive electroanalytical methodology for classification of edible vegetable oils with respect to type (canola, sunflower, corn and soybean) and conservation state (expired and non-expired shelf life). The proposed methodology employs an alcoholic extraction procedure followed by square wave voltammetry (SWV). Two chemometric methods were compared for classification of the resulting voltammograms, namely Soft Independent Modelling of Class Analogy (SIMCA) and Linear Discriminant Analysis (LDA) with variable selection by the Successive Projections Algorithm (SPA). The results were evaluated in terms of errors in a set of samples not included in the modelling process. The best results were obtained with the SPA-LDA method, which correctly classified all samples in terms of type and conservation state.

© 2008 Elsevier B.V. All rights reserved.

1. Introduction

The authenticity and conservation state of edible vegetable oils is a very important issue, due to consumer health and economic reasons. In fact, beneficial and adverse properties for human health depend on the oil type and may be influenced by inadequate storage or expiration of shelf life. Moreover, the retail price varies according to the costs of raw material, processing, refining, bottling, transportation and storage. As a result, more expensive products may become the target of counterfeiting or adulterations with oils having less commercial value [1]. In this context, analytical methodologies are of value to assess compliance with respect to the oil type and expiry date stated in the product label.

Several instrumental techniques may be employed for vegetable oil analysis, such as near [2–6] and mid-infrared [7–10]

spectrometry, chromatography [11], fluorescence [12–14] and chemiluminescence [15,16]. Electroanalytical methods could be used as an alternative. Nevertheless, such an approach has been used mostly for determination of physical properties, such as acid value [17], or specific chemical components, such as tocopherol [18–20], tert-butylhydroquinone [21], tert-butylhydroxyanisole and tert-butylhydroxytoluene [22], rather than direct authentication of oil type and conservation state.

The present paper proposes an electroanalytical methodology for classification of edible vegetable oils with respect to type and conservation state. For this purpose, an extraction procedure with ethanol is employed and square wave voltammetry (SWV) is applied to the extracts. SWV has the advantage of providing large sensitivity with high scanning speed and small capacitive current [23]. Due to the complex nature of a vegetable oil matrix, the resulting voltammograms are formed by the overlapping of several analytical peaks. Therefore, multivariate chemometric methods are used for the classification task. The proposed methodology is applied to a data set with the four types of edible vegetable oils most commercialized in Brazil, namely canola, sunflower, corn and soybean. According to resolution n°. 482, RDC 292/99 from National Agency of Sanitary Vigilance (ANVISA) [24], these oils have sub-

* Corresponding author at: Universidade Federal da Paraíba, Departamento de Química – Laboratório de Automação e Instrumentação em Química Analítica/Quimiometria (LAQA), Caixa Postal 5093, CEP 58051-970 – João Pessoa, PB, Brazil. Tel.: +55 83 3216 7438; fax: +55 83 3216 7437.

E-mail address: laqa@quimica.ufpb.br (M.C.U. Araújo).

tle differences in average chemical composition, except for canola, which has a marked distinction in terms of brassicasterol, oleic and linoleic acid contents. As a result, authentication may be a challenging task, especially with respect to the distinction between soybean, corn and sunflower oil types. Therefore, the development of a simple and non-expensive analytical procedure for this purpose would be of value. In addition, samples with and without expired shelf life are employed to assess the efficiency of the proposed methodology to monitor the conservation state of the oil.

2. Experimental

2.1. Samples

One hundred and fourteen samples of canola, sunflower, corn and soybean oil from different lots and manufacturers were employed. Forty-eight of these samples (canola:13, sunflower:14, corn:14 and soybean:7) had been stored in the original commercial flask without strict environmental control for 12–18 months past the expiry date. Henceforth, these will be termed “expired” samples. For the classification study, the expired samples were gathered into a single group. As a result, five classes will be considered (canola, sunflower, corn, soybean and expired).

2.2. Apparatus

The measurements were carried out with a potentiostat/galvanostat μ AutoLab[®] Type II (Eco Chemie) coupled to a polarographic module 663 VA Stand[®] (Metrohm) fitted with a Ag/AgCl–KCl (3.0 mol L^{−1}) reference electrode and a platinum wire as counter electrode. In order to optimize the experimental conditions, tests were carried out with platinum and gold disk electrodes (Pt-DE and Au-DE, both with 2.0 mm diameter), two different support electrolytes (NaOH and CH₃COOH, both 0.1 mol L^{−1}) and both cathodic and anodic scanning directions.

2.3. Analytical procedure

De-ionised water purified with a Milli-Q Plus system (Millipore) and high purity reagents were used throughout the analytical procedure. No deaeration procedure was necessary.

2.3.1. Extraction

The extraction procedure was adapted from the AOCS (American Oil Chemists' Society) method CA 5a-40 for quantification of free fatty acids in refined vegetable oils. An aliquot of each oil sample was mixed with ethanol under agitation. Four different oil/ethanol proportions (1:4, 1:2, 1:1 and 1:1/2 v/v) were tested. The resulting mixture was maintained at rest for approximately 30 min. A 10 μ L aliquot of the alcoholic phase was then mixed in the electrochemical cell with 10 mL of the support electrolyte and agitated during 60 s. The mixture becomes slightly turbid, which may be caused by the formation of an emulsion.

2.3.2. Electrochemical cleaning of the working electrode

Preliminary investigations revealed that eliminating the oxygen dissolved in the medium was not necessary. In fact, the voltammogram profile was not significantly altered by the presence or absence of oxygen. A similar result was obtained elsewhere [25].

Prior to the acquisition of each voltammogram, the working electrode was subjected to an electrochemical cleaning procedure comprising two steps [25,26]. Initially, the electrode was kept at an anodic potential (AP) during a time t_A to remove contaminants adsorbed in its surface. The electrode was then kept at a cathodic potential (CP) during a time t_C to remove the oxidized layer formed

in the first step. The values of AP, t_A , CP and t_C were optimized according to a 2⁴ central composite design.

The response for each experiment in the design was the signal-to-noise ratio evaluated in terms of Taguchi's Z-parameter [27] as follows. Each voltammogram was registered in triplicate. The mean voltammogram \bar{I}_k and the variance profile s_k^2 were then calculated according to the following equations:

$$\bar{I}_k = \frac{1}{n_{rep}} \sum_{i=1}^{n_{rep}} I_{i,k} \quad (1)$$

$$s_k^2 = \frac{1}{n_{rep} - 1} \sum_{i=1}^{n_{rep}} (I_{i,k} - \bar{I}_k)^2 \quad (2)$$

where $n_{rep} = 3$ is the number of replicates for each experiment and $I_{i,k}$ is k^{th} measured current value for the i^{th} replicate voltammogram. Taguchi's Z-parameter was then calculated as:

$$Z = \sum_{k=1}^{n_p} 10 \log \left(\frac{\bar{I}_k^2}{s_k^2} \right) \quad (3)$$

where n_p is the number of scanned potential values in the voltammogram.

This optimization procedure was carried out by using the alcoholic extract of a soybean oil sample and NaOH 0.1 mol L^{−1} as support electrolyte.

2.3.3. SWV parameters

The alcoholic extract of a soybean oil sample in NaOH 0.1 mol L^{−1} was again employed for optimization of the SWV parameters. After addition of the extract, an equilibrium time of 10 s and a potential scan window from −0.9 to 0.6 V were used. The frequency (f), step height (ΔE_s) and pulse height (ΔE_{sw}) were optimized according to a 2³ composite central design. For this purpose, Taguchi's Z-parameter was employed, as described above.

2.3.4. Chemometrics procedures

The samples were divided into training, test and validation sets by applying the classic Kennard-Stone (KS) uniform sampling algorithm [28] to the voltammograms. Each class was treated separately, as previously described [29]. The number of samples in each set is presented in Table 1.

As previously described [29], the training and test samples were used in the modelling procedures (including Successive Projections Algorithm (SPA) variable selection for Linear Discriminant Analysis (LDA) and determination of principal components in SIMCA) whereas the validation samples were only used in the final evaluation and comparison of the classification models.

The experimental designs were elaborated by using Statistica[®] 6.0. Principal Component Analysis (PCA) and Soft Independent Modelling of Class Analogy (SIMCA) were carried out in Unscrambler[®] 9.7 (CAMO S.A.). The KS and SPA-LDA algorithms were coded in Matlab[®] 6.5.

Table 1
Number of training, test and validation samples in each class.

Class	Set		
	Training	Test	Validation
Canola	9	3	3
Sunflower	10	3	3
Corn	10	3	4
Soybean	10	4	4
Expired	20	10	18
Total	59	23	32

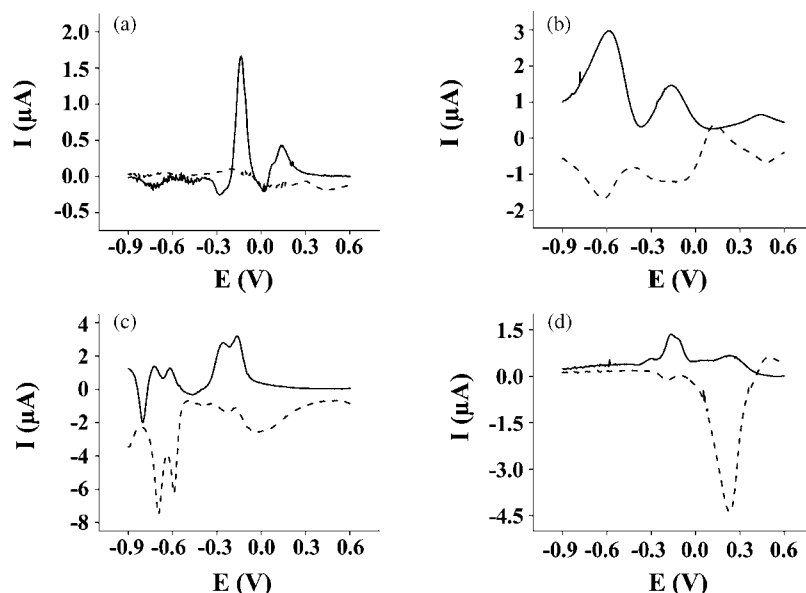


Fig. 1. Voltammogram profiles of a soybean oil sample obtained for scan in the anodic (dashed line) and cathodic (solid line) directions, employing (a) Au-DE and NaOH, (b) Au-DE and CH_3COOH , (c) Pt-DE and NaOH and (d) Pt-DE and CH_3COOH .

3. Results and discussion

3.1. Choice of oil/ethanol proportion in the extraction procedure

This study was carried out with a Pt-DE working electrode, 0.1 mol L^{-1} NaOH support electrolyte and anodic scan direction. The SWV parameters were set to $f=20 \text{ Hz}$, $\Delta E_s=5 \text{ mV}$ and $\Delta E_{\text{sw}}=25 \text{ mV}$. Moreover, the following values were employed in the electrochemical cleaning of the working electrode: $\text{AP}=0.7 \text{ V}$, $t_A=3 \text{ s}$, $\text{CP}=-0.9 \text{ V}$ and $t_C=3 \text{ s}$. These values were chosen on the basis of reference [26].

Four oil/ethanol proportions were tested (1:4, 1:2, 1:1 and 1:½ v/v). The proportion 1:1 was chosen as compromise between larger current values and richer information in the voltammogram profile. This proportion will be employed henceforth.

3.2. Choice of support electrolyte, working electrode, scan direction, and potential scan window

Fig. 1 presents the voltammograms of a soybean oil sample obtained with Pt-DE and Au-DE electrodes, NaOH and CH_3COOH (both 0.1 mol L^{-1}) support electrolytes and cathodic/anodic scanning directions. The parameters for SWV and electrochemical cleaning of the working electrode were the same as those employed in the previous section. The voltammograms in Fig. 1 were obtained after subtraction of the blank signal corresponding to the support electrolyte with a $10 \mu\text{L}$ aliquote of ethanol (same volume of the alcoholic extract of the sample). This subtraction was carried out to emphasize the voltammetric profile of the compounds extracted from the oil sample.

As can be seen, the voltammogram registered in NaOH 0.1 mol L^{-1} with Pt-DE in the cathodic scan (Fig. 1c, solid line) displays a good compromise between large current values and richness of features. Arguably, the response obtained with NaOH is better because this support electrolyte facilitates the electrochemical cleaning of Pt-DE in pulsed techniques, as previously described [30]. Therefore, the Pt-DE electrode with NaOH 0.1 mol L^{-1} support electrolyte and cathodic scan will be employed henceforth. Since the voltammogram obtained under these conditions has very

small current values for potentials larger than 0.3 V , the potential scan window will be restricted to the range 0.3 V to -0.9 V .

3.3. Optimization of the electrochemical cleaning of the working electrode

Table 2 presents the results of the 2^4 central composite design employed to optimize the AP, t_A , CP and t_C parameters. The values for the axial points in the design were chosen in view of the limits

Table 2

2^4 central composite design employed to optimize the electrochemical cleaning of the working electrode. The response values correspond to Taguchi's Z-parameter.

	Experiment	AP (V)	t_A (s)	CP (V)	t_C (s)	Response (Z)
Cubic Design	1	0.5	1	-1.1	1	6752
	2	0.9	1	-1.1	1	7574
	3	0.5	5	-1.1	1	7505
	4	0.9	5	-1.1	1	7897
	5	0.5	1	-0.7	1	5709
	6	0.9	1	-0.7	1	6062
	7	0.5	5	-0.7	1	5752
	8	0.9	5	-0.7	1	6485
	9	0.5	1	-1.1	5	7003
	10	0.9	1	-1.1	5	6973
	11	0.5	5	-1.1	5	7084
	12	0.9	5	-1.1	5	7163
	13	0.5	1	-0.7	5	6081
	14	0.9	1	-0.7	5	6374
	15	0.5	5	-0.7	5	7842
	16	0.9	5	-0.7	5	7312
Axial Points	17	0.4	3	-0.9	3	6791
	18	1.0	3	-0.9	3	7053
	19	0.7	0	-0.9	3	6621
	20	0.7	6	-0.9	3	6837
	21	0.7	3	-1.2	3	8068
	22	0.7	3	-0.6	3	6407
	23	0.7	3	-0.9	0	6181
	24	0.7	3	-0.9	6	6839
Central Points	25	0.7	3	-0.9	3	6786
	26	0.7	3	-0.9	3	6847
	27	0.7	3	-0.9	3	6636

The bold values correspond to the best experimental conditions.

Table 3

2^3 central composite design employed to optimize the SWV parameters. The response values correspond to Taguchi's Z-parameter.

	Experiment	f (Hz)	ΔE_s (mV)	ΔE_{sw} (mV)	Response (Z)
Cubic Design	1	20	2.0	25.0	17290.8
	2	50	2.0	25.0	16527.4
	3	20	5.0	25.0	6953.8
	4	50	5.0	25.0	7641.4
	5	20	2.0	50.0	18074.4
	6	50	2.0	50.0	16160.1
	7	20	5.0	50.0	6330.1
	8	50	5.0	50.0	7359.1
Axial Points	9	10	3.0	37.5	8900.2
	10	60	3.0	37.5	10493.1
	11	35	1.0	37.5	32715.6
	12	35	6.0	37.5	6050.4
	13	35	3.0	16.6	10122.3
	14	35	3.0	58.4	10552.3
Central Points	15	35	3.0	37.5	10720.4
	16	35	3.0	37.5	10676.4
	17	35	3.0	37.5	10176.6

The bold values correspond to the best experimental conditions.

for the region of investigation. In fact, the resulting voltammograms did not display noticeable changes for t_A or t_C larger than 6 s. Moreover, potentials larger than 1.000 V or smaller than -1.200 V could cause the formation of an excess of platinum oxide and/or hydrogen liberation, which would impair the precision of the analysis.

As can be seen in Table 2, the best experimental conditions, which correspond to the largest value of Z (8068 for experiment 21) are AP = 0.7 V, t_A = 3 s, CP = -1.2 V and t_C = 3 s.

3.4. Optimization of SWV parameters

Table 3 presents the results of the 2^3 central composite design employed to optimize the f , ΔE_s and ΔE_{sw} parameters. The values for the axial points in the design were limited by the scan rate (product of f and ΔE_s). Scan rates larger than 360 mV s^{-1} compromise the voltammogram profiles.

As can be seen in Table 3, the best experimental conditions, which correspond to the largest value of Z (32715.6 for experiment 11) are f = 35 Hz, ΔE_s = 1.0 mV and ΔE_{sw} = 37.5 mV.

3.5. Selection of the working range in the voltammogram

Fig. 2 shows the voltammograms for the 114 oil samples acquired under the optimized experimental conditions described above. Each voltammogram in Fig. 2 was obtained after subtraction of the blank signal corresponding to the support electrolyte alone

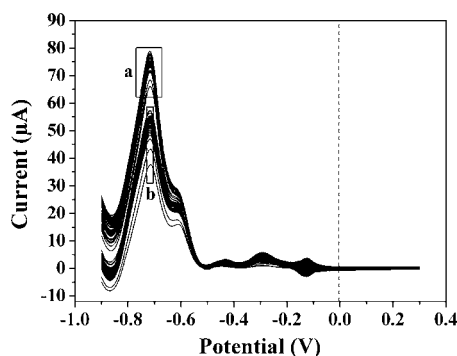


Fig. 2. Voltammograms of the 114 samples, comprising (a) non-expired and (b) expired oils. The working range for chemometric treatment was taken to the left of the dashed vertical line.

(0.1 mol L⁻¹ NaOH). This modification in the blank signal acquisition was adopted to simplify the analytical procedure and thus avoid the propagation of volumetric errors associated to the addition of the 10 μL aliquot of ethanol. As can be seen, the current intensities for potentials larger than 0 V are very small. Therefore, the working range for the chemometric treatment was restricted to cathodic potential values to the left of the vertical dashed line in Fig. 2. This range contains relevant potential values for determination of fatty acids, as described elsewhere [31,32]. After exclusion of the anodic potential values, the resulting voltammograms comprised 800 variables (potentials).

A reproducibility study was conducted by repeating 20 times the analysis of the same oil sample. The standard deviation of the current ranged from 0.04 μA to 1.1 μA over the entire voltammogram, which is considerably smaller than the current values seen in Fig. 2.

The separation between expired and non-expired oil samples is apparent around the -0.7 V potential in the voltammograms presented in Fig. 2. This finding demonstrates that the proposed methodology is valid for monitoring the conservation state of the sample. However, the separation between the oil types (canola, sunflower, corn and soybean) is not clear by visual inspection, which motivates the use of multivariate chemometric techniques.

3.6. Principal Component Analysis (PCA)

Fig. 3 presents the PC2 \times PC1 score plot resulting from the application of PCA to the sample voltammograms. Fig. 3a reveals a clear distinction between expired and non-expired samples, which is in agreement with the separation observed in the voltammograms (Fig. 2). As regards the non-expired samples, the canola type is clearly discriminated from the others, as can be seen in Fig. 3b. On the other hand, there is substantial overlapping among the other types, especially between sunflower and soybean. These findings can be explained on the basis of the average chemical composition of the oils [24]. In fact, the correlation of content values between canola and any of the other types is smaller than 0.77. On the other hand, high correlation values are observed between the composition of corn and sunflower (0.96), corn and soybean (0.98) and especially sunflower and soybean (0.99). These results are in agreement with other works, which employed more sophisticated instrumental techniques, such as electrospray ionization mass spectrometry [33], and near-infrared (NIR), mid-infrared (MIR) and Raman spectrometry [34].

As shown in Fig. 3c, there is no clear distinction between the oil types for the expired samples. This gathering of expired samples in a single group may be ascribed to the process of oxidative rancidity [35]. In this process, free radicals break fatty acid chains, which leads to the formation of several products, such as lipoperoxides, aldehydes, alcohols, ketones, volatile compounds, epoxide compounds and polymers. Since the oil types under study are similar in terms of fatty acid composition, the products of oxidative rancidity tend to be the same. Therefore, the expired samples will be treated as a single group for the classification study presented below.

3.7. SIMCA classification

A SIMCA model was built for each of the five oil classes, according to the default settings of the Unscrambler software. Table 4 presents the classification results obtained by applying the SIMCA models to the test set for four different significance levels of the F -test (1%, 5%, 10% and 25%). It is worth noting that SIMCA errors can be of two types: I (object not included in its own class) and II (object included in a wrong class). Both error types are reported in Table 4. For exam-

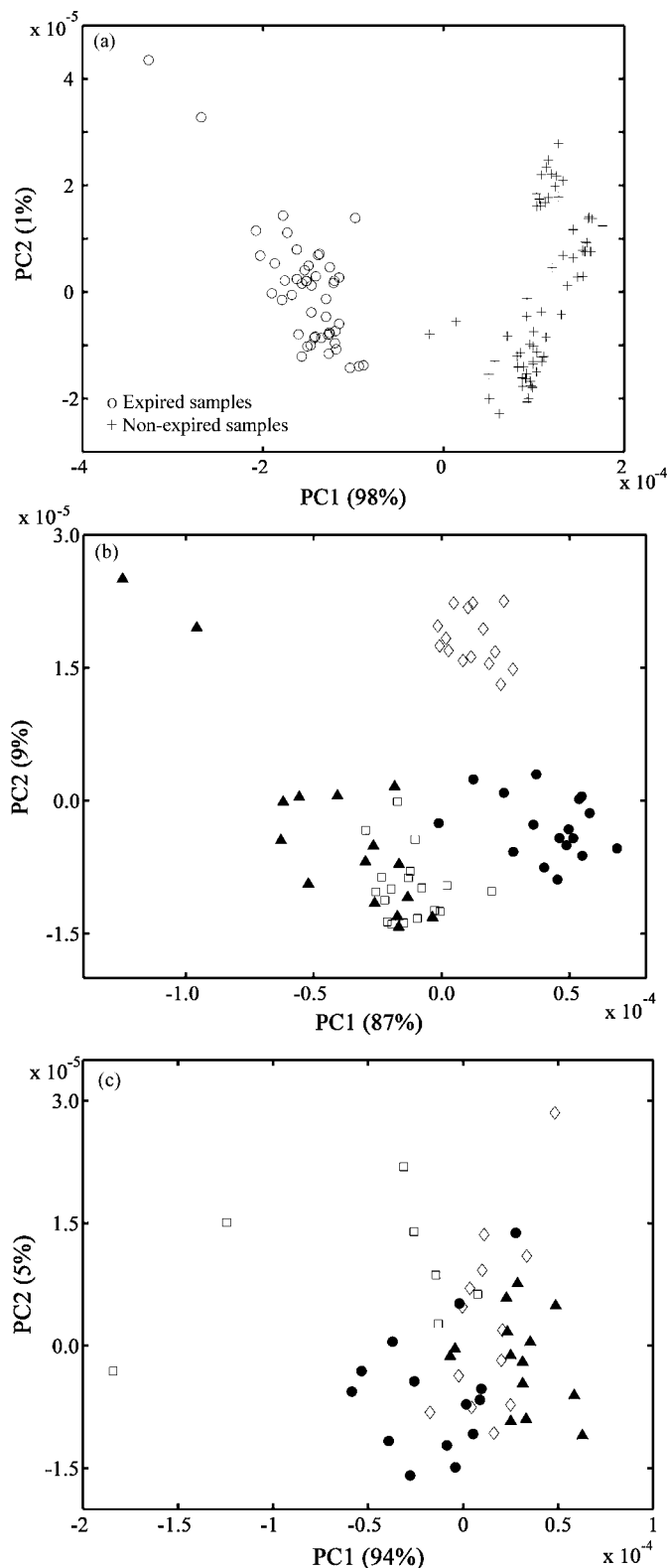


Fig. 3. PC2 \times PC1 score plot for (a) the overall data set, (b) the non-expired samples and (c) the expired samples (\diamond : canola; \blacktriangle : sunflower; \bullet : corn; \square : soybean). The percent variance explained by each PC is indicated in parenthesis.

ple, the canola model presents one type I error (canola sample not included in the canola class) regardless of the significance level of the F-test. On the other hand, the sunflower model presents three type II errors (soybean sample included in the sunflower class) for significance levels of 1%, 5%, and 10% and two type II errors for a significance level of 25%.

The type-II errors indicated in Table 4 corroborate the findings of the PCA study. In fact, regardless of the significance level for the F-test, expired samples were not included in any of the non-expired models and non-expired samples were not included in the expired model. Similarly, canola samples were not included in the other models and other oil types were not included in the canola model. These results are in agreement with the clear separation between expired and canola samples from the remaining classes, as shown in Fig. 3a–b. The largest number of errors in Table 4 correspond to the inclusion of soybean samples in the sunflower model and vice-versa. Again, this finding agrees with the large overlapping between these classes (Fig. 3b) and the high correlation between their average chemical composition, as discussed above. In this context, it is worth noting that the oil type displaying the largest composition correlation with corn is soybean. As a result, the only type-II error

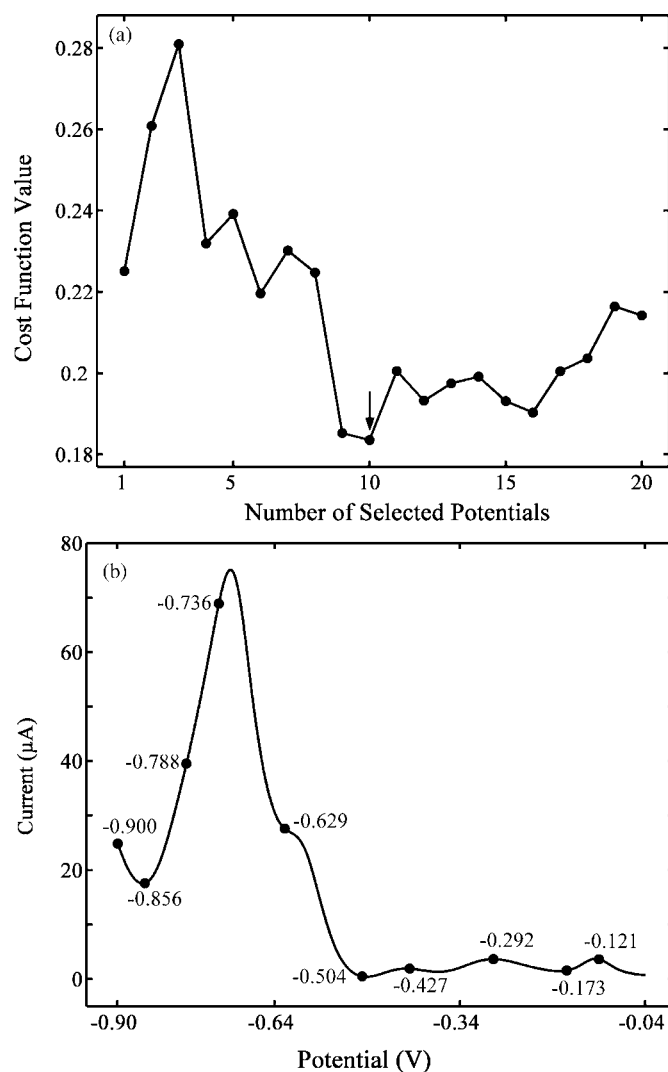


Fig. 4. (a) Graph of the cost function value versus the number of selected potentials in SPA-LDA. The optimum number of potentials corresponds to the point indicated by an arrow. (b) Voltammogram of an oil sample illustrating the potentials selected by SPA-LDA (–0.1208, –0.1732, –0.2917, –0.4274, –0.5043, –0.6293, –0.7361, –0.7884, –0.8557 and –0.8995 V).

Table 4Number of classification errors of the SIMCA models in the vegetable oil validation set for 1%, 5%, 10%, and 25% significance levels for the *F*-test.

Model	Canola (6/97.9%)				Sunflower (4/99.1%)				Corn (3/96.1%)				Soybean (4/97.9%)				Expired (3/97.8%)			
	1	5	10	25	1	5	10	25	1	5	10	25	1	5	10	25	1	5	10	25
Canola	1	1	1	1	–	–	–	–	–	–	–	–	–	–	–	–	–	–	–	–
Sunflower	–	–	–	–	–	–	–	–	–	–	–	–	2	2	2	1	–	–	–	–
Corn	–	–	–	–	–	–	–	–	–	–	–	1	–	–	–	–	–	–	–	–
Soybean	–	–	–	–	3	3	3	2	1	1	1	–	–	–	–	–	–	–	–	–
Expired	–	–	–	–	–	–	–	–	–	–	–	–	–	–	–	–	–	–	–	5

The number of principal components/explained variance employed in each SIMCA model is indicated in parenthesis.

involving corn was the inclusion of a soybean sample in the corn model.

As regards type-I errors, the most noticeable finding in Table 4 concerns the five expired samples not included in their own model. These errors may be ascribed to the large dispersion of this class, which comprises expired oils of four types (Fig. 3c).

3.8. SPA-LDA classification

Fig. 4a presents the cost function of SPA-LDA versus the number of selected potentials. This cost function corresponds to the aver-

age risk of misclassification of samples in the test set [29]. As can be seen, the curve exhibits a minimum point at 10 selected potentials, which are indicated in Fig. 4b. These potentials correspond to informative regions associated to peaks, valleys and half-wave points.

An LDA model generates a number of discriminant functions equal to the number of classes under consideration minus one [36]. Therefore, in the present study, four discriminant functions (DF1, DF2, DF3 and DF4) are generated for the five classes (canola, sunflower, corn, soybean and expired). Fig. 5 presents the resulting DF2 × DF1 and DF3 × DF2 score plots for the data set. As expected, the expired class is plainly discriminated from the remaining samples along the DF1 direction (Fig. 5a). The four non-expired classes are separated by DF2 and DF3, as shown in Fig. 5b. As can be seen in the DF3 × DF2 plot, the canola class is clearly separated from the others. The closest approximation between classes is found between soybean and sunflower, followed by soybean and corn. This finding is in agreement with the discussion concerning the PCA results and chemical composition correlation in Section 3.6.

In contrast to SIMCA, the SPA-LDA model classified all samples in the validation set correctly (i.e., no type-I or type-II errors were obtained). This result can be explained in light of the better separation of the non-expired classes observed in Fig. 5b, as compared to the PCA score plot in Fig. 3b. Therefore, it may be concluded that the variable selection process was valuable for the classification task, as an alternative to the use of the entire working range of potentials (0 to −0.900 V).

4. Conclusions

This paper proposed a simple and non-expensive methodology for classification of edible vegetable oils with respect to type (canola, sunflower, corn and soybean) and conservation state (expired and non-expired shelf life). The proposed methodology employs an extraction procedure followed by square wave voltammetry and chemometric classification methods. The best experimental conditions obtained as the result of an optimization study were the following: (1) extraction with ethanol in the proportion 1:1 (v/v); (2) use of a platinum disk as working electrode; (3) use of 0.1 mol L^{−1} NaOH as support electrolyte; (4) potential scan started in the cathodic direction; (5) electrochemical cleaning of the working electrode with an anodic potential of 0.7 V during 3 s followed by a cathodic potential of −1.2 V during 3 s; (6) SWV with frequency of 35 Hz, step height of 1.0 mV and pulse height of 37.5 mV; (7) potential scan window from 0.3 to −0.900 V; (8) working range from 0 to −0.900 V.

A PCA study applied to the voltammograms in the working range of potentials revealed that the expired oils are plainly separated from the non-expired ones. This finding demonstrates that the proposed methodology is valid for monitoring the conservation state of the sample. However, overlapping was observed between some classes of non-expired oils, especially soybean and sunflower. Such

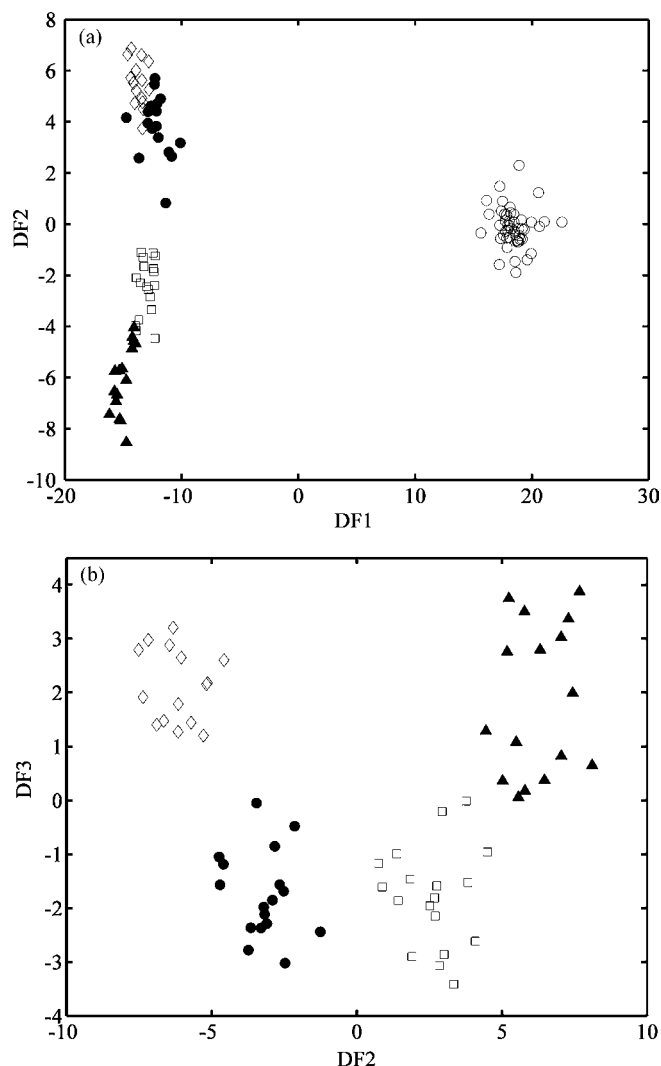


Fig. 5. (a) DF2 × DF1 score plot for the overall data set of 114 oil samples. (b) DF3 × DF2 score plot for the non-expired samples. (◇): canola; (▲): sunflower; (●): corn; (□): soybean and (○): expired).

an overlapping resulted in classification errors when SIMCA models were applied to the set of validation samples. This problem was circumvented by using 10 potentials selected by the SPA-LDA technique, which resulted in the correct classification of all validation samples.

These results suggest that the proposed methodology is a promising alternative for inspection of authenticity and conservation state of edible vegetable oils. Future works could use a flow-batch system [37] to automate the procedures and increase the analytical frequency. Moreover, an investigation concerning the analysis of simulated adulterations of oil samples could be carried out.

Acknowledgments

This work was supported by CAPES (PROCAD grant 0081/05-1, MSc and DSc studentship) and CNPq (research fellowships).

References

- [1] F. Marini, F. Balestrieri, R. Bucci, A.D. Magri, A.L. Magri, D. Marini, *Chemom. Intell. Lab. Syst.* 73 (2004) 85.
- [2] T. Sato, *J. Am. Oil Chem. Soc.* 71 (1994) 293.
- [3] P. Hourant, V. Baeten, M.T. Morales, M. Meurens, R. Aparicio, *Appl. Spectrosc.* 54 (2000) 1168.
- [4] E. Bertran, M. Blanco, J. Coelho, H. Iturriaga, S. MasPOCH, I. Montoliu, *J. Near Infrared Spectrosc.* 8 (2000) 45.
- [5] R.C. Barthus, R.J. Poppi, *Vib. Spectrosc.* 26 (2001) 99.
- [6] D. Franco, M.J. Núñez, M. Pinelo, J. Sineiro, *Eur. Food Res. Technol.* 222 (2006) 443.
- [7] M.D. Guillén, N. Cabo, *J. Sci. Food Agric.* 75 (1997) 1.
- [8] O. Hendl, J.A. Howell, J. Lowery, W. Jones, *Anal. Chim. Acta* 427 (2001) 75.
- [9] A.A. Christy, P.K. Egeberg, *Chemom. Intell. Lab. Syst.* 82 (2006) 130.
- [10] L. Wang, F.S.C. Lee, X. Wang, Y. He, *Food Chem.* 95 (2006) 529.
- [11] J. Malavia, M. Abalos, F.J. Santos, E. Abad, J. Rivera, M.T. Galceran, *J. Chromatogr. A* 1149 (2007) 321.
- [12] E. Sikorska, T. Górecki, I.V. Khmelinskii, M. Sikorski, J. Kozio, *Food Chem.* 89 (2005) 217.
- [13] K.I. Poulli, G.A. Mousdis, C.A. Georgiou, *Anal. Chim. Acta* 542 (2005) 151.
- [14] K.I. Poulli, G.A. Mousdis, C.A. Georgiou, *Anal. Bioanal. Chem.* 386 (2006) 1571.
- [15] K. Papadopoulos, T. Triantis, C.H. Tzikis, A. Nikokavoura, D. Dimotikali, *Anal. Chim. Acta* 464 (2002) 135.
- [16] V. Stepanyan, A. Arnous, C. Petrakis, P. Kefalas, A. Calokerinos, *Talanta* 65 (2005) 1056.
- [17] S.G. Li, H. Zhang, W.T. Xue, *Eur. J. Lipid Sci. Tech.* 109 (2007) 1088.
- [18] M. Coatanea, A. Darchen, D. Hauchard, *Sens. Act. B Chem.* 76 (2001) 539.
- [19] T.G. Diaz, I.D. Merás, A.G. Cabanillas, M.F.A. Franco, *Anal. Chim. Acta* 511 (2004) 231.
- [20] S.G. Li, W.T. Xue, H. Zhang, *Electroanalysis* 18 (2006) 2337.
- [21] W. Surareungchai, D. Kasiwat, *Electroanalysis* 12 (2000) 1124.
- [22] C. Ceballos, H. Fernandez, *J. Am. Oil Chem. Soc.* 77 (2000) 731.
- [23] A.J. Bard, L.R. Faulkner, *Electrochemical Methods Fundamentals and Applications*, 2nd ed., John Wiley & Sons, New York, 2001, 294.
- [24] National Agency of Sanitary Vigilance. Resolution n°. 482, RDC 492/99. Available in <http://www.anvisa.gov.br/legis/resol/482.99.htm>. (access on December 20, 2007).
- [25] Y. Fung, S. MO, *Analyst* 121 (1996) 369.
- [26] C. Bessant, S. Saini, *Anal. Chem.* 71 (1999) 2806.
- [27] D.L. Massart, B.G.M. Vandeginste, L.M.C. Buydens, S. Jong, P.J. Lewi, J. Smeyers-Verbeke, *Handbook of Chemometrics and Qualimetrics: Part A*, Elsevier Science B. V, Amsterdam, 1997, 799.
- [28] R.W. Kennard, L.A. Stone, *Technometrics* 11 (1969) 137.
- [29] M.J.C. Pontes, R.K.H. Galvão, M.C.U. Araújo, P.N.T. Moreira, O.D. Pessoa Neto, G.E. José, T.C.B. Saldanha, *Chemom. Intell. Lab. Syst.* 78 (2005) 11.
- [30] C. Bessant, S. Saini, *J. Electroanal. Chem.* 489 (2000) 76.
- [31] A. Kotani, T. Fuse, F. Kusu, *Anal. Biochem.* 284 (2000) 65.
- [32] C.R.B. Medonça, C.I.D. Bica, C.M.S. Piatnicki, *J. Braz. Chem. Soc.* 14 (2003) 628.
- [33] R.R. Catharino, R. Haddad, L.G. Cabrini, I.B.S. Cunha, A.C.H.F. Sawaya, M.N. Eberlin, *Anal. Chem.* 77 (2005) 7429.
- [34] H. Yang, J. Irudayaraj, M.M. Paradkar, *Food Chem.* 93 (2005) 25.
- [35] F.D. Gunstone, *Vegetable Oils in Food Technology: Composition, Properties and Uses*, CRC Press, Boca Raton, 2002.
- [36] R.O. Duda, P.E. Hart, D.G. Stork, *Pattern Classification*, 2nd ed., John Wiley, New York, 2001.
- [37] R.S. Honorato, M.C.U. Araújo, R.A.C. Lima, E.A.G. Zagatto, R.A.S. Lapa, J.L.C. Lima, *Anal. Chim. Acta* 396 (1999) 91.



Size-dependent electrochemiluminescence behavior of water-soluble CdTe quantum dots and selective sensing of L-cysteine

Lijuan Hua^a, Heyou Han^{a,*}, Xueji Zhang^b

^a College of Science, State Key Laboratory of Agricultural Microbiology, Huazhong Agricultural University, Wuhan 430070, PR China

^b Department of Chemistry, University of South Florida, 4202 East Fowler Avenue, CHE 305, Tampa, FL 33620-5250, USA

ARTICLE INFO

Article history:

Received 12 June 2008

Received in revised form

28 September 2008

Accepted 30 September 2008

Available online 19 October 2008

Keywords:

CdTe

Quantum dots

Size-dependent effect

Electrochemiluminescence

L-Cysteine

ABSTRACT

Water-soluble CdTe quantum dots (QDs) with five sizes (2.25, 2.50, 2.77, 3.12, and 3.26 nm) were synthesized with the hydrothermal method. The electrochemiluminescence (ECL) of CdTe QDs was investigated in detail in air-saturated solution without adding foreign oxidant. It was found that the ECL of CdTe QDs displayed a size-dependent property. With the increasing in the particle size of the CdTe QDs, the ECL intensity was gradually increased, in addition, both ECL peak potentials and ECL onset potentials of CdTe QDs were shifted positively. Influences of some factors on the ECL intensity were investigated. Under the optimal conditions, the ECL intensity had a linear relationship with the concentration of L-cysteine (L-Cys) in the range from 1.3×10^{-6} to 3.5×10^{-5} mol L⁻¹ (R^2 0.996) with a detection limit of 8.7×10^{-7} mol L⁻¹ (S/N = 3). The proposed method was applied to the determination of L-Cys in real samples with satisfactory results. Compared with previous reports, it has better selectivity for the determination of L-Cys.

© 2008 Elsevier B.V. All rights reserved.

1. Introduction

Electrochemiluminescence (ECL) is a special form of chemiluminescence (CL). It has become an important and valuable detection method in analytical chemistry because of its low cost, wide range of analyte, excellent selectivity and high sensitivity [1–3]. Many chemiluminescent reagents were applied in ECL reactions, such as luminol and ruthenium complex, etc. [4–6]. Since they have been extensively studied, it is necessary to look into new luminescent reagents and develop new ECL systems.

Among the miscellaneous functional nanomaterials, quantum dots (QDs) are of considerable interest owing to their variety of superior optical and electrical properties. Recently, some scientists became aware of the potential application of QDs in ECL field. The ECL of Si QDs was first observed by Bard and co-workers in 2002 [7], which introduced a new type of luminescent reagent to ECL systems and opened a new field of ECL studies. Subsequently, the ECL analytical techniques coupled with QDs have been rapidly developed [8–27]. However, these researches were mostly carried out in organic media [7–9,10–12], or by modifying them to electrodes [13–16] in the presence of foreign strong oxidants which are indispensable for the accomplishment of such work. Actually, ECL of QDs

in aqueous solution has a wider potential as a sensor in biological analysis.

Our previous works have first reported the ECL of QDs dispersed in aqueous solution with bare electrode [17,27]. It was demonstrated that water-soluble QDs were promising luminescent materials used in ECL system, which avoided complicated modifying electrode or using toxic organic solution. Generally, the foreign strong oxidants are indispensable for the ECL of QDs, but we recently found that the ECL of QDs can be conducted in air-saturated solution without adding any foreign oxidants. Thus, the ECL systems of QDs were simplified, which was undoubtedly of great importance for expanding potential analytical applications of ECL of QDs. Nevertheless, very few reports have been published on size-dependent ECL properties of QDs, though the unique size-dependent properties of QDs have been the subject of considerable interest [28,29]. Therefore, the goal of our present study is to make an in-depth research on the size-dependent ECL behavior of CdTe QDs.

In this paper, the ECL of CdTe QDs with different sizes were conducted in air-saturated solution without adding any additional oxidants at bare glassy carbon (GC) electrode, which simplified the operating processes of our ECL study. Furthermore, the size-dependent ECL properties of CdTe QDs were investigated in detail. Based on the annihilation of ECL emission from CdTe QDs by L-cysteine (L-Cys), a novel method for the high selectivity determination of L-Cys was developed under the optimal conditions. Our

* Corresponding author. Tel.: +86 27 87288246; fax: +86 27 87288246.
E-mail address: hyhan@mail.hzau.edu.cn (H. Han).

work would expand the potential applications of QDs in the field of ECL.

2. Experimental

2.1. Apparatus

ECL studies were performed using a Model MPI-B from ECL Analyzer Systems (Xi'an Remex Electronic Science & Technology Co. Ltd., Xi'an, China). The voltage of the photo multiplier tube (PMT) was biased at 800 V during the whole processes. A conventional three-electrode system was used for the electrolytic system, a glassy carbon electrode was used as the working electrode, a platinum wire as the counter electrode, and an Ag/AgCl (saturated KCl) electrode as the reference electrode. The ultraviolet–visible (UV–vis) absorption spectra were performed on a Thermo Nicolet Corporation Model evolution 300 spectrophotometer coupled with a 1.00 cm quartz cell. The photoluminescence (PL) spectra were acquired with a PerkinElmer Model LS-55 luminescence spectrometer equipped with a 20 kW xenon discharge lamp as a light source. The Fourier transform infrared (FT-IR) spectra were performed on a Thermo Nicolet Corporation Model avatar 330 spectrometer. The high-resolution transmission electron microscopy (HRTEM) image of the CdTe QDs was acquired on a JEM2010FEF HRTEM (Japan).

2.2. Reagents

CdCl₂·2.5H₂O (99.0%), Tellurium powder (99.99%) and NaBH₄ (96%) were obtained from Tianjin Chemical Reagent Plant (Tianjin, China). Thioglycolic acid (TGA) and Na₂TeO₃ were obtained from Sinopharm Chemical Reagent Co., Ltd. A 0.1 mol L⁻¹ phosphate buffer solution (PBS, pH 7.1) was used throughout this work. L-Cysteine (L-Cys), L-glycine (L-Gly), L-proline (L-Pro), L-glutamic (L-Glu), L-leucine (L-Leu), L-alanine (L-Ala), L-lysine (L-Lys), L-threonine (L-Thr), L-glutamine (L-Gin), L-aspartic acid (L-Asp), L-isoleucine (L-Ile), L-serine (L-Ser), L-valine (L-Val) and L-asparagine (L-Asn), etc. were purchased from Shanghai Boao Biotechnology Co. Ltd. (Shanghai, China). Fresh L-Cys solutions were prepared every day. Human serum was provided from a healthy volunteer. The stock solutions of 0.1 mol L⁻¹ other common amino acids were prepared and stored in a refrigerator. All other reagents were of analytical reagent grade and used as purchased without further purification. Milli-Q (Millipore) water was used throughout.

2.3. Preparation of CdTe QDs

Water-soluble CdTe QDs were synthesized according to the hydrothermal method with slight modifications [30]. Briefly, 10 mL of 0.01 mol L⁻¹ CdCl₂ and 38 mL of ultrapure water were transferred to a small flask. This solution was mixed with 10 μL of TGA and kept bubbling with highly pure N₂. 1.0 mol L⁻¹ NaOH was added to adjust its pH to 11.0, and this mixture became clear. Then 55.5 mg Trisodium citrate and 2.0 mL of 0.01 mol L⁻¹ Na₂TeO₃ were injected into this mixture respectively. Finally, 3.0 mg NaBH₄ was added at N₂ atmosphere. After mixing, about 25 mL of this mixture was transferred to a reaction kettle and kept heated at 180 °C for 60 min, and then water-soluble CdTe QDs could be obtained. By controlling the heating time, different sizes of CdTe QDs were attained. The resulting products were precipitated by acetone and superfluous TGA and Cd²⁺ were removed with centrifugation at 1086 (×g) for 5 min. The resultant precipitate was redispersed in water, reprecipitated by a copious amount of acetone more than two times, and then kept under dark for further use.

2.4. Sample preparation

For preparation of serum, 10 mL of human blood was taken and collected in a sample tube. The serum of blood was separated after putting the sample in an incubator at 37 °C for 30 min for removing red cell. The above serum layer was centrifuged at 1100 (×g) for 6 min to precipitate proteins. The resulting human serum solution was then stored at -70 °C until used.

2.5. Standard procedures for the ECL detection

ECL measurements were carried out in a 0.1 mol L⁻¹ PBS solution (pH 7.1) in the presence of 4.0 × 10⁻⁷ mol L⁻¹ CdTe QDs solution using a conventional three electrode cell mentioned above. The applied working potential ranged from 0 to -2.3 V, and a cycle scan rate was 0.34 V s⁻¹. A high voltage power supply applied 800 V to the PMT, and ECL signals were recorded by a Model MPI-B ECL analyzer. Each data point was an average of five measurements. The different concentrations of standard L-Cys solutions were injected in the ECL cell to obtain the calibration curve. Similarly, sample solutions were injected in the ECL cell to detect the L-Cys concentrations in sample.

3. Results and discussion

3.1. Characterization of water-soluble CdTe QDs

As shown in Fig. 1(A), the prepared CdTe QDs were characterized by UV–vis and the PL spectra. The particle sizes of CdTe QDs were 2.25, 2.50, 2.77, 3.12, and 3.26 nm, respectively, which were calculated in virtue of the following empirical equation [31]:

$$D = (9.8127 \times 10^{-7})\lambda^3 - (1.7147 \times 10^{-3})\lambda^2 + 1.0064\lambda - 194.84$$

In the above equation, *D* (nm) is the diameter of a given QDs, and λ (nm) is the wavelength of the first excitonic absorption peak of the UV–vis absorption spectra. It can be seen that the UV–vis absorption peaks and the PL peaks shifted to longer wavelengths with the increasing QD sizes as a consequence of the well-known quantum size effect. The quantum yield (QY) of the prepared CdTe QDs was obtained in comparison to the PL emission of Rhodamine 6G (QY 95%) [32]. The result supported that the PL QYs of CdTe QDs were 5.5%, 8.5%, 16.0%, 23.6% and 21.4%, respectively.

The CdTe QDs was also studied carefully by HRTEM image (Fig. 1(B)). The morphology and size of CdTe QDs could be observed clearly. The average size of studied CdTe QDs was about 3.16 nm, and considered close to the value of 3.12 nm resulting from the empirical formula which seems to be convenient to calculate the size of CdTe QDs.

The FT-IR spectra were used to character the structure of the prepared CdTe QDs. From Fig. 1(C), TGA showed a peak at 2566 cm⁻¹ for stretch vibration of the S–H bond, which diminished in the spectrum of CdTe QDs. Therefore, it could be concluded that the S–Cd bonds were formatted between TGA and CdTe core. The asymmetric vibration of the carboxyl group in TGA shifted from 1720 to 1551 cm⁻¹, and the symmetric vibration of the carboxyl anion at 1387 cm⁻¹ appeared in the spectrum of CdTe QDs, implying that the COOH in TGA turned to its anion. As a result, the structure of the prepared CdTe QDs could be identified as a cadmium-rich CdTe core covered with excess TGA²⁻ anions, which was similar to the structure of CdSe QDs [33].

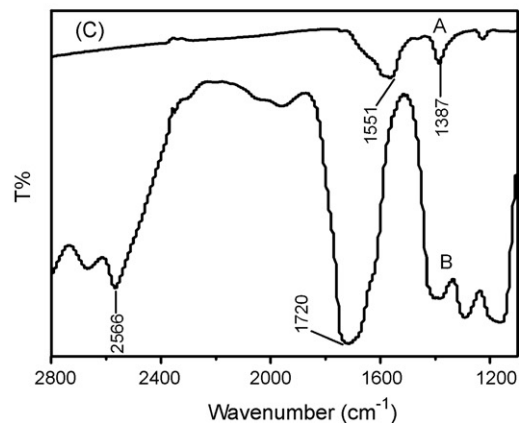
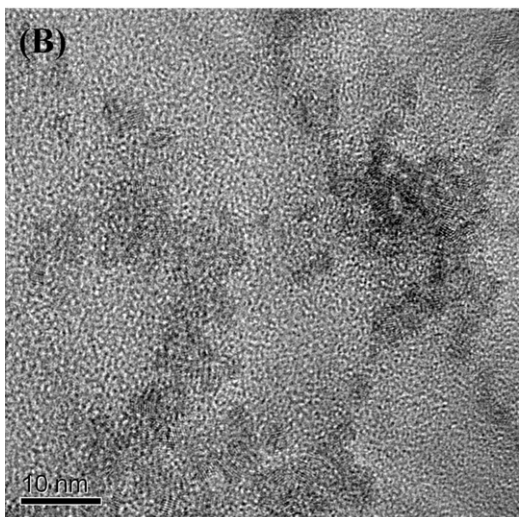
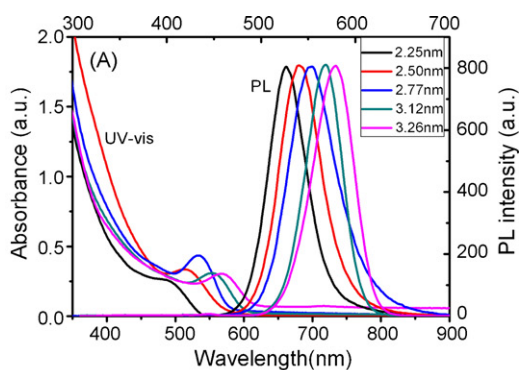


Fig. 1. (A) PL and UV-vis absorption spectra of CdTe QD solution with different sizes of CdTe QDs. (B) The HRTEM image of CdTe QDs, (C) FT-IR spectra of CdTe QDs (a) and TGA (b).

3.2. Size-dependent ECL behavior of CdTe QDs

The size-dependent ECL behavior of CdTe QDs was investigated in air-saturated solution. It was found that the ECL intensity gradually increased while the particle size of CdTe QDs increased, indicating that ECL intensity of CdTe QDs has a size-dependent effect (Fig. 2(A)). Here, the concentrations of CdTe QDs were fixed in all our experiments ($4.0 \times 10^{-7} \text{ mol L}^{-1}$). According to ECL energy match theory [34], the ECL intensity depends on both the quantum efficiency of producing excited-state QDs and the luminescent quantum efficiency of excited-state QDs. The quantum efficiency of producing excited-state QDs enhanced with the increasing sizes

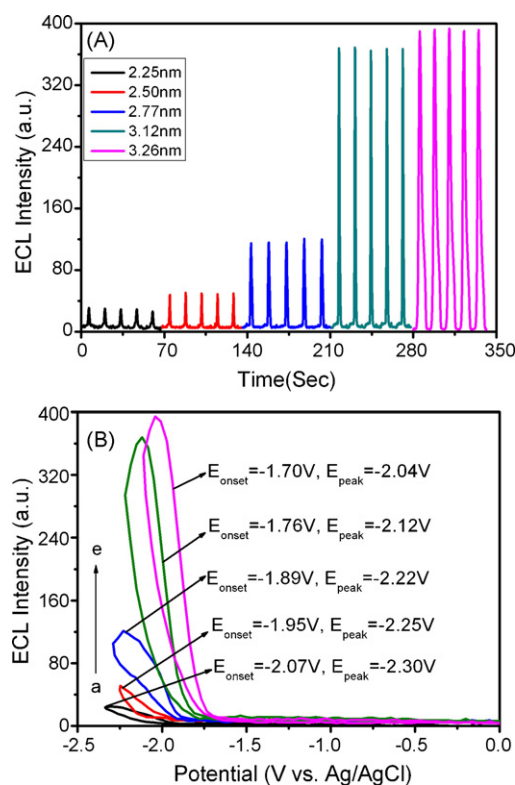


Fig. 2. (A) ECL curves of CdTe QD solution with different sizes. (B) Effects of potential and ECL intensity in CdTe QD solution with different sizes (conditions: $4.0 \times 10^{-7} \text{ mol L}^{-1}$ CdTe QD solution with different sizes; scan rate: 0.34 V s^{-1} ; 0.1 mol L^{-1} pH 7.1 PBS; PMT voltage: 800 V).

of QDs, which was probably resulted from the generated energy of ECL reaction matching degree with the chemical energy for formation of excited state of CdTe QDs [28,29]. It is known that energy band gap of QDs decreased with the increment in particle size [31]. In this case, the increment in ECL intensity was possibly attributed to chemical energy, generated during the ECL reaction of CdTe QDs, more matched the smaller energy band gap of the studied five sizes QDs. The more chemical energy matched the excitation energy need, the stronger the ECL intensity and efficiency. Moreover, the luminescent quantum efficiency of excited-state QDs increased with the increasing QDs sizes, because the confinement energy of excited-state QDs shifted to low energy with the increasing sizes of QDs. In addition, the luminescent quantum efficiency of excited-state QDs was inversely proportional to the confinement energy [35]. As a result, both the quantum efficiency of producing excited-state QDs and the luminescent quantum efficiency of excited-state QDs increased with increment in sizes, which finally resulted in that the ECL intensity of CdTe QDs increased with the particle sizes.

The relationships of ECL peak potentials and ECL onset potentials with the sizes of QDs were illuminated in Fig. 2(B). Both the ECL peak potentials and ECL onset potentials shifted positively with the increasing size or the decreasing band gap of the QDs, indicating that the injection of electrons to the surface of smaller QDs should be more difficult. It has been indicated that the energy band gap of QDs decreased with the increment in particle sizes. The energy levels of QDs move to low energies when the size of QDs increases, since the top of the valence band is shifted toward higher energies and the bottom of the conduction band is moved to lower energies with increasing particle size. This means that the smaller QDs need more energy for injection of electrons to the surface of QDs.

A similar relationship between the band gap of CdTe QDs and their electrochemical behaviors also was observed [28]. Given the fact that the CdTe QDs larger than 4 nm might be unstable, and it was difficult to obtain the large QDs of high quality. Therefore, CdTe QDs of 3.12 nm were chosen to conduct the following experiments. This work possibly provided a promising principle for improving the efficiency of QDs ECL by optimizing the sizes of QDs and the fast preferences of the ECL systems.

The ECL and cyclic voltammetry (CV) curves of the air-saturated blank PBS solution were also observed (not shown). No light emission and current peak were detected. Under the same conditions, the obvious light emission was observed in the CdTe QDs solution. The same experiment was done in the air-saturated blank PBS solution using the GC electrode which has done continuous CVs for 300 cycles in CdTe QDs solution. Similar results were obtained. It means that there nearly was no absorption on the surface of the electrode, or the working electrode was not easily contaminated by CdTe QDs solution in the process of ECL. Therefore, CdTe QDs can be studied as an excellent illuminant in the field of ECL.

3.3. Conditions optimization

The ECL of CdTe QDs was conducted in air-saturated solution without adding any additional oxidants. Therefore, the effect of dissolved oxygen on ECL intensity was investigated. As shown in Fig. 3(A), when dissolved oxygen was removed from the solution by bubbling high-purity N₂, the light emission intensity of ECL decreased dramatically, indicating that dissolved oxygen was an important coreactant for producing ECL of CdTe in the QDs solution. It was very interesting for producing the ECL emission without adding any foreign oxidants, and the operating processes of ECL were simplified. To acquire both simple process and high ECL inten-

sity, air-saturated CdTe QDs solution was recommended in our experiments.

The contrast experiments were also conducted to examine the influence of coexisting substances (e.g., free CdCl₂ and TGA) on ECL of CdTe QDs (Fig. 3(B)). The concentrations of CdCl₂ and TGA solution were in agreement with their concentrations in un-pured CdTe QDs solution. With the same electrochemical parameters, the ECL behaviors of CdCl₂ and TGA solution were studied. Fig. 3(B) (curves d and g) depicted the ECL behaviors of pure TGA in PBS solution, and showed that no ECL signals and current peaks were observed. However, a pair of peak current appeared in pure CdCl₂ solution (curve c), and the ECL signal (curve f) was also quite weak. When TGA solution was added into the CdCl₂ solution, reduction peak current was decreased evidently (curve e), and the ECL signal was not observed. Therefore, the free CdCl₂ and TGA only affected electrochemical behaviors of CdTe QDs (CV curves), but effect on ECL emission was not obvious.

The effect of concentrations of CdTe QDs was studied (Fig. 4(A)). When the concentrations of CdTe QDs were augmented, the formed individual CdTe QDs species were increased in the scanning process, which resulted in the enhancement of the ECL intensity. When the concentration of the CdTe QDs solution exceeded $4.0 \times 10^{-7} \text{ mol L}^{-1}$, the ECL intensity decreased, indicating that the excessive CdTe QDs could inhibit the generation of excited-state CdTe QDs, which was due to an effect called self-absorption in higher concentration [36].

The CdTe QDs was added to the PBS solution and incubated about 5, 10, 15, 20, 25 and 30 min. Then the effect of incubation time on the ECL of CdTe QDs was investigated (Fig. 4(B)). It was found that there was no obvious effect of incubation time on the ECL of

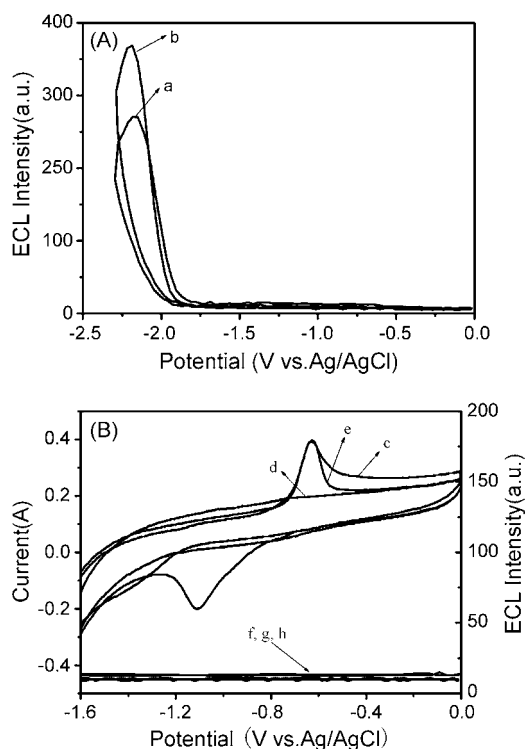


Fig. 3. (A) Effects of dissolved oxygen (a) N₂-saturated CdTe QD solution ($4.0 \times 10^{-7} \text{ mol L}^{-1}$); (b) air-saturated CdTe QD solution ($4.0 \times 10^{-7} \text{ mol L}^{-1}$) and (B) other coreactants (c) CdCl₂; (d) TGA; (e) TGA + CdCl₂ (f–h) ECL curves. (Conditions: scan rate: 0.34 V s^{-1} ; 0.1 mol L^{-1} pH 7.1 PBS; PMT voltage: 800 V .)

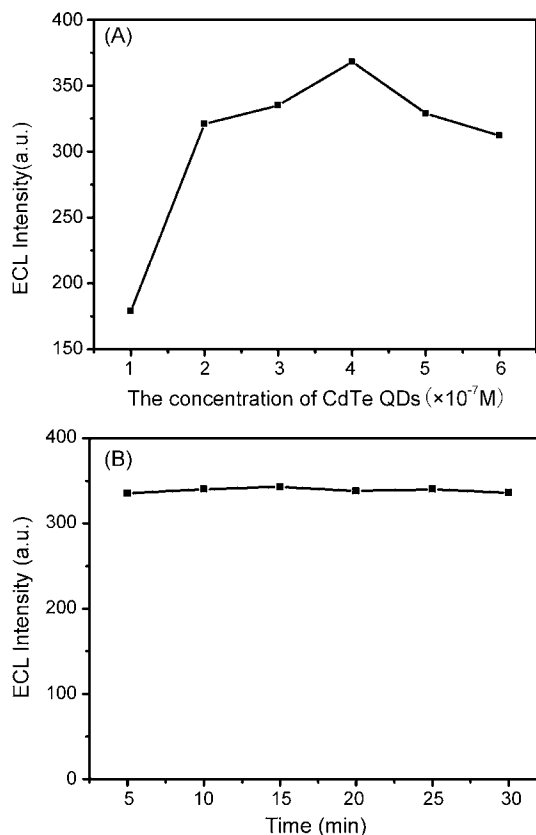


Fig. 4. (A) Effects of concentration of CdTe QDs (conditions: scan rate: 0.34 V s^{-1} ; 0.1 mol L^{-1} pH 7.1 PBS; PMT voltage: 800 V) and (B) incubation time. (Conditions: $4.0 \times 10^{-7} \text{ mol L}^{-1}$ CdTe QD solution; 0.1 mol L^{-1} pH 7.1 PBS; PMT voltage: 800 V .)

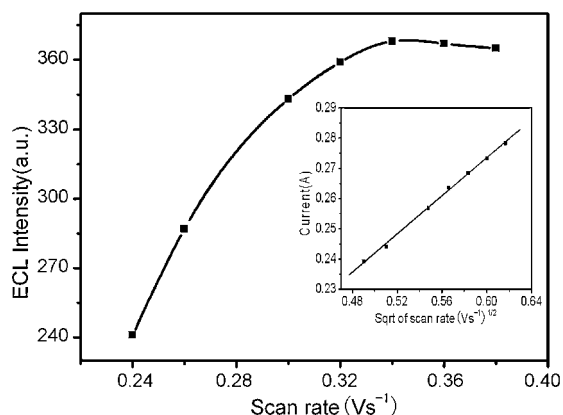


Fig. 5. Effect of scan rate on ECL intensity of CdTe QDs. Inset: Plot of current versus square root of scan rate ($v^{1/2}$) (conditions: 4.0×10^{-7} mol L $^{-1}$ CdTe QD solution; 0.1 mol L $^{-1}$ pH 7.1 PBS; PMT voltage: 800 V).

CdTe QDs in a certain time range, indicating the better stability of ECL.

The scan rate could also affect on the ECL intensity (Fig. 5). With the increasing scan rate, the ECL intensity increased and tended to a constant value at the scan rate of 0.34 Vs^{-1} , indicating the ECL intensity reached the saturation point. Therefore, the scan rate of 0.34 Vs^{-1} was chosen for the following studies. We also found that the cathode peak current was linear with the square root of the scan rate during CV as shown in Fig. 5 (inset), which indicated that this electrochemical reaction was an irreversible diffusion-controlled electrode process.

The studied potential windows were selected as -1.9 to 0 , -2.0 to 0 , -2.1 to 0 , -2.3 to 0 and -2.5 to 0 V, respectively. It was found that the ECL intensities were enhanced, but the ECL signals reached a maximum at a potential window of -2.3 to 0 V. That might be due to the fact that the CdTe QDs in the ECL processes with a high excited electrochemical potential window were unstable. Thus, to achieve the optimum intensity and stability, a potential window of -2.3 to 0 V was selected for the following ECL experiment.

3.4. The quenching effects of L-Cys on the ECL intensity

The quenching effects of L-Cys on the ECL intensity was studied and shown in Fig. 6. Upon addition of L-Cys to the PBS containing 4.0×10^{-7} mol L $^{-1}$ CdTe QDs, the ECL intensity decreased greatly

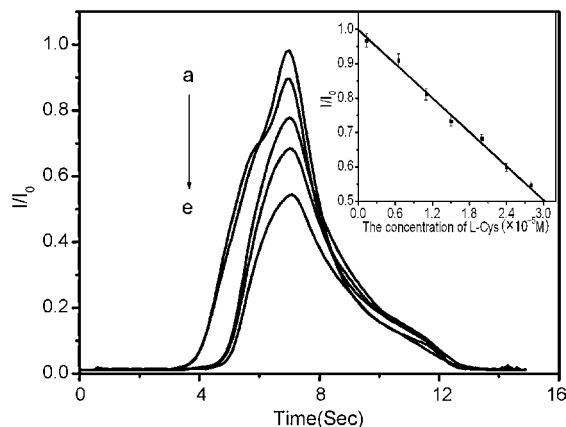
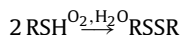


Fig. 6. The quenching effect of L-Cys at 0 (a), 0.65 (b), 1.3 (c), 2.0 (d), and 2.8×10^{-5} mol L $^{-1}$ (e) on the ECL intensity of CdTe QDs. Inset: linear calibration plot for L-Cys (conditions: 4.0×10^{-7} mol L $^{-1}$ CdTe QD solution, scan rate: 0.34 Vs^{-1} ; 0.1 mol L $^{-1}$ pH 7.1 PBS, PMT voltage: 800 V).

with an increase in the concentration of L-Cys. The L-Cys was responsible for the quenching effect according to the following reaction:



According to the above reaction, if L-Cys was added to the system, it would react with the dissolved oxygen or its intermediate species produced in the processes of QD ECL, which resulted in decreasing the ECL intensity. Meanwhile, it confirms the above results about the role of dissolved oxygen. Here, although the stabilizer TGA was also a thiol compound, FT-IR spectrum (Fig. 1(C)) indicated that the ECL emission was quenched by the L-Cys. The structure of CdTe QDs indicated only S–Cd bond without an SH group present in the QDs. Thus, it did not quench the ECL emission and interfere with the detection of L-Cys. Therefore, our present study aims to develop a finer method for the detection of L-Cys based on our above discussion.

3.5. Application to detection of L-Cys

L-Cys is a naturally occurring amino acid with a thiol group, which plays an important role in several biological processes. L-Cys is involved in a variety of key cellular functions including protein synthesis, detoxification, and metabolism, and its insufficiency may cause many diseases. Due to the structural similarity of amino acids and their spectroscopic inertness, most of analytical methods usually involve complicated chromatography separation [37]. Thus, the development of a simple and highly selective method [38] for the detection of L-Cys is obviously of significance.

From the inset of Fig. 6, the ECL intensity decreased linearly with the concentrations of L-Cys. The calibration range for determination of L-Cys was from 1.3×10^{-6} to 3.5×10^{-5} mol L $^{-1}$ with the correlation coefficient of 0.996. The detection limit ($S/N=3$) was found to be 8.7×10^{-7} mol L $^{-1}$. The relative standard deviation (R.S.D.) at the L-Cys concentration of 1.3×10^{-5} mol L $^{-1}$ was 2.0% ($n=5$), indicating an acceptable reproduction.

To study the selectivity for L-Cys determination with the proposed method in amino acid detection, various amino acids were investigated according to the proposed procedure by increasing amounts of them. As shown in Fig. 7, no interference was observed in the presence of L-Pro, L-Glu, L-Ala, L-Gly, L-Leu, L-Val, L-Thr and L-Ile, even when they were present in a 1000-fold concentration. Furthermore, the ECL intensity decreases were all less than 5% relative to L-Cys in the presence of some other common amino acids

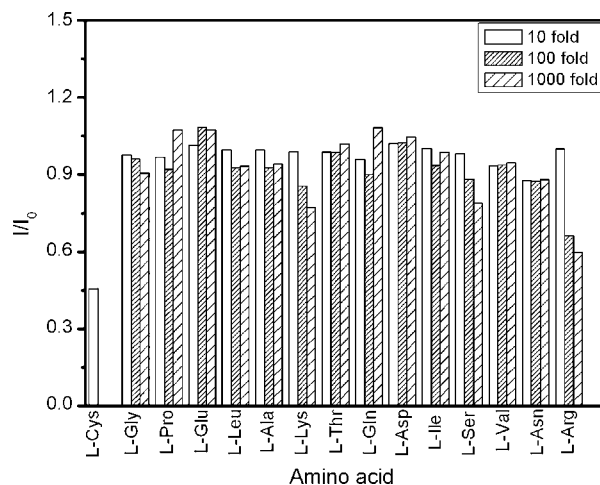


Fig. 7. Interferences of same common amino acid (conditions: 4.0×10^{-7} mol L $^{-1}$ CdTe QD solution; scan rate: 0.34 Vs^{-1} ; 0.1 mol L $^{-1}$ pH 7.1 PBS, PMT voltage: 800 V).

Table 1
Determination of L-Cys in real samples.

Sample	L-Cys added ($\mu\text{mol L}^{-1}$)	L-Cys found ^a ($\mu\text{mol L}^{-1}$)	Recovery (%)	R.S.D. ^a (%)
Synthetic amino acids mixtures				
1	39.0	38.6 \pm 2.6	99.0	6.6
2	126.0	126.0 \pm 2.0	96.9	1.6
3	210.0	204.4 \pm 1.0	97.3	5.5
Human serum				
1	0	364.3 \pm 7.6	4.7	
2	100.0	462.1 \pm 8.4	98.0	2.6
3	200.0	565.7 \pm 10.5	101.0	1.8
4	400.0	735.4 \pm 6.5	92.8	1.0

^a Mean result of five measurements.

with a 100-fold concentration, which also could be neglectable. Therefore, the proposed method is practical for the determination of L-Cys and showed the ideal selectivity.

As a practical use, the proposed method was used to detect L-Cys in synthetic amino acids mixtures and human serum. The recoveries of L-Cys are determined by the standard addition method. The results shown in Table 1. It indicated that the proposed method was suitable for the determination of L-Cys in the presence of other amino acids. Moreover, this method could be also used to successfully detect L-Cys in human serum, and the total concentration were found to be $364.3 \pm 7.6 \mu\text{mol L}^{-1}$. This value fell in the normal range of total L-Cys ($174.0\text{--}378.0 \mu\text{mol L}^{-1}$) in human serum detected by Stabler et al. [39]. Meanwhile, the method had good recoveries, as given in Table 1. These data suggested the fine accuracy and acceptable practicability of the proposed method.

Our following work also extensively studied the quenching effects of other thiol compounds on the ECL intensity, and the similar results could be demonstrated (not shown). Thus, the proposed method could be developed and applied for thiol compounds detection.

4. Conclusions

In summary, we demonstrated that the ECL behavior of CdTe QDs was size dependent. It gives a new path to further improve the efficiency of QD ECL by optimizing the sizes of QDs, and provides a promising strategy for the fast preferences of the ECL system. Furthermore, it was found that the relative high ECL intensity was also observed in air-saturated solution without adding foreign oxidant, and the operating processes of ECL were simplified. A novel method for the high selectivity determination of L-Cys was developed. In contrast to other ECL sensor methods, this proposed method showed simple operating processes and ideal selectivity. Our studies would promote the further studies of QD ECL sensor and has found potential analytical applications.

Acknowledgements

The authors gratefully acknowledge the support for this research by National Natural Science Foundation of China (20675034), Program for New Century Excellent Talents in Chinese Ministry of Education (NCET-05-0668), Program for academic pacesetter of Wuhan (200851430484).

References

- [1] M.M. Richter, Chem. Rev 104 (2004) 3003.
- [2] M.J. Shi, H. Cui, Electrochim. Acta 52 (2006) 1390.
- [3] R. Lei, X. Xu, F. Yu, N. Li, H.W. Liu, K. Li, Talanta 75 (2008) 1068.
- [4] R. Wilson, C. Clavering, A. Hutchinson, Anal. Chem. 75 (2003) 4244.
- [5] J.P. Yuan, T. Li, X.B. Yin, L. Guo, X.Z. Jiang, W.R. Jin, X.R. Yang, E.K. Wang, Anal. Chem. 78 (2006) 2934.
- [6] W. Zhan, A.J. Bard, Anal. Chem. 79 (2007) 459.
- [7] Z. Ding, B.M. Quinn, S.K. Haram, L.E. Pell, B.A. Korgel, A.J. Bard, Science 296 (2002) 1293.
- [8] Y. Bae, N. Myung, A.J. Bard, Nano. Lett. 4 (2004) 1153.
- [9] Y. Bae, D.C. Lee, E.V. Rhogojina, D.C. Jurbergs, B.A. Korgel, A.J. Bard, Nanotechnology 17 (2006) 3791.
- [10] N. Myung, Y. Bae, A.J. Bard, Nano Lett. 2 (2002) 1315.
- [11] N. Myung, Y. Bae, A.J. Bard, Nano Lett 3 (2003) 1053.
- [12] N. Myung, X. Lu, K.P. Johnston, A.J. Bard, Nano Lett. 4 (2004) 183.
- [13] H. Jiang, H.X. Ju, Anal. Chem. 79 (2007) 6690.
- [14] G.Z. Zou, H.X. Ju, Anal. Chem. 76 (2004) 6871.
- [15] G.Z. Zou, H.X. Ju, W.P. Ding, H.Y. Chen, Electroanal. Chem. 579 (2005) 175.
- [16] B. Liu, T. Ren, J.R. Zhang, H.Y. Chen, J.J. Zhu, C. Burda, Electrochem. Commun. 9 (2007) 551.
- [17] H.Y. Han, Z.H. You, J.G. Liang, Z.H. Sheng, Front. Biosci. 12 (2007) 2352.
- [18] S.K. Poznyak, D.V. Talapin, E.V. Shevchenko, H. Weller, Nano Lett. 4 (2004) 693.
- [19] T. Ren, J.Z. Xu, Y.F. Tu, S. Xu, J.J. Zhu, Electrochem. Commun. 7 (2005) 5.
- [20] J.J. Miao, T. Ren, D. Lin, J.J. Zhu, H.Y. Chen, Small 1 (2005) 802.
- [21] S.N. Ding, J.J. Xu, H.Y. Chen, Chem. Commun. 34 (2006) 3631.
- [22] G.F. Jie, B. Liu, J.J. Miao, J.J. Zhu, Talanta 71 (2007) 1476.
- [23] M. Chen, L. Pan, Z. Huang, J. Cao, Y. Zheng, H. Zhang, Mater. Chem. Phys. 101 (2007) 317.
- [24] Z.H. Dai, J. Zhang, J.C. Bao, X.H. Huang, X.Y. Mo, J. Mater. Chem. 17 (2007) 1087.
- [25] G.F. Jie, B. Liu, H.C. Pan, J.J. Zhu, H.Y. Chen, Anal. Chem. 79 (2007) 5574.
- [26] L.H. Shen, X.X. Cui, H.L. Qi, C.C. Zhang, J. Phys. Chem. C 111 (2007) 8172.
- [27] H.Y. Han, Z.H. Sheng, J.G. Liang, Anal. Chim. Acta 596 (2007) 73.
- [28] S.K. Poznyak, N.P. Osipovich, A. Shavel, D.V. Talapin, M.Y. Gao, A. Eychmüller, N. Gaponik, J. Phys. Chem. B 109 (2005) 1094.
- [29] Z.P. Wang, J. Li, B. Liu, J.Q. Hu, X. Yao, J.H. Li, J. Phys. Chem. B 109 (2005) 23304.
- [30] N. Gaponik, D.V. Talapin, A.L. Rogach, K. Hoppe, E.V. Shevchenko, A. Kornowski, A. Eychmüller, H. Weller, J. Phys. Chem. B 106 (2002) 7177.
- [31] W.W. Yu, L.H. Qu, W.Z. Guo, X.G. Peng, Chem. Mater. 15 (2003) 2854.
- [32] J. Georges, N. Arnaud, L. Parise, Appl. Spectrosc. 50 (1996) 1505.
- [33] M.Y. Gao, B. Richter, S. Kirstein, Adv. Mater. 9 (1997) 802.
- [34] A.M. García-Campaña, W.R.G. Baeyens, Chemiluminescence in Analytical Chemistry, Marcel Dekker, New York, 2001.
- [35] L. Brus, J. Chem. Phys. 90 (1986) 2555.
- [36] K.S. Jang, H.C. Ko, B. Moon, H. Lee, Synth. Met. 150 (2005) 127.
- [37] F. Xu, L. Wang, M. Gao, L. Jin, J. Jin, Anal. Bioanal. Chem. 372 (2002) 791.
- [38] B.X. Li, Z.J. Zhang, M.L. Liu, C.L. Xu, Anal. Bioanal. Chem. 377 (2003) 1212.
- [39] S.P. Stabler, P.D. Marcell, E.R. Podell, R.H. Allen, Anal. Biochem. 162 (1987) 185.



Silver UPD ultra-thin film modified nanoporous gold electrode with applications in the electrochemical detection of chloride

Jing-Fang Huang

Department of Chemistry, National Chung Hsing University, Taichung 402, Taiwan, ROC

ARTICLE INFO

Article history:

Received 27 August 2008

Received in revised form

30 September 2008

Accepted 1 October 2008

Available online 17 October 2008

Keywords:

Nanoporous

Ionic liquid

UPD

Sensor

Gold

Silver

Chloride

ABSTRACT

Nanoporous noble metals are usually expected to exhibit much higher surface areas than smooth ones, making them of particular importance in many electrochemical applications. This paper describes a simple electrochemical method to modify a nanoporous Au (NPG) surface by using an under potentially deposited (UPD) Ag adlayer. The NPG electrode was obtained by the dealloying of Zn from $\text{Au}_x\text{Zn}_{1-x}$ in a 40–60 mol% zinc chloride–1-ethyl-3-methylimidazolium chloride (ZnCl_2 –EMIC) ionic liquid. The Ag UPD modified nanoporous gold (NPG/Ag(UPD)) electrode possessed dual properties, including an intrinsic high surface area from the nanoporous structure and the characteristics of the Ag UPD adlayer. The potential utility of using NPG/Ag(UPD) for sensors was demonstrated by its excellent sensitivity and selectivity in the electrochemical determination of chloride ions. An atomic scale metal monolayer obtained in the UPD process was selected as a sensing agent. The long-term storability and operational stability of the electrode were strongly demonstrated. Specifically, two couples of redox waves at ~ 552 mV and ~ 272 mV, respectively, were observed in the cyclic voltammograms (CVs) of the NPG/Ag(UPD) after the adsorption of chloride ions. The first couple of redox waves was related to the UPD and silver stripping and the second couple of redox waves was induced by the adsorption of Cl^- . The Cl^- adsorption process on the NPG/Ag(UPD) electrode followed the transient Langmuir adsorption kinetic model. The ratio of the integrated charges for these two anodic stripping peaks was selectively used to determine dilute chloride ion levels. The calibration curve was linear in the Cl^- concentration range of 0.5–30.0 μM .

© 2008 Elsevier B.V. All rights reserved.

1. Introduction

A nanostructured noble metal with micrometer-sized pores is usually expected to exhibit a much higher surface area than a smooth metal, which is of particular importance in many electrochemical applications, such as electrocatalysis and electrochemical sensors [1–6]. In recent years, the dealloying process was found to be an effective route for fabricating nanoporous noble metals [3,7,8]. Dealloying is a kind of corrosion process that is used to separate the components of an alloy by selective dissolution [9,10]. For instance, if component B is more reactive than component A in a binary alloy A_xB_{1-x} , B will be dissolved from the alloy while A will remain during a dealloying process. This method is relatively easy; however, in the past, high temperature processes, such as arc melting at 1000 °C, were required to prepare the binary alloys [7]. Even though the development of electrochemical deposition offered an advantage, by reducing the operating temperature needed for the preparation of a binary alloy, a drawback to the electrochemical

fabrication of porous metals was that strongly acidic, alkaline, or toxic cyanide electrolyte solutions were used in the typical electrochemical process. Ionic liquids (ILs) are defined as salts that melt below 100 °C. ILs are attracting increasing attention as reaction media, because of their remarkable properties, which include low vapor pressures, high thermal stabilities, and high ionic conductivities [11–15]. Huang et al. demonstrated the replacement of a typical aqueous solution with an ionic liquid, which provided a wide working temperature range, covering from room temperature to above 150 °C. This facilitated the direct formation of alloys on a substrate using the electrodeposition process, simplifying the fabrication step for nanoporous Au and Pt electrodes [3,4].

Although the ultra-high surface area of the nanoporous material is a significant property in numerous research areas, the modified surface of the nanoporous material could be gifted with other unique properties, such as those related to binding sites, charge density, and so forth, further extending their applications. Organic ultra-thin films, such as thiols and sulfides, have been used to modify the surface of electrodes and to functionalize nanoporous gold (NPG) electrodes [3]. It has been demonstrated that organic ultra-thin film modified NPG electrodes show excellent performance in analytical applications, such as in the selective detection of

E-mail address: jfh@dragon.nchu.edu.tw.

copper ions. To the best of our knowledge, there have been fewer studies on using an inorganic modified layer on an NPG electrode. Underpotential deposition (UPD) is a phenomenon wherein a metal monolayer is deposited onto the surface of a foreign metal at a potential that is more positive than the reversible Nernst potential [16]. Metallic UPD adlayers have been demonstrated to alter the composition and chemical properties of an electrode's surface. Metallic UPD should allow for the precise and reproducible control of the surface coverage and for the study of coverage dependent properties, including the structure of the metallic adlayer and its electronic properties [16]. Numerous UPD systems, such as Cu^+ , Pb^{2+} , Bi^{3+} , Ag^+ , etc., on polycrystalline or single crystalline noble metals, such as Pt and Au, have been broadly investigated in a variety of studies [16–24]. Because of this, it was felt that noble metals would be excellent substrates for modification using metallic UPD. In addition, it was expected that a noble metal composed of nanopores would provide a high capacity for the formation of a UPD adlayer because of its ultra-high surface area. Accordingly, such metallic UPD adlayer modified nanoporous noble metals would not only have the original ultra-high surface area but also the additional characteristics of the reproducible metallic UPD adlayer. This would be due to the addition of the metallic UPD adlayer as an ultra-thin film on a substrate with high surface coverage. This paper describes an electrochemical method for modifying an NPG surface using a metallic UPD adlayer. The NPG electrode was obtained by the selective electrochemical dissolution (dealloying) of Zn from $\text{Au}_x\text{Zn}_{1-x}$ alloy in a 40–60 mol% zinc chloride–1-ethyl-3-methylimidazolium chloride (ZnCl_2 –EMIC) ionic liquid, as reported by Huang et al. [3]. A silver UPD system was selected to modify the surface of the NPG electrode. This work demonstrated that the ultra-thin Ag UPD adlayer modified NPG electrode was highly reproducible and compounded a high surface area and the unique properties of the Ag UPD adlayer on the same electrode.

Chloride sensing is an important need in clinical diagnosis, environmental monitoring, and industrial applications [25–30]. In many of these chloride detection applications, there is a need to increase the sensitivity and selectivity. Ion-selective electrodes (ISEs) are popular and commercially available methods for sensing various ions, including chloride [26,31–33]. Optical methods that utilize fluorescence measurement have also been used in the detection of chloride ions [34–38]. Although these methods all have notable performance in many analytical applications, their selectivity and detection limits (typically 5×10^{-5} M) are drawbacks. The stability of the dye molecule used in the optical method also limits this method to related applications. It has been reported that an Ag UPD modified gold electrode can serve as a sensing electrode in the detection of chloride [39,40]. The shift of Ag UPD and stripping peaks on an Au(111) electrode caused from the adsorption of chloride on the Ag adatom provided a possibility for halide sensing, and the current–potential relationship could be used to identify the type of halide and its concentration. However, even after this crystalline electrodes were still limited to some practical operations for sensing applications because preparing and storing them required a more complicated process. To solve this problem, a polycrystalline Au electrode, fabricated by vapor deposition in a high vacuum chamber, was used as a sensing probe to replace the single crystalline electrode [40]. The adsorption of chloride onto the Ag UPD adlayer was used to easily and quantitatively determine the chloride ions in the sample. This is a highly sensitive and selective method for detecting chloride ions (with a detection limit lower than 5×10^{-7} M).

This paper describes a simple electrochemical method for the fabrication of an NPG/Ag(UPD) electrode. This NPG/Ag(UPD) electrode could serve as a possible substrate for the detection of chloride. It possesses dual properties, including an intrinsic high

surface area from the nanoporous structure and the characteristics of the Ag UPD adlayer. It could increase the chloride adsorption capacity and further improve chloride detection performance. This work also demonstrated the potential utility of the NPG/Ag(UPD) electrode for sensors as a result of its excellent sensitivity and selectivity in the electrochemical determination of chloride ions.

2. Experimental

2.1. Reagents

Deionized water was used to prepare all of the solutions. All chemicals were of analytical grade unless otherwise stated. Glassware and polyethylene bottles were soaked in diluted nitric acid and rinsed with deionized water before use. Silver sulfate (JT-Baker), sodium sulfate (JT-Baker), potassium chloride (JT-Baker), potassium bromide (JT-Baker), potassium iodide (JT-Baker), potassium perchlorate (JT-Baker), potassium phosphate (Riedel-de-Haen), sulfuric acid (Aldrich), and zinc chloride 98% (Aldrich), were used without purification.

2.2. Synthesis of ZnCl_2 –EMIC ionic liquid

The EMIC was prepared and purified according to the method described in the literature [3,41]. The ZnCl_2 –EMIC ionic liquid was prepared in a glove box filled with dry nitrogen gas by mixing the proper amounts of ZnCl_2 and EMIC in a beaker, followed by heating at 90 °C for 1 h to ensure that the reaction between the ZnCl_2 and EMIC was complete. The resulting ionic liquids were colorless.

2.3. Fabrication of nanoporous gold (NPG) electrode

The NPG electrode was prepared according to the method proposed by Huang et al. [3]. The electrochemical experiments were accomplished with a CHI 660C potentialstat/galvanostat in a glove box filled with dry nitrogen gas or in an electrochemical cell covered with 99.9% argon gas. A three-electrode electrochemical cell was used for the electrochemical experiments. The reference electrode was a zinc wire (Aldrich, 99.99%) immersed in a partitioned fritted glass tube containing pure 50–50% ZnCl_2 –EMIC ionic liquid. A zinc spiral was used as a counter electrode and immersed in a partitioned fritted glass tube containing pure 40–60% ZnCl_2 –EMIC ionic liquid. The polished gold wire electrode was cleaned by immersion in 70% ethanol, rinsed with deionized water (specific resistivity $18.2 \text{ M}\Omega \text{ cm}^{-1}$), and dried before being used as the working electrode. To conduct the selective dissolution of zinc from an Au–Zn alloy, an Au–Zn surface alloy was made by electrodeposition on an Au wire in a 40–60 mol% ZnCl_2 –EMIC ionic liquid at 120 °C. After this, anodic stripping was used to selectively remove the zinc from the as-prepared Au–Zn alloy in the same ionic liquid, leaving an Au wire electrode with a nanoporous structure.

The microstructure of the NPG electrode was observed with a JEOL JSM-6700F field-emission scanning electron microscope (FE-SEM). The resulting NPG electrode was then electrochemically cleaned using a cycling potential between +1.5 V and 0.0 V versus Ag/AgCl in 0.2 M sulfuric acid until reproducible cyclic voltammograms (CVs) were obtained. The surface area of the nanoporous Au electrode was estimated from the integrated reduction current of gold oxide and a conversion factor of $480 \mu\text{C cm}^{-2}$ [21].

2.4. Modification of the Ag UPD adlayer on the NPG electrode

The Ag UPD process was conducted in a 0.1 M H_2SO_4 aqueous solution containing 1.0 mM Ag_2SO_4 . A typical three-electrode electrochemical cell was used for the electrochemical experiments. The

NPG electrode and a gold wire served as the working and counter electrodes, respectively. To prevent Cl^- interference from the typical Ag/AgCl reference electrode, a silver wire served directly as the quasi-reference electrode. The Ag UPD adlayer was modified on the NPG by a potential scan of 0.65–0.2 V. The potential was stopped at 0.2 V for 1 min to allow the Ag UPD to completely cover the whole surface of the NPG electrode. The as-prepared Ag UPD modified NPG electrode (NPG/Ag(UPD)) was rinsed with deionized water before being used for the detection of chloride.

2.5. The NPG/Ag(UPD) electrode used for the detection of chloride

The NPG/Ag(UPD) electrode was employed as the working electrode for the detection of chloride. First, adsorptive accumulation of chloride ions at the NPG/Ag(UPD) electrode was carried out at an open circuit potential by dipping the electrode into a potassium chloride solution for a specified contact time. The electrode was then removed from the cell, washed thoroughly with deionized water, and transferred to a Cl^- free 0.1 M H_2SO_4 aqueous solution containing 1.0 mM Ag_2SO_4 for CV measurement of the Ag UPD. The integrated charge ratio between the two anodic stripping peaks (a_3 at ~ 272 mV/ a'_1 at ~ 612 mV), due to the accumulated Cl^- ions, was used for a quantitative determination of Cl^- . The NPG/Ag(UPD) electrode was electrochemically cleaned in the 0.2 M H_2SO_4 solution to recycle the NPG electrode and re-modify the Ag UPD adlayer before each measurement.

3. Results and discussion

The SEM image of the NPG electrode prepared by the electrochemical formation and selective electrochemical dealloying of $\text{Au}_x\text{Zn}_{1-x}$ alloys in a 40–60 mol% ZnCl_2 –EMIC ionic liquid, as proposed by Huang et al. [3] showed a continuous porous network with a characteristic ligament size of about 20–30 nm. The diameter of each pore was found to be 10–20 nm, similar to that reported in the literature [3], allowing them to be characterized as nanopores. The as-prepared gold electrode was then characterized by electrochemical methods. Fig. 1 shows cyclic voltammograms of the NPG and polished gold electrodes in 0.2 M H_2SO_4 at 200 mV s^{-1} from 1.5 V to 0.0 V (vs. Ag/AgCl). These voltammograms show the current peaks due to the formation of surface gold oxide on the anodic scan and the subsequent gold oxide reduction on the cathodic scan. Because the NPG electrode had a much higher active surface area, it also had a current response approximately 200 times higher than that of the polished gold electrode. The microscopic surface area A_m of the NPG electrode was estimated from the integrated reduction current of the gold oxide and a conversion factor of $480 \mu\text{C cm}^{-2}$ [21]. The roughness factor, which is the ratio of the microscopic surface area A_m and the geometric area A_g of the polished gold electrode, was determined to be 72. This result also provided strong evidence of an ultra-high surface area for the NPG electrode.

Fig. 2 shows a typical cyclic voltammogram of the Ag UPD onto the NPG electrode in the 0.2 M H_2SO_4 solution containing 1.0 mM Ag_2SO_4 . As can be seen in the insert of Fig. 2, no apparent redox waves were observed on a polished polycrystalline gold electrode, whereas two couples of redox waves, c_1/a_1 and c_2/a_2 at ~ 536 mV/552 mV and ~ 320 mV/448 mV, respectively, were obvious at the NPG electrode in Fig. 2. Although Ag UPD on a polycrystalline Au electrode had been reported in the literature [40], the Ag UPD phenomenon on a common polished polycrystalline gold electrode still was not observed in this work. The polycrystalline Au electrode used in the literature was fabricated by vapor depositing a gold thin film on a glass slide in a high vacuum chamber. The surface microstructure of this electrode should be different from

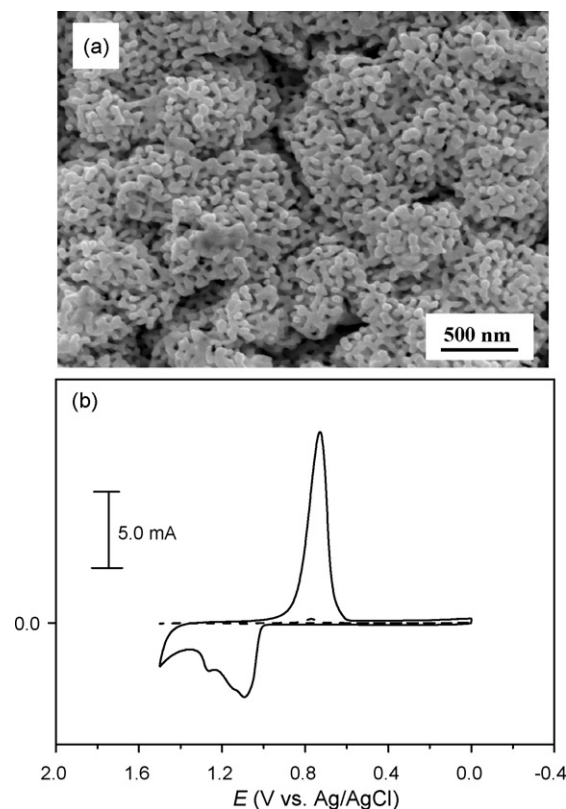


Fig. 1. (a) An SEM image of the NPG electrode. The NPG electrode was obtained by selective anodic stripping of Zn at 1.0 V from gold wire, where the Zn was electrodeposited in a 40–60% ZnCl_2 –EMIC ionic liquid with $Q_c = 0.5 \text{ C cm}^{-2}$ at 120°C ; (b) cyclic voltammograms of the polished gold electrode (dash line) and the NPG electrode (solid line) recorded in a 0.2 M H_2SO_4 solution at 200 mV s^{-1} between 0.0 V and +1.5 V (vs. Ag/AgCl).

the normal polished gold wire used in this work. The difference in the intensity of the Ag UPD signal should be from variations in the surface structure of the substrate because the UPD phenomenon is a surface-constrained electrochemical process and strongly dependent upon the surface structure of the electrode. This also implied that the source of the material used as a probe in a UPD study should significantly effect the observation of the UPD process. The positions of the two couples of redox peaks observed on the NPG

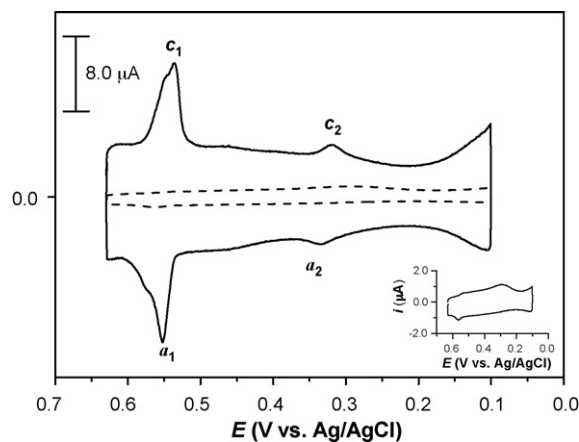


Fig. 2. Cyclic voltammograms of Ag UPD recorded on a polished gold electrode (dash line) and the NPG electrode of Fig. 1a (solid line) in a 0.2 M H_2SO_4 solution containing 1 mM Ag_2SO_4 at 20 mV s^{-1} at 28°C . The insert is the magnification of a CV of Ag UPD on the polished gold electrode.

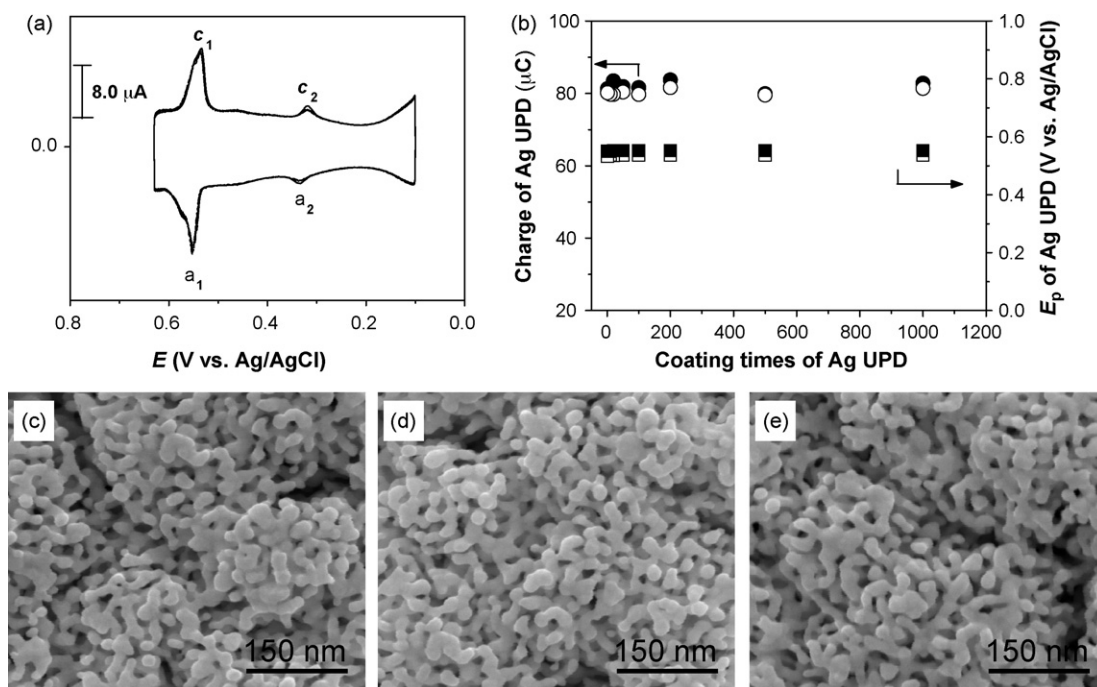


Fig. 3. (a) A multiple-scan CV for the NPG electrode between 0.6 V and 0.1 V at a scan rate of 20 mV/s. (b) The integrated charge, Q , and the peak potential, E_p , of the redox peaks, c_1 (● and ■) and a_1 (○ and □), for the UPD and stripping of Ag recorded as functions of the potential scan cycle. SEM images were obtained for (c) the bare NPG electrode, (d) the NPG/Ag(UPD) electrode and (e) the bare NPG electrode after repeating the Ag UPD modification 1000 times.

electrode in Fig. 2 were similar to those reported by Choi and Laibinis [40]. These peaks were due to Ag UPD and stripping on the NPG electrode. In a comparison of the Ag UPD signals between the polished and NPG electrodes, a high intensity was observed on the NPG electrode because its high surface area provided a high Ag UPD formation capability. The resulting CV also showed that the NPG electrode should be a good candidate for observing the Ag UPD process and that the electrode surface could be easily modified with an Ag UPD thin film using a simple and effective potential scan method.

To study the reproducibility of an NPG electrode modified with an Ag UPD adlayer, a multiple-scan CV was conducted on the NPG electrode between 0.6 V and 0.1 V at a scan rate of 20 mV/s. During this potential scanning, the Ag UPD adlayer could be repeatedly cathodically deposited on and anodically stripped off the NPG electrode. As can be seen, the shapes in the multiple-scan CVs in Fig. 3a are independent of scanning cycles. A linearity between the peak current, i_p , and scan rate, v , was observed but is not shown in this work. These phenomena are consistent with the fact that UPD is a surface-constrained electrochemical process [42]. The integrated charge density for the Ag UPD stripping peak (Q_{a1}/A in which A is the surface area of the electrode) on the NPG surface was $1620 \pm 4 \mu\text{C cm}^{-2}$, which was calculated using the geometric surface area A_g (0.05 cm^2) of the NPG electrode, whereas the

charge density, $22 \pm 2 \mu\text{C cm}^{-2}$, was calculated using the microscopic active surface area A_m (3.61 cm^2) of the NPG electrode. The ultra-high value shown in the first calculated result means the NPG electrode provided a high Ag UPD adlayer formation capacity. The last calculated result was closer to the previously reported value of $20 \pm 2 \mu\text{C cm}^{-2}$, which was found using a polycrystalline Au film fabricated by vapor deposition. This indicated that the high Ag UPD adlayer coverage could be modified on the NPG electrode. Fig. 3b shows the integrated charge, Q , and the peak potential, E_p , of the redox peaks, c_1 and a_1 , for the UPD and stripping of Ag, recorded as functions of the potential scan cycle. It was observed during the potential scan cycle that the integrated charge density and peak potential of the Ag UPD were independent on the cycle of potential scan and that the recovery of the Ag UPD, that is the charge ratio between the UPD and stripping of Ag on the NPG electrode, was close to 100%. This result demonstrated that the microscopic active surface area of the NPG electrode was constant after each Ag UPD modification. It also indicated that the Ag UPD adlayer modification of the NPG electrode was highly reproducible. To further study the surface morphology of the NPG electrode, before and after the modification of the Ag UPD thin film, Fig. 3c–e shows, respectively, representative SEM images obtained for the bare NPG electrode, the Ag UPD coated NPG electrode, and the bare NPG electrode after repeating the Ag UPD modification 1000 times. There was no

Table 1

The rate constant for the adsorption and desorption of Cl^- on the NPG/Ag(UPD) electrode.

Electrode	Rate constant		$\kappa = k_d/k_a (\times 10^{-6} \text{ M})$	Reference
	Adsorption, k_a ($\times 10^2 \text{ L mol}^{-1} \text{ s}^{-1}$)	Desorption, k_d ($\times 10^{-4} \text{ s}^{-1}$)		
NPG/Ag(UPD)	1.1	8.7	7.9 ^a (7.9) ^b	In this work [40]
Au (vapor deposition)/Ag(UPD)	16.0	80.0	4.9 (5.0)	

^a The value of k_a and k_d were estimated from the slope and intercept in the plot of the apparent rates ($k_a C + k_d$) vs. Cl^- concentration.

^b The value was evaluated with Eq. (2).

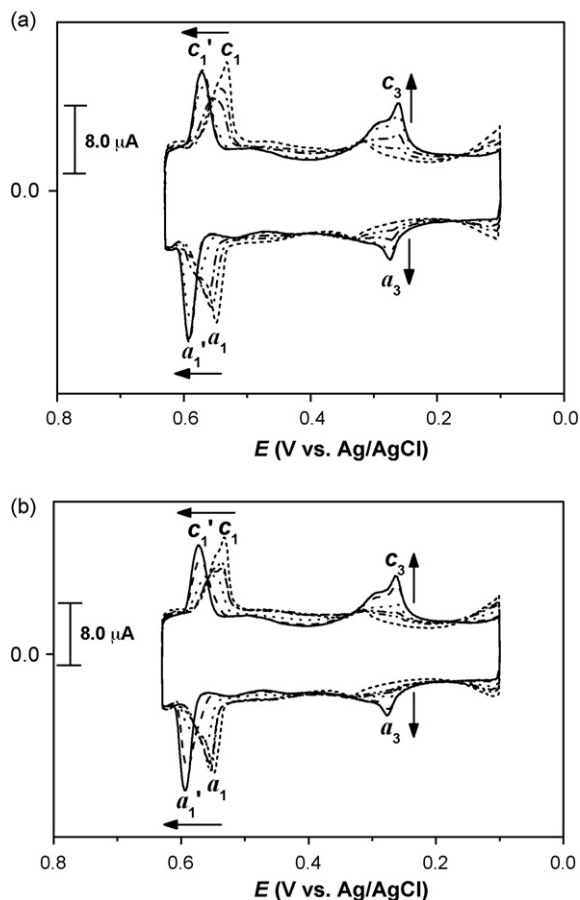


Fig. 4. CVs of Ag UPD and stripping on a NPG/Ag(UPD) electrode that was (a) immersed in a 10.0 μM Cl^- solution at an open circuit potential for various immersion periods, including (short dash) 0.0 min, (dash dot dot) 1.0 min, (dash dot) 3.0 min, (dot) 5.0 min, (dash) 7.0 min, and (solid) 10.0 min, respectively, and (b) immersed in solutions containing various Cl^- concentrations, including (short dash) without the addition of Cl^- , (dash dot dot) 1.0 μM Cl^- , (dash dot) 2.0 μM Cl^- , (dot) 5.0 μM Cl^- , (dash) 10.0 μM Cl^- , and (solid) 20.0 μM Cl^- , respectively, for 1.0 min, recorded in a 0.2 M H_2SO_4 solution containing 1.0 mM Ag_2SO_4 at 20 mV s^{-1} at 28 $^\circ\text{C}$.

significant morphological change, which is indicative of an ultra-thin Ag UPD coating and high reproducibility for the Ag UPD modification of the electrode.

The Cl^- adsorption effect of an Ag UPD ultra-thin film modified single or polycrystalline Au electrode has attracted interest from the chloride-sensing field [39,40]. Our work demonstrated that an NPG/Ag(UPD) electrode simultaneously possesses an ultra-high surface area and the characteristics of the Ag UPD adlayer. It should be a good candidate for a chloride sensing electrode due to its high capacity of Cl^- adsorption from the ultra-high surface area of the NPG electrode. We immersed the NPG/Ag(UPD) electrode into a Cl^- containing solution at an open circuit potential for various immersion periods. After the adsorptive accumulation of chloride ions at the NPG/Ag(UPD) electrode and rinsing it with deionized water, a CV was conducted in a 0.2 M H_2SO_4 solution containing 1.0 mM Ag_2SO_4 . As shown in Fig. 4a, the redox peaks, c_1/a_1 , at 540 mV/550 mV for the UPD and stripping of Ag on the NPG electrode were replaced by a new couple of redox peaks, c'_1/a'_1 , at 605 mV/612 mV, with a gradual positive shift as a function of the immersion period in the Cl^- containing solution. Another new couple of redox peaks, c_3/a_3 , occurred at 262 mV and 272 mV, respectively, and increased with an increase in the exposure period for the NPG/Ag(UPD) electrode in the Cl^- containing solution. Fig. 4b shows the CVs recorded for the NPG/Ag(UPD) electrode immersed in solutions containing various Cl^- concentrations for 1.0 min, after being rinsed with deionized water. The same trend of the peak shift and peak growth of the redox peaks c'_1/a'_1 and c_3/a_3 in Fig. 4a could also be observed during the exposure of the NPG/Ag(UPD) to solutions of increasing Cl^- concentration for a constant immersion period. The assignment of these two new couples of redox peaks, c'_1/a'_1 and c_3/a_3 , was previously reported in the literature [40]. The primary redox peaks, c'_1/a'_1 , were attributed to the average electrochemical state, which indicates a combination of the Cl^- adsorbed NPG/Ag(UPD) sites and the native NPG/Ag(UPD) sites. Although the peak position variation was observed for the Cl^- adsorbed on the NPG/Ag(UPD), the integrated charges of these peaks showed little change through various conditions. For the other couple of redox peaks, c_3/a_3 , generated at 262 mV/272 mV by Cl^- adsorption, their peak intensities gradually increased with Cl^- concentration, but no change in their peak potential could be found. This means the redox peaks, c_3/a_3 , are directly related to the amount of chloride adsorp-

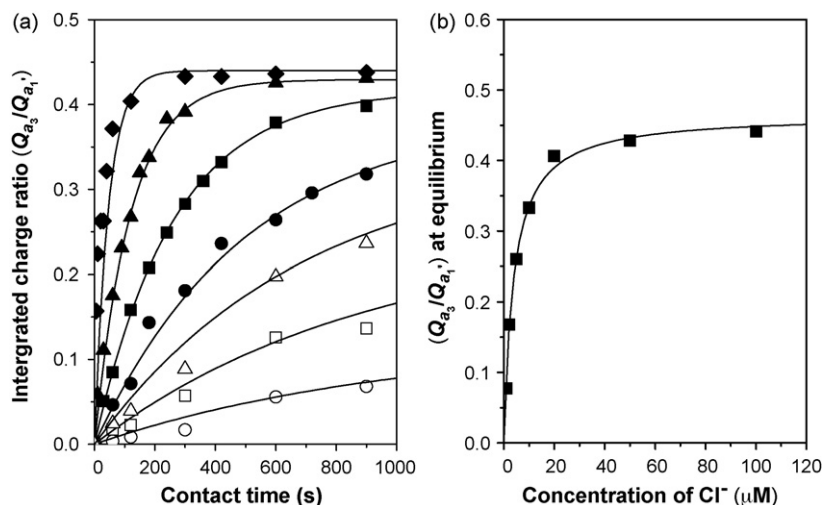


Fig. 5. (a) The ratio of the integrated charges of anodic stripping peaks as a function of the immersion time in a sample containing (\circ) 1.0 μM , (\square) 2.0 μM , (\triangle) 5.0 μM , (\bullet) 10.0 μM , (\blacksquare) 20.0 μM , (\blacktriangle) 50.0 μM and (\blacklozenge) 100.0 μM Cl^- , respectively. Data were fitted with Eq. (1). (b) Equilibrium values of the integrated charge ratio were recorded as a function of Cl^- concentration. Data were fitted with Eq. (2).

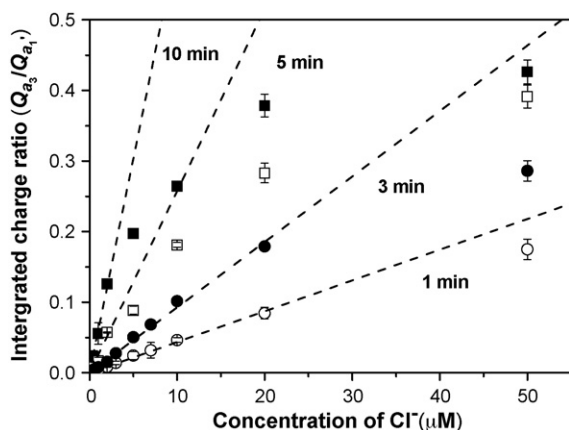


Fig. 6. Calibration plots as the ratio of integrated charges of anodic stripping peaks vs. Cl^- concentration for various immersion periods, including (○) 1.0 min, (●) 3.0 min (□) 5.0 min, and (■) 10.0 min.

tion on the NPG/Ag(UPD) electrode. Since these two couples of redox peaks are related to the Cl^- adsorption, we herein select the anodic stripping peaks, a'_1 and a_3 , as the quantitative signal to determine the amount of Cl^- adsorbed on the NPG/Ag(UPD) electrode. The ratio of the integrated charges of these two anodic stripping peaks, $Q_{a3}/Q_{a'_1}$, is related to Cl^- concentration in the Cl^- containing sample. Fig. 5 shows the ratio of the integrated charges of the anodic stripping peaks, $Q_{a3}/Q_{a'_1}$, as functions of immersion time and Cl^- concentration in the sample. In each Cl^- containing sample, the adsorbed amount of Cl^- generally increased with immersion time, to a limiting plateau where Cl^- adsorption and desorption reached an equilibrium state. At higher concentrations, the measured values of $Q_{a3}/Q_{a'_1}$ reached their equilibrium values much faster than in experiments conducted at lower Cl^- concentrations. With an increase in the Cl^- concentration in the sample, the adsorption rate increased gradually to the maximum plateau. It can be assumed that at the maximum adsorption plateau, the Cl^- adsorption fully covered the NPG/Ag(UPD) electrode. To further study the chloride adsorption/desorption on the NPG/Ag(UPD) electrode, the transient Langmuir adsorption kinetic model was used to study the chloride adsorption kinetics [43]. In this model, the monolayer adsorption can be assumed to be a surface-site filling process in which the adsorption and desorption process compete with each other, and without the effect of mass transport from diffusion. The following equation was used to illustrate the transient Cl^- adsorption:

$$\frac{Q_{a3}}{Q_{a'_1}} = \beta\theta = \beta \frac{k_a}{k_a C + k_d} \{1 - \exp[-(k_a C + k_d)t]\}, \quad (1)$$

where β is a proportional constant that was determined from the maximum value of the integrated charge ratio (0.45), θ is the fractional coverage of the converted sites, C is the concentration of Cl^- , t is the adsorption time, and k_a and k_d are the adsorption and desorption rate constants, respectively. The values of k_a and k_d could be estimated from the slope and intercept in the figure for the apparent rates $(k_a C + k_d)$ versus the Cl^- concentration. A comparison of the adsorption k_a and desorption k_d rate constants in this work with the values reported in the literature is given in Table 1. The slower Cl^- adsorption and desorption rates for the NPG/Ag(UPD) compared to on a smooth polycrystalline Au electrode should be due to the fact that a portion of the active sites for the Cl^- adsorption on the NPG/Ag(UPD) are in the nanopores. It should be more difficult for the Cl^- to adsorb into and escape from these nanopores than from a smooth surface.

Table 2

Interference studies of ions at the NPG/Ag(UPD) electrode in the determination of Cl^- .

Ion	Concentration (μM)	The ratio of integrated charges $Q_{a3}/Q_{a'_1}$	Relative difference from 5.0 μM Cl^-
Cl^-	5	0.050	0.000
SO_4^{2-}	5000	0.050	0.000
NO_3^-	5000	0.053	0.062
PO_4^{3-}	5000	0.048	-0.036
ClO_4^-	5000	0.051	0.022

Fig. 5b shows that the plateau values for $Q_{a3}/Q_{a'_1}$ in Fig. 5a were recorded as a function of Cl^- concentration. It shows the typical Langmuir-like adsorption isotherm. At the plateau values, the Cl^- adsorption and desorption could be assumed to be in a state of equilibrium. Eq. (1) was reduced to give the Langmuir adsorption isotherm ($t \rightarrow \infty$, at equilibrium):

$$\beta \left(\frac{Q_{a3}}{Q_{a'_1}} \right)_{\text{eq}} = \beta\theta_{\text{eq}} = \frac{k_a C}{k_a C + k_d} = \frac{C}{C + \kappa}, \quad (2)$$

where $\kappa = k_d/k_a$. Eq. (2) reasonably describes Fig. 5b. A reciprocal plot of Fig. 5b yielded a value for κ of 7.9×10^{-6} M, as shown in Table 1. This value was consistent with the value estimated from Fig. 5a (7.9×10^{-6} M). The results shown in Fig. 5 indicate that the Cl^- adsorption process on the NPG/Ag(UPD) electrode can be described by the transient Langmuir adsorption kinetic model.

From the discussion above, the NPG/Ag(UPD) electrode has the potential to serve as a new electrode material for chloride detection applications. The fractional chloride coverage estimated from the integrated charge ratio, $Q_{a3}/Q_{a'_1}$, on the electrode was dependent on the Cl^- concentration and contact time in the chloride containing sample. In Fig. 6, the calibration curves for the chloride are shown as the integrated charge ratio, $Q_{a3}/Q_{a'_1}$, against various Cl^- concentrations and immersion periods. We observed a wider dynamic range and lower sensitivity under a shorter contact period than under a longer contact period. In order to reach a proper detection performance, 3 min of contact time was selected

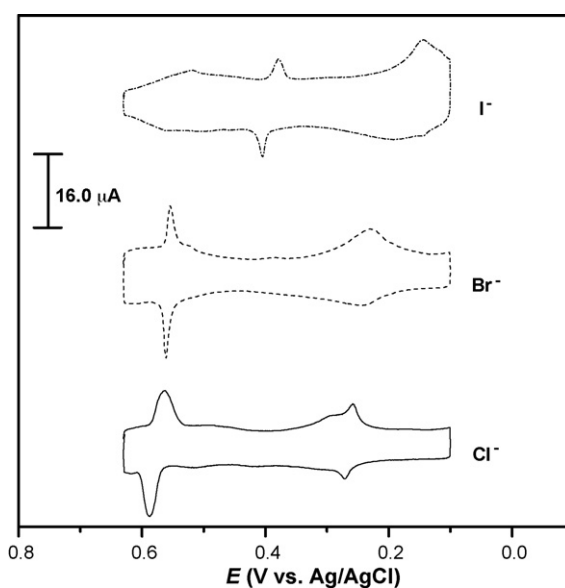


Fig. 7. CVs of Ag UPD and stripping were recorded on the NPG/Ag(UPD) electrode immersed in 20.0 μM : (a) Cl^- (b) Br^- and (c) I^- solutions, respectively, at an open circuit potential for 3.0 min after rinsing with deionized water, taken in a 0.2 M H_2SO_4 solution containing 1 mM Ag_2SO_4 at 20 mV s^{-1} at 28 $^\circ\text{C}$.

as a quantitative standard period. Under this condition, the calibration curve was linear for a Cl^- concentration range of 0.5–30 μM . Compared with most of the results reported in the literature, the detection limit in this work ($<5 \times 10^{-7} \text{ M Cl}^-$) was much lower than ISE-based and optical sensors. Our results were close to those reported by Choi and Laibinis [40], but we used a much simpler and more economical method for preparing the sensing electrode. The long-term storage and operational stability of the electrode in our work were also strongly demonstrated. In the interference study of the NPG/Ag(UPD) electrode against chloride determination, the possible interferents, such as SO_4^{2-} , NO_3^- , PO_4^{3-} , and ClO_4^- were chosen on the basis of their adsorption affinities on the electrode and the frequencies of their occurrence in natural samples. Table 2 shows the integrated charge ratio of 5.0 M Cl^- recorded in the presence of excess amounts of various potential interfering anions. Table 2 shows that the interference from these anions is insignificant. Although it is still difficult to inhibit the interference from other halide ions, Br^- and I^- , during the detection of Cl^- , the distinguishable electrochemical signals for each of these halide ions were obtained in Fig. 7, allowing these ions to be identified directly.

4. Conclusions

In conclusion, a simple yet effective approach to modifying an NPG electrode with an ultra-thin metallic UPD film was presented in this work. A sensitive and selective method for the determination of chloride ions was also described, using the NPG/Ag(UPD) electrode as a sensing probe. While a typical electrodeposition process could easily be used to create a 3D dendritic structure for a metallic modified layer, it is difficult to obtain a microstructure with the desired features. While an atomic scale metal monolayer obtained using the UPD process was selected as the source of the modified layer in our method, the 3D nanostructure of noble metals can still be kept and endowed with the characteristics of the modified UPD metal adlayer. Some of the general advantages of this method include: (1) easy control of the architecture and chemical properties of the NPG electrode after the modification of the metallic UPD adlayer, (2) applicability to a wide variety of UPD systems with metallic properties of interest and (3) potential applicability to other analytical systems, including glucose detection, gas sensing, detection of metal ions, and so forth, or to serve as a new generation of substrates for the development of sensors.

Acknowledgement

This work was supported by the National Science Council of the Republic of China, Taiwan.

References

- [1] M. Michel, A. Taylor, R. Sekol, P. Podsiadlo, P. Ho, N. Kotov, L. Thompson, *Adv. Mater.* 19 (2007) 3859.
- [2] K. Koczkur, Q.F. Yi, A.C. Chen, *Adv. Mater.* 19 (2007) 2648.
- [3] J.F. Huang, I.W. Sun, *Adv. Funct. Mater.* 15 (2005) 989.
- [4] J.F. Huang, I.W. Sun, *Chem. Mater.* 16 (2004) 1829.
- [5] Y.S. Hu, Y.G. Guo, W. Sigle, S. Hore, P. Balaya, J. Maier, *Nat. Mater.* 5 (2006) 713.
- [6] T. Imokawa, K.J. Williams, G. Denuault, *Anal. Chem.* 78 (2006) 265.
- [7] D.V. Pugh, A. Dursun, S.G. Corcoran, *J. Mater. Res.* 18 (2003) 216.
- [8] Y. Ding, M.W. Chen, J. Erlebacher, *J. Am. Chem. Soc.* 126 (2004) 6876.
- [9] R.C. Newman, S.G. Corcoran, J. Erlebacher, M.J. Aziz, K. Sieradzki, *MRS Bull.* 24 (1999) 24.
- [10] A.J. Forty, *Nature* 282 (1979) 597.
- [11] K.R. Seddon, *Nat. Mater.* 2 (2003) 363.
- [12] R.D. Rogers, K.R. Seddon, *Science* 302 (2003) 792.
- [13] M.J. Earle, J. Esperanca, M.A. Gilea, J.N.C. Lopes, L.P.N. Rebelo, J.W. Magee, K.R. Seddon, J.A. Widegren, *Nature* 439 (2006) 831.
- [14] P. Wasserscheid, W. Keim, *Angew. Chem. Int. Edit.* 39 (2000) 3773.
- [15] J.L. Anderson, D.W. Armstrong, G.T. Wei, *Anal. Chem.* 78 (2006) 2892.
- [16] E. Herrero, L.J. Buller, H.D. Abruna, *Chem. Rev.* 101 (2001) 1897.
- [17] L.T. Viyannalage, S. Bliznakov, N. Dimitrov, *Anal. Chem.* 80 (2008) 2042.
- [18] J.W.F. Robertson, D.J. Tiani, J.E. Pemberton, *Langmuir* 23 (2007) 4651.
- [19] O.M. Magnussen, *Chem. Rev.* 102 (2002) 679.
- [20] G.K. Jennings, P.E. Laibinis, *J. Am. Chem. Soc.* 119 (1997) 5208.
- [21] R. Michalitsch, B.J. Palmer, P.E. Laibinis, *Langmuir* 16 (2000) 6533.
- [22] V. Rooryck, F. Reniers, C. Buess-Herman, G.A. Attard, X. Yang, *J. Electroanal. Chem.* 482 (2000) 93.
- [23] C.M. Whelan, M.R. Smyth, C.J. Barnes, G.A. Attard, X.F. Yang, *J. Electroanal. Chem.* 474 (1999) 138.
- [24] K. Ogaki, K. Itaya, *Electrochim. Acta* 40 (1995) 1249.
- [25] J. Bobacka, *Electroanalysis* 18 (2006) 7.
- [26] E. Bakker, Y. Qin, *Anal. Chem.* 78 (2006) 3965.
- [27] J. Bobacka, A. Ivaska, A. Lewenstam, *Chem. Rev.* 108 (2008) 329.
- [28] C. Huber, T. Werner, C. Krause, I. Klimant, O.S. Wolfbeis, *Anal. Chim. Acta* 364 (1998) 143.
- [29] I.H.A. Badr, M. Diaz, M.F. Hawthorne, L.G. Bachas, *Anal. Chem.* 71 (1999) 1371.
- [30] C.D. Geddes, *Sens. Actuator B: Chem.* 72 (2001) 188.
- [31] P. Sjöberg-Eerola, J. Bobacka, T. Sokalski, J. Mieczkowski, A. Ivaska, A. Lewenstam, *Electroanalysis* 16 (2004) 379.
- [32] F. Faridbod, M.R. Ganjali, R. Dinarvand, P. Norouzi, *Sensors* 8 (2008) 2331.
- [33] R. Zielinska, E. Mulik, A. Michalska, S. Achmatowicz, M. Maj-Zurawska, *Anal. Chim. Acta* 451 (2002) 243.
- [34] C. McDonagh, C.S. Burke, B.D. MacCraith, *Chem. Rev.* 108 (2008) 400.
- [35] C. Huber, I. Klimant, C. Krause, O.S. Wolfbeis, *Anal. Chem.* 73 (2001) 2097.
- [36] J.N. Babu, V. Bhalla, M. Kumar, R.K. Mahajan, R.K. Puri, *Tetrahedron Lett.* 49 (2008) 2772.
- [37] S.L.R. Barker, B.A. Thorsrud, R. Kopelman, *Anal. Chem.* 70 (1998) 100.
- [38] P. Langer, R. Muller, S. Drost, T. Werner, *Sens. Actuator B: Chem.* 82 (2002) 1.
- [39] R. Michalitsch, P.E. Laibinis, *Angew. Chem. Int. Edit.* 40 (2001) 941.
- [40] H.G. Choi, P.E. Laibinis, *Anal. Chem.* 76 (2004) 5911.
- [41] J.S. Wilkes, J.A. Levisky, R.A. Wilson, C.L. Hussey, *Inorg. Chem.* 21 (1982) 1263.
- [42] J.F. Huang, I.W. Sun, *J. Electrochem. Soc.* 151 (2004) C8.
- [43] A. Ulman, *An Introduction to Ultrathin Organic Films from Langmuir–Blodgett to Self-Assembly*, Academic Press, New York, 1991.



Phosphotriesterase: A complementary tool for the selective detection of two organophosphate insecticides: Chlorpyrifos and chlorfenvinfos

Georges Istamboulie^a, Didier Fournier^b, Jean-Louis Marty^a, Thierry Noguer^{a,*}

^a Université de Perpignan Via Domitia, IMAGES EA4218, Centre de Phytopharmacie, 52 Avenue Paul Alduy, 66860 Perpignan Cedex, France

^b Institut de Pharmacologie et de Biologie Structurale, UMR CNRS 5089 205, route de Narbonne, 31077 Toulouse Cedex, France

ARTICLE INFO

Article history:

Received 15 July 2008

Received in revised form

26 September 2008

Accepted 29 September 2008

Available online 14 October 2008

Keywords:

Acetylcholinesterase

Phosphotriesterase

Biosensor

Chlorpyrifos

Chlorfenvinfos

ABSTRACT

This work shows the possibility of combining the high sensitivity of genetically-modified *Drosophila melanogaster* acetylcholinesterase (B394) with the ability of phosphotriesterase (PTE) to hydrolyse organophosphate compounds, in the aim of developing a biosensor selective to two insecticides of interest: chlorpyrifos and chlorfenvinfos. The studies clearly demonstrate that chlorfenvinfos is a substrate that acts as competitive inhibitor of PTE, therefore preventing the efficient hydrolysis of other pesticides, including chlorpyrifos. A bi-enzymatic sensor was designed by immobilizing both B394 and PTE in a polyvinylalcohol matrix. The sensor was shown to be able to discriminate between chlorpyrifos and chlorfenvinfos inhibitions.

© 2008 Elsevier B.V. All rights reserved.

1. Introduction

Pesticides are neurotoxic agents widely used for agricultural, industrial, household and warfare purposes. Neurotoxic pesticides mainly act by inhibiting acetylcholinesterase (AChE) [1], an essential enzyme that permits the transmission of electrical signals in the nervous system of most animal beings. Organophosphate (OP) compounds are among the most powerful neurotoxics, they are commonly used as pesticides (insecticides) and chemical warfare agents. Due to their high acute toxicity and risk towards the population, some European directives have been established to limit their presence in water and food resources. For instance, the council directive 98/83/CE concerning the quality of water for human consumption has set a maximum admissible concentration of 0.1 ppb ($\mu\text{g L}^{-1}$) per pesticide and 0.5 ppb for the total amount of pesticides.

Early detection of OP neurotoxins is thus important for protecting water resources and food supplies, but also for defence against terrorist activity, and for monitoring detoxification processes. Accordingly, there are growing demands for field deployable devices for reliable on-site monitoring of OP compounds.

Routine methods are based on extraction, cleanup and analysis normally performed by gas chromatography (GC) or liquid chro-

matography (LC) coupled to sensitive and specific detectors such as nitrogen–phosphorus detectors (NPD) [2–4], flame ionization detectors (FID) [3,4], ultraviolet detectors (UV) or diode array detectors (DAD) [5–7], although recently most methods involve the use of mass spectrometry (MS) as detector to provide ultimate confirmation [8,9]. These methods are highly sensitive and allow the determination of a large number of compounds but they are costly, long and/or complex.

Biosensors have been described for many years as being good candidates as substitutive or complementary tools to these conventional methods, as they can provide real-time qualitative information about the composition of a sample with minimum preparation. Biosensors based on the inhibition of AChE have been widely used for the detection of OP compounds. Among the numerous sensors described, some of them involve the use of recombinant acetylcholinesterases allowing to enhance dramatically the sensitivity of these devices. Such sensors have been recently described in our group for the highly sensitive detection of chlorpyrifos and chlorfenvinfos, two insecticides included since 2001 in a list of priority substances in the field of water policy (decision 2455/2001/EC) [10]. Although these biosensors show a high sensitivity, they often lack of selectivity due to the fact that they react with any cholinesterase inhibitor.

An alternative biosensing route for the detection of these insecticides involves the use of phosphotriesterase (PTE) [11]. This enzyme, also called organophosphate hydrolase (OPH), has the

* Corresponding author. Tel.: +33 4 68 66 22 55; fax: +33 4 68 66 22 23.

E-mail address: noguer@univ-perp.fr (T. Noguer).

ability of hydrolysing ester links of organophosphate compounds, thus liberating the different radicals attached to the phosphate group. Several OPH-based amperometric, potentiometric, or optical biosensors have been already described [12,13]. Recently, Deo et al. [14] have described an amperometric biosensor for organophosphate pesticides based on a carbon nanotube-modified transducer and a PTE biocatalyst. In this sensor, the detection is based on the electrochemical oxidation of *p*-nitrophenol, which is the produced by the PTE-catalysed hydrolysis of the paraoxon or methyl-parathion. However, it must be underlined that only a few insecticides including parathion, methyl-parathion and their oxidation products (paraoxon and paraoxon-methyl) can be detected by this method, as other organophosphate do not generate *p*-nitrophenol upon hydrolysis.

This work presents the development of a biosensor based on the combination of PTE and a highly sensitive recombinant acetylcholinesterase for the selective detection of organophosphate insecticides. In a first step, the activity of PTE towards the main anticholinesterase insecticides was investigated. Then, a bi-enzymatic sensor based on the co-immobilization of AChE and PTE was developed for the detection of chlorpyrifos and chlorfenvinfos.

2. Experimental

2.1. Chemicals and stock solutions

Genetically modified AChE from *Drosophila melanogaster* type B394 and PTE were produced by Protein Bio Sensor (PBS, Toulouse, France). Before immobilisation, enzymatic activities were spectrophotometrically measured using 5,5'-dithiobis(2-nitrobenzoic acid) (DTNB – Ellman's reagent) provided by Sigma. The substrate acetylthiocholine chloride (ATCh) was purchased from Sigma. A 0.1 M ATCh stock solution was daily prepared in water and stored at 4 °C.

The organophosphorus insecticides chlorpyrifos-oxon (phosphoric acid, O,O-diethyl O-(3,5,6-trichloro-2-pyridinyl) ester), chlorpyrifos-oxon-methyl (phosphoric acid, O,O-dimethyl O-(3,5,6-trichloro-2-pyridinyl) ester), dichlorvos (phosphoric acid, O,O-dimethyl O-(2,2'-dichlorovinyl) ester), paraoxon (phosphoric acid, O,O-diethyl O-(4-nitrophenyl) ester), paraoxon-methyl (phosphoric acid, O,O-dimethyl O-(4-nitrophenyl) ester) and chlorfenvinfos (phosphoric acid, 2-chloro-1-(2,4-dichlorophenyl)ethenyl diethyl ester) were purchased from Dr Ehrenstorfer (Augsburg, Germany). Stock solution of pesticides (10^{-3} M) was prepared in acetonitrile and stored at 4 °C.

Azide-unit Pendant Water-soluble Photopolymer (AWP) was provided by Toyo Gosei Kogyo Co. (Chiba, Japan).

The pastes used for screen-printing, i.e. Electrode PE-410, 423SS and 6037SS were obtained from Acheson (Plymouth, UK). Cobalt–phthalocyanine-modified carbon paste was purchased from Gwent Electronic Materials, Ltd. (Gwent, UK). A glycerophthalic paint (Astral, France) was used as insulating layer. Transparent PVC sheets (200 mm × 100 mm × 0.5 mm) were used as printing supports.

2.2. Apparatus

Spectrophotometric measurements were performed using a Hewlett Packard diode array 8451A spectrophotometer. Amperometric measurements were carried out with a 641VA potentiostat (Metrohm, Switzerland), connected to a BD40 (Kipp & Zonen, The Netherlands) flatbed recorder.

Chromatographic determination of pesticides was carried out using a Merck L-6220 HPLC-system fitted with a Supelcosil LC18

reversed phase column (Supelco). The elution solvent used was acetonitrile/water (70:30), at a flow rate of 1 mL/min. The detection of pesticides was performed at 220 nm using a Merck L-4000 UV detector.

Screen-printed electrodes were produced using a semi-automatic DEK 248 printing machine according to a procedure previously described [15], but in a three-electrode configuration. The working electrode was a 4 mm-diameter disk, the auxiliary electrode was a 16 mm × 1.5 mm curved line and the Ag/AgCl pseudo-reference electrode was a 5 mm × 1.5 mm straight line.

2.3. Determination of PTE activity

The activity of PTE was measured using the enzyme in solution, in 10 mM phosphate buffer pH 8, using concentrations of substrate (insecticide) ranging from 10^{-6} M to 10^{-3} M. The activity was measured by two different methods, depending on the substrate used. When using paraoxon derivatives as substrate, the enzyme activity was easily monitored by spectrophotometric measurement of the paranitrophenol produced at 405 nm. Using other substrates (chlorpyrifos-oxon derivatives, dichlorvos, chlorfenvinfos, omethoate and fenamiphos), the activity was measured by HPLC coupled with a UV detector. In that case, the reaction mixture was injected after different reaction times in order to follow the hydrolysis of the pesticide.

2.4. Immobilisation of enzymes

The immobilisation of enzymes was performed by physical entrapment in a polyvinylalcohol-based photopolymer (AWP), as described in previous works [10]. AWP polymer was mixed with enzymatic solution in a ratio 70:30 (v/v). The mixture was vortex-mixed and briefly centrifuged to eliminate the foam. A volume of 3 μ L was then spread onto the working electrode using a micropipette. The concentration of the initial B394 solution was adjusted in order to obtain a final enzyme loading of 1 mU/biosensor. Three types of biosensors were prepared, without PTE or based on the co-immobilization of B394 (1 mU) and PTE in different quantities (0.14 U/biosensor or 0.85 U/biosensor).

The electrodes were exposed to neon light for 3 h at 4 °C to allow the photo-polymerisation between azide groups. After drying for 48 h at 4 °C, the electrodes were ready to use.

2.5. Amperometric measurement principle

Amperometric measurements were performed in stirred solutions using a 5 mL cell. The electrodes were tested in 5 mL of 0.1 M phosphate buffer at a working potential of +100 mV versus Ag/AgCl, which corresponds to the oxidation of thiocholine, the product of the enzymatic hydrolysis of the ATCh substrate in the presence of cobalt–phthalocyanine as electron mediator. The current intensity was recorded and, after current stabilisation, 1 mM ATCh (final concentration in the cell) was injected. The time necessary to reach the plateau was 2–3 min. The measured signal corresponded to the difference of current intensity between the baseline and the plateau. The cell was washed with distilled water between measurements.

The pesticide detection was made in a three-step procedure as follows: first, the initial response of the electrode at the injection of the ATCh (1 mM) was recorded three times, then the electrode was incubated in a solution containing a known concentration of insecticide, and finally the residual response of the electrode was recorded again in the same conditions. The percentage of the inhibition was correlated with the insecticide concentration. The limit of detection was calculated as the insecticide concentration inducing a 10% decrease of the biosensor response.

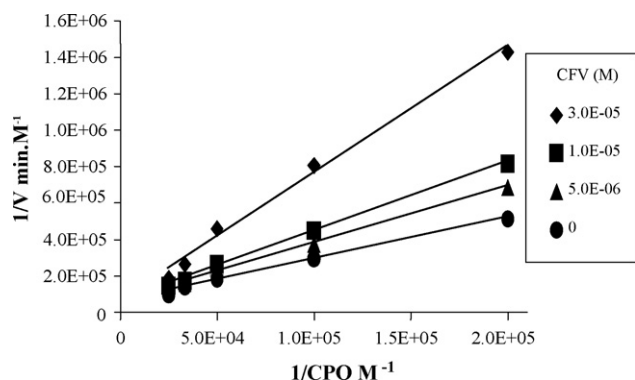


Fig. 1. $1/v$ versus $1/[CPO]$ plot of PTE activity in the presence of different fixed concentrations of CFV (Lineweaver–Burk representation).

3. Results and discussion

3.1. Determination of Michaelis constants (K_m) of PTE enzyme for different organophosphate substrates

The activity of PTE was investigated using eight well-known organophosphate insecticides in order to determine their respective kinetic constants (K_m and V_m). Parathion derivatives (ethyl and methyl) and their oxidation compounds have been widely described as PTE substrates [12,13], mainly due to the easy detection of their hydrolysis product: paranitrophenol. In order to facilitate the comparison between substrates, the maximum velocity was thus expressed throughout this work as paraoxon-ethyl-equivalent activity. The kinetic constants K_m and V_m relative to paraoxon-ethyl were determined spectrophotometrically, their absolute values were 0.25 mM and 14.1 mM min^{-1} , respectively.

The relative values of the kinetic constants obtained for each pesticide are summarized in Table 1.

It clearly appears that PTE has a higher affinity for chlorpyrifos-oxon derivatives than for paraoxon compounds (lower K_m), which are generally used in PTE-based sensors. Both chlorpyrifos-oxon (CPO)-ethyl and chlorfenvinfos (CFV) show a very good affinity for PTE, but even though CFV has a better affinity than CPO, its hydrolysis rate was shown to be 10,000-fold slower than CPO one. Additional “blank” assays without PTE confirmed that CFV was not chemically hydrolysed during the reaction time. The high affinity and the low degradation velocity of CFV indicate that this substrate is likely to act as a competitive inhibitor of PTE for hydrolysis of other organophosphates. Confirmation of this behaviour was obtained by carrying out kinetics of CPO hydrolysis in the presence of different fixed concentrations of CFV. As clearly shown on the Lineweaver–Burk representation ($1/v$ versus $1/[S]$, Fig. 1), an increase of apparent K_m was observed in presence of CFV while no change occurred in the maximum rate (V_m). The replot of $K_{m,app}$ (obtained from Lineweaver–Burk plot) versus the concentration of inhibitor (CFV) allowed us to calculate the competitive inhibition constant (K_i), that was found to be equal to the K_m of PTE for CFV ($K_i = 0.015 \text{ mM} = K_m$) (replot equation: $y = 2.7663x + 4 \times 10^{-5}$). Similar results were obtained using paraoxon as substrate, in that case spectrophotometric measurements allowed to determine a com-

petitive inhibition constant $K_i = 0.017 \text{ mM} = K_m$ (replot equation: $y = 15.8823x + 25 \times 10^{-5}$).

All these features confirmed that CFV acts as a competitive inhibitor of PTE.

3.2. Biosensor characterisation and kinetic study of the immobilised enzyme

The stability of the sensors needs to be evaluated in order to ensure that the decrease in the signal during inhibition measurements is due to enzyme inactivation and not to enzyme leaking. Due to the fact that the developed device is based on a bi-enzymatic system, separate assays must be performed to assess the activity of each enzyme. The operational stability of immobilized B394 acetylcholinesterase was estimated by successively measuring the response of the same enzyme electrode to 1 mM ATCh, at 100 mV versus Ag/AgCl. PTE stability was estimated by measuring the sensor response to 1 mM paraoxon using the same enzyme electrode at 700 mV versus Ag/AgCl. The sensors were washed between tests with distilled water. All three types of sensors were shown to be stable for at least 10 consecutive measurements. The biosensors based on AWP-entrapment presented a good reproducibility, with a signal maximum variation of 5%. The average response to 1 mM ATCh for $n = 5$ electrodes prepared in the same experimental conditions was $290 \pm 15 \text{ nA}$. These reproducibility data refer to the mean value of 10 assays for each electrode.

3.3. Separate detection of CPO and CFV using the bi-enzymatic sensor

3.3.1. Optimization of incubation time

The incubation time of each sensor with various concentrations of pesticides was optimized in order to achieve the highest sensitivity of detection. It was observed that an incubation time of 10 min was sufficient to achieve the maximum inhibition rate whatever the pesticide concentration used. This incubation time was thus applied in further experiments.

3.3.2. Effect of PTE loading on AChE inhibition by CPO and CFV

The inhibition effect of CPO and CFV on sensors incorporating 1 mU of AChE and different amounts of PTE was studied using an incubation time of 10 min. Fig. 2 shows that the inhibitory effect of CPO was decreased when the amount of PTE immobilized on the electrode was increased. In each case, the limit of detection I_{10} , the I_0 , I_{50} , and I_{100} were calculated corresponding to the pesticide concentration inducing 10%, 0%, 50% and 100% inhibition, respectively. These results are summarized in Table 2.

As expected from the determination of the kinetic constants of PTE, the inhibitory effect of CFV was the same whatever the concentration of PTE immobilized on the electrode, this insecticide being not hydrolysed by PTE. Consequently, the responses of a dual-sensor device incorporating B394 and B394 + PTE will be the same if the sample contains only CFV.

A different behaviour was observed when studying CPO determination, due to the rapid hydrolysis of this insecticide by PTE enzyme. For instance, no inhibition was observed for $3 \times 10^{-8} \text{ M}$ CPO using the bi-enzymatic sensor incorporating 0.85 U of PTE,

Table 1

Kinetic constants of PTE enzyme using eight different organophosphate insecticides (substrates). CPO = chlorpyrifos-oxon (ethyl), CFV = chlorfenvinfos.

PTE	CPO-ethyl	CPO-methyl	CFV	Dichlorvos	Paraoxon-methyl	Paraoxon-ethyl	Omethoate and Fenamiphos
K_m (mM)	0.03	0.06	0.017	0.31	1.2	0.25	No hydrolysis
Relative V_m (/paraoxon)	1.8	0.25	0.0002	0.003	0.38	1	

Table 2
Characteristics of the biosensors based on the co-immobilization of B394 acetylcholinesterase (1 mU/sensor) and PTE (0, 0.14 or 0.85 paraoxon-equivalent U/sensor) for the detection of CPO and CFV.

PTE (U/sensor)	Equation	I_0 (M)	I_{10} (M)	I_{50} (M)	I_{100} (M)
CPO					
0	$I = 25.085 \ln(C) + 591.3$	5.8×10^{-11}	8.6×10^{-11}	4.3×10^{-10}	3.0×10^{-9}
0.14	$I = 17.928 \ln(C) + 376.6$	7.5×10^{-10}	1.0×10^{-9}	1.2×10^{-8}	2.0×10^{-7}
0.85	$I = 19.501 \ln(C) + 336.8$	3.2×10^{-8}	5.3×10^{-8}	4.1×10^{-7}	4.1×10^{-6}
CFV					
0 or 0.14 or 0.85	$I = 16.487 \ln(C) + 383.8$	7.7×10^{-11}	1.4×10^{-10}	2.0×10^{-9}	3.3×10^{-8}

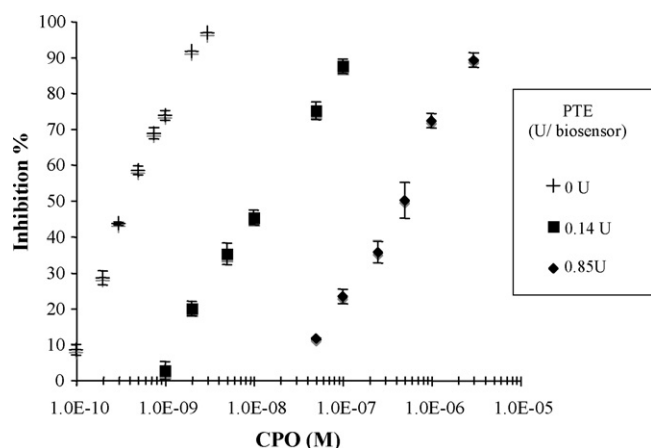


Fig. 2. Detection of CPO using a bi-enzymatic sensor incorporating 1 mU of B394 AChE and different fixed amounts of PTE.

while the same CPO concentration induced a total inhibition of the mono-enzymatic sensor. In such case, PTE can be considered as a discriminating tool allowing the selective detection of CPO and CFV. Globally, the combination of PTE with B394 AChE allowed determining CPO concentrations much higher than those detected using the mono-enzymatic B394-based sensor. For instance, the mono-enzymatic sensor allowed determining CPO concentrations ranging from 3×10^{-9} M to 5.8×10^{-11} M, while the bi-enzymatic sensor incorporating 0.85 U of PTE was usable from 4.1×10^{-6} M to 3.2×10^{-8} M. These features suggest the possibility of developing in the near future sensor arrays incorporating both types of sensors. Due to their complementary working ranges, such devices will allow a dramatic extension of the detectable concentration range, as well as a selective detection of CPO and CFV.

3.4. Effect of mixtures of CPO and CFV on the bi-enzymatic sensor

The bi-enzymatic sensor incorporating 1 mU of B394 AChE and 0.85 U of PTE was used in second step for the assessment of mixtures of CPO and CFV. In Fig. 3 is shown the global inhibition induced by CPO alone or mixed with CFV at concentrations of 7.7×10^{-11} M ($=I_0$), 1.4×10^{-10} M ($=I_{10}$), 5×10^{-10} M ($=I_{30}$) and 2×10^{-9} M ($=I_{50}$). It can be seen that, in the absence of CFV, PTE induced a great decrease of the inhibition rate of B394-based sensor. This feature was due to the hydrolysis of CPO by the PTE enzyme, which was only partial using high concentrations of CPO. When present, CFV induced a competitive inhibition of PTE, which in turn was unable to react with CPO. Consequently, a dramatic increase of the sensor inhibition was observed due to the non-degradation of CPO. For instance, a CPO concentration of 3×10^{-8} M was shown to induce inhibition rates of 0%, 30% and 95% using 0 M, 1.4×10^{-10} M and 2×10^{-9} M

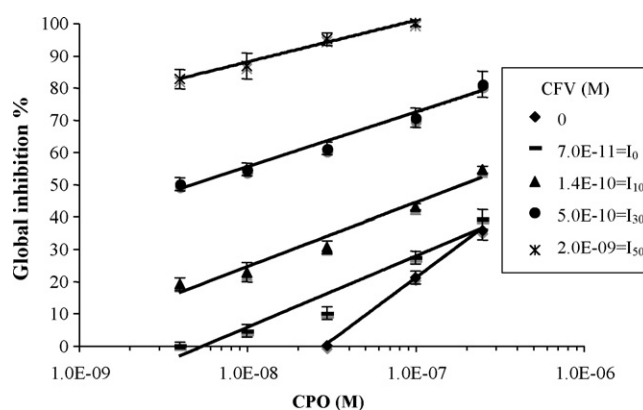


Fig. 3. Effect of CPO and CPO+CFV mixtures on the inhibition rate of a bi-enzymatic sensor incorporating 1 mU of B394 AChE and 0.85 U of PTE. Equations: CFV = 0, $I = 16.877 \ln(C) + 292.6$; CFV = 7.7×10^{-11} M ($=I_0$), $I = 9.587 \ln(C) + 181.4$; CFV = 1.4×10^{-10} M ($=I_{10}$), $I = 8.636 \ln(C) + 186.2$; CFV = 5×10^{-10} M ($=I_{30}$), $I = 7.372 \ln(C) + 190.8$ and CFV = 2×10^{-9} M ($=I_{50}$), $I = 5.622 \ln(C) + 191.1$.

of CFV, respectively. Such effect was observed even using CFV concentrations that do not induce any inhibition of the B394 enzyme (7.7×10^{-11} M).

4. Conclusions

This work shows the possibility of combining the high sensitivity of B394 AChE with the ability of PTE to hydrolyse organophosphate compounds to develop a biosensor selective to chlorpyrifos and chlorfenvinfos. It clearly appeared in this study that chlorfenvinfos binds strongly to PTE but is not hydrolysed by this enzyme. CFV thus acts as a competitive inhibitor of PTE, therefore preventing the efficient hydrolysis of other pesticides. A bi-enzymatic sensor was designed by immobilizing both B394 AChE and PTE in a polyvinylalcohol polymer. The biosensor was used in a first step for the detection of CPO and CFV, and then for the detection of mixtures of these pesticides. In the first case, the sensor was shown to be able to discriminate between the two pesticides, since only CPO is efficiently hydrolysed by the PTE. Using pesticide mixtures, it was shown that due to the competitive inhibition of PTE by CFV, it was difficult to distinguish between inhibitions due to each compound. To become selective, this sensor must be associated with a biosensor incorporating only B394 AChE. Concretely, if both sensors give the same inhibition rate, the inhibition can be attributed to CFV. If an inhibition is observed using B394 and no inhibition occurs with the bi-enzymatic sensor, then the pesticide present is undoubtedly CPO. In between, if the two pesticides are present in the solution, a weaker inhibition is observed using the bi-enzyme sensor, but it is difficult to evaluate the part of each pesticide. In the aim of improving the selectivity of this sensor, future works will focus on the development of sensor arrays involving

different mutant cholinesterases associated or not with PTE. The possible pre-treatment of pesticide mixtures with PTE immobilized on solid-phase columns will be also investigated.

References

- [1] M. Maroni, J. Jarvisalo, F. LaFerla, *Toxicol. Lett.* 33 (1986) 115.
- [2] S. Lacorte, C. Molina, D. Barcelo, *Anal. Chim. Acta* 281 (1993) 71.
- [3] Y. Pico, A.J. Louter, J.J. Vreuls, U.A. Brinkman, *Analyst* 119 (1994) 2025.
- [4] E. Ballesteros, M.J. Parrado, *J. Chromatogr. A* 1029 (2004) 267.
- [5] S. Lacorte, D. Barcelo, *J. Chromatogr. A* 725 (1996) 85.
- [6] J. Norberg, J. Slobodnik, R.J.J. Vreuls, U.A.T. Brinkman, *Anal. Methods Instrum.* 2 (1995) 266.
- [7] V. Pichon, M.C. Hennion, *J. Chromatogr. A* 665 (1994) 269.
- [8] R.B. Geerdink, W.M.A. Niessen, U.A.T. Brinkman, *J. Chromatogr. A* 970 (2002) 65.
- [9] M. Kuster, L.M. De Alda, D. Barcelo, *Mass Spectrom. Rev.* 25 (2006) 900.
- [10] G. Istamboulié, S. Andreescu, J.-L. Marty, T. Noguer, *Biosens. Bioelectron.* 23 (2007) 506.
- [11] A. Mulchandani, W. Chen, P. Mulchandani, J. Wang, K. Rogers, *Biosens. Bioelectron.* 16 (2001) 225.
- [12] A. Mulchandani, P. Mulchandani, W. Chen, J. Wang, L. Chen, *Anal. Chem.* 71 (1999) 2246.
- [13] A. Mulchandani, S. Pan, W. Chen, *Biotechnol. Progr.* 15 (1999) 130.
- [14] R.P. Deo, J. Wang, I. Block, A. Mulchandani, K.A. Joshi, M. Trojanowicz, F. Scholz, W. Chen, Y. Lin, *Anal. Chim. Acta* 530 (2005) 185.
- [15] S. Andreescu, L. Barthelmebs, J.-L. Marty, *Anal. Chim. Acta* 464 (2002) 171.



Improved design for high resolution electrospray ionization ion mobility spectrometry

M.T. Jafari*

Department of Chemistry, Isfahan University of Technology, Isfahan 84156-83111, Iran

ARTICLE INFO

Article history:

Received 3 August 2008

Received in revised form

17 September 2008

Accepted 29 September 2008

Available online 17 October 2008

Keywords:

High resolution

Electrospray ionization

Ion mobility spectrometry

ABSTRACT

An improved design for high resolution electrospray ionization ion mobility spectrometry (ESI-IMS) was developed by making some salient modifications to the IMS cell and its performance was investigated. To enhance desolvation of electrospray droplets at high sample flow rates in this new design, volume of the desolvation region was decreased by reducing its diameter and the entrance position of the desolvation gas was shifted to the end of the desolvation region (near the ion gate). In addition, the ESI source (both needle and counter electrode) was positioned outside of the heating oven of the IMS. This modification made it possible to use the instrument at higher temperatures, and preventing needle clogging in the electrospray process. The ion mobility spectra of different chemical compounds were obtained. The resolving power and resolution of the instrument were increased by about 15–30% relative to previous design. In this work, the baseline separation of the two adjacent ion peaks of morphine and those of codeine was achieved for the first time with resolutions of 1.5 and 1.3, respectively. These four ion peaks were well separated from each other using carbon dioxide (CO₂) rather than nitrogen as the drift gas. Finally, the analytical parameters obtained for ethion, metalaxyl, and tributylamine indicated the high performance of the instrument for quantitative analysis.

© 2008 Elsevier B.V. All rights reserved.

1. Introduction

Ion mobility spectrometry (IMS) was developed for detection and characterization of chemical compounds such as illicit drugs, explosives, pharmaceuticals, environmental pollutants [1]. This technique has been recently used in high-throughput proteomics studies [2–4]. IMS technique can distinguish between compounds on the basis of differences in their reduced mass, charge, and collisional cross section under a weak electric field. Therefore, IMS enables resolution of closely related ionic species. It has also shown to be a valuable structural tool for determining gas-phase ion conformations [5,6].

Ionization source is one important part of an ion mobility spectrometer which produces ions at ambient pressure. Electrospray ionization (ESI), as an ionization source for IMS, converts sample molecules from liquid to gas phase ions. This nonradioactive ionization source has become attractive as a method for IMS determination of biomolecules [7–9]. This method may also be used for detection of inorganic compounds such as uranyl acetate in water [10]. The main advantages of ESI are possibility of direct introduction of liquid samples into IMS, retaining of molecular weight

information due to the soft ionization processes, and formation of multiply charged ions in some instances [1]. A lot of liquid-phase separation techniques have been developed using mass spectrometry (MS) as detector. However, using a mass spectrometer as a detection system in separation techniques has some important problems such as complexity of the instrument and high price. In contrast, IMS has less complex instrumentation, high throughput, ease of operation, and low cost as a detector for liquid chromatography [11,12]. Hence, application of ESI-IMS was demonstrated as a detection method for liquid chromatography [13–16], capillary electrophoresis [17], and flow injection analysis [18]. The main limitation of ESI-IMS is, however, its low resolution which can be attributed to several points. First, a relatively large volume of sample is typically introduced for trace analysis. Solvent evaporation from the electrosprayed fine droplets in the drift region can, therefore, cause broadening of the analyte bands [19,20]. Second, heat transfer from the atmospheric gas to the sprayed droplets is low, and desolvation cannot be completed effectively before the droplets enter the drift region. Third, the electrical potential of the ESI source perturbs the homogeneity of the electric field in the drift region [21,22].

Electrospray ionization was first introduced as an ionization source for IMS in 1972 by Dole and co-workers [23]. They concluded that due to inefficient desolvation of the electrosprayed droplets, ESI would not find the same applicability in IMS as it does in MS, in

* Tel.: +98 311 391 2351; fax: +98 311 391 2350.

E-mail address: jafari@cc.iut.ac.ir.

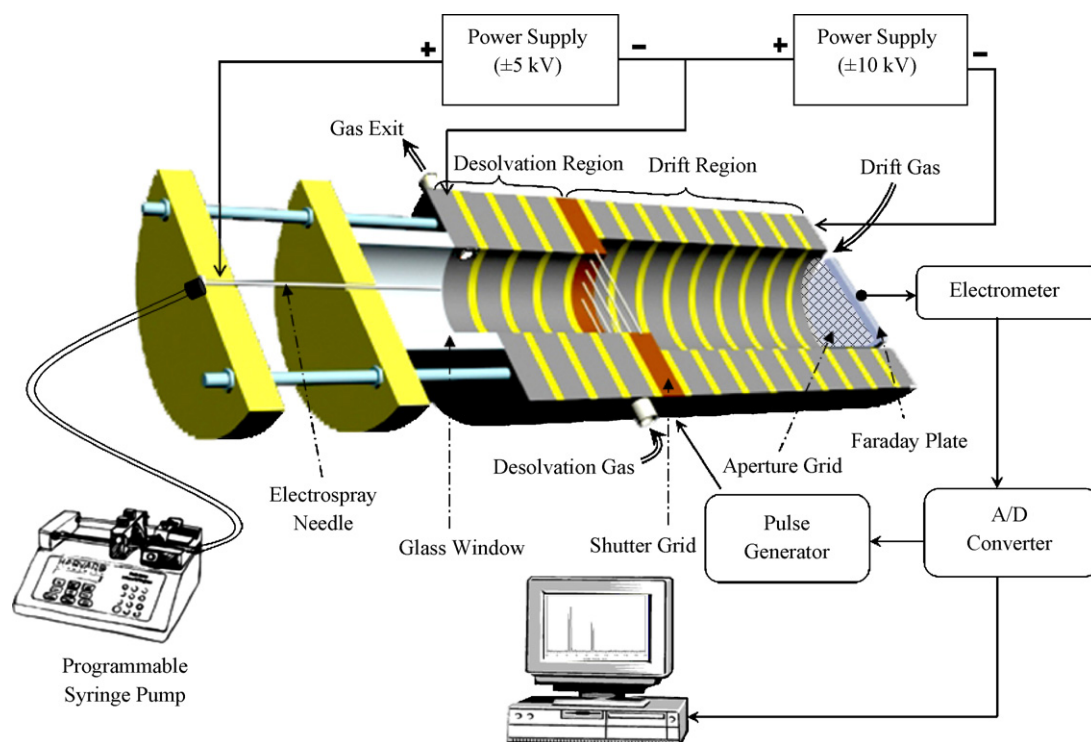


Fig. 1. The schematic diagram of the electrospray ionization-ion mobility spectrometer apparatus with improved design. The diameter of desolvation region was decreased to about half of the drift region diameter and the desolvation gas was entered into the cell at the end of the desolvation region.

which solvent can be readily evaporated under vacuum condition. Later, instrumental improvements such as adding a counterflow of a dry gas and a water-cooled electrospray ion source, suggested by Hill and co-workers, enhanced the desolvation efficiency and prevented needle clogging [19,24–27]. According to the equation derived by Siems et al. [22] for calculation of ion pulse duration measured at half of maximal intensity, lowering the drift tube temperature is an effective way to increase the resolving power of an ion mobility spectrometer. On the other hand, higher temperature of the countercurrent drift gas is necessary for efficient desolvation of the analyte ions.

In addition to the drift gas we recently [28] constructed an ESI-IMS with a preheated dry gas named “Desolvation Gas”. Flowing the desolvation gas through the desolvation region of the IMS cell increased solvent evaporation and resulted in decreasing the drift time and increasing the resolving power. In that design, the electrospray needle was located outside of the cell oven. The consequence was to prevent prespray solvent evaporation problems inside the needle and therefore, needle clogging did not occur during the operation up to 130 °C.

Following these instrumental studies, this paper demonstrates further improvements in the design. In this new design, more efficient desolvation could be achieved by reducing the volume of the desolvation chamber in addition to proper entrance for desolvation gas. These modifications in the proposed design enable the use of higher flow rates at elevated temperature, preventing problems in the electrospray process.

2. Experimental

2.1. Ion mobility spectrometer

The electrospray ionization ion mobility spectrometer used in this research was designed and constructed at Isfahan University of Technology, Isfahan. The schematic diagram of the spectrom-

eter is shown in Fig. 1. The key components of the system included the IMS cell, power supply and pulse generator devices, and signal processing program. The ESI-IMS cell was divided into three different sections named ESI source region, desolvation region, and drift region. This cell was constructed out of our previous design [28], but a number of modifications were made to further increase the operation performance of the instrument. These modifications included: (a) decreasing the volume of the desolvation region by reducing the inside diameter of this region, (b) moving the entrance position of the desolvation gas to the end of the desolvation region, and (c) locating the ESI source (including needle and counter electrode) completely outside of the heating oven.

In this work, the glass cell of the system was substituted with aluminum rings (as conducting rings), which were separated from each other by thin PTFE rings (as insulating rings) of 2 mm thickness. The drift and desolvation conducting rings have the dimensions of 60 mm (o.d.) × 40 mm (i.d.) × 10 mm (width), and 60 mm (o.d.) × 21 mm (i.d.) × 10 mm (width), respectively. The lengths of the drift and desolvation regions are 11 and 5 cm, respectively, but they can be easily shortened or lengthened by removing or adding a number of rings. Electrical contact between conducting rings of drift and desolvation regions was accomplished by using a series of 5.6 MΩ resistors. This configuration provided a uniform electric field inside the drift tube. A high voltage power supply (±10 kV, non-isolated) provided adequate voltage through a voltage divider for the entrance and exit of the desolvation and drift regions. An oven with a sufficient volume (22 L, 12 Bahman Co., Iran) was used to warm up the IMS cell as well as the drift and desolvation gases before entering the cell. The temperature of the heating oven can be chosen from 25 to 200 °C (±0.01). Pure nitrogen was employed as the drift and the desolvation gases with flow rates of 500 and 900 mL min⁻¹, respectively [28]. In order to remove water vapor or other contaminations, the gas was filtered with a 13× molecular sieves (Fluka) trap before entering the IMS cell. As shown in Fig. 1, the entrance tube of the desolvation gas

Table 1
Typical operating conditions during the experimental runs.

Operating parameters	Setting
Needle voltage (kV)	11.40
Target electrode voltage (kV)	9.00
Liquid flow rate ($\mu\text{L min}^{-1}$)	10
Drift field (V cm^{-1})	600
Desolvation field (V cm^{-1})	600
Drift gas flow (N_2) (mL min^{-1})	500
Desolvation gas flow (N_2) (mL min^{-1})	900
Drift tube length (cm)	11
Shutter grid pulse (ms)	0.3
Number of IMS averages	50
Scan time (ms)	20
Number of points per ion mobility spectrum	500

was oriented $\sim 45^\circ$ with respect to the drift tube axis to achieve the same direction as that of the drift gas. This figure also shows that the exhaust tube of the IMS cell is located on the first ring of the desolvation region (target electrode) to exit the warm gas before it reaches the needle tip.

Ion gating was achieved with a Bradbury–Nielsen gate [29] ring (21 mm i.d.) located at the end of the desolvation tube and the entrance of the drift tube. The Bradbury–Nielsen gate was made of electrically isolated alternating parallel alloy 26 wires (50 μm in diameter) with 0.75 mm spacing. The ion gate timing was set manually using a custom-built pulsing electronic device. The logic signals required by the pulsing electronics were generated through a personal computer equipped with an arbitrary waveform generator board. When the potentials applied on the alternating wires were the same as the reference potential, the gate was “open” to allow ions to pass through, whereas when the potentials on the adjacent wires were offset (85 V with respect to the reference potential) an electric field ($\sim 2200 \text{ V cm}^{-1}$) was created orthogonal to the drift field of the spectrometer, and the gate was “closed” to shut off ion transmission. An aperture grid ring, made of an electrical joint between the last drift ring and a wire screen (stainless steel), was located at the end of the drift tube. The function of the aperture grid was to shield the incoming ion cloud from the detector prior to its arrival and hence reduce peak broadening.

The default Faraday plate detector configuration consisted of a stainless steel Plate 21 mm in diameter, positioned ~ 1.0 mm behind the aperture grid. The Faraday plate detector was connected to a home-made current to voltage (A/V) amplifier with a gain of 10^9 V/A . The signal can be amplified, up to 1000 times, using a tunable-gain amplifier. The high-speed A/D module (12-bit dynamic range) was used to measure the spectrometer output and to convert the analog signal to a digital one. All mobility data were collected by data acquisition software and each IMS spectrum was the average of 50 individual spectra. Table 1 summarizes the operating conditions under which the IMS spectra were taken.

2.2. ESI ionization source

In this design, the ESI ionization region, comprising the electrospray needle and counter electrode was located completely outside the heating oven. A small glass-tube (15 cm length and 21 mm i.d.) was used as a window for observing the needle tip by illuminating it with a small diode laser. The glass window was sealed with the aluminum target electrode. A cap for the glass-tube was fabricated by machining a PTFE piece (40-mm o.d. \times 10-mm thick) with a central hole 0.8 mm in diameter. This metal-glass-Teflon seal outside the oven serves as a joint for the varying temperature between the desolvation and ionization regions of the instrument. This modification allowed us to use the instrument without the need for a cooling system for the ESI needle, even at 200°C . This tempera-

ture is the limit of our heating oven. In addition, the glass window allows the operator to observe the needle tip and to optimize the experimental conditions for producing a plume formation and a stable electrospray. A commercially available 26s-gauge polished needle (P/N 7768-01, Hamilton, Reno, NV, U.S.A.) with 0.13 mm i.d., 0.46 mm o.d., and a length of approximately 51 mm was used as the electrospray needle. The position of the ESI needle was adjusted such that its tip was located about 7 mm from the target electrode. A relatively large tip aperture was chosen in this research because it allowed liquid to be delivered through the emitter at a relatively wide range of flow rates. Normally, the flow rate varied from 1 to $40 \mu\text{L min}^{-1}$. The solution was delivered from the same syringe (1.0 mL Hamilton gastight syringe, Reno, NV, U.S.A.) for the entire set of the experiments, to ensure consistency throughout. Sample solution was delivered to the electrospray ion source by a programmable syringe pump (New Era Pump System Inc., U.S.A.). A second high-voltage power supply ($\pm 5 \text{ kV}$, isolated) provided independent voltage control for the ESI ion source up to 15 kV. The electrical contact was applied through a stainless steel zerodead-volume union that connected the emitter with the PTFE capillary transfer line (2.0-mm o.d. \times 0.2-mm i.d., ~ 15 cm long). The corona discharge problem was eliminated by insulating the spray needle with a Teflon tubing [26,28]. The high-voltage power supply and pulse generator devices were prepared from Radyabchem. Co., Isfahan Science & Technology Town. Although the mixture of methanol, water, and acetic acid are commonly used for ESI-IMS, in this work, for better comparison of the results with those of the old instrument, pure methanol was used as the electrospray solvent. Electrospray ionization was normally induced by applying a potential difference of 2.0–3.0 kV between the electrospray needle and the target electrode, which also served as the first ring electrode for the desolvation region. In this work, an electrospray voltage of 11.4 kV (2.4 kV versus the desolvation chamber entrance) was used, and the electrospray flow rate was maintained at $10 \mu\text{L min}^{-1}$ for all experiments unless otherwise mentioned.

2.3. Chemicals and solutions

Methanol used as the electrospray solvent was high performance liquid chromatography (HPLC) grade and was purchased from Merck (Germany). The drug standards of morphine sulfate and codeine phosphate were prepared from Temad Co. (Tehran), and the methadone with concentration of 5 mg mL^{-1} was purchased from Darou pakhsh Co. (Tehran). Pesticides including ethion, Malathion, fenamifos, and metalaxyl were prepared from Accu-standard, Inc. (U.S.A.). All the amines and furfurals used in this work were purchased from Merck. Unless specified, samples were prepared at a concentration of 1.0 mg L^{-1} for obtaining the IMS spectra. Stock standard solutions of $100 \mu\text{g mL}^{-1}$ ethion, metalaxyl, and tributylamine were prepared in methanol. Working solutions (0.01 – $20 \mu\text{g mL}^{-1}$) were prepared by successive dilution of the stock solutions.

3. Results and discussion

3.1. Desolvation efficiency

To investigate the extent of desolvation process with the proposed design, ESI-IMS spectra of some chemicals such as drugs, pesticides, and some amines and furfurals were obtained and the reduced mobility values (K_0) of produced ions were calculated. Comparison of K_0 values obtained through electrospray ionization and the conventional ^{63}Ni can be used as an extent of the desolvation efficiency of sprayed droplets [24]. The ion mobility spectra of

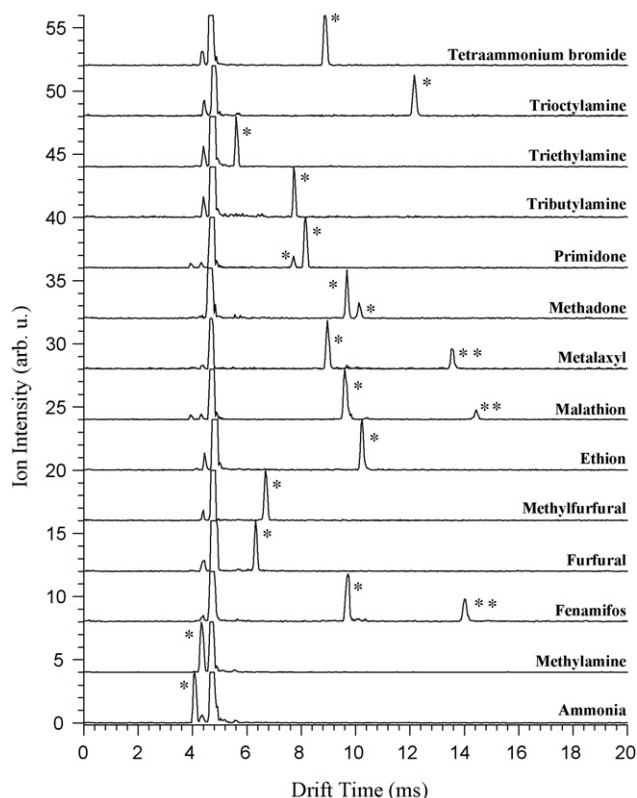


Fig. 2. The ion mobility spectra of the some compounds obtained at the optimum conditions of operating (Table 1). *Constituent ion peak of the compound. **Dimer ion formation.

various classes of compounds obtained in the optimized conditions are shown in Figs. 2 and 4.

Viidanoja et al. [30] suggested that tetraalkylammonium halides are ideal as mobility standards for ESI-IMS because these compounds generate only a single ion mobility peak in addition to their low tendency for clustering. In this work, tetrabutylammonium bromide was used as an external standard for the instrument. The absolute reduced mobility of this compound was calculated to be $1.26 \text{ cm}^2 \text{ V}^{-1} \text{ s}^{-1}$, which is close to $1.33 \text{ cm}^2 \text{ V}^{-1} \text{ s}^{-1}$, reported by Viidanoja et al. [30]. The K_0 value of this compound has not been reported using ^{63}Ni -IMS, presumably due to dissociation in the IMS cell. The reduced mobility values of all the compounds with unknown mobility were determined relative to this value according to Eq. (1).

$$\frac{K_0(\text{unknown})}{K_0(\text{standard})} = \frac{t_d(\text{standard})}{t_d(\text{unknown})} \quad (1)$$

In this equation, t_d is the drift time of the produced ion. The reduced mobility values of the produced ions for all the compounds studied in this work are listed in Table 2. In addition, the reduced mobility values of the compounds that are reported in the literatures using ^{63}Ni and electropray are also tabulated in Table 2.

The reduced mobility values of some of these compounds such as furfural, methylfurfural, methadone and primidone are reported for the first time. As shown in Table 2, most K_0 values compared well with those obtained by ESI-IMS reports as well as with those obtained using ^{63}Ni -IMS. The exceptions were those of low molecular weight (ammonia and methylamine), which appeared in the region of the background solvent peaks. These compounds produce smaller ions than those of others under electrospray process. Based on the previous study conducted by Kobarle and Tang [31], solvation energy will increase when the size of the sprayed ion decreases. As a result, the desolvation process of the smaller ions produced by ammonia and methylamine can be more difficult than that of

Table 2

Reduced mobility values (K_0) and literature K_0 values for several compounds employed in this study.

Compound	Class	Drift Time (ms), ± 0.04	K_0 ($\text{cm}^2 \text{ V}^{-1} \text{ s}^{-1}$)	Lit. K_0 ($\text{cm}^2 \text{ V}^{-1} \text{ s}^{-1}$)	
				(ESI)	(^{63}Ni) ^a
Ammonia	Industrial	4.08	2.74	2.25 [28]	3.02 [24]
Methylamine	Industrial	4.32	2.59	2.21 [28]	2.65 [24]
Triethylamine	Industrial	5.84	1.92	1.84 [28]	1.95 [24]
Tributylamine	Industrial	7.94	1.41	1.35 [28]	1.38 [24]
Trioctylamine	Industrial	12.16	0.92		
Tetrabutylammonium bromide	Industrial	8.88	1.26	1.33 [30]	
Furfural	Industrial	6.32	1.77		
Methylfurfural	Industrial	6.68	1.67		
Ethion	Pesticide	10.24	1.09	1.06 [28]	1.20 [37]
Malathion	Pesticide	9.60	1.17	1.11 [28]	1.30 [37]
		14.44 ^b	0.77	0.76 [28]	
Metalaxyl	Pesticide	9.08	1.23	1.15 [28]	1.37 [38]
		13.60 ^b	0.82	0.77 [28]	
Fenamifos	Pesticide	9.72	1.15	1.08 [28]	
		14.04 ^b	0.80	0.76 [28]	
Methadone	Drug	9.68	1.16		
		10.12	1.11		
Primidone	Drug	7.72	1.45		
		8.16	1.37		
Morphine	Drug	8.96	1.25	1.19 [28]	1.26 [33]
		9.32	1.20	1.15 [28]	1.22 [33]
Codeine	Drug	9.28	1.21	1.14 [28]	1.21 [33]
		9.56	1.17	1.10 [28]	1.18 [33]

^a The reference values were obtained with air as the drift gas.

^b The peak is might be due to the dimer ion formation.

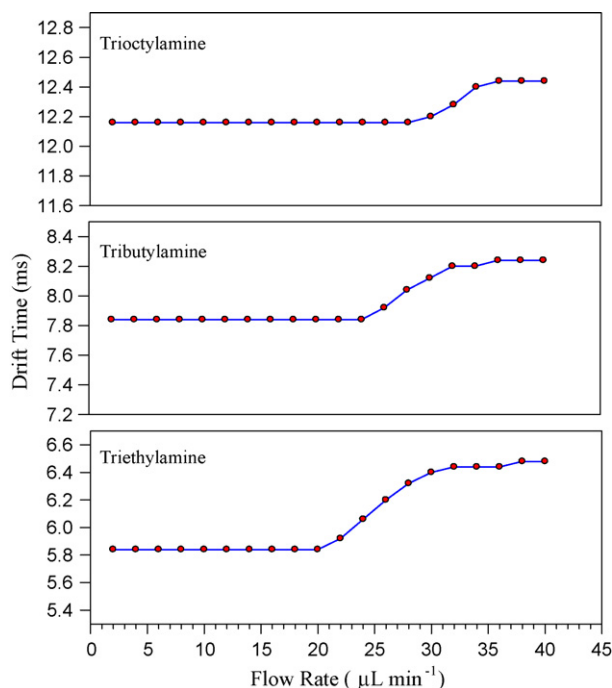


Fig. 3. The drift time of the peak of three compounds (triethylamine, tributylamine, and trioctylamine) was plotted versus flow rate of the sample solutions. The drift time values were constant at flow rates lower than 20, 22, and 30 $\mu\text{L min}^{-1}$ for triethylamine, tributylamine, and trioctylamine, respectively.

larger ions. On the other hand, Hill et al. [24] have reported that the reduced mobility values for ammonia and methylamine determined by ESI-IMS are lower than those obtained by ^{63}Ni -IMS, and suggested that this is the consequence of inadequate desolvation of the analyte ions. Therefore, greater K_0 values obtained for ammonia and methylamine in this work with respect to those obtained through the previous instrument [28] might be due to more efficient desolvation of the compounds used in this work. Decreasing the volume of the desolvation chamber of the instrument to about half of the previous one increased the velocity of the drift gas exiting the drift chamber. This enhances the solvent evaporation of the electrosprayed droplets in the desolvation chamber. Although this geometry has been well known for the reaction region of the ^{63}Ni -IMS cell, it was investigated in ESI-IMS for the first time. In addition, in our old instrument, the desolvation gas was introduced to the cell in middle of the desolvation chamber, whereas in the new design, the gas enters the cell at the end of the desolvation region (near the shutter grid). This modification allows more effective solvent evaporation of the sprayed droplets by the desolvation gas. As Table 2 shows, the reduced mobility values reported in this study are much closer to those obtained by ^{63}Ni -IMS and therefore, it can be assumed that complete desolvation occurred by using proposed design for ESI-IMS.

To further survey the desolvation efficiency of the instrument, the individual IMS spectra of three amine compounds including triethylamine (TEA), tributylamine (TBA), and trioctylamine (TOA) at different flow rates were compared. The drift time of the peak of these compounds were plotted versus flow rate of the solution (Fig. 3). As this figure shows, the t_d values were constant at flow rates lower than 20, 22, and 30 $\mu\text{L min}^{-1}$ for TEA, TBA, and TOA, respectively. At higher flow rates, the ion clusters possess more solvent molecules and the resulting large species are more difficult to desolvate, leading to slower mobility. Therefore, the ion cluster peaks shifted to a lower mobility and their drift time increased. Observation of different flow rates (20, 22, and 30 $\mu\text{L min}^{-1}$) might

Table 3

Comparison of resolving power obtained in this work with that of the previous instrument [28].

Compound	Resolving power, R_p	
	Proposed design	Previous instrument
Ethion	52.6 ± 0.4	41.0
Malathion	51.3 ± 0.8	40.7
Metalaxyl	68.4 ± 0.8	59.7
Tributylamine	45.2 ± 0.5	34.5
Triethylamine	62.3 ± 0.6	
Furfural	70.4 ± 0.7	
Methy-furfural	61.8 ± 0.6	

be due to different sizes of the sample molecules in the order of $\text{TEA} < \text{TBA} < \text{TOA}$. In summary, these results indicate that the complete solvent evaporation could be occurred even at fairly high flow rates, and consequently, would be helpful it to interface to HPLC columns.

3.2. Resolving power and resolution

In order to have an elementary understanding of the separation characteristics of the instrument, resolving power values for different compounds were measured and compared to the previously reported ones. Resolving power in IMS is defined as the drift time, t_d , of an ion divided by the peak width at half height, $w_{1/2}$ [22].

$$R_p = \frac{t_d}{w_{1/2}} \quad (2)$$

The measured resolving powers of the ion mobility spectrometer for some of the test compounds are summarized in Table 3. The resolving power for the studied compounds is quite striking and entirely typical of what was observed with this apparatus. As seen in Table 3, the resolving power values obtained in this work are increased by about 15–30% compared to those obtained with our old instrument [28].

As described in the previous section, this new design speeds up the solvent evaporation process in the desolvation region before the ions are injected into the drift region. This enhances the evaporation of further solvent molecules from the clusters to produce ion clusters with the lower numbers of solvent molecules, producing a narrower peak and consequently a higher resolving power. The resolving power values obtained in this work can be compared with the range of 65–95, reported by Collins and Lee [32], where they used a 27 cm drift tube length and a 200 μs pulse width.

In order to find out the effect of each modification (smaller diameter of the desolvation region and positioning of the desolvation gas) on desolvation efficiency, it is required to do more experiments. In this regard, the resolving power of the ethion and malathion were re-calculated by instrument without the modification of desolvation gas position. The resolving power of ethion and malathion were obtained 49.8 and 49.1, respectively. These data show about 21% increase in resolving power values with respect to our old instrument, and consequently, it seems that the factor of decreasing the diameter of desolvation rings has more effect on improvement of the resolving power of the instrument.

To further investigate the power of the instrument for practical separation of the closely spaced peaks, ion mobility spectra of morphine and codeine were obtained and compared with those obtained previously [28] (Fig. 4). According to Fig. 4, these drugs produce two adjacent ion peaks, M_1 and M_2 for morphine and C_1 and C_2 for codeine.

According to Table 2, the ion clusters are comparable with those obtained by Lawrence [33]. This figure clearly indicates that, in the new instrument, the two peaks are completely baseline resolved for

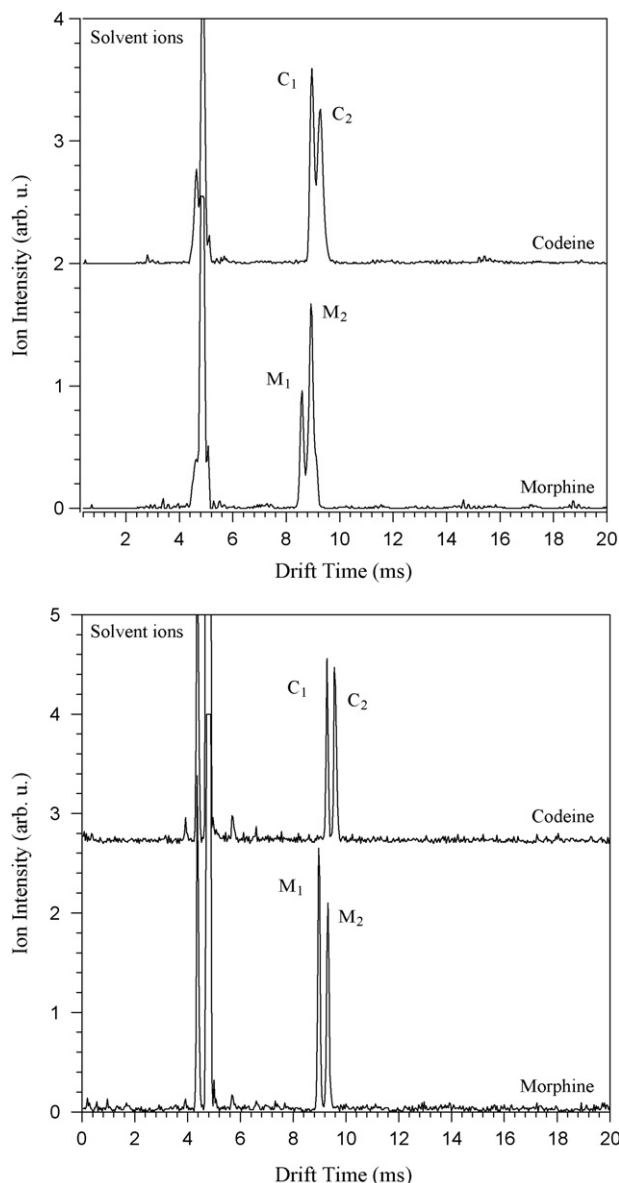


Fig. 4. Comparison of the ion mobility spectra of morphine and codeine obtained in this work (bottom) with those obtained by previous instrument [28] (top). It is clearly indicated that in the new instrument the two peaks are completely baseline resolved for each drug compound.

each drug compound, while this was not the case for the old apparatus. The peak-to-peak resolution, R_{pp} , was calculated for morphine and codeine ion clusters, based on Eq. (3).

$$R_{pp} = \frac{2\Delta t_d}{w_{b1} + w_{b2}} \quad (3)$$

where Δt_d is the difference between drift times of the two adjacent peaks and the w_{b1} and w_{b2} , are their corresponding peak widths. The resolution values were 1.5 and 1.3 for morphine and codeine compounds, respectively. However, the drift time of the M_2 (9.32 ms) and C_1 (9.28 ms) are the same and therefore, each drug interferes with the other one in the analysis of real samples. Since the analysis of these two compounds is very important in biological matrices, full separation of their IMS signals was attempted in this work. Changing the drift gas can drastically improve the separability in ion mobility spectrometry [15,34]. Therefore, the ion mobility spectra of morphine and codeine using nitrogen or carbon dioxide

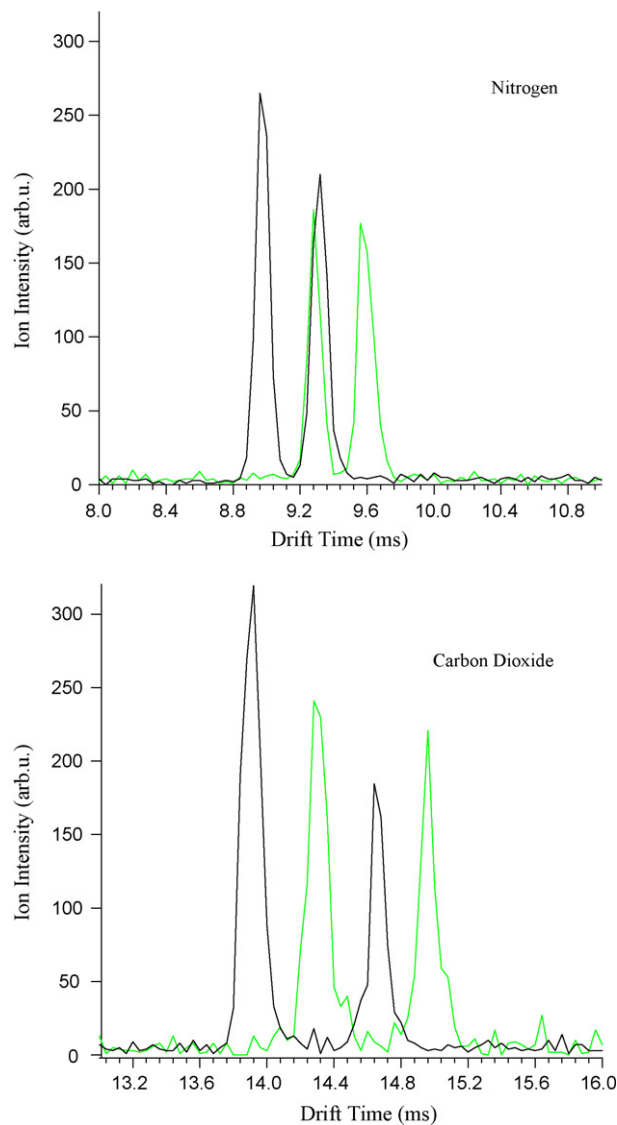


Fig. 5. Overplot of ion mobility spectra of morphine and codeine with N_2 and CO_2 as drift gases. The spectra demonstrate that the use of CO_2 can separate two peaks of morphine from those of the codeine.

as the drift gas were obtained (Fig. 5). According to Fig. 5, M_2 and C_1 peaks were indistinguishable in nitrogen while they were easily separated in carbon dioxide. In this work, two adjusted ion peaks of morphine (M_1 and M_2) were completely separated from those of codeine (C_1 and C_2) for the first time. Consequently, it can be possible to determine these drugs in presence of each other.

3.3. Electrospray ionization efficiency

As described in Section 3.1, complete desolvation can be obtained with present instrument at higher flow rates than that of the previous instrument. It was expected that the intensity of the IMS signal would increase at higher flow rates. But different results were observed, especially at high analyte concentrations. In this regard, we thoroughly investigated the variation of the peak intensity at a wide range of flow rate (from 1 to 40 $\mu L \min^{-1}$). Fig. 6 shows plots of peak intensities extracted from IMS spectra for different concentrations of tributylamine as a function of flow rate.

These plots show three regions including an uphill, plateau, and downhill for all concentrations. When the plots start to plateau, it

Table 4
Analytical parameters for ethion, metalaxyl, and tributylamine using ESI-IMS.

Parameter	Ethion	Metalaxyl	Tributylamine
Calibration curve formula	$Y = 0.01 + 5.63X$	$Y = 0.09 + 2.98X$	$Y = 0.04 + 9.02X$
Linear Range ($\mu\text{g mL}^{-1}$)	0.05–2.20	0.10–1.80	0.02–1.20
Correlation Coefficient, R^2	0.9986	0.9968	0.9970
Detection Limit ($\mu\text{g L}^{-1}$)	16	38	6
Relative Standard Deviation, RSD (%) for $0.4 \mu\text{g mL}^{-1}$ and $n = 5$	6.4	8.1	7.3

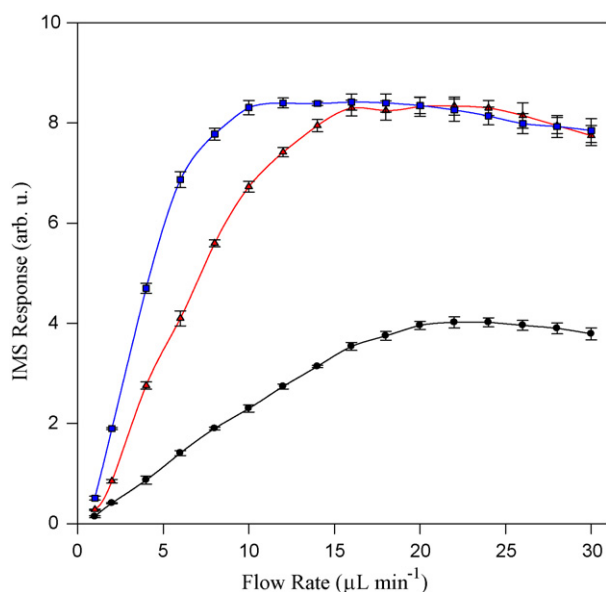


Fig. 6. Plots of IMS response versus flow rate for tributylamine at different concentrations of 0.1 (●), 0.5 (▲), and $1.0 \mu\text{g mL}^{-1}$ (■) included three regions of uphill, plateau, and downhill.

indicates that the total number of ions detected at the Faraday plate has reached maximum and when the plots start to decline, it is clear that total ions produced by electrospray process have decreased. Fig. 6 also shows that when the sample concentration increases, the plateau and downhill regions are shifted to lower flow rates. To interpret these results, we considered the number of ions detected by the Faraday plate (n), as derived by Hill and co-workers [35]:

$$n = n' \text{DE\%} = c f t_g N_{\text{avg}} \text{DE\%} \quad (4)$$

where n' is the total number of analyte molecules introduced to electrospray region and DE% is the detection efficiency percentage. n is dependent on the concentration of analyte (c , in molar), flow rate (f , in L s^{-1}), and shutter grid pulse (t_g , in second). N_{avg} is the Avogadro's number. On the other hand, according to Hill's report [35], the detection efficiency (DE%) is dependent on ionization efficiency (IE%) and ion transmission (TE%) as:

$$\text{DE\%} = \text{IE\%} \times \text{TE\%} \quad (5)$$

The ion transmission (TE%) can be assumed 100% in ESI-IMS due to the large entrance so that it is possible to receive total ion plume produced by the electrospray. In addition, it is clear that in the electrospray process, the ionization efficiency (IE%) increased when the flow rate decreased [35]. Increasing the flow rate at low region, increases the number of ions detected (n), resulting in enhanced peak intensity. In this case n' is a dominant term in Eq. (4) and the plots in Fig. 6 are in uphill region. At the plateau region, when the flow rate further increases, n also increases while the ionization efficiency further decreases, and therefore, the peak intensity remains approximately constant. If the flow rate further increases

after plateau region, ionization efficiency becomes the dominating factor and ion response will eventually decrease.

3.4. Analytical parameters

In this work, a series of standards in the range 0.01 – $20 \mu\text{g mL}^{-1}$ of ethion, metalaxyl, and tributylamine were prepared in methanol and used to determine the analytical parameters of the instrument. When a stable electrospray was achieved, the area of the ion peak produced from IMS system was calculated and considered as the response of ESI-IMS for each concentration of the individual compounds. Ten ion mobility spectra were acquired to obtain the averaged data points. The areas under ion peak(s) were plotted against concentration of these compounds and calibration curve equations were developed by least-squares method. The analytical parameters of the proposed ESI-IMS method for the determination of these compounds are summarized in Table 4.

As this table shows, the linearity range for ethion, metalaxyl, and tributylamine is 0.05 – 2.20 , 0.10 – 1.80 , and 0.02 – $1.20 \mu\text{g mL}^{-1}$, respectively. The data show the linear dynamic range of about 2 orders of magnitude, which is typical for ESI sources and for most IMS systems [36]. Using the standard definition of $S/N = 3$, the detection limits of 16 , 38 , and $6 \mu\text{g L}^{-1}$ were determined for ethion, metalaxyl, and tributylamine, respectively. The detection limits obtained in this work are in the range 10 – $1340 \mu\text{g L}^{-1}$, as reported by Asbury et al. for various compounds [36]. The correlation coefficients were greater than 0.99 for all the compounds. These results compare favorably to the other techniques such as ^{63}Ni -IMS [37,38]. The quantitative results obtained in this work are promising for further development of this method as an analytical tool for the detection of various compounds in liquid samples.

4. Conclusions

An improved design for ESI-IMS cell was introduced and its performance was investigated. In this design, the diameter of desolvation region was decreased and the desolvation gas entered the cell at the end of this region. The consequence of these changes was to increase the desolvation efficiency at higher flow rates and therefore, the resolving power or resolution of the apparatus was enhanced. A resolving power of about 70 could be achieved by only 11 cm drift tube length and $300 \mu\text{s}$ pulse width. It was shown that the baseline separation of two adjacent ion peaks of morphine and codeine could be achieved with resolutions of 1.5 and 1.3, respectively. In this work, thorough investigation of the drift time as well as the IMS signal for ion clusters was studied at a wide range of the sample flow rates. Additionally, the electrospray ionization occurred outside the cell oven, enabling us to use the instrument without needle clogging and disturbance of the electrospray process even at a temperature as high as 200°C . Finally, the calibration curves for determination of ethion, metalaxyl, and tributylamine were obtained, and the analytical parameters revealed capability of the instrument for quantitative analysis.

Acknowledgements

The author is very grateful to the Research Council of Isfahan University of Technology for financial support of this work. Dr. Rezaei and Dr. Khayamian are also specially acknowledged for their valuable helping and discussions. Sincerely thank to Prof. Amini (Isfahan University) and Prof. Amirnasr for their review of the text.

References

- [1] G.A. Eiceman, Z. Karpas, *Ion Mobility Spectrometry*, 2nd ed., CRC Press, Boca Raton, FL, 2005.
- [2] S.J. Valentine, M.D. Plasencia, X. Liu, M. Krishnan, S. Naylor, H.R. Udseth, R.D. Smith, D.E. Clemmer, *J. Proteome Res.* 5 (2006) 2977.
- [3] J.A. Taraszka, X. Gao, S.J. Valentine, R.A. Sowell, S.L. Koeniger, D.F. Miller, T.C. Kaufman, D.E. Clemmer, *J. Proteome Res.* 4 (2005) 1238.
- [4] S. Myung, J.M. Wiseman, S.J. Valentine, T. Zoltán, R.G. Cooks, D.E. Clemmer, *J. Phys. Chem. B* 110 (2006) 5045.
- [5] F.W. Karasek, *Res. Dev.* 21 (1970) 34.
- [6] F.W. Karasek, W.D. Kilpatrick, M.J. Cohen, *Anal. Chem.* 43 (1971) 1441.
- [7] C.S. Hoaglund, S.J. Valentine, C.R. Spurlender, J.P. Reilly, D.E. Clemmer, *Anal. Chem.* 70 (1998) 2236.
- [8] D.E. Clemmer, M.F. Jarrold, *J. Mass Spectrom.* 32 (1997) 577.
- [9] L.W. Beegle, I. Kanik, L. Matz, H.H. Hill, *Anal. Chem.* 73 (2001) 3028.
- [10] H.M. Dion, L.K. Ackerman, H.H. Hill, *Talanta* 57 (2002) 1161.
- [11] A.B. Kanu, H.H. Hill, *Talanta* 73 (2007) 692.
- [12] A.B. Kanu, H.H. Hill, *J. Chromatogr. A* 1177 (2008) 12.
- [13] D.G. McMinin, J.A. Kinzer, C.B. Shumate, W.F. Siems, H.H. Hill, *J. Microcol. Sep.* 2 (1990) 188.
- [14] Y.H. Chen, H.H. Hill, D.P. Wittmer, *J. Microcol. Sep.* 6 (1994) 515.
- [15] G.R. Asbury, H.H. Hill, *J. Microcol. Sep.* 12 (2000) 172.
- [16] L.M. Matz, H.M. Dion, H.H. Hill, *J. Chromatogr. A* 946 (2002) 59.
- [17] R.W. Hallen, C.B. Shumate, W.F. Siems, T. Tsuda, H.H. Hill, *J. Chromatogr.* 480 (1989) 233.
- [18] M. McCooye, L. Ding, G.J. Gardner, C.A. Fraser, J. Lam, R.E. Sturgeon, Z. Mester, *Anal. Chem.* 75 (2003) 2538.
- [19] C.B. Shumate, H.H. Hill, *Anal. Chem.* 61 (1989) 601.
- [20] C. Shumate, *Trends Anal. Chem.* 13 (1994) 104.
- [21] M. Tam, H.H. Hill, *Anal. Chem.* 76 (2004) 2741.
- [22] W.F. Siems, C. Wu, E.E. Tarver, H.H. Hill, P.R. Larsen, D.G. McMinin, *Anal. Chem.* 66 (1994) 4195.
- [23] M.L. Gieniec, J. Cox Jr., D. Teer, M. Dole, 20th Annual Conference on Mass Spectrometry and Allied Topics, Dallas, TX, June 4–9, 1972.
- [24] D. Wittmer, Y.H. Chen, B.K. Luckenbill, H.H. Hill, *Anal. Chem.* 66 (1994) 2348.
- [25] G.R. Asbury, H.H. Hill, *Int. J. Ion Mobility Spectrom.* 2 (1999) 1–8.
- [26] Y.H. Chen, H.H. Hill Jr., D.P. Wittmer, *Int. J. Mass Spectrom. Ion Proc.* 154 (1996) 1.
- [27] D.S. Lee, C. Wu, H.H. Hill Jr., *J. Chromatogr. A* 822 (1998) 1.
- [28] T. Khayamian, M.T. Jafari, *Anal. Chem.* 79 (2007) 3199.
- [29] N.E. Bradbury, R.A. Nielsen, *Phys. Rev.* 49 (1936) 388.
- [30] J. Viidanoja, A. Sysoev, A. Adamov, T. Kotiaho, *Rapid Commun. Mass Spectrom.* 19 (2005) 3051.
- [31] P. Kebarle, L. Tang, *Anal. Chem.* 65 (1993), 972 A.
- [32] D.C. Collins, M.L. Lee, *Fresenius J. Anal. Chem.* 369 (2001) 225.
- [33] A.H. Lawrence, *Anal. Chem.* 58 (1986) 1269.
- [34] L.M. Matz, H.H. Hill, L.W. Beegle, I. Kanik, *J. Am. Soc. Mass Spectrom.* 13 (2002) 300.
- [35] X. Tang, J.E. Bruce, H.H. Hill, *Anal. Chem.* 78 (2006) 7751.
- [36] G.R. Asbury, C. Wu, W.F. Siems, H.H. Hill, *Anal. Chim. Acta* 404 (2000) 273.
- [37] M.T. Jafari, *Talanta* 69 (2006) 1054.
- [38] M.T. Jafari, M. Azimi, *Anal. Lett.* 39 (2006) 2061.



Infrared study of aging of edible oils by oxidative spectroscopic index and MCR-ALS chemometric method

Y. Le Dréau^{a,*}, N. Dupuy^a, J. Artaud^a, D. Ollivier^b, J. Kister^a

^a Université Aix-Marseille, UMR CNRS 6263, ISM², AD²EM, Laboratoire Systèmes Chimiques Complexes, case 451, 13397 Marseille Cedex 20, France

^b Laboratoire de Marseille, Direction Générale de la Concurrence, de la Consommation et de la Répression des Fraudes, 146 traverse Charles-Susini, 13388 Marseille Cedex 13, France

ARTICLE INFO

Article history:

Received 24 June 2008

Received in revised form

30 September 2008

Accepted 6 October 2008

Available online 17 October 2008

Keywords:

Infrared spectroscopy

Edible oils

Aging

Oxidation

Spectroscopic index

PCA

MCR-ALS

ABSTRACT

One of the most suitable analytical techniques used for edible oil quality control is Fourier transform mid infrared spectroscopy (FT-MIR). FT-MIR spectroscopy was used to continuously characterize the aging of various edible oils thanks to a specific aging cell. There were differences in the spectra of fresh and aged oils from different vegetable sources, which provide the basis of a method to classify them according to the oxidative spectroscopic index value. The use of chemometric treatment such as multivariate curve resolution-alternative least square (MCR-ALS) made it possible to extract the spectra of main formed and degraded species. The concentration profiles gave interesting information about the ability of the various oils to support the oxidative treatment and showed that all oils present the same aging process. Both methods led to concordant results in terms of induction times determined by the oxidative spectroscopic index and the appearance of oxidation products revealed by MCR-ALS.

© 2008 Elsevier B.V. All rights reserved.

1. Introduction

Edible oils are mainly constituted by triacylglycerols which are glycerol molecules with three long chain fatty acids attached at the hydroxy groups via ester linkages. Oxidation of lipids as triacylglycerols is an undesirable chemical change that may impact flavour, aroma, nutritional quality of oils with significant implication on human disease and product value. For example, the presence of substantial amount of isolated *trans*-fatty acids has become suspected to arteriosclerosis and heart diseases [1]. Therefore, it is becoming imperative to be able to check the evolution of oils quality which can be altered by oxidation processes induced by oxygen presence and especially accelerated by heating for edible oils. The major compounds produced during vegetable oil oxidation are hydroperoxides, aldehydes, alcohols, acids. . . The oxidation processes are generally considered to occur in three phases: an initiation or induction phase, a propagation phase, and a termination phase. The products of each of these phases will increase and decrease over time making it difficult to quantitatively measure lipid oxidation. A variety of tests have been developed for oil oxidation study. These tests

measure some products of oxidation. Peroxides and hydroperoxides are determined by iodometric titration [2]. Gas chromatography and gas chromatography–mass spectrometry are commonly used to quantify saturated and unsaturated aldehydes or volatile compounds [3]. Non-volatile compounds formed during the oxidation of vegetable oils can be analyzed by liquid chromatography [4]. Depletion of oxygen [5] or substrates has also been determined [6]. These tests give detailed information on oxidation process but are not useful by themselves for predicting oil stability and are very time-consuming by opposition with FT-MIR spectroscopy known as very helpful way to study lipid degradation under oxidative conditions [7–14]. The determination of *trans*-fatty acids [15–17], the study of free fatty acids [18,19] as well as the quality control [20–25] by FT-MIR have been also widely reported. For most of these works, ageing monitoring have been realised in discontinuous way.

In this paper, the development, by FT-MIR, of simple, continuous and rapid method for monitoring oxidation of various edible oils (i.e. to develop a tool to determine their oxidative stability and to compare them) is exposed. It is based on the used of a specific aging cell allowing the characterization oils proceed from various vegetable origins under thermal oxidation stress. In this work, FT-MIR spectra of seven edible oils during thermal oxidation have been collected. Two interpretation ways have been chosen to determine chemical changes in oils during the degradation process and to estimate oil stability.

* Corresponding author. Tel.: +33 4 91 28 27 62; fax: +33 4 91 28 91 52.

E-mail addresses: yldreau@yahoo.com, yveline.le-dreau@univ-cezanne.fr (Y. Le Dréau).

The first one leads to define a new oxidative spectroscopic index based on a reduced spectral range where the modifications have been noticed (from 3050 to 2750 cm^{-1}). The graphic representation of this index allows comparing the behavior of various edible oils.

The second way is based on the use of chemometric treatments of the whole spectra (from 4000 to 400 cm^{-1}) to extract underlying information. Principal component analysis (PCA) has been used as a pre-processing method to obtain a global view of the oil evolution after a thermal oxidation. The interpretation of PCA loadings has permitted to highlight the chemical functions implicated in the oxidative process. SIMPLISMA method associated with multivariate curve resolution-alternative least square (MCR-ALS) has been used to identify more precisely the chemical species produced or degraded during the thermal treatment and to track their evolution. This mathematical method allowed to obtain pure spectra of different species present in oil without prior information of their existence. MCR method based on a number of algorithms [26,27] of which alternative least square (ALS) is actually the widely used for the simultaneous elucidation of spectral and concentration profiles. The interest of this tool is to supply relative quantitative information which traduce the temporal evolution of the relative abundance of the different products during the thermal aging. Results obtained by these two ways have been compared to estimate their concordance.

2. Experimental

2.1. Oil samples

Commercial refined oil samples (peanut oil, rapeseed oils (virgin and refined), walnut oil, grapeseed oil, soybean oil and sunflower oil) were obtained from the Direction Générale de la Concurrence, de la Consommation et de la Répression des Fraudes (DGCCRF) laboratory, Marseille, France.

2.2. Fatty acid determination

Fatty acid compositions (Table 1) of each oil sample before ageing were determined by gas chromatography (GC) of their fatty acid methyl esters as the European standard reference [28]: Oil in *n*-heptane (0.1 g/2 ml) was transmethylated with a cold solution of KOH (2 M) and analyses of obtained fatty acid methyl esters (FAME) were performed on a Perkin–Elmer Autosystem 9000 gas chromatograph (GC) equipped with a split/split-less injector ($t = 250^\circ\text{C}$) and flame ionisation detector (FID) ($t = 250^\circ\text{C}$). A silica capillary column (60 m \times 0.25 mm i.d., 0.25 μm film thickness) coated with DBWAX (polyethylene glycol, JW) was used. The inlet pressure of the hydrogen as carrier gas was 154 kPa with a ratio: 70. The oven temperature program was as follows: 13 min at 200°C , from 200 to 230°C at 6°C min^{-1} , 17 min at 230°C .

Table 1
Fatty acid compositions of oils.

Oils	SAFA%	MUFA%	DUFA%	TUFA%	PUFA%
Walnut	9.5	18.6	57.9	14	71.9
Refined rapeseed	5.7	69.7	15.8	8.8	24.6
Sunflower	11.3	25.3	63.3	0.1	63.4
Grapeseed	10.5	15.4	73.6	0.5	74.1
Virgin rapeseed	7.2	63.7	20.2	8.9	29.1
Soybean	15.2	23.3	53.4	8.1	61.5
Peanut	18.4	61.4	20.1	0.1	20.2

SAFA, saturated fatty acid; MUFA, mono-unsaturated fatty acid; DUFA, di-unsaturated fatty acid; TUFA, tri-unsaturated fatty acid; PUFA, poly-unsaturated fatty acid (= DUFA + TUFA).

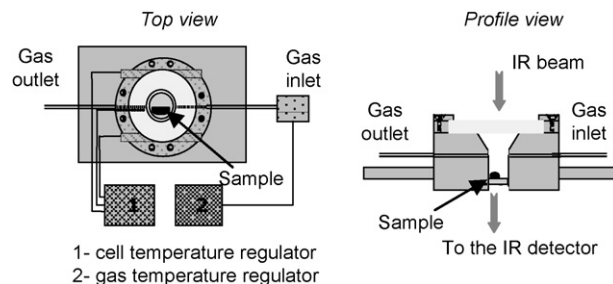


Fig. 1. Principle scheme of the aging cell.

2.3. Infrared spectroscopy

FT-MIR spectra were performed on a Nicolet Protégé 460 spectrometer coupled with a Nicolet Nic-Plan infrared microscope which was fitted with a mercury cadmium tellurium (MCT) detector cooled with liquid nitrogen. The standard analytical conditions were $\times 15$ infrared objective, beam size of $100\ \mu\text{m} \times 100\ \mu\text{m}$. The spectra were acquired using Omnic Nicolet software 5.2. 64 scans of symmetrical interferograms were averaged and the spectrum was calculated from 4000 to $650\ \text{cm}^{-1}$ at $8\ \text{cm}^{-1}$ spectral resolution.

2.4. Ageing test procedure

The ageing test was conducted thanks to an ageing cell developed in our laboratory to study oxidation of petroleum by products [29,30]. So, a continuous oxidation of edible oils (fluid material) was studied by FT-MIR spectroscopy with a vertical IR beam generated by a coupled FT-MIR microscope. The ageing cell (Fig. 1) consisted of a metallic body heated by two heating cartridges connected to a regulator (WATLOW 988), itself connected to a temperature probe fitted in the centre of the cell. A heated gas flow was flushed through the cell. The gas heating block was connected to a second regulator WATLOW 988. The system was equipped with a by-pass to select the gas. Analyses could be performed either under oxidant gas (Synthetic air (80% N_2 , 20% O_2) Air liquide, 99% purity, $50\ \text{ml min}^{-1}$) or under neutral gas (argon, Air liquide, 99% purity, $50\ \text{ml min}^{-1}$), allowing the thermal effect to be distinguished from the oxidative effect during simulated ageing. A NaCl window (13 mm \times 1 mm) supporting the sample (deposited on one half of the window) is fitted at the bottom of the cell. A removable upper NaCl window (32 mm \times 2 mm) is fixed by screws during analysis. The cell was fixed on a Teflon stand itself fitted in the motorized stage of the microscope, so that its movement is not affected.

0.5 mg of oil were placed on the NaCl window in the ageing cell (that correspond to a $10\ \mu\text{m}$ thickness film) and heated from 25°C up to 130°C under argon at $11^\circ\text{C min}^{-1}$. Then the heating was maintained at 130°C under oxidant gas (air) during all the experiment. Gas fills the cell so it is in contact with the surface of the sample. The flow of $50\ \text{mL min}^{-1}$ of argon or air allows the evacuation of volatile compounds produced by ageing. The flow of air allows also to renew the oxygen source. The temperature was chosen after preliminary tests: it allows discriminating oils according to their oxidation resistance. Spectra were rationed to the background collected on a clean area of the NaCl window in the same analytical conditions. Spectra were collected every 15 min.

An oxidative spectroscopic index has been created for monitoring the kinetics of oil aging:

$$I_{\text{C=C}} = \frac{[\text{sp}^2/(\text{sp}^2 + \text{sp}^3)]_{T_t}}{[\text{sp}^2/(\text{sp}^2 + \text{sp}^3)]_{T_0}} \quad (1)$$

where sp^2 is the area of the *cis*-CH stretching vibration band (HC=C band) centered at 3008 cm^{-1} and ($sp^2 + sp^3$) is the area from 3050 to 2750 cm^{-1} including the *cis*-CH band and the CH asymmetric and symmetric stretching bands from CH_3 and CH_2 aliphatic compounds. Areas are measured at given time (T_t) and at the initial time (T_0).

This relative index is based on ratio between area values rather than absolute absorbance values to eliminate all variations due to the preparation and to the thickness of samples. For initial spectra, the index was equal to 1. The experiment was stopped when the band at 3008 cm^{-1} was not detectable any more, corresponding to an index value equal to zero.

The graphic representation of this relative index versus thermal oxidation time made it possible to compare the evolution of various oils on the basis of numerical value rather than to compare series of spectra which are likely not to have the same intensity. To simplify graphs, an average value of index was represented for each oxidation time. It has been obtained after integration of specific areas from three spectra at the same time.

2.5. Software

The chemometric applications are performed by UNSCRAMBLER software version 9.2 from CAMO (Computer Aided Modelling, Trondheim, Norway). All the calculations relating to multivariate resolution with alternative least squares (MCR-ALS) and SIMPLISMA were performed with laboratory-written software under Matlab 6.5 computer environment. These software are available from the authors [31].

2.6. Principal component analysis (PCA)

Principal component analysis (PCA) is a method used for extraction of the systematic variations in a data set [32]. PCA is a tool for unsupervised learning, e.g. extracting information directly from the input data without referring to classes known in advance. This method can be used for classification as well as for description and interpretation. PCA is oriented towards modeling variance/covariance structure of the data matrix into a model which represents the significant variations and which considers the noise as an error. The components are found during the calibration one by one and each principal component represents the main systematic variation in the data set, which can be modeled after the extraction of the previous ones. The common characteristics of all the spectra are modeled in one or several principal components for which the scores are not significantly different according to the species. On the contrary, the information which differentiate the species, contribute to principal component whose scores are significant [33]. The classification may be done on the basis of the scores and the characteristics of each species are established by the interpretation of these specific principal components.

2.7. MCR-ALS

MCR-ALS (multivariate curve resolution-alternative least square) is an effective and efficient multivariate self modeling curve resolution method developed by Tauler [34]. The quality of the relative contributions given by MCR-ALS was evaluated in order to develop a rapid procedure that can be applied to model the behavior of vegetable oils during oxidation.

For the analyzed samples, one matrix $R(n, m)$ made up n row and m columns is obtained. Each row " n " is made up of a spectrum. Each column " m " gives the intensity at a wavenumber. R is the data matrix of n spectra sampled at p wavenumbers. The R matrix is

mathematically decomposed into the product of two-factor matrix.

$$R = CS^T + E \quad (2)$$

Matrix $C(n, q)$ is the concentration matrix describing the evolution of the q chemical components in the samples. Matrix $S^T(q, p)$ is the spectroscopic matrix describing the pure infrared spectra of these components. $E(n, p)$ is the error matrix that provides the data variation not explained by the proposed p contributions. Eq. (1) assumes that data matrix R is bilinear, i.e. that the infrared signal can be decomposed into the sum of individual contributions, each described by a concentration profile in the matrix C and by a pure matrix spectra in matrix S^T . The number of components or contributions q , to be considered in the mathematical decomposition of Eq. (1), can be estimated by singular value decomposition (SVD) analysis [35].

Eq. (1) is solved iteratively using an alternating least square (ALS) procedure based on the two following matrix equations.

$$C = R(S^T)^+ \quad (3)$$

and

$$S^T = C^+R \quad (4)$$

where $(S^T)^+$ and C^+ are the pseudo-inverse matrix of S^T and C [36]. Initial estimate, which are needed to start the ALS procedure described by these two equations, can be obtained by algorithms, such as SIMPLISMA (SIMPLe-to-use Interactive Self Modeling Analysis), which is described elsewhere [37–40]. SIMPLISMA searches for the pure variables where the selectivity of a given component is maximized. In order to obtain proper resolution of the mixture data, user interaction is necessary. Once, the pure variables were determined, they were used to calculate the corresponding pure species spectra because the intensity changes in the pure variables are proportional to the concentration evolutions and, if they are aligned in separated columns, they form the matrix C .

The resolution was improved by applying several constraints during optimization. Some of the possible constraints are:

- *Non-negativity on the concentration profiles*: This is a general constraint used in curve resolution methods [41]. It is applied to the concentration profiles, because the chemical species concentrations are always positive values or zero.
- *Non-negativity on the spectra*: The application of this constraint depends on what instrumental technique is used for detection. In the case of FT-MIR spectra, the intensity of the radiation absorbed or reflected by the sample never takes negative values.

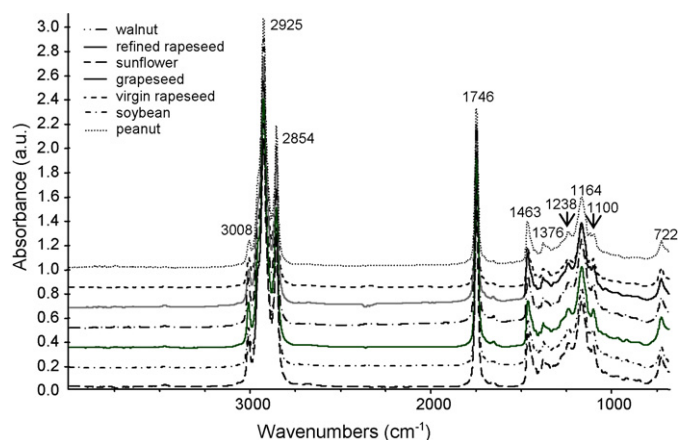


Fig. 2. Spectra of different oils before aging.

Table 2

Assignments of the infrared bands detected in oil spectra.

Wavenumbers (cm ⁻¹)	Function	Type of vibration	Remark
3450	OH	Stretching	Intermolecular bonding
≈3008	CH	Stretching	–CH=CH– (cis-olefin)
2953	CH	Asymmetric stretching	Aliphatic (–CH ₃)
2925	CH	Asymmetric stretching	Aliphatic (–CH ₂)
2854	CH	Symmetric stretching	Aliphatic (–CH ₂)
1746	C=O	Stretching	ν(C=O) ester
1463	CH	Scissoring	Aliphatic (–CH ₂)
1376	CH	Symmetric deformation	Aliphatic (–CH ₃)
1238	CH	Out of plane bending	Aliphatic (–CH ₂)
1164	C–O	Stretching	ν(C–O) ester
1025	C–O–C	Stretching	ν(C–O–C) ester
966	CH	Out of plane bend	trans (–CH=CH–)
722	CH	Rocking	Aliphatic (–CH ₂)

The computed solutions of the algorithms will be presented in terms of the lack-of-fit in percentage (lof (%)) plus the resolved spectral and concentration profiles. The lack-of-fit relates to the difference between the squared sum of the input data and the squared sum of the modeled variation with the resolved MCR-ALS profiles. For one sample it is computed according to the following expression:

$$\text{lof} = \sqrt{\frac{\sum_{i,j}(r_{ij} - \hat{r}_{ij})^2}{\sum_{i,j} r_{ij}^2}} \times 100 \quad (5)$$

where r_{ij} is the experimental absorbance at the j^{th} wavenumber in the i^{th} spectrum and \hat{r}_{ij} is the corresponding value calculated by ALS. A low lack-of-fit percentage indicates that a model fits the data well [42,43]

3. Results and discussion

3.1. Infrared spectra

Spectra of different edible oils before oxidation are presented on Fig. 2. Assignments of the infrared bands (Table 2) were made by comparison with literature data [44]. These spectra seem very similar even if their chemical composition varied. Indeed, even if it was not clearly observed in the resulting infrared spectra, the main differentiation criterion of oils concerned the proportion of double bonds in the aliphatic chain of fatty acids. Table 1 gives these values obtained by GC. Each oil contains saturated (from 6 to 18%), mono-unsaturated (from 15 to 70%), di-unsaturated (from 16 to 74%), and tri-unsaturated (from 0.1 to 14%), fatty acids at different rates. It is

well-known that the higher the percentage of unsaturation is, the more sensitive to oxidation the oil is [45]. Walnut oil has the highest rate of fatty acid tri-unsaturated, so it should be the most sensitive to oxidation. On the contrary, the peanut oil which presents the lowest rate of unsaturated fatty acids should be the most resistant to oxidation.

When oils were heated during 5 h under argon flow, no spectral modifications were observed. Fig. 3 shows spectra of sunflower oil at different times of aging at 130 °C under air flow (i.e. oxidant condition). It presents lot of spectral modifications, so oxygen contents in air was necessary to obtain rapid oxidation. During oxidation band at 3008 cm⁻¹ attributed to double bonds in the aliphatic chain decreases after an induction time as shown on Fig. 3a.

Moreover, spectral modifications in other zones occurred. The band at 3473 cm⁻¹ assigned to the overtone of the triacylglycerol carbonyl absorption shifted and is overlapped by a more intense band at 3464 cm⁻¹ (Fig. 3a). This band is attributed to hydroperoxydes (primary oxidation products) generated in the oxidation process [24]. After the induction time, another band appears in highest wavenumber (3535 cm⁻¹). This band, characteristic of alcohols or secondary oxidation products [15,25,46], increases in intensity. This means that these compounds are produced gradually in time after an induction period.

Therefore, nonoxidated oils show a weak band at 1654 cm⁻¹ attributed to the stretching vibration of the C=C of cis-olefins (Fig. 3b). It decreased and disappeared as the oxidation process advances and a band at 1627 cm⁻¹, assigned to α, β-unsaturated aldehydes and ketones [47] appears. The very weak absorbance of the band at 966 cm⁻¹, associated with bending vibration out of plane of CH functional groups of isolated *trans*-olefins, is covered up after the induction time by two low intensity bands. The first one at 987 cm⁻¹ is associated with the bending vibration of conjugated C–H *trans,trans* and/or *cis,trans* olefinic groups [47]. The second one at 975 cm⁻¹ is assigned to secondary oxidation products such as aldehydes or ketones supporting isolated *trans* double bonds [48]. The band at 987 cm⁻¹ rapidly disappears after the induction time on behalf of increasing of band at 975 cm⁻¹. Therefore, compounds with conjugated double bonds (accountable for the double band at 966 and 987 cm⁻¹) are intermediate compounds in the oxidation process. This fact has been also shown in the oxidation of different edible oils [9,10].

From the outset of oxidation, at the same time that the *cis*-CH band begin to decrease, the broadening of the band at 1746 cm⁻¹, attributed to C=O group carboxyl of triacylglycerol, is observed. By Fourier self deconvolution of this band (Fig. 4), in addition to the band at 1746 cm⁻¹, it appears bands at 1721 cm⁻¹ attributed to the C=O group of aliphatic aldehydes [22], at 1706 cm⁻¹ attributed to

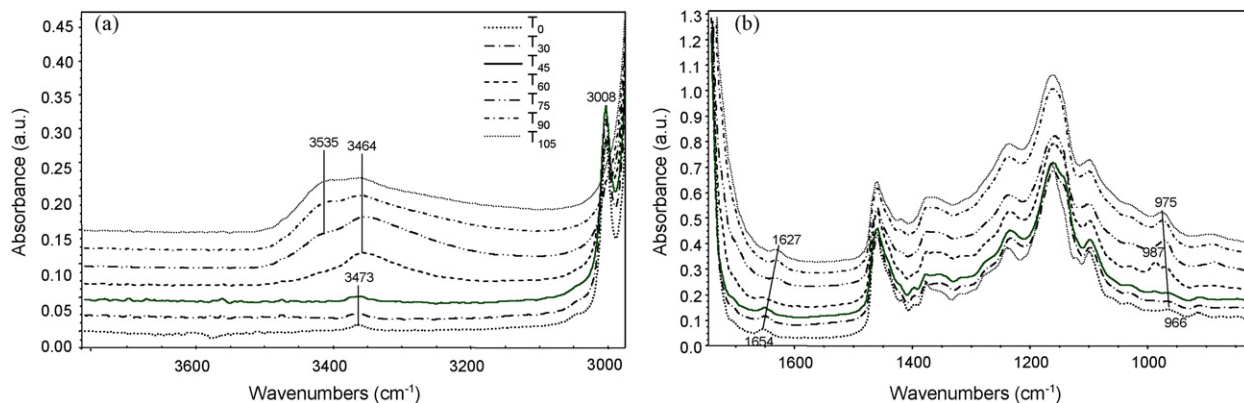


Fig. 3. Spectra of sunflower oil at different times of aging: from 3000 to 4000 cm⁻¹ (a) and from 750 to 1500 cm⁻¹ (b).

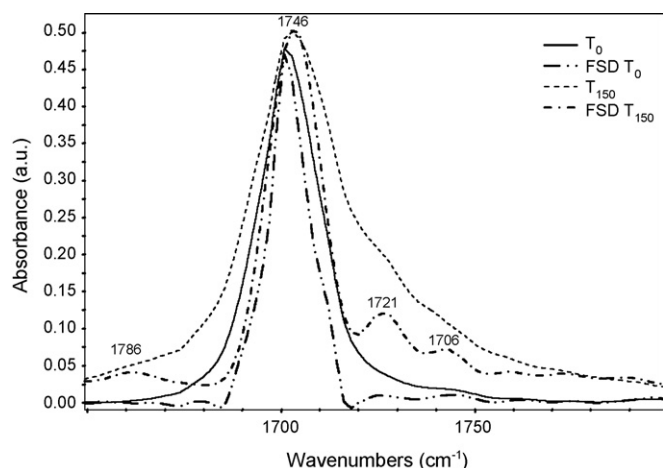


Fig. 4. Spectra and deconvoluted spectra by Fourier self deconvolution (FSD) of sunflower oil at T_0 and T_{150} from 1650 to 1800 cm^{-1} (bandwidth: 22; enhancement factor: 2.0).

Table 3

Characteristic times (min) obtained by the oxidative spectroscopic index for all the oil samples.

Oils	Induction time, T_i	Half life time, $T_{1/2}$	Final time, T_f
Walnut	29	44	63
Refined rapeseed	43	64	92
Sunflower	45	58	79
Grapeseed	57	66	76
Virgin rapeseed	68	89	117
Soybean	73	89	106
Peanut	102	129	165

free fatty acids [48] and at 1786 cm^{-1} which can be attributed to the C=O group of alcohol-acid such as hydroxyacetic acid [49] or to the C=O group of acetic acid [50].

To evaluate the importance of oxidation, oil oxidation kinetic was followed by the calculation of the oxidative spectroscopic index related to the *cis*-CH stretching vibration band at 3008 cm^{-1} . This calculation was performed for all spectra recorded during the oil oxidation kinetics and has conducted to graphs showing the evolution of this index over time (from the beginning of the eating) for all samples (Fig. 5). All curves have a similar profile and can be characterized by two phases and three times. The *induction phase* represents the period of time from the beginning of experiment to the oxidation beginning e.g. the *induction time* (T_i). During this phase, the index value is stable. The *oxidation phase* represents fatty acid degradation. During this phase, the index value decrease from 1 to 0. This phase is characterized by two times: the *half life time*

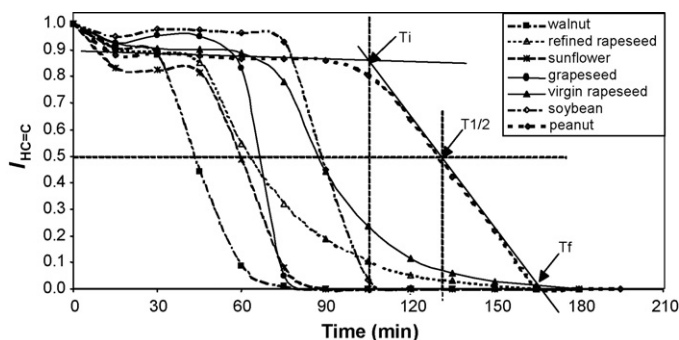


Fig. 5. Evolution of the oxidative spectroscopic index in function of time for all the oils.

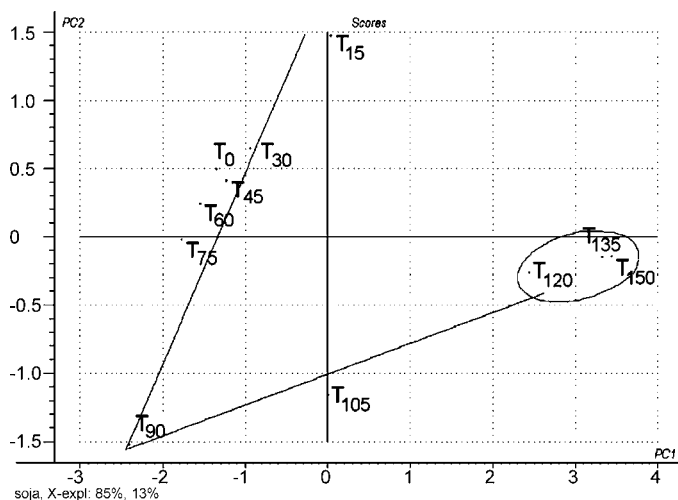


Fig. 6. Principal component analysis (PCA) performed on spectra of oxidized soya oil.

($T_{1/2}$) that corresponds to the necessary time to obtain an index value of 0.5 and the *final time* (T_f) with a zero index value.

The characteristic times of each sample are summarized on Table 3. Walnut oil which shows the lowest values for all three times is the most sensible to thermal oxidation and peanut oil which shows the greatest values for the three times, is the most resistant to thermal oxidation. Even if it is known that quantities of

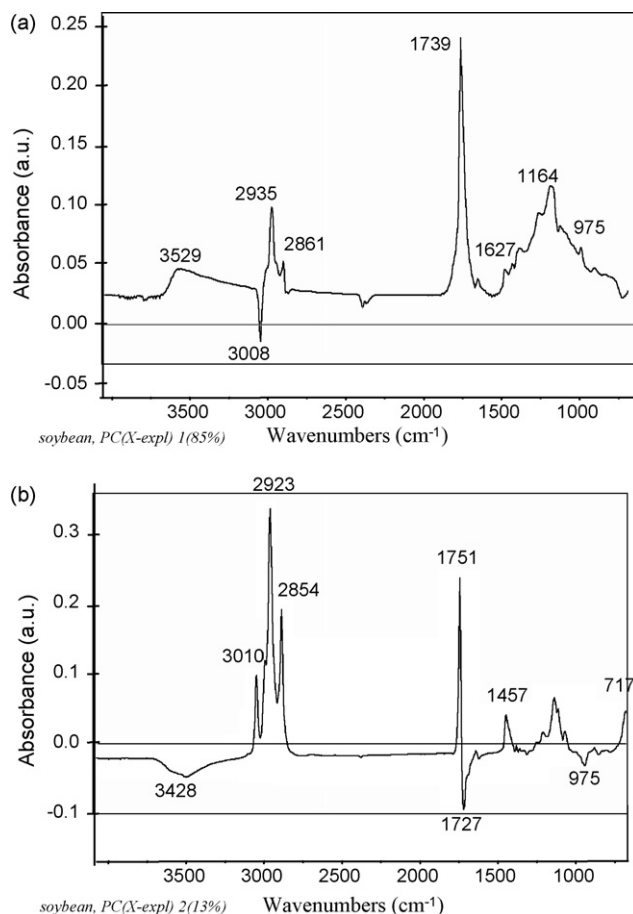


Fig. 7. First (a) and second (b) principal components of the PCA performed on soya oil spectra.

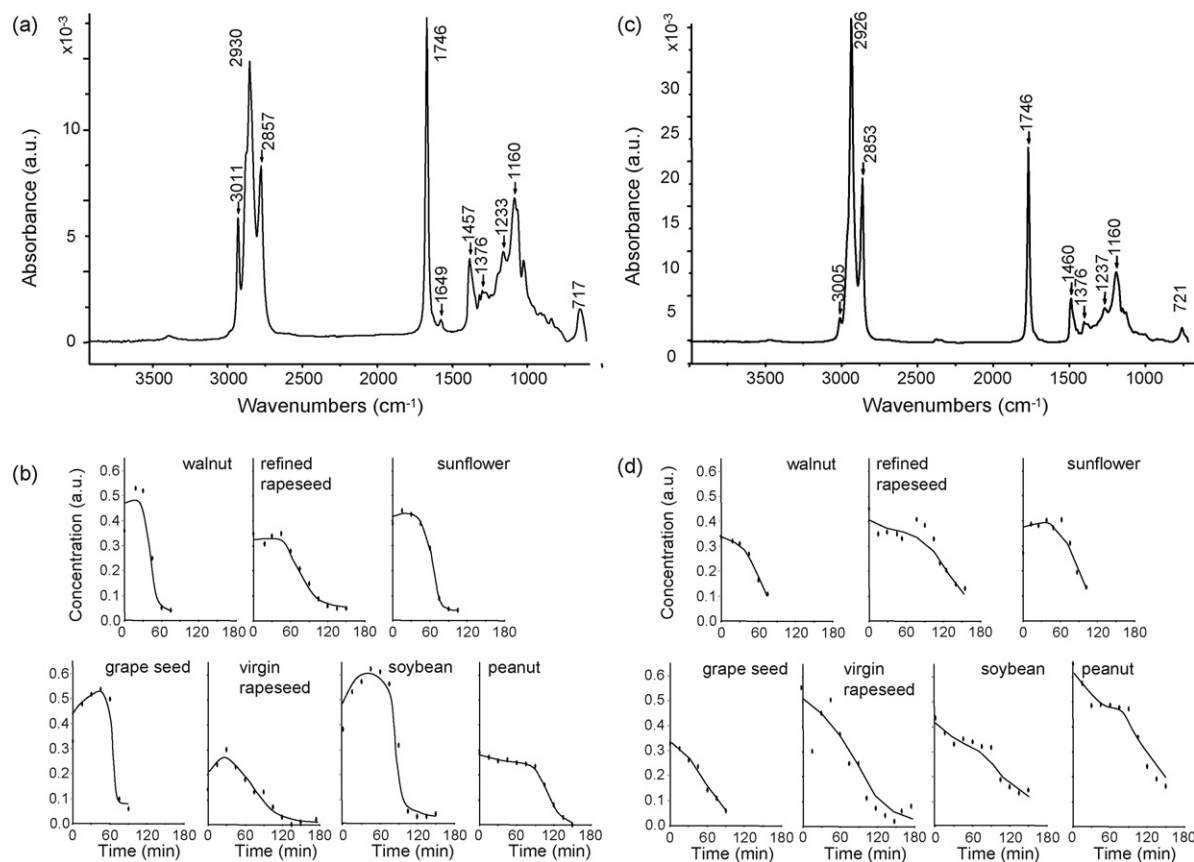


Fig. 8. First extracted spectrum (a) and first associated concentration profile (b) and second extracted spectrum (c) and second associated concentration profile (d) obtained by MCR-ALS performed on all the spectra of all the oxidized oils.

antioxidants present in oil determine its sensitivity to oxidation [51], it seems that the rate of unsaturation influences also oxidation: as a matter of fact, the walnut oil presents the highest concentration of tri-unsaturated fatty acid (TUFA) (14%) and a high concentration of polyunsaturated fatty acid (PUFA) (71.9%) (Table 1), so it must be the most sensitive to oxidation. At the opposite, the peanut oil presents the lowest rates of TUFA (0.1%) and PUFA (20.2%), so it must be the less sensitive to oxidation. Other samples as sunflower oil or grape-seed oil have a different profile: *cis*-CH band remains stable for a longer time than walnut oil but when it starts to decrease, this diminution carries out more abruptly. Table 3 shows a shorter induction time for refined rapeseed oil than for virgin rapeseed oil due to the lost of antioxidant compounds during the refining process.

Although the oxidative spectroscopic index allows a fast comparison of oils and although the analysis of each spectrum (one after the other) makes it possible to show the chemical evolution of oil during its oxidation, it seems interesting to try to take up this evolution thanks to a global study of the whole of spectra of kinetics.

3.2. PCA analysis

When principal component analysis was performed on the spectra recorded as time function at 130 °C, using all the spectral range, similar results were obtained. For each edible oil, spectra recorded at T_0 (25 °C) were different from others recorded at 130 °C because infrared signal is very sensitive to temperature. Therefore, in the entire PCA graph, their position was out of zone. For all the vegetable oils, the two first principal components extracted represent more than 95% of the total variance. The other principal compo-

nents contribute less than 5% of the residual variance, and model the non-significant variations as noise. When spectra are projected (using their scores as coordinates) in the space of the first and second principal components, they are distributed according to the exposition time at 130 °C of the sample. Fig. 6 shows an example obtained with soybean oil. The spectra numbered T_{15} to T_{90} are aligned, with a decreasing of the scores on the first and second principal components. A second straight line from T_{90} to T_{120} is obtained with an increasing of the scores on the first and second principal components. The spectra numbered T_{120} to T_{150} are gathered and present high scores in the first principal component. Therefore, the discrimination between the two groups is done on the first and second principal components (Fig. 7a and b). As the spectra numbered T_{15} to T_{90} are negatively projected as a function of the time exposition of the sample (130 °C and air), they are more correlated with the negative data in the first principal component. The examination of the first principal component spectrum shows high negative contribution at 3008 cm^{-1} (Fig. 7a) attributed to the *cis*-CH stretching vibration band (*cis*-olefin). This spectral information confirms the decrease of this band observed during the kinetics of oxidation and consolidates the choice to use this band to characterize the kinetics of oils and to create the oxidative spectroscopic index. In the same time, a negative projection of the same spectra in the space of the second principal component is observed. The examination of the second principal component spectrum (Fig. 7b) shows high negative contributions at 3428 cm^{-1} , attributed to the O–H of hydroperoxides, and at 1727 and 975 cm^{-1} attributed to the C=O stretching vibration band and/or secondary oxidation products such as aldehydes or ketones supporting isolated *trans* double bonds according to the interpretation of infrared data [44,46].

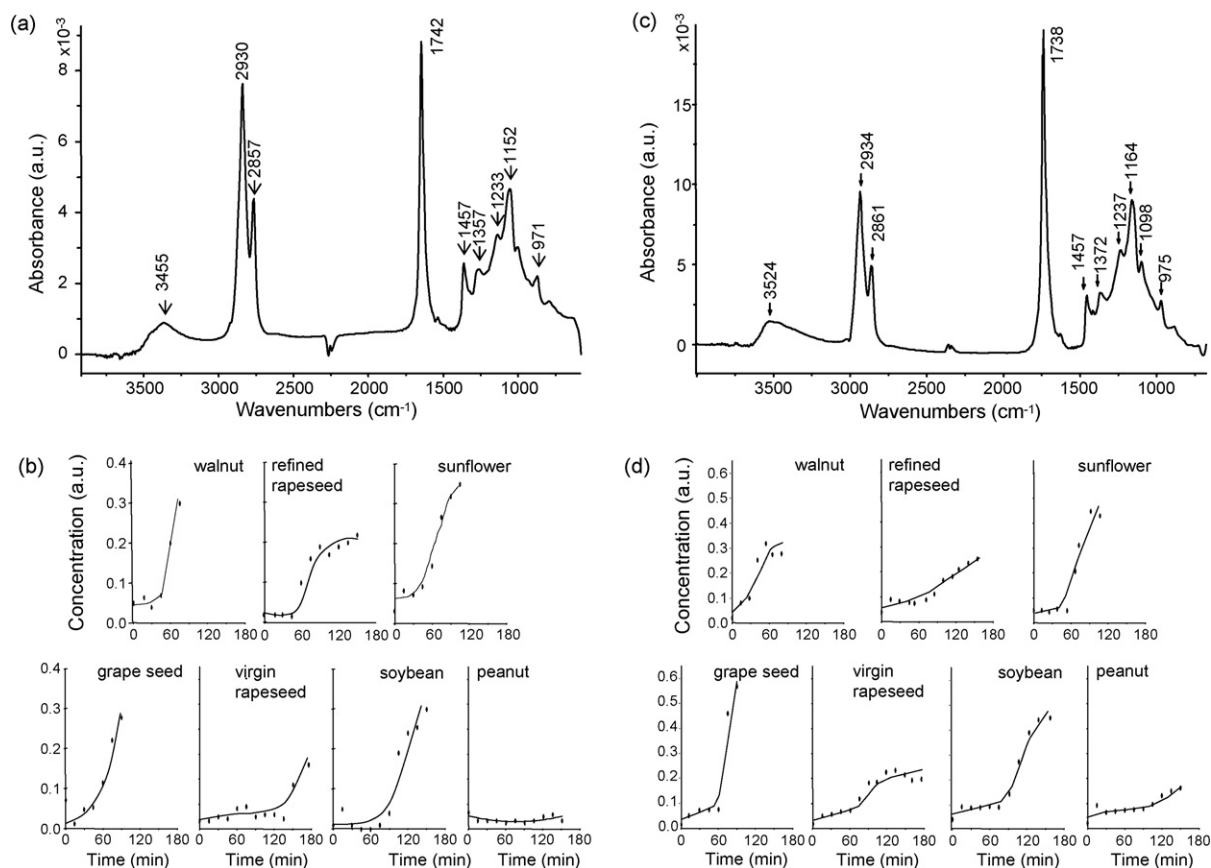


Fig. 9. Third extracted spectrum (a) and third associated concentration profile (b) and fourth extracted spectra (c) and fourth associated concentration profile (d) obtained by MCR-ALS performed on all the spectra of all the oxidized oils.

The spectra numbered T_{105} to T_{150} are positively projected as a function of their time exposition (Fig. 6). They are correlated with the positive data of the first principal component shown on Fig. 7a. The examination of this first principal component spectrum shows high positive contribution at 975, 1739 and 3529 cm⁻¹. According to the interpretation of infrared data, the band at 975 cm⁻¹ can be attributed to the appearance to HC=C out of plane bending vibration of aldehydes or ketones supporting isolated *trans* double bonds [46]. The C=O absorption appears at 1739 cm⁻¹; the shift observed (4 cm⁻¹) between T_0 spectra and the first principal component could be attributed to the transformation of the ester into acid. The appearance of large contribution at 3529 cm⁻¹ could be in first approximation attributed to OH absorption of acid. The spectra numbered T_{105} to T_{150} are always negatively projected in the space of the second principal component shown on Fig. 7b.

The previous results demonstrate that there were sufficient information in the infrared spectra to establish a non-supervised

classification of some groups of samples in function of their aging time. This fact leads to improve the chemometric treatment and to use a curve resolution method to identify the chemical species which contributed to this classification.

3.3. MCR-ALS

Curve resolution approach was applied to all oil spectra. SIMPLISMA was used to estimate the pure spectra and the MCR-ALS optimization program was applied with the following restriction: non-negativity for the spectra and for the concentration. Models with 4–6 components have been computed. The best result [lof = 4.7%] (Eq. (5)) has been obtained with five relevant components according to the Figs. 8 and 9.

The first spectrum (Fig. 8a) was attributed to triacylglycerols of unsaturated acid (3011, 2930, 2857, 1746, 1649, 1457, 1233, 1160 and 717 cm⁻¹). The absorbance of the bands at 3011 and 1649 cm⁻¹,

Table 4
Disappearance or emergence time (min) of compounds isolated by MCR-ALS for each oil sample.

Oils	Time of disappearance beginning (min)		Time of emergence beginning (min)	
	Triacylglycerols of unsaturated <i>cis</i> -acid	Triacylglycerols of mono-unsaturated <i>cis</i> -acid	<i>trans</i> -hydro-peroxyde	Secondary oxidation products
Walnut	30	45	30	30
Refined rapeseed	45	60	45	45
Sunflower	60	60	45	45
Grapeseed	45	0	60	45
Virgin rapeseed	30	30	60	135
Soybean	75	90	75	90
Peanut	90	90	90	No observed

in comparison with the absorbance of the bands at 2930 and 2857 cm^{-1} , was higher than for the other spectra. So, the spectrum was attributed to the triacylglycerols of di or tri-unsaturated *cis*-acid. The associated concentration profile (Fig. 8b) decreases after an induction period in each kinetic. The relative concentration of this second extracted species was less important in spectra of rapeseed and peanut oils that are poor in PUFA, as described in Table 1.

The second spectrum (Fig. 8c) has the same bands than the first one (3005, 2926, 2853, 1746, 1460, 1237, 1160 and 721 cm^{-1}). The intensity of the 3005 cm^{-1} band was very weak compared to the 2926 and 2853 cm^{-1} bands. So, the spectrum was attributed to the triacylglycerols containing mono-unsaturated *cis*-acid. The associated concentration profile (Fig. 8d) decreases from the first to the last spectrum in each kinetic. The relative concentration of this third species was more important for rapeseed and peanut oils that have a high concentration of MUFA (Table 1).

The third spectrum (Fig. 9a) was attributed to a *trans* hydroperoxyde form of triacylglycerols (3455, 1742, 971 cm^{-1}). The associated concentration profile (Fig. 9b) increases up to a maximum in each kinetic except for peanut oil. This oil has the lowest PUFA concentration and the highest SAFA (Table 1) and seems to be potentially less sensitive to oxidation.

The fourth spectrum (Fig. 9c) presents a large band at 3524 cm^{-1} characteristic to the OH stretching vibration of acid, a band at 1738 cm^{-1} attributed to carboxylic acid function and a band at 975 cm^{-1} characteristic to an *trans* double bond on acid, that have allowed to attribute the spectrum to secondary products of oxidation. The associated concentration profile (Fig. 9d) presents a period of poor variation and then increase up to the last spectrum in each kinetic. The final concentration of these products seems to be less important for rapeseed and peanut oils that have a low concentration of PUFA.

During the oxidation process, triacylglycerols decrease after a period of time. In the same way, hydroperoxides and secondary products of oxidation appeared at low concentration at the beginning of the kinetic and their concentration increase after a period of time. Table 4 shows the time when the extracted species appear or disappear. This time was not the same for all the species mathematically extracted. Moreover, the succession “appearance/disappearance” of species is not either the same for all oils. For example, hydroperoxides were not observed in peanut oil and was belatedly detected in virgin rapeseed oil. Triacylglycerols of mono-unsaturated acids disappeared as early as the beginning of the aging process for grapeseed oil while for the other oils, the disappearance occurred after a period of time.

The comparison between Tables 3 and 4 shows that the induction times determined by the oxidative spectroscopic index correspond to the disappearance of triacylglycerols of poly-unsaturated acids and to the appearance of the hydroperoxides presented on Fig. 8a and 9a. The time of the appearance of secondary oxidation products correspond rather to the half life time especially for the most resistant oils to oxidation.

4. Conclusion

The present paper reports on the development by FT-MIR of tool to determine oxidative stability of various edible oils and to compare them. Induction time, half life time and final time determined by oxidative spectroscopic index allow to quickly characterize the sensitivity of oil to a thermic oxidation and then to compare different oils according to their stability. Even if this index does not bring structural, it could be admitted as a simple and fast method to obtain information about the oxidative stability of oils and could

be used as a quality control method. These results have been compared with results obtained by chemometric treatments of the spectra. The use of the MCR-ALS method led to the description of four families of products (disappearance of triacylglycerols containing mono-unsaturated *cis*-acids and triacylglycerols containing poly-unsaturated *cis*-acids, appearance of hydroperoxides and secondary products of oxidation) implicated in the oxidation process, in agreement with oxidative spectroscopic index. Thus, MCR-ALS could be used to determine the contribution of chemical compounds in oxidation phenomena and to deepen the comparison of oils according to their stability.

References

- [1] S. Stender, J. Dyerberg, G. Holmer, L. Ovesen, B. Sandström, Clin. Sci. 86 (4) (1995) 375.
- [2] AOCS, Official Methods and Recommended Practices of the American Oil Chemists' Society, American Oil Chemists' Society, Champaign, IL, 2004.
- [3] E.N. Frankel, Lipid Oxidation, The Oily Press Ltd., Glasgow, UK, 1998, pp. 79–98.
- [4] International Union of Pure and Applied Chemistry, Standard Methods For the Analysis of Oils, Fats and Derivatives, 7th ed., Blackwell, Oxford, 1987, IUPAC Standard Method 2.507.
- [5] M.W. Laubli, P.A. Bruttel, J. Am. Oil Chem. Soc. 63 (6) (1986) 792.
- [6] S.L. Melson, S. Jafar, D. Sykes, M.K. Trigiano, J. Am. Oil Chem. Soc. 71 (12) (1994) 1301.
- [7] J.B. Russel, in: J.C. Allen, R.J. Hamilton (Eds.), Rancidity of Foods, Elsevier Applied Science Publishers, London, 1989.
- [8] M.C.M. Moya Moreno, D. Mendoza Olivares, F.J. Amezcuita Lopez, J.V. Gimeno Adelantado, F. Bosch Reig, Talanta 50 (2) (1999) 269.
- [9] M.C.M. Moya Moreno, D. Mendoza Olivares, F.J. Amezcuita Lopez, V. Peris Martinez, F. Bosch Reig, J. Mol. Struct. 482–483 (1999) 557.
- [10] M.D. Guillén, N. Cabo, J. Sci. Food Agric. 80 (14) (2000) 2028.
- [11] M.D. Guillén, N. Cabo, Food Chem. 77 (4) (2002) 503.
- [12] F.R. Van de Voort, A.A. Ismail, J. Sedman, G. Emo, J. Am. Oil Chem. Soc. 71 (3) (1994) 243.
- [13] T.A. Russin, F.R. Van de Voort, J. Sedman, J. Am. Oil Chem. Soc. 80 (7) (2003) 635.
- [14] B. Muik, B. Lendl, A. Molina-Diaz, M. Valcarcel, M.J. Ayora-Cánada, Anal. Chim. Acta 593 (1) (2007) 54.
- [15] F.R. Van de Voort, A.A. Ismail, J. Sedman, J. Am. Chem. Soc. 72 (8) (1995) 873.
- [16] N. Dupuy, L. Duponchel, J.P. Huvenne, B. Sombret, P. Legrand, Food Chem. 57 (2) (1996) 245.
- [17] A.A. Christy, P.K. Egeberg, E.T. Østensen, Vib. Spectrosc. 33 (1–2) (2003) 37.
- [18] E. Bertran, M. Blanco, J. Coello, H. Iturriaga, S. MasPOCH, I. Montoliu, J. Am. Oil Chem. Soc. 76 (5) (1999) 611.
- [19] M.J.A. Canada, A.R. Medina, B. Lendl, Appl. Spectrosc. 55 (3) (2001) 356.
- [20] Y.W. Lai, E.K. Kemsley, R.H. Wilson, J. Agric. Food Chem. 42 (5) (1994) 1154.
- [21] M.D. Guillén, N. Cabo, Lipids 101 (2) (1999) 71.
- [22] A. Tay, R.K. Singh, S.S. Krishnan, J.P. Gore, Lebensm. -Wiss. Technol. 35 (1) (2002) 99.
- [23] D.A. Rusak, L.M. Brown, S.D. Martin, J. Chem. Educ. 80 (5) (2003) 541.
- [24] B.F. Ozen, I. Weiss, L.J. Mauer, J. Agric. Food Chem. 51 (20) (2003) 5871.
- [25] H. Yang, J. Irudayaraj, M.M. Paradkar, Food Chem. 93 (1) (2005) 25.
- [26] T.H. Jiang, Y. Liang, Y. Ozaki, Chemom. Intell. Lab. Syst. 71 (1) (2004) 1.
- [27] A.A. Christy, P.K. Egeberg, Chemom. Intell. Lab. Syst. 82 (1–2) (2006) 130.
- [28] European standard NF EN ISO 5508, Analysis by GC of Methyl Esters of Fatty Acids AFNOR Paris (1995).
- [29] J. Lamontagne, F. Durrieu, J.P. Planche, V. Mouillet, J. Kister, Anal. Chim. Acta 444 (2) (2001) 241.
- [30] F. Priéri, E. Gresser, Y. Le Dréau, J. Obiols, J. Kister, Appl. Spectrosc. 62 (7) (2008) 810.
- [31] R. Tauler, A. De Juan, Multivariate Curve resolution homepage, <http://www.ub.es/gesq/mcr/mcr.htm>.
- [32] H. Martens, T. Naes, Multivariate Calibration, Wiley, New York, 1989.
- [33] S. Millar, P. Robert, M.F. Devaux, R.C.E. Guy, P. Maris, Appl. Spectrosc. 50 (9) (1996) 1134.
- [34] R. Tauler, Chemom. Intell. Lab. Syst. 30 (1) (1995) 133.
- [35] E.R. Malinowski, Factor Analysis in Chemistry, 2nd ed., Wiley, New York, 1991.
- [36] R. Tauler, A.K. Smilde, B.R. Kowalski, J. Chem. 9 (1) (1995) 31.
- [37] W. Windig, D.A. Stephenson, Anal. Chem. 64 (22) (1992) 2735.
- [38] W. Windig, S. Markel, J. Mol. Struct. 292 (1993) 161.
- [39] P.J. Gemperline, J. Chemom. 3 (1989) 549.
- [40] W. Windig, Chemom. Intell. Lab. Syst. 3 (3) (1988) 159.
- [41] O.S. Borgen, B.R. Kowalski, Anal. Chim. Acta 174 (8) (1985) 1.
- [42] C.B. Zachariassen, J. Larsen, F. van den Berg, R. Bro, A. de Juan, R. Tauler, Chemom. Intell. Lab. Syst. 83 (1) (2006) 13.
- [43] T. Azzouz, R. Tauler, Talanta 74 (5) (2008) 1201.
- [44] M. Safar, D. Bertrand, P. Robert, M.F. Devaux, C. Genot, J. Am. Oil Chem. Soc. 71 (4) (1994) 371.
- [45] W.E. Neff, M. El-Agami, Lebensm. Wiss. Technol. 29 (1996) 772.

- [46] N. Dupuy, C. Wojciechowski, J.P. Huvenne, *Sciences des Aliments* 19 (6) (1999) 677.
- [47] E.N. Frankel, *J. Am. Oil Chem. Soc.* 61 (12) (1984) 1908.
- [48] M.D. Guillén, N. Cabo, *Meat Sci.* 66 (3) (2004) 647.
- [49] H. Kuhne, S. Vaccani, A. Bauder, H.H. Gunthard, *Chem. Phys.* 28 (1–2) (1978) 11.
- [50] T. Shimanouchi, *National Bureau of Standards* 1 (1972) 1.
- [51] D. Tura, C. Gigliotti, S. Pedò, O. Failla, D. Bassi, A. Serraiocco, *Sci. Hortic.* 112 (1) (2007) 108.



Deoxyribonucleic acid modified poly(dimethylsiloxane) microfluidic channels for the enhancement of microchip electrophoresis

Ruping Liang, Pengfei Hu, Guihua Gan, Jianding Qiu*

Department of Chemistry, Nanchang University, Xue fu Road 999, Nanchang 330031, PR China

ARTICLE INFO

Article history:

Received 27 May 2008

Received in revised form

29 September 2008

Accepted 30 September 2008

Available online 17 October 2008

Keywords:

Poly(dimethylsiloxane)

Microchip

Deoxyribonucleic acid

In-channel electrochemical detection

ABSTRACT

In this paper, deoxyribonucleic acid (DNA) was employed to construct a functional film on the PDMS microfluidic channel surface and apply to perform electrophoresis coupled with electrochemical detection. The functional film was formed by sequentially immobilizing chitosan and DNA to the PDMS microfluidic channel surface using the layer-by-layer assembly. The polysaccharide backbone of chitosan can be strongly adsorbed onto the hydrophobic PDMS surface through electrostatic interaction in the acidic media, meanwhile, chitosan contains one protonatable functional moiety resulting in a strong electrostatic interactions between the surface amine group of chitosan and the charged phosphate backbone of DNA at low pH, which generates a hydrophilic microchannel surface and reveals perfect resistance to nonspecific adsorption of analytes. Aminophenol isomers (*p*-, *o*-, and *m*-aminophenol) served as a separation model to evaluate the effect of the functional PDMS microfluidic chips. The results clearly showed that these analytes were efficiently separated within 60 s in a 3.7 cm long separation channel and successfully detected on the modified microchip coupled with in-channel amperometric detection mode at a single carbon fiber electrode. The theoretical plate numbers were 74,021, 92,658 and 60,552 N m^{-1} at the separation voltage of 900 V with the detection limits of 1.6, 4.7 and 2.5 μM ($S/N=3$) for *p*-, *o*-, and *m*-aminophenol, respectively. In addition, this report offered an effective means for preparing hydrophilic and biocompatible PDMS microchannel surface, which would facilitate the use of microfluidic devices for more widespread applications.

© 2008 Elsevier B.V. All rights reserved.

1. Introduction

Miniaturization of chemical analysis systems using microchips is an emerging new technology. Microfluidic devices have attracted increasing attention and provided a powerful platform for chemical and biological assays due to its high sample throughput, low consumption of sample and reagents, automatic control and easy integration [1–3]. Polymer materials such as PDMS, polycarbonate, polystyrene and poly(methyl methacrylate) (PMMA) are best candidates to construct low-cost, disposable and multi-functional microfluidic devices instead of glass and quartz [4–7]. Of all the polymers used for making chips, PDMS has been the most popular due to its low cost, easy handling and sealing with other materials, non-toxicity and versatility [8–10]. In spite of the many advantages of PDMS, its application in microfluidics has not been without problems. The surface modification of PDMS is difficult because the material is inert. Furthermore, PDMS is

extremely hydrophobic, which makes the microchannels difficult to wet with aqueous solution. Due to its high hydrophobicity, PDMS absorbs some organic solvents and some hydrophobic analytes, causing fouling of the material [11–13]. These disadvantages greatly limit the variety of analytes that can be separated on PDMS devices, and generally results in relatively lower separation efficiency. To control of the electroosmotic flow (EOF) and reduction of analyte–wall interaction, the surface modification is of great importance for PDMS microfluidic devices in electrophoresis applications.

Microchannel coatings can be separated into two major categories: permanent coatings and dynamic coatings. Permanent coatings are often regarded as the most effective way for surface modification in order to reduce analyte–wall interactions and to modify the EOF. In permanent coatings chemical compounds (often polymers) are covalently bound to functional groups of the surface or immobilized (e.g., via cross-linking of a polymer) at the surface to become insoluble in the electrolyte. However, permanent coatings are often require organic solvents, high temperature, and more laborious in the production process and might accordingly be less attractive for disposable devices from mass

* Corresponding author. Tel.: +86 791 3969518.

E-mail address: jdqiu@ncu.edu.cn (J. Qiu).

production. Dynamic coating is the easiest way for surface modification. For this propose, dissolved surface-active compounds like polymers or surfactants are utilized, which adsorb strongly at the surface. This can be accomplished by rinsing with a solution of the modifier prior to the analyses or by addition of the modifier to the electrolyte. The successive multiple-ionic-layer approach for dynamic coating was applied to PDMS microfluidic devices by Liu et al. [14]. In this method, polyelectrolyte multilayers are created by exposing a surface to alternating solutions of positively and negatively charged polyelectrolytes. Liu et al. utilized this approach to form polymeric bilayers at PDMS channels with the cationic polymer polybrene followed by a layer of dextrane sulfate as an anionic polymer. Lately, using biomolecules as modifiers attracted increasing attention [15,16]. Thormann and coworkers have reported proteins immobilized on PDMS/AF45-glass channels to reduce adsorption of non-polar molecules and immobilized bioprobes on the surface and perform immunoassays [16]. Chen and coworkers fabricated an albumin-coated PDMS microchip which was used for the separation of dopamine and epinephrine [17]. Recently, the immobilization of DNA and its interaction with some chemical materials had been used in electronic devices, electrochemical sensors and biosensors [18–20]. As is well known, DNA is not only an important biological material due to its genetic function and as a molecular scaffold or template for nanotechnology [21] and nanostructure [22,23], but also an interesting anionic polyelectrolyte consisting of three parts: a phosphate acid group, a basic group (adenine (A), guanine (G), cytosine (C), thymine (T)), and a sugar unit. These units form a well-defined linear helix and repetitive structure by hydrogen bonds between basic groups. This special structure enable DNA be used to make ultrathin films with cationic materials by layer-by-layer (LBL) assembly technique. Shim and coworkers have employed cellulose and DNA to modify a screen-printed electrode for the analysis of neurotransmitters on a glass microchip [24]. However, there is no report on the modification of DNA on the microchannel. In this paper, a stable hydrophilic PDMS microchip is prepared by a simple method for coating microchip capillary channels using the electrostatic LBL assembly technique. This method utilizes a cationic polymer chitosan, coating, followed by a layer of anionic biopolymer DNA to generate and control EOF. Aminophenol isomers, as a group of separation model, were used to evaluate the effect of the functional PDMS microfluidic devices. The surface modification brought the advantages for microfluidic-based separations: generation of stable EOF, enhanced surface hydrophilicity, long lifetime, and improved separation efficiencies.

2. Experimental

2.1. Reagents

Sylgard 184 (PDMS) and curing agent were from Dow Corning (Midland, MI, USA). Carbon fibre ($d = 8 \mu\text{m}$) was purchased from Goodfellow (Oxford, UK). Chitosan (molecular weight 200,000) and 2-morpholinoethanesulfonic acid (MES) were obtained from Sigma–Aldrich (St. Louis, MO, USA). DNA (from calf thymus, 89,370) was purchased from Fluka (Buchs, Switzerland) and used without further purification. Aminophenol isomers, acetic acid and sodium acetate trihydrate were obtained from Shanghai Chemical Reagents Corporation (Shanghai, China). Acetate solution was used as the BGE for the separation of aminophenol isomers. Chitosan (0.05%, w v^{-1}) was dissolved in a 0.4% acetic acid solution and then diluted with water. DNA (0.5 mg mL^{-1}) was prepared by dissolving the calf thymus DNA in 10 mM MES solution and stored at 4°C . All solutions were prepared with doubly distilled water and passed through a $0.22 \mu\text{m}$ cellulose acetate filter (Xinya Purification Factory, Shanghai, China). One millimolar stock solutions of aminophenol isomers were prepared with doubly distilled water before each experiment. Before use, they were diluted with corresponding running buffer to proper concentration. All other reagents were of analytical grade and were used without further purification.

2.2. Fabrication of PDMS/PDMS microchips

The master with a positive relief structure of GaAs for the channels was made using microphtolithographic technique. A cross-type channel of PDMS chip with a 4.0 cm long separation channel (effective separation length, 3.7 cm) and 1.0 cm long injection channel (shown in Fig. 1) and a flat substrate were fabricated from PDMS as the previously described procedure [25]. Briefly, a mixture of elastomer precursor and its curing agent (ratio of 10:1) (sylgard 184) were degassed, poured over the GaAs master, and then cured for 2 h at 70°C . After the replica was peeled from the mold, holes (3 mm diameter) were punched. A flat PDMS substrate (3 mm thick) was obtained via casting and curing the prepolymer mixture in a large flat glass box ($5 \text{ cm} \times 4 \text{ cm}$). The PDMS with microchannels and the PDMS flat were ultrasonically cleaned, subsequently with water, methanol, and water for 10 min, and then dried under an infrared lamp. Finally, they were sealed together to form a reversible PDMS/PDMS microchip. All channels had a maximum depth of $18 \mu\text{m}$. The sampling channel was $30 \mu\text{m}$ in width and the separation channel was $50 \mu\text{m}$ in width.

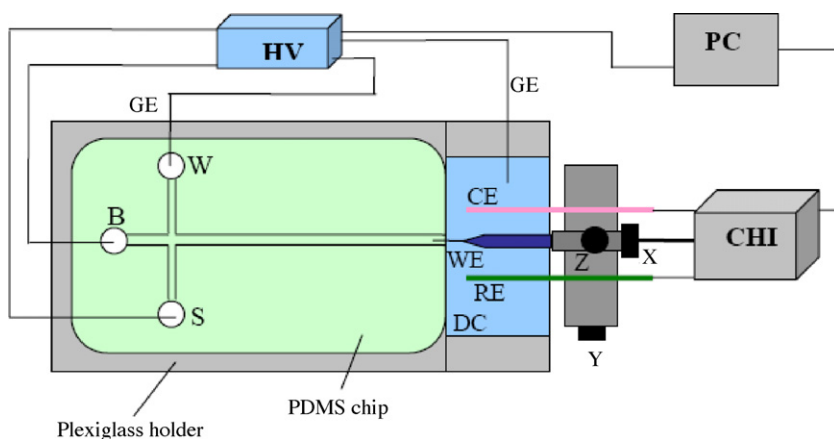


Fig. 1. Schematic diagram of the PDMS microanalysis system. WE: working electrode (the carbon fiber cylindrical electrode); CE: counter electrode (Pt wire); RE: reference electrode (AgCl/Ag); B: running buffer reservoir; S: sample reservoir; W: waste sample reservoir; GE: ground electrode; PC: personal computer; HV: high voltage; CHI: electrochemical workstation; X, Y and Z: adjusting screws in the three dimension adjustor.

2.3. Modification procedure

PDMS channels were modified with chitosan and DNA according to the conventional CE procedures developed by Katayama et al. [26]. Briefly, the channels were rinsed with running buffer and doubly distilled water, respectively, for 10 min each. Once preconditioned, the chitosan solution (pH 5.0, 0.05%, wv⁻¹) was pumped through the microchannels for 10 min by vacuum pump. Then, the DNA (pH 5.0, 500 µg mL⁻¹) solution was pumped through the microchannels and kept for 2 h at 4 °C. Finally, the microchip was flushed with the buffer solution for 5 min. Prior to use, the modified microchip was filled with the buffer solution and stored at 4 °C.

2.4. Characterization measurements of PDMS films

Fourier transformed infrared absorption by total attenuated reflection (ATR-FT-IR) spectra of PDMS films on a wedged ZnSe crystal were recorded using the TENSOR27 spectrometer with a DTGS detector (Bruker, Ettlingen, Germany). A freshly cleaned ZnSe crystal surface was recorded as a reference. All spectra were obtained at 45° angle of incidence for 16 scans with a resolution of 4 cm⁻¹ in the range of 600–4000 cm⁻¹.

2.5. Micro-system arrangement and electrochemical detection

2.5.1. Preparation of single carbon fiber cylindrical electrode

Firstly, a glass capillary with an inner diameter of 0.5 mm was pulled under an alcohol blowtorch to form a fine tip. Then a single carbon fiber with a diameter of 8 µm was carefully inserted into the tip and fixed with epoxy. A copper wire was connected with the carbon fiber through carbon powder at the other end of capillary and then fastened with epoxy. Prior to use, the tip of the carbon fiber was cut with a clean scalpel to form a 2 mm long cylindrical electrode under the microscope (XTS-20, Beijing Tech Instrument Corporation, Beijing, China).

2.5.2. Micro-system arrangement and in-channel electrochemical detection

The microanalysis system is shown in Fig. 1. A PDMS microchip was fixed on a plexiglass holder with a precise three-dimensional system (Shanghai Lianyi Instrument Factory of Optical Fiber and Laser, Shanghai, China) with the precision of ±1 µm in each direction. A working electrode was inserted into the electrode hole on the platform. Here a small amount of silicon grease was used to prevent leaking of the detection cell. The buffer was introduced into the reservoirs and flushed through the channels via vacuum. Detection was performed with a carbon fiber cylindrical electrode, which was activated at constant applied potentials of 1.5 and -1.0 V for 200 s, respectively. Then the end of the carbon fiber was placed in the end of separation channel with a distance of ca. 40 µm from the tip of working electrode to the channel exit under a microscope. An Ag/AgCl reference electrode, a Pt auxiliary and a Pt ground electrode were each placed in the detection cell filled with running buffer. Electrochemical detection was performed using “amperometric *i*-*t* curve” mode with a CHI 660B electrochemical workstation (CHI, Shanghai, China), which was used to provide a constant potential to the detection electrode and to measure the output current. All experiments were performed at room temperature.

2.6. Electrophoresis procedures

A high-voltage power supply, which has an adjustable voltage range of 0–5000 V (Nanjing University, Nanjing, China), was used for supplying high voltage. Parameters such as sampling voltage,

sampling time, separation voltage, and separation time can be set-up and automatically switched via the RS232 communication port of a personnel computer through the program. Before separation experiments the running buffer was introduced directly into the reservoirs and then flushed through the channels under vacuum for several minutes until no bubbles remained in the microchannels. Potentials were then applied to the separation and injection channels for several minutes until the separation and injection currents leveled off. The buffer in sample reservoir was then exchanged with sample solution. Injection of sample into the separation channel was achieved by use of a cross injector. The first injection time must be long enough for the sample to fill the whole injection channel. Data from the first experiment would therefore be ignored because of the long injection time and serious dispersion of the sample into the separation channel. Injection was then performed by applying high voltage of 800 V to the sample reservoir for 4 s through Pt electrodes connected to a high voltage power supply, with the sample waste reservoir grounded, and the other reservoirs floating. When the injection was completed, separation voltage was applied to the buffer reservoir with the detection reservoir grounded, and the other reservoirs floating. The separation current can be monitored in real time.

2.7. Contact angle measurements

A static contact angle measurement was performed on the plate using a JC2000A contact angle analyzer (Shanghai Zhongchen Digital Technic Apparatus Co. Ltd., Shanghai, China) at 25 °C and 60% relative humidity. 3 µL of water droplet was placed on the material with pipette and allowed to rest on the surface for 10 s, and then an image was taken. For each angle reported, at least five sample readings from different surface locations were averaged. The angles reported were reliable to ±2°.

2.8. Measurement of EOF

The EOF measurements were performed using the current monitoring method as the previous literature [27]. Experiments were performed by measuring the current changes. Briefly, the separation channel and detection cell were firstly filled with running buffer. Then the separation and injection sample channels were each rinsed with running buffer for 10 min in sequence. Finally, a diluted buffer (buffer:water = 9:1) was placed in the sample reservoir. Injection was then performed by applying high voltage (800 V) for 4 s. Once the injection was completed, separation voltage of 1000 V was applied and electroosmosis took place, then the lower concentration electrolyte solution migrated from the crossing to the end of the separation channel. The signal of the diluted buffer was monitored at 0 V with a single carbon fiber cylindrical electrode, which was placed in the end of the separation channel. The diluted buffer would lead to an increase in peak current. Migration time of EOF was rapidly obtained. The EOF was calculated according to the equation of $\mu_{\text{eof}} = (L/t)E^{-1}$, where *L* is the effective length of the microchannel, *t* the migration time of the diluted buffer in the separation channel, and *E* is the electric field strength.

3. Results and discussion

3.1. Characterizations of modified PDMS surface

PDMS can adsorb non-polar hydrophobic analytes due to its cross-linked hydrophobic chain, and this is complicated by the fact that PDMS strongly adsorbs biomolecules. A lot of works focused on the resistance to adsorption of biomolecules. On the

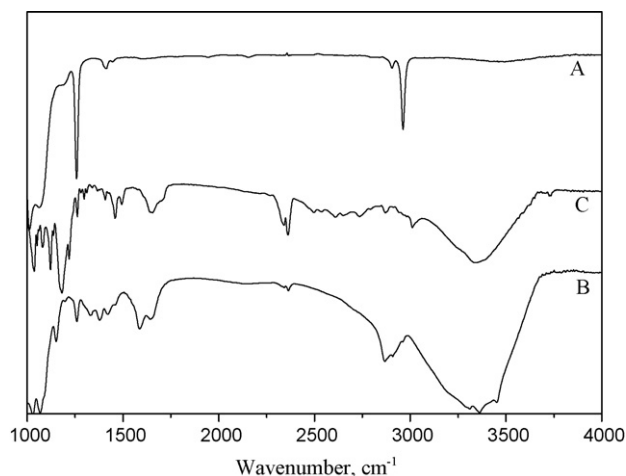


Fig. 2. ATR-FT-IR analysis of the PDMS surface. (A) The native PDMS surface; (B) the chitosan-coated PDMS surface; (C) the chitosan-DNA-coated PDMS surface.

contrary, we just took advantage of this property to produce functional PDMS surface through LBL assembly technique, which is a rich, versatile, and significantly inexpensive approach to the formation of thin films via alternating adsorption of positively and negatively charged species from aqueous solutions, and this method has been applied in many fields such as functional materials and surface modification. In the experiment, DNA was used to modify PDMS microchannels after pre-coating with a layer of chitosan. Biopolymer chitosan ($pK_a = 6.3$) with a lot of primary amino groups is a polysaccharide derived from deacetylation of chitin. Due to the excellent film-forming ability, biocompatibility, non-toxicity, high mechanical strength, cheapness, and susceptibility to chemical modifications, it has been extensively applied for the immobilization of enzymes and the construction of biosensors. The polysaccharide backbone of chitosan was also strongly adsorbed onto the hydrophobic PDMS surface through electrostatic interaction and hydrogen bonding in the acidic media [28]. DNA, as an anionic polymer, has a strong electrostatic interaction with chitosan at low pH ($pH < 7.0$) [29–31]. Therefore, the functional films of chitosan and DNA on the PDMS microfluidic channel surface were constructed using the LBL technique.

Chitosan was positively charged in pH 5.0 acetate buffer, while DNA was negatively charged. Thus, when chitosan was coated on PDMS channel surface, EOF changed its direction from initial cathodic to anodic. Passing DNA solution through the chitosan-coated chip, the EOF reverses its direction again toward the cathode. The changes of EOF suggested that the PDMS surface had been covered by chitosan and DNA. To further demonstrate chitosan and DNA that had been coated on the PDMS surface, ATR-FT-IR experiment was conducted. Fig. 2 shows ATR-FT-IR spectra of the native PDMS, chitosan-coated PDMS and chitosan-DNA-coated PDMS. Compared with native PDMS (curve A), curve B clearly shows that the PDMS surface was coated with chitosan. For the chitosan-DNA-coated PDMS surface, the peak at 1219 cm^{-1} refers to the $\text{CH}_2\text{—O—P—O}$ phosphate group. The chitosan-DNA complex results in the intensity increase or the appearance of H-bonded O—H stretching vibration as well as an asymmetrical PO_2^- vibration at 1182 cm^{-1} , which indicated that DNA had been successfully assembled on the chitosan-coated PDMS surface.

3.2. Hydrophilicity of modified PDMS chip

One of the primary goals of this preparation is to generate hydrophilic channel wall surfaces. The hydrophilicity of the

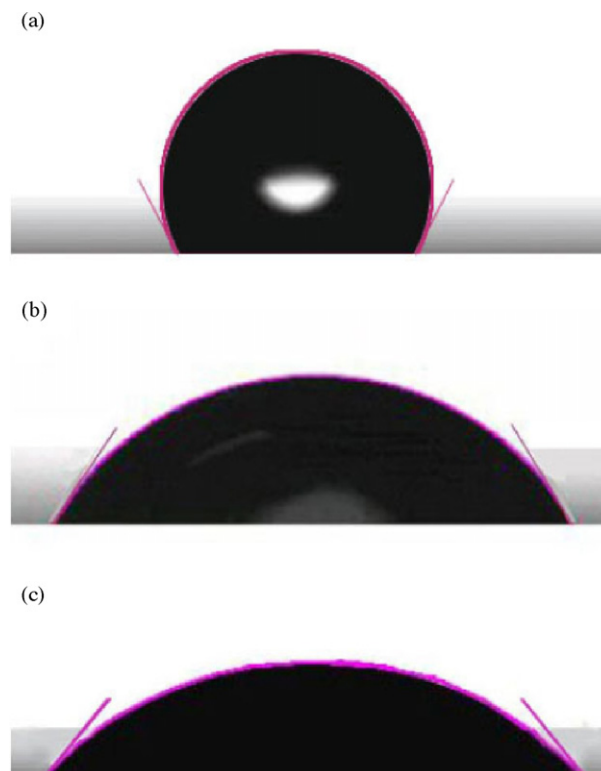


Fig. 3. The contact angle on the (a) native PDMS plate surface; (b) chitosan-DNA modified PDMS plate surface; (c) glass plate.

walls was assessed using water contact angle measurements on the chitosan-DNA modified PDMS plate. Fig. 3 shows the results of contact angle measurements. The initial water contact angles measured on the native PDMS and glass were 115° and 44.5° , respectively. The value for the modified PDMS was 55.5° . The difference of 59.5° between native PDMS and modified PDMS chips indicated that the modified surface was more hydrophilic than native PDMS and close to that of glass.

3.3. EOF of modified PDMS chip

EOF is a useful parameter to investigate the surface modification. Adsorbed molecules directly affect the surface charge density and consequently change the zeta potential, which is necessary for the generation of EOF. The chitosan-DNA-coated PDMS surface resulted in an increase in surface charges and EOF. Fig. 4 shows the relationship of EOF with the buffer pH on the native and coated microchips in 20 mM acetate (pH ranged from 3.5 to 6.5), respectively. The EOF increased sharply from pH 3.5 to 4.5 in the modified chip, and then leveled off in the pH range of 4.5–6.5. Under the same ionic strength, the EOF of the modified microchip was higher than that of the native one, which reflected more surface charges after DNA coating than that of the native one. At pH 5.0 (20 mM acetate), EOF increased from $(1.28 \pm 0.14) \times 10^{-4}\text{ cm}^2\text{ V}^{-1}\text{ s}^{-1}$ ($n=5$, 95% confidence limit) in the native channel to $(4.02 \pm 0.05) \times 10^{-4}\text{ cm}^2\text{ V}^{-1}\text{ s}^{-1}$ ($n=5$, 95% confidence limit) in the modified channel. Since EOF of native PDMS is greatly dependent on the ionic strength and pH of running buffer [32–34], it is unstable and difficult to be controlled. After modification with chitosan-DNA film, EOF became more stable. The RSD of EOF for native PDMS microchip was 4.3% ($n=5$). On chitosan-DNA-coated chips, RSD of EOF was only 0.4% ($n=5$). The reason for higher reproducibility can be contributed to that hydrophilic char-

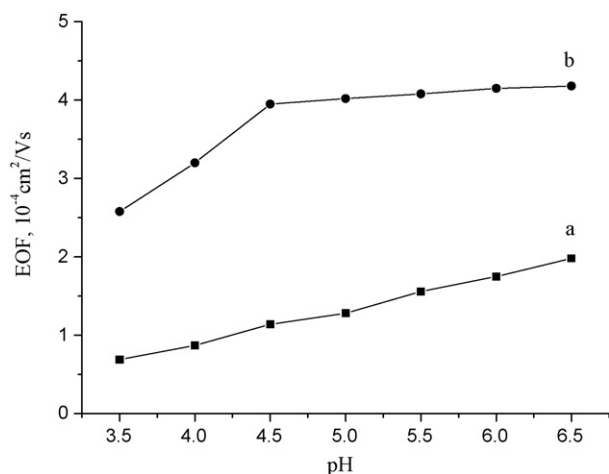


Fig. 4. Effect of pH on EOFs in 20 mM acetate buffer on the native and modified PDMS microchips. (a) Native PDMS microchip; (b) chitosan–DNA-coated PDMS microchip.

acter of chitosan and DNA reduced the proclivity for hydrophobic interaction, leading to significantly lower nonspecific adsorption of analytes.

3.4. Electrophoresis separation of aminophenol isomers

Fig. 5 shows the electropherograms of the separation of aminophenol isomers on native and modified PDMS microchips, respectively. As shown in Fig. 5A, the adsorption of the aminophenol isomers results in lower peak currents and obvious peak broad in the native PDMS microchip. It was observed that migration times gradually increased accompanied with the decrease of peak currents when run numbers increased. These phenomena could be ascribed to the hydrophobic interaction between PDMS and hydrophobic groups of analytes. While PDMS microchannel was modified with chitosan–DNA, the adsorption of analytes was greatly decreased, the separation efficiency and reproducibility were remarkably improved, and the peak shapes of aminophenol isomers became sharper and more symmetric. Furthermore, the separation time dramatically decreased from 140 s on the native chip to 60 s on the coated chip. The theoretical plate numbers of *p*-,

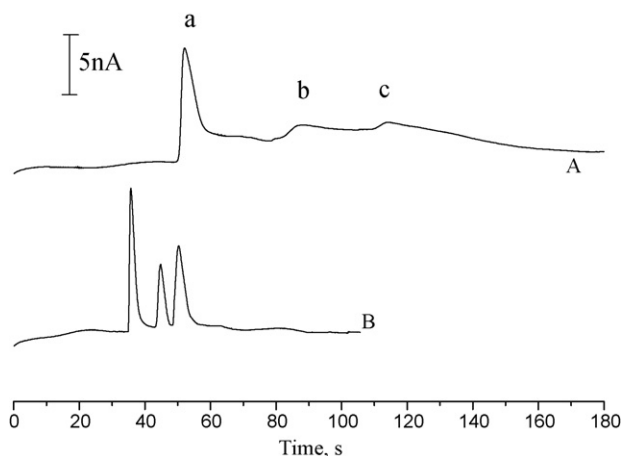


Fig. 5. Electropherograms showing the separations of 200 μM *p*-aminophenol (a), 200 μM *o*-aminophenol (b), and 200 μM *m*-aminophenol (c). (A) Native PDMS microchip; (B) chitosan–DNA-coated PDMS microchip. Conditions: Acetate buffer (20 mM, pH 5.0) as an electrophoresis buffer; sample injection at +800 V for 4 s; separation voltage, +900 V; detection at +1.0 V.

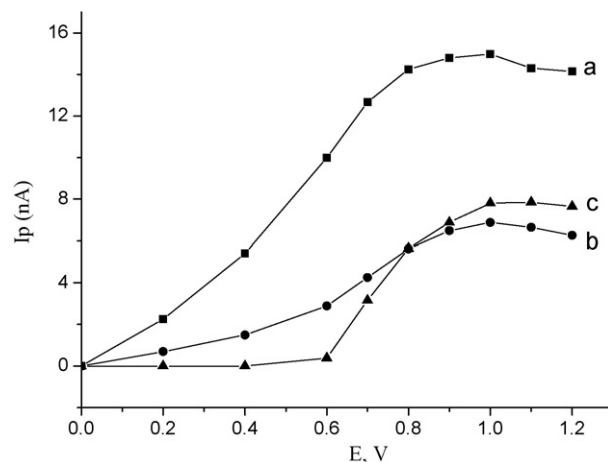


Fig. 6. Hydrodynamic voltammograms for aminophenol isomers on chitosan–DNA-coated PDMS microchip. (a) 200 μM *p*-aminophenol; (b) 200 μM *o*-aminophenol; (c) 200 μM *m*-aminophenol. Other conditions were as in Fig. 5.

o-, and *m*-aminophenol were calculated to be 74,021, 92,658 and 60,552 N m^{-1} for the modified PDMS microchip, which was chosen as an example, and 2714, 3102 and 3292 N m^{-1} for the native PDMS microchip. The peak heights of *o*-, and *m*-aminophenol in the chitosan–DNA modified PDMS microchip were 5.8 and 8 times that of the native ones, respectively. Therefore, not only was the separation time greatly reduced but also high sensitivity and separation efficiency were obtained in the chitosan–DNA modified PDMS microchips.

3.5. Optimization of the electrophoresis conditions

3.5.1. Electrochemical detection

Electrochemical detection would be a good candidate coupled with micro total analysis systems (μ -TAS) for its inherent miniaturization and high sensitivity. Here we use an in-channel amperometric detection mode for microchip with a single carbon fibre cylindrical electrode directly mounted in the end of separation channel. To obtain the optimum detection potential, the hydrodynamic voltammograms were investigated by setting the detection potential from 0 to 1.2 V (Fig. 6). As can be seen in Fig. 6, the three compounds displayed similar curves. The peak current of *p*-aminophenol increased rapidly with the increase in the detection potential until +1.0 V. From +0.2 to +1.0 V the peak current of *o*-aminophenol increased, and the same trend was observed with *m*-aminophenol from +0.6 to +1.0 V. When the applied potential was over +1.0 V (vs Ag/AgCl), the baseline current greatly increased, accompanied with the decrease in the peak currents. Therefore, +1.0 V (vs Ag/AgCl) was selected as the detection potential in this case, where the background current was relatively lower and the S/N ratio was the highest.

3.5.2. Effect of buffer concentration

Based on the previous reports [35,36], acetate (pH 5.0) was chosen as the running buffer. It was found that DNA would not be denatured and desorbed at this pH value. The effect of buffer concentration on the separation efficiency of aminophenol isomers was examined by varying the concentration from 10 to 30 mM, at a fixed pH of 5.0. As shown in Fig. 7, with the increase of the buffer concentration, the corresponding resolutions of the three aminophenol isomers increased, coupled with the increase of migration times. Resolutions were 3.02 for *p*-aminophenol and *o*-aminophenol and 0.87 for *o*-aminophenol and *m*-aminophenol in 10 mM acetate on chitosan–DNA-coated PDMS microchips. When

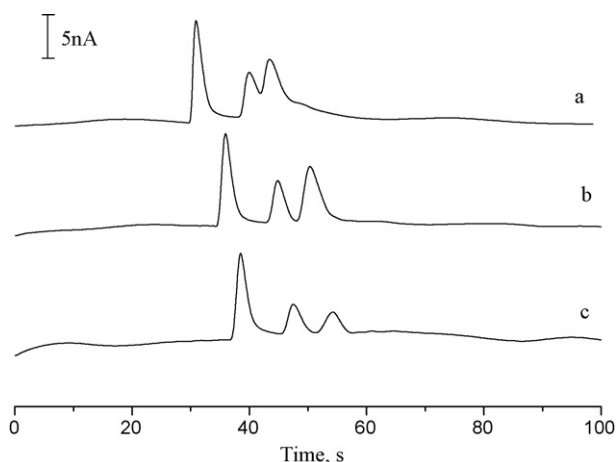


Fig. 7. Electropherograms of 200 μ M *p*-aminophenol, *o*-aminophenol and *m*-aminophenol using the different concentration of acetate buffer on the coated PDMS microchip. (a) 10 mM; (b) 20 mM; (c) 30 mM. Other conditions were as in Fig. 5.

concentration increased to 20 mM, the three aminophenol isomers realized baseline separation, and resolutions increased to 3.15 and 1.58, respectively. While the concentration became over 30 mM, resolutions slightly increased, but the peak currents greatly decreased with the increase of baseline noise. This is because higher concentration of the running buffer usually leads to a slower EOF and an increased Joule heat, and accordingly induces a lower efficiency, sensitivity and stability. Thus, in the experiment, 20 mM acetate was chosen.

3.5.3. Effects of injection time and injection voltage

A sample was injected into the separation channel using a simple crossing mode. The length of the sample plug which greatly influences the separation efficiency can be controlled by injection time and injection voltage. Generally, a high injection voltage results in the desired rectangular shape of the sample plug at the intersection of the cross-channel, and therefore a high separation efficiency will be obtained [37]. However, too high injection voltage will result in higher Joule heat and bubbles in the channel, which will interrupt injection. Here, 800 V was chosen as the optimum injection voltage. The influence of injection time on the responses of aminophenol isomers was also investigated. It is obviously that the peak currents of aminophenol isomers increased greatly with the increase of injection time in the range from 1 to 4 s. However, when injection time was over 4 s, the peak currents increased slowly and the half-peak widths increased quickly. Considering the sensitivity and efficiency, an injection time of 4 s was chosen.

3.5.4. Effect of separation voltage

Since the electrochemical detection principle is based on the coupling of separation electric field on the electrochemical detector, the influence of separation voltage on detection is a major factor in improving detection sensitivity. The influence of separation voltage on the amperometric responses and separation efficiency is shown in Fig. 8. As expected, increasing the separation voltage from 700 to 1200 V (a–f) dramatically decreased the migration time for all three compounds, from 45.4 to 24.6 s (*p*-aminophenol), from 54.5 to 30.6 s (*o*-aminophenol) and from 61.2 to 33.3 s (*m*-aminophenol). In the experiment, the peak currents increased gradually with the voltage between 700 and 900 V and decreased rapidly at higher voltage. The resolution between the *o*- and *m*-aminophenol decreased from 1.65 to 0.78 upon raising the separation voltage between 700 and 1200 V. Also shown (as inset) is the effect of separation voltage upon separation efficiency,

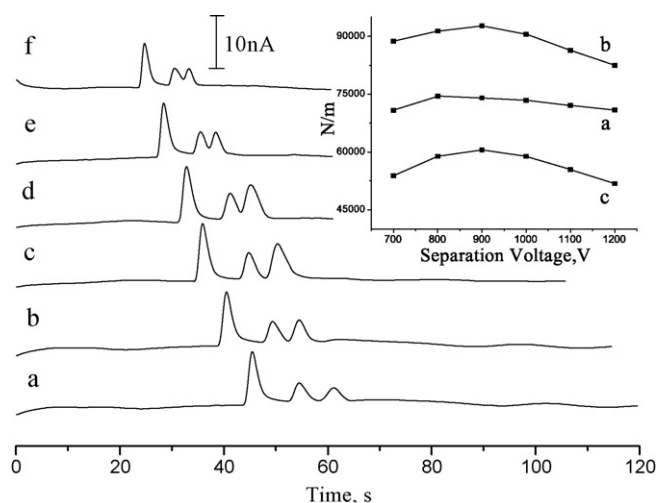


Fig. 8. Electropherograms of aminophenol isomers at different separation voltages: (a) 700 V, (b) 800 V, (c) 900 V, (d) 1000 V, (e) 1100 V and (f) 1200 V. *p*-aminophenol: 200 μ M; *o*-aminophenol: 200 μ M; *m*-aminophenol: 200 μ M. Also shown (as inset) are the resulting plots of plate numbers for (a) *p*-aminophenol; (b) *o*-aminophenol; (c) *m*-aminophenol. Other conditions were as in Fig. 5.

i.e., on theoretical plate number (the number of plates per meter, $N m^{-1}$). For *p*-, *o*-, and *m*-aminophenol, the theoretical plate numbers increased upon the increase in the separation voltage from 700 to 900 V on chitosan–DNA-coated microchip, and then decreased rapidly. The theoretical plate numbers reached maximum values of 74,021 $N m^{-1}$ for *p*-aminophenol at the separation voltage of 800 V, 92,658 $N m^{-1}$ for *o*-aminophenol, and 60,552 $N m^{-1}$ for *m*-aminophenol at 900 V, respectively. In addition, higher separation voltage had a great effect on the background current. Flat baselines were observed using relatively lower separation voltages. Taking into account the amperometric responses, separation efficiency, resolution and separation time, 900 V was chosen in this experiment.

3.6. Reproducibility and stability

It is important to study reproducibility and stability of the modification. Under the optimal condition, the reproducibility on the modified microchips can be investigated according to RSD of EOF, migration time and peak current [38]. RSDs of EOF were 0.4% for run-to-run, 0.9% for day-to-day and 1.5% for chip-to-chip ($n=5$), respectively. Table 1 shows RSDs of migration time and peak current of aminophenol isomers on the coated microchips. The results demonstrate that good reproducibility was achieved on the chitosan–DNA-coated microchips. In addition, more than 50 runs with good resolution were performed continuously. Furthermore, the coated channels also displayed long-term stability. Generally, the native PDMS microchips need to be split into two flats and cleaned with ethanol and water everyday, since the stability become poor due to the adsorption of analytes. While the chitosan–DNA modified chips can be used for more than two weeks, given that they were filled with the running buffer and stored at 4 °C when not in use.

3.7. Linear range and detection limit

The chitosan–DNA modified PDMS microchip displayed well-defined concentration dependence. Under the optimized conditions, the linear range for *p*-aminophenol was from 10 to 600 μ M with the correlation coefficients (r) of 0.9956. The linear ranges were both 25–600 μ M for *o*-aminophenol and *m*-aminophenol,

Table 1The reproducibility of migration time and peak current on the modified microchips ($n = 5$).

	RSD (%) of migration time			RSD (%) of peak current		
	Run-to-run	Day-to-day	Chip-to-chip	Run-to-run	Day-to-day	Chip-to-chip
<i>p</i> -aminophenol	0.4	0.8	2.4	1.5	2.3	2.1
<i>o</i> -aminophenol	0.5	1.0	3.2	2.1	2.7	2.9
<i>m</i> -aminophenol	0.7	1.1	2.8	2.9	3.4	3.7

Table 2Determination of aminophenol isomers in hair dye ($n = 3$).

Analyte	MCE				HPLC
	Sample ($\mu\text{g/g}$)	Added ($\mu\text{g/g}$)	Measured ($\mu\text{g/g}$)	Recovered (%)	Sample ($\mu\text{g/g}$)
<i>p</i> -aminophenol	110 \pm 3.5	200	341 \pm 2.2	110	130 \pm 1.2
<i>o</i> -aminophenol	47.0 \pm 4.3	200	220 \pm 3.1	89	41.0 \pm 1.4
<i>m</i> -aminophenol	1400 \pm 2.6	200	1520 \pm 2.3	95	1700 \pm 0.8

coupled with the correlation coefficients of 0.9994 and 0.9975, respectively. The detection limits for *p*-, *o*-, and *m*-aminophenol were 1.6, 4.7 and 2.5 μM ($S/N = 3$) on the coated microchips, respectively.

3.8. Application

The established method of microchip capillary electrophoresis (MCE) was applied to analyze for commercial permanent hair dye by standard addition analysis. Commercial permanent hair dye was collected from retail stores locally. A precisely weighed quantity (0.2 g) of hair dye product was dissolved in 10 ml of methanol and sonicated for 1 min. This solution was diluted with running buffer and filtered through a 0.22 μm membrane filter. The quantitative analytical results are summarized in Table 2. The hair dye sample was also studied by HPLC (Agilent1200, Santa Clara, CA, USA), which was carried out on an Eclipse C_{18} column (5 μm , 250 mm \times 4.6 mm i.d.). The mobile phase was methanol (10 vol%)–0.1 M acetate buffer pH 4.5 (90 vol%) and was delivered at a flow rate of 0.8 mL min^{-1} . Signal was monitored by UV absorbance at a wavelength of 280 nm. The results from HPLC are listed in Table 2 too. The results from HPLC and MCE showed no significant difference, which showed that the results obtained by the present method are in agreement with those obtained by HPLC. Furthermore, this microsystem only requires 1 min of analysis time, while HPLC needs 15 min to determine aminophenol isomers. Therefore, this cheap and rapid microsystem could be used for the quantitative detection of trace aminophenol isomers in real samples.

4. Conclusions

A simple and efficient protocol for improving EOF and enhancing the separation efficiency based on PDMS surface modification with chitosan and DNA using the LBL assembly technique has been established. With the strategy, aminophenol isomers were successfully separated within 1 min on the chitosan–DNA-coated PDMS microchips, and the application in testing hair dye samples was demonstrated. This surface modification method offers an effective means for preparing biocompatible and hydrophilic PDMS microfluidic chip, and shows an excellent potential for using microfluidic devices in more widespread applications.

Acknowledgements

This work was supported by the Natural Science Foundation of China (Nos. 20605010, 20865003 and 20805023), the Natural Sci-

ence Foundation of Jiangxi Province of China (Nos. 0520075 and 0620039) and the Program for Innovative Research Team of Nanchang University.

References

- [1] D.J. Harrison, K. Fluri, K. Seiler, Z. Fan, C.S. Effenhauser, A. Manz, *Science* 267 (1993) 895.
- [2] W.H. Huang, W. Cheng, Z. Zhang, D.W. Pang, Z.L. Wang, J.K. Cheng, D.F. Cui, *Anal. Chem.* 76 (2004) 483.
- [3] H. Hisamoto, Y. Nakashima, C. Kitamura, S. Funano, M. Yasuoka, K. Morishima, Y. Kikutani, T. Kitamori, S. Terabe, *Anal. Chem.* 76 (2004) 3222.
- [4] S.K. Sia, G.M. Whitesides, *Electrophoresis* 24 (2003) 3563.
- [5] M.A. Roberts, J.S. Rossier, P. Bercier, H. Girault, *Anal. Chem.* 69 (1997) 2035.
- [6] L. Martynova, L.E. Locascio, M. Gaitan, G.W. Kramer, R.G. Christensen, W.A. MacCrehan, *Anal. Chem.* 69 (1997) 4783.
- [7] S.L.R. Barker, M.J. Tarlov, H. Canavan, J.J. Hickman, L.E. Locascio, *Anal. Chem.* 72 (2000) 4899.
- [8] J.C. McDonald, G.M. Whitesides, *Acc. Chem. Res.* 35 (2002) 491.
- [9] D.C. Duffy, J.C. McDonald, O.J.A. Schueller, G.M. Whitesides, *Anal. Chem.* 70 (1998) 4974.
- [10] J.M.K. Ng, I. Gitlin, A.D. Stroock, G.M. Whitesides, *Electrophoresis* 23 (2002) 3461.
- [11] A.M. Spehar, S. Koster, V. Linder, S. Kulmala, N.F. de Rooij, E. Verpoorte, H. Sigrist, W. Thormann, *Electrophoresis* 24 (2003) 3674.
- [12] N.A. Lacher, N.F. de Rooij, E. Verpoorte, S.M. Lunte, J. Chromatogr. A 1004 (2003) 225.
- [13] H. Makamba, J.H. Kim, K. Lim, N. Park, J.H. Hahn, *Electrophoresis* 24 (2003) 3607.
- [14] Y. Liu, J.C. Fanguy, J.M. Bledsoe, C.S. Henry, *Anal. Chem.* 72 (2000) 5939.
- [15] K.S. Phillips, Q. Cheng, *Anal. Chem.* 77 (2005) 327.
- [16] V. Linder, E. Verpoorte, W. Thormann, N.F. de Rooij, H. Sigrist, *Anal. Chem.* 73 (2001) 4181.
- [17] A.J. Wang, J.J. Xu, H.Y. Chen, *J. Chromatogr. A* 1107 (2006) 257.
- [18] C.G. Siontorou, D.P. Nikolelis, U.J. Krull, *Anal. Chem.* 72 (2000) 180.
- [19] A.B. Steel, T.M. Herne, M.J. Tarlov, *Anal. Chem.* 70 (1998) 4670.
- [20] Y.D. Jin, Y. Shao, S.J. Dong, *Langmuir* 19 (2003) 4771.
- [21] E. Winfree, F.R. Liu, L.A. Wenzler, N.C. Seeman, *Nature* 394 (1998) 539.
- [22] C.A. Mirkin, R.L. Letsinger, R.C. Mucic, J.J. Storhoff, *Nature* 382 (1996) 607.
- [23] J. Richter, R. Seidel, R. Kirsch, M. Mertig, W. Pompe, J. Plaschke, H.K. Schackert, *Adv. Mater.* 12 (2000) 507.
- [24] M. Johirul, A. Shiddiky, R.E. Kim, Y.B. Shim, *Electrophoresis* 26 (2005) 3043.
- [25] J.D. Qiu, P.F. Hu, R.P. Liang, *Anal. Sci.* 23 (2007) 1409.
- [26] H. Katayama, Y. Ishihama, N. Asakawa, *Anal. Chem.* 70 (1998) 5272.
- [27] J.J. Xu, N. Bao, X.H. Xia, Y. Peng, H.Y. Chen, *Anal. Chem.* 76 (2004) 6902.
- [28] A.J. Wang, J.J. Xu, H.Y. Chen, *J. Chromatogr. A* 1147 (2007) 120.
- [29] W.D. Cao, C.J. Easley, J.P. Ferrance, J.P. Landers, *Anal. Chem.* 78 (2006) 7222.
- [30] H.Q. Mao, K. Roy, V.L. Troung-Le, K.A. Janes, K.Y. Lin, Y. Wang, J.T. August, K.W. Leong, *J. Control. Rel.* 70 (2001) 399.
- [31] A. Bozkir, O.M. Saka, *Drug Deliv.* 11 (2004) 107.
- [32] G. Ocivirk, M. Munroe, T. Tang, R. Oleschuk, K. Westra, D.J. Harrison, *Electrophoresis* 21 (2000) 107.
- [33] L.E. Locascio, C.E. Perso, C.S. Lee, *J. Chromatogr. A* 857 (1999) 275.
- [34] Z.J. Sui, J.B. Schlenoff, *Langmuir* 19 (2003) 7829.
- [35] M. Pumera, J. Wang, E. Grushka, R. Polsky, *Anal. Chem.* 73 (2001) 5625.
- [36] Y. Xiao, K. Wang, X.D. Yu, J.J. Xu, H.Y. Chen, *Talanta* 72 (2007) 1316.
- [37] N.A. Patanker, H.H. Hu, *Anal. Chem.* 70 (1998) 1870.
- [38] F.B. Erim, A. Cifuentes, H. Poppe, J.C. Kraak, *J. Chromatogr. A* 708 (1995) 356.



Dispersive liquid–liquid microextraction preconcentration of palladium in water samples and determination by graphite furnace atomic absorption spectrometry

Pei Liang*, Ehong Zhao, Feng Li

Key Laboratory of Pesticide & Chemical Biology of Ministry of Education, College of Chemistry, Central China Normal University, Wuhan 430079, PR China

ARTICLE INFO

Article history:

Received 7 August 2008

Received in revised form 15 October 2008

Accepted 21 October 2008

Available online 31 October 2008

Keywords:

Dispersive liquid–liquid microextraction
Palladium

Graphite furnace atomic absorption
spectrometry
Water samples

ABSTRACT

A new method for the determination of palladium was developed by dispersive liquid–liquid microextraction preconcentration and graphite furnace atomic absorption spectrometry detection. In the proposed approach, diethyldithiocarbamate (DDTC) was used as a chelating agent, and carbon tetrachloride and ethanol were selected as extraction and dispersive solvent. Some factors influencing the extraction efficiency of palladium and its subsequent determination, including extraction and dispersive solvent type and volume, pH of sample solution, concentration of the chelating agent and extraction time, were studied and optimized. Under the optimum conditions, the enrichment factor of this method for palladium reached at 156. The detection limit for palladium was 2.4 ng L^{-1} (3σ), and the relative standard deviation (R.S.D.) was 4.3% ($n = 7$, $c = 1.0 \text{ ng mL}^{-1}$). The method was successfully applied to the determination of trace amount of palladium in water samples.

© 2008 Elsevier B.V. All rights reserved.

1. Introduction

The importance of the palladium (Pd) metal has grown many folds in recent years due to the increasing applications for the production of dental and medicinal devices, jewellery, automobile and catalytic converters [1]. Although the benefits of car catalysts are indisputable, the emission of Pd into the environment is largely associated with the production and recycling of catalytic converters in the metal finishing industry as well as the operation of vehicle catalysts. Some of Pd compounds have been reported as potential health risks to humans, causing asthma, allergy, rhino conjunctivitis and other serious health problems [2,3]. The development of analytical methods for the determination of Pd is important for the effective monitoring of pollution levels of this metal in the environment.

Although the concentration of Pd in different compartments of environment continuously increases, it is still at the level of ng g^{-1} (or ng mL^{-1}). Numerous interactions between the analyte and the matrix constituents can significantly influence both the limit of detection and the accuracy of the analytical method. The direct determination of Pd in environmental samples by atomic spectrometric techniques, e.g. graphite furnace atomic

absorption spectrometry (GFAAS) or inductively coupled plasma mass spectrometry (ICP-MS), is usually difficult, and an initial sample pretreatment, such as preconcentration of the analyte and matrix separation, is often necessary [4]. Several methods have been reported for the separation and preconcentration of metal ions, such as coprecipitation [5,6], liquid–liquid extraction (LLE) [7,8], solid-phase extraction (SPE) [9–14] and cloud point extraction (CPE) [15,16], but the disadvantages such as time-consuming, unsatisfactory enrichment factors, large organic solvents and secondary wastes, limit their applications. In recent years, liquid-phase microextraction (LPME) has been developed as a solvent-minimized sample pretreatment procedure since it is inexpensive and minimal exposure to toxic organic solvents [17]. The combination of LPME with electrothermal vaporization inductively coupled plasma atomic emission spectrometry/mass spectrometry (ETV-ICP-AES/MS) or GFAAS has been established as an effective method for the determination of trace elements [18–21]. However, LPME method suffers from some disadvantages such as the fast stirring would tend to format air bubble [22], time-consuming and equilibrium could not be attained after a long time in most cases [23].

In order to overcome the problems, a novel modality of LPME termed as dispersive liquid–liquid microextraction (DLLME), which is based on a ternary component solvent system like homogeneous liquid–liquid extraction and cloud point extraction, was proposed recently [24]. In this method, the appropriate mixture of extraction

* Corresponding author. Fax: +86 27 67867961.

E-mail address: liangpei@mail.ccnu.edu.cn (P. Liang).

solvent and dispersive solvent is injected into an aqueous sample rapidly by syringe, and a cloudy solution is formed. The analyte in the sample is extracted into the fine droplets of extraction solvent. After extraction, phase separation is performed by centrifugation, and the enriched analyte in the sediment phase is determined by chromatography or spectrometry methods. The advantages of the DLLME method are simplicity of operation, rapidity, low cost, high recovery and enrichment factors. This method has been successfully applied for the preconcentration of organic and inorganic species in environmental samples [25–31].

The aim of this work is to combine DLLME with GFAAS and develop a new method for the determination of Pd. In this method, diethyldithiocarbamate (DDTC), which reacts with metallic ions forming a very stable complex and has found numerous applications in trace element separation and preconcentration [32–34], was selected as the chelating reagent. The factors influencing DLLME extraction and GFAAS determination were systematically studied. The method was successfully applied to determine of trace amount of Pd in water samples.

2. Experimental

2.1. Apparatus

A TBS-990 atomic absorption spectrophotometer (Beijing Purkinge General Instrument Co. Ltd, Beijing, China) with a deuterium background correction and a GF990 graphite furnace atomizer system was used. A palladium hollow-cathode lamp operated at 2.0 mA was used as radiation source. Measurements were carried out in the integrated absorbance (peak area) mode at 247.6 nm, using a spectral bandwidth of 0.4 nm. The heating program employed for palladium determination was given as follows: the drying temperature was 120 °C, ramp 15 s, hold 10 s; the pyrolysis temperature was 700 °C, ramp 10 s, hold 10 s; the atomization temperature was 1800 °C, 3 s; the clean temperature was 2100 °C, 4 s. Purge gas flow-rate inside the tube was 200 mL min⁻¹. The pH values were measured with a Mettler Toledo 320-S pH meter (Mettler Toledo Instruments CO. LTD, Shanghai, China). A Model 0412-1 centrifuge (Shanghai Surgical Instrument Factory, Shanghai, P.R. China) was used to accelerate the phase separation.

2.2. Standard solution and reagents

Stock standard solution (100 µg mL⁻¹) of Pd was obtained from the National Institute of Standards (Beijing, China). Working standard solutions were obtained by appropriate dilution of the stock standard solution. The solution of DDTC was prepared by dissolving appropriate amount of DDTC (AR, Shanghai Chemistry Reagent Company, Shanghai, China) in ethanol. All other reagents used were of the highest available purity and of at least analytical reagent grade. Doubly distilled water was used throughout. Pipettes and vessels in the experiments were kept in 10% nitric acid for at least 24 h and subsequently washed four times with double distilled water.

2.3. Dispersive liquid–liquid microextraction procedure

Aliquots of 5.0 mL sample solution containing Pd and 0.10 mg mL⁻¹ DDTC was adjusted to pH 1.0 and placed in a 10 mL screw cap glass test tube with conic bottom. 0.5 mL of ethanol (disperser solvent) containing 40 µL of carbon tetrachloride (extraction solvent) was injected rapidly into the sample solution by using 1.00 mL syringe. A cloudy solution (water, ethanol and carbon tetrachloride) was formed in the test tube. In this step, the complex of Pd

with DDTC was extracted into the fine droplets of carbon tetrachloride. Then, the solution was centrifuged at 3000 rpm for 5 min, and the dispersed fine droplets of carbon tetrachloride were deposited at the bottom of conical test tube (about 25 µL). 20 µL of the sediment phase was removed using a 50-µL microsyringe (minimum scale of 1 µL) and injected into the GFAAS for analysis.

Calibration was performed against aqueous standards submitted to the same DLLME procedure. A blank submitted to the same procedure described above was measured parallel to the sample and calibration solutions. The enrichment factor was calculated as the ratio of the analytical signal of Pd obtained after and before extraction.

2.4. Sample preparation

Portions (10.0 g) of geological standard reference materials (GBW07291 peridotite, provided by the institute of Geophysical and Geochemical Prospecting, Langfang, P.R. China) were roasted in a temperature of 600 °C for 1 h. Then the sample was placed in a PTFE vessel, treated with 20 mL of concentrated HCl and 10 mL of concentrated HNO₃, and digested under pressure at a temperature of 150 °C for 3 h. The sample was evaporated with two portions of 5 mL concentrated hydrofluoric acid to remove silica. Finally, 5 mL of concentrated HCl were added and the solution was evaporated almost to dryness. The residue was dissolved in 0.1 mol L⁻¹ HCl, and the solution was made up to 100 mL with distilled water after the adjustment of pH to 1.0.

River water sample was collected from Yangtze River (Wuhan, P.R. China). Lake water sample was collected from East Lake (Wuhan, P.R. China). Tap water sample was freshly collected from our laboratory, after allowing the water to flow for 5 min. All water samples were filtered through a 0.45-µm membrane filter and analyzed as soon as possible after sampling.

3. Results and discussion

3.1. Effect of extraction solvent and its volume

The type of extraction solvent used in DLLME is an essential consideration for efficient extraction. It should be higher density than water, high extraction capability of the interested compounds and low solubility in water. Chloroform (CHCl₃), carbon disulfide (CS₂) and carbon tetrachloride (CCl₄) were studied as extraction solvent using 0.5 mL of ethanol as the dispersive solvent. Because the solubility of the extraction solvents in water was different, 65, 55 and 40 µL of CHCl₃, CS₂ and CCl₄ were used to obtain 25 µL of the sediment phase at the bottom of the test tube. The obtained enrichment factors were found to be 82, 118 and 156 for CHCl₃, CS₂ and CCl₄ as extraction solvents, respectively. On the other hand, CHCl₃ formed an unstable cloudy solution, and the sediment phase of CS₂ was difficult to be removed by microsyringe. Therefore, CCl₄ was chosen as the extraction solvent in the experiment.

In order to examine the effect of the extraction solvent volume, different volume of CCl₄ (40, 50, 60, 70 and 80 µL) were used as extraction solvent to the same DLLME procedure. By increasing the volume of CCl₄ from 40 to 80 µL, the enrichment factor decreased from 156 to 68, because the volume of the sediment phase increased from 25 to 65 µL. Thereby, 40 µL CCl₄ was used as extraction solvent in the subsequent experiments.

3.2. Effect of type and volume of the disperser solvent

For DLLME method, the dispersive solvent should be miscible with both water and the extraction solvent. Therefore, acetonitrile,

acetone, ethanol and methanol were tested as the dispersive solvent. The effect of these solvents on the extraction efficiency of DLLME was investigated using 0.5 mL of each solvent containing 40 μL of CCl_4 as the extraction solvent. The enrichment factors were 148, 152, 156 and 155 for acetonitrile, acetone, ethanol and methanol, respectively. The results indicate there was no significant statistical difference (*t*-test) between different dispersive solvents. Ethanol was selected for the following experiments due to its less toxicity.

The effect of the volume of ethanol on the extraction efficiency was also examined. To obtain the optimized volume of ethanol, various experiments were performed using different volumes of ethanol (0.40, 0.50, 0.60, 0.70 and 0.80 mL) containing 35, 40, 43, 45 and 48 μL CCl_4 , respectively. It was necessary to change the volume of CCl_4 by changing the volume of ethanol to obtain the constant volume of the sediment phase (25 μL). The result showed that the enrichment factor increased with the increase of the volume of ethanol to 0.50 mL. Reduction in the enrichment factor was observed after the volume of ethanol exceeded 0.50 mL. At low volume, ethanol could not disperse CCl_4 properly and cloudy solution was not formed completely. Reversely, at high volume, the solubility of complex in water increased by the increase of the volume of ethanol. Finally, 0.50 mL ethanol was chosen as the optimum volume.

3.3. Effect of pH

The pH of the sample solution is one of the important factors affecting the formation of complexes and the subsequent extraction. The effect of pH on the DLLME extraction of Pd was studied in the pH range of 0–6. As can be seen in Fig. 1, the highest signal intensity of Pd was obtained at pH 1.0. Therefore, pH 1.0 was selected for the further study.

3.4. Effect of the DDTC concentration

The influence of the DDTC concentration on the DLLME extraction of Pd was evaluated in the concentration range of 0.02–0.2 mg mL^{-1} . The results showed that the signal of Pd was increased with the increase of DDTC concentration up to 0.05 mg mL^{-1} , and then remained constant. In this study, a DDTC concentration of 0.1 mg mL^{-1} was chosen to account for other extractable species that potentially interference with the assaying of Pd.

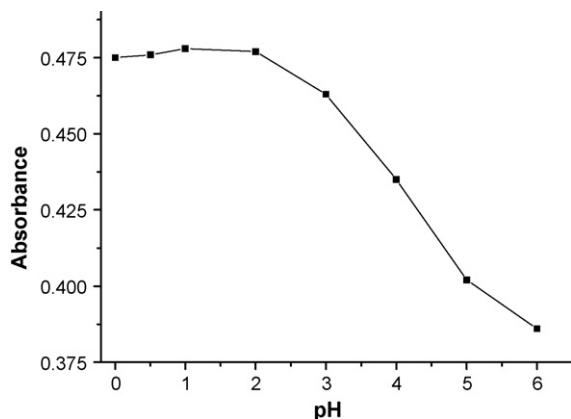


Fig. 1. Effect of pH of the sample solution on the DLLME extraction of Pd. DLLME conditions: Pd, 1.0 ng mL^{-1} ; sample volume, 5.0 mL; dispersive solvent (ethanol) volume, 0.5 mL; extraction solvent (CCl_4) volume, 40 μL ; DDTC concentration, 0.1 mg mL^{-1} .

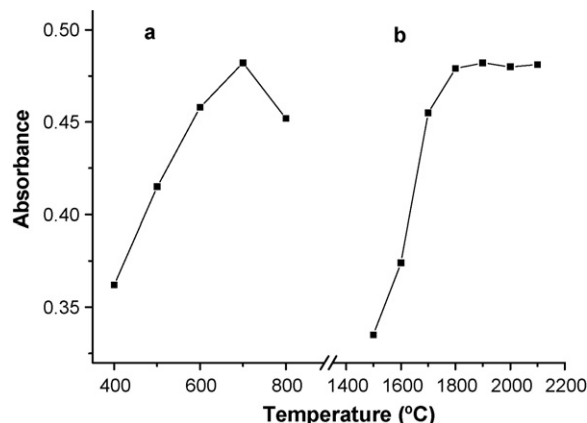


Fig. 2. Pyrolysis curve (a) and atomization curve (b) for Pd. DLLME conditions: Pd, 1.0 ng mL^{-1} ; sample volume, 5.0 mL; pH of sample solution, 1.0; dispersive solvent (ethanol) volume, 0.5 mL; extraction solvent (CCl_4) volume, 40 μL ; DDTC concentration, 0.1 mg mL^{-1} .

3.5. Effect of extraction time

In DLLME, extraction time is defined as interval time between the injection of the mixture of disperser solvent (ethanol) and extraction solvent (CCl_4) and the starting of centrifuge. The effect of extraction time was examined in the range of 5 s to 30 min with the constant experimental conditions. The obtained results showed that the extraction time was no significant influence on the signal of Pd. Because of the infinitely large surface area between extraction solvent and aqueous phase after the formation of cloudy solution, the complex of Pd with DDTC diffuses into the extraction solvent quickly. Therefore, the DLLME method was time-independent, which was the most important advantage of this technique. In this method, the most time-consuming step was the centrifuging of sample solution in the extraction procedure. The process took about 5 min.

3.6. Pyrolysis and atomization curves

The purpose of the pyrolysis step prior to the atomization is to remove the matrix as much as possible to reduce the magnitude of the background signal. In order to avoid Pd losing during the pyrolysis step, the optimal pyrolysis temperature should be selected. Pyrolysis and atomization curves were established using 1.0 ng mL^{-1} Pd solution submitted to the DLLME procedure. Figure 2 shows the pyrolysis and atomization curves for Pd. From the curves, the optimal pyrolysis and atomization temperatures are 700 °C and 1800 °C for Pd. No modifier was used because considerable analyte stabilization was provided by the medium itself.

3.7. Interferences

The potential interference in the present method was investigated. The interference was due to the competition of other metal ions for the chelating agent and their subsequent co-extraction with Pd. In these experiments, solutions containing 1.0 ng mL^{-1} of Pd and the interfering ions were treated according to the recommended procedure. The tolerance limits of the coexisting ions, defined as the largest amount making the recovery of Pd less than 90%. The results showed that at least 5000 $\mu\text{g mL}^{-1}$ of Na^+ , K^+ , SO_4^{2-} , NO_3^- and Cl^- , 2000 $\mu\text{g mL}^{-1}$ of Ca^{2+} and Mg^{2+} and 100 $\mu\text{g mL}^{-1}$ of Al^{3+} , SiO_4^{2-} and PO_4^{3-} had no remarkable interferences with the determination of Pd. Cu^{2+} , Co^{2+} , Zn^{2+} , Cd^{2+} , Ni^{2+} , Mn^{2+} and Pb^{2+} could be

Table 1

Comparison of the published preconcentration methods for Pd with the proposed method.

Preconcentration method	Detection method	Enrichment factor	Detection limit ($\mu\text{g L}^{-1}$)	Reference
Coprecipitation	FAAS	25	1.5	[6]
LLE	Spectrophotometry	–	7	[7]
SPE	ICP-AES	20	0.45	[9]
SPE	FAAS	60	1.5	[11]
SPE	ICP-AES	100	0.2	[12]
SPE	GFAAS	8.7	2.0	[14]
CPE	Spectrophotometry	50	0.47	[15]
CPE	ICP-AES	20	0.3	[16]
DLLME	GFAAS	156	2.4 ng L ⁻¹	This work

Table 2Determination of Pd (ng mL⁻¹) in water samples.

Samples	Added	Found ^a	Recovery (%)
River water	0	3.5 ± 0.5	–
	5	8.6 ± 0.8	102
	10	13.4 ± 1.1	99
Lake water	0	2.3 ± 0.4	–
	5	7.1 ± 0.6	96
	10	12.1 ± 1.0	98
Tap water	0	0.9 ± 0.2	–
	5	5.8 ± 0.5	98
	10	10.9 ± 0.8	100

^a Mean ± S.D., *n* = 5.

tolerated up to 5 $\mu\text{g mL}^{-1}$ and Cr³⁺ and Fe³⁺ could be tolerated up to 1.0 $\mu\text{g mL}^{-1}$.

3.8. Evaluation of method performance

For the purpose of quantitative analysis, a calibration curve for Pd with concentrations ranging over four orders was obtained by spiking the standards directly into distilling water and extracted under the optimal conditions. Linearity was observed over the range of 0.1–5 ng mL⁻¹ with a correlation coefficient (*R*²) of 0.9992. The limit of detection (LOD), based on a signal-to-noise ratio (*S/N*) of 3, was 2.4 ng L⁻¹. The precision of this method was determined by analyzing standard solution at 1.0 ng mL⁻¹ of Pd for seven times in continuous, and the relative standard deviation (R.S.D.) was 4.3%. The enrichment factor was 156 for 5.0 mL sample solution.

Table 1 compares the characteristic data of the proposed method with other preconcentration methods for Pd reported in literatures. As can be seen, the proposed method possesses lower limit of detection and higher enrichment factor than the reported methods with only 5.0 mL sample solution, and is suitable for the determination of trace amount of Pd in various real samples.

3.9. Analysis of real samples

In order to establish the validity of the proposed procedure, the method has been applied to the determination of Pd in geological standard reference materials (GBW07291 peridotite). The determined value (57 ± 6 ng g⁻¹, *n* = 5) is in good agreement with the certified value (60 ± 9 ng g⁻¹).

The proposed method was applied to determine of Pd in river water, lake water and tap water samples. In addition, the recovery experiments of different amounts of Pd were carried out, and the

results are shown in Table 2. The results indicate that the recoveries in the range of 96–102% are reasonable well for trace analysis.

4. Conclusion

A new method of DLLME combined with GFAAS has been proposed for the determination of Pd in water samples. The advantage of method is simple, rapid and the minimization of waste generation. The proposed method possesses lower limit of detection and higher enrichment factor than other reported preconcentration methods for Pd, which makes it suitable for the determination of trace amount of Pd in various real samples.

References

- [1] C.R.M. Rao, G.S. Reddi, Trends Anal. Chem. 19 (2000) 565.
- [2] R. Merget, G. Rosner, Sci. Total Environ. 270 (2001) 165.
- [3] K. Ravindra, L. Bencs, R.V. Griecken, Sci. Total Environ. 318 (2004) 1.
- [4] B. Godlewska-Zylkiewicz, Microchim. Acta 147 (2004) 189.
- [5] Y. Wang, M.L. Chen, J.H. Wang, J. Anal. Atom. Spectrom. 21 (2006) 535.
- [6] M. Soyulak, M. Tuzen, J. Hazard. Mater. 152 (2008) 656.
- [7] A.N. Anthemidis, D.G. Themelis, J.A. Stratis, Talanta 54 (2001) 37.
- [8] L. Pan, Y.C. Qin, B. Hu, Z.C. Jiang, Chem. Res. Chin. Univ. 23 (2007) 399.
- [9] Y.W. Wu, Z.C. Jiang, B. Hu, Geostand. Geoanal. Res. 28 (2004) 383.
- [10] Y. Wang, J.H. Wang, Z.L. Fang, Anal. Chem. 77 (2005) 5396.
- [11] R.S. Praveen, S. Daniel, T.P. Rao, S. Sampath, K.S. Rao, Talanta 70 (2006) 437.
- [12] M.R. Jamali, Y. Assadi, F. Shemirani, M. Salavati-Niasari, Talanta 71 (2007) 1524.
- [13] A.M. Zou, M.L. Chen, Y. Shu, J.H. Wang, J. Anal. Atom. Spectrom. 22 (2007) 392.
- [14] C.B. Ojeda, F.S. Rojas, J.M.C. Pavon, Microchim. Acta 158 (2007) 103.
- [15] F. Shemirani, R.R. Kozani, M.R. Jamali, Y. Assadi, M.R.M. Hosseini, Int. J. Environ. Anal. Chem. 86 (2006) 1105.
- [16] L. Tavakoli, Y. Yamini, H. Ebrahimzadeh, A. Nezhadali, S. Shariati, F. Nourmohammadian, J. Hazard. Mater. 152 (2008) 737.
- [17] E. Psillakis, N. Kalogerakis, Trends Anal. Chem. 22 (2003) 565.
- [18] L.B. Xia, B. Hu, Z.C. Jiang, Y.L. Wu, Y. Liang, Anal. Chem. 76 (2004) 2910.
- [19] L.B. Xia, Y.L. Wu, B. Hu, J. Mass Spectrom. 42 (2007) 803.
- [20] J. Cao, P. Liang, R. Liu, J. Hazard. Mater. 152 (2008) 910.
- [21] H.F. Maltez, D.L.G. Borges, E. Carasek, B. Welz, A.J. Curtius, Talanta 74 (2008) 800.
- [22] G. Shen, H.K. Lee, Anal. Chem. 74 (2002) 648.
- [23] F. Ahmadi, Y. Assadi, M.R.M. Hosseini, M. Rezaee, J. Chromatogr. A 1101 (2006) 307.
- [24] M. Rezaee, Y. Assadi, M.R.M. Hosseini, E. Aghaee, F. Ahmadi, S. Berijani, J. Chromatogr. A 1116 (2006) 1.
- [25] M.A. Farajzadeh, M. Bahrani, J.A. Jonsson, Anal. Chim. Acta 591 (2007) 69.
- [26] J.S. Chiang, S.D. Huang, Talanta 75 (2008) 70.
- [27] P. Liang, J. Xu, Q. Li, Anal. Chim. Acta 609 (2008) 53.
- [28] E.Z. Jahromi, A. Bidari, Y. Assadi, M.R.M. Hosseini, M.R. Jamali, Anal. Chim. Acta 585 (2007) 305.
- [29] N. Shokoufi, F. Shemirani, Y. Assadi, Anal. Chim. Acta 597 (2007) 349.
- [30] H.M. Jiang, Y.C. Qin, B. Hu, Talanta 74 (2008) 1160.
- [31] M. Shamsipur, M. Ramezani, Talanta 75 (2008) 294.
- [32] S. Dadfarnia, A.M. Haji Shabani, M. Gohari, Talanta 64 (2004) 682.
- [33] X.P. Yan, Y. Li, Y. Jiang, Anal. Chem. 75 (2003) 2251.
- [34] P. Wu, Y. Gao, G.L. Cheng, W.S. Yang, Y. Lv, X.D. Hou, J. Anal. Atom. Spectrom. 23 (2008) 752.



Immobilization of trypsin on silica-coated fiberglass core in microchip for highly efficient proteolysis

Ting Liu, Sheng Wang, Gang Chen*

School of Pharmacy and Institute of Biomedical Sciences, Fudan University, 220 Handan Rd, Shanghai 200032, China

ARTICLE INFO

Article history:

Received 1 August 2008

Received in revised form 3 October 2008

Accepted 7 October 2008

Available online 17 October 2008

Keywords:

Mass spectrometry

Glass fiber

Microchip

Miniaturization

Bioreactor

Proteolysis

ABSTRACT

In this report, trypsin was immobilized on silica-coated fiberglass core in microchip to form a core-changeable bioreactor for highly efficient proteolysis. To prepare the fiber core, a layer of organic–inorganic hybrid silica coating was prepared on the surface of a piece of glass fiber by a sol–gel method with tetraethoxysilane (TEOS) and 3-aminopropyltriethoxysilane (APTES) as precursors. Subsequently, trypsin was immobilized on the coating with the aid of glutaraldehyde. Prior to use, the enzyme-immobilized fiber was inserted into the channel of a microchip to form an in-channel fiber bioreactor. The novel bioreactor can be regenerated by changing its fiber core. The scanning electron microscopy images of the cross-section of a trypsin-immobilized fiber indicated that a layer of $\sim 1\ \mu\text{m}$ thick film formed on the glass substrate. The feasibility and performance of the unique bioreactor were demonstrated by the tryptic digestion of bovine serum albumin (BSA) and cytochrome *c* (Cyt-*c*) and the digestion time was significantly reduced to less than 10 s. The digests were identified by MALDI-TOF MS with sequence coverages of 45% (BSA) and 77% (Cyt-*c*) that were comparable to those obtained by 12-h conventional in-solution tryptic digestion. The fiber-based microchip bioreactor provides a promising platform for the high-throughput protein identification.

© 2008 Elsevier B.V. All rights reserved.

1. Introduction

Since the pioneering work of Manz and Harrison, microfluidic chips are of considerable recent interest owing to their high degree of integration, portability, minimal sample/reagent consumption, high performance and speed [1,2]. These microchip analysis systems hold considerable promise for biomedical and pharmaceutical analysis, clinical diagnostics, forensic investigations, and environmental monitoring [3–5]. They can dramatically change the scale and speed at which chemical analysis is performed. It is particularly suitable for the low volume samples in the field of biomedical analysis where the available volumes are usually small. Microfluidic devices are powerful platforms for handling small-volume samples (nL to μL) in microchannels to perform enzymatic reactions [6], immunoassay [7], etc.

One of the important applications of microchip bioreactors is the protein digestion in the field of proteomics. Proteolysis is the key process for protein sequencing in proteome research. It is of high importance to develop efficient ways to achieve a high-quality proteolytic digestion for the MS peptide mapping because the

conventional in-solution digestion of proteins is time consuming [8].

Recent efforts have been made to fabricate microfluidic enzymatic reactors by immobilizing proteases on the channel walls of microchips. The bioreactors were further coupled with mass spectrometry (MS) to perform the efficient digestion of low-level proteins and peptide mapping [9–14]. In comparison to the free enzymes in solution, the enzymes immobilized in microchannels were reported to be much more stable and highly resistant to environmental changes, and provide molecular-level interactions between the immobilized enzymes and the flowing protein substrates. The proteolytic enzyme, usually trypsin, has been immobilized on the channel walls in microchips by sol–gel encapsulation [9,10], covalent linking [11,12], and multiplayer assembly [13,14] approaches to fabricate bioreactors for proteolysis. Among these immobilization approaches, the sol–gel encapsulation method has attracted much more attention. Because the trypsin-containing layers were permanently modified on the channel wall, the microchip could not be used when the enzyme activity decreased to some extent.

Fibers made from various substances are versatile materials and have found wide analytical applications such as solid-phase microextraction [15], optic sensors [16], electrochemical sensors [17], capillary electrochromatography [18], liquid chromatogra-

* Corresponding author. Tel.: +86 21 5423 7313; fax: +86 21 6418 7117.

E-mail address: gangchen@fudan.edu.cn (G. Chen).

phy [19], gas chromatography [20], etc. It is a challenging task to integrate fibers on microchips to construct novel platforms for protein digestion.

In this work, a piece of trypsin-immobilized glass fiber was inserted into the channel of a microchip to fabricate a core-changeable microfluidic bioreactor that could be regenerated by changing the core that consisted of a piece of glass fiber and a layer of trypsin-immobilized organic–inorganic hybrid silica coating. The silica coating was prepared on a piece of glass fiber by a sol–gel method with tetraethoxysilane (TEOS) and 3-aminopropyltriethoxysilane (APTES) as precursors, offering a porous surface to accommodate trypsin. Trypsin was immobilized on the primary amino group-containing coating with the aid of glutaraldehyde. The in-channel fiber bioreactor has been coupled with matrix-assisted laser desorption/ionization time-of-flight mass spectrometry (MALDI-TOF MS) for the digestion and peptide mapping of bovine serum albumin (BSA) and cytochrome c (Cyt-c). The fabrication details, characterization, feasibility, and performance of the core-changeable microchip bioreactors are reported in the following sections.

2. Experimental

2.1. Reagents

TEOS, APTES, acetonitrile (ACN), ammonium bicarbonate (NH_4HCO_3), methyl methacrylate (MMA), benzoin ethyl ether, 2-2'-azo-bis-isobutyronitrile, absolute ethanol, tris(hydroxymethyl)aminomethane (Tris), and sodium hydroxide were all purchased from Shanghai Chemical Reagent Company (SinoPharm, Shanghai, China). BSA, Cyt-c from horse heart, trypsin from bovine pancreas, benzamidine hydrochloride, trifluoroacetic acid (TFA), sodium azide (NaN_3), and α -cyano-4-hydroxycinnamic acid (CHCA) were supplied by Sigma (St. Louis, MO, USA). Normal human serum was kindly donated by the Clinical Laboratory of Zhongshan Hospital (Shanghai, China).

2.2. Fabrication of poly(methyl methacrylate) microchip

The poly(methyl methacrylate) (PMMA) microchip (15 mm \times 75 mm \times 3 mm) used in this work had a simple cross layout. The original waste reservoir was cut off to leave the channel

outlet for inserting fiber core. The chips consisted of a 58-mm long main channel (between the injection cross and the channel outlet) and a 5-mm long injection channel. The channels had a trapezoidal cross-section with a top width of $\sim 280\ \mu\text{m}$, a bottom width of $\sim 100\ \mu\text{m}$, and a depth of $\sim 110\ \mu\text{m}$. The channel plates of the PMMA microchips were fabricated by the in situ surface polymerization of MMA prepolymer molding solution between a silicon template and a commercially available PMMA plate. The fabrication details of the PMMA microchips have been described previously [21]. The silicon template was fabricated by standard photolithography and wet chemical etching [22].

2.3. Preparation of core-changeable microchip bioreactor

Fig. 1 illustrates the procedure of the immobilization of trypsin on the surface of glass fiber. Prior to modification, a piece of 12 cm long glass fiber ($\sim 90\ \mu\text{m}$ diameter) was rinsed with doubly distilled water and ethanol and dried at room temperature. It was then dipped in 1 M NaOH aqueous solution for 15 min at room temperature and thoroughly rinsed with doubly distilled water. To prepare organic–inorganic hybrid sol, a mixture solution containing 11.2 mL of TEOS, 11.8 mL of APTES, and 21.5 mL of absolute ethanol was mixed with 3.2 mL of 1 M ammonium hydroxide aqueous solution. The mixture was vortexed at room temperature for 1 h. After the glass fiber was immersed in the coating solution for 5 min, it was taken out and was allowed to air dry for 2 h. And then, it was successively dipped in 2.5% (w/v) glutaraldehyde in 50 mM phosphate buffer (pH 8.0) at room temperature and 5 mg/mL trypsin in 50 mM phosphate buffer (pH 8.0) containing 50 mM benzamidine (a protease inhibitor) and 5 mg/mL sodium cyanoborohydride (NaBH_3CN) at 4°C for 3 and 12 h, respectively. After the non-specifically adsorbed trypsin was removed by rinsing with 50 mM phosphate buffer (pH 8.0), the trypsin-immobilized fiber core was immersed in 1 M Tris-HCl (pH 8.0) for 2 h to deplete the residual aldehyde groups. The fiber core could be stored in 50 mM Tris-HCl buffer (pH 7.5) containing 10 mM CaCl_2 and 0.02% NaN_3 at 4°C when it was not in use. Scanning electron microscopy (SEM) images of the surface and cross-section of the trypsin-immobilized glass fiber were obtained by using a PHILIPS XL 30 scanning electron microscope (Netherlands) and were illustrated in Figs. 2 and 3.

Prior to use, the modified part of the glass fiber was inserted into the main channel of a PMMA microchip under a magnifier to

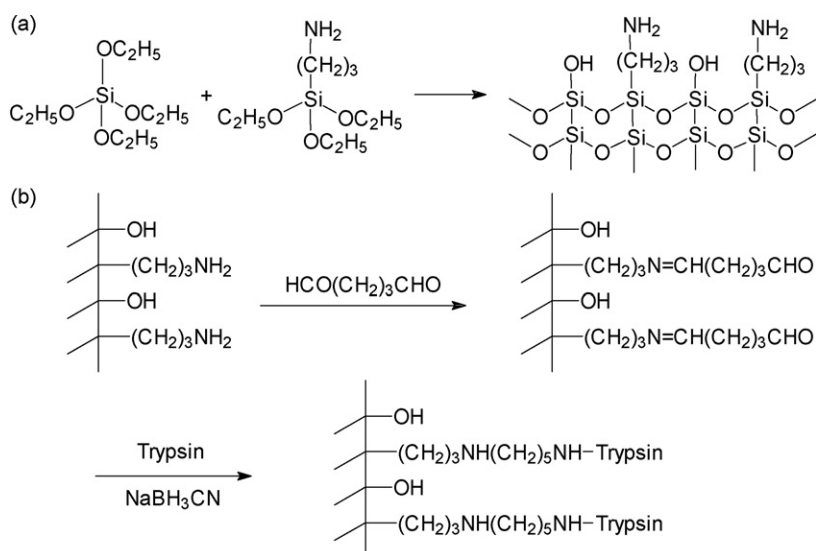


Fig. 1. Schematic diagram showing (a) the formation of the organic–inorganic hybrid silica coating and (b) trypsin immobilization.

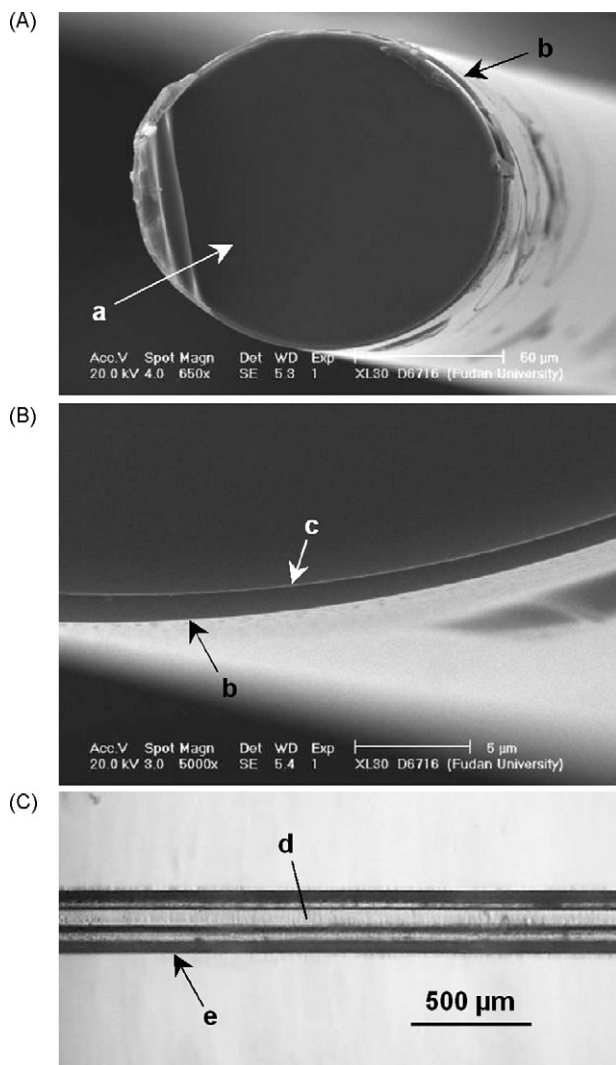


Fig. 2. SEM images of (Panel a) the cross-section of a trypsin-immobilized glass fiber and (Panel b) the edge part of the cross-section. Conditions: accelerating voltage, 20 kV; magnification, (Panel a) 650 \times and (Panel b) 5000 \times . (a) Glass substrate, (b) trypsin-immobilized organic–inorganic hybrid silica coating, (c) the boundary between (a) and (b). (Panel c) Typical microscopic photograph of a trypsin-immobilized fiber core (d) in the microchannel (e) of a PMMA microchip.

form an in-channel fiber bioreactor. The length of the fiber core in the needle was 5.8 cm while the length of the fiber protruded outside the channel outlet was approximately 3 mm, facilitating its removal. The trypsin-immobilized fiber core in the present needle bioreactor could be easily changed by hands. Fig. 2c illustrates the typical microscopic photograph of a trypsin-immobilized fiber core in the microchannel of a PMMA microchip.

2.4. On-chip protein digestion and identification

As shown in Fig. 4a, the on-chip protein digestion system consists of a syringe pump and a core-changeable microchip bioreactor. At 37 °C, protein solutions in 10 mM NH_4HCO_3 buffer solution (pH 8.1) were driven through the in-channel bioreactor (Fig. 4b) by the syringe pump at a flow rate of 2 $\mu\text{L}/\text{min}$ via one hole on the chip, while the other two holes were sealed with small plastic stoppers. Effluents accumulated on the channel outlet were collected by a pipette and then identified by MALDI-TOF MS. All MS experiments were performed on a 4700 Proteomics Analyzer (Applied Biosys-

tems, Framingham, MA, USA). Prior to MALDI-TOF MS analysis, a volume of 0.5 μL of each digest was spotted on a MALDI plate. After the solvent evaporated, 0.5 μL of matrix solution (4 mg/mL CHCA dissolved in 50% aqueous ACN containing 0.1% TFA) was dropped on the dried samples. The MS instrument was operated at an accelerating voltage of 20 kV. A 200-Hz pulsed Nd:YAG laser at 355 nm was used. Prior to use, the MS instrument was calibrated with the tryptic digest of myoglobin in an internal calibration mode. GPS Explorer software from Applied Biosystems with Mascot as a search engine and SwissProt as a database were used to identify proteins. The missed cleavages of peptides were allowed up to 1. For comparison, BSA and Cyt-c were also digested by using conventional in-solution proteolysis in 10 mM NH_4HCO_3 buffer (pH 8.1) for 12 h at 37 °C (trypsin/substrate ratio, 1:40, w/w).

3. Results and discussion

As illustrated in Fig. 1, trypsin was immobilized on the surface of organic–inorganic hybrid silica coating that was modified on glass fiber via a sol–gel approach. TEOS and APTES hydrolyzed in aqueous ethanol at a molar ratio of 1:1 to form sol. After the sol was coated on a piece of glass fiber, it would further condense to form a layer of organic–inorganic hybrid silica coating which contained a great deal of primary amino groups. In this work, glutaraldehyde, a commonly used cross-linking agent, was employed to immobilize trypsin on the coating. Benzamidine was added in the immobilization solution to minimize the autolysis of trypsin. Glutaraldehyde could react with the primary amino groups of trypsin and the coating to form Schiff bases to immobilize trypsin. Because this reaction was reversible, the C=N bonds in Schiff bases were further reduced to C–N bonds with reducing agent (NaBH_3CN) to enhance the stability of the immobilized trypsin.

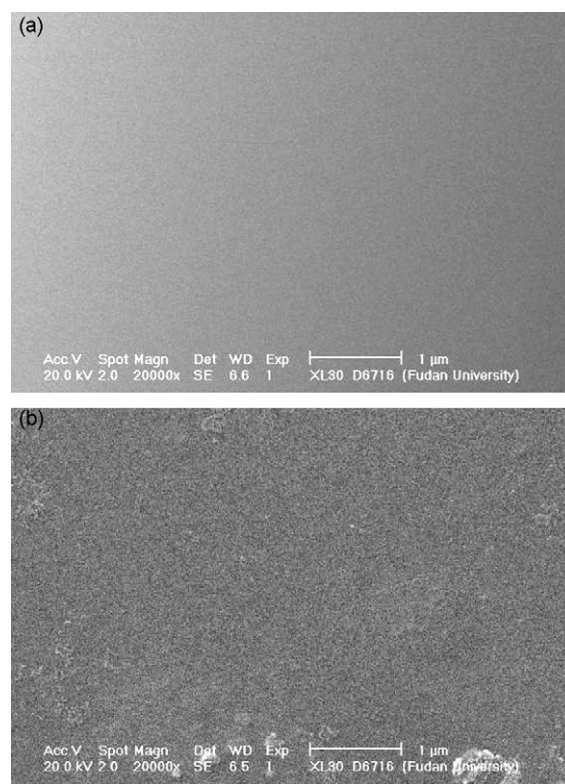


Fig. 3. SEM images of the surfaces of (a) glass fiber and (b) trypsin-immobilized organic–inorganic hybrid silica coating on glass fiber. Conditions: accelerating voltage, 20 kV; magnification, 20,000 \times .

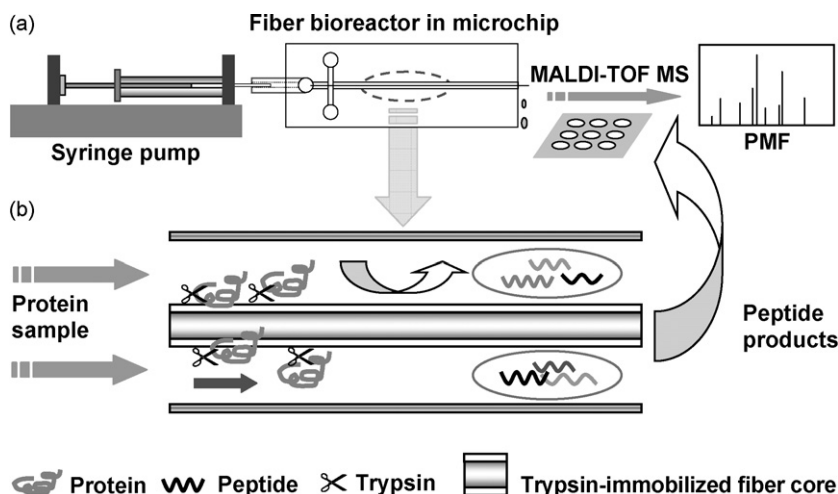


Fig. 4. Schematic diagrams showing (a) the processes of protein digestion and MALDI-TOF MS peptide mapping and (b) the amplified in-channel fiber bioreactor.

The present core-changeable microchip bioreactor takes the advantages of both the changeable enzyme-immobilized fiber and microfluidic chips, offering a fast, flexible, and reliable enzymatic methodology for highly efficient proteolysis and other biological applications with enzymes involved. The most promising advantage of the unique microchip bioreactor is that it can be regenerated by simply changing the enzyme-immobilized fiber core. Fig. 4 illustrates the processes of protein digestion and MALDI-TOF MS peptide mapping and the amplified in-channel fiber bioreactor. As shown in Fig. 4b, the micron-scale openings between the enzyme-immobilized fiber core and the microchannel offer the possibility to perform microfluidic protein digestion. After carefully exam-

ining the final microchip bioreactor by an optical microscope, it was observed that the body of the enzyme-immobilized fiber core in the microchannel was complete and intact (Fig. 2c). The fiber core was well accommodated in the middle of the microchannel.

The trypsin-immobilized fiber core is the crucial part of the present core-changeable microfluidic bioreactor. In this work, it was made of a piece of glass fiber because it was rigid and could be easily inserted into or removed from the microchannel. Fig. 2a shows the SEM images of the cross-section of a trypsin-immobilized glass fiber. It can be seen clearly that a layer of coating has formed on the surface of the glass fiber. The thick-

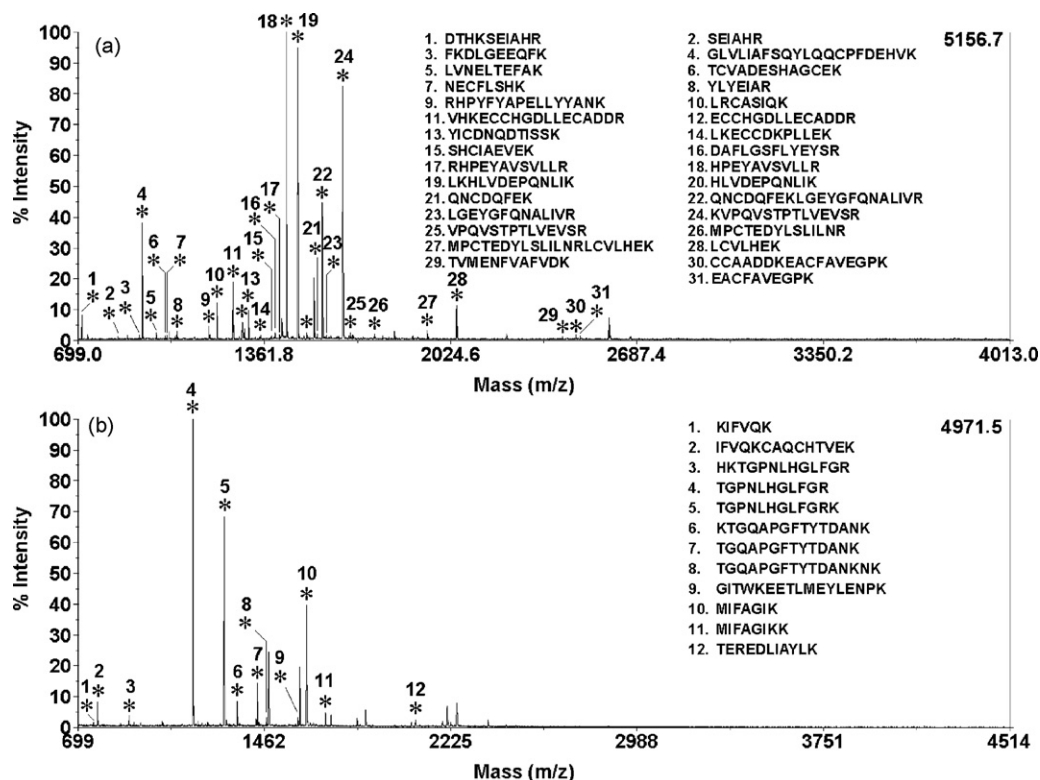


Fig. 5. MALDI-TOF mass spectra of the digests of (a) BSA and (b) Cyt-c obtained by using a core-changeable microchip bioreactor at a flow rate of 2.0 $\mu\text{L}/\text{min}$ (digestion time, <10 s; all peptides matched were marked with “*”). The concentrations of proteins were 200 ng/ μL in 10 mmol/L NH_4HCO_3 aqueous solution (pH 8.1).

ness of the modification layer was estimated to be in the range of 0.8–1.0 μm (Fig. 2b). Fig. 3 illustrates the SEM images of the surfaces of pristine glass fiber and trypsin-immobilized organic–inorganic hybrid silica coating on glass fiber. Fig. 3b indicates that a layer of rough sol–gel coating has formed and continuously distributed on the surface glass fiber. The porous trypsin-immobilized sol–gel coating offered an interface with high specific surface area for the interaction between immobilized trypsin and proteins.

The feasibility and performance of the unique core-changeable microfluidic bioreactor were demonstrated by the tryptic digestion of BSA and Cyt-c in connection with MALDI-TOF MS peptide mapping. At a flow rate of 2.0 $\mu\text{L}/\text{min}$, the time of the interaction between the protein samples and the immobilized trypsin on the fiber core was estimated to be less than 10 s. Fig. 5 displays the peptide mass fingerprinting (PMF) spectra of the tryptic digests of 200 ng/ μL BSA and 200 ng/ μL Cyt-c obtained by using the in-channel fiber bioreactor. Both samples were well digested and positively identified. The identified peptide residues obtained by using the microchip bioreactor were presented in Tables 1 and 2. It was found that 31 and 12 tryptic peptides from BSA and Cyt-c were identified with the corresponding amino acid sequence coverage of 45% and 77% for BSA and Cyt-c, respectively. The results indicate that 277 out of the 607 possible amino acids of BSA and 81 out of the 104 possible amino acids of Cyt-c have been identified (Table 3). As illustrated in Fig. 5, the intensities of peptides 4, 18, 19, 21, 22, and 24 in the digest of BSA and peptides 4, 5, 7, and 10 in the digest of Cyt-c were much stronger.

Table 1

Identified peptides of BSA obtained by using a core-changeable microchip bioreactor and 12-h conventional in-solution digestion coupled with MALDI-TOF MS.

Position	Peptide sequence	Microreactor	In-solution
25–34	DTHKSEIAHR	• ^a	•
29–34	SEIAHR	•	
35–44	FKDLGEEQFK	•	
45–65	GLVLIASFQYLQQCPFDEHVK	•	
66–75	LVNELTEFAK	•	•
76–88	TCVADESHAGCEK	•	•
123–130	NECFLSHK	•	•
161–167	YLYEIAK	•	•
161–168	YLYEIAK	•	•
168–183	RHPYFYAPPELLYYANK	•	•
169–183	HPYFYAPPELLYYANK	•	•
198–204	GACLLPK	•	•
221–228	LRCASIQK	•	•
264–280	VHKECCHGDLLECADDR	•	•
267–280	ECCHGDLLECADDR	•	•
286–297	YICDNQDTISSK	•	•
298–309	LKECCDKPLLEK	•	•
310–318	SHCIAEVEK	•	•
347–359	DAFLGSFLYEYSR	•	•
360–371	RHPEYAVSVLLR	•	•
361–371	HPEYAVSVLLR	•	•
400–412	LKHLVDEPQNLIK	•	•
402–412	HLVDEPQNLIK	•	•
413–420	QNCDQFEK	•	•
413–433	QNCDQFEKLGEGYGFQNALIVR	•	•
421–433	LGEYGFQNALIVR	•	•
437–451	KVPQVSTPTLVEVSR	•	•
438–451	VPQVSTPTLVEVSR	•	•
469–482	MPCTEDYLSLILNR	•	•
469–489	MPCTEDYLSLILNRLCVLHEK	•	•
483–489	LCVLHEK	•	•
508–523	RPCFSALTPDETYVPK	•	•
524–544	AFDEKLFTFHADICTLPDTEK	•	•
569–580	TVMENFVAFVDK	•	•
581–597	CCAADDKEACFAVEGPK	•	•
588–597	EACFAVEGPK	•	•

^a The matched peptides are labeled with “•”.

Table 2

Identified peptides of Cyt-c obtained by using a core-changeable microchip bioreactor and 12-h conventional in-solution digestion coupled with MALDI-TOF MS.

Position	Peptide sequence	Microreactor	In-solution
8–13	KIFVQK	• ^a	
9–22	IFVQKCAQCHTVEK	•	•
26–38	HKTGPNLHGLFGR	•	
28–38	TGPNLHGLFGR	•	•
28–39	TGPNLHGLFGRK	•	•
39–53	KTGQAPGFTYTDANK	•	
40–53	TGQAPGFTYTDANK	•	
40–55	TGQAPGFTYTDANKNK	•	•
56–72	GITWKEETLMLEYLENPK	•	•
80–86	MIFAGIK	•	
80–87	MIFAGIKK	•	•
89–99	TEREDLIAYLK	•	•

^a The matched peptides are labeled with “•”.

For comparison, the MALDI-TOF mass spectra of the digests of 200 ng/ μL BSA and 200 ng/ μL Cyt-c obtained by using 12-h conventional in-solution digestion were also measured (not shown). All matched peptides were presented in Tables 1 and 2. The results indicated that 22 and 7 peptides were found matched with the amino acid sequence coverages of 37% (identified amino acids, 230) and 75% (identified amino acids, 78) for BSA and Cyt-c, respectively. Table 3 summarizes the MALDI-TOF MS results of the digests obtained by using different digestion approaches. The identification results obtained by the core-changeable microchip bioreactor were comparable to those based on conventional in-solution digestion. More importantly, the digestion time was significantly reduced from 12 h for in-solution digestion to less than 10 s for the present on-chip digestion. The significantly enhanced digestion efficiency of the in-channel fiber bioreactor could be attributed to the high concentration of trypsin immobilized in the organic–inorganic hybrid silica coating on glass fiber and the higher surface area of the fiber bioreactor in the channel, which increased the frequency of the interaction between trypsin and proteins [10].

The operational stability and reproducibility of the fiber-packed channel bioreactor is of crucial importance for its application in the high-throughput protein analysis. A solution of 200 ng/ μL Cyt-c was digested to test the stability of the microfluidic bioreactor. The microchip was used at $\sim 37^\circ\text{C}$ for 2 h consecutively, and the tryptic digests were analyzed with MALDI-TOF MS every 15 min. The sequence coverages of the eight consecutive runs were 77, 77, 75, 72, 70, 70, 65, and 57, indicating that the stability and operational bioactivity of the immobilized trypsin were satisfactory. For the first six runs, the sequence coverages were around 74% with the relative standard deviation (R.S.D.) of 4.4%. In the case of the seventh run, the sequence coverage decreased to 65%, which indicated the beginning of the significant loss of the enzyme activity. The enhanced stability of trypsin can be attributed to the minimization of autolysis in the organic–inorganic hybrid silica network on the surface of glass fiber, offering a promising platform for highly efficient proteolysis. In comparison, trypsin dissolved in 50 mM Tris–HCl (pH 8.0) almost lost its activity completely within 1 day at 25°C [23].

The suitability of the core-changeable microchip bioreactor to complex proteins was demonstrated by digesting human serum. Normal human serum contains 60–75 g/L of proteins. The weight percentages of human serum albumin (HSA), α -1-globulin, α -2-globulin, β -globulin, and γ -globulin in the total serum protein are in the ranges of 53.3–70.5%, 4.4–9.3%, 6.4–10.3%, 6.7–10.6%, 11–16.8%, respectively [24]. In this work, a sample of normal human serum was diluted in 10 mM NH_4HCO_3 solution (pH 8.1) containing 5 ng/ μL trypsin at a ratio of 1:500 after it was denatured in a 95°C water bath for 15 min. Subsequently, 100 μL of the mixture

Table 3
Summary of MALDI-TOF MS results of the digests of BSA and Cyt-c obtained by using a core-changeable microchip bioreactor and conventional in-solution digestion coupled with MALDI-TOF MS.

Digestion methods	Protein	Accession no. ^a	Digestion time	Sequence coverage (%)	Peptides matched	Amino acids identified
Microreactor	BSA	P02769	10 s	45	31	277
In-solution	BSA	P02769	12 h	37	22	230
Microreactor	Cyt-c	P00004	10 s	77	12	81
In-solution	Cyt-c	P00004	12 h	75	7	78

^a P02769 and P00004 are the accession numbers of serum albumin precursor.bovine and cytochrome c. horse, respectively.

was allowed to flow through the channel containing a trypsin-immobilized fiber core at a flow rate of 2.0 $\mu\text{L}/\text{min}$ at $\sim 37^\circ\text{C}$. The MALDI-TOF mass spectrum of the digest was shown in Fig. 6. The results indicated that 26 peptides were found to match to HAS (Table 4).

Since the present microreactor was prepared by simply inserting a piece of trypsin-immobilized glass fiber in the microchannel, the major advantage of the core-changeable microfluidic bioreactor over the conventional enzymatic microreactors with the enzyme permanently immobilized on the channel walls was that the enzymatic activity could be easily regenerated by changing the fiber core. According to the stability test conducted above, the prepared microreactor should be regenerated after six times of usage for the digestion of proteins. The regeneration process was quite simple. After the old fiber core was removed, the empty channel was then flushed with 0.1 M HCl aqueous solution and doubly distilled water for 5 min each. Subsequently, a piece of new trypsin-immobilized fiber core was inserted into the channel. In order to investigate the “core-to-core” reproducibility, seven pieces of trypsin-immobilized fibers have been evaluated based on the digestion of 200 ng/ μL Cyt-c in the same microchip. The digested products were then analyzed with MALDI-TOF MS. The obtained seven PMF spectra (not shown) were identical with the same sequence coverage of 77% except that the peak heights changed to some extent, indicating the satisfactory reproducibility of the present IR-assisted proteolysis approach.

Besides the high digestion efficiency, an additional advantage of the present approach is its simplicity, which is promising for the automated high-throughput protein analysis using a microchip platform containing multiple parallel in-channel fiber bioreactors. Although only trypsin microreactor has been demonstrated in this work, the unique fiber-based microchip will find more applica-

Table 4
Identified peptides of HAS in human serum obtained by using a core-changeable microchip bioreactor coupled with MALDI-TOF MS.

Position	Peptide sequence
8–17	FKDLGEENFK
39–48	LVNEVTEFAK
134–141	KYLYEIAR
135–141	YLYEIAR
135–142	YLYEIARR
143–157	HPYFYAPELLFFAKR
179–187	LDELRLDEGK
197–206	CASLQKFGER
207–215	AFKAWAVAR
216–222	LSQRFPK
315–333	NYAEAKDVFLGMFLYEYAR
321–333	DVFLGMFLYEYAR
321–334	DVFLGMFLYEYARR
334–345	RHPDYSVVLRLR
335–345	HPDYSVVLRLR
370–386	VFDEFKPLVEEPQNLIK
387–399	QNCLEFEQLGEYK
400–407	FQNALLVR
411–425	KVPQVSTPTLVEVSR
412–425	VPQVSTPTLVEVSR
470–481	VTKCCTESLVNR
482–497	RPCFSALEVDETYVPK
498–518	EFNAETFTFHADICTLSEKER
522–531	KQTALVELVK
539–554	EQLKAVMDDFAAFVEK
543–557	AVMDDFAAFVEKCKC

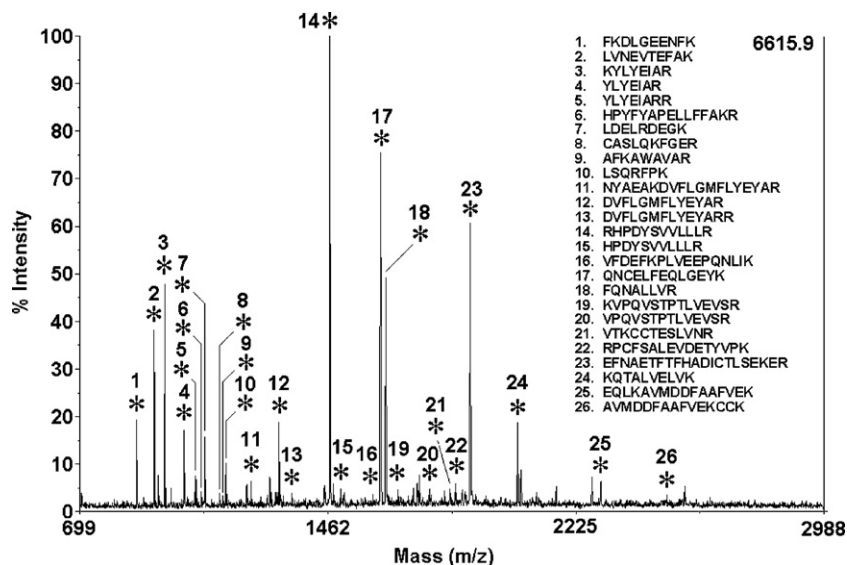


Fig. 6. MALDI-TOF mass spectrum of the tryptic digest of 1:500 diluted human serum in 10 mM NH_4HCO_3 solution (pH 8.1) obtained by using a core-changeable microchip bioreactor at a flow rate of 2.0 $\mu\text{L}/\text{min}$ (digestion time, <10 s; all peptides matched were marked with “*”).

tion in the fabrication of other bioanalytical microdevices. Recently, a novel immobilized trypsin reactor based on organic–inorganic hybrid silica monoliths has been developed by Zhang's group [25]. In the presence of cetyltrimethyl ammonium bromide (CTAB), hybrid silica monolithic support was prepared in a piece of fused silica capillary by sol–gel approach with TEOS and APTES as precursors. Because trypsin was covalently immobilized in the monolith by using glutaraldehyde, the amount of immobilized trypsin was higher than that on the surface of fiber core in the present core-changeable microreactor. The monolithic bioreactor could not be used when the enzyme activity decreased to some extent. However, our fiber-based microchip bioreactor has no such limitation because it can be regenerated by changing its trypsin-immobilized fiber core.

4. Conclusions

It can be concluded that the core-changeable microchip bioreactor coupled with MALDI-TOF MS is a promising strategy for the efficient protein digestion and peptide mapping. Porous organic–inorganic hydride silica was coated on the surface of glass fiber for immobilizing trypsin to fabricate the fiber core of a microchip bioreactor. The main advantage of the in-channel fiber bioreactor was that it could be regenerated by changing the fiber core because trypsin was immobilized on the changeable fiber rather than permanently on the channel wall. SEM and microscopic images showed that the quality of the present microchip bioreactor was satisfactory. The unique features of this approach are the very short digestion time (<10 s) and its minimal sample/reagent consumption. The higher sequence coverage and numbers of the matched peptides indicate the excellent performance of the novel enzymatic microreactor. The present in-channel fiber can also be employed as supports for various functional materials such as stationary phases, extraction materials, and other enzymes and will find more applications in microchip capillary electrochromatography, microextraction on chip, microchip capillary electrophoresis, microfluidic enzymatic reactors for other purposes, etc.

Acknowledgments

This work was financially supported by 863 program of China (2007AA04Z309 and 2004AA639740), NSFC (200875015, 20675017 and 20405002) and National Key Technology R&D Program (2006BAI19B02).

References

- [1] D.J. Harrison, A. Manz, Z. Fan, H. Lüdi, H.M. Widmer, *Anal. Chem.* 64 (1992) 1926–1932.
- [2] D.J. Harrison, K. Flury, K. Seiler, Z. Fan, C.S. Effenhauser, A. Manz, *Science* 261 (1993) 895–897.
- [3] Y. Chen, L. Zhang, G. Chen, *Electrophoresis* 29 (2008) 1801–1814.
- [4] X. Yao, H.X. Wu, J. Wang, S. Qu, G. Chen, *Chem. Eur. J.* 13 (2007) 846–853.
- [5] P.S. Dittrich, K. Tachikawa, A. Manz, *Anal. Chem.* 78 (2006) 3887–3908.
- [6] J. Wang, M.P. Chatrathi, B. Tian, *Anal. Chem.* 73 (2001) 1296–1300.
- [7] K. Sato, M. Tokeshi, T. Odake, H. Kimura, T. Ooi, M. Nakao, T. Kitamori, *Anal. Chem.* 72 (2000) 1144–1147.
- [8] Z.Y. Park, D.H. Russell, *Anal. Chem.* 72 (2000) 2667–2670.
- [9] K. Sakai-Kato, M. Kato, T. Toyooka, *Anal. Chem.* 75 (2003) 388–393.
- [10] H.Y. Qu, H.T. Wang, Y. Huang, W. Zhong, H.J. Lu, J.L. Kong, P.Y. Yang, B.H. Liu, *Anal. Chem.* 76 (2004) 6426–6433.
- [11] D.S. Peterson, T. Rohr, F. Svec, J.M.J. Frechet, *Anal. Chem.* 74 (2002) 4081–4088.
- [12] H.Z. Fan, G. Chen, *Proteomics* 7 (2007) 3445–3449.
- [13] Y. Liu, W. Zhong, S. Meng, J.L. Kong, H.J. Lu, P.Y. Yang, H.H. Girault, B.H. Liu, *Chem. Eur. J.* 12 (2006) 6585–6591.
- [14] Y. Liu, H.J. Lu, W. Zhong, P.Y. Song, J.L. Kong, P.Y. Yang, H.H. Girault, B.H. Liu, *Anal. Chem.* 78 (2006) 801–808.
- [15] Y. Chen, J. Pawliszyn, *Anal. Chem.* 76 (2004) 5807–5815.
- [16] O.S. Wolfbeis, *Anal. Chem.* 78 (2006) 3859–3874.
- [17] W.H. Oldenzien, G. Dijkstra, T.J.F.H. Cremers, B.H.C. Westerink, *Anal. Chem.* 78 (2006) 3366–3378.
- [18] K. Jinno, H. Watanabe, Y. Saito, T. Takeichi, *Electrophoresis* 22 (2001) 3371–3376.
- [19] R.D. Stanelle, M. Mignanelli, P. Brown, R.K. Marcus, *Anal. Bioanal. Chem.* 384 (2006) 250–258.
- [20] Y. Saito, A. Tahara, M. Imaizumi, T. Takeichi, H. Wada, K. Jinno, *Anal. Chem.* 75 (2003) 5525–5531.
- [21] G.X. Xu, J. Wang, Y. Chen, L.Y. Zhang, D.R. Wang, G. Chen, *Lab. Chip* 6 (2006) 145–148.
- [22] J. Chen, Y.H. Lin, G. Chen, *Electrophoresis* 28 (2007) 2897–2903.
- [23] I.M. Lazar, R.S. Ramsey, J.M. Ramsey, *Anal. Chem.* 73 (2001) 1733–1739.
- [24] P. Luraschi, E.D. Dea, C. Franzin, *Clin. Chem. Lab. Med.* 41 (2003) 782–786.
- [25] J.F. Ma, Z. Liang, X.Q. Qiao, Q.L. Deng, D.Y. Tao, L.H. Zhang, Y.K. Zhang, *Anal. Chem.* 80 (2008) 2949–2956.



Standard addition analysis of fluoroquinolones in human serum in the presence of the interferent salicylate using lanthanide-sensitized excitation-time decay luminescence data and multivariate curve resolution

Valeria A. Lozano^a, Romà Tauler^b, Gabriela A. Ibañez^{a,*}, Alejandro C. Olivieri^{a,**}

^a Departamento de Química Analítica, Facultad de Ciencias Bioquímicas y Farmacéuticas, Universidad Nacional de Rosario and Instituto de Química Rosario (IQUIR-CONICET), Suipacha 531, Rosario (S2002LRK), Argentina

^b Instituto de Investigaciones Químicas y Ambientales de Barcelona, Consejo Superior de Investigaciones Científicas, Jordi Girona 18, Barcelona (08034), Spain

ARTICLE INFO

Article history:

Received 5 September 2008

Received in revised form 2 October 2008

Accepted 5 October 2008

Available online 21 October 2008

Keywords:

Lanthanide-sensitized luminescence

Excitation-time decay data

Multivariate curve resolution

Standard addition

Fluoroquinolone analysis

ABSTRACT

Three fluoroquinolone antibiotics (ciprofloxacin, norfloxacin and danofloxacin) have been determined in human serum in the presence of the potential interferent salicylate, by processing lanthanide-sensitized excitation-time decay matrix data for their terbium (III) complexes. The algorithm employed, multivariate curve resolution-alternating least-squares, is one of the few methodologies which permit the achievement of the second-order advantage in the presence of a high degree of overlapping between the time decay profiles for the analyte and the interferent complexes. Furthermore, the presence of analyte–background interactions makes it necessary to employ the standard addition method for successful quantitation. Both simulations and experiments showed that the modified standard addition method was suitable for this purpose, in which the test data matrix was subtracted from the standard addition matrices, and quantitation proceeded using classical external calibration procedure. The analyte concentration ranges were all within the therapeutic range, i.e., 0–6 mg L⁻¹ in serum, with final concentrations in the measuring cell in the order of 0.2 mg L⁻¹.

© 2008 Published by Elsevier B.V.

1. Introduction

Fluoroquinolone antibacterial agents are among the most important class of synthetic antibiotics in human and veterinary medicine, because of their broad activity spectrum and good oral absorption [1]. Several methods have been reported for the quantitative determination of fluoroquinolone antibiotics in human serum: high-performance liquid [2–12] and thin-layer [13] chromatographies, capillary electrophoresis [14,15], rotating electrode amperometry [16], spectrophotometry [17,18], and flow-injection analysis with chemiluminescence detection [19].

Quinolones often exhibit native fluorescence, which can be applied to their determination. The fluorescence signal can be enhanced in the solid phase [20], and also in micellar media, improving the sensitivity and detection limit [21], and allowing the simultaneous determination of several quinolones by chemometrics-improved spectrofluorimetry [22,23]. Quinolones containing α -carbonyl carboxylic acid groups form stable com-

plexes with terbium ions. The ligand-lanthanide complexes absorb energy at a wavelength which depends on the organic ligand, and emit radiation at the characteristic wavelength of terbium (III) (546 nm) [21,24,25]. The luminescence of these systems arises from an intramolecular energy transfer process from the excited triplet state of the analyte to the emitting level of the lanthanide ion, with the intensity depending on the substituent attached to the nitrogen atom of the pyridone ring [21,26]. Moreover, the luminescence signal may be increased using a micellar medium and/or a second ligand leading to the formation of ternary complexes. This synergist ligand removes water molecules from the coordination sphere of the lanthanide ion, and the micellar environment protects the analyte–lanthanide chelate against non-radiative processes [25]. Furthermore, the use of a deoxygenating agent such as sodium sulphite avoids the non-radiative deactivation of the triplet state caused by dissolved oxygen [21]. Lanthanide-sensitized luminescence in the univariate calibration mode [1,21,24–31] has been applied to the determination of a number of fluoroquinolones in serum.

In several methods described to quantify fluoroquinolones salicylic acid has been found to be a serious interferent [25,26,28]. Salicylic acid forms luminescent terbium chelates in the presence of EDTA [32,33], providing the basis for the interferent effect of this

* Corresponding author.

** Corresponding author. Tel.: +54 341 4372704; fax: +54 341 4372704.

E-mail address: aolivieri@bioyf.unr.edu.ar (A.C. Olivieri).

drug. If a test sample contains salicylic acid, or other potentially interfering constituents, univariate calibration cannot be applied, but multivariate data (particularly second-order data) can be useful in this regard.

It is known that analyte quantitation in the presence of responsive potential interferences can be performed by measuring second-order signals and processing them with appropriate second-order multivariate algorithms, achieving the second-order advantage [34–37]. Recently, lanthanide-sensitized excitation-time decay (LSETD) luminescence matrix data have been shown to be useful in obtaining the second-order advantage, allowing the determination of benzoate in beverages in the presence of the interferent saccharin [38].

In the present report, we discuss the analysis of three fluoroquinolones (ciprofloxacin, norfloxacin and danofloxacin) in human serum samples, in the presence of salicylate as a potential interferent, by measuring and processing LSETD matrix data. The system under investigation presents several analytical challenges: (1) the background serum significantly modifies the signal intensity arising from the analyte–lanthanide complex in comparison with that recorded in aqueous solutions, and (2) the second-order signals from the analyte–lanthanide and interferent–lanthanide complexes display very similar luminescence time decay profiles.

The effect of a background on the analyte response leading to a change in the slope of the univariate signal–concentration relationship can be corrected by standard addition calibration [39]. However, responsive non-analytes in a test sample constitute an interference in univariate analysis, requiring the achievement of the second-order advantage for successful quantitation. In the presence of both responsive interferences and background-driven changes on the analyte intensity, second-order calibration using the standard addition mode is needed for analyte quantitation [40–43]. This is the reason why LSETD matrix data have been employed for the present study.

On the other hand, if analyte and interferent profiles are highly overlapped in one of the data dimensions, only few algorithmic approaches are able to decompose the overall signal into contributions from the analyte and the remaining constituents [44]. Multivariate curve resolution-alternating least-squares (MCR-ALS) [45] has been recently shown to be able to accomplish this task, at least when external calibration is applied [44]. In this report, we show that standard addition coupled to MCR-ALS is useful to determine fluoroquinolones in human serum in the presence of salicylate as interferent, by processing second-order LSETD data for their terbium (III) complexes. However, rather than implementing the classical mode of standard addition, we found that better results are obtained with a modified approach, in which matrix data from the test sample are subtracted from the standard addition matrices, and quantitation is subsequently done using the external calibration methodology. Simulations show that this modified mode is more reliable, because it leads to a lower degree of overlapping in the time decay dimension. Although MCR-ALS has been previously implemented using standard addition [46], to the best of our knowledge, this is the first time that standard addition second-order data are analyzed in the presently described manner.

2. Experimental

2.1. Equipment

An SLM Aminco Bowman Series 2 luminescence spectrometer was used, equipped with a 7W Xenon pulsed lamp, and connected to a PC microcomputer with the AB2 software which runs under OS2. Instrumental parameters were: slit widths, 8 nm (excitation) and 16 nm (emission), delay, 225 μ s; gate, 800 μ s; minimum flash period, 5 ms; photomultiplier tube (PMT) sensitivity, 550 mV; masked detector. The temperature of the cell compartment was kept constant at 25 °C by circulating distilled water from a thermostated tank (Cole-Parmer).

Individual excitation spectra were recorded at the emission wavelength of 545 nm. For the time decay measurements, excitation and emission wavelengths were 271 and 545 nm, respectively, while the time gate varied from 225 to 800 μ s in periods of 25 μ s. The LSETD data matrices were collected with the emission wavelength fixed at 545 nm, using excitation wavelengths from 240 to 350 nm each 5 nm (23 data points), and decay times from 225 to 800 μ s each 25 μ s (24 data points). In this way, the excitation-time matrices were of size 23 \times 24. These LSETD matrices were then saved in ASCII format, and transferred to a PC Sempron AMD microcomputer for subsequent manipulation by the second-order multivariate curve resolution program MCR-ALS.

2.2. Reagents

All reagents were of analytical grade. The following solutions were prepared: (1) stock solutions of ciprofloxacin (100.0 mg L⁻¹, Fluka, Sigma–Aldrich, Steinheim, Germany), norfloxacin (50.0 mg L⁻¹, Sigma–Aldrich, Steinheim, Germany) and danofloxacin (50.0 mg L⁻¹, Riedel-de Haën, Sigma–Aldrich, Steinheim, Germany) in acetic acid 50 mmol L⁻¹ (Merck, Buenos Aires, Argentina), (2) sodium salicylate (1000 mg L⁻¹, Merck, Darmstadt, Germany) in distilled water, (3) terbium (III) (2.00×10^{-2} mol L⁻¹) from terbium chloride hexahydrate (Fluka, Buchs, Switzerland) in distilled water, (4) sodium dodecyl sulphate (SDS, 1.20×10^{-1} mol L⁻¹, Merck, Darmstadt, Germany) in distilled water, (5) sodium sulphite (7.50×10^{-2} mol L⁻¹, Merck, Darmstadt, Germany) in distilled water, and (6) a sodium acetate/acetic acid buffer (1.00 mol L⁻¹, pH 6.50) in distilled water. Eight different serum samples were taken from healthy volunteers.

2.3. Procedure

For the determination of each fluoroquinolone in serum in the presence of salicylate, appropriate aliquots of the corresponding stock solutions were added to different sera, with the analyte and interferent concentrations randomly selected from the therapeutic ranges. They were deproteinized (1:2 acetonitrile), and the supernatant (0.24 mL for ciprofloxacin and 0.20 mL for the remaining two analytes) was placed in a 2.00 mL volumetric flask. The required amounts of the stock solutions of terbium (III), SDS, sodium sulphite and acetic/acetate buffer were then added to this flask, and completion to the mark was achieved with distilled water. The final concentrations of terbium (III), SDS, sulphite and buffer were 1.00×10^{-3} mol L⁻¹, 4.80×10^{-3} mol L⁻¹, 7.50×10^{-3} mol L⁻¹ and 0.10 mol L⁻¹, respectively. The solution was placed in the cuvette and LSETD matrix was measured. Three successive additions of analyte stock solution (2.0 μ L for ciprofloxacin and 2.8 μ L for the other two analytes) were then carried out, in such a way that the analyte concentrations were respectively increased by (1) 0.10, 0.20 and 0.30 mg L⁻¹ for ciprofloxacin, and (2) 0.07, 0.14 and 0.21 mg L⁻¹ for norfloxacin and danofloxacin (concentration changes by dilution were considered negligible). After each addition, the samples were homogenized. The final concentration ranges for the analyzed drugs were as follows (values refer to the measuring cell): ciprofloxacin, from 0.00 to 0.24 mg L⁻¹, norfloxacin and danofloxacin, from 0.00 to 0.20 mg L⁻¹, and the potential interferent salicylate, from 4.00 to 12.00 mg L⁻¹. We estimate the uncertainties in all these analyte concentrations to be of the order of ± 0.01 mg L⁻¹. The degree of serum dilution (1:25) was

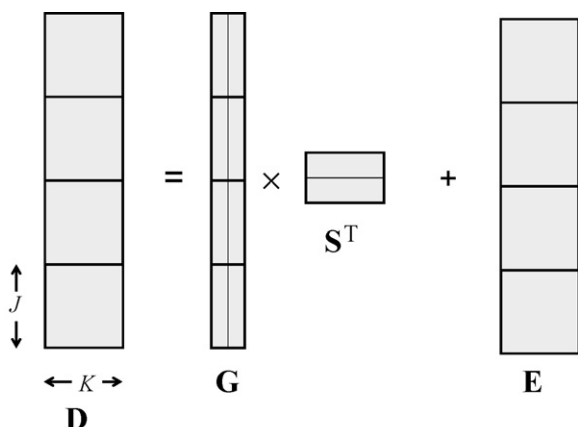


Fig. 1. Schematic illustration of the MCR-ALS decomposition of the augmented matrix **D** [see Eq. (1)]. The gray rectangles placed on top of each other represent the data matrices for each experimental sample contained in **D**. Matrix **G** is shown as comprising the time decay profiles for two sample components, while matrix **S** contains two rows, each describing the excitation spectrum of the sample components.

such that the maximum serum concentrations of the studied drugs were 6 mg L^{-1} for the three fluoroquinolones, and ca. 300 mg L^{-1} for salicylate. All these concentration ranges are within the therapeutic values of the studied drugs in human serum [47].

3. Theory

3.1. MCR-ALS

In this second-order multivariate method, an augmented data matrix is created from the test data matrices and (1) calibration data matrices in the external calibration mode, or (2) standard addition matrices in the standard addition mode. If the matrices are of size $J \times K$, where J is the number of time decay points and K the number of wavelengths, the rows represent the spectral mode and the columns the temporal mode. Augmentation can be performed in the column direction or in the row direction, depending on the type of experiment being analyzed and also on the presence of severe overlapping in one of the data modes [44,45]. In the presently studied case, the luminescence half-lives for the terbium (III) complexes of the analyte and the potential interference are very similar, and hence it is useful to implement the temporal- (i.e., column-) augmentation mode, where the matrices are placed on top of each other (Fig. 1). The bilinear decomposition of the augmented matrix is then performed according to the expression:

$$\mathbf{D} = \mathbf{G}\mathbf{S}^T + \mathbf{E} \quad (1)$$

where the rows of **D** contain the excitation spectra measured for different samples at several decay times, the columns of **G** contain the time decay profiles of the intervening species, the columns of **S** their related spectra, and **E** is a matrix of residuals not fitted by the model. Fig. 1 shows the decomposition of matrix **D** in an illustrative scheme. Appropriate dimensions of **D**, **G**, **S** and **E** are $(IJ) \times K$, $(IJ) \times N$, $K \times N$ and $(IJ) \times K$, respectively (I is the total number of samples in matrix **D**, and N the number of responsive components). Decomposition of **D** is achieved by iterative least-squares minimization of the Frobenius norm of **E**. The minimization is started by supplying estimated spectra for the various components, which are employed to estimate $\hat{\mathbf{G}}$ (with the 'hat' implying an estimated matrix) from Eq. (1):

$$\hat{\mathbf{G}} = \mathbf{D}(\mathbf{S}^T)^+ \quad (2)$$

where the superscript '+' indicates the generalized inverse. With matrix $\hat{\mathbf{G}}$ from Eq. (2) and the original data matrix **D**, the spectral matrix **S** is re-estimated by least-squares:

$$\hat{\mathbf{S}} = \mathbf{D}^T(\hat{\mathbf{G}}^+)^T \quad (3)$$

and finally **E** is calculated from Eq. (1) using **D** and the estimated $\hat{\mathbf{G}}$ and $\hat{\mathbf{S}}$ matrices. These steps are repeated until convergence, under suitable constraining conditions during the ALS process, for example, non-negativity in spectral and time profiles. It is important to point out that MCR-ALS requires initialization with system parameters as close as possible to the final results. One may supply, for example, the species spectra, as obtained from either pure analyte standards or from the analysis of the so-called 'purest' spectra, based on the SIMPLISMA (simple interactive self-modelling mixture analysis) methodology, a multivariate curve resolution algorithm which extracts pure component spectra from a series of spectra of mixtures of varying composition [48]. In the present work we have employed the latter alternative in all cases.

After MCR-ALS decomposition of **D**, concentration information contained in **G** can be used for quantitative predictions, by first defining the analyte concentration score as the area under the profile for the i th sample:

$$a(i, n) = \sum_{j=1+(i-1)J}^{iJ} G(j, n) \quad (4)$$

where $a(i, n)$ is the score for the component n in the sample i . In the regular standard addition mode (herein named mode 1), the scores are employed to build a pseudo-univariate standard addition calibration graph against the added analyte concentrations, predicting the concentration in the test samples in the usual univariate manner [49]:

$$[a(1, n)|a(2, n)|\dots|a(I, n)] = m_1[0|\mathbf{y}^T] + n_1 \quad (5)$$

$$y_u = \frac{n_1}{m_1} \quad (6)$$

where n indicates the analyte, y_u is the predicted concentration, and \mathbf{y} the vector [size $(I-1) \times 1$] of nominal concentrations added to the sample.

In the modified standard addition mode 2, the test data matrix is digitally subtracted from each of the standard addition matrices, creating a new data set comprised of the unknown matrix and data matrices representing the contribution of the pure analyte, embedded in the background of the test sample. A new augmented data matrix is created with these matrices, and subjected to MCR-ALS decomposition. It should be noted that in this alternative calibration mode, an additional restriction can be imposed during the ALS minimization, namely the so-called correspondence among components and samples, which involves information as to whether a given component is present or absent in certain samples. In this case, the interferent is only present in the test sample, and this information is valuable during the decomposition of the augmented data matrix.

After decomposition, the analyte scores are defined as in Eq. (4) above, as the corresponding areas under the profile for each sample. Quantitation is then possible using the standard calibration mode, i.e.:

$$[a(2, n)|a(3, n)|\dots|a(I, n)] = m_2\mathbf{y}^T + n_2 \quad (7)$$

$$y_u = \frac{a(1, n) - n_2}{m_2} \quad (8)$$

where it is assumed that sample No. 1 is the test sample and samples 2, ..., I are the standard additions. The reasons for implementing this modified standard addition mode will be clear below.

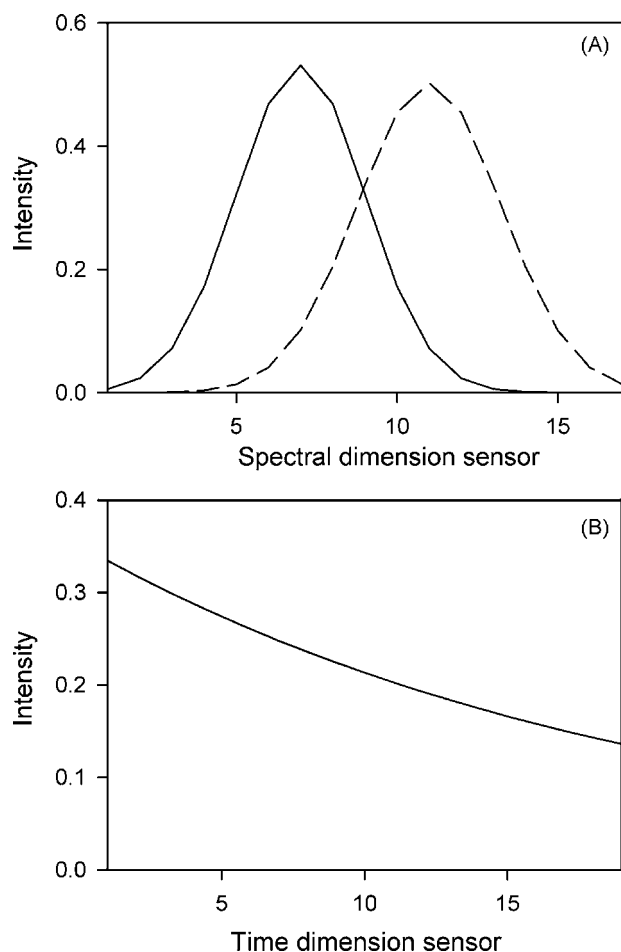


Fig. 2. (A) Excitation spectra for both components of the simulated system. (B) The corresponding time-decay profiles (solid line, analyte; dashed line, interferent). In all cases, the intensities have been normalized to unit length.

3.2. Simulations

In order to illustrate the behavior of MCR-ALS in both calibration modes discussed in the previous section, simulations were carried out for a model system. A single calibrated analyte and a single interferent were included in all test samples. Thus, proper resolution of this system requires adherence to the second-order advantage. For each test sample, three additional ones were created by simulating the addition of the analyte. The excitation-time decay matrix data were generated starting from noiseless spectral and time profiles which are shown in Fig. 2A and B, respectively. As can be seen, both components have identical time decay profiles, but differ in their excitation spectra. From the profiles shown in Fig. 2, a set of second-order signals was built for 100 test samples, with the analyte and the interferent both at concentrations chosen at random from the range 0–1 (in arbitrary units). For each of these matrices, three standard additions were simulated, adding the analyte in concentrations which were 0.5, 1 and 1.5 units in excess with respect to the original concentration. Finally, noise was added to all matrices, taken from a gaussian distribution having a standard deviation equal to 5% of the maximum signal.

The second-order data for each of the 100 test samples were then joined to those for the standard additions, and each four-sample data set was submitted to second-order calibration with MCR-ALS in both standard addition modes described below.

Table 1

Cross-validation PCA analysis of a typical simulated test sample data matrix and of the augmented matrices in both standard addition modes.

n^a	RSSE ^b	PRESS ^c	PRESS(n)/RSSE($n - 1$)
Test data matrix			
1	2.40×10^{-5}	2.92×10^{-5}	–
2	2.21×10^{-5}	3.14×10^{-5}	1.05
3	1.94×10^{-5}	3.36×10^{-5}	1.18
4	1.76×10^{-5}	3.36×10^{-5}	1.33
Augmented data matrix: mode 1			
1	2.56×10^{-4}	3.61×10^{-4}	–
2	2.50×10^{-5}	3.36×10^{-5}	0.11
3	2.30×10^{-5}	3.72×10^{-5}	1.20
4	2.21×10^{-5}	3.97×10^{-5}	1.34
Augmented data matrix: mode 2			
1	5.76×10^{-4}	7.29×10^{-4}	–
2	2.50×10^{-5}	3.48×10^{-5}	0.05
3	2.30×10^{-5}	3.72×10^{-5}	1.20
4	2.21×10^{-5}	4.10×10^{-5}	1.37

^a n = number of PCs. The number of significant PCs is given in bold.

^b RSSE = residual sum of squared errors after matrix reconstruction with the indicated number of PCs.

^c PRESS = predicted error sum of squares corresponding to leave-one-out cross-validation with the indicated number of PCs.

3.3. Software

Simulations were carried out using in-house MATLAB 7.0 routines [50]. The codes available on the internet for MCR-ALS [51,52] and PARAFAC [53] were employed for multivariate analysis. The latter method was applied through a MATLAB graphical user interface which is also available on the Web [54].

4. Results and discussion

4.1. Simulated data

4.1.1. Rank analysis

Before proceeding with the discussion of the MCR-ALS results for the simulated system, it is interesting to note that the performance of the resolution strongly depends on the knowledge of the global and local properties of the data set, particularly on those related to the mathematical and chemical rank [55,56]. The mathematical rank can be defined as the number of significant principal components (PCs) as obtained from principal component analysis (PCA), whereas the chemical rank is the known number of responsive chemical species [55,56]. A data matrix is considered full rank if the mathematical and chemical ranks coincide [55,56]. Usually, the number of PCs which explains the spectral variance in a matrix is assessed by comparing the residual sum of square errors (RSSE) of the matrix reconstruction with increasing number of PCs, with the predicted error sum of squares (PRESS) of leave-one-out cross-validation, as described, for example, in Ref. [57]. The correct number of PCs is the one leading to a ratio PRESS(n)/RSSE($n - 1$) which is not larger than 1, where n is a given number of PCs. Table 1 shows the results obtained for a single simulated test data matrix. As can be seen, the test data matrix is classified as rank-deficient, because the number of significant PCs is one, whereas the number of known contributing species is two. Although some selectivity exists in the spectral domain, the identical time profiles lead to the existence of a single significant principal component for this system.

To overcome the rank deficiency problem, matrix augmentation can be applied, which breaks the rank-deficiency and thus facilitates resolution [55,56]. Application of SVD to the augmented matrices obtained in both standard addition modes correctly esti-

mates the rank, i.e., two (Table 1). Thus the augmented data matrices are full rank, because the number of significant PCs and the number of chemical species coincide.

In a recent paper, it has been shown that an excellent alternative for the analysis of the present problem is the MCR-ALS algorithm [44]. The latter one is able to break the collinearity in one of the data dimensions by resorting to matrix augmentation, making possible the quantitation of a given analyte in the presence of interferents with profiles which strongly overlap those for the analyte. Although the former results have been obtained for kinetic systems, they can be easily adapted to the present case, where the time dimension is replaced by the time decay of the lanthanide-sensitized luminescence signal.

4.1.2. Prediction results

Analysis of the simulated test samples was first performed using the classical standard addition mode 1. Each test data matrix was augmented in the manner described above, and the augmented matrix was subjected to MCR-ALS analysis, imposing the restrictions of non-negativity in all profiles, and initializing the least-squares fit with the spectral profiles for both sample components as provided by the SIMPLISMA methodology. After the fitting has converged, MCR-ALS retrieved satisfactory spectral profiles, as can be observed in Fig. 3A, which shows the fitted spectra for both sample components, which can be compared to those in Fig. 2A. The retrieved time profiles for the successive data matrices are shown in Fig. 3B, illustrating how the analyte concentrations (solid line) grow in going from the test sample (the left sub-matrix) to the standard additions (the three adjacent sub-matrices), whereas the interferent (dashed line) remains almost constant, as expected. This figure illustrates the remarkable success of MCR-ALS in decomposing a data set where two components have identical profiles in the time dimension.

After decomposition of the augmented matrix in this first standard addition mode, the obtained scores for the test samples were converted to analyte concentration by means of the well-known standard addition Eqs. (5) and (6). The prediction results showed that the root mean square error (RMSE) was 0.017 units, corresponding to a relative error of prediction (REP) of 3.4% with respect to the mean test concentration (0.5 units). Although these figures of merit appear to be satisfactory, implementation of the alternative standard addition mode rendered even better prediction results, as explained below.

In the alternative mode of standard addition described above (mode 2), MCR-ALS analysis resorted to similar initialization conditions and restrictions during the least-squares fit, with the additional information provided by the correspondence among species and samples. The spectral profiles recovered by the algorithm (not shown) were again very similar to those shown in Fig. 2A, while those corresponding to the time dimension, presented in Fig. 3C, are interpreted as involving an interferent profile which does only contribute to the test sample, and analyte profiles in the three right sub-matrices which allow to calibrate a pseudo-univariate model [Eq. (7)], where the left sub-matrix score is then interpolated [Eq. (8)]. This implies that quantitation can be done using the classical standard calibration equations.

The analyte prediction results in this second mode were considerably better than for the first mode of analysis: the RMSE decreased to 0.007 concentration units, corresponding to a REP of only 1.4%. We ascribe this improved analytical performance to a lower degree of overlap in the augmented time direction when the alternative mode 2 of standard addition is applied. In order to quantitate the degree of overlap (S_{12}) in the time decay profiles between components 1 and 2, an analogous expression to the squared correlation

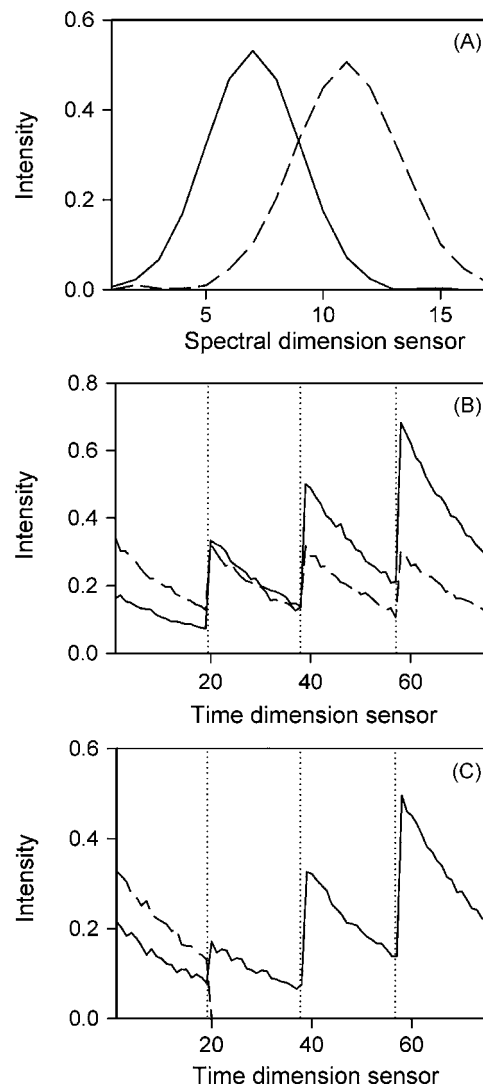


Fig. 3. Profiles retrieved by MCR-ALS when processing a typical test sample of the simulated system, together with the standard addition matrices. (A) Spectral profiles, common to all samples in the regular standard addition mode 1 (those for the modified standard addition mode 2 are identical). (B) Time-decay profiles for successive matrix samples in the regular standard addition mode 1. The dotted lines separate the different samples: from left to right, test sample and the three standard additions. (C) Time-decay profiles for successive matrix samples in the modified standard addition mode 2. The dotted lines separate the different samples: from left to right, test sample and the results of subtracting the test sample data from the three standard additions. In all cases, the solid line indicates the analyte and the dashed line the interferent.

coefficient can be employed:

$$S_{12} = \frac{\|\mathbf{t}_1^T \mathbf{t}_2\|}{\|\mathbf{t}_1\| \|\mathbf{t}_2\|} \quad (9)$$

where \mathbf{t}_1 and \mathbf{t}_2 are the time profiles for components 1 and 2, respectively along the augmented time dimension, i.e., each of these profiles has (IK) elements (see Fig. 3B and C). In general, the value of S_{12} ranges from zero to one, corresponding to the extreme situations of no overlapping and complete overlapping, respectively. Using Eq. (9), the overlap for the regular mode 1 and modified standard addition mode 2 are 0.90 and 0.26, respectively. This result justifies the better predictive ability of the modified mode 2.

4.2. Experimental data

4.2.1. Optimization of the luminescence signal

General conditions for generating lanthanide-sensitized luminescence from their fluoroquinolone complexes were taken from the literature [21,30]. For each of the chemical variables which are likely to have an effect on the intensity of the LSETD signal arising from the ciprofloxacin terbium (III) complex, univariate optimizations were carried out. The concentration of terbium (III) was varied (6 points) between 2.0×10^{-4} and $4 \times 10^{-3} \text{ mol L}^{-1}$, with an optimum at $1.0 \times 10^{-3} \text{ mol L}^{-1}$. The SDS concentration ranged from 6.0×10^{-4} to $1.8 \times 10^{-2} \text{ mol L}^{-1}$ (six different values), with an optimum at $4.8 \times 10^{-3} \text{ mol L}^{-1}$. For the sulphite concentration, five concentrations between 4.5×10^{-3} and $1.5 \times 10^{-2} \text{ mol L}^{-1}$ were checked, and the optimum results were obtained at $7.5 \times 10^{-3} \text{ mol L}^{-1}$. Finally, four pH values were tried: 4.0, 5.5, 6.5 and 7.0, with the best results obtained at pH 6.5. The optimum conditions were then set for all subsequent experiments and for all three analytes.

4.2.2. The need of standard addition

The first issue to be assessed was whether the analysis of the presently studied fluoroquinolones in serum requires the use of standard addition. We found that the latter technique was indeed required, because of a significant change in the slope of the univariate regression of lanthanide-sensitized luminescence intensities of the terbium (III) complexes with respect to analyte concentrations. In order to verify this assertion, several univariate calibration curves were built for each analyte in the presence of serum, which were compared to that obtained in water solution. The results for ciprofloxacin in water, for example, with six different concentrations in the range $0.0\text{--}0.50 \text{ mg L}^{-1}$ were slope = 185(2), intercept = 2.2(5), $r^2 = 0.9985$ (standard deviation in the last significant figures in parenthesis), while in a typical serum background, slope = 142(3), intercept = 10(1), $r^2 = 0.9999$. The results suggest a significant change in slope (a decrease of 43 units in slope, ca. 17 times larger than the average standard deviation). Moreover, the elliptical joint confidence regions for each pair of slope and intercept do (drawn at 95% confidence level) do not overlap, confirming the differential behaviour of the analyte signal in the absence and presence of serum. These results can be attributed, in principle, to analyte–background interactions, requiring standard addition for successful analyte quantitation. Recently, it has been suggested that an alternative to standard addition is to employ external calibration in the presence of background [58]. However, in the present case it was found that each serum produces a specific change in analyte response which significantly varies from serum to serum, making this latter alternative unfeasible.

In the presence of unexpected sample components producing luminescent terbium (III) complexes, such as salicylate, standard addition should be complemented with the measurement of second-order excitation-time decay data, in order to be able to achieve the second-order advantage [40–43]. It should be noticed that blank serum samples did not produce any significant luminescence signal under the present working conditions, confirming that the only effect of the background serum was a change in the intensity of the analyte–terbium complex.

4.2.3. Spectral and time decay profiles

Fig. 4 shows a typical landscape of LSETD data for a serum sample spiked with both ciprofloxacin and salicylate. This is the type of signals which can in principle provide the required second-order advantage, as recently described [38]. It should be noticed that all LSETD matrices for the present study have been obtained by keeping the emission wavelength fixed at 545 nm, the emis-

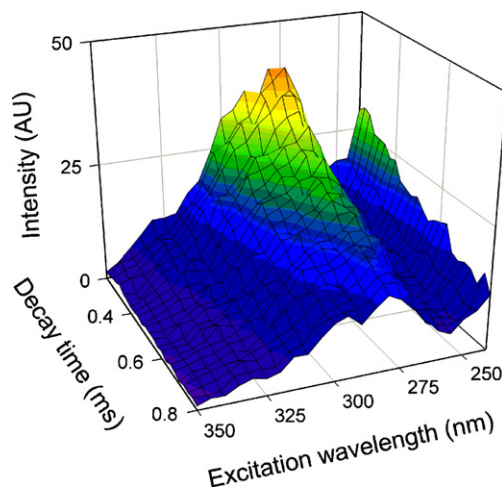


Fig. 4. Three-dimensional LSETD matrix as a function of time decay and excitation wavelength, corresponding to a serum sample spiked with ciprofloxacin 0.14 mg L^{-1} and salicylate 11.8 mg L^{-1} .

sion line for the terbium (III) with maximum intensity. Since the emission always proceeds from an excited state of the lanthanide ion, this dimension does not provide selectivity to the analysis, and this is the reason why it is kept constant. One important

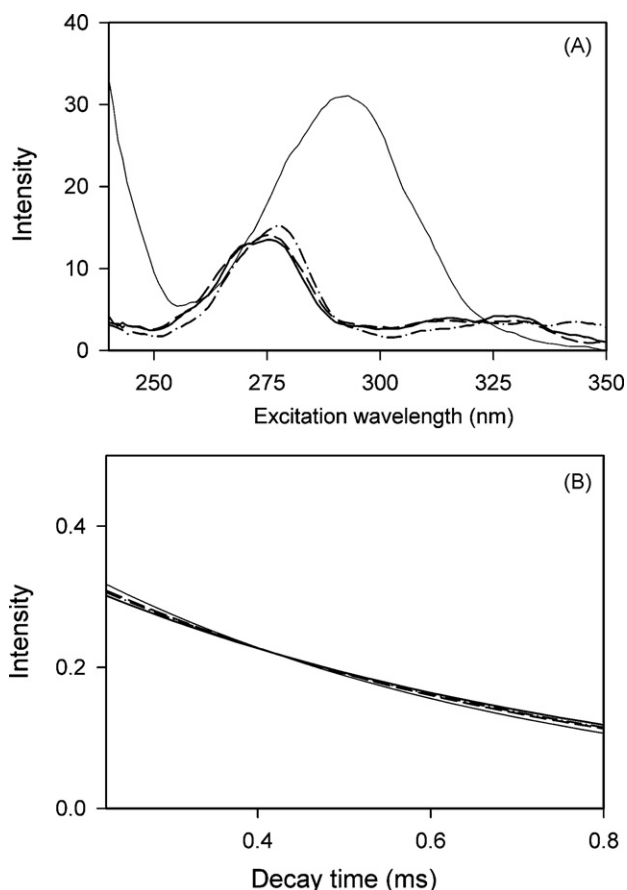


Fig. 5. (A) Thick lines: excitation lanthanide-sensitized luminescence spectra for the terbium (III) complexes of the studied analytes in serum, all at concentrations 0.1 mg L^{-1} : ciprofloxacin, solid line, norfloxacin, dashed line, danofloxacin, dashed-dotted line. Thin line: the corresponding excitation spectrum for salicylate (8.0 mg L^{-1} in serum). (B) Time decay curves for all the components shown in part (A), after normalization to unit length. Lines are denoted as in plot (A).

Table 2

Cross-validation PCA analysis of a data matrix for a typical serum sample spiked with both ciprofloxacin and salicylate, and of the corresponding standard addition augmented matrix.

n^a	RSSE ^b	PRESS ^c	PRESS(n)/RSSE($n-1$)
Test data matrix			
1	1.01	1.12	–
2	0.96	1.15	1.06
3	0.91	1.16	1.20
4	0.86	1.19	1.39
Augmented data matrix: mode 2			
1	1.67	1.71	–
2	1.39	1.44	0.68
3	1.32	1.40	1.00
4	1.28	1.39	1.01

^a n = number of PCs. The number of significant PCs is given in bold.

^b RSSE = residual sum of squared errors after matrix reconstruction with the indicated number of PCs.

^c PRESS = predicted error sum of squares corresponding to leave-one-out cross-validation with the indicated number of PCs.

requirement for the application of most second-order multivariate calibration algorithms is that there is sufficient selectivity in both data modes between the calibrated analyte and the interferents. In the present case, the excitation mode shows good selectivity

between analyte and salicylate (Fig. 5A). However, in the time mode the selectivity is rather poor, as shown in Fig. 5B. The life times corresponding to the profiles shown in the latter figure, obtained by non-linear least-squares regression to the exponential decay expression $f(t) = \exp(-t/\tau)$ are ciprofloxacin, 0.60(1), norfloxacin, 0.62(1), danofloxacin, 0.57(1) and salicylate, 0.59(1) (values in ms, with the standard deviation in the last significant figure in parenthesis), confirming that they are all very similar. In fact, the degrees of overlap between the time decay profiles for each of the lanthanide complexes of the fluoroquinolones and of the interferent salicylate, quantified through Eq. (9) are 0.9991, 0.9998 and 0.9996 for ciprofloxacin, norfloxacin and danofloxacin, respectively.

4.2.4. Second-order multivariate analysis

Preliminary results using second-order standard addition and data processing using parallel factor analysis [59] provided unsatisfactory results for all three analytes. We ascribe these poor results to the high collinearity among the time decay profiles of Fig. 5B.

Because the selectivity in the time dimension is very poor, the experimental fluoroquinolone–salicylate system resembles the simulated data analyzed in Section 4.1.1. Therefore, MCR-ALS was selected as the second-order multivariate calibration algorithm of choice. However, due to the significant change in the slope of the

Table 3

Prediction results for the test serum samples spiked with both ciprofloxacin and salicylate.

Sample	Nominal analyte (mg L ⁻¹)	Salicylate (mg L ⁻¹)	Serum type ^a	Predicted analyte (mg L ⁻¹)	MCR components ^b
1	0.22	9.80	A	0.24	1
2	0.22	9.80	D	0.19	1
3	0.24	10.80	A	0.23	1
4	0.19	7.30	A	0.19	1
5	0.14	11.80	B	0.16	2
6	0.00	8.00	B	0.02	2
7	0.13	4.00	B	0.12	1
8	0.13	4.00	D	0.15	1
9	0.17	5.50	C	0.17	2
10	0.17	5.50	D	0.20	2
11	0.11	6.10	C	0.14	2
12	0.18	11.20	C	0.15	1
13	0.18	11.20	D	0.19	2
14	0.08	6.40	E	0.08	1
15	0.08	10.00	E	0.10	1
16	0.08	10.00	F	0.10	2
RMSE				0.02	
REP%				8.3	

^a The letter identifies the type of serum employed in sample preparation.

^b Number of components employed in the MCR decomposition of the augmented matrix, as determined by PCA (see text).

Table 4

Prediction results for the test serum samples spiked with both norfloxacin and salicylate.

Sample	Nominal analyte (mg L ⁻¹)	Salicylate (mg L ⁻¹)	Serum type ^a	Predicted analyte (mg L ⁻¹)	MCR components ^b
1	0.10	8.00	A	0.09	1
2	0.10	8.00	B	0.12	2
3	0.18	8.20	C	0.14	2
4	0.18	8.20	D	0.25	2
5	0.12	9.80	C	0.12	1
6	0.08	9.00	E	0.09	1
7	0.08	9.00	F	0.09	1
8	0.00	6.70	F	0.02	2
9	0.15	9.30	G	0.20	2
10	0.20	9.00	G	0.25	2
11	0.16	6.10	H	0.10	1
12	0.14	4.60	H	0.12	1
13	0.09	5.10	H	0.09	1
RMSE				0.03	
REP%				15	

^a The letter identifies the type of serum employed in sample preparation.

^b Number of components employed in the MCR decomposition of the augmented matrix, as determined by PCA (see text).

Table 5

Prediction results for the test serum samples spiked with both danofloxacin and salicylate.

Sample	Nominal analyte (mg L ⁻¹)	Salicylate (mg L ⁻¹)	Serum type ^a	Predicted analyte (mg L ⁻¹)	MCR components ^b
1	0.10	10.00	A	0.11	2
2	0.10	10.00	B	0.10	2
3	0.10	8.00	A	0.11	2
4	0.10	8.00	B	0.11	2
5	0.18	8.20	C	0.18	1
6	0.12	9.80	C	0.12	1
7	0.08	9.00	C	0.09	1
8	0.00	6.70	D	0.02	2
9	0.00	6.70	F	-0.01	2
10	0.15	9.30	D	0.19	2
11	0.20	9.00	E	0.14	1
12	0.16	6.10	E	0.17	1
13	0.14	4.60	F	0.17	1
14	0.09	5.10	F	0.10	2
RMSE				0.02	
REP%				10	

^a The letter identifies the type of serum employed in sample preparation.^b Number of components employed in the MCR decomposition of the augmented matrix, as determined by PCA (see text).

signal–concentration relationship for the analytes in the presence of the human serum background, MCR-ALS was implemented in the standard addition mode. As discussed in connection with the simulated data sets, the best alternative is to use the second mode of standard addition, which was subsequently employed in all the fluoroquinolone analyses described below.

As explained in connection with the simulated data, rank analysis was performed by PCA of the augmented matrices before application of MCR-ALS decomposition. Table 2 shows results for the PCA study of a typical spiked serum sample where the contribution of salicylate is detectable. As can be appreciated, the test data matrix is rank-deficient, because PCA can only detect a single significant PC, whereas two significant PCs are required to explain the spectral variability across the augmented data matrix. These two components correspond to the responsive analyte and the potential interferent. This rank analysis was performed for all of the test samples before application of MCR-ALS. In certain cases, although the sera were spiked with the analyte and also with the potential interferent, the rank of the augmented matrices was found to be one. In all of these latter cases, the matrices were still full rank, because it was verified that the signal arising from the terbium (III) complex of salicylate was undistinguishable from the instrumental noise, and MCR-ALS provided a satisfactory fit by considering a single responsive component whose spectral characteristics were those of the complexes of the analytes. It may be noticed that although salicylate leads to an intense spectrum (Fig. 5A) when complexed to terbium (III), when either of the analytes is present the intensity from the salicylate complex is smaller, probably as a consequence of a competitive effect which favours complex formation with the analytes.

Fig. 6 shows the MCR-ALS decomposition results for a typical spiked serum sample containing ciprofloxacin and salicylate, and requiring two responsive components for successful data processing. Fig. 6A displays the retrieved spectral profiles, which are seen to resemble those for the terbium complexes of the analyte and the potential interferent (compare with Fig. 5A). Although the profiles of Fig. 6A are normalized to unit length, it is apparent that the main spectral features of ciprofloxacin and salicylate (maxima at around 275 and 300 nm, respectively) are well reproduced. On the other hand, Fig. 6B shows the progression of time decay profiles in the standard addition study of a typical test sample. The left sub-plot corresponds to the test sample itself, while the three remaining matrices are those obtained after subtracting the test sample matrix from each of the standard addition matrices (in the

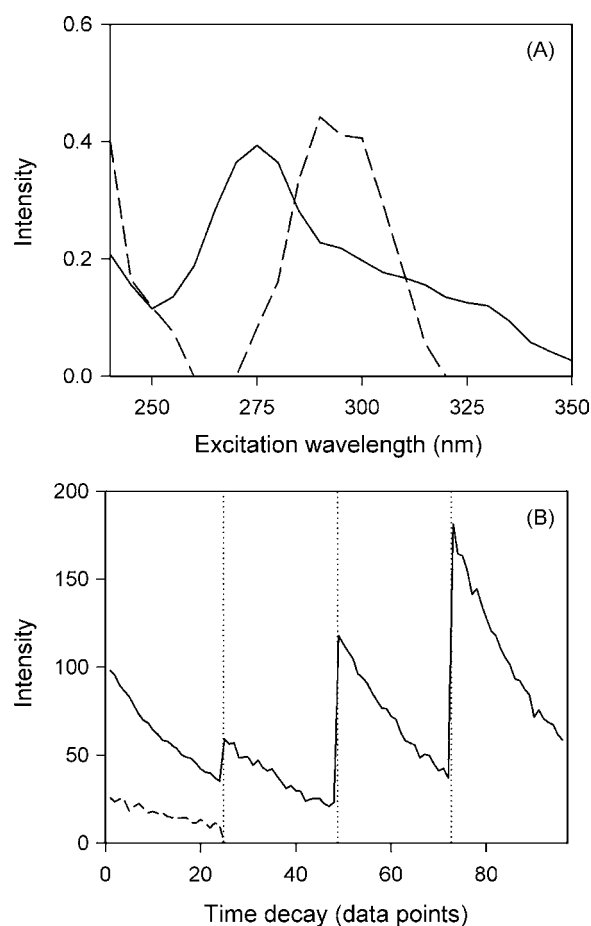


Fig. 6. MCR-ALS results for a typical serum sample, spiked with the analyte ciprofloxacin (0.14 mg L⁻¹) and salicylate (11.8 mg L⁻¹). (A) Excitation lanthanide-sensitized luminescence profiles for the terbium (III) complexes of both sample components. (B) Time-decay profiles for successive matrix samples in the standard addition mode 2. The dotted lines separate the different samples: from left to right, test sample and the results of subtracting the test sample data from the three standard additions. In all cases, the solid line indicates the analyte and the dashed line the interferent. The vertical scales are arbitrary.

latter three sub-plots, therefore, the profile for the interferent is absent). Fig. 6A and B are illustrative of the success of MCR-ALS in decomposing the contributions from the analyte and from the interferent, even when the time decay profile for the salicylate complex is almost identical to that of the ciprofloxacin complex.

4.2.5. Prediction results

Tables 3–5 collect the prediction results for all the spiked samples analyzed using the above-discussed methodology. It could be argued that the samples having a single responsive component could also be analyzed using univariate standard addition, by picking the signal intensity at the analyte excitation and time maxima. However, we prefer to report the results provided by MCR-ALS analysis, because: (1) it provides higher sensitivity and (2) all results are compared on a common basis.

Overall, the results are encouraging: root mean square errors (RMSE), expressed in mg L^{-1} , are 0.02, 0.03 and 0.02 for ciprofloxacin, norfloxacin and danofloxacin, respectively, i.e., in the ppb range. They correspond to REP% (relative errors of prediction) of 8.3, 15 and 10%, respectively, all reasonable in view of the complexity of the present analysis. Although it is difficult to assess the limit of detection for standard addition using MCR-ALS, the results suggest that this figure of merit is around 0.02 mg L^{-1} for all three analytes, based both on the values of the RMSEs and on the fact that blank serum samples, only containing salicylate, are also predicted to contain $0.01\text{--}0.02 \text{ mg L}^{-1}$ (Tables 3–5).

It should be stressed that the above analysis cannot be performed by univariate calibration of luminescence signals, because of the presence of potentially interfering compounds in a given sample, such as salicylic acid. Only second-order data analysis resorting to the second-order advantage can be employed for this purpose. This strategy is able to model the presence of unexpected sample components generating interference, allowing for accurate analyte quantitation in complex samples.

5. Conclusions

Fluoroquinolones can be quantitated in human serum in the presence of salicylate by suitable processing of second-order lanthanide-sensitized excitation-time decay luminescence data. Because of the presence of a responsive interferent whose instrumental signal overlaps with that from the analytes, successful analysis requires second-order data processing using multivariate curve resolution, which is able to overcome the following challenges: (1) presence of unknown constituents in a test sample, (2) background matrix effects leading to changes in the analyte signal, and (3) very similar time decay profiles for the analyte and the interferent.

Acknowledgments

Universidad Nacional de Rosario, CONICET (Consejo Nacional de Investigaciones Científicas y Técnicas, Project No. PIP 5303) and ANPCyT (Agencia Nacional de Promoción Científica y Tecnológica, Project No. PICT-25825) and AEIC (Agencia Española de Cooperación Internacional, Project A/8864/07) are gratefully acknowledged for financial support. V.A.L. thanks ANPCyT for a fellowship.

References

- [1] S. Morales-Muñoz, J.L. Luque-García, M.D. Luque de Castro, J. Chromatogr. A 1059 (2004) 25.
- [2] A. Zotou, N. Miltiadou, J. Pharm. Biomed. Anal. 28 (2002) 559.
- [3] U. Neckel, C. Joukhadar, M. Frossard, W. Jaeger, M. Mueller, B.X. Mayer, Anal. Chim. Acta 463 (2002) 199.

- [4] T. Zupancic, B. Pihlar, J. Chromatogr. A 975 (2002) 199.
- [5] O.R. Idowu, J.O. Peggins, J. Pharm. Biomed. Anal. 35 (2004) 143.
- [6] A. Espinosa-Mansilla, A. Muñoz de la Peña, D. González-Gómez, F. Salinas-López, Talanta 68 (2006) 1215.
- [7] Z. Vybiralova, M. Nobilis, J. Zoulova, J. Kvetina, P. Petr, J. Pharm. Biomed. Anal. 37 (2005) 851.
- [8] A. Espinosa-Mansilla, A. Muñoz de la Peña, D. González-Gómez, F. Salinas-López, J. Chromatogr. B 822 (2005) 185.
- [9] C. González, L. Moreno, J. Small, D.G. Jones, S.F. Sánchez Bruni, Anal. Chim. Acta 560 (2006) 227.
- [10] I.M. van Geijlswijk, A.R.H. van Zanten, Y.G. van der Meer, Ther. Drug. Monit. 28 (2006) 278.
- [11] J.L. Vilchez, L. Araujo, A. Prieto, A. Navalón, Anal. Chim. Acta 516 (2004) 135.
- [12] T. Galaon, S. Udrescu, I. Sora, V. David, A. Medvedovici, Biomed. Chromatogr. 21 (2007) 40.
- [13] Y.L. Feng, C. Dong, J. Chromatogr. Sci. 42 (2004) 474.
- [14] M. Hernandez, C. Aguilar, F. Borruil, M. Calull, J. Chromatogr. B 772 (2002) 163.
- [15] M. Ferdig, A. Kaleta, T. Diep Thanh Vo, W. Buchberger, J. Chromatogr. A 1047 (2004) 305.
- [16] A.A.J. Torriero, E. Salinas, J. Raba, J.J. Silber, Biosens. Bioelectron. 22 (2006) 109.
- [17] M.E. El-Kommos, G.A. Saleh, S.M. El-Gizawi, M.A. Abou-Elwafa, Talanta 60 (2003) 1033.
- [18] M. Rizk, F. Belal, F. Ibrahim, S. Ahmed, Z.A. Sheribah, J. AOAC Int. 84 (2001) 368.
- [19] H.W. Sun, L.Q. Li, X.Y. Chen, Anal. Bioanal. Chem. 384 (2006) 1314.
- [20] J.L. Vilchez, O. Ballesteros, J. Taoufik, G. Sánchez-Palencia, A. Navalón, Anal. Chim. Acta 444 (2001) 279.
- [21] J.A. Ocaña, F.J. Barragán, M. Callejón, Talanta 63 (2004) 691.
- [22] A. Muñoz de la Peña, A. Espinosa-Mansilla, D. González-Gómez, A.C. Olivieri, H.C. Goicoechea, Anal. Chem. 75 (2003) 2640.
- [23] D.M. Fang, H.L. Wu, Y.J. Ding, L.Q. Hu, A.L. Xia, R.Q. Yu, Talanta 70 (2006) 58.
- [24] Y. Wang, L. Feng, C. Jiang, Spectrochim. Acta A 61 (2005) 2909.
- [25] R.C. Rodríguez-Díaz, M.P. Aguilar-Caballeros, A. Gómez-Hens, Anal. Chim. Acta 494 (2003) 55.
- [26] R.C. Rodríguez-Díaz, M.P. Aguilar-Caballeros, A. Gómez-Hens, Anal. Lett. 37 (2004) 1163.
- [27] R.M. Cuenca-Trujillo, M.J. Ayora-Canada, A. Molina-Díaz, J. AOAC Int. 85 (2002) 1268.
- [28] S. Panadero, A. Gómez-Hens, D. Pérez-Bendito, Anal. Chim. Acta 303 (1995) 39.
- [29] C.J. Veiopoulou, P.C. Ioannou, E.S. Lianidou, J. Pharm. Biomed. Anal. 15 (1997) 1839.
- [30] J.A. Ocaña, M. Callejón, F.J. Barragán, Analyst 125 (2000) 1851.
- [31] E.J. Llorent-Martínez, J.F. García-Reyes, P. Ortega-Barrales, A. Molina-Díaz, Anal. Chim. Acta 532 (2005) 159.
- [32] N. Arnaud, J. Georges, Analyst 124 (1999) 1075.
- [33] S. Panadero, A. Gómez-Hens, D. Pérez-Bendito, Anal. Chim. Acta 329 (1996) 135.
- [34] G.M. Escandar, N.M. Faber, H.C. Goicoechea, A. Muñoz de la Peña, A.C. Olivieri, R.J. Poppi, Trends Anal. Chem. 26 (2007) 752.
- [35] R. Bro, Crit. Rev. Anal. Chem. 36 (2006) 279.
- [36] Á. Rinnan, J. Riu, R. Bro, J. Chemometrics 21 (2007) 76.
- [37] K.S. Booksh, B.R. Kowalski, Anal. Chem. 66 (1994) 782A.
- [38] V.A. Lozano, G.A. Ibañez, A.C. Olivieri, Anal. Chim. Acta 610 (2008) 186.
- [39] R.C. Castells, M.A. Castillo, Anal. Chim. Acta 423 (2000) 179.
- [40] M.M. Sena, M.G. Trevisan, R.J. Poppi, Quim. Nova 28 (2005) 910.
- [41] J.A. Arancibia, A.C. Olivieri, G.M. Escandar, Anal. Bioanal. Chem. 374 (2002) 451.
- [42] M. Bahram, R. Bro, Anal. Chim. Acta 584 (2007) 397.
- [43] V. Gómez, R. Cuadros, I. Ruisánchez, M.P. Callao, Anal. Chim. Acta 600 (2007) 233.
- [44] M.J. Culzoni, H.C. Goicoechea, G.A. Ibañez, V.A. Lozano, N.R. Marsili, A.C. Olivieri, A.P. Pagani, Anal. Chim. Acta 614 (2008) 46.
- [45] A. De Juan, E. Casassas, R. Tauler, in: R.A. Meyers (Ed.), Encyclopedia of Analytical Chemistry, John Wiley & Sons, Ltd., Chichester, 2000, p. 9800.
- [46] E. Peré-Trepát, S. Lacorte, R. Tauler, Anal. Chim. Acta 595 (2007) 228.
- [47] L.L. Brunton (Ed.), Goodman & Gilman's The Pharmacological Basis of Therapeutics, 11th edition, McGraw-Hill Inc., New York, 2006.
- [48] W. Windig, J. Guilment, Anal. Chem. 63 (1991) 1425.
- [49] J.N. Miller, J.C. Miller, Statistics and Chemometrics for Analytical Chemistry, Pearson-Prentice Hall, New York, 2005, Chapter 2.
- [50] MATLAB 7.0, The Mathworks, Natick, Massachusetts, 2003.
- [51] <http://www.ub.es/gesq/mcr/mcr.htm>.
- [52] J. Jaumot, R. Gargallo, A. de Juan, R. Tauler, Chemom. Intell. Lab. Syst. 76 (2005) 101.
- [53] www.models.kvl.dk/source/.
- [54] www.chemometry.com.
- [55] J. Saurina, S. Hernández-Cassou, R. Tauler, A. Izquierdo-Ridors, J. Chemometrics 12 (1998) 183.
- [56] A. Izquierdo-Ridors, J. Saurina, S. Hernández-Cassou, R. Tauler, Chemom. Intell. Lab. Syst. 38 (1997) 183.
- [57] R.G. Brereton, Chemometrics, Data Analysis for the Laboratory and Chemical Plant, Wiley, Chichester, UK, 2003, p. 199.
- [58] M.J. Culzoni, H.C. Goicoechea, A.P. Pagani, M.A. Cabezon, A.C. Olivieri, Analyst 131 (2006) 718.
- [59] R. Bro, Chemom. Intell. Lab. Syst. 38 (1997) 149.



Rapid determination of Δ^9 -Tetrahydrocannabinol in saliva by polymer monolith microextraction combined with gas chromatography–mass spectrometry

Dan Luo^{a,b}, Fei Chen^a, Kuang Xiao^a, Yu-Qi Feng^{a,*}

^a Department of Chemistry, Wuhan University, Wuhan 430072, PR China

^b Shanghai Office, Analytical Applications Center, Shimadzu International Trading (Shanghai) Co. Ltd., Shanghai 200020, PR China

ARTICLE INFO

Article history:

Received 28 June 2008

Received in revised form 1 October 2008

Accepted 2 October 2008

Available online 17 October 2008

Keywords:

Δ^9 -Tetrahydrocannabinol

Saliva

Polymer monolith microextraction (PMME)

Gas chromatography–mass spectrometry

ABSTRACT

A method was developed for the determination of Δ^9 -Tetrahydrocannabinol (THC) in saliva by polymer monolith microextraction (PMME) combined with gas chromatography–mass spectrometry. The poly(methacrylic acid-co-ethylene glycol dimethacrylate) (p(MAA-co-EGDMA)) monolithic capillary column was selected as the extraction medium of PMME, which showed high extraction capacity towards THC in saliva. To reach optimum PMME extraction performance, several PMME parameters were investigated, including matrix pH, flow rate for extraction, sampling volume and elution solvent. Under the optimal conditions, good extraction efficiency was obtained with no matrix interference in the process of extraction and the subsequent GC–MS analysis. In the selected-ion monitoring (SIM) mode, the limit of detection (LOD) for THC was 0.68 ng/mL. The linearity range of the method was 3–300 ng/mL. Excellent reproducibility of the method was exhibited by intra- and inter-day precisions, yielding the relative standard deviations (R.S.D.s) less than 12%; recoveries higher than 89%. The proposed method was proved to be rapid, sensitive, and competently applied to the determination of THC in saliva samples.

© 2008 Elsevier B.V. All rights reserved.

1. Introduction

Cannabis is the most commonly used illicit drug throughout the world, and Δ^9 -Tetrahydrocannabinol (THC) is the primary psychoactive constituent; it predominantly acts on the central nervous and cardiovascular systems, and may produce behavioral effects, including feelings of euphoria and relaxation, lack of concentration, hallucinations, and mood changes such as panic reactions and paranoia at high doses [1–3]. Thus the illicit use of cannabis has been an issue of concern in the law enforcement community.

Qualitative and quantitative analyses of cannabinoids have been performed based on radioimmunoassay (RIA) [4,5], HPLC [6–8], GC [9,10], LC–MS [11–13] and GC–MS [14–16]. RIA techniques are highly sensitive for the cannabinoids; however, false positives may often occur because of cross-reactivities. In addition, HPLC methods require specific detectors (e.g. amperometric detector) to replace the traditional ultraviolet detector because the latter is not sufficiently sensitive. Thus GC–MS was the most popular method because of its high sensitivity and low false positive rate. However, derivatization is essential for the detection of THC metabolites like

THC–COOH by GC–MS, which is laborious and time-consuming. If the analyte of interest could be analyzed by GC–MS without derivatization, thus the time of analysis will be greatly reduced.

In recent years, there is an increased interest in the use of saliva as an alternative testing matrix to detect drug abuse. At first, THC is the target analyte in saliva samples and its metabolites are generally accepted to be at extremely low levels; THC could be directly analyzed by GC–MS without derivatization. Moreover, saliva is relatively free of interfering substances compared to other physiological fluids like urine and plasma [17], and can be easily collected under direct supervision in a noninvasive way [18,19], and furthermore, salivary drug concentrations have similar time profiles to plasma concentrations [20,21]. Therefore, measurement of THC in saliva is reported to offer a more accurate value of concentration during cannabis intoxication [17]. Previous reports indicate that levels of cannabinoids in saliva range from 50 to 1000 ng/mL shortly after cannabis exposure. After 3–4 h, levels fall below 50 ng/mL and remain detectable at a cutoff limit of 1 ng/mL up to 10 h depending on the strength of the cannabis cigarette smoked [22]. However, saliva samples have two main limitations: the specimen volume is often small and the analyte concentration is lower than that in urine [23]. As a result, saliva testing is a great challenge for us and sensitive pretreatment method is highly demanded.

Solid-phase microextraction is widely used as a viable tool for the analysis of drugs in biological fluids due to its simplicity,

* Corresponding author. Tel.: +86 27 87867564; fax: +86 27 68754067.

E-mail address: yqfeng@whu.edu.cn (Y.-Q. Feng).

solvent-free characteristic and convenience of automation. Yonamine et al. [24] employed a 100 μm polydimethylsiloxane (PDMS) fiber as an extraction medium; the limit of detection (LOD) of THC was 5 ng/mL. Hall et al. [17] also chose PDMS to extract cannabinoids, but involved addition of glacial acetic acid before SPME, and the results showed that the extraction efficiency was enhanced since acetic acid could remove resulting protein and cellular debris. Recently, Guido [25] adopted the method of stir-bar sorptive extraction, the LOD of THC could be lower than 1 ng/mL, while the pretreatment time was as long as 90 min, unable to meet the needs of rapid detection.

In our previous research, polymer monolith microextraction (PMME) based on the use of a capillary monolithic column of poly(methacrylic acid-co-ethylene glycol dimethacrylate) (*p*(MAA-co-EGDMA)) has been successfully coupled to capillary electrophoresis (CE) [26], HPLC [27,28] and HPLC-MS [29,30] for the determination of basic drugs and angiotensin II receptor antagonists in biological matrices. Compared to the fiber coating SPME, this monolithic structure has a larger surface area, which yields a higher extraction capacity. At the same time, polymer sorbent possesses hydrophilic carboxylic acid groups in the hydrophobic bone structure and has been demonstrated to be biocompatible in dealing with complicated sample matrix [31–33]. Moreover, the convective mass transfer procedure and low pressure-drop offered by the porous structure can facilitate the extraction process [31–33].

In this article, a PMME technique using a *p*(MAA-co-EGDMA) monolithic capillary combined with GC-MS detection was developed for the determination of THC in saliva samples. After PMME, the eluate could be directly injected into GC-MS system without derivatization, and less time consumption and lower detection limit have been achieved compared to those previous methods [17,24,25].

2. Experimental

2.1. Reagents and materials

Δ^9 -Tetrahydrocannabinol standard solution (1.0 mg/mL in methanol, 0.3 mL) was purchased from The State Food and Drug Administration (Beijing, China). Δ^9 -Tetrahydrocannabinol- d_3 (THC- d_3 , 100 $\mu\text{g/mL}$ in methanol, 1 mL) was supplied from Cerilant Corporation (Texas, USA) and used as internal standard. THC and its isotopic internal standard (THC- d_3) are easily oxidated especially when they get light, thus the stock solutions of THC and THC- d_3 were stored at 4 $^\circ\text{C}$ in darkness under nitrogen atmosphere. The experiment results showed that the stock solutions were stable for almost three months.

Methanol (HPLC-grade) was obtained from Fisher Company Inc. (Fairfield, OH, USA). Acetone (Analytical-grade) was manufactured by the Shanghai Chemical Reagent Company (Shanghai, China). Purified water was obtained with a Milli-Q apparatus (Millipore, Bedford, MA).

2.2. Instrumentation

GC-MS analysis was performed using a Shimadzu GC-MS QP2010plus equipped with an AOC-20i+s autosampler (Kyoto, Japan); data acquisition and analysis were performed using software of GCMSsolution (Shimadzu, Kyoto, Japan).

The extraction device with a *p*(MAA-co-EGDMA) monolith in fused silica capillary (2 cm \times 530 μm) for PMME was purchased from Micromole Separation Testing Technology (Beijing, China). It is composed of an extraction pinhead and the syringe barrel, as shown in Fig. 1 [26].

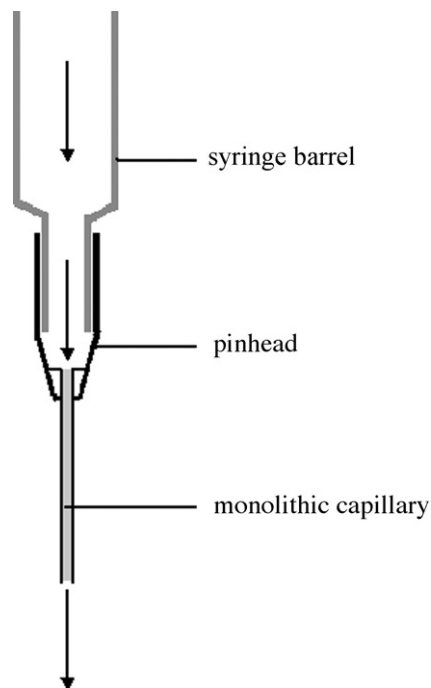


Fig. 1. Scheme of the PMME [26].

2.3. Sample preparation

Saliva samples were collected from drug-free healthy volunteers. Each collection should be at least 2 h apart from eating and drinking. To obtain the saliva samples, each volunteer was told not to swallow the saliva but to store it in their mouths. After 5 min, saliva was collected in Eppendorf tubes and stored at -20°C immediately. The saliva samples were centrifuged for 5 min at 12,000 rpm (4 $^\circ\text{C}$) when they were used. Two hundred microliters of drug-free saliva samples were selected, and 10 μL of IS working solution (0.4 $\mu\text{g/mL}$, methanol) was then added. After standing 30 min to intermix completely, the mixture were diluted to 1 mL with phosphate buffer (20 mM, pH 7.0), and filtered with a 0.45 μm nylon membrane filter, and then sample solution could be directly taken for extraction.

2.4. PMME procedure

As shown in Fig. 2 [26], the whole procedure included preconditioning, sorption, clean-up and desorption. A syringe infusion pump (CP 3000, Silugao high-technology development, Beijing, China) was employed for the delivery of the sample. For pre-treatment, 0.3 mL methanol in the syringe was ejected via the monolithic capillary at 0.15 mL/min, and then 0.3 mL phosphate buffer (20 mM, pH 7.0) was used to wash the monolithic capillary at 0.15 mL/min. For the sorption, in a similar way, 1 mL sample solution was pumped through the capillary at 0.08 mL/min, and then 0.2 mL phosphate buffer (20 mM, pH 7.0) was driven through at the same velocity to get rid of the residual matrix in order to avoid the interference for separation. And then, the residual phosphate buffer solution was expelled from the pinhead and monolithic capillary by air via a clean syringe. For the desorption, 0.05 mL acetone was ejected via the monolithic capillary at 0.04 mL/min and the eluate was collected in a vial for the subsequent analysis by GC-MS, the whole extraction procedure could be finished less than 20 min.

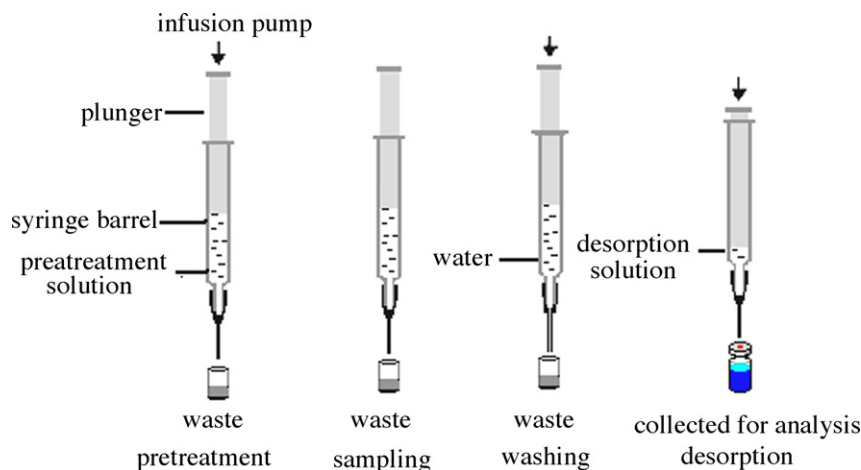


Fig. 2. Scheme of the PMME process [26].

2.5. GC–MS analysis

The separation was achieved on a fused silica capillary column (HP-5MS, 30 m \times 0.25 mm i.d., film thickness 0.25 μ m) (Agilent Technologies, Palo Alto, CA, USA). The oven temperature was programmed at 120 °C for 2 min, increased to 175 °C at 20 °C/min and held for 2 min, and then increased to 295 °C at 15 °C/min, and held for 10 min. Splitless injection mode was used, and the splitless time was 1 min; helium (purity 99.999%) with a flow rate of 1.2 mL/min was used as carrier gas. The injection port, ion source and interface temperatures were 260, 200 and 280 °C, respectively. The electron-impact (EI) mass spectra of the analytes were recorded by SCAN mode (scan range 50–450 m/z) to determine retention times and characteristic mass fragments. For quantitative analysis, the chosen characteristic mass fragments were monitored in the selected-ion monitoring (SIM) mode: m/z 299, 314 and 231 for THC, m/z 302, 317 and 234 for THC- d_3 , while m/z 299 and 302 were selected for quantification measurement of THC and THC- d_3 , respectively. Ion ratio acceptance criterion was a deviation $\leq 30\%$ ion ratio from the calibration sample.

3. Results and discussion

3.1. Optimization of conditions for PMME

To achieve the best extraction efficiency of the *p*(MAA-co-EGDMA) monolithic capillary towards THC, various conditions like the extraction equilibrium profile, extraction flow rate and pH value need to be optimized.

Since polymer monolith might collapse under higher pressure condition (~ 300 psi), saliva samples should be diluted with phosphate solution prior to extraction to reduce viscosity of sample solution and keep the monolith working under lower pressure. The THC standard and IS solution were added to 1.0 mL samples, and then the samples were diluted at ratios of 1:1, 1:3, 1:5, and 1:10 (v/v). The experimental results indicated that the monolith worked at pressure of ~ 100 psi when the saliva sample was diluted at a ratio of 1:5.

The extraction equilibrium profile was monitored by increasing the volume of the extracted sample from 0.2 to 2 mL (corresponding to 120–1200 ng of THC) at a constant flow rate. It can be seen from Fig. 3 that the amount of THC extracted increased with the increasing volume of the extracted sample; the extraction equilibrium was not reached after 2 mL of sample solution was supplied. The sharp slopes of the profile indicated that the monolithic capillary

exhibited remarkable extraction capacity toward THC. To achieve sufficient sensitivity within a short time, 1 mL sample was selected for subsequent analysis.

p(MAA-co-EGDMA) monolithic contains many carboxyl groups in its backbone, which can exhibited in aqueous solution as anionic or intermediate form; this extraction is therefore pH-dependent. The pH optimization was conducted in 20 mM phosphate matrix solution over the pH range 3–9; the pH of the carrier solution was changed simultaneously. As shown in Fig. 4, the extraction efficiency was high and constant in the range of 3–6; while with the higher pH more than 6, the extraction efficiency was dropped dramatically. This can be explained by the fact that the interaction between the analyte and the monolithic capillary was mainly based on the hydrophobic interaction. In the alkaline matrix, the amount of the ionized carboxylic groups of the polymer extraction phase increased, leading to the decrease in hydrophobic interaction between THC and the extraction material. So the pH of sample matrix would be adjusted to pH 4. However, the saliva sample at pH 4 exhibited poor extraction efficiency for THC. Considering that the impurities of saliva matrix may affect the extraction, we chose saliva sample as matrix, and review the capacity of actual sample analysis. The results exhibited that as the pH value is increased, the

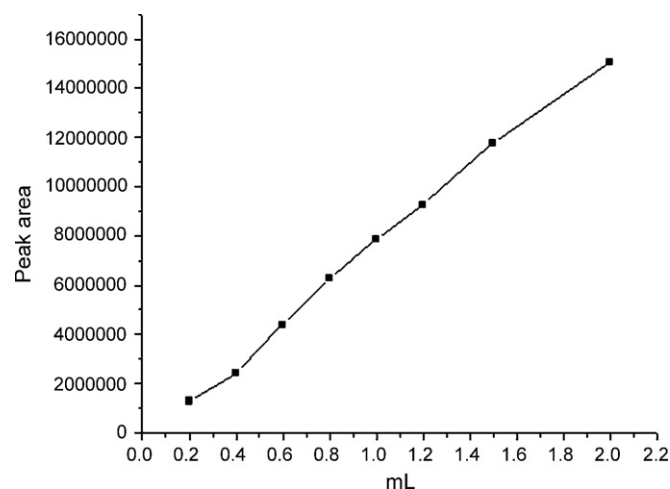


Fig. 3. The extracted sample equilibrium profile of Δ^9 -Tetrahydrocannabinol for the PMME. The sample solution was 20 mM phosphate solution at pH 4.0 spiked with THC at 600 ng/mL. Operating conditions: extraction flow rate 0.08 mL/min, desorption flow rate 0.04 mL/min.

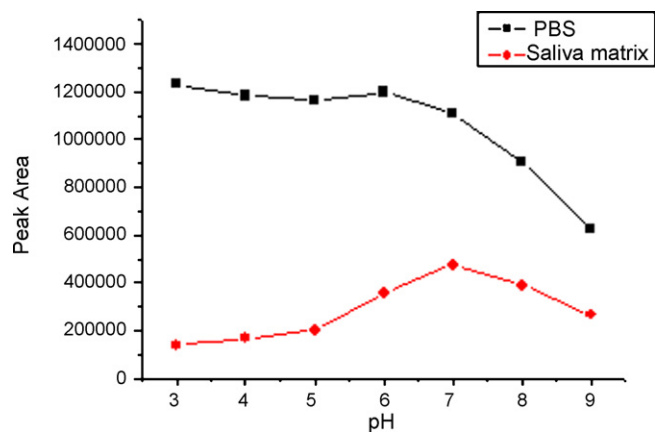


Fig. 4. The effect of matrix pH on extraction efficiency (in phosphate buffered solution (PBS) and in saliva matrix).

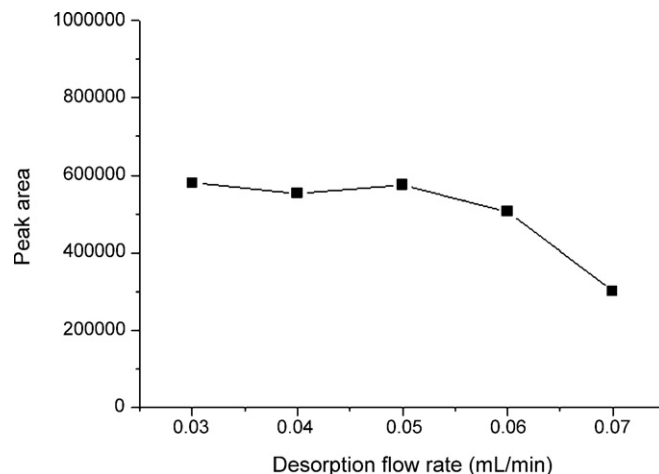


Fig. 6. Desorption flow rate profile of THC for PMME. Sample solution spiked with THC at 600 ng/mL.

extraction efficiency increased firstly, and then decreased, with the maximum value at pH 7.0. Moreover, even under the optimized condition (pH 7.0), the extraction efficiency for THC in saliva matrix was found to be 40% of that in aqueous solution. This may be explained by the fact that competitive adsorption occurred between the saliva matrix and THC, and the coexistence such as protein and cell debris in saliva samples might interact with THC. As a result, pH 7.0 was chosen for the following extraction process.

The extraction flow rate of the sample solution was optimized in the range of 0.03–0.10 mL/min. As shown in Fig. 5, the flow rate had no significant influence on the extraction efficiency. Therefore, a flow rate of 0.08 mL/min was selected due to the shorter extraction time and the acceptable pressure (~100 psi) of the monolith column.

Acetone was selected as the desorption solvent; the eluate can go directly for GC–MS analysis. The desorption procedure was optimized to achieve accurate quantification of THC. After sample extraction, 0.05 mL acetone was used to elute the THC for three times, and then each 0.05 mL eluate was collected for detection. It was found that the first 0.05 mL acetone could elute more than 90% extracted THC from the monolithic capillary. Furthermore, the flow rate of the desorption solution was optimized in the range of 0.03–0.07 mL/min as seen in Fig. 6, and the flow rate of 0.04 mL/min was found to be suitable considering the extraction efficiency and extraction time.

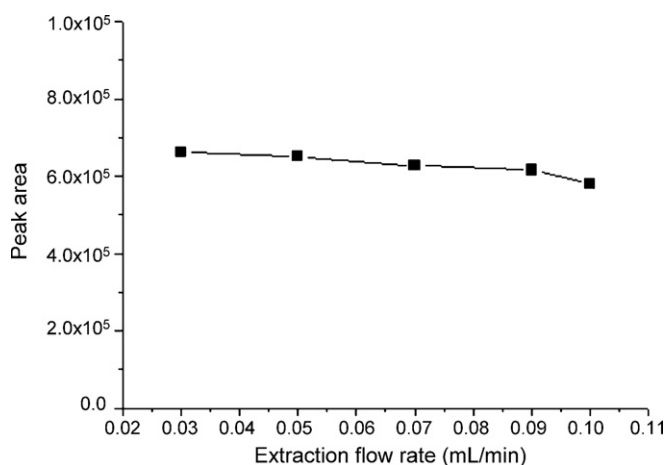


Fig. 5. Extraction flow rate profile of THC for PMME. The sample solution was 20 mM phosphate solution at pH 4.0 spiked with THC at 600 ng/mL.

3.2. Selection of quantitative ions and qualitative ions

The application of the GC–MS method for the determination of THC was verified using an internal standard for quantification. At first, the analytical performance of the optimized GC–MS was determined by a standard solution of THC and THC-d₃ in pure solvents. SCAN mode was applied firstly to determine retention times and characteristic mass fragments, and then, the SIM mode was employed to achieve suitable sensitivity. Fig. 7 is the mass spectra of THC (a) and THC-d₃ (b), fragments of *m/z* 299 and 302, corresponding to the characteristic fragment of these two compounds' loss of -CH₃, was selected as quantification ions of target and IS because of their high sensitivities and the fact that there was no interference peak in these two channels at the retention time near those of THC and THC-d₃. Reference ions *m/z* 214, 231 for THC and *m/z* 217, 234 for THC-d₃ were also monitored. The ion ratios used (*m/z* 299/214/231 and *m/z* 302/217/234) for confirmatory purpose was studied in all sample matrixes. Similarity index (SI) over three spiked concentration (3, 50, 300 ng/mL) levels were satisfied: 81 for 3 ng/mL; 87 for 50 ng/mL; 94 for 300 ng/mL. Mass chromatograms of a blank saliva sample (a), as well as saliva sample spiked with 10 ng/mL THC (b) with IS at 20 ng/mL are shown in Fig. 8. It can be seen that no interfering peaks originating from saliva matrix were observed.

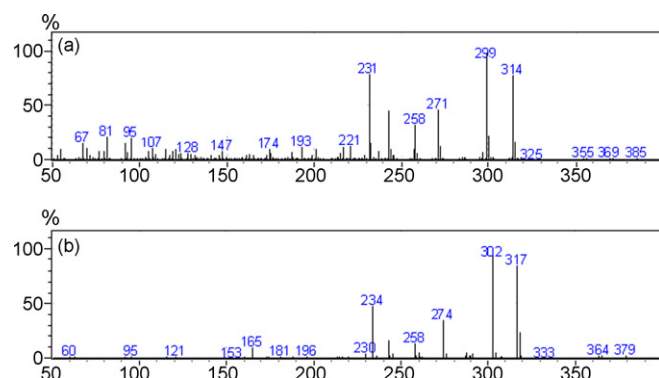


Fig. 7. Mass spectra of Δ⁹-Tetrahydrocannabinol (a) and Δ⁹-Tetrahydrocannabinol-d₃ (b).

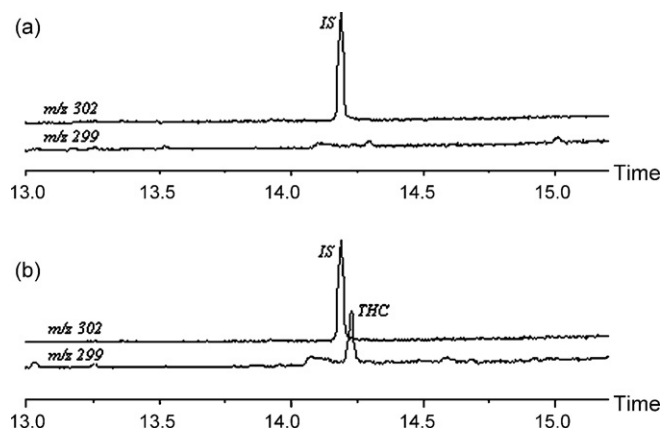


Fig. 8. Chromatograms of a blank saliva sample (a) and saliva sample spiked with 10 ng/mL THC (b) with IS at the concentration of 20 ng/mL. Retention time: THC, 14.21 min; IS, 14.19 min.

3.3. Method validation

The monolithic capillary showed high stability since no significant changes in the back-pressure and extraction efficiency of the capillary column were found in the experiments.

The application of the PMME–GCMS method for the determination of THC was verified using an internal standard for quantification. The internal calibration was performed by plotting peak area ratios (THC/IS) versus concentration ratios of THC and THC- d_3 . The sample solutions were spiked with stock solution to get final concentrations of THC at 3, 10, 20, 50, 100, 300 ng/mL and THC- d_3 at 20 ng/mL for calibration curves. The SIM mode was employed to achieve suitable sensitivity. The calibration curve was $Y = -0.05 + 0.02X$ with correlation coefficient of $R > 0.999$. Detection and quantification limits were calculated as the concentration corresponding to a signal 3 and 10 times the standard deviation of the baseline noise and the limit of detection and quantification of this method were 0.68 and 2.26 ng/mL, respectively.

The extraction recoveries were determined by analysis of the spiked THC-free samples at different concentrations; the spiking levels ranged from 3 to 300 ng/mL. The recoveries were calculated by comparing the extracted amounts of THC from those of the samples with the corresponding spiking amounts on calibration curves. The recoveries and relative standard deviations (R.S.D.s) are summarized in Table 1; mean recoveries were in the range of 89.8–96.5%.

The reproducibility of the developed method was determined by the inter- and intra-day precision. The precision was acquired by samples spiked at three levels of concentration (3, 50, 300 ng/mL). Five extraction of sample solution over a day gave the intra-day R.S.D.s; while inter-day precisions data were obtained by analysis of the samples extracted on five consecutive days. Excellent method reproducibility was achieved. The intra-day precisions for 3, 50, 300 ng/mL were found to be 9.4, 7.1 and 3.1%, respectively; the inter-day precisions for 3, 50, 300 ng/mL were 11.6, 8.7 and 8.1%, respectively.

Table 1
Recoveries (%) obtained for PMME of Δ^9 -Tetrahydrocannabinol in saliva samples.

Fortified concentration (ng/mL)	Recovery (%)	R.S.D.s (%) (n = 3)
3	90.7	10.9
50	89.8	6.5
300	96.5	5.7

Table 2

Determination of Δ^9 -Tetrahydrocannabinol in saliva samples from six volunteers.

	Sample 1	Sample 2	Sample 3	Sample 4	Sample 5	Sample 6
Spiked recovery (%)	86.3	92.5	93.6	84.8	90.1	82.4
R.S.D.s (n = 3)	10.5	7.6	8.9	11.2	6.3	12.9

3.4. Quantitative analysis of THC in human saliva

Based on the procedures described above, the PMME/GC–MS technique was applied for the analysis of THC in saliva samples. Saliva samples of six drug-free healthy volunteers (including a smoker) were spiked with 6 ng/mL THC, and all samples obtained were analyzed in three replicates. According to Table 2, R.S.D. were less than 12.9%, and no interfering peaks originating from saliva matrix were observed.

4. Conclusion

PMME using *p*(MAA-co-EGDMA) monolithic capillary combined with GC–MS provides a simple, fast, sensitive, and selective procedure for the identification and determination of THC in saliva samples. This monolithic capillary provides excellent extraction capacity toward THC, and the good permeability ensures the quick extraction procedure, with the time consume less than 20 min. Moreover, a faster analysis can be obtained by fixing two or more extraction device on single syringe infusion pump. In conclusion, this proposed PMME advocated an environmentally friendly and rapid sample pretreatment technique compared with other THC pretreatment methods reported previously, and has the potential to be applied to the determination of other drug abuse.

Acknowledgments

This work was partly supported by grants from the National Science Fund for Distinguished Young Scholars (No. 20625516) and National Key Technologies R&D Program of China (2006BAF07B03). Shimadzu international trading (Shanghai) Co. Ltd. is thanked for providing the GC–MS QP2010 plus.

References

- [1] C.D.R. de Oliveira, M. Yonamine, R.L.D. Moreau, J. Sep. Sci. 30 (2007) 128.
- [2] M. Pellegrini, E. Marchei, R. Pacifici, S. Pichini, J. Pharm. Biomed. 36 (2005) 939.
- [3] R.H. Lowe, E.L. Karschner, E.W. Schilke, A.J. Barnes, M.A. Huestis, J. Chromatogr. A 1163 (2007) 318.
- [4] S.J. Gross, J.R. Soares, S.L. Wong, R.E. Schuster, Nature 252 (1994) 581.
- [5] J.D. Teale, E.J. Forman, L.J. King, V. Marks, Nature 249 (1974) 154.
- [6] C. Abbata, R. Galy, A. Benyamina, M. Reynaud, L. Bonhomme-Faivre, J. Pharm. Biomed. 41 (2006) 1011.
- [7] O. Zoller, P. Rhy, B. Zimmerli, J. Chromatogr. A 872 (2000) 101.
- [8] E. Kramer, K.A. Kovar, J. Chromatogr. B 731 (1999) 167.
- [9] J.M. Rosenfeld, J. Chromatogr. A 843 (1999) 19.
- [10] A.J. Poortman-van der Meer, H. Huizer, Forensic Sci. Int. 101 (1999) 1.
- [11] O. Quintela, D.M. Andrenyak, A.M. Hoggan, D.J. Crouch, J. Anal. Toxicol. 31 (2007) 157.
- [12] M. Laloup, M.D.R. Fernandez, M. Wood, G.D. Boeck, C. Henquet, V. Maes, N. Samyn, J. Chromatogr. A 1082 (2005) 15.
- [13] M. Concheiro, A. de Castro, O. Quintela, A. Cruz, M. López-Rivadulla, J. Chromatogr. B 810 (2004) 319.
- [14] J.Y. Kim, M.K. In, Rapid Commun. Mass Spectrom. 21 (2007) 1339.
- [15] T. Nadulski, F. Pragst, J. Chromatogr. B 846 (2007) 78.
- [16] T. Nadulski, F. Sporkert, M. Schnelle, A.M. Stadelmann, P. Roser, T. Scheffer, F. Pragst, Anal. Toxicol. 29 (2005) 782.
- [17] B.J. Hall, M. Satterfield-Doerr, A.R. Parikh, J.S. Brodbelt, Anal. Chem. 70 (1998) 1788.
- [18] N. Fucci, N. de Giovanni, M. Chiarotti, Forensic Sci. Int. 134 (2003) 40.
- [19] J.K.M. Aps, L.C. Martens, Forensic Sci. Int. 150 (2005) 119.
- [20] M.A. Huestis, E.J. Cone, J. Anal. Toxicol. 28 (2004) 394.
- [21] R.S. Niedbala, K.W. Kardos, D.F. Fritch, S. Kardos, T. Fries, J. Waga, J. Robb, E.J. Cone, J. Anal. Toxicol. 25 (2001) 289.

- [22] L.K. Thompson, E.J. Cone, J. Chromatogr. 421 (1987) 91.
- [23] M. Laloup, M.D.M.R. Fernandez, M. Wood, G.D. Boeck, C. Henquet, V. Maes, N. Samyn, J. Chromatogr. A 1082 (2005) 15.
- [24] M. Yonamine, N. Tawil, R.L.M. Moreau, O.A. Silva, J. Chromatogr. B 789 (2003) 73.
- [25] D. Guido, Labor Prax. 4 (2006) 22.
- [26] M. Zhang, F. Wei, Y.F. Zhang, J. Nie, Y.Q. Feng, J. Chromatogr. A 1102 (2006) 294.
- [27] H.J. Zhang, J.F. Huang, H. Wang, Y.Q. Feng, Anal. Chim. Acta 565 (2006) 129.
- [28] H.J. Zhang, J.S. Li, H. Wang, Y.Q. Feng, Anal. Bioanal. Chem. 386 (2006) 2035.
- [29] J.F. Huang, H.J. Zhang, Y.Q. Feng, J. Agric. Food Chem. 54 (2006) 9279.
- [30] J.F. Huang, H.J. Zhang, B. Lin, Q.W. Yu, Y.Q. Feng, Rapid Commun. Mass Spectrom. 21 (2007) 2895.
- [31] Y. Fan, Y.Q. Feng, S.L. Da, Z.G. Shi, Z.G. Anal. Chim. Acta 523 (2004) 251.
- [32] J. Nie, Q. Zhao, J.F. Huang, B.R. Xiang, Y.Q. Feng, J. Sep. Sci. 29 (2006) 650.
- [33] Y. Wen, M. Zhang, Q. Zhao, Y.Q. Feng, J. Agric. Food Chem. 53 (2005) 8468.



Review

Flow injection based methods for fast screening of antioxidant capacity

Luís M. Magalhães, Miguel Santos, Marcela A. Segundo*, Salette Reis, José L.F.C. Lima

REQUIMTE, Serviço de Química-Física, Faculdade de Farmácia, Universidade do Porto, Rua Aníbal Cunha, 164, 4099-030 Porto, Portugal

ARTICLE INFO

Article history:

Received 31 July 2008

Received in revised form 19 October 2008

Accepted 24 October 2008

Available online 31 October 2008

Keywords:

Antioxidant capacity

Flow injection analysis

Automatic methods

DPPH

ABTS

Folin-Ciocalteu

Electrochemical methods

ABSTRACT

The role and importance of antioxidants in different fields, ranging from physiology to food technology, have become evident in the past years, requiring adequate analytical methodologies. Therefore, the determination of antioxidant capacity as a routine or screening analysis fosters its automation. In this context, several flow injection methods based on scavenging of 2,2'-azinobis-(3-ethylbenzothiazoline-6-sulphonate) radical cation (ABTS^{•+}) or 2,2-diphenyl-1-picrylhydrazyl radical (DDPH[•]) or based on the determination of total reducing capacity have been proposed. The objective of the present review is to critically compare the different approaches, regarding their degree of automation, their performance vs. the respective batch procedure and its applicability to real samples.

© 2008 Elsevier B.V. All rights reserved.

Contents

1. Introduction.....	1559
2. Flow methods based on scavenging of 2,2'-azinobis-(3-ethylbenzothiazoline-6-sulphonate) radical cation (ABTS ^{•+}).....	1560
3. Flow methods based on scavenging of 2,2-diphenyl-1-picrylhydrazyl radical (DDPH [•]).....	1562
4. Flow methods for determination of total reducing capacity.....	1563
5. Conclusions.....	1565
Acknowledgements.....	1566
References.....	1566

1. Introduction

In the past years, the importance of antioxidants in the protection of organisms or tissues, or of nonliving systems against oxidative stress has become evident. This statement is supported by studies performed in a variety of areas, including physiology [1,2], pharmacology [3,4], nutrition [5–7] and even food processing [8,9]. In all these areas of research fast, reliable methods for antioxidant assessment are needed [10,11]. Generally, the ideal method for determination of antioxidant properties should assess the effect of a compound/sample in reaction conditions that mimic those found when oxidative stress is induced in vivo by reactive nitrogen species (RNS) and reactive oxygen species (ROS). However, this kind of

assessment may be considered exaggerated for screening purposes, considering the individual testing against numerous ROS/RNS (e.g. H₂O₂, O₂^{•−}, HO[•], HOCl, ¹O₂, NO[•], and ONOO[−]) and the conditions of assay in vivo (e.g. use of cultured cell lines or lab animals). In this scenario, in vitro methods to determine “total antioxidant capacity” are ideal as an exploratory screening step prior to characterization or isolation of bioactive compounds [12].

Along the past two decades, several methods, including the ABTS^{•+} (2,2'-azinobis-(3-ethylbenzothiazoline-6-sulphonate) radical cation) assay [13,14], the DPPH[•] (2,2-diphenyl-1-picrylhydrazyl radical) assay [15], the ferric reducing antioxidant power (FRAP) assay [16], and the electrochemical estimation of total reducing capacity [17,18] have been proposed for assessment of antioxidant capacity. Considering that these methods are routinely used for screening purposes, their automation is relevant. In this respect, automation using flow injection based methods can offer several advantages, besides the enhancement of sample throughput, when

* Corresponding author. Tel.: +351 222078994; fax: +351 222078961.

E-mail address: msegundo@mail.ff.up.pt (M.A. Segundo).

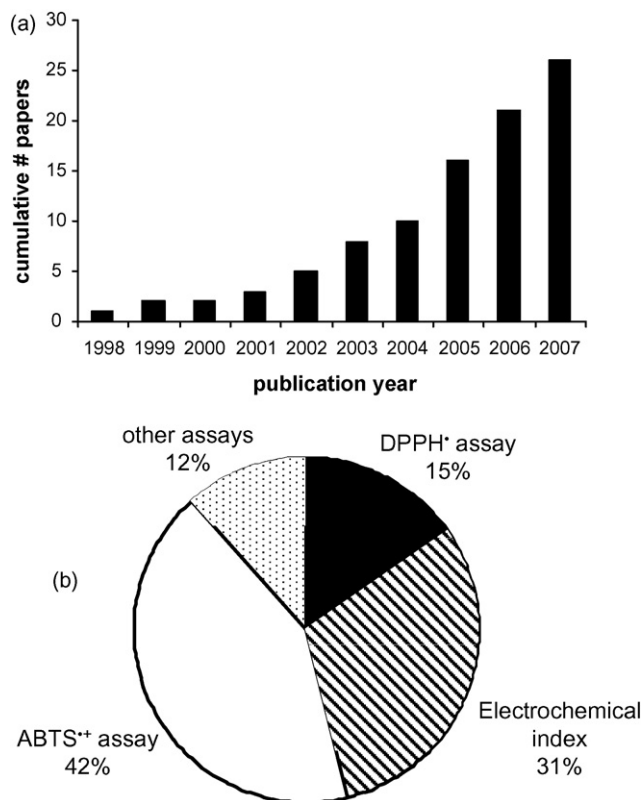


Fig. 1. (a) Cumulative distribution of papers dealing with automatic flow based determination of total antioxidant capacity per publication year. (b) Distribution of the same papers regarding assay type. Papers from 2008 are not included.

compared to conventional batch methods. For this particular application, the features of flow injection analysis (FIA) [19] systems provide a strict control of reaction conditions in both space and time, which are essential for determination of species that are sensitive to environmental conditions (light, temperature, presence of O₂, for instance). Furthermore, the evolution of FIA to sequential injection analysis [20] (SIA), described as a mechanically simpler alternative to FIA, and to other strategies based on the flow network concept [21] expanded the benefits of automation. This last type of flow systems includes multi-commutation [22,23], multi-syringe flow injection analysis (MSFIA) [24,25] and multipumping [26], where the manifold channels are connected to computer-controlled devices (solenoid valves or micro-pumps) that enable the flexible access to reagent(s), sample and carrier in any software-defined combination.

The aim of this review is to establish a critical comparison between the different automatic flow based systems developed until the present moment for fast screening of antioxidant capacity and to highlight the advantages of automatic methods toward the corresponding batch procedure. As depicted in Fig. 1a, the number of publications devoted to this subject has grown significantly, especially in the past 3 years. Moreover, different assays have been automated (Fig. 1b). In fact, more than half of the proposed applications are based on the utilization of colored, radical species (ABTS^{•+} or DPPH[•]) that mimic the ROS/RNS found in vivo. Other methods aimed the determination of “total reducing capacity”, for which the amperometric determination of an “electrochemical index” accounts for about 31% of the flow systems reported. Considering this division, an overview is presented in the next sections.

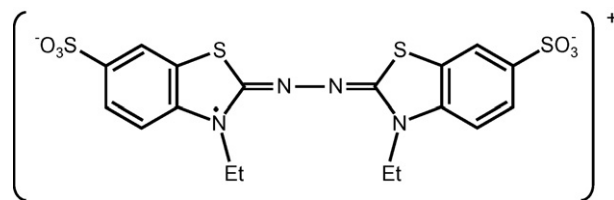


Fig. 2. ABTS^{•+} chemical structure.

2. Flow methods based on scavenging of 2,2'-azinobis-(3-ethylbenzothiazoline-6-sulphonate) radical cation (ABTS^{•+})

One of the most common methods for assessing the antioxidant capacity is the ABTS^{•+} or TEAC (trolox equivalent antioxidant capacity) assay based on the scavenging of 2,2'-azinobis-(3-ethylbenzothiazoline-6-sulphonate) radical cation (Fig. 2) [13]. Generally, the sample to be tested is added to a solution containing a certain amount of ABTS^{•+}. After a period of time that may vary between 1 and 30 min, the concentration of the remaining ABTS^{•+} is determined spectrophotometrically [14]. ABTS is commercially available but the ABTS^{•+} radical cation must be formed prior to determination. Several strategies have been described for performing this step, based on (i) chemical reaction using manganese dioxide [27], or 2,2'-azobis(2-amidinopropane) dihydrochloride [28], or potassium persulfate [14]; (ii) enzymatic reaction using metmyoglobin [13] or horseradish peroxidase [29]; (iii) electrochemical generation [30].

The automation of ABTS^{•+} assay (Table 1) was first implemented by Pellegrini et al. [31] using a single channel flow injection system similar to that presented in Fig. 3a. Therefore, after injecting a sample containing antioxidant compound(s), a negative peak representing the decolorization of ABTS^{•+} was obtained (Fig. 4a), whose area was proportional to the concentration of ABTS^{•+} that was reduced. The TEAC value corresponds to the trolox concentration providing a discoloration of ABTS^{•+} equal to that caused by the sample. The proposed flow injection system was applied for the evaluation of antioxidant capacity of pure compounds (ascorbic acid, caffeic acid, ferulic acid, gallic acid, naringenin, quercetin, α -tocopherol, and vanillic acid) and results were compared to the batch assay. In general, the two set of results were in good agreement, with exception of naringenin. The applicability of the technique was tested by measuring the antioxidant capacity of several common beverages (beer, coffee, cola, fruit juices, and tea) and results were not statistically different from the batch assay, using trolox as standard compound.

Bompadre et al. [32] reported that the previous FIA-ABTS^{•+} assay partially failed when more complex biological samples, such as plasma, were analyzed. Hence, they proposed minor changes (sample volume, reaction coil configuration) in the flow manifold and also introduced temperature control. Therefore, the temperature and time/way of exposure of the active compounds present in the samples with ABTS^{•+} were strictly controlled. Using these experimental conditions, the authors showed that the temperature was a critical aspect in the measurement of plasma antioxidant capacity whilst its influence was less important in the assay of non-complex biological samples (mouthrinse, white wines). Hence, the temperature of the reaction coil was fixed at 35 °C whilst the reaction time was defined as 1.3 min. The improved FIA-ABTS^{•+} method was useful to screen rapidly, without dilution, and with high repeatability the antioxidant capacity of both non-complex biological mixtures and plasma samples. The same flow injection system was later applied to determine the antioxidant capacity of enriched toothpastes [33].

Table 1
Flow-based methods for determination of scavenging capacity against ABTS^{•+}.

Flow method	Generation of reactive species	pH value	Detection system	Quantification	Type of sample	Determination rate (h ⁻¹)	RSD (%)	Reference
FIA	Chemical (K ₂ S ₂ O ₈)	Unbuffered	Vis (734 nm)	Area of negative peak	Beer, coffee, cola, juices, tea	30	<1.7	[31]
FIA	Chemical (K ₂ S ₂ O ₈)	7.4	Vis (n.g.)	% of inhibition, calculated from maximum decrease of absorbance	Mouthrinse, white wine and plasma	~22	<2.7	[32]
FIA	Enzymatic (H ₂ O ₂ + HRP)	4.6	Vis (414 nm)	Height of negative peak	Honey and wine	120	<5	[34]
FIA	Electrochemical (in-line)	7.4	Vis (734 nm)	Height of negative peak	Coffee, red wine, tea	32	<1.95	[42]
FIA	Enzymatic (H ₂ O ₂ + HRP, in-line)	7.4	Biamperometry	Peak height	Juices, tea, wine	42	n.g.	[43]
FIA	Enzymatic (glucose + GOD/H ₂ O ₂ + HRP, in-line)	7.4	Biamperometry	Peak height	Spirits and wine	~37	n.g.	[44]
SIA	Chemical (K ₂ S ₂ O ₈)	Unbuffered, 5.4 and 7.4	Vis (734 nm)	% of decolourization, calculated from maximum decrease of absorbance	Beer, juices, milk, tea, yoghurt	9–20	n.g.	[36]
SIA	Chemical (K ₂ S ₂ O ₈)	7.5	Vis (734 nm)	% of inhibition, calculated from maximum decrease of absorbance	Wine	15 or 42	<2.4	[39]
MSFIA	Enzymatic (H ₂ O ₂ + HRP)	4.6	Vis (734 nm)	Height of negative peak	Beer, juices, tea, wine	12 or 18	<3.1	[41]

FIA, flow injection analysis; SIA, sequential injection analysis; MSFIA, multisyringe flow injection analysis; Vis, spectrophotometry; HRP, horseradish peroxidase; GOD, glucose oxidase; n.g., not given.

A double-line FIA system (Fig. 3b) was also proposed for the ABTS^{•+} assay [34]. Compared to the previous single channel systems, this novel manifold allowed the addition of reagent to the whole sample, avoiding the possibility of its depletion in the central zone of the sample plug. Furthermore, a higher sample throughput was attained (four times higher, Table 1) and the concentration gradients formed along the injected sample bolus were also exploited to obtain information on the reaction kinetics of ABTS^{•+} scavenging through a single injection. As the flow injection signals are the output of two kinetic processes occurring simultaneously, i.e. physical dispersion and chemical reaction, the authors observed that the TEAC values obtained for fast-reacting scavengers as ascorbic acid and caffeic acid were independent from the time of measurement. Physical dispersion was the only process that influenced the analytical signal. On the opposite, the TEAC values of slow-reacting scavengers, such as (+)-catechin, (–)-epicatechin, ferulic acid, and gallic acid increased using the peak tail readings because of their longer reaction time. The same authors had previously developed a continuous, stopped flow method to study the effect of reaction time (10, 360, and 600 s) and pH (4.6, 5.4, and 7.4) on the ABTS^{•+} scavenging reaction [35]. They concluded that the TEAC values were dependent on reaction time as well as on pH value for almost all studied antioxidant compounds, due to the differences in the rate of reaction for antioxidants and for trolox (reference compound). Due to the variation of TEAC with pH, it was suggested that it is crucial to measure the ABTS^{•+} scavenging capacity at the pH of the system to which the expected results are going to be applied.

This importance of reaction time and pH upon the results obtained in the ABTS^{•+} assay was also reported by Lima et al. [36] who proposed a SIA–ABTS^{•+} manifold to automate this assay (Table 1). A well-stirred mixing chamber, placed in a side port of the selection valve, was incorporated to the system (Fig. 3c), allowing a thorough mixing between the sample and ABTS^{•+} and making possible to use one single standard solution to perform the calibration procedure (based on aspiration of variable volumes of sample). By changing the carrier solution, different pH values

were studied (non-buffered, 5.4 and 7.4). For almost all antioxidants tested (trolox, ascorbic acid, caffeic acid, gallic acid, catechin, α-tocopherol), the authors verified that higher sensitivity values were obtained for the highest pH value, which is expected for reactions based on an electron transfer mechanism, which are favored under alkaline conditions [37].

Considering that the complexity of samples requires the utilization of more than one method for the evaluation of antioxidant capacity [38] and taking advantage of the high versatility of computer-controlled automatic methods, the ABTS^{•+} assay was performed along with other methodologies using the same manifold without the need for system reconfiguration. Hence, a SIA system was proposed to accommodate in the same manifold the spectrophotometric ABTS^{•+} assay and the fluorimetric H₂O₂ scavenging capacity assay [39]. Initially, 300 μL of sample and 25 μL of ABTS^{•+} solution were sequentially aspirated. However, the intercalation of ABTS^{•+} plug between two equal sample segments of 150 μL resulted in more efficient mixing, without needing a mixing chamber as reported before [36]. Using trolox as standard compound, the applicability of the proposed system was assessed by processing several pure compounds (ascorbic acid, caffeic acid, catechin, gallic acid, and taxifolin) as well as Portuguese white and red wines. Regarding the application to wine samples, a higher dilution level was necessary for the ABTS^{•+} assay. Thus, in order to introduce the same sample in the system and analyze it sequentially by the two methods, an additional dilution was carried out in-line through two dilution coils incorporated in the side ports of the selection valve. A similar SIA system, comprising only the ABTS^{•+} assay, has also been proposed for the quantification and simultaneous evaluation of antioxidant activity of a non-steroidal anti-inflammatory drug (etodolac) [40].

Recently, an automatic flow procedure based on MSFIA was developed for the sequential spectrophotometric determination of ABTS^{•+} scavenging capacity and Folin-Ciocalteu (FC) reducing capacity [41]. The manifold configuration included several reaction coils for reaction development when the two methods were per-

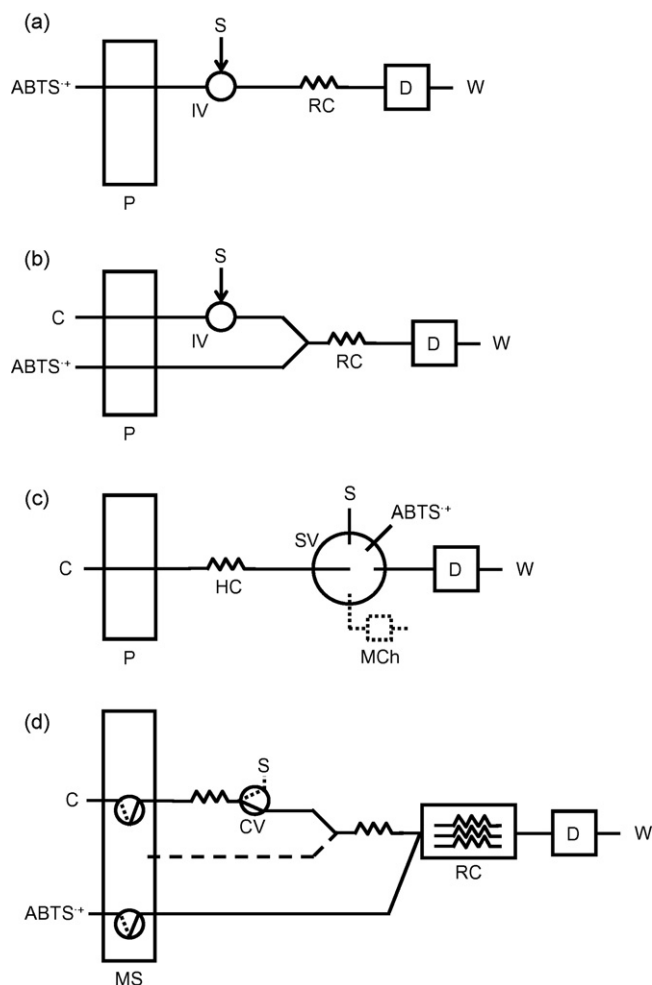


Fig. 3. Schematic representation of automatic flow based systems for determination of $\text{ABTS}^{\bullet+}$ scavenging capacity resorting to single (a) or double line (b) flow injection analysis, sequential injection analysis (c), and multisyringe flow injection analysis (d). P: pump; IV: injection valve; S: sample; RC: reaction coil; D: detector; W: waste; C: carrier; SV: selection valve; HC: holding coil; MCh: mixing chamber; MS: multisyringe; CV: commutation valve.

formed in tandem (Fig. 3d). The proposed method was applied to a large number of beverages ($n=72$) divided in six groups, namely red wines, white wines, juices, herbal infusions, tea infusions and beers. Besides the application to routine analysis, this manifold

was particularly useful for evaluation of the correlation between these two antioxidant assays, showing that this correlation may vary according to the type of sample analyzed.

The automatic $\text{ABTS}^{\bullet+}$ assays described above relies on the radical cation preformed off-line by chemical or enzymatic oxidation of ABTS (Table 1). As the kinetics of ABTS oxidation is slow, requiring a few hours for reaction completeness (16 or 3 h for chemical or enzymatic generation, respectively), the preparation of this solution is often performed on the day before its utilization. Therefore, to avoid this time-consuming procedure and taking a step further toward a fully automatic method, the in-line generation of $\text{ABTS}^{\bullet+}$ radical cation has been proposed, resorting to electrochemical oxidation or to enzymatic reaction. In this context, Ivekovic et al. [42] proposed a manifold for the spectrophotometric $\text{ABTS}^{\bullet+}$ assay, comprising a flow-through electrolysis cell, where the radical species was generated in-line by electrochemical oxidation of ABTS. The electrolysis cell was operated under constant current conditions, with the working electrode potential fixed at 700 ± 5 mV, and the amount of the $\text{ABTS}^{\bullet+}$ generated in-line was established by the flow rate and the value of the current imposed on the cell. The applicability of the method was demonstrated by analysis of nineteen compounds and several common beverages (coffee, red wine, and teas).

Recently, in-line enzymatic generation of $\text{ABTS}^{\bullet+}$ radical with electrochemical determination of antioxidant capacity was implemented by Milardovic et al. [43]. The FIA method developed is based on the continuous flow of $\text{ABTS}/\text{H}_2\text{O}_2$ solution through a tubular flow-through bioreactor containing immobilized horseradish peroxidase, which catalyses the oxidation of ABTS. The $\text{ABTS}^{\bullet+}$ radical generated was further merged with antioxidant compound/sample and the residual reduced concentration of $\text{ABTS}^{\bullet+}$ was measured in a biamprometric detector containing an interdigitated electrode. The current intensity obtained was proportional to the $\text{ABTS}^{\bullet+}$ scavenging capacity. To minimize the possible reaction between unreacted H_2O_2 and antioxidant(s), the authors reduced the inlet H_2O_2 concentration from $120 \mu\text{M}$ (optimization studies) to $30 \mu\text{M}$ (application to food samples). The system was applied to water-soluble pure compounds and to tea, juice and wine samples, with a good agreement with the spectrophotometric batch procedure. Nevertheless, the authors verified that the $\text{ABTS}/\text{H}_2\text{O}_2$ solution was unstable during a working day, and thus proposed a novel FIA system in which the $\text{ABTS}^{\bullet+}$ radical was bienzymatically produced from glucose oxidase and horseradish peroxidase enzymes, separately immobilized in tubular flow-through reactors [44]. In this case, the H_2O_2 necessary for ABTS oxidation was continuously formed in-line through the oxidation of glucose. The manifold was applied to alcoholic beverages and TEAC values lower than those provided by the batch procedure were attained, probably due to the shorter reaction time. However, it should be emphasized that none of these strategies circumvent the possible interference of the unreacted H_2O_2 , which may be considerably increased with the progressive inactivation of the immobilized peroxidase.

3. Flow methods based on scavenging of 2,2-diphenyl-1-picrylhydrazyl radical (DPPH•)

Another common assay for the determination of antioxidant capacity is the DPPH• (2,2-diphenyl-1-picrylhydrazyl radical) assay, based on the reduction by antioxidants of this purple chromogen radical (Fig. 5) to the corresponding pale yellow hydrazine [45]. Compared to the $\text{ABTS}^{\bullet+}$ assay, some advantages may be highlighted, namely the stability and commercial availability of DPPH• radical. Generally, this assay is performed in organic or organic/aqueous media. In fact, Stasko et al. reported recently that DPPH• coagulates in water/ethanol solutions containing more

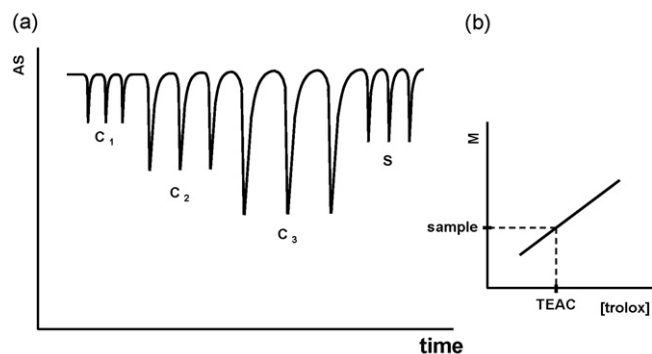


Fig. 4. (a) Analytical signal (AS) obtained for determination of scavenging capacity using chromogenic radicals ($\text{ABTS}^{\bullet+}$ or DPPH^{\bullet} , for instance). (b) Calibration curve applied in TEAC assay, where M stands for the area or the peak height or the percentage of inhibition calculated from AS.

Table 2
Flow-based methods for determination of scavenging capacity against DPPH•.

Flow method	pH value	Detection system	Quantification	Type of sample	Determination rate (h ⁻¹)	RSD (%)	Reference
FIA	Unbuffered	ESR	Height of negative peak	Coffee, red wine, tea	13	<3.2	[50]
SIA	Unbuffered and 4.8	Vis (525 nm)	Percentage of inhibition, calculated from height of negative peak	Herbal and mushroom extracts	45	<1.8	[53,56]
MSFIA	Unbuffered	Vis (517 nm)	Absorbance decrease after 120 s	Beers, juices, tea, wines	13	<1.0	[57]
MSFIA	Unbuffered, 4.1 and 7.6	Vis (517 nm)	Absorbance decrease after 180 s	n.a.	14	n. g.	[59]

FIA, flow injection analysis; SIA, sequential injection analysis; MSFIA, multisyringe flow injection analysis; ESR, electron spin resonance spectrometry; Vis, spectrophotometry; n.a., not applicable; n.g., not given.

than 60% of water, which hinders its application to hydrophilic compounds [46]. The laboratory procedure is technically simple, involving the determination of the remaining DPPH• using spectrophotometry [15], electron spin resonance (ESR) spectroscopy [47] or electrochemistry [48,49]. The assay time is longer than that established for the ABTS^{•+} assay, varying between 20 min up to 6 h [15].

Initially, the DPPH• assay was automated using a FIA system coupled to ESR spectrometry [50,51] (Table 2). In this method, the DPPH• solution was continuously fed into a flow-through flat cell, providing a constant ESR signal at a fixed magnetic field strength (335.3 mT). When the radical scavenger compound/sample solution was injected into the carrier stream, the signal was suppressed and a negative peak appeared whose height was proportional to the concentration of the radical scavenger. The low determination rate (13 h⁻¹) was due to the low resistance to pressure of the flow cell (flow rates higher than 0.32 mL min⁻¹ were not applicable). The results obtained for pure compounds (ascorbic acid, cysteine, trolox) as well as for beverages were compared with a HPLC-DPPH• method [52]. Lower values were found for some samples, which were explained by the difference in the reaction time applied in the HPLC method (20 min) and in the FIA method (<2 min).

Later, a spectrophotometric SIA-DPPH• methodology for rapid and routine screening of pronounced antioxidant/radical scavenging capacity in natural samples was proposed [53]. As described before for the ABTS^{•+} assay [39], a sandwich strategy was implemented to circumvent the mixing problems inherent to SIA [54,55]. Hence, the DPPH• zone (20 µL) was intercalated between two zones (25 µL each) of the antioxidant test solution. The applicability of this SIA system was demonstrated for pure compounds (ascorbic acid, caffeic acid, catechin, epicatechin, and rutin) and for routine screening regarding the presence of antioxidant compounds in a large series of lyophilized herbal and mushroom extracts. The results were compared to the batch procedure and, despite the lower results attained for two samples the proposed method is definitely acceptable for screening purposes. In fact, it was recently applied for a screening study in 88 plant extracts from Central Euro-

pean taxons belonging to the families Asteraceae and Cichoriaceae [56].

Recently, an automatic DPPH• assay was developed using a flow procedure based on multisyringe flow injection analysis and spectrophotometric detection [57]. A stopped flow approach was implemented to monitor the absorbance decrease along time and to evaluate the reaction kinetics qualitatively upon the tested sample. Furthermore, after studying the influence of the initial DPPH• concentration on the calculated percentage of inhibition, the authors suggested the expression of antioxidant capacity as the absorbance variation (or concentration of radical consumed) rather than the percentage of consumed DPPH•, as this last value is dependent of the initial DPPH• concentration. The sample dilution factor was also assessed and it was verified that it did not influence the values obtained for samples which were composed mainly by fast scavengers, whilst for samples containing or originating slow reacting compounds, the dilution was a key aspect in achieving results similar to that obtained by the end-point time-consuming batch method. For these samples (white and red wines) that did not exhaust its scavenging capacity within the period of measurement (about 3 min), a mathematical model [58] was successfully applied to estimate the total DPPH• consumed. Hence, the combination of automation and mathematical treatment of results enabled a significant reduction of analysis time (from 2 h to 3 min).

A similar MSFIA system was developed to evaluate the DPPH• reaction conditions concerning pH and solvent [59]. Benefiting from the reduction of environmental contamination by manipulation of organic solvents, such as methanol, in a contained media (flow conduits), the influence of pH (unbuffered, 4.1, and 7.6) and solvent (methanol and ethanolic solution 50%, v/v) during the first 3 min of the DPPH• scavenging reaction was studied. Using the same configuration, the reaction conditions were adjusted in-line and, for those situations in which a stable value of absorbance was attained within the time period of absorbance monitoring, the number of DPPH• molecules reduced per molecule of antioxidant was calculated.

4. Flow methods for determination of total reducing capacity

The oxidation potential (reducing capacity) of specific compound(s) or sample is conceptually related to their expected antioxidant capacity. Indeed, oxidation potential and antioxidant capacity are inversely related, so that when the oxidation potential of an analyte is low it means that this analyte would be oxidized easily, corresponding to a high antioxidant capacity. Considering this rationale, flow-based methods have been developed to improve the measurement of overall reducing/antioxidant capacity of pure compounds and of a wide variety of food products (Table 3). This

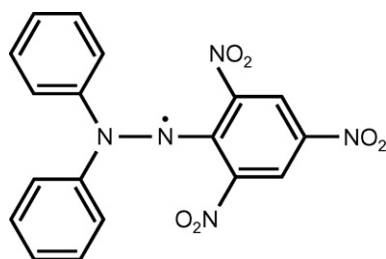


Fig. 5. DPPH• chemical structure.

Table 3

Flow-based methods for determination of total reducing/antioxidant capacity.

Assay	Flow method	pH value	Detection system	Quantification	Type of sample	Determination rate (h ⁻¹)	RSD (%)	Reference
Total phenolics	FIA	2.0	CL	Peak height	Wine	120	<0.8	[61]
CL-antioxidant capacity	FIA	7.4	CL	Height of negative peak	Olive oil	180	<2.8	[62]
Reduction of Fe(III) complex	FIA	≥7.0	Potentiometry	Height of negative peak	Fruit extract, herbal infusion and tea	100	<1.8	[64]
Folin-Ciocalteu reducing capacity	MSFIA	>12	Vis (750 nm)	Peak height	Beer, juices, tea, wine	12	<1.3	[41,66]
Amperometric reducing capacity	FIA	n.g.	Amperometry (+0.4 V)	Peak height	Wine	<90	n.g.	[18]
Amperometric reducing capacity	FIA	n.g.	Amperometry (+0.5 V)	Peak height	Olive oil	90	<3.5	[68]
Amperometric reducing capacity	FIA	n.g.	Amperometry (+0.5 V)	Peak height	Vegetable extracts	60	<3.5	[70]
Amperometric reducing capacity	FIA	4.0	Amperometry (+0.5 V)	Peak height	Herbal extracts	60	n.g.	[71]
Amperometric reducing capacity	FIA	4.5	Amperometry (+0.5 V)	Peak height	Honey, propolis and royal jelly	n.g.	<2.5	[72]
Amperometric reducing capacity	FIA	4.0	Amperometry (+0.8 V, +0.5 V)	Peak height	Tea infusions	n.g.	<3.2	[77]
Amperometric reducing capacity	FIA	4.6	Amperometry (+0.7 V)	Peak height	LMW fractions of whey	60	<2.7	[73,74]
Amperometric reducing capacity	FIA	7.5	Amperometry (+0.8 V, +0.5 V, +0.3 V)	Peak height	Apple, pear, green beans, juices, wines	~60	<7	[75]

CL, chemiluminescence; FIA, flow injection analysis; LMW, low molecular weight; MSFIA, multisyringe flow injection analysis; Vis, spectrophotometry.

property has been determined either through a redox reaction between the antioxidant compounds present in the sample and an oxidizing reagent (such as acidic potassium permanganate, ferric ion, or tungstate-molybdate) or through amperometric methods, based on the measurement of current intensity obtained at a fixed potential.

In food samples, except for carotenoids and vitamins C and E, the most readily oxidizable compounds are those containing (poly)phenolic groups. In fact, polyphenols are the most abundant antioxidants in our diet, since the average daily intake is about 1 g, which is almost 10-fold the intake of vitamin C, 100-fold the intake of vitamin E, and 500-fold the intake of carotenoids [60]. For this reason, the assessment of “total phenolic” content has been directly related with the reducing/antioxidant properties of food products. In this context, Costin et al. proposed a FIA system for the determination of the total phenolic/antioxidant levels in wine after chemiluminescence (CL) generated by these compounds upon oxidation with acidic (pH 2) potassium permanganate in the presence of sodium polyphosphate [61]. For this, the sample was injected in a double-line system where the carrier stream merged with acidic potassium permanganate just before the flow-through CL cell. The proposed method was applied to pure compounds (caffeic acid, catechin, epicatechin, ferulic acid, gallic acid, 4-hydroxycinnamic acid, quercetin, rutin, and vanillin) and to several red and white wine samples. The CL peak height showed a good correlation with the batch DPPH• assay, showing that this method is suitable for rapid estimation of antioxidant or total phenolic content.

Recently, a high-throughput FIA system for CL measurement of antioxidant capacity in olive oils has been proposed [62]. In this case, a three-line system was devised, comprising the initial mixing between olive oil sample (in 80:20 methanol/water) and CL-generating solution containing luminol, horseradish peroxidase and *p*-iodophenol, followed by addition of a H₂O₂ solution. In opposition to the system mentioned above, the presence of antioxidant compounds inhibited the CL signal due to scavenging of H₂O₂ and other reactive species (hydroxyl and superoxide radicals, for instance) that are concomitantly formed [63]. Olive oil samples (*n* = 50) were analysed and no correlation was found between these results and those from ABTS•⁺ and DPPH• methods. The authors suggested that the discrepancies were due to the different reaction time applied in each method (1 h for ABTS•⁺ and DPPH• and 1 s for CL-FIA).

Shpigun et al. [64] developed a flow injection potentiometric method for the evaluation of antioxidant capacity relying upon ferric-reducing ability. The change in the composition of the carrier solution ([Fe(CN)₆]³⁻/[Fe(CN)₆]⁴⁻ redox-reagent) due to redox reaction between water-soluble antioxidants and the oxidant Fe(III) was monitored potentiometrically by a combined platinum electrode. The height of the transient negative signal was proportional to the reducing/antioxidant capacity of the compound/sample and a linear relationship between the analytical signal and the logarithm of the concentration of test compound was attained. The proposed FIA-potentiometric method was applied to pure compounds (ascorbic acid, caffeic acid, chlorogenic acid, L-cysteine, gallic acid, pyrocatechol, pyrogallol, tannic acid, uric acid, and trolox) and also to a variety of food samples. As this assay relies on a chemistry similar to that applied in the widely applied FRAP assay [16,65], based on the reduction of ferric ion to ferrous ion, the presence of the well known pro-oxidant species Fe(II) in the reaction medium may be regarded as a shortcoming.

The automation of FC assay for determination of total reducing capacity, measured as the cumulative capacity of both phenolic and nonphenolic compounds to reduce the FC reagent (tungstate-molybdate acid complexes) was recently implemented by MSFIA system using spectrophotometric detection [66]. In this case, the carbonate buffer solution used for pH adjustment in the batch procedure [67] was replaced by sodium hydroxide solution as the rate of reduction of FC reagent (and also the decomposition of the reaction product) is substantially increased in higher alkaline medium. The strict control of reaction time offered by MSFIA minimized the interference of the decomposition of reaction product, enabling the reduction of reaction time from 2 h (batch method) to 4 min, with similar results for all samples analyzed (wines, beers, teas, soft drinks and juices). Furthermore, by changing the working conditions through software control without manifold reconfiguration, different strategies for mixing of sample and reagent were exploited (continuous flow of FC reagent, merging zones, and intercalated zones approach), in order to attain lower reagent consumption and higher determination throughput. Later, this assay was also implemented in a MSFIA manifold that enabled the sequential determination of this parameter and the ABTS•⁺ scavenging capacity [41].

The flow methods abovementioned use reactive species (oxidants) to evaluate the reducing/antioxidant capacity of pure

compounds and samples. In contrast, the flow methods using amperometric detection rely on the physico-chemical properties of the molecule(s) present in the sample, essentially polyphenols, and do not require the use of reactive species, radicals or non-radicals. This is an important issue as the antioxidant capacity assessed is strongly dependent on the oxidant species applied [38].

Mannino et al. developed a single-line FIA system for the determination of the antioxidant capacity with an electrochemical detector operating at a fixed potential [18]. The authors observed that at the lower potential established (+0.4 V vs. Ag/AgCl reference electrode) only some polyphenolic compounds, having particular structural features like three phenolic groups or two phenolic groups in *o*- or *p*-position, can be oxidized. Therefore, this methodology was proposed for evaluation of “antioxidant power” in wines. For white wines, results comparable to those from the Folin-Ciocalteu assay were obtained. For red wines, this correlation was poor, justified by the higher proportion of phenols of “good antioxidant properties” found in these samples.

Later, the same research group extended this procedure to the evaluation of the “antioxidant power” of olive oils as a model of lipophilic samples [68]. The olive oil samples were injected in a carrier stream of chloroform containing tetrabutylammonium bromide and acetic acid, and further directed to an electrochemical detector operating at a potential of +0.5 V (vs. Ag/AgCl reference electrode). This method offered a sound alternative to the normally used Rancimat method [69] that, owing to the severity of the oxidation conditions used, is not useful for the prediction of olive oil shelf-life. A similar system was proposed by Buratti et al. [70], who investigated the electrochemical properties of lipophilic compounds present in vegetables, such as carotenoids, chlorophylls, tocopherols, and capsaicin as well as several vegetable extracts. In this case, the carrier stream was composed by methyl *tert*-butyl ether, methanol, and sodium dodecyl sulphate. For both systems, the results obtained by the FIA-electrochemical method were compared to those of the ABTS^{•+} assay and a good correlation was found.

More recently, a similar FIA system was applied to assess the antioxidant activity of herb extracts from the *Labiatae* family [71] and also to the evaluation of antioxidant power of honeybee products (honey, propolis, and royal jelly) [72]. In both systems, the carrier was a methanolic solution containing acetic acid/acetate buffer and sodium perchlorate. For all types of sample analyzed, the results provided by the FIA-amperometric method showed a good correlation with DPPH[•] assay.

An amperometric single channel FIA manifold was also proposed to assess the antioxidant capacities of low molecular weight fractions of whey [73]. In this case, the oxidation potential was fixed at +0.7 V (vs. Ag/AgCl reference electrode) and trolox was used as standard compound. The results provided by this system showed a good correlation with those provided by spectrophotometric batch methods: ABTS^{•+} and FRAP assays [74]. Nevertheless, the authors pointed out some limitations to its applicability, namely to compounds with low diffusion coefficient, such as proteins. Furthermore, fouling problems due to protein adsorption at the working electrode were also reported, requesting off-line protein removal prior to determination.

Blasco et al. [75] have proposed a new screening electrochemical protocol to determine total polyphenolics in foods. They introduced the concept of the “Electrochemical Index”, defined as the total polyphenolic content obtained by electrochemistry. For this, a single-channel FIA system with amperometric detection using a glassy carbon disk electrode was employed. Basically, the electrochemical protocol consisted in the measurement of the amperometric current at neutral pH (7.5) and at different oxidation potentials. Since the selectivity increases after a decrease of

the oxidation potential, different degrees in the total polyphenolic fractions could be attained. In this way, it was suggested that the total polyphenolics measured under no selective oxidation conditions (+0.8 V) represent the “electrochemical index” while the total polyphenolics measured under more selective conditions (+0.5 V) represent the high antioxidant polyphenolic fraction. The present electrochemical protocol was applied to several food products (peel, pulp and juices of apple and pear, wines, and fresh and processed green beans). The results obtained using the electrochemical protocol were well correlated with “total phenolics” obtained using the Folin-Ciocalteu assay. Later, the same research group exploited the analytical possibilities of the “electrochemical index” to estimate the antioxidant capacity in honey samples [76]. The results obtained at both potentials applied (+0.5 and +0.8 V) exhibited a high correlation with the DPPH[•] assay. A similar approach was recently taken by Buratti et al. [77] using an innovative, low cost detection cell placed in a FIA system for analysis of tea infusions. In this case, the current resulting from the oxidation of electroactive compounds at +0.8 V or +0.5 V were correlated to Folin-Ciocalteu phenolic index or to DPPH[•] assay, respectively.

Finally, Pérusse and Leech [78] proposed a voltammetric flow injection system for determination of methylene blue, produced off-line by the oxidation of benzoyl-leuco methylene blue in the presence of 13-hydroperoxy-9,11-octadecadienoic acid and myoglobin. When antioxidant compounds/samples were added to the previous reaction media, the formation of methylene blue was inhibited, providing a lower FIA signal. It should be emphasized that the automation of the protocol was restricted here to the determination of the reaction product, with a limited exploitation of FIA features.

5. Conclusions

In general, the reported flow based automatic methods presented several features, such as simplicity, versatility, low cost, and high sample throughput that are advantageous for rapid and reliable determination of reducing/antioxidant capacity in both pure compounds and complex matrices. Besides this, the reaction/determination takes place in a contained environment, minimizing the operator exposition to organic solvents used in the DPPH[•] or lipophilic-electrochemical assays. Furthermore, the reaction conditions (time, mixing, pH) are strictly controlled, improving the repeatability of results.

One of the main advantages brought by the association of flow based methods–antioxidant assessment is the significant decrease on analysis time. This was achieved in different ways, depending on the objectives for which the application was developed. For screening procedures [53] the analysis time can be shorter than that employed in the batch procedure as reaction completeness is not expected. The objective in this case was to attain a “positive” or “negative” result in order to further investigate the compound/extract analyzed. However, when results comparable to end-point methods were aimed, the direct translation of batch methods to flow systems was not feasible, especially for samples containing slow reacting antioxidants. In this case, other solutions were implemented, such as the change on reaction media performed for the Folin-Ciocalteu assay [66] or the application of a mathematical model to the absorbance profile obtained in the first 3 min of reaction in order to predict the DPPH[•] consumption at the end-point time [57].

The flexibility of flow management offered by computer controlled flow techniques fostered the implementation of two different assays in the same manifold, which were performed sequentially. In this way, the sample was processed by both methods at the same time, avoiding discrepancies that may arise due

to sample modification over time and a more reliable comparison between methods.

The flow-based systems reported here were mainly applied to food samples, namely wine, beer, coffee, fruit juices, tea, olive oil, honey and also to plant extracts. The majority of these samples were liquid, which afforded their direct introduction into the systems. In some cases, in-line dilution was performed automatically, implemented in a dilution coil [39] or in a mixing chamber [36], both placed at lateral ports of SIA-selection valve. In fact, sample dilution is undeniably an important factor on antioxidant assays as the time necessary to attain the reaction end-point will decrease for lower antioxidant concentrations [58,79]. For flow based systems, sample dilution is a key parameter to attain results comparable to end-point methods as the reaction time is comparably shorter. For instance, as reported for the DDPH method, the antioxidant capacity assessed for a red wine sample varied from 97% to 67% of the batch end-point value when sample dilution was 1:333 or 1:67. Therefore, in order to check if results are time-biased, it is recommended to process different dilutions of the same sample whenever using flow based systems.

Finally, the combination of single-line FIA systems with amperometric detection provided a simple way of measuring the antioxidant/reducing capacity in the absence of a challenging oxidant species. Nevertheless, the different manifolds proposed were based on the application of different oxidation potentials and pH values (Table 3). In addition, the electrochemical properties of samples have been quantified using different reference standard compounds such as caffeic acid [18], β -carotene [70], (+)-catechin [18,75], galangin [72], gallic acid [76] and trolox [73]. As reported by Avila et al. [76], the values obtained for honey samples were strongly influenced by the oxidation potential, the pH and the reference compound used. Therefore, continued efforts to standardize the analytical conditions are unequivocally necessary in order to obtain comparable results within and between methods.

Acknowledgements

L.M. Magalhães thanks FCT and FSE (III Quadro Comunitário de Apoio) for the PhD grant SFRH/BD/12539/2003. This work was financially supported by FCT through project PTDC/SAU-FCF/67718/2006.

References

- [1] J.M. McCord, *Am. J. Med.* 108 (2000) 652.
- [2] M. Valko, D. Leibfriz, J. Moncol, M.T.D. Cronin, M. Mazur, J. Telser, *Int. J. Biochem. Cell Biol.* 39 (2007) 44.
- [3] D. Galaris, A. Barbouti, P. Korantzopoulos, *Curr. Pharm. Des.* 12 (2006) 2875.
- [4] C.F. Tseng, S.J.T. Mao, *Curr. Pharm. Anal.* 2 (2006) 369.
- [5] J.M. Peake, K. Suzuki, J.S. Coombes, *J. Nutr. Biochem.* 18 (2007) 357.
- [6] G. Ruel, C. Couillard, *Mol. Nutr. Food Res.* 51 (2007) 692.
- [7] A. Kubo, D.A. Corley, *Am. J. Gastroenterol.* 102 (2007) 2323.
- [8] R.B. Jones, N. Z. J. Crop Hortic. Sci. 35 (2007) 219.
- [9] J.C. Rickman, D.M. Barrett, C.M. Bruhn, *J. Sci. Food Agric.* 87 (2007) 930.
- [10] R.L. Prior, X.L. Wu, K. Schaich, *J. Agric. Food Chem.* 53 (2005) 4290.
- [11] R. Kohen, A. Nyska, *Toxicol. Pathol.* 30 (2002) 620.
- [12] L.M. Magalhães, M.A. Segundo, S. Reis, J.L.F.C. Lima, *Anal. Chim. Acta* 613 (2008) 1.
- [13] N.J. Miller, C. Rice-Evans, M.J. Davies, V. Gopinathan, A. Milner, *Clin. Sci.* 84 (1993) 407.
- [14] R. Re, N. Pellegrini, A. Proteggente, A. Pannala, M. Yang, C. Rice-Evans, *Free Radic. Biol. Med.* 26 (1999) 1231.
- [15] W. Brandwilliams, M.E. Cuvelier, C. Berset, *LWT-Food Sci. Technol.* 28 (1995) 25.
- [16] I.F.F. Benzie, J.J. Strain, *Anal. Biochem.* 239 (1996) 70.
- [17] S. Chevion, M.A. Roberts, M. Chevion, *Free Radic. Biol. Med.* 28 (2000) 860.
- [18] S. Mannino, O. Brenna, S. Buratti, M.S. Cosio, *Electroanalysis* 10 (1998) 908.
- [19] J. Ruzicka, E.H. Hansen, *Anal. Chim. Acta* 78 (1975) 145.
- [20] J. Ruzicka, G.D. Marshall, *Anal. Chim. Acta* 237 (1990) 329.
- [21] E.A.G. Zagatto, B.F. Reis, C.C. Oliveira, R.P. Sartini, M.A.Z. Arruda, *Anal. Chim. Acta* 400 (1999) 249.
- [22] B.F. Reis, M.F. Gine, E.A.G. Zagatto, J.L.F.C. Lima, R.A. Lapa, *Anal. Chim. Acta* 293 (1994) 129.
- [23] F.R.P. Rocha, B.F. Reis, E.A.G. Zagatto, J.L.F.C. Lima, R.A.S. Lapa, J.L.M. Santos, *Anal. Chim. Acta* 468 (2002) 119.
- [24] F. Albertús, B. Horstkotte, A. Cladera, V. Cerdà, *Analyst* 124 (1999) 1373.
- [25] M.A. Segundo, L.M. Magalhães, *Anal. Sci.* 22 (2006) 3.
- [26] M. Amatatongchai, O. Hofmann, D. Nacapricha, O. Chailapakul, A.J. De Mello, *Anal. Bioanal. Chem.* 387 (2007) 277.
- [27] N.J. Miller, J. Sampson, L.P. Candeias, P.M. Bramley, C.A. Rice-Evans, *FEBS Lett.* 384 (1996) 240.
- [28] R. Van den Berg, G.R.M.M. Haenen, H. Van den Berg, A. Bast, *Food Chem.* 66 (1999) 511.
- [29] A. Cano, J. Hernandez-Ruiz, F. Garcia-Canovas, M. Acosta, M.B. Arnao, *Phytochem. Anal.* 9 (1998) 196.
- [30] A.M. Alonso, C. Dominguez, D.A. Guillen, C.G. Barroso, *J. Agric. Food Chem.* 50 (2002) 3112.
- [31] N. Pellegrini, D. Del Rio, B. Colombi, M. Bianchi, F. Brighenti, *J. Agric. Food Chem.* 51 (2003) 260.
- [32] S. Bompadre, L. Leone, A. Politi, M. Battino, *Free Radic. Res.* 38 (2004) 831.
- [33] M. Battino, M.S. Ferreiro, T. Armeni, A. Politi, S. Bompadre, A. Massoli, P. Bullon, *Free Radic. Res.* 39 (2005) 343.
- [34] E.P. Labrinea, C.A. Georgiou, *J. Agric. Food Chem.* 53 (2005) 4341.
- [35] E.P. Labrinea, C.A. Georgiou, *Anal. Chim. Acta* 526 (2004) 63.
- [36] M.J.R. Lima, I.V. Toth, A.O.S.S. Rangel, *Talanta* 68 (2005) 207.
- [37] M.C. Foti, C. Daquino, C. Geraci, *J. Org. Chem.* 69 (2004) 2309.
- [38] E.N. Frankel, A.S. Meyer, *J. Sci. Food Agric.* 80 (2000) 1925.
- [39] P.C.A.G. Pinto, M.L.M.F.S. Saraiva, S. Reis, J.L.F.C. Lima, *Anal. Chim. Acta* 531 (2005) 25.
- [40] J.B. Garcia, M.L.M.F.S. Saraiva, J.L.F.C. Lima, *Anal. Chim. Acta* 573 (2006) 371.
- [41] L.M. Magalhães, M.A. Segundo, S. Reis, J.L.F.C. Lima, I.V. Toth, A.O.S.S. Rangel, *Anal. Chim. Acta* 592 (2007) 193.
- [42] D. Ivekovic, S. Milardovic, M. Roboz, B.S. Grabaric, *Analyst* 130 (2005) 708.
- [43] S. Milardovic, I. Kerekovic, R. Derrico, V. Rumenjak, *Talanta* 71 (2007) 213.
- [44] S. Milardovic, I. Kerekovic, V. Rumenjak, *Food Chem.* 105 (2007) 1688.
- [45] M.S. Blois, *Nature* 181 (1958) 1199.
- [46] A. Stasko, V. Brezova, S. Biskupic, V. Misik, *Free Radic. Res.* 41 (2007) 379.
- [47] C.A. Calliste, P. Trouillas, D.P. Allais, A. Simon, J.L. Duroux, *J. Agric. Food Chem.* 49 (2001) 3321.
- [48] S. Milardovic, D. Ivekovic, V. Ruwenjak, B.S. Grabaric, *Electroanalysis* 17 (2005) 1847.
- [49] S. Milardovic, D. Ivekovic, B.S. Grabaric, *Bioelectrochemistry* 68 (2006) 175.
- [50] H. Ukeda, Y. Adachi, M. Sawamura, *Talanta* 58 (2002) 1279.
- [51] H. Ukeda, *Bunseki Kagaku* 53 (2004) 221.
- [52] T. Yamaguchi, H. Takamura, T. Matoba, J. Terao, *Biosci. Biotechnol. Biochem.* 62 (1998) 1201.
- [53] M. Polasek, P. Skala, L. Opletal, L. Jahodar, *Anal. Bioanal. Chem.* 379 (2004) 754.
- [54] M.A. Segundo, A.O.S.S. Rangel, *Anal. Chim. Acta* 458 (2002) 131.
- [55] H.R. Silva, M.A. Segundo, A. Rangel, *J. Braz. Chem. Soc.* 14 (2003) 59.
- [56] V. Kolecár, L. Opletal, E. Brojerova, Z. Rehakova, F. Cervenka, K. Kubikova, K. Kuca, D. Jun, M. Polasek, J. Kunes, L. Jahodar, *J. Enzym. Inhib. Med. Chem.* 23 (2008) 218.
- [57] L.M. Magalhães, M.A. Segundo, S. Reis, J.L.F.C. Lima, *Anal. Chim. Acta* 558 (2006) 310.
- [58] J.C. Espin, C. Soler-Rivas, H.J. Wichers, *J. Agric. Food Chem.* 48 (2000) 648.
- [59] L.M. Magalhães, M.A. Segundo, C. Siquet, S. Reis, J.L.F.C. Lima, *Microchim. Acta* 157 (2007) 113.
- [60] A. Scalbert, G. Williamson, *J. Nutr.* 130 (2000) 2073S.
- [61] J.W. Costin, N.W. Barnett, S.W. Lewis, D.J. McGillivray, *Anal. Chim. Acta* 499 (2003) 47.
- [62] K.S. Miniotti, C.A. Georgiou, *Food Chem.* 109 (2008) 455.
- [63] I. Parejo, C. Petrakis, P. Kefalas, *J. Pharmacol. Toxicol. Methods* 43 (2000) 183.
- [64] L.K. Shpigun, M.A. Arharova, K.Z. Brainina, A.V. Ivanova, *Anal. Chim. Acta* 573 (2006) 419.
- [65] I.F.F. Benzie, J.J. Strain, *Methods Enzymol.* 299 (1999) 15.
- [66] L.M. Magalhães, M.A. Segundo, S. Reis, J.L.F.C. Lima, A.O.S.S. Rangel, *J. Agric. Food Chem.* 54 (2006) 5241.
- [67] V.L. Singleton, R. Orthofer, R.M. Lamuela-Raventos, *Methods Enzymol.* 299 (1999) 152.
- [68] S. Mannino, S. Buratti, M.S. Cosio, N. Pellegrini, *Analyst* 124 (1999) 1115.
- [69] M.W. Laubli, P.A. Bruttel, *J. Am. Oil Chem. Soc.* 63 (1986) 792.
- [70] S. Buratti, N. Pellegrini, O.V. Brenna, S. Mannino, *J. Agric. Food Chem.* 49 (2001) 5136.
- [71] M.S. Cosio, S. Buratti, S. Mannino, S. Benedetti, *Food Chem.* 97 (2006) 725.
- [72] S. Buratti, S. Benedetti, M.S. Cosio, *Talanta* 71 (2007) 1387.
- [73] J. Chen, L. Gorton, B. Akesson, *Anal. Chim. Acta* 474 (2002) 137.
- [74] J. Chen, H. Lindmark-Mansson, L. Gorton, B. Akesson, *Int. Dairy J.* 13 (2003) 927.
- [75] A.J. Blasco, M.C. Rogerio, M.C. Gonzalez, A. Escarpa, *Anal. Chim. Acta* 539 (2005) 237.
- [76] M. Avila, A.G. Crevillen, M.C. Gonzalez, A. Escarpa, L.V. Hortiguera, C.D. Carretero, R.A.P. Martin, *Electroanalysis* 18 (2006) 1821.
- [77] S. Buratti, M. Scampicchio, G. Giovanelli, S. Mannino, *Talanta* 75 (2008) 312.
- [78] P. Perusse, D. Leech, *Electroanalysis* 15 (2003) 573.
- [79] D. Villano, M.S. Fernandez-Pachon, A.M. Troncoso, M.C. Garcia-Parrilla, *Talanta* 64 (2004) 501.



Preliminary study of UV ageing process of proteinaceous paint binder by FT-IR and principal component analysis

E. Manzano^a, N. Navas^a, R. Checa-Moreno^b, L. Rodríguez-Simón^c, L.F. Capitán-Vallvey^{a,*}

^a Department of Analytical Chemistry, University of Granada, c/Fuentenueva s/n, Granada E-18071, Spain

^b Laboratorio Central de Sanidad Animal, M.A.P.A., c/Camino del Jau s/n, Santa Fe, Granada E-18320, Spain

^c Department of Paint and Restoration, University of Granada, Avd. Andalucía s/n, Granada E-18071, Spain

ARTICLE INFO

Article history:

Received 20 April 2008

Received in revised form

30 September 2008

Accepted 6 October 2008

Available online 17 October 2008

Keywords:

FT-IR spectroscopy

Principal component analysis

UV ageing process

Proteinaceous binders

Cultural heritage conservation

ABSTRACT

This work presents a preliminary study on the ageing process of proteinaceous binder materials used in painting under UV light. With this aim, two sets of model samples were prepared: samples prepared using a single protein material and complex samples prepared in a similar way to the sequence of layers in a real painting from lowest to highest complexity (protein, drying oils, pigment and varnish). The study focuses on acquiring information about the possible degradation process of proteinaceous binders due to ageing and how this process be affected by the presence of characteristic non-proteinaceous painting materials, such as lipids from linseed oil, terpenic compounds from varnish and inorganic pigments. Samples simulated the accelerated ageing process, as did the UV light exposition. The FT-IR spectra were recorded after 100, 500, 1000 and 1500 h of exposition. The study of the accelerated ageing process was performed by means of principal component analysis (PCA) using the FT-IR spectra obtained. Loadings from the significant principal components were analysed to find the FT-IR frequency (cm^{-1}) involved in the degradation process. The study showed the lack of any relevant modification on the proteins in the single model samples. On the contrary, the complex model samples showed the ageing process. The accelerated ageing process can be explained by a principal component from PCA. The most affected IR region was $2900\text{--}3600\text{ cm}^{-1}$, where the amide band was included.

© 2008 Published by Elsevier B.V.

1. Introduction

The colour or pictorial layer of paintings is mainly composed of pigments and organic binders. Egg yolk, glair, animal glue, milk or casein, drying oils, gums, plant resins, animal resins and waxes are the most common organic materials used as binding media historically in Europe [1]. The paint medium determined the painting technique, and moreover, could be helpful for the authentication of the artwork. On the other hand, organic materials used in art generally need special attention in the conservation of paintings, due to their tendency to undergo degradation, transformation and oxidation processes with respect to the inorganic constituent. Therefore a major problem with organic binders used in objects of Cultural Heritage is their short lifetime due to their susceptibility to various degrading processes. Particularly, in art paintings, discolouration, cracking and degradation are the results of chemical and physicochemical processes that usually originate from oxygen and exposure to UV light [1]. Nevertheless, the stability of proteins

in various atmospheric conditions is said to be exceptional as compared with the yellowing and brittleness of aged oils and resins [2]. This may be the reason why the ageing process of oils and resins has been widely discussed [3–5], while the ageing of the proteins used in painting has scarcely been studied [2].

Analytical studies of binding material have mainly been accomplished by gas chromatographic techniques [6–10]. Fourier transform infrared (FT-IR) spectroscopy has also been traditionally used in the study of works of art to characterise both the inorganic and organic constituents in painting materials from a wide variety of artworks [11–13]. This technique has the advantage of being fast and needs no treatment sample procedure. On the other hand, FT-IR – as spectroscopic technique – provides complex data sets represented by the spectra of the samples, suitable for being treated by multivariate analysis techniques. In recent years, chemometric techniques have been increasingly more used in the field of Cultural Heritage since they can extract information from correlated data sets, such as spectroscopic sets [14]. Several of these efforts have focused on studying the degradation produced by ageing processes [15–20]. One example of this is a method for monitoring the surface conservation of wooden objects by Raman Spectroscopy and multivariate control charts [15]. Similar approaches, but using

* Corresponding author.

E-mail address: lcapitan@ugr.es (L.F. Capitán-Vallvey).

ATR-FT-IR [16,17,19] and FT-Raman [18] spectroscopy were also proposed for monitoring and testing the state of conservation of painted surfaces. Recently, this approach based on multivariate control charts has also been used to monitor the surface of paper samples exposed to UV light by ATR-FTR-IR spectroscopy [20]. Multivariate calibration by means of partial least squares algorithm was also applied to analyse the pigments on the surface of a painting [21], although the ageing process of the protein binding material was not the goal of these works. Multivariate techniques have been mainly applied to characterise binder materials but using data sets from GC-MS [22,23]. Recently a comparison between traditional and pattern recognition strategy (SIMCA) in the classification of old proteinaceous binders has been proposed [24]. The use of near IR spectroscopy in a classification study of binding media used in paintings was also reported [25].

The objective of this preliminary work was to evaluate the accelerated ageing process – represented by the UV light exposure – of proteinaceous binding materials in simulated pictorial samples both when proteins were single and when they were in a complex matrix. The painting materials chosen for the study (gypsum, egg albumin, jersey cow casein, rabbit epidermis collagen, linseed oil, white lead pigment and terpenic resin) were representative of proteinaceous and lipid binders, inorganic pigments and varnish used for many years and throughout historical epochs. Complex samples were constructed adding non-proteinaceous materials (from the above-mentioned) to a protein thin layer in order to simulate the strata arrangement in an original painting. The analyses of samples were performed periodically by recording their FT-IR spectra after exposure to UV radiation. PCA was applied to FT-IR spectra to reduce its multidimensional space into a smaller space in order to extract information about the protein ageing process by studying similarities in the samples. Despite the complexity of the samples, PCA analysis made it possible to detect IR changes related to the accelerated ageing treatment, proving its usefulness in extracting information from complex data sets. This work represents a first approach to studying the UV ageing process of proteinaceous binding materials by using FT-IR spectroscopy along with chemometric tools such as PCA.

2. Experimental

2.1. Instrument and software

The FT-IR spectra were collected using a NICOLET spectrometer 20SXB, working in transmission mode. The instrument was connected to a Pentium 200 and the instrument software was OMNIC v 4.1, running under Windows 2000 Professional (Microsoft Corporation, USA). The FT-IR spectra were recorded from 3999 to 400 cm^{-1} with a resolution of 2 cm^{-1} and 200 scan.

High-speed exposure unit SUNTEST CPS, Heraeus (Hanau, Germany), equipped with a Xenon lamp; a special UV glass filter was used for limiting the radiation at wavelengths greater than 295 nm, corresponding to outdoor solar exposure. Irradiance was set at 765 W m^{-2} , and the maximum and minimum temperatures of the samples were maintained between 30–35 °C and 15–20% relative humidity measured by the thermohygrometer Station OREGON, mod. EMR812HGN (Portland, OR, USA).

System of Gel Air Dryer, BIO-RAD Laboratories S.A. (Madrid, Spain).

Analytical balance METTLER-TOLEDO model AE163, with the weight range between 0–30 g and 0–160 g, and precision 0.01 and 0.1 mg, respectively.

Ultrasound bath, 6l capacity, Selecta model Ultrasons-H of J.P. Selecta S.A. (Barcelona, Spain).

Chemometric data treatments were performed using Statistical Product and Service Solutions program (SPSS, for Windows ver. 15, USA) and Excel 2000 (Microsoft Corporation, USA).

2.2. Reagents

The standard proteins used to prepare the samples were albumin, skin veal collagen and bovine milk α -casein, all purchased from Sigma (Barcelona, Spain). In addition, three similar protein binding media were also prepared according to old recipes [26] to obtain standards similar to those used by ancient artists, specifically albumin from hen eggs, collagen from rabbit glue and casein from bovine jersey milk (homemade samples). The drying oil used to prepare complex samples was linseed oil (boiled linseed oil) purchased from Talens (Apeldoorn, Holland). The pigment selected to mix with the linseed oil was lead white or basic carbonate of lead ($\text{PbCO}_3 \cdot \text{Pb(OH)}_2$) purchased from Maimeri & Co. (Milano, Italy). Dammar varnish glossy, purchased from Talens (Apeldoorn, Holland) was used for the upper varnish layer.

2.3. Model samples

All samples were prepared on 45 mm \times 20 mm glass slides. Two sets of model samples were prepared. The first was made up of the single protein samples prepared by just painting the glass slides with a single layer of the studied proteins (P1–P6 samples; Table 1). The second set contained samples that were constructed increasing their complexity by adding a new layer in every slide sample of the set. Therefore a gypsum ground layer was disposed on all glass slides and then over this inner layer of gypsum the following layers were arranged sequentially: a thin layer of rabbit glue (P8 sample), a thin layer of linseed oil (P9 sample), a thin layer of a mixture composed of lead white and linseed oil at a ratio of 2:1 (w/w) (sample P10), and an outer layer in sample P11 which was a thin layer of dammar varnish (Table 1). This second set was prepared according to the usual complexity of a real painting, simulating its sequence of layers: ground layer, pictorial layer and protection layer. P7 sample only containing ground gypsum layer.

The different materials used to prepare the layers were carefully spread on the glass slide with a paintbrush. After spreading each layer, the slide was dried to a constant weight using a gel air dryer system. The weight was controlled after every layer deposit in order to estimate the percentage of weight that each layer represented on the slide, including the proteinaceous layer. The protein percentage values were 10.3% for P8, 5.8% for P9, 5.4% for P10 and 8.1% for P11. These percentages, higher than 5% in all cases, were attributable to the presence of some proteinaceous material coming from binders in the samples; a lower percentage in real samples might suggest

Table 1
Sets of model samples.

Single protein set samples		Complex matrix set samples (Collagen or rabbit glue set samples)			
samples	single protein	samples	ground	pictorial layer	protection layer
P1	albumin (standard)	P8	gypsum	rabbit glue	none
P2	hen egg albumin	P9	gypsum	rabbit glue + linseed oil	none
P3	collagen of skin veal (standard)	P10	gypsum	rabbit glue + linseed oil mixed white lead	none
P4	collagen of rabbit glue	P11	gypsum	rabbit glue + linseed oil mixed white lead	dammar varnish
P5	α -casein of bovine milk (standard)				
P6	casein from milk (bovine jersey)				

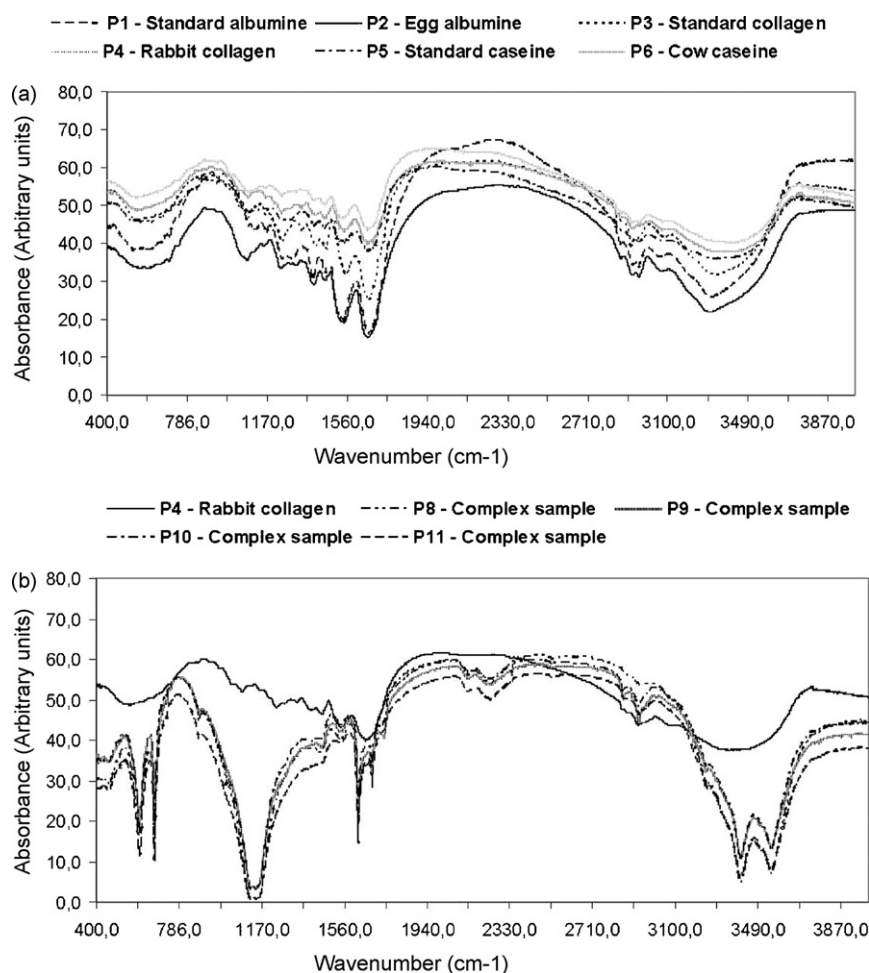


Fig. 1. Averaged FT-IR spectra of the samples studied before UV exposure ($t = 0$ h): (A) single model samples and (B) complex model samples and single collagen sample.

traces of amino acids in non-proteinaceous materials or the action of some microorganism especially in wall paintings [27,28].

2.4. UV light exposure

In order to provide complete information about the whole model samples prepared on glass slides (Table 1), five random samples were taken from each slide and the KBr pastilles were prepared. In this way, every glass slide was represented by five KBr pastilles. Simulation of exposure to sunlight was achieved by irradiation with light from a UV lamp emitting over 310 nm at 765 W m^{-2} . FT-IR spectra were registered after 0, 100, 500, 1000 and 1500 h of exposition. The five FT-IR spectra from the same glass model sample slide at the same time of the UV light exposure were averaged in order to achieve FT-IR spectra that were as representative as possible. These averaged spectra were used to describe the state of conservation of the respective model sample before and after the UV ageing treatment.

Table 2
IR regions analysed by PCA.

IR region (cm^{-1})	Sample analysed
600–1450	All samples
1500–1750	All samples
1750–1850	P8, P9, P10, P11 (set of complex samples)
2900–3600	All samples

3. Results and discussion

3.1. Model sample selection

Albumin, collagen and casein were selected to study their UV ageing process since they have been widely used in painting as preparation layer and as binding media. From the point of view of the conservation state, it is important to know if the ageing process produces some significant physical and chemical changes in these proteinaceous materials (Table 1). Linseed oil was selected because it has been widely used as a medium in pictorial layers in oil paintings due to its good optical and mechanical properties with respect to other drying oils, i.e. walnut, poppyseed. Lead white has been

Table 3
PCA. Single protein set samples.

IR region (cm^{-1})	PC	Variance account (%)	Variance accumulated (%)
600–1450	PC1	91.4	91.4
	PC2	6.8	98.2
	PC3	0.9	99.0
1500–1750	PC1	98.2	98.2
	PC2	1.0	99.2
	PC3	0.7	99.8
2900–3600	PC1	96.4	96.4
	PC2	2.7	99.1
	PC3	0.7	99.9

one of the most commonly used pigments in the history of painting. A mixture of white lead and linseed oil was laid in a thin layer over the protein layer to test the ion Pb(II) influence on the drying speed of the linseed oil and the consequent action of the lipid oxidants – formed during this drying – on the degradation process of

rabbit glue, the natural protein selected for this study [29]. Finally, dammar glossy was chosen as the outer layer since this varnish containing terpenic resin as dammar and is more stable and less acid than other natural resins, such as mastic. This varnish has also been widely used throughout different artistic periods.

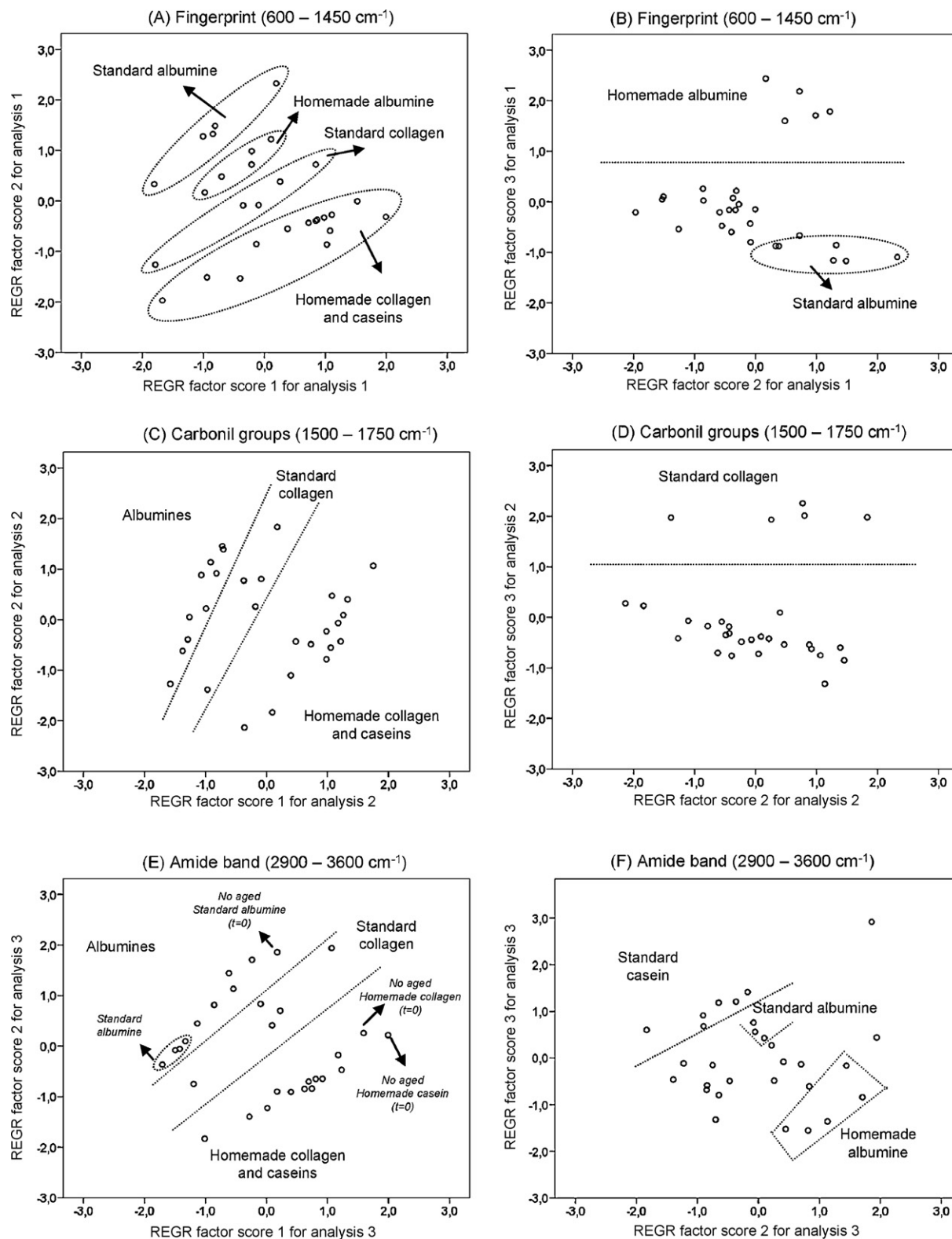


Fig. 2. Score plots of PC1 and PC2 and score plots of PC2 and PC3 for the three FT-IR regions studied in the single protein set samples.

Complex model samples P8, P9, P10 and P11 were constructed adding new layers in order to simulate the complex composition of a real painting. It is well known that, despite the composition changes throughout historical epochs, paintings are made up of different layers. On the inner layer, namely the preparation layer, the pictorial layer itself is scattered and formed by the pigments mixed with organic binders such as proteins, sugars, drying oils or waxes and finally an outer varnish layer. For this study, pictorial films simpler than real paint were prepared (Table 1, complex matrix set samples). The objective in including this set was to test the influence of new layers on the possible changes in the proteinaceous binder when samples were exposed to the accelerated ageing process.

3.2. PCA analysis

The FT-IR spectra were registered from 400 to 3999 cm^{-1} and formed by 3734 data points. At each time studied, the different model samples prepared on glass slides were characterised by the average spectrum of the five FT-IR spectra recorded as explained in

Section 2. In this way, these FT-IR average spectra were less affected by the position where the powder was taken in the glass slide to make the KBr pellets. Fig. 1 shows these average IR spectra for single protein samples (A) and the complex samples (B) right after their preparation ($t=0$), thus, without undergoing any ageing process.

Models samples were split into two sets for PCA analysis. The first contained all the samples with a single protein and the second included the samples that emulated real layer situations in a painting, here called complex matrix sets (Table 1). Several IR regions were selected to carry out the PCA analysis in accordance with the sample composition. Table 2 shows these IR regions, the characteristic band tested in each one and the samples where they were used. The fingerprint region was selected to apply PCA because of its unique absorption patterns for every compound and then for every mixture. The IR region between 1500 and 1750 cm^{-1} was used as representative of absorption bands at 1650 cm^{-1} attributed to C=O amide I and to 1518 cm^{-1} N–H amide II [30], and the band at 1653 cm^{-1} caused by C=C double bonds in the fatty acids [31] were also included in this IR region. The region between 1750 and 1850 cm^{-1} was analysed when the samples contained oil. It

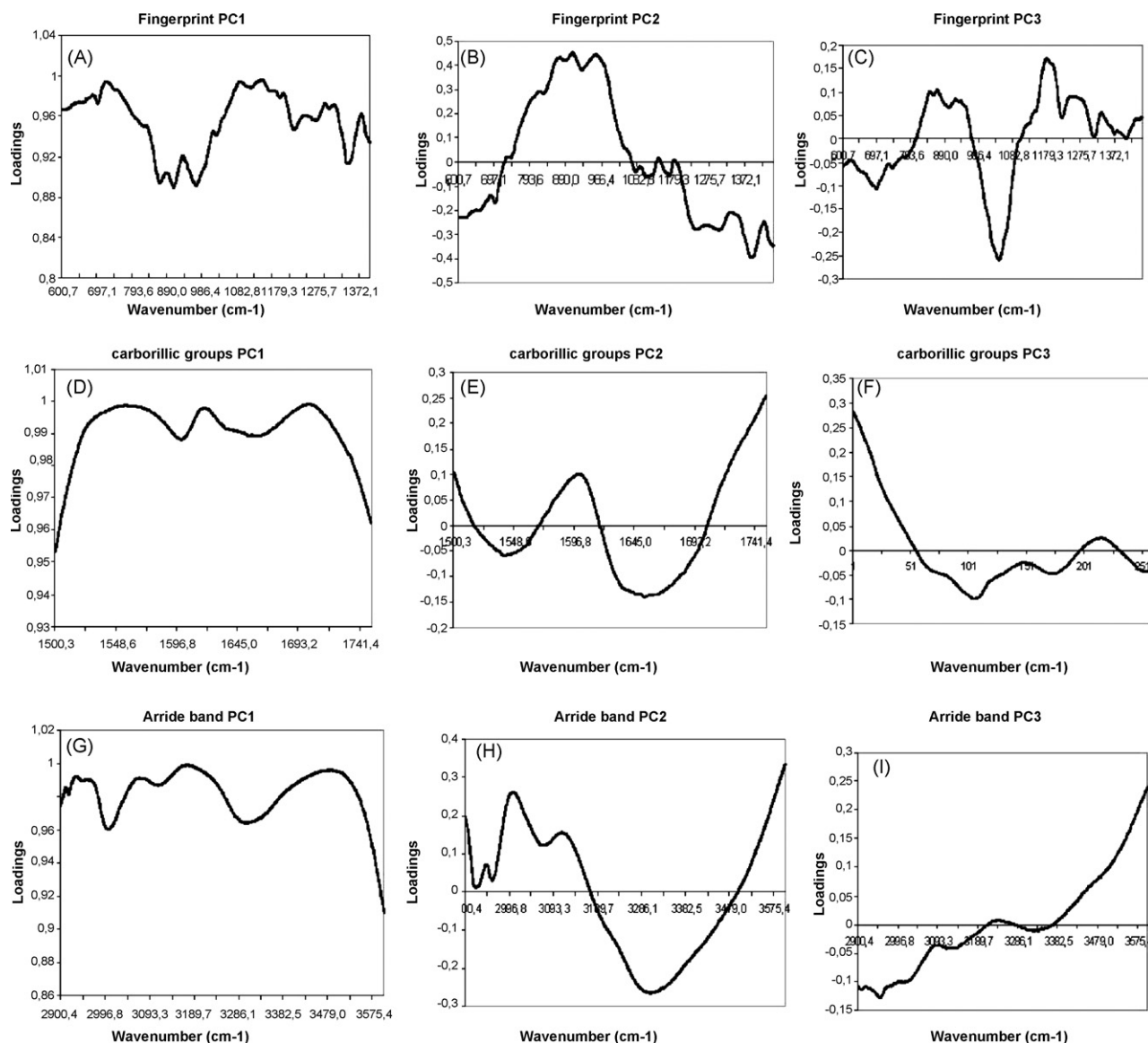


Fig. 3. Loading plots of PC1, PC2 and PC3 from the three FT-IR regions studied in the single protein set samples.

includes the intense signal from the carbonyl group at 1744 cm^{-1} from ester bonds and the absorption shoulder centred at 1776 cm^{-1} characteristic of aged oil drying [31]. The IR region from 2900 to 3600 cm^{-1} was also tested since it includes aliphatic vibrations around 3000 cm^{-1} from fatty acids, the protein amide band A (around 3300 cm^{-1}) and B (around 3100 cm^{-1}), and also includes

bands from hydroxyl groups or hydroperoxide, both products of oxidation from drying oil [29].

PCA were performed using both the covariance data matrixes (scaling by mean-centered data) and the correlation data matrixes (scaling by unit variance). The results were clearly better when PCA were performed on the correlation data matrixes, so the results shown and discussed here correspond to autoscaled data. A simple centring data procedure is often adopted for spectral data [18,32], because the applied autoscaling procedure assigns the same relevance to each IR spectral region. Thus spectral regions with small variation – no relevant IR bands – can acquire the same importance as large IR bands related to important functional groups. Therefore in this work, only IR bands containing the greatest variability were selected to apply PCA (not the whole IR spectrum). This may explain why results were more interpretable when data were autoscaled since no relevant bands were included in the PCA.

3.2.1. Single protein models

The PCA of the data matrix from the samples containing a single protein showed no pattern distribution with respect to ageing treatment. There were no groupings of samples that underwent the same ageing process in any of the IR regions studied when the scores of the samples were projected onto the plane of the two first PCs or when using the second and third PCs (Fig. 2). The total variance explained by the three first PCs in the entire PCA were always higher than 99.0% (Table 3). It can therefore be inferred that the ageing process did not introduce systematic chemical changes that could be detected by multivariate analysis of the IR spectrum. Moreover, the fingerprint region presented the best ability to grouping different kinds of protein samples (Fig. 2); it was possible to distinguish four different groups projecting the scores onto the plane of the two first PCs (Fig. 2A). In the case of albumin samples, the PCA could even differentiate protein belonging to standard or homemade samples. The collagen samples were also split into two groups, but homemade collagen samples were placed together with all the casein samples. Since grouping appeared diagonally on the plane of the two first PCs for the entire IR region, it was necessary to use both PCs to group the protein samples. Fig. 3 shows the loading plots of the three first PCs in the different IR regions studied. It can be seen that no peaks appeared with the greatest weight in PC1; rather the weight was distributed across the whole IR region. Scores projected onto the plane of the second and third PCs were less informative for the other three IR regions analysed.

Fingerprint and carbonyl groups regions split the samples into two groups by the third PC. The first isolated homemade albumin from the rest of the samples and the second isolated the standard collagen. The amide band region grouped types of protein but not as well as the two first PCs of the fingerprint region. No sample distribution within the groups was related to the ageing process. By just analysing scores from amide band projected onto the plain of the two first PCs it was possible to observe that three of the five non-aged samples ($t=0$) were placed outside of their respective kind of samples. They were standard albumin, homemade collagen and homemade casein samples. This could be attributed to a drying process during the first hours. It can be assumed that once the water was evaporated from the samples, no further changes were detected by the PCA, in agreement with the consulted bibliography [2,33,34].

3.2.2. Complex models

The results found when the PCA was performed on the data matrix from the complex samples were different from those shown above. The most informative IR region was found to be the amide band, even to characterise the kind of samples. The results from the

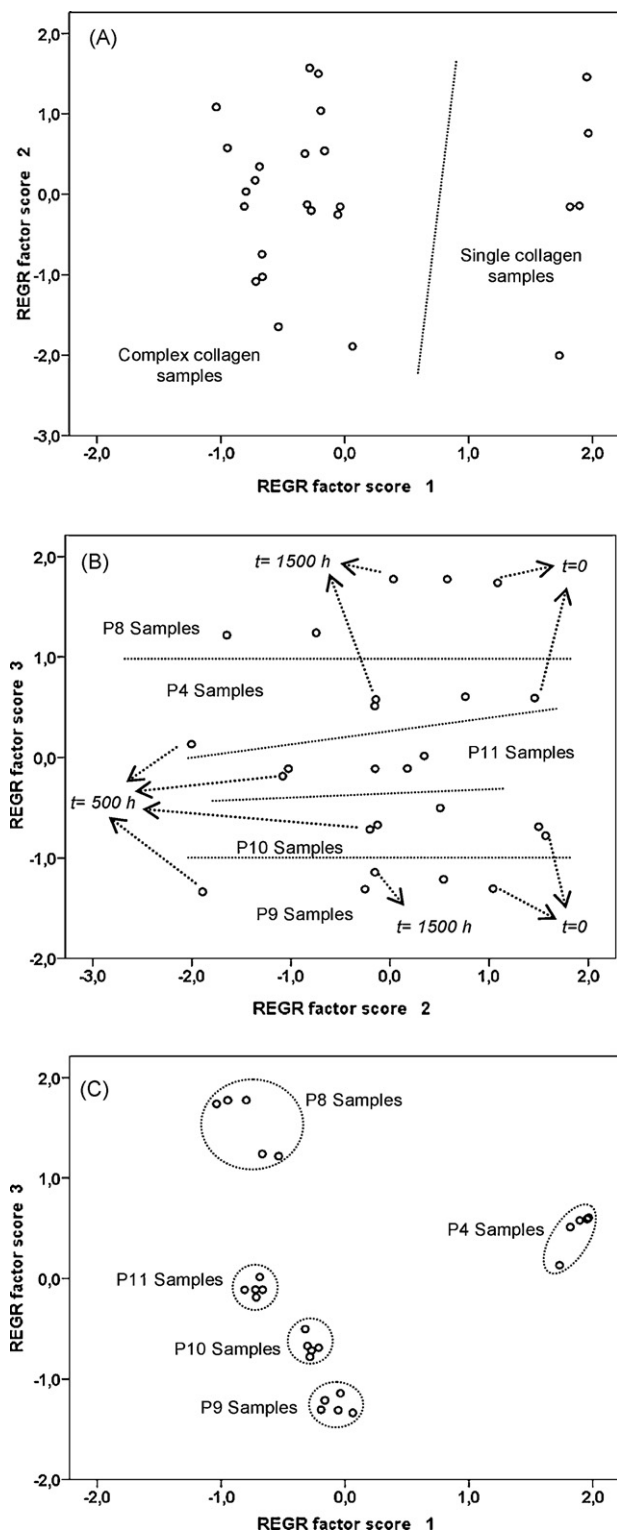


Fig. 4. Score plot of PC1 and PC2, score plot of PC2 and PC3 and score plot of PC3 and PC1 for the FT-IR regions.

Table 4
PCA. Complex model set samples.

IR region (cm ⁻¹)	PC	Variance account (%)	Variance accumulated (%)
600–1450	PC1	83.4	83.4
	PC2	15.6	98.9
	PC3	0.6	99.6
1500–1750	PC1	85.1	85.1
	PC2	9.8	94.9
	PC3	4.3	99.2
1750–1850	PC1	99.2	99.2
	PC2	0.7	99.9
	PC3	0.1	99.9
2900–3600	PC1	60.9	60.9
	PC2	37.5	98.4
	PC3	1.5	99.9

PCA analysis are reported in Table 4. The first three PCs were significant and explain 99.0% of the total variance. The scores plotted in the plane of PC1 and PC2 showed a separation of samples containing gypsum from the sample without gypsum throughout PC1 (Fig. 4). From the IR spectrum (Fig. 1) it can be seen that the main variability in the samples was introduced by the presence of gypsum, therefore this information was included in the first PC. Samples prepared with gypsum had negative or zero scores in the PC1. Samples prepared without gypsum were characterised by high PC1 scores. From the analysis of the loading plots (Fig. 5), this can be seen clearly, as frequencies higher than 3177 cm⁻¹ had the largest weight on PC1; this IR region leading the separation among samples with and without gypsum. The scores plotted in the plane of the PC2 and PC3 and their loading plots are shown in Figs. 4 and 5, respectively. The separation of kinds of sample along the PC3 can be clearly seen. The PC3 score decreased in the following order: samples prepared only with collagen and gypsum (P8) > collagen (P4) > collagen, gypsum, linseed oil, pigment and varnish (P11) > collagen, gypsum, linseed oil and pigment (P10) > collagen, gypsum, linseed oil (P9). Samples prepared with linseed oil gave negative scores on PC3. The analysis of the loadings clearly reveals that PC3 mainly accounts for the peaks at 2930 cm⁻¹ because this peak had the highest positive weight on this PC3. The work by Marengo et al. [18] analysing the exposure to UV light of ultramarine blue mixed with linseed oil and spread on canvas attributed this peak to the presence of linseed oil in the samples. No aged samples gave positive values on the PC which accounted for the peak at 2933 cm⁻¹ and this result can be used to indicate the degradation of this oil by the accelerated ageing UV process. In this analysis, samples prepared without linseed oil were those that gave positive score values on the PC3, and samples containing linseed oil gave negative score values on this PC3. Therefore, the decrease of the signal at 2933 cm⁻¹ observed here would correlate with the presence or absence of linseed oil in the sample.

The variability explained in the PC2 was related to the ageing process. In accordance with Marengo et al. [18–20], performing PCA on the non-ageing and ageing samples together, possible new phenomena induced by the ageing treatments can account for a specific PC. The results obtained corroborated this affirmation. The distribution of the sample in groups along the PC2 showed that non-ageing samples had the highest scores, samples suffering a 500-h ageing process had the lowest scores, and most ageing samples had zero or close to zero scores on this PC3 (Fig. 4). From the analysis of the corresponding loading plots (Fig. 5), the IR region affected by the accelerated UV ageing process can be estimated. The band around 3180 cm⁻¹ had the largest weight on the PC2. This frequency was not associated with a characteristic peak in the IR spectrum (Fig. 6). The conclusion that emerged from the analysis of the loading plots

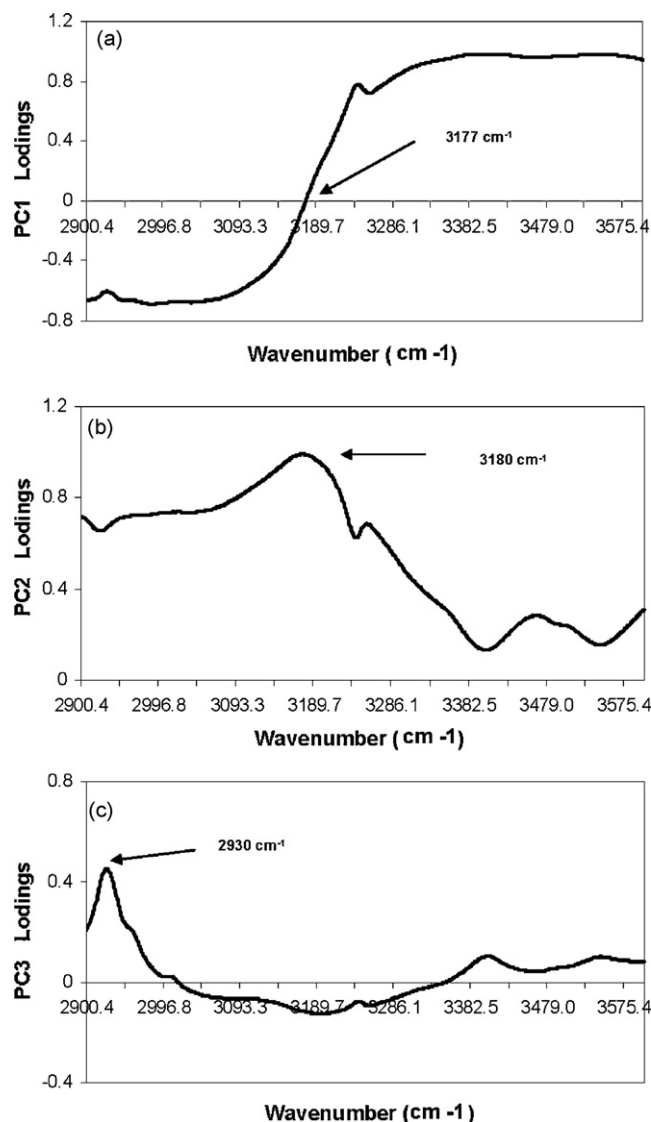


Fig. 5. Loading plots of: PC1 (a), PC2 (b) and PC3 (c) from 2900 to 3600 cm⁻¹ of the complex set samples.

and the IR spectra of the ageing complex samples could be that the samples from 0 to 500 h suffer a general decrease in intensity in the whole IR region, being more affected around 3180 cm⁻¹; the ageing of the samples from 500 to 1500 h appears to have increased the intensity of this region with the corresponding scores rising to zero or close to zero. It was not possible to explain the results chemically since the frequencies with the largest weights on the PC2 were not characteristic of any group present in the complex samples. It may be that the ageing process is involved with protein since the amide band was included in this IR region, but no solid conclusion could be inferred. Despite the different sample compositions, PCA can detect distribution patterns associated with the UV ageing of complex samples. Once the information represented in the PC2 is eliminated, the score plots of the PC1 and PC3 grouped types of complex samples perfectly, as can be seen in Fig. 4. The ageing process accounted for in a PC was found only by analysing this IR region. The PCA of the other IR regions did not provide as much information. Now that the capability of the PCA of IR data matrix to detect and extract the results of the ageing process in the PC has been tested, more efforts must be made which focus on the analysis of data matrix from samples characterised with lesser variability in

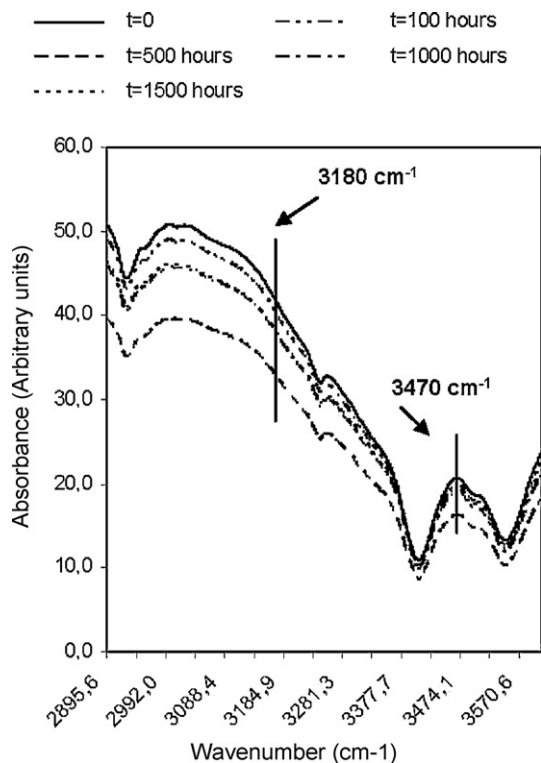


Fig. 6. Averaged FT-IR spectra of P9 complex sample before and after UV exposure.

their composition, in order to be able to interpret the results more easily.

4. Conclusion

Although the samples used in this study were a simple model of a painted work of art, this paper constituted a first effort to systematically study the accelerated UV ageing process of proteins used as binding materials in paints by using PCA on FT-IR data. Two model samples were prepared in order to investigate how the complexity of the sample affects the UV accelerated ageing process of proteinaceous binder material. One of these model samples was formed by samples prepared using only protein, and the other was prepared increasing the complexity of its composition, emulating real paintings. The PCA of the IR data matrix provided valuable information about the ageing process. First of all, no changes were detected in samples containing a single protein. From the analysis of the scores plots using the first three PCs, no pattern distribution of the samples associated with ageing were found. When the samples emulated real samples, changes were detected in a PC since the pattern distribution of the scores could be related to the accelerated UV ageing process. The most affected IR region was between 2900 and 3600 cm^{-1} , region that includes the amide band. Nevertheless no conclusion could be made about the chemical process since, apart

from a general change in the intensity, particular changes on characteristic IR peaks were not detected. However, this paper shows the capability of the PCA on FT-IR data matrix to detect changes produced by an accelerated ageing process. This work represents an initial step in a long-term research project focusing on the interaction experienced by proteinaceous binders with the usual compounds that could be found in an original painting, such as lipids, waxes, sugars and pigments. Efforts must be made to focus on the analysis of data matrices from samples characterised by less variability in their composition, in order to be able to interpret the results more easily.

Acknowledgements

We acknowledge financial support from the *Ministerio de Educación y Cultura, Dirección General de Enseñanza Superior* (Spain) from Projects BHA2003-08671 and HUM2006-09262.

References

- [1] R. Mills, R. White, *The Organic Chemistry of Museum Objects*, 2nd ed., Butterworth-Heinemann, London, 2003.
- [2] A. Karpowicz, *Stud. Conserv.* 26 (1981) 153.
- [3] J. Mallegol, L. Gonon, J. Lemaire, J.-L. Gardenette, *Polym. Degrad. Stab.* 72 (2001) 191.
- [4] J. Mallegol, J.-L. Gardenette, J. Lemaire, *J. Am. Oil Chem. Soc.* 967 (1999) 76.
- [5] S. Boyatzis, E. Ioakimoglou, P. Argitis, *J. Appl. Polym. Sci.* 84 (2002) 936.
- [6] V. Pitthar, P. Finch, *Chromatographia* 3 (2001) 317.
- [7] L. Rampazzi, F. Cariati, G. Tanda, M.P. Colombini, *J. Cult. Heritage* 2 (2002) 237.
- [8] V. Pitthard, M. Griesser, S. Stanek, T. Bayerova, *Macromol. Symp.* 238 (2006) 37.
- [9] H. Ling, N. Maiqian, G. Chiavari, R. Mazzeo, *Microchem. J.* 85 (2007) 347.
- [10] G. Gautier, M.P. Colombini, *Talanta* 73 (2007) 95.
- [11] M. Bacci, M. Fabbri, M. Piccolo, S. Porcinai, *Anal. Chim. Acta* 446 (2001) 15.
- [12] M. Castillejo, M. Martín, M. Ouja, D. Silva, R. Torres, C. Domingo, J.V. García-Ramos, S. Cortés-Sánchez, *Appl. Spectrosc.* 55 (2001) 992.
- [13] F. Capitelli, *J. Anal. Appl. Pyrol.* 71 (2004) 405.
- [14] G. Musumarra, M. Fichera, *Chemometr. Intell. Lab. Syst.* 44 (1998) 363.
- [15] E. Marengo, E. Robotti, M.C. Liparota, M.C. Gennaro, *Anal. Chem.* 75 (2003) 5567.
- [16] E. Marengo, E. Robotti, M.C. Liparota, M.C. Gennaro, *Talanta* 63 (2004) 987.
- [17] E. Marengo, E. Robotti, M.C. Liparota, M. Bobba, M.C. Gennaro, *Talanta* 66 (2005) 1158.
- [18] E. Marengo, M.C. Liparota, E. Robotti, M. Bobba, M.C. Gennaro, *Anal. Bioanal. Chem.* 381 (2005) 884.
- [19] E. Marengo, M.C. Liparota, E. Robotti, M. Bobba, *Vib. Spectrosc.* 40 (2006) 225.
- [20] E. Robotti, M. Bobba, A. Panepinto, E. Marengo, *Anal. Bioanal. Chem.* 388 (2007) 1249.
- [21] E. Marengo, M.C. Liparota, E. Robotti, M. Bobba, *Anal. Chim. Acta* 553 (2005) 111.
- [22] R. Aruga, P. Mirto, A. Casolli, G. Palla, *Fresenius J. Anal. Chem.* 365 (1999) 365.
- [23] A. Casoli, P. Misti, G. Palla, *Fresenius J. Anal. Chem.* 352 (1995) 372.
- [24] R. Checa, E. Manzano, G. Mirón, L.F. Capitán-Vallvey, *Talanta* 75 (2008) 697.
- [25] A. Jurado-López, M.D. Luque de Castro, *Anal. Bioanal. Chem.* 380 (2004) 706.
- [26] C. Cenini, *The Craftsman's Handbook. Il Libro dell'Arte*, Dover Publications, Inc., New York, 1960.
- [27] S.M. Halpine, *Studies in the History of Art 51. Monograph Series II. Conservation Research*, National Gallery of Art, Washington, 1995.
- [28] F. Ronca, *Stud. Conserv.* 39 (1994) 100.
- [29] J. Weerd, A. Loon, J.J. Boon, *Stud. Conserv.* 50 (2005) 3.
- [30] M. Favaro, P.A. Vigato, A. Andreotti, M.P. Colombini, *J. Cult. Heritage* 6 (2005) 295.
- [31] R.J. Meilunas, J.G. Bentsen, A. Steinberg, *Stud. Conserv.* 35 (1990) 33.
- [32] D.L. Massart, B.G.M. Vandeginste, S.N. Deming, Y. Micotte, L. Kaufman, *Chemometrics: A Textbook*, Elsevier, Amsterdam, 1988.
- [33] P.O. Souillac, C.R. Middaugh, J.H. Rytting, *Int. J. Pharm.* 235 (2002) 207.
- [34] M.P. Colombini, F. Modugno, *J. Sep. Sci.* 27 (2004) 147.



Authentication of fattening diet of goat kid according to their fatty acid profile from perirenal fat

Tania Mellado-González^a, Mónica Narváez-Rivas^b, M. Jesús Alcalde^c,
Tomás Cano^d, Manuel León-Camacho^{b,*}

^a Departamento de Bromatología y Nutrición, Universidad Autónoma de Tamaulipas, UAM Reynosa-Aztlán, Mexico

^b Food Characterization and Quality Department, Instituto de la Grasa (C.S.I.C.), Spain

^c Agroforestry Science Department, University of Seville, Spain

^d OCA, Oficina Comarcal Agraria de Úbeda, Spain

ARTICLE INFO

Article history:

Received 13 May 2008

Received in revised form

29 September 2008

Accepted 29 September 2008

Available online 1 November 2008

Keywords:

Goat kid

Fatty acids

Gas Chromatography

Pattern recognition

ABSTRACT

Fatty acids of forty-two samples of perirenal fat of goat kids reared on three different feeding systems: goat milk (B), milk replacer (R) and milk-based starter (F) have been analyzed by Gas Chromatography flame ionization detector. The lipids were extracted by melting of perirenal fat in a microwave oven. The fat was then filtered and dissolved in hexane. This analysis was performed on a column (100 m × 0.25 mm i.d. and 0.25 μm film thickness) coated with a polar stationary phase HP-88 and flame ionization detector was used. Hydrogen (25 psi inlet constant pressure) was used as carrier gas. Programmed temperature was kept at 175 °C and held isothermally for 10 min, and was then raised to 205 °C at a rate of 3 °C/min and held isothermally for 10 min. By using the fatty acids as chemical descriptors, pattern recognition techniques were applied to differentiate between goat milk, milk replacer and milk-based starter fattening diet of goat kid. C18:2 and C18:3 acids were found to be the most differentiating variables.

© 2008 Elsevier B.V. All rights reserved.

1. Introduction

The meat of suckling goat kid comes from animals that have taken only milk in its short life, because they are slaughtered approximately when they are one month old.

In ruminants, the biohydrogenation process that takes place in the rumen due to a microbial synthesis is influenced by the rumen pH [1,2] and diet. In the mammary gland this process occurs by enzymatic reactions that modify the trans fatty acids (TFA) formed during ruminal metabolism. The TFA formed in these processes pass to milk [3].

In addition, recent experiments have demonstrated that the ruminant diet has an important role in the fatty acid profile of milk fat because if the kind of feeding is modified the milk nutritional value can be improved [4–8].

Most of the fat in kid carcass is in perirenal and subcutaneous deposits [9], only about 1% is as intra-muscular fat. The fat of goat kid is less saturated than others the frequent consumption (chicken, beef, pork and lamb) [10]. Besides, the researchers look

for ways to change the fatty acid composition of the meat through the feed [11,12], especially by reducing the concentrations of SFA (saturated fatty acids) and increasing n-3 PUFA (polyunsaturated fatty acids), because the saturated fat is involved in various cardiovascular diseases and cancers [13]. In this sense, it is recommended that PUFA/SFA ratio above 0.4 and n-6/n-3 PUFA ratio less than 4 to take less risks [14].

The kid at this age is still a pre-ruminant because it has not developed the bacterial flora that can saturate the fat of foods consumed and therefore the composition of its fat depending on the composition of the diet.

Some authors have reported that the diet of the mother can affect the milk fat composition and the fatty acid composition of milk replacers for goat kids depends largely on the vegetable fat added. In addition, they relate the sensorial quality difference (odour and flavour) of the freshly cooked goat kid meat with two feeding types of animal (goat milk and milk replacer) [15].

A study realized with suckling lambs reported that the fatty acid profile in deposit fat was influenced by the type of rearing and by dietary fat composition and a higher presence of *trans*-C18:1 (elaidic) in milk source can be precursor of *c9,t11*-C18:2 [16].

There are few studies that establish an analytical method to differentiate between the feeding with goat milk or milk replacer. In

* Corresponding author at: Instituto de la Grasa (C.S.I.C.) Avda. Padre García Tejero, 4, 41012 Seville-Spain. Tel.: +34 954611550; fax: +34 954616790.

E-mail address: mleon@cica.es (M. León-Camacho).

Table 1
Composition of fatty acids function (%) of goat kid perirenal fat samples.

Sample ^a	Zone	C10:0	C12:0	C14:0	C16:0	C16:1	C17:0	C17:1	C18:0	t-C18:1 ω 9	C18:1 ω 9	C18:1 ω 7	C18:2	C20:0	C18:3	C20:1
1B	Torreperojil	0.46	0.79	7.60	27.72	1.85	0.90	0.33	23.10	1.31	32.52	1.33	1.74	0.06	0.07	0.22
2B	Baeza	0.33	0.80	7.94	28.80	1.88	0.72	0.25	20.28	1.89	33.42	1.15	1.97	0.15	0.05	0.36
3B	Baeza	0.31	0.75	7.63	28.50	1.85	0.73	0.24	20.65	1.84	33.80	1.15	2.01	0.12	0.07	0.36
4B	Baeza	0.62	1.10	9.07	31.31	1.79	0.87	0.29	19.39	2.68	28.11	1.19	2.74	0.14	0.08	0.62
5B	Ubeda	0.47	0.82	7.70	27.79	1.77	0.91	0.30	23.87	1.29	31.67	1.35	1.71	0.09	0.08	0.20
6B	Torreperojil	0.48	0.82	7.97	28.33	1.91	0.95	0.30	23.00	1.28	31.59	1.31	1.70	0.06	0.09	0.19
7B	Torreperojil	0.71	1.15	9.66	31.93	1.78	0.80	0.29	18.62	2.51	28.10	1.15	2.61	0.05	0.06	0.58
8B	Torreperojil	0.59	1.05	9.07	31.35	1.73	0.84	0.29	19.51	2.68	28.09	1.21	2.72	0.09	0.09	0.68
9B	Torreperojil	0.32	0.75	7.57	28.34	1.85	0.71	0.24	20.57	1.84	34.06	1.17	2.04	0.08	0.07	0.39
10B	Ubeda	0.64	1.09	8.94	31.10	1.62	0.77	0.29	19.70	2.55	28.55	1.20	2.69	0.16	0.08	0.62
11B	Ubeda	0.46	0.65	7.09	26.12	1.94	1.02	0.31	22.07	1.38	34.84	1.37	2.19	0.09	0.09	0.38
12B	Ubeda	0.63	0.97	8.35	27.96	1.86	0.93	0.33	20.92	1.45	32.48	1.36	2.17	0.17	0.08	0.34
13R	Baeza	0.15	8.86	15.26	26.58	2.10	0.31	0.15	9.42	0.26	28.81	2.64	4.78	0.18	0.46	0.04
14R	Torreperojil	0.17	9.49	15.97	27.27	2.19	0.33	0.15	10.27	0.31	29.58	2.70	4.93	0.20	0.47	0.05
15R	Torreperojil	0.13	8.23	14.54	25.89	2.01	0.29	0.14	8.57	0.21	28.04	2.58	4.63	0.16	0.45	0.03
16R	Baeza	0.16	9.18	15.61	26.92	2.15	0.32	0.15	9.85	0.28	29.20	2.67	4.85	0.19	0.47	0.05
17R	Baeza	0.14	8.54	14.90	26.24	2.06	0.30	0.14	9.00	0.23	28.43	2.61	4.70	0.17	0.46	0.04
18R	Torreperojil	0.16	9.28	15.73	27.04	2.16	0.32	0.15	9.99	0.29	29.33	2.68	4.88	0.19	0.47	0.05
19R	Ubeda	0.14	8.44	14.78	26.12	2.04	0.30	0.14	8.86	0.22	28.30	2.60	4.68	0.17	0.45	0.04
20R	Torreperojil	0.15	9.07	15.49	26.81	2.13	0.32	0.15	9.71	0.28	29.07	2.66	4.83	0.18	0.46	0.05
21R	Ubeda	0.14	8.65	15.02	26.35	2.07	0.30	0.14	9.14	0.24	28.56	2.62	4.73	0.17	0.46	0.04
22R	Ubeda	0.18	9.87	16.40	27.68	2.25	0.34	0.15	10.78	0.34	30.04	2.74	5.02	0.21	0.48	0.06
23B	Ubeda	1.12	1.52	9.93	26.98	1.70	0.79	0.22	20.92	0.99	32.44	1.29	1.72	0.10	0.09	0.20
24B	Ubeda	0.90	1.56	11.48	32.42	1.92	0.83	0.24	17.38	1.47	28.70	0.93	1.67	0.10	0.05	0.33
25B	Ubeda	0.75	1.05	7.78	26.61	2.27	1.13	0.51	20.00	1.97	34.10	1.37	1.94	0.07	0.07	0.39
26B	Baeza	1.16	1.94	12.60	36.46	2.29	0.76	0.24	13.91	1.27	26.17	1.15	1.52	0.15	0.08	0.29
27B	Baeza	0.98	1.35	9.88	30.59	2.01	1.04	0.27	19.43	1.82	28.97	1.22	1.90	0.12	0.08	0.34
28B	Baeza	0.67	1.14	10.67	32.62	1.91	0.94	0.24	19.08	1.30	28.07	1.09	1.76	0.11	0.05	0.36
29B	Baeza	0.44	0.67	7.67	28.97	1.86	0.94	0.29	21.84	1.49	32.59	1.12	1.67	0.09	0.04	0.32
30B	Baeza	0.38	0.66	6.99	26.90	1.84	1.13	0.27	23.07	1.51	32.98	1.25	2.48	0.10	0.05	0.38
31B	Baeza	0.49	0.77	7.88	27.56	2.27	0.87	0.32	18.62	1.30	36.33	1.40	1.68	0.09	0.07	0.34
32B	Baeza	0.93	1.44	10.45	30.98	2.06	1.00	0.24	18.53	1.70	29.01	1.18	1.95	0.14	0.06	0.32
33F	Ubeda	0.15	5.71	12.22	33.74	1.40	0.26	0.04	9.40	1.04	29.12	1.41	5.18	0.10	0.13	0.09
34F	Ubeda	0.11	3.85	10.70	32.78	1.66	0.29	0.04	10.56	1.17	31.44	1.42	5.65	0.10	0.12	0.11
35F	Torreperojil	0.10	4.34	12.02	33.21	1.66	0.25	0.05	9.73	1.07	30.38	1.35	5.56	0.07	0.11	0.09
36F	Baeza	0.11	3.91	10.72	33.06	1.59	0.29	0.05	10.60	1.15	31.08	1.46	5.62	0.12	0.13	0.11
37F	Torreperojil	0.12	4.30	12.04	32.38	1.36	0.22	0.03	11.00	1.07	30.39	1.47	5.32	0.09	0.12	0.08
38F	Torreperojil	0.09	4.61	12.79	34.10	1.46	0.27	0.04	9.87	1.02	28.72	1.34	5.43	0.09	0.10	0.07
39F	Torreperojil	0.10	3.28	10.76	32.82	1.45	0.26	0.04	11.38	0.99	31.38	1.47	5.74	0.09	0.14	0.09
40F	Baeza	0.15	5.67	13.01	32.42	1.59	0.27	0.04	8.50	1.17	30.08	1.39	5.37	0.12	0.13	0.11
41F	Ubeda	0.10	4.13	11.18	31.09	1.38	0.24	0.05	11.90	1.12	31.30	1.58	5.56	0.14	0.13	0.09
42F	Baeza	0.14	4.89	12.35	33.47	1.46	0.24	0.04	9.34	1.04	30.05	1.37	5.28	0.12	0.12	0.08

^a B = fattening with goat milk; R = fattening with milk replacer; F = fattening with milk-based starter.

this sense, it has been proposed the determination of C15:0, C17:0 and C17:1 to establish raising systems of goat kids [17].

In this paper a study of the fatty acid profiles of 42 goat kid perirenal fat samples, belonging to three fattening diet system (Goat milk, milk replacer and milk-based starter), has been carried out. After the extraction of the perirenal fat, the fatty acids have been analyzed by Gas Chromatography (GC) with flame ionization detection (FID), one of the most useful analytical methods to determine fatty acid profile. Differences in the composition of the fatty acid profile have been used to differentiate between the fattening diet systems. Principal Component (PCA) and cluster analyses (CA) were applied for classification purposes to the fatty acid profile to infer differences between groups according to the fattening diet.

2. Materials & methods

2.1. Reagents and solutions

n-Hexane, fraction from petroleum, Multisolvant™ HPLC ACS grade was supplied by Scharlau (Barcelona, Spain). Potassium hydroxide 85% PA-ACS grade and methanol PA-ACS-ISO grade were supplied by Merck (Germany). All other materials were of analytical grade.

2.2. Animal samples

A total of forty-two samples of perirenal fat were analyzed from goat kid murciano-granadina breed. The animals were slaughter when one month old. Twenty two samples corresponding to animals with a fattening diet based exclusively on goat milk, ten corresponding to animals fed with milk replacer, (consisted of 63% powdered skimmed milk, vegetable oils, 10% whey and cereal products) and ten corresponding to animals fed with milk-based starter (consisted of 30% powdered whey, 15.5% milk and soybean proteins, gluten, 13% vegetable oils and 11% animal fat). Table 1 shows the identification code assigned to each sample. The samples were taken from different zones of production from Spanish province of Jaen (Baeza, Torreperogil and Ubeda). All the animals included in the study were reared intensively.

In order to measure the dietary effects on the fatty acid composition of the animals studied, sixteen samples of goat milk, two samples of milk replacer and two samples of milk-based starter were collected and analyzed.

2.3. Analytical procedure

2.3.1. Extraction of the milk and perirenal fat

Milk fat extraction was performed following the method recommended by the International Norm. FIL-IDF 1A [18]. According to this method, 7.5 mL of ammonium hydroxide (25%) and 50 mL of ethanol were added to 50 mL of goat milk in a 500 mL decanting funnel. After shaking, the mixture was extracted twice, first using 250 mL of 1/1 diethyl ether/hexane, then with 150 mL of the same mixture. The supernatant portions were combined, dried over anhydride sodium sulphate and evaporated to dryness in a rotatory evaporator at 35 °C under reduced pressure.

Perirenal fat of goat kid was cut up and melted in a microwave oven [19] for 3 min at 360 W of power; the fat sample was then immediately filtered through Albet filter paper before analysis.

2.3.2. Fatty acids analysis

To prepare Fatty Acids Methyl Esters (FAME), method IUPAC was used [20], so that fatty acids were extracted with *n*-hexane and then methylated with 2N KOH in methanol. Afterwards, samples were analyzed by Gas Chromatography (GC) using A Varian

Table 2

Fatty acids species identified by the GC method. Identification based on the relative retention time to C18:1ω9 (see Fig. 1).

Peak	Fatty acid	T _{RR}
1	C10:0	0.42
2	C12:0	0.48
3	C14:0	0.57
4	C16:0	0.72
5	C16:1	0.79
6	C17:0	0.82
7	C17:1	0.89
8	C18:0	0.93
9	<i>trans</i> -C18:1ω9	0.98
10	C18:1ω9	1.00
11	C18:1ω7	1.01
12	C18:2	1.10
13	C20:0	1.17
14	C18:3	1.21
15	C20:1	1.25

T_{RR}: means relative retention time.

3800 gas chromatograph (Varian Co, Palo Alto, CA, USA) equipped with a Flame Ionization Detector, a fused silica capillary column of 100 m × 0.25 mm, 0.25 μm film thickness of HP 88 stationary phase and a Varian 8400 automatic injector was used. The injector temperature was kept at 360 °C, while the detector temperature was 370 °C. Hydrogen (25 psi inlet constant pressure) was used as carrier gas, while the make-up gas was nitrogen at 30 mL min⁻¹. Split injection mode was used with a ratio of 1:50.

In order to obtain better resolution, fat samples from milk and prerirenal were analyzed under different GC conditions:

To analyze milk fat the initial oven temperature was kept at 80 °C, and was then raised to 205 °C at a rate of 3 °C/min and held isothermally for 8.33 min.

For perirenal fat samples, the initial oven temperature was kept at 175 °C and held isothermally for 10 min, and was then raised to 205 °C at a rate. of 3 °C/min and held isothermally for 10 min.

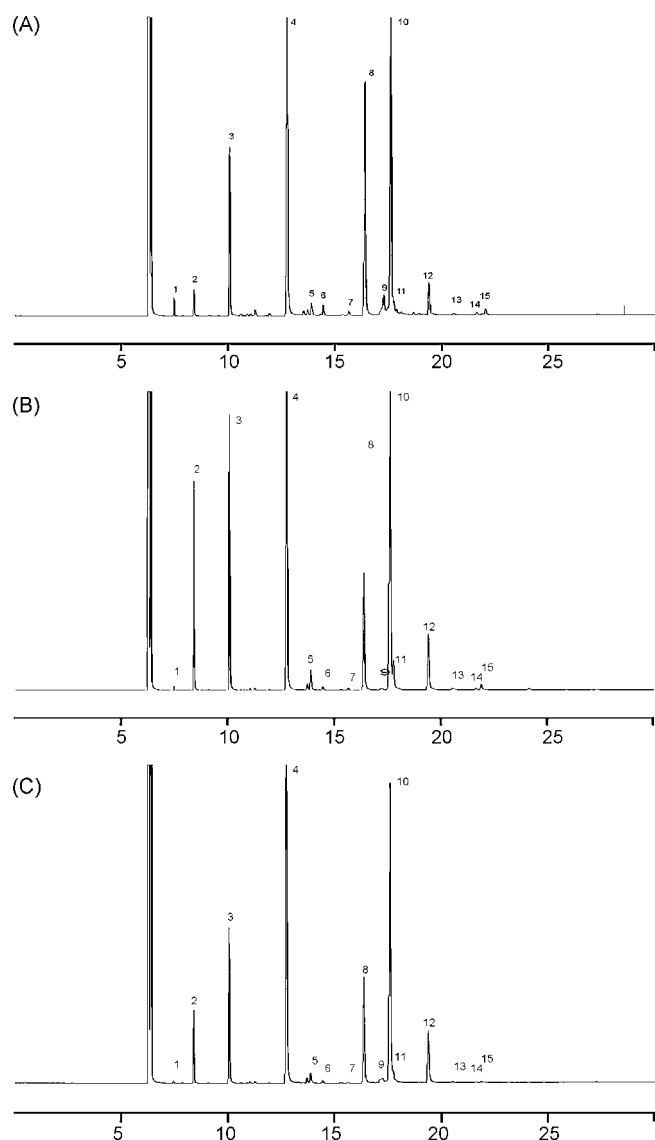
2.4. Data analysis

Fifteen fatty acids have been analyzed in the perirenal fat samples and they were considered the chemical descriptors (Table 2). A data matrix whose rows are the samples and whose columns are the variables was built (Table 1). Each element of this matrix x_{ij} corresponds to the content of the fatty acid j for the sample i . Pattern recognition techniques used in this work included Principal Component Analysis (PCA) and Hierarchical Agglomerative Clustering (HAC). PCA is a vector space transform often used to reduce multidimensional data set to lower dimensions for analysis or to reveal their internal structure. If a multivariate data set is visualized as a set of coordinates in a high dimensional data space, PCA supplies the user with a lower dimensional picture. HAC starts with every single object in a single cluster; then, in each successive iteration, it agglomerates the closest pair of clusters by satisfying some similarity criteria until all the data are in a single cluster. The PCA and HCA analysis was conducted using the statistical package: STATISTICA from Statsoft™ (Tulsa, OK, USA).

3. Results and discussion

3.1. Fatty acid profile of perirenal fat

Fifteen fatty acids molecular species were identified according to their relative retention times to C18:1ω9 acid (Table 2). Fig. 1 shows the corresponding individual chromatograms of goat milk (Fig. 1A), milk replacer (Fig. 1B) and milk-based starter (Fig. 1C)

**Table 3**

Composition of fatty acids function (%) of fattening samples.

Fatty acid	Goat milk		Milk replacer		Milk-based starter	
	Means	σ	Means	σ	Means	σ
C4:0	1.55	0.31	0.01	0.00	0.02	0.00
C6:0	2.06	0.29	0.33	0.00	0.29	0.00
C8:0	2.74	0.32	4.23	0.06	3.36	0.04
C10:0	9.54	1.15	3.40	0.02	2.68	0.01
C10:1	0.21	0.08	0.00	0.00	0.11	0.00
C11:0	0.05	0.03	0.00	0.00	0.05	0.00
C12:0	4.16	0.79	27.50	0.02	22.69	0.01
C13:0	0.05	0.02	0.01	0.01	0.01	0.00
C14:0	9.62	1.20	10.62	0.02	9.44	0.02
C14:1	0.12	0.04	0.00	0.00	0.00	0.00
iso C15:0	0.35	0.12	0.01	0.01	0.03	0.01
anteiso C15:0	0.56	0.17	0.02	0.00	0.04	0.00
C15:1	0.05	0.01	0.00	0.00	0.00	0.00
iso C16:0	0.14	0.04	0.02	0.03	0.03	0.01
C16:0	26.41	4.00	15.71	0.06	26.35	0.07
C16:1	0.59	0.17	0.94	0.02	0.11	0.00
iso C17:0	0.28	0.05	0.03	0.05	0.00	0.00
anteiso C17:0	0.16	0.09	0.00	0.00	0.00	0.00
C17:0	0.47	0.11	0.13	0.01	0.07	0.01
C17:1	0.20	0.05	0.11	0.01	0.01	0.00
C18:0	13.03	3.19	6.23	0.03	4.59	0.02
t-C18:1ω9	1.17	0.36	0.00	0.00	0.54	0.01
C18:1ω9	22.74	3.38	22.63	0.04	22.82	0.04
C18:1ω7	0.64	0.09	1.96	0.02	0.80	0.01
C18:2 c,t	0.05	0.01	0.00	0.00	0.09	0.00
C18:2 t,c	0.08	0.01	0.00	0.00	0.10	0.01
C18:2 c,c	1.94	0.33	5.08	0.00	5.37	0.00
C20:0	0.24	0.03	0.15	0.02	0.22	0.03
C18:3	0.34	0.11	0.34	0.00	0.09	0.00
C20:1	0.46	0.15	0.53	0.02	0.12	0.01

milk-based starter used in goat kid diet. The goat milk presents a higher content of short chain fatty acids (less than 12 carbon atoms), which are not found in samples of perirenal fat analyzed, except the C10:0 acid. A lower C12:0 acid content is found in this milk. The C14:0 acid content is similar to those of the milk replacer and milk-based starter and the C16:0 acid content is similar to that found in the milk-based starter and higher than that in milk replacer. The goat milk shows a higher content of C18:0 acid, a similar content of C18:1ω9 and a lower content of C18:2 than the others types of feeding. This is in accordance with the fatty acid profiles observed for the perirenal fat analyzed.

3.2. PCA-based display methods and cluster analysis

PCA was applied to the data matrix. PC1 and PC2 explain up to 79.90% of the total variance, being 59.30% explained by PC1 and 20.60% by PC2. To visualize the trends of the data (Fig. 2), the loadings for variables were represented in the space of the two principal components (PCs) obtained from PCA [23]. The variables C12:0, C14:0, C18:0, C18:1ω7, C18:2 and C18:3 appear with the highest absolute values, so they are the descriptors with a major contribution to PC1 and the most differentiating variables. C10:0, C17:0, C17:1, *trans*-C18:1ω9, C20:0 and C20:1 appear with minor absolute values and consequently they contribute to a minor extent to PC1. C16:0, C16:1 and C18:1ω9 have the lowest differentiating character. The scores of the samples appear in Fig. 3. As can be observed, all the goat milk samples appear at the positive side of PC1 while milk replacer and milk-based starter samples appear at the negative side. Then, all the milk-based starter samples appear at the positive side of PC2 while milk replacer appears at the negative side. Therefore, a complete separation of the fattening diet was achieved by PCA. Among the most promising features, the two most characteristics compounds are: C18:2 and C18:3. These results are in good agreement with the fact that samples situated at the right side of the plot

Fig. 1. Gas-chromatogram of the fatty acid profile of goat kid perirenal fat samples: (A) goat milk; milk replacer (B) and milk-based starter (C); peaks identification: see Table 2.

fattening diet samples of perirenal fat. In this figure, the peaks of the fatty acids eluted by the atom carbon number and unsaturations number respectively (Table 2), except the C18:3 acid, which eluted after C20:0 acid. The first group of peaks (C10:0–C16:1) of interest elutes at a retention time between 7.4 and 14.0 min, the peaks C17:0 and C17:1 elute between 14.4 and 15.7 min, the group of fatty acids with carbon number = 18 (stearic, elaidic, oleic, cis-vaccenic and linoleic) elutes between 16.0 and 19.5 min. C18:1ω9 acid is the major fatty acid of the goat kid perirenal fat [17,21] and elutes at 17.6 min. The peaks corresponding to C20:0, C18:3 and C20:1 appear after 20.0 min. The peaks of the chromatogram that show a more remarkable difference between the three fattening diet types are C12:0, C18:1ω7, C18:2 and C18:3. Some authors [15,17,22] showed that no noticeable levels of C4–C8 were found in kid fat, because these short-chain fatty acids are metabolised. For the samples from the goat milk, the higher peaks are C16:0, C18:0 and C18:1ω9. On the other hand, for the milk replacer ones C14:0, C16:0 and C18:1ω9 give the higher peaks and for the milk-based starter ones C16:0 and C18:1ω9 give the higher peaks. Table 3 shows the fatty acid composition of goat milk, milk replacer and

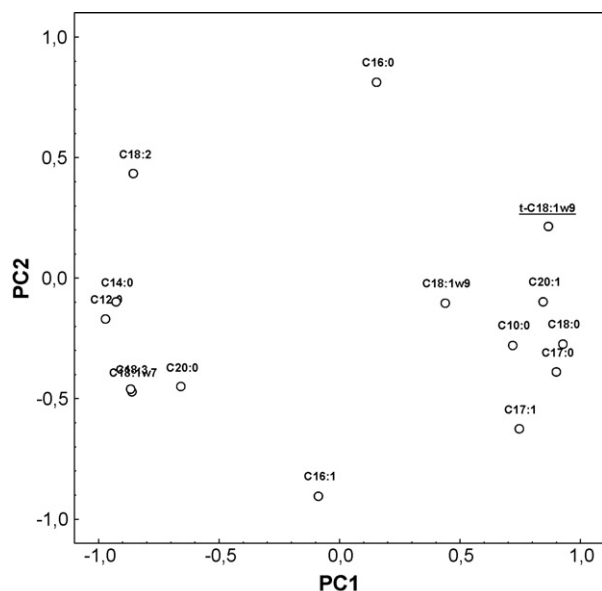


Fig. 2. Loadings plot for the first PCs.

(goat milk) exhibit low contents of C18:2, whereas samples situated at the left side (milk replacer and milk-based starter) are characterized by higher contents for this variable. Besides, goat milk exhibits low contents of C18:3. On the contrary, the milk-based starter samples present slightly higher values of the descriptor C18:3 (at the left side of the plot) and milk replacer samples present high values for this variable. C18:2 appears in animals feeding with cereal, vegetable oils and seed-based diet while C18:3 is higher in animals that have consumed grass.

Once the variables that most contributed to discrimination were identified, a hierarchical agglomerative cluster analysis of samples was performed using the variables C18:2 and C18:3, to check their discriminating ability. The City-block (Manhattan) distance was used as a similarity measurement and the Ward's method as an amalgamation rule [24]. In Fig. 4, the resulting dendrogram can be observed. Three well-separated clusters appear, one of them containing all goat milk cases (B), another containing all milk-based starter cases (F) and the other containing the milk replacer samples (R). No conflicts appeared. From the above results it may be deduced that the content in C18:2 and C18:3 fatty acids plays an

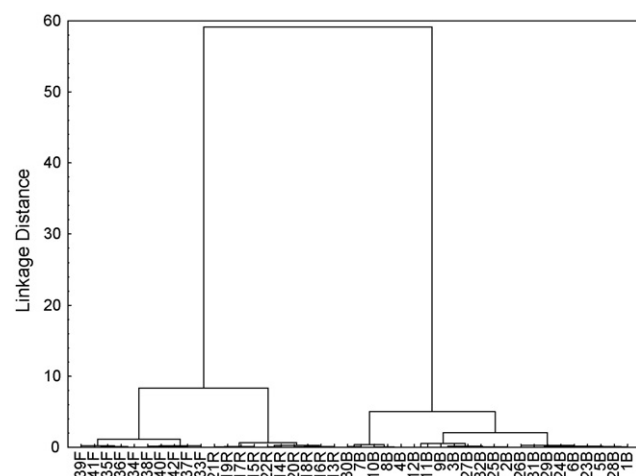


Fig. 4. Dendrogram of the goat kid perirenal fat samples by using C18:2 and C18:3 variables.

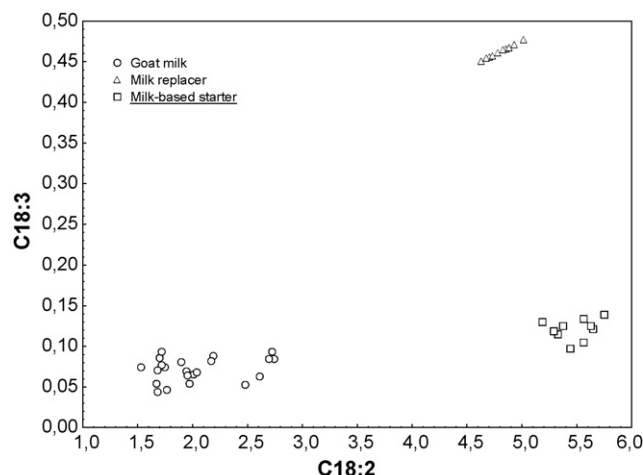


Fig. 5. Variable-variable plot C18:2–C18:3.

essential role in the classification of the goat kid perirenal fat samples into the goat milk/milk-based starter/milk replacer feeding. Furthermore, based on the results deduced from PCA and HAC, a simple classification method for the studied samples emerged (was disclosed).

3.3. Classification of samples

A very simple way for classification of samples is the one based on the variable-variable plot. A C18:2–C18:3 plot for the studied samples is depicted in Fig. 5. As can be seen, goat milk, milk-based starter and milk replacer classes are perfectly separated. Accordingly, based on the C18:2 and C18:3 content, any new sample may be easily classified.

Acknowledgements

The authors are grateful to the farmers and Torreperojil Slaughterhouse for the collaboration and given help.

References

- [1] W. Kaufmann, *Livest. Prod. Sci.* 3 (1976) 103.
- [2] A.A. AbuGhazaleh, B.N. Jacobson, *Anim. Feed Sci. Technol.* 136 (2007) 11.
- [3] M. Ledoux, P. Juaneda, J.-L. Sébédio, *Eur. J. Lipid Sci. Technol.* 109 (2007) 891.

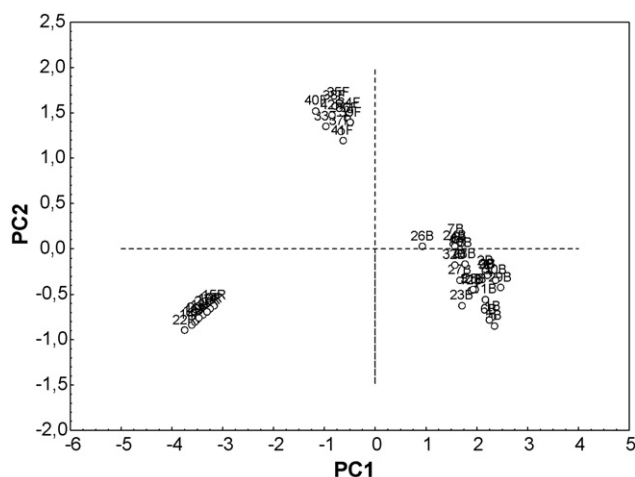


Fig. 3. Scores plot for the first PCs.

- [4] L. Biondi, M.A. Valvo, M. Di Gloria, E. Scinardo Tenghi, V. Galofaro a, A. Priolo, *Small Rumin. Res.* 75 (2008) 17.
- [5] A. Cabiddu, M. Addis, G. Pinna, M. Decandia, M. Sitzia, G. Piredda, A. Pirisi, G. Molle, *Anim. Feed Sci. Technol.* 131 (2006) 292.
- [6] J.J. Lóor, M. Doreau, J.M. Chardigny, A. Ollier, J.L. Sebedio, Y. Chilliard, *Anim. Feed Sci. Technol.* 119 (2005) 227.
- [7] M. Matsushita, N.M. Tazinafo, R.G. Padre, C.C. Oliveira, N.E. Souza, J.V. Visentainer, F.A.F. Macedo, N.P. Ribas, *Small Rumin. Res.* 72 (2007) 127.
- [8] P.V.D. Andrade, Ph. Schmidely, *Livest. Sci.* 104 (2006) 77.
- [9] A. Marichal, N. Castro, J. Capote, M.J. Zamorano, A. Arguello, *Livest. Prod. Sci.* 83 (2003) 247.
- [10] USDA, Official United States Standards for Grades of Carcass Beef, USDA, Agricultural Marketing Service, Washington, DC, USA, 1989.
- [11] M.J. Potchoiba, C.D. Lu, F. Pinkerton, T. Sahlu, *Small Rumin. Res.* 3 (1990) 583.
- [12] M. Enser, K.G. Hallett, B. Hewett, G.A.J. Fursey, J.D. Wood, G. Harrington, *Meat Sci.* 49 (1998) 329.
- [13] A. Trichopoulou, P. Lagiou, *Am. J. Clin. Nutr.* 66 (1997) 9615.
- [14] L. Van Horn, M. McCain, P.M. Kris-Etherton, F. Burke, J.A. Carson, C.M. Champagne, W. Karmally, G. Sikand, *J. Am. Diet Assoc.* 108 (2008) 287.
- [15] S. Bañón, R. Vila, A. Price, E. Ferrandini, M.D. Garrido, *Meat Sci.* 72 (2006) 216.
- [16] M.T. Osorio, J.M. Zumalacárregui, A. Figueira, J. Mateo, *Small Rumin. Res.* 73 (2007) 127.
- [17] A. Rojas, C. López-Bote, A. Rota, L. Martín, P.L. Rodríguez, J.J. Tovar, *Small Rumin. Res.* 14 (1994) 61.
- [18] International Norm, FIL-IDF 1A, 1969.
- [19] E. De Pedro, M. Casillas, C.M. Miranda, *Meat Sci.* 45 (1997) 45.
- [20] IUPAC 2.301., Standard Methods for the Analysis of Oils, Fats and Derivatives, 7th ed., Blackwell Scientific Publications, 1987.
- [21] K.H. Yeon, G. Van Trierum, K.W. Lee, A.C. Beinen, *Small Rumin. Res.* 8 (2003) 83.
- [22] M. Todaro, A. Corrao, C.M.A. Barone, R. Schinelli, M. Occidente, P. Giaccone, *Small Rumin. Res.* 44 (2002) 75.
- [23] M. Meloun, J. Militky, M. Forina, *Chemometrics for Analytical Chemistry*, Ellis Horwood, New York, 1992, p. 204.
- [24] J.H. Ward, *J. Am. Statist. Assoc.* 58 (1963) 236.



Short communication

A sequential extraction procedure for an insight into selenium speciation in garlic

Sandra Mounicou^{a,*}, Mihaly Dernovics^b, Katarzyna Bierla^a, Joanna Szpunar^a^a Laboratoire de Chimie Analytique Bio-inorganique et Environnement, CNRS UMR 5254, Hélioparc, 2, av. Pr. Angot, F-64053 Pau, France^b Department of Applied Chemistry Corvinus University of Budapest 1118 Budapest, Villanyi ut 29-33 Hungary

ARTICLE INFO

Article history:

Received 9 April 2008

Received in revised form 14 October 2008

Accepted 17 October 2008

Available online 31 October 2008

Keywords:

Selenium

Garlic

Sequential extraction

SEC–ICP MS

AEC–ICP MS

Ion-pairing RPC–ICP MS

ABSTRACT

A sequential extraction procedure was developed for the fractionation of different classes of selenium species present in garlic. The consecutive steps included leaching with water, extraction of cell-wall bound species after lysis with a mixture of cellulase, chitinase and β -glucanase completed by a proteolytic attack, extraction with HCl to liberate the residual organic bound species and finally, extractions with sulfite solution and CS_2 to complete the mass balance by the recovery of Se^0 and Se^{2-} , respectively. Selenium speciation in the aqueous fractions was probed by anion-exchange and ion-pairing reversed-phase HPLC–ICP MS after purification by preparative size-exclusion LC. It was found to be strongly affected by the sample redox conditions. The peak identity was matched with a mixture of 9 compounds expected to be present in allium plants; electrospray QTOF MS turned out to be unsuccessful. Selenite, selenate and selenomethionine were the dominating species present.

© 2008 Elsevier B.V. All rights reserved.

1. Introduction

Speciation of selenium in garlic and other allium plants has been a topic of intense research since the introduction of gas chromatography with element specific detection to probe volatile selenium species and some non-volatile compounds after their derivatization [1–3]. The subsequent development of HPLC–ICP MS methods opened the way to the investigation of non-volatile selenium metabolites which could not be derivatized [4–9]. Reversed-phase was the principal chromatographic separation mechanism used [4]. The separation efficiency could be considerably improved by using ion-pairing either with trifluoroacetic acid (TFA) [5] or with heptafluorobutyric acid (HFBA) [8,9] thus diminishing the risk of peak misidentification by retention time matching. Most of studies resulted in the detection of Se-methylselenocysteine [5–9]. Selenomethionine and Se-*n*-propylselenocysteine were also reported but a number of peaks usually remained unidentified [5].

An alternative technique for the identification of Se species is electrospray MS/MS. It was first proposed for the standardless identification of Se-species in Se-rich yeast [10]. In garlic, it allowed the identification of γ -glutamyl-Se-methylselenocysteine by McSheehy et al. [11] (later confirmed by others [12,13]) and

of γ -glutamyl-Se-methylselenomethionine [14]. However, a number of species detected in HPLC–ICP MS chromatograms could not be identified by electrospray MS/MS because of the insufficient ionisation in the experimental (sample preparation and chromatographic) conditions used.

Data on selenium speciation in garlic are limited to the water-soluble fraction of which the selenium concentration strongly varies (if at all reported!). The objectives of this work were: (i) to propose a fractionation procedure allowing an insight into the chemical forms of the entire selenium present in the sample, and (ii) to propose the most comprehensive to date probe of Se-containing standards to be used as a retention time matching spike in order to get an insight into the selenium speciation in the aqueous phase when HPLC–ESI QTOF MS fails.

2. Experimental

2.1. Instrumentation

An AktaTM prime automated LC system combined with a fraction collector (Pharmacia, Uppsala, Sweden) was used for the fractionation with preparative size-exclusion chromatography. Selenium was off-line detected in the collected fractions by means of an ELAN 6000 ICP MS (PE SCIEX, Concord, Canada) on the ⁸²Se isotope. Analytical scale chromatographic separations were performed using a Model 1100 HPLC pump (Agilent, Santa Clara, CA, USA) as the deliv-

* Corresponding author. Tel.: +33 559407764; fax: +33 559407781.

E-mail address: sandra.mounicou@univ-pau.fr (S. Mounicou).

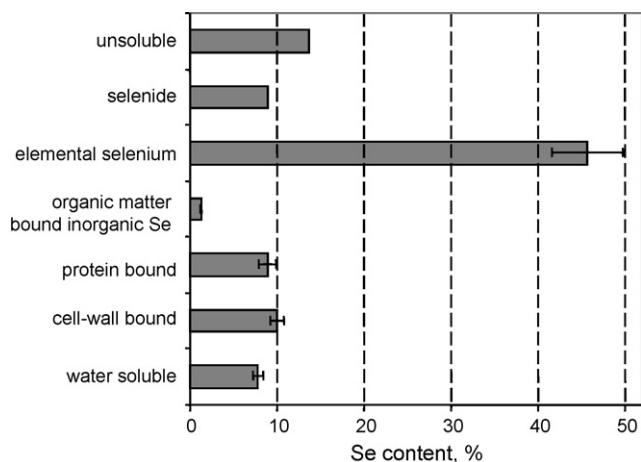


Fig. 1. Recovery of selenium during the sequential extraction procedure.

ery system. Injections were performed using a Rheodyne valve with a 100- or 200- μ L sample loop. The exit of the column was directly connected to the Meinhard nebulizer (Glass Expansion, Romainmotier, Switzerland) of the ICP MS equipped with a collision cell (Agilent 7500c, Agilent, Tokyo, Japan) by means of polyetheretherketone (PEEK) tubing. Hydrogen gas was used to pressurize the collision cell. Fractions from the preparative chromatography were lyophilized at a temperature of -50°C using a Model LP3 lyophilizer (Jouan, France). DigiPrep (SCP Science, Courtaboeuf, France) was used for sample digestion.

2.2. Reagents, solutions and materials

Analytical reagent grade chemicals and enzymes purchased from Sigma–Aldrich (Saint-Quentin Fallavier, France) and water (18.2 M Ω cm) obtained from a Milli-Q system (Millipore, Bedford, MA) were used throughout unless stated otherwise. The chromatographic mobile phases were degassed by purging with helium. The standard Se compounds were purchased from Aldrich or custom synthesized. Metallothionein-I (MT-1), metallothionein-II (MT-2), cyanocobalamin, selenomethionine (SeMet) and selenate (Se VI) were used as calibration standards for size exclusion chromatography. A commercial sample of freeze-dried garlic with a total Se concentration of 650 $\mu\text{g/g}$ (determined as described below) was analysed.

2.3. Procedures

2.3.1. Total selenium determination

A 200-mg garlic sample was digested with 1.25 mL of a mixture of HNO_3 and H_2O_2 (4:1, v/v) in a 50-mL polypropylene tube (Digi-Tube, SPC Science) using the following temperature program: 0.5 h up to 65°C and 4 h at 65°C . 10 mL of water was added to decrease the HNO_3 concentration in the solution fed to the ICP MS. Total selenium was measured by ICP MS using the method of standard additions at two levels. The ^{76}Se and ^{78}Se isotopes were used for quantification; Rh and Ga were used as internal standards.

2.3.2. Sequential extraction

Sequential extraction protocol included the following steps:

- (1) **Water extraction:** 0.2 g of a garlic sample was sonicated for 2 h with 10 mL of H_2O . The supernatant was recovered by centrifugation (30 min at $1780 \times g$). The protocol was repeated 3 times; the 3 supernatants were pooled and lyophilized.

The lyophilisate was dissolved in 3 mL water and centrifuged ($5400 \times g$, 10 min). The supernatant was chromatographed and the residue leached further as described below.

- (2) **Enzymatic cell wall lysis:** a mixture of lysing enzymes from *Trichoderma harzianum* (cellulase, protease, chitinase, β -glucanase; 20 mg) was added to the residue together with 5 mL 50 mM $\text{CH}_3\text{COONH}_4$ pH 6. The sample was incubated for 12 h at 37°C and then centrifuged to separate the supernatant (cell-wall bound species) and the residue.
- (3) **Proteolysis:** an aliquot of 5 mL 50 mM Tris–HCl buffer (pH 7.5) containing 18 mg of protease (type XIV) was added to the residue after the lysis. The sample was incubated during 24 h at 37°C . The supernatant was separated by centrifugation.
- (4) **HCl extraction:** diluted HCl (0.1 M) was added to the residue and the sample was incubated for 1 h at 37°C to liberate inorganic Se bound to organic matter. The supernatant was separated by centrifugation.

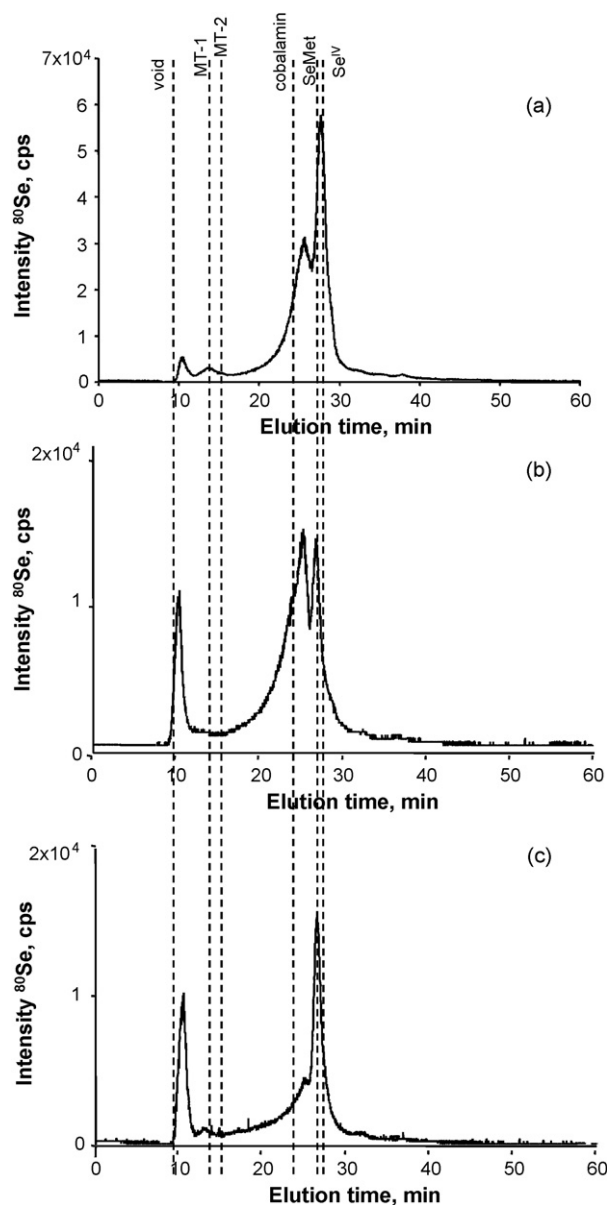


Fig. 2. SEC–ICP MS chromatograms of sequential extracts of garlic after (a) aqueous extraction, (b) extraction with the lysing enzymes, and (c) proteolysis.

Table 1
Chromatographic conditions.

Separation mechanism	Analytical SEC	Preparative SEC	Anion exchange	Reversed phase
Column	Superdex peptide (10 mm × 300 mm × 13 μm)	Superdex 30 HiLoad 26/60	Hamilton PRPX-100 (4.1 mm × 250 mm × 10 μm)	C8 Alltima (4.6 mm × 250 mm × 5 μm)
Eluent	100 mM ammonium acetate pH 7.5	10 mM ammonium acetate pH 9.5	Ammonium acetate, pH 5.1. A: 25 mM; B: 250 mM	0.05% HFBA. A: in H ₂ O; B: in MeOH
Elution program	Isocratic	Isocratic	0–5 min: 0% B; 5–15 min: 0–100% B; 25–26 min: 100–0% B; 26–35 min: 0%B	0–5 min: 5% B; 5–30 min: 5–40% B; 30–35 min: 40% B; 35–37 min: 40–5% B; 37–40 min 5% B
Injection volume	100 μL	3 mL	100 μL	100 μL
Flow rate (mL/min)	0.7	2.2	1.5	0.9

- (5) *Sulphite extraction*: 5 mL of 1 M Na₂SO₃ (pH 7) was added to the residue prior to an incubation for 24 h at 37 °C. The supernatant and the residue were separated by centrifugation.
- (6) *CS₂ extraction*: 1 mL H₂O was added to the residue followed by the addition of 4 mL CS₂. The mixture was incubated for 4 h and it was hand-shaken regularly. After centrifugation, the residual plant particles became agglomerated in the upper water phase, while the CS₂-containing layer was localised on the lower part of the centrifuge tube due to its higher density. Therefore this layer was recovered by piercing the bottom of the tube.

The absence of selenium in the residue was verified by ICP MS following the HNO₃–H₂O₂ digestion.

The extraction was carried out in triplicate until the sulphite extraction, followed by a single analysis of the CS₂ residue.

2.3.3. Chromatographic conditions

The optimized chromatographic conditions were given in Table 1. ICP-MS detection of Se was carried out using the ⁸⁰Se isotope.

3. Results

3.1. Sequential extraction of selenium species

The method development was based on a procedure proposed elsewhere for yeast [15,16]. However, as driselase (the enzymatic cocktail containing a mixture of cellulases and hemicellulases dedicated to dissolve the yeast cell wall) was found less efficient for garlic, a preparation of lysing enzymes containing in addition chitinase, β-glucanase and protease was used instead. In contrast to yeast, a considerable fraction of selenium turned out to remain in the residue after proteolysis. It is also to note that after the lysing steps of cell wall and proteins, red particles became visible in the sample. Therefore two additional steps dedicated to fractionate the remaining selenium were introduced: one based on the extraction with sulphite solution was supposed to remove elemental selenium (Se⁰) [17,18] and the other, based on extraction with CS₂, was expected to be specific to selenides [19].

The distribution of selenium among different fractions is shown in Fig. 1. The procedure accounted for ca. 90% of the selenium present; the remaining ca. 10% was left in the insoluble residue after the last extraction step. The dominating form was elemental selenium Se⁰ accounting for almost half of the selenium present. The presence of elemental selenium in allium plants has been already reported by direct analytical techniques [20]. Together with ca. 10% of Se present as selenides, it shows a strongly inorganic character of selenium in the analysed sample. The remaining selenium was quasi-uniformly distributed between water soluble, cell-wall bound, and protein-bound fractions, each of them corresponding to ca. 10% of the total selenium content. The fraction of selenium weakly and non-specifically bound to organic matter was negligi-

ble and accounted for ca. 1% of the total selenium. The efficiency of the water extraction was found to be similar regardless of the temperature of the extracting solution which indicates negligible contribution of volatile selenium species to the total selenium content.

3.2. Selenium distribution as a function of molecular weight

An insight into speciation of selenium in the aqueous extracts was attempted by analytical scale size-exclusion LC-ICP MS. The chromatograms obtained for the water, cell wall lysis and proteolytic extracts are shown in Fig. 2. All of them show a similar morphology with a signal in the exclusion volume of the column

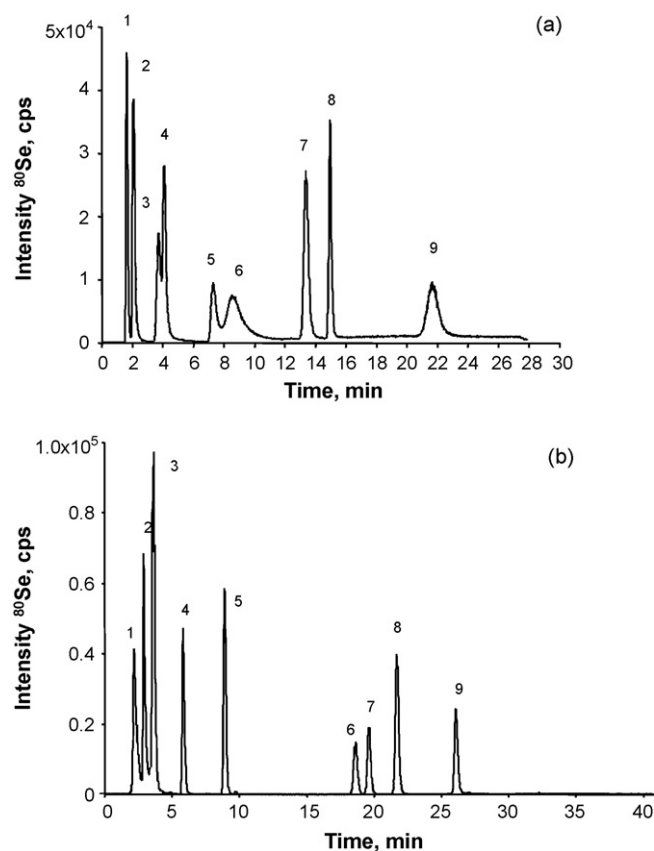


Fig. 3. HPLC-ICP MS analysis of a mixture of 9 selenium species using (a) anion-exchange (1: selenocystine; 2: Se-methylselenocystine; 3: selenomethionine; 4: methylseleninic acid; 5: Se(IV); 6: Se-allylselenocystine; 7: γ-glutamyl methyl selenocystine; 8: Se(VI); 9: γ-glutamyl selenomethionine), (b) ion-pairing reversed-phase separation (1: SeVI; 2: SeIV; 3: methylseleninic acid; 4: selenocystine; 5: Se-methylselenocystine; 6: selenomethionine; 7: γ-glutamyl methyl selenocystine; 8: Se-allyl-selenocystine; 9: γ-glutamyl selenomethionine) mechanisms.

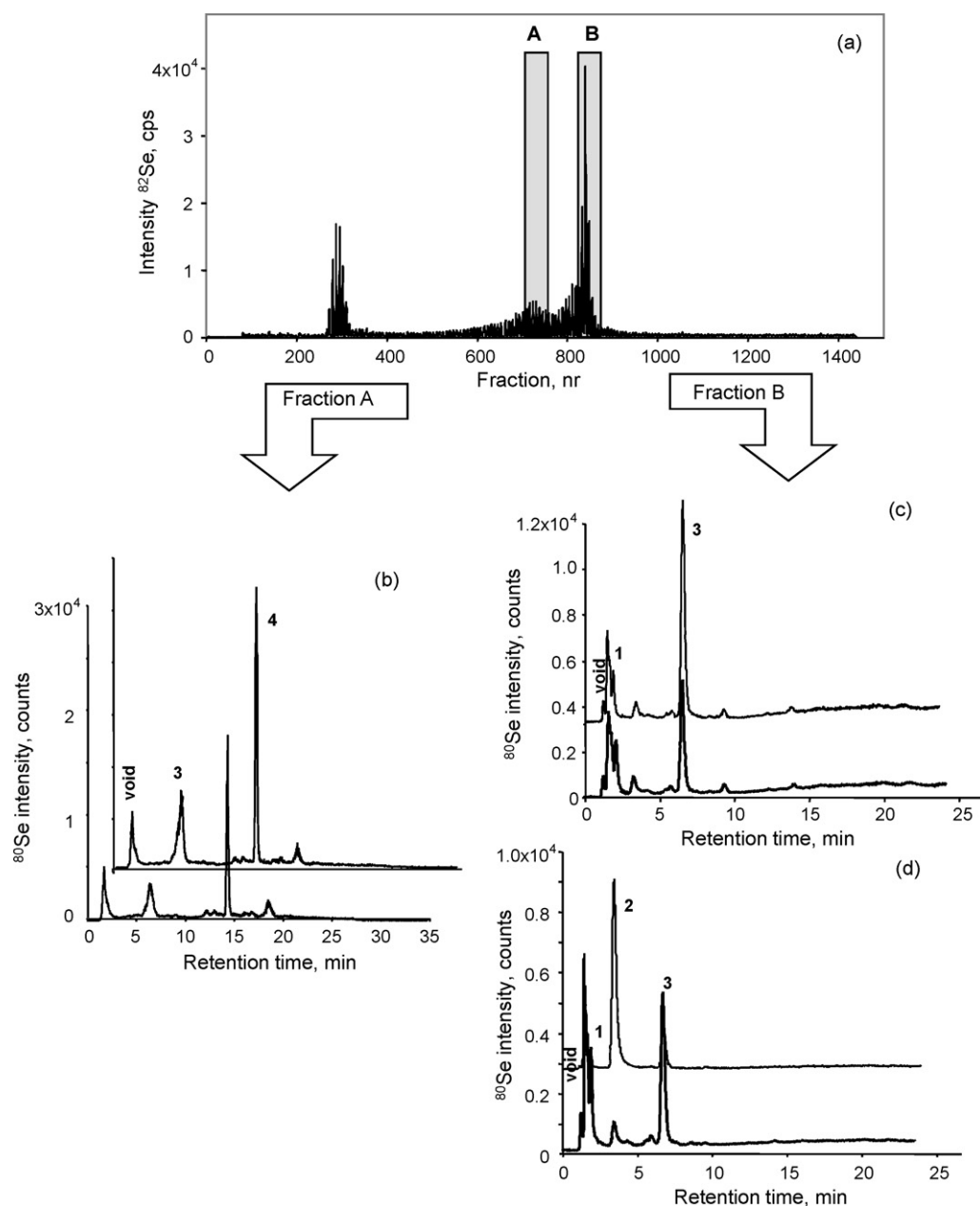


Fig. 4. Identification of selenium species in the low-molecular weight fraction isolated by size-exclusion chromatography. (a) preparative scale Size-exclusion chromatogram; (b–d) anion-exchange chromatograms of the fractions highlighted in (a). **Bold line:** chromatogram of the fraction. **Thin line:** chromatogram of the fraction spiked with (b) Se(VI); (c) Se(IV); (d) selenomethionine. Signal identification: 1, Se-methylselenocysteine; 2, selenomethionine; 3, Se(IV); 4, Se(VI).

(typical to Se non-specifically bound to cellular debris). Most of selenium elutes with the low-molecular weight fraction which corresponds to 90% of Se in the water extract; 75% in the cell wall lysis extract and 65% in the proteolytic extract.

In order to get an insight into the Se-speciation in the low-molecular fraction, the size-exclusion LC was upscaled to the semi-preparative scale. The low-molecular weight selenium rich fraction ($7.8 \pm 0.6\%$) of the water extract was collected and analysed, in the first attempt by direct nanoHPLC–ESI QTOF MS/MS. The analysis of the data set did not allow the detection of any selenium isotopic pattern confirming the detection of a selenium species. An approach by HPLC–ICP MS, expected to be more sensitive and robust was therefore attempted.

3.3. HPLC–ICP MS analysis of selenium species

The identification of Se-species by HPLC–ICP MS has usually been based on the matching of retention times with those of standard compounds. This implies (i) that the efficiency of the separation mechanism used is sufficient to produce peaks corresponding to a single compound and (ii) that authentic standards of the compounds to be found and quantified are available. In this work, a mixture of 9 Se-species reported elsewhere to be present in allium plants as such or as sulphur analogues was prepared and used to optimize the separation by anion-exchange HPLC and by ion-pairing reversed-phase HPLC. The chromatograms obtained are shown in Fig. 3a and b, respectively. The use of anion-exchange HPLC is particularly recommended for the positive identification

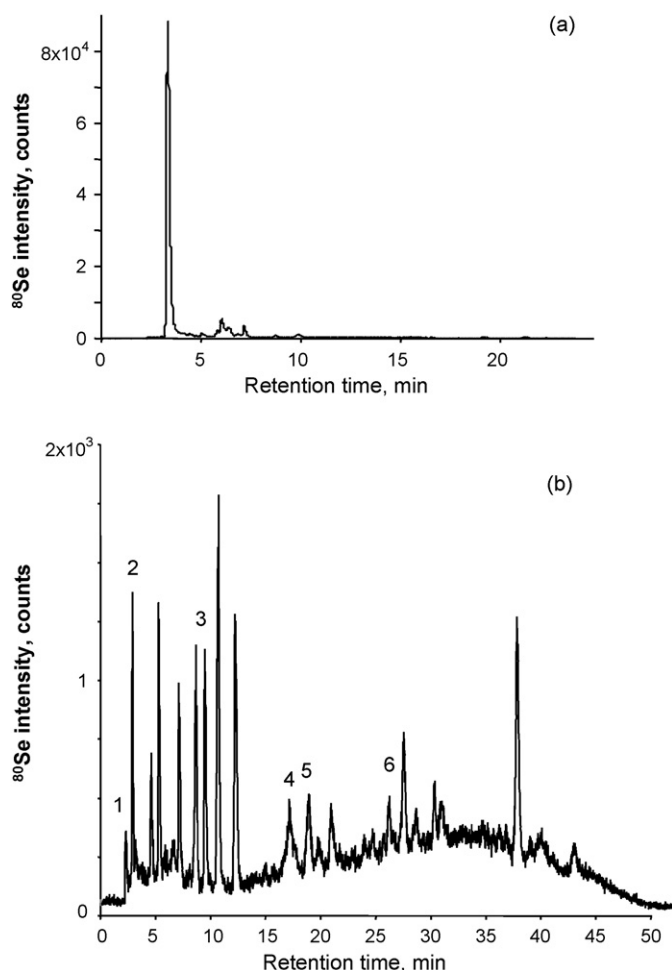


Fig. 5. Analysis of major Se fraction in size-exclusion chromatography by ion-pairing RP HPLC-ICP MS. (a) Fraction after lyophilisation and dissolution in water; (b) fraction after lyophilisation and dissolution in water with addition of DDT. The numbers mark the compounds identified by retention time matching: 1, Se(VI); 2, Se(IV); 3, Se-methylselenocysteine; 4, selenomethionine; 5, γ -glutamyl-Se-methylselenocysteine; 6, γ -glutamyl-Se-methylselenomethionine.

of inorganic selenium species (selenate and selenite) which elute close to the void in reversed-phase chromatography and suffer the most from the decreased retention in the presence of a matrix or from the co-elution with unretained species.

3.4. Identification of selenium species in the low-molecular weight Se fraction of garlic

The use of a 10-fold higher volume column on the semi-preparative scale allowed a clear distinction of a minor fraction preceding the major one within the LMW fraction isolated by size-exclusion chromatography (Fig. 4a). The speciation of selenium in these fractions was investigated by anion-exchange HPLC and ion-pairing RP HPLC in the conditions optimized in Fig. 3. For the purpose of identification the extracts were spiked by each of the 9 standards and chromatographed. The anion-exchange chromatograms showing retention time matches are shown in Fig. 4b–d. They show that the dominant species are inorganic selenium. Se(IV) accounts for 2/3 of selenium in the major fraction and inorganic selenium [Se(IV) and Se(VI)] accounts for ca. 75% of the total selenium in the minor fraction. The presence of Se(IV) in both fractions suggests that selenite was non-specifically attached to other molecules, these bonds being destroyed dur-

ing freeze-drying of the collected fraction. Selenate is the major compound in the minor fraction. Out of other species selenomethionine could be identified in the major fraction (Fig. 4d). A positive match was also obtained for Se-methylselenocysteine but the peak was not chromatographically pure. The recovery in RP HPLC was $94 \pm 4\%$ and $88 \pm 6\%$ for fractions 1 and 2, respectively. In anion-exchange HPLC $41 \pm 12\%$ and $89 \pm 8.4\%$ could be recovered, respectively.

The chromatogram obtained by RP HPLC-ICP MS shows a single peak in the void (Fig. 5a). This can be partly due to the matrix effect still decreasing the retention of Se(IV) and Se(VI). It was observed, however, that the addition of a reducing reagent (dithiothreitol) resulted in the disappearance of the large peak in the void and in the formation of a number of peaks covering a large range of retention times (Fig. 5b). A similar phenomenon was observed for selenomethionine in yeast extracts [21,22]. Some of these peaks co-eluted with Se(IV), Se-methylselenocysteine and, to a lesser extent Se(VI), selenomethionine, γ -glutamyl-Se-methylselenocysteine, and γ -glutamyl-Se-methylselenomethionine (cf. Fig. 5b). The dominance of inorganic selenium was confirmed in the extract after cell wall lysis; on the other hand the proteolytic extract contained predominantly selenomethionine (chromatograms not shown).

The water-soluble selenate or selenite as well as the insoluble elemental selenium and selenides accounting altogether for over 95% of selenium recovered after extraction is not typical in the light of earlier reports claiming γ -glutamyl-Se-methylselenocysteine as the major (90%) species [11,13]. Considerable contribution of inorganic selenium was, however, reported in other plants such as Japanese pungent radish (45%) [23], or shallot (28%) [13]. Speciation of selenium in garlic is strongly dependent on the sample origin as it was reported elsewhere for the Se-enriched yeast [14].

4. Conclusion

The study proposes a method able to characterize a garlic sample in terms of distribution of selenium among the different origins (water soluble, cell-wall bound, protein bound, elemental and selenide). Retention time matching with the most comprehensive to date set of standards allows the identification of many species provided the analysis is carried out in reduced conditions. This approach is more valuable compared to the performance of HPLC-ESI MS because the latter one cannot detect the compounds of interest under similar sample preparation conditions [24].

References

- [1] E. Block, X.J. Cai, P.C. Uden, X. Zhang, B.D. Quimby, J.J. Sullivan, *Pure Appl. Chem.* 68 (1996) 937.
- [2] X.J. Cai, P.C. Uden, E. Block, X. Zhang, B.D. Quimby, J.J. Sullivan, *J. Agric. Food Chem.* 42 (1994) 2081.
- [3] R. Lobinski, J.S. Edmonds, K.T. Suzuki, P.C. Uden, *Pure Appl. Chem.* 72 (2000) 447.
- [4] H. Ge, X.J. Cai, J.F. Tyson, P.C. Uden, E.R. Denoyer, E. Block, *Anal. Commun.* 33 (1996) 279.
- [5] S.M. Bird, H. Ge, P.C. Uden, J.F. Tyson, E. Block, E. Denoyer, *J. Chromatogr. A* 789 (1997) 349.
- [6] M. Kotrebai, M. Birringer, J.F. Tyson, E. Block, P.C. Uden, *Anal. Commun.* 36 (1999) 249.
- [7] M. Kotrebai, P.C. Uden, *Spectrochim. Acta Part B* 54 (1999) 1573.
- [8] M. Kotrebai, M. Birringer, J.F. Tyson, E. Block, P.C. Uden, *Analyst* 125 (2000) 71.
- [9] M. Kotrebai, J.F. Tyson, E. Block, P.C. Uden, *J. Chromatogr. A* 866 (2000) 51.
- [10] C. Casiot, V. Vacchina, H. Chassaing, J. Szpunar, M. Potin-Gautier, R. Lobinski, *Anal. Commun.* 36 (1999) 77.
- [11] S. McSheehy, W. Yang, F. Pannier, J. Szpunar, R. Lobinski, J. Auger, M. Potin-Gautier, *Anal. Chim. Acta* 421 (2000) 147.
- [12] M. Shah, S.S. Kannamkumath, J.C.A. Wuilloud, R.G. Wuilloud, J.A. Caruso, *J. Anal. At. Spectrom.* 19 (2004) 381.
- [13] Y. Ogra, K. Ishiwata, Y. Iwashita, K.T. Suzuki, *J. Chromatogr. A* 1093 (2005) 118.

- [14] E.H. Larsen, R. Lobinski, K. Burger-Meyer, M. Hansen, R. Ruzik, L. Mazurowska, P.H. Rasmussen, J.J. Sloth, O. Scholten, C. Kik, *Anal. Bioanal. Chem.* 385 (2006) 1098.
- [15] J.R. Encinar, M. Sliwka-Kaszynska, A. Polatajko, V. Vacchina, J. Szpunar, *Anal. Chim. Acta* 500 (2003) 171.
- [16] C. Casiot, J. Szpunar, R. Lobinski, M. Potin-Gautier, *J. Anal. At. Spectrom.* 14 (1999) 645.
- [17] S. Gao, K.K. Tani, D.W. Peters, M.J. Herbel, *J. Environ. Qual.* 29 (2000) 1275.
- [18] D.J. Velinsky, G.A. Cutter, *Anal. Chim. Acta* 235 (1990) 419.
- [19] V.J. Molinski, G.W. Leddicotte, The Radiochemistry of Selenium, in: Nuclear Science Series of National Academy of Sciences, National Research Council, Washington, DC, 1965, Committee on Nuclear Science.
- [20] S. Glinska, B. Gabara, *Folia Histochem. Cytobiol.* 38 (2000) 143.
- [21] A. Polatajko, B. Banas, J.R. Encinar, J. Szpunar, *Anal. Bioanal. Chem.* 381 (2005) 844.
- [22] E.H. Larsen, M. Hansen, T. Fan, M. Vahl, *J. Anal. At. Spectrom.* 16 (2001) 1403.
- [23] Y. Ogra, T. Kitaguchi, K. Ishiwata, N. Suzuki, Y. Iwashita, K.T. Suzuki, *J. Anal. At. Spectrom.* 22 (2007) 1390.
- [24] E. Dumont, Y. Ogra, F. Vanhaecke, K.T. Suzuki, R. Cornelis, *Anal. Bioanal. Chem.* 384 (2006) 1196.



Increasing the sensitivity of the spectrophotometric determinations of the oxygen content in YBCO superconducting samples using the I_3^- -starch compound

Tsvetanka K. Nedeltcheva^{a,*}, Stela Iv. Georgieva^{a,*},
Latinka K. Vladimirova^a, Angelina K. Stoyanova-Ivanova^b

^a Department of Analytical Chemistry, University of Chemical Technology and Metallurgy, Kl. Ohridski 8, 1756 Sofia, Bulgaria

^b Institute of Solid State Physics, Bulgarian Academy of Sciences, 72 Tzarigradsko Chaussee Blvd., 1784 Sofia, Bulgaria

ARTICLE INFO

Article history:

Received 2 June 2008

Received in revised form

30 September 2008

Accepted 6 October 2008

Available online 19 October 2008

Keywords:

YBCO superconductors

Oxygen content

Spectrophotometry

Starch

Iodine

ABSTRACT

The conditions for formation of the I_3^- -starch compound and measuring its absorbance have been found, and a spectrophotometric method has been developed for the determination of the oxygen content in $YBa_2Cu_3O_y$ superconducting bulk samples. The method involves the following stages: a decomposition of the sample in an acid medium in the presence of iodide ions under inert atmosphere; formation of a complex between Cu(II) and glycine; binding the I_3^- -complex with a starch and the absorbance measurement of the colored I_3^- -starch compound. The coefficient of the active oxygen is calculated by the ratio of the absorbances of two solutions and the method does not require both calibration and precise measuring sample mass. The accuracy of the results is confirmed applying the comparative spectrophotometric method that uses the yellow I_3^- -complex. The precision of the results evaluated by the relative standard deviation is 2%. The developed method is sensitive and allows a sample mass about 2 mg to be used. The analysis is rapid and requires a simple and inexpensive apparatus. Thus the new method would be useful for an express analytical control of the oxygen content of YBCO-superconducting materials produced for the electronics.

© 2008 Elsevier B.V. All rights reserved.

1. Introduction

The oxygen content acts as a regulating factor of the structure and the electrical properties of YBCO superconducting materials and that is why its control has to be done [1–4]. Various “wet” methods have been developed for the determination of the oxygen content, such as iodometric titrations [5–9], thermogravimetric analyzes [10], volumetric measurements [10], coulometric titrations [11–13], spectrophotometric analyzes [14,15].

Last years YBCO and other superconducting materials have been studied for electronic applications. The amount of the superconducting materials for these applications is small (sometimes it is 1–5 mg) and to determine the oxygen content in them coulometry and spectrophotometry among the methods given up could be used. The sample mass for analyzes in coulometric titrations [12] is about 10 mg, in micro-coulometry [13] the mass is reduced to 5 mg. The spectrophotometric method [14,15] uses a sample mass in the limits of 8–10 mg. The coulometry however needs pre-

cisely measuring the sample mass, while the spectrophotometric method does not require. The spectrophotometric method does not need calibration to be done also. This method uses iodide ions as reducers and the coefficient of the active oxygen is calculated as a ratio between the absorbances of two solutions containing the yellow colored I_3^- -complex. The absorbance in the numerator corresponds to the quantity of Cu(III) in the sample, and that in the denominator—to the total copper quantity.

In this work experiments were made to reduce the sample mass in the spectrophotometric method pointed out above. The capability of I_3^- and the starch to form an intensive colored compound [16] was tested and a sensitive spectrophotometric method for the determination of the oxygen content in YBCO superconducting materials was developed.

2. Experimental

2.1. Solutions and apparatus

The following reagents were used: $1.63 \times 10^{-3} \text{ mol l}^{-1}$ Cu(II) prepared by dissolving CuO (p.a.) in 1 mol l^{-1} sulfuric acid; 0.112, 0.300, 0.630, 1.12, 1.68 and 2.52 mol l^{-1} KI prepared daily

* Corresponding author.

E-mail address: tco4ko.75@abv.bg (S.Iv. Georgieva).

from KI (p.a., Merck); 0.1 mol l^{-1} hydrochloric acid; 0.1 mol l^{-1} sodium hydroxide solution; sodium acetate–acetic acid buffer ($C_{\text{NaAc}} = 0.08 \text{ mol l}^{-1}$; $\text{pH} = 4.9 \pm 0.1$); 2 mol l^{-1} glycine solution; 0.2%, 0.4%, 0.8% and 1.6% solutions of starch in water (v):glycerine (v) mixture (1:1)—the solutions are stable for several weeks; potassium iodide (p.a.; Merck); nitrogen gas (99.99).

The assembly for sample dissolution is described in [15]. The absorbance was measured by a single-beam Spekol 11 spectrophotometer (Carl Zeiss, Jena) using cells with a path length of 1 cm. Double-beam Spectrophotometer Cary (Varian) was used to record the spectra.

2.2. Procedure

2.2.1. Analysis of model solutions

Proper volume of the Cu(II) solution, 2 ml of the buffer solution, and 3 ml of the KI solutions were introduced in a measuring flask of 10 ml. After a 10 min stay in a dark place, 1 ml of the starch solutions was added and the solution was diluted up to the mark. The starch solution and the distilled water were added drop by drop with continuously shaking of the flask. The absorbance of the I_3^- -starch compound was measured at $\lambda = 545 \text{ nm}$ against a blank solution. The spectra of the compound were recorded against distilled water.

2.2.2. Analysis of YBCO bulk sample

1.5–2.0 mg of a bulk sample, previously powdered and homogenized, was placed in a hemispherical glass container and put on the bottom of one of the beakers. Two measures of 2.5 g KI were placed in the beakers. A volume of 6 ml of the hydrochloric acid was introduced in each of the funnels. The oxygen from the beakers and the solutions was removed by purging with a nitrogen gas for 10 min. The hydrochloric acid solutions were introduced to the beakers and the potassium iodide was carefully dissolved before the sample made contact with the solution. Then the nitrogen gas was stopped, the glass container was turned off and the sample was decomposed and dissolved by stirring. The funnels were removed and volumes of 9 ml of the acetate buffer were added to the sample and blank solutions. After this procedure, 6 ml of the sodium hydroxide solution were added to each of the beakers and the stirring of the solutions was stopped. Three measured flasks of 10.0 ml each with stopper numbered 1, 2 and 3 were prepared (see Table 1). A volume of 5.00 ml and two of 2.00 ml were taken from the sample solution and transferred into flasks 1, 2 and 3, respectively. Two blank sample volumes of 3.00 ml each were added to flasks 2 and 3, which contained 2 ml of the sample solution. Thereafter, 2.00 ml of glycine solution were added to flasks 1 and 3 and 2.00 ml of distilled water were added to flask 2. The solutions were homogenized and 1 ml of the 0.8% starch solution was added to each flask drop by drop shaking the flask, then the solutions were diluted up to the mark of 10 ml by distilled water. After 5 min the absorbances were measured at $\lambda = 545 \text{ nm}$ as the absorbance of the solutions in flasks 1 and 2 was read against the solution in flask 3. It is recommended two parallel sets of solutions to be made and

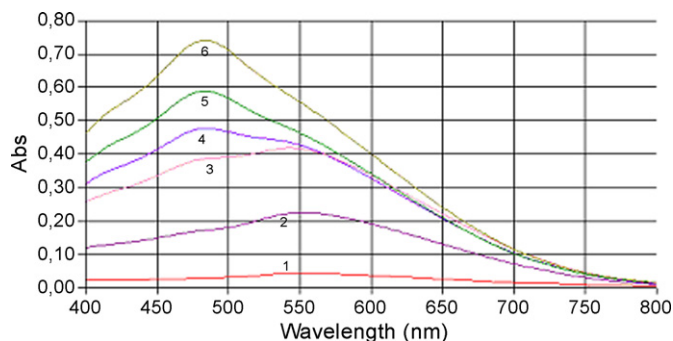


Fig. 1. Spectra of the I_3^- -starch compound at $C_{\text{Cu}} = 3.84 \times 10^{-5} \text{ mol l}^{-1}$, starch 0.08% and concentrations of KI in mol l^{-1} : (1) 0.034, (2) 0.090, (3) 0.19, (4) 0.34, (5) 0.50 and (6) 0.76.

the coefficient of the active oxygen to be calculated by the mean absorbances.

3. Results and discussion

The experiments with model solutions were carried out in the presence of the reagents that are used in the method for the determination of the oxygen content of YBCO samples [14,15]. First the I_3^- -complex is formed in solutions containing Cu(II) concentration in the limits of 0.6×10^{-5} to $6 \times 10^{-5} \text{ mol l}^{-1}$, a sodium acetate–acetic acid buffer ($\text{pH} = 4.9 \pm 0.1$), equimolar quantities of sodium hydroxide solution and hydrochloric acid and different concentrations of KI. After that the starch solution is added and the I_3^- -starch compound is formed. It was established that starch concentrations of 0.02%, 0.04%, 0.08% and 0.16% in the solutions for the absorbance measurement do not exert any effect on the absorption spectrum of the I_3^- -starch compound, and a starch concentration of 0.08% was chosen. The potassium iodide concentration was varied from 0.034 to 0.76 mol l^{-1} and the spectra of the I_3^- -starch compound were recorded at six concentrations of KI (Fig. 1). The absorbance of the I_3^- -starch compound increases when the concentration of KI increases which can be due to the changes in the extent of binding the iodine in I_3^- -complex or to the harmful oxidation process of the iodide ions from the oxygen air. To evaluate the influence of the oxidation process, six blank solutions with KI concentration as these given in Fig. 1 were prepared and their absorbances were measured towards $\text{d}_2\text{H}_2\text{O}$. The absorbances of first three solutions with lower KI concentration were approximately equal to zero. The last three solutions with concentrations of KI: 0.34, 0.50 and 0.76 mol l^{-1} exhibits maximum values of the absorbance as follows: 0.010, 0.055 and 0.120, respectively. The potassium iodide concentration of 0.34 mol l^{-1} was selected at which the sensitivity is high and the absorbance of the blank solution is still low.

Two spectral maxima were observed at wavelengths of 485 and 545 nm. For KI concentrations up to 0.19 mol l^{-1} the absorbance at 545 nm is the higher one. In contrast, when KI concentrations are between 0.34 and 0.76 mol l^{-1} the maximum at 485 nm is more pronounced. The wavelength of the right maximum ($\lambda = 545 \text{ nm}$) at which a concentration of KI between 0.19 and 0.50 mol l^{-1} exerts small effect on the absorbance (Fig. 1) has been chosen for the absorbance measurement. The choice of the wavelength value has been determined by the fact indicated in the spectrophotometric method [14,15] that the KI concentration in the sample solution is not precisely equal to this in blank. Beer's law at the wavelength of 545 nm and for KI concentration of 0.34 mol l^{-1} has been tested. A linear correlation between the absorbance of the I_3^- -starch compound and the concentration of Cu(II) was found

Table 1
Preparation of the solutions for absorbance measurement.

Number of the flask	Volumes (ml)				
	Sample	Blank sample ^a	Glycine	$\text{d}_2\text{H}_2\text{O}$	Starch
Flask 1	5	–	2	–	1
Flask 2	2	3	–	2	1
Flask 3 – comparative solution	2	3	2	–	1

^a The blank sample passes through all stages of the procedure, simultaneously with the sample for analyze.

Table 2

Chemical reactions of the analytical method.

Stages of the analytical procedure	Chemical reactions
1. Decomposition of the sample	$2\text{Cu}^{2+} + 7\text{I}^- \leftrightarrow 2\text{CuI}_2^- + \text{I}_3^-$ (1) $\text{Cu}^{3+} + 5\text{I}^- \rightarrow \text{CuI}_2^- + \text{I}_3^-$ (2)
2. Introduction of the glycine	$\text{I}_3^- + 2\text{CuI}_2 + 2\text{iGly} \leftrightarrow 2\text{CuGly}_i + 7\text{I}^-$ (3) $2\text{Cu}^{3+} + 3\text{I}^- + 2\text{iGly} \rightarrow 2\text{CuGly}_i + \text{I}_3^-$ (4)
3. Inserting the starch	$\text{I}_3^- + \text{starch} \rightarrow \text{I}_3^- - \text{starch}$ (5)

($r=0.995$) and the regression equation at $P=95\%$ and $f=13$ is $A=(1.25 \pm 0.01) \times 10^4 C_{\text{Cu(II)}}$.

The procedure for analysis of YBCO bulk samples is similar to this given in works [14,15]. The sample is dissolved in hydrochloric acid in the presence of iodide ions under inert atmosphere. Cu(II) and Cu(III) react with iodide ions according Eqs. (1) and (2) (see Table 2). Three solutions with different volumes of the sample and blank solutions, and glycine in two of them are prepared (see Table 1). The iodine in the solution without glycine is equivalent to the total copper. The iodine in the solutions with glycine is equivalent only to the copper (III) according to Eqs. (3) and (4) in Table 2. The starch is added to the three solutions and this stage is the main innovation of the procedure. The starch binds I_3^- in a colored stable compound (see Eq. (5) in Table 2) and its absorbance is measured. The iodide and starch concentrations in the solutions for the absorbance measurement are the same as these found by the experiments with model solutions. The absorbance is measured at 545 nm, corresponding to the wavelength of the right maximum of the spectrum, by the reason pointed out before. The molar absorptivity of the I_3^- -starch compound is about ten times higher than that of I_3^- -compound [17], and thus the sensitivity of the method is 10 times increased. That is why a smaller sample mass, a lower quantity of KI and a lower hydrochloric acid concentration were used in the procedure. The novelty is also the shorter time for purging the solutions with nitrogen gas. As a result the time of the sample analyses is decreased.

In order to test the procedure, a monophasic $\text{YBa}_2\text{Cu}_3\text{O}_y$ superconducting bulk sample (X-ray tested [18]), synthesized by solid-phase technology [18], was used. The values of the δ -coefficient of the active oxygen in $\text{YBa}_2\text{Cu}_{3-\delta}\text{Cu}_2^{2+}\text{O}_{6.5+\delta}$ superconductors were calculated by the formula:

$$\delta = \frac{A_1}{A_2}$$

where A_1 is the absorbance of the solution in flask 1, and A_2 is the absorbance of the solution in flask 2. The absorbances A_1 and A_2

of the solutions were read against the absorbance of the solution in flask 3. The mean δ -value obtained from 13 determinations was $\delta = 0.448 \pm 0.007$ ($P=95\%$, $f=12$). The precision of the method evaluated by the relative standard deviation was 2%. To test the accuracy of the mean result a comparative method, using the absorbance measurement of the yellow I_3^- -compound was applied [14,15]. The mean result from five determinations of the same YBCO sample was $\delta = 0.45 \pm 0.01$ ($P=95\%$, $f=3$). The coincidence of the two δ -values is a proof for the absence of systematic errors in all stages of the new method and mainly in the new stage: "Formation of the I_3^- -starch compound" included in the developed method.

4. Conclusions

The developed method is sensitive and accurate. The analysis is rapid, needs a small sample quantity (about 2 mg) and uses simple and inexpensive apparatus. Thus the new method would be useful for an express analytical control of the oxygen content of YBCO-superconducting materials produced for the electronics.

References

- [1] S. Kambe, Y. Murakoshi, R. Sekine, M. Kawai, K. Yanada, S. Oshima, K. Okuyama, *Physica C* 178 (1991) 71.
- [2] J.L. Tallon, C. Bermihard, H. Shaked, R.L. Hitterman, J.D. Jordensen, *Phys. Rev. B* 51 (1995) 12911.
- [3] J.D. Jorgensen, D.G. Hinks, P.G. Radaelli, S. Pie, P. Lightfoot, B. Dabrowski, C.U. Segre, B.A. Hunter, *Physica C* 184 (1991) 185–189.
- [4] A. Fukuoka, M. Karppinen, M. Itoh, K. Hamada, H. Yamauchi, *J. Supercond.* 31 (1995) 8.
- [5] D.C. Harris, T.A. Hewson, *J. Solid State Chem.* 69 (1987) 182.
- [6] A.I. Nazzari, V.Y. Lee, *Physica C* 153–155 (1988) 1367.
- [7] T. Nedeltcheva, A. Stoyanova-Ivanova, L. Kostadinova, I. Ivanova, *Fresen. J. Anal. Chem.* 196 (1992) 342.
- [8] W.M. Chen, J. Chen, X. Jin, *Physica C* 132 (1997) 276.
- [9] T. Nedeltcheva, P. Simeonova, V. Lovchinov, *Anal. Chim. Acta* 312 (1995) 227–229.
- [10] M. Karppinen, A. Fukuoka, L. Niinisto, H. Yamauchi, *Supercond. Sci. Technol.* 9 (1996) 121–135.
- [11] R. Chavdarova, T. Nedeltcheva, L. Vladimirova, *Anal. Chim. Acta* 353 (1997) 325–328.
- [12] Y. Yasukawa, H. Yamauchi, M. Karppinen, *Appl. Phys. Lett.* 8 (2002) 502.
- [13] F. Sato, M. Fujihara, S. Kambe, O. Ishii, *Physica C* 445–448 (2006) 102–106.
- [14] T. Nedeltcheva, L. Vladimirova, *Anal. Chim. Acta* 437 (2001) 259.
- [15] A. Stoyanova-Ivanova, T. Nedeltcheva, L. Vladimirova, *Cent. Eur. J. Chem.* 432 (2005) 3.
- [16] X. Yu, C. Houtman, R.H. Atalla, *Carbohydr. Res.* 129–141 (1996) 292.
- [17] T. Nedeltcheva, *Anal. Chim. Acta* 312 (1995) 223–226.
- [18] A.K. Stoyanova-Ivanova, S.D. Terzieva, A.D. Staneva, V. Mikli, R. Traksmas, Y.B. Dimitriev, V.T. Kovachev, *CEJC Volume 4* (1) (2006) 166.



Sensing parts per million levels of gaseous NO₂ by a optical fiber transducer based on calix[4]arenes

Shin-Ichi Ohira, Eranda Wanigasekara, Dmitry M. Rudkevich¹, Purnendu K. Dasgupta*

Department of Chemistry and Biochemistry, The University of Texas at Arlington, Arlington, TX 76019-0065, USA

ARTICLE INFO

Article history:

Received 9 September 2008

Received in revised form 16 October 2008

Accepted 17 October 2008

Available online 25 October 2008

Keywords:

Calixarene

Fiber optic sensor

Nitrogen dioxide

ABSTRACT

Calixarenes are interesting building blocks in supramolecular receptor design. They can be easily functionalized to give the desired guest binding and sequestration properties. We demonstrate here the use of simple alkylated calixarenes as novel NO₂ sensors. Upon reacting with gaseous NO₂, alkylated calixarenes form stable calixarene-NO⁺ (nitrosonium) complexes that have a deep purple color. This specific and selective formation of the colored complex was used to develop a fiber optic based colorimetric NO₂ sensor. Several alkylated calixarenes are used and tested as sensing materials. The calixarene compound was immobilized on a fine mesh silica-gel coated thin layer chromatography plate. The sensing plate was coupled with a fiber optic based photodetector. Gas samples were sampled in a manner where they impinged on the surface of sensing plate. The light transmission through the plate was continuously monitored. For a 5 min sample, the limit of detection was 0.54 ppmv with 1,3-alternate O-hexyl calix[4]arene (**1a**). There were no significant response differences between different conformations of calixarenes such as 1,3-alternate or cone. This chemistry can form the basis of a colorimetric sensor that relies on extant filter tape technology.

With calixarenes however, such a reaction is potentially reversible – color formed upon reaction with NO₂ can be reversed by flushing the sensing plate by purified air. While we found that the removal of the developed color can be accelerated by simultaneous heating and suction, permitting the reuse of the same sensing area multiple times, we also observed that the sensitivity gradually decreased. The nitrosonium calixarene derivative tends to transform to the nitrated form; this process is catalyzed by light. Several methylated calixarenes were synthesized and tested but a fully satisfactory solution has proven elusive.

© 2008 Elsevier B.V. All rights reserved.

1. Introduction

Calixarenes have been called “chemical chameleons” because of the synthetic flexibility with which they can be functionalized or derivatized [1]. Calix[4]arenes in particular are extensively used in host–guest chemistry because of their ability to reversibly form stable inclusion complexes; the interest in calix[4]arenes for applications in analytical and separation chemistry has been steadily growing [2–5]. The conformational rigidity and flexibility of these supramolecular receptors vary upon incorporation of a guest molecule/ion: this allows the utilization of calix[4]arenes as fundamental building blocks that can be tailored to make calix[4]arenes with desired functionalities for quantitative and qualitative applications.

Calixarene derivatives have been utilized to make solid phase micro extraction fibers that are particularly well suited for extracting phenols from water/wastewater [6]. They have been successfully used as stationary phases in capillary gas chromatography [7] and high performance liquid chromatography [8]. Derivatized calixarenes have been used as molecular receptors in determination of ions, e.g., Ag⁺ [9–13], Hg²⁺ [6,14–16], Ni²⁺ [17], Th⁴⁺ [18], UO₂²⁺ [9,18–20], HPO₄^{2−} [21,22], Na⁺ [23–26], K⁺ [27], Cd²⁺ [28], Pb²⁺ [20,29,30], Mn²⁺ [31], Co²⁺ [32], Au³⁺ [10], Ti⁴⁺ [16,33,34] and Cs⁺ [35]. In most cases, the derivatized calixarenes provided a more selective sensing element for ion selective electrodes (ISE) relative to extant alternatives. Optical transduction has also been used: Ma et al. [17] measured Ni²⁺ ions using chromogenic azocalix[4]arenes that absorbed red light when Ni²⁺ was entrapped by the calixarene. Jain et al. have used calix[4]resorcinarene-hydroxamic acid for optical measurement of UO₂²⁺ [20].

Recent studies of molecular recognition and sensing of NO₂ with calixarenes show that a purple charge transfer complex is formed with a relatively high binding constant [36]. These experiments were conducted with relatively high concentrations of NO₂. It is

* Corresponding author. Fax.: +1 817 272 3808.

E-mail address: dasgupta@uta.edu (P.K. Dasgupta).

¹ Deceased.

well known that NO_2 exists in its dimeric form of N_2O_4 at higher concentrations and N_2O_4 can disproportionate to NO^+NO_3^- ; this process is favored in the presence of aromatic compounds which can provide a π -electron rich site for NO^+ to bind [37–39]. Nitrosonium ion (NO^+) (van der Waals diameter, $<2\text{ \AA}$) generated from $\text{NO}_2/\text{N}_2\text{O}_4$ thus binds well to the interior (internal diameter $\sim 6\text{ \AA}$) of calix[4]arene. The reversible development of a purple color both in solution phase and with the pure solid phase upon reaction of calixarene with NO_2 (g) was previously reported [36] leading to an enhanced interest in the remarkable complexation and molecular encapsulation abilities of calixarenes towards NO_2 and other environmentally important gases [40]. Thus far, such experiments have been limited to pure or high concentration NO_2 with qualitative investigations on color development. In ambient air or even in internal combustion engine exhaust (where concentrations range from single digit to triple digit parts per million by volume (ppmv) NO_2 [41]), NO_2 is present in much lower concentrations than tests made with calixarene-based sensors thus far, it remains an open question whether the calixarene- NO^+ binding constant is high enough to drive the formation of an inclusion complex at such low concentrations. Nitrogen dioxide is one of six criteria air pollutant designed by US-EPA [42]. Of particular interest to us is a sensor that can directly measure NO_2 levels in engine exhaust and in source monitoring; there is a worldwide interest in such sensors [43]. We describe here the working characteristics of a simple optical fiber-based NO_2 sensor that is based on alkylated calix[4]arenes as the sensing element.

2. Experimental

2.1. Instruments and standard gases

^1H NMR spectra were recorded at $295 \pm 2\text{ K}$ on a JEOL Eclipse 300 MHz spectrometer. The chemical shifts were measured relative to the residual non-deuterated solvent resonance. Ultraviolet–visible spectra were obtained with HP 8453A photodiode array spectrophotometer. Nitrogen dioxide was generated from a gravimetrically calibrated permeation tube [44] made in-house

from a fluorinated ethylene propylene tube (50 mm \times 6.3 mm o.d., 0.38 mm wall thickness), providing an output of $\sim 30\text{ }\mu\text{g NO}_2/\text{min}$ at 30°C . Dilution air was generated by a chromatographic pure air generator (Model 737, AACCO, www.aadcoinst.com) and metered with mass flow controllers (Tylan General, Torrance, CA).

2.2. Synthesis of calixarenes

See Fig. 1 for all structures. Parent calix[4]arene **1** and [1.1.1.1] Metacyclophanes **3** (Pappalardo's cyclophane) were synthesized by minor modification of procedures reported in literature [45–47]. Calixarenes **1a**, **1b**, **2a**, **2b**, **2c** and alkylated [1.1.1.1] Metacyclophanes, **3a**, **3b** were prepared according to the published procedures [48–50].

A representative procedure for the synthesis of compounds **1a**, **1b** is as follows. An alkyl bromide (0.03 mol) was added to a suspension of tetrahydroxycalix[4]arene **1** (0.01 mol) and K_2CO_3 (4.2 g, 0.03 mol) in MeCN (200 mL), and the reaction mixture was refluxed under nitrogen for 48 h. The precipitate was filtered off, and the solution was evaporated to dryness. The residue was redissolved in CH_2Cl_2 (200 mL), and the solution was washed with water ($3 \times 150\text{ mL}$) and dried over MgSO_4 . After evaporation, the solid residue was treated with MeOH (200 mL) to yield the corresponding 5,27-bis(alkyloxy)-26,28-hydroxycalix[4]arene. An alkyl bromide (0.04 mol) was added to a suspension of this compound (0.01 mol) and Cs_2CO_3 (50 g, 0.15 mol) in MeCN (300 mL), and the reaction mixture was refluxed under nitrogen for 48 h. After cooling, the precipitate was filtered off and treated with a mixture of water (100 mL) and CH_2Cl_2 (100 mL). The organic layer was separated, washed with water ($2 \times 100\text{ mL}$), dried over MgSO_4 , and evaporated. After evaporation, the solid residue was recrystallized from 10:1 MeOH- CHCl_3 to give desired 1,3-alternate O-alkyl calix[4]arene.

A representative procedure for the alkylation of compounds **2a**, **2b**, **2c**, **3a**, **3b** is as follows. Sodium hydride (0.11 g of 60% suspension in mineral oil, 2.7 mmol) was added to the solution of tetrahydroxycalix[4]arene or Pappalardo's cyclophane [45,46] (0.2 g, 0.34 mmol) in freshly distilled DMF (20 mL), and the mixture was stirred under

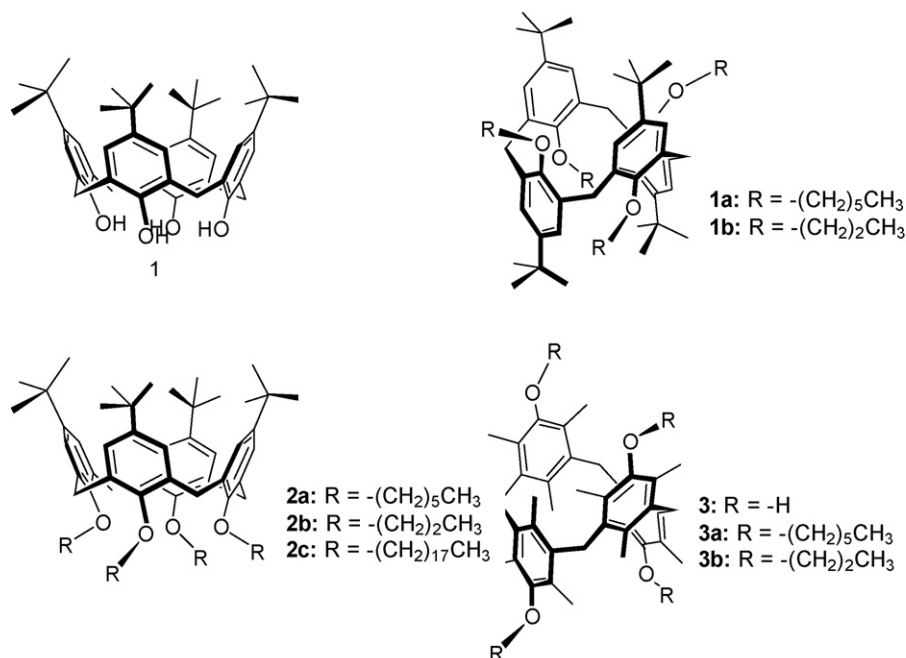


Fig. 1. Structures of calix[4]arenes used in this work.

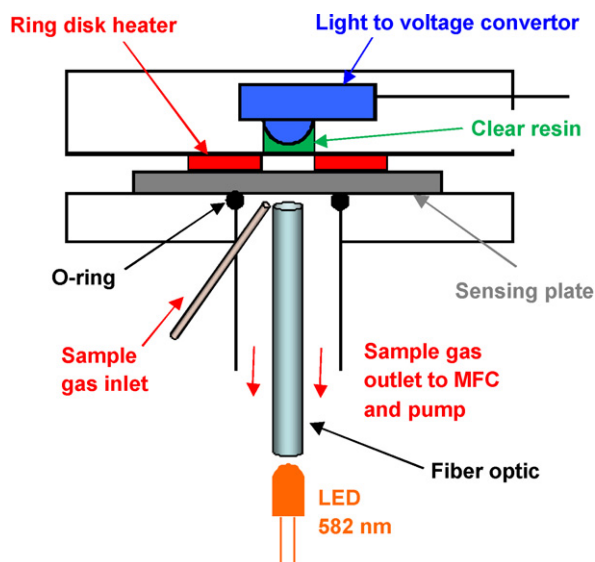


Fig. 2. The gas collection/detection system shown schematically.

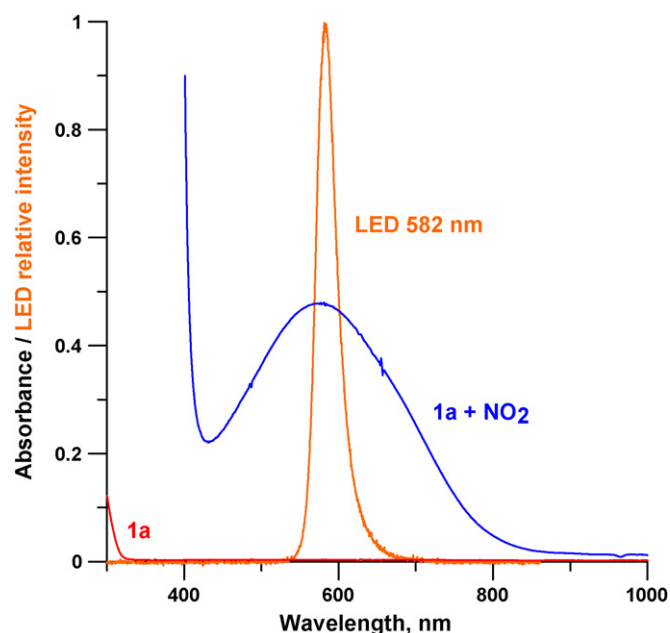


Fig. 3. Spectra obtained with calix[4]arene and NO₂. Structure of compound **1a** (1,3-alternate O-hexyl calix[4]arene) is shown in Fig. 1.

nitrogen for 30 min. An alkyl bromide (2.04 mmol) was then added, and the reaction mixture was stirred at 70 °C for 48 h. After evaporation of the solvent, the precipitate was collected and dissolved in CH₂Cl₂ (20 mL). The solution was washed with water (3 × 20 mL), dried over MgSO₄, and evaporated. The residue was recrystallized from MeOH–CHCl₃ to afford the desired product as a white powder.

Structures of all synthesized compounds were confirmed by ¹H NMR and were in agreement with previously published results [45–47].

2.3. Preparation of sensing plates

Transparent polyester-backed thin layer chromatography (TLC) plates (4410-221, Whatman) were impregnated with test calixarene compounds to form the sensing elements. TLC plates were cut in 25 mm squares, and then put into deionized water for 30 min to remove water soluble contaminants. The plates were dried with a pure dry air stream for 2–3 h, washed with CHCl₃ and then dipped into a solution of 0.6 mM calixarene in CHCl₃, withdrawing and drying in a pure air stream for 15 min. This method of impregnation was chosen based on preliminary experiments; details are provided in supporting information (SI).

2.4. Gas collection/detection set up

As shown in Fig. 2, the impregnated sensing plate was placed between two 5 mm thick black acrylic plates. The bottom plate is connected to a 6.3 mm o.d. tube that serves both as the entrance of a 1.5 mm core jacketed fiber optic (NT02-550, www.edmundoptics.com) and as the sample air exit (that leads to an aspiration pump). The fiber optic and the air aspiration line are separated at the bottom with a tee, not shown in this figure. The sample gas enters through a Teflon-lined stainless steel tube of 0.8 mm i.d. and impinges on the impregnated plate at an angle of ~45°. The sample inlet is provided with an all-fluorocarbon wetted path 3-way solenoid valve (360T031, www.NResearch.com). The fiber optic tip is located ~1 mm from the center of the exposed area of the plate. The sampling flow rate was held constant at 0.35 standard liters per minute (SLPM), unless otherwise stated, by a mass flow controller (Tylan General, Torrance, CA) and a miniature air aspiration pump (T2-01, www.Parker.com). The distal end of the fiber optic was coupled to a

flattened-top surface-polished light emitting diode (LED) [51]. The LED (HLMP3850, Agilent) had its peak emission at 582 nm and was driven at 25 mA. The aperture in the top plate had a light to voltage converter (TSL257, www.taosinc.com) for detecting the transmitted light. The front of the aperture was filled in with a clear urethane resin (20–2620, www.epoxies.com). This measure increased the transmitted light signal 2×. A flat ring-shaped heater (Polyimide Thermofoil® (HK5186R25.0L12B, http://www.minco.com, 12.7 mm o.d., 2.4 mm i.d., 0.3 mm thickness) was incorporated behind the sensing plate with the heater aperture concentric with the detector aperture so the transmitted light was not blocked. The detector signal was acquired through a universal serial bus based data acquisition module of 14-bit resolution (USB-1408FS, www.measurementcomputing.com) on a laptop computer using software written in-house.

3. Results and discussion

3.1. Color development with calix[4]arenes and NO₂

Gaseous NO₂ was bubbled through 0.1 mM 1,3-alternate O-hexyl calix[4]arene (**1a**) in CHCl₃. Whereas the pure compound has no significant absorption within the 350–1000 nm range, broadband visible absorption with a λ_{max} of 560 nm was observed after treatment with NO₂. Fig. 3 shows the absorption spectrum with the emission spectrum of the interrogation LED also shown thereon. Compounds **1b**, **2a** and **2b** were similarly tested – there were no significant differences in the λ_{max} or the absorbance. Monitoring the solution by ¹H NMR before and after the NO₂ absorption produced results very analogous to those reported in [32].

3.2. Response with sensing plate and 1,3-alternate O-hexyl calix[4]arene

Langmuir–Blodgett monolayer film approaches for sensing NO₂ gas with porphyrin [52–54] or calixarene/porphyrin [55] compounds. We have chosen to work with TLC plates both because of ease of preparation and the large surface area of this material

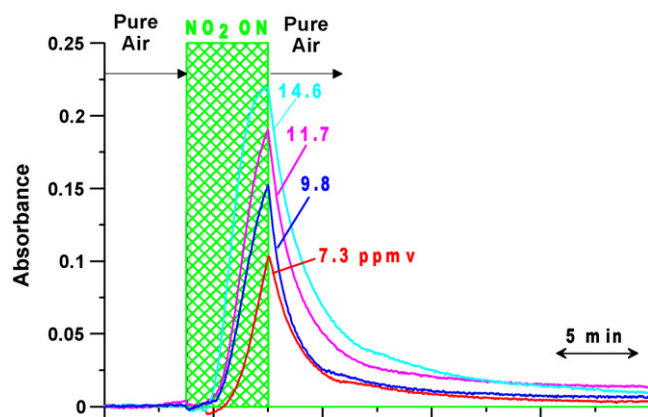


Fig. 4. Response to NO_2 obtained with **1a** (1,3-alternate O-hexyl calix[4]arene). The plates were exposed to standard NO_2 gas for 5 min at 0.35 SLPM.

that provides appreciable capacity to absorb the calixarene. Even at low ppm levels of NO_2 , the formation of a purple product could be readily observed. Initial results with different types of TLC plates indicated that the best results are obtained small particle porous silica with a pore size of 60 Å. The impregnation of calixarene by dip-coating provides a relatively uniform impregnation pattern. Visual comparison of sensing plates prepared by different methods and after exposure to NO_2 under otherwise identical conditions is shown in Fig. S1 in SI.

The response of a sensing plate impregnated with 1,3-alternate O-hexyl calix[4]arene to various concentrations of NO_2 gas of known concentration was studied for 5 min periods on fresh sensing areas, followed by sampling of pure air. The results are shown in Fig. 4. The sensing area was changed after every single measurement. It is clear that even at low ppmv levels of NO_2 and with the calixarene as a solid adsorbate, the chemical sensing principle is still effective. Depending on the exact exposure concentration, the observed lag time before the first rise in the absorbance signal varies but is generally less than 2 min. The absorbance then rises steeply and during the middle of the exposure period, dA/dt attains a maximum as shown in Fig. 5. Towards the end of the

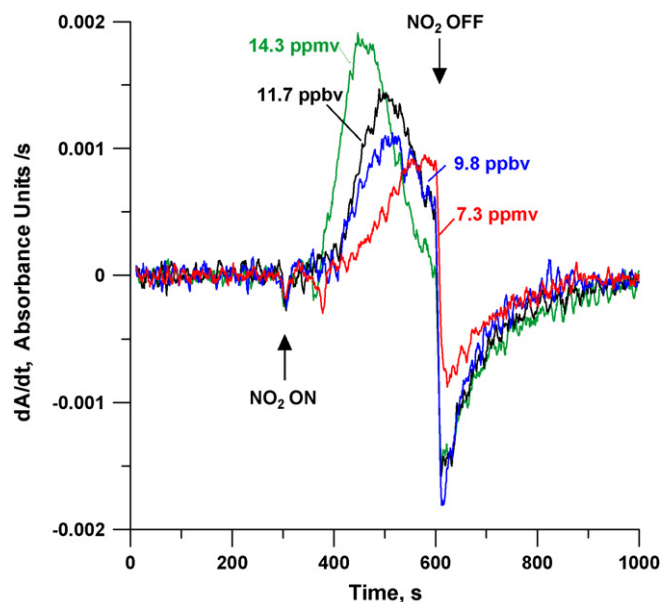


Fig. 5. The rate of change of absorbance during the sample/zeroing cycle. The conditions are as same as Fig. 4.

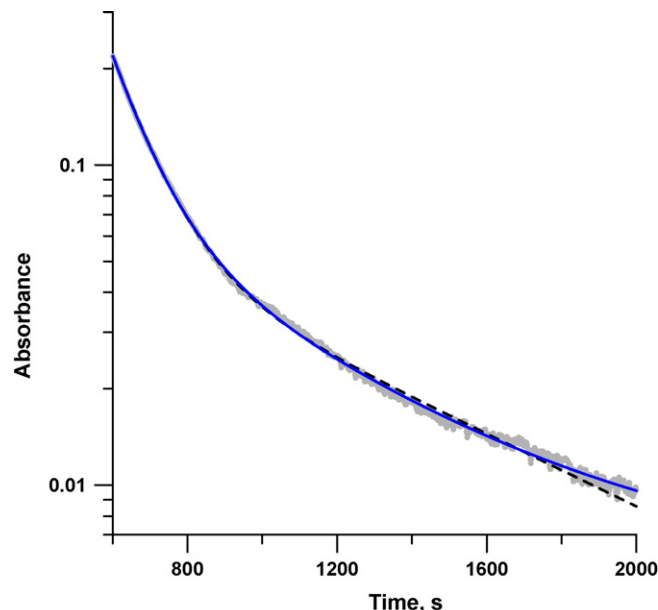


Fig. 6. Decay of absorbance from plate exposed to 14.6 ppmv NO_2 (gray line). The decay starts at $t = 601$ s. The best fit to Eqs. (3) and (4) are respectively shown in the dashed and solid (blue) traces. See text for further details. (For interpretation of the references to color in this figure legend, the reader is referred to the web version of the article.)

exposure period dA/dt actually decreases, suggesting that this is an equilibrium process.

The absorbance at the end of the 5 min sampling period (the maximum) bears a linear relationship with the sample concentration (See Fig. S2 in SI for a plot):

$$A_{582\text{ nm}} = 0.0161 \pm 0.00188 [\text{NO}_2, \text{ ppmv}] - 0.0086 \pm 0.00210, \quad r^2 = 0.9735 \quad (1)$$

For a 5 min sample, the limit of detection obtained with three times of standard deviations of blank was 0.54 ppmv. A plot of dA/dt_{max} against concentration is shown in Fig. S3 in SI and is also linear, this actually exhibits slightly better linearity than Eq. (1) above:

$$\frac{dA}{dt_{\text{max}}} (\text{mAU/s}) = 0.1421 \pm 0.0107 [\text{NO}_2, \text{ ppmv}] - 0.2612 \pm 0.1196, \quad r^2 = 0.9888 \quad (2)$$

As may be anticipated, if the flow rate is decreased, the upper linear limit can be significantly increased; these data are not separately discussed here.

3.3. Decay profile and reversibility

It is readily observed that as soon as the NO_2 flow is turned off and zero air is sampled, the observed absorbance begins to decrease, seemingly in an exponential pattern. An exponential return to the baseline will indeed be expected if there is a single entity, e.g., the NO_2 -calixarene complex that is formed upon NO_2 exposure that then decomposes in a first order and presumably in a unimolecular manner. A closer look at the decay pattern however suggests that this is not the situation. Consider Fig. 6; the gray trace shows the original data for the decay from the 14.6 ppm exposure, beginning with the moment NO_2 exposure is stopped and zero air flow is begun. This figure is plotted with a logarithmic ordinate. It

is clear that this is not a simple linear plot that will be indicative of a first order unimolecular decomposition of the inclusion complex. Rather, the plot suggests there may be two different superimposed rate processes. We chose to explore how well a double exponential decay model (where two separate species are considered to be responsible together for the initial signal and which then decay with two different first order rate constants) fit the observed data. The basic model of the absorbance as a function of time t (A_t ; $t=0$ corresponds to cessation of NO_2 exposure) thus states.

$$A_t = A_{t=0}[fe^{-k_1t} + (1-f)e^{-k_2t}] \quad (3)$$

where fractions f and $1-f$ respectively decay with rate constants of k_1 and k_2 . The dash trace in Fig. 6 is the best fit to this model with $f=0.757$, k_1 and k_2 being 9.04×10^{-3} and $1.30 \times 10^{-3} \text{ s}^{-1}$. A further refinement comes from the observation that after a significant exposure to NO_2 , even after substantial time is allowed for zero air flow, the residual absorbance does not completely return to the initial zero value. In fact after multiple exposures, we can visually see a residual yellowish color on the plate that does not disappear. To accommodate this, we modify Eq. (3) to:

$$A_t = A_{t=0}[fe^{-k_1t} + (1-f)e^{-k_2t} + b((1-f)(1-e^{-k_2t}))] \quad (4)$$

which takes into account that the second pathway results in a product that itself absorbs some light. The best fit to Eq. (4) involves $f=0.703$, k_1 and k_2 being 9.62×10^{-3} and $1.93 \times 10^{-3} \text{ s}^{-1}$, and $b=0.0868$ and is depicted by the blue trace. It is obvious that within the noise limits of the original trace, this model seems to fit the observed behavior perfectly. Fig. S4 in SI shows the same for the 11.7 ppm exposure where not only the model fits as well but the respective fitted parameters of importance are also close: $f=0.709$, $k_1=1.15 \times 10^{-2}$ and $k_2=2.96 \times 10^{-3} \text{ s}^{-1}$. This analysis thus suggests that two separate products are formed in approximately 70:30 ratios and their fate is not the same.

3.4. Reversibility, reusability and sensor interrogation light intensity

As Fig. 4 suggests, the absorbance decay to attain a stable low value takes a long time, >20 min. It would be desirable to accelerate this process for reuse of the sensor. At this time we had not also fully carried out the analysis of the decay process that we have presented in the previous section. We determined the effects of (a) pulling a vacuum on the sensor plate (sample inlet closed (sample inlet closed, sample aspiration pump on), (b) heating (1.5 V applied to the heater), and (c) simultaneous application of both heat and vacuum. Vacuum alone was not very effective. Heating reduced the time needed for regeneration (strictly, time to return to the same baseline value obtained by 20 min of pure air flush) to $\sim 50\%$. Simultaneous heating and vacuuming worked best: we were able to reduce the time necessary for “regeneration” to 5 min. The fact that heating displaces the equilibrium to less sorption of NO_2 provides in principle an opportunity to move the center of the dynamic range of the sensor up and down by varying the operational temperature; warmer temperatures would also benefit the response time by decreasing the equilibrium sorption/desorption time. Presently we presumed that room temperature sampling and regeneration by heating–vacuuming will provide an opportunity for reusing the same sensor area.

When we performed repeated analysis, however, it was clear that the response gradually decreases with each repeated cycle. We assumed that the loss may be due to actual loss of the calixarene from the plate. Increasing the impregnating solution concentration nearly 10-fold to 5 mM or attaching long hydrocarbon tails up to C-18 (compound **2c**) did not significantly alter the pattern of loss

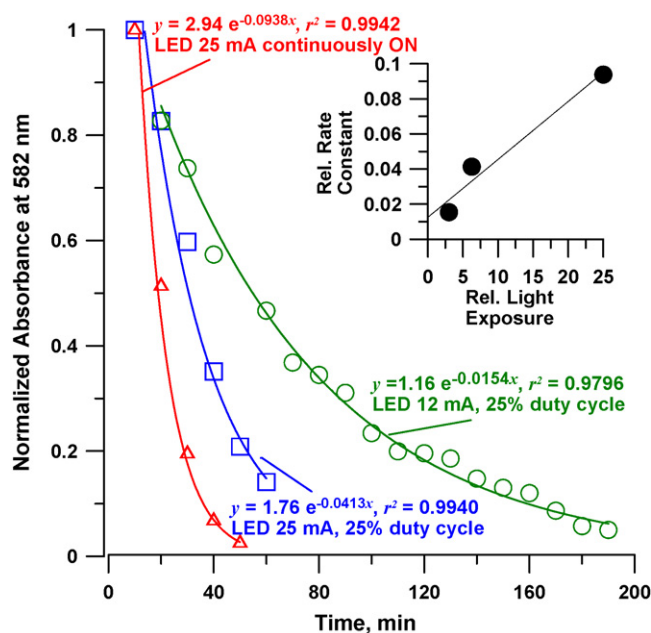


Fig. 7. Loss of response upon exposure to 30 ppmv NO_2 for 5 min and regeneration for 5 min under three different conditions of light interrogation. (a) Triangles show LED continuously ON with $i=25$ mA; (b) squares show LED ON with 25% duty cycle ($i=25$ mA); (c) circles show the same as b except $i=12$ mA. Inset shows the relative rate constants for first order decay plotted against relative light exposure. These were obtained with **1a** (1,3-alternate O-hexyl calix[4]arene).

of response upon use. Detailed observation with parametric variations then indicated that the extent of this decrease is directly related to the observed absorbance at the end of the sampling cycle, i.e., the amount of NO_2 present on the plate and also on the amount of light exposure from the LED source (Fig. 7).

While it has been shown that nitrosonium-calixarene complexes can be stable [56], it is also known that aromatic nitration can occur when calixarenes interact with NO_2 in chloroform or dichloromethane solution [57]. However, that such nitration could occur in the solid phase or with gas–solid reactions and further, be photocatalyzed, were unanticipated. Fig. 7 shows the decay of the response after relatively high amounts of NO_2 was put on the plate by sampling 30 ppmv NO_2 for 5 min. The plate was then regenerated by simultaneous heating and vacuum for 5 min under three different illumination conditions: (a) The LED was driven at 25 mA and it was on continuously for the entire exposure period, (b) the LED was operated with a 25% duty cycle 15 s ON, 45 s OFF and (c) same as b, except that the ON state drive current (to which the emitted light intensity is linearly related) was 12 mA. It will be observed that the loss of response in all three cases fits first order decay equations well. When the relative rate constants are plotted against the relative amounts of light exposures (see inset, Fig. 7), the data suggests that while the reaction may indeed be photocatalyzed, some loss of response will proceed even in the dark. Indeed, we found that there was loss of response even when we attempted to interrogate with a long wavelength LED with a much lower photon energy (λ_{max} 760 nm, driven at 10 mA, LED-760-40M32, <http://www.roithner-laser.com>).

Tin (IV) chloride has been reported to stabilize the nitrosyl calixarene inclusion complex, thus minimizing the nitration of phenyl rings in calixarene [36]. We incorporated SnCl_4 in the impregnating solution but did not observe any marked improvement in response stability.

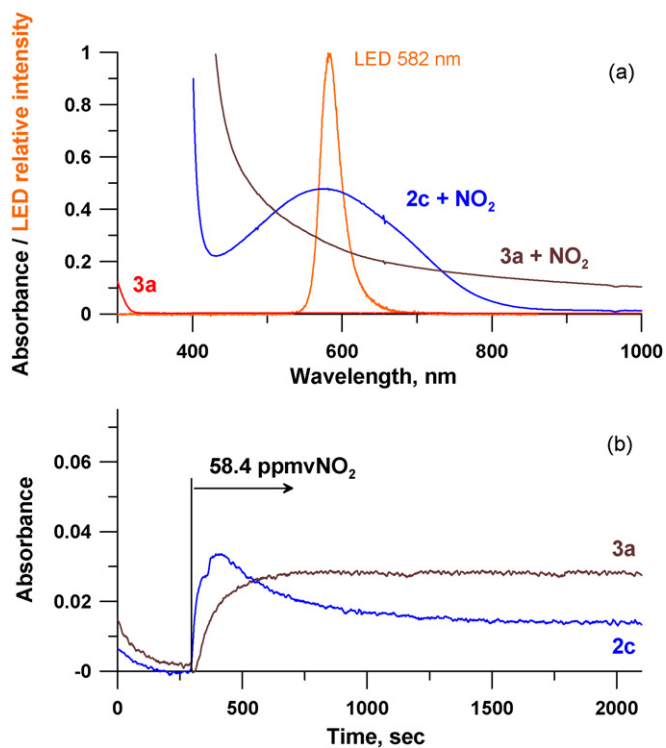


Fig. 8. Response of functionalized calix[4]arenes with NO_2 . (a) Spectra with NO_2 and (b) response with NO_2 . The 582 nm LED spectrum is shown for reference. These data were obtained with **2c** (1,3-alternate O-octadecyl calix[4]arene) and **3a** (O-hexyl calix[4]arene).

3.5. Search for other derivatives

We looked for other means of preventing nitration by synthesizing calixarenes where the preferred nitration points were blocked (compounds **3a** and **3b**). On exposure to NO_2 , these compounds produced brown, rather than purple products (Fig. 8(a)). The sensitivities for NO_2 detection of the compounds in series **3** are much lower than that of **2a** (compare Fig. 4 with Fig. 8(b)). Also, while **2c** does produce a purple product, it is too much less sensitive than **2a**. Perhaps more importantly, the reaction of NO_2 with the compounds in series **3** proved not at all reversible (Fig. 8). Possibly, *ipso* nitration [58] occurred.

Nitrogen dioxide is a hydrophobic gas that has high solubility in apolar solvents [59]. We found that solutions of NO_2 in CHCl_3 absorb strongly in the near UV. With calix[4]arenes, especially hydrophobic calix[4]arenes, we presumed that there may be better collection efficiencies for NO_2 and the resulting product could be measured in the near UV. However, in practice, the sensitivity was significantly poorer than with compound **2a**, either in the visible or in near UV.

4. Conclusions

We show a calixarene based optical sensor for NO_2 , the sensitivity of which is widely tunable as a function of temperature; it is known that calixarenes selectively bind NO_2 . The basic sensing technique should be useful for many other gas analysis applications. 1,3-alternate O-hexyl calix[4]arene showed good sensitivity to low ppmv levels of NO_2 . Presently the chemistry is readily applicable to one-time use sensors such as impregnated glass or paper filter sensors [60] but is only partially reversible towards repeated use. The lure for a truly reversible sensor nevertheless remains alluring and the findings in this paper should prove important in designing such sensors.

Acknowledgements

On behalf of our deceased co-author DMR, we gratefully acknowledge the award of the Sloan Fellowship to him. This work was partly supported by the award of a Japan Society for Promotion of Science Fellowship to SO and partly by a US Environmental Protection Agency Science To Achieve Results (STAR) grant (RD-83107402) to PKD. However, this manuscript has not been subjected to review by these agencies and no endorsements should be inferred.

Appendix A. Supplementary data

Supplementary data associated with this article can be found, in the online version, at doi:10.1016/j.talanta.2008.10.024.

References

- [1] E. van Dienst, W.I.I. Bakker, J.F.J. Engbersen, W. Verboom, D.N. Reinhoudt, *Pure Appl. Chem.* 65 (1993) 387.
- [2] M. Ulewicz, *Pol. J. Chem.* 82 (2008) 1237.
- [3] T. Kajiura, N. Iki, M. Yamashita, *Coord. Chem. Rev.* 251 (2007) 1734.
- [4] I. Mohammed-Ziegler, F. Billes, J. Inclusion Phenom. Macro. Chem. 58 (2007) 19.
- [5] L. Baklouti, N. Cheriaa, M. Mahouachi, A. Othman, R. Abidi, J.S. Kim, Y. Kim, J. Vicens, *Mini-Rev. Org. Chem.* 3 (2006) 219.
- [6] F. Zhou, X. Li, Z. Zeng, *Anal. Chim. Acta* 538 (2005) 63.
- [7] J. Xing, C.-Y. Wu, T. Li, Z.-L. Zhong, Y.-Y. Chen, *Anal. Sci.* 15 (1999) 785.
- [8] M. Liu, L.-S. Li, S.-L. Da, Y.-Q. Feng, *Talanta* 66 (2005) 479.
- [9] L. Chen, X. He, B. Zhao, Y. Liu, *Anal. Chim. Acta* 417 (2000) 51.
- [10] S. Yajima, Y. Iwane, E. Nomura, H. Taniguchi, K. Kimura, *Anal. Chim. Acta* 556 (2006) 189.
- [11] T. Shinohara, H. Higuchi, Y. Senba, K. Ohto, K. Yoshizuka, K. Inoue, *Anal. Sci.* 17 (2001) 889.
- [12] K. Ohto, H. Yamaga, E. Murakami, K. Inoue, *Talanta* 44 (1997) 1123.
- [13] K.M. O'Connor, G. Svehla, S.J. Harris, M.A. McKervey, *Talanta* 39 (1992) 1549.
- [14] C.G. Talanova, N.S.A. Elkarim, V.S. Talanov, R.A. Bartsch, *Anal. Chem.* 71 (1999) 3106.
- [15] R.K. Mahajan, R. Kaur, I. Kaur, V. Sharma, M. Kumar, *Anal. Sci.* 20 (2004) 811.
- [16] V.S. Talanov, E.D. Roper, N.M. Buie, G.G. Talanova, *Tetrahedron Lett.* 48 (2007) 8022.
- [17] Q. Ma, H. Ma, M. Su, Z. Wang, L. Nie, S. Liang, *Anal. Chim. Acta* 439 (2001) 73.
- [18] N. Demirel, M. Merdivan, N. Pirinccioglu, C. Hamamci, *Anal. Chim. Acta* 485 (2003) 213.
- [19] M. Sonoda, M. Nishida, D. Ishii, I. Yoshida, *Anal. Sci.* 15 (1999) 1207.
- [20] V.K. Jain, S.G. Pillai, R.A. Pandya, Y.K. Agrawal, P.S. Shrivastav, *Talanta* 65 (2005) 466.
- [21] F. Kivileham, W.J. Mace, H.A. Moynihan, D.W.M. Arrigan, *Anal. Chim. Acta* 585 (2007) 154.
- [22] V.K. Gupta, R. Ludwig, S. Agarwal, *Anal. Chim. Acta* 538 (2005) 213.
- [23] K. Kimura, T. Miura, M. Matsuo, T. Shono, *Anal. Chem.* 62 (1990) 1510.
- [24] A. Cadogan, Z. gao, A. Lewenstam, A. Ivaska, *Anal. Chem.* 64 (1992) 2496.
- [25] B.T.T. Lan, K. Tóth, *Anal. Sci.* 14 (1998) 191.
- [26] K. Cunnigham, G. Svehla, S.J. Harris, M.A. McKervey, *Analyst* 118 (1993) 341.
- [27] T. Katsu, Y. Yokoyama, K. Ueda, K. Kohno, T. Yamato, *Anal. Sci.* 21 (2005) 175.
- [28] S. Zhang, W. Huang, *Anal. Sci.* 17 (2001) 983.
- [29] J. Radecki, I. Grzybowska, A. Hameurlaine, W. Dehaen, *Anal. Sci.* 20 (2004) 1599.
- [30] N.M. Bule, V.S. Talanov, R.J. Butcher, G.G. Talanova, *Inorg. Chem.* 47 (2008) 3549.
- [31] D.D. Malkhede, P.M. Dhadke, S.M. Khopkar, *Anal. Sci.* 15 (1999) 781.
- [32] A. Gupta, S.M. Khopkar, *Talanta* 42 (1995) 1493.
- [33] E.D. Ropoer, V.S. Talanov, R.J. Butcher, G.G. Talanova, *Supramol. Chem.* 20 (2008) 217.
- [34] G.G. Talanova, E.D. Roper, N.M. Buie, M.G. Gorbunova, R.A. Bartsch, V.S. Talanov, *Chem. Commun.* (2005) 5673.
- [35] V.S. Talanov, G.G. Talanova, M.G. Gorbunova, R.A. Bartsch, *J. Chem. Soc., Perkin Trans. 2* (2002) 209.
- [36] G.V. Zyryanov, Y. Kang, D.M. Rudkevich, *J. Am. Chem. Soc.* 125 (2003) 2997.
- [37] J.C. Evans, H.W. Rinn, S.J. Kuhn, G. Olah, *Inorg. Chem.* 3 (1964) 857.
- [38] C.C. Addison, *Chem. Rev.* 80 (1980) 21.
- [39] E. Bosch, J.K. Kochi, *J. Org. Chem.* 59 (1994) 3314.
- [40] J.H. Hines, E. Wanigasekara, D.M. Rudkevich, R.D. Rogers, *J. Mater. Chem.* 18 (2008) 4050.
- [41] Y. Yamada, Y. Seno, Y. Masuoka, K. Yamashita, *Sens. Actuators B* 49 (1998) 248.
- [42] The United States Environmental Protection Agency. Six common air pollutants. <http://www.epa.gov/air/urbanair>. Accessed September 3, 2008.
- [43] NTT Energy and Environment System Laboratories. NO_2 Sensors. <http://www.ntt.co.jp/islab/kankyo/eng/research/environment/assessment.html#no2s>. Accessed September 3, 2008.

- [44] E.E. Hughes, H.L. Rook, E.R. Deardorff, J.H. Margeson, R.G. Fuerst, *Anal. Chem.* 49 (1977) 1823.
- [45] C.D. Gutsche, M. Iqbal, *Org. Synth.* 68 (1990) 234.
- [46] C.D. Gutsche, J.A. Levine, P.K. Sujeeth, *J. Org. Chem.* 50 (1985) 5802.
- [47] S. Pappalardo, G. Ferguson, J.F. Gallagher, *J. Org. Chem.* 57 (1992) 7102.
- [48] M. Staffilani, G. Bonvicini, J.W. Steed, K.T. Holman, J.L. Atwood, M.R.J. Elsegood, *Organometallics* 17 (1998) 1732.
- [49] V.G. Organo, A.V. Leontiev, V. Sgarlata, H.V.R. Dias, D.M. Rudkevich, *Angew. Chem. Int. Ed.* 44 (2005) 3043.
- [50] G.V. Zyryanov, D.M. Rudkevich, *J. Am. Chem. Soc.* 126 (2004) 4264.
- [51] P.K. Dasgupta, I.-Y. Eom, K.J. Morris, J. Li, *Anal. Chim. Acta* 500 (2003) 337.
- [52] O. Worsfold, C.M. Dooling, T.H. Richardson, M.O. Vysotsky, R. Tregonning, C.A. Hunter, C. Malins, *J. Mater. Chem.* 11 (2001) 399.
- [53] T.H. Richardson, C.M. Dooling, O. Worsfold, L.T. Jones, K. Kato, K. Shinbo, F. Kaneko, R. Tregonning, M.O. Vysotsky, C.A. Hunter, *Colloid Surf. A – Physicochem. Eng. Aspects* 198–200 (2002) 843.
- [54] T.H. Richardson, C.M. Dooling, L.T. Jones, R.A. Brook, *Adv. Colloid Interface Sci.* 116 (2005) 81.
- [55] T.H. Richardson, R.A. Brook, F. Davis, C.A. Hunter, *Colloid Surf. A – Physicochem. Eng. Aspects* 284–285 (2006) 320.
- [56] R. Rathore, S.V. Lindeman, K.S.S.P. Rao, D. Sun, J.K. Kochi, *Angew. Chem. Int. Ed.* 39 (2000) 2123.
- [57] R. Rathore, E. Bosch, J.K. Kochi, *Tetrahedron* 50 (1994) 6727.
- [58] E. Bosh, J.K. Kochi, *J. Org. Chem.* 59 (1994) 3314.
- [59] A. Luzar, D. Bratko, *J. Phys. Chem. B* 109 (2005) 22545.
- [60] K. Kawamura, K. Kerman, M. Fujihara, N. Nagatani, T. Hashiba, E. Tamiya, *Sens. Actuators B* 105 (2005) 495.



Flow injection analysis system based on amperometric thin-film transducers for free chlorine detection in swimming pool waters

Rosa Olivé-Monllau^a, Jahir Orozco^b, César Fernández-Sánchez^b, Mireia Baeza^{a,*}, Jordi Bartrolí^a, Cecilia Jimenez-Jorquera^b, Francisco Céspedes^a

^a Grup de Sensors i Biosensors, Departament de Química, Facultat de Ciències, Edifici C-Nord, Universitat Autònoma de Barcelona, 08193 Bellaterra (Cerdanyola del Vallès), Spain

^b Instituto de Microelectrónica de Barcelona (IMB-CNM), CSIC. Campus UAB, 08193 Bellaterra, Spain

ARTICLE INFO

Article history:

Received 7 May 2008

Received in revised form 2 October 2008

Accepted 6 October 2008

Available online 18 October 2008

Keywords:

Free chlorine analysis

FIA system

Gold miniaturized thin-film transducer

Amperometric detection

Swimming pool water

ABSTRACT

This work reports on the performance of a user-friendly flow injection analysis (FIA) system for the monitoring of free chlorine. A methacrylate flow cell integrating a gold thin-film microelectrode, together with an on-chip gold counter electrode, both fabricated by microfabrication technology, provided robustness, low output impedance, rapid response and low cost to the proposed flow system. An external Ag/AgCl reference electrode placed downstream the chip completes the electrochemical cell. Amperometric detection of chlorine was carried out at a set potential of +350 mV, without oxygen interference. The proposed flow system responded linearly to chlorine concentrations in a range from 0.2 to 5 mg l⁻¹, with a sensitivity of 0.23 μ A l mg⁻¹, the estimated limit of detection being 0.02 mg l⁻¹. In addition, the system response was kept stable for at least 10 days ($\pm 3\sigma$ criterion), by keeping the flow system in an inert atmosphere when not in use. Fifteen samples of swimming pool waters were analyzed and no matrix effects were detected. Also, results were in good agreement with those obtained by a standard method. The excellent analytical performance of the system together with its good working stability would also enable its application for the detection of chlorine in other matrices such as tap water or chlorine stock solutions.

© 2008 Elsevier B.V. All rights reserved.

1. Introduction

Chlorine is a powerful oxidizing agent used in water disinfection, bleaching and other numerous manufacturing processes [1]. The hazard of an insufficient disinfection, the objectionable odour in treated water, as well as the increase of trihalomethane levels produced by chlorine overfeeding make the measurement and control of chlorine concentration highly recommendable in waters where disinfection processes are required. Up to now, different standard methods, mainly based on classical volumetric approaches, have been defined to analyze free chlorine in tap water and wastewater [2–4]. The increasing need to generate more rapid and automatic chemical information has led to the development of different analytical laboratory methods for the determination of free chlorine, which rely on optical [5,6] or electrochemical techniques [7–13]. Among them, electrochemical techniques are very versatile and, in turn, provide several advantages such as low cost processing, fast and reproducible data acquisition and easy handling.

Free chlorine concentration (the sum of dissolved chlorine gas (Cl₂), hypochlorous acid (HClO) and hypochlorite anion (ClO⁻) depending on the pH of the medium) is of special importance to define levels of the quality of disinfection in swimming pool waters. Its determination is currently carried out by means of the standard *N,N*-diethyl-*p*-phenylenediamine (DPD) colorimetric method [2,14]. This method is simple but it is not highly precise and cannot be applied in continuous systems.

The development of autonomous analytical systems for free chlorine monitoring, which overcome the above-mentioned drawbacks is of high interest. Several methods for the continuous detection of residual chlorine in either tap water [12,15] or environmental water samples [8] have been reported. They offer several advantages with respect to analytical systems working in batch, such as rapidity, accuracy, minimal reagent consumption and on-line monitoring of the target analyte. Indeed, such systems enable the real-time on-site reading of chlorine concentrations, thus minimizing variations of the sample composition due to transportation or storage.

Miniaturized solid-state thin-film electrochemical transducers [16,17], fabricated by microfabrication processes appear to be useful for environmental applications working in harsh conditions. They were easily integrated within small detection probes designed

* Corresponding author. Tel.: +34 93 5814927; fax: +34 93 5812379.

E-mail address: mariadelmar.baeza@uab.cat (M. Baeza).

for specific in-field measurements [18–21] and also integrated in flow systems for on-line measurements [8–10]. Previous works on the use of such devices for chlorine determination have been reported [14,22]. However, they were just applied to tap water analysis. Moreover, potential steps had to be carried out in between measurements in order to extend the device lifetime, making the approach less appealing from a practical point of view.

Here, the application of amperometric thin-film electrodes combined with a flow injection analysis system for the sensitive detection of free chlorine is reported. Gold and platinum electrodes were applied in batch conditions using voltammetric techniques. Au electrodes were selected and implemented in a FIA system and then evaluated for the continuous detection of this target analyte. The benefits of using this approach in terms of analytical performance and device stability are described and demonstrated by carrying out the successful analysis of chlorine in complex matrices coming from a swimming pool.

2. Experimental

2.1. Reagents and solutions

Ethanol (95%), acetone, $K_3Fe(CN)_6$, sodium hypochlorite (10–13%) and potassium dihydrogen phosphate were all purchased from Sigma–Aldrich (St. Louis, MO, USA) and used as received. All other chemicals were of analytical reagent grade. All solutions were prepared using de-ionized water from a Milli-Q system (Millipore, Billerica, MA, USA).

2.2. Devices and apparatus

Au and Pt microelectrodes were fabricated at the Instituto de Microelectrónica de Barcelona (IMB-CNM) according to standard photolithographic technology. The fabrication process is explained elsewhere [23]. The chips fabricated with a size of $3\text{ mm} \times 3.5\text{ mm}$ included a 2.77 mm^2 counter electrode, separated $0.5\text{ }\mu\text{m}$ from a 1.62 mm^2 working electrode. An image of one chip is depicted in Fig. 1(inset).

An amperometric cell was used for batch measurements. It contained an Au or Pt microelectrode as working electrode, an external Pt counter electrode (XE100, Radiometer Analytical, Villeurbanne CEDEX, Lyon, France) and a Ag/AgCl/10% (w/v) KNO_3 reference electrode (0726.100 Metrohm, Herisau, Switzerland). A μ -Autolab potentiostat/galvanostat (EcoChemie B.V, Utrecht, The Netherlands), using GPES 4.7 software package (General Purpose

Electrochemical System) was used for batch voltammetric and amperometric measurements.

Amperometric measurements with the FIA system were carried out by means of an amperimeter LC-4C (Bio analytical Systems Inc., USA) together with a data acquisition card ADC-42 (Technology Limited, St. Neots, Cambridgeshire, UK) and a personal computer for data recording and visualization. An Au working electrode chip also including an Au counter electrode, as described above, were inserted in a home made flow cell (6.3 mm^3 internal volume) based on two methacrylate blocks [24]. A double junction Ag/AgCl reference electrode ORION 900200 was placed downstream the microelectrode cell by means of a methacrylate assembly. The electrode external solution was the same one used as the carrier in the flow system. A scheme of the FIA system is depicted in Fig. 1. Together with the flow cell, it incorporates a manifold with three channels, one for the sample and calibration solutions, one for the conditioning solution used for analysis of the swimming pool water samples (that adjusted the ionic strength and pH of the sample) and one for the carrier solution. A four-channel peristaltic pump (Gilson) for liquid pumping equipped with silicon pump tubing (Elkay Products), a six-port injection valve (Hamilton) and 0.7 mm -internal diameter Teflon tubing (Omnifit) completed the system.

2.3. Analytical performance

All experiments were performed at room temperature. Microelectrodes were initially cleaned using a brush successively wetted in 95% ethanol, de-ionized water and acetone. Then, they were dried with nitrogen and electrochemically activated by repeated potential cycling (15 times) in a window between $+0.8$ and -2.2 V , in a 0.1 M KNO_3 solution. The electrochemical behaviour of the cleaned electrodes was tested in a 0.1 M KNO_3 solution containing $1.0\text{ mM K}_3Fe(CN)_6$ at 50 mV s^{-1} .

Hydrodynamic curves were plotted to define the optimal amperometric detection potential. These experiments were carried out in a 4.0 mg l^{-1} free chlorine solution, prepared by dilution of a 2000 mg l^{-1} stock solution in DI water. A fixed potential of $+1.05\text{ V}$ was firstly applied for 30 s followed by successive step potentials, ranging from $+1.0$ to 0.0 V , the output current intensity being then recorded.

The chronoamperometric response of the microelectrodes to free chlorine was initially evaluated in batch, in a 0.1 M phosphate buffer background solution, pH 5.5, containing 0.1 M KNO_3 (PBS) and adding successive amounts of the analyte. A pre-conditioning step was performed between each measurement by applying a

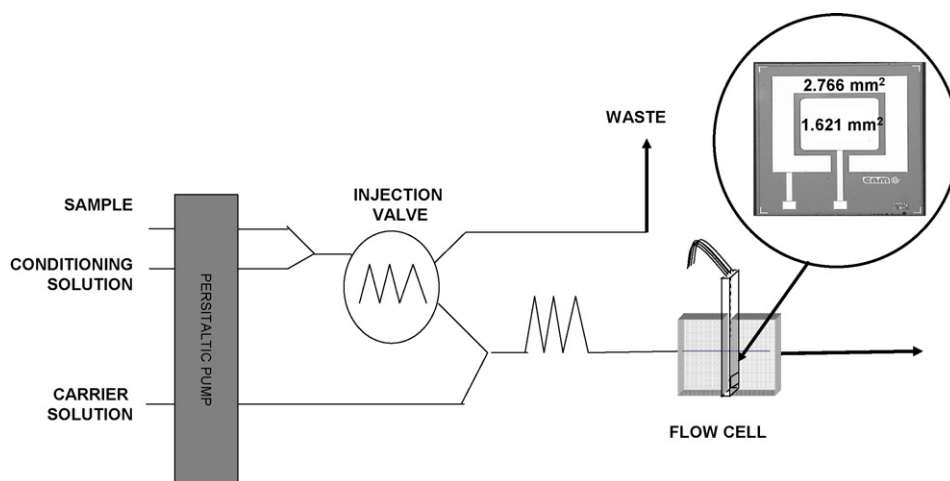


Fig. 1. Schematic representation of the FIA setup for chlorine analysis. Inset: Optical image of an Au microelectrode including an on-chip Au counter electrode.

potential of +0.35 V for 10 s in the background electrolyte solution. Chlorine detection in the described FIA system was performed at a set potential of +0.35 V. PBS was used as the flow carrier in the FIA system. The analytical response was evaluated using different standard solutions, in a concentration range between 0 and 5 mg l⁻¹, prepared by dilution of the stock solution with DI water.

For the analysis of swimming pool waters samples, an additional flow channel was introduced in a system (Fig. 1) in order to carry out a pre-conditioning step. This consisted in the dilution of the sample in 0.2 M PBS, pH 5.5, containing 0.2 M KNO₃. Fifteen real samples were collected from the swimming pool located at the sport facilities of the Universitat Autònoma de Barcelona (UAB). Six synthetic samples were prepared by dilution of the stock solution with DI water. The samples were analyzed immediately using the described FIA system and results compared with those obtained using the standard DPD colorimetric method [2,14]. These free chlorine analyses were carried out with reagents provided by HACH Lange Company and the absorbance was measured by means of a commercial colorimeter. All chlorine measurements obtained were in the mg l⁻¹ range.

3. Results and discussion

3.1. Electrochemical characterization of microelectrodes

Cyclic voltammetric experiments were carried out to evaluate the electrochemical performance of the fabricated microelectrodes. An electrochemical activation process, described in Section 2, was found to be necessary in order to get a clean metal surface. Cyclic voltammograms recorded in a ferricyanide solution with 15 microelectrode devices, showed their excellent performance and the high response reproducibility attained. The peak current of the ferricyanide reduction process, the cathodic peak current to anodic peak current ratio and the peak potential difference values were 2.93 μ A (SD = 0.06), 1.04 (SD = 0.02) and 70 mV (SD = 2), respectively.

3.2. Chronoamperometric experiments

In order to avoid interferences such as chloramines or oxygen, setting the polarization potential appropriately is highly desirable [12]. Herein, a hydrodynamic curve was plotted (Fig. 2). This curve showed a plateau at which the reduction of the hypochlorite species to give chloride took place. This plateau expanded from +350 to +475 mV and from +350 to +625 mV, for Au and

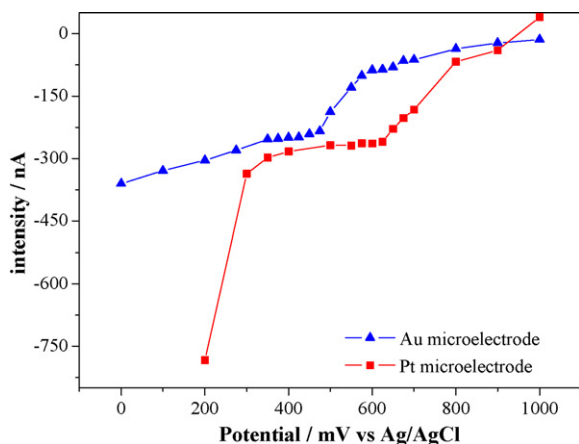


Fig. 2. Free chlorine hydrodynamic curves recorded with both Au and Pt microelectrodes. 4.0 ppm of Free chlorine concentration was 4.0 mg l⁻¹. Measurements were carried out in PBS pH 5.5.

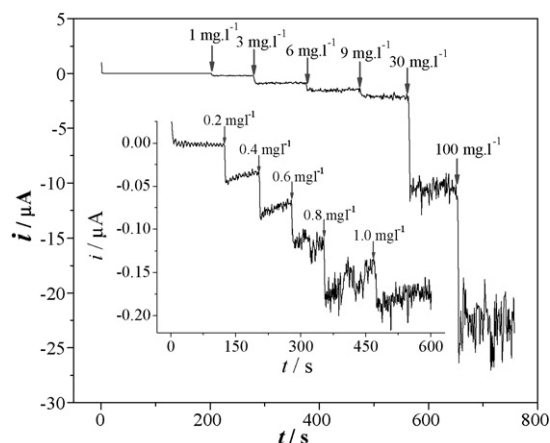


Fig. 3. Amperometric dynamic response of an Au microelectrode in a chlorine concentration range from 0.2 to 100 mg l⁻¹. Inset: amplified plot of the lower chlorine concentration range.

Pt microelectrodes, respectively. It was noticed that at potentials below +350 mV, the dissolved oxygen reduction over Pt and Au microelectrodes takes place, being Au less influenced than Pt. Such observation was also made elsewhere [14]. Therefore, in order to guarantee the absence of oxygen interferences an optimum potential of +350 mV was chosen for subsequent measurements. This value is in agreement with the working potential used by other authors, at pH 5.5 [8,25,26].

The Au electrode response to changes in concentration of free chlorine was evaluated by chronoamperometric measurements. Fig. 3 shows the electrode dynamic response to different additions of free chlorine. A linear relationship between the chlorine concentration and the cathodic current (in absolute value) was observed for three different concentration ranges (measurements carried out in triplicate). The lower linear range expands from 0.2 to 1 mg l⁻¹, the sensitivity being 0.191 μ A l mg⁻¹ (RSD = 1%, r^2 = 0.996, 95% confidence). The limit of detection (LOD) was estimated using the $3S_B/m$ IUPAC criteria [27], where m is the slope of the linear calibration plot and S_B corresponds to the standard deviation of the sensor response in the absence of chlorine (blank). This was 0.08 mg l⁻¹ of free chlorine, which is in agreement with values reported by other authors [8,15]. Regarding the free chlorine concentration in the water supply systems [28], these sensors may be suitable for monitoring free chlorine in tap water.

The Au microelectrode also responded linearly in a wider concentration range between 0.2 and 10 mg l⁻¹, with a sensitivity of 0.23 μ A l mg⁻¹ (RSD = 5%, r^2 = 0.993, 95% confidence). This concentration range is suitable for monitoring free chlorine in swimming pool waters taking into account that levels are usually found between 0.5 and 2.0 mg l⁻¹ [29].

A third linear concentration range was found between 10 and 100 mg l⁻¹ free chlorine. The electrode sensitivity was 0.21 μ A l mg⁻¹ (RSD = 6%, r^2 = 0.9999, n = 3, 95% confidence). Herein, it is shown that Au microelectrodes may be really useful to analyze samples with high levels of free chlorine, such as liquefied chlorine stock solutions, disinfecting solutions for cleaning in place (CIP) or sanitization in place (SIP) systems [9,30].

These results showed that the gold microelectrode response was highly reproducible in all the concentration ranges studied. A similar behaviour was also observed for chlorine concentrations up to 250 mg l⁻¹. However, fouling of the electrode surface was here more accused, which made it necessary to apply an electrochemical treatment, in-between calibrations, similar to the one described for the initial electrode activation.

It is important to remark that similar results were obtained with Pt microelectrodes in terms of sensitivity, reproducibility and linear range. However, the estimated limit of detection was higher and the estimated repeatability (consecutive measurements in the same chlorine solution carried with the same electrode) was worse. This behaviour may be explained by the fast fouling of the Pt microelectrode surface in the presence of free chlorine and the fact that gold microelectrodes are less influenced by dissolved oxygen than platinum ones, as pointed out above [8,15]. Therefore, Au microelectrodes were chosen and applied in the FIA system.

3.3. Amperometric flow injection analysis

The hydrodynamic experimental parameters of the FIA system were set at $2\text{ cm}^3\text{ min}^{-1}$ flow rate, $600\text{ }\mu\text{l}$ injection volume, 85 cm long reaction coil and $+350\text{ mV}$ potential (previously set in batch, as described above). The analysis time for each sample was 2 min (time from injection to steady-state signal). Several analytical parameters were evaluated, that is, signal repeatability, system reproducibility and long term stability.

In order to evaluate the signal repeatability, a 2 ppm standard solution was used. A RSD value of 1% was obtained for 12 consecutive chlorine measurements, the mean current value being $-0.53\text{ }\mu\text{A}$.

The Au microelectrode response in the FIA system was evaluated in a range between 0.2 and 5 mg l^{-1} (Fig. 4). This concentration range was chosen because it matches the minimum and maximum legal chlorine concentration permitted by the current Spanish legislation in swimming pool waters [29,31]. The mean sensitivity, for three calibration plots and 95% confidence, was $0.23\text{ }\mu\text{A l mg}^{-1}$, with a RSD of 4% . The obtained results showed a linear response in the whole evaluated range. Fig. 4 also shows the excellent repeatability and reproducibility of the FIA system. In order to get a careful estimation of the experimental LOD, three calibration plots in a narrow concentration interval from 0.01 to 0.1 mg l^{-1} were performed. A LOD of 0.02 mg l^{-1} , according to the $3S_b/m$ IUPAC criteria, was obtained.

It is well known that metallic electrodes undergo a degradation process in contact with chlorine solutions [14,22]. Therefore, a study of the degradation of the Au microelectrode surface in the FIA system was required. The microelectrode voltammetric response was recorded in a $1\text{ mM K}_3\text{Fe(CN)}_6$ in 0.1 M KNO_3 solution before and after carrying out the calibration process. As it is shown in Fig. 5, the electrochemical response of the microelectrode to $\text{Fe}^{3+}/\text{Fe}^{2+}$ redox pair decreased significantly after a chlorine cali-

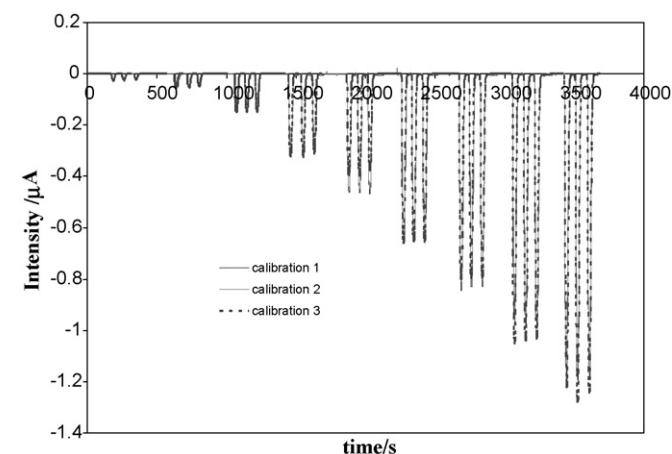


Fig. 4. Amperograms recorded with the FIA system for three calibrations experiments carried out from 0.2 to 5 mg l^{-1} chlorine concentrations.

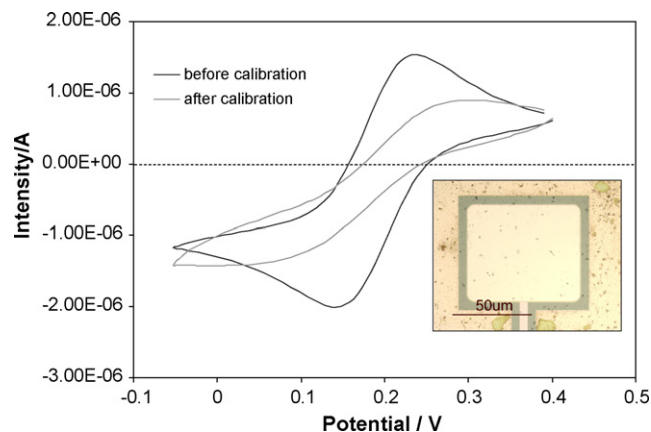


Fig. 5. Cyclic voltammograms recorded before and after performing a chlorine calibration. Inset: optical image of the surface of an Au microelectrode surface after carrying out a calibration experiment.

bration step. This behaviour might be explained by the degradation of the Au surface in contact with the analyte solution and oxidation of the counter electrode as was observed by optical microscopy. (See inset image of microelectrode surface after a calibration run.) This behaviour was also reported elsewhere [15].

In order to make an estimation of the loss of sensitivity due to the decrease of microelectrode active surface, successive calibration plots were carried out for 4 days without performing activation steps and keeping the microelectrodes in the flow system. Results are shown in Table 1. Sensitivity values were reproducible when considering those calibration processes carried out the same day. By contrast, the mean sensitivity values obtained during the 4-day period decreased significantly. The sensor response steadily deteriorated until it lost linearity in the fourth working day. Regarding this results, a simple approach was implemented that resulted in a great improvement in the sensor lifetime. This consisted of keeping the electrochemical cell in an inert atmosphere while not in use. Indeed, N_2 gas was pumped in the flow channel for 5 min and then the FIA system was sealed. Calibration experiments were then carried out with two different gold microelectrodes for several days. The shift in the mean sensitivity values (calculated from the values of consecutive calibrations carried out within one working day) was plotted against time for each microelectrode. The mean value of the calibration plots carried out the first working day was used to calculate the control/nominal sensitivity value. The upper and lower control limits were set at three times the standard deviation ($3S$) of this value. Results showed that after 10 days the sensitivity was still within the control limits (Fig. 6). This demonstrates that the simple procedure explained above increased the sensor lifetime for at least 10 days. The sensitivity of the calibration curves recorded with both Au microelectrodes showed a coefficient of variation around 5% ($n = 13$). It is important to underline the necessity

Table 1

Calibration parameters obtained with the flow system for successive chlorine calibration experiments.

Day	Sensitivity ($\mu\text{A l mg}^{-1}$)	R^2 ($n = 3$)
1	$-0.23 (\pm 0.01)$	0.996
2	$-0.20 (\pm 0.02)$	0.994
	$-0.20 (\pm 0.02)$	0.995
3	$-0.15 (\pm 0.02)$	0.990
	$-0.15 (\pm 0.02)$	0.990
4	$-0.18 (\pm 0.05)$	0.950
	$-0.19 (\pm 0.04)$	0.970

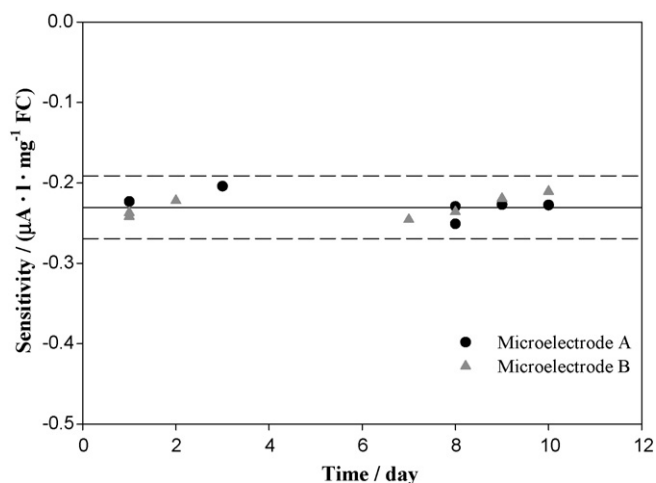


Fig. 6. Variation of the Au microelectrode sensitivity upon carrying out measurements for a 10-day period of time. All values lie between the $\pm 3\sigma$ interval.

of carrying out an electrochemical activation step, as described in the experimental section, after a 10-day working period in order to keep the good performance of the Au microelectrodes in the FIA system for longer periods of time. Overall, it is shown here that the proposed approach enables the reliable amperometric monitoring of free chlorine for up to 10 consecutive days.

3.4. Analysis of swimming pool water samples

Swimming pool water is a complex matrix that contains not only chlorine, but also compounds like chloramines, uric acid, citric acid and organic matter. Additionally, the high volatility of chlorine makes sample conservation very challenging. In order to overcome matrix effects, a new channel upstream the sample injection valve was inserted in the FIA system (Fig. 1, conditioning solution channel). The flow rate used was the same in the three flow channels (2 ml min^{-1}). This extra-channel induces the dilution of the sample by a factor of 2. This was tested by carrying out several consecutive calibration plots. The average sensitivity was $0.10 \pm 0.02 \mu\text{A l mg}^{-1}$ ($n=4$, 95% confidence), this value being less than half the sensitivity value obtained without the conditioning solution channel ($0.23 \mu\text{A l mg}^{-1}$). Besides, the LOD was also affected by this dilution factor, this being 0.06 mg l^{-1} free chlorine. Nevertheless the

in-line sample conditioning was suitable to minimize matrix effects and extend the system lifetime for continuous measurements of swimming pool samples.

Twenty-one samples were analyzed with the proposed system for a period of several days. Fifteen samples were directly collected from the swimming pool, and six samples were synthetically prepared and used as control. Results were compared with those obtained from the standard method using linear regression analysis (Fig. 7). A good correlation was found, which means that no significant differences were observed between both methods. The values of the slope and intercept were $0.94 (\pm 0.05)$ and $0.03 (\pm 0.06)$, respectively (r^2 0.984, $n = 21$, 95% confidence).

4. Conclusions

The amperometric detection of chlorine using thin-film Au microelectrodes integrated in a FIA system was successfully carried out at those concentration levels required for the analysis of this species in swimming pool water samples. Besides, the proposed microelectrodes responded linearly in a wide concentration range, which make them suitable for other applications such as a tap water and chlorine stock solution analyses.

Degradation of metallic surfaces upon being in contact with chlorine solutions seems to make Au microelectrodes unsuitable for continuous chlorine detection. This drawback was here overcome by implementing a simple procedure consisting in keeping the detection system in an inert atmosphere when not in use. Thus, the sensor lifetime was extended for at least 10 days. Matrix effects were avoided by inserting an extra-channel in the flow system that enabled the sample dilution before reaching the detection system by a factor of 2. An excellent agreement between the results obtained with the proposed system and a standard method for chlorine determination was achieved, thus demonstrating the potential of the FIA system for the rapid and reliable monitoring of chlorine levels in swimming pool waters. In order to further improve the detection system lifetime, future work will be directed towards the deposition of a suitable membrane at the microelectrode surface that prevented its degradation by the action of this target species more efficiently.

Acknowledgements

The work has been supported by the DPI2003-08229-C03 project from the Spanish Ministry of Science and Education (MEC). R. Olivé-Monllau and J. Orozco's thanks Universitat Autònoma de Barcelona (UAB) and MEC for the award of PIF and a FPI studentship, respectively.

References

- [1] G.C. White, Handbook of Chlorination, Van Nostrand Reinhold, New York, 1986.
- [2] U.E.P.A Methods 330.1 to 330.5, 1978.
- [3] UNE-EN ISO 7393-1 to 73-93-3, 2000.
- [4] Standard Methods for the Examination of Water and Wastewater, 21st Edition, 2005.
- [5] J.B. Claver, M.C.V. Miron, L.F. Capitan-Vallvey, *Analytica Chimica Acta* 522 (2004) 267.
- [6] M. Ralfs, J. Heinze, *Sensors and Actuators B-Chemical* 44 (1997) 257.
- [7] Edstrom-Industries, Forms of Chlorine in water (4230-MI4148), WI, USA www.edstrom.com.
- [8] J.Y. Jin, Y. Suzuki, N. Ishikawa, T. Takeuchi, *Analytical Sciences* 20 (2004) 205.
- [9] S.Y. Kishioka, T. Kosugi, A. Yamada, *Electroanalysis* 17 (2005) 724.
- [10] F. Koder, M. Umeda, A. Yamada, *Analytica Chimica Acta* 537 (2005) 293.
- [11] W. Matuszewski, M. Trojanowicz, *Analytica Chimica Acta* 207 (1988) 59.
- [12] A. Okumura, A. Hirabayashi, Y. Sasaki, R. Miyake, *Analytical Sciences* 17 (2001) 1113.
- [13] A.P. Soldatkin, D.V. Gorchkov, C. Martelet, N. Jaffrezic-Renault, *Sensors and Actuators B-Chemical* 43 (1997) 99.

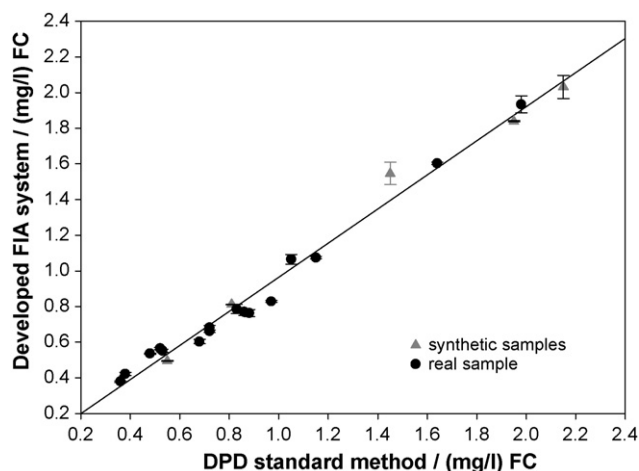


Fig. 7. Linear regression analysis comparing the standard method (DPD colorimetric) and the described FIA system.

- [14] L. Moberg, B. Karlberg, *Analytica Chimica Acta* 407 (2000) 127.
- [15] F.J. Del Campo, O. Ordeig, F.J. Munoz, *Analytica Chimica Acta* 554 (2005) 98.
- [16] J.K. Atkinson, A.W.J. Cranny, W.V. Glasspool, J.A. Mihell, *Sensors and Actuators B-Chemical* 54 (1999) 215.
- [17] K. Cammann, *Sensors and Actuators B-Chemical* 6 (1992) 19.
- [18] J. Artigas, A. Beltran, C. Jimenez, A. Baldi, R. Mas, C. Dominguez, J. Alonso, *Computers and Electronics in Agriculture* 31 (2001) 281.
- [19] L. Campanella, C. Colapicchioni, G. Crescentini, M.P. Sammartino, Y. Su, M. Tomassetti, *Sensors and Actuators B-Chemical* 27 (1995) 329.
- [20] J.H. Lee, A. Jang, P.R. Bhadri, R.R. Myers, W. Timmons, F.R. Beyette, P.L. Bishop, I. Papautsky, *Sensors and Actuators B-Chemical* 115 (2006) 220.
- [21] J. Orozco, A. Baldi, P.L. Martin, A. Bratov, C. Jimenez, *Analytica Chimica Acta* 579 (2006) 95.
- [22] O. Ordeig, R. Mas, J. Gonzalo, F.J. Del Campo, F.J. Munoz, C. de Haro, *Electroanalysis* 17 (2005) 1641.
- [23] J. Orozco, G. Suarez, C. Fernandez-Sanchez, C. McNeil, C. Jimenez-Jorquera, *Electrochimica Acta* 53 (2007) 729.
- [24] J. Artigas, C. Jimenez, C. Dominguez, S. Minguez, A. Gonzalo, J. Alonso, *Sensors and Actuators B-Chemical* 89 (2003) 199.
- [25] A. van den Berg, M. Archenault, K.-H. M. A. van der Schoot, G. A. d.R. N.F, *Proceedings of the Seventh International Conference on Solid-State Sensors and Actuators*, 1993, p. 936.
- [26] A. Vandenberg, A. Grisel, E. Verneynorberg, B.H. Vanderschoot, M. Koudelkahep, N.F. Derooij, *Sensors and Actuators B-Chemical* 13 (1993) 396.
- [27] G.L. Long, J.D. Winefordner, *Analytical Chemistry* 55 (1983) A712.
- [28] *Drinking Water Contaminants*, 2003.
- [29] Boletín oficial del estado (BOE). Ley 14, 25 abril, 1986, p. 102.
- [30] G. Agius, S. Burkeen, J. Mynatt, *Master Brewers Association of the Americans* 41 (2004) 42.
- [31] *Diari Oficial de la Generalitat de Catalunya*, DOGC, Decret 95, 22 Febrero, Generalitat de Catalunya, 2000, p. 2338.



Application of tandem column solid phase extraction and flame atomic absorption spectrometry for the determination of inorganic and organically bound forms of iron in wine

Pawel Pohl*, Bartłomiej Prusisz

Analytical Chemistry Division, Faculty of Chemistry, Wrocław University of Technology, Wybrzeże Stanisława Wyspiańskiego 27, 50-370 Wrocław, Poland

ARTICLE INFO

Article history:

Received 21 April 2008

Received in revised form 2 October 2008

Accepted 6 October 2008

Available online 17 October 2008

Keywords:

Wine

Iron

Fractionation

Solid phase extraction

Flame atomic absorption spectrometry

ABSTRACT

A tandem column solid phase extraction (SPE) procedure has been devised to examine the fractionation of Fe in wine. Wine was filtered through a 0.45 μm filter and then, the filtrate was driven through an adsorbing Amberlite XAD-7HP column followed by a cation exchange Dowex 50W-x8-200 column. Three different Fe groupings are discriminated and assessed, including hydrophobic species of Fe bound to phenolic substances and related species (phenolic fraction), cationic species comprising simple Fe ions and labile Fe forms (cationic fraction), in addition to anionic and/or neutral Fe complexes with organic acids (residual fraction). The suitability of the procedure has been evaluated analyzing four bottled red wines. The results obtained were verified using another tandem column assemblage in which an adsorbing Amberlite XAD-16 column was exchanged by the Amberlite XAD-7HP column. The fractionation pattern ascertained for Fe in analyzed wines is discussed in reference to previously published works. In addition, a conditioning treatment and preparation of Amberlite XAD resins have been revised.

© 2008 Elsevier B.V. All rights reserved.

1. Introduction

The method development in the determination of distinct Fe speciation or fractionation forms in wine is of special significance because individual metal species affect wine quality and exhibit differentiated toxicity and bioavailability [1–3]. Normally, in fermented wines the main part of Fe is present in the form of ferrous ions, Fe(II), while the content of ferric ions, Fe(III), is much lower. When wine is exposed to air during a further enological treatment, Fe(II) ions can be readily oxidized to Fe(III) form and a wine spoilage may be activated. The extent of this process is dependent on the concentrations of both inorganic Fe(II, III) forms as well as their mutual ratio, and strictly determine wine stability, color and clarity [4,5]. It is because the Fe inorganic forms actively participate in the formation of the reactive oxygen species which subsequently oxidize wine components, mostly phenolics, and other compounds, e.g., ethanol, glycerol, sugars or organic acids [6–9].

Because of Fe bioavailability, interactions of Fe(II, III) ions with phenolic compounds are also of a great concern. It is supposed that complexes of Fe with phenolics are less available. Moreover, some proteins can bind inorganic Fe ions or complexes of proteins

together with Fe ions and phenolics may be formed. All these Fe species significantly inhibit its absorbability from wine [10].

For the reasons stated above it is evident that dependable analytical methods enabling to speciate Fe in wine are very useful in retrieving the information necessary to understand spoilage processes occurred in wine and potential Fe toxicity related to wine consumption [1,3,11,12]. However, the speciation and fractionation studies in which both inorganic and organically bound Fe species can be determined are very few [13]. Ultrafiltration with molecular weight cut-offs ranged from 100 000 to 1 000 Da was applied before and provided the size fractionation pattern of compounds interacting with Fe in wine and being distributed between insoluble-suspended and dissolved fractions [11]. The determination of dissolved and suspended Fe species was also achieved using a sequential cloud point extraction [13]. The Fe species associated with tannins and other phenolic and insoluble compounds were isolated using micelles of non-ionic surfactants. In addition, free Fe species were also entrapped into micelles in the supernatant resulting from centrifugation of the precipitated organically bound Fe species but as a water-insoluble complex with ammonium pyrrolidone dithiocarbamate (APDC).

Solid phase extraction (SPE) appears to be a very advantageous method for the speciation and fractionation of Fe in wine due to differences in chemical properties of the existing Fe species. Typically, Fe(II, III) inorganic species can be distinguished after chelation of one or both forms with appropriate complexing agents and reten-

* Corresponding author. Tel.: +48 71 320 3445; fax: +48 71 320 2494.
E-mail address: pawel.pohl@pwr.wroc.pl (P. Pohl).

tion of the resulted Fe(II) and/or Fe(III) complexes, differing in charge and hydrophobicity, on selected resins [14–17]. The determinations of Fe(II, III) inorganic species are preceded by removing Fe species bound to tannins and other phenolic substances [15,16].

When using both ion exchange and non-ionic adsorbing resins for SPE it is possible to determine inorganic and organically bound Fe species, but such approach has been reported so far only in a few contributions [14,16,17]. Moreover, a careful analysis of the experimental conditions under which the speciation of Fe was undertaken in the cited works indicate some inconsistencies that could have affected the fractionation analysis and caused certain artifacts in fractionation patterns of Fe obtained for studied wines. Accordingly, to determine inorganic Fe(II, III) species retained on a strong cation exchanger Dowex 50W-x8, Ajlec and Stupar [14] prepared wine samples in a 0.1 mol l^{-1} HNO_3 solution. To estimate organic Fe species retained on an adsorbing resin Amberlite XAD-2, they used a 0.02 mol l^{-1} HNO_3 solution to prepare wine solutions. As a result, no organically bound Fe species fraction was found in analyzed wines. These species might have been retained on the cation exchanger or decomposed due to an equilibrium alteration. In a two-step fractionation scheme reported by Karadjova et al. [16] sample volumes analyzed at the second step (1 ml) seem to be very small for a convenient column operation, when considering resin masses (0.5–1 g) and dead volumes of the respective SPE columns. In addition, both Amberlite XAD resins required a special treatment aimed at blocking hypothetical cation exchange active sites responsible for sorption of simple Fe ions. Finally, Tasev et al. [17] used a self-made sorbent containing silica gel beads and pieces of a filter paper soaked with a trioctylmethylammonium chloride (TOMACI) solution to retain organically bound Fe species, or, in the second turn, the sum of the latter Fe species and Fe(III) inorganic species previously complexed with oxalic acid. All organically bound Fe species were suspected to be negatively charged and retained on the sorbent through attractions with TOMA^+ ions. However, organically bound Fe species could rather be retained on the sorbent due to some hydrophobic interactions with the surface of the silica gel and the use of MIBK for the elution reveals this conclusion. Besides, wine samples were diluted before the analysis what could have altered to some extent the equilibrium between the species.

The present study was attempted to devise a new simpler and more consistent fractionation scheme based on SPE for partitioning the Fe species. Two tandem column assemblages, *i.e.*, Amberlite XAD-7HP–Dowex 50W-x8-200 and Amberlite XAD-16–Dowex 50W-x8-200, were proposed and their suitability for the determination of three different classes of Fe species in wine was assessed. Additionally, the method of Amberlite XAD resins preparation for the fractionation analysis was revised. Both tandem column systems described were used for the fractionation of Fe in four bottled Bulgarian, Moldavian and Ukrainian red wines. The separated fractions were operationally defined and referred to Fe species bound to hydrophobic and high molecular weight organic compounds, mostly phenolic species (phenolic fraction), inorganic Fe forms being the sum of simple Fe(II, III) ions and labile Fe species (cationic fraction), and finally negatively charged complexes of Fe(III) with low molecular weight organic acids and other inorganic ligands, in addition to neutral Fe(II, III) species (residual fraction).

2. Experimental

2.1. Apparatus and materials

A Perkin-Elmer 1100B atomic absorption spectrometer (Germany), equipped with a single slot 10-cm titanium burner head for air-acetylene flame, a plastic mixing chamber with a flow spoiler, a

stainless steel nebulizer, and a drain siphon interlock, was applied for measurements. A two standard addition method was used for the determination of the Fe content in all solutions. Operating parameters recommended by the instrument manufacturer were used, including gas flow rates of 8.0 and 2.5 l min^{-1} , respectively, for air and acetylene, a spectral bandwidth of 0.2 nm, and a hollow cathode lamp current of 15 mA. A time-shared background correction of measured absorbance at 248.3 nm was performed using a deuterium lamp. A time-average integration (hold mode) with an integration time of 1 s and three replicates was used for a signal readout. The detection limit (DL) of 0.01 mg l^{-1} and the upper linearity range of 10 mg l^{-1} were established for Fe.

A digital pH-meter PM1 (TMS Electronics, Poland) with a combined electrode was used for the measurements of pH in wine. A Supelco (USA) filtration apparatus consisted of a 250-ml glass reservoir, a tapered funnel base and a 1000-ml flask was used for wine filtration through $0.45 \mu\text{m}$ pore size Nylon 66 membrane filters (Supelco).

Non-ionic hydrophobic adsorbing resins Amberlite XAD-7HP (mesh size 20–60, cross-linked aliphatic acrylic polymer, surface area $450 \text{ m}^2 \text{ g}^{-1}$, pore size distribution 300–450 Å, dipole moment 1.8 D) and Amberlite XAD-16 (mesh size 20–60, cross-linked styrene–divinylbenzene copolymer, surface area $900 \text{ m}^2 \text{ g}^{-1}$, pore size distribution 80–320 Å, dipole moment 0.3 D), and a strong acidic cation exchanger Dowex 50W-x8-200 (mesh size 100–200, cross-linked styrene–divinylbenzene copolymer) were used for SPE. Polymeric sorbents were supplied by Supelco and were packed into Supelco glass columns (10 mm ID) equipped with coarse frits and Teflon stopcocks.

2.2. Reagents and solutions

Analytical grade chemical reagents from POCh (Poland), including concentrated nitric acid (HNO_3), concentrated hydrochloric acid (HCl), acetic acid ($\text{C}_2\text{H}_4\text{O}_2$), citric acid ($\text{C}_6\text{H}_8\text{O}_7 \cdot \text{H}_2\text{O}$, CA), tannic acid ($\text{C}_{76}\text{H}_{52}\text{O}_{46}$, TA), sodium hydroxide (NaOH), potassium hydrogen phthalate ($\text{C}_8\text{H}_5\text{KO}_4$), potassium chloride (KCl), sodium chloride (NaCl), calcium chloride ($\text{CaCl}_2 \cdot 6\text{H}_2\text{O}$), magnesium chloride ($\text{MgCl}_2 \cdot 6\text{H}_2\text{O}$), sodium acetate ($\text{C}_2\text{H}_3\text{NaO}_2$), methanol (CH_4O) and ethanol ($\text{C}_2\text{H}_6\text{O}$) were applied in the study. Although the predominant inorganic form of Fe in wine is Fe(II) ions, this form is readily oxidized to Fe(III) ions in the presence of O_2 dissolved in wine during its handling. The latter ions are also much willingly complexed by phenolic substances as compared to Fe(II) ions. For that reason Fe(III) ions were used in the experimental study. Merck (Germany) stock single-element standard solution (1000 mg l^{-1}) of Fe(III) was used to prepare its 20-ml working solutions at a concentration of 10 mg l^{-1} . These solutions also contained 10% (v/v) of ethanol, and Na, K, Ca and Mg at concentrations of 160, 1600, 120 and 360 mg l^{-1} , respectively, which corresponded to an average content of these constituents in wine [2]. Working solutions were adjusted to pH 3.0, 3.5, 4.0, 4.5 and 5.0 using 2 ml of 0.10 mol l^{-1} two-component buffer solutions containing $\text{C}_8\text{H}_5\text{KO}_4$ and HCl or NaOH, or $\text{C}_2\text{H}_3\text{NaO}_2$ and $\text{C}_2\text{H}_4\text{O}_2$. Solutions of CA or TA (5000 mg l^{-1}) were used to complex Fe(III) ions; the final concentration of both acids in working solutions was 500 mg l^{-1} . Doubly distilled water was used throughout.

2.3. Resin wetting and column preparation

Amberlite XAD resins as received were dried at first in an oven for 4 h at 110°C . The loss on drying of the initial mass of 58% for the Amberlite XAD-7HP resin and 64% in case of the Amberlite XAD-16 resin was found. Then, 1.5-g portions of the dried resins were placed in beakers and wetted with 20 ml of methanol. The mixtures

were stirred and the resins were allowed to stand for 20 min. Next, the resin beads were washed with doubly distilled water. For that aim, methanol was decanted and replaced with 20 ml of water. The mixtures were stirred again and the resins were allowed to stand for next 20 min. The latter operation was repeated and the resulted resin slurries were poured into the columns. The excess of water was drained and the resin beds formed were washed with 10 ml of a 1 mol l^{-1} HCl solution. Finally, they were rinsed with 20 ml of water to reach the column effluents neutral.

In case of Dowex 50W-x8-200, a 1.0-g portion of the resin as received was wetted with 20 ml of water. The mixture was stirred and the resin was allowed to stand for 20 min. This operation was repeated using a fresh portion of water. Finally, the resulted resin slurry was poured into the column. Next, the resin bed formed was washed with 10 ml of 1 mol l^{-1} HCl solution and the excess of HCl was removed by rinsing the column with 20 ml of water. Afterward, 10 ml of a 1 mol l^{-1} NaOH solution was passed through the column and rinsed with 20 ml of water.

All solutions and water were driven through the columns at a flow rate of 2 ml min^{-1} which was maintained by means of a 4-channel MasterFlex L/S peristaltic pump (Cole-Parmer, USA).

2.4. Column operation

To investigate sorption properties of polymeric sorbents used in the present study, i.e., Amberlite XAD-7HP, Amberlite XAD-16 and Dowex 50W-x8-200, 20-ml working solutions of simple Fe(III) ions or complexes of Fe(III) with CA and TA were passed through the resin beds at the flow rate of 1 ml min^{-1} . Portions (5 ml) of column effluents were collected and subsequently analyzed on the presence of Fe. The amounts of different Fe forms retained under certain experimental conditions were assessed subtracting the amounts of Fe not sorbed by the resins from the initial Fe amount present in working solution loaded onto the columns. Retention efficiencies (in %) were calculated relating these values to the original Fe content in working solution.

The suitability of HCl and HNO_3 solutions at concentrations corresponded to 1, 2 and 4 mol l^{-1} for the recovery of Fe-TA complexes from Amberlite XAD resins and simple Fe(III) ions from Dowex 50W-x8-200 was also examined. Working solutions of Fe (pH 4.5) were driven through the columns at the flow rate of 1 ml min^{-1} . Por-

tions (5 ml) of column effluents were saved and analyzed to assess the amounts of Fe retained. Next, 10 ml of tested stripping solutions were passed at the same flow rate to recover the solutes. Relevant portions of eluates (10 ml) were collected and analyzed on the presence of Fe. Recovery efficiencies (in %) were calculated relating the amounts of Fe recovered from the columns to the original content of Fe in working solutions; the amounts of Fe retained on the resins during the sample loading step were considered.

All retention and recovery efficiencies were mean values for three or six independent replicates. The respective column blanks were evaluated and taken into account in final results.

2.5. Sample treatment and fractionation procedure

Four commercially available bottled red wines from Bulgaria, Moldavia and Ukraine were analyzed. After opening, 150 ml of each wine was filtered through a $0.45 \mu\text{m}$ pore size membrane filter. The filtrate was immediately subjected to a further treatment. The total Fe concentrations in wines and their filtrates were determined after a 5-fold dilution of 2-ml sample portions and a subsequent acidification with 0.5 ml of concentrated HNO_3 . The analysis was performed in three separate samples and using two standard additions. Adequate blind samples were measured and considered in calculations.

The analytical procedure used for the fractionation of Fe in wine is schematically shown in Fig. 1. Briefly, 20-ml portion of filtered wine was driven at the flow rate of 1 ml min^{-1} through the first column (Amberlite XAD-7HP) connected with the second column (Dowex 50W-x8-200). When the effluent of the first column was passing through the second column, its 5-ml portion was sampled to evaluate the amount of Fe species bound to phenolic compounds and retained on the Amberlite XAD-7HP adsorbent (phenolic Fe species fraction). In addition, a 5-ml portion of the second column effluent was also collected to assess the amount of Fe species not retained on both sorbents (residual Fe species fraction). When the sample was passed through both columns, they were disconnected and cationic Fe species (cationic Fe species fraction) retained on the Dowex 50W-x8-200 column were eluted by passing 10 ml of a 2 mol l^{-1} HCl solution through the resin bed at the flow rate of 1 ml min^{-1} . All effluents and eluates were analyzed on the presence of Fe using two standard additions. Results of Fe fractionation

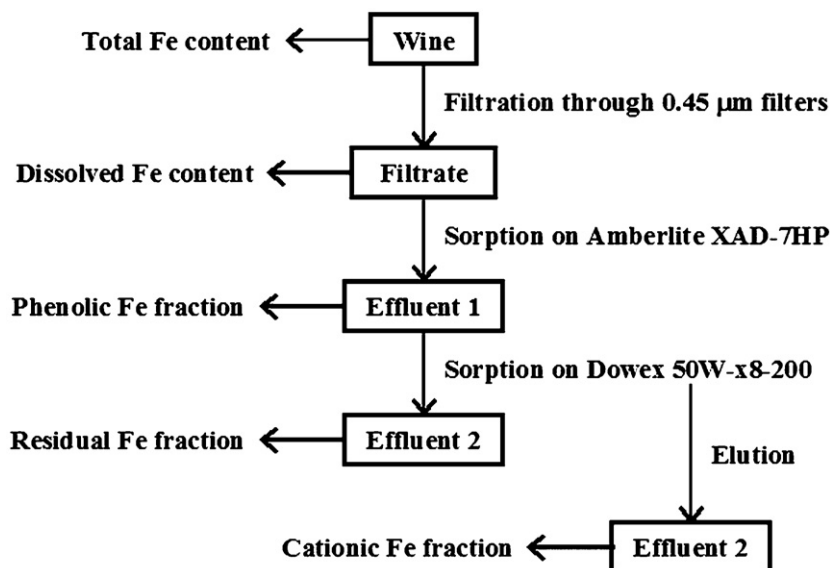


Fig. 1. The scheme of the fractionation procedure of Fe in wine.

analysis in wines achieved using Amberlite XAD-7HP–Dowex 50W-x8-200 linked columns were compared to those obtained with another tandem column assemblage in which Amberlite XAD-16 was used instead of Amberlite XAD-7HP.

3. Results and discussion

For a long time, non-polar macroreticular Amberlite XAD resins have been reputed to be convenient materials for the estimation of the fraction of Fe bound to high molecular weight polyphenolic substances [18]. Particularly, styrene–divinylbenzene copolymeric resins like Amberlite XAD-2 (Rohm and Haas) or its analogue SM-2 (Bio-Rad) were often applied for the determination of complexes of Fe or other metals with different humic substances in a variety of water samples. It was because of a high affinity of these resins toward the molecules with hydrophobic moieties [19–23]. However, the use of both adsorbents was connected with retention of substantial amounts of free bi- and trivalent metal cations. Free and inorganically complexed metal cations were also retained by the macroreticular acrylic ester resins like Amberlite XAD-7 or its substitute SM-7 [24,25]. It was believed this phenomenon was related to cation exchange attributed to the presence of polar impurities being products of a polymeric chain oxidation in case of styrene–divinylbenzene resins [26], or free carboxylic acid sites resulted from an incomplete ester methylation [25]. This drawback was usually overcome by treating the resins with In(III) ions in order to block the active cation exchange sites [19,20,22].

In the 1970s and the 1980s the supposition about cation exchange sites was likely to be true, but through the years, the production of adsorbing resins has been completely changed. These days, Amberlite XAD resins manufactured by Rohm and Haas company are of consistent and uniform quality, in compliance with GMP standards and complying with the latest requirements of different regulatory authorities. Therefore, the reason for which non-ionic hydrophobic resins are still reported to retain simple metal ions [16,27,28] should be quite different and it was revised in the present study.

3.1. Revision of resin conditioning treatment

Indeed, when using the Amberlite XAD-7HP resin and passing working solutions of simple Fe(III) ions through the columns at the flow rate of 1 ml min^{−1}, it was found that from 18 to 46% of the initial amount of Fe is retained on the resin at pH 3–5, adjusted using adequate phthalate buffers (Table 1). As can be seen, under the same conditions, the non-ionic hydrophobic adsorbing resin Amberlite XAD-16 exhibits even a higher retention of Fe(III) ions. In this case, Fe was recovered from column effluents with the efficiency of 27–37%, which indicates that the resin sorbs from 63 to 73% of the initial amount of Fe during loading the solutions on the columns.

Table 1

The retention efficiencies of the Fe(III) ions on the Amberlite XAD adsorbents from the solutions containing phthalate buffers. A, untreated resin; B, In(III)-treated resin.

pH	Retention efficiency ^a (%)			
	Amberlite XAD-7HP		Amberlite XAD-16	
	A	B	A	B
3.0	22 ± 3	30 ± 2	71 ± 4	76 ± 2
3.5	18 ± 3	43 ± 2	63 ± 2	73 ± 3
4.0	30 ± 2	44 ± 4	65 ± 4	81 ± 3
4.5	20 ± 2	43 ± 2	73 ± 3	82 ± 2
5.0	46 ± 3	49 ± 3	72 ± 3	80 ± 3

^a The mean values (*n* = 3) with figures behind being standard deviations.

Regarding lately reported comments on sorption of bi- and trivalent metal cations from aqueous solutions of pH 3–5 on non-ionic Amberlite XAD-8 [16] and Amberlite XAD-7 [27] adsorbing resins used for the fractionation analysis of Al, Cu, Fe and Zn, it was decided to condition both adsorbing resins with In(III) ions. Such a treatment was expected to block probable cation exchange active sites and eliminate or decrease retention of simple Fe(III) ions. Accordingly, 100 ml of a 100 mg l^{−1} In(III) solution were passed through Amberlite XAD-7HP and Amberlite XAD-16 resin beds at the flow rate of 1 ml min^{−1} and then, the columns were washed with 20 ml of water. However, this procedure has not led to a decrease of Fe(III) ions sorption at all. It was established that the In(III)-treated Amberlite XAD-7HP resin retains from 30 to 49% of the initial amount of Fe in loaded solutions (Table 1).

The behavior of the In(III)-treated Amberlite XAD-16 resin toward simple Fe(III) ions is also comparable to this of the untreated resin. Column effluents collected after passing working solutions through the resin were found to contain only 18–27% of the initial Fe amount and this points retention of 73–82% of simple Fe(III) ions on the In(III)-treated Amberlite XAD-16 resin.

Sorption of divalent Cu and Zn and trivalent Fe cations on the Amberlite XAD-8 resin was previously reported to occur in the presence of tartrate buffers [16], while trivalent Al cations were found to be retained by the Amberlite XAD-7 adsorbent when they were present in solutions containing phthalate buffers [27]. Contrary, divalent Mn and Zn cations were established not to be sorbed from solutions containing phthalate buffers on the Amberlite XAD-7 resin [29]. Therefore, it was supposed that other reason than cation exchange capacity of polar impurities present in resin structures could be responsible for retention of simple Fe(III) ions. Likely, organic acids of buffers used for the pH adjustment could bind respective metal cations, and then, individual tartrate or phthalate metal complexes formed could be possibly retained on the resins.

Accordingly, phthalate buffers used at first were replaced with much simpler acetate buffers. As a result, no retention of simple Fe(III) ions was found when loading working solutions of Fe(III) on columns packed with both Amberlite XAD adsorbents at the flow rate of 1 ml min^{−1}. Recoveries of Fe from column effluents obtained after passing solutions of pH 3–5 were in the range of 100–101% and of 99–103%, respectively, for Amberlite XAD-7HP and Amberlite XAD-16 resins. In addition, when using the Amberlite XAD-7HP resin, it was checked that In(III) ions are not sorbed on the column from solutions adjusted to pH 3–5 using respective acetate buffers. This demonstrates that Amberlite XAD resins do not contain any cation exchange active sites. Metals could be retained due to the formation of respective hydroxides and hydrolyzed forms of metals [28] or different metal complexes, as it is reported here.

3.2. Evaluation of resin sorption and desorption behavior

3.2.1. Amberlite XAD-7HP and Amberlite XAD-16

After revising preparation conditions of Amberlite XAD-7HP and Amberlite XAD-16 resins, their sorption and desorption behavior toward other Fe species, i.e., low- and high molecular weight species, was examined. It was important inasmuch as the results obtained through the proposed tandem column SPE fractionation schemes are operationally defined and relate to sorption properties of the resins applied. Furthermore, investigating interactions between different Fe species and resins studied, a better consideration about a distribution of the species is made then. Since Fe(III) is partially complexed in wine by citric and oxalic acids to give negatively charged complexes [14,15], whereas phenolic substances of wine, including mostly flavonoids and tannins, willingly bind Fe ions to form hydrophobic species [1,3,13,16], complexes of Fe(III)

Table 2

The retention efficiencies of the Fe(III)–TA complex on the Amberlite XAD adsorbents from the solutions containing acetate buffers.

pH	Retention efficiency ^a (%)	
	Amberlite XAD-7HP	Amberlite XAD-16
3.0	20 ± 1	15 ± 2
3.5	20 ± 1	15 ± 2
4.0	34 ± 2	21 ± 2
4.5	83 ± 3	49 ± 2
5.0	85 ± 1	50 ± 1

^a The mean values ($n=6$) with figures behind being standard deviations.

with CA and TA were selected in the present study to represent two different classes of Fe species in wine.

Working solutions of simple Fe(III) ions with added CA (at a concentration of 500 mg l⁻¹) were prepared at pH 3–5 using acetate buffers and driven through the columns at the flow rate of 1 ml min⁻¹. Solvents passed through the resin beds were collected and the Fe content was determined to assess the amount of Fe sorbed on the resins. It was found that both Amberlite XAD resins do not retain anionic Fe–CA complexes in the investigated pH range. Iron was recovered from column effluents with efficiencies changed from 100 ± 1% (pH 4.5) to 102 ± 3% (pH 3.5) in case of Amberlite XAD-7HP and from 99 ± 2% (pH 4.0) to 101 ± 1% (pH 3.0) in case of Amberlite XAD-16.

The study of sorption conditions of Fe–TA complexes included the effect of the solution pH, the mass of the resin and the flow rate at which working solutions were driven through the resin beds. At the outset, working solutions of Fe(III) ions with added TA (at a concentration of 500 mg l⁻¹) and adjusted to pH 3–5 with acetate buffers were passed through the columns at the flow rate of 1 ml min⁻¹. Effluents were collected and the content of Fe was determined to evaluate the amounts of Fe sorbed on both Amberlite XAD resins and calculate respective retention efficiencies (Table 2). It was found that at pH 3–4 Fe–TA complexes are hardly retained by both adsorbing resins probably due to an inefficient complex formation. Indeed, it has been recently established that the stability constant for the Fe–TA complex formed at corresponding pH is about 4 orders of magnitude lower than for this formed at higher pH values [30]. At pH 5.0, the stability constant for the Fe–TA complex has been evaluated to be of order of 10⁹ [30] and accordingly, retention efficiencies of Fe assessed at pH 4.5 and 5.0 for Amberlite XAD-7HP were found to be higher than 80%. Very comparable results were lately reported for an activated carbon, which sorbed Fe–TA complexes at pH 4.5–7.0 with efficiencies ranged from 60 to 80% [31].

Unfortunately, retention efficiencies of the Fe–TA complex at pH 4.5 and 5.0 determined for Amberlite XAD-16 are lower than those obtained for Amberlite XAD-7HP. It was probably attributed to a lower dipole moment and a pore size distribution of the Amberlite XAD-16 resin as compared to the latter resin. Lately, relatively high polarity (1.8 D) and porosity (25 µm) of Amberlite XAD-8 in contrast to Amberlite XAD-2, for which the dipole moment of 0.3 D and the porosity of 0.42 µm were ascertained, were also concluded to be responsible for higher sorption of different phenolic substances [16]. Additionally, higher sorption efficiencies of the Fe–TA complex observed for Amberlite XAD-7HP might be due to other than only hydrophobic interactions between the solute and the sorbent, e.g., formation of hydrogen bonds between phenolic hydroxyl groups of TA and carbonyl groups of a polyacrylic ester matrix [32].

Considering retention efficiencies of Fe achieved for both adsorbents, the effect of different resin masses, that is 0.6, 0.9, 1.2, 1.5 and 1.8 g, on the sorption rate was investigated. Solutions containing the Fe–TA complex and prepared at pH 4.5 were driven at the flow rate

of 1 ml min⁻¹ through the columns containing different amounts of Amberlite XAD-7HP and Amberlite XAD-16 resins. Respective effluents were collected and analyzed on the presence of Fe. It was found that retention efficiencies of Fe for both resins remains unchanged when using resin masses higher than 0.9 g. Relative standard deviations for average retention efficiencies assessed using 1.2, 1.5 and 1.8-g resin beds were lower than 1 and 5%, respectively, in case of Amberlite XAD-7HP and Amberlite XAD-16.

The effect of the sample flow rate was studied by passing solutions of the Fe–TA complex (pH 4.5) through 1.5-g resin beds of both Amberlite XAD resins at 1, 2, 3 and 4 ml min⁻¹. After analyzing column effluents it was found that retention efficiencies are not affected only at flow rates of 1 and 2 ml min⁻¹. Increasing the flow rate up to 4 ml min⁻¹ it was found that retention efficiencies of Fe are reduced by 15% for Amberlite XAD-7HP and 22% in case of Amberlite XAD-16. Therefore, the resin mass of 1.5 g and the flow rate of 1 ml min⁻¹ were used for both resins in further experiments.

Using favorable conditions, the effect of different HCl and HNO₃ solutions was studied to select the eluent that would provide complete elution of sorbed Fe–TA complexes. It was found that 1 mol l⁻¹ solutions of both acids produces quantitative recoveries of the complex of Fe(III) with TA (pH 4.5) retained on Amberlite XAD resins applied here. Accordingly, recovery efficiencies of 100 ± 1% (HNO₃) and 99 ± 2% (HCl) for Amberlite XAD-7HP and of 100 ± 2% (HNO₃) and 99 ± 1% (HCl) for Amberlite XAD-16 were obtained when using these solutions. A 2 mol l⁻¹ HCl solution was also established to result in high recovery efficiencies of Fe, i.e., 98 ± 2% (Amberlite XAD-7HP) and 98 ± 1% (Amberlite XAD-16). Unfortunately, a 2 mol l⁻¹ HNO₃ solution, reported before to be suitable for recovery of organically bound metals from Amberlite XAD resins [16,27,29], was found to be unsatisfactory. It resulted in 91 and 81% desorption of Fe, respectively, from Amberlite XAD-7HP and Amberlite XAD-16 resins.

3.2.2. Dowex 50W-x8-200

Strong acidic cation exchangers Dowex 50W have been very often used for the fractionation of metals in dietary samples, enabling separation of a broadly meant fraction of cationic metal species primarily comprising simple metal ions and their labile forms [16,29,33,34]. Since Dowex 50W-x8-200 was used in the present study for the evaluation of the cationic fraction, sorption properties of this resin toward Fe(III) ions and complexes of Fe(III) with CA and TA were examined.

Studying the retention efficiency of simple Fe(III) ions at pH 3–5, respective Fe working solutions were passed through 1.0-g resin beds at the flow rate of 1 ml min⁻¹ and column effluents were collected prior to the analysis. It was found that the Dowex 50W-x8-200 resin quantitatively retains Fe(III) ions in the investigated pH interval. Concentrations of Fe measured in all column effluents were lower than the DL for Fe. It corresponds to Fe retention efficiencies higher than 100%.

Since the total ion exchange capacity for Dowex 50W-x8-200 is relatively high (1.7 meq ml⁻¹), the effect of the resin mass was not investigated. However, considering the height of resin beds (15 mm for the wetted resin), the influence of the flow rate at which solutions of Fe(III) ions at pH 4.5 were driven through the columns on the Fe sorption rate was examined. When using flow rates higher than 2 ml min⁻¹ retention efficiencies for Fe were found to gradually decrease probably due to a shorter contact time of the solute with the resin [29,34]. When the flow rate of 4 ml min⁻¹ was applied, 15% decrease in the retention efficiency of Fe was noted.

It was also established that a 2 mol l⁻¹ HCl solution is the most adequate eluent providing 100 ± 1% recovery of Fe from Dowex 50W-x8-200. The recovery efficiency of 95 ± 2% was achieved when

a 1 mol l⁻¹ HCl solution was used. Other solutions examined, i.e., 1 and 2 mol l⁻¹ HNO₃, were found to be inappropriate for recovery of Fe. Correspondingly, these solutions yield recovery efficiencies of 75 and 89%.

When passing solutions of Fe(III) ions with added CA through the columns at the flow rate of 1 ml min⁻¹, it was established that Fe is not sorbed on the Dowex 50W-x8-200 resin at pH 4–5. This is probably due to the formation of anionic hydroxy Fe(III) citrate complexes, namely [Fe(III)(OH)₂Citrate]²⁻ and [Fe(III)(OH)Citrate]⁻ [35]. Under these conditions, from 98 ± 2% (pH 4.0) to 99 ± 2% (pH 5.0) of the initial amount of Fe in working solutions loaded onto the columns was recovered from column effluents. At lower pH, Fe was found to be partially retained by the resin, i.e., 27% at pH 3.0 and 16% at pH 3.5, but except for anionic citrate complexes of Fe, there could be also present its cationic forms in loaded solutions, e.g., hydroxy cations [35].

When passing working solutions of Fe(III) ions with addition of TA, it was found that Fe is not sorbed on the resin at pH 4.5 and 5.0. Apparently, 93 ± 1% (pH 4.5) and 97 ± 1% (pH 5.0) of the initial amount of Fe in loaded solutions was established to be present in column effluents. It points out that the Fe–TA complex formed might be negatively charged, as it was formerly assumed [17], or more likely, have a high hydrophobicity. At lower pH, Dowex 50W-x8-200 was found to sorb from 68 ± 1% (pH 4.0) to 75 ± 1% (pH 3.0) of Fe present in working solutions. Correspondingly, from 32 to 25% of the initial amount of Fe was determined in respective column effluents.

3.3. Iron fractionation in wine

The experimental evidence of Fe partitioning and the determination of inorganic and organically bound Fe species in wine have been occasionally reported in the literature [13,14,16,17]. Besides, there are some inconsistencies in already published works in which SPE was used. They cope with possible alteration of the equilibrium between the Fe species due to wine acidification and dilution [14,17], artifacts in fractionation patterns of Fe due to the use of single SPE columns for separation of different Fe species [14,17] and difficulties in column operation related to small volumes of samples taken for the analysis [16]. In the latter case, it probably resulted in total recoveries of 65–83% for all Fe fractions distinguished in wine [16].

Hence, a simpler procedure based on the use of tandem column SPE was proposed in the present study for the classification of Fe species in wine. The fractionation scheme applied (Fig. 1) enables

separation of three different fractions of the Fe species. Considering the sorption behavior of resins used, it includes the phenolic fraction (retained on the first column), the cationic fraction (retained on the second column) and the residual fraction (not retained by both columns). Due to a very strong sorption of Fe species bound to phenolic compounds, their quantitative elution with selected eluents (1 mol l⁻¹ HNO₃ and 2 mol l⁻¹ HCl solutions) was not possible. As a result, a non-elution approach was applied to evaluate the content of the phenolic Fe fraction. After passing 20 ml of undiluted and filtered wine portions through the first column, 5-ml portions of column effluents were collected prior to the determination of Fe forms not sorbed on Amberlite XAD resins. This approach has the advantage that it is simpler and faster than the plain elution and takes away a doubt about the recovery efficiency.

The total Fe concentrations in analyzed wines were found to be within 3.1–6.4 mg l⁻¹. It was assessed after 5-fold dilution of wine with water and acidification with concentrated HNO₃. The validity of this direct analysis procedure was proved analyzing wine samples after their wet digestion with concentrated HNO₃ and 30% H₂O₂. The concentrations found for both procedures do not differ significantly at the 0.05 level.

Differences between concentrations of Fe determined in wines and those found in filtrates resulted from wine filtration through 0.45 µm pore size filters were also statistically insignificant at the same level of significance. This indicates that Fe in studied bottled red wines is not present in the form of the particular fraction as was reported before for other bottled wines [16]. In addition, this was confirmed by the analysis of sample solutions obtained after digestion of filters through which 150-ml wine portions were passed. In all resulted sample solutions concentrations of Fe measured were found to be below the DL for Fe.

Results of Fe fractionation in red wines achieved with the procedure proposed are given in Table 3. As can be seen that the cationic Fe fraction, mostly containing simple Fe(II, III) ions and labile Fe species, is the predominant class of Fe species in red wines. The contribution of this fraction to the total Fe content was ascertained to be from 51 to 68%. This is comparable to findings reported in former works dedicated to the fractionation of Fe in wine, where the fraction of simple Fe(II, III) ions with labile Fe species amounted for 27–60% [16] or 38–58% [17].

The contribution of the phenolic Fe fraction associated with the presence of Fe forms bound to phenolic substances and other related high molecular weight organic species such as polysaccharides and proteins was found to change from 11 to 39% of the total Fe content. A corresponding finding for this fraction was previously

Table 3

The content of Fe in red wines and their filtrates, and the fraction distribution of Fe obtained using Amberlite XAD-7HP–Dowex 50W-x8-200 and Amberlite XAD-16–Dowex 50W-x8-200 tandem column systems.

	W1 (Bulgarian)	W2 (Bulgarian)	W3 (Moldavian)	W4 (Ukrainian)
pH	3.4	3.9	4.3	4.6
Total content in wine (mg l ⁻¹)	4.8 ± 0.4	4.4 ± 0.3	6.4 ± 0.1	3.1 ± 0.2
Total content in filtrate ^a (mg l ⁻¹)	4.6 ± 0.1	4.2 ± 0.1	6.4 ± 0.1	3.2 ± 0.3
Fractionation distribution ^b –Amberlite XAD-7HP–Dowex 50W-x8-200 tandem column system				
Phenolic fraction (%)	20 ± 3	11 ± 2	39 ± 2	31 ± 1
Cationic fraction (%)	62 ± 7	68 ± 2	51 ± 1	51 ± 1
Residual fraction (%)	19 ± 1	19 ± 1	10 ± 1	19 ± 1
Sum of fractions (%)	101 ± 8	98 ± 3	100 ± 2	101 ± 2
Fractionation distribution ^b –Amberlite XAD-16–Dowex 50W-x8-200 tandem column system				
Phenolic fraction (%)	20 ± 1	12 ± 1	36 ± 3	34 ± 2
Cationic fraction (%)	58 ± 1	64 ± 1	50 ± 2	50 ± 1
Residual fraction (%)	24 ± 4	22 ± 1	12 ± 2	18 ± 1
Sum of fractions (%)	102 ± 4	98 ± 2	98 ± 4	102 ± 2

^a Wine portions were passed through 0.45 µm membrane filters.

^b Mean values (*n* = 3) with figures behind being pooled standard deviations.

determined in Ref. [16] and it contributed to 18–27%. A greater donation of the phenolic Fe fraction (37–53%) was also found [17], however, in the cited work, besides the phenolic species, this fraction could also contain anionic complexes of Fe with low molecular weight organic acids present in wine.

The residual Fe groupings were established to be the less abundant fraction in analyzed red wines. These species contributed to 10–19% of the total content of Fe and were presumed to be mainly anionic and/or neutral complexes of Fe with organic acids of the primary origin, e.g., citric, oxalic, tartaric, malic, or secondary products of alcoholic fermentation. This assumption can be approved by results related to the anionic Fe species fraction separated and determined in wine using an anion exchanger Dowex 1-x8. As reported, the donation of this fraction to the total Fe content was within 2–19% [16].

Due to lack of a relevant reference material with specified amounts of different operationally defined fractions of Fe, the quality and control of results of the fractionation analysis obtained applying the tandem Amberlite XAD-7HP–Dowex 50W-x8-200 column system was assured by their comparison with results achieved using the tandem Amberlite XAD-16–Dowex 50W-x8-200 column system. The assessed fraction distribution of Fe in analyzed red wines is given in Table 3. It can be seen that the results achieved for both tandem column systems are very consistent. Additionally, for both procedures percentage differences between sums of Fe concentrations found in discriminated fractions and respective total dissolved Fe contents are within –3 to +2%. This proves the validity and reliability of the fractionation approach proposed and described in the present study.

4. Conclusions

It seems that retention of free metal cations by non-ionic macroreticular hydrophobic Amberlite XAD adsorbing resins does not result from cation exchange at moieties of polar impurities having exchange capacity. More likely, complexes of these metals with anionic constituents of buffering solutions used for sample preparation are formed and sorbed on the resins. Therefore, the treatment of resins with solutions of In(III) or Bi(III) salts described in the literature appears to be unnecessary. Only a careful selection of buffering solutions is required and this should consider possible interactions between their constituents and investigated metal ions.

Fractionation procedures implementing SPE for the discrimination of Fe species in wine according to their charge, hydrophobicity or stability seem to be very useful in examining the chemistry of wine oxidation and its susceptibility to browning. Using different polymeric sorbents these procedures can supply in a very convenient manner practical information on the presence of inorganic and organically bound Fe species.

The approach devised in the present study is based on the use of tandem column SPE. It is simpler than its ancestors and maintains the original Fe speciation present in wine. This is very important because any changes in the initial speciation of Fe made during the sample treatment can increase the risk of errors in fractionation patterns of Fe in wine. Due to lack of a relevant reference material, the quality of the Fe partitioning approach devised was assured by comparing results achieved when using two different adsorbing resins in the SPE fractionation procedure.

Acknowledgment

P. Pohl acknowledges receiving the Return Fellowship of the Alexander von Humboldt Foundation in 2007.

References

- [1] K. Pyrzynska, *Chem. Speciation Bioavailability* 19 (2007) 1.
- [2] P. Pohl, *Trends Anal. Chem.* 26 (2007) 941.
- [3] G. Scollary, *Analyst* 25 (1997) M26.
- [4] P. Benitez, R. Castro, J.A.S. Pazo, C.G. Barroso, *Food. Res. Int.* 35 (2002) 785.
- [5] P. Benitez, R. Castro, C.G. Barroso, *Anal. Chim. Acta* 458 (2002) 197.
- [6] H. Li, A. Guo, H. Wang, *Food Chem.* 108 (2008) 1.
- [7] J. Cacho, J.E. Castells, A. Esteban, B. Laguna, N. Sagrista, *Am. J. Enol. Viticult.* 46 (1995) 380.
- [8] V.F. Laurine, A.L. Waterhouse, *J. Agr. Food Chem.* 54 (2006) 4668.
- [9] J.C. Danilewicz, *Am. J. Enol. Viticult.* 54 (2003) 73.
- [10] K. Argyri, M. Komaitis, M. Kapsokafalou, *Food Chem.* 96 (2006) 281.
- [11] A.J. McKinnon, G.R. Scollary, *Talanta* 44 (1997) 1649.
- [12] Z. Muranyi, L. Papp, *Microchem. J.* 60 (1998) 134.
- [13] E.K. Paleologos, D.L. Giokas, S.M. Tzouwara-Karayanni, M.I. Karayannis, *Anal. Chim. Acta* 458 (2002) 241.
- [14] R. Ajlec, J. Stupar, *Analyst* 114 (1989) 137.
- [15] A. Bakar Tawali, G. Schwedt, *Fresenius' J. Anal. Chem.* 357 (1997) 50.
- [16] I. Karadjova, B. Izgi, S. Gucer, *Spectrochim. Acta, Part B* 57 (2002) 581.
- [17] K. Tasev, I. Karadjova, S. Arpadjan, J. Cvetkovic, T. Stafilov, *Food Control* 17 (2006) 484.
- [18] Y. Sugimura, Y. Suzuki, Y. Miyake, *Deep-Sea Res.* 25 (1978) 309.
- [19] M. Hiraide, Y. Arima, A. Mizuike, *Anal. Chim. Acta* 200 (1987) 171.
- [20] M. Hiraide, M. Ishii, A. Mizuike, *Anal. Sci.* 4 (1988) 605.
- [21] M. Hiraide, T. Ueda, A. Mizuike, *Anal. Chim. Acta* 227 (1989) 421.
- [22] M. Hiraide, S. Hiramatsu, H. Kawaguchi, *Fresenius' J. Anal. Chem.* 348 (1994) 758.
- [23] T.M. Florence, *Talanta* 29 (1982) 345.
- [24] C.-C. Wan, S. Chiang, A. Corsini, *Anal. Chim. Acta* 54 (1982) 1433.
- [25] C.-C. Wan, S. Chiang, A. Corsini, *Anal. Chim. Acta* 57 (1985) 719.
- [26] D.J. Mackey, *J. Chromatogr. A* 236 (1982) 81.
- [27] S.B. Erdemoglu, K. Pyrzynska, S. Gucer, *Anal. Chim. Acta* 411 (2000) 81.
- [28] S. Tokalioglu, S. Kartal, L. Elci, *Anal. Sci.* 16 (2000) 1169.
- [29] P. Pohl, B. Prusisz, *Talanta* 71 (2007) 1616.
- [30] S. Sungur, A. Uzar, *Spectrochim. Acta, Part B* 69 (2008) 225.
- [31] A. Ucer, A. Uyanik, S. Cay, Y. Ozkan, *Sep. Purif. Technol.* 44 (2005) 11.
- [32] B. Pan, B. Pan, W. Zhang, Q. Zhang, S. Zheng, *J. Hazard. Mater.* 158 (2008) 293.
- [33] S.B. Yasar, S. Gucer, *Anal. Chim. Acta* 505 (2004) 43.
- [34] P. Pohl, B. Prusisz, *Anal. Chim. Acta* 502 (2004) 83.
- [35] G.W. Quinn, D.M. Taylor, *Analyst* 117 (1992) 689.



Chemical activation of egg shell membrane for covalent immobilization of enzymes and its evaluation as inert support in urinary oxalate determination

C.S. Pundir*, Manu Bhambi, Nar Singh Chauhan

Biochemistry Research laboratory, Department of Biochemistry & Genetics, MD University, Rohtak 124001, Haryana, India

ARTICLE INFO

Article history:

Received 22 August 2008

Received in revised form 1 October 2008

Accepted 1 October 2008

Available online 14 October 2008

Keywords:

Biosensors

Egg shell membrane

Immobilization

Oxalate oxidase

Lipase

Peroxidase

Glucose oxidase

ABSTRACT

Egg shell membrane is a novel, robust, microporous, cost effective, easily available organic support material. In recent studies egg shell membranes were utilized as organic support for enzyme immobilization. But low conjugation yield limits its application as good support for biotechnological industries. In present study egg shell membrane was chemically treated to introduce free functional groups for covalent linkage of proteins to increase its conjugation yield and stability of conjugate complex. Many enzymes were tested for immobilization on modified egg shell membrane like oxalate oxidase, glucose oxidase, peroxidase and lipase. A fifteen to sixteen fold increase in conjugation yield was observed when immobilization was performed after chemical treatment in comparison to immobilization on native membrane with slight change in specific activity of immobilized enzyme which ranges from 5% to 15%. Egg shell membrane bound enzymes showed slight changes in their kinetic properties after immobilization. Egg shell membrane bound oxalate oxidase shows detection limit of 1.5 μM when used for urinary oxalate determination. Egg shell membrane support shows no interference to enzyme activity and a good correlation of 0.99 was observed with the values estimated using commercially available Sigma kit. The immobilized oxalate oxidase, glucose oxidase, peroxidase and lipase were stable up to duration of 180 days and there is respective loss of 10%, 13%, 24%, and 33% of initial activity. Overall result strengthens our view of using chemically modified egg shell membrane as solid support for better immobilization of enzymes and can be used in various biotechnological applications.

© 2008 Elsevier B.V. All rights reserved.

1. Introduction

Chicken egg is one of most common food articles and utilized all over the globe. In egg, yolk is edible part and shell is thrown away as waste. Egg shell is a complex stratified structure having outer layer of calcified shell and inner layer of thin shell membranes. These membranes retain albumen and prevent penetration of bacteria [1]. The egg shell membranes contain proteins as major constituents with small amounts of carbohydrates and lipids. Organic matter of egg shell membrane contains two glycosaminoglycans including hyaluronic acid and chondroitin sulfate-dermatan sulfate copolymer, sialic acid etc. [2].

Nowadays egg shell membranes have been used for different purposes. There are many distinctive properties associated with egg shell membrane like high porosity, antibacterial, anti-inflammatory. Egg shell membrane comprises of high amount of minerals and amino acids. Due to these properties egg shell

membranes have multiple applications in therapeutic, nutraceutical, metallurgy, bioremediation areas, either as such or after processing. Along with this, due to large surface area, porous structure and non-interference to analyte, egg shell membrane were chosen as good support for biosensor construction [3–8].

Due to often conflicting requirements of a good support, various organic/inorganic materials have been used as support for immobilization of enzyme. However, some common problems are associated with all these supports, such as low stability, affinity towards microbial attacks, involvement of various chemicals, cost and reusability etc. which leads to progressive replacement of these supports [9–11].

The inert structure and presence of collagen and excess of minerals provide less free functional groups for enzymatic coupling. To overcome these problems poly functional groups were adsorbed on membrane surface to increase protein molecule coupling through cross linking agent [6–8]. But adsorption is less stable process and concurrently leads to less stability of immobilized enzymes over the support surface [9,10,12]. Beside this, presence of hyaluronic acid and proteins, these membranes are always susceptible to microbial attack [2,13].

* Corresponding author. Tel.: +91 1262 292480 (O)/272012 (R); fax: +91 1262 294640.

E-mail address: pundircs@rediffmail.com (C.S. Pundir).

In present study various model enzymes belonging to hydro-lase, oxidoreductase family were used. Chemical treatment of egg shell membrane leads to increases in conjugation yield by fifteen to sixteen fold. When egg shell membrane bound oxalate oxidase was used to determine urinary oxalate concentration, it showed a good correlation of 0.9982 with commercially available oxalate determination kit with minimum detection limit of 1.5 μ M. These results indicate use of this modified membrane as excellent support for immobilization of various enzymes and their application in diagnostics, therapeutics etc.

2. Materials and methods

2.1. Reagents

Ammonia (I), nickel chloride, α -amylase, lipase and glucose oxidase from Sisco Research Laboratory (India), Horse radish peroxidase (HOPD), oxalic acid, 4-aminophenazone, glutaraldehyde from Sigma, were used. Leghorn white egg was purchased from local market. All other chemicals were of analytical reagent (AR) grade. Oxalate oxidase was extracted and purified from sorghum leaves [11]. Enzyme was purified and homogeneity was checked with poly-acrylamide gel electrophoresis.

2.2. Pretreatment and activation of egg shell membrane

Egg shell membrane was carefully extracted from egg after removing egg yolk and outer calcified shell. Egg shell membranes were washed with distilled water to remove all residual particles. Egg shell membrane was cut in rectangular pieces of dimension 4 cm \times 2 cm. A few pieces of membrane were washed again with distilled water and transferred to cleaned test tube having reagent A (10 ml of liquid ammonia and 50 mg of nickel chloride). The membranes were incubated in reagent A for 5 h and after incubation membranes were washed with distilled water to remove excess of reagent A. These pretreated membranes were affixed onto one end of virgin plastic strip (12 cm length \times 1 cm diameter). Affixed egg shell membrane was treated with reagent B (2.5% glutaraldehyde in 0.1 M sodium phosphate buffer, pH 7.0) for 2 h at ambient temperature (RT). Plastic strips having affixed membranes are removed from reagent B and washed many times with distilled water.

2.3. Immobilization of enzymes

Enzyme samples for immobilization were prepared in 0.1 M sodium phosphate buffer (pH 7.0) by suspending calculated protein amount in given buffer. The activated egg membrane affixed to plastic strip was incubated in enzyme solution and kept for 10 h at 4 °C in dark to allow coupling between enzyme and pretreated egg shell membrane. The strip was removed and washed many times with buffer (0.1 M sodium phosphate buffer, pH 7.0) to remove unbound enzyme to membrane. Protein concentration was calculated in wash out solution to calculate conjugation yield. To calculate protein concentration in wash out solution, whole buffer solution (remaining enzyme solution after enzyme immobilization onto activated egg shell membrane + buffer drained after washing of egg shell membrane) was collected in sterile container and protein concentration was calculated in buffer as leftover protein in solution after treatment. These values were used to calculate conjugation yield by using Eq. (1).

Conjugation yield (protein immobilized/surface area)

$$\rightarrow \frac{(\text{total protein (enzyme) in solution before treatment} - \text{leftover protein in solution after treatment})}{\text{surface area (cm}^2\text{)}} \quad (1)$$

3. Scanning electron microscopy (SEM)

Scanning electron microscopy of untreated, chemically activated and enzyme bound membranes was performed at AIIMS, Delhi (India).

4. Enzyme assays

Enzymatic activities for free and immobilized enzyme were checked and change in specific activity was observed after enzyme immobilization. The assay of oxalate oxidase was carried out based on the measurement of H_2O_2 [11,14]. Horse radish peroxidase assay was based on Trinder's colour reaction [16]. Activity of free lipase was assayed according to Gotthiff Naher with modification [17,18]. Native glucose oxidase (GOD) was assay performed using glucose as substrate [19]. The assay of egg shell membrane bound oxalate oxidase, peroxidase, glucose oxidase and lipase was done as described above except that free enzymes were replaced by affixed egg shell membrane bound enzymes and reaction buffer was increased by 0.1 ml and the reaction mixture was incubated at shaking water bath for continuous mixing of reagents.

5. Kinetic properties of immobilized enzyme

Changes in kinetic parameters of immobilized oxalate oxidase, peroxidase, glucose oxidase and lipase were observed and compared with kinetic parameters of free enzyme. To validate various physiological parameters like optimum pH, temperature, incubation period and substrate concentration, enzyme assays were performed. To determine the optimum pH of immobilized enzyme the pH of reaction buffer was varied from pH 4.0 to 9.0 using different buffer systems within their effective pH range like 0.05 M sodium succinate for pH 4.0–6.0, 0.05 M sodium phosphate for pH 6.0–7.5 and 0.05 M Tris–Cl for pH 7.5–9.0. Similarly optimum temperature of immobilized enzyme was observed after incubating reaction mixture at different temperatures ranging from 25 °C to 55 °C at an interval of 5 °C. To study the effect of substrate concentration on the initial velocity of immobilized enzyme, assays were performed in gradient of substrate concentration ranging from 0.02 mM to 5 mM for oxalate oxidase, 0.1 mM to 10 mM for glucose oxidase, 0.1 mM to 2 mM for peroxidase and 1 mM to 10 mM for lipase. Immobilized oxalate oxidase was checked for interference by KCl, NaCl, CaCl_2 , CuSO_4 , MgSO_4 , and MnCl_4 salts [18,21].

6. Urinary oxalate determination

Urine samples from patients suffering from hyperoxaluria and kidney stones were collected from PGIMS hospital Rohtak, India and processed immediately to check concentration of oxalic acid [11,15,19,20]. Results were evaluated using different statistical parameters and correlation was observed between commercially available colorimetric kits.

7. Reuse of immobilized enzyme

To reuse the immobilized enzyme, egg shell membrane bound enzyme was washed by dipping it in a series of 4–5 test tubes containing 1 ml of 0.05 M sodium phosphate buffer pH 6.5. The immobilized enzyme was stored in same buffer at 4 °C when not in use. Microbial growth was checked for native and chemically treated membranes during the storage.

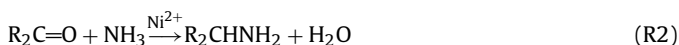
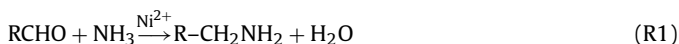
8. Results and discussion

Egg shell membrane is a complex porous structure made up of proteins, glycolipids, carbohydrates and minerals [1]. Being an inert support, it had been used as a good support for biosensor construction [6–8]. Excess of collagen and minerals leads to lesser number of functional groups for enzymatic coupling, thus low conjugation yield [2]. This low conjugation yield limits use of egg shell membrane in other biotechnological applications possessing paramount property like high surface area, porous structure, inert nature etc.

In many studies, to come up with this problem, additives like bovine serum albumin etc. have been used to induce more functional groups for covalent linkage of biocatalysts [6–8]. But use of these additives sometimes affects stability of enzyme linkage to egg shell membrane and limits their reusability. So in present study egg shell membrane was chemically treated to induce free functional group on egg shell membrane components for enzymatic coupling. This chemically modified egg shell membrane was later used for immobilization of various enzymes and successful immobilization was shown.

9. Treatment of egg shell membrane

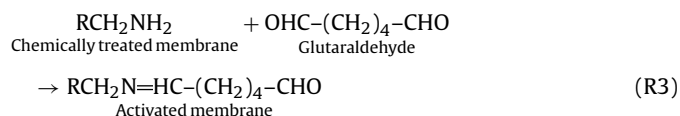
As per earlier studies, good quantity of glycosaminoglycan like hyaluronic acid, chondroitin sulfate–dermatan sulfate copolymer and sialic acid was observed in egg shell membrane [1–3]. Chemical structures of these components comprise of a free keto/aldehyde group. In present study, egg shell membranes were treated with ammonia in the presence of nickel as catalyst and induce free amine group on its glycosaminoglycan components (Reactions (R1) and (R2)). Different conditions were tried for calculating optimized concentration of ammonia and nickel for egg shell membrane activation. It was observed that higher concentration (>100 mg) of nickel makes egg shell membrane pigmented and rigid. These changes due to increased concentration of nickel decrease conjugation yield of protein. Even when diluted solution of ammonia (50% and 70%) was used, it lowers conjugation yield (65% and 77% respectively). Similarly other combinations like lower concentration of nickel (>40 mg), increase/decrease in incubation temperature etc. lead to decrease in conjugation yield. Finally it was observed that when egg shell membrane amination reaction takes place at room temperature for 5 h in 10 ml anhydrous ammonia with 50 mg of nickel, it results into optimal conjugation yield.



Here R = glycosaminoglycan and sialic acid carbon ring structure associated with free aldehyde and keto group in egg shell membrane.

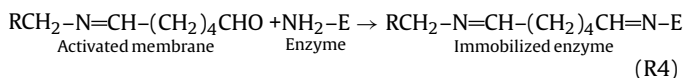
10. Activation of chemically modified egg membrane

Chemically treated egg shell membrane was activated with glutaraldehyde, a bifunctional cross linking agent for optimal reaction [6,11,15,18]. During this step one aldehyde group of glutaraldehyde reacts with chemically induced free amine group of shell membrane components and other aldehyde groups remain free.



11. Immobilization of enzyme on activated egg membrane

Activated egg shell membrane was incubated with enzyme for covalent linkage of enzyme and activated support material. In this process effective collision between aldehyde group of activated membrane and amine group of enzyme leads to covalent coupling of enzyme to activated egg shell membrane (Reaction (R4)).



Conjugation yield was observed for various enzymes and compared with when immobilization was performed without prior treatment of membrane (Table 1). A fifteen to sixteen fold higher conjugation yield was observed when protein immobilization was performed after membrane treatment in comparison to when immobilization was performed on native membrane. These increases in conjugation yield also confirm introduction of more functional groups of egg shell membrane for glutaraldehyde coupling and later on enzymatic coupling. Enzymatic assay were performed for immobilized enzyme to calculate change in specific activity of enzyme after immobilization. There is slight change in specific activity of immobilized enzyme which ranges from 5% to 15%. This change in specific activity might be due to conformational change in enzyme structure which can lead to inactivation of few enzyme molecules. There is only a slight loss of enzyme specific activity which can be neglected at the cost of reusability of enzyme after enzyme immobilization.

11.1. Scanning electron microscopy (SEM) of egg membrane

The surfaces of egg shell membranes (i) chemically treated with immobilized oxalate oxidase (Fig. 1: 1a and 1b); (ii) untreated with immobilized oxalate oxidase (Fig. 1: 2a and 2b) and (iii) chemically treated without immobilized enzyme (Fig. 1: 3a and 3b) were observed under scanning electron microscope. A change in surface morphology of support after immobilization process was a strong evidence of oxalate oxidase immobilization. Similarly in the present

Table 1
Change in conjugation yield of treated and untreated egg shell membrane with different enzymes.

	Conjugation yield ($\mu\text{g}/\text{cm}^2$)			
	Lipase	Peroxidase	Glucose oxidase	Oxalate oxidase
Untreated egg shell membrane	12.0 \pm 0.7 ^a	6.5 \pm 0.5	12.5 \pm 0.5	ND ^b
Treated egg shell membrane	183.5 \pm 0.5	113.0 \pm 0.37	200.0 \pm 0.8	190 \pm 1.8

^a Standard deviation was calculated from triplicate values.

^b Value were not determined for this parameter.

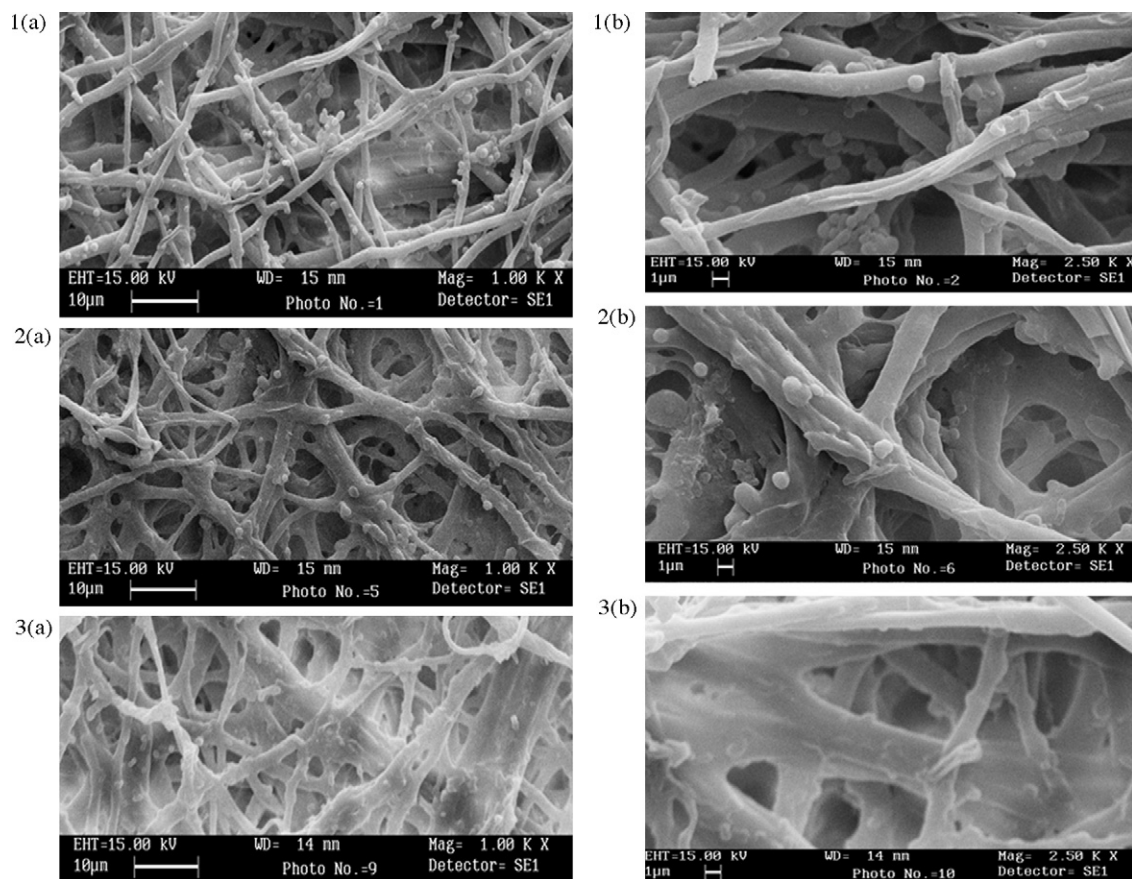


Fig. 1. Scanning electron micrographs of chemically modified egg shell membrane with immobilized oxalate oxidase (1a and 1b) or without (3a and 3b) and untreated egg shell membrane with immobilized enzyme (2a and 2b). In figure micrograph a, b belong to same sample shown at different parameters, figure a represents sample picture with scale of 10 μm and b with 1 μm scale.

study Fig. 1: 1a and 1b showed sporadic globules of immobilized oxalate oxidase on egg shell membrane components, fig. 2a and 2b showed protein fibers along with sporadic globules of immobilized oxalate oxidase but in lesser amount as compared to Fig. 1: 1a and 1b. Fig. 1: 3a and 3b showed egg shell membrane components without immobilized enzymes. Significant difference can be observed in number of protein globules attached to egg shell membrane components. These results strengthen the observation of better immobilization of enzyme on chemically treated egg membrane.

12. Change in kinetic parameters

Kinetic properties of immobilized enzymes were observed under different physiological conditions like change in temperature, time of incubation, pH of reaction mixture etc. Enzyme undergoes minor changes in its kinetic properties after immobilization which reveals stability of enzyme and non-interference from egg shell membrane support (Table 2). Slight change in optimum pH of immobilized enzyme was observed in comparison to native enzyme. The pH activity relationship of any given enzyme depends on the acid base behavior of enzyme and substrate and many other factors which are usually difficult to analyze quantitatively. A major reason for alteration in optimum pH can also be due to change in H^+ concentration in enzymatic microenvironment as loss of some $-\text{NH}_2$ groups due to covalent coupling [11,12,14].

There is increase in optimum temperature for immobilized enzymes as compared to native enzyme, which might be due to slow transfer of heat from surrounding to catalytic system due to immobilization support barrier. Because of this reason the temper-

ature of system and surrounding varies and catalytic system needs slightly higher temperature of surrounding to maintain optimum catalytic temperature in system. Change in optimum temperature was also observed in many other immobilization based studies [12]. After immobilization of enzyme on egg shell membrane, change in K_m and V_{max} was observed. K_m of oxalate oxidase was slightly increased, while in case of other enzymes like peroxidase, lipase and glucose oxidase there is slight decrease. Rate of enzyme catalysis was measured in terms of V_{max} . Either slight decrease (in case of glucose oxidase and peroxidase) or an increase (in case of lipase and oxalate oxidase) in V_{max} was observed. K_m and V_{max} of enzyme depend upon many factors like substrate affinity, change in microenvironment of enzyme after immobilization and product inhibition etc. Due to change in microenvironment of enzyme after immobilization, diffusibilities of substrate and products were different from native enzyme so change in K_m and catalytic efficiency were generally observed [11,12,15,16,19,20].

Immobilized enzyme was checked for interference with various metal salt ions and metabolites like KCl, NaCl, CaCl_2 , CuSO_4 , MgSO_4 , MnCl_4 , glucose, urea, cholesterol and ascorbic acid which is major interference in various biological samples like blood plasma, urine etc. The immobilized oxalate oxidase maintains its native activity in the presence of interferents which reveals stable conformation of immobilized enzyme (Table 3).

Only slight changes were observed in kinetic property of immobilized enzyme in reference to native enzyme which reveals that egg shell membrane proves a better and inert support for enzyme immobilization.

Table 2

Change in kinetic parameter of immobilized enzyme in comparison to native enzyme.

Kinetic parameters	Free oxalate oxidase	Immobilized oxalate oxidase	Free glucose oxidase	Immobilized glucose oxidase	Free peroxidase	Immobilized peroxidase	Free lipase	Immobilized lipase
pH	5.0	6.5	5.5	5.5	7.0	5.5	7.5	7.0
Temperature (°C)	37	40	37	40	25	40	35	40
K_m (mM)	0.55	0.78	6.2	0.35	0.24	0.17	4.2	1.2
V_{max}	0.285 $\mu\text{mol H}_2\text{O}_2/\text{min/ml}$	1.1 $\mu\text{mol H}_2\text{O}_2/\text{min}$	0.12 $\mu\text{mol H}_2\text{O}_2/\text{min/ml}$	0.11 $\mu\text{mol H}_2\text{O}_2/\text{min}$	20.0 $\mu\text{mol H}_2\text{O}_2/\text{min/ml}$	19.2 $\mu\text{mol H}_2\text{O}_2/\text{min}$	0.0015 $\mu\text{mol FFA}/\text{min/ml}$	3.6 $\mu\text{mol FFA}/\text{min/ml}$

Table 3

Effect of different salts and metabolites on the activity of immobilized oxalate oxidase onto chemically activated egg shell membrane.

Salt tested ^a	Relative activity (%) of immobilized oxalate oxidase ^b
None	100
NaCl	100 \pm 2
KCl	101 \pm 3
CuSO ₄	138 \pm 5
MgSO ₄	140 \pm 4
CaCl ₂	87 \pm 3
MnCl ₂	164 \pm 6
Ascorbic acid	95 \pm 2
Urea	93 \pm 3
Glucose	98 \pm 3
Cholesterol	88 \pm 7

^a Standard assay condition were used except for the addition of various salts (10^{-2} M conc.), 0.10 mM of urea, 17 $\mu\text{mol/l}$ of ascorbic acid, 0.9 mM of glucose and 2.00 mM of cholesterol as indicated above.

^b The value mentioned below is mean value of experiment performed in triplicate.

13. Urinary oxalate determination

Egg shell membrane bound oxalate oxidase was used for estimation of oxalic acid concentration in urine samples. Pretreated urine samples were checked for the presence of oxalic acid after replacing substrate with 0.1 ml of urine sample. Chemically activated egg shell membrane bound enzymes show linearity from 0.01 mM to 1.5 mM with $90 \pm 2\%$ recovery of added oxalic acid in urine (10 mg/l and 20 mg/l) in reference to native egg shell membrane bound enzyme showing linearity from 0.07 mM to 1.5 mM with $81 \pm 3\%$ recovery of added oxalic acid in urine (10 mg/l and 20 mg/l). The functioning range of immobilized oxalate oxidase lies in the same range as the oxalate concentration in healthy and patient blood and urine samples. Minimum detection limit of oxalic acid was 1.5 μM , 10.0 μM when chemically activated egg shell membrane immobilized oxalate oxidase and native egg shell membrane bound enzyme was used to estimate oxalic acid concentration. Minimum detection limit of oxalic acid with chemically activated egg shell membrane immobilized oxalate oxidase is lower than estimated in our earlier studies and comparable to other studies [11,15,19–21]. The oxalic acid concentration calculated using chemically activated egg shell membrane immobilized oxalate oxidase was statistically validated and the value had 2.3% or 4.3% coefficient of variation with or within batch samples. Value of oxalates calculated using egg shell membrane immobilized oxalate oxidase was compared with commercially available colorimetric kit and good correlation of 0.9982 was observed (Fig. 2). These results indicate its better use as diagnostic kit for estimation of oxalic acid concentration in biological samples which is indicator of hyperoxaluria, pre-hyperoxaluria, stages of kidney stone formation [11,19]. These results show that egg shell membrane is an inert support and had no interference with enzyme activity.

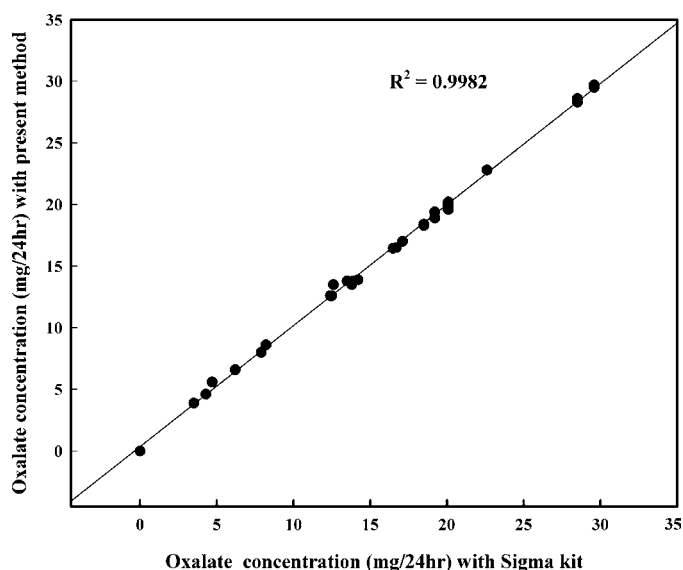


Fig. 2. Correlation between oxalate values determined in urine samples with immobilized oxalate oxidase on egg shell membrane and commercially available kit.

13.1. Reuse of immobilized oxalate oxidase

The immobilized enzymes were checked for reusability and stability for long-term use as diagnostic kits or other applications. The chemically activated egg shell membrane immobilized oxalate oxidase, glucose oxidase, peroxidase and lipase were checked for stability up to the duration of 180 days and there is respective loss of 10%, 13%, 24%, and 33% of initial activity when reaction system was incubated in reaction buffer at 4 °C after enzymatic assay. In comparison of native egg shell membrane immobilized oxalate oxidase, glucose oxidase, peroxidase and lipase were found stable only up to the duration of 60 days as egg membrane starts decaying afterwards in reaction buffer along with microbial growth which together leads to loss of enzymatic activity. Reusability and stability analysis reveals that chemically activated egg shell membrane can be used as an inert, cheaper and stable support for various biotechnological applications.

14. Conclusion

In the present study egg shell membrane was modified chemically and used as a support for immobilizing a variety of enzymes. Besides its abundance and low cost, this support also possesses a good biocompatibility with excellent self life. The present work proves that chemical modification of egg shell membrane increases conjugation yield without significant change in immobilized enzyme activity. Along with increased conjugation yield, chemically activated egg shell membrane bound oxalate oxidase shows better stability, self life, reusability and lower detection

limit as compared to native egg shell bound oxalate oxidase, when both immobilized systems were used for urinary oxalate determination. These observations increase its applicability as immobilization support. Egg shell membrane as an immobilization support is very promising platform not only for developing diagnostic kit, enzymatic pads and biosensors but also for other biotechnological industries. These egg shell membranes can be used in inert drug delivery to intestine. Being porous in nature egg shell membrane with immobilized oxidative enzymes can also be used for skin grafting and early recovery from burn and injuries.

References

- [1] D.R. Jones, M.T. Musgrove, J. Food Prot. 70 (2007) 2004.
- [2] T. Nakano, N. Ikawa, L. Ozimek, Poult. Sci. 81 (2002) 709.
- [3] D.A. Carrino, J.E. Dennis, T.M. Wu, J.L. Arias, M.S. Fernandez, J.P. Rodriguez, D.J. Fink, A.H. Heuer, A.I. Caplan, Connect. Tissue Res. 35 (1996) 325.
- [4] S. Ishikawa, S. Sekine, N. Miura, K. Suyama, K. Arihara, M. Itoh, Biol. Trace Elem. Res. 102 (2004) 113.
- [5] M. Arami, L.N. Yousefi, N.M. Mahmoodi, Chemosphere 65 (2006) 1999.
- [6] Y. Zhang, G. Wen, Y. Zhou, S. Shuang, C. Dong, M.M. Choi, Biosens. Bioelectron. 22 (2007) 1791.
- [7] S. Tembe, B.S. Kubal, M. Karve, S.F. D'Souza, Anal. Chim. Acta 612 (2008) 212.
- [8] B. Li, D. Lan, Z. Zhang, Anal. Biochem. 374 (2008) 64.
- [9] W. Tischer, V. Kasche, Trends Biotechnol. 17 (1999) 326.
- [10] S. Laschi, M. Mascini, Med. Eng. Phys. 28 (2006) 934.
- [11] C.S. Pundir, N.S. Chauhan, M. Bhambi, Anal. Biochem. 374 (2008) 272.
- [12] J.P. Kennedy, Hand Book of Enzyme Technology, Marcel Dekker Inc., New York, 1985.
- [13] T. Ohya, Y. Kaneko, Biochim. Biophys. Acta 198 (1970) 607.
- [14] Satyapal, C.S. Pundir, Biochim. Biophys. Acta 1161 (1993) 1.
- [15] M. Bhambi, C.S. Pundir, Biotechnol. Appl. Biochem. 47 (2007) 125.
- [16] A.K. Bhargava, H. Lal, C.S. Pundir, J. Biochem. Biophys. Methods 39 (1999) 125.
- [17] G. Naher, Pharm. Unserer Zeit. 5 (1976) 171.
- [18] S. Gupta, Yogesh, S. Javiya, M. Bhambi, C.S. Pundir, K. Singh, A. Bhattacharya, Int. J. Biol. Macromol. 42 (2008) 145.
- [19] C.S. Pundir, Satyapal, Clin. Chem. 44 (1998) 1364.
- [20] N.K. Kuchhal, M. Thakur, C.S. Pundir, Ann. Clin. Biochem. 37 (2000) 74.
- [21] K. Rani, P. Garg, C.S. Pundir, Anal. Biochem. 332 (2004) 32.



Liquid chromatographic fingerprint of 3-methylflavone-8-carboxylic acid established for its synthesis control analysis

Jun-Qin Qiao, Dong Sheng, Hong-Zhen Lian*

Key Laboratory of Analytical Chemistry for Life Science (Ministry of Education of China), School of Chemistry & Chemical Engineering and Center of Materials Analysis, Nanjing University, 22 Hankou Road, Nanjing 210093, China

ARTICLE INFO

Article history:

Received 7 May 2008
Received in revised form
23 September 2008
Accepted 26 September 2008
Available online 9 October 2008

Keywords:

High-performance liquid chromatography (HPLC)
Chromatographic fingerprints
3-Methylflavone-8-carboxylic acid (MFCA)
Methyl 3-propionylsalicylate (MPS)
Relative impurities

ABSTRACT

A high-performance liquid chromatographic method was proposed for the separation of relative impurities in industrial 3-methylflavone-8-carboxylic acid (MFCA) and its intermediate methyl 3-propionylsalicylate (MPS). Benzoic acid (BA), MPS, 6-chloro-3-methylflavone-8-carboxylic acid (MFCA-Cl) and methyl 5-chloro-3-propionylsalicylate (MPS-Cl) in MFCA, and MPS-Cl in MPS were respectively quantified by an external standard method. As results showed, the linearity of standard curves was excellent with the relative coefficients of over 0.999 for all the detected components, and the intra- and inter-day precisions of impurities determination were satisfactory with the relative standard deviation of not more than 8.0%. Under the selected experimental condition, the chromatographic fingerprints of MFCA and MPS were drawn synthetically, and the transfer of impurities in the stepwise reactions of MFCA manufacture was elucidated. The fingerprints have great potential in instructing the production of MFCA for industrial use and in conducting the conversion of relative impurities.

© 2008 Elsevier B.V. All rights reserved.

1. Introduction

3-Methylflavone-8-carboxylic acid (MFCA), a derivative of flavonoids, has smooth muscle relaxing activity and antispasmodic effect due to its ability of inhibiting phosphodiesterase enzyme [1–3]. It can increase bladder volume capacity and decrease micturition pressure [2], but the effect is low [4]. Additionally, it has relaxant effect on the prostatic tissues, so a potential use of it is suggested in benign prostatic obstruction [5]. In fact, MFCA is dominantly used as an intermediate for the synthesis of a list of compounds with various pharmaceutical functions. For example, a type of derivatives of MFCA, including dimethylaminoethyl 5-chloro-3-propionylsalicylate, morpholinoethyl 5-bromo-3-propionylsalicylate, β -piperidinoethyl 5-chloro-3-propionylsalicylate, and the like, have coronary vasodilation activities by increasing the coronary blood flow. With these activities, the compounds find applications in treating angina and in preventing the paroxysm of myocardial infarction and are also usable as a remedial agent for treating the pollakisuria anosognosia or as a diuretic having an activity of relaxation for convulsion of smooth muscle of the low urinary tract [6]. Another type of MFCA derivatives, including

(1 α ,2 α ,3 α)-6N-[3-benzyl-3-azabicyclo[3.1.0]hexyl]-3-methyl-4-oxo-2-phenyl-4H-1-benzopyran-8-carboxamide, N-[3-benzyl-3-azabicyclo[3.1.0]hexyl-1-(aminomethyl)-yl]-3-methyl-4-oxo-2-phenyl-4H-1-benzopyran-8-carboxamide, and the like, are able to provide a protocol for treatment or prophylaxis of an animal or a human suffering from a disease or disorder of the respiratory systems such as bronchial asthma, chronic obstructive pulmonary disorders, pulmonary fibrosis, urinary system which induce such urinary disorder as urinary incontinence, lower urinary tract systems, etc., and gastrointestinal system such as irritable bowel syndrome, obesity, diabetes and gastrointestinal hyperkinesis [7].

The synthesis technologies of MFCA are different from each other due to various starting materials. Some impurities in MFCA have strong impact on downstream pharmaceuticals, so they must be strictly controlled. However, the study of MFCA mainly focuses on its preparation [8–10]. Although several methods including radiometric assay [11], gas chromatography (GC) [12–14], high performance liquid chromatography (HPLC) [15–18] and capillary electrophoresis (CE) [19] have been reported for the determination of MFCA as medical metabolite in biological fluids, there has been no report about the analysis of relative impurities in industrial MFCA up to date.

One typical process of preparing MFCA is started with methyl 5-chloro-3-propionylsalicylate (MPS-Cl) with the synthesis route as shown in Fig. 1, in which MPS-Cl is converted to MPS first.

* Corresponding author. Tel.: +86 25 83686075; fax: +86 25 83325180.
E-mail address: hzlian@nju.edu.cn (H.-Z. Lian).

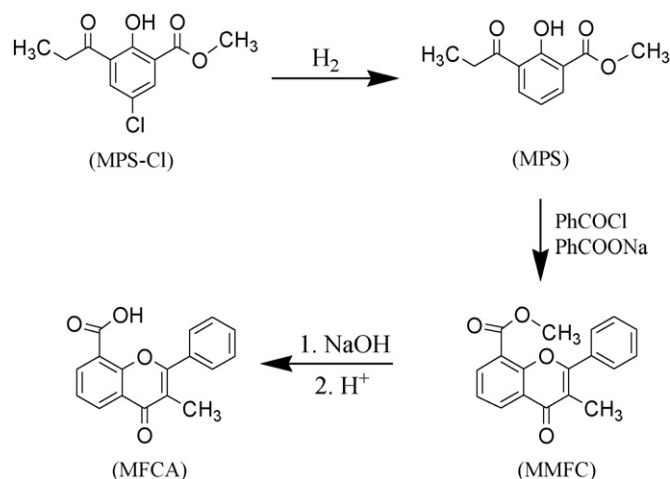


Fig. 1. Reaction of MFCA synthesis.

2. Experimental

2.1. Apparatus

Instrumentation for analysis was a Waters Alliance 2695 Separations Module equipped with a vacuum degasser, a quaternary pump, an auto-sampler and a 996 UV–Vis photodiode-array detector (PDA) (Waters, Milford, USA). The separation was controlled and the chromatograms were recorded with a Waters Empower chromatography manager system.

2.2. Chemicals

Reference substance (RS) of benzoic acid (99.5%) was purchased from Shanghai First Reagent Factory (Shanghai, China); RSs of MFCA, MPS, MPS-Cl and MFCA-Cl (all 99.0%) were provided by Dongjiang Chemical Factory (Taizhou, China); methanol and acetonitrile were both HPLC grade (Merck, Darmstadt, Germany). Perchloric acid (70–72%, guaranteed reagent) was obtained from Tianjin Third Reagent Factory (Tianjin, China). Wahaha purified water (Wahaha Group Ltd., Hangzhou, China) was used throughout the experiment.

2.3. Chromatographic conditions

HPLC separation was carried out on a Phenomenex Gemini C_{18} column (150 mm \times 4.6 mm i.d., 5 μ m) (Guangzhou Phenomenex Scientific Co., Ltd., Guangzhou, China). The column temperature was maintained at 30 °C. An isocratic elution with acetonitrile, water and 0.1% (v/v) perchloric acid (40:10:50, v/v/v) was employed at a flow rate of 1.0 mL min^{-1} . The injection volume was 10 μ L. The effluent was monitored by PDA detector set at 240 nm.

2.4. Procedure

MFCA sample solutions for relative impurity analysis were prepared in triplicate by accurately weighing approximately 10.00 mg MFCA sample into 10 mL volumetric flasks, and adding methanol to make up to the mark after sonication for about 10 min. MPS sample solutions for relative impurity analysis were prepared in triplicate by accurately weighing approximately 20.00 mg MPS sample into 10 mL volumetric flasks, and adding methanol to make up to the mark after sonication for about 10 min.

3. Results and discussion

3.1. Optimization of chromatographic conditions

3.1.1. Mobile phase

Considering most analytes of interest are weakly acidic compounds, perchloric acid was added into mobile phase in order to suppress their dissociation. The proportion of 0.1% perchloric acid

MPS-Cl is similar to methyl 3-propionylsalicylate (MPS) both in structure and in reactivity, so there will be side reactions accompanied if there is unconverted MPS-Cl in MPS (Fig. 2).

It can be estimated that the potential impurities existing in final MFCA are MPS-Cl, MPS, methyl 3-methylflavone-8-carboxylate (MMFC), methyl 6-chloro-3-methylflavone-8-carboxylate (MMFC-Cl), MFCA-Cl, etc. In addition, benzoic acid (BA) may also exist in MFCA due to the hydrolyzation of remanent benzoyl chloride ($PhCOCl$) and sodium benzoate ($PhCOONa$). From the viewpoint of chromatographic fingerprint of fine chemicals [20,21], the six compounds mentioned above constitute the basic “impurity group” of MFCA for industrial use. The reason why it is called “basic” is because the structure of some impurities is not clear. However, this ambiguity does not embarrass the establishment of chromatographic fingerprint [22]. In this impurity group, MFCA-Cl has the worst influence on MFCA downriver products, so its residue must be eliminated in the process of production. Obviously, if a sufficient conversion of MPS-Cl to MPS is ensured, the content of MFCA-Cl in MFCA should be reduced greatly.

Considering the lack of specificity of radiometric assay, tedious operation of methylation for GC analysis, and narrow linearity range accompanied with high detection limit of CE method, HPLC was chosen at last for the MFCA and MPS analyses owing to its characteristics of rapidness and sensitivity. By using HPLC, not only the relative impurities in MFCA but also the relative impurities in MPS can be well separated and determined under the same chromatographic condition. In this experiment, the chromatographic fingerprints of industrial MFCA and MPS were prepared contextually, furthermore, the transformation of relative impurities in the synthesis process of MFCA from MPS-Cl was also investigated.

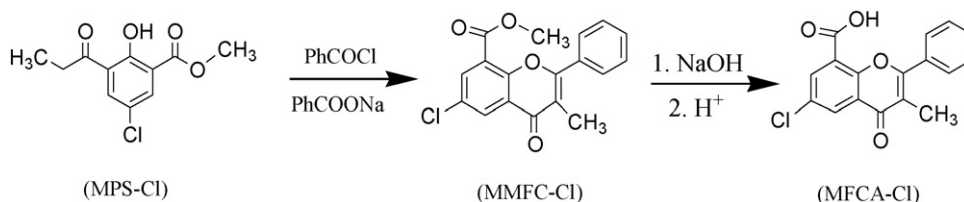


Fig. 2. Side-reaction in MFCA synthesis.

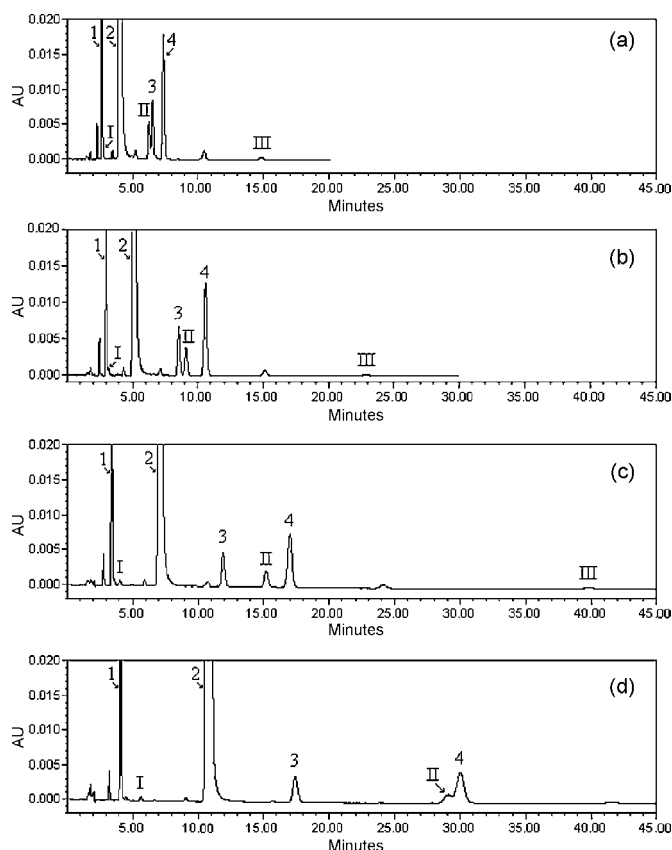


Fig. 3. Chromatograms of MFCA and its relative impurities under different mobile phases. Column: Phenomenex Gemini C₁₈, 150 mm × 4.6 mm i.d., 5 μm; column temperature: 30 °C; mobile phase: (a) 50% CH₃OH + 50% HClO₄ (0.1%); (b) 45% CH₃OH + 5% H₂O + 50% HClO₄ (0.1%); (c) 40% CH₃OH + 10% H₂O + 50% HClO₄ (0.1%); (d) 35% CH₃OH + 15% H₂O + 50% HClO₄ (0.1%). Flow rate: 1.0 mL min⁻¹; injection volume: 10 μL; wavelength for UV detection: 240 nm. Peaks: 1—BA; 2—MFCA; 3—MPS; 4—MFCA-Cl; I, II and III. Unknown impurities.

solution in mobile phase was kept at 50%, and the separation was optimized by changing the contents of methanol and water.

MFCA sample solution spiked with BA, MPS and MFCA-Cl RSs was analyzed under four different mobile phases apart: mobile phase 1 (methanol: 0.1% perchloric acid = 50:50, v/v), mobile phase 2 (methanol:water:0.1% perchloric acid = 45:5:50), mobile phase 3 (methanol:water:0.1% perchloric acid = 40:10:50) and mobile phase 4 (methanol:water:0.1% perchloric acid = 35:15:50). Results indicated that the retention times of all the analytes became longer and longer as the ratio of methanol declined gradually (Fig. 3). Using mobile phase 1 to elute, it is apparent that the peaks of MPS (t_R = 6.54 min) and unknown impurity II could not realize baseline separation; when mobile phase 2 was used, the peaks of BA (t_R = 2.70 min) and unknown impurity I (t_R = 3.18 min) almost overlapped; under mobile phase 4, the peak of unknown impurity II (t_R = 29.20 min) was covered by that of MFCA-Cl, and the peak of unknown impurity III missed. However, all the components in MFCA sample solution could be well separated under mobile phase 3 with good peak shapes and moderate separation times. So mobile phase 3 was chosen at last for the separation of MFCA and its related impurities.

Using the same procedure to analyze MPS sample solution spiked with MPS-Cl RS, the separation performance of MPS and its impurities eluted by the four different mobile phases mentioned above are shown in Fig. 4. The peaks of unknown impurity V and impurity VI were completely covered by the peak of MPS under mobile phase 1, and a little better separation between impurity V

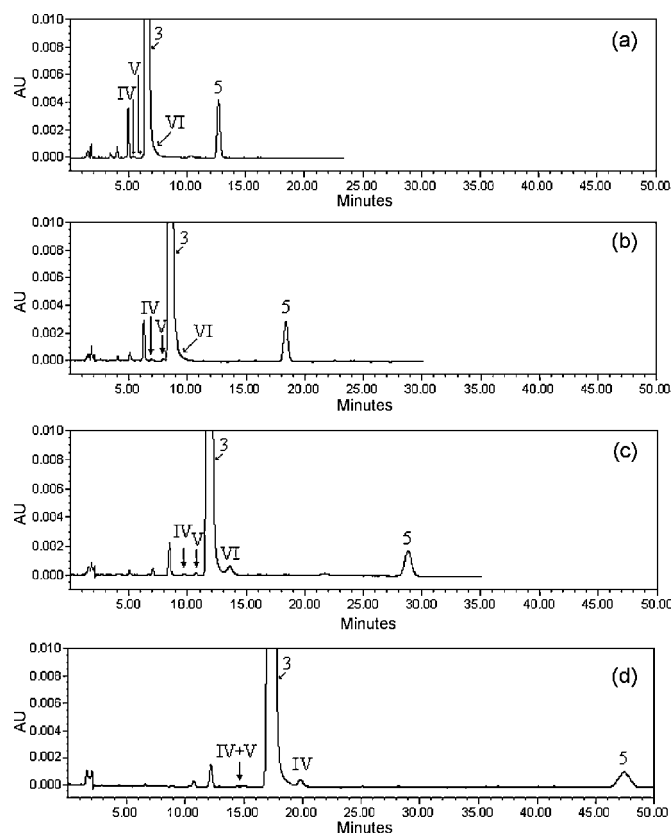


Fig. 4. Chromatograms of MPS and its relative impurities under different mobile phases. Chromatographic conditions, including mobile phase of a, b, c and d, are the same as in Fig. 3. Peaks: 3—MPS; 5—MPS-Cl; IV, V and VI. Unknown impurities.

and MPS was achieved under mobile phase 2 while the peak of impurity VI did not be observed either; when mobile phase 3 was applied, the separation effect improved significantly and almost all the related impurities in MPS could realize baseline separation; although there was an even better separation between MPS and unknown impurity VI under mobile phase 4, the peaks of unknown impurities IV and V before MPS peak were too near with each other, and the total separation time was too long. Therefore, in order to improve the separation efficiency and obtain a good separation effect, mobile phase 3 was chosen also for the separation of MPS and its related impurities. In that case the stepwise control analysis during MFCA manufacture becomes more convenient. Under the same HPLC condition, Figs. 3 and 4c make up the integrated chromatogram of all the related substances falling on the impurity group of industrial MFCA.

3.1.2. Detection wavelength

On-line PDA UV spectra (Fig. 5) show that, the maximum absorption of BA was at 226.3 and 271.5 nm; MFCA and MFCA-Cl had similar spectrum but with slightly different characteristic absorption at 240.5, 290.6 and 314.6 nm, and at 242.9, 296.6 and 324.2 nm, respectively, and likewise, MPS and MPS-Cl had similar spectrum but with slightly different characteristic absorption at 324.2 and at 338.6 nm, respectively. The basic structures of MFCA-Cl and MPS-Cl are similar to that of MFCA and MPS, respectively. However, MFCA-Cl and MPS-Cl have one more -Cl on benzene, p electrons of Cl atom can form p- π conjugated bond with π electrons of benzene ring, so the UV absorption of MFCA-Cl and MPS-Cl displayed red shift compared with MFCA and MPS, respectively. Although the residue of MFCA-Cl is very low in final MFCA industrial product, it has a significant effect on downstream drugs of MFCA, so its content is

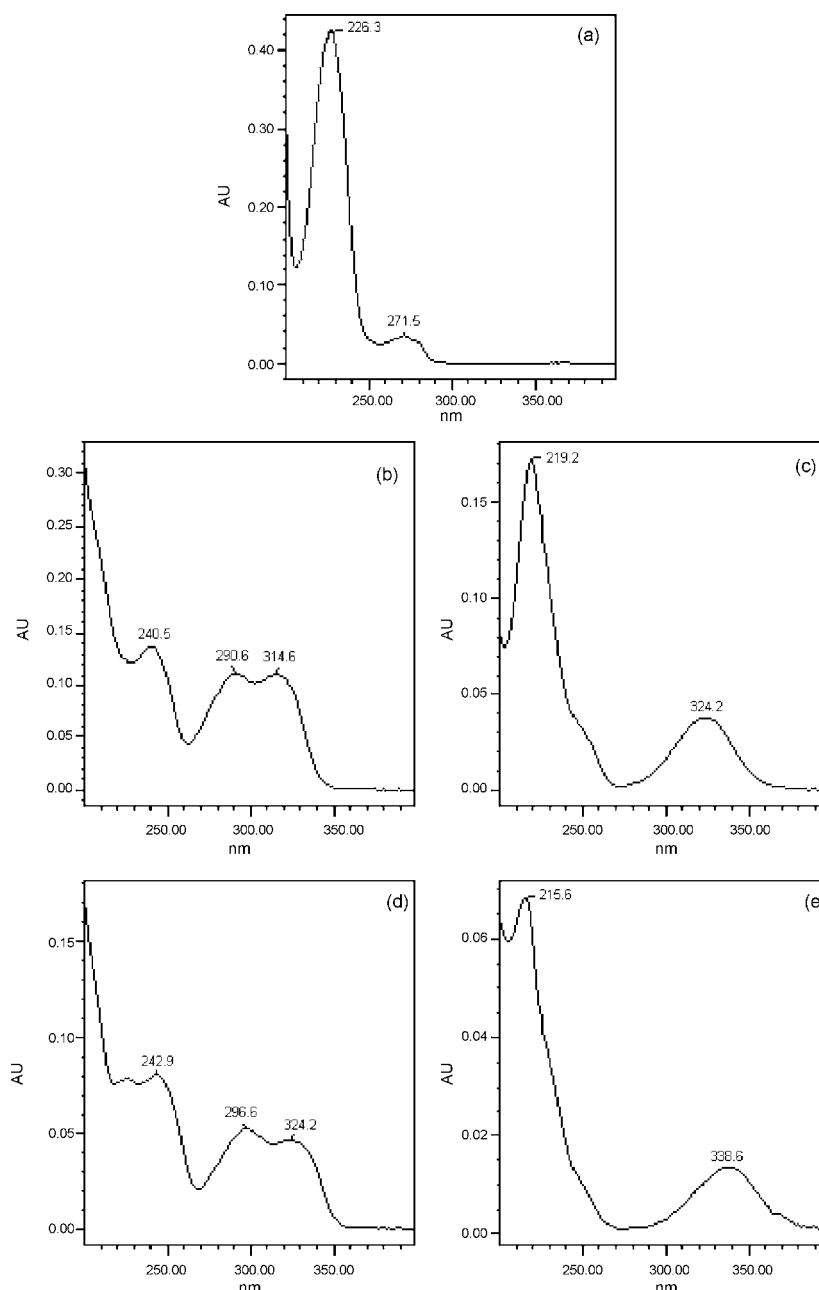


Fig. 5. On-line UV spectra of BA (a), MFCA (b), MPS (c), MFCA-Cl (d) and MPS-Cl (e). Chromatographic conditions are the same as in Figs. 3 and 4c.

the most concerned. In spite that all the impurities of interest had quite strong absorption at 220 nm, the absorption at this wavelength was near terminal absorption, which caused serious baseline noise; whereas, BA, MPS and MPS-Cl also had rather strong absorption under 240 nm, and the signal-to-noise ratio was much higher than that under 220 nm. So 240 nm was chosen as the detection wavelength throughout the experiment.

3.2. Calibration curve and detection limit

Individual BA, MFCA, MPS, MFCA-Cl and MPS-Cl stock solutions used for calibration purpose were prepared by separately weighing 10.00 mg of RS into five 10 mL volumetric flasks and adding methanol to make up to the mark after 10 min sonication. Then transfer each stock solution 0.50 mL into a 10-mL volumetric flask, mix and add methanol to the volume. Mixed standard solutions at

concentration of 1.00×10^{-5} to 5.00×10^{-2} mg mL⁻¹ each component were prepared by serial dilution of the above mixed standard solution with methanol.

Linearity of calibration curve was obtained from the regression of peak area versus concentration of standard. The limit of detection (LOD) was defined as the concentration where the peak height was three times the background (Table 1). Mixed standard solution of 0.0005 mg mL⁻¹ was injected five times consecutively, the peak area relative standard deviations (R.S.D.s) of MFCA, BA, MPS, MPS-Cl and MFCA-Cl were 1.2%, 2.6%, 5.4%, 1.3% and 1.1%, respectively.

It can be seen from the chromatogram of a mixed standard solution (Fig. 6a) that, the retention times of MFCA-Cl and MPS-Cl were respectively longer than those of MFCA and MPS. That is because, although -Cl has polarity, it is a hydrophobic group [23], and the p electrons on Cl atom can easily move to benzene ring and result in p- π conjugate, reducing the polarity and increasing the

Table 1
Calibration curves and detection limits.

No.	Component	Linear equation	<i>r</i>	Linear range (mg mL ⁻¹)	LOD (mg mL ⁻¹)
1	MFCA	$A = -9107.08 + 2.00E7C$	0.9997	0.0001–0.50	0.00005
2	BA	$A = -137.05 + 1.78E7C$	0.9999	0.00005–0.05	0.00005
3	MPS	$A = 11.38 + 1.73E7C$	0.9999	0.0001–0.50	0.00005
4	MFCA-Cl	$A = 11.38 + 1.74E7C$	0.9999	0.0001–0.05	0.00005
5	MPS-Cl	$A = 326.89 + 1.48E7C$	1.0000	0.0002–0.05	0.00010

hydrophobicity of the whole compounds. In addition, the retention times of MPS and MPS-Cl were respectively longer than those of MFCA and MFCA-Cl, this is because the hydrophobicity of MPS and MPS-Cl containing –OH is much stronger than that of MFCA and MFCA-Cl containing –COOH.

3.3. Analysis of relative impurities in MFCA and MPS

The first sample solutions of MFCA and MPS were repeatedly injected five times apart (Fig. 6b and c). The peak area R.S.D.s were 5.3%, 1.7% and 0.7% for BA, MPS and MFCA-Cl in MFCA sample solution, and 0.6% for MPS-Cl in MPS sample solution. The triplicate analytical results of impurities (mean \pm expanded uncertainty, $\bar{R} \pm U$) in MFCA and MPS industrial products, respectively, with intra- and inter-day precisions, are summarized in Table 2. In our experiment, we made the expanded uncertainty U , a symmetric interval around the result \bar{R} , be calculated from the formula: $U = KS$, where S is the standard deviation, and $K = 2$ was taken for a probability imposed at the 95% confidence levels [24–26]. The value of R.S.D.s and the uncertainties for all the impurities measured displayed a good precision of the established HPLC method.

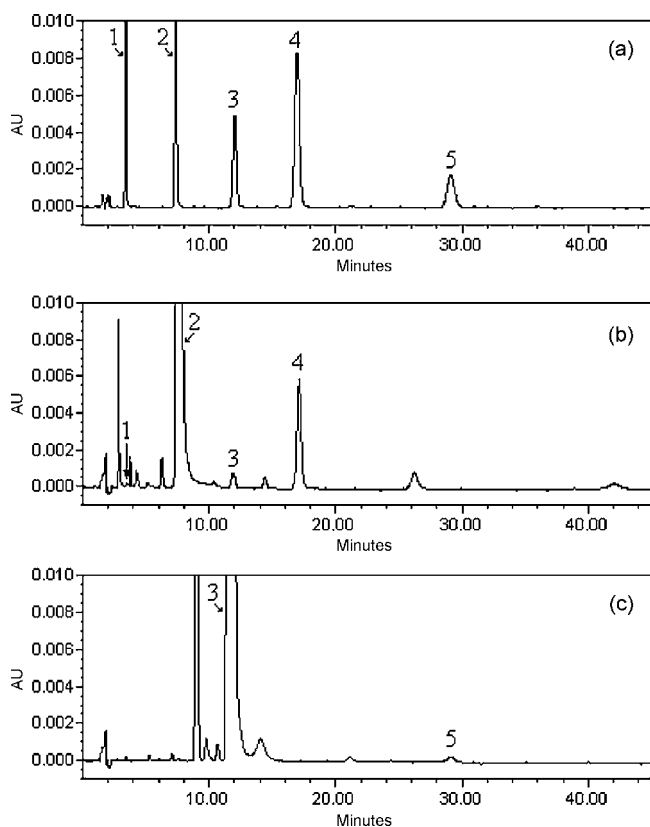


Fig. 6. Chromatograms of mixed standard (a), MFCA sample (b) and MPS sample (c). Chromatographic conditions and peak numbers are the same as in Figs. 3 and 4c.

Table 2
Determination of impurities in industrial MFCA and MPS.

	Intra-day (<i>n</i> = 3)		Inter-day (<i>n</i> = 3)	
	Content ($\bar{R} \pm U$, %)	R.S.D. (%)	Content ($\bar{R} \pm U$, %)	R.S.D. (%)
Industrial MFCA				
BA	0.0060 \pm 0.0010	8.1	0.0058 \pm 0.0006	5.1
MPS	0.1079 \pm 0.0028	1.3	0.1029 \pm 0.0103	5.0
MFCA-Cl	0.3408 \pm 0.0048	0.7	0.3327 \pm 0.0160	2.4
MPS-Cl	ND	–	ND	–
Industrial MPS				
MPS-Cl	0.0363 \pm 0.0018	2.5	0.0347 \pm 0.0027	3.9

MFCA analyzed here was made from the MPS, so Fig. 6b combined with Fig. 6c represents typical chromatographic fingerprints of industrial MFCA and its former intermediate MPS.

To our best knowledge, there has been no document reported for the MFCA analysis with high performance liquid chromatography–mass spectrometry (HPLC–MS) up to now. So in our further research, an HPLC–MS method will be developed for the validation and measurement of the unknown impurities falling on the chromatograms of industrial MFCA and MPS. In that case, the chromatographic fingerprints of MFCA and MPS will become more refined and can service better for MFCA production.

3.4. Impurity transfer in the process of MFCA synthesis

The analytical results show that although the content of MPS-Cl in MPS was only 0.0363%, the content of MFCA-Cl in MFCA was up to 0.3327%. This is because the electron-withdrawing action of Cl atom makes S_N2 nucleophilic reaction activity of MPS-Cl is much higher than that of MPS, therefore the rate of conversion of MPS-Cl into MFCA-Cl is much higher than that of MPS into MFCA. Correspondingly, MFCA-Cl was not detected in another MFCA sample synthesized from MPS containing no MPS-Cl via the same route. It is demonstrated that the transfer from MPS-Cl to MFCA-Cl would be strengthened in the course of reaction. Therefore, the dechlorination degree of MPS-Cl has an immediate effect on the residue of MFCA-Cl in MFCA. We have previously pointed out that, for a multi-step reaction, even as the slowest unit reaction determines the entire reaction speed, the unit reaction producing an impurity most difficult to remove determines the final product quality [20]. For the synthesis of MFCA, the dechlorination of MPS-Cl by hydrogenation is easy to do, however, it is probably difficult to remove MFCA-Cl from MFCA. Meanwhile, from the economy angle, the later and the deeper the reaction proceeds, the more the cost will be. Therefore, the rate of transformation from MPS-Cl to MPS should be furthest increased in order to improve the final product quality and decrease the economic input for production.

4. Conclusion

The relative impurities in industrial MFCA and its intermediate MPS were successfully separated by using carefully optimized HPLC method. Under an identical chromatographic condition, both the contents of BA, MPS, MFCA-Cl and MPS-Cl in MFCA, and the

content of MPS-Cl in MPS can be determined apart with accurate and reliable results. Moreover, chromatographic fingerprints of MFCA and MPS were established on the basis of satisfactory separation and determination. The production of MFCA and the transformation of impurities can be controlled rapidly and effectively using the combined chromatographic fingerprints.

Acknowledgments

This work was supported by National Natural Science Foundation of China (20575027), National Basic Research Program of China (973 program, No. 2009CB421601), National Science Funds for Creative Research Groups (20521503), and Analysis & Test Fund of Nanjing University. We are grateful to Prof. Wan-fang Lu for her helpful and instructive comments.

References

- [1] M. Conti, I. Setnikar, Arch. Int. Pharmacodyn. Ther. 213 (1975) 186.
- [2] P. Cazzulani, C. Pietra, G.A. Abbiati, R. Ceserani, D. Oliva, M. Civelli, A. Tajana, D. Nardi, Arzneim.-Forsch. 38 (1988) 379.
- [3] P. Cazzulani, R. Panzarasa, C. Luca, D. Oliva, G. Graziani, Arch. Int. Pharmacodyn. Ther. 268 (1984) 301.
- [4] O. Koichi, S. Noriko, D. Masami, Yakuri to Chiryo (1973–2000) 14 (1986) 7321.
- [5] M. Caine, S. Gin, C. Pietra, R. Ruffmann, Urology 37 (1991) 390.
- [6] I. Hiroshige, F. Kenichi, N. Ikuzo, 3-Methylflavone-8-carboxylic acid derivatives. EP 107 (804) (1984).
- [7] M. Anita, S. Sanjay, S. Kumar, G. Jang Bahadur, A preparation of flavone derivatives, useful as muscarinic receptor antagonists. WO 2004 056 811, 2004.
- [8] Mitsui Petrochemical Industries, Ltd., Flavone derivatives. Jpn. Kokai Tokkyo Koho, JP 59 104 375, 1984.
- [9] M. Nobuo, S. Hiroshi, H. Seiichi, N. Kenichi, 3-Methylflavone-8-carboxylic acid basic esters. JP 49 080 035, 1974.
- [10] S. Enrico, 2-Piperidinoethyl 3-methylflavone-8-carboxylate. DE 2 059 296, 1972.
- [11] A. Cova, I. Setnikar, Drug Res. 25 (1975) 1707.
- [12] E. Pedersen, Urol. Int. 32 (1977) 202.
- [13] M. Bertoli, F. Conti, M. Conti, A. Cova, I. Setnikar, Pharmacol. Res. Commun. 8 (1976) 417.
- [14] T. Ariga, K. Tanaka, K. Hattori, Sankyo Kenkyusho Nempo 26 (1974) 94.
- [15] M.T. Sheu, G.C. Yeh, W.T. Ke, H.O. Ho, J. Chromatogr. B: Biomed. Appl. 75 (2001) 79.
- [16] A. El-Gindy, S. Sallam, R.A. Abdel-Salam, J. Pharmaceut. Biomed. 44 (2007) 274.
- [17] Y. Huang, Q. Yu, M.Z. Liang, J.X. Wang, Y.P. Qin, Y.G. Zou, West Chin. J. Pharmaceut. Sci. 15 (2000) 9.
- [18] Y. Wang, T.J. Wang, T.L. Zhang, Chin. J. Pharmaceut. Anal. 22 (2002) 202.
- [19] C.X. Zhang, Z.P. Sun, D.K. Ling, J.S. Zheng, J. Guo, X.Y. Li, J. Chromatogr. Biomed. Appl. 123 (1993) 287.
- [20] H.Z. Lian, Fine Chem. Intermed. 34 (2004) 1.
- [21] H.Z. Lian, Y.N. Wei, Talanta 71 (2007) 264.
- [22] Y.N. Wei, C. Li, H.Z. Lian, Rock Min. Anal. 26 (2007) 81.
- [23] H.Z. Lian, L. Mao, J. Miao, X.Q. Xu, Z. Zhang, Chem. J. Chin. Univ. 17 (1996) 713.
- [24] R. Kellner, J.-M. Mermet, M. Otto, M. Valcárcel, H.M. Widmer (Eds.), Analytical Chemistry, second ed., Wiley-VCH, Weinheim, 2004.
- [25] J. Caro, M. Gallego, Talanta 76 (2008) 847.
- [26] T. Watanabe, K. Kato, N. Matsumoto, T. Maeda, Talanta 72 (2007) 1655.



Short communication

Development and validation of LC methods with visible detection using pre-column derivatization and mass detection for the assay of voglibose

Nanduri V.V.S.S. Raman^a, Kura Ratnakar Reddy^a, Adapa V.S.S. Prasad^a, Karipeddi Ramakrishna^{b,*}^a Hetero Drugs Ltd. (R&D), Plot No. B. 80 & 81, APIE, Balanagar, Hyderabad 500 018, India^b College of Science, GITAM University, Visakhapatnam 530 045, India

ARTICLE INFO

Article history:

Received 15 July 2008

Received in revised form

24 September 2008

Accepted 24 September 2008

Available online 4 October 2008

Keywords:

Method development

Validation

Pre-column derivatization

Mass detection

Assay

Voglibose

ABSTRACT

Two sensitive and selective liquid chromatographic methods were developed for the assay of voglibose (VB) and validated as per International Conference on Harmonization (ICH) guidelines. First method is based on the pre-column derivatization of VB followed by visible detection (LC–VD) and second method involves mass spectrometric detection (LC–MS). In LC–VD method, VB was derivatized with sodium metaperiodate and 3-methyl-2-benzothiazolinone hydrazone hydrochloride monohydrate (MBTH). The derivatized color product of VB (DCPVB) was run through Novapak C18 (300 × 3.9 mm, 4 μm) column using the mobile phase containing buffer (0.01 M mixture of sodium di hydrogen orthophosphate and disodium hydrogen orthophosphate, pH 6.0) and acetonitrile in 35:65 v/v ratio. The eluted DCPVB was monitored at 667 nm. The fixation of optimum conditions in LC–VD method is described. DCPVB structure was confirmed by mass spectral analysis. In LC–MS method, VB was passed through Venusil XBPPH (150 × 4.6 mm, 5 μm) column using a 95:5 v/v mixture of 0.01% formic acid and methanol as mobile phase. The assay concentrations of VB in pure form and in tablets for LC–VD and LC–MS methods are 25 and 5 ng ml^{−1}, respectively.

© 2008 Elsevier B.V. All rights reserved.

1. Introduction

Voglibose (3,4-Dideoxy-4-[[2-hydroxy-1-(hydroxymethyl)ethyl]amino]-2-C-(hydroxy methyl)-D-epiinositol, VB) [1,2], is an alpha-glucosidase inhibitor used for lowering post-prandial blood glucose levels in people with diabetes mellitus. In literature only one article for the determination of VB was found [3]. This article describes two liquid chromatographic methods one with fluorescence detection (LC–FD) using post-column derivatization and other with mass detection (LC–MS). Since VB does not have chromophoric groups, post-column derivatization technique was opted in LC–FD method. But this method requires high temperature and elutes VB at longer retention time. Hence, we have opted pre-column derivatization technique with visible detection (LC–VD) [4,5] because for pre-column derivatization, no special equipment is required, no restrictions on the reaction conditions like reaction time, reaction temperature, number of reagents etc. In addition, small volumes of reagents are sufficient for derivatization and the derivatized products often permits easier selection of stationary and mobile phases than the original compounds. We have also

developed a highly sensitive LC–MS method for the assay of VB. Both the methods were validated as per ICH guidelines [6].

2. Experimental

2.1. Chemicals and reagents

Sodium di hydrogen orthophosphate, disodium hydrogen orthophosphate, formic acid, HPLC grade acetonitrile and methanol were procured from Merck, India. 1% solution of sodium metaperiodate (Sigma–Aldrich Corporation, Bangalore, India) and 1% solution of 3-methyl-2-benzothiazolinone hydrazone hydrochloride monohydrate (MBTH, Sigma–Aldrich Corporation, Bangalore, India) were prepared in Milli Q water (Millipore, Bangalore, India).

2.2. Sample preparation

One milligram per millilitre stock solution of VB was prepared by dissolving 100 mg in 100 ml of Milli Q water. This solution is further diluted with Milli Q water to get the solutions with desired concentrations for validation. Tablet powder equivalent to 100 mg of VB was dissolved in 50 ml of water and sonicated for 30 min. This solution is filtered into a 100 ml volumetric flask and diluted up to the mark with 100 ml of Milli Q water to get 1 mg ml^{−1} tablet

* Corresponding author.

E-mail address: karipeddi_rk@yahoo.com (K. Ramakrishna).

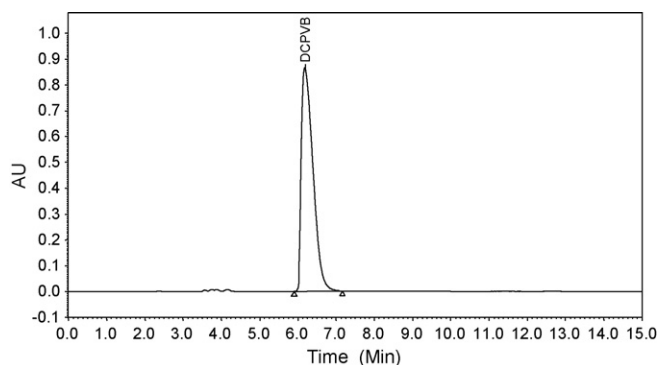


Fig. 1. LC-VD chromatogram of DCPVB.

solution. This solution is further diluted with Milli Q water to get the solutions with desired concentrations for specificity.

2.3. LC-VD conditions

LC-VD analysis was carried out on Waters Alliance 2695 separation module equipped with 2996 PDA detector (Waters Corporation, Milford, USA) and empower software. Novapak C18 (300 × 3.9 mm, 4 μm, Waters Corporation, Milford, USA) column and 35:65 v/v mixture of buffer (0.01 M mixture of sodium di hydrogen orthophosphate and disodium hydrogen orthophosphate, pH 6.0) and acetonitrile were used as stationary and mobile phases, respectively. The flow rate of the mobile phase was kept at 1.0 ml min⁻¹.

Aliquots of VB solutions (200, 225, 250, 275 and 300 ng ml⁻¹) were prepared by diluting 1 mg ml⁻¹ VB stock solution with water and taken into a series of 10 ml volumetric flasks. To these flasks, 1.5 ml each of NaIO₄ and MBTH solutions were added and kept for 10 min. Then the solutions were made up to the mark with water and cyclomixed to get DCPVB solutions. The final concentration of VB in the DCPVB solutions were 20.0, 22.5, 25.0, 27.5 and 30.0 ng ml⁻¹. 100 μl of each DCPVB solution was injected and the eluted DCPVB at retention time ~6.4 min was monitored at 667 nm (Fig. 1).

2.4. LC-MS conditions

LC-MS analysis was carried out on Shimadzu LCMS-2010 EV system (Shimadzu Corporation, Japan) having LCMS solution software in electro spray ionization (positive) mode. Selective ion monitoring of VB was done. Interface, curve dissolution line and detector voltages are 4.4 kV, 0.0 V and 1.5 kV, respectively. Nebulization gas flow is 1.5 l min⁻¹. Interface, curve dissolution line and heat block temperatures are 250, 230 and 200 °C, respectively. Venusil XBPPH (150 × 4.6 mm, 5 μm) column and a 95:5 v/v mixture of 0.01% formic acid and methanol were used as stationary and mobile phases, respectively. The flow rate of the mobile phase was 0.4 ml min⁻¹. VB solutions (4.0, 4.5, 5.0, 5.5 and 6.0 ng ml⁻¹) were prepared in a 50:50 v/v mixture of 0.01% formic acid and methanol. The total ion chromatogram of VB in SIM mode and its mass spectrum are presented in Figs. 2 and 3, respectively.

3. Results and discussion

3.1. LC-VD method development

Initially, 250 ng ml⁻¹ of VB was taken into a 10 ml volumetric flask and 1 ml each of NaIO₄ and MBTH solutions were added. DCPVB was developed within 2 min., then the total volume was

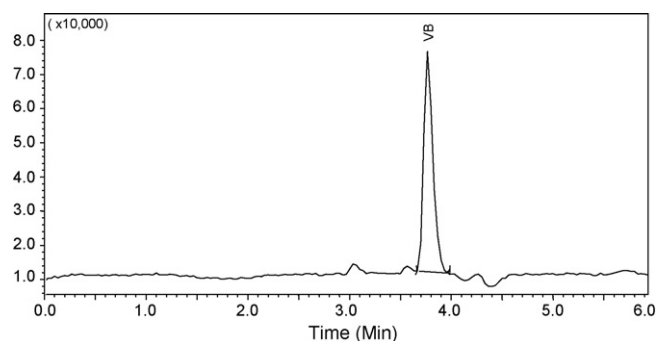


Fig. 2. Total ion chromatogram of VB in SIM mode.

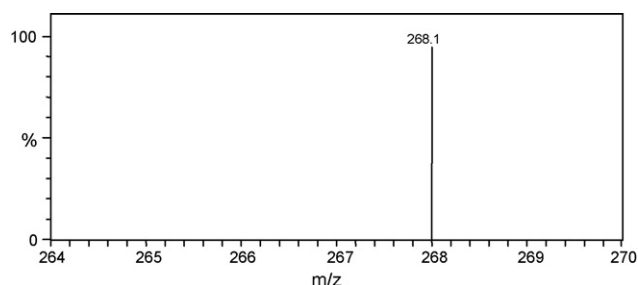
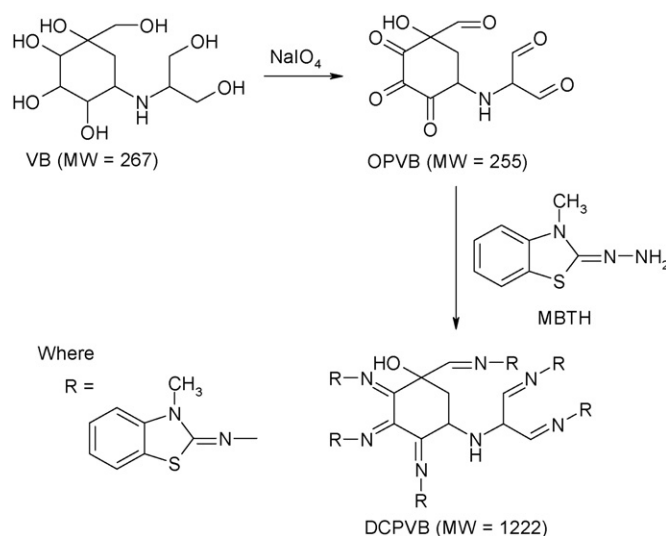


Fig. 3. Mass spectrum of VB.

made up to the mark with water and the resulting solution was used for LC-VD method development. DCPVB was run through literature conditions [2] viz. Cosmosil 5NH₂-MS column (150 × 4.6 mm, 5 μm) as stationary phase and a 2:1 v/v mixture of acetonitrile and 30 mM NaH₂PO₄ (pH 6.5) as mobile phase. DCPVB was not eluted in this condition. Hence, the above column was replaced with Novapak C18 (300 mm × 3.9 mm × 4 μm) column and the same mobile phase was maintained with a flow rate of 1.0 ml min⁻¹. DCPVB was eluted in this condition, but blank interference and peak tailing were observed. Then, it was planned to modify mobile phase and hence, buffer (0.01 M mixture of sodium di hydrogen orthophosphate and disodium hydrogen orthophosphate, pH 6.0) and acetonitrile in 30:70 ratio was opted. In this condition, peak tailing is reduced, but DCPVB eluted too early. Finally by altering the



Scheme 1. Formation of derivatized colored product of VB through oxidation product.

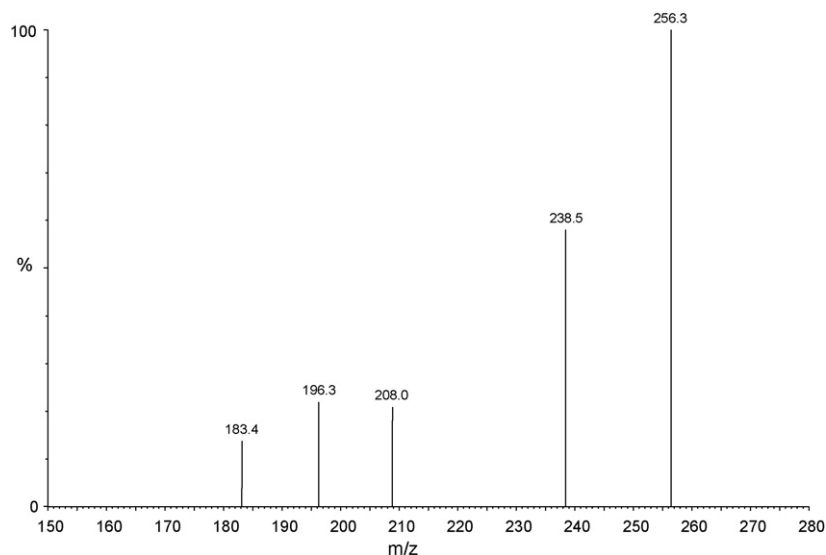


Fig. 4. Mass spectrum of OPVB.

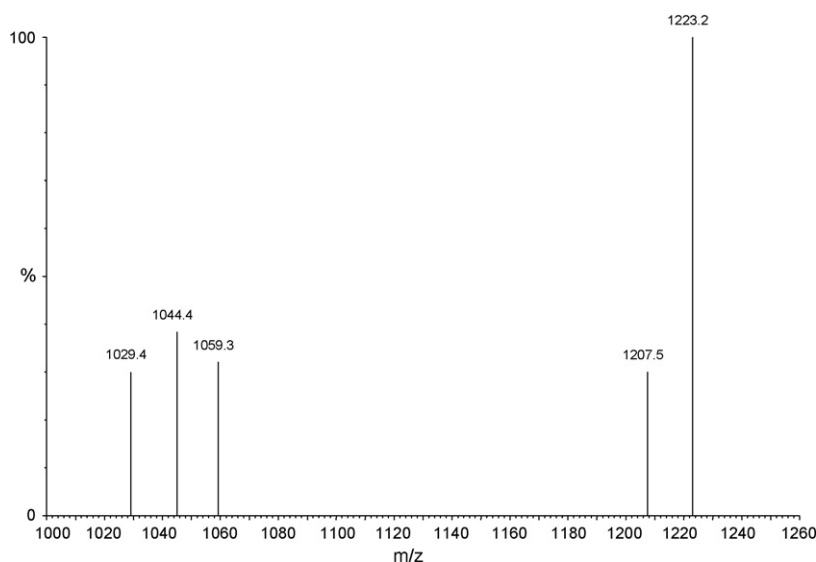


Fig. 5. Mass spectrum of DCPVB.

mobile phase ratio as 35:65 v/v, adequate retention time (~ 6.4 min) was obtained. PDA detector showed 667 nm as the appropriate wave length for the monitoring of DCPVB. Room temperature was found to be adequate for the analysis. After LC–VD method development, the completeness of the DCPVB formation was studied. Maximum detector response was observed with 1.5 ml each of NaIO_4 and MBTH solutions. Maximum color intensity of DCPVB was obtained with in 10 min. and stable up to 120 min. Hence, it is recommended to derivatize VB freshly with 1.5 ml each of NaIO_4 and MBTH reagents and run DCPVB through HPLC system between 10–120 min. of its preparation.

3.2. Chemistry of colored species formed in LC–VD method

DCPVB forms in two steps [7–9] as represented in Scheme 1. In the first step, VB undergoes oxidation with sodium metaperiodate and forms its oxidation product (OPVB). VB ($M_w = 267$) contains seven alcoholic groups among which three are primary, three are secondary and one is tertiary in nature. The three primary alcohols

were oxidized to aldehydes and three secondary alcohols to ketones by sodium metaperiodate. The tertiary alcohol was not oxidized. Hence, there is a loss of 12 hydrogens and hence the molecular weight of proposed OPVB is 255. This was confirmed by LC–MS/MS system (Waters 2695 Alliance liquid chromatograph coupled with quattro micro mass spectrometer with MassLynx software, Waters Corporation, Milford, USA). Analysis was done in electro spray ionization (positive) mode and the mass spectrum of OPVB (Fig. 4)

Table 1
Analytical data of proposed methods.

Parameter	LC–VD	LC–MS
Linear range (ng ml^{-1})	20–30	4–6
Slope	1721	1002
Intercept	2108	1516
Correlation coefficient	0.9998	0.9999
Repeatability [#]	0.53	0.72
Intermediate precision [#]	1.72	1.08

[#] %RSD of six determinations at assay level.

Table 2
Accuracy and specificity of proposed methods.

Parameter	LV–VD method (assay \pm %RSD)			LC–MS method (assay \pm %RSD)		
	20 ng ml ⁻¹	25 ng ml ⁻¹	30 ng ml ⁻¹	4 ng ml ⁻¹	5 ng ml ⁻¹	6 ng ml ⁻¹
Accuracy from VB pure substance	99.4 \pm 0.91	99.5 \pm 0.65	99.3 \pm 0.98	99.6 \pm 0.18	99.1 \pm 0.17	99.2 \pm 0.22
Specificity from VB tablets	98.5 \pm 1.12	98.9 \pm 1.34	98.8 \pm 1.52	98.4 \pm 1.76	98.8 \pm 1.56	98.9 \pm 1.52

showed m/z value as 256 ($M+1$). In the second step, since aldehydes and ketones couples with primary amines to form schiff bases with the loss of water molecules, OPVB coupled with MBTH reagent and formed DCPVB. The mass spectrum of DCPVB (Fig. 5) taken on LC–MS/MS system in atmospheric pressure chemical ionization (positive) mode showed m/z value as 1223 ($M+1$) and confirmed the structure of DCPVB.

3.3. Validation of LC–VD and LC–MS methods

The proposed LC–VD and LC–MS methods for the assay of VB were validated as per ICH guidelines [6] in terms of linearity, precision, accuracy, specificity and robustness. Linearity test solutions for the proposed methods were prepared in the range of 80–120% of 25 and 5 ng/ml of VB test concentration for LC–VD and LC–MS methods, respectively (20.0, 22.5, 25.0, 27.5 and 30.0 ng ml⁻¹ for LC–VD, 4.0, 4.5, 5.0, 5.5 and 6.0 ng ml⁻¹ for LC–MS method). Calibration curves were drawn by plotting the peak areas versus concentrations of VB and linear least squares analysis data is presented in Table 1. Precision was evaluated in terms of repeatability and intermediate precision. Repeatability of the methods was checked by injecting six VB assay preparations (25 ng ml⁻¹ for LC–VD and 5 ng ml⁻¹ for LC–MS method) on the same day. The intermediate precision of the methods was also verified by applying same procedure on six different days using a different analyst. The low %RSD values presented in Table 1 indicate the good precision of the method. The accuracy of the proposed methods were evaluated by assaying VB by both the methods at three concentrations (20, 25 and 30 ng/ml for LC–VD and 4, 5 and 6 ng ml⁻¹ for LC–MS method). Each assay was carried out three times. The low %RSD values for three assays at all the concentrations (Table 2) show the best accuracy of the proposed methods. Specificity of the methods is determined in terms of peak purity. In LC–VD method, photodiode array detector ensured the homogeneity and purity of VB peak. LC–MS shows m/z value of VB peak as 268 ($M+1$) that matches with its molecular weight (267) and indicates the specificity of the method. Since the specificity is the ability to assess the analyte in the presence of components which may be expected to be present, the assays were carried out using their tablets at three concentrations (20, 25 and 30 ng/ml for LC–VD and 4, 5, 6 ng ml⁻¹ for LC–MS method). Each assay was carried out three times. The low %RSD values for three assays at all the concentrations from their tablets (Table 2) also indicate the speci-

ficity of the proposed methods. Robustness of the methods was checked by altering chromatographic conditions deliberately. The flow rate of the mobile phase was altered by 0.2 units in LC–VD and 0.1 unit in LC–MS method. The effect of column temperature on retention time was studied at 25 and 30 °C instead of 28 °C (room temperature). All the other mobile phase components were held constant. These deliberate modifications do not show significant effect on the chromatographic performance indicating the robustness of the methods. In LC–MS method, VB was stable up to 7 h in its mobile phase and hence it is suggested to complete the analysis before 7 h of sample preparation.

4. Conclusions

This article describes validated LC–VD and LC–MS methods for the assay of voglibose. In LC–VD method, the pre-column derivatization process is simple, requires minute quantities of reagents, no temperature is required, color product forms within 10 min. and stable up to 6 h. LC–MS method is more sensitive because it can assay VB at 5 ng ml⁻¹ concentration. Hence, the present methods can successfully be applied for the assay of voglibose in pure form and tablets, which is non chromophoric in nature.

Acknowledgments

The authors are highly thankful to Dr. Bandi Parthasarathi Reddy, CMD, Hetero Drugs Limited, Hyderabad for his encouragement and providing facilities to carry this research work.

References

- [1] The Merck Index (Merck & Co., Inc. Whitehouse Station, NJ, USA), 14th edition, 2006, p. 1727.
- [2] C. Xiaolong, Z. Yuguo, S. Yinchu, Curr. Med. Chem. 13 (2006) 109–116.
- [3] J.S. Woo, J.K. Ryu, J. Pharm. Biomed. Anal. 42 (2006) 328–333.
- [4] W. Li, H. Jia, K. Zhao, Talanta 71 (2007) 385–390.
- [5] Y.M. Martinez, R.H. Hernandez, P.C. Falco, J. Chromatogr. A 1164 (2007) 329–333.
- [6] International Conference on Harmonisation Guideline on Validation of Analytical Procedures; Q2 (R1), 2005.
- [7] C.S.P. Sastry, P.Y. Naidu, C.S.R. Lakshmi, M.N. Reddy, C. Ravi, Talanta 47 (1998) 85–93.
- [8] A.V.S.S. Prasad, T. Siva Rao, C.S.P. Sastry, U.V. Prasad, Ind. J. Pharm. Sci. 64 (2002) 270–272.
- [9] G. Gori, P. Meneghetti, A. Sturaro, G. Parvoli, L. Doretti, G.B. Bartolucci, Chromatographia 40 (1995) 336–340.



Evaluation of the arsenic binding capacity of plant proteins under conditions of protein extraction for gel electrophoretic analysis

Anne-Christine Schmidt*, Sandra Steier, Matthias Otto

TU Bergakademie Freiberg, Faculty of Chemistry and Physics, Institute of Analytical Chemistry, Leipziger Str. 29, D-09596 Freiberg, Germany

ARTICLE INFO

Article history:

Received 17 July 2008

Received in revised form 14 October 2008

Accepted 17 October 2008

Available online 31 October 2008

Keywords:

Protein extraction

Plant samples

Arsenic-binding proteins

Gel electrophoresis

Atomic spectrometry

ABSTRACT

As prerequisite for the investigation of arsenic-binding proteins in plants, the general influence of different extraction parameters on the binding behaviour of arsenic to the plant protein pool was investigated. The concentration of the extraction buffer affected the extraction yield both for proteins and for arsenic revealing an optimal buffer concentration of 5 mM Tris/HCl, pH 8. The addition of 1 or 2% (w/v) SDS to the extraction buffer produced a two- to threefold enhancement of the total protein extraction yield but strongly suppressed the simultaneous extraction of arsenic from $80 \pm 8\%$ extraction yield obtained without SDS to $48 \pm 2\%$ in presence of 2% (w/v) SDS. The arsenic binding capacity of the protein fraction obtained after extraction with Tris buffer and protein precipitation by trichloroacetic acid in acetone was estimated to be $1.4 \pm 0.6\%$ independently on the original spiking concentration of arsenic provided in the form of monomethylarsonate to the extracts. Due to the low total protein concentrations of the plant extracts that varied in the range from 75 to $412 \mu\text{g mL}^{-1}$ depending on the extraction parameters, high arsenic concentrations of 263 – $1001 \text{ mg (kg protein mass)}^{-1}$ resulted for spiking concentrations of 10 mg As L^{-1} . The optimized protein isolation procedure was applied to plants grown under arsenic exposure and revealed a similar arsenic binding capacity as for the spiked protein extracts.

© 2008 Elsevier B.V. All rights reserved.

1. Introduction

Toxic effects of arsenic are ascribed to its interaction with biochemical pathways, enzymes, and other biomolecules. In plants, arsenic is taken up from contaminated soils and waters via the roots is further translocated to shoots and leaves [1]. Whereas some plant species are damaged, other kinds of plants show an elevated arsenic tolerance and hyperaccumulate this toxic metalloid [2,3]. Analytical approaches are mainly focused on soluble arsenic species [1,4]. Their possible bindings to biomolecules dissociate during extraction or chromatographic separation. The binding of arsenic to the tripeptide glutathione and to special thiol-rich polypeptides called phytochelatins was demonstrated in plant extracts [5–7] but their analysis is difficult due to limited stability. Arsenic-bindings to high molecular weight compounds such as proteins were found in model solutions [8,9]. However, owing to the fact that many plant enzymes have free thiol groups which can react with arsenic, studies concerning the analysis of arsenic-binding proteins in real plant samples are missing probably due to the difficulty in sample preparation and conservation of the bindings. A first approach concerning this topic was performed by the analysis of the distribution

of arsenic species between the fractions of soluble proteins, structure proteins, and non-proteins of arsenic-accumulating plants by means of a fractionated sample preparation procedure [10].

One- and two-dimensional gel electrophoresis are a powerful tool for the analysis of protein patterns of biological samples containing a complex mixture of differently sized proteins. Moreover, a subsequent determination of metals or other heteroelements in the separated protein bands by means of laser ablation inductively coupled plasma mass spectrometry (LA-ICPMS) or X-ray spectroscopic techniques provide the possibility to detect metal- or metalloid–protein complexes [11,12]. Because sample preparation is considered to be the most crucial step for protein analysis by gel electrophoretic separations and very little is known about its influence on the stability of arsenic–protein bindings, it is necessary to investigate the effects of these various parameters.

In contrast to animal or bacterial samples, plant tissues represent a challenging sample type for protein isolation and analysis because they contain plenty of substances such as phenolic compounds, carbohydrates, organic acids, lipids, and terpenes that interfere with the gel electrophoretic separation of proteins [13,14]. Therefore, purification steps such as protein precipitation are necessary to remove non-protein contaminants. Furthermore, protein precipitation serves as a very effective preconcentration step for proteins from diluted protein sources such as plant materials. Because trichloroacetic acid (TCA) in acetone has been proven as

* Corresponding author. Tel.: +49 3731 393255; fax: +49 3731 393666.

E-mail address: Anne-Christine.Schmidt@chemie.tu-freiberg.de (A.-C. Schmidt).

an efficient precipitating agent for purification of plant proteins for subsequent gel electrophoretic separation [15–17] this type of precipitation was also applied in the current study. A further advantage of the TCA/acetone precipitation consists in the immediate inactivation of proteolytic and other modifying enzymes that are released from broken cells during extraction [18]. However, in some cases a washing of the protein precipitate is necessary prior to gel electrophoresis to remove co-precipitated contaminants [14].

To search for real arsenoproteins in biological samples, the exploration of the behaviour of arsenic during extraction, precipitation, and purification of proteins for gel electrophoresis becomes obligatory. In the present investigations, the arsenic binding capacity of plant proteins extracted under different conditions was determined exemplary of a biologically important arsenic compound, monomethylarsonic acid (MMA(V)). This methylated arsenic species is assumed to be produced from inorganic arsenite during biomethylation and was also found in plants grown on arsenic-enriched substrates [19,20]. Further, due to their strong toxicity, monomethylarsonate salts were used as herbicides [21]. The influences of different parameters varied during sample preparation on the extraction efficiencies obtained both for total arsenic and for total protein as well as on gel electrophoretic separations of the extracted plant proteins were evaluated. After optimization of the sample preparation procedure by means of arsenic spiking experiments, the optimized extraction parameters were applied to plants cultivated under arsenic exposure in order to quantify the fraction of accumulated arsenic that was associated to proteins.

2. Experimental

2.1. Plant material

Leaf and stalk material from simply cultivable nasturtium plants (*Tropaeolum majus* L.) served as protein source for the preparation of protein extracts. In addition to control plants grown on humus soil characterized by a background arsenic level of $<5 \text{ mg kg}^{-1}$ dry mass, some plants were cultivated under arsenic exposure during 8 weeks after an initial arsenic-free germination and growth phase of 4 weeks. The arsenic compound monomethylarsonate (MMA(V), obtained in the form of monosodium acid methane arsonate sesquihydrate from Chem Service, West Chester, PA, USA) was applied to the soil used for plant cultivation twice per week in 100 mL portions containing 5 mg arsenic. The plants were harvested and divided into leaves and stalks, and stored frozen at -20°C .

2.2. Preparation of the extraction media

The solid buffer substances tris(hydroxymethyl)aminomethane (Tris, p.a., from Merck, Darmstadt, Germany) and ammonium acetate (HPLC grade, from J.T. Baker B.V., Deventer, Holland) used for the extraction experiments were dissolved in deionized water to prepare 100 mM buffer stock solutions. To vary the pH for the extraction media, the pH value of the buffer solutions was adjusted with 2 M HCl (prepared from 32% HCl, p.a., Sigma–Aldrich, Steinheim, Germany) or with 100% acetic acid (p.a., Merck, Darmstadt, Germany), respectively, and controlled by a pH electrode (HI 9321 microprocessor pH meter, HANNA instruments, Kehl am Rhein, Germany). Different buffer concentrations were prepared by dilution of these stock solutions with deionized water.

The reducing agent dithiothreitol (DTT, 1 M stock solution in water from Sigma–Aldrich) was added to the extraction buffer system to a final concentration of 50 mM. Further extraction buffer additives were the protease inhibitor phenylmethylsulfonyl fluoride (PMSF, 0.1 M stock solution in ethanol from Sigma–Aldrich)

at a concentration of 2 mM in the final extracts and 10 mg of the adsorbents for polyphenolic compounds polyvinylpyrrolidone (PVPP, from Sigma–Aldrich) in an extract volume of 10 mL. The concentration of the tenside sodium dodecyl sulfate (SDS, $\geq 98\%$ from Sigma–Aldrich) in the extraction buffer was varied between 0, 0.5, 1, and 2% (w/v).

2.3. Combined protein and arsenic extraction protocol for plant tissues

The flow-chart of the entire extraction and purification protocol is pointed out in Fig. 1. The extractions were performed in 30 mL polypropylene centrifuge tubes (Nalge Nunc International Corporation, Rochester, NY, USA). For the centrifugation steps the Avanti™ Centrifuge J-30I (Beckmann Coulter, Fullerton, CA, USA) was used. The ultrasound treatments were carried out in a water bath. For some samples, the final protein pellet was washed with 4 mL 90% (v/v) ethanol containing 2 mM DTT for 2 h, and centrifuged again at $10,000 \times g$ and 4°C for 10 min. The precipitating agent acetone was purchased in p.a. quality from Merck, Darmstadt, Germany, and trichloroacetic acid (TCA, $\geq 99.5\%$) from Sigma–Aldrich, Steinheim, Germany.

2.4. Microwave digestion of extraction residues and protein pellets

The filtration and centrifugation residues arising from the extraction procedure as well as the precipitated protein pellets (Fig. 1) were mineralized by means of microwave digestion with 3 mL 65% HNO_3 and 1 mL 30% H_2O_2 (both in suprapur quality from Merck, Darmstadt, Germany) in 20 mL Teflon vessels using the following program (Microwave system Start 1500, MLS, Leutkirch, Germany): step 1: 3 min heating to 85°C at a power of 700 W; step 2: 5 min heating to 145°C at a power of 1000 W; step 3: 3 min heating to 210°C at 1000 W; step 4: 15 min maintaining the temperature at 210°C and the power at 1000 W; step 5: cooling to 20°C for 20 min at 0 W. The resulting digests were filled up to 8 mL with deionized water. Three blank samples containing 3 mL HNO_3 and 1 mL H_2O_2 were processed as the other samples.

2.5. Protein quantification by the Bradford assay

For preparation of the Bradford reagent, 50.7 mg Coomassie Brilliant Blue G-250 (from Sigma–Aldrich) were dissolved in a mixture of 25 mL 95% (v/v) ethanol (p.a., from Merck) and 50 mL 85% (w/v) orthophosphoric acid (ultra, Sigma–Aldrich). This solution was filled up with deionized water to a final volume of 500 mL and filtrated to remove insoluble dye particles. 200 μL of the dye reagent solution were mixed with 800 μL aqueous sample solution and incubated for 10 min. A calibration line was compiled by measuring the UV absorption at 595 nm for six different concentrations of bovine serum albumine (BSA, 200 mg mL^{-1} stock solution in water from Sigma–Aldrich) using a photometer (Ultrospec 1000, Pharmacia Biotech). The linear range was estimated to 0.1 to 4.0 $\mu\text{g mL}^{-1}$ ($r = 0.984$). The leaf protein extracts were diluted 1:100, 1:50, or 1:10 with water in order to produce absorption values that were consistent with this calibration range. The absorption value of a mixture of 200 μL dye reagent and 800 μL deionized water was subtracted as blank value from all BSA and sample values.

2.6. ICP-OES and HG-ETA-AAS for determination of total arsenic contents

The total arsenic contents in the raw protein extracts as well as in the microwave digests of the extraction residues and of the

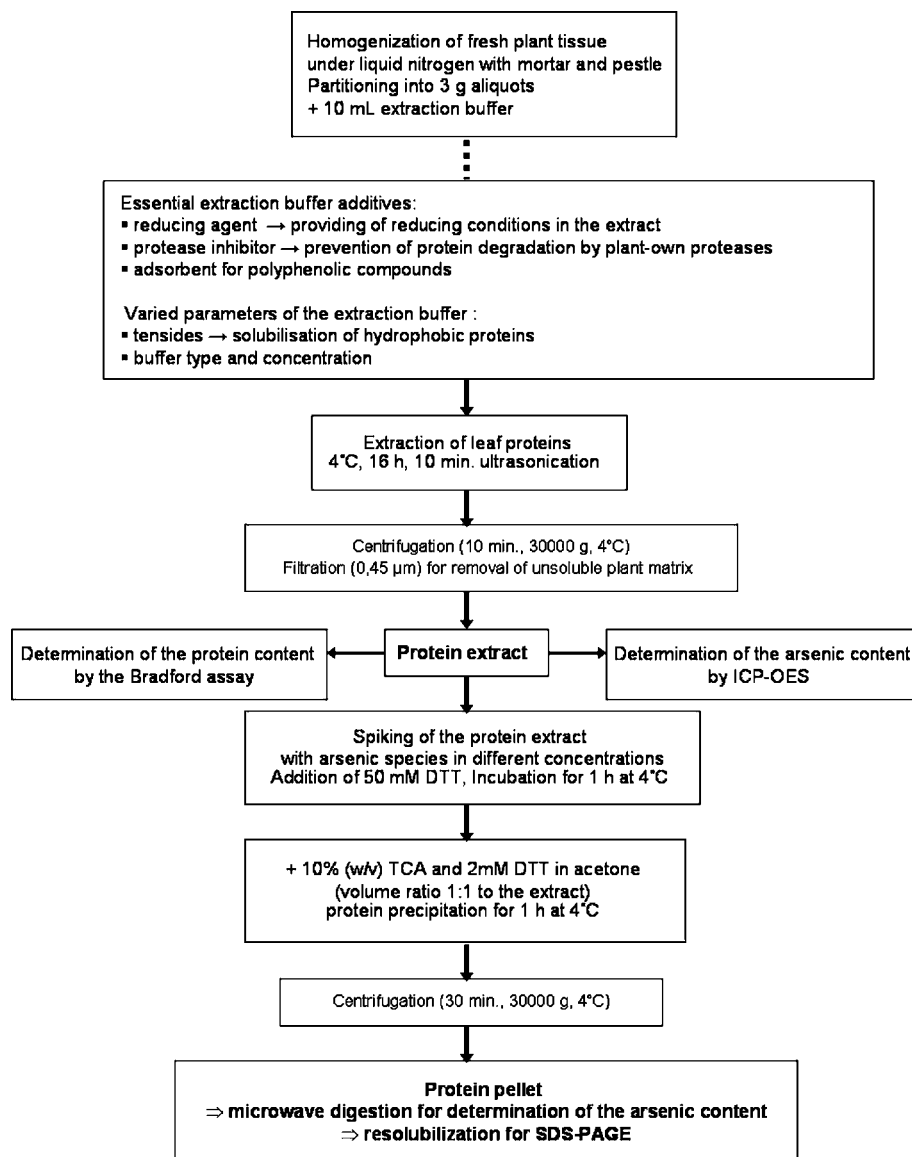


Fig. 1. Flow chart for the protein isolation protocol developed for the estimation of the arsenic binding capacity of plant proteins.

precipitated protein pellets were determined using inductively coupled plasma optical emission spectrometry (ICP-OES, iCAP 6500 device, Thermo Electron, Dreieich, Germany). The sample was infused at a flow rate of 2 mL min^{-1} into a concentric nebulizer (Mira Mist) associated to a glass cyclone spray chamber. The emission of As was measured axially in the argon plasma torch at the wavelengths 189.0, 193.7, and 228.8 nm.

Since a high load of organic solvent extinguishes the plasma torch of an ICP, the arsenic contents in the ethanolic wash solutions were measured using atomic absorption spectrometry with hydride generation and electrothermal atomization (HG-ETA-AAS). The samples were pre-reduced with ascorbic acid and potassium iodide for 1 h. To form volatile hydrides of the arsenic compounds, NaBH_4/HCl was added. A combination of a FIAS 400 for hydride generation in the flow injection mode and an atomic absorption spectrometer (ZL 4100, PerkinElmer) with an electrothermal atomizer was used. The hydrides were enriched in a graphite furnace (permanently modified with Pd). The absorption intensity of As was measured at 193.7 nm. An external calibration in the solvent ethanol was performed.

The arsenic concentrations of the respective buffer and reagent solutions were subtracted from the arsenic contents of the samples as blank values.

2.7. SDS-PAGE

The protein pellets obtained after TCA/acetone precipitation of the leaf protein extracts were re-solubilized in SDS-PAGE sample buffer prepared according to Lämmli [22] (62.5 mM Tris/HCl buffer, pH 6.8, 2% (w/v) SDS, 5% (v/v) β -mercaptoethanol ($\geq 98\%$, electrophoresis grade, Sigma-Aldrich), 20% (v/v) glycerol ($\geq 99\%$, Sigma-Aldrich), 0.1% (w/v) bromophenol blue (sodium salt, Sigma-Aldrich), in deionized water) to reach final protein concentrations of $5 \mu\text{g } \mu\text{L}^{-1}$. After denaturation at 95°C for 5 min, protein amounts of 25–100 μg were loaded onto $20 \times 20 \text{ cm}$ gels in the Protean II XL electrophoresis cell (Bio-Rad Laboratories GmbH, München, Germany). The running buffer for the electrophoresis was 25 mM Tris/HCl buffer, pH 8.3, with 192 mM glycine and 0.1% (w/v) SDS. A current of 13 and 18 mA was regulated in a 2 cm long stacking gel (5% T), and in the 0.75-mm thick separating gel (15% T),

respectively, using the Power Pac™ Basic power supply (Biorad). The gels were transferred into the staining solution (0.1% (w/v) Coomassie Brilliant Blue G 250, 0.77 M (NH₄)₂SO₄, and 2% H₃PO₄ mixed with the fixation agent 100% methanol in the volume ratio 4:1), shaken over night and destained with deionized water by shaking.

3. Results and discussion

3.1. Effect of different extraction parameters on the extracted protein concentration

At first, the proteins were extracted from the plant tissue using an aqueous extraction buffer in order to gain a protein-containing solution for spiking and incubation with arsenic. For this purpose a weakly alkaline Tris/HCl buffer was chosen that is a widespread buffer for biological samples and a running buffer for gel electrophoretic protein separations.

Among the parameters varied for the buffer solution, the buffer concentration had an influence on the extraction yield (Fig. 2). 5 and 10 mM Tris buffer, pH 8, caused a more efficient protein extraction from plants exposed to arsenic during their growth period compared to 1 and 25 mM buffer. From leaves considerably higher amounts of protein could be extracted than from stalks. A Tris buffer concentration of 5 mM was chosen instead of 10 mM in order to minimize the salt load of the samples for SDS-PAGE. Moreover, the 5 mM buffer caused a higher extraction yield for arsenic (see below, Fig. 3). The pH value of the Tris buffer system that was varied between 6.8, 8.0, and 9.0, did not affect the protein extraction yield. With all these buffer solutions the fraction of water-soluble, cytosolic proteins was extracted. A significant enhancement of the extracted protein concentration was caused by the addition of the surfactant sodium dodecyl sulfate (SDS) to the aqueous Tris buffer system (Table 1). Whereas a mass concentration of 0.5% SDS was not sufficient to solve higher amounts of proteins from the leaf material, 1% and 2% (w/v) SDS led to a more than twofold and more than threefold increase, respectively, of the protein yield compared to the extraction without SDS addition. SDS exhibits a particular extraction capability for hydrophobic membrane proteins which are not soluble in aqueous solutions [23]. Thereby, its extraction efficiency is larger than for other types of surfactants such as DoTAB or SB 3–12 [24].

Because plant extracts are characterized by high concentrations of phenolic substances which interfere with the gel electrophoresis due to modification of proteins as well as by high protease activities, a protease inhibitor, phenylmethylsulfonyl fluoride (PMSF), and

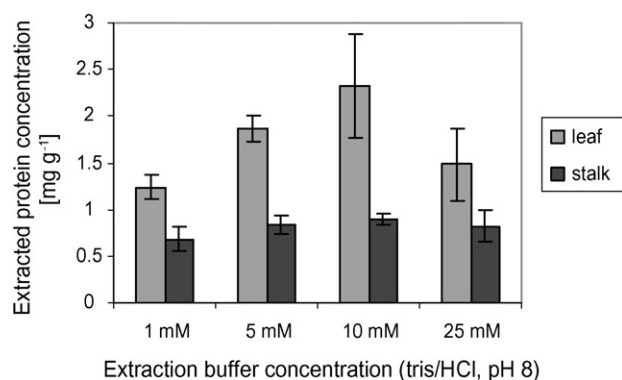


Fig. 2. Effect of Tris buffer concentration on the extracted protein concentration from homogenized leaves and stalks of *Tropaeolum majus* grown under MMA(V) exposure. Average values with standard deviations for three independent samples are given.

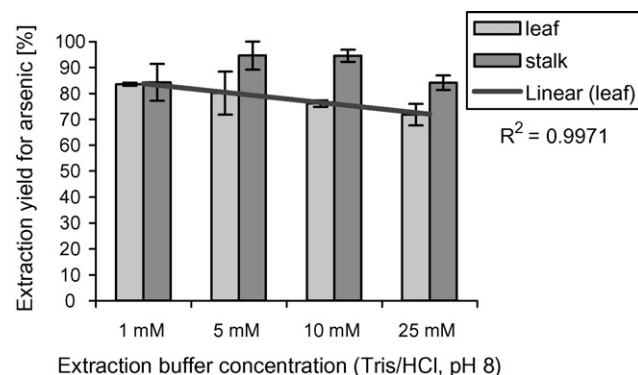


Fig. 3. Dependence of the extraction yield obtained for arsenic from leaves and stalks of *Tropaeolum majus* cultivated under MMA(V) exposure on the concentration of the extraction buffer. Average values with standard deviations for three independent samples are given.

an adsorbent for phenolic compounds, polyvinylpolypyrrolidone (PVPP), were added to the protein extract solutions. These additives did not influence the extracted protein amounts estimated by the Bradford assay (Table 1).

In order to test a further buffer type which provides another pH milieu, ammonium acetate adjusted to pH 4.0 was compared to the Tris/HCl system, pH 8.0, regarding the extraction yield obtained for proteins from control plants and plants cultivated under MMA(V) exposition. Similar protein amounts were solved from the plants by both buffer types. No substantial differences to the control plants were observed for the protein concentrations extracted from arsenic exposed plants.

The Bradford assay used for the determination of protein concentrations in the current study has become widely accepted for protein quantification in biological samples due to its sensitivity and uncomplicated feasibility. Nevertheless, the Bradford assay provides semi-quantitative data particularly for complex samples since the dye binding varies depending on the kind of proteins. Further, the surfactant SDS which was a constituent of some of the samples listed in Table 1, interferes with the protein quantification. But no better alternatives are currently available for protein quantification in biological samples, because other protein assays which are based on Cu(II) reduction are widely more susceptible to reducing agents like DTT [25] which was present in all samples.

3.2. Extraction yield for arsenic under different parameters optimized for protein extraction

The influence of the parameters optimized for the extraction of proteins from leaf and stalk tissue on the simultaneous extraction

Table 1

Effect of different buffer additives on the extracted protein concentrations from leaves of *Tropaeolum majus*.

Buffer additives	Extracted protein concentration μg mL ⁻¹ leaf extract	mg g ⁻¹ fresh leaf tissue
–	149 ± 37	0.5 ± 0.1
2 mM PMSF	127 ± 6.1	0.4 ± 0.02
2 mM PMSF, 1 g L ⁻¹ PVPP	133 ± 13	0.4 ± 0.04
2 mM PMSF, 1 g L ⁻¹ PVPP, 0.5% (w/v) SDS	116 ± 23	0.4 ± 0.07
2 mM PMSF, 1 g L ⁻¹ PVPP, 1% (w/v) SDS	273 ± 40	0.9 ± 0.1
2 mM PMSF, 1 g L ⁻¹ PVPP, 2% (w/v) SDS	412 ± 130	1.3 ± 0.4
2% (w/v) SDS	309 ± 24	1.1 ± 0.09

10 mL of 5 mM Tris/HCl buffer solution at pH 8.0 with 50 mM DTT was used as extraction buffer for 3 g fresh leaf material. Average concentrations from $n = 3$ –6 parallel samples are listed.

of arsenic was examined. Whereas a 10 mM Tris buffer provided the highest extraction yield for proteins (compare Fig. 2), the extraction efficiency for arsenic from leaves decreased linearly with increasing buffer concentration from 82% down to 71% (Fig. 3). As mentioned above (Section 3.1), the 5 mM Tris buffer system was chosen as the best compromise for a simultaneous extraction of arsenic and proteins from leaves. For stalks, higher arsenic yields resulted in the extracts both with 5 and 10 mM Tris buffer than with 1 and 25 mM buffer concentrations. Altogether, high extraction efficiencies were obtained with the Tris/HCl buffer systems ranging between 75 and 90%, so that it can be assumed that the main part of the arsenic accumulated in the plant tissues is present in the protein extract and can possibly bind to proteins. For comparison, $78.3 \pm 6.9\%$ ($n=40$) of the total arsenic accumulated in leaves of the same plants cultivated under MMA(V) exposure were extracted with 10 mM sodium phosphate buffer, pH 7.0, giving a similar extraction yield as with the 10 mM Tris buffer. In another study dealing with the analysis of cadmium-binding proteins, the extraction efficiency for Cd obtained by a HEPES-NaOH buffer, pH 7.6, that was used for the extraction of proteins from spinach leaves, was evaluated to 63–100% [26].

With the addition of 2% (w/v) SDS to the extraction buffer system the extraction yield for arsenic declined to $47.5 \pm 2.3\%$ ($n=3$) in case of 5 mM Tris buffer and to $43.4 \pm 1.7\%$ ($n=3$) in case of 5 mM acetate buffer. Presumably, the micelles formed by the surfactant in the solution phase exclude the hydrophilic, polar arsenic compounds. However, the protein-associated arsenic should not be excluded.

The leaves exhibited a total arsenic content of $21.5 \pm 0.5 \text{ mg kg}^{-1}$ fresh mass ($n=5$). In contrast, the control plants were characterized by a background arsenic level of $0.3 \pm 0.1 \text{ mg kg}^{-1}$ fresh leaf mass ($n=4$). The arsenic species distribution of the plants exposed to MMA(V) was investigated recently [20]. The analysis of leaf extracts revealed that As(III), MMA(V) and another unknown metabolite, possibly MMA(III), dominated to 20, 21, and 59%, respectively, the total water-extractable arsenic species content in the cells.

3.3. Determination of the arsenic binding capacity of protein extracts spiked with monomethylarsonate under the influence of varied extraction parameters

In order to determine the binding capacity of proteins extracted from leaf cells under varying extraction conditions, different amounts of arsenic species were added to the raw protein extract. In order to simulate native conditions, a reducing environment was maintained in the extracts by adding the reducing agent DTT. In addition to the prevention of protein aggregation by disulfide bonds, the reducing agent provides binding sites for arsenic in the form of free thiol groups of proteins which are susceptible to oxidation under non-physiological oxidative conditions. A fundamental impact of the presence of a reducing agent in the sample solution on arsenic bindings to sulfur-containing proteins was observed in mass spectrometric studies [9]. Further, a non-denaturing extraction buffer system was chosen and all extraction, incubation, and precipitation steps were performed at 4 °C. The final results of the arsenic spiking experiments are pointed out by the arsenic

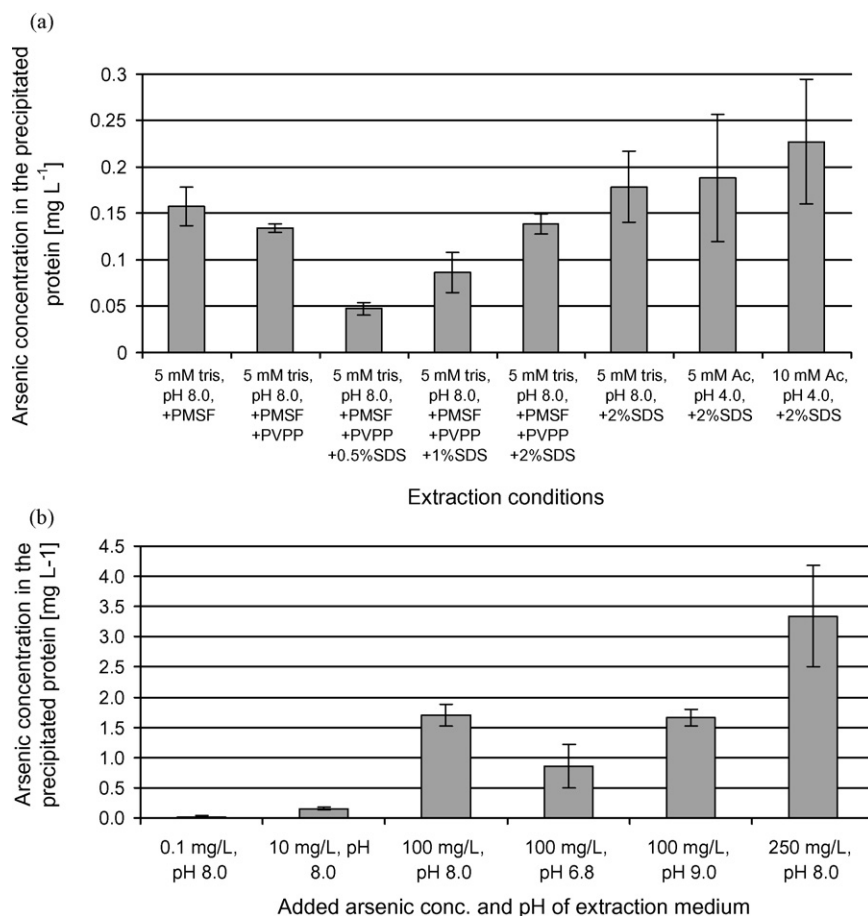


Fig. 4. Influence of the extraction conditions on the arsenic concentration in the precipitated protein fraction. (a) Addition of 10 mg As L⁻¹ extract volume before protein precipitation. Variation of extraction conditions: two different extraction buffers and pH values, addition of PMSF, PVPP, and different amounts of SDS (b) Addition of different amounts of arsenic to the extract before protein precipitation. Extraction with 5 mM Tris buffer at different pH values.

Table 2

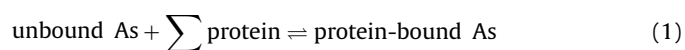
Portions of arsenic found in the protein fraction after precipitation related to the original arsenic amount added to the raw protein extract under different extraction conditions.

Arsenic spiking concentration in the raw extract (mg L ⁻¹)	Extraction buffer	Extraction additives	Arsenic portion in the protein precipitate (% of spiked amount)
10	5 mM Tris/HCl, pH 8.0	PMSF	2.1 ± 0.3
10	5 mM Tris/HCl, pH 8.0	PMSF + PVPP	1.8 ± 0.06
10	5 mM Tris/HCl, pH 8.0	PMSF + PVPP + 0.5%SDS	0.63 ± 0.09
10	5 mM Tris/HCl, pH 8.0	PMSF + PVPP + 1%SDS	1.2 ± 0.28
10	5 mM Tris/HCl, pH 8.0	PMSF + PVPP + 2%SDS	1.8 ± 0.15
10	5 mM Tris/HCl, pH 8.0	2%SDS	2.4 ± 0.5
10	5 mM acetate, pH 4.0	2%SDS	1.0 ± 0.42
10	10 mM acetate, pH 4.0	2%SDS	1.1 ± 0.36
100	5 mM Tris/HCl, pH 6.8	–	0.7 ± 0.3
100	5 mM Tris/HCl, pH 8.0	–	1.04 ± 0.26
100	5 mM Tris/HCl, pH 9.0	–	1.2 ± 0.22
250	5 mM Tris/HCl, pH 8.0	–	1.4 ± 0.1

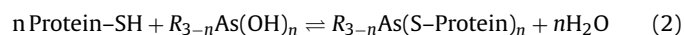
Average values with standard deviations for $n = 3$ –5 parallel prepared samples are listed.

concentrations found in the protein fraction after TCA/acetone precipitation (Fig. 4). Despite of same arsenic amounts added to the raw protein extract, the arsenic concentrations in the protein precipitates vary depending on the extraction conditions (Fig. 4a). The enhancement of the protein extraction by rising additions of SDS to the extraction buffer (see Table 1) was accompanied by decreased arsenic concentrations in the protein precipitates compared to SDS-free samples. This behaviour can be possibly ascribed to the masking of potential arsenic-binding proteins in the SDS micelles as well as to a denaturation of the proteins resulting in a spatial shielding of potential arsenic-binding sites. Besides, other types of proteins were extracted using SDS than with aqueous buffer systems. An opposed effect emerged with rising SDS concentration probably due to the strong enhancement of extracted protein amounts.

With increasing arsenic spiking concentrations in the original extracts the arsenic concentrations in the protein precipitates increased (Fig. 4b). However, the ratio of the arsenic fraction associated to the protein precipitate to the initially spiked arsenic amount remained nearly constant. An average value for this ratio expressed in % values in Table 2 of $1.37 \pm 0.55\%$ ($n = 12$) resulted for all varied extraction parameters and of $1.39 \pm 0.51\%$ ($n = 6$) for all extraction experiments performed without SDS. These findings suggest a binding equilibrium (Eq. (1)) between free arsenic in the solution phase and protein-bound arsenic that is controlled by varied extraction parameters to a small degree (Table 2).



The underlying reaction mechanisms can only be presumed because pool data are obtained with the current analytical procedure. The most likely reaction type should be based on the affinity of trivalent arsenic to sulfur (Eq. (2)). However, also other types of binding could be involved such as non-covalent associations or chemi- or physisorption to the surface of the protein precipitate.



with $n \leq 3$ and R = organic residue with an As–C bond.

The portion of arsenic found in the final protein precipitate seems to be low related to the initially spiked arsenic amount. However, related to the absolute protein mass of the extracts high arsenic concentrations in the range from 263 to 1001 mg kg⁻¹ result depending on the sample type for original spiking concentrations of 10 mg As L⁻¹.

In order to purify the protein pellet from non-protein impurities, a washing step was performed with 4 mL ethanol. In the final wash solutions, arsenic concentrations of 0.016 ± 0.0031 mg L⁻¹ ($n = 6$) were detected. This corresponds to an arsenic loss of $5.7 \pm 1.3\%$

($n = 6$) that is resolved from the protein pellet by the washing step. The quality of the 1D gel electrophoretic separation was not improved by this wash operation. In contrast, the protein bands were considerably weaker presumably due to a partial protein loss during washing.

3.4. Determination of the arsenic binding capacity of leaf proteins from plants cultivated under MMA(V) exposure

For the investigation of the arsenic binding capacity of leaf proteins from plants grown under MMA(V) exposure those parameters that proved to be most effective for the extraction of proteins in the preceding experiments (Section 3.1) were employed. Due to the presence of 2% (w/v) SDS in the extractant solution both hydrophilic water-soluble proteins and hydrophobic membrane proteins were solved from the leaf tissue. In contrast to the protein samples spiked with arsenic after completing the extraction (Section 3.3), the assumed arsenoproteins were already formed in the cells before the extraction process. Therefore, the discussed SDS based inhibition of the arsenic–protein binding should not play a role.

The arsenic concentrations in the leaf extracts used for the subsequent protein precipitation amounted to 5.4 ± 1.1 mg L⁻¹ ($n = 3$) in case of Tris buffer (pH 8) extraction and to 4.1 ± 0.3 mg L⁻¹ ($n = 3$) in case of acetate buffer (pH 4) extraction. Based on these protein extracts, $0.82 \pm 0.03\%$ ($n = 3$) and $0.61 \pm 0.13\%$ ($n = 3$) of the total arsenic quantity present in the original Tris or acetate buffer extracts, respectively, were recovered in the protein precipitates. These low relative values correspond to high arsenic concentrations related to the protein mass of the extracts: 323.3 ± 2.9 mg kg⁻¹ ($n = 3$) for the Tris buffer extractions and 129.0 ± 23.5 mg kg⁻¹ ($n = 3$) for the acetate buffer extractions.

From these results a similar protein binding capacity can be deduced for leaves of plants cultivated under MMA(V) exposure and for leaf extracts of control plants that were spiked with MMA(V) before protein precipitation.

3.5. SDS-PAGE of extracted leaf proteins

The sample preparation scheme (Fig. 1) that was optimized regarding arsenic and protein extraction is suited for SDS-PAGE of complex plant protein samples with elevated as well as with background arsenic levels and provides a high reproducibility (Fig. 5). In studies dealing with the analysis of metal-binding proteins or metalloproteins the precipitation step was omitted in order to prevent metal dissociation. Unfortunately, this non-denaturing sample preparation leads to a strongly reduced number of protein bands in the 1D-PAGE [26,27]. This was also observed in our study. A direct application of the raw buffer extracts onto the gels delivered no

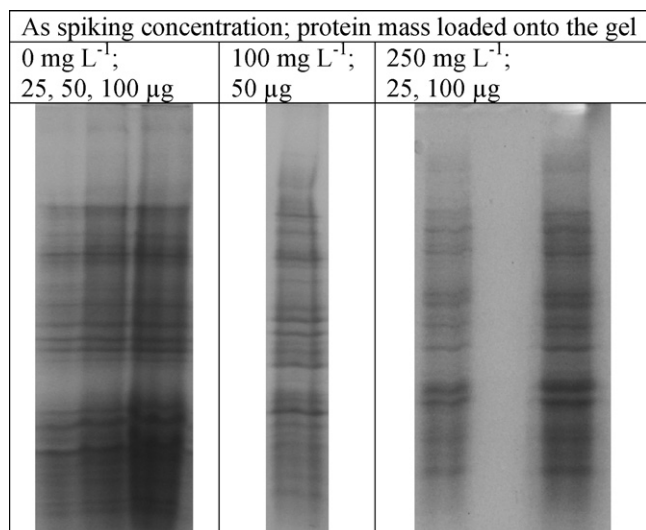


Fig. 5. SDS-PAGE results for leaf protein extracts obtained with 5 mM Tris/HCl buffer, pH 8/50 mM DTT and protein precipitation with 10% (w/v) TCA/2 mM DTT in acetone.

evaluable protein separation. The precipitation of proteins by TCA in acetone produced a significant improvement of the 1D-GE results both regarding number and intensity of different protein bands. The contrast between the protein bands and the background staining was also considerably improved because the protein precipitation serves as an efficient purification step. A danger for dissociation of non-covalent or coordinative arsenic–protein bindings, which are relied on a definite three-dimensional protein structure, can be assumed to occur during the denaturing protein precipitation. However, covalent arsenic bindings proposed in Eq. (2) should not be affected.

4. Conclusion

The discussed experiments demonstrate the influencing factors that must be considered during the whole sample preparation procedure for the analysis of arsenic-binding proteins in plants.

The arsenic binding capacity of the total leaf protein pool was determined after protein extraction and precipitation for arsenic spiking experiments of the raw protein extracts as well as for plants grown under arsenic exposure. It can be concluded that, on average, only 1% of the original arsenic amount in the raw protein extract is recovered in the precipitated protein fraction after TCA/acetone treatment. However, related to the total protein mass, high arsenic concentrations in the upper mg kg⁻¹ range result. Despite of higher protein concentrations in the extract after addition of SDS, the binding capacity of the protein precipitate for arsenic was not elevated.

In the future, alternative protein extraction protocols such as phenol-based strategies and alternative precipitation agents such as TCA in water or ammonium sulfate should be tested with regard to their influence on the arsenic–protein associations. In addition to MMA(V) other arsenic species should be included and kinetic binding studies should be performed. The stability of arsenic–protein bindings under the particular conditions of the SDS-PAGE should be examined using arsenic-binding standard proteins such as thioredoxin. In order to extend the separation performance of the gel electrophoresis, an isoelectric focusing step should be conducted before SDS-PAGE in terms of a two-dimensional approach.

Acknowledgements

We are much obliged to Ines Volkmann from the Helmholtz Centre of Environmental Research Leipzig, Department of Analytical Chemistry, for carrying out the SDS-PAGE analyses.

References

- [1] A.C. Schmidt, W. Reisser, J. Mattusch, R. Wennrich, K. Jung, J. Anal. At. Spectrom. 19 (2004) 172.
- [2] Z.C. Huang, T.B. Chen, M. Lei, Y.R. Liu, T.D. Hu, Environ. Sci. Technol. 42 (2008) 5106.
- [3] A.C. Schmidt, J. Mattusch, W. Reisser, R. Wennrich, Chemosphere 56 (2004) 305.
- [4] K.A. Mir, A. Rutter, I. Koch, P. Smith, K.J. Reimer, J.S. Poland, Talanta 72 (2007) 1507.
- [5] A.P. Navaza, M. Montes-Bayón, D.L. Le Duc, N. Terry, A. Sanz-Medel, J. Mass Spectrom. 41 (2006) 323.
- [6] W. Zhang, Y. Cai, Anal. Chem. 75 (2003) 7030.
- [7] A. Raab, J. Feldmann, A.A. Meharg, Plant Physiol. 134 (2004) 1113.
- [8] A.C. Schmidt, J. Koppelt, M. Neustadt, M. Otto, Rapid Commun. Mass Spectrom. 21 (2007) 153.
- [9] A.C. Schmidt, M. Neustadt, M. Otto, J. Mass Spectrom. 42 (2007) 771.
- [10] A.C. Schmidt, J. Mattusch, R. Wennrich, Microchim. Acta 151 (2005) 167.
- [11] G. Ballihaut, F. Claverie, C. Pecheyran, S. Mounicou, R. Grimaud, R. Lobinski, Anal. Chem. 79 (2007) 6874.
- [12] I. Feldmann, C.U. Koehler, P.H. Roos, N. Jakubowski, J. Anal. At. Spectrom. 21 (2006) 1006.
- [13] J.K.C. Rose, S. Bashir, J. Giovannoni, M.M. Jahn, S.R. Saravanan, Plant J. 39 (2004) 715.
- [14] W. Wang, R. Vignani, M. Scali, M. Cresti, Electrophoresis 27 (2006) 2782.
- [15] S.C. Carpentier, E. Witters, K. Laukens, P. Deckers, R. Swennen, B. Panis, Proteomics 5 (2005) 2497.
- [16] N. Islam, M. Lonsdale, N.M. Upadhyaya, T.J. Higgins, H. Hirano, R. Akhurst, Proteomics 4 (2004) 1903.
- [17] B.E. Maserti, C.M. Della Croce, F. Luro, R. Morillon, M. Cini, L. Caltavuturo, J. Chromatogr. B 849 (2007) 351.
- [18] F.S. Wu, M.Y. Wang, Anal. Biochem. 139 (1984) 100.
- [19] A. Raab, P.N. Williams, A. Meharg, J. Feldmann, Environ. Chem. 4 (2007) 197.
- [20] A.C. Schmidt, N. Haufe, M. Otto, Talanta 76 (2008) 1233.
- [21] S. Gao, R.G. Burau, J. Environ. Qual. 26 (1997) 753.
- [22] U.K. Lämmli, Nature 277 (1970) 680.
- [23] A. Görg, W. Weiss, M.J. Dunn, Proteomics 4 (2004) 3665.
- [24] S.H. Park, S.R. Bean, J. Agric. Food Chem. 51 (2003) 7050.
- [25] L.S. Ramagli, in: A.J. Link (Ed.), Methods in Molecular Biology, vol. 112: 2-D Proteome Analysis Protocols, Humana Press Inc., Totowa, NJ, 1999, pp. 99–103.
- [26] A. Polatajko, M. Azzolini, I. Feldmann, T. Stuezel, N. Jakubowski, J. Anal. At. Spectrom. 22 (2007) 878.
- [27] C. Schmidt de Magalhães, M.A.Z. Arruda, Talanta 71 (2007) 1958.



Chlorine gas sensors using one-dimensional tellurium nanostructures

Shashwati Sen^a, Madhvi Sharma^a, Vivek Kumar^c, K.P. Muthe^a, P.V. Satyam^b,
Umananda M. Bhatta^b, M. Roy^d, N.K. Gaur^c, S.K. Gupta^{a,*}, J.V. Yakhmi^a

^a Technical Physics & Prototype Engineering Division, Bhabha Atomic Research Centre, Mumbai 400085, India

^b Institute of Physics, Sachivalaya Marg, Bhubaneswar, Orissa 751005, India

^c Department of Physics, Barkatullah University, Bhopal, MP 462026, India

^d Chemistry Division, Bhabha Atomic Research Centre, Mumbai 400085, India

ARTICLE INFO

Article history:

Received 7 August 2008

Received in revised form

23 September 2008

Accepted 24 September 2008

Available online 17 October 2008

Keywords:

Nanotubes

Gas sensor

Band gap

Impedance spectroscopy

Grain boundary

ABSTRACT

Tellurium nanotubes have been grown by physical vapor deposition under inert environment at atmospheric pressure as well as under vacuum conditions. Different techniques such as scanning electron microscopy (SEM), transmission electron microscopy (TEM), X-ray diffraction (XRD) and optical absorption have been utilized for characterization of grown structures. Films prepared using both types of tellurium nanotubes were characterized for sensitivity to oxidizing and reducing gases and it was found that the relative response to gases depends on the microstructure. Nanotubes prepared at atmospheric pressure (of argon) showed high sensitivity and better selectivity to chlorine gas. Impedance spectroscopy studies showed that the response to chlorine is mainly contributed by grain boundaries and is therefore enhanced for nanotubes prepared under argon atmosphere.

© 2008 Elsevier B.V. All rights reserved.

1. Introduction

Investigations on the growth and characteristics of quasi one-dimensional structures (Q1D) are important as they provide inherently enhanced integration density of devices, have novel physical effects due to reduced dimensionality and have high surface to volume ratio desirable for some applications [1]. A variety of inorganic materials including elemental and compound semiconductors have been synthesized in various nano-forms [2]. Tellurium is a low band gap semiconductor and is useful for various applications such as optical recording, thin film transistors, strain sensitive devices, infrared detectors, gas sensors and thermoelectric devices [3,4]. Due to anisotropic crystal structure, Te is amenable to the growth of one-dimensional nanostructures as nanowires and nanotubes.

In earlier studies, we have investigated pure Te thin films as room temperature gas sensors for H₂S, NH₃ and NO [5–7]. However, there are no reports on application of Te nanostructures as gas sensors or Te thin films for detection of chlorine gas. Chlorine is a widely used chemical in many industrial processes and is very harmful when emitted into environment. It may be detected by sophisti-

cated techniques as gas chromatography, chemical detecting tubes and electrochemical sensors [8–10]. Sensors based on semiconductor oxides such as In₂O₃ and WO₃ have also been employed for the detection of this gas but most of them require elevated temperatures for operation [11,12]. Patil and Patil have reported room temperature detection of Cl₂ gas at high concentrations (300 ppm) using CuO modified ZnO [13]. In a recent report, Sb-doped, SnO₂ films with nanoporous structure have been employed for room temperature chlorine sensing [14]. As tellurium thin films have been shown to detect many reducing and oxidizing gases at room temperature [5–7], it is desirable to explore Te nanostructures for sensitivity to chlorine.

In most of the studies reported in the literature, nanostructures of Te have been grown by solution routes such as reduction of TeO₂ or orthotelluric acid by hydrazine and oxidation of NaHTe in the presence of surfactants [15–18]. Nanostructures have also been prepared by hydrothermal and solvothermal processes. Few groups have reported the growth of Te nanostructures by vapor phase techniques. Geng et al. [19] have synthesized Te nanobelts from Al₂Te₃ in a furnace under Ar gas flow. Mohanty et al. [20] have synthesized Te nanotubes with triangular cross-section and some with hexagonal cross-section by evaporation of Te in a tubular furnace in the presence of Ar gas at intermediate pressure of 1–1.5 Torr and deposition temperature of 150–200 °C. They reported the growth of nanowires and nanorods in case of Si (1 1 1) and sapphire (0 0 1)

* Corresponding author. Tel.: +91 22 25593863; fax: +91 22 25505296.

E-mail address: dr Gupta@barc.gov.in (S.K. Gupta).

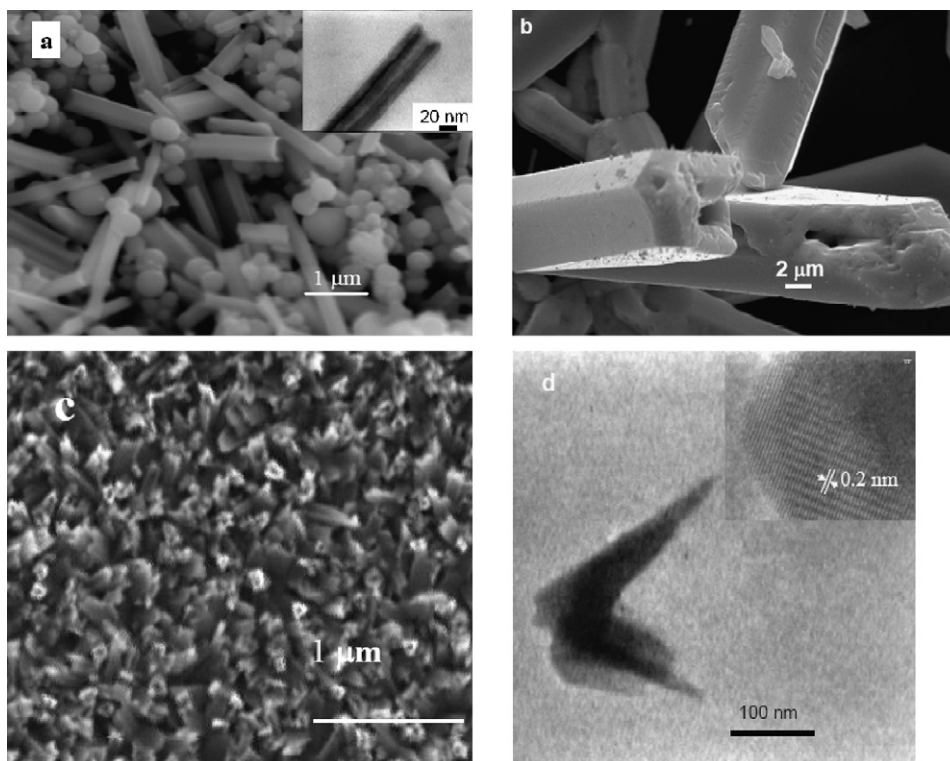


Fig. 1. SEM images of typical (a) type-I sample—Te nanotubes grown in furnace, (b) type-II sample—Te micro-rods and (c) type-III sample—Te nanotubes on silicon. (d) TEM and HRTEM images of type-III sample. Inset of (a) shows TEM of a type-I nanotube.

substrate, respectively [21]. Metraux and Grobéty [22] have grown Te nanostructures on Si (1 1 1) substrate and aluminium foil by heating Te in an induction furnace (in the presence of magnetic field). They observed formation of nanotubes on both substrates under argon ambient at 1 mbar pressure. However, at 10^{-7} mbar, the formation of nanowires on aluminium foil and platelets on Si (1 1 1) was observed. Interestingly, when the depositions were carried out in a high vacuum coating unit (thus without the assistance of magnetic field) the formation of dendritic Te filaments was observed which led to the inference that the presence of magnetic field is primarily responsible for the observed growth behavior. Recently Wang et al. [23] reported the growth of ultra-wide Te nanobelts by vapor deposition in a horizontal quartz tube at evaporation temperature of 350°C under vacuum conditions. Similarly, Chen et al. [24] have fabricated Te nanowires of different orientations, on NaNO_2 floccules by vacuum deposition at 10^{-5} mbar. Thus we find that diverse Te nanostructures have been obtained by tuning the growth conditions. As the microstructure of materials affects their functionality [25], we expect suitable Te nanostructures to show selective response for detection of desired gases.

Here, we report the growth of Te nanotubes at atmospheric pressure in a horizontal quartz tube and under high vacuum conditions. The gas sensing characteristics of these nanostructures were investigated and Te nanotubes prepared under atmospheric pressure were found to detect chlorine gas at room temperature at very low concentration of 0.5 ppm. Impedance spectroscopy studies showed that the response to chlorine is mainly due to resistance changes at grain boundaries.

2. Experimental

Growth of Te nanostructures was carried out at atmospheric pressure as well as under vacuum conditions. At atmospheric pres-

sure, the growth was carried out under argon atmosphere in a tubular furnace as described earlier [26]. Briefly, Te powder was loaded in an alumina boat and placed in a 1-m long quartz tube. The furnace temperature was raised to 550°C in presence of Ar gas flow ($150\text{ cm}^3/\text{min}$) and maintained at this temperature for 2 h. Te nanotubes were found to deposit on quartz tube in the direction of gas flow at temperature of $30\text{--}50^{\circ}\text{C}$. Micro-rods (whiskers) of Te were found to grow in the high temperature ($350\text{--}400^{\circ}\text{C}$) zone of the furnace. Similar deposits were also obtained on different substrates placed in the tube.

In the case of synthesis carried out by thermal evaporation under vacuum, high purity Te powder was loaded in a molybdenum boat. The depositions on Si (1 1 1) substrates (maintained at 100°C) were carried out under vacuum of 2×10^{-5} mbar at a rate of 10 Å/s maintained using a quartz crystal thickness monitor.

Microstructure of the grown Te was studied by scanning electron microscopy (SEM) using TESCAN make VEGA MV2300T/40 system. The chemical composition was obtained by energy dispersive X-ray (EDX) analysis, while structural information was obtained by X-ray diffraction (XRD) spectra obtained by employing $\text{Cu K}\alpha$ radiation. TEM analysis was carried out using JEOL 2010 UHR system and the images were recorded using a $20\times$ Gatan camera. For TEM, powder of Te nanostructures grown in furnace and scraped powder from silicon substrates in case of Te grown in high vacuum were utilized. Powders were dispersed in propanol by ultrasonication and a drop of this solution was placed on carbon-coated Cu grid. The impedance spectroscopy measurements were carried out using AUTOLAB make potentiostat–galvanostat (model PGSTAT 302).

For study of gas sensitivity, Te grown in horizontal furnace was dispersed in ethanol to make a suspension, which was painted on a glass plate (called type-I sample) with two pre-deposited gold electrodes and thick film gold contacts were made on individual whiskers of tellurium (called type-II samples). In case of Te deposited on Si (1 1 1) substrates under vacuum (called type-III

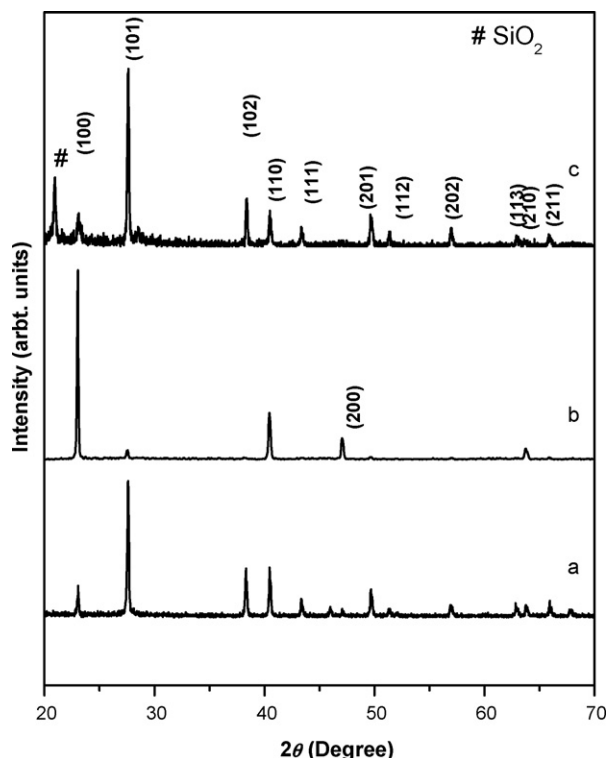


Fig. 2. XRD spectra of: (a) type-I, (b) type-II and (c) type-III samples (peak marked # corresponds to SiO_2).

samples), Au electrodes were thermally evaporated on nanostructured Te film. Electrical contacts were made by soldering silver wires to the gold pads, using indium solder. The sensitivity towards different gases was determined by measuring the resistance in atmosphere and on exposure to different gases using Keithley multimeter. The measurement setup has been described elsewhere [5]. All the sensitivity measurements were carried out at room temperature. Sensitivity to some of the gases was also studied using Te thin films deposited on alumina substrates (called type-IV samples).

On exposure to oxidizing gases such as NO and Cl_2 the resistance of all the samples was found to decrease while on exposure to reducing gases such as H_2S and NH_3 , the resistance increased, as expected for p-type nature of Te. The response (S) to different gases is defined by

$$S = \left| \frac{(R_a - R_g)}{R_a} \right|$$

where R_a and R_g are the resistances of the sensors in air and gas, respectively. It may be noted a factor of 4 change in resistance corresponds to $S = 3$ for a reducing gas (where $R_g > R_a$) and $S = 0.75$ for an oxidizing gas (where $R_a > R_g$). The response time is defined as the time taken to attain 90% of the change in resistance and the recovery time is the time taken by the sensors to return back to 10% of its original resistance.

3. Results and discussion

SEM and TEM micrographs of various samples are shown in Fig. 1 and corresponding X-ray diffraction spectra are shown in Fig. 2. SEM micrograph of low temperature deposit at atmospheric pressure (type-I samples) showed presence of nanotubes (Fig. 1a). Inset of this figure shows the TEM image of a single nanotube. Detailed characterization and growth mechanism of these nanotubes has been

reported earlier [26]. The tubes had outer diameter of 100–500 nm, wall thickness of ~10 nm and maximum length up to 3 μm . All the tubes were found to be hexagonal in shape and their size was independent of the nature of the substrate. Deposits in quartz tube at temperatures of 350–400 $^\circ\text{C}$ were found to consist of Te micro-rods as shown in Fig. 1b (type-II samples). The whiskers had a hexagonal cross-section with a diameter of 2–4 μm and length ranging from 1 to 10 mm.

Depositions under vacuum were carried out at a substrate temperature of 100 $^\circ\text{C}$, as films at this temperature were found to be crystalline in earlier studies [6]. Si (1 1 1) substrates were used due to their good lattice matching with Te [22]. SEM of these samples (type-III) showed growth of nanotubes with diameter of 70–150 nm (Fig. 1c). The size distribution of the nanotubes was found to be quite narrow in this case as compared to type-I samples. TEM image (Fig. 1d) showed that the nanotubes had prong-like structure with tubes showing split at the end as reported in earlier study [26]. The HRTEM image at the tip of these prongs showed the lattice spacing of ~0.2 nm corresponding to the (0 0 3) direction of Te, confirming the growth direction to be along c-axis. Our result of nanotubes deposition under vacuum conditions is in contrast with that of Metraux and Grob  ty [22] who have not observed the formation of Te nanostructures when depositions were performed in a high vacuum coating unit.

X-ray diffraction spectra of different structures are shown in Fig. 2. Powder diffraction spectra were measured for type-I and type-II samples and grazing angle XRD was obtained for type-III samples due to their thin film nature. All of the samples are found to be single crystalline Te. All the peaks could be indexed for the hexagonal structure of tellurium with, space group $P3_121$ and lattice parameters of $a = b = 4.49$ and $c = 5.9$ \AA . This shows that samples are high quality Te crystals without any impurity phase. It is seen that relative intensity of (1 0 0) peak in whiskers (spectrum b) is quite large compared to sample of type-I (spectrum a). This is because these are c-axis oriented whiskers of large size and lie parallel to the substrate during XRD. In case of spectra (c) we also observe a peak corresponding to SiO_2 as these Te nanotubes (type-III sample) have been grown on Si substrate with thin oxide layer. The variation in relative intensities of peaks in three spectra arises due to different orientations of crystallites.

Because of the anisotropic nature of Te lattice, it shows tendency to form 1D structures with Te adatoms having greater tendency of sticking along c-axis. In case of growth in furnace at atmospheric pressure, formation of nanowires and nanotubes by vapor–solid (VS) mechanisms has been described earlier [26]. In this case we observe nanotubes at temperature of 30–50 $^\circ\text{C}$ irrespective of the nature of the substrate. However this temperature is not sufficient for epitaxial growth of Te on a given substrate. In the case of vacuum deposition at 100 $^\circ\text{C}$, the growth of crystalline Te is governed by surface kinetics as Te adatoms gain sufficient energy to occupy favorable lattice sites on the substrate. For Si (1 1 1) substrate, $3a_{\text{surface}} \text{ Si}(1\ 1\ 1) = 2a_{\text{bulk}} \text{ Te}$ (where a_{surface} and a_{bulk} are lattice parameters on surface of silicon and bulk crystalline Te) with a mismatch of only ~0.9%. This leads to preferential nucleation of Te (0 0 1) parallel to Si (1 1 1) [22]. The Te adatoms continue to find and attach themselves to the energetically favorable sites leading to the formation of oriented tubes.

Optical absorption spectra and photoluminescence studies provide information about defects in semiconductors. UV–vis absorption spectra were recorded for different samples and the results are shown in Fig. 3. The value of optical band gap was estimated using Mott and Davis model for direct allowed transitions in semiconductors using equation:

$$\alpha(\nu)h\nu = B(h\nu - E_{\text{gap}})^{m/2}$$

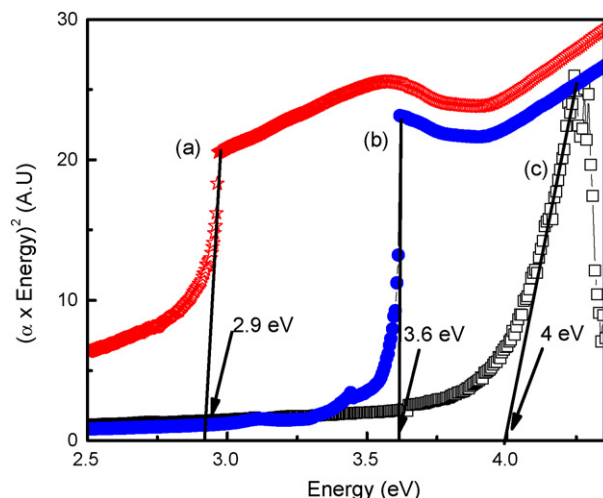


Fig. 3. Optical absorption spectra of: (a) type-I (b) type-II and (c) type-III samples.

where α is the absorption coefficient, E_{gap} is the optical band gap, $h\nu$ is the energy of incident photon, B is a constant and $m = 1$ for direct transitions. To determine the band gap, we have plotted $(\alpha h\nu)^2$ as function of $(h\nu)$. The absorption in the 3–6 eV region for Te has been attributed to transitions from bonding to antibonding states [27,28]. Band gap for type-I nanotubes is seen to be less than that of whiskers (type-II) and type-III nanotubes indicating larger number of defects or states in the gap for type-I samples. The defects in the structure are important as they may contribute to interaction with gases but have disadvantage of reducing mobility of carriers. Thus it is expected that type-I samples may act as better sensor material due to increased defects.

Response of different samples was studied for many gases and Table 1 gives typical response to H_2S , NH_3 , NO and Cl_2 gases. It is found that (a) response of whiskers to all gases is quite small compared to other samples, (b) both whiskers and thin films have better response to H_2S in comparison to Cl_2 and NO and (c) type-I samples have maximum sensitivity for detection of Cl_2 . Small response of whiskers is understandable as these have much smaller surface area compared to other samples. To understand the better sensitivity of nanotubes to chlorine, we have performed impedance spectroscopy measurements on type-I and type-III samples on exposure to 4 ppm of chlorine and H_2S gases and the results are shown in Fig. 4. The impedance spectra have been analyzed using equivalent circuit as shown in Fig. 4(c). It consists of two RC networks consisting of R_{Bulk} and C_{Bulk} for intragrain region and R_{Grain} and C_{Grain} for grain boundary region. R_0 is additional frequency independent resistance. Values of various parameters obtained from impedance spectra (before and after exposure to gases) are given in Table 2 for two types of samples. Type-I samples show only grain boundary contribution. This is understandable as these have been prepared by dispersion of nanotubes in solution and coating on substrates that yield very poor grain to grain connectivity. Type-III samples

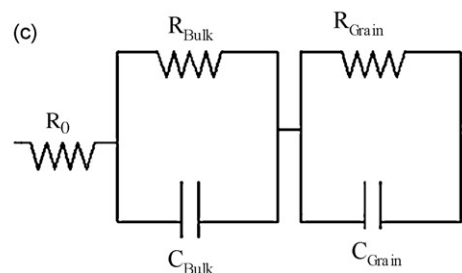
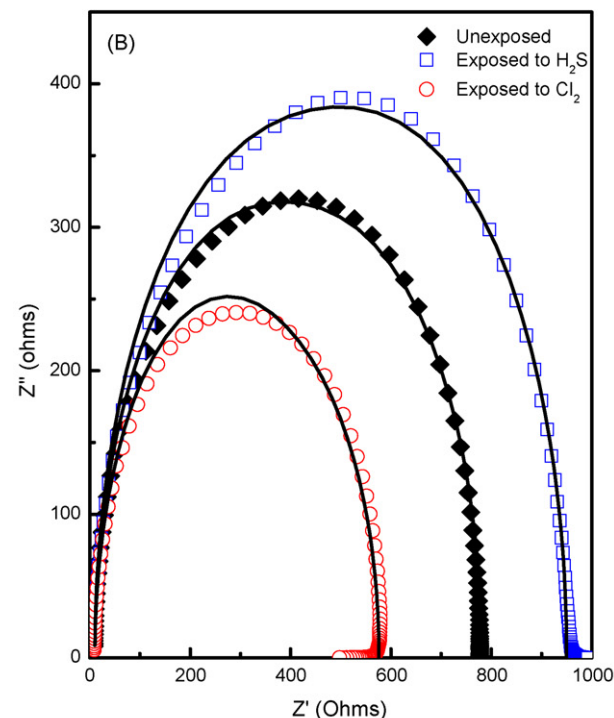
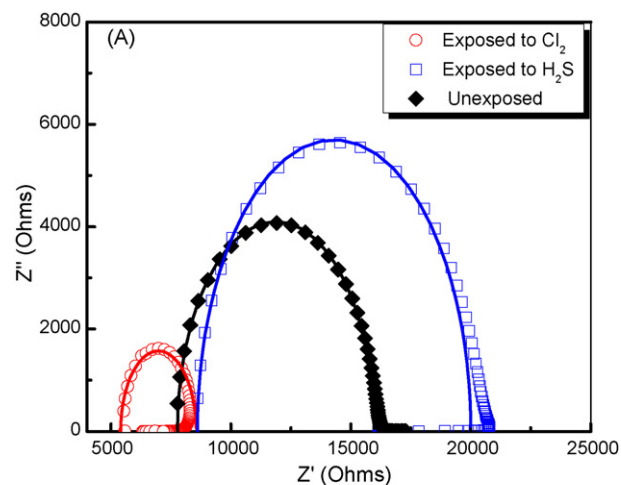


Fig. 4. Impedance spectra before and after exposure to 4 ppm of Cl_2 and H_2S gases at room temperature for typical (a) type-I and (b) type-III samples. The scattered points show experimental data and the solid lines represent fitting obtained with the values given in Table 2. (c) Shows the equivalent circuit used for analysis.

Table 1

Typical response of different Te samples to H_2S , NH_3 , NO and Cl_2 gases at concentration of 8 ppm.

Gas	Response to gases for samples of type			
	I (nanotubes)	II (whiskers)	III (nanotubes)	IV (thin films)
H_2S	0.33	0.087	0.18	1.85
NH_3	0.0204	0.009	0.026	0.1
Cl_2	0.75	0.043	0.43	0.57
NO	0.47	0.009	0.27	0.30

show both intragrain and intergrain (grain boundary) contributions and it is found that grain boundary region has much higher contribution in response to Cl_2 in comparison to intragrain region. On the other hand, contributions of intragrain and grain boundary regions towards response to H_2S are similar. A similar and in fact,

Table 2

Parameters obtained by fitting of impedance spectroscopy data to equivalent circuit for type-I and type-III samples. Parameters have been measured before and during exposure to H₂S and Cl₂ gases at 4 ppm concentration.

Parameter	Type-I sample (atm. pressure)			Type-III sample (vacuum deposited)		
	Unexposed	Cl ₂ exposed	H ₂ S exposed	Unexposed	Cl ₂ exposed	H ₂ S exposed
R_0 (Ω)	7770	5300	8600	10	10	10
R_{Bulk} (Ω)	–	–	–	400	390	440
C_{Bulk} (F)	–	–	–	2.21×10^{-8}	2.147×10^{-8}	2×10^{-8}
R_{Grain} (Ω)	8200	3150	11,400	370	176	500
C_{Grain} (F)	1.29×10^{-7}	1.01×10^{-6}	1.16×10^{-7}	8.6×10^{-8}	1.45×10^{-7}	6.63×10^{-8}

often higher contribution of intragrain region to H₂S is in agreement with earlier studies on thin films [5]. A higher contribution of grain boundary region towards response to chlorine explains better sensitivity of nanotube samples to this gas in comparison to thin film and whisker samples. This also explains best response of type-I samples to chlorine.

As type-I samples have good response to chlorine, these were further studied. Response of a typical sensor to chlorine at 2 ppm concentration is shown in Fig. 5(a). A response time of 30 s and recovery time of 2 h is observed for a typical sample. Response of another film to chlorine at different concentrations is shown in Fig. 5(b). The recovery time is found to increase with concentration of Cl₂ however, the resistance of the film is found to recover to its base resistance even when exposed to 8 ppm of gas indicat-

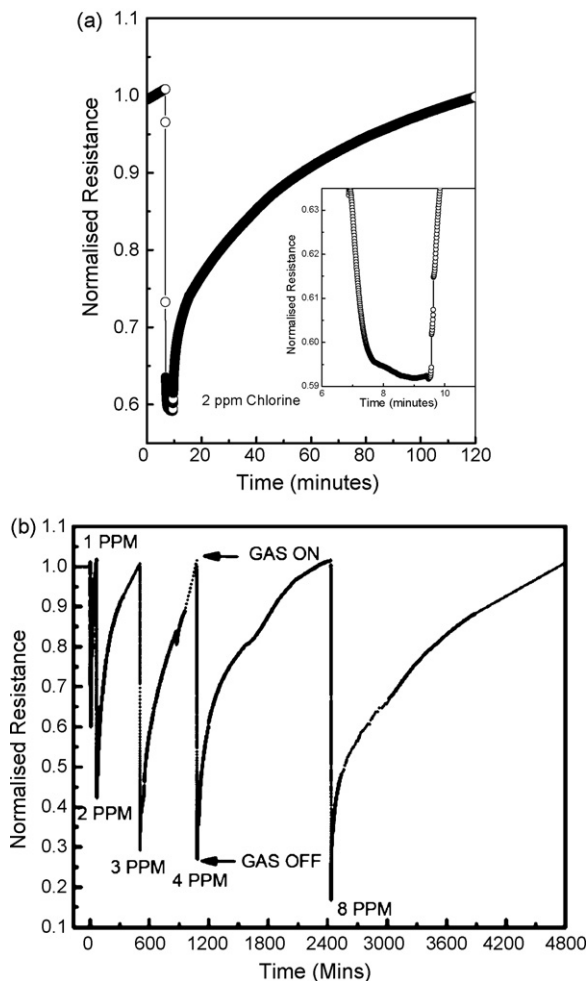


Fig. 5. (a) Response of a type-I sensor to 2 ppm chlorine. Inset gives expanded view to show saturation at 2 ppm. (b) Response and recovery characteristics for different concentrations of Cl₂ gas for another type-I sample.

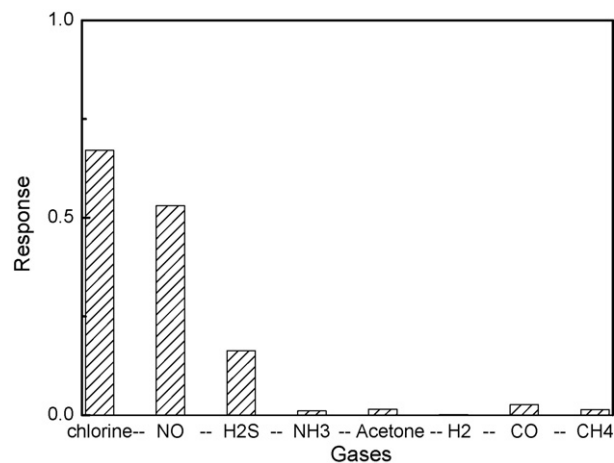


Fig. 6. Response of a typical type-I sample to H₂S, NO, Cl₂, acetone, NH₃, CO and CH₄ gases at 4 ppm and H₂ at 2% concentration.

ing a reversible change on exposure to chlorine gas. Investigations to reduce recovery time are being carried out. Response of a typical type-I sample to many oxidizing and reducing gases is shown in Fig. 6. It is observed that these samples are quite selective for response to chlorine.

The mechanism of response of Te to oxidizing or reducing gas has been reported in earlier studies [4]. Te is a p-type semiconductor and adsorption of oxygen (in normal air) leads to trapping of electrons and therefore introduction of holes in the lattice. This reduces the resistance. The resistance is further reduced on adsorption to oxidizing gases that trap electrons (such as Cl₂), and increased on exposure to reducing gases that remove the adsorbed oxygen.

4. Conclusion

The growth of Te nanotubes has been carried out via a one-step physical vapor deposition process at atmospheric pressure as well as under high vacuum conditions. Te nanotubes grown under atmospheric conditions in a horizontal furnace showed high sensitivity towards Cl₂ gas at room temperature. It is found that chlorine has larger influence on grain boundary resistance compared to intragrain resistance leading to better response of nanostructure materials.

References

- [1] J.G. Lu, P. Chang, Z. Fan, Mater. Sci. Eng. R 52 (2006) 49.
- [2] C.N.R. Rao, F.L. Deepak, G. Gundiah, A. Govindraj, Prog. Solid State Chem. 31 (2003) 5.
- [3] T. Ikari, H. Berger, F. Levy, Mater. Res. Bull. 21 (1986) 99.
- [4] S. Sen, K.P. Muthe, N. Joshi, S.C. Gadkari, S.K. Gupta, Jagannath, M. Roy, S.K. Deshpande, J.V. Yakhmi, Sens. Actuator B 98 (2004) 154.
- [5] S. Sen, V. Bhandarkar, K.P. Muthe, M. Roy, S.K. Deshpande, R.C. Aiyer, S.K. Gupta, J.V. Yakhmi, V.C. Sahni, Sens. Actuator B 115 (2006) 270.

- [6] V. Bhandarkar, S. Sen, K.P. Muthe, M. Kaur, M. Senthil Kumar, S.K. Deshpande, S.K. Gupta, J.V. Yakhmi, V.C. Sahni, *Mater. Sci. Eng. B* 131 (2006) 156.
- [7] V. Bhandarkar, S. Sen, K.P. Muthe, S.K. Deshpande, S. Bhattacharya, S.K. Gupta, *Asian J. Phys.* 14 (2005) 97.
- [8] A. Galdikas, Z. Martunas, A. Setkus, *Sens. Actuator B* 7 (1992) 633.
- [9] D.H. Dawson, D.E. Williams, *J. Mater. Chem.* 6 (3) (1996) 409.
- [10] T. Miyata, T. Hikosaka, T. Minami, *Sens. Actuator B* 69 (2000) 16.
- [11] J. Tamaki, *Sens. Actuator B* 83 (2002) 190.
- [12] T.V. Belysheva, L.P. Bogovtseva, *J. Anal. Chem.* 61 (2006) 494.
- [13] D.R. Patil, L.A. Patil, *Sens. Actuator B* 123 (2007) 546.
- [14] A. Chaparadza, S.B. Rananavare, *Nanotechnology* 19 (2008) 245501.
- [15] B. Mayer, Y.N. Xia, *J. Mater. Chem.* 12 (2002) 1875.
- [16] R. Zheng, W. Cheng, E. Wang, S. Dong, *Chem. Phys. Lett.* 395 (2004) 302.
- [17] Z. Liu, Z. Hu, J. Liang, S. Li, Y. Yang, S. Peng, Y. Qian, *Langmuir* 20 (2004) 214.
- [18] Z. Liu, Z. Hu, Q. Xie, B. Yang, J. Wu, Y. Qian, *J. Mater. Chem.* 13 (2003) 159.
- [19] B. Geng, Y. Lin, X. Peng, G. Meng, L. Zhang, *Nanotechnology* 14 (2003) 983.
- [20] P. Mohanty, T. Kang, B. Kim, *J. Phys. Chem.* 110 (2006) 791.
- [21] P. Mohanty, J. Park, B. Kim, *J. Nanosci. Nanotechnol.* 6 (2006) 3380.
- [22] C. Métraux, B. Grobety, *J. Mater. Res.* 19 (2004) 2159.
- [23] Q. Wang, G.-D. Li, Y.-L. Liu, S. Xu, K.-J. Wang, J.-S. Chen, *J. Phys. Chem. C* 111 (2007) 12926.
- [24] H. Chen, H. Lu, Y. Nie, J. Zhang, M. Zhang, Q. Dai, S. Gao, S. Kan, D. Li, G. Zou, *Phys. Lett. A* 362 (2007) 61.
- [25] B. Lui, H. Zeng, *J. Am. Chem. Soc.* 126 (2004) 8124.
- [26] S. Sen, U.M. Bhatta, V. Kumar, K.P. Muthe, S. Bhattacharya, S.K. Gupta, J.V. Yakhmi, *Cryst. Growth Des.* 8 (1) (2008) 238.
- [27] R. Swan, A.K. Ray, C.A. Hogarth, *Phys. Stat. Sol. A* 127 (1991) 555.
- [28] U.K. Gautam, C.N. Rao, *J. Mater. Chem.* 14 (2004) 2530.



Digital image-based flame emission spectrometry

Wellington Silva Lyra, Vagner Bezerra dos Santos, Amália Geiza Gama Dionízio, Valdomiro Lacerda Martins, Luciano Farias Almeida, Edvaldo Nóbrega Gaião, Paulo Henrique Gonçalves Dias Diniz, Edvan Cirino Silva*, Mário César Ugulino Araújo

Universidade Federal da Paraíba, CCEN, Departamento de Química, Caixa Postal 5093, CEP 58051-970 João Pessoa, PB, Brazil

ARTICLE INFO

Article history:

Received 25 April 2008

Received in revised form

25 September 2008

Accepted 26 September 2008

Available online 17 October 2008

Keywords:

Digital image

Red–green–blue colour system

Flame emission spectrometry

Alkaline metal determination

Pharmaceutical formulations

Water analysis

ABSTRACT

A digital image-based flame emission spectrometric (DIB-FES) method for the quantitative chemical analysis is proposed here for the first time. The DIB-FES method employs a webcam to capture the digital images which are associated to a radiation emitted by the analyte into an air–butane flame. Since the detection by webcam is based on the RGB (red–green–blue) colour system, a novel mathematical model was developed in order to build DIB-FES analytical curves and estimate figures of merit for the proposed method. In this approach, each image is retrieved in the three R, G and B individual components and their values were used to define a position vector in RGB three-dimensional space. The norm of this vector is then adopted as the RGB-based value (analytical response) and it has revealed to be linearly related to the analyte concentration. The feasibility of the DIB-FES method is illustrated in three applications involving the determination of lithium, sodium and calcium in anti-depressive drug, physiological serum and water, respectively. In comparison with the traditional flame emission spectrometry (trad-FES), no statistic difference has been observed between the results by applying the paired *t*-test at the 95% confidence level. However, the DIB-FES method has offered the largest sensitivities and precision, as well as the smallest limits of detection and quantification for the three analytes. These advantageous characteristics are attributed to the trivariate nature of the detection by webcam.

© 2008 Elsevier B.V. All rights reserved.

1. Introduction

Recently, Maleki et al. [1] and Gaião et al. [2] have exploited the potential of digital images to carry out quantitative chemical analyses. Such digital images have been obtained with up to 24 bits (16.7 million colours) by using the RGB (red–green–blue) colour system [3,4]. In their first work [1], the authors have used the digital images for simultaneous determination of Al (III) and Fe (III) in alloys using the chrome azurol S (CAS) as chromogenic reagent. In this case, a neural network model based on the RGB values obtained from the digital images captured from the Al (III)–CAS and Fe (III)–CAS complexes was built. Gaião et al. [2] have used digital images obtained from a webcam to develop a novel digital image-based (DIB) titration method, which was successfully applied to the determination of total alkalinity in mineral and tap waters.

In the works mentioned above, the digital images present the colour of the emergent radiation, which is a complementary colour of the absorbed radiation by the absorbent molecular species. Thus,

the digital images are indirectly associated to the molecular absorption phenomenon that provides the basis to the well-known UV–Vis spectrometry [5]. However, the literature does not show the use of digital images to perform chemical analysis based on flame emission.

In this paper, a digital image-based flame emission spectrometric (DIB-FES) method for quantitative chemical analysis is proposed. The DIB-FES method also employs, as elsewhere [2], a webcam to capture the digital images, but now they are associated to a radiation emitted by the analytes into an air–butane flame [5]. Since the detection by webcam is based on the RGB colour system, a novel mathematical approach was developed in order to build linear analytical curves and estimate figures of merit for the DIB-FES method. Three applications involving different matrices and analytes were carried out in order to demonstrate the feasibility and potentiality of the proposed methodology. The first one involves the determination of lithium in an anti-depressive drug, which is nowadays a relevant problem from a public sanitation point of view. The second application concerns the sodium determination in physiological serum, which is a universally adopted solution to provide sodium ions to the human organism. The third application consists in the water analysis involving the determination of calcium, which has as function to improve the flocculation and coagulation

* Corresponding author. Fax: +55 83 3216 7438.

E-mail address: edvan@quimica.ufpb.br (E.C. Silva).

Nomenclature

C	concentration of the analyte (mg L^{-1})
I	intensity of emission (arbitrary units)
k	constant of proportionality (arbitrary units)
LOD	limit of detection (mg L^{-1})
LOQ	limit of quantification (mg L^{-1})
\bar{R}_s , \bar{G}_s , and \bar{B}_s	average value of the red, green and blue component of the sample solution (arbitrary units)
\bar{R}_b , \bar{G}_b , and \bar{B}_b	average value of the red, green and blue component of the blank solution (arbitrary units)
\bar{R}_{s-b} , \bar{G}_{s-b} , and \bar{B}_{s-b}	differences between average values of the red, green and blue components of the standard/sample solution and blank solution (arbitrary units)
$\ \mathbf{v}\ $	norm of a vector \mathbf{v} in the RGB tridimensional space (arbitrary units)
$\ \mathbf{v}_b\ $	norm of the vector associated to blank solution (arbitrary units)
$s_{\bar{R}}$, $s_{\bar{G}}$, and $s_{\bar{B}}$	standard deviation of the average values of the red, green and blue components of the vector associated to blank solution (arbitrary units)
s_b	standard deviation of the norm of the vector associated to blank solution (arbitrary units)
\mathbf{v}_1 , \mathbf{v}_2 , \mathbf{v}_3 , \mathbf{v}_4 , and \mathbf{v}_5	vector associated to first, second, third, fourth, and fifth standard solution respectively (arbitrary units)

Greek letters

α	intersection of the analytical curve
β	slope of the analytical curve

efficiency in water treatment plants. For comparison purposes, all mentioned analytes were determined by using the traditional flame emission spectrometry (also named flame photometry) [5]. It is worth noting that in all applications carried out in this work, all the samples chosen do not present spectral interference and/or matrix effect.

2. Experimental

2.1. Reagents, samples, and solutions

Stock solutions of $1000 \text{ mg L}^{-1} \text{ Li}^+$, Na^+ and Ca^{2+} were prepared from their previously dried carbonate salts by means of dissolution with HCl 1:1 (v/v). The stock solution of $10.0 \text{ g L}^{-1} \text{ La}^{3+}$ was prepared from its previously dried chloride salt at 110°C . The working standard solutions of Li^+ ($6.0\text{--}30.0 \text{ mg L}^{-1}$), Na^+ ($1.8\text{--}9.0 \text{ mg L}^{-1}$) and Ca^{2+} ($10.0\text{--}50.0 \text{ mg L}^{-1}$) were prepared by suitable dilutions from their respective stock solutions.

The water samples were acquired from a local water treatment plant. Aliquots of the stock solution of La^{3+} were added to the water samples and Ca^{2+} working standard solutions in order to minimize the decreasing in the calcium emission signal. After dilution, these solutions presented $1.0 \text{ g L}^{-1} \text{ La}^{3+}$.

Six brands of an anti-depressive drug with a nominal content of $300 \text{ mg Li}_2\text{CO}_3$ were purchased from local drugstores. For each brand, a portion of 10 tablets was grinded in a mortar to yield a fine powder. An appropriate amount of the powder ($400\text{--}450 \text{ mg}$) was dissolved in 25 mL of $0.1 \text{ mol L}^{-1} \text{ HCl}$ solution, shaking the mixture with a magnetic stirring for 10 min. Afterwards, a filtration to remove the insoluble particles was performed, and

the resulting solution was diluted to a final volume of 1 L with water.

Six samples of physiological serum with a nominal concentration of 0.90% (w/v) NaCl were also purchased in a local drugstore.

Before the analysis, all samples were suitably diluted with water in order to interpolate the analytical signals in a linear response range.

Chemicals of analytical grade and water recently distilled-deionized by a Milli-Q (Millipore) system were used throughout the work.

2.2. Apparatus

A schematic diagram and a photograph of the analytical system assembled for digital images acquisition are shown in Fig. 1. It comprises a model Instant Creative Webcam [6], which was connected to an universal serial bus (USB) inlet of a Pentium III 650 MHz microcomputer (PC). In order to avoid interferences of the ambient light, the webcam was coupled to a cardboard tube with approximately 4.0 cm of internal diameter and 13.0 cm of length. The other edge of the tube was coupled to a small window of the photometer chimney. This tube was finally placed into a black wood box with approximately $20.0 \text{ cm} \times 16.0 \text{ cm} \times 11.0 \text{ cm}$, as illustrated in Fig. 1.

A model NK-2004 Digimed flame photometer was used for the FES measurements. This instrument was operated according to recommendations of the manufacturer for the maximum sensitivity with an air–butane flame.

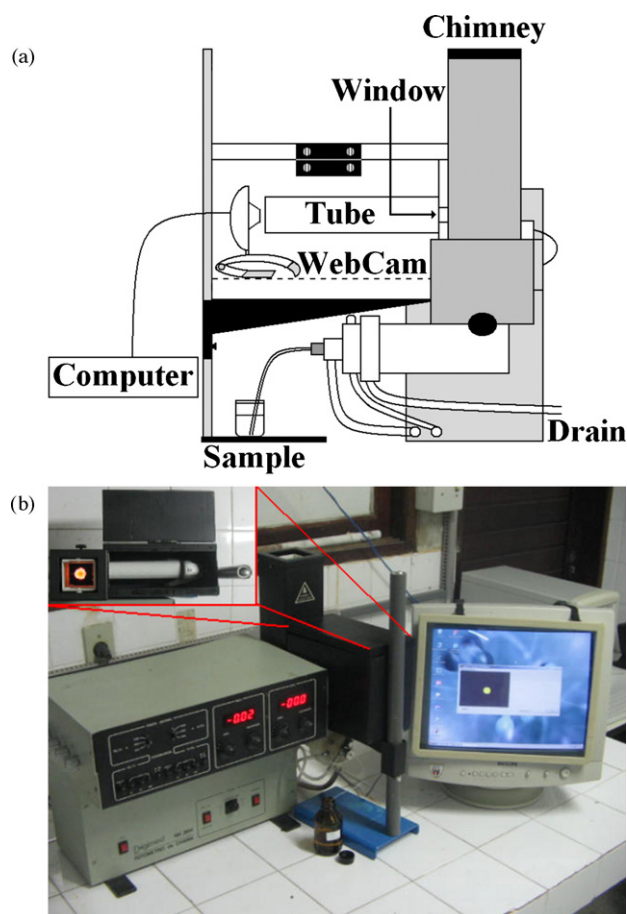


Fig. 1. Schematic diagram (a) and photograph (b) of the analytical system assembled for acquisition of the digital images. For further details, see the text.

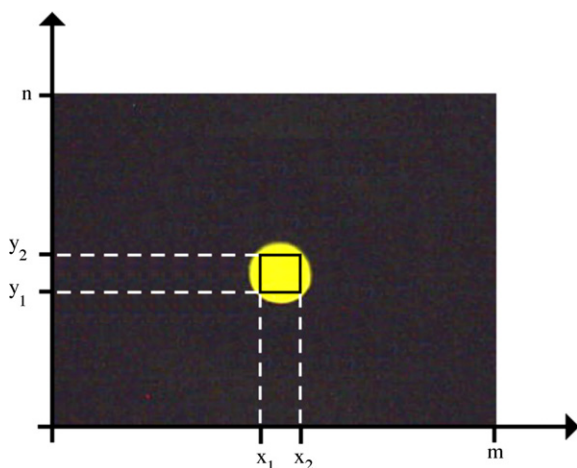


Fig. 2. Digital image with $n \times m$ pixels obtained from one of the calibration solutions. x_1 , x_2 , y_1 and y_2 are coordinates that delimit the flame region more adequate for analytical treatment.

2.3. Digital image acquisition and region selection for data treatment

The webcam was configured to capture 24-bits digital images (16.7 million colours) at rate of 34 images s^{-1} and $352 \text{ pixels} \times 288 \text{ pixels}$ of spatial resolution [6]. Nevertheless, the region selected for data treatment, which is delimited in the image illustrated in Fig. 2, is a matrix with $25 \text{ pixels} \times 25 \text{ pixels}$ (where $x_2 - x_1 = 25$ and $y_2 - y_1 = 25$). The images were captured and stored as “bmp” format files by means of the software written in Kylix (version 3.0).

The region of the flame in Fig. 2, named interconal area [5], is localized approximately 2.5 cm above the bottom of the flame. This area is commonly used for emission measurements in the trad-FES, because it presents a thermal equilibrium and it is often rich in free atoms. Such region has revealed to be appropriated to build the DIB-FES analytical curves.

In order to delimit the region for data treatment (Fig. 2), the user selects such region only in the first digital image by using the mouse. After that, the software automatically uses the same coordinates of the delimited region for all digital images (calibration solutions and samples). Right after that, the software performs the scan of the pixels (column-by-column) on the delimited region of each image. Then, it retrieves the values of the R , G and B individual components from each pixel. Thereafter, the software calculates the \bar{R} , \bar{G} and \bar{B} average values of all pixels. These values are used to localize a point in the RGB three-dimensional space and to define a position vector \mathbf{v} (see Fig. 4) associated to a digital image from each calibration solution or sample. The norm “ $\|\cdot\|$ ” of the vector \mathbf{v} is adopted as the RGB-based value for building the analytical curves by using the mathematical approach described in the next section.

2.4. RGB-based value, analytical curve and figures of merit

A mathematical approach aiming at a linear relationship between the proposed RGB-based value and analyte concentration is developed as follows.

The norm “ $\|\cdot\|$ ” of the vector \mathbf{v} is calculated as

$$\|\mathbf{v}\| = \sqrt{\bar{R}_{s-b}^2 + \bar{G}_{s-b}^2 + \bar{B}_{s-b}^2} \quad (1)$$

where \bar{R}_{s-b} , \bar{G}_{s-b} and \bar{B}_{s-b} are the results of the difference between the \bar{R}_s , \bar{G}_s and \bar{B}_s average values of all pixels from delimited region

(Fig. 2) in digital images from the calibration solutions or samples and \bar{R}_b , \bar{G}_b and \bar{B}_b from the blank.

By assuming that the number of photons that reaches the photo-transducer of the webcam is proportional to the emission intensity of the source (I) and that the relationship between “ I ” and the analyte concentration (C) for a specific concentration range is linear, the following equation is valid:

$$\|\mathbf{v}\| = kC \quad (2)$$

Thereafter, Eq. (2) describes, as experimentally attested in present work (see Fig. 5), a linear relationship between the vector norm $\|\mathbf{v}\|$ and the concentration of the analyte. As mentioned in previous section, $\|\mathbf{v}\|$ is the RGB-based value here employed to build DIB-FES analytical curves. Moreover, the vectors associated to the digital images from each analyte should be positioned onto a same support line in the RGB three-dimensional space (see Fig. 4).

The fitted regression models were checked by using analysis of variance (ANOVA). After that, the analytical performance of the DIB-FES method was assessed using the sensitivity, limit of detection (LOD), limit of quantification (LOQ) and relative standard deviation (R.S.D.). These figures of merit were also compared with those estimated to evaluate the performance of the trad-FES method.

The values of some figures of merit were obtained according to the IUPAC recommendations reported elsewhere [7,8]. However, the standard deviation of the blank (s_b), LOD and LOQ were estimated for the DIB-FES method by using a novel approach proposed in this work. This treatment is necessary by considering that the analytical response is now associated to a vector norm based on three experimental variables, namely the R , G and B components. For this purpose, the mathematical approach described below should be adopted.

According to Eq. (1), the vector norm $\|\mathbf{v}_b\|$ associated to the digital image from the blank is given by

$$\|\mathbf{v}_b\| = \sqrt{\bar{R}_b^2 + \bar{G}_b^2 + \bar{B}_b^2} \quad (3)$$

where \bar{R}_b , \bar{G}_b and \bar{B}_b are the average values of all pixels from delimited region (Fig. 2) in the digital images from the blank.

Since $\|\mathbf{v}_b\|$ is based on three variables, the associated standard deviation (s_b) should be estimated by using the expression below, which is derived employing error propagation equations described elsewhere [9]

$$s_b = \sqrt{\frac{(\bar{R}_b s_{\bar{R}})^2 + (\bar{G}_b s_{\bar{G}})^2 + (\bar{B}_b s_{\bar{B}})^2}{\bar{R}_b^2 + \bar{G}_b^2 + \bar{B}_b^2}} \quad (4)$$

where $s_{\bar{R}}$, $s_{\bar{G}}$ and $s_{\bar{B}}$ are the standard deviations associated to the \bar{R}_b , \bar{G}_b and \bar{B}_b values resulting of the digital images from the blank, respectively.

Finally, LOD and LOQ are calculated by using the s_b value estimated by Eq. (4) and the following expressions:

$$\text{LOD} = \frac{3s_b}{\beta} \quad (5)$$

and

$$\text{LOQ} = \frac{10s_b}{\beta} \quad (6)$$

where “ β ” is the slope from the analytical curve based on Eq. (2) and estimated by linear least-squares regression fitting.

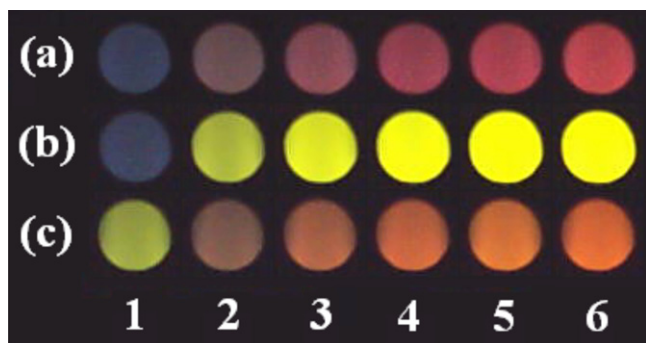


Fig. 3. Digital images captured during the flame emission from lithium (a), sodium (b), and calcium (c) in calibration solutions used to build DIB-FES analytical curves.

3. Results and discussion

3.1. Digital images and emission phenomenon

In Fig. 3 are illustrated the digital images associated to the radiation emitted by lithium (a), sodium (b), and calcium (c) from five calibration solutions with different concentrations. The first image of the sequences is associated to background radiation emitted when the blank solution is aspirated by the photometer (Fig. 1).

As can be seen in Fig. 3a, the images present the red primary colour (remarkably the images 5 and 6) for which the intensity

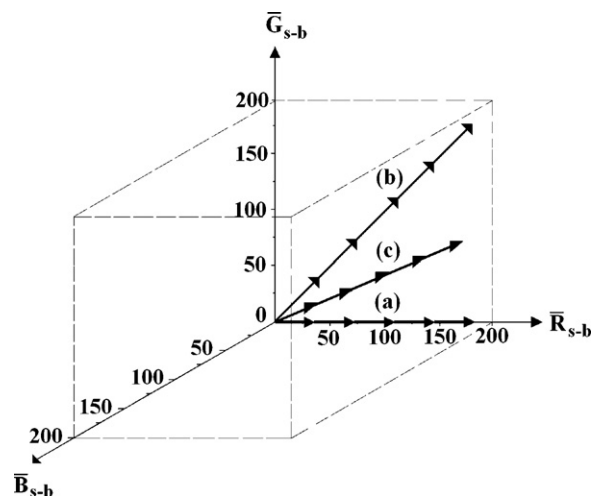


Fig. 4. The norm of the vectors $\mathbf{v}_1\text{--}\mathbf{v}_5$ of each calibration solution and the values of \bar{R}_{s-b} , \bar{G}_{s-b} and \bar{B}_{s-b} for digital images from lithium (a), sodium (b) and calcium (c).

raises as the Li^+ concentration in calibration solutions increases. This radiation corresponds to the resonance lines (duplet) observed around 671 nm in the spectrum of the lithium, which result from the electronic transition from a 2p excited state to the 2s ground state [5].

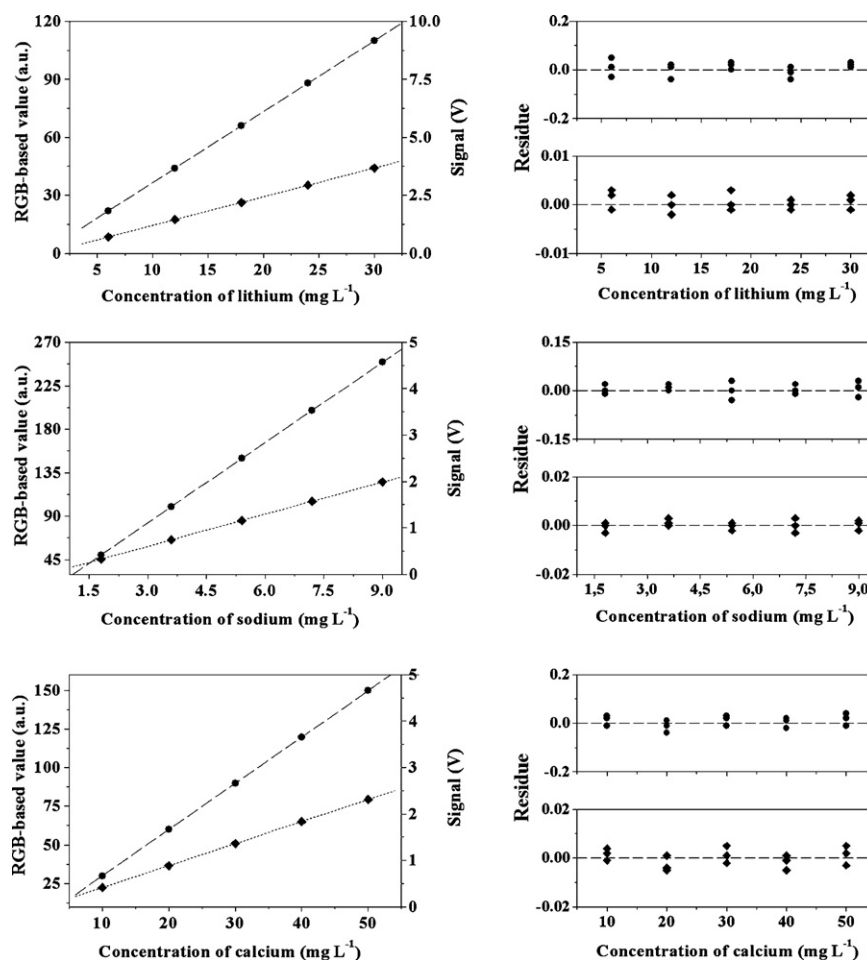


Fig. 5. DIB-FES (dashed line) and trad-FES (dotted line) analytical curves and residual plots for the three determined analytes.

Table 1

Analysis of variance for the fit of a linear model ($Y = \alpha + \beta X$) of the analytical curves (Fig. 5).

Analyte	Degrees of freedom	Mean square (MS)	
		DIB-FES	trad-FES
Lithium	1 ^a	1.45×10^4	16.57
	13 ^b	8.50×10^{-4}	3.26×10^{-6}
	3 ^c	1.16×10^{-3}	3.44×10^{-6}
	10 ^d	7.58×10^{-4}	3.20×10^{-6}
Sodium	1 ^a	7.47×10^4	5.20
	13 ^b	4.12×10^{-4}	4.43×10^{-6}
	3 ^c	3.84×10^{-4}	4.34×10^{-6}
	10 ^d	4.20×10^{-4}	4.47×10^{-6}
Calcium	1 ^a	2.69×10^4	6.78
	13 ^b	5.81×10^{-4}	1.20×10^{-5}
	3 ^c	8.06×10^{-4}	1.57×10^{-5}
	10 ^d	5.13×10^{-4}	1.09×10^{-5}

^a Regression.

^b Residual.

^c Lack of fit.

^d Pure error.

The images in Fig. 3b present the yellow secondary colour, which results from a balanced mixture of the primary colours red + green [2–4]. Such yellow light outcomes from the electronic transition from the 3p excited state to 3s ground state, yielding the resonance lines (D duplet) at 589.6 and 589.0 nm in sodium spectrum [5].

Regarding the images shown in Fig. 3c, it can be seen that they present an orange tertiary colour resulting from the mixture red + green with a larger contribution of red colour. This colour is associated to the emission band from the CaOH species produced in an air–butane flame [5].

In all cases (Fig. 3a–c) the intensity of the colour raises as the analyte concentration in calibration solutions increases. As a result, an increasing concentration of the emitting species yields a proportional increase in the photons amount reaching the photo-transducer of the webcam.

3.2. Relationships between $\|\mathbf{v}\|$ and \bar{R}_{s-b} , \bar{G}_{s-b} and \bar{B}_{s-b} values

Fig. 4a reveals that the vectors \mathbf{v}_1 – \mathbf{v}_5 , associated respectively to each digital image from Li^+ calibration solutions, are localized onto a same straight line whose direction coincides with the \bar{R}_{s-b} axis. It means that there is no significant differences between the \bar{G}_s and \bar{B}_s values and \bar{G}_b and \bar{B}_b , that is, the values of \bar{G}_{s-b} and \bar{B}_{s-b} are close to zero. In case of the sodium (Fig. 4b), \bar{R}_s and \bar{G}_s values present equivalent contributions for the norm of the vectors \mathbf{v}_1 – \mathbf{v}_5 and, consequently, these vectors are lie on bisectrix line between \bar{R}_{s-b} and \bar{G}_{s-b} axis. In Fig. 4c is shown that \bar{R}_s and \bar{G}_s values associated to digital images from the Ca^{2+} calibration solutions also contribute for the vector norm, but in this case, present different proportions. Thus, the straight line onto which the vectors \mathbf{v}_1 – \mathbf{v}_5 are localized presents

a direction closer to the \bar{R}_{s-b} axis due to the larger contribution of this component.

3.3. Analytical curves, analysis of variance and performance of the DIB-FES method

Fig. 5 shows the DIB-FES and trad-FES analytical curves obtained in the determination of lithium, sodium and calcium in anti-depressive drug, physiological serum and water, respectively. For both techniques, a linear behaviour between the analytical responses and analyte concentrations for all analytes was observed. Such inference based on a visual inspection can be confirmed by means of the results of ANOVA shown in Table 1 and model residual plots presented in Fig. 5. According to the recommendations found elsewhere [10], the *F*-test for lack of fit should be applied too. For this purpose, the experimental design should also contemplate genuine repeated measurements at least in one of the concentrations levels. In the present work, the analytical curves were built on the basis of three repeated measurements in five levels. Thus, the values of pure errors were calculated by using the mean squares (MS) shown in Table 1.

In all cases, values of $\text{MS}_{\text{lack of fit}}/\text{MS}_{\text{pure error}}$ and $\text{MS}_{\text{regression}}/\text{MS}_{\text{residual}}$ are smaller and much higher than the value of the point of *F*-distribution at the 95% confidence level and corresponding degrees of freedom, respectively. As a result, no evidence of lack of fit for the linear models is observed, and the linear regressions are highly significant. In order to corroborate this conclusion, an analysis of the residual plots (Fig. 5) was also performed. It can be noticed a random distribution of the residuals around zero for all analytes.

Since the DIB-FES and trad-FES analytical curves do not present lack of fit according to ANOVA test, the figures of merit were estimated for both methods and the results are present in Table 2. As can be seen, the DIB-FES method yielded analytical curves with the largest slopes for all analytes. Consequently, the proposed method has a higher sensitivity than those presented by the trad-FES technique. This advantageous characteristic may be attributed to the trivariate detection of the webcam, yielding analytical responses with larger sensitivities. The DIB-FES method also presented better performance in terms of the figures of merit LOD and LOQ. For this purpose, 20 digital images from the blank of each analyte were acquired and used to calculate $s_{\bar{R}}$, $s_{\bar{G}}$ and $s_{\bar{B}}$, as well as the value of s_b .

3.4. Analytical determinations

As presented in Table 3, DIB-FES and trad-FES methods have yielded similar results in the determination of the three analytes. In fact, it was not verified statistic difference between the results by applying the paired *t*-test at the 95% confidence level. However the DIB-FES method presented a better precision as revealed by the smaller values of overall R.S.D. ($n=5$). This satisfactory precision may be ascribed to the multivariate nature of the monitored signal in RGB image-based analytical determinations [2,11].

Table 2

Linear regression parameters, LOD and LOQ of the DIB-FES and trad-FES methods.

Analyte	Regression parameters ($Y = \alpha + \beta X$)				Values of merit figures ($\times 10^{-1}$)			
	α		β		LOD (mg L ⁻¹)		LOQ (mg L ⁻¹)	
	DIB-FES	trad-FES	DIB-FES	trad-FES	DIB-FES	trad-FES	DIB-FES	trad-FES
Lithium	0.07751	−0.03276	3.66879	0.12385	0.9	2.8	3.1	9.3
Sodium	0.01750	−0.09190	27.71650	0.23130	0.4	0.8	1.5	3.0
Calcium	−0.03100	−0.06417	2.99590	0.04754	1.0	2.6	3.2	8.5

Table 3

Contents of lithium, sodium and calcium determined by the DIB-FES and trad-FES methods.

Samples	Analytical method	
	DIB-FES	trad-FES
Anti-depressive	Li ₂ CO ₃ (mg)	
(1)	299.8 ± 0.6	299.5 ± 1.1
(2)	300.0 ± 0.4	300.0 ± 1.4
(3)	299.0 ± 0.5	299.1 ± 1.3
(4)	299.2 ± 0.6	299.8 ± 1.2
(5)	299.5 ± 0.4	298.9 ± 1.5
(6)	299.4 ± 0.3	299.6 ± 1.6
Overall R.S.D.	0.5	1.4
Physiologic serum	NaCl (% w/v)	
(1)	0.88 ± 0.04	0.89 ± 0.07
(2)	0.89 ± 0.02	0.88 ± 0.06
(3)	0.89 ± 0.02	0.90 ± 0.05
(4)	0.89 ± 0.03	0.89 ± 0.06
(5)	0.88 ± 0.05	0.89 ± 0.07
(6)	0.90 ± 0.01	0.89 ± 0.06
Overall R.S.D.	0.02	0.06
Water	Free CaO (in g L ⁻¹)	
(1)	25.0 ± 0.2	24.9 ± 1.5
(2)	25.2 ± 0.2	25.2 ± 1.7
(3)	24.7 ± 0.1	24.9 ± 1.6
(4)	24.8 ± 0.2	24.5 ± 1.0
(5)	25.0 ± 0.3	25.1 ± 1.2
(6)	24.8 ± 0.2	24.7 ± 1.6
Overall R.S.D.	0.2	1.4

4. Conclusions

In this paper is presented the use of digital images obtained with a webcam as a novel detection technique in flame emission spectrometry for implementing quantitative chemical analyses. A simple mathematical model based on RGB colour system and vector norm concept was proposed to build linear analytical curves, as well as to estimate figures of merit of DIB-FES method. This novel treatment is justified considering that the analytical response is now associated to a vector norm based on three experimental variables, namely the R, G and B components.

The proposed DIB-FES method was successfully applied to the determination of lithium, sodium and calcium in anti-depressive drug, physiological serum and water, respectively. In all the applications, LOD, LOQ, precision and sensitivity were better than those

obtained from the trad-FES analysis. In case of lithium determination, the proposed method presented values of LOD and LOQ much smaller than those obtained through the method recently reported in the literature [12].

By using an inexpensive webcam as analytical detector, the proposed strategy offers an promising alternative to traditional flame emission photometry. In addition, since it can dispense a wavelength selector, this characteristic could be exploited to reduce the cost and simplify the instrumentation for flame emission methods. On the other hand, the absence of wavelength selector makes the analytical response from the webcam more susceptible to spectral interference and/or matrix effect, especially in analytical determinations involving complex matrices. Such drawbacks may be overcome by using multivariate calibration methods [11]. In this context, the feasibility for the use of the Generalized Standard Addition Method (GSAM) [13,14] is presently under investigation.

Finally, besides the advantages associated to the low cost and the better figures of merit mentioned above, the main advantages of using a webcam as analytical detector compared with the trad-FES are a larger sensitivity due to trivariate nature of the detection and spatial-resolution-related characteristic inherent to digital images. This last advantage will be explored in future works.

Acknowledgement

The authors thank the Brazilian agency CNPq for scholarship.

References

- [1] N. Maleki, A. Safavi, F. Sedaghatpour, Talanta 64 (2004) 830.
- [2] E.N. Gaião, V.L. Martins, W.S. Lyra, L.F. Almeida, E.C. Silva, M.C.U. Araújo, Anal. Chim. Acta 570 (2006) 283.
- [3] R.S. Berns, Principles of Colour Technology, 3rd ed., Wiley, NY, 2000.
- [4] P. Geladi, H. Grahn, Multivariate Image Analysis, 2nd ed., Wiley, NY, 1996.
- [5] D.A. Skoog, J.J. Leary, Principles of Instrumental Analysis, 4th ed., Saunders College Publishing, NY, 1992.
- [6] <<http://www.waz.com.br/Webcam/creative.Webcam.instant.php?codprod=87960>> (accessed April 2008).
- [7] IUPAC, Pure Appl. Chem. 45 (1976) 99.
- [8] IUPAC, Pure Appl. Chem. 45 (1976) 105.
- [9] D.A. Skoog, D.M. West, F.J. Holler, Fundamentals of Analytical Chemistry, 7th ed., Saunders College Publishing, Philadelphia, 1996.
- [10] N.R. Draper, H. Smith, Applied Regression Analysis, 3rd ed., Wiley, NY, 1998.
- [11] K.R. Beebe, R.J. Pell, B. Seasholtz, Chemometrics—A Practical Guide, Wiley, NY, 1998.
- [12] C.M.L. Silva, V.G.K. Almeida, R.J. Cassela, Talanta 73 (2007) 613.
- [13] B.E.H. Saxberg, B.R. Kowalski, Anal. Chem. 51 (1979) 1031.
- [14] E.C. Silva, V.L. Martins, A.F. Araújo, M.C.U. Araújo, Anal. Sci. 15 (1999) 1235.



Diimine ligand as a novel chemiluminescence enhancer of luminol-containing compounds

Chaivat Smanmoo, Mutsumi Yamasuji, Tomoko Sagawa, Takayuki Shibata, Tsutomu Kabashima, De-Qi Yuan, Kahee Fujita, Masaaki Kai*

Faculty of Pharmaceutical Sciences, School of Biomedical Sciences, Nagasaki University, 1-14 Bunkyo-Machi, Nagasaki 852-8521, Japan

ARTICLE INFO

Article history:

Received 15 July 2008

Received in revised form 6 October 2008

Accepted 6 October 2008

Available online 17 October 2008

Keywords:

Chemiluminescence enhancer

Enhancer

Isoluminol

Luminol

Luminol-containing polymer

ABSTRACT

A series of diimine ligands (DLs) have been synthesized and evaluated for their non-enzymatic chemiluminescence (CL) enhancement of isoluminol or luminol-containing compounds. Of the DLs, *N,N'*-bis(*m*-hydroxybenzylidene)propylenediamine (DL **10**) was found to greatly enhance their CLs approximately 40 folds for isoluminol, 10 folds for luminol and 6 folds for a luminol-containing polymer. The CL enhancement of the compounds was observed in the presence of CH_3CN , H_2O_2 , tetra-*n*-propylammonium hydroxide (TPA), and Fe (III) ion. The possible mechanism of this CL enhancement was discussed on the basis of the chelate formation of the ligand and the metal ions.

© 2008 Elsevier B.V. All rights reserved.

1. Introduction

The use of chemiluminescent reagents in immunoassay and DNA-hybridization assay has gained its popularity since no isotopic labeling is required. Besides, it offers a rapid assay with good sensitivity and selectivity for analytes [1]. The most well-known chemiluminescence (CL) detection system is based on the enzymatic system coupled with enzyme-labeled horseradish peroxidase (HRP) or alkaline phosphatase (ALP) [2–4]. However, these assays are limited by the instability of enzymes [5,6]. Therefore, the non-enzymatic assay for CL detection with extremely high sensitivity is highly required. In order to increase the sensitivity of the non-enzymatic assay, an effective CL enhancer is desirable in the CL reaction. The presence of CL enhancers is beneficial to the CL reaction as they increase the intensity of light emission and prolong the emission [7]. In the last decade, several CL enhancers have been developed for the enzymatic CL reaction, mainly in HRP assays. These CL enhancers are based on the phenol derivative, e.g. lophine and its derivatives, phenylboronic acid derivatives, 6-hydroxybenzothiazole and phenol derivatives [8–12]. Recently, Cui and co-workers [13] extensively studied a number of phenol compounds for the non-enzymatic CL enhancement in the

luminol- $\text{KIO}_4\text{-H}_2\text{O}_2$ system. However, these CL enhancers only twice enhanced the CL of luminol.

Recently, we have developed sensitive macromolecular probes for the CL detection of proteins on a solid-phase membrane [14]. The probe exhibits strong CL depending on the number of luminol moieties that are incorporated into the macromolecular dextran backbone. Therefore more suitable CL enhancers for this macromolecular probe are necessary in order to further increase the sensitivity of this non-enzymatic CL detection system. This paper describes the development of a novel solid-phase CL enhancer based on diimine ligands (DL) for the luminol-containing compound. A newly synthesized diimine ligand (DL **10**), *N,N'*-bis(*m*-hydroxybenzylidene)propylenediamine, was found to significantly enhance the CL of isoluminol, luminol and luminol-containing dextran-based polymer. The CL enhancement by this DL was due to the complexation between DL **10** and Fe (III) which is crucial for the primary oxidation of isoluminol or luminol moiety (Fig. 1).

2. Experimental

2.1. Reagents and apparatus

Tetra-*n*-propylammonium hydroxide (TPA, 1.0M solution in water) was purchased from Sigma-Aldrich, USA. FeCl_3 , luminol, isoluminol, several diamines and benzaldehydes were obtained

* Corresponding author. Tel.: +81 95 819 2438; fax: +81 95 819 2438.

E-mail address: ms-ai@nagasaki-u.ac.jp (M. Kai).

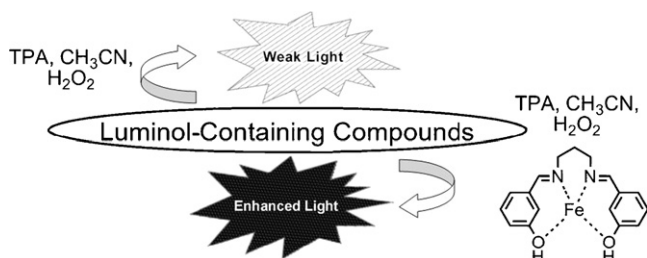


Fig. 1. The presented diagram for the CL enhancement of luminol-containing compounds by DL **10**.

from TCI Co., Japan. Dextran (MW approximately 2×10^6) was obtained from Amersham Biosciences, UK. Biotin-AC₅-hydrazide was obtained from Dojindo, Japan. Sodium borohydride and sodium periodate were obtained from Wako Chemicals, Japan. All chemicals were of analytical grade reagents and were used as received without further purification. The water was prepared using MILLI-XQ (Millipore Corp., USA). All organic solvents (acetonitrile and dimethyl sulfoxide) were freshly dried over 4 Å molecular sieves. Glasswares for the synthesis of diimine ligand were flame-dried and cooled under nitrogen atmosphere before use. The gel liquid chromatography (GLC) was carried out using a TSK gel T2000SW column (Tosoh, Japan). Elemental analysis for the synthesized compound was analyzed by Tokyo Chemical Industry, Japan. CL measurements were performed with a BLR-201 luminescence reader (Aloka, Japan). The detection of CL imaging was achieved using a Lumino CCD AE-6930 densitograph (Atto Co., Japan) and the data were processed by a computer running Densitometer Analyst version 4.0 software. For NMR experiments, residual proton signals from the deuterated solvents were used as references of chloroform (¹H 7.25 ppm, ¹³C 77 ppm) and DMSO (¹H 2.50 ppm).

2.2. Synthesis of *N,N'*-bis(*m*-hydroxybenzylidene)propylenediamine (DL **10**)

3-Hydroxybenzaldehyde (1.06 mL, 10 mmol) and distilled water (30 mL) were added into a 250 mL bottom flask at room temperature. 1,3-Propylenediamine (0.44 mL, 5 mmol) was subsequently added in one portion and the flask was kept at room temperature with vigorous stirring for 6 h. The yellow precipitate was filtered off affording the crude compound which was the recrystallized with methanol to afford DL **10** as yellow crystals (1.29 g, 92%); mp 80 °C; ¹H NMR (400 MHz, CDCl₃) δ (ppm) 2.09 (2H, quintet, *J* 6.8 Hz, NCH₂CH₂CH₂N), 3.69 (4H, t, *J* 6.8, NCH₂CH₂CH₂N), 6.76 (2H, dd, *J* 2.0 and 9.80, ArCH), 6.95 (2H, d, *J* 7.25, ArCH), 7.22 (2H, s, ArCH), 7.51 (2H, dd, *J* 7.80 and 8.0, ArCH), 8.22 (2H, s, CH=N), 9.55 (2H, s, OH), 8.22 (2H, s, 2 × CH=N); ¹³C NMR (75 MHz, CDCl₃) δ 31.7 (CH₂), 59.1 (CH₃), 124.9 (ArCH), 129.4 (ArCH), 131.7 (ArCH), 135.0 (ArCH), 160.0 (C=N); HRMS *m/z* (ESI) calc. for C₁₇H₁₈N₂O₂ [M⁺+Na] 282.1368, found 282.1674. Other DLs were synthesized according to the above procedure.

2.3. Synthesis of luminol-containing dextran-based polymer

Dextran (MW approximately 2×10^6) 400 mg was dissolved in H₂O (80 mL), followed by the precipitation with 300 mL of methanol. The precipitated dextran was re-dissolved in 60 mL of distilled water before reacting with sodium periodate (317 mg, 1.48 mmol). The oxidation of dextran was monitored by UV-spectrophotometer at the wavelength at 310 nm. After 30% oxidation, the oxidized dextran was precipitated with 400 mL of

methanol, and then dissolved in 80 mL of DMSO. To this reaction mixture, biotin-AC₅-hydrazide (30 mg, 0.08 mmol) was added and allowed to stir at room temperature for 3 h. Glacial acetic acid (16 mL) and luminol (240 mg, 1.35 mmol) were subsequently added into the reaction mixture and left stirring at 60 °C overnight. The modified dextran was precipitated with 300 mL of methanol followed by dissolving the modified dextran in ethylene glycol (30 mL). Sodium borohydride (870 mg, 23 mmol) was subsequently added into the reaction mixture and left stirring at room temperature for 4 h. The resultant biotin and luminol-containing dextran was precipitated with 300 mL of methanol. The precipitate was dissolved in 10 mL of Milli-Q water followed by re-precipitation with 300 mL of methanol. The dextran-based polymeric CL compound was then dried *in vacuo* and its purity was checked by gel liquid chromatography.

2.4. Procedure of liquid-phase CL detection of isoluminol or luminol enhanced by DLs

Chemiluminescent reactions were carried out in 10 mm × 75 mm disposable culture tubes. After the addition of 30 μL of 5.0 μM isoluminol or luminol in CH₃CN, 90 μL of 1.0 M TPA in H₂O, 30 μL of CH₃CN, 30 μL of 10 mM DLs in H₂O, 20 μL of 8.8 M H₂O₂ in H₂O, 30 μL of 10 mM FeCl₃ in H₂O into the tube, the tube was immediately placed in a luminescence reader. The signal of all reactions was displayed and integrated for 1.0 min. The kinetics of the CL reaction was monitored on a recorder connected to the luminescence reader.

2.5. CL Imaging of luminol-containing dextran-based polymer enhanced by DL **10** on a nylon membrane

Three different amounts of dextran-based polymeric CL compounds (500, 250 and 130 ng) were spotted directly on a nylon membrane and dried *in vacuo* for 10 min. The nylon membrane was then washed with 2 mL of 100% methanol at 37 °C for 10 min before drying the membrane *in vacuo*. The membrane was then immersed into a CL emitting reagents (300 μL of CH₃CN, 700 μL of 1.0 M TPA in H₂O, and 50 μL of 10 mM DL **10** in H₂O) for 10 s. Then, 50 μL of 8.8 M H₂O₂ and 50 μL of 10 mM FeCl₃ were added into the emitting solution and left standing for 10 s before the CL detection for 1.0 min with CCD camera.

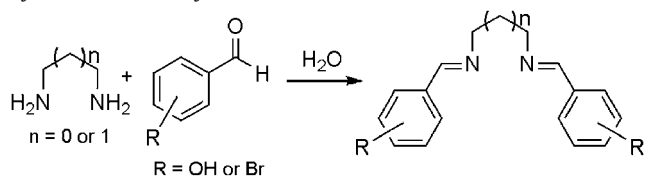
3. Results and discussion

3.1. Characteristics of DLs

Recently, we have developed a non-enzymatic CL detection of a luminol-containing dextran-based polymer on a nylon membrane in which TPA, CH₃CN, H₂O₂ and FeCl₃ were employed in the CL-reaction system [14]. Attempting to enhance the CL of isoluminol and luminol employing a classical CL enhancer, *p*-iodophenol, led to no enhancement in our reaction system. This enhancer is most effective for the enzymatic CL reaction with HRP and luminol. Therefore, binding of *p*-iodophenol into the HRP pocket might be one of the responsibilities for the CL enhancement.

During the course of study, we found that DL **1** exhibited weak CL enhancement of isoluminol. Encouraging by this finding, a number of DLs were prepared for the investigation of their CL enhancing ability. Isoluminol and luminol were chosen as representative CL compounds and used for subsequent optimized experiments. Ten DLs were obtained with good to excellent yields (75–92%) (Table 1). These DLs could be soluble at 10 mM concentration in water.

Table 1
Synthetic scheme and yields of DLs.



Diimine ligand (DL)	Structure	Yield (%) ^a	Diimine ligand (DL)	Structure	Yield (%) ^a
DL 1		75	DL 6		86
DL 2		90	DL 7		82
DL 3		84	DL 8		87
DL 4		78	DL 9		90
DL 5		79	DL 10		92

^a Isolated yield.

3.2. The effect of DL concentration for the CL enhancement of isoluminol

The different concentrations of various DLs were investigated (Fig. 2). Of investigated concentrations, 10 mM DL 10 exhibited the strongest CL enhancement of isoluminol. After the optimization of Fe(III) concentrations, 10 mM Fe(III) gave the strongest CL enhancement of isoluminol. Increasing concentration of DLs resulted in significant decrease of CL intensity. This may imply the interruption of the catalytic oxidation of isoluminol. The concentration between DL 10 and Fe(III) at 1:1 ratio was optimal since at this ratio the highest CL enhancement of isoluminol was observed. Therefore, this ratio was chosen for further experiments.

3.3. Kinetic profiles of CL emission of isoluminol in the presence and absence of DL 10

The CL emission-time profiles of the reactions were investigated (Fig. 3). The CL signals of the reactions were shown to be rapidly emitted in the presence of Fe(III), although the CL signals were much weaker in the absence of DL 10. In the presence of Fe(III),

the CL reactions were initiated immediately within 3 s and reached the maximum after 30 s and declined slowly to the baseline after 50 s. In the absence of Fe(III), the CL reaction initiated after 3 s and reached the maximum after 150 s, although its CL intensity was

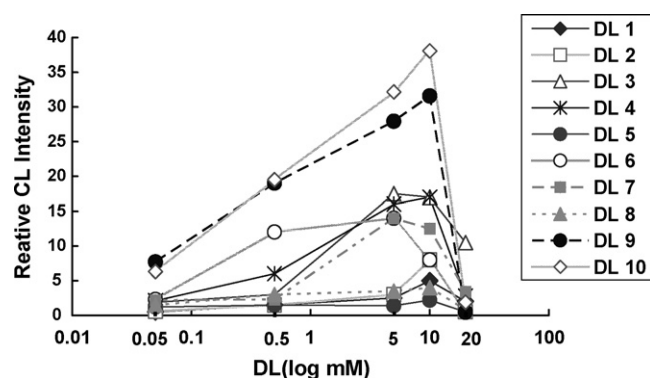


Fig. 2. The effect of DL concentration on the CL enhancement of isoluminol. The CL reaction was performed according to the procedure of the Section 2.4.

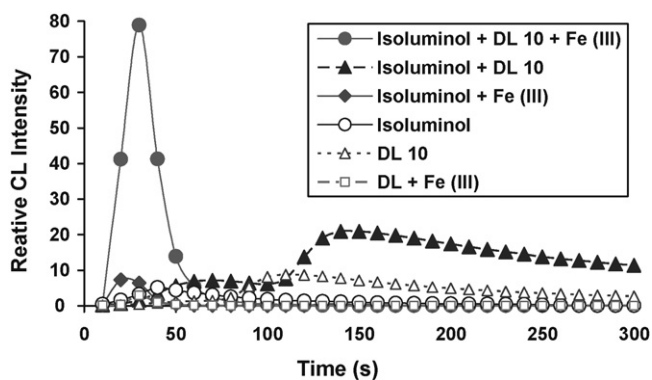


Fig. 3. Time-course for CL emission of isoluminol in the presence of DL **10** and/or FeCl_3 . The CL reaction was performed according to the procedure of the Section 2.4, and for non-addition of the reagents, their solvents were used.

much lower. It was clear that DL **10** significantly enhanced the CL of isoluminol.

3.4. A screening of DLs for the CL enhancement of isoluminol and luminol

Various DLs (10 mM) were further screened for the CL enhancement of either isoluminol or luminol (5.0 μM each) under the optimized conditions (Fig. 4). Of all ligands screened, DLs **9** and **10** strongly enhanced both CL of isoluminol and luminol. The degree of enhancement for isoluminol in the presence of DL **10** was 40 fold higher than that without DL **10**. Other DLs moderately enhanced both CL of isoluminol and luminol.

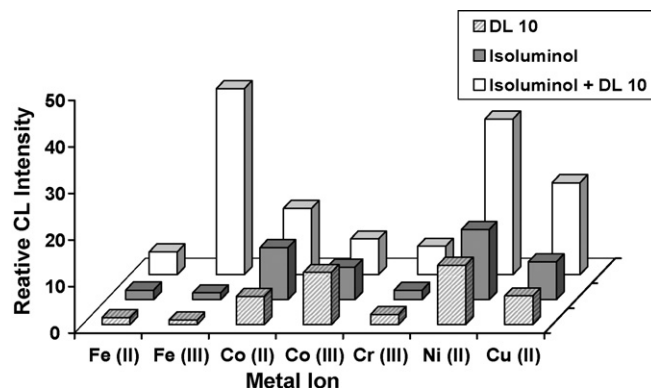


Fig. 5. The effect of various metal ions on the CL enhancement of isoluminol with DL **10**. The CL reaction was performed according to the procedure of the Section 2.4, and for non-addition of the reagents, their solvents were used.

3.5. Metal screening for the CL enhancement of isoluminol by DL 10

The CL of (iso)luminol is known to be efficiently catalyzed in the presence of metal ions [15]. Therefore, the effect of various metal ions (10 mM each) on the CL enhancement of isoluminol was investigated in our reaction system (Fig. 5). Of these metal ions screened, Fe (III) was the best metal catalyst for the CL emission of isoluminol in the presence of DL **10**. Although in the presence of Ni (II) or Cu (II) ion, the strong CL emission was obtained, the CL enhancement of isoluminol was less degree as compared with Fe (III) catalyst.

3.6. Proposed mechanism for CL enhancement of isoluminol and luminol by DL 10

At this stage, the mechanism for the CL enhancement of (iso)luminol by DL **10** is still not conclusive, since the crystal of the diimine and Fe (III) complex could not be obtained to analyse its structure with an X-ray diffraction instrument. However, the complex between Fe (III) and DL **10** might effectively enhance the catalysis of the generation of hydroxyl or hydroxyl-like radicals which are important species for the primary oxidation of (iso)luminol. This primary oxidation of (iso)luminol may be a crucial step contributing to the CL enhancement of the proposed system. If the complexation between Fe (III) and DL is one of the important factors for the overall CL enhancement of the proposed system, DLs **4** and **10** should exhibit similar degree of CL enhancement since these DLs are isomers. However, DL **10** exhibited with a higher degree of CL enhancement of both isoluminol and luminol. The differences of these DLs are i) the position of the hydroxyl group (*ortho*- and *meta*-positions for DLs **4** and **10**, respectively).

As shown in Fig. 6, the energy-optimized modeling indicated that the bond length between chelated Fe (III) and nitrogen atom is 1.738 Å for DL **4** and 1.875 Å for DL **10**. The bond length between Fe (III) and oxygen atom is 1.905 Å and 2.029 Å for DLs **4** and **10**, respectively. It indicated that DL **10** provides a bigger room to accommodate Fe (III) than DL **4**. This spacious room for Fe (III) accommodation might be responsible for facilitating the proper conformation of DL to perform a stable complexation between Fe (III). This might be an important factor responsible for the overall CL enhancement of the proposed system. The effect of spacer group of diimine moiety was more pronounced for DLs **3** and **9** compared to DLs **4** and **10**. The methylene spacer reduces the bond length between the nitrogen or oxygen atoms and the chelated Fe (III) which lead to the shrinkage of the spacer for Fe (III) accommodation. In addition to the position of the hydroxyl group, the

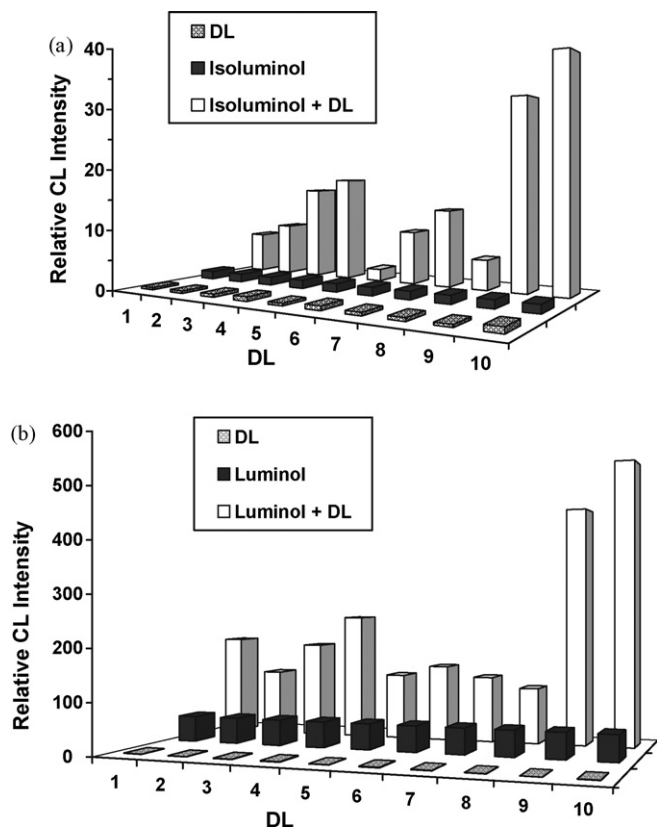


Fig. 4. Screening of DLs for the CL enhancement of (a) isoluminol and (b) luminol. The CL reaction was performed according to the procedure of the Section 2.4, and for non-addition of the reagents, their solvents were used.

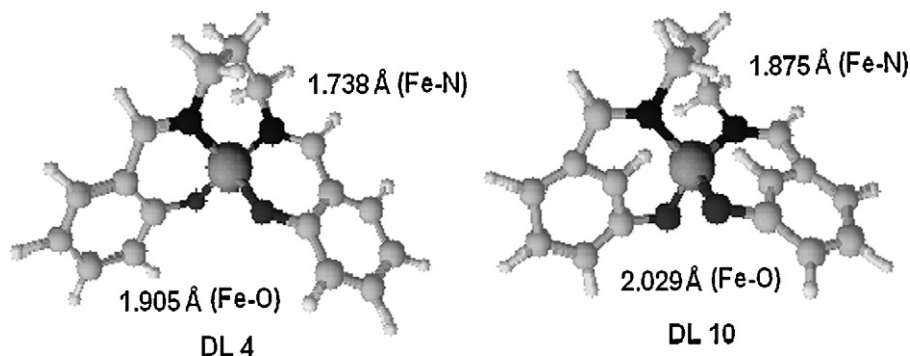


Fig. 6. Energy-optimized structures of DLs **4** and **10** chelating Fe (III).

length of the spacer group was also an important factor for the CL enhancement of the proposed system.

3.7. CL enhancement of a luminol-containing compound by DL **10**

Finally, DL **10** was employed for the CL enhancement of a luminol-containing dextran-based polymer on a nylon membrane (Fig. 7). In the presence of DL **10**, the CL of the dextran-based polymeric compound was enhanced six-fold higher as compared with the absence of DL **10**. The reason that less degree of CL enhancement was observed may be due to the less exposure of luminol units buried inside the dextran-based macromolecular structure to the CL emitting reagents. In this detection system, a maximum CL emission should be detected within 5 min for flashing-CL mode adapted to a CCD camera. Therefore, a high concentration of H_2O_2 in the presence of a strongly alkaline organic base was required in order to emit the CL fast on the membrane. During this solid-phase CL reaction, a yellow precipitation was observed which might be $Fe(OH)_3$ after the addition of $FeCl_3$ without DL **10**. However, this precipitation did not occur in the presence of DL **10** because of the chelation of the metal ion with the diimine.

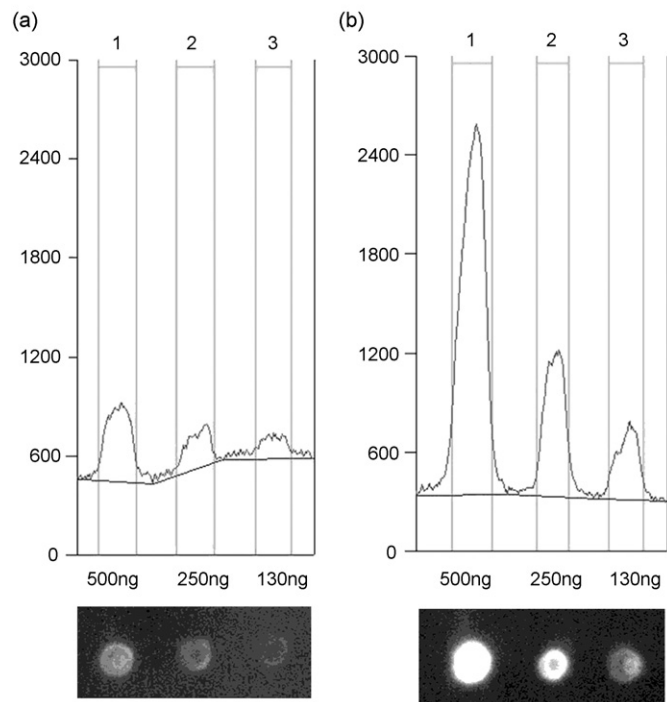
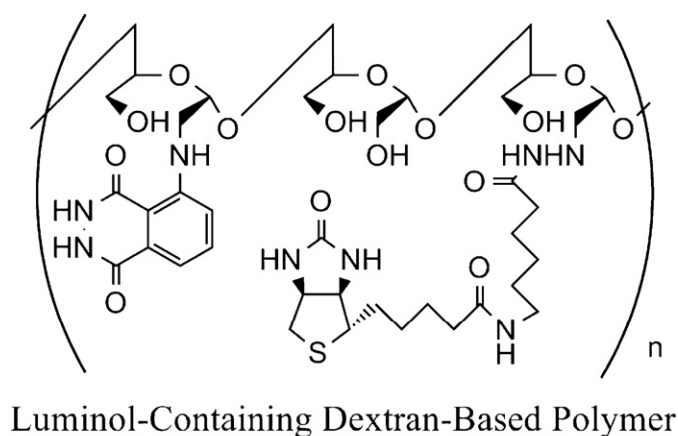


Fig. 7. Non-enzymatic CL enhancement (a) with and (b) without DL **10** for the imaging detection of a luminol-containing dextran-based polymer. The polymer (ca. 2,500,000 Da containing ca. 3000 units of luminol in the molecule) was spotted at 500, 250 and 130 ng on a nylon membrane.

4. Conclusions

In conclusion, DL **10** has been first time synthesized and evaluated for its CL enhancement of the (iso)luminol-containing compounds. The possible mechanism for the CL enhancement by DL **10** is proposed on the basis of the complex formation between Fe (III) and the ligand. This complex might be responsible for the primary oxidation of (iso)luminol residues in the compound which is crucial for the CL enhancement of the present system. The flexible spacer of the propylene group in DL **10** might also provide a better conformation of DL **10** to accommodate Fe (III) ion. This finding permits to use the ligand as an enhancer for the sensitive and non-enzymatic CL detection of luminol-containing compounds.

Acknowledgements

We thank the Japan Society for the Promotion of Science (JSPS) for the financial support and this work was also supported partly from Japanese Ministry of Health, Welfare and Labor.

References

- [1] T.P. Whitehead, L.J. Kricka, T.J.N. Carter, G.H.G. Thorpe, Clin. Chem. 25 (1979) 1531.
- [2] R. Iwata, H. Ito, T. Hayashi, Y. Sekine, N. Koyama, M. Yamaki, Anal. Biochem. 231 (1995) 170.
- [3] I. Bronstein, B. Edwards, J.C.J. Vote, Biolumin. Chemilumin. 4 (1989) 99.
- [4] A.P. Schaap, H. Akhavan, L.J. Romano, Clin. Chem. 35 (1989) 1863.

- [5] G.H.G. Thorpe, L.J. Kricka, S.B. Moseley, T.P. Whitehead, Clin. Chem. 31 (1985) 1335.
- [6] T.P. Whitehead, G.H.G. Thorpe, T.J.N. Carter, Nature 305 (1983) 158.
- [7] Y. Dotsikas, Y.L. Loukas, Talanta 71 (2007) 906.
- [8] L.J. Kricka, G.H.G. Thorpe, R.A.W. Stott, Pure Appl. Chem. 59 (1987) 651.
- [9] T.J.N. Carter, C.J. Groucutt, R.A. W Scott, European Patent, EP 87959, 1982.
- [10] L.J. Kricka, M. Cooper, X. Ji, Anal. Biochem. 240 (1996) 119.
- [11] D.N. Lee, H.J. Park, D.H. Kim, S.W. Lee, S.J. Park, B.H. Kim, W.Y. Lee, Bull. Korean Chem. Soc. 23 (2002) 13.
- [12] F. Kennedy, N.M. Shavaleev, T. Koullourou, Z.R. Bell, J.C. Jeffery, S. Faulkner, M.D. Ward, Dalton Trans. (2007) 1492.
- [13] H. Xu, C.-F. Duan, C.-Z. Lai, M. Lian, Z.-F. Zhang, L.-J. Liu, H. Cui, Luminescence 21 (2006) 195.
- [14] H. Zhang, C. Smanmoo, T. Kabashima, J. Lu, M. Kai, Angew. Chem. Int. Ed. 46 (2007) 8226.
- [15] S. Hanaoka, J.-M. Lin, M. Yamada, Anal. Chim. Acta 409 (2000) 65.



Synthesis and spectral characteristics of two novel intramolecular charge transfer fluorescent dyes

Shengmei Song^{a,b}, Dong Ju^a, Junfen Li^a, Duxin Li^a, Yanli Wei^a, Chuan Dong^a,
Peihua Lin^a, Shaomin Shuang^{a,*}

^a Research Center of Environmental Science and Engineering, Department of Chemistry, Shanxi University, Shanxi 030006, PR China

^b Department of Chemistry, Shangqiu Normal University, Shangqiu 476000, PR China

ARTICLE INFO

Article history:

Received 11 July 2008

Received in revised form 1 October 2008

Accepted 2 October 2008

Available online 17 October 2008

Keywords:

Carbazole

Fluorene

Pyrazoline

Synthesis

Fluorescence

Intramolecular charge transfer (ICT)

ABSTRACT

The synthesis and absorption/fluorescence properties of two novel intramolecular charge transfer (ICT) compounds of (fluorene-2-yl)-(9-ethylcarbazole-3-yl) ketene and 1-phenyl-3-(fluorenone-2-yl)-5-(9-ethylcarbazole-3-yl)-2-pyrazoline were reported. The primary structure of the target compounds was characterized by IR and ¹H NMR. The systems contained a fluorenone or a propenon group as an electron acceptor (A) and an N-ethylcarbazole and a pyrazoline group as electron donors (D). From the emissive properties it was concluded that the electronic coupling between D and A was sufficient to allow charge transfer in these molecules. The ICT maximal emission displayed a large wavelength shift and Stokes shifts increased in response to the increase of the solvent polarity. The highly solvatochromic properties made the two compounds of great interest as new classes of fluorescent probes, electroluminescent and electrofax materials.

© 2008 Elsevier B.V. All rights reserved.

1. Introduction

The intramolecular charge transfer (ICT) compound is one kind of the most important molecule materials, which is functionalized by electron-donating (D) and electron-accepting (A) groups through a π -conjugated linker. The molecules with D- π -A structures have attracted increasing attention since they can serve as electroactive and photoactive materials in molecular electronics, such as biochemical fluorescent technology [1–4], efficient nonlinear optical (NLO) [5–7], electrogenerated chemiluminescence [8–11], organic light-emitting diodes (OLEDs) [12–14] and solar cells [15–18]. Carbazole is known not only as an efficient short-wavelength emitter but also as a strong electron-donating chromophore. The conjugative coupling with electron-accepting moieties through a π -spacer results in a charge transfer band caused by the intramolecular D–A interactions. To utilize these characteristics in practical optoelectronic materials, many conjugated carbazole polymers have been prepared and the properties were extensively investigated [19,20]. Pyrazoline and its derivatives are formed by benzeno-hydrazone cyclization, and they have N atoms which attain conjugation by donating electron. So they

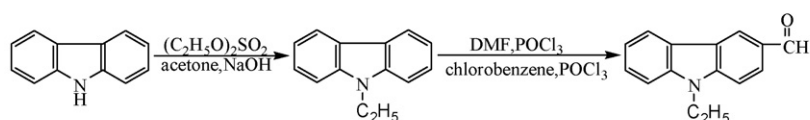
have higher hole-transport efficiency and some photoelectron characteristics [21]. Fluorene and its derivatives, as blue luminescent materials with wide energy gap and high luminescence efficiency, have drawn much attention of materials chemists and device physicists [10,22]. Chalcone and its derivatives are the products of aldol cross-condensation between aromatic aldehydes and ketones and their molecular structures have great flexibility allowing them bind to different receptors [23]. So if the strong electron-donor (D) of carbazole/pyrazoline moieties and strong electron-acceptor (A) of fluorenone/chalcone moieties are synthesized in one molecule, it would bring excellent efficiency.

Based on this target, two novel ICT fluorescent dyes were synthesized which were (fluorene-2-yl)-(9-ethylcarbazole-3-yl) ketene (compound c) and 1-phenyl-3-(fluorenone-2-yl)-5-(9-ethylcarbazole-3-yl)-2-pyrazoline (compound e). The general routes for the synthesis of compounds a–e were shown in Scheme 1. N-Ethyl-carbazole moiety was linked to fluorenone by pyrazoline ring to form compound e and combined with fluorene by propenon group to form compound c. Their structures were characterized by IR, ¹H NMR and fluorescence spectra. In order to correlate the polarity influence of the solvent on the absorption maxima and fluorescence emission wavelengths, the polarity parameters used well expressed local interactions between the solute and the solvent, i.e., the E_T (30) (defined by Reichardt) [24,25] and Δf following the Lippert–Mataga equation [26,27] which indicated that

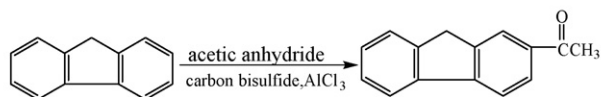
* Corresponding author. Tel.: +86 351 7018842; fax: +86 351 7011322.

E-mail address: sms Huang@sxu.edu.cn (S. Shuang).

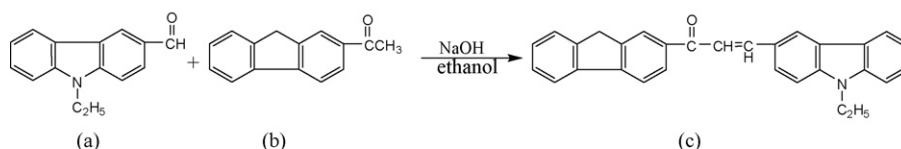
Scheme 1.1



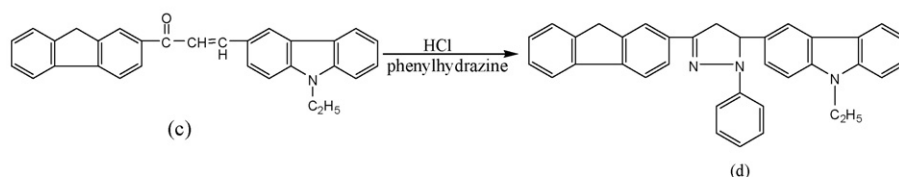
Scheme 1.2



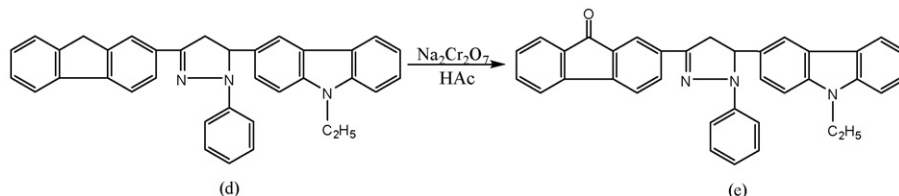
Scheme 1.3



Scheme 1.4



Scheme 1.5



Scheme 1. General routes for the synthesis of compounds a–e.

- (1.1) Synthesis of 9-ethyl-3-formylcarbazole (compound a).
- (1.2) Synthesis of 2-acetylfluorene (compound b).
- (1.3) Synthesis of (fluorene-2-yl)-(9-ethylcarbazol-3-yl)-ketene (compound c).
- (1.4) Synthesis of 1-phenyl-3-(fluorene-2-yl)-5-(9-ethylcarbazol-3-yl)-2-pyrazoline (compound d).
- (1.5) Synthesis of 1-phenyl-3-(fluorenone-2-yl)-5-(9-ethylcarbazol-3-yl)-2-pyrazoline (compound e).

the emission wavelength of the compounds was red-shifted and the Stokes shifts increased with the increase of solvent polarity. Experiments showed that the long-wavelength (LW) emission of the two dyes could be quenched by protic solvents. In addition, the fluorescence quantum yields of the dyes were obtained and the fluorescence quantum yield of compound e was larger than compound c.

2. Experimental

2.1. Materials and methods

2.1.1. Apparatus and reagents

Melting points were determined on x-5 melting point detector. IR spectra were recorded with an FTIR 1730. ¹H NMR spectra were obtained on a Bruker 300 MHz instrument. The absorption and fluorescence spectrum were recorded on TU-1901 dual-beam UV–visible spectrophotometer (Beijing Purkinje General Instru-

ment Co., Ltd., Beijing, China) equipped with 1.0 cm quartz cells and Cary Eclipse spectrofluorometer (Varian, USA) equipped with a 150 W xenon lamp source and 1.0 cm quartz cell.

All the reagents were purchased from Beijing Chemical Plant without further purification prior to use.

2.1.2. Procedures

The synthesis of compounds was described in Section 2.2, and the general routes were shown in Scheme 1. All spectral experiments were carried out at 20–25 °C. Excitation and emission slits width were both set at 5 nm.

2.2. Synthesis and characterization

2.2.1. Synthesis of N-ethylcarbazole (Scheme 1.1)

According to the method from ref. [28], 5 g of carbazole, 9.3 g of diethyl sulfate and 65 ml of acetone were blended into a three-necked flask with a mechanical stirrer, and the solution changed

from colourless to red brown. Then the solution which was obtained from 4.5 g of NaOH and 3 ml of distilled water was added in and the colour of the solution changed from red brown into white, at last into soil yellow. After stirring rapidly for 15 min, the reaction mixture was poured into a beaker containing 600–700 ml distilled water, white precipitate appeared. After being placed statically and filtered, the product was recrystallized from anhydrous ethanol, and 4.38 g of white fine needle-like crystals were obtained. The yield was 75.1%, and the melting point was 72–74 °C, which was consistent with literature values [28].

2.2.2. Synthesis of 9-ethyl-3-formylcarbazole (compound a) (Scheme 1.1)

10 g of *N*-ethylcarbazole, 100 ml of chlorobenzene and 15 ml of dimethyl formamide dried off with anhydrous magnesium sulfate were blended into a 250 ml four-necked flask equipped with a stirrer. Then 10 ml of phosphorus oxychloride was added dropwise and it was stirred at 65–70 °C for 5 h. It was obtained a yellow solid adhered to the flask inner wall. After addition of adequate amount of distilled water, all solid was dissolved yielding a dark blue solution. Some dark blue oil was obtained after steam distillation and was solidified by adding petroleum ether. The product was recrystallized from anhydrous ethanol, and 8.3 g of yellow granular solid was obtained. The yield was 72.4%, and the melting point was 86–88 °C.

IR (KBr) cm^{-1} : 3040, $\gamma_{\text{C-H}}$ (carbazole); 2950, $\gamma_{\text{C-H}}$ ($-\text{CH}_2\text{CH}_3$); 2850, 2750, $\gamma_{\text{C-H}}$ ($-\text{CHO}$); 1715, $\gamma_{\text{C=O}}$ ($-\text{CHO}$); 1590, 1490, $\gamma_{\text{C=C}}$ (carbazole); 1450, 1390, $\delta_{\text{C-H}}$ ($-\text{CH}_2\text{CH}_3$); 1147, $\delta_{\text{C-N}}$ (carbazole); 900–700, $\delta_{\text{C-H}}$ (carbazole).

$^1\text{H NMR}$ (CDCl_3) δ (ppm): 1.5 (3H, $-\text{CH}_3$), 4.4 (2H, $-\text{CH}_2-$), 7.3–8.7 (7H, carbazole-), 10.1 (1H, $-\text{CHO}$).

2.2.3. Synthesis of 2-acetyl fluorene (compounds b) (Scheme 1.2)

2 g of fluorene and 25 ml of carbon disulfide were added in a three-necked flask equipped with a mechanical stirrer, stirring until fluorene was dissolved, 3.2 g of anhydrous aluminum chloride was added in. Keeping the carbon disulfide refluxing slowly, 1.3 g of acetic anhydride was added drop-by-drop. Then the reaction was kept 1 h in 46–47 °C water bath. After filtration, the precipitate was transferred to a beaker and 40 ml of carbon disulfide was added, stirred for 10 min (to dissolve the fluorene which did not react and other impurities) and filtration was done. 20 ml of dilute hydrochloric acid solution (100 g water: 4 g concentrated hydrochloric acid) was added in and fully stirred, then the first hydrolysis was coupled with the second hydrolysis. Then a light orange solid (2.1 g) was obtained by water washing and drying after filtration, the yield was 84%, and the melting point was 124–126 °C.

IR (KBr) cm^{-1} : 3010, 2972, $\delta_{\text{C-H}}$ (fluorene); 1679, $\gamma_{\text{C=O}}$ ($-\text{COCH}_3$); 1606, 1566, $\gamma_{\text{C=C}}$ (fluorene); 1421, 1400, $\delta_{\text{C-H}}$ ($-\text{COCH}_3$); 1292, 1265, 1228, $\delta_{\text{C-H}}$ ($-\text{CH}_2-$, fluorene); 854, 771, 738, $\delta_{\text{C-H}}$ (fluorene).

$^1\text{H NMR}$ (CDCl_3) δ (ppm): 2.65–2.64 (3H, $-\text{COCH}_3$), 4.00–3.88 (2H, the $-\text{CH}_2-$ of fluorene), 7.2–7.9 (7H, fluorene)

2.2.4. Synthesis of (fluorene-2-yl)-(9-ethylcarbazol-3-yl)-ketene (compound c) (Scheme 1.3)

1.1 g of *N*-ethyl-3-formyl carbazole, 1 g of 2-acetyl fluorene and 80 ml of ethanol were added in 250 ml conical flask, and the solution was obtained by stirring at room temperature. Then 10% NaOH aqueous solution (3 ml) was dropped in. The reaction was kept for 24 h at room temperature. The solid was obtained after filtration, and the product was recrystallized from anhydrous ethanol after washed by distilled water. The golden yellow powder (0.8 g) was obtained. The yield was 43%, and the melting point was 176–178 °C.

IR (KBr) cm^{-1} : 3421, 2972, $\delta_{\text{C-H}}$ (fluorine- skeleton, carbazole- skeleton, $-\text{CH}=\text{CH}-$); 1678, 1606, $\gamma_{\text{C=C}}$ (fluorine- skeleton,

carbazole- skeleton, $-\text{CH}=\text{CH}-$); 1577, $\gamma_{\text{C=O}}$ ($-\text{CO}-$); 1490, 1471, $\delta_{\text{C-H}}$ ($-\text{CH}_2\text{CH}_3$).

$^1\text{H NMR}$ (CDCl_3) δ (ppm): 1.5 (3H, $-\text{CH}_3$), 4.4–4.3 (2H, $-\text{CH}_2-$), 2.5–2.2 (2H, the $-\text{CH}_2-$ of fluorene), 3.9–3.7 (2H, $-\text{CH}=\text{CH}-$), 7.1–8.1 (14H, fluorine- skeleton, carbazole- skeleton), ethanol solvent peaks were also observed.

2.2.5. Synthesis of

1-phenyl-3-(fluorene-2-yl)-5-(9-ethylcarbazole-3-yl)-2-pyrazoline (compound d) (Scheme 1.4)

0.2 g (fluorene-2-yl)-5-(*N*-ethylcarbazole-3-yl) ketene was dissolved in 10 ml of ether glycol, and the reactive system was kept refluxing. Then 0.2 ml of phenylhydrazine and 0.2 ml of concentrated hydrochloric acid were dropped in, and the reaction was kept for 8 h. Appropriate distilled water was added to cool the reactive system to room temperature. After being placed statically, filtrated and dried, 0.2 g brown solid powder was obtained. The yield was 83%, and the melting point was 150 °C.

IR (KBr) cm^{-1} : 3411, 2871, $\delta_{\text{C-H}}$ (fluorine- skeleton, carbazole- skeleton); 1676, 1598, $\gamma_{\text{C=C}}$ (fluorine- skeleton, carbazole- skeleton); 1560, $\gamma_{\text{C=N}}$ (pyrazoline ring); 1490, 1458, $\delta_{\text{C-H}}$ ($-\text{CH}_2\text{CH}_3$); 1330, 1232, $\delta_{\text{C-H}}$ (pyrazoline ring, $-\text{CH}_2-$, $-\text{CH}-$); 1124, $\delta_{\text{C-N}}$ (carbazole- skeleton); 806, 746, 694, $\delta_{\text{C-H}}$ (fluorine- skeleton, carbazole- skeleton). From the IR spectra of compounds c and d, it could be seen that the 1577 cm^{-1} carbonyl absorption peaks in compound d disappeared apparently, and the intensity of 1676 cm^{-1} double bond absorption peak weakened, all these proved that pyrazoline ring had been formed.

$^1\text{H NMR}$ (CDCl_3) δ (ppm): 1.3 (3H, $-\text{CH}_3$), 4.3–3.9 (2H, $-\text{CH}_2-$), 2.7–2.6 (2H, the $-\text{CH}_2-$ of fluorene), 2.3–2.0 (2H, the $-\text{CH}_2-$ of pyrazoline ring), 3.5 (1H, the $-\text{CH}=\text{CH}$ of pyrazoline ring), 7.1–8.0 (19H, phenyl, fluorine- skeleton, carbazole- skeleton).

2.2.6. Synthesis of 1-phenyl-3-(fluorenone-2-yl)-5-(9-ethylcarbazole-3-yl)-2-pyrazoline (compound e) (Scheme 1.5)

0.2 g precursors of target compounds were dissolved in 5 ml acetic acid, and 0.9 g sodium dichromate was added in. The system was kept refluxing and 0.8 ml acetic anhydride was dropped in. The reaction was kept for 10 h. The solution changed into green, and appropriate distilled water was added to cool the reactive system to room temperature. After being placed statically, filtrated and dried, the khaki solid powder 0.1 g was obtained. The product was recrystallized from anhydrous ethanol after washed by distilled water. The yield was 48%, and the melting point was 192 °C.

IR (KBr) cm^{-1} : Comparing the IR spectra, other characteristic peaks have the same profile as in IR spectra of compound d, but they were shifted to longer wavelengths.

$^1\text{H NMR}$ (DMSO) δ (ppm): 1.057 (3H, $-\text{CH}_3$), 2.0–1.9 (2H, $-\text{CH}_2-$), 3.7–3.4 (2H, the $-\text{CH}_2-$ of pyrazoline ring), 7.4–8.1 (19H, phenyl, fluorene- skeleton, carbazole- skeleton).

2.2.7. Note

We conceived that the fluorene-group of product c was oxidated into fluorenone-group. Two synthesis routes were used: first, fluorenone acetylation reaction was adopted to obtain 2-acetyl fluorenone, but the final product was 2-carboxyl-fluorenone. This was probably due to fluorenone being the strong electron acceptor, and acetylation reaction could not be pursued. Second, the fluorene moiety was oxidated directly to fluorenone after the formation of compound c, also without success, which may be because the double bond on propenon group was oxidated more easily than fluorene.

Table 1

Maximum excitation and emission wavelengths of five compounds a–e in chloroform solvent.

Compounds	Excitation (nm)	Emission (nm)
a	259	336
b	262	417
c	420	498
d	373	503
e	347	515

3. Results and discussions

3.1. The maximum excitation and emission spectra of five compounds in CHCl_3

With the increase of the conjugate system, the maximum excitation and emission wavelengths of compounds a–e were shifted to longer wavelengths. The spectra data of five compounds in chloroform were listed in Table 1.

3.2. Effect of solvent on the absorption spectra

Typical absorption spectra of compounds c and e were shown in Fig. 1, and all spectra were normalized with respect to the peak maximum. In Fig. 1a, all the electronic absorption spectra of compound c presented two main bands, whose maxima were located in the between 250 and 300 nm, and larger than 300 nm. The short-

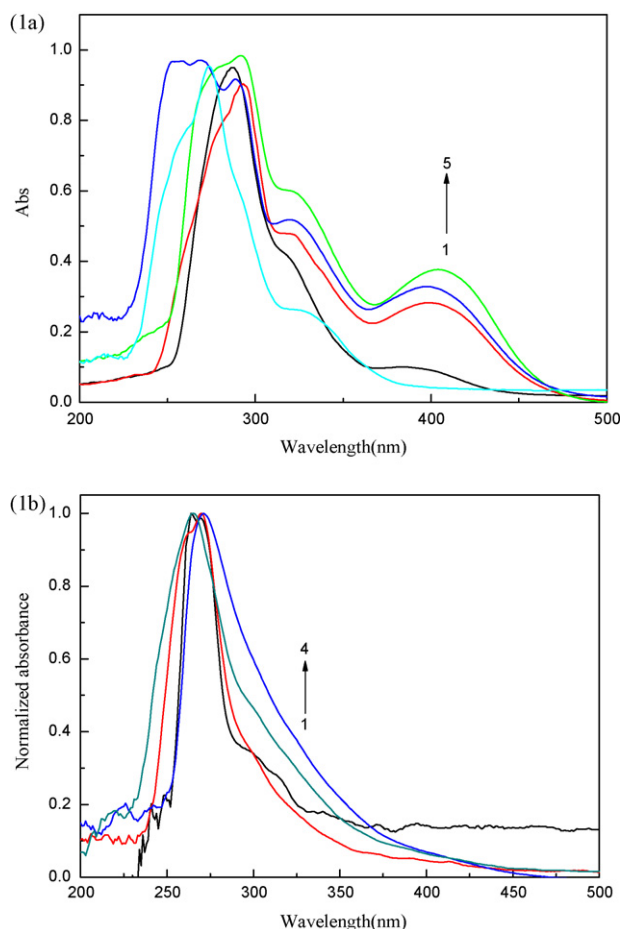


Fig. 1. UV-vis absorption spectra of compounds c (a) and e (b) in different solvents. Solvents: (a): (1) H_2O , (2) CCl_4 , (3) CHCl_3 , (4) methanol, (5) DMSO; (b): (1) CHCl_3 , (2) CHCl_4 , (3) methanol, (4) DMSO.

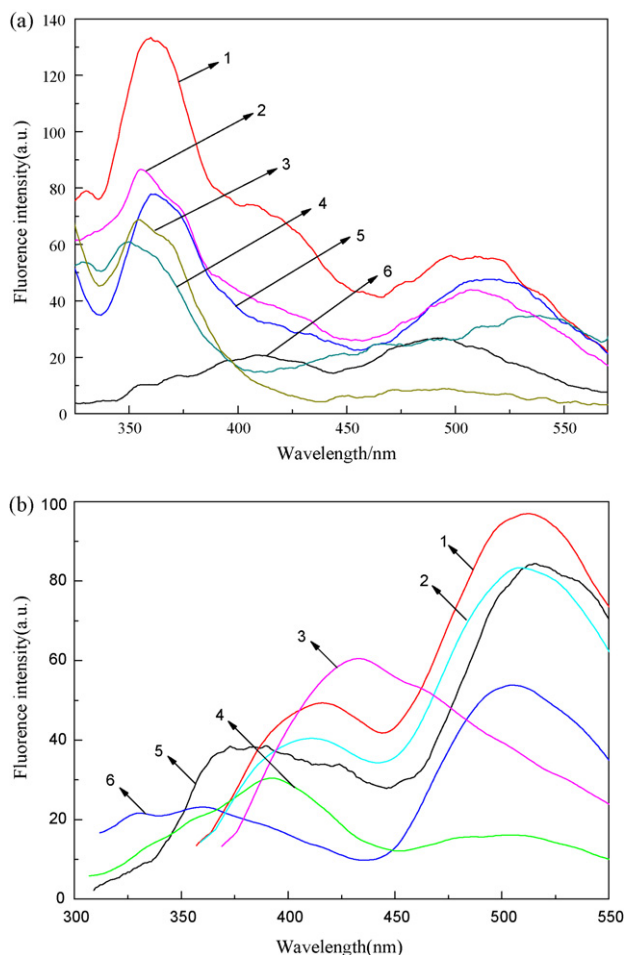


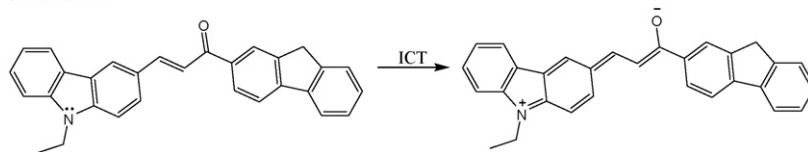
Fig. 2. The emission spectra of compounds c (a) and e (b). Solvents: (a): (1) DMF, (2) acetonitrile, (3) THF, (4) ethanol, (5) DMSO, (6) CHCl_3 ; (b): (1) acetone, (2) butanone, (3) methanol, (4) diethyl ether, (5) DMSO, (6) THF.

wavelength bands were attributed to the π – π^* transitions whereas the long-wavelength bands were attributed to ICT transitions. The short-wavelength bands and long-wavelength bands exhibited bathochromic firstly then hypsochromic with the increase of the solvent polarity. Normally, the bathochromic shift occurs when the dipole moment of the probe increases during the electronic transition (i.e., the ground-state dipole moment μ_g < excited-state dipole moment μ_e), and the excited state was formed in a solvent cage of already partly oriented solvent molecules [24]. The hypsochromic shift perhaps indicated the effects of hydrogen-bonding. The absorption of long-wavelength bands increased first then decreased as solvents polarity increased and the absorption strength completely disappeared in the water indicating that polar solvent can quench ICT fluorescence. The absorption spectrum of compound e (Fig. 1b) displayed negligible solvatochromism with the increase of the solvent polarity. But the long-wavelength bands were not observed perhaps due to absence of the ICT phenomenon in ground state of compound e. The comparison of c and e illuminated the ICT was easier in compound c.

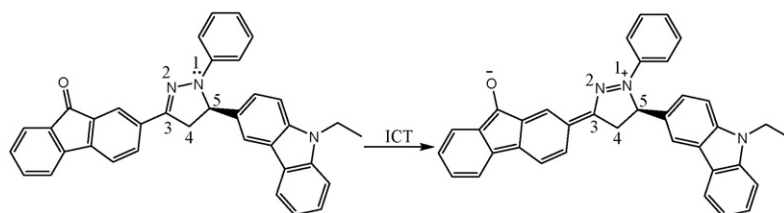
3.3. Effect of solvent on the fluorescence emission spectra

Following the absorption experiments, steady-state fluorescence spectra of compounds c and e were obtained in different solvents. A total of 11 organic solvents were tested, and some representative emission spectra were shown in Fig. 2. The peak

Scheme 2.1



Scheme 2.2



Scheme 2. ICT process of compound e (2.2).

maximum shifted to red as the solvent polarity increased. Compound c had two fluorescence peaks farther from each other than compound e in the excited state. Fig. 2a presented fluorescence spectra of compounds c in various solvents and the excitation wavelength was at 293 nm. Perhaps the conjugated double bonds at the vinyl of the molecules inhibited the rotation of the separate chromophores at excited state, making the charge transfer between atoms in the plane way to form dual-fluorescence. Compound e showed the doubled fluorescence possibly because there was single bond between the separate chromophores which made it possible that the chromophore rotate surrounding the single bond. The ICT at excited state of compound e was complete charge transfer-twist intramolecular charge transfer (TICT), so the emission wavelengths of dual-fluorescence were nearer than that of compound c. The structure of compounds c and e were shown in Scheme 2. The electrons were expected to be delocalized between the nitrogen atoms of the carbazole-like/pyrazoline ring and the oxygen of the fluorenone-like ring. In addition, hydrogen-bonding between the solvent and nitrogen/oxygen atoms of compounds may induce electron redistribution. This might be the reason that emission wavelength shifted to longer wavelength in all protic solvents with strong hydrogen-bonding ability.

3.4. General solvent effect and the Lippert–Mataga relation

ICT molecules are sensitive to changes in the external environment which produces the dramatic fluorescence spectral changes [29,30]. The position of the peak maximum (ν_f) for each fluorescence spectrum was plotted against the solvent polarity parameter $E_T(30)$ in Fig. 3. Fig. 3 showed that the maximum emission shifted from 481 to 553 nm in compound c and from 500 to 527 nm in compound e with the increase of the solvent polarity parameter. It confirmed that the solvent polarity affected the fluorescence of compounds c and e.

To better understand the solvent polarity effect, the Lippert–Mataga relation was applied. This relation has been widely used to correlate the energy difference between absorption ($h\nu_a$) and emission ($h\nu_f$), also known as Stokes' shift, with solvent polarity represented by Δf . This relation was given in Eq. (1). It involves both the dielectric constant and the refractive index (n) of the solvents [27,31]:

$$\nu_a - \nu_f = \frac{2(\mu_E - \mu_G)^2}{hca^3} \Delta f + \text{constant} \quad (1)$$

In Eq. (1), ν_a and ν_f are the wavenumbers (cm^{-1}) corresponding to the absorption and the emission, respectively, h is Planck's con-

stant, c is the speed of light, and a is the radius of the solvent cavity in which the fluorophore resides. For an elongated shape of the molecule, a is usually estimated as 40% of its longest axis [32]. The term (Δf) involving ϵ and n is called the orientation polarizability, which only accounts for the spectral shifts due to the reorientation of the solvent molecules. Therefore, the Lippert–Mataga relation is based on the assumption that the energy difference is only proportional to the solvent orientation polarizability (known as the

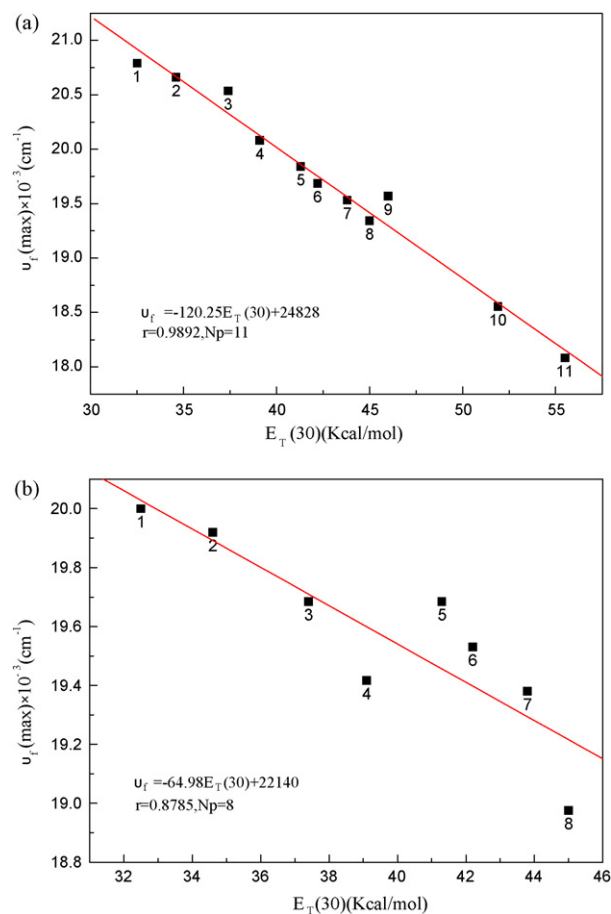


Fig. 3. The emission maximum vs. the solvent polarity parameter $E_T(30)$ of compounds c (a) and e (b). The numbers refer to the solvents: (1) CCl_4 , (2) diethyl ether, (3) THF, (4) chloroform, (5) butanone, (6) acetone, (7) DMF, (8) DMSO, (9) acetonitrile, (10) ethanol, (11) methanol.

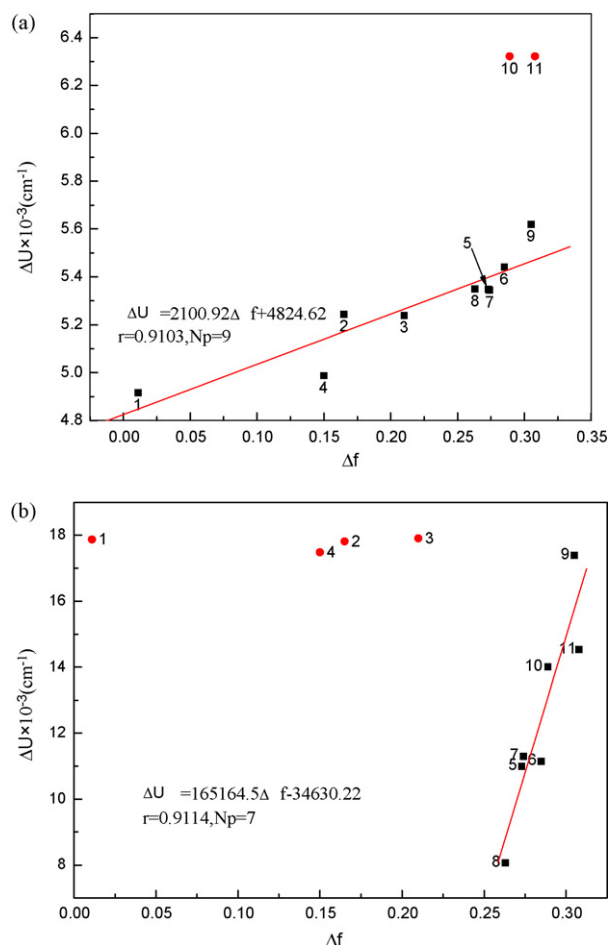


Fig. 4. Stokes shifts as a function of solvent orientation polarizability (Δf) of compounds **c** (a) and **e** (b). The numbers refer to the solvents: (1) CCl_4 , (2) diethyl ether, (3) THF, (4) chloroform, (5) butanone, (6) acetone, (7) DMF, (8) DMSO, (9) acetonitrile, (10) ethanol, (11) methanol.

general solvent effect). Inability of Stokes' shift to increase linearly with Δf usually implies that specific solvent effects are involved.

$$\Delta f = \frac{\epsilon - 1}{2\epsilon + 1} - \frac{n^2 - 1}{2n^2 + 1} \quad (2)$$

Fig. 4 showed the Lippert–Mataga plots of compounds **c** and **e** in 11 organic solvents. The estimation from the Lippert–Mataga equation is based on the assumption that the photophysical properties of compounds **c** and **e** can be described by the theory of general solvent effect; hence, it may not hold if specific solvent effects are involved. Actually, Stokes' shifts of compound **c** observed for solvents ethanol, methanol and water did not follow the trend (Fig. 4a) because hydroxyl group (OH) existed in these solvents and it had strong ability to form hydrogen-bonding. Stokes' shifts of compound **e** followed a linear trend in solvents with a polarity (Δf) larger than 0.21, however, they did not show significant difference when the polarity was smaller than 0.21. This suggested that the solvent polarity might not be the only factor affecting the spectral shifts. Specific solvent effects including hydrogen-bonding, acid–base chemistry, and charge transfer interactions can also result in nonlinear Lippert–Mataga plots. As mentioned before, compounds **c** and **e** can form hydrogen bonds with the solvent, and it can transfer electrons between them (Scheme 2). This complicated the interpretation of how the solvent affected the absorption and emission spectra of compounds **c** and **e**. From the Lippert–Mataga equation, the slope of this line yields the dipole

moment difference between the ground and excited states ($\Delta\mu$), according to [27,31],

$$\text{slope} = \frac{2(\Delta\mu)^2}{hca^3} \quad (3)$$

The estimated dipole moment differences were 2.68 D (debye) of compound **c** and 41.19 D of compound **e** respectively based on the assumption that the Onsager cavity radius a equals 3.24 and 4.68 Å respectively, which were 40% of the optimized distance between the two farthest atoms of the molecule in the direction of charge separation [27,33]. Such a large dipole moment difference usually indicated the occurrence of ICT induced by the solvent after excitation [33–38]. Scheme 2 described the mechanism by which the ICT occurred. In most cases, solvent polarity is believed to be the effect driving an ICT, but for compounds **c** and **e**, another important factors, hydrogen-bonding, should be considered as well. Most solvents used in this study can form hydrogen bonds with compounds **c** and **e**. Alcohols with a hydroxyl group (OH), in addition to their large solvent polarity, may favor the occurrence of an ICT and result in the large dipole moment difference. For compound **e**, in the less polar region ($\Delta f < 0.21$), the Stokes shifts were almost the same. However, sameness is probably a coincidence because an ICT should not occur in the nonpolar solvents where no hydrogen bonds can be formed with compound.

3.5. Quenching of ICT fluorescence by protic solvent

In protic solvents, the intensity of the long-wavelength emission decreased from alcohol to water. In fact, the LW band completely disappeared in water, which limited their applicability as a polarity probe in such solvents. In order to prove that the solvent polarity is the source of this effect, the quenching of compounds **c** and **e** in DMSO ($\Delta f = 0.263$) by water ($\Delta f = 0.32$) was measured (see Fig. 5).

Fig. 5a exhibited that the fluorescence intensity of the LW emission band decreased as the water concentration increased. The decreased fluorescence intensity was also accompanied by a red-shift of the emission maximum. The fluorescence spectra shifted to longer wavelength by 33 nm in the presence of 17.2 M water in DMSO. In Fig. 5b, no change in fluorescence wavelengths could be detected on addition of water during this quenching, which was consistent with a slight change in polarity. In Fig. 5 insert, F_0/F was plotted vs. the concentration of water (mol/L). From these S–V plots, K_{sv} values of 0.08 and 0.36 L mol^{−1} were calculated which indicated that **e** was more sensitive to polarity than **c**.

3.6. Influence of structure and solvent on the fluorescence quantum yields

The fluorescence quantum yields Y_f of compounds **c** and **e** in solvents of different polarity were obtained using the following relation [35].

$$Y_{fu} = Y_{fs} \frac{F_u A_s n_u^2}{F_s A_u n_s^2} \quad (4)$$

where F represents the corrected fluorescence peak area, A the absorbance at the excitation wavelength, n the refractive index of the solvent used, Y_f the fluorescence quantum efficiency and the subscripts “s” and “u” refer to the standard and unknown respectively, and resorcinolphthalein dissolved in 0.1 M NaOH solution was used as the standard.

Although the compounds were not highly fluorescent, the fluorescence quantum yields depended strongly on the solvent polarity (refer to Table 2). Fluorescence quantum yields decreased from CCl_4 to butanone then increased with the increase of the solvent polarity, because the region of highly polar solvents such as

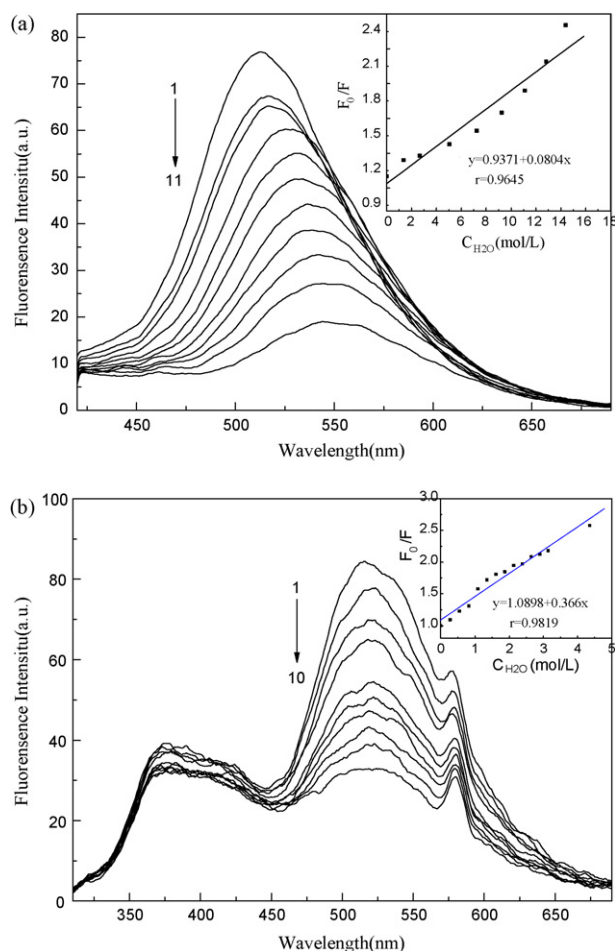


Fig. 5. Fluorescence spectra of compounds c (a) and e (b) in DMSO containing various % (v/v) of water. The concentration of water % (v/v): (a): (1) 0, (2) 2.4, (3) 4.8, (4) 9.1, (5) 13.0, (6) 16.7, (7) 20.0, (8) 23.1, (9) 25.9, (10) 28.6, (11) 31.0; (b): (1) 0, (2) 0.50, (3) 0.99, (4) 1.48, (5) 1.96, (6) 2.34, (7) 2.91, (8) 4.31, (9) 5.6, (10) 7.83. (Insert) plot of fluorescence F_0/F vs. concentration of water (mol/L).

acetonitrile and ethanol can form hydrogen bond. There are two mechanisms for substituted chalcones involved during the course of increasing solvent polarity. One mechanism is the increase in the fluorescence quantum yield with a suitable enhancement of ICT: the so-called “negative solvatokinetic effect”. Several suggestions, such as “biradicaloid charge transfer”, “proximity effect” and “conformational changes”, have been proposed to explain the behavior of the “negative solvatokinetic effect”. The other mechanism is a reduction in the fluorescence quantum yield by strong ICT: the so-called “positive solvatokinetic effect”. For compounds c and e, both the mechanisms had effects on their

fluorescence quantum yields. As the solvent polarity increased, from carbon tetrachloride to butanone, the fluorescence behavior was controlled by the second mechanism. However, in solvents with polarity larger than butanone, the fluorescence quantum yields increased. The phenomenon can be explained by molecule structure. The charge transfer mechanism of pyrazoline was the competition between $N1 \rightarrow N2 \rightarrow C3$ conjugate charge transfer and $N1 \rightarrow C5$ non-conjugate charge transfer. $N1$ atom of pyrazoline ring was donating-electron source of charge transfer. And replace moiety of linking $C3$ was electron acceptor which was affected by the replace moiety of $C5$. The substituent in the 5-position of pyrazoline was donating-electron moiety, which enhanced donating-electron ability of its 1-position. So the quantum yield of compound e was larger. In the compound c, fluorene moiety (A) has linked with 9-ethylcarbazole moiety (D) by conjugate bound of chalcone group. Two moieties (A and D) were situated in the same plane. It was a conjugate intramolecular electron-transfer compound showing fluorescence. In the compound e, 9-ethylcarbazole moiety (D) had linked in $C5$ position, although the space with conjugate section was farther, but D was vertical to A, so the distance between A and D was shortened and this was beneficial to its fluorescence.

4. Conclusions

This study reports the synthesis and photophysical properties of two novel ICT fluorescent compounds both containing fluorene and carbazole groups. The primary structures of the two compounds have been characterized by IR and 1H NMR, and the fluorescence spectra studies together with correlation of spectroscopic properties with various solvent polarity parameters revealed that compound e was more sensitive to solvent polarity due to stronger ICT process than compound c. Such A- π -D systems might be used as excellent optoelectronics materials and sensitive fluorescent probe.

Though fluorescence quantum yields of compound e were not very high, it may be used to probe its microenvironment in biological systems of interest. Future work directed to use e as fluorescence probe for HSA is anticipated to be promising. Similar work is progressing in our laboratory, and the results will be released soon.

Acknowledgements

This work was supported by the National Science Foundation of China (no. 20875059) and the Youth Science Foundation of Shanxi Province (no. 20051005). All the authors express their deep thanks.

References

- [1] Y.-L. Tsai, C.-C. Chang, C.-C. Kang, T.-C. Chang, J. Lumin. 127 (2007) 41.
- [2] B. Hugon, F. Anizon, C. Bailly, R.M. Golsteyn, A.P.S. Léonce, J. Hickman, B. Pfeiffer, M. Prudhomme, Bioorg. Med. Chem. 15 (2007) 5965.
- [3] T. Taskin, F. Sevin, J. Mol. Struct.: Theochem. 803 (2007) 61.
- [4] E. Conchon, F. Anizon, B. Aboab, R.M. Golsteyn, S. Léonce, B. Pfeiffer, M. Prudhomme, Bioorg. Med. Chem. 16 (2008) 4419–4430.
- [5] K.R. Yoon, S.-O. Ko, S.M. Lee, H. Lee, Dye Pigment 75 (2007) 567.
- [6] K.R. Yoon, S.-O. Ko, H. Lee, Synthetic Met. 157 (2007) 627.
- [7] I.K. Moon, C.-S. Choi, N. Kim, Polymer 48 (2007) 3461.
- [8] Z.J. Zhao, X.J. Xu, X.P. Chen, X.M. Wang, P. Lu, G. Yu, Y.Q. Liu, Tetrahedron 64 (2008) 2658.
- [9] H. Chen, X. Xu, H.G. Yan, X.R. Cai, Y. Li, Q. Jiang, M.G. Xie, Chin. Chem. Lett. 18 (2007) 1496.
- [10] W. Li, J. Qiao, L. Duan, L.D. Wang, Y. Qiu, Tetrahedron 63 (2007) 10161.
- [11] K.R.J. Thomas, J.T. Lin, Y.-T. Tao, C.-W. Ko, J. Am. Chem. Soc. 123 (2001) 9404.
- [12] H.-P. Zhao, X.-T. Tao, F.-Z. Wang, Y. Ren, X.-Q. Sun, J.-X. Yang, Y.-X. Yan, D.-C. Zou, X. Zhao, M.-H. Jiang, Chem. Phys. Lett. 439 (2007) 132.
- [13] X.H. Li, J. Gui, H. Yang, W.J. Wu, F.Y. Li, H. Tian, C.H. Huang, Inorg. Chim. Acta 361 (2008) 2835–2840.
- [14] V. Van Dijken, J.J.A.M. Bastiaansen, N.M.M. Kiggen, B.M.W. Langeveld, C. Rothe, A. Monkman, I. Bach, P. Stössel, K. Brunner, J. Am. Chem. Soc. 126 (2004) 7718.
- [15] Y.H. Zhou, P. Peng, L. Han, W.J. Tian, Synth. Met. 157 (2007) 502.

Table 2

Fluorescence quantum yields of compounds c and e in different solvents.

Solvents	Compound c	Compound e
Carbon tetrachloride	0.049	0.588
Diethyl ether	0.050	0.149
Tetrahydrofuran	0.028	0.197
Chloroform	0.008	0.0062
Butanone	0.006	0.052
Acetone	0.034	0.122
DMSO	0.083	0.164
Acetonitrile	0.055	0.044
Ethanol	0.122	0.278
Methanol	0.020	0.032

- [16] Y. Ooyama, Y. Shimada, Y. Kagawa, Y. Yamada, I. Imae, K. Komaguchi, Y. Harima, *Tetrahedron Lett.* 48 (2007) 9167.
- [17] D.X. Li, J.G. Ren, J.F. Li, Z.W. Wang, G.M. Bo, *Dye Pigment* 49 (2001) 181.
- [18] D.X. Li, Z.W. Wang, Z.Q. Guo, W.D. Lan, *Dyes Pigments* 39 (3) (1998) 133.
- [19] J. Simokaitiene, J.V. Grazulevicius, V. Jankauskas, R. Rutkaite, J. Sidaravicius, *Dye Pigment* 79 (2008) 40–47.
- [20] H.X. Shao, X.P. Chen, Z.X. Wang, P. Lu, *J. Lumin.* 127 (2007) 349.
- [21] J. Barbera, C. Koen, G. Raquel, H. Stephan, P. André, L.S. José, *J. Mater. Chem.* 8 (1998) 1725.
- [22] V.P. Barberis, J.A. Mikroyannidis, *Synthetic Met.* 156 (2006) 1408.
- [23] L.P. Guan, X.M. Yin, H.M. Quan, Z.S. Quan, *Chin. J. Org. Chem.* 24 (2004) 1274.
- [24] C. Reichardt, H.F. Ebel (Eds.), *Solvents and Solvent Effects in Organic Chemistry*, second ed., VCH, Basel, 1988.
- [25] C. Reichardt, *Chem. Rev.* 94 (1994) 2319.
- [26] D.R. Lide (Ed.), *CRC Handbook of Chemistry and Physics*, 71st ed., CRC Press, Boca Raton, FL, 1990.
- [27] S.Y. Fung, J. Duhamel, P. Chen, *J. Photochem. Photobiol. A* 11 (2006) 11446.
- [28] G. Bai, J. Li, D. Li, C. Dong, X. Han, P. Lin, *Dye Pigment* 75 (2007) 93.
- [29] O. Sire, B. Alpert, C.A. Royer, *Biophys. J.* 70 (1996) 2903.
- [30] M. Mazumdar, P.K. Parrack, B. Bhattacharyya, *Eur. J. Biochem.* 204 (1992) 127.
- [31] J.R. Lakowicz, *Principles of Fluorescence Spectroscopy*, second ed., Kluwer Academic/Plenum Publishers, New York, 1999.
- [32] M.W. Wong, M.J. Frisch, K.B. Wiberg, *J. Am. Chem. Soc.* 113 (1991) 4776.
- [33] J. Dey, I.M. Warner, *J. Photochem. Photobiol. A* 116 (1998) 27.
- [34] K. Nagy, S.G.L. Biczó, *J. Photochem. Photobiol. A* 107 (2003) 8784.
- [35] T.C. Werner, R.M. Hoffman, *J. Phys. Chem.* 77 (1973) 1611.
- [36] C.J. Seliskar, L. Brand, *J. Am. Chem. Soc.* 93 (1971) 5414.
- [37] P. Bosch, A. Fernández-Arizpe, J.L. Mateo, A.E. Lozano, P. Noheda, *J. Photochem. Photobiol. A* 133 (2000) 51.
- [38] Y.H. Pang, S.M. Shuang, M.S. Wong, Z.H. Li, C. Dong, *J. Photochem. Photobiol. A* 170 (2005) 15.



Separation/preconcentration of trace amounts of Cr, Cu and Pb in environmental samples by magnetic solid-phase extraction with Bismuthiol-II-immobilized magnetic nanoparticles and their determination by ICP-OES

Jibrin Sabo Suleiman, Bin Hu*, Hanyong Peng, Chaozhang Huang

Department of Chemistry, Wuhan University, Wuhan 430072, China

ARTICLE INFO

Article history:

Received 30 June 2008

Received in revised form

24 September 2008

Accepted 26 September 2008

Available online 14 October 2008

Keywords:

Separation/preconcentration

Cr, Cu and Pb

Environmental samples

Magnetic nanoparticles

Bismuthiol-II

ICP-OES

ABSTRACT

A new method for separation/preconcentration of trace amounts of Cr, Cu and Pb in environmental samples by magnetic solid-phase extraction (SPE) with Bismuthiol-II-immobilized magnetic nanoparticles and their determination by ICP-OES has been developed. The separation of the target analytes from the aqueous solution containing the target analytes and Bismuthiol-II-immobilized magnetic nanoparticles was simply achieved by applying external magnetic field. Optimal experimental conditions including pH, sample volume, eluent concentration and volume and co-existing ions have been studied and established. Under the optimal experimental conditions, the detection limits for Cr, Cu and Pb with enrichment factors of 96, 95 and 87 were found to be 0.043, 0.058 and 0.085 ng mL⁻¹ and their relative standard deviations (R.S.D.s) were 3.5%, 4.6% and 3.7% ($n=5$, $C=2$ ng mL⁻¹), respectively. The method was validated with certified reference material (GBW50009-88) of environmental water sample and the analytical results coincided well with the certified values. Furthermore, the method was successfully applied to the determination of target analytes in river and lake water samples. Compared with established methods, the proposed method is characterized with high enrichment factor, fast separation and low detection limits.

© 2008 Elsevier B.V. All rights reserved.

1. Introduction

Both chromium and copper are essential elements and have an important role in the glucose, lipid and protein metabolism [1–2], while lead is an extremely toxic element. Lead has been used at least since biblical times in a variety of products in inorganic form, while its impact as a major environmental pollutant was recognized until the last century [3]. Therefore, the determination of trace amounts of Cr, Cu and Pb in environmental water is of great significance from the public health and environmental point of view.

In recent years, continuous progress has been made in analytical instrumentation; however, direct determination of trace metal ions in environmental samples is difficult sometimes due to various factors, particularly their low concentrations and matrix effects. Under these circumstances, in order to determine trace levels of Cr, Cu and Pb, a separation and enrichment step prior to their determinations could be a good choice. Several methods have been proposed for separation and preconcentration of trace Cr, Cu and Pb including: cloud point extraction [4], precipitation/co-precipitation [5], liquid–liquid extraction [6], and solid-phase extraction (SPE) [7].

Among these techniques, SPE procedures, either off- or on-line, are considered superior to other procedures for their simplicity, consumption of small volumes of organic solvent, and ability to achieve a higher enrichment factor. It is commonly acknowledged that the adsorption materials play a very important role in SPE, because adsorption materials determine the analytical sensitivity, precision and selectivity in SPE techniques. The current researches in SPE are mainly focused on the development of new sorbents. To date, many adsorbents, such as active carbon [8], cellulose [9], nanometer-sized materials [10], egg-shell membrane [11] and modified silica beads [12,13], have been employed in SPE. To improve the selectivity, these adsorbents are normally modified by attaching organic and inorganic molecules to their surface.

Nanometer-sized materials have attracted substantial interest in the scientific community because of their special properties [14,15]. The size range of nanoparticles is from 1 to almost 100 nm, which falls between the classical fields of chemistry and solid-state physics. The relatively large surface area and highly active surface sites of nanoparticles enable them to have a wide range of potential applications, including shape-selective catalysis [16], chromatographic separations [17], sorption of metal ions [18], enzyme encapsulation [19], DNA transfection [20], and drug delivery [21]. Magnetic nanoparticles, as a new kind of nanometer-sized mate-

* Corresponding author. Fax: +86 27 68754067.

E-mail address: binhu@whu.edu.cn (B. Hu).

rial, are widely used in the fields of biotechnology and biomedicine for applications such as cell labeling and separation [22], magnetic resonance imaging (MRI) (as a contrast agent) [23], enzyme and protein separations [24], targeted drug delivery [25], and magnetic ferrofluids hyperthermia [26]. These particles are superparamagnetic, which means that they are attracted to a magnetic field, but retain no residual magnetism after the field is removed. Therefore, suspended superparamagnetic particles adhered to the target can be removed very quickly from a matrix using a magnetic field, but they do not agglomerate after removal of the field. Hu et al. [27] employed magnetic Fe_2O_3 nanoparticles as adsorption material for the removal and recovery of Cr(VI) from wastewater, and the adsorption capacity was found to be very high. However, it should be pointed out that pure inorganic nanoparticles (such as Fe_3O_4 and Fe_2O_3) can easily form large aggregates, which may alter their magnetic properties [24]. Moreover, these nanometer-sized metal oxides are not target-selective and are unsuitable for samples with complicated matrices [28]. The modification of these magnetic nanoparticles with a suitable coating has been proven to be one of the most efficient ways [29].

As a reagent commonly used in spectrophotometry, Bismuthiol can form stable complex with Cd, Cu and Pb under special conditions due to functional groups of $-\text{SH}-$ and $-\text{NH}-$ [30,31]. In this study, silica-coated magnetic nanoparticles (SCMNPs) immobilized with Bismuthiol II were synthesized. These magnetic nanoparticles were employed as an SPE adsorbent for separating and concentrating trace amounts of Cr, Cu and Pb from environmental samples. The levels of these elements were then determined by ICP-OES.

2. Experimental

2.1. Instrumentation

A 1150 W, 27.12 MHz Spectro Genesis EOP ICP-OES (Kleve, Germany) with a cross flow nebulizer and a Scott model spray chamber was employed for the determination of target elements. The auxiliary gas (Ar) flow rate, carrier gas (Ar) flow rate and plasma gas (Ar) flow rate were 1.0, 1.0 and 12 L min^{-1} , respectively, and the wavelengths used were Cr(II) 267.716 nm; Cu(I) 324.754 nm and Pb(II) 220.353 nm. The solution uptake rate was 2.0 mL min^{-1} and the integration time was 12 s. The Bismuthiol-II-immobilized silica-coated magnetic nanoparticles (BSCMNPs) were characterized by NEXUS 870 FI-IR (Thermo, Madison, USA) and a JEM-100CXII electron microscope (JEOL, Tokyo, Japan). The pH values were controlled with a Mettler Toledo 320-S pH meter (Mettler Toledo Instruments Co. Ltd., Shanghai, China) supplied with a combined electrode. An SY1200 model Ultrasonicator (Shengyuan Instrument Factory, Shanghai, China) was used to disperse the nanoparticles in solution. An Nd-Fe-B magnet ($8.0 \text{ mm} \times 6.0 \text{ mm} \times 1.6 \text{ mm}$) was used for magnetic separation.

2.2. Standard solution and reagents

All reagents used were of “specpure” or at least analytical reagent grade. Highly pure deionized water ($18.2 \text{ M}\Omega \text{ cm}$) obtained from a Labconco system (Labconco Co., Kansas City, MO, USA) was used throughout this work. Stock solutions (1 g L^{-1}) of Cr, Cu and Pb were prepared by dissolving $\text{CrCl}_3 \cdot 6\text{H}_2\text{O}$, $\text{CuSO}_4 \cdot 5\text{H}_2\text{O}$ and $\text{Pb(NO}_3)_2$ (The First Reagent Factory, Shanghai, China) in 1% (v/v) HCl, 1% (v/v) HNO_3 and 1% (v/v) HNO_3 , respectively. Standard stock solutions (1 g L^{-1}) of other elements were prepared from their salts by a conventional method [32]. Bismuthiol-II was obtained from East China Normal University (Shanghai, China).

Glycerol was obtained from Shanghai Zhanyun Chemical Co. Ltd. (Shanghai, China). Tetraethoxysilane (TEOS) (Wuhan University Chemical Factory, Wuhan, China) were used for the preparation of sorbent.

2.3. Preparation of silica-coated magnetic nanoparticles (SCMNPs)

The magnetic nanoparticles (MNPs) were prepared according to Ref. [29] with some little modifications. Briefly, $\text{FeCl}_3 \cdot 6\text{H}_2\text{O}$ (11.68 g) and $\text{FeCl}_2 \cdot 4\text{H}_2\text{O}$ (4.30 g) were dissolved in 200-mL deionized water under nitrogen gas with vigorous stirring at 85°C . Then, 20 mL of 30% aqueous ammonia was added to the solution. The color of bulk solution changed from orange to black immediately. The magnetic precipitates were washed twice with deionized water and once with 0.02 mol L^{-1} sodium chloride. The washed magnetite was stored in deionized water at a concentration of 40 g L^{-1} . Then, the magnetite suspension prepared above (20 mL) was placed in a 250-mL round-bottom flask and allowed to settle. The supernatant was removed, and an aqueous solution of TEOS (10% (v/v), 80 mL) was added, followed by glycerol (60 mL). The pH of the suspension was adjusted to 4.6 using glacial acetic acid, and the mixture was then stirred and heated at 90°C for 2 h under a nitrogen atmosphere. After cooling to room temperature, the suspension was washed sequentially with deionized water ($3 \times 500 \text{ mL}$), methanol ($3 \times 500 \text{ mL}$), and deionized water ($5 \times 500 \text{ mL}$). The silica magnetite composite was stored in deionized water at a concentration of 40 g L^{-1} .

2.4. Preparation of Bismuthiol-II-immobilized silica-coated magnetic nanoparticles (BSCMNPs)

Silica-coated magnetite (25 mL) prepared as described above was washed with ethanol ($2 \times 100 \text{ mL}$) and then homogeneously dispersed to 150 mL with 1% Bismuthiol. The solution was transferred to a 500-mL beaker and ultrasonicated for 2 h. After that, the resulting nanoparticles were washed with deionized water three times and twice with methanol, then dried into powders at room temperature under vacuum.

2.5. General procedure

The procedure for the magnetic solid-phase extraction is presented in Fig. 1 and the details are as follows: a portion of sample solution containing $10 \mu\text{g}$ analyte ions was transferred to a 200-mL beaker, the pH value was adjusted to 7 with 0.1 mol L^{-1} HNO_3 and 0.1 mol L^{-1} aqueous ammonia, and the final volume was diluted to 200 mL. Then, 100 mg of BSCMNPs were added, and the solution was ultrasonicated for 10 min to facilitate adsorption of the metal ions onto the nanoparticles. Then the magnetic adsorbent was separated easily and quickly using a magnet and the supernatants were decanted directly. The magnet was removed, and a solution containing 1.0 mol L^{-1} HNO_3 was added as eluent and ultrasonicated again for 5 min. Finally, the magnet was used again to settle the magnetic nanoparticles, and the eluate was pipetted into a test tube for subsequent ICP-OES analysis.

Highly pure deionized water was chosen as the blank solution and subjected to SPE and the blank values were determined. These blank values were subtracted from the values determined for the different metal ions to give the final experimental measurements.

2.6. Sample preparation

Water samples were collected from the East Lake and Yangtze River of Wuhan, P.R. China. The samples were filtered before

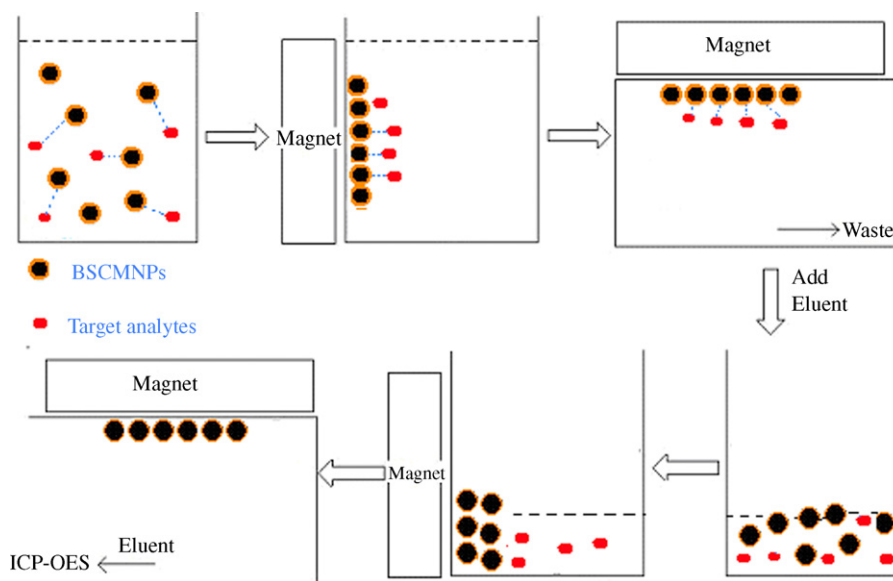


Fig. 1. Procedure for magnetic solid-phase extraction.

analysis through a 0.45- μm membrane filter (Tianjing Jinteng Instrument Factory, Tianjin, China) and stored in polyethylene container for subsequent usage after they were acidified to pH 1 with concentrated HNO_3 .

3. Results and discussion

3.1. Characterization of Bismuthiol-II-immobilized SCMNP

In order to ascertain the immobilization of Bismuthiol-II on SCMNP, the characterization was performed by FI-IR spectroscopy, and Fig. 2 is the graphical representation of the FI-IR spectra for BSCMNPs, SCMNP and Bismuthiol-II. As could be seen, BSCMNPs contained $-\text{SH}$ and $-\text{NH}-$ spectral band at 2435 cm^{-1} and 1491 cm^{-1} which is similar to the characteristics spectral band of Bismuthiol-II at 2431 cm^{-1} for $-\text{SH}$ and 1489 cm^{-1} for $-\text{NH}-$. A comparison of these characteristic spectral bands indicated that the surface SCMNP contained $-\text{SH}$ and $-\text{NH}-$ functional groups as a result of the immobilization procedure.

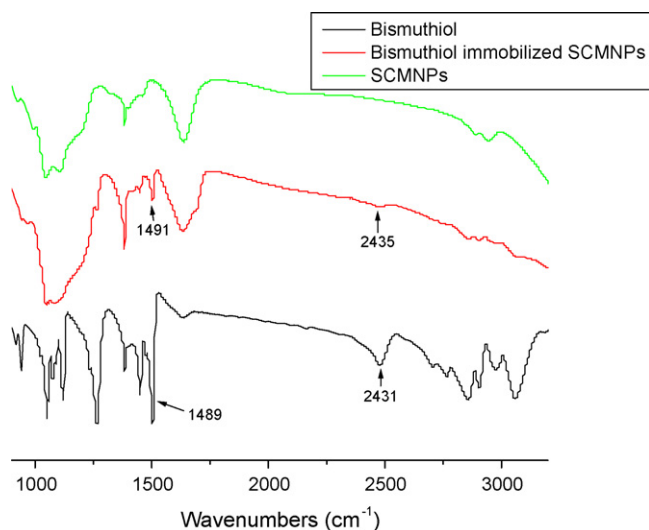


Fig. 2. IR spectra of BSCMNPs.

The BSCMNPs particles were also characterized by TEM. The experimental results showed the average diameter of the BSCMNPs was in the range of 50–70 nm.

3.2. Effect of pH

In order to determine the optimal pH required for quantitative adsorption of target analytes, it is important to study the effect of pH in a wider range. The effect of pH on the adsorption of target metal ions with concentration of $0.05\text{ }\mu\text{g mL}^{-1}$ over the pH range from 1 to 9 was studied. As could be seen from Fig. 3, quantitative adsorption ($>90\%$) was obtained for Cr, Cu and Pb within the pH range of 3–9. This indicated that BSCMNPs was selective to Cr, Cu and Pb in the pH range of 3–8. Considering the fact that Bismuthiol II could be decomposed at high acidity [33], pH 7 was selected for all subsequent experiments.

3.3. Effect of elution

With respect to the stripping of target analytes from the magnetic particles, HNO_3 were employed. Fig. 4 showed the effect of

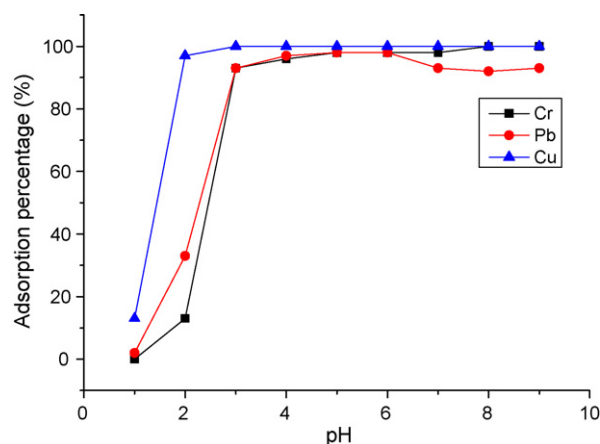


Fig. 3. Effect of pH on the adsorption percentage (%) of the studied elements on BSCMNPs. The concentration of the metal ions: $0.05\text{ }\mu\text{g mL}^{-1}$.

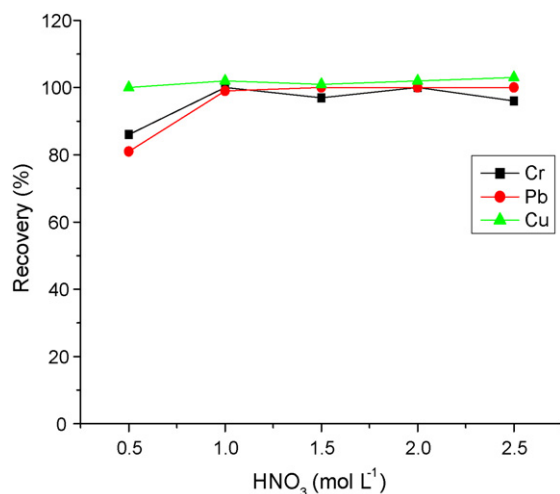


Fig. 4. The effect of elution concentration (HNO_3) on the recovery of the studied analytes on BSCMNPs.

concentration of HNO_3 on the recovery of the target analyte. As could be seen, quantitative recovery for all the studied target analytes could be obtained with $1\text{--}2.5\text{ mol L}^{-1}$ HNO_3 . In this work, 1 mol L^{-1} HNO_3 was chosen for further experiment.

The effect of elution volume for quantitative elution of the studied ions was investigated. The results showed that 1 mL of 1 mol L^{-1} HNO_3 was sufficient to recover the analytes quantitatively.

3.4. Effect of sample volume

In order to obtain a higher enrichment factor, a larger volume of sample solution is required. To study the effect of sample volume, the sample solutions of $10, 25, 50, 100, 150$ and 200 mL containing $0.05\text{ }\mu\text{g}$ of target analytes were operated according to the general procedure. It was found that quantitative recoveries for all target analytes were obtained when sample volumes were less than 150 mL . Hence, sample volume of 100 mL was selected for subsequent experiments.

3.5. Effect of ultrasonic time

Ultrasonic times for adsorption and elution were also optimized in order to minimize the time required for sample processing. The experimental results indicated that quantitative recovery of all analytes in 100-mL sample solution was achieved when the ultrasonication time was greater than 10 min for adsorption and greater than 5 min for elution. Therefore, an ultrasonication time of 10 min was used for adsorption and 5 min was used for elution in subsequent experiments.

3.6. Effect of sediment time

Conventional SPE usually requires filtration or centrifugation to separate the adsorbent from aqueous solutions, which

makes the method time-consuming. In this study, the adsorbent could be separated rapidly from the sample solution using an external magnetic field, due to the superparamagnetism of these nanoparticles. The effect of sediment time on the recovery of metal ions was investigated, and no significant effect was observed when the sedimentation time was greater than 2 min . A sediment time of 2.5 min was therefore selected in subsequent experiments.

3.7. Effect of co-existing ions

The optimal experimental conditions described above were used to study whether other co-existing ions, such as K^+ , Na^+ , Ca^{2+} , Mg^{2+} , Al^{3+} , Fe^{3+} , Zn^{2+} , Cl^- , SO_4^{2-} and NO_3^- could act as interferences during the preconcentration/separation and analyte determination steps of the two-step method. The experimental results showed that recoveries of the target analytes were remained above 90% even in the presence of the following ions: 3 mg mL^{-1} K^+ and Na^+ , 2 mg mL^{-1} Ca^{2+} and Mg^{2+} , $50\text{ }\mu\text{g mL}^{-1}$ Al^{3+} , $10\text{ }\mu\text{g mL}^{-1}$ Fe^{3+} and Zn^{2+} , 4 mg mL^{-1} Cl^- and 2 mg mL^{-1} SO_4^{2-} and NO_3^- , indicating that the method has a good tolerance to matrix interference.

3.8. Adsorption capacity study and sorbent regeneration

The adsorption capacity study used here was adapted from the method recommended by Maquieira et al. [32]. The static adsorption capacities of BSCMNPs were found to be $8.6, 5.3$ and 9.4 mg g^{-1} for Cr, Cu and Pb, respectively.

Regeneration is one of the key factors for evaluating the performance of the adsorption material. In this work, it was found that the BSCMNPs can be re-used up to three times without loss of analytical performance. Considering that 5 g of BSCMNPs could be prepared in one batch and only 100 mg of BSCMNPs was used for one extraction operation, this reusable time is acceptable.

3.9. Analytical performance

Under the optimal experimental conditions, the detection limits for Cr, Cu and Pb with enrichment factors of $96, 95$ and 87 were found to be $0.043, 0.058$ and 0.085 ng mL^{-1} and their relative standard deviations (R.S.D.s) were $3.5\%, 4.6\%$ and 3.7% ($n=5$, $C=2\text{ ng mL}^{-1}$), respectively. The enrichment factor was calculated as follows:

enrichment factor

$$= \frac{\text{the slope of calibration after preconcentration}}{\text{the slope of the calibration before preconcentration}}$$

A comparison of LODs obtained by this method with that obtained by several other approaches for determining Cr, Cu and Pb is shown in Table 1. As can be seen, the LODs obtained by this method are much lower than those obtained by SPE-ICP-OES [34–36] and SPE-FAAS [37].

Table 1

Comparison of detection limits (ng mL^{-1}) for determination of Cr, Cu and Pb using different analytical techniques.

Analytical technique	Sorbent	Cr	Cu	Pb	Ref.
MSPE-ICP-OES	BSCMNPs	0.043	0.058	0.085	This work
SPE-ICP-OES	<i>p</i> -DMABD-modified nanometer-sized SiO_2	0.79	1.27	1.79	34
SPE-ICP-OES	Nanometer-sized TiO_2	1.14	0.34	–	35
SPE-ICP-OES	PAN-modified nanometer-sized TiO_2	3.5	2.8	–	36
SPE-FAAS	Multiwalled carbon nanotubes	–	0.47	0.28	37

Table 2

Analytical results for certified reference material GBW50009-88 environmental water (mean \pm S.D., $n = 3$).

Element	Certified (ng mL ⁻¹)	Found (ng mL ⁻¹)
Cr	1.49 \pm 0.06	1.42 \pm 0.04
Cu	1.49 \pm 0.06	1.33 \pm 0.03
Pb	1.21 \pm 0.05	1.23 \pm 0.06

Table 3

Analytical results for real water samples (mean \pm S.D., $n = 3$).

Sample	Element	Added (ng mL ⁻¹)	Found (ng mL ⁻¹)	Recovery (%)
River water	Cr	0	0.32 \pm 0.11	–
		2.00	2.08 \pm 0.14	90
	Cu	0	3.22 \pm 0.12	–
		2.00	5.22 \pm 0.11	99
	Pb	0	2.35 \pm 0.12	–
		2.00	4.51 \pm 0.14	104
Lake water	Cr	0	1.88 \pm 0.14	–
		2.00	3.85 \pm 0.32	99
	Cu	0	1.13 \pm 0.07	–
		2.00	3.16 \pm 0.36	101
	Pb	0	3.01 \pm 0.18	–
		2.00	4.8 \pm 0.28	96

3.10. Analytical applications

To evaluate the accuracy of the developed method, the certified reference material GBW50009-88 environmental water were analyzed, and the analytical results are shown in Table 2. As can be seen, the determined values obtained by this method are in good agreement with the certified values. The developed method was also applied to the analysis of two kinds of environmental water samples. The analytical results, along with the recoveries for the spiked samples, are given in Table 3. As could be seen, recoveries for the target analytes ranged from 90 to 104%.

4. Conclusion

A new magnetic silica sorbent of Bismuthiol II-immobilized magnetic nanoparticles has been prepared by the sol–gel method. The modified nanoparticles are highly monodisperse and magnetically separable and have been successfully employed for the magnetic solid-phase extraction of trace Cr, Cu and Pb from environmental water. The developed method is simple, rapid and sensitive and very suitable for rapid adsorption of heavy metals from large volume of sample solution.

Acknowledgements

The Science Fund for Creative Research Groups of NSFC (No. 20621502) and NCET-04-0658, MOE of China were acknowledged for their financial supports.

References

- [1] M.R. Ganzali, L.H. Babhaei, A. Badiel, G.M. Ziarani, A. Tarlani, Anal. Sci. 20 (2004) 725–729.
- [2] N. Zhang, J.S. Suleiman, M. He, B. Hu, Talanta 75 (2008) 536–543.
- [3] F. Zheng, B. Hu, Talanta 73 (2007) 372–379.
- [4] A.N. Tang, D.Q. Jiang, X.P. Yan, Anal. Chim. Acta 507 (2004) 203–208.
- [5] D. Atanassova, V. Stefanova, E. Russeva, Talanta 47 (1998) 1237–1243.
- [6] O.M. El-Hussaini, N.M. Rice, Hydrometallurgy 72 (2004) 259–264.
- [7] M. Soylak, M. Tüzen, D. Mendil, I. Turkekul, Talanta 70 (2006) 1129–1135.
- [8] V. Strelko, D.J. Malik, M. Streat, Sep. Sci. Technol. 39 (2004) 1885–1905.
- [9] M.L. Chen, Y. Tian, J.H. Wang, J. Anal. Atom. Spectrom. 23 (2008) 876–880.
- [10] J. Yin, Z.C. Jiang, G. Chang, B. Hu, Anal. Chim. Acta 540 (2005) 333–339.
- [11] A.M. Zou, X.W. Chen, M.L. Chen, J.H. Wang, J. Anal. Atom. Spectrom. 23 (2008) 412–415.
- [12] A.M. Zou, M.L. Chen, X.W. Chen, J.H. Wang, Anal. Chim. Acta 598 (2007) 74–81.
- [13] A.M. Zou, M.L. Chen, Y. Shu, M. Yang, J.H. Wang, J. Anal. Atom. Spectrom. 22 (2007) 392–398.
- [14] G.P. Rao, C. Lu, F.S. Su, Sep. Purif. Technol. 58 (2007) 224–231.
- [15] A. Henglein, Chem. Rev. 89 (1989) 1861–1873.
- [16] R. Garro, M.T. Navarro, J. Primo, J. Catal. 233 (2005) 342–350.
- [17] J.G. Hou, Q. Ma, X.Z. Du, H.L. Deng, J.Z. Gao, Talanta 62 (2004) 241–246.
- [18] P. Liang, B. Hu, Z.C. Jiang, Y.C. Qin, T.Y. Peng, J. Anal. Atom. Spectrom. 16 (2001) 863–866.
- [19] T.K. Jain, I. Roy, T.K. De, A. Maitra, J. Am. Chem. Soc. 120 (1998) 11092–11095.
- [20] Y. Aoyama, T. Kanamori, T. Nakai, T. Sasaki, S. Horiuchi, S. Sando, T. Niidome, J. Am. Chem. Soc. 125 (2003) 3455–3457.
- [21] N. Murthy, Y.X. Thng, S. Schuck, M.C. Xu, J.M.J. Frechet, J. Am. Chem. Soc. 124 (2002) 12398–12399.
- [22] R.S. Faye, S. Aamdal, H.K. Hoifodt, Clin. Cancer Res. 10 (2004) 4134–4139.
- [23] J.C. Frias, Y.Q. Ma, K.J. Williams, Nano Lett. 6 (2006) 2220–2224.
- [24] H.H. Yang, S.Q. Zhang, X.L. Chen, Z.X. Zhuang, J.G. Xu, X.R. Wang, Anal. Chem. 76 (2004) 1316–1321.
- [25] F. Wiekhorst, C. Seliger, R. Jurgons, J. Nanosci. Nanotechnol. 6 (2006) 3222–3225.
- [26] R. Hergt, R. Hiergeist, I. Hilger, J. Magn. Magn. Mater. 270 (2004) 345–357.
- [27] J. Hu, G.H. Chen, M.C. Irene, Water Res. 39 (2005) 4528–4536.
- [28] X.L. Pu, Z.C. Jiang, B. Hu, H.B. Wang, J. Anal. Atom. Spectrom. 19 (2004) 984–989.
- [29] C.Z. Huang, B. Hu, J. Sep. Sci. 31 (2008) 760–767.
- [30] Analytical Chemistry Institute of Hangzhou University, The Handbook of Analytical Chemistry (I), 2nd section, Chemical Industry Press, Hangzhou, Beijing, 1997, pp. 308–314 (in Chinese).
- [31] X.Q. Liu, Z.Y. Ma, J.M. Xing, H.Z. Liu, J. Magn. Magn. Mater. 270 (2004) 1–6.
- [32] A. Maquieira, H.A.M. Elmahadi, R. Puchades, Anal. Chem. 66 (1994) 3632–3638.
- [33] A. Majumdar, B.R. Singh, Bismuthiol II as an analytical reagent, Part VI, Fresen. J. Anal. Chem. 155 (1957) 86–90.
- [34] Y.M. Cui, X.J. Chang, Y.H. Zhai, X.B. Zhu, H. Zheng, N. Lian, Microchem. J. 83 (2006) 35–41.
- [35] P. Liang, Y.C. Qin, B. Hu, T.Y. Peng, Z.C. Jiang, Anal. Chim. Acta 440 (2001) 207–213.
- [36] L.H. Yang, B. Hu, Z.C. Jiang, H.L. Pan, Microchim. Acta 144 (2004) 227–231.
- [37] A.H. El-Sheikh, J.A. Sweileh, Y.S. Al-Degs, Anal. Chim. Acta 604 (2007) 119–126.



A simple capillary electrophoresis with electrochemical detection method for determination of the hydrolysis rate constant of chlorogenic acid

Ping Tong^{a,b}, Lan Zhang^{a,b,**}, Yu He^a, Yuwu Chi^a, Guonan Chen^{a,*}

^a Ministry of Education Key Laboratory of Analysis and Detection for Food Safety (Fuzhou University), Fuzhou, Fujian 350002, China

^b Analytical and Testing Center, Fuzhou University, Fuzhou, Fujian 350002, China

ARTICLE INFO

Article history:

Received 29 May 2008

Received in revised form 7 October 2008

Accepted 11 October 2008

Available online 31 October 2008

Keywords:

Capillary electrophoresis

Electrochemical detection

Hydrolysis rate constant

Chlorogenic acid

Caffeic acid

ABSTRACT

A method based on the kinetics stability study on hydrolysis of chlorogenic acid by capillary zone electrophoresis with electrochemical detection (CE-ED) has been developed in this paper. Both cyclic and hydrodynamic voltammograms of chlorogenic acid and its hydrolysis product caffeic acid have been investigated. The conditions for separation of chlorogenic acid and caffeic acid, such as the buffer pH and concentration, the separation voltage, and the injection time have been optimized. Under the optimum CE running conditions, the effects of reaction temperature and pH values of the hydrolysis solutions on the hydrolysis rate constants were further studied. The hydrolysis rate constants of chlorogenic acid were obtained from the concentration change of hydrolysis during the process of hydrolysis. Based on the fact, a simple and economical method for the determination of the hydrolysis rate constant and activation energy of hydrolysis reaction has been developed.

© 2008 Elsevier B.V. All rights reserved.

1. Introduction

It is reported that about 30% of the pharmaceuticals in the world are based on crude drug. Especially in the field of antibiotic and anti-cancer drugs, nearly 60–80% of them come from crude drugs. So the investigation and exploitation of crude drugs becomes very important and popular nowadays. Chlorogenic acid and caffeic acid are the main active ingredients in many traditional crude drugs, such as *Lonicera japonica Thunb*, *Eucomia ulmoide*, *Taraxacum sinicum Kitag*, etc. [1]. Some related researches showed that chlorogenic acid and caffeic acid had many physiological activities, such as anti-bacteria, antioxidative and other protective effects [2]. As some literatures indicated that chlorogenic acid showed a tendency to hydrolyze to produce caffeic acid and quinic acid in alkaline aqueous solution [3]. Although caffeic acid displays some similarities to chlorogenic acid in the clinical application, there is different content requirement for different officinal. It is described by Pharmacopoeia of People's Republic of China that when the content of chlorogenic acid in *Lonicera japonica Thunb* is less than 1.5% and the content of caffeic acid is below 0.02% in *Taraxacum sinicum Kitag*, the curative effect may be consumedly lower [4]. Since the treat-

ment processes of the crude drugs may affect the curative effect, it is necessary to look for a simple and economical analytical method to evaluate and control the whole process.

The kinetic study, such as the determination of physicochemical constant can be very useful for guiding the extraction of active ingredients in the crude drugs. It is well known that some physicochemical constants are very important in the pharmaceutical industry [5] and phytochemistry research [6]. For example, the rate constant is one of the leading physicochemical parameters for investigation on the degradation of crude drugs. Hydrolysis is a major degradation mode, and the hydrolysis rate constant is related to the stability of drug. Moreover, the activation energy can be used to evaluate whether the degradation reaction can happen or not. Thus, it is a meaningful thing to found a simple and effective method to estimate the rate constants and activation energy of the hydrolytic reaction of some components in crude drugs, it can be a guide to select appropriate storage conditions and control drug quality. For crude drugs, there are still many tasks to be carried out in this field.

The most common method for determination of the rate constant is ultraviolet (UV) spectrophotometer [7,8], however, the limitations and shortages of this method are also well known. Firstly, it is impossible to simultaneously determine and observe the change of the concentration of the reactant and product in the hydrolysis process directly, when the product has the same best ultraviolet absorption wavelength as reactant, the quantitative analysis of reactant is greatly affected. Secondly, UV method has its

* Corresponding author.

** Corresponding author at: Department of Chemistry, Fuzhou University, Fuzhou, Fujian 350002, China. Tel.: +86 591 87893315; fax: +86 591 83713866.

E-mail addresses: zlan@fzu.edu.cn (L. Zhang), gnchen@fzu.edu.cn (G. Chen).

own limitation in the aspect of sensitivity. In addition, for UV spectrophotometer, complicated pretreatments are usually required. Capillary electrophoresis (CE) as an important separation technology with the advantage of minimal sample volume requirement, short analysis time and high separation efficiency, it has been used as a powerful tool for the drug analysis, such as determination of the main component, estimation of impurities and the separation of the chiral substance [9–13]. More recently, CE has been developed to measure the physicochemical constants and the kinetic study of some reactions [6,14–16]. But there are seldom studies focusing on the hydrolysis rate constant of compound by using CE [17–21].

CE coupling with electrochemical detection (CE-ED) offers high sensitivity and good selectivity for separation and detection of electroactive analytes, and it has been widely applied in the quantitative analysis including the main active ingredients of crude drugs [22–24]. There were some reports about quantitative determinations of chlorogenic acid and caffeic acid in crude drugs [25–30], but still no description is related to the kinetic study for hydrolysis of chlorogenic acid. In this study, CE-ED was used as an effective method for directly measuring the hydrolysis rate constant and activation energy of chlorogenic acid, and demonstrating its use for studying the hydrolysis reaction. Under the optimum separation conditions, chlorogenic acid and its hydrolysate caffeic acid could be fast separated within 7 min, and the experimental results indicated that this method was easy, efficient and intuitive to obtain the hydrolysis rate constant and activation energy.

2. Theory

As mentioned in introduction, chlorogenic acid can be hydrolyzed to produce caffeic acid and quinic acid in alkaline aqueous solution. The hydrolysis reaction can be described as Fig. 1.

As water is superfluous during the hydrolysis, the concentration of water can be considered to be constant in the reaction. So, the hydrolysis of chlorogenic acid is a first-order reaction and the kinetic equation is described as follow:

$$-\frac{dC}{dt} = kC \quad (1)$$

The kinetics equation can be also expressed as,

$$\ln C = -kt + \ln C_0 \quad (2)$$

where C is the concentration of chlorogenic acid at the hydrolysis time t , which can be determined by CE-ED, and C_0 is the initial concentration of chlorogenic acid, then k is the rate constant of hydrolysis reaction. Since the kinetic reaction is first-order, when $\ln C$ is plotted against t , a straight line can be obtained, and the slope of the line is the first-order rate constant k .

As shown in Arrhenius equation, the relationship between k and absolute temperature of the reaction T can be described as follow,

$$\ln k = A e^{-E/(RT)} \quad (3)$$

where A is apparent frequency factor, E is activation energy of the reaction; R is the mole gas constant ($8.314 \text{ J K}^{-1} \text{ mol}^{-1}$). In addition, Eq. (3) can also be expressed as,

$$\ln k = -\frac{E}{RT} + \ln A \quad (4)$$

when $\ln k$ is plotted with T^{-1} , a straight line (slope = $-E/R$) is obtained. So the activation energy E can be calculated according to the slope ($E = -\text{slope} \times R$).

3. Experimental

3.1. Materials

Chlorogenic acid and caffeic acid were purchased from the Chinese Institute of Biological Products Control (Beijing, China). Other chemicals were of analytical-reagent grade. All solutions were freshly prepared with doubly distilled water and filtrated through a $0.22 \mu\text{m}$ membrane filter before use.

Stock solution of chlorogenic acid (1.8 mmol/L) and caffeic acid (3.4 mmol/L) were prepared by using 5% (v/v) methanol–buffer solution (pH 7.0, $8 \text{ mmol/L KH}_2\text{PO}_4$ – $4 \text{ mmol/L Na}_2\text{B}_4\text{O}_7$ solution) and diluted to the desired concentration with the running buffer just prior to use. Both solutions were kept in a 4°C refrigerator and were stable for at least 2 months.

Buffer solution was prepared from the mixture of $0.1 \text{ mol/L KH}_2\text{PO}_4$ and $0.05 \text{ mol/L Na}_2\text{B}_4\text{O}_7$. And then the desired concentrations of buffers were obtained by diluting with distilled water. The pH values of buffers were adjusted accurately by $0.1 \text{ mol/L H}_3\text{PO}_4$ or 0.1 mol/L KOH with a pH meter. The running buffer used for electrophoresis was $8 \text{ mmol/L KH}_2\text{PO}_4$ – $4 \text{ mmol/L Na}_2\text{B}_4\text{O}_7$, unless indicated otherwise.

3.2. Apparatus

The CE-ED assembly was self-constructed in this laboratory and was similar to that described previously [31]. A high-voltage power supply (Shanghai Institute of Nuclear Research, China) provided a voltage of up to 30 kV between the ends of the capillary. The inlet end of the capillary was held at a positive potential and the outlet end was grounded; the apparatus was housed in an interlock box to prevent the operator from accidental shock. It was reported that for end-column amperometric detection method when the capillary internal diameters was less than $25 \mu\text{m}$, the potential field effect on background noise could be negligible [32,33]. In this experiment, a 30 cm length of $25 \mu\text{m}$ i.d., $360 \text{ o.d. } \mu\text{m}$ uncoated fused-silica capillary was used (Yongnian Optical Fiber Factory, Heibei, China). The unused capillary had been flushed with 0.1 mol/L sodium hydroxide solution for four hours before use, then rinsed with 0.1 mol/L HCl and doubly distilled water for 10 min each. Between run, the capillary was rinsed with 0.05 mol/L sodium hydroxide solution, doubly distilled water and running buffer for 5 min , respectively.

A conventional three-electrode electrochemical cell consisting of a $300 \mu\text{m}$ diameter carbon disc working electrode, a platinum auxiliary electrode, and a Ag/AgCl (saturated KCl) electrode as reference electrode, was connected to a BAS LC-4C electrochemical detector (Bioanalytical Systems Inc., West Lafayette, IN, USA). Before use, the working electrode was successively polished with emery paper and alumina powder, sonicated in water, and finally exactly leveled with the outlet of the capillary and shaped a wall-jet configuration. The data were recorded by TL9902 analytical system of chromatogram.

The hydrolysis was carried out in a constant temperature water bath (Medical Treatment Instrument Factory, Jiangsu, China).

3.3. Hydrolysis procedures

The constant temperature water bath was adjusted to the desired temperatures at which the hydrolysis was carried out (70 , 80 and 90°C , respectively). One tube was filled with $600 \mu\text{L}$ of 0.12 mmol/L chlorogenic acid solution and the other was full of the same volume of $8 \text{ mmol/L KH}_2\text{PO}_4$ – $4 \text{ mmol/L Na}_2\text{B}_4\text{O}_7$ buffer solutions. Both of them were placed into the constant temperature water bath for 20 min . The buffer solution was then added to the above tube containing chlorogenic acid and mixed by shaking. In a

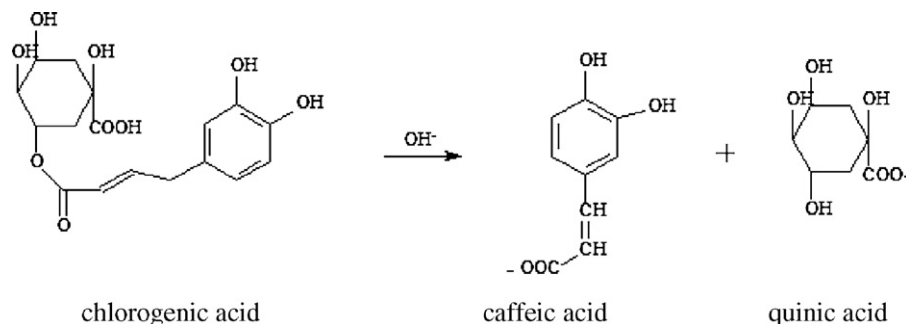


Fig. 1. Hydrolysis reaction of chlorogenic acid.

certain interval time, an accurate volume of 100 μL of hydrolysates was transferred to another tube, and then ice was used in order to terminate the hydrolysis reaction. At last the solution was analyzed by CE-ED, and the measurement was repeated for three times at least. The hydrolysis times ranged from 1 to 8 h.

4. Results and discussion

4.1. Electrochemical characteristic

Due to the fact that the molecular structure of both chlorogenic acid and caffeic acid possessing hydroxyl groups, the two analytes are anticipated to be electroactive at electrode, and this has been verified by cyclic voltammetry. The optimal detection potential for CE was determined by measuring the hydrodynamic voltammograms (HDVs) potential ranging from 800 to 1050 mV for chlorogenic acid and caffeic acid. As a compromise of higher current responses and lower noise, the applied potential of working electrode was maintained at ± 900 mV (versus Ag/AgCl). The experiment indicated that the working electrodes could present good stability and high reproducibility at the optimum potential for more than two months.

4.2. Optimum conditions for electrophoresis

To determine the optimum conditions for the separation and detection of chlorogenic acid and caffeic acid, a standard mixture solution was analyzed to optimize the composition of the buffers and the voltage.

In this study, single constituent buffer was firstly considered, but poor Rs were obtained. It was found that the satisfied separation and good sensitivity could be obtained when the KH_2PO_4 – $\text{Na}_2\text{B}_4\text{O}_7$ buffer solution was used as the carrier buffer. This is likely due to the following reasons. On the one hand, as demonstrated in the literature [34], $\text{B}_4\text{O}_7^{2-}$ and hydroxyl of glucose in the structure of chlorogenic acid could form ligand, then Rs of chlorogenic acid and caffeic acid would be improved. On the other hand, it was also described [35] that the effective mobility (μ_{ef}), Rs and analysis time (t_{A}) was increased with the cation in buffer solution according to the order of Li, Na, and K. As a result, it was considered that KH_2PO_4 was more helpful than NaH_2PO_4 for this analysis system.

Both pH and concentration of the buffer play a key role in CE method. It had been mentioned that chlorogenic acid could be hydrolyzed to produce caffeic acid and quinic acid in alkaline aqueous solution, so neutral solution was suitable for the running buffer of electrophoresis. In this study, buffer solutions with different pH values (6.8, 7.0, 7.2, 7.4 and 7.6) were tested. In the range from 7.0 to 7.6, the two current response peaks were separated completely, however, their current response reduced with the increase of the pH value. So, pH 7.0 was selected as the optimum pH. The

effect of the concentration of the buffer was also investigated. On the promise of enough resolution of two analytes, low concentration of buffer was employed to reduce the migration time and improve sensitivity. As a compromise, 8 mmol/L KH_2PO_4 –4 mmol/L $\text{Na}_2\text{B}_4\text{O}_7$ solution was selected.

The effect of separation voltage on separation efficiency of CZE was investigated in the range of 12–24 kV. In this range, the migration times of the analytes were significantly shortened and the current signals were increased a little when the separation voltage increased. However, when it was higher than 18 kV, the Rs were reduced to less than 1.6. Therefore, 18 kV was selected as the separation voltage. Electrokinetic sampling was used in our experiment. The injection time ranging from 4 to 14 s was optimized, and 10 s was selected as the injection time in this experiment.

The typical electropherogram of a standard mixture solution consisted of chlorogenic acid (8.3×10^{-5} mol/L) and caffeic acid (1.5×10^{-4} mol/L) was obtained under the optimum conditions and shown in Fig. 2. It can be seen from Fig. 2 that these two analytes were completely separated within 7 min at room temperature.

4.3. Validity of CE-AD method

Under the optimized conditions, a standard mixture solution was tested to determine the repeatability of the peak current and migration time for the two analytes. The relative standard deviations (RSDs) of peak current and migration time were 2.7% and 1.1% for chlorogenic acid, 3.4% and 1.1% for caffeic acid, respectively ($n = 7$).

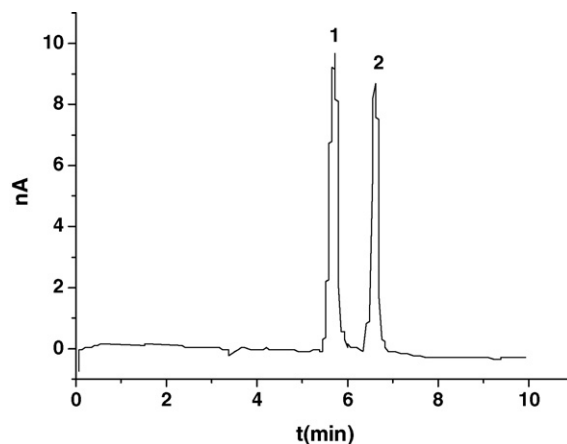


Fig. 2. Electropherograms of standard mixture. (1) Chlorogenic acid (8.3×10^{-5} mol/L); (2) caffeic acid (1.5×10^{-4} mol/L), working potential: 900 mV; injections: 18 kV \times 10 s; separation voltage: 18 kV; running buffer: 8 mmol/L KH_2PO_4 –4 mmol/L $\text{Na}_2\text{B}_4\text{O}_7$ (pH 7.0).

Table 1
Regression equations and the detection limits^a.

Compounds	Regression equation $Y = a + bX^b$	Correlation coefficient	Linear range ($\mu\text{mol/L}$)	Detection limits ^c ($\mu\text{mol/L}$)
Chlorogenic acid	$y = -0.1906 + 0.1071x$	0.9995	0.48–122	0.09
Caffeic acid	$y = -0.2102 + 0.0559x$	0.9991	0.76–226	0.19

^a Conditions were the same as in Fig. 2.

^b Where Y is the peak current (in 1 nA) and X is the compound concentration (in $\mu\text{mol/L}$).

^c The detection limits were calculated according to IUPAC recommendations ($\text{LOD} = 3\delta_b/s$).

A series of the standard mixture solutions of chlorogenic acid and caffeic acid with the concentration in the range of 0.48–122 and 0.76–226 $\mu\text{mol/L}$, respectively, were tested to determine the linearity for this pair of hydro-analytes at the carbon disc electrode ($n=3$). The detection limits was obtained as 0.09 and 0.19 $\mu\text{mol/L}$, respectively by IUPAC recommendation ($\text{LOD} = 3\delta_b/s$). The results of detection limits and regression analysis on calibration curves are presented in Table 1. The calibration curves exhibited an excellent linear response, $R = 0.9995$ and 0.9991 for chlorogenic acid and caffeic acid, respectively over three orders magnitude of the concentration.

Furthermore, the recoveries of spiked sample was determined to examine the accuracy of the proposed method. A standard mixture solution of 5.6×10^{-5} and 1.1×10^{-4} mol/L of chlorogenic acid and caffeic acid, respectively, was selected as the spiked sample. Then two different concentrations of standard mixture solution were added to the spiked sample, and the recoveries of chlorogenic acid and caffeic acid were in the range of 105–111% and 98.1–116%, respectively.

4.4. Kinetic study on hydrolysis of chlorogenic acid

According to the Section 3.3, the hydrolysis of chlorogenic acid was carried out in the constant temperature water bath (90 °C). Fig. 3 shows the typical electropherograms of chlorogenic acid and hydrolyzate caffeic acid at 90 °C in 8 mmol/L KH_2PO_4 –4 mmol/L $\text{Na}_2\text{B}_4\text{O}_7$ (pH 9.0) buffer solution when the hydrolysis time were 1, 2, 3, and 4 h, respectively. As shown in Fig. 3, the change of the peak currents of peak 1 and peak 2 demonstrates the change of concentrations of chlorogenic acid and caffeic acid during the process

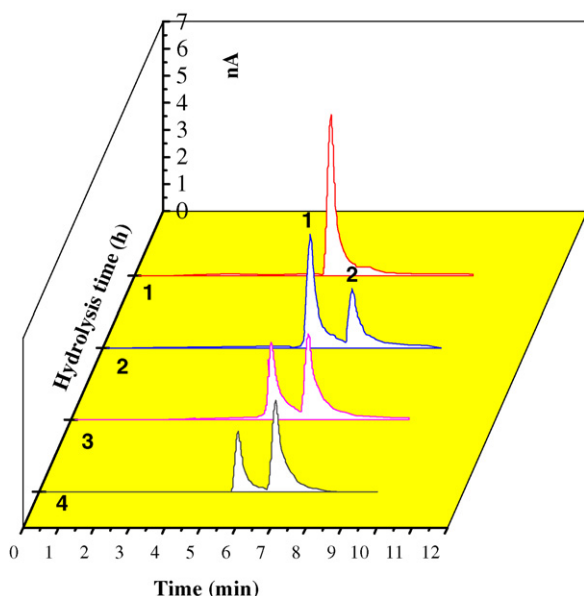


Fig. 3. Electropherogram showing of the hydrolysis of chlorogenic acid. Conditions were the same as in Fig. 2.

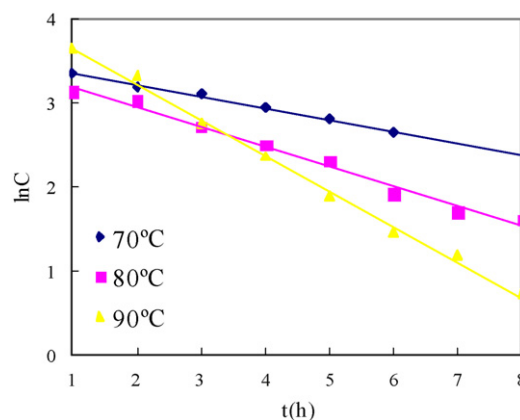


Fig. 4. Relationship between $\ln C$ and t for chlorogenic acid hydrolysis reaction at various temperatures in pH 9.0 solution.

of hydrolysis. The peak current of chlorogenic acid was decreased gradually with the hydrolysis time increased, while the peak current of caffeic acid was increased at the same time.

As we known, kinetic constant of hydrolysis depends on the temperature closely. The hydrolysis of chlorogenic acid at temperature of 70 and 80 °C was carried out in the same way and then the variation of the concentration with hydrolysis time was observed. Fig. 4 shows the relationship between $\ln C$ and t for chlorogenic acid hydrolysis reaction (at pH 9.0) at various temperatures (at 70, 80, 90 °C), and it exhibits a good linearity. The experimental results indicated that the hydrolysis velocity decreased with the decreasing of reaction temperature under the same acidity (pH 9.0).

Then the hydrolytic reaction in a buffer solutions with pH of 8.0 was carried out, and the result showed that it would take at least 15 h to complete the hydrolysis reaction at 90 °C under pH 8.0, while only 12 h under pH 9.0. This indicated that the hydrolysis rate constant was closely related to the alkalinity of the hydrolysis solution. Higher alkalinity would be helpful to increase the reaction rate.

In the light of Eq. (2) of Section 2, a straight line can be obtained by plotting $\ln C$ against t (h) at different alkalinity of the hydrolysis solution. The slope of the line is $-k$, and k is the rate constant of hydrolysis reaction. In order to obtain the activation energy of chlorogenic acid hydrolysis reaction, the plot of $\ln k$ versus $1/T$ is mapping according to Eq. (4) of Section 2. A good linearity between $\ln k$ and absolute temperature T^{-1} is approximately in accordance with Van't Hoff Rule. The regression equation, correlation coefficients, and the calculated activation energy in two pH values solutions are shown in Table 2. The activation energies under pH

Table 2
Influence of pH on activation energy of chlorogenic acid hydrolysis^a.

pH	Regression equation	Correlation coefficient	E_a (kJ mol^{-1})
8.0	$\ln k = -8615.0/T + 22.842$	0.9986	71.62
9.0	$\ln k = -7007.7/T + 18.436$	0.9994	58.26

^a Conditions were the same as in Fig. 2.

8.0 and pH 9.0 are 71.62 and 58.26 kJ mol⁻¹, respectively. It was shown that higher pH would lower the activation energy of hydrolysis reaction. The good straight-line illustrated *E* was approximately a constant, which is independent of *T* in the tested temperature range.

5. Conclusion

In this work, capillary electrophoresis with electrochemical detection was found to be a useful technique for studying the kinetic aspects of chlorogenic acid hydrolysis in aqueous solution. Except for the determination of hydrolysis rate constant, the method would promise to be applied to the study of other physico-chemical constant, such as the dissociation constant (*pK_a*), binding constant and so on for other compounds existed in the crude drugs.

Acknowledgements

The authors are grateful for the National Nature Sciences Foundation of China (20675016, 20735002, 20775014), the Key Program of Science and Technology Department of Fujian Province (2007I0020, 2007Y0060), the Nature Sciences Funding of Fujian Province (2007J0219, B0510006, 2008J0228), the Key Special Purpose Funding of Physical Education Bureau of Fujian Province (HX2005-74), the Plan of University New Century Outstanding Talented Man of Fujian Province, China (HX2006-101).

References

- [1] W.J. Sun, S.C. Xie, The Quantitative Analysis Of the Ingredients of Crude Drugs, China Press of Medicine Science, Beijing, 2003.
- [2] Chinese Herbal Medicine Information Center of State Administration of Medicine, Manual of Active Ingredient of Botanic Medicine People's Medical Publishing House, Beijing, 1982.
- [3] S.Y. Shi, The Analytical Method of the Active Ingredients of Chinese, People's Medical Publishing House, Beijing, 1982.
- [4] Pharmacopoeia Commission of People's Republic of China, Pharmacopoeia of People's Republic of China, Chemical Industry Press, Beijing, 2000.
- [5] A. Afdeef, J.E.A. Comer, S.T. Thomson, Anal. Chem. 65 (1993) 42.
- [6] X.M. Fang, F.Y. Gong, J.Y. Ye, et al., Chromatographia 46 (1997) 137.
- [7] N. Marti, G.H.B. Hoa, J. Kozelka, Inorg. Chem. Commun. 1 (1998) 439.
- [8] E. Furusjö, L.G. Danielsson, Anal. Chim. Acta 373 (1998) 83.
- [9] X.K. Wang, Y.Z. He, L.L. Qian, Talanta 74 (2007) 1.
- [10] N. Helali, N.T. Tran, L. Monser, et al., Talanta 74 (2008) 694.
- [11] X.Y. Zheng, M.H. Lu, L. Zhang, et al., Talanta 76 (2008) 15.
- [12] K.D. Altria, M.A. Kelly, B.J. Clark, Trends Anal. Chem. 17 (1998) 214.
- [13] N. Anastos, N.W. Barnett, S.W. Lewis, Talanta 67 (2005) 269.
- [14] N.B. Li, J.P. Duan, H.Q. Chen, et al., Talanta 59 (2003) 493.
- [15] J.Y. Hsiao, S.H. Wu, W.H. Ding, Talanta 68 (2006) 1252.
- [16] A.A. Christy, P.K. Egeberg, Talanta 51 (2000) 1049.
- [17] X.P. Xing, Y.H. Cao, L.C. Wang, J. Chromatogr. A 1072 (2004) 267.
- [18] G. Chen, J.N. Ye, H.M. Bao, et al., J. Pharm. Biomed. Anal. 29 (2002) 843.
- [19] L.N. Song, R.M. Fang, Y.Z. Fang, Chem. J. Chin. Uni. 4 (2000) 541.
- [20] L. Zhang, P. Tong, G.N. Chen, J. Chromatogr. A 1098 (2005) 194.
- [21] L. Zhang, Q. Chen, G.N. Chen, et al., Chin. J. Anal. Chem. 31 (2003) 799.
- [22] G. Chen, H.W. Zhang, J.N. Ye, Anal. Chim. Acta 423 (2000) 69.
- [23] G. Chen, H.W. Zhang, J.N. Ye, Talanta 53 (2000) 471.
- [24] G. Chen, J.X. Zhang, J.N. Ye, J. Chromatogr. A 923 (2001) 255.
- [25] Y.Y. Peng, F.H. Liu, J.N. Ye, Electroanalysis 17 (2005) 356.
- [26] A.F. Wang, Y. Zhou, F. Wu, P.G. He, Y.Z. Fang, J. Pharm. Biomed. Anal. 35 (2004) 959.
- [27] Y.H. Cao, Y. Wang, J.N. Ye, J. Pharm. Biomed. Anal. 39 (2005) 60.
- [28] X. Yao, G. Chen, Anal. Bional. Chem. 388 (2007) 475.
- [29] D. Sterbova, J. Vlcek, V. Kuban, J. Sep. Sci. 29 (2006) 308.
- [30] S.J. Sheu, C.L. Chieh, W.C. Weng, J. Chromatogr. A 2 (2001) 285.
- [31] W. Wang, B. Qiu, X.Q. Xu, et al., Electrophoresis 26 (2005) 903.
- [32] X.H. Huang, R.N. Zare, S. Sloss, et al., Anal. Chem. 63 (1991) 189.
- [33] W. Lu, R.M. Cassidy, Anal. Chem. 66 (1994) 200.
- [34] Y. Chen, Capillary Electrophoresis Technology and Application, Chemical Industry Press, Beijing, 2000.
- [35] Y.Z. Deng, J.L. He, High Performance Capillary Electrophoresis, Science Press, Beijing, 1996.



Hybrid sequential injection–flow injection manifold for the spectrophotometric determination of total sulfite in wines using o-phthalaldehyde and gas-diffusion

Paraskevas D. Tzanavaras, Eleni Thiakouli, Demetrius G. Themelis*

Laboratory of Analytical Chemistry, Department of Chemistry, Aristotle University of Thessaloniki, 54124 Thessaloniki, Greece

ARTICLE INFO

Article history:

Received 24 June 2008

Received in revised form

24 September 2008

Accepted 29 September 2008

Available online 14 October 2008

Keywords:

Sulfite

Determination

Gas-diffusion

Sequential injection

Spectrophotometry

o-Phthalaldehyde

Wine

ABSTRACT

A new automated spectrophotometric method for the determination of total sulfite in white and red wines is reported. The assay is based on the reaction of o-phthalaldehyde (OPA) and ammonium chloride with the analyte in basic medium under SI conditions. Upon on-line alkalization with NaOH, a blue product is formed having an absorption maximum at 630 nm. The parameters affecting the reaction – temperature, pH, ionic strength, amount concentration and volume of OPA, amount concentration of ammonium chloride, flow rate and reaction coil length – and the gas-diffusion process – sample and HCl volumes, length of mixing coil, donor flow rate – were studied. The proposed method was validated in terms of linearity ($1\text{--}40\text{ mg L}^{-1}$, $r = 0.9997$), limit of detection ($c_L = 0.3\text{ mg L}^{-1}$) and quantitation ($c_Q = 1.0\text{ mg L}^{-1}$), precision ($s_r = 2.2\%$ at 20 mg L^{-1} sulfite, $n = 12$) and selectivity. The applicability of the analytical procedure was evaluated by analyzing white and red wine samples, while the accuracy as expressed by recovery experiments ranged between 96% and 106%.

© 2008 Elsevier B.V. All rights reserved.

1. Introduction

Sulfite is a naturally occurring by-product of the fermentation process in winemaking. Sulfites are added to wine and many other food products in order to preserve their freshness and shelf life. It plays two important roles. Firstly, it is an anti-microbial agent, and as such is used to help curtail the growth of undesirable fault producing yeasts and bacteria. Secondly, it acts as an antioxidant, safeguarding the wine's fruit integrity and protecting it against browning. In winemaking, this usually takes the form of sulphur dioxide. If SO_2 is not added, the aging process of wine is greatly accelerated [1,2]. Since the 1980s, the use of sulfites has come under increased scrutiny due to potential health concerns. United States Food and Drug Administration regulations require food and wine producers to indicate "contains sulfites" on the label of any product that has at least 10 mg L^{-1} . These regulations, which went into effect in 1986, were instituted because sulfite-sensitive individuals who are deficient in the natural enzyme to metabolize it can experience allergic reactions [3,4].

It is therefore important to develop reliable methods for the efficient quality control of sulfite in wines both during production and storage after bottling. Recently reported analytical meth-

ods (2000–2008) for the determination of sulfite apply a variety of instrumental approaches: electroanalytical approaches [5–10] including amperometric biosensors [11–13] are popular among scientists due to the properties of the analyte, capillary electrophoresis coupled to either UV [14] or conductivity detection [15,16], fluorescence/chemiluminescence [17–19], vapour generation ICP-OES [20], FTIR [21], piezoelectric sensors [22] and light scattering detection [23].

UV–vis spectrophotometry is an interesting alternative for routine applications as it offers cost-effective and widely available instrumentation, low operational costs and simple handling. On this basis, two batch spectrophotometric methods [24,25] and two optical sensors [26,27] have been reported recently for the determination of sulfites. Although they offer adequate analytical figures of merit they suffer for the necessity of synthesizing the analytical reagent [24] and the sensing membranes [26,27] making them rather unattractive to routine analyses.

Flow injection techniques have offered invaluable analytical tools for over thirty years in terms of rapidity, cost-effectiveness, precision and accuracy. Recent reports on FI to the analysis of sulfites include a variety of approaches based on amperometry [28,29], chemiluminescence [30], fluorescence [31], conductivity [32] and most commonly spectrophotometric detection [33–36]. A potential disadvantage of FI is the complicated, multi-channelled manifolds that are often proposed by analytical scientists. This is particularly evident in the case of sulfite, where a gas-diffusion step is

* Corresponding author. Tel.: +30 2310997804; fax: +30 2310997719.
E-mail address: themelis@chem.auth.gr (D.G. Themelis).

also incorporated in the majority of the assays [28,29,31–36]. Four-channelled [32,35], five-channelled [31] or even six-channelled setups [33,36] have therefore been recommended. To overcome this limitation Ruzicka and Marshall introduced sequential injection analysis, where all necessary analytical steps are carried out in a practically single-channelled mode [37]. To our knowledge, only two SI methods have been reported so far for the determination of sulfite. The first is based on the well-known formaldehyde–pararosaniline system with photometric detection [38] and the second on the use of a boron-doped diamond electrode and amperometric detection [39]. Both assays employ on-line gas-diffusion while the former utilizes three pumps [38] and the latter a continuously flowing acceptor stream to avoid disturbances of the electrochemical detector from the discontinuous operation of SI [39].

The scope of the present study is to propose a new automated method for the determination of total sulfite in wines. The method is based on a promising batch chemical system in terms of both selectivity and sensitivity [40]. The analyte reacts with o-phthalaldehyde (OPA) in the presence of ammonia in phosphate buffer medium. Upon addition of NaOH to the reaction mixture, a deep blue product is formed having an absorption maximum at 630 nm. In order to accomplish this two stage process, a hybrid SI–FI system was utilized. Sulfite was separated from the wine matrix through an on-line gas-diffusion process incorporated in the SI manifold, followed by reaction with OPA in the presence of ammonia. The reaction mixture was merged on-line with a continuously flowing of NaOH prior to detection. The proposed method offers considerable advantages for routine analysis: automation through a practically two-channelled manifold; simple and low cost instrumentation including photometric detection; commercially available reagents; no complicated sample pretreatment prior to analysis; adequate sensitivity and linearity for this kind of determination; selectivity against potential interfering species and acceptable sampling rate.

2. Material and methods

2.1. Instrumentation

A schematic diagram of the hybrid SI–FI manifold used is shown in Fig. 1. It was comprised of the following parts: a micro-

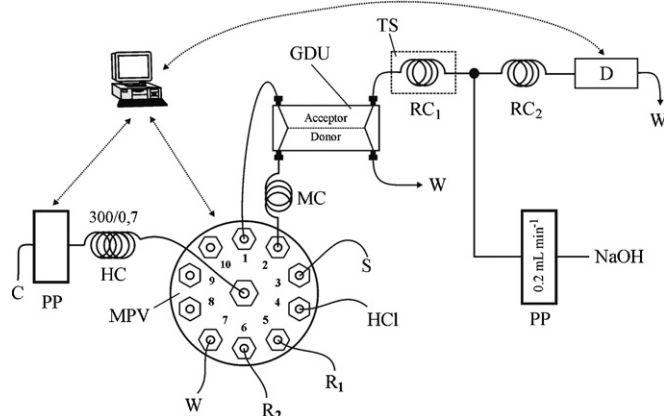


Fig. 1. Schematic depiction of the hybrid SI–FI setup: C: water as carrier; PP: peristaltic pump; HC: holding coil; MPV: multi-position valve; S: sample; HCl: 1.0 mol L^{−1} HCl solution; R₁: OPA ($c = 1 \times 10^{-2}$ mol L^{−1}); R₂: ammonium chloride ($c = 2 \times 10^{-2}$ mol L^{−1})/phosphate buffer (pH 8.5, 7.5×10^{-2} mol L^{−1}); W: waste; MC: mixing coil (30 cm/0.5 mm i.d.); GDU: gas-diffusion unit; TS: thermostat; RC₁ and RC₂: reaction coils (60 cm/0.5 mm i.d.) and D: spectrophotometric detector ($\lambda_{\text{max}} = 630$ nm).

electrically actuated 10-port valve (Valco, Switzerland); a Tecator (Hoganas, Sweden) 5023 FIStar double-beam spectrophotometer equipped with a 1-cm long flow cell of 18- μ L internal volume; a Gilson (Minipuls3, France) peristaltic pump for the SI steps; a peristaltic pump of a Tecator 5010 FI analyzer for delivering the NaOH solution; a ChemifoldTM Type V gas-diffusion unit (Tecator, Sweden).

The hardware was interfaced to the controlling PC through a multi-function I/O card (6025 E, National Instrument, Austin, TX). The control of the system and the data acquisition from the detector were performed through a special program developed in house using the LabVIEW 5.1.1 instrumentation software package (National Instrument, Austin, TX).

PTFE gas-diffusion membranes were also provided by Tecator and were typically replaced on a weekly basis. The flow system used 0.5 mm i.d. Teflon tubing throughout, while Tygon pump tubes were used for aspirating/delivering the solutions.

2.2. Reagents

All reagents were of analytical grade and provided by Merck (Darmstadt, Germany) unless stated otherwise. All other reagents used for interferences experiments were purchased from either Sigma–Aldrich or Merck and were salts of analytical grade as well. Ultra-pure quality water, produced by a Milli-Q system (Millipore, Bedford, US) was used for preparation of all the solutions.

The stock sulfite solution ($\gamma(\text{SO}_3^{2-}) = 1000 \mu\text{g mL}^{-1}$) was prepared daily in 0.1 mol L^{−1} NaOH. Working standards were prepared by appropriate dilutions of the stock solution also in 0.1 mol L^{−1} NaOH in order to match the alkalinity of the samples after treatment.

The OPA working solution ($c(\text{OPA}) = 1 \times 10^{-2}$ mol L^{−1}) was prepared by dispersing an accurately weighed amount of the reagent in 100 μ L MeOH and diluting to 10 mL with de-ionized water. The resulting solution was ultra-sonicated for 5 min to facilitate complete dissolution. The reagent was found to be stable for 1 week if kept refrigerated and protected from the light.

The stock NH₄Cl solution ($c(\text{NH}_4\text{Cl}) = 0.1$ mol L^{−1}) was prepared in de-ionized water. Working solutions were prepared by dilution of the stock in 7.5×10^{-2} mol L^{−1} phosphate buffer (pH 8.5).

A 1 mol L^{−1} NaOH stock solution was prepared by dissolving the appropriate amount of NaOH pellets in de-ionized water. HCl stock solution (3 mol L^{−1}) was prepared by proper dilution of the concentrated acid ($\rho = 1.19$, $w = 37\%$) in water.

2.3. SI–GD procedure for aqueous solutions

The optimum SI sequence is shown in Table 1. In brief, each cycle began with filling of the acceptor stream of the gas-diffusion unit with the ammonium chloride–buffer mixture (steps 1–6). Sampling involved delivering of a “sandwiched” acidified sample zone through the donor line (steps 7–14). During the detection step, OPA reagent was aspirated and the reaction mixture was propelled at the confluence point where it was merged with the continuous-flowing NaOH stream and driven towards the spectrophotometric detector (steps 15–18). The duration of the cycle was 360 s, corresponding to a sampling rate of 10 h^{−1}.

At the beginning and end of a working day all ports and lines of the SI manifold were flushed with 3 mL of de-ionized water. It should be noted that when changing between samples, an additional washing step was performed in order to avoid carryover effects; 3 \times 200 μ L of the new sample/standard was aspirated to the HC, and then flushed through port 7 to waste (W).

Table 1
SI sequence for the determination of sulfite.

Step a/a	Time (s)	Valve position	Pump action	Flow rate (mL min ⁻¹)	Action description
1	1	6	Off	–	Selection of acceptor port
2	10	6	Aspirate	1.8	Aspiration of acceptor (R ₂) in the HC
3	1	1	Off	–	Selection of detector port
4	10	1	Deliver	0.9	Filling the acceptor groove of the GDU
5	1	7	Off	–	Selection of waste port
6	20	7	Deliver	1.8	Flushing of the HC
Sampling					
7	1	4	Off	–	Selection of HCl reagent port
8	5	4	Aspirate	0.6	Aspiration of HCl in the HC
9	1	3	Off	–	Selection of sample port
10	10	3	Aspirate	1.2	Aspiration of sample in the HC
11	1	4	Off	–	Selection of HCl reagent port
12	5	4	Aspirate	0.6	Aspiration of HCl in the HC
13	1	2	Off	–	Selection of donor port
14	100	2	Dispense	0.4	Propulsion of mixture to the donor channel
Detection					
15	1	5	Off	–	Selection of OPA port (R ₁)
16	7.5	5	Aspirate	0.6	Aspiration of OPA in the HC
17	1	1	Off	–	Selection of detector port
18	180	1	Deliver	0.2	Propulsion of mixture to the detector

2.4. Analysis of wine samples

The method was applied to the analysis of white and red wines. 5 mL of each sample was treated with an equal volume of 1 mol L⁻¹ NaOH in order to liberate bound sulfites from the wine matrix, since due to their nucleophilic character they tend to react with endogenous wine components such as aldehydes [41–43]. The mixture was diluted to a final volume of 50 mL with de-ionized water prior to injection in the SI system.

3. Results and discussion

3.1. Preliminary experiments

Preliminary experiments were carried out in order to investigate whether the chemical system proposed by Abdel-Latif for the determination of sulfite [40] could be automated using sequential injection analysis. The experiments confirmed that the sulfite–OPA–ammonium reaction mixture had to be merged with a highly alkaline NaOH solution in order to achieve adequate sensitivity in the visible region ($\lambda_{\text{max}} = 630 \text{ nm}$). However, effective alkalization could not be performed under sequential injection conditions, in a practically single-channelled mode. It was therefore necessary to develop a hybrid sequential–flow injection manifold, by incorporating a continuously flowing NaOH stream prior to spectrophotometric detection, as can be seen in Fig. 1.

Although the method proposed by Abdel-Latif was claimed to be highly selective, a gas-diffusion step was introduced in the automated setup in order to avoid potential interferences from the wine samples matrix, including color and amino acids. It should be noted that Abdel-Latif in order to compensate the effect of such interferences used the first derivative of the absorption spectrum [40].

3.2. Study of the color-forming reaction

The various instrumental and chemical variables that affect the chemical reaction were investigated without the gas-diffusion step – using the univariate approach – at 10 mg L⁻¹ sulfites. A hybrid SI–FI manifold similar shown in Fig. 1 was used throughout the study, adopting a three-zones configuration. In brief, sample, ammonium-buffer and OPA zones were aspirated sequen-

tially in the holding coil and propelled towards the confluence point where they were merged with the NaOH stream. The final reaction product was monitored spectrophotometrically at 630 nm. The starting values of the studied variables were: $T = 25^\circ\text{C}$; $V(\text{sample}) = V(\text{ammonium-buffer}) = V(\text{OPA}) = 50 \mu\text{L}$; $q_v(\text{detector}) = 0.6 \text{ mL min}^{-1}$; $c(\text{OPA}) = 5 \times 10^{-3} \text{ mol L}^{-1}$; $l(\text{RC}_2) = 60 \text{ cm}$; 0.5 mm i.d. ; $c(\text{NH}_4\text{Cl}) = 1 \times 10^{-2} \text{ mol L}^{-1}$; pH 8.5 ($5 \times 10^{-2} \text{ mol L}^{-1}$ phosphate buffer) and $c(\text{NaOH}) = 0.5 \text{ mol L}^{-1}$. It should be noted that the length of the thermostated reaction coil (RC_1) was kept at 60 cm/0.5 mm i.d. and the flow rate of the NaOH stream at 0.2 mL min^{-1} throughout this study.

The effect of temperature on the reaction was investigated in the range of 25–70 °C. The experimental results are depicted in Fig. 2A. As can be seen, an almost linear increase in the signals was observed within the studied range. Higher temperatures produced irreproducible results due to bubbles formation even if a restriction coil was used at the detector waste-line. 70 °C was therefore selected for further studies.

The effect of the flow rate of the reaction mixture towards the confluence point prior to detection was studied in the range of 0.6–0.2 mL min⁻¹. The experimental results are shown in Fig. 2B. The signals increased by ca. 165% by decreasing the flow rate within the studied range. The value of 0.2 mL min⁻¹ was selected for subsequent experiments.

The reaction coil RC_2 determines the contact-time between the reaction mixture and the NaOH solution. Its effect was studied between 30 and 90 cm (0.5 mm i.d. in all cases). Maximum absorbance was observed at 60 cm, while longer coils resulted in lower absorbance values due to pre-dominance of dispersion effects.

The effect of the amount concentration of NaOH was studied in the range of 0.25–1.0 mol L⁻¹. No significant variations were recorded within this range. The value of 0.5 mol L⁻¹ was selected for further experiments.

The amount concentration of ammonium chloride had a more marking effect on the sensitivity of the developed method. An almost linear increase in absorbance was obtained between 0.5 and $2 \times 10^{-2} \text{ mol L}^{-1}$, while the phenomenon was less pronounced in the range of $2\text{--}5 \times 10^{-2} \text{ mol L}^{-1}$. The value of $2 \times 10^{-2} \text{ mol L}^{-1}$ was preferred for subsequent studies.

The effect of the pH on the reaction was investigated in the range of 7.0–10.0 using $5 \times 10^{-2} \text{ mol L}^{-1}$ phosphate buffer in all

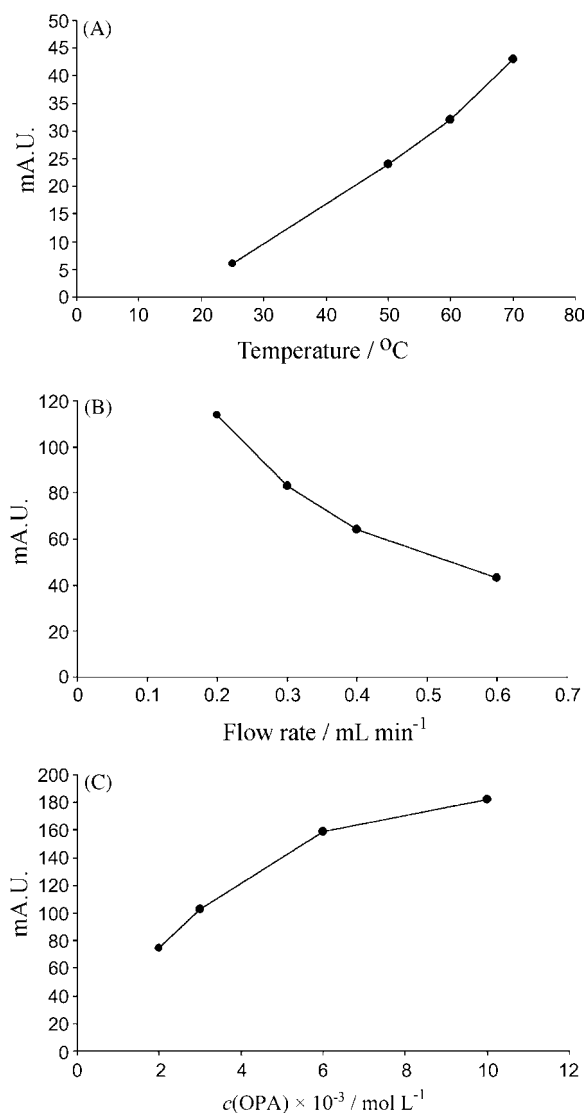


Fig. 2. Study of instrumental and chemical variables: (A) effect of temperature; (B) effect of the acceptor flow rate and (C) effect of the amount concentration of OPA. For experimental details see Section 3.2.

cases. A plateau was obtained in the range of 8.0–9.0, while the signals decreased for lower and higher pH values. This behavior is an advantage of the proposed assay, since no strict pH control is required. The ionic strength of the buffer had a moderate effect on the signals in the range of $1\text{--}5 \times 10^{-2} \text{ mol L}^{-1}$ and practically no effect up to 0.1 mol L^{-1} . The value of $7.5 \times 10^{-2} \text{ mol L}^{-1}$ was selected for further experiments.

Variation of the amount concentration of OPA between 0.2 and $1 \times 10^{-2} \text{ mol L}^{-1}$ resulted in a non-linear increase in the measured absorbance (Fig. 2C). Higher OPA amount concentrations resulted in the formation of blue precipitates within the flow lines, a phenomenon that has also been previously observed in flow injection manifolds [31]. These precipitates could be removed effectively only by flushing the system with acetone. The amount concentration of $1 \times 10^{-2} \text{ mol L}^{-1}$ was selected for subsequent investigations.

Finally, the effect of the volume of the OPA reagent was studied in the range of $25\text{--}100 \mu\text{L}$. Steady state in absorbance was observed within the range of $50\text{--}100 \mu\text{L}$, with a small decrease at $25 \mu\text{L}$. A volume of $75 \mu\text{L}$ was preferred for further investigations.

3.3. Study of the gas-diffusion step

The gas-diffusion step was studied using the hybrid SI–FI setup shown in Fig. 1 and under the selected values of the variables mentioned in the previous section. The investigated variables were the flow rate of the donor stream, the sample injection volume, the volume and amount concentration of the HCl solution and the length of the mixing coil (MC). It should be noted that in order to achieve efficient acidification of the sample, the latter was “sandwiched” between two HCl zones of equal volumes. The starting values of these variables were: q_v (donor) = 0.6 mL min^{-1} ; V (sample) = $50 \mu\text{L}$; V (HCl) = $2 \times 50 \mu\text{L}$; c (HCl) = 1.0 mol L^{-1} and l (MC) = $60 \text{ cm}/0.5 \text{ mm i.d.}$

The flow rate of the donor stream is a critical parameter in on-line gas-diffusion procedures since it determines the time contact between the sample and the semi-permeable membrane and therefore the efficiency of the diffusion process. Its effect was investigated in the range of $0.2\text{--}0.6 \text{ mL min}^{-1}$. Higher sensitivity was obtained at a flow rate of 0.2 mL min^{-1} , while no significant differences were observed in the range of $0.3\text{--}0.6 \text{ mL min}^{-1}$. A flow rate of 0.4 mL min^{-1} was selected as a compromise between sensitivity and sampling frequency.

The effect of the sample injection volume was studied in the range of $50\text{--}300 \mu\text{L}$. The experiments showed an almost linear dependence between the volume and the measured absorbance. The value of $200 \mu\text{L}$ was preferred in terms of sensitivity and sampling rate. On the other hand, no significant variations were obtained for HCl volumes in the range from 100 (2×50) to 200 (2×100) μL . The volume of $100 \mu\text{L}$ was therefore selected for subsequent experiments.

Another potentially critical parameter affecting the gas-diffusion process is the amount concentration of HCl. Since the standards and wine samples contain a final NaOH amount concentration of 0.1 mol L^{-1} , a sufficiently acidic environment must be ensured in order to promote the formation of gaseous sulfur dioxide. The experiments showed a ca. 40% increase on sensitivity in the range of $0.2\text{--}1.0 \text{ mol L}^{-1}$ HCl, while leveling-off was obtained thereafter. The latter value was selected for further studies.

Finally, the effect of the length of the MC was studied in the range of $30\text{--}90 \text{ cm}$. The length of the mixing coil determines the extent of overlapping between the sample and HCl zones and, therefore, the efficiency of the formation of sulfur dioxide and gas-diffusion step. However, the experiments showed no variations within the investigated range. 30 cm was selected as it provided adequate overlapping of the zones.

3.4. Method validation

The developed method was validated in terms of linearity, limits of detection and quantitation, precision, selectivity and accuracy using the SI setup shown in Fig. 1.

3.4.1. Linearity

Linearity was obeyed in the range of $1\text{--}40 \text{ mg L}^{-1}$ sulfite following the regression equation

$$A = 13.7(\pm 2.3) + 12.6(\pm 0.1)\gamma(\text{sulfite})$$

where A is the absorbance as measured by the flow through detector in mA.U. and γ (sulfite) is the mass concentration of the analyte in mg L^{-1} . The validity of the calibration curve was evaluated by the value of the regression coefficient, the distribution of the residuals and response factor (R.F.) test [44]. The acceptance limit for the regression coefficient was a value of >0.999 , while for the response factor test was set to be within $\pm 5\%$ of the experimental slope as

Table 2
Study of interferences.

Interfering species	Specie/analyte mass concentration ratio	Percent recovery, <i>R</i> (%) ^a (20 mg L ⁻¹ SO ₃ ²⁻)
Glycine	100	101
Tartaric, citric, oxalic, malic, malonic, ascorbic, boric	100	97–102
SO ₄ ²⁻ , NO ₃ ⁻ , F ⁻ , SCN ⁻ , CH ₃ COO ⁻ , CO ₃ ²⁻	100	96–102
Ca(II), Mg(II), Zn(II), Fe(III), Cu(II)	50	97–103
CN ⁻	10	102
Ethanol	20% ^b	99

^a The acceptance limit is 95–105%.

^b Corresponds to a volume fraction of 20% in the test sample.

given by the equation:

$$R.F. = \frac{\text{peak height (mAU)} - \text{intercept}}{\gamma(\text{sulfite})}$$

The regression coefficient was 0.9996. The values of the R.F. ranged between −4.8% (at 2.0 mg L⁻¹ sulfite) and +1.3% (at 25 mg L⁻¹ sulfite), verifying the validity of the regression line. The plot of the residuals indicated random distribution around the “zero” line.

3.4.2. Limits of detection and quantitation

The limits of detection and quantitation (*c*_L and *c*_Q) of the proposed assay were calculated according to the IUPAC recommendations, as 3.3*s*_b/*m* and 10*s*_b/*m*, respectively, where *s*_b is the standard deviation of the blank measurements (*n* = 8), and *m* is the slope of the calibration graph [45]. On this basis, the *c*_L and *c*_Q of the proposed method were calculated to be 0.3 and 1.0 mg L⁻¹ sulfite, respectively. These values are adequate for the determination of the analyte in real wine samples.

3.4.3. Precision

The within-day precision of the proposed method was evaluated by repeated injections (*n* = 12) of a sulfites standard solution at the 20 mg L⁻¹ level. The relative standard deviation was 2.2%. The between-day precision for five consecutive at the same concentration level was less than 8%.

3.4.4. Study of interferences

The selectivity of the assay against several potentially interfering species was examined by analyzing mixtures of the species with the analyte at a sulfite mass concentration of 20 mg L⁻¹. The study of interferences was focused on metals, anions and organic acids that may co-exist with sulfites in real samples. The experimental results are shown in Table 2. As OPA is a well-known reagent for amino acids, glycine was investigated as a model compound at a maximum mass ratio of 100:1. The incorporation of the gas-diffusion step in the method, offered sufficient selectivity against such compounds. On the other hand, cyanide ions react with OPA [46] and are volatile under acidic conditions forming HCN. However, the experiments showed that cyanides are adequately tolerated at a 10:1 ratio. Finally, ethanol was found to be tolerable at satisfactory volume fraction of 20% that is above the usual percentage in wine samples. It should be noted that the acceptance criterion for non-interference was set at percent recoveries in the range of 95–105% compared to a sulfite standard solution at the same mass concentration.

3.4.5. Accuracy

The accuracy of the developed method was validated by recovery experiments after spiking wine and red wine samples (diluted

Table 3
Accuracy of the proposed assay.

Wine sample ^{a,b}	Sulfite added (mg L ⁻¹)	Sulfite found (mg L ⁻¹)	Recovery, <i>R</i> (%)
White A	5.0	5.3	106
	10.0	9.9	99
	15.0	15.3	102
White B	5.0	5.0	100
	10.0	10.2	102
	15.0	15.5	103
Red A	5.0	4.8	96
	10.0	10.1	101
	15.0	14.7	98
Red B	5.0	5.1	102
	10.0	9.7	97
	15.0	15.0	100

^a Mean of three results.

^b Spiked after 1:10 sample dilution.

Table 4
Determination of total sulfites in white and red wine samples.

Wine sample	Sulfite found by SI (mg L ⁻¹) ^a ± SD	Reference method ^b (mg L ⁻¹)
White A	114 ± 3	108
White B	132 ± 5	136
White C	101 ± 2	105
White D	112 ± 4	116
Red A	63 ± 2	60
Red B	91 ± 2	89
Red C	88 ± 3	92

^a Mean of three results.

^b Based on iodimetric titration [47].

1:10) with known amounts of sulfite standards, in the range of 5–15 mg L⁻¹. These experiments included in Table 3, verified the accuracy of the proposed assay since the calculated percent recoveries ranged between 96% and 106%.

3.5. Analysis of wine samples

The applicability of the developed SI method was evaluated by analyzing white and red wine samples for total sulfite. Samples were treated as described in Section 2.4 and analyzed using the sequence as shown in Table 1. The experimental results are included in Table 4. The total sulfite content ranged between 63 and 132 mg L⁻¹. The validity of the results was confirmed by comparison of the found values to those derived by the EU recommended iodine-based titrimetric approach [47]. Good agreement was observed in all cases, as the relative errors were in the range of −4.5% to +5.2%. As expected, higher total sulfite values were found in white wines, which is in accordance with the literature [1,2].

4. Conclusions

The present study reports a new automated assay for the determination of total sulfite in white and red wines by incorporation of a gas-diffusion step in a hybrid SI-FI manifold and spectrophotometric detection. The proposed method offers adequate sensitivity (*c*_L = 0.3 mg L⁻¹) and linear determination range (up to 40 mg L⁻¹), no complicated procedures prior to analysis, acceptable sampling rate of 10 h⁻¹ and readily available instrumentation and reagents. Thorough validation in terms of precision, accuracy and selectivity confirmed the applicability of the developed analytical assay. The percent recoveries from the analysis of real samples were in the range of 96–106%.

References

- [1] L. Pizzoferrato, G. Lullo, E. Quattucci, *Food Chem.* 43 (1998) 275.
- [2] C.M.N. Azevedo, K. Araki, H.E. Toma, L. Agnes, *Anal. Chim. Acta* 387 (1999) 175.
- [3] A.F. Gunnison, D.W. Jacobsen, *CRC Crit. Rev. Toxicol.* 17 (1987) 185.
- [4] H. Valley, P.J. Thompson, *Thorax* 56 (2001) 763.
- [5] U.T. Yilmaz, G. Somer, *Anal. Chim. Acta* 603 (2007) 30.
- [6] S. McLeod, D.E. Davey, *Anal. Chim. Acta* 600 (2007) 72.
- [7] M.H. Pournaghi-Azar, R.E. Sabzi, *Electroanalysis* 16 (2004) 860.
- [8] T. Garcia, E. Casero, E. Lorenzo, F. Pariente, *Sens. Actuator B* 106 (2005) 803.
- [9] D.R. Shankaran, K.-I. Iimura, T. Kato, *Electroanalysis* 16 (2004) 556.
- [10] R. Carballo, V.C. Dall'Orto, A. Lo Balbo, I. Rezzano, *Sens. Actuator B* 88 (2003) 155.
- [11] M. Zhao, D.B. Hibbert, J.J. Gooding, *Anal. Chim. Acta* 556 (2006) 195.
- [12] A.K. Abass, J.P. Hart, D. Cowell, *Sens. Actuator B* 62 (2000) 148.
- [13] M.K. Sezgin, E. Dinckaya, *Talanta* 65 (2005) 998.
- [14] G. Jankovskiene, Z. Daunoravicius, A. Padarauskas, *J. Chromatogr. A* 934 (2001) 67.
- [15] M. Masar, M. Dankova, E. Olvecka, A. Stachurova, D. Kaniansky, B. Stanislawski, *J. Chromatogr. A* 1084 (2005) 101.
- [16] M. Masar, M. Dankova, E. Olvecka, A. Stachurova, D. Kaniansky, B. Stanislawski, *J. Chromatogr. A* 1026 (2004) 31.
- [17] X.-F. Yang, X.-Q. Guo, Y.-B. Zhao, *Anal. Chim. Acta* 456 (2002) 121.
- [18] Z. Xin-qi, L. Dong-hui, Z. Hong, X. Jin-gou, *Anal. Chim. Acta* 448 (2001) 71.
- [19] R.L. Bonifacio, N. Coichev, *Anal. Chim. Acta* 517 (2004) 125.
- [20] J. Cmelik, J. Machat, E. Niedobova, V. Otruba, V. Kanicky, *Anal. Bioanal. Chem.* 383 (2005) 483.
- [21] S.K. Verma, M.K. Deb, *J. Agric. Food Chem.* 55 (2007) 8319.
- [22] B. Palenzuela, B.M. Simonet, A. Rios, M. Valcarcel, *Anal. Chim. Acta* 535 (2005) 65.
- [23] R.C. Rodriguez-Diaz, M.P. Aguilar-Caballeros, A. Gomez-Hens, *J. Agric. Food Chem.* 52 (2004) 7777.
- [24] S.S.M. Hassan, M.S.A. Hamza, A.H.K. Mohamed, *Anal. Chim. Acta* 570 (2006) 232.
- [25] M.M.S. Abdul Galil, M.S. Yogendra Kumar, M.A. Sathish, G. Nagendrappa, *J. Anal. Chem.* 63 (2008) 239.
- [26] K.R.B. Silva, I.M. Raimundo, I.F. Gimenez, O.L. Alves, *J. Agric. Food Chem.* 54 (2006) 8697.
- [27] S. de Marcos, N. Alcubierre, J. Galban, J.R. Castillo, *Anal. Chim. Acta* 502 (2004) 7.
- [28] T.J. Cardwell, M.J. Christophersen, *Anal. Chim. Acta* 416 (2000) 105.
- [29] D. Corbo, M. Bertotti, *Anal. Bioanal. Chem.* 374 (2002) 416.
- [30] D. He, Z. Zhang, Y. Huang, *Anal. Lett.* 38 (2005) 563.
- [31] H. Mana, U. Spohn, *Anal. Chem.* 73 (2001) 3187.
- [32] S. Faldt, B. Karlberg, W. Frenzel, *Fresenius J. Anal. Chem.* 371 (2001) 425.
- [33] J. Carinhanha, C. Santos, M. Korn, *Microchim. Acta* 153 (2006) 87.
- [34] D. Melo, E.A.G. Zagatto, I.L. Mattos, N. Maniasso, *J. Braz. Chem. Soc.* 14 (2003) 375.
- [35] M.A. Segundo, A.O.S.S. Rangel, A. Cladera, V. Cerda, *Analyst* 125 (2000) 1501.
- [36] G.T. Atanassov, R.C. Lima, R.B.R. Mesquita, A.O.S.S. Rangel, I.V. Toth, *Analyst* 128 (2000) 77.
- [37] J. Ruzicka, G.D. Marshall, *Anal. Chim. Acta* 237 (1990) 329.
- [38] M.A. Segundo, A.O.S.S. Rangel, *Anal. Chim. Acta* 427 (2001) 279.
- [39] C. Chinwongamorn, K. Pinwattana, N. Praphairaksit, T. Imato, O. Chailapakul, *Sensors* 8 (2008) 1846.
- [40] M.S. Abdel-Latif, *Anal. Lett.* 27 (1994) 2601.
- [41] R. Walker, *Food Addit. Contam.* 2 (1985) 5.
- [42] B.L. Wedzicha, *Chem. Br.* 27 (1991) 1030.
- [43] J.B. Adams, *Food Chem.* 59 (1997) 401.
- [44] J.M. Green, *Anal. Chem.* 68 (1996) 305A.
- [45] J. Mocak, A.M. Bond, S. Mitchell, G. Scollary, *Pure Appl. Chem.* 69 (1997) 297.
- [46] Y. Nomura, K. Nagakubo, H.S. Ji, A. Watanabe, T. Akimoto, S. McNiven, K. Hayashi, Y. Arikawa, I. Karube, *Environ. Sci. Technol.* 34 (2000) 2618.
- [47] E. Mataix, M.D. Luque de Castro, *Analyst* 123 (1998) 1547.



A LC–MS method allowing the analysis of HMX and RDX present at the picogram level in natural aqueous samples without a concentration step

Olivier Vigneau, Xavier Machuron-Mandard*

Commissariat à l'Energie Atomique, Centre DAM Ile-de-France, Bruyères-le-Châtel, 91297 Arpajon Cedex, France

ARTICLE INFO

Article history:

Received 13 June 2008

Received in revised form

19 September 2008

Accepted 29 September 2008

Available online 1 November 2008

Keywords:

LC/MS

ESI

Explosive

HMX

RDX

ABSTRACT

The introduction of chloroform into the nebulising gas of a LC/MS electrospray interface (ESI), in a perfectly controlled way, leads to the formation of intense adducts $[M+Cl]^-$ when a mobile phase containing HMX (1,3,5,7-tetranitro-1,3,5,7-tetrazacyclooctane or octogen) and RDX (1,3,5-trinitro-1,3,5-triazacyclohexane or hexogen) is eluted. This LC/MS method allows the direct analysis of aqueous samples containing HMX and RDX at the picogram level without a concentration step. The method is used to determine HMX and RDX concentrations in ground water samples from a military site.

© 2008 Elsevier B.V. All rights reserved.

1. Introduction

In the group of organic explosives, HMX and RDX are, among the military explosives, the most widely used (Fig. 1). Because of their toxicity (RDX is a possible human carcinogen [1]), the monitoring of the explosives released into the environment is an important topic. Those compounds can be detected in soils or in natural waters [2]. So, the use of suitable and efficient analytical methods devoted to trace analysis is therefore required.

The thermal lability of HMX and RDX (named as nitramines) preferably leads to the use of liquid chromatography (LC) instead of gas chromatography (GC) [3]. Usually, as described in the US EPA Method 8330, the analysis of aqueous samples containing explosives is carried out by LC/UV after a concentration step [4]. A sample volume equal to 1 L is necessary. This method is tedious, time-consuming and UV detection leads to a poor sensitivity ($1\text{--}10\text{ }\mu\text{g L}^{-1}$).

The 2004 edition of the drinking water standards and health advisories of the US Environmental Protection Agency (US EPA) recommends a maximum of $400\text{ }\mu\text{g L}^{-1}$ for HMX and a maximum of $2\text{ }\mu\text{g L}^{-1}$ for RDX in drinking water for a life-time exposure [1]. The estimated quantitation limits of the EPA Method 8330,

when no concentration step is achieved, are equal to $13\text{ }\mu\text{g L}^{-1}$ for HMX and $14\text{ }\mu\text{g L}^{-1}$ for RDX [5]. Owing to its poor sensitivity, this method is not fully fulfilled for direct analysis of aqueous samples containing traces of RDX. Thanks to its good sensitivity, mass spectrometry allows the detection of a specific ion at traces level. The development of atmospheric pressure ionisation (API) interface in mass spectrometry allows direct detection of traces of explosives by LC/MS, without a concentration step [6–8]. The complete separation of different explosives having very different physical properties (such as nitramines, nitric esters and nitroaromatics) in a same run cannot be easily realised on conventional reverse phase columns. LC separation with porous graphitic carbon (PGC) column followed by MS detection with negative adduct formation allows the analysis of nitramines, nitric esters and nitroaromatics in a single method [9,10]. Tachon et al. compare the analysis by LC/MS of explosives with an atmospheric pressure chemical ionisation (APCI) interface for forensic investigations [9]. The described LC/APCI-MS method claims good performances in terms of selectivity, sensitivity and robustness. However, the limits of detection for HMX and RDX are respectively equals to 3.6 ng and 2.2 ng. Holmgren et al. used the same method (LC separation with PGC column followed by APCI/MS) and obtained the quite similar limits of detection for HMX (0.7 ng) and RDX (3.2 ng) [10]. The main drawback of APCI interface is that it requires a high temperature (typically a minimum of $300\text{ }^{\circ}\text{C}$) to ensure the complete vaporisation of the mobile phase leading to partial loss of heat labile compounds. For example, the thermal decomposition values of HMX and RDX are

* Corresponding author. Tel.: +33 169265127.

E-mail addresses: olivier.vigneau@cea.fr (O. Vigneau), xavier.machuron-mandard@cea.fr (X. Machuron-Mandard).

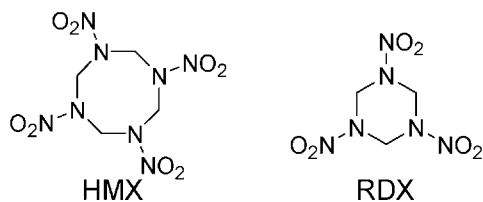


Fig. 1. Structural formulae of HMX and RDX.

respectively equals to 280 °C and 213 °C [11]. So, in APCI part of the RDX molecules decompose yielding NO_2^- species which leads to adduct formation with a second RDX molecule producing abundant $[\text{M}+\text{NO}_2]^-$ cluster ions [6]. This parameter could hamper the analysis of environmental samples containing ultratraces of such explosives.

In the case of nitramines analysis, ESI is the most suitable interface [8]. The drawback of the use of ESI instead of APCI is that nitroaromatics are more difficult to ionise. In ESI, most of the explosives are detected as adduct-species with the exception of nitroaromatics (such as trinitrotoluene, dinitrobenzene, trinitrobenzene) [12,13]. Indeed, the use of additives can enhance the analyte ionisation efficiency leading to higher mass spectrometer sensitivity. In ESI, HMX and RDX are difficult to ionise due to a lack of acidic hydrogen and because their mass spectra are composed of multiple ions [6,14]. To enhance the sensitivity and to allow a better identification of the explosives, some papers report the use of additives such as ammonium salts or organic acids [6,7,12,14,15]. In the presence of those salts, the mass spectra of HMX and RDX are composed of intensive ions of $[\text{M}+\text{X}]^-$ ($\text{X} = \text{Cl}, \text{CH}_3\text{COO}, \text{NO}_3$ or HCOO).

Mathis and McCord present a comprehensive method to allow the screening of a panel of high explosives (HMX, RDX, EGDN, NG and TNT) [12]. Different ammonium salts (nitrate, formate, acetate and chloride) are added to the mobile phase in order to perform multiple negative adduct formation of the different energetic compounds analysed. By adding those salts directly to the chromatographic mobile phase additional specificity and selectivity is obtained. Indeed, information relating to the relative extent of adduct formation (based on intensity ratios) in addition to adduct stability is used to provide a multiplexed detection scheme. No information on the limits of detection obtained is given.

A sensitive method for HMX quantification in environmental samples using LC/ESI-MS is reported by Pan et al. [14]. A detection limit of 0.78 pg for HMX is obtained (lowest detection limit obtained to date) by adding a small amount of acetic acid to the mobile phase and operating at relatively low heated capillary temperature.

The introduction of the additives could be done in various points of the LC/MS apparatus. Indeed, it could be introduced in the aqueous mobile phase, by a post-column system or into the gas feed of the API interface of the mass spectrometer (in the case of a volatile additive).

In this paper, a LC/MS method allowing the direct analysis of natural water samples contaminated by HMX or RDX at the pictogram level without preparation of the sample is described. The analysis of HMX and RDX is conducted because these compounds respond poorly when analysed by GC/MS. Nitroaromatics can be easily analysed by GC/MS so this work only focuses on the analysis of nitramines.

The influence of the additive introduction either in the mobile phase of the LC part or into the nebulising gas of the electrospray (ESI) interface is compared. The post-column process is not considered here because the introduction of the additive by a post-column apparatus dilutes the analyte and spreads the chromatographic peaks [16]. A system is described, allowing the introduction of a

liquid additive into the nebulising gas of the electrospray ionisation (ESI) interface of a mass spectrometer, in a perfectly controlled way, leading to limits of detection for HMX and RDX at pictogram level.

2. Experimental

2.1. Chemicals

RDX and HMX standards are provided by Supelco (Saint Quentin Fallavier, France) as 1 mg mL⁻¹ solutions in acetonitrile. An intermediate solution containing 1 mg L⁻¹ of each compound in acetonitrile is prepared. This solution is used to prepare calibrated aqueous solutions at different concentrations. Methanol and acetonitrile are both HPLC grade and are provided by VWR (Fontenay-sous-Bois, France). HPLC grade chloroform is purchased from Sigma-Aldrich (Saint Quentin Fallavier, France). Ammonium chloride salt is from Merck (Fontenay-sous-Bois, France). Ultra-pure water used for the preparation of mobile phases and standard solutions is obtained from a Millipore MilliQ-10 system. Standard solutions and samples are filtered with syringe filters before analysis (PALL Acrodisc CR 25 mm Syringe filter with 0.45 µm PTFE membrane) provided by VWR (Fontenay-sous-Bois, France).

2.2. Standard LC/MS apparatus

A VARIAN 1200L triple quadrupole mass spectrometer, equipped with an ESI interface, coupled with a VARIAN liquid chromatograph is used. In the negative mode, synthetic air is employed as nebulising gas and nitrogen is used as drying gas. The liquid chromatographic system is composed of two VARIAN 210 pumps, a vacuum membrane degasser and a VARIAN 410 MIDAS autosampler. This configuration is used when the additive is added to the mobile phase. In this case, the chromatographic separation is achieved with a VARIAN column (Pursuit C18 reversed-phase type, 25 cm × 2 mm × 5 µm) using an isocratic mobile phase made of water and methanol (50/50, v/v) at a flow-rate of 0.2 mL min⁻¹. Ammonium chloride is employed as an additive and dissolved in the aqueous mobile phase. It is introduced in the aqueous phase at low concentration ($C = 1 \times 10^{-3}$ mol L⁻¹ in water) leading to an ammonium chloride concentration in the mobile phase equal to 0.5×10^{-3} mol L⁻¹. The sample injection volume is 100 µL.

2.3. Modified LC/MS apparatus

Our patented system [17], allowing the introduction of the additive into the nebulising gas of the ESI interface, needs the modification of the gas feed. A syringe-pump, a syringe and a stainless steel tee are connected to the nebulising gas supply of the ESI interface (Fig. 2). The liquid ionisable additive is introduced in the syringe and its flow rate is controlled by the syringe pump. A timer triggered by the autosampler controls the time and the length of the additive's introduction. This introduction occurs during a short time window centred around the retention time of the analyte. The additive is sprayed by the nebulising gas and is carried to the ESI needle. At the tip of the needle, the analytes – carried by the LC eluent – and the additive are ionised leading to the formation of the adduct ions (e.g. $[\text{M}+\text{X}]^-$ in a negative mode). Then, those ions are transferred to the analyser of the mass spectrometer. Note that in principle, any mass spectrometer equipped with an ESI interface can be used. The LC eluent is directed to the waste for the first 6 min and after 17 min of analysis via a six-port valve. The fraction of eluent between 6 min and 17 min is introduced in the ESI needle of the mass spectrometer. In this case, the chromatographic separation is achieved with a VARIAN column (Pursuit C18 reversed-phase type,

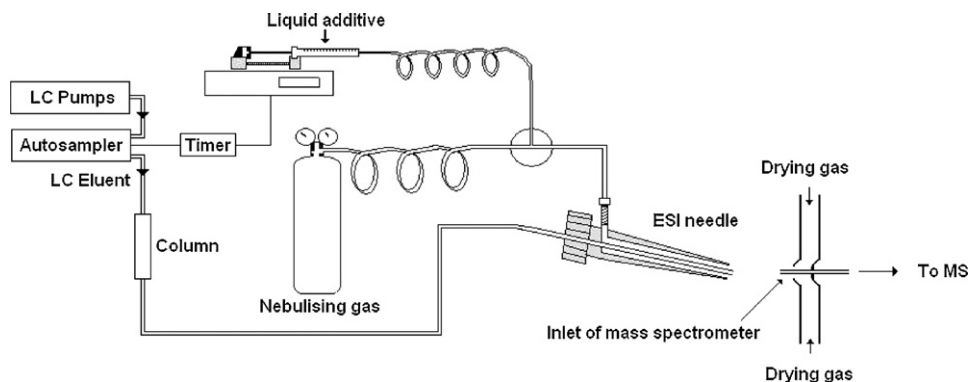


Fig. 2. Introduction of a liquid ionisable additive in the nebulising gas of the ESI interface.

25 cm \times 2 mm \times 5 μ m) using an isocratic mobile phase of water and methanol (70/30, v/v) at a flow-rate of 0.2 mL min⁻¹. The sample injection volume is 100 μ L.

2.4. Sample preparation

All water samples are kept at 4 °C in the dark during shipment and storage. Prior to their analysis, the samples are filtered through syringe filters. Each extract volume is placed into an autosampler vial (2 mL) for LC/MS analysis.

2.5. Identification and quantification of HMX and RDX

HMX and RDX are identified, in selected ion monitoring (SIM) mode, by their retention time, the presence in their mass spectra of the ions [HMX+³⁵Cl]⁻ (m/z = 331 Th), [HMX+³⁷Cl]⁻ (m/z = 333 Th), [RDX+³⁵Cl]⁻ (m/z = 257 Th) and [RDX+³⁷Cl]⁻ (m/z = 259 Th) and the abundance ratio of the ions [M+³⁵Cl]⁻ and [M+³⁷Cl]⁻ for which a ratio of 3 to 1 is expected.

The quantification of HMX and RDX is achieved, also in SIM mode, by measuring the area of the chromatographic peak corresponding to the ions [HMX+³⁵Cl]⁻ (m/z = 331 Th) and [RDX+³⁵Cl]⁻ (m/z = 257 Th).

3. Results and discussion

3.1. Introduction of an additive in the mobile phase

In our first experiments, ammonium chloride is used as an additive. The continuous introduction of this mobile phase in the electrospray interface has deleterious effects [18–20]. The use of salt in the LC eluent clogs up the mass spectrometer, since the evaporation of solvent leads to a deposit of the salt involving a decrease in sensitivity. After 24 h of constant introduction of the LC eluent in the electrospray interface, the sensitivity of the mass spectrometer decreases dramatically. Indeed, as can be seen in Fig. 3, the signal response of ions corresponding to [HMX+Cl]⁻ and [RDX+Cl]⁻ is reduced by practically 50% after 24 h of repeated analyses of a water sample containing traces of HMX and RDX (2 μ g L⁻¹ of each). So, the liquid ionisable additives (such as chloroform or methylene chloride) with a low boiling point are more suitable because of their volatility. Those additives can be introduced in the LC eluent [16,21] but their concentration could not be modified easily and some additives are not fully miscible with the aqueous mobile phase. So, the introduction of the additive is realised by another way.

3.2. Introduction of an additive into the nebulising gas of the ESI interface

As mentioned above, to introduce an additive into the nebulising gas of the electrospray interface, it is better to use an ionisable volatile organic compound. In the case of the analysis of ethylene glycol dinitrate (EGDN), Lawrence [22] used diffusion tubes to dope the gas stream of an ion mobility spectrometer with dichloromethane and to produce chloride adducts. However, this process does not permit careful control of the dopant concentration. So, in our experiments the introduction of the vapors of ionisable additives (such as chloroform, methylene chloride, nitromethane...), in a perfectly controlled way, is realised into the gas feed of an electrospray interface of a mass spectrometer to improve the analyte ionisation efficiency. This process needs a slight modification of the ESI interface (Fig. 2).

In the presence of chloride ions and in negative mode, HMX and RDX are known to give the corresponding adducts [HMX+Cl]⁻ and [RDX+Cl]⁻ [15,23]. In our system, the chloride ions are produced by ionisation of chloroform (CHCl₃) [24] or methylene chloride (CH₂Cl₂) [25] at the ESI needle. This is confirmed by the presence of two abundant ions at m/z values equal to 35 Th and 37 Th with a 3:1 ratio in mass abundance.

Fig. 4 demonstrates the need to control the flow rate of additive injected in the nebulising gas. The chromatographic peak areas

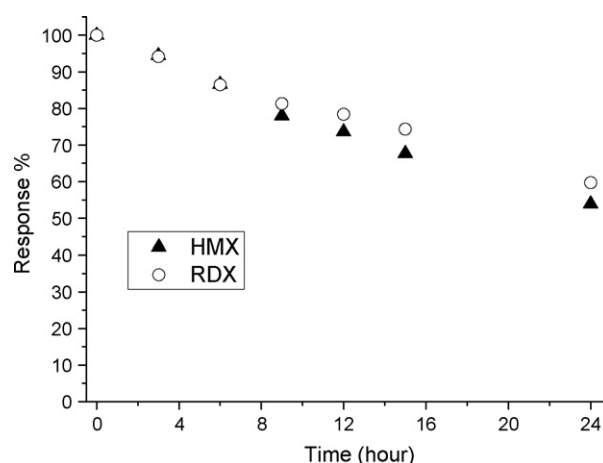


Fig. 3. Decrease of the signal response in LC/ESI-MS after 24 h of repeated analyses of an aqueous mixture of HMX and RDX (2 μ g L⁻¹ of each), with a chromatographic mobile phase containing ammonium chloride (0.5 \times 10⁻³ mol L⁻¹). The values are calculated as the ratio of signal values at different time to the signal value obtained at the beginning of the study (t = 0 h).

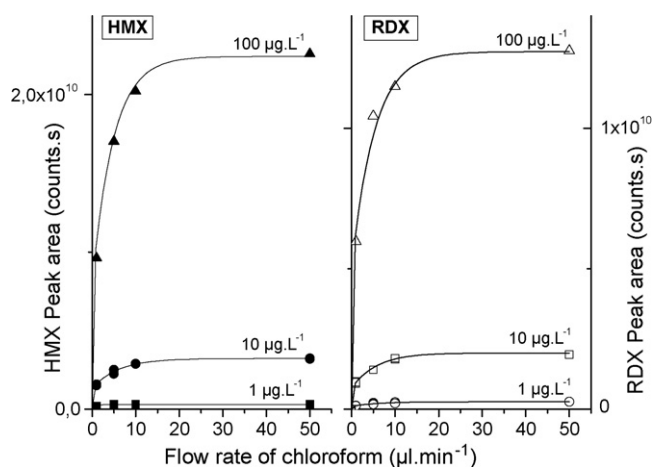


Fig. 4. Influence of the flow rate of chloroform introduced into the gas feed of the ESI interface on the chromatographic peak areas at different concentrations of HMX and RDX (1–100 $\mu\text{g L}^{-1}$ of each).

of analytes at different concentrations (1–100 $\mu\text{g L}^{-1}$) are studied when increasing flow rates of chloroform introduced in the nebulising gas. When the chloride concentration increases (by increasing the flow rate of chloroform), the fractions of $[\text{HMX}+\text{Cl}]^-$ and $[\text{RDX}+\text{Cl}]^-$ raise, which results in an increase of peak areas of each analyte. Moreover, as can be seen, a minimum of flow rate is necessary to ensure a maximum response signal for HMX and RDX. The flow rate must be adapted to a range of concentration of the analytes to obtain a stable signal even if a slight variation of the flow rate of additive occurs. The minimum flow rate of chloroform for the concentration range 0.02 $\mu\text{g L}^{-1}$ to 5 $\mu\text{g L}^{-1}$ in nitramines (HMX and RDX) is equal to 2 $\mu\text{L min}^{-1}$. For the 5–20 $\mu\text{g L}^{-1}$ concentration range of nitramines, a minimum of 10 $\mu\text{L min}^{-1}$ is required. The minimum flow rate of chloroform required for the concentration range of HMX and RDX between 20 and 100 $\mu\text{g L}^{-1}$ is 20 $\mu\text{L min}^{-1}$.

3.3. Detection limit (LOD) and quantification limit (LOQ) for HMX and RDX

In all the following experiments, chloroform is used as additive and is introduced into the gas feed of the ESI thanks to our system. Calibration standards at six concentrations (0.1–5 $\mu\text{g L}^{-1}$) are prepared by diluting the intermediate standard solution in water. The limits of detection and the limits of quantification for HMX and

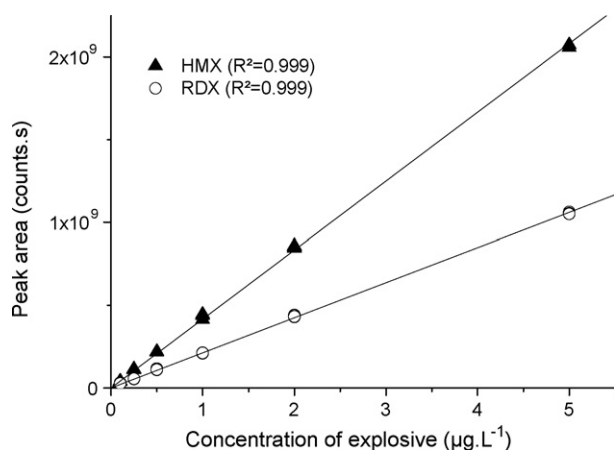


Fig. 5. Calibration curves for HMX and RDX when chloroform is injected in the nebulising gas (flow rate = 2 $\mu\text{L min}^{-1}$).

Table 1

LOD and LOQ obtained for HMX and RDX compared to EPA recommendations.

Product	LOD ($\mu\text{g L}^{-1}$)	LOQ ($\mu\text{g L}^{-1}$)	US EPA recommendations ($\mu\text{g L}^{-1}$)
HMX	0.02	0.05	400
RDX	0.02	0.05	2

RDX (4 replicates for each calibration level) are determined. Those solutions are analysed with an injection of chloroform in the nebulising gas, between the 6th and 17th minute of the run, at a flow rate of 2 $\mu\text{L min}^{-1}$. As shown in Fig. 5, a good linearity is achieved ($R^2 = 0.999$) for both compounds.

The limit of detection and the limit of quantification are obtained from a statistical analysis of the signal response. For a distribution of values presumed to be Gaussian, for a risk value of 5%, the LOD value is equal to 3.29 s_B . For the purpose of simplification, the conventional value is set to 3 s_B . Usually, the LOQ value is set to 10 s_B [26]. In LC, the blank standard deviation is not directly available [26] therefore the weighted linear regression method is used to estimate the LOD and the LOQ for HMX and RDX. The values obtained are summarised in Table 1. A good correlation is observed with experimental results obtained with standard solutions containing the analytes at the LOD and LOQ concentration levels. The two chromatograms shown on Fig. 6 illustrate the response in LC/MS when standard solutions containing HMX and RDX, both at 0.02 $\mu\text{g L}^{-1}$ and 0.05 $\mu\text{g L}^{-1}$ are injected. With a sample loop volume of 100 μL , the LOD obtained for HMX and RDX equals an injected mass of 2 pg.

The system allowing additive introduction into the gas feed of an ESI interface could have a great interest to enhance the sensitivity in liquid chromatography/atmospheric pressure ionisation by anion attachment mechanism. Our process, could be used instead of salts or post-column derivation to improve the detection and the identification of various compounds [27,28], such as monosaccharides [29], oligosaccharides [30], chlorinated paraffins [16], lipids [31] or penicillins [32] with an ESI interface.

3.4. Application of the method for natural ground water samples

As mentioned before, because of their potential to cause adverse health effects on people exposed to them, the monitoring of explosives released into the environment is an important topic. At this time, there is a lack of European regulations and guidelines regarding explosives. Health advisories have been established for HMX and RDX by US EPA and those are used as reference.

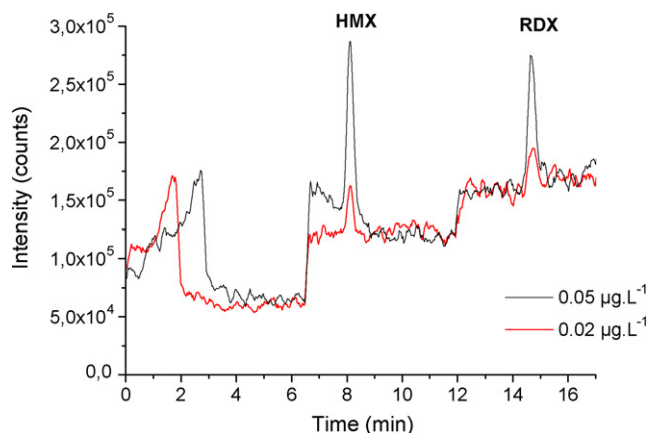


Fig. 6. Chromatograms obtained after injection of 100 μL of solutions containing 0.02 $\mu\text{g L}^{-1}$ and 0.05 $\mu\text{g L}^{-1}$ of HMX and RDX.

Table 2

HMX and RDX concentrations measured in three natural ground water samples of a military site (six replicates for each sample). The data are subjected to statistical analysis by the Student–Fisher test, with a 95% confidence level and Student–Fisher constant of 2.57. Results are presented as mean \pm error.

Sample	[HMX] ($\mu\text{g L}^{-1}$)	[RDX] ($\mu\text{g L}^{-1}$)
Ground water sample 1	1.3 \pm 0.1	0.42 \pm 0.02
Ground water sample 2	0.41 \pm 0.02	<0.02 ^a
Ground water sample 3	0.24 \pm 0.01	0.02 < x < 0.05 ^b

^a RDX is not detected in the sample, if RDX is present its concentration is lower than LOD.

^b RDX concentration is between LOD and LOQ.

The analysis of three natural groundwater samples, obtained from a military site is realised. All samples are analysed six times. The quantitative data (six replicates by sample) are subjected to statistical analysis by the Student–Fisher test, with a level of significance of 0.05 (i.e. at the 95% confidence level with a Student–Fisher constant of 2.57). Results, reported in Table 2, are presented as mean \pm error.

Ultra-traces of HMX and RDX in those ground water samples have been measured. The actual military site is located on a Second World War battlefield. HMX and RDX are known to be present in leachate from various types of soils and are likely to migrate into groundwater [33,34] despite a low water solubility [35] but there is also evidence of their persistence in soil for several years [36]. Indeed, a study carried out at the Los Alamos National Laboratory, over a period of 20 years, estimates the half-life of HMX and RDX at 39 years and 36 years, respectively [36]. So, the absence of significant degradation, a leaching and a transport from soil to groundwater may explain the presence of traces of HMX and RDX in the samples.

4. Conclusion

A sensitive method, allowing the direct analysis by LC/MS of groundwater samples containing HMX and RDX at concentrations as low as 0.02 $\mu\text{g L}^{-1}$, is described. The greatest advantage of our sensitive method is that any concentration step is necessary to be fulfilled with the US EPA recommendations. It can also be useful in forensic analysis because after a bomb attack, the post-blast residues left on the bombing site are present only at trace level.

The anion attachment mechanism is important in the electrospray process. Negative ion adduct formation could be used to improve the sensitivity of detection for some analytes which do not have sites with permanent charge or ionisable groups. Electron deficient atoms, which bind to electronegative atoms such as the hydrogen present on hydroxyl groups, could offer binding sites for anions. Our patented system could be of great interest to enhance the identification and the sensitivity to various compounds ionised with an ESI interface. It also could be used in negative or in positive

mode, according to the additive used. The system is also compatible with an atmospheric pressure chemical ionisation (APCI) interface.

References

- [1] EPA, 2004 Edition of the Drinking Water Standards and Health Advisories, United States Environmental Protection Agency, EPA 822-R-04-005, 2004.
- [2] A. Halasz, C. Groom, E. Zhou, L. Paquet, C. Beaulieu, S. Deschamps, A. Corriveau, S. Thiboutot, G. Ampleman, C. Dubois, J. Hawari, J. Chromatogr. A 963 (2002) 411.
- [3] J. Yinon, J.E. McClellan, R.A. Yost, Rapid Commun. Mass Spectrom. 11 (1997) 1961.
- [4] EPA, Nitroaromatics and Nitramines by High Performance Liquid Chromatography (HPLC), United States Environmental Protection Agency, Office of Solid Waste, Method 8330 SW-846 Update III, 1997.
- [5] EPA, Method 8330: Determination of Concentration of Nitroaromatics and Nitramines by High-Performance Liquid Chromatography (HPLC), US Army Corps of Engineers, Cold Regions Research & Engineering Laboratory.
- [6] A. Gapeev, M. Sigman, J. Yinon, Rapid Commun. Mass Spectrom. 17 (2003) 943.
- [7] C.S. Evans, R. Sleeman, J. Luke, B.J. Keely, Rapid Commun. Mass Spectrom. 16 (2002) 1883.
- [8] D.A. Cassada, S.J. Monson, D.D. Snow, R.F. Spalding, J. Chromatogr. A 844 (1999) 87.
- [9] R. Tachon, V. Pichon, M. Barbe-Le Borgne, J.-J. Minet, J. Chromatogr. A 1154 (2007) 174.
- [10] E. Holmgren, H. Carlsson, P. Goede, C. Crescenzi, J. Chromatogr. A 1099 (2005) 127.
- [11] J. Akhavan, Chemistry of Explosives, 2nd ed., Royal Society of Chemistry, Dorchester, 2004.
- [12] J.A. Mathis, B.R. McCord, Rapid Commun. Mass Spectrom. 19 (2005) 99.
- [13] A. Schreiber, J. Efer, W. Engewald, J. Chromatogr. A 869 (2000) 411.
- [14] X. Pan, K. Tian, L.E. Jones, G.P. Cobb, Talanta 70 (2006) 455.
- [15] J. Yinon, S. Zitrin, Modern Methods and Applications in Analysis of Explosives, 1st ed., John Wiley & Sons, Eastbourne, 1996.
- [16] Z. Zencak, M. Oehme, Rapid Commun. Mass Spectrom. 18 (2004) 2235.
- [17] X. Machuron-Mandard, O. Vigneau, French Patent 0650209, 2006.
- [18] T.L. Constantopoulos, G.S. Jackson, C.G. Enke, J. Am. Soc. Mass Spectrom. 10 (1999) 625.
- [19] S. Kromidas, More Practical Problem Solving in HPLC, 1st ed., Wiley-VCH, 2005.
- [20] R. King, R. Bonfiglio, C. Fernandez-Metzler, C. Miller-Stein, T. Olah, J. Am. Soc. Mass Spectrom. 11 (2000) 942.
- [21] A. Colorado, Varian Inc. LC/MS Application Note 18, 2004.
- [22] A.H. Lawrence, P. Neudorfl, Anal. Chem. 60 (1988) 104.
- [23] I. Cotte-Rodriguez, Z. Takats, N. Talaty, H. Chen, R.G. Cooks, Anal. Chem. 77 (2005) 6755.
- [24] J.M. Warman, M.C. Sauer Jr., Int. J. Radiat. Phys. Chem. 3 (1971) 237.
- [25] S. Matejcek, G. Senn, A. Kiendler, A. Stamatovic, T.D. Mark, J. Chem. Phys. 107 (1997) 8955.
- [26] J. Vial, A. Jardy, Anal. Chem. 71 (1999) 2672.
- [27] S. Gao, Z.-P. Zhang, H.T. Karnes, J. Chromatogr. B 825 (2005) 98.
- [28] X. Zhao, J. Yinon, J. Chromatogr. A 977 (2002) 59.
- [29] H.R. Liang, T. Takagaki, R.L. Foltz, P. Bennett, J. Chromatogr. B 824 (2005) 36.
- [30] J. Zhu, R.B. Cole, J. Am. Soc. Mass Spectrom. 12 (2001) 1193.
- [31] X. Han, H. Cheng, J. Lipid Res. 46 (2005) 163.
- [32] S. Horimoto, T. Mayumi, K. Aoe, N. Nishimura, T. Sato, J. Pharm. Biomed. Anal. 30 (2002) 1093.
- [33] H. Abadin, J.J. Liccione, Toxicological Profile for HMX, Agency for Toxic Substances and Disease Registry, 1997.
- [34] C. Smith-Simon, S. Goldhaber, Toxicological Profile for RDX, Agency for Toxic Substances and Disease Registry, 1995.
- [35] J. Yinon, Forensic and Environmental Detection of Explosives, 1st ed., John Wiley & Sons, Chichester, 1999.
- [36] F.W. Dubois, J.F. Baytos, Weathering of Explosives for Twenty Years, Los Alamos National Laboratory, LA 11931, 1991.



Characterization of 2-phenylbenzo[g]quinoxaline derivatives as viscosity-sensitive fluorescent probes

Ke Wang, Wen Shi, Jia Jia, Suming Chen, Huimin Ma*

Beijing National Laboratory for Molecular Sciences, Institute of Chemistry, Chinese Academy of Sciences, Beijing 100190, China

ARTICLE INFO

Article history:

Received 18 July 2008

Received in revised form 7 October 2008

Accepted 11 October 2008

Available online 21 October 2008

Keywords:

Viscosity-sensitive fluorescent probe

Rotatable single bond

2-Phenylbenzo[g]quinoxaline derivatives

Electronic effect of substituted groups

ABSTRACT

To develop viscosity-sensitive fluorescent probes, five different substituted 2-phenylbenzo[g]quinoxaline derivatives (**3a–e**) were designed and synthesized by using benzo[g]quinoxaline as a fluorophore and phenyl ring bearing a rotatable single bond as a viscosity-sensitive unit. The fluorescence properties of these compounds were investigated in the media of the ethylene glycol–glycerol mixture with varied viscosity. It is found that 2-(4-hydroxyphenyl)benzo[g]quinoxaline (**3d**) and 2-(4-dimethylaminophenyl)benzo[g]quinoxaline (**3e**) carrying stronger electron-donating groups in the phenyl ring show more sensitive fluorescence response to viscosity, revealing their potential use in viscosity detection and the key role of the substituted groups. The effects of solvent polarity and pH on the fluorescent properties of **3d** and **3e** were also discussed. The present study might be useful in developing viscosity-sensitive fluorescent probes.

© 2008 Elsevier B.V. All rights reserved.

1. Introduction

Viscosity is an important physicochemical parameter and many physiological diseases are related to the alteration of viscosity in local environment. For example, hypercholesterolemia [1], atherosclerosis [2], cell malignancy [3] and diabetes [4,5] have been attributed to the change in cell membrane viscosity. On a more macroscopic scale, the viscosity of blood plasma also shows correlation with some disease states, such as infections and infarction [6], hypertension [7] and diabetes [8]. Thus the measurement of viscosity in biological systems is of great importance for the understanding of various diseases. The traditional method for determining viscosity is by virtue of a mechanical viscometer, which however suffers from some drawbacks, such as time-consuming measurement process and inconvenience in monitoring viscosity on a microscopic scale.

Because of its convenience and high sensitivity as well as its high spatial and temporal resolution capability, fluorescence spectroscopy has been widely used in various fields [9–11]. Up to now, a number of viscosity-sensitive fluorescent probes, such as 3,3-dimethyl-2-phenyl-3H-indole [12], 2-(p-

dimethylaminostyryl)benzo-xazole [13], molecular rotors [14,15] and *N*-aryl-9-aminoacridinium derivatives [16], have been developed, and some of them have been utilized to monitor the assembly processes of tubulin [14] and the viscosity change in cell membrane [15]. However, most of the reported viscosity-sensitive fluorescent probes have a relatively short-wavelength emission, which may suffer from the interferences of background fluorescence from common biological matrixes. Obviously, the development of viscosity-sensitive fluorescent probes with long-wavelength emission is still a challenge. Moreover, systematic studies on the relationship between structures and analytical properties of viscosity-sensitive fluorescent probes would be significant.

In our opinion, the fluorescent probes that are sensitive to viscosity should contain two units. One is the fluorophore, which is used to produce fluorescence signal; the other is the viscosity-sensitive moiety capable of rotating. With the increase of viscosity, the internal rotation is hindered and the concerned nonradiative de-excitation is thus decreased, accompanying the enhancement of fluorescence intensity. Based on this principle, five different substituted 2-phenylbenzo[g]quinoxaline derivatives were designed and synthesized by using benzo[g]quinoxaline as a fluorophore and phenyl ring bearing a rotatable single bond as a viscosity-sensitive unit (**3a–e**, Fig. 1), and their fluorescence properties were investigated in the present work. Herein, we describe the results of such a study.

* Corresponding author. Tel.: +86 10 62554673; fax: +86 10 62559373.

E-mail address: mahm@iccas.ac.cn (H. Ma).

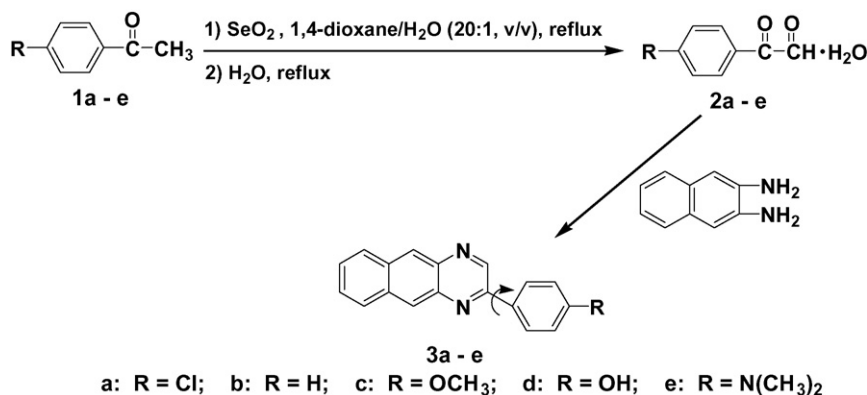


Fig. 1. Synthesis of the 2-phenylbenzo[g]quinoxaline derivatives.

2. Experimental

2.1. Apparatus and reagents

A Hitachi F-2500 spectrofluorimeter was used for fluorescence measurements. The absorption spectra were recorded in 1 cm cells with a Techcomp UV-8500 spectrophotometer (Shanghai, China). A model HI-98128 pH-meter (Hanna Instruments Inc., USA) was used for pH measurements. Electrospray ionization mass spectra (ESI-MS) were measured with LC-MS2010 (Shimadzu, Japan). Elemental analyses were carried out with a Flash EA 1112 instrument. ¹H NMR spectra were measured on a Bruker DMX-400 spectrometer at 400 MHz in CDCl₃ or *d*₆-DMSO with tetramethylsilane as the internal standard. The viscosity of the mixture of ethylene glycol and glycerol with different volume ratios was measured using Brookfield Dial Reading Viscometer (USA). A model HI-98128 pH-meter (Hanna Instruments Inc., USA) was used for pH measurements.

4-Dimethylaminoacetophenone and 4-hydroxyacetophenone (TCI, Japan), 4-chloroacetophenone (Merck), 4-methoxyacetophenone and acetophenone (Beijing, China), selenium dioxide (Shanghai, China) and 2,3-diaminonaphthalene (Acros) were used as received. The solvents and other chemicals employed were all of analytical grade.

2.2. Synthesis of different substituted 2-phenylbenzo[g]quinoxaline derivatives

As illustrated in Fig. 1, the 2-phenylbenzo[g]quinoxaline derivatives (**3a-e**) can be synthesized by the reaction of **2a-e** with 2,3-diaminonaphthalene. Different substituted phenylglyoxal hydrate (**2a-e**) was prepared via the oxidation of the corresponding acetophenone (**1a-e**) by selenium dioxide following the known method of the literature [17]. In brief, a mixture of 1,4-dioxane (10 mL), water (0.5 mL), selenium dioxide (1.11 g, 0.01 mol) and the corresponding acetophenone (**1a-e**) (0.01 mol) was refluxed for 3 h, and then filtered to remove selenium. The filtrate was concentrated by rotary evaporation. The oily residue was mixed with 20 mL of water, and then refluxed for 3 h with stirring. The resulting solution was clarified with charcoal, except for the preparation of **2e**. Upon cooling, the hydrate **2a-e** was crystallized from the above solution.

The general procedure for the synthesis of **3a-e** is as follows: the mixture of 2,3-diaminonaphthalene (0.3 mmol) and the corresponding phenylglyoxal hydrate (0.3 mmol) in 3 mL 1,4-dioxane was stirred at room temperature for 30 min, and then the reaction mixture was diluted with 30 mL of water. After stirring for an additional 5 min, the formed precipitate was filtered and purified by

silica-gel column chromatography with the different volume ratios of ethyl acetate and petroleum ether as eluent.

2-(4-Chlorophenyl)benzo[g]quinoxaline (3a): Yield: 87%. ¹H NMR (400 MHz, CDCl₃, 298 K) δ 7.59 (d, *J* = 8.3 Hz, 2H), 7.61–7.64 (m, 2H), 8.14–8.16 (m, 2H), 8.25 (d, *J* = 8.3 Hz, 2H), 8.77 (s, 1H), 8.79 (s, 1H), 9.38 (s, 1H). ESI-MS, *m/z* (relative intensity): 290.9 (100%) [M+H]⁺, 292.9 (30%) [M+2+H]⁺. Elemental analysis: calcd. for C₁₈H₁₁ClN₂: C 74.36, H 3.81, N 9.63%; found, C 74.42, H 3.84, N 9.62%.

2-Phenylbenzo[g]quinoxaline (3b): Yield: 81%. ¹H NMR (400 MHz, CDCl₃, 298 K) δ 7.57–7.62 (m, 5H), 8.13–8.15 (m, 2H), 8.29 (d, *J* = 7.3 Hz, 2H), 8.74 (s, 1H), 8.78 (s, 1H), 9.41 (s, 1H). ESI-MS, *m/z*: 257.2 [M+H]⁺. Elemental analysis: calcd. for C₁₈H₁₂N₂: C 84.35, H 4.72, N 10.93%; found, C 84.43, H 4.72, N 10.87%.

2-(4-Methoxyphenyl)benzo[g]quinoxaline (3c): Yield: 72%. ¹H NMR (400 MHz, CDCl₃, 298 K) δ 3.93 (s, 3H), 7.12 (d, *J* = 8.5 Hz, 2H), 7.57–7.61 (m, 2H), 8.11–8.13 (m, 2H), 8.27 (d, *J* = 8.5 Hz, 2H), 8.67 (s, 1H), 8.71 (s, 1H), 9.38 (s, 1H). ESI-MS, *m/z*: 287.2 [M+H]⁺. Elemental analysis: calcd. for C₁₉H₁₄N₂O: C 79.70, H 4.93, N 9.78%; found, C 79.61, H 5.03, N 9.74%.

2-(4-Hydroxyphenyl)benzo[g]quinoxaline (3d): Yield: 67%. ¹H NMR (400 MHz, *d*₆-DMSO, 298 K) δ 7.0 (d, *J* = 8.6 Hz, 2H), 7.63–7.65 (m, 2H), 8.22–8.25 (m, 2H), 8.31 (d, *J* = 8.6 Hz, 2H), 8.72 (s, 1H), 8.74 (s, 1H), 9.58 (s, 1H), 10.13 (s, 1H). Negative ESI-MS, *m/z*: 271.1 [M-H]⁻. Elemental analysis: calcd. for C₁₈H₁₂N₂O: C 79.39, H 4.44, N 10.29%; found, C 79.27, H 4.58, N 10.47%.

2-(4-Dimethylaminophenyl)benzo[g]quinoxaline (3e): Yield: 69%. ¹H NMR (400 MHz, CDCl₃, 298 K) δ 3.10 (s, 6H), 6.87 (d, *J* = 8.6 Hz, 2H), 7.51–7.57 (m, 2H), 8.08 (d, *J* = 7.4 Hz, 2H), 8.23 (d, *J* = 8.6 Hz, 2H), 8.61 (s, 1H), 8.63 (s, 1H), 9.36 (s, 1H). ESI-MS, *m/z*: 300.2 [M+H]⁺. Elemental analysis: calcd. for C₂₀H₁₇N₃: C 80.24, H 5.72, N 14.04%; found, C 80.28, H 5.81, N 14.06%.

2.3. Fluorescence measurements

The compound **3a-e** was dissolved in *N,N*-dimethylformamide (DMF) to prepare its stock solution of 1 mM.

To test the effect of viscosity, 50 μL of the stock solution of **3a-e** was mixed with 10 mL of the ethylene glycol–glycerol mixture in a test tube, and then the fluorescence of the resulting solution was measured at 20 °C.

The effect of solvent polarity was examined by measuring the absorbance and fluorescence of 50 μL of the stock solution of **3d** or **3e** in 10 mL of different solvents at 20 °C.

Because of poor water solubility of **3d** and **3e**, the effect of pH was studied by measuring the fluorescence of 50 μL of the stock solution of **3d** or **3e** in 10 mL of 0.1 M NaCl aqueous solution containing 10–20% (v/v) DMF with varied pH values; the different pH

was adjusted with diluted NaOH or HCl, and measured with a model HI-98128 pH-meter.

3. Results and discussion

3.1. Design and synthesis of **3a–e** as viscosity-sensitive fluorescent probe

As is known, viscosity-sensitive fluorescent probes are the molecules that undergo internal rotations resulting in viscosity-dependent changes in their emissive properties [18]. Obviously, in this kind of probe, not only a fluorophore but also a rotatable moiety should be engineered [19]. To design such molecules, here we take advantage of the property of 2-phenylbenzo[g]quinoxalines (**3a–e** in Fig. 1). Firstly, benzo[g]quinoxaline is a large conjugated skeleton, which may act as a fluorophore emitting a long-wavelength light. Secondly, the phenyl ring linked to benzo[g]quinoxaline by a free single bond may serve as a rotatable unit. Upon the increase of viscosity, the possibility of internal rotations would be reduced and thus the fluorescence intensity is increased. Moreover, the substituted group (R) with different electron-donor capacity in the phenyl ring may have some effect on the sensitivity to viscosity. As a result, five 2-phenylbenzo[g]quinoxaline derivatives with varied substituted groups (**3a–e**) were synthesized in this work, among which **3a** and **3b** are the known compounds [20,21], whereas the other three (**3c–e**) are new ones.

3.2. Effect of viscosity on the fluorescence properties of **3a–e**

To investigate the effect of viscosity on the fluorescence properties of **3a–e**, the mixture of ethylene glycol and glycerol with different volume ratios was chosen as a testing media of varied viscosity, because these two alcohols have comparable polarity and in this case the viscosity would be the only influential factor in the media [22].

As shown in Fig. 2, with increasing viscosity, both the fluorescence intensities and the emission wavelengths from **3a–c** do not change remarkably. However, the fluorescence intensities of **3d** and **3e** (Figs. 3 and 4) exhibit a great increase with increasing viscosity, but their emission wavelengths hardly alter. These results show that the five 2-phenylbenzo[g]quinoxaline derivatives display a distinct sensitivity to viscosity. That is, the compounds **3d** and **3e** give a sensitive fluorescence response to the viscosity of media, while the other three (**3a–c**) do not show this behavior. The major difference in chemical structure among the five compounds lies on the substituted group. Furthermore, it is known that the electron-donating ability of the substituted groups is $\text{Cl} < \text{H} < \text{OCH}_3 < \text{OH} < \text{N}(\text{CH}_3)_2$ [23]. Therefore, it may be concluded that, for the 2-phenylbenzo[g]quinoxaline derivatives, the fluorescence response to viscosity depends on the electron-donor capacity of their substituted groups in the phenyl ring (Fig. 1), and stronger electron-donating groups such as OH and $\text{N}(\text{CH}_3)_2$ would be necessary to achieve high sensitivity to viscosity.

The reason for the above effect of the substituted groups is rather complicated, but a possible explanation can be made in terms of the formation of twisted intramolecular charge transfer (TICT) state, which can de-excite nonradiatively [24–26]. In other words, in the molecule **3a–e**, when the electron-donor capacity of the substituted group in phenyl ring [e.g., OH and $\text{N}(\text{CH}_3)_2$] is strong enough, the benzo[g]quinoxaline moiety may serve as an electron acceptor. In this case, the formation of the D- π -A architecture through the phenyl ring would be favorable, thereby benefiting the generation of TICT state. Upon increase of viscosity, the formation of TICT state is hindered, thus leading to the increase in fluorescence

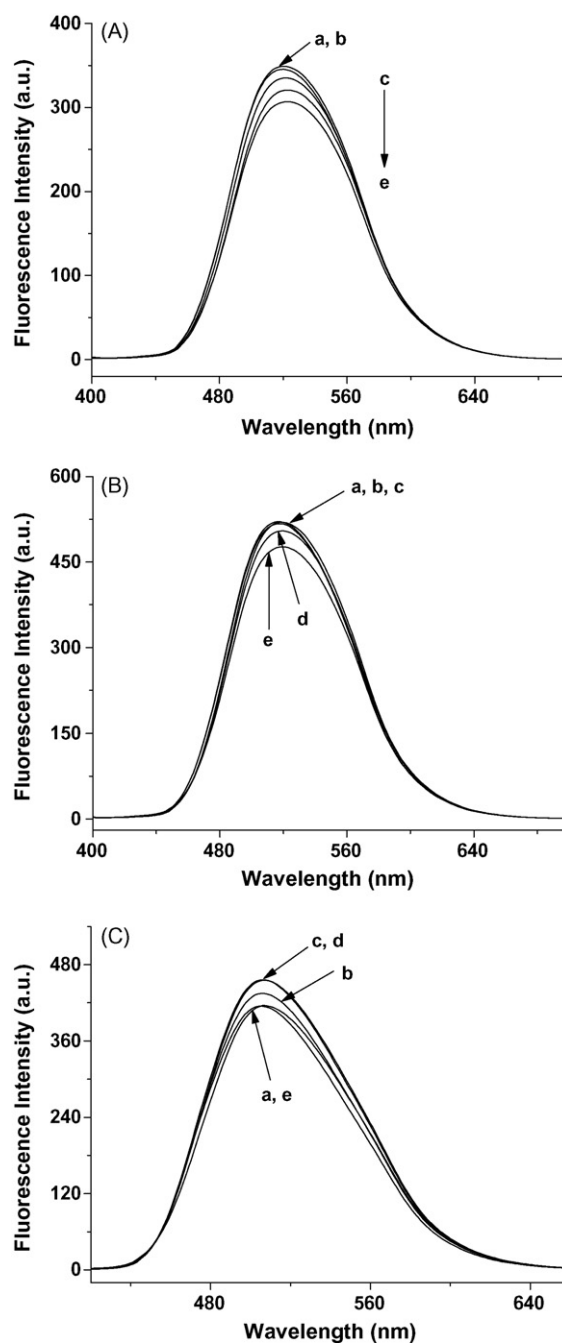


Fig. 2. The fluorescence emission spectra of 5 μM of (A) **3a** with $\lambda_{\text{ex}} = 382$ nm, (B) **3b** with $\lambda_{\text{ex}} = 380$ nm and (C) **3c** with $\lambda_{\text{ex}} = 392$ nm in the varied viscosity media of the ethylene glycol/glycerol (v/v) mixtures: (a) ethylene glycol only; (b) 7:3; (c) 5:5; (d) 3:7; (e) glycerol only. All the spectra were recorded at 20 °C, with both excitation and emission slit widths of 10 nm and a 400 V PMT voltage.

intensity. As depicted in the inset of Fig. 3, the relationship between the fluorescence intensity of **3d** and the viscosity of media can be described through Förster and Hoffmann equation [27,28] with a good linearity:

$$\log I = C + x \log \eta$$

where I = fluorescent emission intensity; η = solvent viscosity; x = dye-dependent constant; C = concentration and temperature constant.

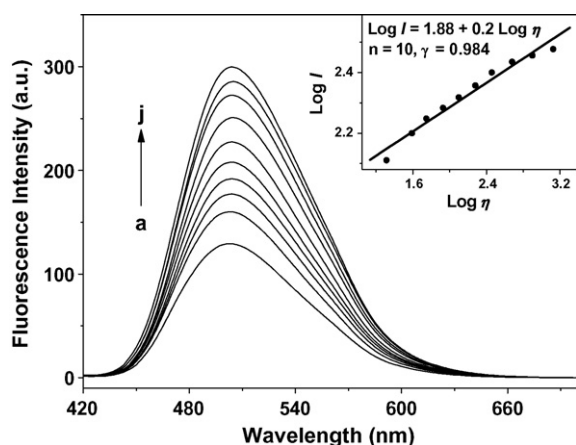


Fig. 3. The fluorescence emission spectra of 5 μ M of **3d** in the varied viscosity media of the ethylene glycol/glycerol (v/v) mixtures: (a) ethylene glycol only; (b) 8:2; (c) 7:3; (d) 6:4; (e) 5:5; (f) 4:6; (g) 3:7; (h) 2:8; (i) 1:9; (j) glycerol only. All the spectra were recorded at 20 °C and $\lambda_{\text{ex}} = 394$ nm, with both excitation and emission slit widths of 10 nm, and a 400 V PMT voltage. The inset shows the linear relationship between $\log I$ and $\log \eta$.

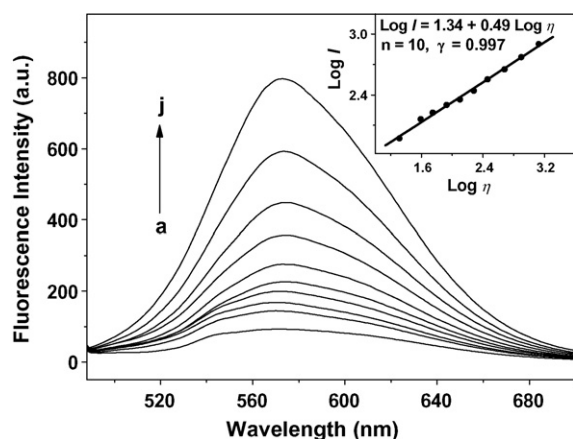


Fig. 4. The fluorescence emission spectra of 5 μ M of **3e** in the varied viscosity media of the ethylene glycol/glycerol (v/v) mixtures: (a) ethylene glycol only; (b) 8:2; (c) 7:3; (d) 6:4; (e) 5:5; (f) 4:6; (g) 3:7; (h) 2:8; (i) 1:9; (j) glycerol only. All the spectra were recorded at 20 °C and $\lambda_{\text{ex}} = 453$ nm, with both excitation and emission slit widths of 10 nm, and a 700 V PMT voltage. The inset shows the linear relationship between $\log I$ and $\log \eta$.

Similarly, the fluorescence intensity of **3e** also gives a linear response to viscosity (the inset of Fig. 4). The above results suggest that the viscosity of media may be determined on the basis of the change in fluorescence intensity of **3d** or **3e** for some systems. Moreover, **3d** and **3e** have a long-wavelength emission of >500 nm. This is very desirable to avoid the short-wavelength fluorescence interferences. Because **3d** and **3e** show better response to viscosity, in the subsequent experiments the fluorescence properties of these two compounds are further studied by examining the effects of other factors such as polarity and pH.

3.3. Effect of solvent polarity on fluorescence properties of **3d** and **3e**

The dielectric constants of the solvents usually reflect their polarity. As shown in Table 1, with the decrease of solvent polarity, **3d** shows a great hypsochromic shift in the fluorescence emission maxima from 489 nm in dimethylsulfoxide to 461 nm in hexane, with the exception in alcohols that may produce the solute–solvent specific interactions like hydrogen bonding [29,30]. In addition, dual fluorescence emission was found in nonpolar solvents such as tetrahydrofuran, toluene and *n*-hexane. This may result from the fluorescence emissions of the so-called local excited (LE) state and intramolecular charge transfer (ICT) state. Similar phenomena from 2-(*p*-dimethylaminostyryl)benzoxazole have been observed by Fayed [13]. Interestingly, the fluorescence quantum yield of **3d** does not change largely in these tested solvents ($\Phi = 0.017$ – 0.034), except in glycerol, which has a rather high viscosity and causes a great increase in quantum yield ($\Phi = 0.081$).

Similarly, with the decrease of solvent polarity, **3e** also displays a notable hypsochromic shift in fluorescence emission maxima from 604 nm in dimethylsulfoxide to 491 nm in hexane with the exception in alcohols. However, the fluorescence quantum yield of **3e** increases greatly from 2.75×10^{-3} in dimethylsulfoxide to 0.23 in hexane (Table 1), suggesting that the fluorescence intensity of **3e** is also sensitive to polarity.

The above results indicate that the fluorescence emission wavelengths of **3d** and **3e** exhibit a sensitive response to solvent polarity. Therefore, **3d** and **3e** may also be useful for polarity monitoring.

3.4. Effect of pH on the fluorescence properties of **3d** and **3e**

As depicted in Fig. 5, the fluorescence intensity of **3d** exhibits a rapid decrease when pH is over 7.6. This may be interpreted

Table 1
Fluorescence properties of **3d** and **3e** in different solvents.

Solvent	D^a	η^b (mPa s)	3d			3e		
			λ_{ex} (nm)	λ_{em} (nm)	Φ^c	λ_{ex} (nm)	λ_{em} (nm)	Φ^c
Dimethylsulfoxide	47.2	2.47	393	489	0.030	450	604	2.75×10^{-3}
Glycerol	46.5	1495	394	504	0.081	451	570	3.98×10^{-3}
Ethylene glycol	41.4	20.6	394	503	0.034	453	572	6.13×10^{-4}
DMF	38.2	0.85	391	482	0.030	450	594	6.65×10^{-3}
Acetonitrile	36.6	0.375	383	473	0.024	438	586	7.19×10^{-3}
Methanol	33	0.59	391	494	0.017	434	566	3.38×10^{-4}
Ethanol	25.3	1.2	392	491	0.025	450	568	1.37×10^{-3}
Acetone	21	0.32	385	471	0.020	438	576	0.025
Dichloromethane	9.1	0.44	388	470 (br) ^d	0.029	439	563	0.11
Tetrahydrofuran	7.5	0.55	387	448, 470	0.022	438	562	0.12
Toluene	2.4	0.587	388	447, 470	0.018	435	521	0.18
<i>n</i> -Hexane	1.9	0.313	383	438, 461	0.017	420	491	0.23

^a Dielectric constant (D).

^b Viscosity (η) of the solvents at 20 °C are from the literatures [22,31].

^c The fluorescence quantum yield (Φ) of **3d** and **3e** was determined by using 9,10-diphenyl-anthracene ($\Phi = 0.95$ in cyclohexane) and fluorescein ($\Phi = 0.95$ in 0.1 M NaOH) as a standard [32], respectively.

^d Broad peak.

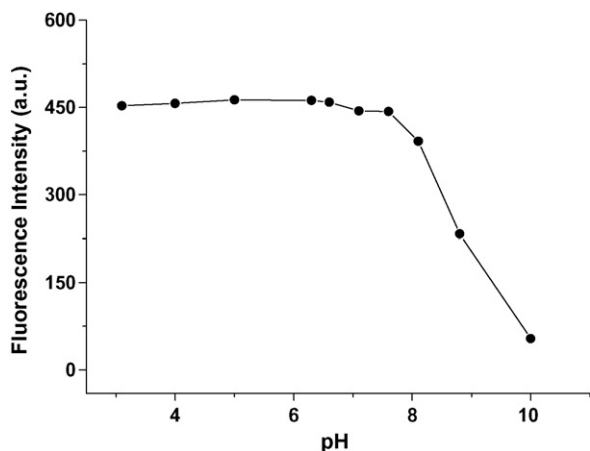


Fig. 5. The effect of pH on the fluorescence emission intensity of 5 μ M of **3d** in 0.1 M NaCl aqueous solution containing 10% (v/v) DMF. The fluorescence intensity was measured at $\lambda_{\text{ex}} = 391$ nm with both excitation and emission slit widths of 10 nm, and a 700 V PMT voltage.

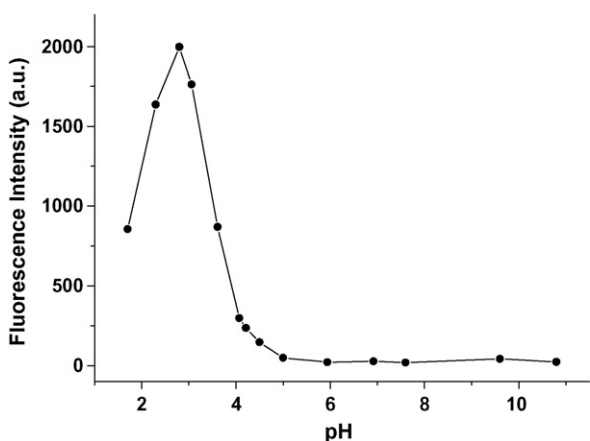


Fig. 6. The effect of pH on the fluorescence emission intensity of 5 μ M of **3e** in 0.1 M NaCl aqueous solution containing 20% (v/v) DMF. The fluorescence intensity was measured at $\lambda_{\text{ex}} = 379$ nm with both excitation and emission slit widths of 10 nm, and a 700 V PMT voltage.

by the change in electron-donor capability of the OH group. The ionization of the OH group in basic media forms O^- , which has a stronger electron-donating ability and causes the increase in ICT [33], accompanied by the decrease of fluorescence intensity.

The effect of pH on the fluorescence intensity of **3e** is somewhat complex. As shown in Fig. 6, the increase of pH values causes a fast rise in fluorescence intensity of **3e**, a maximum at about pH 3, and then a rapid decrease. The phenomenon can be repeatedly produced. This may be attributed to different deprotonations of the multiple electronegative atoms [13,34] in the molecule during the pH transition, which affects the ICT.

For accurate detection of viscosity, the influence of pH on the fluorescence intensity should be excluded. As can be seen from Figs. 5 and 6, the fluorescence intensity of **3d** and **3e** is not affected in the range of pH 3–7 and 5–11, respectively, suggesting that the measurement of viscosity should be performed in these pH regions. The fluorescence intensity of **3e** is rather low in the range of pH 5–11, which is due to the very low viscosity of the aqueous media. However, when the viscosity of a medium is raised, the fluorescence

intensity will be increased (Fig. 4), and thus the viscosity change can be measured.

4. Conclusions

Five different substituted 2-phenylbenzo[g]quinoxalines bearing a rotatable moiety of phenyl ring have been synthesized and characterized as viscosity-sensitive fluorescence probes. Among them, only **3d** and **3e** with stronger electron-donating groups exhibit sensitive fluorescence responses to viscosity, indicating that these two compounds may be of great potential use in viscosity detection, and strong electron-donor groups in the phenyl ring are crucial to afford high sensitivity. These findings might be useful in developing viscosity-sensitive fluorescent probes.

Acknowledgements

Financial support from the NSF of China (Nos. 20875092, 90813032 and 20525517), 863 Program and the Chinese Academy of Sciences is acknowledged.

References

- [1] M.M. Gleason, M.S. Medow, T.N. Tulenko, *Cric. Res.* 69 (1991) 216.
- [2] G. Deliconstantinos, V. Villiotou, J.C. Stavrides, *Biochem. Pharmacol.* 49 (1995) 1589.
- [3] M. Shinitzky, *Physiology of Membrane Fluidity*, CRC Press, Boca Raton, 1984, pp. 1–51.
- [4] O. Nativ, M. Shinitzky, H. Manu, D. Hecht, C.T. Roberts, D. LeRoith, Y. Zick, *Biochem. J.* 298 (1994) 443.
- [5] W. Osterode, C. Holler, F. Ulberth, *Diabet. Med.* 13 (1996) 1044.
- [6] J. Harkness, *Biorheology* 8 (1971) 171.
- [7] R.L. Letcher, S. Chien, T.G. Pickering, J.E. Sealey, J.H. Laragh, *Am. J. Med.* 70 (1981) 1195.
- [8] D.E. McMillan, *Metabolism* 31 (1982) 274.
- [9] K.J. Huang, W.Z. Xie, H. Wang, H.S. Zhang, *Talanta* 73 (2007) 62.
- [10] K.J. Huang, H. Wang, Y.H. Guo, R.L. Fan, H.S. Zhang, *Talanta* 69 (2006) 73.
- [11] B. Tang, T.X. Yue, J.S. Wu, Y.M. Dong, Y. Ding, H.J. Wang, *Talanta* 64 (2004) 955.
- [12] M. Belletête, R.S. Sarpal, G. Durocher, *Chem. Phys. Lett.* 201 (1993) 145.
- [13] T.A. Fayed, *J. Photochem. Photobiol. A: Chem.* 121 (1999) 17.
- [14] C.E. Kung, J.K. Reed, *Biochemistry* 28 (1989) 6678.
- [15] M.A. Haidekker, T. Ling, M. Anglo, H.Y. Stevens, J.A. Frangos, E.A. Theodorakis, *Chem. Biol.* 8 (2001) 123.
- [16] A. Granzhan, H. Ihmels, G. Viola, *J. Am. Chem. Soc.* 129 (2007) 1254.
- [17] G. Fodor, Ö. Kovács, *J. Am. Chem. Soc.* 71 (1949) 1045.
- [18] V. Bernard, *Molecular Fluorescence: Principles and Applications*, Wiley, Weinheim, 2002, p. 230.
- [19] X.Q. Chen, M. Sun, H.M. Ma, *Curr. Org. Chem.* 10 (2006) 477.
- [20] A. Gazit, H. App, G. McMahon, J. Chen, A. Levitzki, F.D. Bohmer, *J. Med. Chem.* 39 (1996) 2170.
- [21] J. Pató, G. Kéri, L. Örfi, F. Wáczek, Z. Horváth, P. Bánhegyi, I. Szabadkai, J. Marosfalvi, B. Hegymegi-Barakonyi, Z. Székelyhidi, Z. Greff, A. Choidas, G. Bacher, H. Daub, S. Obert, A. Kurtenbach, P. Habenberger, Patent WO200294796-A2 (2002).
- [22] M.A. Haidekker, T.P. Brady, D. Lichlyter, E.A. Theodorakis, *Bioorg. Chem.* 33 (2005) 415 (and references therein).
- [23] R.O. Loutfy, K.Y. Law, *J. Phys. Chem.* 84 (1980) 2803.
- [24] M.S.A. Abdel-Mottaleb, R.O. Loutfy, R. Lapouyade, *J. Photochem. Photobiol. A: Chem.* 48 (1989) 87.
- [25] G. Jones, W.P. Jackson, C.Y. Choi, *J. Phys. Chem.* 89 (1985) 294.
- [26] J.A. van Gompel, G.B. Schuster, *J. Phys. Chem.* 93 (1989) 1292.
- [27] M.A. Haidekker, T.P. Brady, D. Lichlyter, E.A. Theodorakis, *J. Am. Chem. Soc.* 128 (2006) 398.
- [28] Th. Förster, G. Hoffmann, *Z. Phys. Chem.* 75 (1971) 63.
- [29] M.K. Singh, H. Pal, A.C. Bhasikuttan, A.V. Sapre, *Photochem. Photobiol.* 68 (1998) 32.
- [30] S.Y. Dong, H.M. Ma, X.J. Duan, X.Q. Chen, J. Li, *J. Proteome Res.* 4 (2005) 161.
- [31] J.A. Dean, *Lange's Handbook of Chemistry*, 15th ed., McGraw-Hill, New York, 1999, pp. 5.90–5.129.
- [32] J.R. Lakowicz, *Principles of Fluorescence Spectroscopy*, 2nd ed., Kluwer Academic/Plenum Pub, New York, 1999, pp. 52–53.
- [33] S.L. Wang, T.I. Ho, *J. Photochem. Photobiol. A: Chem.* 135 (2000) 119.
- [34] M.H. Su, Y. Liu, H.M. Ma, Q.L. Ma, Z.H. Wang, J.L. Yang, M.X. Wang, *Chem. Commun.* (2001) 960.



Development of a highly sensitive and specific monoclonal antibody-based enzyme-linked immunosorbent assay (ELISA) for detection of Sudan I in food samples

Yuzhen Wang^a, Dapeng Wei^b, Hong Yang^c, Yuan Yang^d, Weiwei Xing^a, Yuan Li^a, Anping Deng^{a,*}

^a Key Laboratory of Green Chemistry & Technology, Ministry of Education of China, College of Chemistry, Sichuan University, Chengdu 610064, China

^b West China School of Preclinical and Forensic Medicine, Sichuan University, Chengdu 610041, China

^c West China School of Pharmacy, Sichuan University, Chengdu 610041, China

^d Chengdu Center for Disease Control and Prevention, Chengdu 610041, China

ARTICLE INFO

Article history:

Received 23 August 2008

Received in revised form 4 October 2008

Accepted 7 October 2008

Available online 18 October 2008

Keywords:

Sudan I

Monoclonal antibody

ELISA

Food samples

HPLC

ABSTRACT

The use of Sudan I as an additive in food products has been prohibited in the European Union and many other countries. In this study, a highly sensitive and specific monoclonal antibody (mAb)-based indirect competitive enzyme-linked immunosorbent assay (ELISA) for the detection of Sudan I in food samples was developed. The hapten derivative with a three-carbon-atom length of carboxylic spacer at the azobond *para*-position was synthesized and coupled to carrier proteins. The hapten-bovine serum albumin (BSA) conjugate was used as an immunogen, while the hapten-ovalbumin (OVA) conjugate was applied as a coating antigen. The mAb against Sudan I was produced by hybridoma technique and the corresponding ELISA was characterized in terms of sensitivity, specificity, precision and accuracy. At optimal experimental conditions, the standard curve was constructed in concentrations of 0.1–100 ng mL⁻¹. The values of IC₅₀ for nine standard curves were in the range of 1.1–2.0 ng mL⁻¹ and the LOD at a signal-to-noise ratio of 3 (S/N=3) was 0.07–0.14 ng mL⁻¹. The cross-reactivity values of the mAb with Sudan II, III and IV were 9.5%, 33.9% and 0.95%; no cross-reactivity was found with other six edible colorants: Lemon yellow, Bright blue, Indigotin, Kermes, Amarant and Sunset yellow, indicating the assay displays not only high sensitivity but also high specificity as well. The organic solvent effect on the assay was tested. It was observed that the ELISA was tolerated to 30% of methanol and 10% of acetonitrile without significant loss of IC₅₀ value. Six food samples were spiked with Sudan I and the methanolic extracts after appropriate dilution were analyzed by ELISA. Acceptable recovery rates of 88.2–110.5% and coefficients of variation of 2.5–17.4% were obtained. The ELISA for nine spiked samples was confirmed by high-performance liquid chromatography (HPLC) with a high correlation coefficient of 0.9840 (*n*=9). The mAb-based ELISA proven to be a feasible quantitative/screening method for Sudan I analysis in food samples with the properties of high sensitivity, specificity, simplicity of sample pretreatment, high sample throughput and low expense.

© 2008 Elsevier B.V. All rights reserved.

1. Introduction

Sudan I [1-(phenylazo)-2-naphthol] belongs to Sudan dyes which include Sudan I, II, III, and IV (molecular structures were shown in Table 1). These chemicals are inexpensive fat-soluble azo-compounds which are mainly used as coloring additives in manufacturing of some products, such as oils, wax products, and ball point inks since their bright and vivid colors could improve luster of commercial products [1]. Sudan I is classified as a carcinogen by the International Agency for Research on Cancer (IARC)

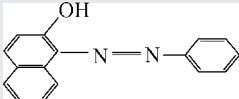
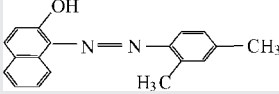
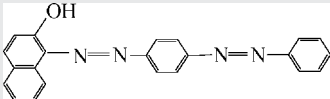
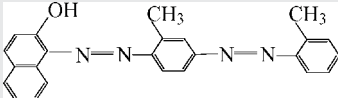
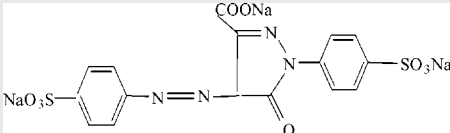
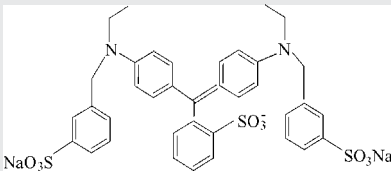
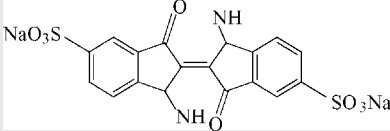
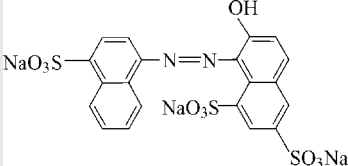
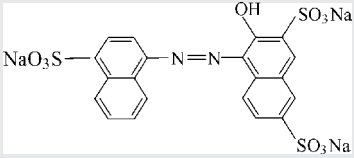
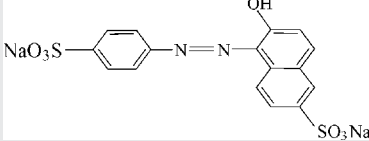
[2]. There is evidence that Sudan I is potentially carcinogenic in rodents and causes damage to genetic material since it can react with a given sequence of DNA *in vitro* [3]. It is also considered a possible genotoxic carcinogen and mutagen to human. For these reasons, in European Union and many other countries, Sudan I and other Sudan dyes are not permitted as additives in food products for any purpose at any levels. However, Sudan dyes are still illegally utilized as additives in foods by some merchants, particularly in those containing chilli powders, relishes, chutneys, seasonings, sauces and ready meals. In the last years, the presence of Sudan I and other Sudan dyes found in food products in China and Europe has caused a great panic among customers [4]. Therefore, for the assurance of consumer health, control of Sudan dyes in food products is very crucial and the development

* Corresponding author. Tel.: +86 28 85471302; fax: +86 28 85412907.

E-mail address: denganping6119@yahoo.com.cn (A. Deng).

Table 1

Cross-reactivity of the monoclonal antibody with Sudan I–IV and other six edible colorants.

Compound	Chemical structure	IC ₅₀	CR (%)
Sudan I		1.9 ^a	100
Sudan II		20	9.5
Sudan III		5.6	33.9
Sudan IV		200	0.95
Lemon yellow		>10,000	<0.01
Bright blue		>10,000	<0.01
Indigotin		>10,000	<0.01
Kermes		>10,000	<0.01
Amaranth		>10,000	<0.01
Sunset yellow		>10,000	<0.01

^a In the CR testing, IC₅₀ of 1.9 ng mL⁻¹ was obtained.

of a simple, economic and rapid analytical method is urgently required.

The standard analysis method is based on liquid chromatography approved by the European Union [5]. Other liquid chromatographic methods associated with different detectors such as UV [6], APCI-MS [7–8], ESI-MS [9], DAD [10], DAD-ESI-MS [11], ESI-MS/MS [12], capillary LC/Q-TOF-MS [13], CL [14], electrochemi-

cal detection [15], etc. for the analysis of Sudan dyes in different food samples have been reported. Generally, chromatographic methods are high cost and time-consuming, mainly because of complicated, expensive instrument and extensive sample preparation. Therefore, other techniques for detecting Sudan dyes were also developed. Molecularly imprinted polymers based extraction method coupled with HPLC detection were reported for selectively measurement of

Sudan dyes in foods [16]. Sudan I, II, III and IV were also separated by capillary electrophoresis combined with UV-detection, with an LOD of 96 ng mL^{-1} [17]. Multi-wall carbon nanotube-based electrochemical sensor for determination of Sudan I was reported, with the detection limit of 5 ng mL^{-1} [18]. Recently, Huang et al. found that Sudan dyes react with silver nitrate to produce silver nanoparticles, resulting in obvious plasmon resonance scattering signals at 452 nm, which was used to determine $0.2\text{--}2.4 \mu\text{mol}$ Sudan I, however, sensitivity was low and selectivity rather poor [19].

Immunoassays, especially enzyme-linked immunosorbent assays (ELISAs), are analytical methods which are based on the specific interaction between an antibody and corresponding antigen. The most significant advantages of ELISAs over the traditional instrumental methods are their high sensitivity and specificity, simple sample preparation, high throughput, and therefore, low cost per sample. ELISAs have been widely used for the determination of both large and small analytes such as proteins, microorganisms [20,21], antibiotics [22], hormones [23], pesticides [24] halogenated and aromatic pollutants [25,26], and even heavy metals [27] in the biological, medical, agricultural, and environmental area.

In our previous study, a polyclonal antibody (pAb) based ELISA for the determination of Sudan I in food samples was developed [28]. To our knowledge, that was the first report of the immunoassay for Sudan I, a notorious illegal additive in food products. However, as expected, the drawbacks of the pAb are mainly on its limited supply and heterogeneous affinity binding with the corresponding antigen. Recently, a monoclonal antibody (mAb)-based ELISA to detect Sudan dyes and Para red was published [29]. In that paper, however, the Sudan I derivative was simply synthesized by azocoupling reaction using 2-naphthol and diazotized 4-aminobenzoic acid. The functional group, e.g. carboxylic group, which is used for coupling Sudan I molecule to carrier protein, was directly attached to the benzene ring. As there was no spacer between Sudan I molecule and carrier protein, the Sudan I molecule might be partially embedded in the protein, e.g. the Sudan I molecule might be incompletely exposed to immunological system of immunized animal. Consequently, the monoclonal antibody exhibited high specific affinity binding with Sudan III and para red, showing group specific instead of target analyte specific. To overcome the problems associated with pAb and to produce high specific monoclonal antibody, the aims of this study are to adopt a novel synthesizing approach for the preparation of Sudan I derivative, to produce monoclonal antibody (mAb) against Sudan I with homogeneous and specific affinity binding and unlimited antibody supply, and to develop a sensitive and specific mAb-based ELISA for Sudan I detection in foods. In this study, Sudan I derivative with a three-carbon-atom length of linking spacer bearing a carboxylic group at the end was synthesized and covalently coupled to carrier proteins for the preparation of immunogen and coating antigen. The mAb against Sudan I was prepared by hybridoma technique and used to establish an indirect competitive ELISA. The proposed ELISA was validated by a conventional HPLC method for the analysis of Sudan I in food samples.

2. Experimental

2.1. Chemicals, apparatus, buffers and solutions

2.1.1. Chemicals

Sudan I, II, III, IV (HPLC grade), bovine serum albumin (BSA), ovalbumin (OVA), casein, 3,3',5,5'-tetramethylbenzidine (TMB), Tween-20, methanol (HPLC grade), dimethyl sulfoxide (DMSO), dimethylformamide (DMF), *N,N'*-dicyclohexylcarbodiimide (DCC),

N-hydroxysuccinimide (NHS), Freund's complete and incomplete adjuvants, horseradish peroxidase labeled goat anti-mouse IgG conjugate (HRP-GaMIgG), hypoxanthine aminopterin thymidine (HAT), hypoxanthine thymidine (HT), polyethylene glycol (PEG 4000), amarant, kermes, indigotin, bright blue and Lemon yellow were purchased from Sigma (Luis, Mo. 63178, USA). RPMI 1640 was bought from GibcoBri (Paisley, Scotland). Cell medium and fetal calf serum was from Minhai (Lanzhou, China). Mouse SP2/0 myeloma cell was bought from the Cell Bank of Chinese Science Academy (Shanghai, China). BALB/C mice were purchased from Experimental Animal Center of Sichuan University (Chengdu, China).

2.1.2. Apparatus

ELISA reader (Sunrise Remote/Touch Screen) and microtiter plate washer (M12/2R) were bought from Columbus plus (Tecan, Grödig, Austria). CO_2 incubator (HF 151 UV) was from Heal-For Development Ltd. (Shanghai, China). Spectrophotometer UV-2300 was from Techcomp (Shanghai, China). Microtiter plate shaker (KJ-201C Oscillator) was from Kangjian Medical Apparatus, Co., Ltd. (Jiangsu, China). Polystyrene microtiter plates (96-well) were from Haimen Plastic (Jiangsu, China). Deionized-RO water supply system (DZG-303A) was purchased from AK Company (Chengdu, Joint Company between Chengdu and Taiwan).

2.1.3. Buffers and solutions

(1) Coating buffer: 0.05 mol L^{-1} carbonate buffer, pH 9.8; (2) coating antigen stock solution: 1 mg mL^{-1} of coating antigen prepared with coating buffer; (3) assay buffer: 0.01 mol L^{-1} phosphate-buffered saline (PBS) pH 7.4, containing 145 mmol L^{-1} NaCl; (4) washing buffer (PBST): assay buffer with 0.1% (v/v) of Tween-20; (5) blocking solution: 1% of casein in assay buffer; (6) acetate buffer: 100 mmol L^{-1} sodium acetate acid buffer, pH 5.7; (7) substrate solution ($\text{TMB} + \text{H}_2\text{O}_2$): $200 \mu\text{L}$ of 10 mg mL^{-1} TMB dissolved in DMF, $20 \mu\text{L}$ of 5% H_2O_2 and 1 mL of acetate buffer were added to 20 mL of pure water; (8) stop solution: sulfuric acid (5%). (9) Sudan I standard solutions at the concentrations of 0, 0.1, 0.3, 1.0, 3.0, 10, 30 and 100 ng mL^{-1} were prepared by diluting the stock solution (1 mg mL^{-1} , by dissolving Sudan I red powder in DMF) with methanol:water (5:95, v/v).

2.2. Synthesis of Sudan I derivative

Sudan I-3-propanoic acid [Sudan I-C3, Fig. 1(a)] was synthesized in three steps according to the procedures described in Ref. [28]. Briefly, malonic acid was firstly reacted with 4-nitrobenzaldehyde in freshly distilled pyridine with acetamide as a catalyst. Then, the synthesized 3-(4-nitrophenyl)acrylic acid was reduced by hydrogen with palladium-C catalyst. Finally, the hydrogen reduction product 3-(4-aminophenyl)propanoic was reacted with 2-naphthol to form Sudan I-3-propanoic acid. The structure of synthesized Sudan I-C3 was confirmed by NMR spectrum.

2.3. Preparation of immunogen and coating antigen

The carboxylic acid-derivative Sudan I-C3 was conjugated to BSA and OVA by the DCC/NHS ester method as described in the literature [30]. Briefly, equimolar amounts (0.15 mmol) of Sudan I-C3, NHS, and DCC were dissolved in $300 \mu\text{L}$ of DMF and the mixture was incubated overnight at 25°C . The solution was centrifuged at $12,000 \text{ rpm}$ (e.g. $13,400 \times g$) for 10 min and the supernatant was added slowly to 100 mg of protein (BSA or OVA) dissolved in 5 mL of 0.13 mol L^{-1} NaHCO_3 under stirring. After incubation for 4 h at

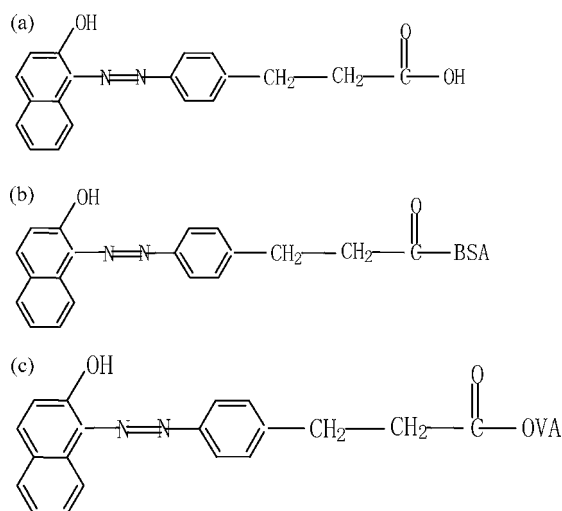


Fig. 1. The structures of: (a) Sudan I-C3, (b) Sudan I-C3-BSA and (c) Sudan I-C3-OVA.

25 °C, the solution was centrifuged and the supernatant was intensively dialyzed in 0.01 mol L⁻¹ (NH₄)₂CO₃ for 4 days with several changes of the dialyzing buffer solution. Finally, the Sudan I-protein conjugates were lyophilized and stored in the refrigerator until use. Sudan I-C3-BSA conjugate (Fig. 1(b)) was used as immunogens for antibody preparation, while the Sudan I-C3-OVA conjugate was served as coating antigens (Fig. 1(c)) for ELISA establishment.

2.4. Production of monoclonal antibody

2.4.1. Immunization

Two female BALB/C mice (6–8 weeks old) were immunized with Sudan I-C3-BSA subcutaneously. The dose of immunogen for each mouse was 100 µg of Sudan I-C3-BSA dissolved in physiological saline and emulsified with an equal volume of Freund's complete adjuvant. In next two sequential booster immunizations, 100 µg of immunogen emulsified with the same volume of incomplete Freund's adjuvant was given to each mouse in the same way at 2-week intervals after the initial immunization. Small volume of blood was collected from tail for testing antibody titer. The mice were given the final booster injection intraperitoneally without adjuvant before cell fusion.

2.4.2. Cell fusion

Three days after the final booster injection, the mice were sacrificed and their spleen cells were removed. The spleen cells were fused with mouse SP2/0 myeloma cells at the ratio of 10:1 in the presence of 50% polyethylene glycol 4000 which was used as fusion agent. The fused cells (hybridomas) were distributed in 96-well culture plates supplemented with hypoxanthine aminopterin thiamidine (HAT) medium containing 20% fetal calf serum with peritoneal macrophages as feeder cells from young BALB/C mice. The growth of hybridomas in the plates was incubated at 37 °C with 5% CO₂.

2.4.3. Hybridoma selection and cloning

After incubated for 2 weeks, culture supernatants were screened by indirect ELISA: 96-well microtiter plates were coated with the Sudan I-C3-OVA conjugate (100 µL/well in 0.05 mol L⁻¹ carbonate buffer, pH 9.6) overnight at 4 °C. The plates were washed three times with PBST and then blocked with 1% casein in PBS (120 µL/well) for 1 h at 37 °C. After the plates were washed three times with PBST, the plates received 50 µL/well of hybridomas supernatants, incubated

at 37 °C for 2 h. After washing, 100 µL of HRP-GaMlgG diluted in PBS was added to each well, and incubated for 1 h at 37 °C. After another washing step, the substrate solution (100 µL/well) was added. The reaction was stopped with sulfuric acid (80 µL/well) after 15 min and the absorbance was read at 450 nm. The hybridomas which produced antibody-recognizing Sudan I were subcloned for three times using the limiting dilution method. Stable antibody-producing clones were expanded and cryopreserved in liquid nitrogen.

2.4.4. Purification of monoclonal antibody

Parts of stable subclones were expanded and then injected into female BALB/C mice intraperitoneally which were preinjected with 0.5 mL of liquid paraffin 1 week ago. Ten days after the injection, the ascites were collected and subjected to purification by ammonium sulfate precipitation. The purified mAb was stored at -20 °C in the presence of 50% glycerol.

2.5. The procedures of indirect competitive ELISA

An indirect competitive ELISA format was adopted for analyzing Sudan I. The ELISA procedures were as follows. Sudan I-C3-OVA diluted with carbonate buffer, pH 9.8 was added to the wells of a microtiter plate (200 µL/well). The plate was incubated overnight at 4 °C and then washed with PBST using an automated plate washer. Some binding sites not occupied by the coating antigen were then blocked by the blocking buffer (280 µL/well) for 1 h at room temperature. After the plate was washed as before, standard solutions or samples (100 µL/well) and diluted mAb (100 µL/well) were added and incubated for 1 h at room temperature. After washing, GaMlgG-HRP was added (200 µL/well) and the plate incubated for 1 h at room temperature. Then, the plate was washed and the substrate solution (200 µL/well) added. After incubation with shaking for about 20 min, sulfuric acid (5%, 80 µL/well) was added and the absorbance measured at 450 nm using a microplate reader. Calibration curves were constructed in the form of (B/B₀) × 100% vs. log C, where B and B₀ was the absorbance of the analyte at the standard point and at zero concentration of the analyte, respectively.

2.6. Cross-reactivity

The specificity of the produced mAb was investigated by cross-reactivity (CR) experiment. Nine compounds were selected for testing CR (Table 1). Sudan II, Sudan III, and Sudan IV are fat-soluble and their use for food production is prohibited. The remaining six chemicals, Lemon yellow, Bright blue, Indigotin, Kermes, Amarant and Sunset yellow, are water-soluble and as edible additives widely used in food manufacturing. Standard solutions of testing compounds were prepared in the concentration range of 0.001–1000 ng mL⁻¹ with methanol:water (5:95, v/v) and applied to the ELISA procedures. CR was expressed as percent IC₅₀ values based on 100% response of Sudan I, e.g. CR(%) = (IC₅₀ for Sudan I/IC₅₀ for competing compound) × 100%. The IC₅₀ can be considered a measure (inverse) of the affinity of an antibody for a given analyte.

2.7. Fortification of Sudan I in food samples

Nine food samples including chilli powder I, II, chilli sauce I, tomato sauce I, II, hot-pot seasoning I, II and sausage I, II were collected from local supermarkets in Chengdu (China). Another sample, Chilli sauce II, was obtained from Chengdu Center for Disease Control and Prevention, Chengdu, which was confirmed to be positive. All samples were screened by ELISA. To examine the assay parameters of accuracy and precision, six collected samples, e.g. chilli powder I, chilli sauce I, II, tomato sauce I, hot-pot seasoning I and sausage I were used for fortification experiment. Chilli powder,

chilli sauce and tomato sauce can be directly applied for fortification, while hot-pot seasoning and sausage need to be homogenized before fortification. The procedures of fortification were as follows. An appropriate amount of samples were weighed into glass tubes with glass stoppers and fortified with Sudan I dissolved in methanol up to the final concentration of 2–10 μg Sudan I/g of sample. The fortified samples were shaken for 10 min and then kept at room temperature overnight. The extraction of spiked samples with pure methanol was performed by sonification for 20 min, vigorously shaking for 1 min, followed by centrifugation at 10,000 rpm for 10 min. The supernatants were diluted with methanol:water (5:95, v/v) at an appropriate fold to reduce the matrix effect and measured by ELISA. For each sample, three separate extractions were performed and each sample was determined in four replicate. Unspiked samples were extracted in the same way and used as blanks.

2.8. HPLC–UV analysis

HPLC was performed according to the procedure of Calbiani et al. [12]. Sudan I standard solutions or sample extracts were passed through a 0.45 μm cellulose acetate membrane filter (Alltech, Unterhaching, Germany) prior to HPLC detection. A HPLC system (Alltech, USA) with a C18 column (250 mm \times 4.6 mm, 5.0 μm particle size, Alltech, USA) was equilibrated with mobile phase consisting of methanol:2% aqueous acetic acid (90:10, v/v) at a flow rate of 1 mL min⁻¹. The volume of standard or extract in each analysis was 20 μL . Sudan I was monitored at 478 nm by UV detector. The HPLC workstation software (Alltech, USA) was used for the instrument control and data analysis. Peak areas were used for quantification. The calibration curve for Sudan I was constructed with standards of 0, 0.01, 0.05, 0.1, 0.5, 1.0, 2.0 and 5.0 $\mu\text{g mL}^{-1}$.

3. Results and discussion

3.1. Synthesis of Sudan I derivative

The most important requirement to develop an ELISA for small molecular compound like Sudan I is to modify the molecular structure of the target analyte properly, e.g. to synthesize a hapten derivative which bears a spacer to be coupled covalently to the carrier protein. Both the position at the hapten molecule where the spacer is attached and the length of the spacer may play an important role for a successful antibody generation. Generally, the molecular structure of the hapten should be left unchanged as far as possible and further, a spacer length of 3–5 C-atoms is considered most suitable [31,32]. In this study, Sudan I-derivative with a three-carbon-atom spacer length was synthesized (Fig. 1(a)). The spacer is attached at the para position of the azobond, far away from the naphthol moiety. The structure of Sudan I-C3 was confirmed by NMR method. The data from NMR method are: ¹H NMR (200 MHz, CDCl₃): δ 14.30 (b, 1H), 8.55 (d, J = 4.2 Hz, 1H), 7.73–7.50 (m, 4H), 7.41–7.14 (m, 4H), 6.89 (d, J = 3.96, 1H), 3.45 (b, 1H), 3.05 (t, J = 7.50 Hz, 2H), 2.76 (t, J = 7.46 Hz, 2H).

3.2. Synthesis of immunogen and coating antigen

The Sudan I-C3 derivative bearing a carboxylic acid group at the end of the spacer was activated by DCC/NHS ester method and then covalently coupled with a carrier protein (BSA or OVA). The conjugates of Sudan I-C3-BSA and Sudan I-C3-OVA were respectively used as immunogen and coating antigen. The UV spectra of BSA, Sudan I and the Sudan I-C3-BSA conjugate are shown in Fig. 2. It was observed that the characteristic peaks of Sudan I and BSA were located at 478 and 280 nm, respectively. It was also noted that the

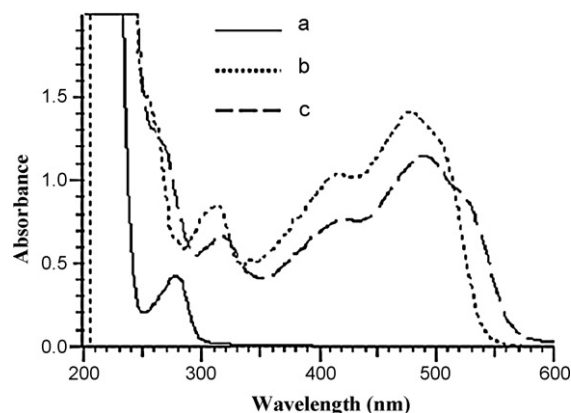


Fig. 2. UV spectra of: (a) BSA, (b) Sudan I and (c) Sudan I-C3-BSA conjugate.

characteristic peaks of Sudan I and BSA were all appeared on the spectrum of Sudan I-C3-BSA conjugate, but with somewhat red shift after conjugation. The spectra shown in Fig. 2 clearly indicated that the coupling of hapten to BSA was success. The UV spectra of Sudan I-C3-OVA conjugate were similar to those in Fig. 2 and therefore not showed herein.

3.3. Production of monoclonal antibody

Two BALB/C mice were immunized with Sudan I-C3-BSA. After third injection, it was observed that antisera collected from two immunized mice displayed high affinity binding with coating antigen. Three days after the final booster injection, the mice were killed and their spleen cells were removed. As the titer of antisera from two mice was similar, the spleen cells from two mice were mixed and used for the fusion experiments. After incubated for 2 weeks, the supernatants from hybridoma cells were screened by an indirect competitive ELISA. The hybridomas which produced antibody recognition with Sudan I were subcloned for three times using the limiting dilution method. Monoclonal antibodies were then produced in mouse ascites and purified with saturated ammonium precipitation.

3.4. Optimization of assay conditions

Usually, in the development of ELISA, criteria used to optimize experimental conditions includes: IC₅₀, e.g. the concentration of standard solution producing 50% of inhibition; detection limit (LOD), the lowest analyte concentration at a signal-to-noise ratio of 3; and maximum absorbance (B_0) limited in the range of 0.5–1.5 according to the Lambert–Beer law generally. To develop a highly sensitive and specific ELISA, the optimum assay conditions such as the concentration of coating antigen, dilution of antiserum and HRP-GaMlgG, etc, should be determined based on these criteria.

The assay conditions were optimized according to checkerboard titration method [33]. The optimal concentration of coating antigen OLA-OVA was found to be 20 ng mL⁻¹; the best dilution for mAb was 1:50,000; suitable dilution of GaMlgG-HRP was 1:20,000.

3.5. Sensitivity and stability of the assay

Under optimal assay conditions, the ELISA standard curve for Sudan I detection was constructed in concentrations of 0.1–100 ng mL⁻¹. The sensitivity was expressed by IC₅₀ value, the lower of the IC₅₀ value, the higher sensitivity of the assay would be. The stability of assay based on mAb was tested by running ELISA procedures for nine individual times within 4 weeks. Fig. 3 is

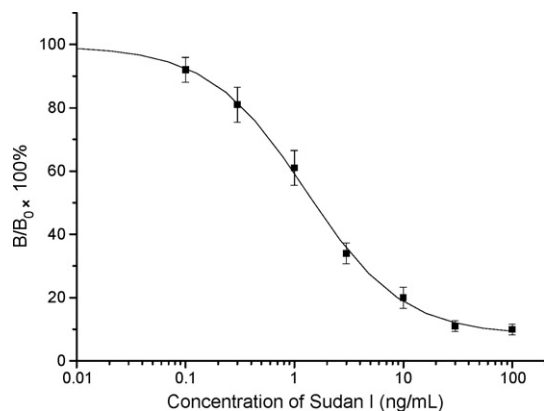


Fig. 3. The standard curve of Sudan I. Vertical bars represent the standard derivations of $B/B_0 \times 100\%$ ($n=9$). The IC_{50} was in the range $1.1\text{--}2.0\text{ ng mL}^{-1}$ and the LOD was $0.07\text{--}0.14\text{ ng mL}^{-1}$.

the average calibration curve constructed from nine performances. The relative standard deviation (R.S.D.) of the absorbance in four replicates for each calibration point on nine curves was within 10%. The IC_{50} value for nine standard curves was in the range of $1.1\text{--}2.0\text{ ng mL}^{-1}$, and the LOD at a signal-to-noise ratio of 3 ($S/N=3$) was $0.07\text{--}0.14\text{ ng mL}^{-1}$, indicating high sensitivity and stability of the assay.

3.6. Specificity of the assay

The assay specificity was evaluated by cross-reactivity (CR) of the mAb with three structurally related compounds of Sudan dyes (Sudan II, III and IV) and other six colorants (Sunset yellow, Amarant, Kermes, Indigotin, Bright blue, and Lemon yellow). The molecular structures of the testing compounds, the IC_{50} and CR values for each compound were given in Table 1. From Table 1, it can be seen that the CR values of the antibody with Sudan II, III and IV were 9.5%, 33.9% and 0.95%, respectively. The high CR of mAb with Sudan III can be explained by the fact that Sudan III and Sudan I exhibited the highest structural homology among all Sudan dyes. Lesser recognition of mAb with Sudan II and Sudan IV might be caused by the methyl group(s) attached in *ortho*- and *para*-positions to the linking azo group. From Table 1, it was also noticed that there was no cross-reactivity (i.e. CR was below 0.01%) of mAb with other colorants. Even the chemicals Sunset Yellow and Amaranth which share both the naphthol ring and attached azo group with Sudan I were not recognized by the antibody because of the large sulfonic acid group(s) preventing the antibody approach. To summarize, high specific monoclonal antibody was obtained against Sudan I after immunization with Sudan I derivatives containing C3-spacer arms attached to the benzene ring.

3.7. Effect of organic solvents on the assay

As methanol and acetonitrile are water miscible and commonly used for the extraction of analytes from different matrices, the effect of above two organic solvents on ELISA was tested by running assay procedures using Sudan I standard solutions prepared in methanol or acetonitrile at the concentration of 0%, 1%, 2%, 5%, 10%, 20%, 30%, 40% and 50%, respectively. As illustrated in Fig. 4, in the case of acetonitrile, the IC_{50} value was slightly increased within concentration 0–10%, however, when acetonitrile was more than 10%, IC_{50} value was rapidly increased. Similar finding was observed in the case of methanol, but the extent of the assay tolerance to the organic solvent was different. When the concentration of methanol was less than 30%, the IC_{50} values seemed to be constant, but when

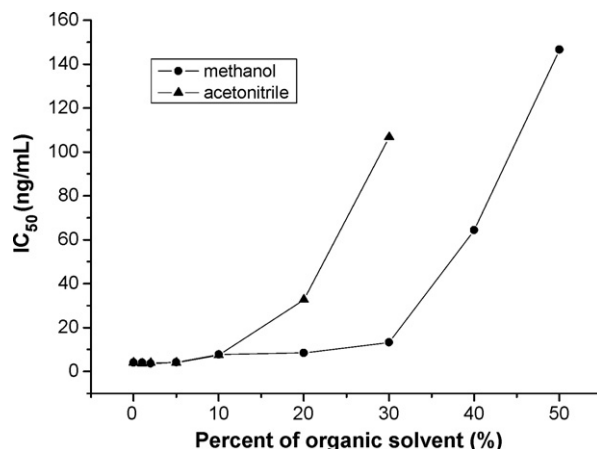


Fig. 4. Effect of methanol and acetonitrile on IC_{50} value of the assay.

methanol concentration was more than 30%, a significantly increasing IC_{50} value was appeared. It was demonstrated from Fig. 4 that the ELISA was tolerated to 30% of methanol or 10% of acetonitrile without significant loss of assay sensitivity. The effect of organic solvent on the immunoassay might be explained by somewhat denaturation of antibody at organic solvent environment, especially at high concentration [34]. As high tolerance and low price, methanol was chosen for extraction of food samples in this study.

3.8. Accuracy and precision of the assay

Ten collected food samples without fortification were analyzed by ELISA. It was found that only chilli sauce II was positive sample, with the Sudan I concentration of $1.03\text{ }\mu\text{g/g}$ of sample. The other nine sample were considered negative samples as content of Sudan I was undetectable by ELISA.

To test accuracy and precision of the ELISA, six food samples including chilli powder I, chilli sauce I, tomato sauce I, hot-pot seasoning I, sausage I and chilli sauce II were fortified with Sudan I at concentration of 2, 5 and $10\text{ }\mu\text{g/g}$ of sample. The fortified samples were extracted with pure methanol. Unspiked samples were served as blanks. The methanolic extracts were diluted with 5% methanol aqueous at 1:200–1:1000 folds depending on the different types of sample to eliminate the matrix effect completely. The diluted extracts were analyzed by ELISA. Assay precision and accuracy was estimated by measuring four replicates. The results of accuracy and precision obtained from each spiked sample measured by ELISA were shown in Table 2. Acceptable recovery rates of 88.2–110.5% and intra-assay coefficients of variation of 2.5–17.4% ($n=4$) were obtained. On the other hand, the inter-assay coefficients of variation were less than 20% ($n=3$).

3.9. Validation of the assay with HPLC

The HPLC calibration curve for Sudan I was constructed in the range of 0, 0.01, 0.05, 0.1, 0.5, 1.0, 2.0 and $5.0\text{ }\mu\text{g mL}^{-1}$ with an LOD of 5 ng mL^{-1} . With the selected parameters (see Section 2) the retention time of Sudan I was 12 min. The linear equation of the HPLC standard curve was $Y=51904x+680.37$ ($r=0.9990$, $n=8$).

To validate the applicability of the ELISA, nine fortified food samples including chilli powder I (spiked at concentration of 5 and $20\text{ }\mu\text{g/g}$ sample, respectively), chilli sauce I (spiked at concentration of 2 and $10\text{ }\mu\text{g/g}$), tomato sauce I (spiked at concentration of $5\text{ }\mu\text{g/g}$), hot-pot seasoning I (spiked at concentration of $10\text{ }\mu\text{g/g}$), sausage I (spiked at concentration of $5\text{ }\mu\text{g/g}$) and the chilli sauce II (spiked at concentration of 0 and $2\text{ }\mu\text{g/g}$) were measured by HPLC

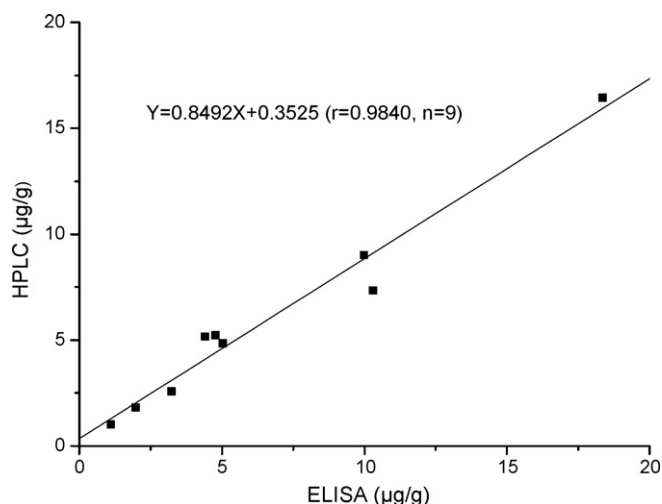
Table 2

The results of recovery and coefficient of variation for Sudan I determination from six fortified food samples by ELISA.

Sample	Fortified (μg/g)	Detected (μg/g)	Recovery (%)	CV (%) (n = 4)
Chilli powder I	2	1.98 ± 0.05	99.0	2.5
	5	5.03 ± 0.23	100.6	4.6
	10	9.21 ± 0.38	92.1	4.1
Chilli sauce I	2	1.90 ± 0.15	95.0	7.9
	5	5.30 ± 0.56	106.0	10.6
	10	9.99 ± 1.38	99.9	13.8
Tomato sauce I	2	1.90 ± 0.15	95.0	7.9
	5	4.41 ± 0.19	88.2	4.3
	10	9.28 ± 0.87	92.8	9.4
Hot-pot seasoning I	2	1.95 ± 0.09	97.5	4.6
	5	4.97 ± 0.45	99.4	9.1
	10	10.30 ± 0.47	103.0	4.6
Sausage I	2	2.19 ± 0.38	109.5	17.4
	5	4.78 ± 0.37	95.6	7.7
	10	10.02 ± 0.49	100.2	4.9
Chilli sauce II ^a	2	3.24 ± 0.18	110.5	5.6
	5	6.43 ± 0.48	108.0	7.5
	10	11.55 ± 0.87	105.2	7.5

No detectable Sudan I was found in the other blank samples.

^a The concentration of Sudan I in unspiked chilli sauce II measured by ELISA was 1.03 μg/g of sample. Thus the recovery rates were calculated as: (3.24–1.03)/2 = 110.5%, (6.43–1.03)/5 = 108.0% and (11.55–1.03)/10 = 105.2%.

**Fig. 5.** Correlation between the proposed ELISA and HPLC for spiked samples.

and ELISA simultaneously and the measured results were compared. As shown in Fig. 5, good correlation was obtained between ELISA (x) and HPLC (Y) with the linear regression equation of $Y = 0.8492x + 0.3525$ ($r = 0.9840$, $n = 9$). These results suggested that Sudan I in food samples could be simply, rapidly and accurately detected by ELISA without any cleanup procedures.

4. Conclusion

In this study, the hapten derivative with a three-carbon-atom length of carboxylic spacer at the azobound *para*-position was synthesized and coupled to carrier proteins. Monoclonal antibody

against Sudan I was prepared by hybridoma technique and a highly sensitive and specific indirect ELISA for the detection of Sudan I in different kinds of food samples was developed. The ELISA was tolerated to 30% of methanol and 10% of acetonitrile without significant loss of IC_{50} value. Interferences caused by sample matrix could be easily overcome by a simple dilution step before immunochemical analysis. Recovery rates of 88.2–110.5% and coefficients of variation of 2.5–17.4% demonstrated high accuracy and precision of the assay. The method was also validated by HPLC with good correlation. The proposed ELISA could be a feasible quantitative/screening method for Sudan I analysis in food samples due to its high sensitivity and simplicity, rapidity, lower expenses and high sample throughput.

Acknowledgements

This research work was financially supported by grants from the Scientific Research Foundation for the Returned Overseas Chinese (No. 2006331-11-3) and from the Promotion Program Foundation of Sichuan University of China (No. 0082204127090).

References

- [1] P. Moller, H. Wallin, *Mutat. Res.* 462 (2000) 13.
- [2] M. Stiborova, V. Martinek, H. Rydlova, P. Hodek, E. Frei, *Cancer Res.* 62 (2002) 5678.
- [3] M. Stiborova, B. Asfaw, E. Frei, H.H. Schmeiser, M. Wiessler, J. Hradec, *Carcinogenesis* 11 (1990) 1843.
- [4] C. Yu, Q. Liu, L. Lan, B. Hu, *J. Chromatogr. A* 1188 (2008) 124.
- [5] European Commission, *New Method Declaration* 03/99.
- [6] M. Mazzetti, R. Fascioli, I. Mazzoncini, G. Spinelli, I. Morelli, A. Bertoli, *Food Addit. Contam.* 21 (2004) 935.
- [7] F. Tateo, M. Bononi, *J. Agric. Food Chem.* 52 (2004) 655.
- [8] L. Di Donna, L. Maiuolo, F. Mazzotti, D. De Luca, G. Sindona, *Anal. Chem.* 76 (2004) 5104.
- [9] H.W. Chen, X. Zhang, M.B. Luo, *Chin. J. Anal. Chem.* 34 (2006) 464.
- [10] V. Cornet, Y. Govaert, G. Moens, J. Van Loc, J.M. Degroot, *J. Agric. Food Chem.* 54 (2006) 639.
- [11] M. Ma, X.B. Luo, B. Chen, S.P. Sub, S.Z. Yao, *J. Chromatogr. A* 1103 (2006) 170.
- [12] F. Calbiani, M. Careri, L. Elviri, A. Mangia, I. Pistara, I. Zagnoni, *J. Chromatogr. A* 1042 (2004) 123.
- [13] F. Calbiani, M. Careri, L. Elviri, A. Mangia, I. Zagnoni, *J. Chromatogr. A* 1058 (2004) 127.
- [14] Y.T. Zhang, Z.J. Zhang, Y.H. Sun, *J. Chromatogr. A* 1129 (2006) 34.
- [15] O. Chailapakul, W. Wonsawat, W. Siangproh, K. Grudpan, Y. Zhao, Z. Zhu, *Food Chem.* 109 (2008) 876.
- [16] S. Wang, Z. Xu, G. Fand, Z. Duan, Y. Zhang, S. Chen, *J. Agric. Food Chem.* 55 (2007) 3869.
- [17] E. Mejia, Y.S. Ding, M.F. Mora, C.D. Garcia, *Food Chem.* 102 (2007) 1027.
- [18] T. Gan, K. Li, K. Wu, *Sens. Actuators B* 132 (2008) 134.
- [19] L.P. Wu, Y.F. Li, C.Z. Huang, Q. Zheng, *Anal. Chem.* 78 (2006) 5570.
- [20] M.C. Castro, R. Garci, G.J. Rodri, G. Rodri, M.L. Marina, *Food Chem.* 100 (2007) 468.
- [21] X.J. Li, A.F. Du, W.M. Cai, Y.H. Hou, L.H. Pang, X. Gao, *Exp. Parasitol.* 115 (2007) 242.
- [22] H.Y. Zhang, Z.J. Duan, L. Wang, Y. Zhang, S. Wang, *J. Agric. Food Chem.* 54 (2006) 4499.
- [23] Z.L. Li, S. Wang, N.A. Lee, R.D. Allan, I.R. Kennedy, *Anal. Chim. Acta* 503 (2004) 171.
- [24] H.B. Gao, Y. Ling, T. Xu, W.W. Zhu, H.Y. Jing, W. Sheng, Q.X. Li, J. Li, *J. Agric. Food Chem.* 54 (2006) 5284.
- [25] A.P. Deng, V. Kolar, M. Franek, *Anal. Bioanal. Chem.* 373 (2002) 685.
- [26] D. Matschulat, A.P. Deng, R. Niessner, D. Knopp, *Analyst* 130 (2005) 1078.
- [27] D. Knopp, *Ecol. Chem. Eng.* 13 (2006) 383.
- [28] H. Dan, M. Yu, D. Knopp, R. Niessner, A.P. Deng, *J. Agric. Food Chem.* 55 (2007) 6424.
- [29] C. Ju, Y. Tang, H. Fan, J. Chen, *Anal. Chim. Acta* 621 (2008) 200.
- [30] M. Franek, A.P. Deng, V. Kolar, J. Socha, *Anal. Chim. Acta* 444 (2001) 131.
- [31] J.P. Sherry, *Crit. Rev. Anal. Chem.* 54 (1992) 217.
- [32] M.-P. Marco, S. Gee, B.D. Hammock, *Trends Anal. Chem.* 14 (1995) 415.
- [33] I.S. Kim, S.J. Setford, S. Saini, *Anal. Chim. Acta* 422 (2000) 167.
- [34] Y. Goda, M. Iirobc, A. Kobayashi, S. Fujimoto, M. Lke, M. Fujita, *Anal. Chim. Acta* 528 (2005) 47.



Enhanced separation of seven quinolones by capillary electrophoresis with silica nanoparticles as additive

Yanqing Wang^a, Willy R.G. Baeyens^b, Changgang Huang^a, Guangtao Fei^c, Li He^d, Jin Ouyang^{a,*}

^a College of Chemistry, Beijing Normal University, Beijing 100875, PR China

^b Department of Pharmaceutical Analysis, Faculty of Pharmaceutical Sciences, Ghent University, Harelbekestraat 72, B-9000 Ghent, Belgium

^c Institute of Solid State Physics, Chinese Academy of Sciences, Hefei 230031, PR China

^d Affiliated Hospital of Tsinghua University, Beijing 100084, PR China

ARTICLE INFO

Article history:

Received 12 June 2008

Received in revised form

30 September 2008

Accepted 1 October 2008

Available online 14 October 2008

Keywords:

Capillary zone electrophoresis

Quinolones

Silica nanoparticles

Enhanced separation

ABSTRACT

This paper describes the enhanced separation of lomefloxacin, sparfloxacin, fleroxacin, norfloxacin, ofloxacin, gatifloxacin and pazufloxacin by capillary zone electrophoresis (CZE) using silica nanoparticles (SiNPs) as running buffer additive. The impact of SiNPs concentration on the resolution and selectivity of separation was investigated and a given value of SiNPs was finally chosen under the optimum conditions. The addition of the SiNPs to the running buffer enabled electroosmotic flow (EOF) decrease and permitted full interaction between SiNPs and analytes. The influence of separation voltage, pH and buffer concentration on the separation in the presence of SiNPs was examined. Interactions between drugs and nanoparticles during the separation are discussed; the determination of interaction constants is also achieved. A good resolution of seven quinolones was obtained within 15 min in a 50 cm effective length fused-silica capillary at a separation voltage of +10 kV in a 12 mM disodium tetraborate-phosphate buffer (pH 9.08) containing 5.2 $\mu\text{g mL}^{-1}$ SiNPs.

© 2008 Elsevier B.V. All rights reserved.

1. Introduction

Since their discovery in the 1980s, the fluoroquinolone chemotherapeutic compounds (FQs) have been widely used in the treatment of various bacterial infections [1]. This class of anti-infective drugs exhibits activity against Gram-positive and Gram-negative bacteria which is caused by the inhibition of two bacterial enzymes: DNA gyrase and topoisomerase IV enzymes [2]. These compounds have the advantages of fewer toxic side effects and enhanced pharmacokinetic properties. Due to the cited characteristics and their universal applications, FQs are being studied intensively for more frequent application in the treatment of various diseases.

So far, several methods have been developed for the analysis of FQs [3–6]. Among these, high-performance liquid chromatography (HPLC) has been most universally used for their separation [7–10]. However, the disadvantages of HPLC include tedious sample preparation procedures, large volumes of eluting solutions and additives as well as the total analysis time. Capillary electrophoresis (CE) is being increasingly applied to FQs separation because of short

analysis times and low consumption of reagents [11–16], although its selectivity is not always satisfying. Furthermore, as was investigated during the present FQs separation, some buffer additives such as surfactants, ion-pairing agents and organic modifiers are to be employed and a chemometrics scheme should be used [17,18].

Nanomaterials have been applied in CE owing to their unique properties (electric, chemical, magnetic and mechanical) [19], representatives being gold nanoparticles [20], polymer nanoparticles [21,22] and carbon nanotubes [23–26]. The advantage of applying these materials is that they provide additional interaction sites. They can also serve as large surface area platforms for organofunctional groups, which can interact with the capillary surface, the analytes or both, leading to enhanced selectivity and separation efficiency.

Compared to other nanomaterials, silica nanoparticles (SiNPs) contain hydroxyl functional groups with different binding sites on the surface, and since recently they attract extensive attention in CE. It has been reported that SiNPs are used as a pseudostationary phase, which is similar to the use of polymeric nanoparticles and ionic polymers that act as pseudostationary phases to affect the electrophoretic mobilities of analytes and thus their selectivity [27–31]. Ohno et al. [32] used SiNPs in micro-CE to obtain good separation of DNA. Kuo et al. [33] first used SiNPs in the analysis of biologically active amines by using native laser-induced fluorescence (LIF). In that study, the capillaries were dynamically coated

* Corresponding author at: College of Chemistry, No. 44, Beijing Normal University, Beijing 100875, PR China. Fax: +86 10 62799838.

E-mail address: jinyang@bnu.edu.cn (J. Ouyang).

with poly(vinylpyrrolidone) (PVP) and poly(ethylene oxide) (PEO); the SiNPs had a strong interaction with PEO and the adsorption of SiNPs on the PEO through hydrogen bonding and hydrophobic patches became the main contributor for the improved separation [33]. To the best of our knowledge, no study on the direct introduction of SiNPs in buffer solution as additive in CE has been reported so far for the separation of FQs.

The aim of the present paper is to study the application of SiNPs as buffer additive in CE for the separation of seven quinolone antibacterial agents (lomefloxacin, sparfloxacin, fleroxacin, norfloxacin, ofloxacin, gatifloxacin, pazufloxacin). As will be shown, the introduction of certain SiNPs in the buffer solution could successfully improve the separation. The interactions between the SiNPs and the analytes may be the main driving forces for the observed enhanced separation.

2. Experimental

2.1. Materials and solution preparation

SiNPs were a gift from the Institute of Solid State Physics, Chinese Academy of Sciences (Hefei, P.R. China). Lomefloxacin, sparfloxacin, fleroxacin, norfloxacin, ofloxacin, gatifloxacin and pazufloxacin (Fig. 1) were provided by the Beijing Institute for the Control of Biological Products (Beijing, P.R. China). Disodium tetraborate, sodium dihydrogen phosphate and phosphoric acid (85%) were purchased from Beijing Chemical Plant (Beijing, P.R. China). All chemicals for the buffer solutions were of analytical grade. All solutions were prepared using purified water (Millipore, Milford, MA, USA). The buffer was prepared by dissolving disodium tetraborate and sodium dihydrogen phosphate in Milli-Q water at a concentration of 12 mM

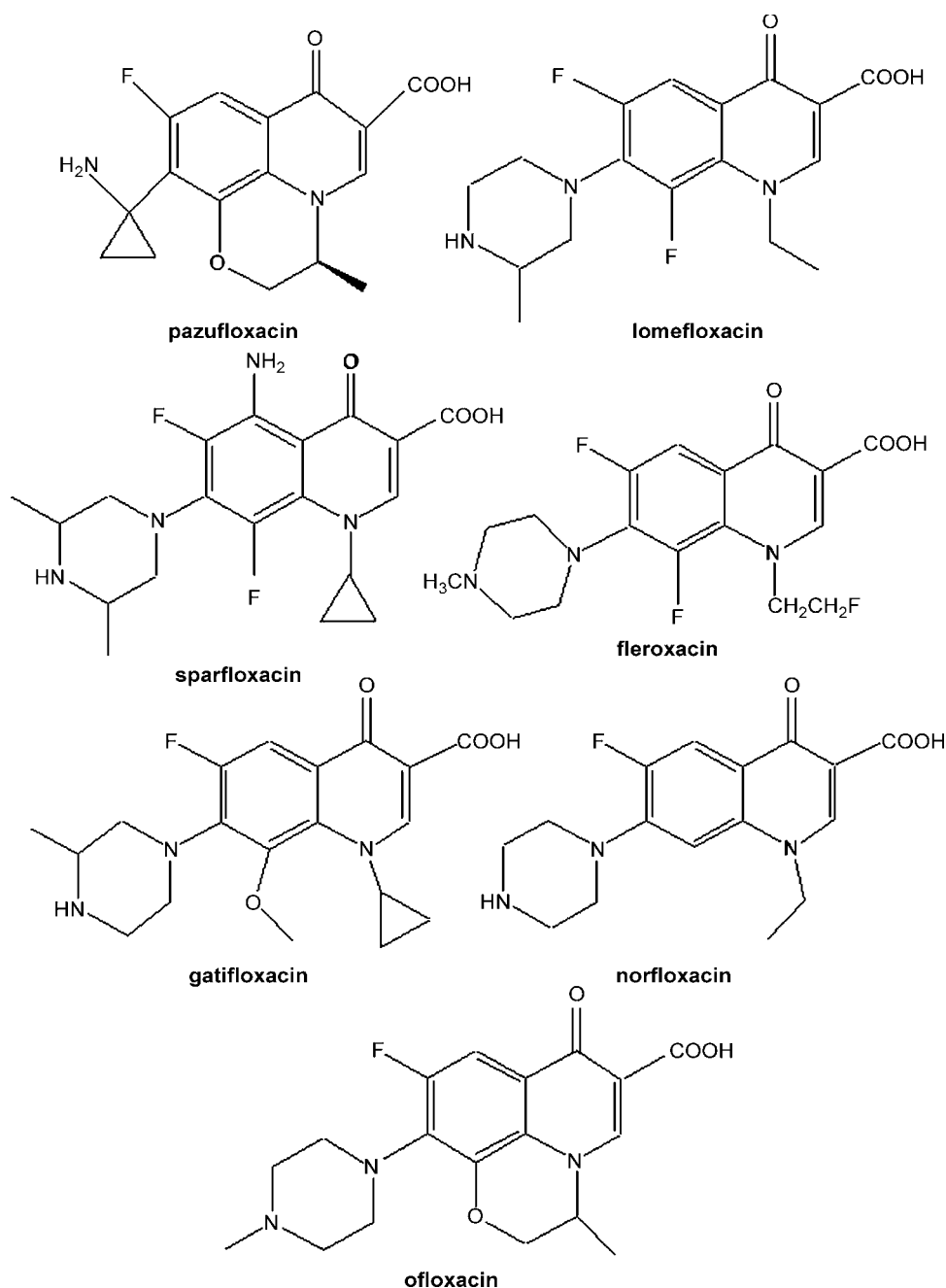


Fig. 1. Structures of the analytes.

and 38 mM, respectively. The pH was adjusted using NaOH or H_3PO_4 .

The SiO_2 suspension was prepared by adding SiO_2 nanoparticles in Milli-Q water through ultrasonication with a bath sonicator (KQ-50DE, Kunshan ultrasonic apparatus Ltd., Jiangsu, P.R. China) for about 5 min at the initial concentration of $20 \mu\text{g mL}^{-1}$. Next, the suspension was added to the buffer which was used for the separation.

Stock solutions of seven quinolone antibacterials were prepared by dissolving under ultrasonic treatment in Milli-Q water to provide a concentration of about $600 \mu\text{g mL}^{-1}$ for sparfloxacin, $500 \mu\text{g mL}^{-1}$ for norfloxacin, $750 \mu\text{g mL}^{-1}$ for fleroxacin, $420 \mu\text{g mL}^{-1}$ for gatifloxacin, $700 \mu\text{g mL}^{-1}$ for ofloxacin, $350 \mu\text{g mL}^{-1}$ for lomefloxacin hydrochloride and $400 \mu\text{g mL}^{-1}$ for pazufloxacin. All solutions were filtered using $0.45 \mu\text{m}$ syringe filters (Microfiltration System, CA, USA) and degassed in an ultrasonic bath for 10 min before rinsing the column.

2.2. Apparatus

A 1229 capillary electrophoresis apparatus (Beijing Institute of New Technology Application, P.R. China) equipped with a UV detector installed at 254 nm was used for all measurements. Fused-silica capillary columns (uncoated) $50 \mu\text{m}$ I.D. \times $375 \mu\text{m}$ O.D., with a total length of 65 cm and effective length of 50 cm were used as the separation capillary (Photoconduction Fiber Plant, Yongnian Country, Hebei Province, P.R. China). All electropherograms were obtained at average ambient laboratory temperatures of $25 \pm 2^\circ\text{C}$.

2.3. Procedures

When a new capillary was used, it was conditioned by a pressure flush of 1.0 M NaOH solution (60 min) for silanol activation, 0.2 M NaOH (10 min), deionized water (10 min) and buffer solution (5 min). Between runs, the capillary was washed sequentially with 0.2 M NaOH (5 min), deionized water (5 min) and buffer solution (5 min). At this stage, the capillary was ready for the analysis.

3. Results and discussion

3.1. Characterization of SiNPs

The pristine SiNPs contain hydroxyl functional groups with different binding sites on the surface. Appropriate nanoparticles dispersions introduced in the running buffer play an important role for investigating their effects upon separation. The transmission electron microscope (TEM) image of the SiNPs is shown in Fig. 2. From the image it can be noticed that the size of the SiNPs is less than 100 nm, which shows about 30 nm at average.

3.2. Optimization of separation with/without SiNPs

At first, the SiNPs were not applied in the running buffer. The separations occurred under different conditions: separation voltages of 6–15 kV, pH values from 8.7–9.4, and buffer concentrations – the concentration (mmol) ratio of disodium tetraborate and sodium dihydrogen phosphate varying from 6:44 to 40:10 – were investigated. However, under the optimum separation conditions, the seven quinolones only exhibited poor separation as shown in Fig. 3a. Hence, SiNPs were explored as buffer additive so as to improve the separation. An improved resolution by using certain amounts of SiNPs was obtained as shown in Fig. 3c. It can be observed that in the presence of $5.2 \mu\text{g mL}^{-1}$ SiNPs, gatifloxacin and ofloxacin were separated, and also norfloxacin and ofloxacin were

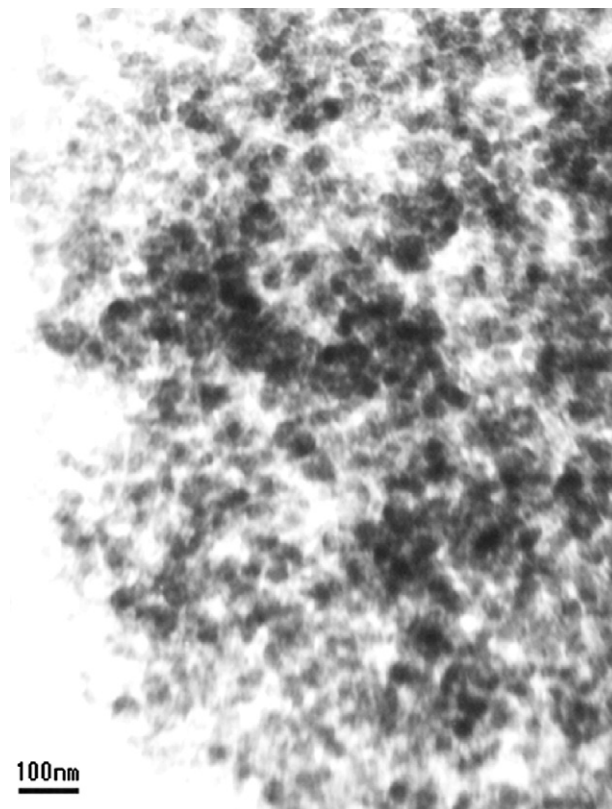


Fig. 2. TEM image of SiNPs.

resolved. In order to further study how the SiNPs affected separation, a series of experiments were performed investigating different voltages, pH and buffer concentrations in the presence of SiNPs; the impact of SiNPs concentration was examined likewise.

3.3. Influence of voltage and buffer concentration upon separation in the presence of SiNPs

The separation voltages were optimized over the range of 8–20 kV. Voltages higher than 20 kV or lower than 8 kV were not beneficial for the resolution of all compounds. The maximum resolution occurred at 10 kV, which was chosen as the final separation voltage. Apparently no important separational differences were observed when changing the cited conditions in the absence or presence of SiNPs when the voltage changed.

Different buffer concentrations in the presence of $5.2 \mu\text{g mL}^{-1}$ SiNPs were also investigated. As shown in Fig. 4, the resolution of norfloxacin and ofloxacin slightly improved with increasing disodium tetraborate concentrations; however, the separation of gatifloxacin and sparfloxacin became more difficult. The best results occurred when the disodium tetraborate concentration was 12 mM. Slight disodium tetraborate hydrolysis during the separation may lead to a minor change of the buffer pH value, which in turn affects the surface properties of SiNPs. Hence, a further study of pH impact upon the electrophoretic behavior of SiNPs during separation was investigated as described below.

3.4. Impact of pH on separation

As for the impact of pH on the resolution of separation, pH values ranging from 8.7–9.4 were examined. It seemed that the effects of pH upon the separation of gatifloxacin and sparfloxacin, norfloxacin and ofloxacin were stronger than for the other analytes; the

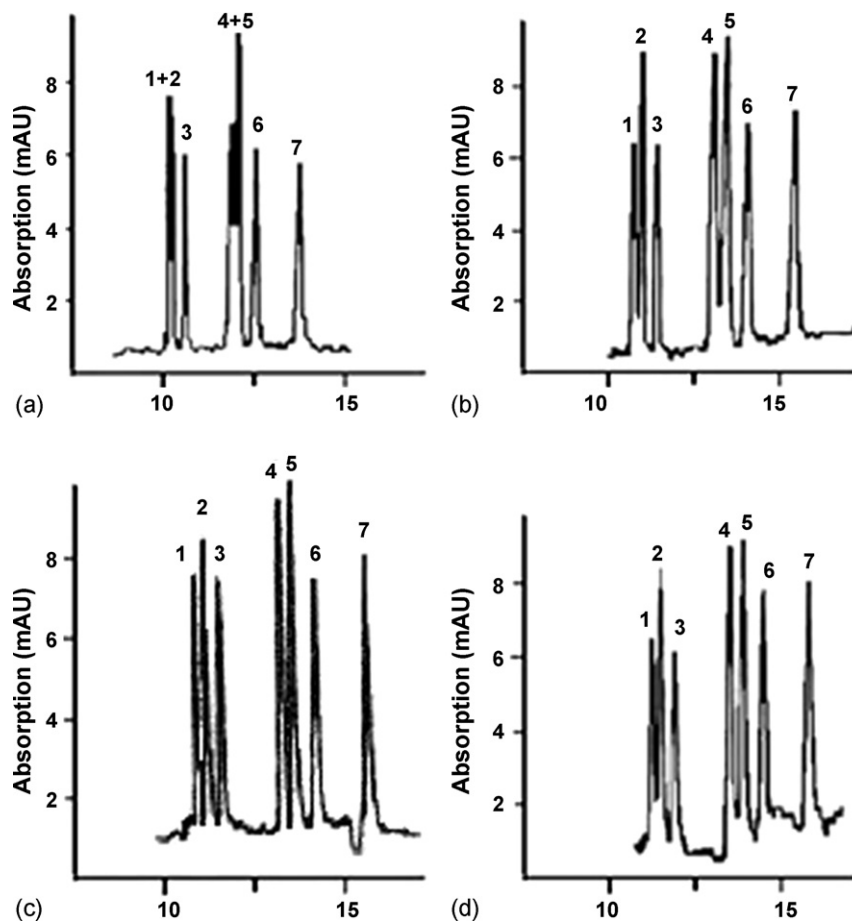


Fig. 3. Electropherograms of seven quinolones in the absence of SiNPs (a) and in the presence of $3.6 \mu\text{g mL}^{-1}$ SiNPs (b), $5.2 \mu\text{g mL}^{-1}$ SiNPs (c), $5.7 \mu\text{g mL}^{-1}$ SiNPs (d). 1, Gatifloxacin; 2, sparfloxacin; 3, lomefloxacin; 4, norfloxacin; 5, ofloxacin; 6, fleroxacin; 7, pazufloxacin; allied conditions: pH 9.08, separation voltage +10 kV, buffer solution of 12 mM disodium tetraborate-phosphate, hydrodynamic injection time 7 s.

increase of pH was beneficial to the separation of gatifloxacin and sparfloxacin but had an opposite effect on norfloxacin and ofloxacin (Fig. 5); as concerns selectivity (Fig. 6), pH obviously affected the latter but with little impact on the separation of gatifloxacin and sparfloxacin. In order to achieve good resolution and, simultaneously, satisfying selectivities, 9.08 was chosen as the final pH value. It can be seen that pH exerts a major impact upon the separa-

tion in the presence of SiNPs. The change of pH apparently alters the surface properties of SiNPs, leading to a modified interaction between analytes and SiNPs. The results also indicated that the migration time of the solutes distinctly prolonged with increasing pH (10.40, 10.40, 10.64, 11.64, 12.0, 12.54, 13.58 min for gatifloxacin, sparfloxacin, lomefloxacin, norfloxacin, ofloxacin, fleroxacin and pazufloxacin, respectively, at pH values of 8.70, 12.23, 12.44, 12.71, 13.95, 13.95, 14.30; 15.24 min for the analytes at pH 9.40).

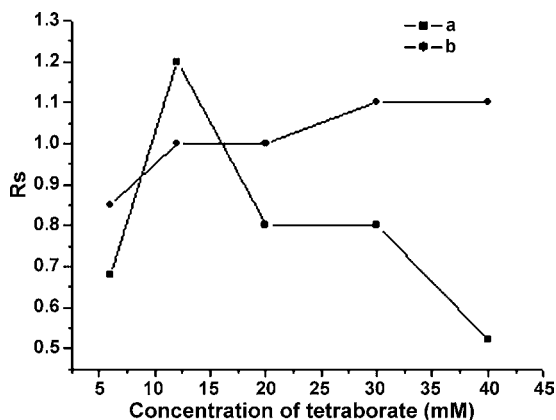


Fig. 4. Effect of buffer concentration on the resolution in the presence of $5.2 \mu\text{g mL}^{-1}$ SiNPs. (a) Gatifloxacin and sparfloxacin, (b) norfloxacin and ofloxacin. R_s = resolution. Other conditions as in Fig. 3.

3.5. Impact of SiNPs concentration on separation

In the present experiment, the amount of SiNPs in the buffer solution was gradually increased and its impact on separation was investigated. From the electropherograms shown in Fig. 3, it was observed that at lower SiNPs concentrations, the improvement was slight; when it reached $5.2 \mu\text{g mL}^{-1}$, the improvement was most significant. When above this level, there was little change upon separation, only, as for this case, it was considered that the addition of SiNPs to the buffer solution could decrease electroosmotic flow (EOF), resulting in good resolution. In order to demonstrate the supposition that EOF decreased with increasing SiNPs concentrations, experiments were carried out to evaluate the effect of SiNPs concentration upon EOF when the other conditions remained the same, acetone being chosen as neutral EOF marker. The results are shown in Fig. 7. It can be seen that EOF indeed decreased with increasing SiNPs: $\mu_{eo} = 5.34 \times 10^{-4} \text{ cm}^2 \text{ V}^{-1} \text{ s}^{-1}$ in the absence of SiNPs, which decreased to $3.61 \times 10^{-4} \text{ cm}^2 \text{ V}^{-1} \text{ s}^{-1}$ when the SiNPs concentration

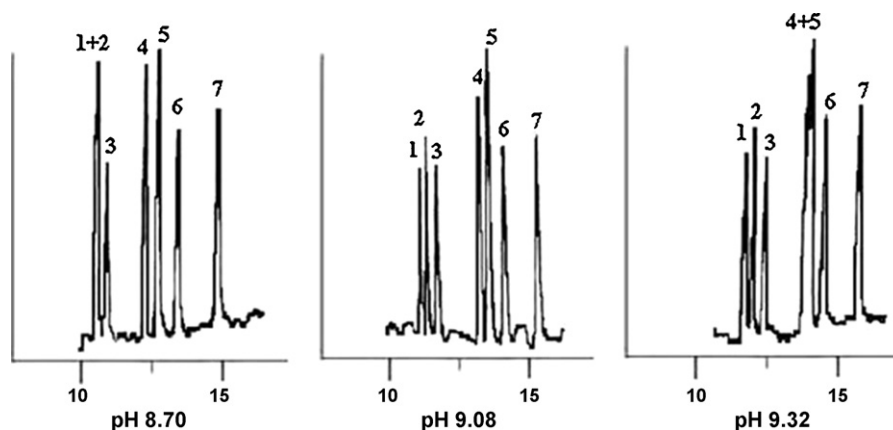


Fig. 5. Electropherograms of seven quinolones with increasing pH values in the presence of $5.2 \mu\text{g mL}^{-1}$ SiNPs. 1, Gatifloxacin; 2, sparfloxacin; 3, lomefloxacin; 4, norfloxacin; 5, ofloxacin; 6, fleroxacin; 7, pazufloxacin. Other conditions as in Fig. 3.

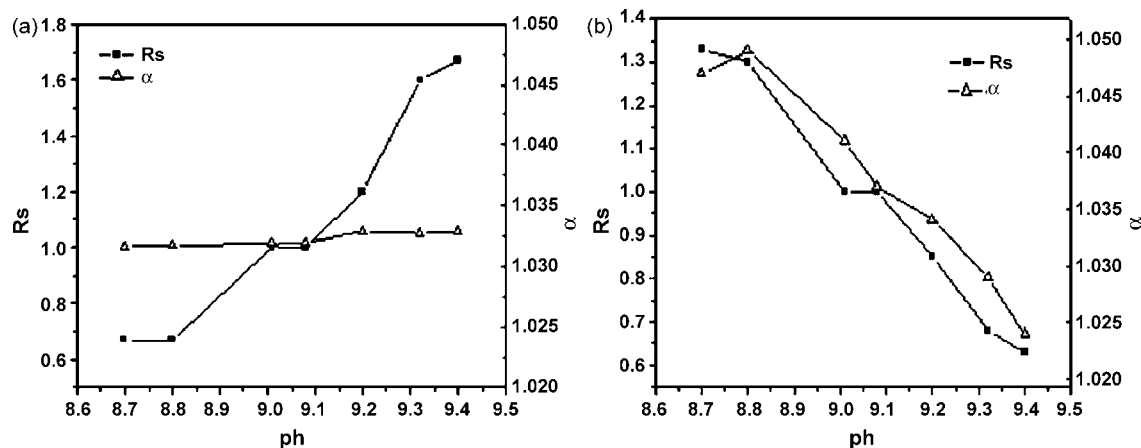


Fig. 6. Influence of pH upon resolution and selectivity in the presence of $5.2 \mu\text{g mL}^{-1}$ SiNPs. (a) Gatifloxacin and sparfloxacin. (b) Norfloxacin and ofloxacin. Rs = resolution and α = selectivity. Other conditions as in Fig. 3.

reached a certain value; no obvious change of EOF occurred above this value. The lowest EOF was obtained when the SiNPs concentration was $5.2 \mu\text{g mL}^{-1}$. Under these conditions, apparently full interaction between analytes and nanoparticles occurs, leading to good resolution. Because of the high pH (9.08), it remains obvious that both SiNPs and capillary wall exhibit negative charges, SiNPs not adsorbing on the capillary wall but rather keeping away from it. The presence of SiNPs in the buffer thus increases the total

ionic strength, then makes the zeta potential of the capillary wall decrease, resulting in EOF decrease. Also, it is assumed that the increase in viscosity by the addition of SiNPs represents another reason for decrease of EOF.

It also should be noticed that the separation time prolonged with increasing SiNPs concentration: at a concentration of $3.6 \mu\text{g mL}^{-1}$, the time was 10.49, 10.64, 10.91, 11.95, 12.18, 12.59 and 13.49 min for gatifloxacin, sparfloxacin, lomefloxacin, norfloxacin, ofloxacin, fleroxacin and pazufloxacin, respectively; when it reached $5.2 \mu\text{g mL}^{-1}$, the time was 10.82, 10.99, 11.28, 12.43, 12.76, 13.16 and 14.13 min for the analytes. Above this value, the time slightly prolonged and separation could not be improved. All results were in accordance with the change of EOF. Moreover, the separation of gatifloxacin and sparfloxacin, norfloxacin and ofloxacin was influenced more substantially than of the other analytes by the addition of SiNPs. This influence was most obvious at the level of $5.2 \mu\text{g mL}^{-1}$.

3.6. Interactions during separation

Although an exact mechanism for the quinolone separation applying SiNPs as buffer additive at high pH has not been clearly established so far, the enhanced separation may probably be explained as follows. An interaction between SiNPs and the analytes is most likely the main reason for the separation, as distinct separational improvements are observed. In order to confirm this

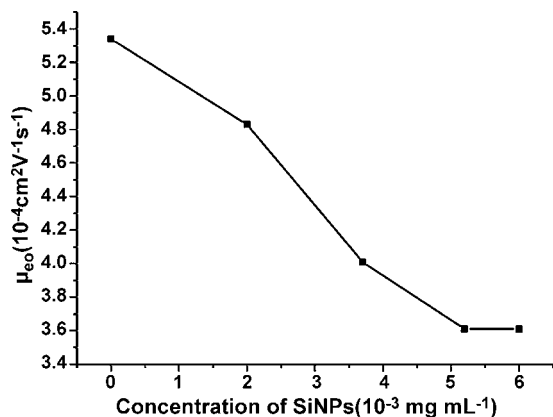


Fig. 7. Influence of SiNPs concentrations on EOF. Other conditions as in Fig. 3.

vision, the interaction constants between SiNPs and all analytes were determined and the data were calculated as described in reference [34]. The interaction constant is obtained by using the following equations:

$$\mu = \frac{Ll}{V} \left(\frac{1}{t} - \frac{1}{t_0} \right) \quad (1)$$

$$\frac{\mu_0 - \mu}{\mu - \mu_\infty} = KC \quad (2)$$

where L and l are total length and effective length of the capillary, respectively, t and t_0 are the migration times of analytes and EOF, respectively, V is the separation voltage, μ_0 the electrophoretic mobility of the analytes in the absence of SiNPs and μ_∞ the electrophoretic mobility when combining SiNPs and the analytes; K is the interaction constant between them, C is the concentration of SiNPs.

We obtained t , t_0 , μ_0 values at different concentrations of SiNPs, and obtained the μ value at different concentrations of SiNPs through Eq. (1), next a series of data points was obtained through Eq. (2), then the K value being obtained. From the data shown in Table 1, it can be observed that the interaction constants of all analytes are in the following order: gatifloxacin < sparfloxacin < lomefloxacin < norfloxacin < ofloxacin < fleroxacin < pazufloxacin, which is in accordance with the separation order and which demonstrates our view.

As for the structures of the seven quinolones, they have two pK_a values because of the dissociation of the carboxylic group and the deprotonation of the N_4 of the piperazine ring. Their pK_a values generally vary from 6 to 9, for instance, pK_{a1} 6.03 and pK_{a2} 8.38 for gatifloxacin [35], pK_{a1} 6.23 and pK_{a2} 8.57 for sparfloxacin [36], pK_{a1} 5.97 and pK_{a2} 7.65 for ofloxacin [37], pK_{a1} 5.94 and pK_{a2} 8.22 for norfloxacin [38], pK_{a1} 6.59 and pK_{a2} 8.05 for fleroxacin [39]. Under pH 9.08 conditions, the adsorption of SiNPs on the capillary wall could hardly occur; it is presumed that the interaction between the analytes and SiNPs may be the main reason for the separation improvement. The results of the binding constants data can demonstrate this supposition; moreover the carboxylic group on the piperazine ring takes a negative charge, the-NH remaining in the molecular form. In the present study, the most obvious improvements occurred in the separation of gatifloxacin and sparfloxacin, norfloxacin and ofloxacin. It is estimated that gatifloxacin and sparfloxacin interact with SiNPs by hydrogen bonding. Because of the existence of $-NH_2$ and $-F$ groups in the sparfloxacin structure, its interaction with SiNPs will be stronger than for gatifloxacin. Norfloxacin and ofloxacin may adsorb on the surface of SiNPs, and the sorption will be distinguishing based on their different structures [40,41]. In addition, the change of pH may alter the surface properties of SiNPs, which hence may alter the interactions between SiNPs and analytes.

Table 1
Determination of the combination constants between analytes and nanoparticles^a.

Parameter ^b	Analytes ^c						
	Gati	Spar	Lome	Norf	Oflo	Flero	Pazu
$\mu_0 \times 10^{-8}$ ($m^2 V^{-1} s^{-1}$)	-1.08	-1.16	-1.53	-1.69	-1.73	-1.87	-2.25
$\mu_\infty \times 10^{-8}$ ($m^2 V^{-1} s^{-1}$)	-0.73	-0.79	-0.81	-1.53	-1.70	-1.79	-1.87
$K \times 10^{-3}$ ($mL \mu g^{-1}$)	2.81	3.00	3.06	3.41	3.41	3.91	4.65

^a Separation conditions: pH 9.08, separation voltage +10 kV, buffer solution of 12 mM disodium tetraborate-phosphate, hydrodynamic injective time 7 s.

^b μ_0 and μ_∞ are the electrophoretic mobilities of the analytes in the absence of SiNPs and the combination of SiNPs and analytes, K is the combination constant.

^c Gati, gatifloxacin; Spar, sparfloxacin; Lome, lomefloxacin; Norf, norfloxacin; Oflo, ofloxacin; Flero, fleroxacin; Pazu, pazufloxacin.

Table 2
Detection limits, linearity and repeatability^a.

Analyte ^b	Equation for calibration curves	Linear range ($\mu g mL^{-1}$)	R^2	Detection limit ($\mu g mL^{-1}$) (S/N=3)	Concentration level ($\mu g mL^{-1}$) (S/N=3)	Peak area RSD (%) $n=4$	Separation time RSD (%) $n=4$
Gati	$y = 0.9449x + 42.299$	5–420	0.9929	2.0	20	6.12	0.21
Spar	$y = 0.7112x - 1.0727$	5–400	0.9979	2.5	20	7.60	0.84
Lome	$y = 0.5348x - 3.2536$	10–350	0.9990	7.0	35	5.30	0.67
Norf	$y = 1.2651x - 5.4262$	7–500	0.9990	3.5	20	6.43	0.91
Oflo	$y = 0.9449x + 42.299$	5–300	0.9929	3.0	20	4.91	0.70
Flero	$y = 0.782x + 17.879$	8–500	0.9904	3.5	20	4.63	0.98
Pazu	$y = 0.6621x + 29.336$	6–400	0.9968	2.0	20	7.46	0.10

^a Separation conditions: pH 9.08, separation voltage +10 kV, buffer solution of 12 mM disodium tetraborate-phosphate containing $5.2 \mu g mL^{-1}$ SiNPs, hydrodynamic injective time 7 s.

^b Gati, gatifloxacin; Spar, sparfloxacin; Lome, lomefloxacin; Norf, norfloxacin; Oflo, ofloxacin; Flero, fleroxacin; Pazu, pazufloxacin.

Table 3Recovery of analytes in human serum^a.

Analyte ^b	Equation for calibration curves	R ²	Added (μg mL ⁻¹)	Found (μg mL ⁻¹)	Recovery (%)	Peak area RSD (%) n = 4	Separation time RSD (%) n = 4
Gati	$y = 0.0279x - 0.4077$	0.9894	65.0	58.0	89.2	8.20	0.81
			120.0	107.1	89.2		
			205.0	191.2	93.1		
Oflo	$y = 0.0791x - 11.804$	0.9858	125.0	113.0	88.9	5.34	0.94
			190.0	173.1	91.1		
			290.0	273.0	94.1		
Flero	$y = 0.0442x - 2.3992$	0.9979	90.0	83.4	92.2	4.60	2.70
			200.0	183.1	91.5		
			240.0	222.5	92.7		
Lome	$y = 0.0516x - 6.529$	0.9903	165.0	151.6	92.1	5.04	1.89
			185.0	173.4	92.5		
			205.0	188.2	91.7		
Pazu	$y = 0.1886x - 17.243$	0.9985	120.0	113.5	94.6	8.13	2.04
			200.0	193.7	96.9		
			250.0	234.8	93.9		
Spar	$y = 0.0498x - 0.909$	0.9822	85.0	83.1	97.8	3.33	2.28
			110.0	109.4	99.5		
			155.0	143.6	92.6		
Norf	$y = 0.0816x - 7.803$	0.9309	170.0	159.4	93.8	3.31	2.94
			215.0	204.6	95.2		
			265.0	251.0	94.7		

^a Separation conditions: pH 9.08, separation voltage +10 kV, buffer solution of 12 mM disodium tetraborate-phosphate containing 5.2 μg mL⁻¹ SiNPs, hydrodynamic injective time 7 s.

^b Gati, gatifloxacin; Spar, sparfloxacin; Lome, lomefloxacin; Norf, norfloxacin; Oflo, ofloxacin; Flero, fleroxacin; Pazu, pazufloxacin.

3.7. Linearity, detection limits and repeatability

A series of standard mixture solutions of the seven analytes were tested to determine the signal linearity for all analytes using UV detection. The results of this regression analysis on calibration curves, linear range and detection limits as well as repeatability are presented in Table 2. The RSD was less than 7.60% for peak areas and less than 0.98% for separation times of the analytes.

3.8. Application to human serum

In order to demonstrate the feasibility of the present method in real samples, the recoveries of seven quinolones in human serum were examined under the optimized experimental conditions. In this experiment, healthy human serum was used. It was diluted 10 times with buffer solution, whereafter the analytes were added, no clean-up procedure being involved. As shown in Table 3, the recovery of the analytes was more than 89.2%, the RSDs for peak areas and separation times were less than 8.20% and 2.94%, respectively. The results indicate that the present method can be applied to the analysis of real samples.

4. Conclusion

The addition of SiNPs as buffer additive could successfully improve the separation of quinolones, not only with respect to resolution but also in terms of selectivity. The influence of the SiNPs concentration upon separation was investigated. The impact of the separation voltage, pH, and buffer concentration upon the electrophoretic behavior of SiNPs was also examined. It was found that the separation voltages had little influence upon the electrophoretic behavior of SiNPs, while pH changes could alter the surface properties of SiNPs, leading to a modified interaction between SiNPs and analytes, improving separation. Application of the present method to human serum was also achieved. The results showed that the method has potential use in real sample analysis. The application of SiNPs to the separation as reported in this

paper is most likely to be extended to other areas. Furthermore, the ease of SiNPs modification also can extend their future applications.

Acknowledgements

The authors gratefully acknowledge the support from the National Nature Science Foundation of China (20675010), the Bilateral Scientific and Technological Cooperation Flanders–China (011S0503) and the National Basic Research Program of China.

References

- [1] M.V.N. de Souza, Med. Chem. 5 (2005) 1009.
- [2] G. Carlucci, J. Chromatogr. A 812 (1998) 343.
- [3] K.P.R. Chowdary, G.D. Rao, Indian Drugs 34 (1997) 107.
- [4] L. Fratini, E.E.S. Schapoval, Int. J. Pharm. 127 (1996) 279.
- [5] F. Belar, A.A. Al-Majed, A.M. Al-Obaid, Talanta 50 (1999) 765.
- [6] V. Andreu, C. Blasco, Y. Picó, TrAC 26 (2007) 534.
- [7] S. Joshi, J. Pharm. Biomed. Anal. 28 (2002) 795.
- [8] V.F. Samanidou, C.E. Demetriou, I.N. Papadoyannis, Anal. Bioanal. Chem. 375 (2003) 623.
- [9] L.A. Shervington, M. Abba, B. Hussain, J. Donnelly, J. Pharm. Biomed. Anal. 39 (2005) 769.
- [10] M.I.R.M. Santoro, N.M. Kassab, A.K. Singh, E.R.M. Kedor-Hackman, J. Pharm. Biomed. Anal. 40 (2006) 179.
- [11] A.F. Faria, M.V.N. de Souza, M.V. de Almeida, M.A.L. de Oliveira, Anal. Chim. Acta 579 (2006) 185.
- [12] B.Y. Deng, C.N. Su, Y.H. Kang, Anal. Bioanal. Chem. 385 (2006) 1336.
- [13] A. Juan-García, G. Font, Y. Picó, Electrophoresis 27 (2006) 2240.
- [14] H.X. Lu, X.P. Wu, Z.H. Xie, X.C. Lin, L.Q. Guo, C. Yan, G.N. Chen, J. Sep. Sci. 28 (2005) 2210.
- [15] M. Hernandez, F. Borrull, M. Calull, J. Chromatogr. B-Anal. Technol. Biomed. Life Sci. 742 (2000) 255.
- [16] F.J. Lara, A.M. García-Campaña, F. Ales-Barrero, J.M. Bosque-Sendra, L.E. García-Ayuso, Anal. Chem. 78 (2006) 7665.
- [17] J.L. Beltran, E. Jimenez-Lozano, D. Barron, J. Barbosa, Anal. Chim. Acta 501 (2004) 137.
- [18] S.W. Sun, L.Y. Chen, J. Chromatogr. A 766 (1997) 215.
- [19] K. Okuyama, I.W. Lenggoro, Chem. Eng. Sci. 58 (2003) 537.
- [20] M.F. Huang, C.C. Huang, H.T. Chang, Electrophoresis 24 (2003) 2896.
- [21] C. Nilsson, S. Birnbaum, S. Nilsson, J. Chromatogr. A 1168 (2007) 212.
- [22] N. Na, Y.P. Hu, J. Ouyang, W.R.G. Baeyens, J.R. Delanghe, T. De Beer, Anal. Chim. Acta 527 (2004) 139.

- [23] Z.H. Wang, G.A. Luo, J.F. Chen, S.F. Xiao, Y.M. Wang, *Electrophoresis* 24 (2003) 4181.
- [24] J.H.T. Luong, P. Bouvrette, Y.L. Liu, D.Q. Yang, E. Sacher, J. *Chromatogr. A* 1074 (2005) 187.
- [25] X. Xiong, J. Ouyang, W.R.G. Baeyens, J.R. Delanghe, X.M. Shen, Y.P. Yang, *Electrophoresis* 27 (2006) 3243.
- [26] N. Na, Y.P. Hu, J. Ouyang, W.R.G. Baeyens, J.R. Delanghe, Y.E.C. Taes, M.X. Xie, H.Y. Chen, Y.P. Yang, *Talanta* 69 (2006) 866.
- [27] P. Viberg, M. Jornten-Karlsson, P. Petersson, P. Spegel, S. Nilsson, *Anal. Chem.* 74 (2002) 4595.
- [28] B. Maichel, E. Kenndler, *Electrophoresis* 21 (2000) 3160.
- [29] C.P. Palmer, *Electrophoresis* 21 (2000) 4054.
- [30] S. Schulte, C.P. Palmer, *Electrophoresis* 24 (2003) 978.
- [31] W.D. Qin, *Electrophoresis* 28 (2007) 3017.
- [32] T. Ohno, T. Matsuda, H. Suzuki, M. Fujimoto, *Adv. Powder Technol.* 17 (2006) 167.
- [33] I.T. Kuo, Y.F. Huang, H.T. Chang, *Electrophoresis* 26 (2005) 2643.
- [34] S.G. Penn, E.T. Bergstrom, I. Knights, G.Y. Liu, A. Ruddick, D.M. Goodall, J. *Phys. Chem.* 99 (1995) 3875.
- [35] F.F. Adriana, M.V.N. de Souza, M.V. de Almeida, M.A.L. de Oliveira, *Anal. Chim. Acta* 579 (2006) 185.
- [36] Y.X. Furet, J. Deshusses, J.C. Pechere, *Antimicrob. Agents Chemother.* 36 (1992) 2506–2511.
- [37] Ph. Schmitt-Kopplin, J. Burhenne, D. Freitag, M. Spiteller, A. Kettrup, J. *Chromatogr. A* 837 (1999) 253.
- [38] D. Barroñ, E. Jiménez-Lozano, A. Irlles, J. Barbosa, J. *Chromatogr. A* 871 (2000) 381.
- [39] V. Sanz-Nebot, I. Toro, J. Barbosa, J. *Chromatogr. A* 933 (2001) 45.
- [40] K.W. Goyne, J. Chorover, J.D. Kubicki, A.R. Zimmerman, S.L. Brantley, J. *Colloid Interface Sci.* 283 (2005) 160.
- [41] O. Lorphensri, J. Intravijit, D.A. Sabatini, T.C.G. Kibbey, K. Osathaphan, C. Saiwan, *Water Res.* 40 (2006) 1481.



Thermo-reversibility of the fluorescence enhancement of acridine orange induced by supramolecular self-assembly

Hong Wang, Weiping Zhang, Xueling Dong, Yajiang Yang*

School of Chemistry and Chemical Engineering, Huazhong University of Science and Technology, Wuhan 430074, China

ARTICLE INFO

Article history:

Received 12 August 2008

Received in revised form 19 October 2008

Accepted 21 October 2008

Available online 5 November 2008

Keywords:

Thermo-reversibility

Fluorescence enhancement

Supramolecular hydrogels

Gelators

Self-assembly

ABSTRACT

Fluorescence enhancement of acridine orange (AO) in supramolecular hydrogels formed by self-assembly of the gelators 3-[(2R)-2-(octadecylamino)-3-phenylpropanoyl]amino}butyrate (TC₁₈PheBu) and 1,3:2,4-di-O-benzylidene-D-sorbitol (DBS) was investigated by steady-state and varying temperature fluorescence, polarized fluorescence and time-resolved fluorescence techniques. The results showed that the fluorescence intensities of AO in the gels remarkably increased in comparison with AO aqueous solutions, and increased with an increase of the gelator concentrations. The varying temperature fluorescence analysis indicated that fluorescence intensities of AO in the gels decreased upon an increase of temperature, and vice versa. This can be attributed to aggregation and dissociation of the gelators in the systems, since the fluorescence enhancement of AO was induced by self-assembly of the gelators. Polarized fluorescence analysis indicated that the values of anisotropy (*r*) of AO are significantly higher than that in water. This further confirmed that the three-dimensional network formed by the gelator aggregates constrained the rotation of AO entrapped within the gels, resulting in high values of anisotropy. Time-resolved fluorescence analysis indicated that the rates of fluorescence decay in the gels are lower than that in water. These results reveal thermo-reversibility of the fluorescence enhancement of AO in supramolecular hydrogels.

© 2008 Elsevier B.V. All rights reserved.

1. Introduction

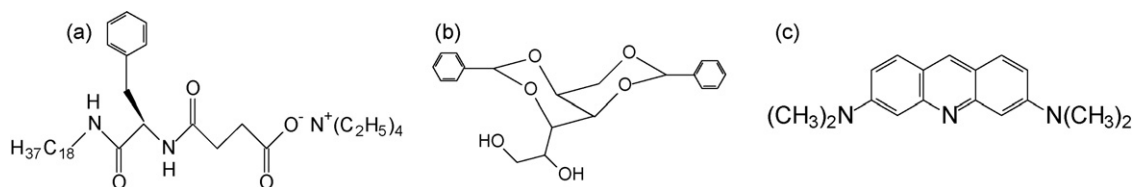
Gelation of organic or aqueous fluids by low molecular weight gelators has been the subject of increasing attention [1,2]. These gelators can self-assemble into three-dimensional network structures at low concentration, ultimately resulting in formation of supramolecular organogels or hydrogels. The thermo-reversibility and chemical sensitivity of supramolecular gels plays an important role in potential applications, including drug delivery systems [3], templates for preparation of nano-materials [4], gel electrolytes [5] and molecular recognition [6]. The fluorescence enhancement occurring in supramolecular gels has received particular attention in recent years.

The investigations of fluorescence enhancement in supramolecular gels are mainly concerned with the fluorescence arising from the gelator with fluorescent moieties. Park and co-workers utilized a fluorescent trifluoromethyl-based cyanostilbene derivative as gelator to gelatinize tetrahydrofuran (THF) and found that its fluorescence intensity in the gels was 460 times stronger than that in THF solution [7]. Ihara and co-workers found that the

fluorescence intensity of the resultant organogel was more than 1000 times higher than that of the solution when salicylideneaniline derivative with cholesterol moieties was used as gelator [8]. Strongly enhanced emission and a longer lifetime were found in the binary gels based on L-tartaric acid and stilbazoles compared with that in the original solution [9,10]. The fluorescence behaviors of guest molecules in supramolecular gel, for example, the energy transfer from the fluorescent moieties of a supramolecular hydrogel toward a hosted fluorophore [11] and the fluorescent lifetime of 8-anilino-1-naphthalene sulfonic acid (ANS) in supramolecular hydrogels [12] are also reported. Seo and Chang found that the fluorescence intensity of norfloxacin in organogel was 10 times stronger than that in the corresponding solutions when using this gel as norfloxacin carrier [13]. These investigations mainly involved the fluorescence enhancement arising from the gelator with fluorescent moieties in supramolecular gels. However, little attention has been paid to the fluorescence enhancement of specific fluorescent substances as guest entrapped in supramolecular hydrogels. Particularly, the temperature dependence of the fluorescence enhancement of the guest molecules in supramolecular gels has not been reported to our knowledge.

Taking into account that the thermo-reversibility is an important property of supramolecular gels, we have prepared two types of supramolecular hydrogels through the self-assembly of the

* Corresponding author. Tel.: +86 27 87547141; fax: +86 27 87543632.
E-mail address: yjyang@mail.hust.edu.cn (Y. Yang).



Scheme 1. Molecular structures of TC₁₈PheBu (a), DBS (b) and AO (c).

gelator 3-[[[(2R)-2-(octadecylamino)-3-phenylpropanoyl]amino]butyrate (TC₁₈PheBu) [14] and 1,3:2,4-di-O-benzylidene- β -sorbitol (DBS) in water and in dimethyl sulfoxide/water (DMSO/H₂O, 1/2, v/v), respectively. acridine orange (AO) was used as the guest fluorescent molecule. Scheme 1 shows the molecular structures of these compounds. The temperature dependence of the fluorescence enhancement was mainly investigated by using varying temperature fluorescence and polarized fluorescence techniques. Potential applications of our results in drug delivery and fluorescent sensors are envisaged.

2. Experimental

2.1. Materials

Acridine orange hemi (zinc chloride) salt (AO) was purchased from Sigma–Aldrich. Gelator 3-[[[(2R)-2-(octadecylamino)-3-phenylpropanoyl]amino]butyrate (TC₁₈PheBu) was synthesized according to the procedure described previously [14]. 1,3:2,4-di-O-benzylidene- β -sorbitol (DBS) was purchased from Hubei Huabang Chemicals Ltd. Dimethyl sulfoxide (DMSO) is of analytical grade and used as received. Ultrapure water was produced by a Millipore Direct-Q system.

2.2. Preparation of supramolecular hydrogels

In a 5 mm cuvette, a weighed amount of TC₁₈PheBu was mixed with an AO (1.0×10^{-7} mol/L) aqueous solution. The mixture was heated in a water bath (ca. 85 °C) until the solid completely dissolved and subsequently allowed to cool to room temperature. The resultant supramolecular hydrogels (designated as TC₁₈PheBu gel) were placed in the dark for 3 h before testing. Similarly, supramolecular hydrogels were prepared by mixing of DBS and DMSO/H₂O (1/2, v/v) with AO (designated as DBS gel). An AO aqueous solution was used as a reference.

2.3. Fluorescent and polarized optical microscopies

The gel samples containing AO (1.0×10^{-5} mol/L) were prepared on a glass plate according to the methods described above. The samples were measured by fluorescent optical microscopy (FOM, IX71, Olympus) and polarized optical microscopy (POM, BH-2, Olympus).

2.4. Photophysical measurements

Steady-state and polarized fluorescence measurements were performed with a spectrofluorimeter (FP-6500, Jasco) equipped with a heating/cooling temperature controller and polarizing prisms. The anisotropy values (r) were calculated using the following equations [15]:

$$r = \frac{I_{VV} - GI_{VH}}{I_{VV} + 2GI_{VH}} \quad G = \frac{I_{HV}}{I_{HH}}$$

Herein I is the emission intensity and G is instrumental correction factor. The subscripts denote the orientation (H for horizontal and V for vertical) of the excitation and emission polarizer. The excitation wavelength was 460 nm and emission wavelength was 525 nm.

2.5. Measurements of time-resolved fluorescence [16]

The time-resolved fluorescence of the gels and solutions were recorded on a luminescence spectrometer (Victor3, PerkinElmer) with a setting of 2 μ s counting window, 340 nm of excitation wavelength and 535 nm of emission wavelength. The count cycle was 1000 μ s. The volume of all samples was 250 μ L.

3. Results and discussion

3.1. Fluorescent phenomena of AO in supramolecular hydrogels

As shown in Fig. 1, the fluorescent molecule acridine orange exhibits different fluorescent phenomena in water and in supramolecular hydrogels formed by the gelators. Fig. 1A shows the fluorescent optical microscopy image of an AO aqueous solution, indicating that no fluorescent phenomenon is observed. Fig. 1B and D shows FOM images of AO entrapped within both the TC₁₈PheBu gel and the DBS gel. The isolated fluorescent spots can be clearly observed, indicating strong fluorescence emission of AO. Apparently, such distinct fluorescent phenomena of AO should be attributed to the special local environment within the supramolecular hydrogels. As we reported previously, TC₁₈PheBu can self-assemble through intermolecular interactions in water into fibrillar aggregates with diameters in the range of 40–60 nm [14]. Fig. 1C and E shows polarized optical microscopy images of the TC₁₈PheBu gel and the DBS gel, respectively. The observed pattern in Fig. 1C exhibits tree branch-like crystallites consisting of

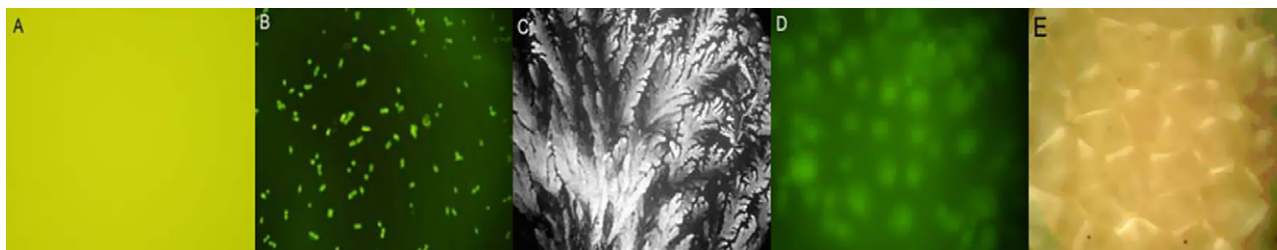


Fig. 1. (A) FOM image of an AO aqueous solution (400 \times). (B and C) FOM and POM images of TC₁₈PheBu gels (200 \times). (D and E) FOM and POM images of DBS gels (200 \times).

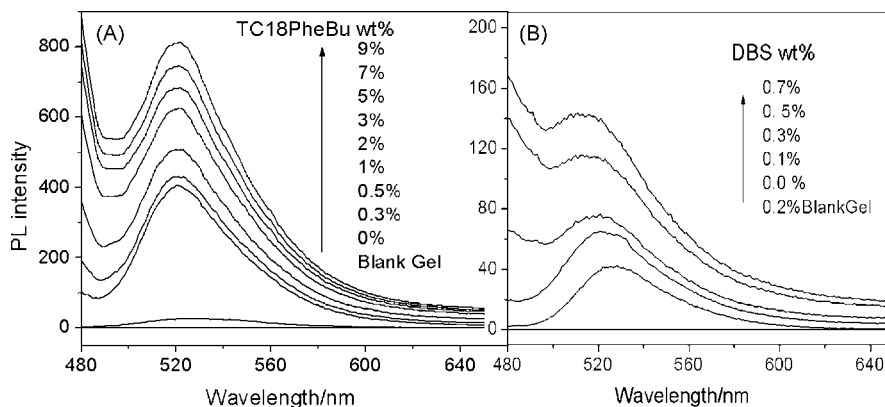


Fig. 2. Fluorescent spectra of AO versus the concentrations of TC₁₈PheBu (A) and DBS (B).

TC₁₈PheBu aggregates. The typical Maltese cross in Fig. 1E reveals the spherical crystallites consisting of DBS aggregates. These gelator aggregates further entangle each other and ultimately form three-dimensional networks. TC₁₈PheBu is an organic compound with long hydrophobic chains and DBS is also a strong hydrophobic compound. Since local environments surrounding their aggregates are hydrophobic, homogenous aqueous solution becomes heterogeneous gel system. In this case, hydrophilic AO was entrapped within the hydrophilic micro-environment formed by the three-dimensional network, leading to more heterogeneous dispersion of AO in the system. As a result, distinct fluorescent phenomena in water and the supramolecular hydrogels are observed.

To further study the fluorescence phenomena of AO in supramolecular hydrogels, steady-state fluorescence spectra of AO in both gels with varied concentration of gelators were measured. Results are shown in Figs. 2 and 3.

In Fig. 2, it was found that there was no fluorescence in both blank TC₁₈PheBu gels and the DBS gels (gels without AO). A slight blue shift of fluorescence spectra of AO in DBS gel from 524 to 511 nm was observed, which may result from the lower polarity of the supramolecular gel in comparison with corresponding solution [17]. From Fig. 3, the fluorescent intensity of the AO aqueous solution at maximum emission wavelength was very low (ca. 25). Interestingly, the fluorescent intensities of AO in both gels dramatically increased upon the formation of gelator aggregates. For instance, the fluorescent intensity of AO in a TC₁₈PheBu gel formed by 9.5 wt% of TC₁₈PheBu was 33 times stronger than that of an AO solution. Similarly, the fluorescent intensity of AO in a DBS gel

formed by 0.7 wt% of DBS was approximately 3 times stronger than that of an AO solution. Thus, the present results imply that the fluorescence enhancement of AO is induced by the self-assembly of the gelator.

3.2. Time-resolved fluorescence of AO in supramolecular hydrogels

In general, long fluorescent lifetimes imply strong fluorescent intensities. Fig. 4 shows the fluorescent lifetime decay of AO in water and in both gels. In the case of the TC₁₈PheBu gel, the decay rates of the fluorescent lifetime were slower than that of an aqueous solution. In the case of the DBS gel, the decay rates of the fluorescent lifetime for both the solution and gel were rather close. It explains the low times of fluorescent enhancement in DBS gels as shown in Fig. 3B. According to the Stokes–Einstein equation [13], the rotation correlated time of fluorescent molecules is related to the viscosity of the system and the molecular volume, i.e. the higher the viscosity and the larger the molecular volume, the longer the rotation correlated time. Apparently, the viscosity of both gels is much higher than that of aqueous solutions although their viscosities have not been exactly determined herein. As discussed for Fig. 1, AO is isolated by a three-dimensional network consisting of gelator aggregates. Under these circumstances, the formation of gelator aggregates restricts the rotation and vibration of AO molecules. In other words, the possibility of nonradiative relaxation is reduced, as, for example, collision quenching between AO molecules. Since the DBS gel formed by 0.2 wt% of DBS, contain low density three-

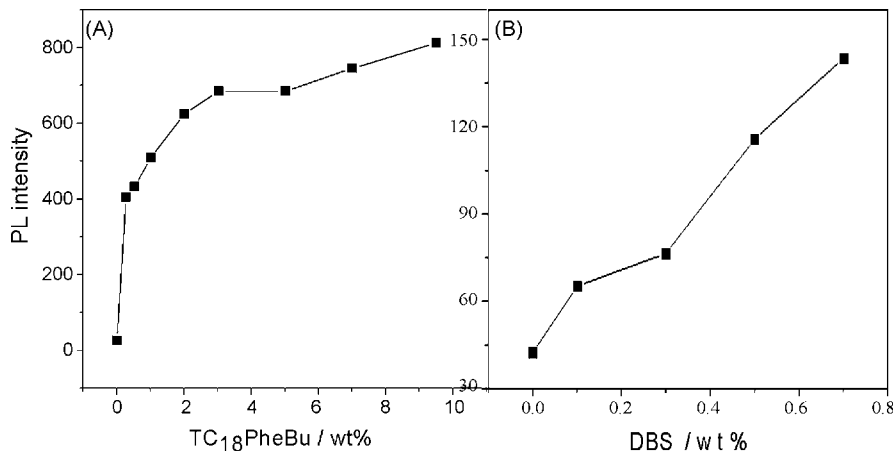


Fig. 3. Fluorescent intensities of AO at the maximum emission wavelength versus the concentrations of TC₁₈PheBu (A) and DBS (B).

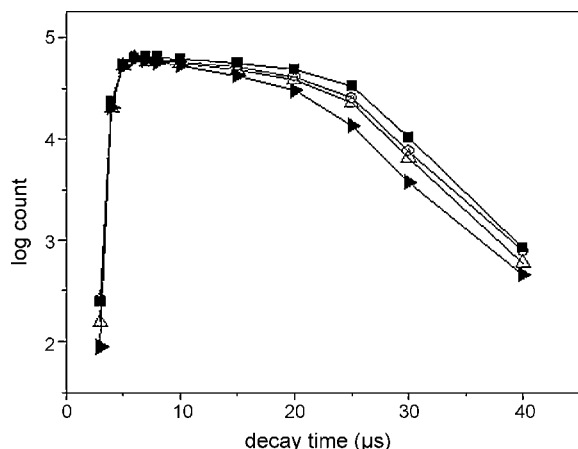


Fig. 4. Time-resolved fluorescence of AO in both gels and corresponding solutions. (▲ and ■) AO in water and in TC₁₈PheBu gel formed by 2 wt% of TC₁₈PheBu. (△ and ○) AO in DMSO/H₂O solution and in DBS gel formed by 0.2 wt% of DBS.

dimensional networks, the decay rates of fluorescent lifetime for both the DBS solution and the DBS gel are rather similar.

Supramolecular hydrogels formed by gelators show typical thermo-reversibility mainly due to the temperature dependence of the aggregation and dissociation of gelators. Herein, varying tem-

perature fluorescence spectra of AO in both gels were measured (Fig. 5). Obviously, the fluorescent intensities of AO in both gels at the maximum emission wavelength decreased gradually with an increase of temperature. It was found that the fluorescent intensities of an AO solution were almost temperature independent. The tendency in the decrease became smaller in the temperature range between 50 and 65 °C, indicative of a gel–sol transition, which can be attributed to the dissociation of gelator aggregates. The gel–sol transition temperature for the gel formed 2 wt% of TC₁₈PheBu was ca. 50 °C [14]. In our experiment, it was ca. 61 °C for the gel formed by 0.2 wt% of DBS. When the system was allowed to cool to 25 °C, the fluorescent intensities of AO in both gels became again the same as those in the initial status due to self-assembling of the gelator. As discussed for Fig. 1, gelator aggregates further entangle each other and ultimately form three-dimensional networks. This network structure starts to relax and collapse due to dissociation of gelator aggregates during the process of temperature rising, leading to the decreased fluorescent intensities of AO. This further confirms the suggestion in the discussion of Figs. 2 and 3, namely that the fluorescence enhancement of AO is induced by self-assembly of the gelator. Like thermo-reversibility of supramolecular gels, fluorescence enhancement of AO in supramolecular hydrogels also exhibits thermo-reversibility, which could be valuable for the development of fluorescent sensors and fluorescent switches.

Considering the relationship between the anisotropy values (r) arising from polarized fluorescence spectra and local environment

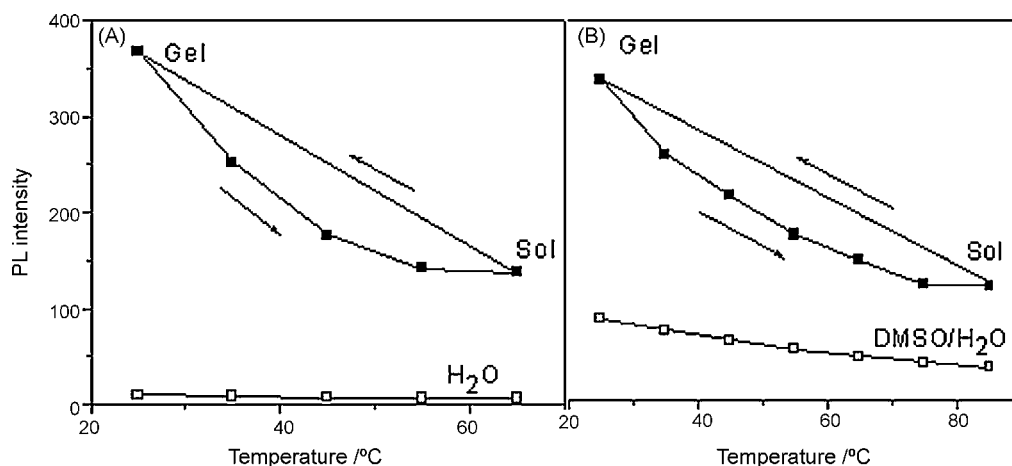


Fig. 5. Fluorescent intensities of AO in TC₁₈PheBu gel formed by 2 wt% of TC₁₈PheBu (A) and DBS gel formed by 0.2 wt% of DBS (B) versus temperature. (■) Gels. (□) Solutions.

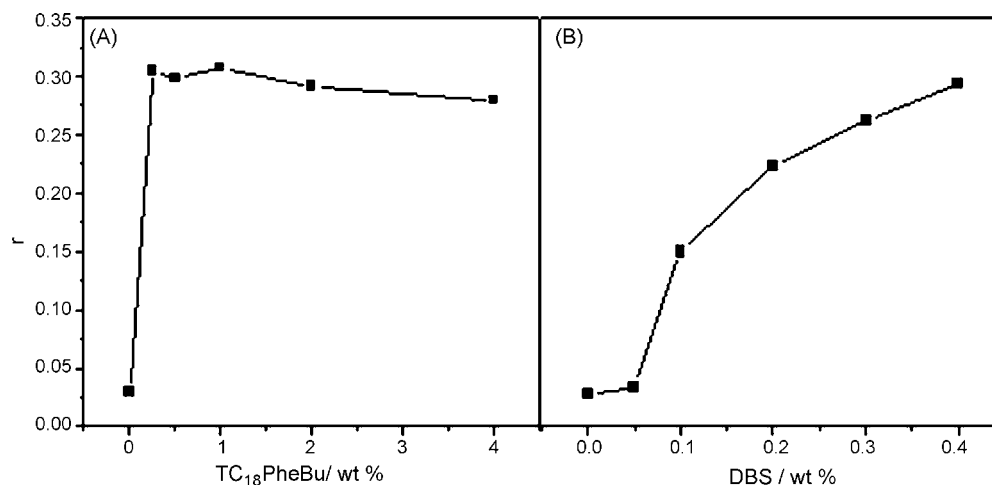


Fig. 6. The values of anisotropy (r) of AO within both gels versus the concentrations of TC₁₈PheBu (A) and DBS (B).

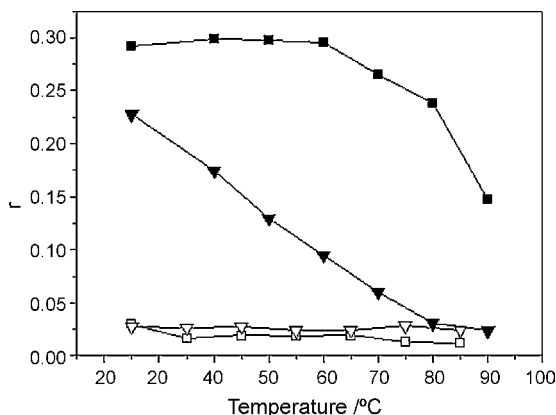


Fig. 7. The anisotropy values of AO in both gels versus temperature. (■ and □) AO in TC₁₈PheBu gels formed by 2 wt% of TC₁₈PheBu and in water, respectively. (▼ and ▽) AO in DBS gels formed by 0.2 wt% of DBS and DMSO/H₂O solutions.

where fluorescent molecules are entrapped, polarized fluorescence spectra of AO in both gels were measured (Fig. 6). The anisotropy values of AO were rather small in water and in DMSO/H₂O solutions. In general, the value of the anisotropy is related to the rates of rotation of fluorescent substances, which depends upon the local environment where the fluorescent molecules are entrapped. For instance, the values of anisotropy were very small (ca. 0.03) when AO was dissolved in water or in DMSO/H₂O solutions. However, these values were 10 times larger (ca. 0.3) when AO was entrapped in both gels formed by 2 wt% of TC₁₈PheBu and 0.4 wt% of DBS, respectively. The distinct difference could be ascribed to restriction of the rotation of AO within the three-dimensional networks formed by gelator aggregates, resulting in a rapid increase of the values of anisotropy. This result confirms that fluorescence enhancement of AO entrapped within the gel is induced by self-assembly of the gelator as discussed for Figs. 2 and 3. We note that the values of anisotropy in TC₁₈PheBu gel did not further increase with an increase of the TC₁₈PheBu concentration. In the case of the DBS gel, anisotropy values could not be obtained when higher concentration of DBS was applied due to the restricted solubility of DBS in DMSO/H₂O solutions. This result is consistent with the discussion of Figs. 2 and 3 (vide supra).

Fig. 7 shows the relationship of the anisotropy values of AO at λ_{\max} (525 nm) and temperature. Obviously, the values of anisotropy of AO in water and in DMSO/H₂O solutions was almost independent of the temperature. In the case of the TC₁₈PheBu gel, the anisotropy values of AO remained constant when the temperature was below the gel–sol transition temperature (ca. 50 °C). However, they rapidly decreased when the temperature was higher than the gel–sol transition temperature. At 90 °C, the value of anisotropy was only 50% of initial status. In the case of the DBS gel, the trend of the decrease differed from that of the TC₁₈PheBu gel, which be rationalized by the different molecular structures and local viscosities where AO is entrapped. However, quite generally the value of anisotropy decreased with an increase of temperature. As discussed

above, three-dimensional network structures relaxed and collapsed when the temperature is increased, resulting in a decrease of the anisotropy values due to AO molecules which are now free from the restriction.

4. Conclusions

Fluorescent AO entrapped within supramolecular hydrogels formed by TC₁₈PheBu and DBS shows typical fluorescent enhancement in comparison with aqueous AO solutions. Steady-state fluorescence spectra of AO in supramolecular hydrogels indicate that the fluorescence enhancement of AO is induced by self-assembly of the gelators. The decay rates of fluorescent lifetimes of AO in both gels were slower than that of an aqueous AO solution. Varying temperature fluorescence spectra of AO in both gels reveal thermo-reversibility of these fluorescent enhancements, which could be significant for the development of fluorescent sensors and switches. Polarized fluorescence spectra of AO in supramolecular hydrogels indicate that the anisotropy values of AO increased with an increase of the gelator concentrations and decreased with an increase of temperature. This is ascribed to the collapse of three-dimensional network structures, resulting in freeing of AO from restriction in rotation. These observations confirm that fluorescence enhancement of AO entrapped within the gel is induced by self-assembly of the gelator.

Acknowledgments

Financial support from National Key Scientific Research Program of China (No. 2006CB933301) is gratefully acknowledged. We thank the Analytical and Testing Center of HUST for the fluorescence measurements.

References

- [1] P. Terech, R.G. Weiss, *Chem. Rev.* 97 (1997) 3133.
- [2] M. George, R.G. Weiss, *Acc. Chem. Res.* 39 (2006) 489.
- [3] S. Cao, X. Fu, N. Wang, H. Wang, Y. Yang, *Int. J. Pharm.* 357 (2008) 95.
- [4] M. Kimura, S. Kobayashi, T. Kuroda, K. Hanabusa, H. Shirai, *Adv. Mater.* 16 (2004) 335.
- [5] Y. Meng, Y. Yang, *Electrochem. Commun.* 9 (2007) 1428.
- [6] X. Fu, Y. Yang, N. Wang, H. Wang, Y. Yang, *J. Mol. Recognit.* 20 (2007) 238.
- [7] B.K. An, D.S. Lee, J.S. Lee, Y.S. Park, H.S. Song, S.Y. Park, *J. Am. Chem. Soc.* 126 (2004) 10232.
- [8] P. Xue, R. Lu, G. Chen, Y. Zhang, H. Nomoto, M. Takafuji, H. Ihara, *Chem. Eur. J.* 13 (2007) 8231.
- [9] C. Bao, R. Lu, M. Jin, P. Xue, C. Tan, G. Liu, Y. Zhao, *Org. Biomol. Chem.* 3 (2005) 2508.
- [10] H. Yang, T. Yi, Z. Zhou, Y. Zhou, J. Wu, M. Xu, F. Li, *Langmuir* 23 (2007) 8224.
- [11] M. Montalti, L.S. Dolc, L. Prodi, N. Zaccaroni, M.C.A. Stuart, K.J.C. van Bommel, A. Friggeri, *Langmuir* 22 (2006) 2299.
- [12] S. Mukhopadhyay, Krishnamoorthy S Ira G., U. Maitra, *J. Phys. Chem. B* 107 (2003) 2189.
- [13] S.H. Seo, J.Y. Chang, *Chem. Mater.* 17 (2005) 3249.
- [14] X. Fu, N. Wang, Y. Yang, *J. Colloid Interf. Sci.* 315 (2007) 376.
- [15] K. Das, E. Dertz, J. Paterson, W. Zhang, G.A. Kraus, J.W. Petrich, *J. Phys. Chem. B* 102 (1998) 1479.
- [16] R. Thakar, Y. Chen, P.T. Snee, *Nano Lett.* 7 (2007) 3429.
- [17] L. Wang, Y. Shao, J. Zhang, M. Anpo, *Opt. Mater.* 28 (2006) 1232.



Comparison of tungsten coil electrothermal vaporization and thermospray sample introduction methods for flame furnace atomic absorption spectrometry

Peng Wu^a, Yunchang Zhang^{b,1}, Rui Liu^b, Yi Lv^b, Xiandeng Hou^{a,b,*}

^a Analytical & Testing Center, Sichuan University, Chengdu, Sichuan 610064, China

^b College of Chemistry, Sichuan University, Chengdu, Sichuan 610064, China

ARTICLE INFO

Article history:

Received 20 July 2008

Received in revised form 7 October 2008

Accepted 7 October 2008

Available online 19 October 2008

Keywords:

Flame furnace

Atomic absorption spectrometry

Tungsten coil

Electrothermal vaporization

Thermospray

ABSTRACT

Flame furnace atomic absorption spectrometry (FF-AAS) is a newly developed flame atomic absorption spectrometric technique based on arranging a flame furnace onto the top of the flame burner head. In this fundamental investigation, 25 elements were carefully tested by using either thermospray FF-AAS or tungsten coil electrothermal vaporization FF-AAS, of which 15 volatile and semi-volatile elements (Cd, Tl, Ag, Pb, Zn, Hg, Cu, Sb, Bi, Te, In, As, Se, Sn and Au) exhibited better limits of detection compared to those by conventional FAAS; however, non-volatile or refractory elements (Fe, Co, Ni, Cr, Mn, Pd, Pt, Al, Be and V) showed inferior sensitivities by the proposed methods.

© 2008 Elsevier B.V. All rights reserved.

1. Introduction

Flame atomic absorption spectrometry (FAAS) nowadays is still one of the most frequently used analytical techniques for elemental determination [1]. However, its relatively low sensitivity largely hampers its further applications in ultratrace analysis. Conventionally, the detection power of FAAS can be improved by “atom trapping” techniques [2]. Recently, flame furnace AAS (FF-AAS) has been proposed by Gáspár and Berndt with two variants: beam injection FF-AAS [3–5] and thermospray FF-AAS [6–8]. In FF-AAS, a nickel or quartz tube is located in the standard air-acetylene flame as the atomization cell (flame furnace), and sample solution is introduced directly into the tube via beam injection or thermospray. The detection power can be greatly improved for volatile and semi-volatile elements in FF-AAS due to the complete introduction of sample solution and a prolonged residence time of atoms in the absorption zone.

Atomization temperature is a critical parameter in all types of atomic spectrometric techniques as it affects the atomization effi-

ciency directly. In FF-AAS, the temperature inside the flame furnace is about 1000 °C [9], which is much lower than that of the flame. The temperature is determined by the flame gas (about 2500 °C), its contact with the wall of the tube, and the amount of liquid sample introduced. It should be mentioned that the main practical limitation of the FF-AAS system is that the temperature inside the flame furnace is not high enough to promote efficient atomization, especially for less volatile elements such as Cr, Mg, Fe, Co and Ni [3]. Up to date, only those elements with low appearance temperatures (for instance, Cd, Pb, Hg and Cu) can find good analytical performance in FF-AAS [10–13]. The sensitivity improvement is associated with the volatility of the elements, i.e., the lower the appearance temperature of an element, the more significant sensitivity improvement [3,6].

Electrothermal vaporization (ETV) has long been considered as an excellent approach for introducing dry sample aerosol into plasma-based spectroscopic cells [14]. With ETV, the energy of the atomization cell itself is not wasted on the desolvation of the sample so that greater energy is available for atomization. An additional benefit of ETV is its capability to easily accommodate complex sample matrices. It is also a micro-analytical technique, capable of working with micro amount of liquid samples or even solid samples. Graphite furnace (GF) is the predominant ETV device in analytical atomic spectrometry [14,15], but tungsten coil vaporizers have also been used in analytical atomic spectrometry. GF vaporizers are typically originated from conventional graphite furnace

* Corresponding author at: Analytical & Testing Center, Sichuan University, Chengdu, Sichuan 610064, China. Tel.: +86 28 8541 5695.

E-mail addresses: houxu@scu.edu.cn, houxu@scu.edu.cn (X. Hou).

¹ Current address: National Institute of Measurement & Testing Technology, Sichuan 610021, China.

AAS (GF-AAS) and thus the outstanding characteristics of GF-AAS are thus well retained in GF vaporizers, such as high atomization efficiency and powerful capability for matrix removal during the pyrolysis step. On the other hand, the advantages of tungsten coil (W-coil) vaporizers include freedom from carbide forming interferences, lower surface porosity, higher heating rate, much lower power supply, and compactness [16–18]. It should be pointed out that W-coil ETV has disadvantages such as limited sampling volume, impurity of W-coil material, and lower temperature stability compared to graphite ETV. Nevertheless, W-coil has already been frequently used as an ETV for ICP-based spectrometry [19–22]. In this work, W-coil ETV is coupled to an FF-AAS system for introducing dry sample aerosol. Sample aerosol was first vaporized from the W-coil surface and then delivered into the flame furnace via a mixture of Ar and H₂ gas, and the temperature of the flame furnace would not be significantly lowered by sample introduction. In addition, thermospray FF-AAS was also investigated in order to compare the performance of the methods by introducing dry aerosol and liquid sample into FF-AAS.

2. Experimental

2.1. Instrumentation

A Model GGX-9 flame atomic absorption spectrometer (Geological Instrument Co., Beijing, China) equipped with a deuterium lamp for background correction was used in this work. The manufacturer-recommended working parameters (analytical wavelength, slit width, and hollow cathode lamp current) were used for the atomic absorbance measurements. A quartz tube (10/11 mm i.d./o.d., and 10.5 cm in length) was used as the flame furnace. The arrangement of the quartz tube on the flame was similar to our previous work [10]. Generally, 5.5 L/min air–1.5 L/min acetylene was used for the flame.

For thermospray sampling (mode A in Fig. 1), a peristaltic pump (Model HL-2D, Huxi Analytical Instrumental Co., Shanghai, China) was used to aid the sampling and a quartz capillary (10 cm in length and 0.4/1 mm i.d./o.d.) as the thermospray device. The quartz tube had additional holes on the bottom for the flame to spread in. For W-coil ETV (mode B in Fig. 1), a “T” type quartz furnace without

additional holes (4 cm in length for the “T” tip) was connected directly to the ETV device via a silica tube to minimize the dead volume of the transport. The construction of the W-coil ETV device is the same as described in our previous work [23]. A commercial DC power supply (HY 1791-10S, 0–30 V, Huai'an Yangguang Electronics Ltd. Co., Huai'an, China), which was redesigned and controlled by a Single Chip Micryoco (SCM), was used as a programmable power supply for the W-coil ETV. Mixed gas of Ar/H₂ was used as the carrier gas to deliver the sample aerosol into the flame furnace. For all elements, gas flow rates at 400 mL/min Ar and 80 mL/min H₂ were used.

An ICP-OES instrument (Iris Advantage, Thermo Jarrell Ash Corporation, MA, USA) was used to determine the possible analyte loss during W-coil ETV FF-AAS measurements. The major instrumental parameters were: power, 1150 W; sampling rate, 2.0 mL/min; nebulizer pressure, 27 psi; and integration time, 20 s. Analytical lines for each element were recommended by the manufacturer. Two-line scheme was used for the background correction.

2.2. Operation procedure

For thermospray sampling, a similar operation procedure as described in our previous report [10] was adapted; and for W-coil ETV sampling, 20 μ L sample solution was manually pipetted onto the coil surface through the sample introduction hole using a microsyringe. Then, a rubber plug was inserted into the hole, and the heating program was started: 3.2 A, 65 s for desolvation; 7.8 A, 5 s for vaporization; and 8.2 A, 4 s for cleaning.

3. Results and discussion

3.1. Optimization of major experimental conditions and general performance

In this work, 25 elements were investigated using either TS-FF-AAS or W-coil ETV-FF-AAS. The optimization for the W-coil ETV-FF-AAS determination was carried out first by evaluating the effect of argon and hydrogen flow rates, the vaporization temperature (the current) and the duration. Argon plays a key role in transporting the vaporized analyte aerosol from the W-coil ETV to the flame furnace. For most of the elements, when the argon flow rate was below 300 mL/min, the atomic absorbance signal increased with argon flow rate, but the precision of measurements was poor; when it was higher than 600 mL/min, decreased residence time of analyte atoms in the absorption zone led to decreased signal. Therefore, 400 mL/min of argon flow rate was chosen for the subsequent experiments. This result was somewhat different from the previous work involving W-coil ETV for sample introduction into quartz tube atomizer of Ar/H₂ flame atomic fluorescence spectrometry, probably because the dead volume in this work was smaller, as the W-coil electrothermal vaporizer was directly connected to the “T” type quartz flame furnace. Hydrogen was used to protect the tungsten coil from oxidation, and its flow rate of 80 mL/min was used as a compromise of safety consideration and effective protection of the W-coil. Considering efficient atomization/vaporization and safety, vaporization temperature was set at about 2000 °C (7.8 A) for 5 s for all elements.

All calibration curves were established by using single element standard solutions and peak-height absorbance for quantification. Limits of detection (LODs) were evaluated based on 3 σ of 11 measurements of a blank solution. Among these elements, 15 volatile and semi-volatile elements (Cd, Tl, Ag, Pb, Zn, Hg, Cu, Sb, Bi, Te, In, As, Se, Sn and Au) exhibited improved LODs compared to those of conventional FAAS (Table 1); other elements (Fe, Co, Ni, Cr, Mn, Pd,

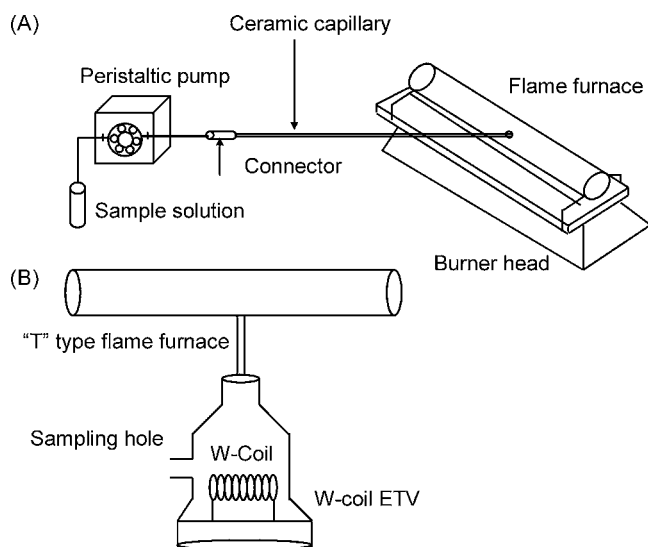


Fig. 1. Instrumental arrangement of flame furnace AAS system (not to scale). (A) thermospray; and (B) W-coil electrothermal vaporization. In thermospray, the quartz tube with additional holes facing flame was used, while in W-coil electrothermal vaporization, the “T” type quartz tube had no additional holes.

Table 1Limits of detection (3σ) and upper linear ranges for 21 elements by TS-FF-AAS and W-coil ETV-FF-AAS, respectively, in comparison with those by FAAS and GF-AAS.

Element	Limits of detection ($\mu\text{g/L}$)				Upper linear range ($\mu\text{g/mL}$)			Improved power of detection (over FAAS) ^a		Temperature of GF-AAS ($^{\circ}\text{C}$) ^b	
	FAAS	GF-AAS ^c	TS-FF-AAS	W-coil ETV ^d	FAAS	TS-FF-AAS	W-coil ETV	TS-FF-AAS	W-coil ETV	Pyrolysis	Atomization
Cd	20	0.002	0.5	0.5	2	0.1	0.05	34	39	300	900
Ag	40	0.005	4	0.9	5	0.4	0.2	13	21	450	1100
Pb	400	0.05	25	25	40	2	0.6	25	31	800	1200
Tl	300	0.1	20	10	50	2	0.5	20	30	700	1200
Hg	3000	0.6	700	–	500	20	–	20	–	200	750
Zn	40	0.02	2	3	2	0.05	0.1	16	15	700	1100
Cu	120	0.014	5	2	6	0.2	0.2	15	17	850	2100
Sb	500	0.05	20	15	50	2	1	34	34	800	2300
Bi	100	0.05	20	15	20	2	0.5	19	30	350	1600
Te	200	0.1	10	10	20	2	1	23	22	400	2300
Sn	30000	0.1	900	1000	500	20	40	102	46	800	2300
In	500	–	300	10	50	10	1	4	43	750	2100
As	20000	0.05	600	30	100	10	10	26	18	400	2100
Se	2000	0.05	100	100	20	2	5	20	6	300	2300
Au	200	0.15	200	50	20	5	10	1.8	1.2	800	1900
Fe	100	0.06	4000	250	10	50	10	0.045	0.6	1100	2100
Co	100	0.15	1000	300	5	20	10	0.15	0.27	1100	2100
Ni	80	0.07	400	200	10	10	5	0.33	0.26	1000	2500
Cr	100	0.004	–	250	100	–	5	–	0.34	1200	2500
Mn	20	0.005	400	10	2	20	0.5	0.2	2.4	900	1800
Pd	150	0.09	600	200	5	10	5	0.4	1	1100	2200

^a Defined as the slope ratio of calibration curves by the proposed method to FAAS.^b Recommended by Thermo-Electron Corporation.^c Values from Ref. [24], with 50 μL sample volume.^d Based on a sampling volume of 20 μL .

Pt, Al, Be and V) involved in this work are non-volatile or refractory elements, and inferior sensitivity over direct FAAS was observed for these elements by TS-FF-AAS or W-coil ETV-FF-AAS. Although marked sensitivity increase was obtained by FF-AAS, it cannot rival GF-AAS which still represents one of the most sensitive approach for elemental analysis [24]. Details are further discussed in the following sections.

3.2. Volatile and semi-volatile elements

FF-AAS has exhibited better performance for volatile and semi-volatile elements, especially for Hg, Cd, Pb and Zn, over traditional FAAS [3,6,8]. Such effects were also observed in the present work using either thermospray or W-coil ETV as the sampling tool for FF-AAS. Meanwhile, it was found that the typical linear range of the calibration curve for W-coil ETV FF-AAS was shorter than that of TS-FF-AAS (Table 1), just as the case of GF-AAS in comparison with FAAS. It can be seen from Table 1 that the improved power of detection of W-coil ETV-FF-AAS over FAAS is generally larger than that of TS-FF-AAS for most elements except Sn, As and Se. In TS-FF-AAS, the energy of flame furnace is partially used for desolvation of aqueous sample and not totally for atomization, so the sampling volume should be strictly controlled to achieve the best analytical performance. In this work, 20 μL sample solution was chosen for use; and for the purpose of comparison, 20 μL sample solution was also injected for W-coil ETV-FF-AAS measurements. One of the advantages of ETV is that it permits the atomization source to drive its full energy for atomization/ionization. For Hg, however, no appreciable signal was obtained by W-coil ETV-FF-AAS because it was totally vaporized in the desolvation step due to the extremely high volatility of its metal form.

The analyte transport efficiency in electrothermal vaporization has been carefully studied by Holcombe et al. in ETV-ICP-MS system [25,26], and they found that analyte loss was inevitable during the transport. Although the dead volume in this work was greatly

minimized, the analyte loss was still observed during the transport; and the analyte loss was higher in the case of W-coil ETV. The ICP-OES results showed that Cu, Sn and Au were detectable in the washing solutions of the vaporization cell as well as the connection tube (treated with 10 mL nitric acid after the measurements of the calibration curves). Therefore, the driven force for the sensitivity difference of TS-FF-AAS and W-coil ETV FF-AAS is probably the temperature/energy for atomization in the flame furnace. In fact, transport tubes of different length were also tested for Cd, Pb and Ag, and decreased atomic absorbance signal with the length of the transport tube was observed as expected, and this further confirmed the analyte loss during their transport in W-coil ETV FF-AAS.

It is also interesting to find that although the W-coil ETV-FF-AAS for As and Se determination is not as sensitive as TS-FF-AAS, the LODs obtained by W-coil ETV-FF-AAS are better than (As) or equivalent (Se) to those by TS-FF-AAS. The resonance lines of As (193.7 nm) and Se (196.0 nm) lie in the vacuum ultraviolet region (<200 nm), so flame gases cause serious background and lead to poor precision by FAAS. In TS-FF-AAS, a tube (flame furnace) with additional holes for flame gases to enter in was used, and this deteriorates the blank signals during the low temperature atomization [27]. In W-coil ETV-FF-AAS, on the other hand, a “T” type tube without additional holes was employed and better stability for blank signals was obtained, leading to improved LODs over TS-FF-AAS.

3.3. Non-volatile elements

Non-volatile elements investigated in this work includes Fe, Co, Ni, Cr, Mn and Pd. Gáspár and Berndt have reported that the sensitivity for Na, Li, Mg, Mn, Cr, Fe, Co and Ni by FF-AAS was lower than that by conventional FAAS [3], and this was also true in the present work except Mn by W-coil ETV-FF-AAS (Table 1). Although Donati et al. used TS-FF-AAS to determine Co in biological samples,

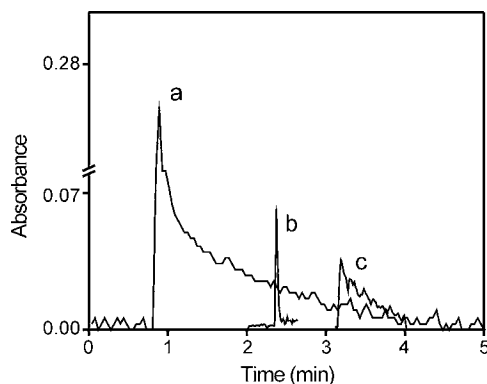


Fig. 2. Atomic absorption profiles of iron obtained by TS-FF-AAS and W-coil ETV-FF-AAS. (curve a) 20 $\mu\text{g/mL}$ Fe by W-coil ETV-FF-AAS; (curve b) 5 $\mu\text{g/mL}$ Fe by W-coil ETV-FF-AAS; and (curve c) 20 $\mu\text{g/mL}$ Fe by TS-FF-AAS.

derivatization of Co with APDC is needed based on the thermochemical behavior of Co-PDC complex [28]. Most probably the high appearance temperature for these elements led to the sensitivity loss by FF-AAS, and no calibration curve can even be established for Cr using TS-FF-AAS in this work because of the relatively low temperature of flame furnace.

ICP-OES analysis showed that appreciable amount of analyte was condensed in the transport tube and the flame furnace. Because the appearance temperatures of these elements are higher than those volatile and semi-volatile elements, after sputtering from the tungsten coil, their free atoms are prone to congregate together and condensed on the inner wall of the tube. Fig. 2 showed the typical Fe signal profiles obtained by TS-FF-AAS and W-coil ETV-FF-AAS, and the phenomena were generally the same for other elements. In TS-FF-AAS, the signal tailing is serious (Fig. 2 curve c). After Fe solution entering into the flame furnace, due to its high appearance temperature and the low energy of flame furnace, very small amount of Fe can be atomized, and this leads to the low sensitivity of TS-FF-AAS. Meanwhile, the relatively “cold” tube wall can trap free atoms, subsequent release of Fe atoms from the flame furnace is expected to be much slower than that of volatile elements [29], leading to a tailed signal profile.

For W-coil ETV-FF-AAS, a well-shaped signal profile can be obtained at a low concentration of Fe (Fig. 2 curve b), while the signal tailing can also occur at a high concentration (Fig. 2 curve a). Most probably in W-coil ETV, the temperature of the flame furnace would not decrease significantly upon the sample introduction, and thus the trap effect of the furnace toward the atom cloud is minimal when the atom population is small. But the trap did exist because the signal profile tailed again at a higher concentration (Fig. 2 curve a).

The results of Mn determination by TS-FF-AAS in this work is different from Nascentes et al.’s results for direct determination of Mn in beer samples, in which a sevenfold of detection limit improvement was obtained [30]. This is probably originated from different experimental conditions, such as geometry and analyte medium, thus leading to varied atomization mechanism and efficiency.

3.4. Refractory elements

In this work, we also investigated some refractory metals, namely Pt, Al, Be and V, by TS-FF-AAS and W-coil ETV-FF-AAS, respectively. None of these elements produced measurable signals in either TS-FF-AAS or W-coil ETV-FF-AAS. It is known that nitrous oxide-acetylene flame is usually used for these elements

in FAAS [31,32], and the pyrolysis temperatures and atomization temperatures for these elements are above 1200 °C and 2600 °C, respectively. It is obvious that the flame furnace cannot atomize these elements, so neither TS-FF-AAS nor W-coil ETV-FF-AAS is good for the determination of these elements. Besides, the common atomization mechanism for these elements is often a three-step process in graphite furnace [33]. Take Al as an example, aluminum salt firstly decomposes to Al_2O_3 at 1100 K, then Al_2O_3 vaporizes at 1750 °C and enters into the gas phase to disassociate to AlO. Finally, free Al atoms are generated by pyrolytic decomposition of AlO. Obviously, the energy of the flame furnace can only satisfy the first step in TS-FF-AAS. In W-coil ETV-FF-AAS, the energy of W-coil may be enough for the atomization of Al [34], but free Al atoms would quickly condensate on the transport tube as well as the flame furnace, and this was also confirmed with ICP-OES analysis.

4. Conclusion

W-coil ETV was employed to deliver dry sample aerosol into the flame furnace, and it compared favorably with thermospray for sample introduction. The sensitivity improvement of different elements was directly associated with their volatility. For the volatile and semi-volatile elements, the sensitivity of W-coil ETV and thermospray sampling was similar; while for those non-volatile elements, W-coil ETV was generally better because the energy of the flame furnace is not needed for desolvation. In the case of refractory elements, neither thermospray nor W-coil ETV sampling can gain detectable sensitivity as the low temperature flame furnace cannot atomize these elements efficiently, and the analyte loss is significant during the sample transport in the case of W-coil ETV-FF-AAS.

Acknowledgements

Xiandeng Hou acknowledges the financial support for this project from the National Natural Science Foundation of China [No. 20675053] and the Ministry of Education of China [20070610008].

References

- [1] B. Welz, M. Sperling, *Atomic Absorption Spectrometry*, Wiley-VCH, Weinheim, 1999.
- [2] H. Matusiewicz, *Spectrochim. Acta B* 52 (1997) 1711.
- [3] A. Gáspár, H. Berndt, *Anal. Chem.* 72 (2000) 240.
- [4] A. Gáspár, H. Berndt, *Anal. Bioanal. Chem.* 372 (2002) 695.
- [5] J. Neira, H. Berndt, *Fresenius J. Anal. Chem.* 368 (2000) 649.
- [6] J. Davies, H. Berndt, *Anal. Chim. Acta* 479 (2003) 215.
- [7] A. Gáspár, E. Szeles, H. Berndt, *Anal. Bioanal. Chem.* 372 (2002) 136.
- [8] A. Gáspár, H. Berndt, *Spectrochim. Acta B* 55 (2000) 587.
- [9] M.L. Brancalion, E. Sabadini, M.A.Z. Arruda, *Anal. Chem.* 79 (2007) 6527.
- [10] P. Wu, Y.C. Zhang, Y. Lv, X.D. Hou, *Spectrochim. Acta B* 61 (2006) 1310.
- [11] Y. Li, Y. Jiang, X.P. Yan, *Electrophoresis* 26 (2005) 661.
- [12] E. Ivanova, H. Berndt, E. Pulvermacher, *J. Anal. Atom. Spectrom.* 19 (2004) 1507.
- [13] E.R. Pereira-Filho, H. Berndt, M.A.Z. Arruda, *J. Anal. Atom. Spectrom.* 17 (2002) 1308.
- [14] H. Bin, S. Li, G.Q. Xiang, M. He, Z.C. Jiang, *Appl. Spectrosc. Rev.* 42 (2007) 203.
- [15] J.M. Carey, J.A. Caruso, *Crit. Rev. Anal. Chem.* 23 (1992) 397.
- [16] X.D. Hou, B.T. Jones, *Spectrochim. Acta B* 57 (2002) 659.
- [17] K. Levine, K.A. Wagner, B.T. Jones, *Appl. Spectrosc.* 52 (1998) 1165.
- [18] P. Wu, X.D. Wen, Y. Lu, X.D. Hou, *Chin. J. Anal. Chem.* 34 (2006) S278.
- [19] A.C. Davis, C.P. Calloway, B.T. Jones, *Talanta* 71 (2007) 1144.
- [20] A.C. Davis, B.W. Alligood, C.P. Calloway, B.T. Jones, *Appl. Spectrosc.* 59 (2005) 1300.
- [21] P. Barth, S. Hauptkorn, V. Krivan, *J. Anal. Atom. Spectrom.* 12 (1997) 1359.
- [22] P. Barth, S. Hauptkorn, V. Krivan, *J. Anal. Atom. Spectrom.* 12 (1997) 1351.
- [23] P. Wu, X.D. Wen, L. He, Y.H. He, M.Z. Chen, X.D. Hou, *Talanta* 74 (2008) 505.
- [24] Perkin-Elmer, *The Guide to Techniques and Applications of Atomic Spectroscopy*, Perkin-Elmer, Norwalk, 2003, p. 7.
- [25] G. Ertas, J.A. Holcombe, *Spectrochim. Acta B* 58 (2003) 1597.
- [26] J. Venable, J.A. Holcombe, *Spectrochim. Acta B* 56 (2001) 1431.
- [27] F. Rosini, C.C. Nascentes, J.Y. Neira, J.A. Nóbrega, *Talanta* 73 (2007) 845.

- [28] G.L. Donati, C.C. Nascentes, A.R.A. Nogueira, M.A.Z. Arruda, J.A. Nobrêga, *Microchem. J.* 82 (2006) 189.
- [29] P. Wu, R. Liu, H. Berndt, Y. Lv, X.D. Hou, J. *Anal. Atom. Spectrom.* 23 (2008) 37.
- [30] C.C. Nascentes, M.Y. Kamogawa, K.G. Fernandes, M.A.Z. Arruda, A.R.A. Nogueira, J.A. Nobrêga, *Spectrochim. Acta B* 60 (2005) 749.
- [31] J.B. Willis, *Spectrochim. Acta B* 52 (1997) 667.
- [32] J.B. Willis, *Nature* 207 (1965) 715.
- [33] B. Deng, *The Principles, Technologies and Applications of Atomic Absorption Spectrometry*, Tsing Hua Univ. Press, 2004.
- [34] P.O. Luccas, J.A. Nobrêga, P.V. Oliveira, F.J. Krug, *Talanta* 48 (1999) 695.



Fluorescence detection of total count of *Escherichia coli* and *Staphylococcus aureus* on water-soluble CdSe quantum dots coupled with bacteria

Xiuheng Xue^a, Jian Pan^{a,*}, Huiming Xie^a, Juhua Wang^b, Shuang Zhang^a

^a Engineering Research Center of Bio-Process, Ministry of Education, Hefei University of Technology, 193 Tun Xi Road, Hefei, Anhui 230009, China

^b College of Animal Science and Technology, Anhui Agricultural University, Hefei, Anhui 230036, China

ARTICLE INFO

Article history:

Received 18 June 2008

Received in revised form 13 October 2008

Accepted 14 October 2008

Available online 25 October 2008

Keywords:

Escherichia coli

Staphylococcus aureus

Rapid detection

Fluorescence

CdSe quantum dots

ABSTRACT

The aim of this paper was to demonstrate a fluorescence measurement method for rapid detection of two bacterial count by using water-soluble quantum dots (QDs) as a fluorescence marker, and spectrofluorometer acted as detection apparatus, while *Escherichia coli* (*E. coli*) and *Staphylococcus aureus* (*S. aureus*) were as detection target bacteria. Highly luminescent water-soluble CdSe QDs were first prepared by using thioglycolic acid (TGA) as a ligand, and were then covalently coupled with target bacteria. The bacterial cell images were obtained using fluorescence microscopy. Our results showed that CdSe QDs prepared in water phase were highly luminescent, stable, and successfully conjugated with *E. coli* and *S. aureus*. The fluorescence method could detect 10^2 – 10^7 CFU/mL total count of *E. coli* and *S. aureus* in 1–2 h and the low detection limit is 10^2 CFU/mL. A linear relationship of the fluorescence peak intensity and log total count of *E. coli* and *S. aureus* have been established using the equation $Y = 118.68X - 141.75$ ($r = 0.9907$).

© 2008 Elsevier B.V. All rights reserved.

1. Introduction

Rapid and sensitive detection of total bacteria count is extremely important in biotechnology, medical diagnosis, and food safety. Because of slow detection speed and complicated procedures, plate count, as a conventional method, could not ideally meet the requirements of fast and efficient microbe detection any more. Recently, several new methods including enzyme linked immunosorbent assay (ELISA) [1], polymerase chain reaction (PCR) [2], diffraction-based cell detection [3], and flow cytometry detection [4] have been reported. However, most of current available methods for detecting trace amounts of bacteria need either amplification or enrichment of the target bacteria in the sample, and moreover the apparatus are expensive. Therefore, simple and sensitive methods, which do not need target amplification or enrichment, are currently being pursued. It has been shown that fluorescence analysis is a rapid, technically simple, and efficient method for directly isolating target bacteria from originals or pre-enriching samples without any expensive apparatus [5,6]. Furthermore, demands of greater sensitivity, speed, and ease of manipulation in detecting microbes are also increasing as evidenced by fluorescent markers have been developed one after another [7–10].

Quantum dots (QDs), as novel fluorescent markers, have been applied broadly to biological imaging and analysis including cell staining [11,12], DNA detection [13], cell surface receptor targeting [14], and detection for pathogenic bacteria [15,16]. Unlike conventional fluorescent dyes, QDs have long-term photostability, high quantum yield, broad absorption spectra and narrow, symmetric emission [17,18]. Hence, the sensitivity can be improved, and the optical systems can be simplified if the conventional dyes were replaced by QDs as a fluorescent labeling [16]. These advantages suggested that QDs bio-conjugates have greater potential in microbe monitoring, such as detection of total bacterial count and pathogen [16,19].

Immunoassays with QDs-labeled antibodies and enzymes have been well documented to rapidly detect and identify pathogens bacteria [16,20], while limited information is available regarding to use QDs for detecting total bacterial count. It was supposed that surface of water-soluble QDs, coated with TGA or MPA in aqueous phase during preparation, could be easily coupled with bacteria to detect bacterial count. So far, although use of QDs as a biological imaging tool has clearly been established for eukaryotic cells [21,22], relatively little is known about if QDs could be truly coupled with bacteria and feasible in detecting bacterial count.

In this study, a fluorescence measurement method was demonstrated for rapid detection of two bacterial count using water-soluble QDs as marker, spectrofluorometer as detection

* Corresponding author. Tel.: +86 551 2901862; fax: +86 551 2901862.
E-mail address: dunwuyin@126.com (J. Pan).

apparatus and *Escherichia coli* and *Staphylococcus aureus* as detection target bacteria.

2. Materials and methods

2.1. Materials

Fluorescein isothiocyanate (FITC) and tetramethyl rhodamine methyl ester (TMRM) were purchased from Sigma–Aldrich (St. Louis, USA). Cadmium chloride, sodium borohydride, selenium powder and sodium hydroxide (Shanghai Chemical Reagents Company, Shanghai, China) were used for the preparation of CdSe-QDs. Thioglycolic acid (TGA, Chengdu Kelong Chemical Reagents Co., Chengdu, China) was employed for surface modification of CdSe-QDs. 1-Ethyl-3-(3-dimethylaminopropyl)-carbodiimide (EDC, Shanghai Medpep Co., Shanghai, China) was used for activator. Other inorganic reagents include the sodium phosphate monobasic, sodium phosphate dibasic heptahydrate, hydrochloric acid, phosphate buffered saline (PBS, pH 7.4). All reagents were of analytical grade without further purification. Ultra pure water was used throughout.

2.2. Synthesis of water-soluble CdSe quantum dots

Water-soluble CdSe QDs solution was prepared as reported in Ref. [19] using the reaction between Cd^{2+} and NaHSe solution with TGA as stabilizer. Mixture of NaHB and Se was incubated for 2 h at 4 °C to synthesize NaHSe. For preparation of Cd precursor solution, a solution of CdCl_2 and TGA were mixed, and pH value was then adjusted to 11. This solution was placed in a three-necked flask, and was deoxidized with N_2 bubbling for 30 min. Under vigorous stirring, the prepared oxygen free NaHSe solution was injected. Typical molar ratio of Cd:Te:TGA was 2:1:4 in our experiments. The resulting mixture solution was heated to 90 °C and refluxed to 2 h for obtaining the green CdSe QDs. The CdSe QDs precipitates were rinsed with ethanol and dried by vacuum oven, and then were stored at 4 °C in dark.

2.3. Bacterial aerobic plate count

Microbial strains of *S. aureus* and *E. coli* were kind gifts from the lab of Dr. Yu (Anhui Entry-Exit Inspection and Quarantine Bureau, China). They were cultured in 100 mL of Luria Bertani (LB) broth. After incubation overnight at 37 °C, the bacterial cells were centrifuged for 10 min at $1600 \times g$. The bacteria were washed twice with the sterilized PBS (pH 7.4) and then resuspended in PBS (pH 7.4) under gentle vortex mixing. Aerobic plate count was determined by inoculating 1 mL of samples onto nutrient agar plates and incubated aerobically at 37 °C for 24 h and colonies counted.

2.4. QDs coupled with bacterial

At the mid-log phase, *E. coli* and *S. aureus* solutions were centrifuged for 10 min at approximately $1600 \times g$, and the supernatant was discarded. After discarding the supernatant, the bacterial pellet was resuspended in 10 mL PBS by vortexing for approximately 10 s. GTA-coated water-soluble CdSe quantum dots were conjugated to *E. coli* and *S. aureus* using EDC as a coupling reagent. For measuring the best condition of water-soluble CdSe quantum dots coupled with the bacterial cells, 50–400 μL (1.0 mg/mL) CdSe QDs and 100 μL 0.1 mg/mL EDC were reacted together with bacteria for 10–40 min at 37 °C, and then the mixtures were purified using ultra-filtration membrane (0.22 μm) to wash away the excess CdSe QDs. Further, fluorescence intensity and fluorescence images of different *E. coli*

and *S. aureus* were identified by labeling water-soluble CdSe QD of solution certain concentrations. Moreover, EDC was not added into the reaction solution in contrast.

2.5. Fluorescence microscopy

An IX-71 Olympus microscope system (Tokyo, Japan), equipped with a DP30BW cooled CCD camera and 500–560 nm BP emission filter was used to observe the images of bacterial cells.

2.6. Fluorescence spectra

Absorption spectra were obtained using a UV-1600 spectrophotometer (Beijing, China). Fluorescence intensity and emission spectra of CdSe QDs coupled with bacteria were recorded with the excitation wavelength fixed at 400 nm using an F-970 spectrofluorometer (Shanghai, China).

3. Results and discussion

3.1. Spectrum and stability of water-soluble CdSe QDs

CdSe QDs were synthesized in aqueous phase using the reaction between Cd^{2+} and NaHSe solution in the presence of TGA as a stabilizer. Fig. 1 shows the absorption spectrum and fluorescent emission spectra of green CdSe QDs used in bacterial cells labeling in this study. The absorption spectrum (curve a) indicates that CdSe QDs have a wider range of absorption, and the absorption peak is at 400 nm and 460 nm. Their broad absorption spectra allows for the efficient excitation at any wavelength with a single light source. The emission spectrum (curve b) is characterized by good symmetry and relatively narrow spectral width, which provided sufficient spectral resolution for quantitative detection of the fluorescence intensity. Generally, when using conventional organic dyes as fluorescent labeling, their narrow excitation spectra and broad emission spectra make simultaneous measurements very difficult. CdSe QDs allow the use of a single excitation wavelength, which greatly simplified the optical system used to make these measurements and makes simultaneous detection easier [23–25]. In this study, for studies difference of

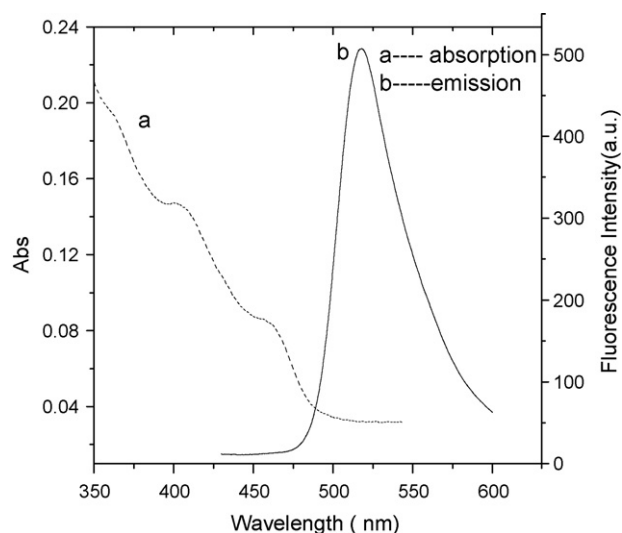


Fig. 1. Absorption spectra (curve a) and fluorescence emission spectra (curve b) of water-soluble CdSe quantum dots. Excitation wavelength is at 400 nm, and the emission peak is at 524 nm.

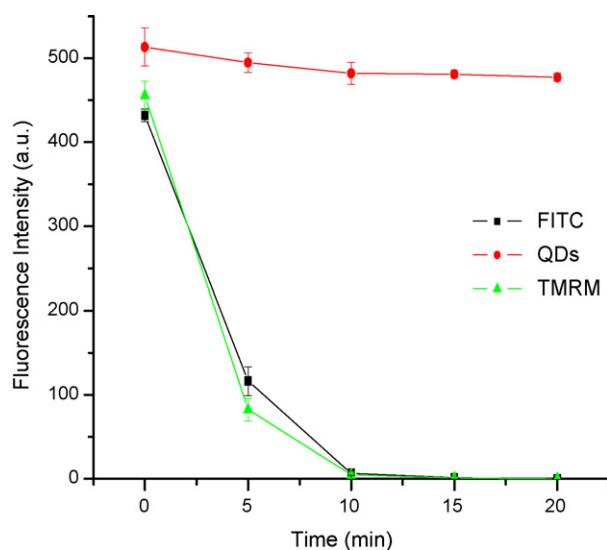


Fig. 2. Fluorescent intensities and photostability of water-soluble CdSe QDs, FITC and TMRM. Liquid solutions containing similar concentrations (1.0 mg/mL) were exposed under respective optimal excitation wavelengths and fluorescent intensities were measured at 5 min intervals.

fluorescence property both CdSe QDs and organic dye, fluorescence intensity of CdSe QDs was compared to that of FITC and TMRM. The comparison results indicate that water-soluble CdSe QDs solutions have high fluorescence intensity. CdSe QDs have improved brightness compared with two typical fluorescence dyes, which makes it easier for quantitative measurement of fluorescence intensity.

The photostability of water-soluble CdSe QDs was further compared against FITC and TMRM (Fig. 2). In the solution state, the fluorescence intensity was measured every 5 min and versus time data was directly obtained from the spectrofluorometer, which was excited continuously at its optimal excitation. The results show that the CdSe QDs are more stable than FITC and TMRM. As shown in Fig. 2, within 5 min, total fluorescence intensity of FITC and TMRM were reduced about 70%. The fluorescence signature of FITC and TMRM was evenly disappeared at 10 min, whereas it was not change that of CdSe QDs within 20 min.

These data illustrated that CdSe QDs display high luminescence, good water-solubility and photo-stability. It was similar to the reports in the references about applications of CdSe QDs in biological imaging and analysis [11–16].

3.2. The best condition of water-soluble CdSe quantum dots coupled with bacterial cells

In order to identify whether the water-soluble CdSe QDs bind on the bacterial cells, in this experiment, *E. coli* and *S. aureus* was chosen as detection target bacteria because they possess different cell walls and the component which was well understood. To determine the best integration time of CdSe QDs coupled with bacteria, 50–400 μ L (1.0 mg/mL) CdSe QDs and *E. coli* and *S. aureus* were reacted together for 40 min, respectively. The fluorescence intensity of different integration time was obtained at 524 nm. As shown in Fig. 3, prior to 25 min, fluorescence intensity both of *E. coli* and *S. aureus* increase linearly with integration time, but the fluorescence intensity was not increase approximately 30 min after addition of the CdSe QDs solution to the bacteria in log phase. Thus the best integration times of CdSe QDs coupled with bacteria was 30 min in this study. 400 μ L (1.0 mg/mL) CdSe QDs and *E. coli* and *S. aureus*

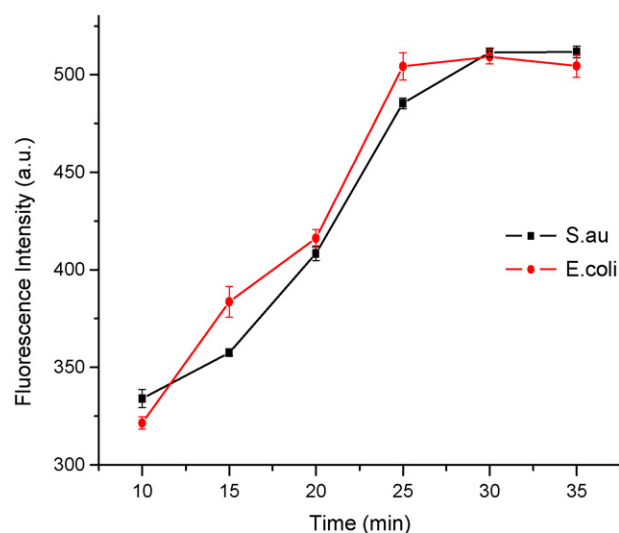


Fig. 3. Effect of integration time on the fluorescence intensity of the water-soluble CdSe QDs bind on *E. coli* and *S. aureus* (10^7 CFU/mL of *E. coli* and *S. aureus*).

were respectively reacted together for 10–40 min at 37 °C to determine the likely CdSe QDs concentrations of CdSe QDs coupled with bacteria. As shown in Fig. 4, fluorescence intensity both of *E. coli* and *S. aureus* coupled with CdSe QDs solution increased with CdSe QDs concentrations from 50 μ L to 400 μ L, but CdSe QDs coupled with bacteria was restricted with QDs concentrations and did not increase when CdSe QDs concentrations achieved 350 μ L. Thus, to prepare effective QDs–bacterial conjugates, the minimum level of the concentration of the CdSe QDs was 350 μ L, and integration times of CdSe QDs coupled with bacteria was approximately 30 min in this level.

3.3. Microscopic image and the principle of the bacterial cells coupled with water-soluble CdSe quantum dot

The fluorescence microscopy images demonstrate that the fluorescence signals of the *E. coli* and *S. aureus* cells coupled with water-soluble CdSe QDs were clear seen approximately 30 min after

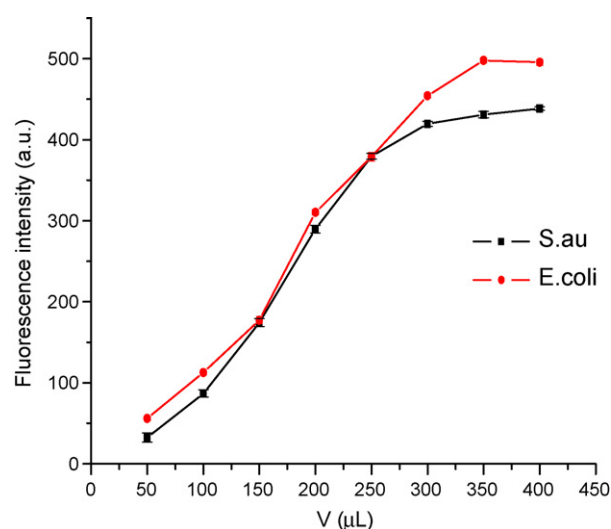


Fig. 4. Effect of water-soluble CdSe QDs concentrations on the fluorescence intensity of the QDs bind on *E. coli* and *S. aureus* in log phase (10^7 CFU/mL of *E. coli* and *S. aureus*). The concentration of QDs is 1.0 mg mL^{-1} .

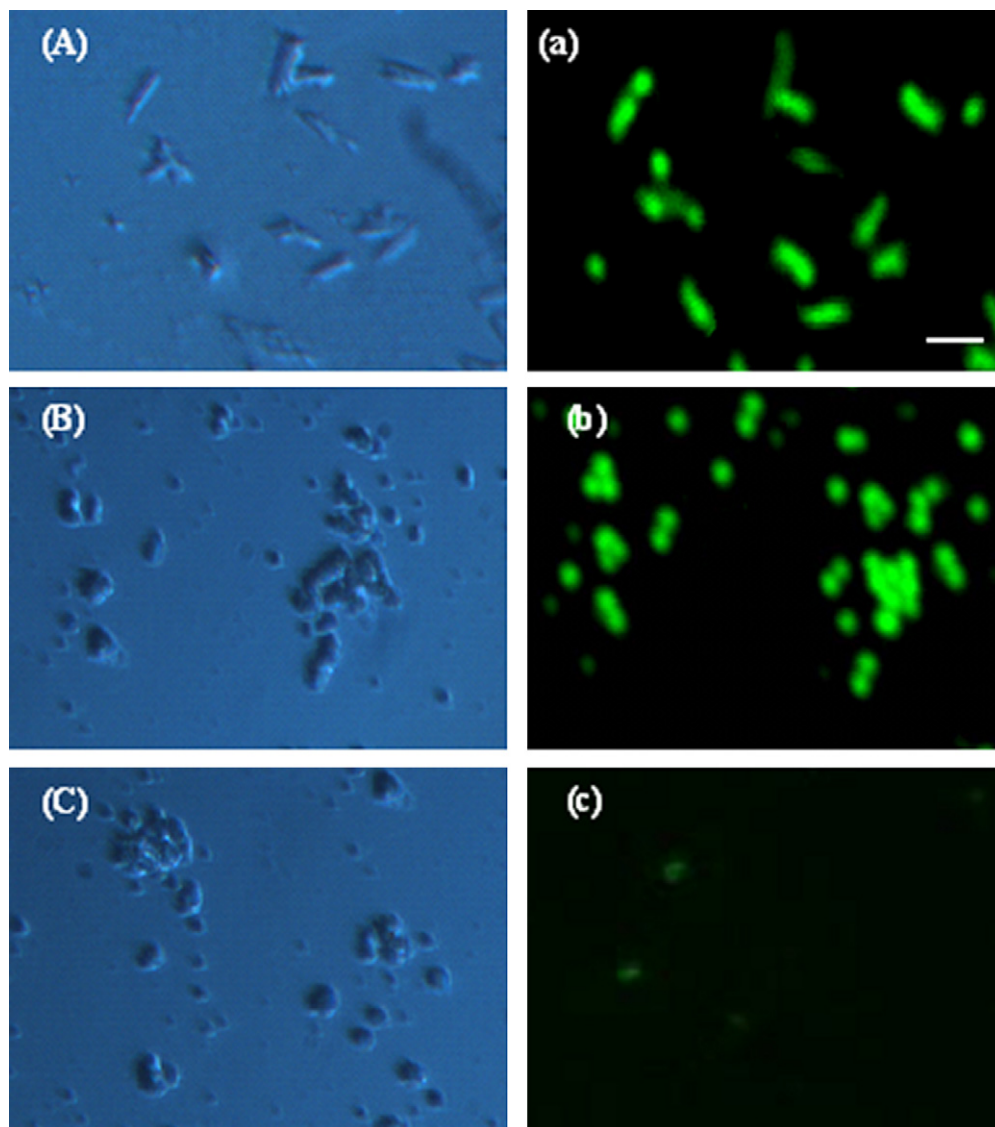


Fig. 5. Fluorescence and bright-field images (1000 \times) of *E. coli* and *S. aureus* cells. (A) and (a) indicate bright-field and fluorescence images of *E. coli* cells (10^7 CFU/mL cell suspension) treated with QDs and EDC, (B) and (b) indicate the images of *S. aureus* cells (10^7 CFU/mL cell suspension) under the same condition. A lot of luminescent dots were observed under a fluorescent microscope (a, b). (C) and (c) show, respectively, images of *E. coli* cells (10^7 CFU/mL cell suspension) treated with QDs (without EDC) in bright fields and fluorescent. Few luminescent dots were observed under a fluorescent microscope (c). The scale bars are 1 μ m.

addition of the CdSe QDs solution and EDC to the bacteria in log phase. A lot of luminescent the *E. coli* and *S. aureus* cells were observed under a fluorescent microscope (Fig. 5a and b). In contrast, the fluorescence signals of the *E. coli* and *S. aureus* cells without addition of the EDC were invisible in control experiments (Fig. 5c). It also showed that only a few CdSe QDs bind on the well surface of *E. coli* and *S. aureus* cells.

Furthermore, these images reveal water-soluble CdSe QDs bind on the *E. coli* and *S. aureus*, but it is nonspecific. The possible mechanisms are that the water-soluble CdSe QDs with surface carboxylic acids bind on the surface of Skin cells [26,27]. But another published paper indicated that QDs are able to label to bacteria only if the particles are <5 nm in diameter. They through that the diameter of the particles was about 3–4 nm could pass through bacterial cell walls

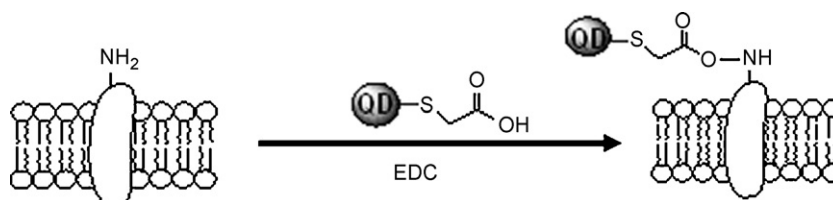


Fig. 6. Diagrammatic sketch of principle for bacterial coupled with water-soluble CdSe quantum dots.

and membrane entry the cell, so the QDs could label to bacteria. But the luminescent bacterial cells were observed approximately 12 h after addition of the QD solution to the bacteria in log phase [21]. In this study, we used CdSe QDs as a fluorescent labeling and EDC as a crosslinking agent to explore whether the water-soluble CdSe QDs bind on the surface of two bacterial cells. EDC is a commonly used coupling agent that can link between amine groups of proteins and carboxylic group of some compounds [28,29], so EDC was chosen to confirm whether CdSe QDs were effectively conjugated with amine groups of bacteria. As shown in Fig. 5, the fluorescence signals of the two bacterial cells with addition of the EDC are clear and bright (Fig. 5a and b), but the fluorescence signals of the bacterial cells without addition of the EDC become invisible (Fig. 5c). It indicated that the water-soluble CdSe QDs bind on the surface of two bacterial cells. Since the surface of CdSe QDs were coated with certain GTA, the thiol group of GTA was linked to the surface of CdSe QDs by thiol group–Cd coordination, and the functional carboxylic group was free, which can be easily coupled with amine groups the surface of bacteria, such as proteins, peptides and amino acids.

Fig. 6 illustrates the coupling process of bacteria with QDs. For simplification, only one protein is shown on one bacterial cell membrane and one protein on one QD conjugate. In fact, one bacterial cell membrane carries numerous proteins and one protein typically bind on numerous QD conjugate. Briefly, the detection was based on coupling amino group of bacterial cell membranes with QD bio-labeling.

3.4. Fluorescence detection of total count of *E. coli* and *S. aureus*

The fluorescence intensity of 10^1 – 10^7 CFU/mL total count of *E. coli* and *S. aureus* was presented in Fig. 7. As shown in this figure, the fluorescence intensity peak intensity increases with increasing cell count in the range of 10^1 – 10^7 CFU/mL *E. coli* and *S. aureus* cells. The fluorescence peak intensity increases with increasing two bacterial count and a linear relationship could be established using the equation $Y = 118.68X - 141.75$ ($r = 0.9907$) over the range of 10^2 – 10^7 CFU/mL.

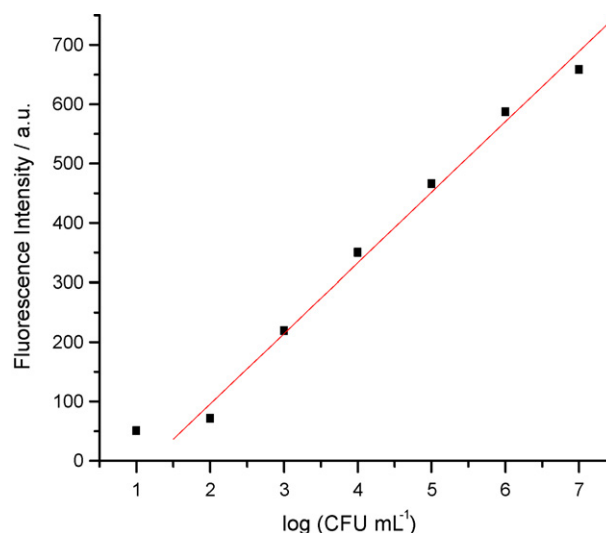


Fig. 7. Variation in differential fluorescence signal intensity with total count of *E. coli* and *S. aureus*. The concentration of water-soluble CdSe QDs is 1.0 mg/mL. The detection target bacteria are mixture of *E. coli* and *S. aureus*. The relationship between fluorescence signal intensity and log total count of *E. coli* and *S. aureus* follows the equation of $Y = 118.68X - 141.75$ ($r = 0.9907$). The low detection limit is 10^2 CFU/mL.

Fig. 8 shows the fluorescence images of 10^2 , 10^4 and 10^7 CFU/mL *E. coli* and *S. aureus* cells. The luminescent bacterial cells become visible approximately 30 min after addition of the QDs solution to the 10^2 – 10^7 CFU/mL bacteria. However, the signals of the blank and the samples of 10^1 CFU/mL bacterial are indistinguishable, which might not be coupled with CdSe QDs or might be due to the high background reflection. The detection limit obtained in this study is 10^2 CFU/mL. The fluorescence method could detect 10^2 – 10^7 CFU/mL total count of *E. coli* and *S. aureus* in 1–2 h from adding a sample solution to obtaining the final result, with a detection limit of 10^2 CFU/mL, that of at least 10–20 times lower than conventional plate count.

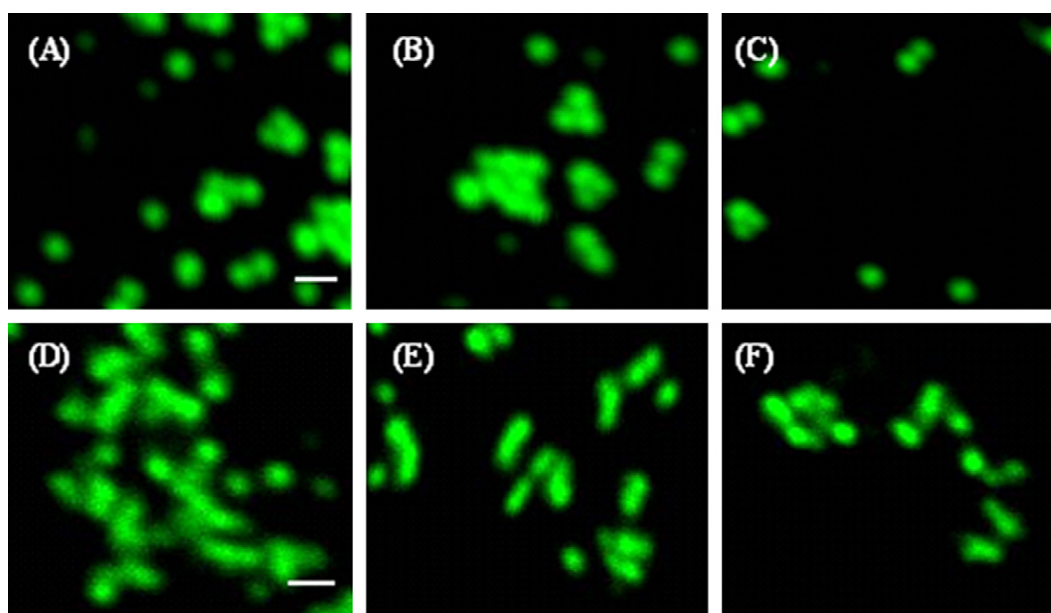


Fig. 8. Fluorescence images of bacterial cells coupled with water-soluble CdSe QDs (1000 \times). (A–C) The images of different quantities *S. aureus* cells coupled with QDs when exposed to 10^7 , 10^4 , 10^2 CFU/mL cells suspension, respectively. (D–F) The images of *E. coli* cells coupled with QDs in the same quantities bacterial cells. The scale bars are 1 μ m.

4. Conclusions

This study has prepared highly luminescent and stable water-soluble CdSe QDs using thioglycolic acid (TGA) as a ligand. A sensitive and rapid fluorescence detection method of total bacterial count has been demonstrated based on the water-soluble CdSe quantum dots coupled with bacterial. The fluorescence method could detect 10^2 – 10^7 CFU/mL total count of *E. coli* and *S. aureus* in 1–2 h and the low detection limit is 10^2 CFU/mL. The fluorescence peak intensity increases with increasing total count of *E. coli* and *S. aureus* and a linear relationship could be established using the equation $Y = 118.68X - 141.75$ ($r = 0.9907$) over the range of 10^2 – 10^7 CFU/mL.

Acknowledgement

This work was financially supported by the Eleventh Five-Year Plan Key Project of Anhui China (06003015B).

References

- [1] G. Bonwick, C. Smith, J. Walliams, Food Sci. Technol. 17 (2003) 32–34.
- [2] P. Belgrade, W. Benett, D. Hadley, J. Richards, P. Stratton, R. Mariella Jr., F. Milanovich, Science 284 (1999) 449.
- [3] P.M. St. John, R. Davis, N. Cady, J. Czajka, C.A. Batt, H.G. Craighead, Anal. Chem. 70 (1998) 1108.
- [4] F. Patolsky, G. Zheng, O. Hayden, M. Lakadamyali, X. Zhuang, C.M. Lieber, Proc. Natl. Acad. Sci. U.S.A. 101 (2004) 14017.
- [5] L.M. Scolaro, M. Castriciano, A. Romeo, S. Patane, E. Cefali, M. Allegrini, J. Phys. Chem. B 106 (2002) 2453.
- [6] S. Santra, B. Liesenfeld, C. Bertolino, D. Dutta, Z.H. Cao, W.H. Tan, B.M. Moudgil, R.A. Mericle, J. Lumin. 117 (2006) 75–82.
- [7] M.Y. Choi, J.A. Pollard, M.A. Webb, J.L. Mchale, J. Am. Chem. Soc. 125 (2003) 810.
- [8] J.H. Kim, D. Morikis, M. Ozkan, Sens. Actuators B 102 (2004) 314.
- [9] X.J. Zhao, L.R. Hilliard, S.J. Mechery, Y.P. Wang, R.P. Bagwe, S.G. Jin, W.H. Tan, Proc. Nat. Acad. Sci. U.S.A. 101 (2004) 15027.
- [10] R. Hamid, Y. Rotshteyn, L. Rabadi, R. Parikh, P. Bullock, Toxicol. Vitro 18 (2004) 703–710.
- [11] J.K. Jaiswal, H. Mattoussi, J.M. Mauro, S.M. Simon, Nat. Biotechnol. 21 (2003) 47.
- [12] X. Wu, H. Liu, J. Liu, K.N. Haley, J.A. Treadway, J.P. Larson, N. Ge, F. Peale, M.P. Bruchez, Nat. Biotechnol. 21 (2003) 41.
- [13] M. Han, X. Gao, J.Z. Su, S. Nie, Nat. Biotechnol. 19 (2001) 631.
- [14] S.J. Rosenthal, I. Tomlinson, E.M. Adkins, S. Schroeter, S. Adams, L. Swafford, J. McBride, Y. Wang, L.J. DeFelic, R.D. Blakely, J. Am. Chem. Soc. 124 (2002) 4586.
- [15] M.A. Hahn, J.S. Tabb, T.D. Krauss, Anal. Chem. 77 (2005) 4861.
- [16] J.A. Kloepper, R.E. Mielke, J.L. Nadeau, Appl. Environ. Microbiol. 5 (2005) 2548–2557.
- [17] D. Matthew, Y.J. Hirschey, D. Galen Han, A. Butler Stucky, J. Biol. Inorg. Chem. 11 (2006) 663–669.
- [18] H.D. Duong, J.I. Rhee, Talanta 73 (2007) 899–905.
- [19] J.F. Weng, X.T. Song, L. Li, H.F. Qian, K.Y. Chen, X.M. Xu, C.X. Cao, J.C. Ren, Talanta 70 (2006) 397–402.
- [20] Z.D. Liu, S.F. Chen, C.Z. Huang, S.J. Zhen, Q.G. Liao, Anal. Chim. Acta 599 (2007) 279–286.
- [21] J.A. Kloepper, R.E. Mielke, M.S. Wong, K.H. Nealson, G. Stucky, J.L. Nadeau, Appl. Environ. Microbiol. 69 (2003) 4205–4213.
- [22] J.A. Kloepper, R.E. Mielke, J.L. Nadeau, Appl. Environ. Microbiol. 71 (2005) 2548–2557.
- [23] J.K. Jaiswal, H. Mattoussi, J.M. Mauro, S.M. Simon, Nat. Biotechnol. 21 (2003) 47–51.
- [24] L.J. Yang, Y.B. Li, Analyst 131 (2006) 394–401.
- [25] A. Watson, X. Wu, M. Bruchez, Biotechniques 34 (2003) 296–300.
- [26] P. Jessica, J.E. Ryman-Rasmussen, N.A. Riviere, Monteiro-Riviere, Nano Lett. 7 (2007) 1344–1348.
- [27] H.Y. Liu, T.Q. Vu, Nano Lett. 7 (2007) 1044–1049.
- [28] S.P. Wang, N. Mamedova, N.A. Kotov, W. Chen, J. Studer, Nano Lett. 2 (2002) 817.
- [29] A. Schroedter, H. Weller, Nano Lett. 2 (2002) 1363.



Glutathione-capped CdTe quantum dots for the sensitive detection of glucose

Jipei Yuan^a, Weiwei Guo^a, Jianyuan Yin^b, Erkang Wang^{a,*}

^a State Key Laboratory of Electroanalytical Chemistry, Changchun Institute of Applied Chemistry, Chinese Academy of Sciences, Graduate School of the Chinese Academy of Sciences, Changchun, Jilin 130022, China

^b Department of Traditional Chinese Medicinal Chemistry, Pharmacy College, Jilin University, Changchun, Jilin 130021, China

ARTICLE INFO

Article history:

Received 12 August 2008

Received in revised form 20 October 2008

Accepted 21 October 2008

Available online 31 October 2008

Keywords:

Quantum dots
H₂O₂-sensitive
Glucose
Detection

ABSTRACT

A simple and sensitive assay system for glucose based on the glutathione (GSH)-capped CdTe quantum dots (QDs) was developed. GSH-capped CdTe QDs exhibit higher sensitivity to H₂O₂ produced from the glucose oxidase catalyzed oxidation of glucose, and are also more biocompatible than other thiols-capped QDs. Based on the quenching of H₂O₂ on GSH-capped QDs, glucose can be detected. The detection conditions containing reaction time, the concentration of glucose oxidase and the sizes of QDs were optimized and the detection limits for glucose was determined to be 0.1 μM; two detection ranges of glucose from 1.0 μM to 0.5 mM and from 1.0 mM to 20 mM, respectively were obtained. The detection limit was almost a 1000 times lower than other QDs-based optical glucose sensing systems. The developed glucose detection system was simple and facile with no need of complicated enzyme immobilization and modification of QDs.

© 2008 Elsevier B.V. All rights reserved.

1. Introduction

Semiconductor nanocrystals (quantum dots, QDs) exhibit unique properties such as size-dependent emission, narrow emission peak and resistance to photo-bleaching [1]. Intensive researches have been done in the study of synthesis and photophysical properties of QDs during the past two decades [2–5]. Although the development of QDs-based chemical (bio) analysis had a relative late start compared with their intensive applications in bioimaging, a rapid progress has been achieved within the latest several years by analytical scientists with several review papers published very recently [2,6–10]. Taking full advantages of the QDs unique property, various pathways were adopted to develop optical sensors based on the variation of QDs photoluminescence (PL) intensity induced by the changes of QDs surface conditions. Previous studies were focus on the QDs-based sensing system for ions [11–13] and small molecules [14,15]. In order to achieve the selective analysis, the surfaces of QDs were modified with host molecules to selectively encapsulate ions or small molecules [16,17]. On the other hand, sensing analytes or bio-recognition events were also achieved through fluorescence resonance energy transfer or electron transfer process with QDs as fluorescence labels

[18–23]. QDs display great potential in the analytical areas especially in the development of biosensing systems.

Glucose is a major component of animal and plant carbohydrates, and the detection of glucose is of great importance in food analysis as well as in diagnosing metabolites. Various methods have been developed for glucose by electrochemical and optical analysis and so on [24–28]. Recently, several groups paid efforts to the design of QDs based optical sensing systems for glucose determination. Cavaliere-Jaricot group [29] and Huang group [30] reported on the glucose detection based on the quenching of QDs photoluminescence (PL) emission by H₂O₂ and acidic changes produced by glucose oxidase (GOD) catalyzed glucose oxidation, respectively. Rhee group [31] functionalized the mercaptopropionic acid (MPA) capped QDs with GOD and horseradish peroxidase (HRP), and then glucose was sensed by the quenching of QDs through FRET from QDs to the enzymatic reactions. However, the detection limits were relatively high (at 0.1 mM level). In order to achieve the sensitive detection of glucose, a QDs–bienzyme hybrid system has been developed by our group. An efficient QDs PL quencher benzoquinone (BQ) was produced from GOD–HRP catalyzed with glucose and hydroquinone as substrates, and the highly sensitive detection of glucose was achieved with detection limit of 10 nM [32], however the detection range was relatively narrow. Very recently, Willner group [33] proposed that controlling the photophysical properties of QDs by H₂O₂ might provide versatile method to develop QDs-based sensors as numerous oxidase generated H₂O₂, and then detection of glucose and acetylcholine esterase inhibition were performed to prove the feasibility with the H₂O₂-sensitive QDs

* Corresponding author at: State Key Laboratory of Electroanalytical Chemistry, Changchun Institute of Applied Chemistry, Chinese Academy of Sciences, Changchun, 130022, China. Tel.: +86 431 85262003; fax: +86 431 85689711.

E-mail address: ekwang@ciac.jl.cn (E. Wang).

(mercaptoundecanoic acid and GSH-capped CdSe/ZnS QDs) functionalized with enzymes. A lower detection limit of 0.1 mM for H_2O_2 was achieved and the requirement of QDs PL quencher was avoided.

In this manuscript, the GSH-capped CdTe QDs were proved to be more sensitive to H_2O_2 than the CdSe/ZnS QDs. The sensitivity of QDs with different sizes on H_2O_2 was investigated and results showed that QDs with smaller size presented higher sensitivity. Utilizing the sensitivity of the GSH-capped QDs PL emission on H_2O_2 , a simple glucose detection method was further developed based on the oxidation of glucose by GOD. The detection limit of glucose was determined to be 0.1 μM . Also, two wide detection ranges of glucose were obtained from 1.0 μM to 0.5 mM and from 1.0 mM to 20 mM. Compared with other thiols-capped QDs, GSH-capped QDs was more biocompatible, as GSH can detoxify Cd^{2+} ions [34]. The avoidance of modification of QDs and GOD made this method simple and facile.

2. Experimental

2.1. Reagents

All the starting materials of CdTe QDs synthesis were obtained from commercial suppliers and were used without further purification. Mercaptosuccinic acid (MSA) was obtained from Aldrich Chemical (Milwaukee, WI, USA). Glutathione (reduced form) was purchased from Beijing Dingguo Biotechnology (Beijing, China). Glucose oxidase (from *Aspergillus niger*) was purchased from Sigma (St. Louis, MO, USA). Chemicals used are at least analytical grade. Frozen human serum samples were obtained from Hospital of Chinese Integrative Medicine of Jilin Province (Changchun, China). All the solutions were prepared with water purified by a Milli-Q system (Millipore, Bedford, MA, USA).

2.2. Instrumentation

UV/vis absorption spectra were recorded by a CARY 500 UV/vis–near IR Varian spectrophotometer. Fluorescence experiments were recorded on a PerkinElmer LS 55 luminescence spectrometer. Transmission electron microscopy (TEM) measurements were made on a JEOL 2000 transmission electron microscope operated at an accelerating voltage of 200 kV. Samples for TEM characterization were prepared by placing a drop of QDs colloid solution onto a carbon-coated copper grid and drying at room temperature.

2.3. Synthesis of CdTe QDs

Four millilitres of 0.04 M cadmium chloride was diluted to 25 mL in a one-necked flask, and trisodium citrate dihydrate (0.1 g), glutathione (0.05 g) or mercaptosuccinic acid (0.1 g), Na_2TeO_3 (0.01 M, 1 mL) and NaBH_4 (0.05 g) were added with stirring. The mixture was reacted at 90 °C under open-air conditions for a certain period of time. The obtained QDs were precipitated with ethanol and the precipitates were separated by centrifugation and were redissolved in 50 mM phosphate buffer solution (pH 7.4). The precipitation process was repeated for three times in order to eliminate the free glutathione ligands and salts in the crude CdTe QDs colloids.

2.4. Fluorescence experiments

Thirty microlitres of QDs colloids were diluted with phosphate buffer solution and a certain volume of H_2O_2 was added into the diluted colloids. Under the excitation wavelength of 400 nm, the fluorescence spectra of QDs were recorded. The slot widths of the excitation and emission were both 10.0 nm.

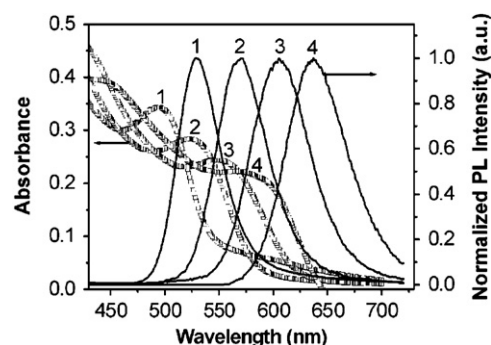


Fig. 1. UV/vis absorption and PL emission spectra of synthesized GSH-capped CdTe QDs with four sizes ((1) 2.17 nm; (2) 2.86 nm; (3) 3.28 nm; (4) 3.45 nm).

3. Results and discussion

3.1. Optical characterization of GSH-capped CdTe QDs

The synthesis of GSH-capped CdTe QDs have been achieved by several groups [34,35]. Here in this work, the water-soluble GSH-capped QDs were easily synthesized according to the CdTe QDs synthesis method proposed by our group previously [36]. The UV/vis absorption and PL emission spectra of synthesized GSH-capped CdTe QDs with different sizes were shown in Fig. 1. The diameters of QDs were calculated following Peng's method [37]. The obtained QDs exhibited a broad absorption spectra and narrow and symmetrical emission peaks with the excitation wavelength at 400 nm.

3.2. Comparison of responses of GSH-capped QDs and MSA-capped QDs on H_2O_2

The effects of H_2O_2 on the PL emission of both the GSH and MSA-capped CdTe QDs were studied and compared. It was found in our experiment that the PL emission of GSH-capped QDs was more easily influenced by the presence of H_2O_2 compared with MSA-capped QDs. The time-dependent experiments of both GSH and MSA-capped QDs– H_2O_2 system were investigated with the PL spectra of the mixture of QDs and 1 mM H_2O_2 were recorded every 3 min for 6 times. As shown in Fig. 2, with the increase of the scan times, the PL intensity of QDs decreased, and the PL emission of GSH-capped QDs was quenched more intensively by H_2O_2 . Results of the sixth scan showed that there was a 71.8% decrease of the PL intensity of GSH-capped QDs, while only a decrease of 30.9%

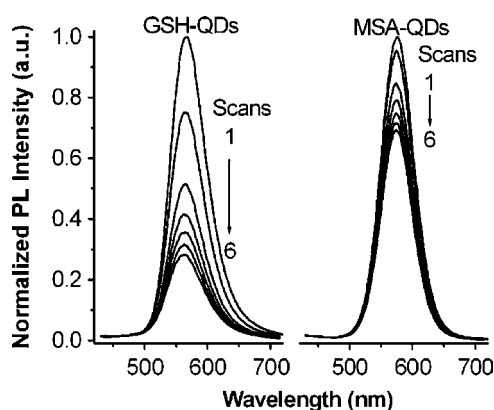


Fig. 2. PL spectra represented comparison of the six sequential scans of GSH-capped QDs and MSA-capped QDs with the addition of 1 mM H_2O_2 . Scan rate, 500 nm/min; scan delays, 3 min.

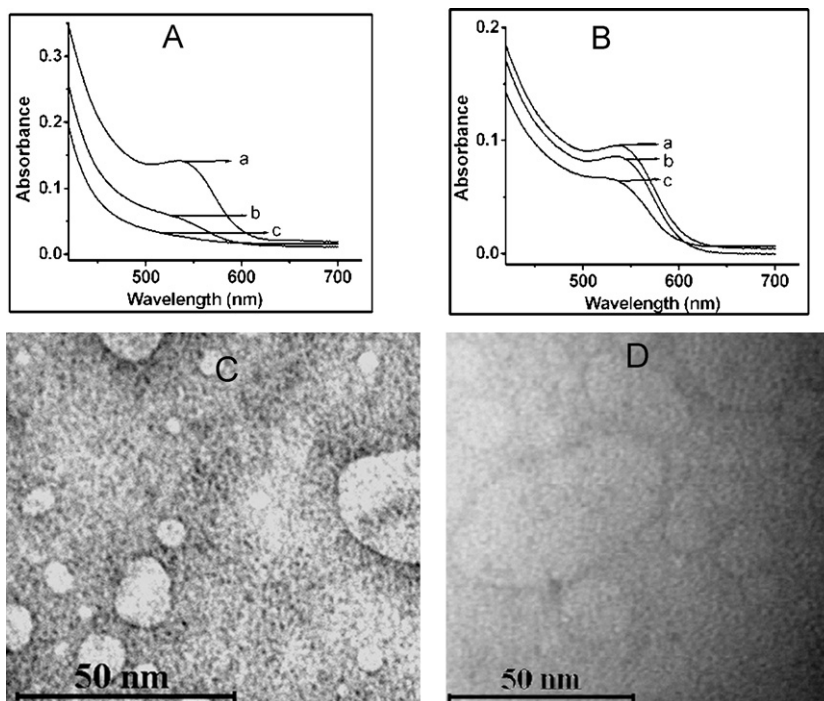


Fig. 3. UV/vis absorption spectra of GSH-capped CdTe QDs (A) and MSA-capped CdTe QDs (B) before (a) and after the addition of 0.01 M H_2O_2 for 10 min (b) and 6 h (c), respectively; and the TEM images of GSH-capped CdTe QDs before (C) and after the addition of 0.01 M H_2O_2 (D).

occurred to the MSA-capped QDs. The quenching effect of H_2O_2 on GSH-capped QDs was more than two times intensive than that on MSA-capped QDs. And the quenching effect of H_2O_2 on GSH-capped CdTe QDs was more intensive than that on CdSe/ZnS QDs as a quenching effect of about 40% was observed as reported previously [33]. The quenching effect of H_2O_2 on the PL emission of GSH-capped CdTe QDs might be due to the oxidation of QDs surfaces. Li group reported that QDs could be destroyed by H_2O_2 in alkaline solution [38]; however, the detailed mechanism was not very clear yet [33]. In this work, TEM images of GSH-capped CdTe QDs before and after the H_2O_2 treatment were obtained, and the UV/vis spectra of both GSH-capped CdTe QDs and MSA-capped CdTe QDs before and after the addition of 0.01 M H_2O_2 were also compared. As shown in Fig. 3A and B, UV/vis absorption peak of GSH-capped CdTe QDs decreased intensively after reacting with H_2O_2 for 6 h, indicating that the lattice structure of QDs were partly destroyed by H_2O_2 , while the decrease of UV/vis absorption peak of MSA-capped CdTe QDs was at a relatively lower extent. TEM images of GSH-capped CdTe QDs indicated that the QDs were non-aggregated after the addition of H_2O_2 , which can also be proved by the fact that there was no blue-shift or red-shift of PL spectra observed. The above results showed that GSH-capped CdTe QDs were more easily to be oxidized and then destroyed compared with MSA-capped QDs. The obtained results were consistent with the phenomenon observed by Li group [38], the lattice structure of GSH-capped CdTe QDs can be partly destroyed after the oxidation of H_2O_2 , leading QDs PL quenching effect. Based on GSH-capped CdTe QDs, glucose detection with higher sensitivity can be established.

3.3. Detection of H_2O_2 by the quenching PL emission of GSH-capped CdTe QDs

In order to achieve the sensitive detection of H_2O_2 , the quenching kinetics of GSH-capped CdTe QDs by H_2O_2 was investigated. Results showed that the QDs PL intensity decreased with the increase of incubation time of GSH-capped QDs with H_2O_2 within

5 min, and it was found that linear relationship existed between the PL intensity decrease and incubation time. As the decrease of PL intensity became slow down after 5 min, an incubation time of 5 min was chosen in our experiment.

Utilizing the intensive quenching effects on GSH-capped CdTe QDs, optical sensing method of H_2O_2 can be established. The quenching effect of H_2O_2 with different concentrations on GSH-capped CdTe QDs with size of 2.50 nm was studied and shown in Fig. 4 with the incubation time of 5 min. PL intensity of QDs decreased gradually with the increase of H_2O_2 concentration. The detection limit of H_2O_2 was determined to be 1.0 μM , which was 100 times lower than other QDs PL quenching-based H_2O_2 detection method [29,33]. An extremely wide linear range was obtained between I_0/I (I_0 and I are the PL intensity of QDs in the absence/presence of quencher) and the concentration of H_2O_2 with the concentration range between 0.1 mM and 10 mM.

3.4. Glucose sensing system based on the GSH-QDs and glucose oxidase system

The sensitive detection of H_2O_2 with broad linear range based on GSH-capped CdTe QDs made it possible to develop a sensitive glucose determination system with the coupling of GSH-capped CdTe QDs and GOD that catalyzed oxidation of glucose to produce H_2O_2 . The responses of GSH-capped CdTe QDs on 1.0 mM glucose, 3.2 mg/mL GOD and the mixture of glucose and GOD were investigated. As shown in Fig. 5, the mixture of glucose and GOD with 5 min incubation exhibited a quenching effect of 40% on GSH-capped QDs, while glucose and GOD itself presented no influences on the PL spectra of QDs. The above results showed that quenching effects were attributed to H_2O_2 generated from glucose oxidation.

To achieve sensitive detection of glucose, some key factors that influence the glucose detection were studied. The concentration of GOD was optimized. With the increase of GOD concentration, the quenching effect of 1 mM glucose also enhanced. I/I_0 was linear

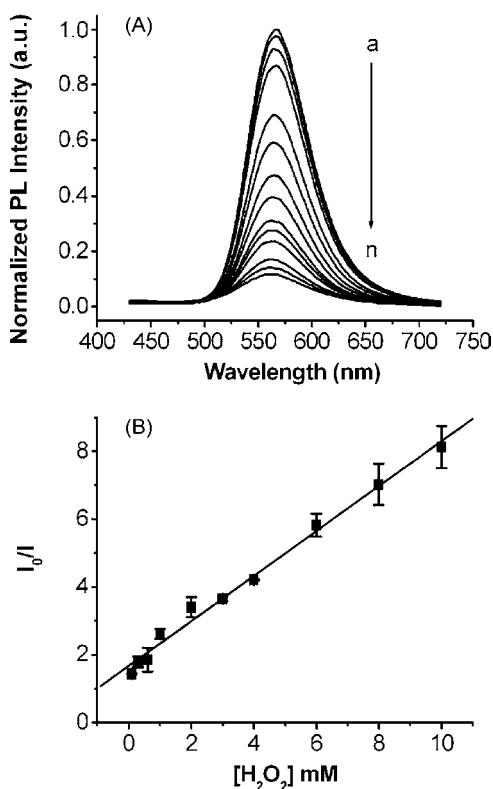


Fig. 4. (A) PL spectra represent the quenching effect of H_2O_2 with concentrations a to n, 0, 1.0 μM , 10 μM , 50 μM , 0.1 mM, 0.3 mM, 0.6 mM, 1.0 mM, 2.0 mM, 3.0 mM, 4.0 mM, 6.0 mM, 8.0 mM, 10 mM. (B) Linear relationship between I_0/I and the concentration of H_2O_2 . Incubation time of QDs and H_2O_2 , 5 min; 50 mM phosphate buffer solution (pH 7.4).

with the concentration of GOD within 0.16 mg/mL, and when the concentration of GOD was above 0.16 mg/mL, the quenching effects did not enhance any more. Thus 0.16 mg/mL GOD was utilized in the following experiments. Then, the enzymatic reaction time was studied. A linear relationship of I_0/I and reaction time of 1.0 mM glucose–0.16 mg/mL GOD system within 5 min were observed. The enzymatic reaction can reach its equilibrium within 5 min, and the incubation time of 5 min was chosen.

The size of QDs is a crucial parameter that decides the sensitivity and detection range of glucose detection. With the decrease of QDs size, more atoms of the total number of atoms comprising the

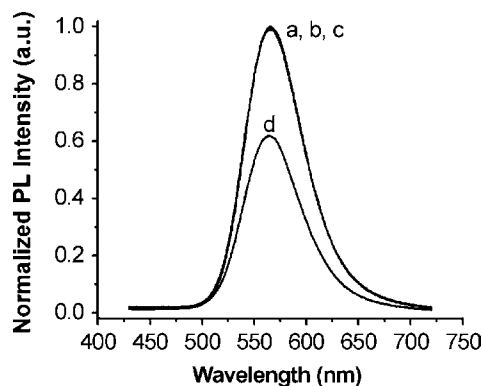


Fig. 5. PL spectra represent the quenching effect of GOD–glucose system on GSH-capped QDs; (a) QDs; (b) QDs with the addition of 1 mM glucose; (c) QDs with the addition of 0.32 mg/mL GOD; (d) QDs with the addition of 1 mM glucose and 0.32 mg/mL GOD. Enzymatic incubation time, 5 min; incubation time of QDs and glucose–GOD system, 5 min; 50 mM phosphate buffer solution (pH 7.4).

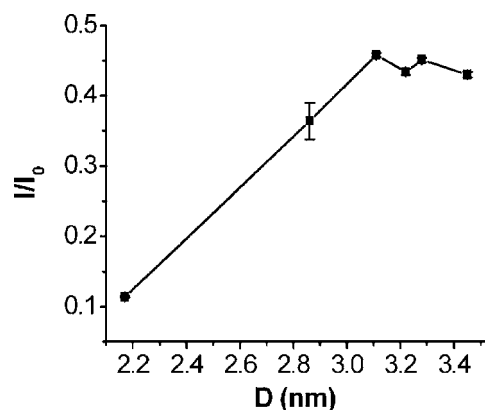


Fig. 6. Relationship between the quenching effects (I/I_0) of 1 mM H_2O_2 on GSH-capped CdTe QDs PL intensity and QDs diameters. Incubation time of QDs and H_2O_2 , 5 min; 50 mM phosphate buffer solution (pH 7.4).

particle will locate at the particle surface, and the QDs with smaller diameter can be more sensitive to their surfaces. We investigated the response of PL intensity of QDs with different sizes on 1 mM H_2O_2 . As shown in Fig. 6, the quenching effect ($1 - I/I_0$) of H_2O_2 on QDs PL intensity enhanced with the decrease of their diameters (D). The quenching extent of 1 mM H_2O_2 on the PL intensity of QDs with the size of 2.17 nm was about 88.6%, while a quenching effect of about 63.6% was achieved when the QDs size was 2.86 nm. When the sizes of QDs were above 3.11 nm, the quenching effects of H_2O_2 were almost the same and at about 55% levels.

Here, we further investigated the influences of QDs sizes on glucose detection. GSH-capped CdTe QDs with three different diameters (2.17 nm, 2.50 nm and 3.11 nm) were utilized in this study. As to the determination of glucose, the glucose with various concentrations was first oxidized with the catalysis of 0.16 mg/mL GOD in 50 mM phosphate buffer (pH 7.4) for 5 min, and then certain volume of QDs was added into above reaction system for another 5 min and underwent fluorescence experiments. Under the optimized reaction conditions, the response of QDs PL intensity on glucose with different concentrations was shown in Fig. 7. It can be seen from Fig. 7A that QDs with diameter of 2.17 nm were more sensitive to glucose than that of 2.50 nm and 3.11 nm. Fig. 7B showed the Stern–Volmer curves that represented the relationship of I_0/I and the concentration of glucose.

Different detection limits can be obtained when QDs with different sizes were used. Utilizing QDs with smaller size, determination of glucose with higher sensitivity can be achieved. The detection limit of glucose was determined to be 0.1 μM utilizing QDs of 2.17 nm, which was 10 times lower than that obtained using QDs of 2.50 nm and 3.11 nm. The linear ranges of glucose detection were also different when using QDs of different diameters as seen in Table 1. With QDs diameters of 2.17 nm and 2.50 nm, two linear ranges were obtained; while only one linear range can be obtained when the diameter of QDs was 3.11 nm as shown in Fig. 8. The detailed linear ranges and linear regression equations of glucose detection with QDs diameters with 2.17 nm, 2.50 nm and 3.11 nm were listed below.

For QDs of 2.17 nm, two linear ranges were obtained. In the range from 1.0 μM to 0.5 mM, I_0/I was linear with the concentration of glucose with the linear regression equation of $(I_0/I) = 1.1 + 2744 C_{\text{glucose}}$ ($r = 0.995$), and in the range from 1.0 mM to 20 mM $(I_0/I) = 2.9 + 138.8 C_{\text{glucose}}$ ($r = 0.993$). For QDs of 2.50 nm, in the range from 1.0 μM to 0.5 mM $(I_0/I) = 1.1 + 1064.1 C_{\text{glucose}}$ ($r = 0.996$); and in the range from 1.0 mM to 15 mM $(I_0/I) = 1.8 + 33.1 C_{\text{glucose}}$ ($r = 0.993$). For QDs of 3.11 nm, in the range from 0.05 mM to 1.0 mM $(I_0/I) = 1.1 + 620.5 C_{\text{glucose}}$ ($r = 0.986$). The above results indicated

Table 1
Comparison of QDs PL quenching-based optical detection methods for glucose and the detection ranges of glucose based on GSH-capped CdTe QDs with different sizes.

QDs	Ligands	Enzymes	Quenching mechanism	Detection range	Reference
CdSe/ZnS@ SiO ₂	Not given	GOD	H ₂ O ₂	0.5–3 mM	[29]
CdSe/ZnS	MSA	GOD	Acidic change	0.2–10 mM or 2–30 mM	[30]
CdSe/ZnS	MPA	GOD-HRP	FRET	0–5.0 g/L, 0.2–5.0 g/L or 1.0–5.0 g/L	[31]
CdTe	MSA	GOD-HRP	BQ	1.0 μM to 0.15 mM and 0.15–1.0 mM	[32]
CdSe/ZnS	GSH	GOD	H ₂ O ₂	Not given	[33]
CdTe (2.17 nm)	GSH	GOD	H ₂ O ₂	1.0 μM to 0.5 mM and 1.0–20 mM	Current method
CdTe (2.50 nm)	GSH	GOD	H ₂ O ₂	1.0 μM to 0.5 mM and 1.0–15 mM	Current method
CdTe (3.11 nm)	GSH	GOD	H ₂ O ₂	0.05 mM to 1.0 mM	Current method

that the detection limits became poor and detection range became narrow with the increase of QDs diameters.

The detection limit of this method was much lower than other H₂O₂ and acidic change influenced QDs PL emission-based methods [29,30]. The detection range of rather wide, as glucose with concentration from 1.0 μM to 20 mM could be quantified. Detail comparison of the glucose detection method based on quenching of QDs PL emission was also listed in Table 1. Also, the proposed method exhibited excellent reproducibility with the relative standard deviation (R.S.D.) of 3.82% for 12 reduplicate detection of 1.0 mM glucose.

3.5. Interference and real sample analysis

Certain metal ions such as Cu(II) [39], Co(II) [40] and Hg(II) [41] can intensively quench the PL emission of CdTe QDs as reported

previously, and these metal ions will interfere with the glucose detection. Na⁺ with concentration of 300 mM exhibits no obvious influence on QDs PL emission. Similar to all the H₂O₂-based bioassays, some reducing substances in the plasma or other body fluids may interfere with the glucose assay as they can consume

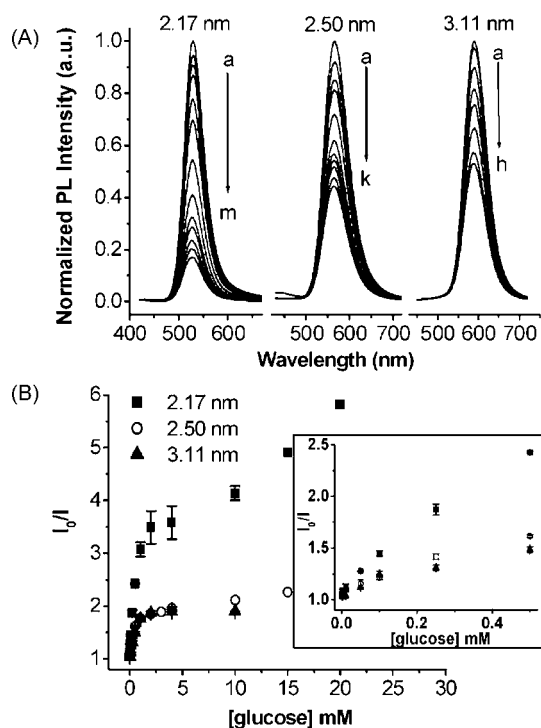


Fig. 7. (A) PL spectra represent the quenching effect of glucose–GOD system with different glucose concentrations on QDs PL intensity with three different QDs diameters; for 2.17 nm QDs, glucose concentration from a to m, 0, 0.1 μM, 1.0 μM, 10 μM, 50 μM, 0.1 mM, 0.25 mM, 0.5 mM, 1.0 mM, 2.0 mM, 10 mM, 15 mM, 20 mM; for 2.50 nm QDs, a–k, 0, 1.0 μM, 50 μM, 0.1 mM, 0.25 mM, 0.5 mM, 1.0 mM, 2.0 mM, 4.0 mM, 10 mM, 15 mM; for 3.11 nm QDs, a–h, 0, 1.0 μM, 50 μM, 0.1 mM, 0.25 mM, 0.5 mM, 1.0 mM, 2.0 mM. (B) The relationship between I_0/I and the concentration of glucose using QDs with different diameters; inset, relationship between I_0/I and the concentration of glucose within 0.5 mM. 0.16 mg/mL GOD; enzymatic incubation time, 5 min; incubation time of QDs and glucose–GOD system, 5 min; 50 mM phosphate buffer solution (pH 7.4).

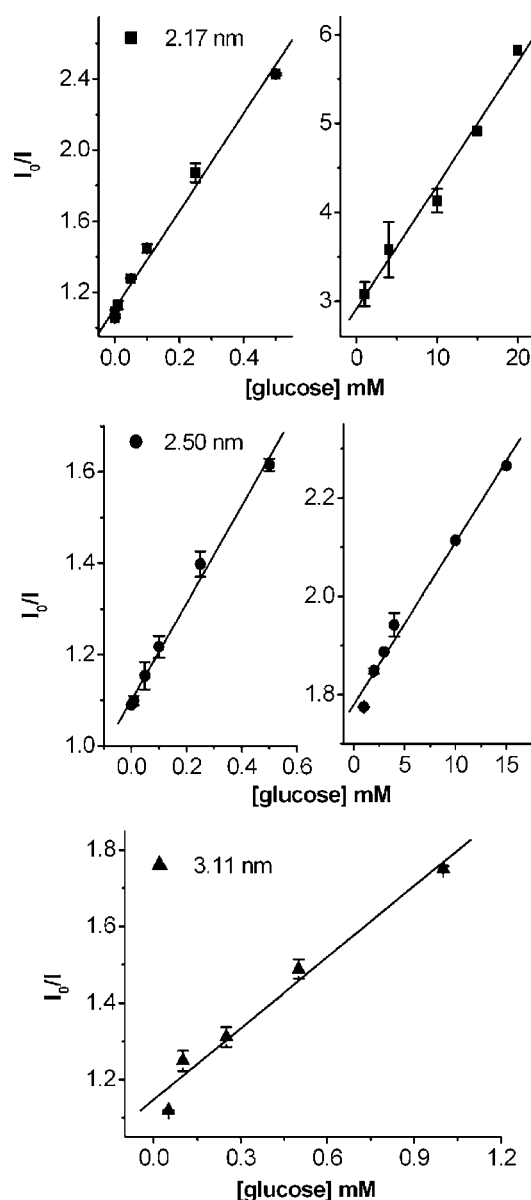


Fig. 8. Linear regression curves of glucose detection using QDs with diameters of 2.17 nm, 2.50 nm and 3.11 nm, respectively. 0.16 mg/mL GOD; enzymatic incubation time, 5 min; incubation time of QDs and glucose–GOD system, 5 min; 50 mM phosphate buffer solution (pH 7.4).

Table 2

Glucose content determination in serum samples.

Sample	Content determined by local hospital (mM)	Content determined by this method (mM)	Relative error (%)
1	5.46	5.27	−3.48
2	5.79	6.40	10.54
3	6.31	6.37	0.95
4	9.37	9.79	4.48
5	9.60	9.43	−1.77

H₂O₂ produced from GOD catalyzed glucose oxidation. It should be noticed that ethylenediaminetetraacetic acid dipotassium salt (EDTA2K) that is usually used as anticoagulant existing in the anticoagulant blood, can bind to the surface Cd site on CdTe QDs and reduce the stability of QDs reaction with QDs [42], resulting serious interference on glucose detection.

To investigate the feasibility of the sensing system for analysis glucose in biological samples, glucose concentration in human serum was examined. Serum was mixed with phosphate buffer solution that containing 0.16 mg/mL GOD, allowing inhibition for 5 min, and a certain volume of GSH-QDs was added into the mixture for another 5 min. The quenching extent of QDs PL intensity was used to calculate the glucose concentration in serum. Serum glucose detection results were listed in Table 2. It can be seen that the glucose concentration determined using the current method were close to the values provided by the local hospital.

4. Conclusion

With the utilizing of GSH-capped CdTe QDs that was highly sensitive to H₂O₂, a sensitive glucose determination system was developed. Quantitative detection of glucose ranging from 1.0 μM to 20 mM with a detection limit of 0.1 μM was achieved. The relatively low detection limit, wide detection range and the simple determination procedure make this GSH-capped CdTe QDs-based method component for glucose detection. And also, based on GSH-capped CdTe QDs, sensing systems for various analytes or bio-processes that produce H₂O₂ could also be developed.

Acknowledgements

This work was supported by NSFC 20575064, 20675076, 20735003 and Chinese Academy of Sciences KCJX2. YW. H09, H11.

References

- [1] A.P. Alivisatos, Science 271 (1996) 933.
- [2] J.M. Costa-Fernandez, R. Pereiro, A. Sanz-Medel, Trends Anal. Chem. 25 (2006) 207.
- [3] L.E. Brus, J. Chem. Phys. 79 (1983) 5566.
- [4] L. Spanhel, M. Haase, H. Weller, A. Henglein, J. Am. Chem. Soc. 109 (1987) 5649.
- [5] M.G. Bawendi, M.L. Steigerwald, L.E. Brus, Annu. Rev. Phys. Chem. 41 (1990) 477.
- [6] K.E. Sapsford, T. Pons, I.L. Medintz, H. Mattoussi, Sensors 6 (2006) 925.
- [7] X. Wang, M.J. Ruedas-Rama, E.A.H. Hall, Anal. Lett. 40 (2007) 1497.
- [8] P. Jorge, M.A. Martins, T. Trindade, J.L. Santos, F. Farahi, Sensors 7 (2007) 3489.
- [9] F.M. Raymo, I. Yildiz, Phys. Chem. Chem. Phys. 9 (2007) 2036.
- [10] M. Zayats, I. Willner, Adv. Biochem. Eng. Biotechnol. 109 (2008) 255.
- [11] Y. Chen, Z. Rosenzweig, Anal. Chem. 74 (2002) 5132.
- [12] J.G. Liang, X.P. Ai, Z.K. He, D.W. Pang, Analyst 129 (2004) 619.
- [13] K.M. Gattas-Asfura, R.M. Leblanc, Chem. Commun. (2003) 2684.
- [14] J. Liang, S. Huang, D. Zeng, Z. He, X. Ji, X. Ai, H. Yang, Talanta 69 (2006) 126.
- [15] Q. Liao, Y. Li, C. Huang, Chem. Res. Chin. U 23 (2007) 138.
- [16] C.Y. Chen, C.T. Cheng, C.W. Lai, P.W. Wu, K.C. Wu, P.T. Chou, Y.H. Chou, H.T. Chiu, Chem. Commun. (2006) 263.
- [17] S. Banerjee, S. Kar, S. Santra, Chem. Commun. (2008) 3037.
- [18] A.R. Clapp, I.L. Medintz, H. Mattoussi, Chem. Phys. Chem. 7 (2006) 47.
- [19] K.E. Sapsford, L. Berti, I.L. Medintz, Angew. Chem. Int. Ed. 45 (2006) 4562.
- [20] F. Patolsky, R. Gill, Y. Weizmann, T. Mokari, U. Banin, I. Willner, J. Am. Chem. Soc. 125 (2003) 13918.
- [21] L. Shi, V. De Paoli, N. Rosenzweig, Z. Rosenzweig, J. Am. Chem. Soc. 128 (2006) 10378.
- [22] I. Yildiz, M. Tomasulo, F.M. Raymo, Proc. Natl. Acad. Sci. U.S.A. 103 (2006) 11457.
- [23] D.B. Cordes, S. Gamsey, B. Singaram, Angew. Chem. Int. Ed. 45 (2006) 3829.
- [24] T. Ferri, S. Maida, A. Poscia, R. Santucci, Electroanalysis 13 (2001) 1198.
- [25] Y. Wu, S. Hu, Bioelectrochemistry 70 (2007) 335.
- [26] B.Y. Wu, S.H. Hou, F. Yin, Z.X. Zhao, Y.Y. Wang, X.S. Wang, Q. Chen, Biosens. Bioelectron. 22 (2007) 2854.
- [27] Y. Lv, Z. Zhang, F. Chen, Talanta 59 (2003) 571.
- [28] J. Li, X.Q. Lin, Biosens. Bioelectron. 22 (2007) 2898.
- [29] S. Cavaliere-Jaricot, M. Darbandi, E. Kucur, T. Nann, Microchim. Acta 160 (2008) 375–383.
- [30] C.P. Huang, S.W. Liu, T.M. Chen, Y.K. Li, Sens. Actuators B 130 (2008) 338.
- [31] H.D. Duong, J. I. Rhee Talanta 73 (2007) 899.
- [32] J. Yuan, W. Guo, E. Wang, Biosens. Bioelectron. 23 (2008) 1567.
- [33] R. Gill, L. Bahshi, R. Freeman, I. Willner, Angew. Chem. Int. Ed. 47 (2008) 1676.
- [34] H. Qian, C. Dong, J. Weng, J. Ren, Small 2 (2006) 747.
- [35] Y. Zheng, S. Gao, J.Y. Ying, Adv. Mater. 19 (2007) 376.
- [36] H.F. Bao, E.K. Wang, S.J. Dong, Small 2 (2006) 476.
- [37] W.W. Yu, L. Qu, W. Guo, X. Peng, Chem. Mater. 15 (2003) 2854.
- [38] Z. Wang, J. Li, B. Liu, J. Hu, X. Yao, J. Li, J. Phys. Chem. B 109 (2005) 23304.
- [39] B. Chen, Z. Ping, Anal. Bioanal. Chem. 381 (2005) 986.
- [40] J. Li, D. Bao, X. Hong, D. Li, J. Li, Y. Bai, T. Li, Colloid Surf. A 257 (258) (2005) 267.
- [41] Y.S. Xia, C.Q. Zhu, Talanta 75 (2008) 215–221.
- [42] Z. Tang, Y. Wang, S. Shanbhag, N. Kotov, J. Am. Chem. Soc. 128 (2006) 7036.



Studies on the aconitine-type alkaloids in the roots of *Aconitum Carmichaeli* Debx. by HPLC/ESIMS/MSⁿ

Hao Yue^{a,b}, Zifeng Pi^a, Fengrui Song^a, Zhiqiang Liu^a, Zongwei Cai^b, Shuying Liu^{a,*}

^a Changchun Center of Mass Spectrometry, Changchun Institute of Applied Chemistry, Chinese Academy of Sciences, 5625 Renmin Street, Changchun 130022, China

^b Department of Chemistry, Hong Kong Baptist University, Kowloon, Hong Kong SAR, China

ARTICLE INFO

Article history:

Received 4 August 2008

Received in revised form 9 October 2008

Accepted 11 October 2008

Available online 22 October 2008

Keywords:

HPLC/ESIMS/MSⁿ

FTICR/ESIMS

Aconitine-type alkaloids

Aconitum Carmichaeli

C₁₉-norditerpenoid

ABSTRACT

Studies of aconitine-type alkaloids in the Chinese herb *Aconitum Carmichaeli* were performed by HPLC/ESIMS/MSⁿ and FTICR/ESIMS in positive ion mode. The characteristic fragmentation pathways in the MSⁿ spectra were summarized based on previously published research literature and further study. According to the fragmentation pathways of mass spectrometry, results from the analysis of standard compounds and reports from literature, 111 compounds were identified or deduced in a total of 117 found compounds in *A. Carmichaeli*. In the 11 monoester-diterpenoid alkaloids (MDA), 10 diesterditerpenoid alkaloids (DDA) and 81 lipo-alkaloids, the novel alkaloids including 1 MDA, 2 DDA and 48 lipo-alkaloids were detected. In addition, 1 DDA, 7 lipo-alkaloids and 2 alkaloids with small molecular weights that possess C₁₉-norditerpenoid skeleton were reported in *A. Carmichaeli* for the first time.

© 2008 Elsevier B.V. All rights reserved.

1. Introduction

Aconitum Carmichaeli is widely distributed in the northern hemisphere of China [1]. Aconitine-type alkaloid extracts from the roots of *A. Carmichaeli* have analgetic, diuretics, anti-inflammatory and cardiotoxic actions [2–4]. At the same time, they also present enormous toxicity [5,6]. The NMR and MALDI/TOFMS techniques have been applied to characterize structure of the compounds isolated from the *Aconitum* genus [7–10]. In our previous work, the fragmentation pathways of aconitine-type alkaloids in extracts of *Aconitum Kusnezoffii* and *A. Carmichaeli* were studied by ESIMS/MSⁿ and MALDI/TOFMS [11–13]. A series of aconitine-type alkaloids had been detected based on the known fragmentation pathways. Because high performance liquid chromatography (HPLC) coupled with mass spectrometry (MS) provides selective and sensitive for the analysis of complex mixtures without complicated component isolation, it has been applied to the analysis of known aconitine-type compounds [14–16]. Moreover, FTICR/ESIMS (Fourier transform ion cyclotron resonance) has been also played an important role in the identification of compound's structures due to the fact that it not only provide structural information on the analysis, but also determines the precise mass/charge ratio and the elemental composition of ions.

Aconitine-type alkaloids share a common C₁₉-norditerpenoid skeleton. Traditionally, they can be divided into three major types according to the substitute at the C₈ position of the diterpenoid skeleton. These are monoester-diterpenoid alkaloids (MDA), diester-diterpenoid alkaloids (DDA) and lipo-alkaloids, in which the C₈ position is occupied by hydroxyl group, an acetyl or a fatty acid acyl, respectively. The structures of the known alkaloids are summarized in Table 1.

In this study, HPLC/ESIMS/MSⁿ was used to identify aconitine-type alkaloids in *A. Carmichaeli* (Fuji). Firstly, the fragmentation pathways for the characterization of structure of aconitine-type alkaloids were studied by ESIMS/MSⁿ. According to the obtained characteristic fragmentation pathways, a total of 111 alkaloids in Fuji were characterized and identified by HPLC/ESIMS/MSⁿ and FTICR/ESIMS. Fifty-one novel alkaloids were firstly detected in Fuji (alkaloids denoted double asterisk in Table 2).

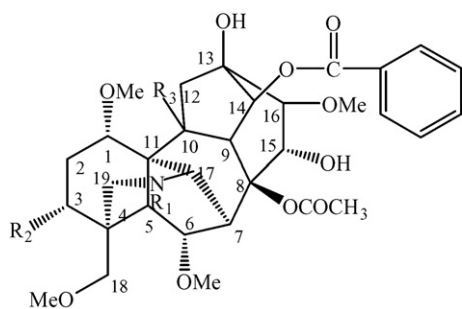
2. Experimental

2.1. Materials

Standards of aconitine (AC), hypaconitine (HA), and mesaconitine (MA) were purchased from the Chinese Authenticating Institute of Material and Biological Products (Beijing, China). Other alkaloid standards were kindly provided by the west China College of pharmacy, Sichuan University. Fuji (Processed roots of *A. Carmichaeli*) were purchased from a Changchun drugstore.

* Corresponding author. Tel.: +86 431 85262613.

E-mail address: mslab@ciac.jl.cn (S. Liu).

Table 1The structures of some known aconitine-type alkaloids in *Aconitum*.

Aconitines	[M+H] ⁺	R ₁	R ₂	R ₃
Hypaconitine	616	CH ₃	H	H
Deoxyaconitine	630	C ₂ H ₅	H	H
Mesaconitine	632	CH ₃	OH	H
Aconitine	646	C ₂ H ₅	OH	H
10-OH-mesaconitine	648	CH ₃	OH	OH
10-OH-aconitine	662	C ₂ H ₅	OH	OH

When C₈ is occupied by OH group, monoester-diterpenoid aconitines is formed. When C₈ is occupied by a fatty acyl, such as linoleic, oleic, nonadecenoic acid and lipo alkaloids is formed.

Methanol and acetonitrile were HPLC grade and other reagents used were analytical grade. Deionized water was prepared using a Millipore water purification system.

All standards were prepared in dichloromethane at the concentrations of 75 µg mL⁻¹. Five grams dried power of Fuzi was soaked with 50 mL ether for 12 h after mixing with 10% aqueous ammonia at room temperature. Then the extracted solution was diluted with methanol and filtered through a syringe filter (0.45 µm), before being analyzed by HPLC–ESIMS/MSⁿ and ESI–FTICR–MS.

2.2. HPLC–ESI–MSⁿ

The HPLC system consisted of a Waters (Milford, MA, USA) 2690 with a photodiode-array 969 detector coupled with a Millennium³² workstation. HPLC/ESIMS/MSⁿ experiments were performed using a LCQ ion trap mass spectrometer (Finnigan MAT, San Jose, CA, USA) equipped with an electrospray source in the positive ion mode which is capable of analyzing ions up to *m/z* 2000. The electrospray voltage was set to 5.0 kV. The capillary temperature was 260 °C. The HPLC was connected to the mass spectrometer via the UV cell outlet. Nitrogen gas was used as both a sheath gas and an auxiliary gas. The collision gas used was helium gas, and the collision energy (%) for the MSⁿ analyses ranged from 25 to 42%.

To develop a chromatographic method about three type aconitine-alkaloids, three columns (Agilent Zobax XDB-C18, Waters C18, and Agilent RP18 column) were used in various conditions. A series of parameters were set to optimize the separation, including organic modifiers, buffer concentrations, column temperatures and flow rates. According to the experimental results, good separation could be carried out by using an Agilent RP18 column (150 mm × 2.6 mm, 5 µm). The mobiles used for HPLC separation were acetonitrile (A) and water (0.2% triethylamine and 0.5% acetic acid) (B). The gradient elution of mobile was 0–50 min 15–50% B, 50–90 min 50–80% B and 90–130 min 50–80% B. The flow rate was set at 0.6 mL min⁻¹, and the column temperature was maintained at 23 °C.

2.3. ESI–FTICR–MS

The high-resolution mass spectrometry was performed using an IonSpec Ultima 7.0T FTICR instrument (IonSpec, CA, USA) with an

electrospray source in the positive ion mode. The probe heater was set at 100 °C and the source heater was set at 80 °C. The probe HV was set to 3.8 kV. The sample cone voltage was set to –30 V. The extractor cone was set to 5 V. The desolvation gas was set to 0.1 V. The cone gas was set to 0.85 V, and the collision gas N₂ was set to 100 ms pulse (40 Torr).

3. Results and discussion

3.1. ESIMS/MSⁿ analysis

In the previous work, the specific fragmentation pathways of the aconitine-type alkaloids were studied [11,17–19]. In some literature reports, the explanation on the neutral losses of CO and CH₃OH in MSⁿ spectra of DDA was different. The proposed general mechanism for successive losses of AcOH, CO, C₆H₅COOH, H₂O and CH₃OH from DDA was deduced, as shown in Scheme 1 (HA is as an example). The predominant daughter ion (*m/z* 556) in MS/MS spectrum of HA corresponded to a neutral loss AcOH from HA. The formation of [M+H–AcOH–CH₃OH–CO]⁺ suggested that the AcOH eliminated from C₇ and C₈ and the CH₃OH eliminated from C₁₅ and C₁₆. Then the enol was yielded and tautomerized into carbonyl and CO was lost. The conclusion about the losses of CO by Li agreed well with our analytical results [18]. The loss CH₃OH within the daughter ion [M+H–AcOH–CH₃OH]⁺ was eliminated from the methoxyl on C₁₆ and the proton on C₁₅ because the loss CO was detected in MS³ spectrum of [M+H–AcOH–CH₃OH]⁺. In the MS³ experiment with the precursor ion at *m/z* 556, *m/z* 524 [F+H–CH₃OH]⁺, 506 [F+H–CH₃OH–H₂O]⁺, 496 [F+H–CH₃OH–CO]⁺, 432 [F+H–3CH₃OH–CO]⁺, 402 [F+H–CH₃OH–BzOH]⁺ and 338 [F+H–3CH₃OH–BzOH]⁺ [11]. The unknown aconitine-type compounds could be identified according to the fragmentation pathways.

3.2. HPLC/ESIMS/MSⁿ and ESI–FTICR–MS

When using the total ion chromatograms (TIC) of *A. genus* extracts alone (not shown), the identification of peaks was difficult. But a total 117 peaks can be identified by extracted ion chromatograms (EIC), according to the information of retention time (*t_R*), protonated molecules ([M+H]⁺), the product ions and data reported from literature (Table 2).

3.2.1. Diester-diterpenoid alkaloids and their analogues

Fig. 1 shows typical EIC at *m/z* 616, 632, 646 of Fuzi extracts. The compounds with *m/z* 616 (*t_R* 23.26 min), 632 (*t_R* 20.28 min), 646 (*t_R* 22.45 min) corresponded to HA, MA and AC, respectively, which were confirmed by *t_R* and the comparison with the MS/MS data obtained from the analysis of standards (Table 2–peaks 24, 17 and 21). The peaks at 17.97 min and *m/z* 648, 20.73 min and *m/z* 662, as well as 26.67 min and *m/z* 630 had the similar fragmentation pathways of AC (Table 2–peak 12, 19 and 29). The loss of acetic acid is the dominant fragmentation. According to the MS/MS data and the literature reports [11], it could be concluded that *m/z* 630, 648 and 662 corresponded to the protonated molecules of deoxyaconitine (DA), 10-OH-mesaconitine and 10-OH-aconitine, respectively.

For the *m/z* 614 ion in EIC, there were two peaks at *t_R* 25.68 min (Table 2–peak 28) and 29.88 min (Table 2–peak 32) (Fig. 2a). Peak 28 showed the neutral losses of acetic acid (60 Da), methanol (32 Da), and carbon monoxide (28 Da) in the ESIMS/MS analysis (Fig. 2b). Peak 32 did not give the fragment ion of [M+H–AcOH–CH₃OH–CO]⁺ (*m/z* 494), but showed the [M+H–AcOH–H₂O]⁺ ion at *m/z* 536 in the MS/MS spectrum compared with that of peak 28 (Fig. 2c). This difference indicated that they are isomers. Only peak 28 has a hydroxyl group at C₁₅ because of the neutral losses of CO according

Table 2Compounds identified in *Aconitum Carmichaeli* by HPLC–MSⁿ and FTICR–MS.

	<i>t</i> _R	[M+H] ⁺	Alkaloids		<i>t</i> _R	[M+H] ⁺	Alkaloids
1	3.45	438	Neoline ^{**}	60	48.48	850	8-ndd-Benzoylhypaconine
2	4.93	454	Fuziline ^{**}	61	48.73	864	8-ndd-Benzoyldeoxyaconine
3	5.38	438	Neoline ^{**}	62	49.91	868	8-ndc-Benzoyldeoxyaconine
4	6.44	422	Talatzamine ^{**}	63	50.25	852	8-ndn-Benzoylhypaconine
5	8.35	452	Chasmanine [*]	64	50.48	810	8-ttd-Benzoylaconine
6	9.58	464	14-Acetyltalatzamine ^{**}	65	50.67	866	8-linolen-10-OH-Benzoylmesaconine [*]
7	10.57	606	14-Benzoyl-10-OH-mesaconine [*]	66	51.90	890	8-htt-Benzoyldeoxyaconine
8	12.61	620	14-Benzoyl-10-OH-aconine [*]	67	52.55	824	8-pmd-Benzoylmesaconine
9	13.51	590	14-Benzoylmesaconine [*]	68	52.69	890	8-htt-Benzoyldeoxyaconine
10	15.48	604	14-Benzoylaconine ^{**}	69	53.37	840	8-str-Benzoylhypaconine
11	16.54	574	14-Benzoylhypaconine ^{**}	70	54.78	840	8-pme-Benzoylaconine ^{**}
12	17.97	648	10-OH-mesaconitine ^{**}	71	55.01	840	8-hdc-Benzoyldeoxyaconine
13	18.01	558	14-Benzoyl-3,13-deoxyaconine	72	55.71	850	8-linolen-Benzoylmesaconine ^{**}
14	18.63	588	14-Benzoyldeoxyaconine ^{**}	73	56.96	868	8-lino-10-OH-Benzoylmesaconine ^{**}
15	19.71	556	Dehydrated benzoylhypaconine ^{**}	74	58.32	812	8-pdn-Benzoylmesaconine ^{**}
16	20.02	500	Aconine ^{**}	75	58.43	864	8-linolen-Benzoylaconine ^{**}
17	20.28	632	Mesaconitine ^{**}	76	59.10	800	8-ttac-Benzoylmesaconine
18	20.55	542	14-Benzoylnoeline	77	59.64	834	8-linolen-Benzoylhypaconine ^{**}
19	20.73	662	10-OH-aconitine [*]	78	60.16	882	8-lino-10-OH-Benzoylaconine ^{**}
20	21.67	588	Dehydrated 14-benzoyl-10-OH-mesaconine ^{**}	79	61.34	826	8-pme-Benzoylmesaconine ^{**}
21	22.45	646	Aconitine ^{**}	80	61.92	826	8-pdn-Benzoylaconine ^{**}
22	22.83	572	Dehydrated benzoylmesaconine ^{**}	81	62.47	858	8-esp-Benzoylhypaconine
23	23.01	618	8-Methoxyl-14-benzoylaconine [*]	82	62.99	796	8-pdn-Benzoylhypaconine
24	23.26	616	Hypaconitine ^{**}	83	63.91	848	8-linolen-Benzoyldeoxyaconine ^{**}
25	24.33	600	13-Deoxyhypaconitine	84	64.33	784	8-ttac-Benzoylhypaconine
26	25.06	700	Unknown	85	65.11	852	8-lino-Benzoylmesaconine ^{**}
27	25.22	628	Foreaconitine ^{**}	86	66.47	810	8-pme-Benzoylhypaconine
28	25.68	614	3,13-Deoxyaconitine	87	67.42	844	8-pal-10-OH-Benzoylmesaconine ^{**}
29	26.67	630	Deoxyaconitine ^{**}	88	67.84	814	8-pdc-Benzoylmesaconine ^{**}
30	27.01	570	Dehydrated deoxyaconitine ^{**}	89	68.86	866	8-lino-Benzoylaconine ^{**}
31	27.88	684	Unknown	90	71.10	836	8-lino-Benzoylhypaconine ^{**}
32	29.88	614	Chasmaconitine	91	73.58	858	8-pal-10-OH-Benzoylaconine ^{**}
33	30.23	668	Unknown	92	74.98	798	8-pdc-Benzoylhypaconine ^{**}
34	31.62	726	Unknown	93	75.23	840	8-htn-Benzoylmesaconine
35	32.78	770	Unknown	94	77.63	850	8-lino-Benzoyldeoxyaconine ^{**}
36	34.93	784	Unknown	95	78.81	884	8-ole-10-OH-Benzoylaconine [*]
37	35.85	900	8-esc-10-OH-Benzoylmesaconine [*]	96	79.28	824	8-htn-Benzoylhypaconine
38	37.28	868	8-ndc-Benzoyldeoxyaconine	97	80.85	828	8-pal-Benzoylmesaconine ^{**}
39	39.03	902	8-dcs-Benzoylaconine	98	83.80	812	8-pdc-Benzoyldeoxyaconine
40	42.36	904	8-esp-10-OH-Benzoylaconine	99	83.90	796	8-pal-Benzoyl-15-deoxyhypaconine
41	42.99	904	8-hct-Benzoylaconine	100	84.00	854	8-ole-Benzoylmesaconine ^{**}
42	44.98	882	8-esc-Benzoyldeoxyaconine	101	86.78	842	8-pal-Benzoylaconine ^{**}
43	45.22	882	8-ecn-Benzoylmesaconine ^{**}	102	88.69	822	8-ole-Benzoyl-15-dexoyhypaconine
44	45.96	882	8-ndd-10-OH-Benzoylmesaconine	103	90.33	812	8-pal-Benzoylhypaconine ^{**}
45	46.12	868	8-esc-Benzoylhypaconine	104	92.60	868	8-ndn-Benzoylmesaconine ^{**}
46	46.23	866	8-htt-Benzoylhypaconine	105	93.12	834	8-lino-Benzoyl-3,13-deoxyaconine
47	46.35	866	8-ndn-Benzoyldeoxyaconine	106	93.87	880	8-ndt-10-OH-Benzoylmesaconine
48	46.86	938	8-tsn-Benzoylaconine	107	94.10	838	8-ole-Benzoylhypaconine ^{**}
49	46.86	938	8-ttec-Benzoyldeoxyaconine	108	97.22	796	8-pdc-Benzoyl-3,13-deoxyaconine
50	46.97	938	8-psc-Benzoylhypaconine	109	99.65	842	8-hdc-Benzoylmesaconine [*]
51	46.98	938	8-tten-Benzoylmesaconine	110	101.14	826	8-pal-Benzoyldeoxyaconine ^{**}
52	47.01	922	8-tsn-Benzoyldeoxyaconine	111	103.52	864	8-ecd-Benzoylhypaconine
53	47.01	922	8-tten-Benzoylhypaconine	112	105.72	852	8-ole-Benzoyldeoxyaconine [*]
54	47.05	922	8-tds-Benzoylmesaconine	113	106.66	856	8-hdc-Benzoylaconine [*]
55	47.14	952	8-psc-Benzoyldeoxyaconine	114	112.63	826	8-hdc-Benzoylhypaconine [*]
56	47.14	952	8-tten-Benzoylaconine	115	122.32	810	8-pal-Benzoyl-3,13-deoxyaconine
57	47.31	854	8-ndc-Benzoylhypaconine	116	125.89	856	8-str-Benzoylmesaconine
58	47.86	936	8-tten-Benzoyldeoxyaconine	117	126.84	838	8-str-Benzoyl-3,13-deoxyaconine
59	48.35	936	8-tds-Benzoylaconine				

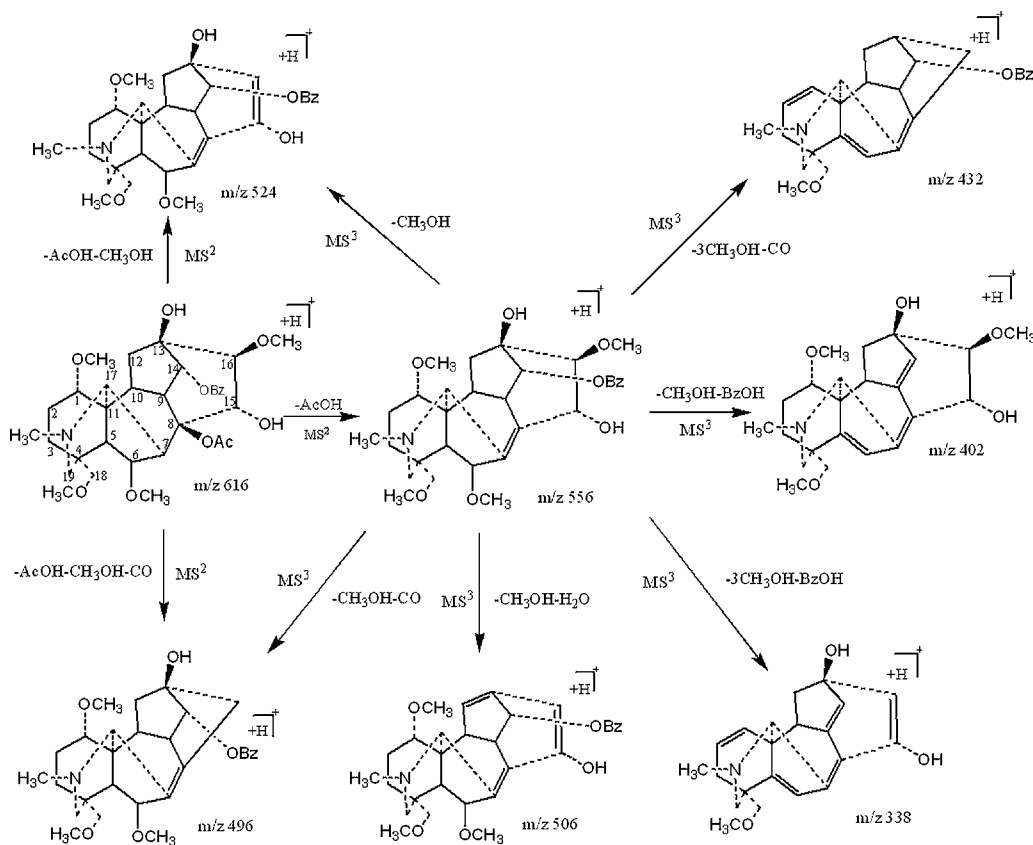
Ttd, ttac, pdn, pdc, pmd, pme, pal, htn, hdc, linolen, lino, ole, str, ndt, ndd, ndn, ndc, esp, ecd, ecn, esc, dcs, hct, htt, tsd, tsn, tten, ttec and psc represent the residues of tetradecadienoic acid, tetradecanoic acid, pentadecenoic acid, pentadecanoic acid, palmitadienoic acid, palmitoleic acid, palmitic acid, heptadecenoic acid, heptadecanoic acid, linolenic acid, linoleic acid, oleic acid, stearic acid, nonadecatrienoic acid, nonadecadienoic acid, nonadecenoic acid, nonadecanoic acid, eicosapentaenoic acid, eicosadienoic acid, eicosenoic acid, docosanoic acid, heneicosapentaenoic acid, heneicosatetraenoic acid, tricosadienoic acid, triosenic acid, tetradecenoic acid, tetracosanoic acid and pentacosanoic acid, respectively.

^{*} Denotes the known alkaloids in *Aconitum* L.

^{**} Denotes the known alkaloids in *A. Carmichaeli*.

to fragmentation pathways of the aconitine-type alkaloids. In a full-scan high-resolution mass spectra both alkaloids showed the same protonated molecular ion [M+H]⁺ at *m/z* 614.33209. The proposed formula was C₃₄H₄₈NO₉⁺ and measurement error was −0.44 ppm. From the obtained results of structural information, the compound

of peak 32 was identified as chasmaconitine from the described fragmentation pathways that were reported previously (Table 3) [20]. The characteristic product ions of [M+H−AcOH−H₂O]⁺ in the MS/MS spectrum of chasmaconitine was yielded from the neutral loss of acetic acid at C₈ and C₁₅ and H₂O at C₁₃ and C₁₆. Compared



Scheme 1. Proposed fragmentation pathway of DDA in ESI-MSⁿ.

with the structure of chasmaconitine, the unique product ions of peak 28 may be attributed from OH substitution at C₁₅ and not at C₁₃. Therefore, the compound corresponding to peak 28 was identified as 3,13-deoxy-aconitine, whose structure was tentatively deduced and shown in Table 3. Similarly, the peak 25 (*m/z* 600) eluted at 24.33 min showed the characterized fragments, such as [M+H-AcOH]⁺, [M+H-CH₃OH]⁺, [M+H-AcOH-CH₃OH]⁺, [M+H-AcOH-2CH₃OH]⁺ and [M+H-AcOH-CH₃OH-CO]⁺ in MS/MS spectrum (Fig. 3). Its high-resolution mass spectrometry data gave the proposed formulae of C₃₃H₄₆NO₉⁺ with the observed mass of 600.31611 and measurement error of -1.00 ppm. Thus,

the peak at *t_R* 24.33 min corresponded to 13-deoxy-hypaconitine, which was confirmed by comparing the MS² spectra with those of hypaconitine and 3,13-deoxyaconitine (Table 3).

Additionally, the peak (*m/z* 628) eluted 25.22 min showed the same retention time and MS/MS data as those of the standard foreaconitine. The daughter ions of foreaconitine in MS/MS spectrum were as following: *m/z* 568 [M+H-AcOH]⁺, 596 [M+H-CH₃OH]⁺, 536 [M+H-AcOH-CH₃OH]⁺ and 504 [M+H-AcOH-2CH₃OH]⁺. The compound (Table 2-peak 27) had been found and identified in *A. Carmichaeli* [9].

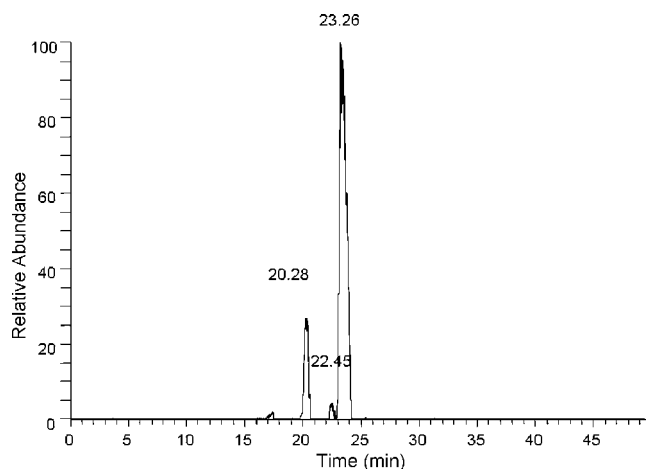


Fig. 1. The extracted ion chromatogram of mesaconitine (20.28 min), aconitine (22.45 min) and hypaconitine (23.26 min).

Table 3

The possible structure of diterpenoid alkaloids found firstly in Fuzi.

The image shows a complex polycyclic diterpenoid alkaloid skeleton. The carbons are numbered 1 through 19. Substituents include a benzoyloxy group at C-16, a methoxy group at C-18, and various other groups labeled R1, R2, R3, R4, and R5. Stereochemistry is indicated with wedged and dashed bonds.

Alkaloids	<i>t_R</i> (min)	[M+H] ⁺	R ₁	R ₂	R ₃	R ₄	R ₅
3,13-Deoxy-aconitine	25.89	614.33209	C ₂ H ₅	H	ACO	OH	H
Chasmaconitine	29.88	614.33209	C ₂ H ₅	H	ACO	H	OH
13-Deoxy-hypaconitine	24.50	600.31611	CH ₃	H	ACO	OH	H
8-Methoxy-14-benzoylaconine	23.01	618.32664	C ₂ H ₅	OH	CH ₃ O	OH	OH

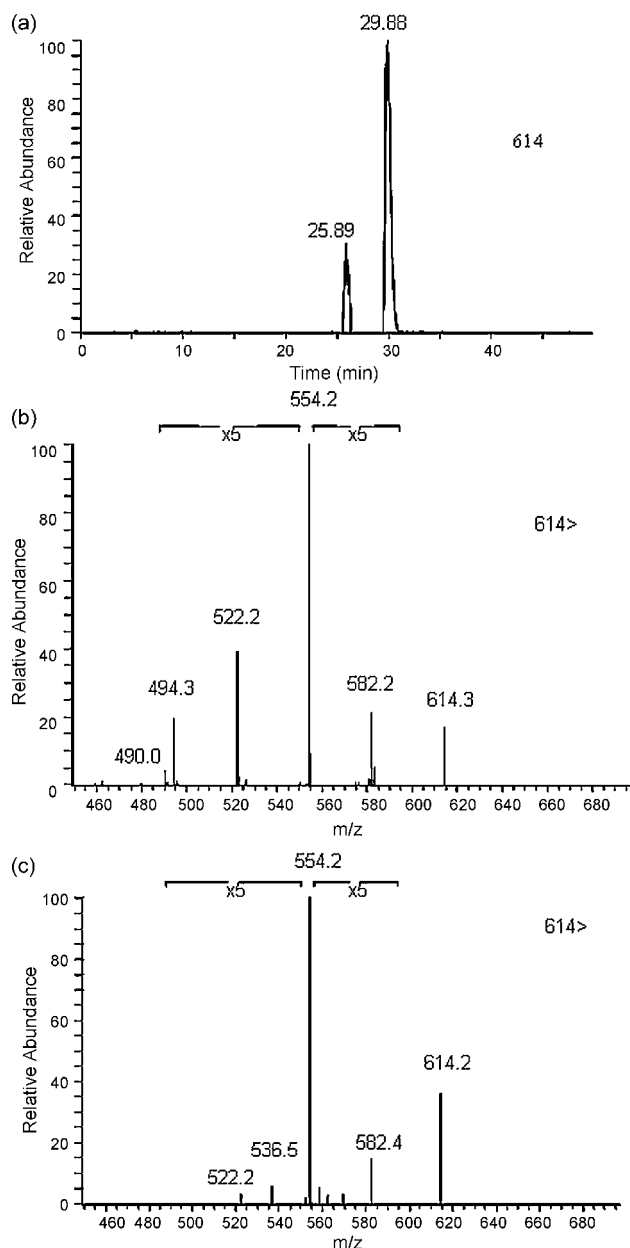


Fig. 2. The extracted ion chromatograms of m/z 614 (a) as well as the corresponding MS/MS spectra of peaks at 25.89 min (b) and 29.88 min (c).

3.2.2. Monoester-diterpenoid alkaloids

Monoester-diterpenoid aconitines showed less toxicity than DDA. During the processing of *Aconitum* roots, DDA is decayed to MDA. MDA can be divided into two types according to the substitution at the C_8 and C_{15} positions, namely the hydrolyzed MDA, in which the C_8 position is occupied by a hydroxyl group, and the pyrolysed MDA, in which the C_8 and C_{15} positions are assigned to $C=C$ bond. Peak 9 (m/z 590) eluted at 13.51 min showed the product ions at m/z 572 [$M+H-H_2O$] $^+$, 558 [$M+H-CH_3OH$] $^+$, 540 [$M+H-H_2O-CH_3OH$] $^+$, 526 [$M+H-2CH_3OH$] $^+$ and 522 [$M+H-2H_2O-CH_3OH$] $^+$ in the MS/MS spectrum. The compound could thus be identified as 14-benzoylmesaconine by comparing its MS/MS data with those of mesaconitine. Similarly, other six hydrolyzed MDA were identified (Table 2). On the other hand, peak 22 at 22.83 min and m/z 572 showed fragment ions in MS/MS spectrum as well as the MS³ data of

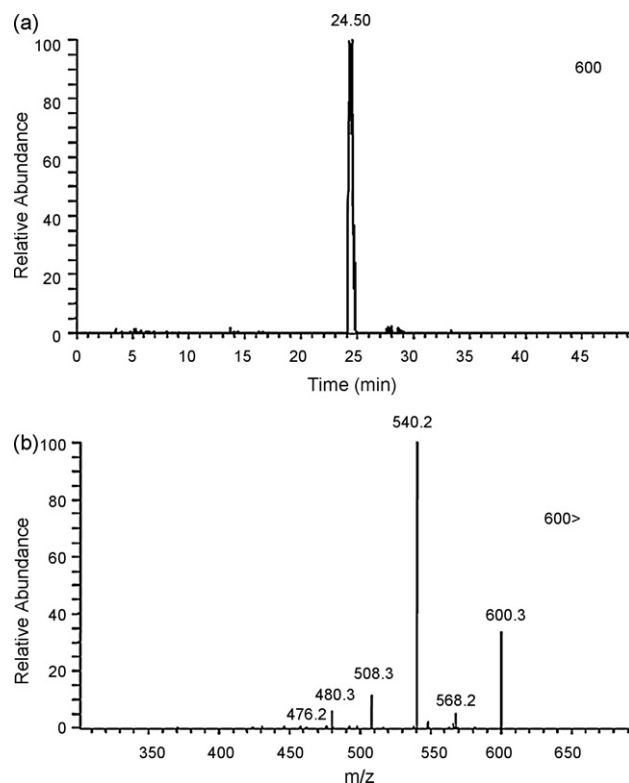


Fig. 3. The extracted ion chromatogram of m/z 600 (a) and MS/MS spectrum (b).

mesaconitine. The compound was assigned to deacetoxy benzoylmesaconine that was major component of processed Fuzi heated with sand. Accordingly, three pyrolysed MDA can also be identified and are summarized in Table 2. 14-benzoyl-3,13-deoxyaconine (Table 2-peak 13) was possibly resulted from the hydrolysis of 3,13-deoxyaconitine.

3.2.3. Lipo-alkaloids

In general, MS³ spectra of the predominant [$M-lipo$] $^+$ ion of lipo-alkaloids was the same as that of [$M-AcOH$] $^+$ of the related DDA. For example, MS³ spectra of 8-lino-benzoylaconitine and aconitine were similar. Based on the obtained fragmentation pathways, a total of 81 lipo-alkaloids were found and identified from the HPLC/ESIMS/MSⁿ analysis. For example, three peaks of retention time at 48.48, 55.71 and 77.63 min were detected with the protonated molecules at m/z 850 in Fuzi extract (Fig. 4a). Their MS/MS spectra gave predominant product ions at m/z 556, 572 and 570, corresponding to the neutral losses of nonadecadienoic acid (nnd, 294 Da), linolenic acid (linolen, 278 Da) and linoleic acid (lino, 280 Da), respectively (Fig. 4b–d). The MS³ results indicated that they were derived from HA, MA and DA. Therefore, it was likely that the ions at m/z 850 corresponded to 8-ndd-benzoylhypaconine (Table 2-peak 60), 8-linolen-benzoylmesaconine (Table 2-peak 72) and 8-lino-benzoyldeoxyaconine (Table 2-peak 94). To the best of our knowledge, this was the first report about 8-ndd-benzoylhypaconine being involved in the extraction of *Aconitum Carmichaeli*. Similarly, the MS/MS data of ion at m/z 852 gave three major predominant product ions at m/z 556 (t_R 50.25 min), 572 (t_R 65.11 min), and 570 (t_R 105.72 min), corresponding to the neutral losses of 296 Da (nonadecenoic acid), 280 Da (linoleic acid) and 282 Da (oleic acid), respectively (Fig. 5). Thus, the ions at m/z 852 corresponded to the protonated 8-ndn-benzoylhypaconine (Table 2-peak 63), 8-lino-benzoylmesaconine (Table 2-peak 85) and

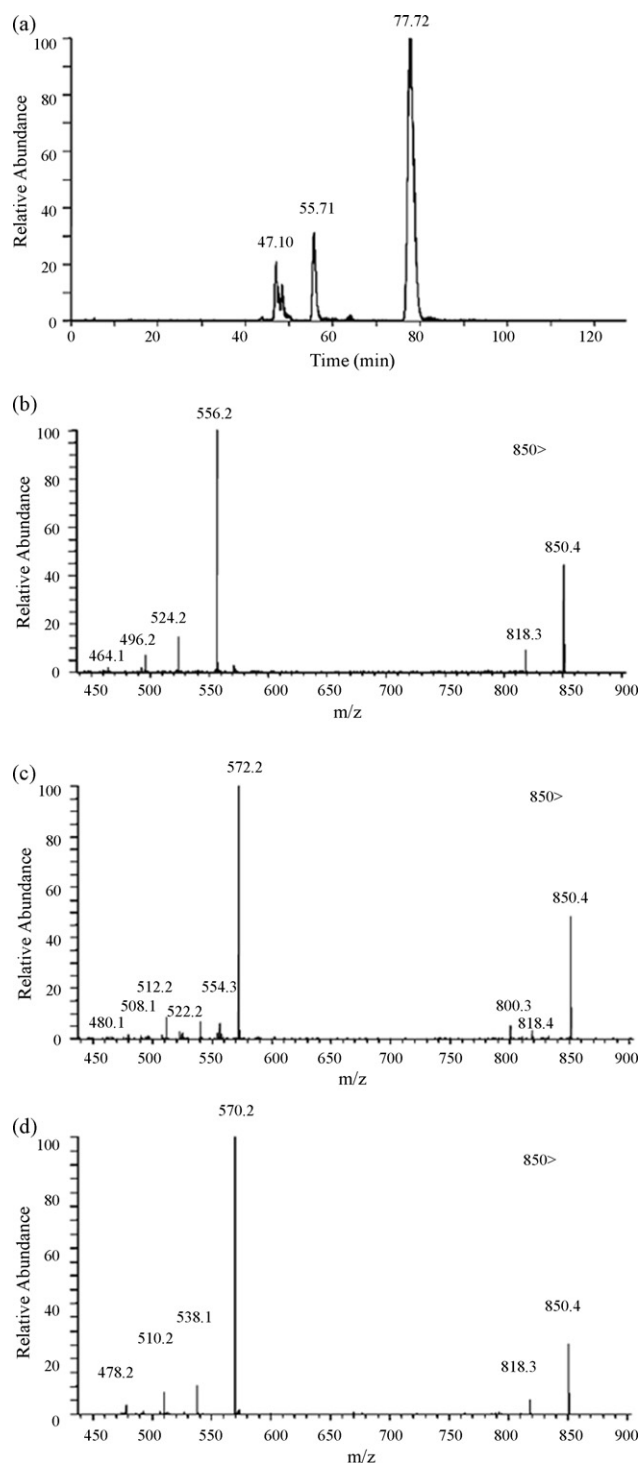


Fig. 4. The extracted ion chromatogram of m/z 850 (a), MS/MS spectra of peak at 47.10 min (b), 55.71 min (c) and 77.72 min (d).

8-ole-benzoyldeoxyaconin (Table 2-peak 112), respectively. 8-ndn-benzoylhypaconine identified in this study was also reported for the first time.

The peaks at m/z 834 were eluted at 59.64 min (Table 2-peak 77) and 93.12 min (Table 2-peak 105) (Fig. 6a). Peak 77 was easily confirmed as 8-linolen-benzoylhypaconine by its fragment ions [10]. Peak 105 produced the fragment ions at m/z 802 [$M+H-CH_3OH$] $^+$, 554 [$M+H-lino$] $^+$ (predominate ion), 522 [$M+H-lino-CH_3OH$] $^+$, and 494 [$M+H-lino-CH_3OH-CO$] $^+$, similar to

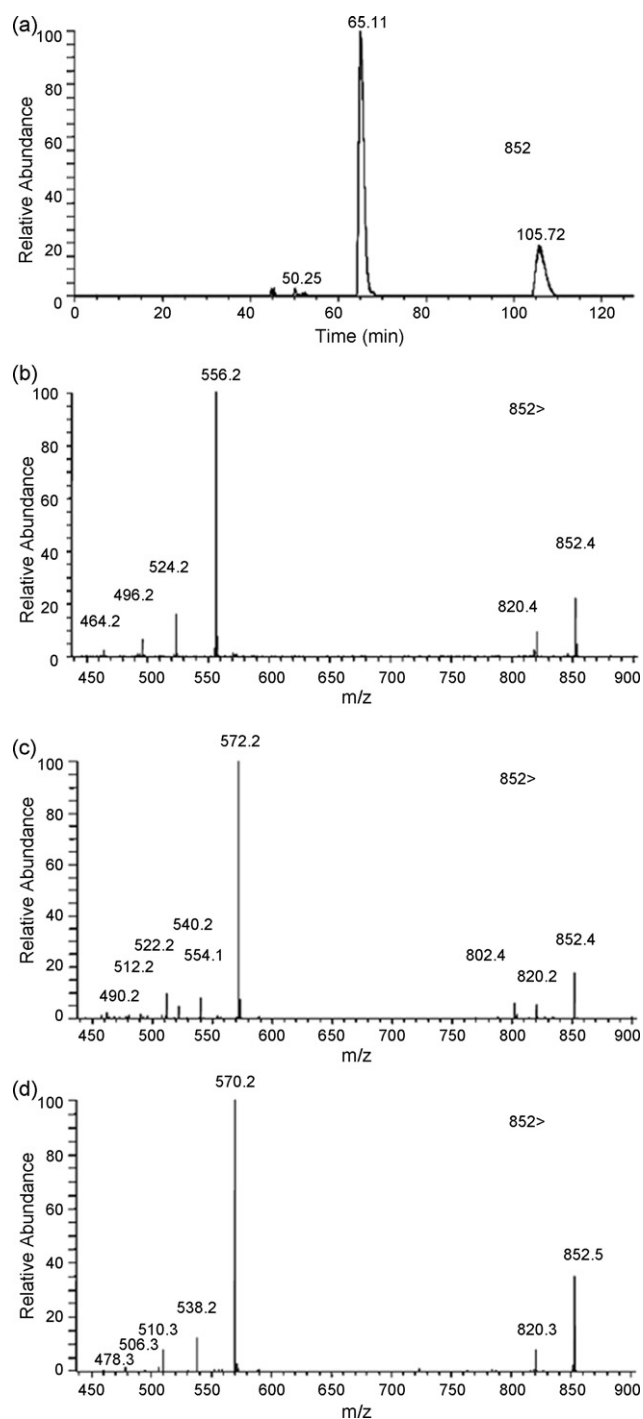


Fig. 5. The extracted ion chromatogram of m/z 852 (a), MS/MS spectra of peak at 50.25 min (b), 65.11 min (c) and 105.72 min (d).

the MS/MS spectrum of protonated 3,13-deoxyaconitine (Fig. 6b). The MS³ data of its [$M+H-lino$] $^+$ was the same as that of [$M+H-AcOH$] $^+$ of 3,13-deoxyaconine. Thus, peak 105 was identified as 8-lino-benzoyl-3,13-deoxyaconine which had not been previously reported. Additionally, the peaks at m/z 796 eluted at 62.99 min (Table 2-peak 82), 83.90 min (Table 2-peak 99) and 97.22 min (Table 2-peak 108), gave three major product ions at m/z 556, 540 and 554, corresponding to the neutral losses of 240 Da (pentadecanoic acid), 256 Da (palmitic acid) and 242 Da (pentadecanoic acid). The MS³ spectra of the ions at m/z 556, 540 and 554

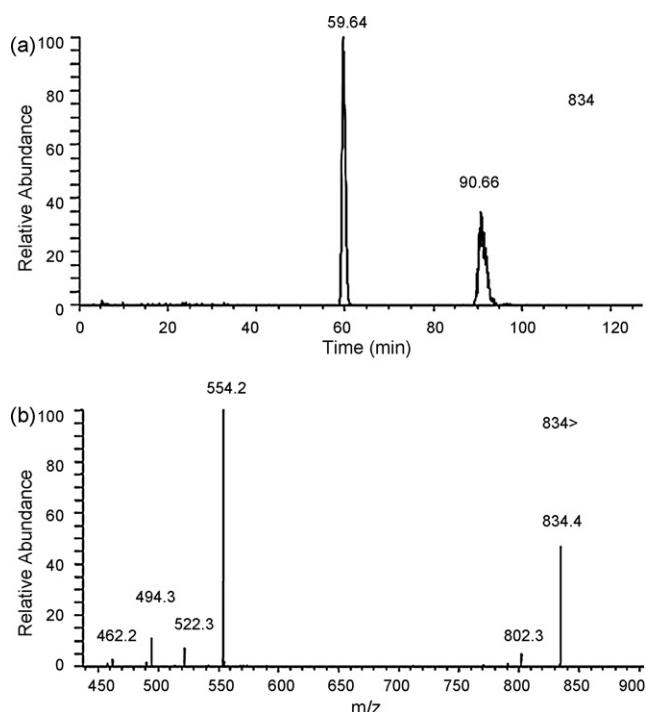


Fig. 6. The extracted ion chromatogram of m/z 834 (a) and MS/MS spectrum of peak at 90.66 min (b).

were similar to those of peak 24, 33 and 26, respectively. These compounds were confirmed as 8-pdn-benzoylhypaconine (peak 82), 8-pal-14-benzoyl-15-deoxyhypaconine (peak 99) and 8-pdc-benzoylchasmaconine (peak 108), all of which were reported for the first time. As mentioned above, all lipo-alkaloids found in Fuzi, including 48 kinds of unknown lipo-alkaloids and 7 kinds of known lipo-alkaloids in *Aconitum*, were listed in Table 2. Lipo-alkaloids with occurrence of the 14C, 21C, 23C, 24C, 25C saturated or unsaturated fatty acid residues at C₈ had not been reported previously in *Aconitum* genera.

3.2.4. Other alkaloids

Peak 23 (m/z 618) gave the product ions of $[M+H-H_2O]^+$ (m/z 600), $[M+H-CH_3OH]^+$ (m/z 586), $[M+H-CH_3OH-H_2O]^+$ (m/z 568), $[M+H-2CH_3OH]^+$ (m/z 554), $[M+H-2CH_3OH-H_2O]^+$ (m/z 536), $[M+H-3CH_3OH]^+$ (m/z 522) in the ESIMS/MS spectrum (Fig. 4). Compared with the literature reports, it was identified as 8-methoxy-14-benzoylaconine, which was already found in *Aconitum pseudostapfianum* (Table 3) [21,22].

In addition, some low m/z ions were detected within the retention time of 10 min. For example, peak 1 and 3 (m/z 438 at 3.45 and 5.38 min) were identified as isomer of neoline, as a result of the comparisons of the retention time, $[M+H]^+$ ion and characteristic fragment ions with those data of related authentic standards. The differentiation of compounds 1 and 3 could not be performed by ESIMS. Peak 2 eluted at 4.93 min and m/z 454 has the similar neutral losses to neoline, including product ions at m/z 436 $[M+H-H_2O]^+$, 418 $[M+H-2H_2O]^+$, 404 $[M+H-H_2O-CH_3OH]^+$, 386 $[M+H-2H_2O-CH_3OH]^+$ and 372 $[M+H-H_2O-2CH_3OH]^+$. Thus, peak 2 was identified as fuziline which was the general compound in *Aconitum* [23,24]. Similarly, talatizamine (m/z 422 and 6.44 min), chasmanine (m/z 452 and 8.35 min) and 14-acetyltalatizamine (m/z 464 and 9.58 min) were confirmed by the previously reported methods [25]. When C₈ acetyl and C₁₅ benzoyl of DDA were substituted by hydroxyl,

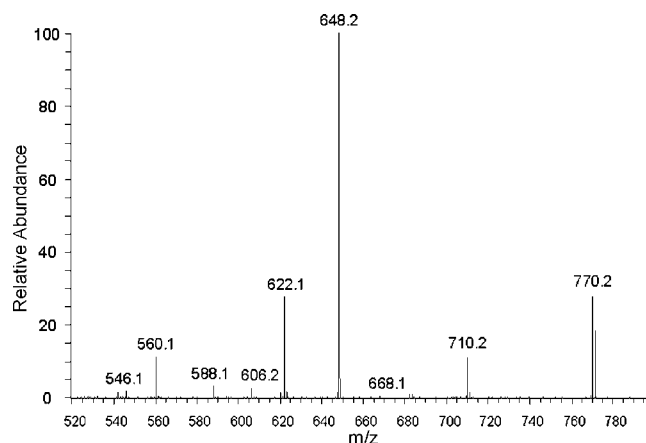


Fig. 7. MS/MS spectrum of peak at 32.78 min and m/z 770.

corresponding amine compounds were produced. Only acanine (m/z 500) in hydrolysate of DDA was found at 20.02 min (data not shown), mostly due to the instability of aconitine in DDA.

Interestingly, another type of DDA was detected by HPLC-ESIMS/MS in Fuzi. For example, in the MS/MS spectrum of m/z 770 (Fig. 7), the predominated fragment ion was at m/z 648 $[M+H-BzOH]^+$, and other ions were interpreted as 710 $[M+H-AcOH]^+$, 668 $[M+H-AcOH-CH_2CO]^+$, 588 $[M+H-BzOH-AcOH]^+$, 560 $[M+H-BzOH-AcOH-CO]^+$ and 546 $[M+H-BzOH-AcOH-CH_2CO]^+$. These six compounds showed the fragmentation pathways that were different from that of the known DDA. But the lipo-alkaloids corresponding to the fragmentations were not identified in this study.

Acknowledgements

This work was supported by the National Natural Science Foundation of China (No. 30472134, 30672600) and 973 project (No. 2006CB5047060). The authors gratefully acknowledge Prof. F.P. Wang and D.L. Chen (West China College of Pharmacy, Sichuan University, China) for their kind help.

References

- [1] N.G. Bisset, *Ethnopharmacology* 4 (1981) 247.
- [2] A. Ameri, *Eur. J. Pharmacol.* 342 (1998) 183.
- [3] H.K. Desai, B.P. Hart, R.W. Caldwell, J.Z. Huang, S.W. Pelletier, *J. Nat. Prod.* 61 (1998) 743.
- [4] Y. Suzuki, T. Oyama, A. Ishige, T. Isono, A. Asami, Y. Ikeda, M. Noguchi, Y. Omiya, *Planta Med.* 60 (1994) 391.
- [5] M. Mizugaki, K. Ito, Y. Ohyama, S. Konishi, S. Tanaka, K. Kurasawa, *J. Anal. Toxicol.* 22 (1998) 336.
- [6] Y. Ohno, *J. Toxicol.-Toxin Rev.* 17 (1998) 1.
- [7] S.H. Shim, J.S. Kim, S.S. Kang, K.H. Son, K. Bae, *J. Asian Nat. Prod. Res.* 8 (2006) 451.
- [8] L. Cai, D.L. Chen, S.Y. Liu, F.P. Wang, *Chem. Pharm. Bull.* 54 (2006) 779.
- [9] S.H. Shim, J.S. Kim, S.S. Kang, *Chem. Pharm. Bull.* 51 (2003) 999.
- [10] W. Wu, Z.T. Liang, Z.Z. Zhao, Z.W. Cai, *J. Mass Spectrom.* 42 (2007) 58.
- [11] Y. Wang, Z.Q. Liu, F.R. Song, S.Y. Liu, *Rapid Commun. Mass Spectrom.* 16 (2002) 2075.
- [12] Y. Wang, L. Shi, F.R. Song, Z.Q. Liu, S.Y. Liu, *Rapid Commun. Mass Spectrom.* 17 (2003) 279.
- [13] W.X. Sun, S.Y. Liu, Z.Q. Liu, F.R. Song, S.P. Fang, *Rapid Commun. Mass Spectrom.* 12 (1998) 821.
- [14] H.G. Zhang, Y. Sun, M.Y. Duan, Y.J. Chen, D.F. Zhong, H.Q. Zhang, *Toxicol.* 46 (2005) 500.
- [15] M. Hayashida, H. Hayakawa, K. Wada, T. Yamada, M. Nihira, Y. Ohno, *Legal Med.* 5 (2003) S101.
- [16] R. Kaneko, S. Hattori, S. Furuta, M. Hamajima, Y. Hirata, K. Watanabe, H. Seno, A. Ishii, *J. Mass Spectrom.* 41 (2006) 810.

- [17] Y. Wang, F.R. Song, Q.X. Xu, Z.Q. Liu, S.Y. Liu, *J. Mass spectrom.* 38 (2003) 962.
- [18] R. Li, Z.J. Wu, F. Zhang, L.S. Ding, *Rapid Commun. Mass Spectrom.* 20 (2006) 157.
- [19] L.H. Chen, L.J. Jin, Z.M. Su, Y.Q. Qiu, Y. Wang, S.Y. Liu, *Chem. J. Chinese Univ.* 26 (2005) 2340.
- [20] M.S. Yunusov, *Nat. Prod. Rep.* 10 (1993) 471.
- [21] A.U. Rahman, M.I. Choudhary, *Nat. Prod. Rep.* 16 (1999) 619.
- [22] H. Yue, Z.F. Pi, H.L. Li, F.R. Song, Z.Q. Liu, S.Y. Liu, *Photochem. Anal.* 19 (2008) 141.
- [23] A. Katz, *J. Nat. Prod.* 53 (1990) 204.
- [24] P.G. Xiao, F.P. Wang, F. Gao, L.P. Yan, D.L. Chen, Y. Liu, *Acta Phytotaxon. Sin.* 44 (2006) 1.
- [25] Z.B. Li, L. Xu, J.Z. Wang, D.L. Chen, X.X. Jian, F.P. Wang, *Nat. Prod. Res. Develop.* 12 (2000) 16.



Amperometric determination of cyanides at the low ppb level by automated preconcentration based on gas diffusion coupled to sequential injection analysis

Constantinos K. Zacharis^{a,*}, Paraskevas D. Tzanavaras^a,
Anastasios N. Voulgaropoulos^{a,*}, Bo Karlberg^b

^a Laboratory of Analytical Chemistry, Department of Chemistry, Aristotle University of Thessaloniki, GR-54124 Thessaloniki, Greece

^b Department of Analytical Chemistry, Stockholm University, SE-10691 Stockholm, Sweden

ARTICLE INFO

Article history:

Received 1 July 2008

Received in revised form

18 September 2008

Accepted 29 September 2008

Available online 1 November 2008

Keywords:

Cyanide

Gas diffusion

Sequential injection

Amperometric detection

Water samples

ABSTRACT

A simple, sensitive method for determining free cyanides is described. The assay is based on automated gas diffusion of the analyte using sequential injection analysis (SIA) coupled to amperometric detection on a silver working electrode. The effects of varying several parameters affecting the analytical procedure (including the flow rates of the donor and acceptor streams, the concentrations of the reagents and the sample volumes) were studied. The validity and quality of the method were also assessed, by examining its linearity, limits of detection and quantitation, precision, selectivity to potentially interfering substances. Its sensitivity can be enhanced by applying a simple preconcentration step, following which limits of detection were found to be 0.05–0.12 $\mu\text{g L}^{-1}$. Application of the proposed assay to the analysis of tap, mineral and table water samples spiked at concentrations ranging from 1 to 10 $\mu\text{g L}^{-1} \text{CN}^-$, yielded satisfactory recoveries (88–112%).

© 2008 Elsevier B.V. All rights reserved.

1. Introduction

Hydrogen cyanide and its simple sodium and potassium salts are among the most rapidly acting poisons affecting the central nervous system (CNS) of both animals and humans. Cyanides are both human-made and naturally occurring substances, which are released to the environment from industrial sources and car emissions [1] in addition to being present in plants of several species as cyanogenic glycosides and produced by certain bacteria, fungi, and algae.

Hydrogen cyanide is rapidly absorbed by the gastrointestinal and respiratory tracts, while in solution and possibly the concentrated vapor, it can be absorbed directly through the intact skin [2]. It exerts its toxic effects by forming a complex with the Fe(III) of mitochondrial cytochrome oxidase, thereby preventing use of oxygen by cells [3]. The most specific symptom in acute cyanide poisoning is the bright red color of venous blood, which provides evidence of the inability of the tissues to use oxygen [4].

Recommendations and regulations regarding its use and permitted levels are updated periodically as more information becomes available. Typical examples include the following [5]. The highest concentration of cyanide allowed in drinking water by the US EPA (Environmental Protection Agency) is 200 $\mu\text{g L}^{-1}$ or 0.2 ppm. Limits are also set for amounts of hydrogen cyanide in stored foods that have been treated with cyanide to control pests (e.g. 50 ppm for citrus fruits by the US EPA) and in workplace air (11 mg m^{-3} averaged over an 8-h workday and 40-h workweek by the US Occupational Safety and Health Administration [1]).

Official methods for determining cyanides in environmental samples are mainly based on spectrophotometric [6], potentiometric [7] and amperometric detections [8]. Typical spectrophotometric assays involve converting the analyte to cyanogen chloride by chloramine-T and subsequent reaction with pyridine and barbituric acid. The applicable range is 5–500 $\mu\text{g L}^{-1}$ [6]. Off-line distillation is employed for total cyanide determinations [9]. Substances that can cause substantial increases in measurements of cyanides include thiocyanates, therefore approaches have been proposed for the simultaneous determination of both of these classes of analytes [10–14]. Alternatives to the pyridine–barbituric acid system include the isonicotinic acid–barbituric acid [15] and γ -picoline–barbituric acid [16] methods. Potentiometry [7] using

* Corresponding authors. Tel.: +30 2310997721/7673; fax: +30 2310997719.

E-mail addresses: zacharis@chem.auth.gr (C.K. Zacharis),

voulgaro@chem.auth.gr (A.N. Voulgaropoulos).

cyanide-selective electrodes enables the determination of free CN^- in various samples at concentrations exceeding $50 \mu\text{g L}^{-1}$. In addition to taking precautions to avoid potential problems caused by known interfering species, such as sulfides and hydrogen ions, special care should be taken to maintain precise temperature control. Cyanide ion-selective electrodes (CN-ISEs) have also been successfully incorporated into automated flow injection (FI) systems [17–19], improving the sensitivity and sampling rates of analyses. Finally, amperometric detection using a silver working electrode incorporated in a FI system [8] offers a wide determination range, of $2 \mu\text{g L}^{-1}$ to 5mg L^{-1} , with a limit of detection (LOD) of $0.5 \mu\text{g L}^{-1}$.

FI coupled to gas diffusion (GD) has proven to be a popular and effective approach for the determination of cyanides, exploiting the formation of gaseous HCN in acidic media [20–28]. Reported assays have been carried out using: spectrophotometric detection [20–22], with LODs in the range of 0.025 – $100 \mu\text{g L}^{-1}$; fluorimetry [23–25], with generally lower LODs in the range of 0.4 – $0.5 \mu\text{g L}^{-1}$; and electrochemical detection [26–28], offering LODs in the range of 0.2 – $26 \mu\text{g L}^{-1}$. The sampling throughputs per hour of these FI–GD setups range between 4 [29] and 60 [22]. From a selectivity perspective, sulfide ions seem to be the major interfering species in FI–GD determinations of cyanides [22,26–28]. Apart from the well-established pre-treatment protocol using lead salts [6–8], attempts have been made to overcome this problem by using oxidants in the donor stream to oxidise sulfides to sulfates [22,26]. However, precipitation of MnO_2 in the flow system when using KMnO_4 and the generation of increased signals from the detector due to the conversion of SCN^- to HCN limit their applicability.

Sequential injection (SI) analysis—the second generation of FI techniques—has been developed as an advantageous alternative to traditional FI [30]. SI has unique sample handling potential due to the combined use of a multi-position valve and a bi-directional propulsion system. SI has also been effectively coupled to gas diffusion, combining the advantages of both techniques. SI–GD determinations of ammonia [29,31,32], free chlorine [33], sulfide [34], sulfur dioxide [35], dissolved carbon [36] and urea [37] have been reported recently. However, to the best of our knowledge, no SI–GD method has been previously reported for the determination of cyanides.

The present study reports the first development and application of a SI–GD method for determining trace free cyanides. Cyanides were converted on-line to HCN by acidification followed by diffusion through the hydrophobic PTFE membrane of a GD unit incorporated in the SI manifold. The analyte was detected amperometrically in the alkaline acceptor stream using an Ag working electrode avoiding the need for complex reactions prior to measurement. Due to the static nature of the acceptor stream enrichment of the analyte and therefore increased sensitivity was achieved by repetitive preconcentration cycles. The detection limits offered by the proposed method are better or comparable to those of the most sensitive methods reported to date [8,19,23,24,28] and far below limits set by international standards and regulations. The applicability of the method was evaluated by analyzing several tap, mineral and table water samples.

2. Experimental

2.1. Apparatus

A schematic diagram of the SI–GD configuration is outlined in Fig. 1. The FIALab 3000 system (FIALab Instruments, WA, USA) consisted of a Cavo 1000 μL syringe pump (Tecan, Switzerland) and a Cheminert® six-port selection valve (Valco VICI, Houston, USA). The SI analyzer was controlled by the FIALab software. The volume of the holding coil (HC) was $700 \mu\text{L}$. PTFE tubing (0.5 mm i.d.) was

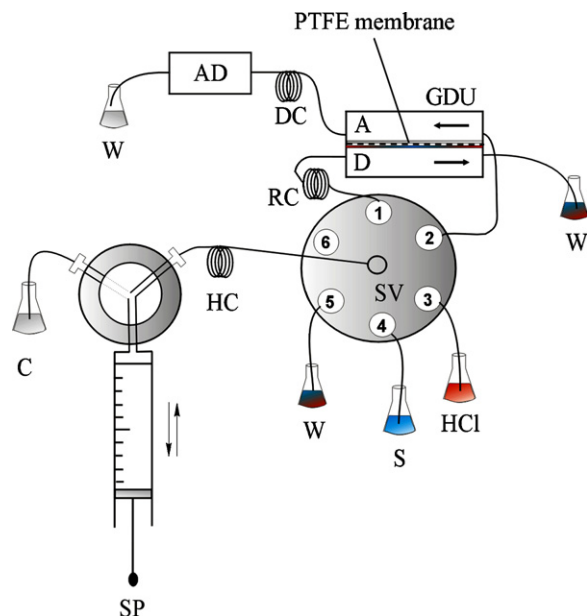


Fig. 1. Schematic diagram of the SIA–GD instrumentation, where C = carrier (0.2 mol L^{-1} NaOH), SP = syringe pump ($V = 1000 \mu\text{L}$), HC = holding coil ($700 \mu\text{L}$), SV = selection valve, S = sample, HCl = HCl solution at 0.5 mol L^{-1} , RC = reaction coil ($60 \text{ cm}/0.5 \text{ mm i.d.}$), DC = dilution coil ($60 \text{ cm}/0.5 \text{ mm i.d.}$), W = waste, A = acceptor, D = donor, GDU = gas-diffusion unit, AD = amperometric detector. For further details see Section 2.1.

used throughout including connections, holding, reaction and delay coils.

The flow-through amperometric cell of a Cyanide Solution® 3000 Analyzer (Alpkem®, O.I. Analytical, College Station, TX, USA) comprised an Ag working electrode and a Pt counter electrode. The reference electrode (Ag/AgCl) was separated from the flowing stream by an ion-exchange Nafion membrane. The detector was operated at a potential of 0.0 V . The resulting current (pA) was monitored by the WinFLOW™ software (O.I. Analytical) and was graphically represented as a peak. The amperometric detector was equilibrated at the beginning of each working day for at least 30 min by continuous propulsion of a NaOH solution (0.2 mol L^{-1}) at a flow rate of 0.9 mL min^{-1} using a peristaltic pump (Gilson Minipuls3, Villiers-le-Bel, France). Typical, weekly maintenance of the detector included polishing of the active surface of the working electrode using alumina and refilling of the reference solution. On daily usage, the flow-cell was stored filled with a NaOH solution. De-ionized water was used for longer storage periods.

A Chemifold™ Type V gas diffusion unit (Tecator, Sweden) was employed throughout this work. The dimensions of the gas-diffusion groove were $72 \text{ mm} \times 2 \text{ mm}$. PTFE gas-diffusion membranes were also provided by Tecator and were typically replaced on weekly basis.

2.2. Chemicals and solutions

KCN, NaOH and HCl were all of analytical grade and provided by Merck (Darmstadt, Germany). All other reagents used for assessing the effects of potentially interfering substances were purchased from Sigma–Aldrich or Merck and were also of analytical grade. Water was purified by a Milli-Q system (Millipore, Bedford, MA, USA) and used for preparing all solutions.

Stock CN^- solutions ($\gamma\text{-CN}^- = 1000 \mu\text{g mL}^{-1}$) were prepared in 0.1 mol L^{-1} NaOH, kept refrigerated at 4°C for a week, and then replaced. Working standards were prepared by diluting the stock solution as appropriate in 0.01 mol L^{-1} NaOH.

Table 1
Protocol sequence for the CN^- determinations using SI–GD.

	Step a/a	Time (s)	Valve position	Pump action	Flow rate (mL min^{-1})	Action description
Sample loading (steps 1–12)	1	1	3	Off	–	Selection of HCl reagent port
	2	5	3	Aspirate	0.6	Aspiration of HCl
	3	1	4	Off	–	Selection of sample port
	4	6.25	4	Aspirate	1.2	Aspiration of sample
	5	1	3	Off	–	Selection of HCl reagent port
	6	5	3	Aspirate	0.6	Aspiration of HCl
	7	1	4	Off	–	Selection of sample port
	8	6.25	4	Aspirate	1.2	Aspiration of sample
	9	1	3	Off	–	Selection of HCl reagent port
	10	5	3	Aspirate	0.6	Aspiration of HCl
	11	1	1	Off	–	Selection of donor port
	12	300	1	Dispense	0.2	Propulsion of mixture in the donor channel
Detection	13	1	2	Off	–	Selection of acceptor port
	14	66.6	2	Dispense	0.9	Propulsion of CN^- towards the detector
	15		End of cycle			

Stock solutions of NaOH and HCl (2 mol L^{-1}) were prepared by dissolving the appropriate amount of NaOH pellets in de-ionized water and appropriate dilution of the concentrated acid ($d = 1.19$, 37%) in water, respectively.

Carrier and reagent solutions were filtered through $0.45 \mu\text{m}$ membrane filters (Schleicher & Schuell, Dassel, Germany) and degassed ultrasonically for 10 min prior to use.

2.3. Safety

Cyanide ions and salts are extremely poisonous and should be handled with great care. All solutions must be prepared in a well-ventilated hood, while the waste tank from SI experiments should contain NaOH in order to avoid any risk of HCN formation. Cyanide-containing wastes were disposed by converting the cyanides to the less toxic cyanate ions via alkaline chlorination using NaOH and NaOCl.

2.4. SI–GD procedure for aqueous solutions

The assay sequence is shown in Table 1. Each run began by washing the donor and acceptor channels with $1000 \mu\text{L}$ of carrier (0.2 mol L^{-1} NaOH) at a flow rate of 1.2 mL min^{-1} . Samples (S, $2 \times 125 \mu\text{L}$) and HCl (R, $3 \times 50 \mu\text{L}$) were sequentially aspirated in the holding coil (HC) through ports 4 and 3 of the selection valve, respectively. The aspiration pattern was R/S/R/S/R and the “sandwiched” sample zones were propelled to the donor channel (D) of the GD unit through port 1 at a flow rate of 0.2 mL min^{-1} . Gaseous hydrogen cyanide was formed as the sample and HCl solution zones were allowed to overlap and mix in a 60-cm long reaction coil (RC). The analyte diffused through the pores of the PTFE membrane and was trapped in the static acceptor channel (A). The analyte was preconcentrated by repeating the sample loading cycle 2–5 times according to the desired sensitivity (sequence steps 1–12). The acceptor was propelled towards the amperometric detector at a flow rate 0.9 mL min^{-1} through a 60-cm long delay coil (DC). The height of the resulting peaks was equivalent to the CN^- concentration in the sample, and was used for all measurements. Three replicates were analyzed in all instances.

When switching between samples or standards an additional washing step was performed, to avoid carryover effects, in which $3 \times 200 \mu\text{L}$ portions of the new sample/standard were aspirated into the HC, and then flushed through port 5 to the auxiliary waste (W).

2.5. Analysis of water samples

Tap water samples were collected from three different areas of the city of Thessaloniki, while commercially available mineral and

table water were purchased from the local market. All samples were checked for residual chlorine and sulfides using suitable potassium iodide–starch and lead acetate test strips (Fluka). All tests were negative for sulfides. The presence of residual chlorine in tap water was eliminated by ascorbic acid, while sulfide ions—if present—could be removed by adding lead acetate. The pH of the samples was brought to 12 by adding 1 mL of a 6 mol L^{-1} NaOH solution per liter of sample, followed by filtration through $0.45 \mu\text{m}$ filters to remove suspended material.

3. Results and discussion

3.1. Preliminary experiments

Flow-through electrochemical detectors may require several seconds, or even more, for baseline stabilization, and there are inevitably disturbances to the flow in serial injection analyses because of the discontinuity of the pumping of the carrier towards the detector. Hence, it is essential to establish the behavior of the detector in terms of its response times, reproducibility and baseline stability under SI conditions. In this study, the initial experimental parameters for preliminary studies included $\gamma(\text{CN}^-) = 200 \mu\text{g L}^{-1}$, $V(S) = 100 \mu\text{L}$ and 0.1 mol L^{-1} NaOH as carrier.

In order to evaluate the stability of the amperometric detector experiments were performed, using the setup shown in Fig. 1 without the GD unit, in which $100 \mu\text{L}$ portions of a cyanide standard or blank solution were aspirated into the HC and propelled to the amperometric detector at a flow rate of 0.9 mL min^{-1} . A sharp negative “spike peak” was recorded even during blank experiments when the selection valve (SV) switched to the detector port, possibly due to slight pressure differences between SI channels. It was therefore necessary to “delay” the analyte peak in order to avoid possible inaccuracies in signal evaluation. A 60-cm long delay coil (DC) positioned between the SV and the detector provided sufficient delay (ca. 8 s) with acceptable loss of sensitivity due to additional dispersion.

Another important parameter affecting the response of electrochemical detectors is the flow rate of the carrier stream (q_v), due to mass transfer kinetic effects on the active surface of the working electrode [38]. Therefore, the effects of the carrier flow rate on the sensitivity, repeatability and sample throughput of the system were also investigated. The signals were not significantly affected in the range of 0.48 – 0.9 mL min^{-1} , but decreased sharply at higher flow rates, up to 1.5 mL min^{-1} . Repeatability was satisfactory in all cases ($s_r < 2.0\%$, $n = 3$). A flow rate of 0.9 mL min^{-1} was selected for further investigations.

The effect of the NaOH carrier amount concentration on the amperometric detector response was investigated in the range of

0.05–0.5 mol L⁻¹. The carrier flow rate was fixed at 0.9 mL min⁻¹. An approximately 35% increase in peak height was observed in the range 0.05–0.2 mol L⁻¹ and practically leveled-off thereafter. The value of 0.2 mol L⁻¹ NaOH was therefore selected for subsequent experiments. It should be noted that the NaOH carrier stream also serves as the acceptor stream when the GD unit is incorporated in the SI system.

Coupling the GD unit to the SI system yielded irreproducible results ($s_r > 10\%$) when the donor and acceptor streams flowed in the same direction. Similar problems were previously reported by Cerda and co-workers for the SI–GD determination of ammonia [32]. The cited authors overcame these problems by positioning the acceptor channel in a “closed loop” of an additional valve. In our study we simply reversed the flow direction of the donor stream, thereby avoiding the potentially undesirable effects of pressure differences, as shown in Fig. 1. The relative standard deviation of the signals was improved, being less than 2% ($n = 6$).

3.2. Study of SI and chemical parameters

In order to proceed to the final system design, several SI variables (aspiration order, sample and HCl volumes, reaction coil length, and the flow rate of the donor stream) were studied using the univariate approach. The starting values of the SI and chemical variables were: $\gamma(\text{CN}^-) = 200 \mu\text{g L}^{-1}$, $V(\text{CN}^-) = V(\text{HCl}) = 100 \mu\text{L}$, $q_v(\text{donor}) = 0.3 \text{ mL min}^{-1}$, $c(\text{HCl}) = 1.0 \text{ mol L}^{-1}$ and $l(\text{RC}) = 60 \text{ cm}$. The flow rate and amount concentration of NaOH in the acceptor stream and the length of the delay coil were as mentioned in the preliminary studies section above.

Effective diffusion of gaseous HCN from aqueous samples requires acidification of all of the alkaline cyanide solution. It is therefore essential to ensure efficient overlapping of the HCl and sample zones in order to maintain high diffusion yields and sensitivity. For this reason, the effects of varying the aspiration order of the HCl and sample zones were examined. The results showed that the diffusion is highest when two zones of sample (S) are “sandwiched” between three HCl (R) zones (R/S/R/S/R). This pattern was adopted throughout the remainder of this study.

The flow rate of the donor stream is also an extremely important parameter in on-line gas-diffusion analyses, since it determines the length of time that the acidified samples are in contact with the PTFE membrane. Experiments in which this parameter was varied showed that reducing the donor stream flow rate from 0.6 to 0.1 mL min⁻¹ resulted in a 250% increase in peak heights (Fig. 2). A donor flow rate of 0.2 mL min⁻¹ was selected for further analyses as a compromise between sensitivity and sampling throughput.

The influence of the total volume of the injected sample was studied in the range 50–300 μL , under the optimal aspiration pattern of R/S/R/S/R. An almost linear increase in the recorded current with increases in volume was observed in the range of 50–250 μL , but the relationship was substantially less linear with a further increase to 300 μL . Therefore the sample injection volume of 250 μL ($2 \times 125 \mu\text{L}$) was selected as optimal. Increases in peak heights were also observed with increases in the total volume of HCl from 75 to 150 μL , but further increases in volume, to 225 μL , had little additional effect. Thus, 150 μL ($3 \times 50 \mu\text{L}$) was selected for further analyses.

The influence of the length of the reaction coil (a potentially important parameter, since it affects the extent of overlapping zones) was investigated in the range of 10–70 cm, using 0.5 mm i.d. PTFE tubing in all cases. The maximum current was obtained at a length of 60 cm, indicating that this length allowed adequate mixing and acidification of the sample, and was thus adopted for subsequent experiments.

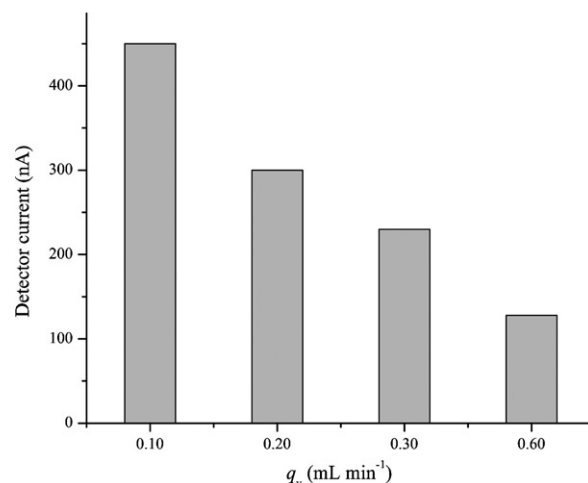


Fig. 2. Effect of varying the donor flow rate on the cyanide determination.

The effects of varying two chemical variables were also studied. The HCl concentration was varied in the range of 0.5–1.5 mol L⁻¹, and peak heights were found to be virtually unaffected across the studied range. Thus, 0.5 mol L⁻¹ provided sufficient acidity and was selected as optimal. This hypothesis was confirmed by varying the amount of NaOH in the samples from 0.005 to 0.02 mol L⁻¹, since no significant effects on peak height were observed across this range, so all samples and standards were preserved in 0.01 mol L⁻¹ NaOH.

3.3. Preconcentration of CN⁻ by SI–GD

An additional advantage of coupling SI to gas diffusion is the potential it offers to preconcentrate analytes by exploiting the static nature of the acceptor zone [32]. This can be done by simply repeating N times the injection-loading sequence of the sample to the donor stream, thereby enriching the static acceptor solution with the analyte. This approach is not commonly applied in flow injection analyses since the donor and acceptor streams usually flow continuously in the same or opposite directions.

Using the finalized SI setup shown in Fig. 1 and performing one injection-loading cycle ($N = 1$), a linear relationship between analyte concentration and peak height was observed in the range of 0.4–200.0 $\mu\text{g L}^{-1}$. The regression equation and corresponding LOD are included in Table 2.

In order to increase further the sensitivity of the assay, preconcentration experiments were carried out with test solutions containing 1.0 and 10.0 $\mu\text{g L}^{-1}$ CN⁻, and N (numbers of preconcentration cycles) of 1–3 and 5. The results of these experiments are shown in Fig. 3. As can be clearly seen, the developed setup allows efficient preconcentration of the analyte, yielding a linear relationship between peak height and N (across the studied range) at both concentrations tested. The repeatability of the preconcentration step was satisfactory, since the s_r values were $< 5\%$ in all cases ($n = 5$), due to the high reproducibility of the SI–GD hardware's performance. Typical SI peaks at 1 $\mu\text{g L}^{-1}$ concentration level after one and five preconcentration steps are depicted in Fig. 4. In order to evaluate the analytical performance of the preconcentration procedure additional calibration curves were constructed for $N = 2$ and 3. The corresponding regression equations and LOD/LOQ values are also shown in Table 2. Linearity, as expressed by the regression coefficients, was satisfactory in all cases, while the detection limits were in the range of 0.05–0.12 $\mu\text{g L}^{-1}$, depending on the number of preconcentration cycles. However, it should be noted that the sampling throughput will be reduced ca. three-fold reduction when

Table 2
Regression equations and limits of detection (LOD) obtained for 1–3 preconcentration cycles.

<i>N</i> ^a	Range (μg L ⁻¹)	Regression equation	<i>R</i> ²	LOD (μg L ⁻¹)	Sampling rate (h ⁻¹)
1	0.4–200	<i>Y</i> ^b = 4895 (±14) × γ(CN ⁻) + 2543 (±301)	0.9999	0.12	9
2	0.25–100	<i>Y</i> = 9553 (±35) × γ(CN ⁻) + 2149 (±218)	0.9997	0.07	5
3	0.17–70	<i>Y</i> = 13951 (±47) × γ(CN ⁻) + 3008 (±274)	0.9991	0.05	3

^a *N*: number of preconcentration cycles.
^b *Y*: peak height in pA.

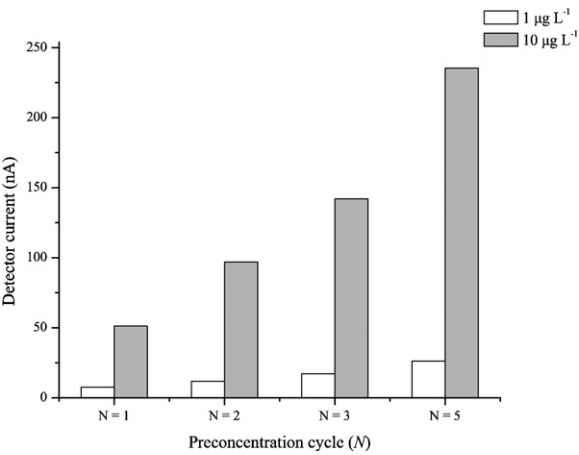


Fig. 3. Effects of preconcentration cycles (*N* = 1–5) on the cyanide peak height.

two or three preconcentration steps are applied rather than a single loading cycle.

3.4. Method validation

The quality of the developed method was evaluated in terms of its linearity, LOD, LOQ, repeatability and selectivity. Linearity was evaluated using response factor (R.F.) tests [39], setting as an acceptance limit the deviation of the R.F. of each point of the calibration curve to be within ±5% of the experimental slope, as given by the equation:

$$R.F. = \frac{\text{peak height (pA)} - \text{intercept}}{\gamma[\text{CN}^-]}$$

For a single preconcentration cycle (*N* = 1) the R.F. values were less than ±3% for cyanide concentrations in the range of 2–200 μg L⁻¹. Higher R.F. values in the range of 5–10% were obtained with lower

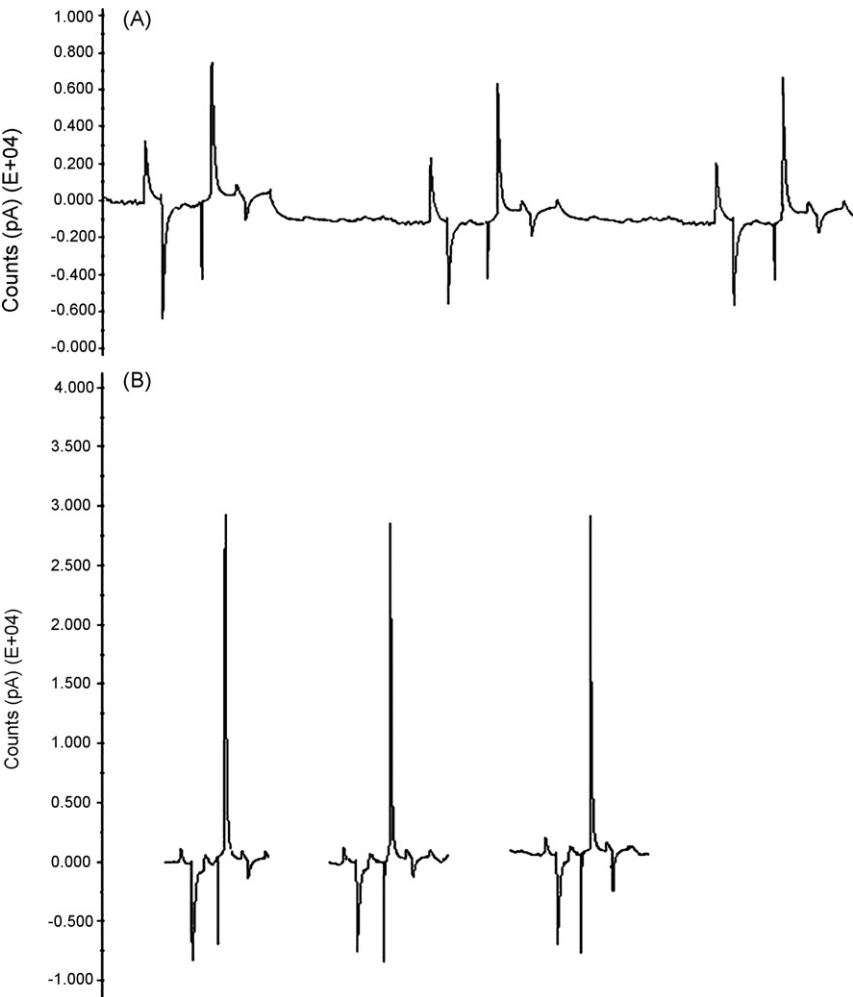


Fig. 4. Typical SI peaks for γ(CN⁻) concentrations of 1 μg L⁻¹ after *N* = 1 (A) and *N* = 5 (B) preconcentration cycles.

concentrations close to the LOQ ($0.5\text{--}2.0\text{ }\mu\text{g L}^{-1}$). Similar results were obtained using two or three preconcentration cycles; the R.F. values exceeded the 5% limit only for cyanide concentrations lower than $1.0\text{ }\mu\text{g L}^{-1}$, but were less than 10% in both cases.

The limits of detection and quantitation (LOD and LOQ, respectively) were calculated according to the IUPAC criteria ($3 \times s_b/m$ and $10 \times s_b/m$, respectively) where s_b is the standard deviation of the blank measurements ($n=8$), and m is the slope of the calibration graph [40]. The results can be found in Table 2.

The repeatability (within-day precision) of the developed assay was evaluated at three CN^- concentrations: 1.0 , 5.0 and $10.0\text{ }\mu\text{g L}^{-1}$, with three preconcentration cycles ($N=3$) as a “worst case scenario”. Each standard was analyzed in triplicate at the beginning, middle and end of a working day ($n=3 \times 3$). The respective s_r values were 5.1, 3.6 and 2.8%, confirming that the procedure has a high degree of precision. The day-to-day precision of the proposed method was evaluated by constructing calibration curves for six consecutive days at six cyanide levels in the range of $5\text{--}200\text{ }\mu\text{g L}^{-1}$. The experimental results confirmed the precision of the assay, as the R.S.D. of the slopes of the obtained regression lines was <8%.

The selectivity of the assay for cyanide versus several species was examined by measuring the amperometric detector responses they induced both in the absence of the analyte (to determine their potential to interfere with cyanide measurements) and in the presence of $100\text{ }\mu\text{g L}^{-1}\text{ CN}^-$, to determine the tolerance of the method. Unless otherwise stated, interferents were equilibrated with the sample for 1 h prior to analysis.

Sulfide ions are known to interfere strongly in the amperometric determination of cyanides because following acidification H_2S diffuses through the PTFE membrane and produces a positive response at the detector [8,27,28]. Conversely, they can also react with the analyte, forming SCN^- ions, thereby reducing its concentration in real samples and leading to underestimates of cyanide concentrations. The most widely accepted procedure for removing these interferents is to precipitate S^{2-} with PbCO_3 as PbS [8]. When this procedure was applied here, and the resulting solutions were filtered through $0.45\text{ }\mu\text{m}$ filters immediately after the reaction, S^{2-} could be tolerated at concentrations up to 5 mg L^{-1} , corresponding to a mass ratio of $\text{S}^{2-}/\text{CN}^- = 50$.

Formaldehyde and acetaldehyde do not induce responses by the amperometric detector in the absence of cyanide, but they both react with the analyte in aqueous solutions to form cyanohydrins. However, these species were tolerated up to mass ratios of 50 when treated with 3.5% ethylene diamine and 10 for untreated samples.

Species such as SCN^- , I^- , Br^- , NO_3^- , NO_2^- , NH_4^+ , SO_4^{2-} , OCN^- , ascorbic and oxalic acids were not found to interfere, either in the absence or presence of cyanides up to mass concentration ratios of 100, and hypochlorite (OCl^-) ions only seriously interfere in the presence of the analyte. By adding ascorbic acid (ca. 0.5 mg mL^{-1} of sample), a OCl^-/CN^- mass concentration ratio of 10/1 causes a negative interference of ca. 40%.

3.5. Analysis of water samples

The applicability of the SI method in practice was evaluated by analyzing tap, mineral and table water samples. All samples were collected and treated as described in Section 2.4, and they were analyzed both without ($N=1$) and with preconcentration ($N=2$ and 3). Each sample was analyzed in triplicate, and the experimental results are shown in Table 3. No cyanide was detected in any of the assayed samples. The accuracy of the results was checked by spiking the samples with known concentrations of the analyte in the range of $1.0\text{--}10.0\text{ }\mu\text{g L}^{-1}$. Percent recoveries were in the range of 88–112% at the $1\text{ }\mu\text{g L}^{-1}$ level. Higher recoveries, in the range of

Table 3
Analysis of water samples.

Sample	CN^- added ($\mu\text{g L}^{-1}$)	Recovery (%)		
		$N=1$	$N=2$	$N=3$
Tap water (I)	–	N.D. ^a	N.D.	N.D.
	1.0	89	92	93
	2.0	94	96	96
	5.0	102	98	103
	10.0	98	103	104
Tap water (II)	–	N.D.	N.D.	N.D.
	1.0	108	88	96
	2.0	92	91	94
	5.0	95	104	99
	10.0	105	106	98
Tap water (III)	–	N.D.	N.D.	N.D.
	1.0	89	111	112
	2.0	95	92	94
	5.0	101	101	94
	10.0	105	97	103
Mineral water (I)	–	N.D.	N.D.	N.D.
	1.0	91	95	93
	2.0	105	103	99
	5.0	103	101	97
	10.0	99	97	102
Mineral water (II)	–	N.D.	N.D.	N.D.
	1.0	93	109	92
	2.0	96	95	98
	5.0	105	99	94
	10.0	96	106	95
Table water	–	N.D.	N.D.	N.D.
	1.0	110	108	92
	2.0	108	96	104
	5.0	96	102	94
	10.0	105	99	106

^a N.D. = not detected.

91–108% were obtained at cyanide concentrations between 2.0 and $10.0\text{ }\mu\text{g L}^{-1}$.

4. Conclusions

SI has wide potential applications in automated analytical methods due to the opportunities it provides for the precise, robust and yet flexible handling and manipulation of liquid samples. Exploiting these features, a simple and sensitive assay was developed for the determination of free cyanides in water samples at low-ppb levels. The employment of an amperometric detector renders the method practically reagentless. The GD unit not only increased selectivity but the “static nature” of the acceptor stream enabled the incorporation of an enrichment-preconcentration step by repetitive loading of the sample. The limit of detection of the developed protocols ranged between 0.05 and $0.12\text{ }\mu\text{g L}^{-1}$ depending on the number of preconcentration cycles. These values are well below the recommended limits in environmental samples set by international U.S. and European authorities. Analyte recoveries from real samples ranged between 88 and 112%. Another highly desirable feature of the proposed protocol is the compact and readily available instrumentation which is suitable for *in situ* and field analysis. The combination of SI, gas diffusion and amperometric detection resulted in an efficient, reliable tool for screening free cyanides at low levels in environmental samples.

Acknowledgement

The authors thank Assistant Professor S. Sotiropoulos (Chemistry Department, Laboratory of Physical Chemistry, Aristotelian

University of Thessaloniki, Greece), for the donation of Nafion membranes.

References

- [1] ATSDR (Agency for Toxic Substances Disease Registry), Toxicological Profile for Cyanide, U.S. Public Health Service, 2006.
- [2] United States Environmental Protection Agency, Health Effects Assessment for Cyanides. Prepared by the Environmental Criteria and Assessment Office, Cincinnati, OH for the Emergency and Remedial Response Office, Washington, DC, EPA/540/1-86-011, 1984.
- [3] H.L. Hardy, G.W. Boylen Jr., in: L. Parmeggiani (Ed.), Encyclopaedia of Occupational Health and Safety, vol. 1, 3rd ed., International Labour Office, Geneva, 1983, p. 5747.
- [4] R. Hartung, in: G.D. Clayton, E. Clayton (Eds.), Patty's Industrial Hygiene and Toxicology, vol. 2C, John Wiley & Sons, New York, NY, 1982, pp. 4845–4900.
- [5] United States Environmental Protection Agency, Methods for Chemical Analysis of Water and Wastes, Environmental Monitoring and Support Laboratory, Cincinnati, OH, 1983.
- [6] United States Environmental Protection Agency (EPA), Titrimetric and Manual Spectrophotometric Determinative Methods for Cyanide, Method 9014-1, 1996.
- [7] United States Environmental Protection Agency (EPA), Potentiometric Determination of Cyanide in Aqueous Samples and Distillates with Ion-Selective Electrode, Method 9213, 1996.
- [8] United States Environmental Protection Agency (EPA), Available Cyanide by Flow Injection, Ligand Exchange, and Amperometry, Method OIA-1677, 1999.
- [9] United States Environmental Protection Agency, Total and Amenable Cyanide: Distillation, Method 9010B, 1996.
- [10] S. Nagashima, Anal. Chem. 56 (1984) 1944.
- [11] A. Sharma, R.J. Thibert, Microchim. Acta 1 (1985) 357.
- [12] A. Tanaka, K. Mashiba, T. Deguchi, Anal. Chim. Acta 241 (1988) 259.
- [13] A. Tanaka, K. Deguchi, T. Deguchi, Anal. Chim. Acta 261 (1992) 281.
- [14] A. Afkhami, N. Sarlak, A.R. Zarei, Talanta 71 (2007) 893.
- [15] S. Nagashima, T. Ozawa, Int. J. Environ. Anal. Chem. 10 (1981) 99.
- [16] S. Nagashima, Anal. Chim. Acta 91 (1977) 303.
- [17] M.A.B. Marin, E.M. Ganzarolli, A. Lehmkuhl, I. Goncalves de Souza, R.R. Urzedo de Queiroz, J. Autom. Methods Manag. Chem. 21 (1999) 23.
- [18] M.A.B. Marin, R. Carvalho de Silva, A. Lehmkuhl, J. Borda de Silva, E.M. Ganzarolli, R.R. Urzedo de Queiroz, Quim. Nova 23 (2000) 23.
- [19] B. Vallejo-Pecharroman, M.D. Luque de Castro, Analyst 127 (2002) 267.
- [20] Z. Zhu, Z. Fang, Anal. Chim. Acta 198 (1987) 25.
- [21] J.A. Sweileh, Anal. Chim. Acta 336 (1996) 113.
- [22] H. Sulistyarti, T.J. Cardwell, S.D. Kolev, Anal. Chim. Acta 357 (1997) 103.
- [23] E. Miralles, D. Prat, R. Compano, M. Granados, Analyst 123 (1998) 217.
- [24] E. Miralles, R. Compano, M. Granados, M.-D. Prat, Fresenius J. Anal. Chem 365 (1999) 516.
- [25] Y. Nomura, K. Nagakubo, H.-S. Ji, A. Watanabe, T. Akimoto, S. McNiven, K. Hayashi, Y. Arikawa, I. Karube, Environ. Sci. Technol. 34 (2000) 2618.
- [26] W. Frenzel, C.Y. Liu, J. Oleksy-Frenzel, Anal. Chim. Acta 233 (1990) 77.
- [27] E.B. Milosavljevic, L. Solujic, J.L. Hendrix, Environ. Sci. Technol. 29 (1995) 426.
- [28] L. Solujic, E.B. Milosavljevic, M.R. Straka, Analyst 124 (1999) 1255.
- [29] I. Lukkari, J. Ruzicka, G.D. Christian, Fresenius J. Anal. Chem. 346 (1993) 813.
- [30] J. Ruzicka, G.D. Marshall, Anal. Chim. Acta 237 (1990) 329.
- [31] M.T. Oms, A. Cerda, A. Cladera, V. Cerda, R. Forteza, Anal. Chim. Acta 318 (1996) 251.
- [32] M.T. Oms, A. Cerda, V. Cerda, Electroanalysis 8 (1996) 387.
- [33] R.B.R. Mesquita, A.O.O.S. Rangel, Talanta 68 (2005) 268.
- [34] M.S.P. Silva, J.C. Masini, Quim. Nova 27 (2004) 545.
- [35] M.A. Segundo, A.O.O.S. Rangel, Anal. Chim. Acta 427 (2001) 279.
- [36] O. Tue-Ngeum, R.C. Sandford, J. Jakmunee, K. Grudpan, I.D. McKelvie, P.J. Worsfold, Anal. Chim. Acta 554 (2005) 17.
- [37] M.J.R. Lima, S.M.V. Fernandes, A.O.S.S. Rangel, J. Agric. Food Chem. 52 (2004) 6887.
- [38] B. Karlberg, G.E. Pacey, Flow injection Analysis, a Practical Guide, Elsevier Science Publishers, Amsterdam, 1989.
- [39] J.M. Green, Anal. Chem. 68 (1996) 305A.
- [40] J. Mocak, A.M. Bond, S. Mitchell, G. Scollary, Pure Appl. Chem. 69 (1997) 297.



Preconcentration of nickel and cadmium by TiO₂ nanotubes as solid-phase extraction adsorbents coupled with flame atomic absorption spectrometry

Qing-xiang Zhou^{a,*}, Xin-ning Zhao^{a,b}, Jun-ping Xiao^c

^a School of Chemistry and Environmental Sciences, Henan Normal University, Henan Key Laboratory for Environmental Pollution Control, Key Laboratory for Yellow River and Huaihe River Water Environment and Pollution Control, Ministry of Education, Xinxiang 453007, China

^b Environment Protection Bureau of Xinxiang, Xinxiang 453000, China

^c Department of Chemistry, University of Science and Technology Beijing, Beijing 100083, China

ARTICLE INFO

Article history:

Received 18 June 2008

Received in revised form 6 October 2008

Accepted 7 October 2008

Available online 19 October 2008

Keywords:

TiO₂ nanotubes

Solid-phase extraction

Flame atomic absorption spectrometry

ABSTRACT

TiO₂ nanotubes, a new nanomaterial, are often used in the photocatalysis. Due to its relatively large specific surface areas it should have a higher enrichment capacity. However, very few applications in the enrichment of pollutants were found. This paper described a new procedure to investigate the trapping power of TiO₂ nanotubes with cadmium and nickel in water samples as the model analytes and flame atomic absorption spectrometry for the analysis. The possible parameters influencing the enrichment were optimized. Under the optimal SPE conditions, the method detection limits and precisions (R.S.D., $n=6$) were 0.25 ng mL⁻¹ and 2.2% for cadmium, 1 ng mL⁻¹ and 2.6% for nickel, respectively. The established method has been successfully applied to analyze four realworld water samples, and satisfactory results were obtained. The spiked recoveries were in the range of 90.2–99.2% for them. All these indicated that TiO₂ nanotubes had great potential in environmental field.

© 2008 Elsevier B.V. All rights reserved.

1. Introduction

Heavy metals have been put much more attention nowadays because the toxic effect of them at low concentration has been found. Some of them could be accumulated in body tissues and then throw a threat on the human health. So novel, sensitive analytical methods for the determination of heavy metal ions at trace levels are highly desired. Atomic absorption spectrometry is an often used instrument in the analysis of elements. However, sample pretreatment is a necessary procedure because the sample matrices are usually complex. Recently, many methods for sample pretreatment have been developed and they all gained great achievements such as solid-phase extraction, supported liquid membrane, and liquid phase micro-extraction. Wang and coauthors have contributed great to preconcentration of the heavy metal ions. They have developed several novel metal ions sorption technology such as cell-immobilized micro-column in the presence of an external magnetic field, sequential injection reductive bio-sorption on the surface of egg-shell membrane, immobilizing *Chorella vulgaris* and *Saccharomyces cerevisiae* cell onto silica beads for bio-sorption, cellulose fibre packed micro-column and

octadecyl immobilized surface [1–5]. These technologies were successfully applied to the preconcentration of Cd²⁺ at ultratrace level, Cr⁶⁺ and chromium speciation, and Mn²⁺ and Cr³⁺, and provided alternative modes for the determination of trace metal ions.

In recent years, nanostructure material has attracted great attention in many fields [6–10]. Titanium dioxide, TiO₂, a novel nanomaterial, has been in the centre of focus and many reports about its application have been reported. The properties of TiO₂ nanopowder determined that it could enrich some environmental pollutants. Recently, some papers proved that achievements had been obtained using TiO₂ material as solid-phase extraction packing material to preconcentration and determination of some heavy metals. Liu and Liang have used a micro-column packed with immobilized nanometer TiO₂ to separate and preconcentration of gold prior to its determination by flame atomic absorption spectrometry (FAAS) [11], and the results indicated that there had a better detection limit of 0.21 ng mL⁻¹, moreover satisfactory results had been achieved with the method applied for the determination of trace amounts of Au in geological and water samples. Zhang et al. applied titanium dioxide as solid-phase adsorbent to concentrate As, Se and Sb in river water and seawater [12] and favorable results were obtained. TiO₂ nanoparticles have also been successfully explored the adsorptive ability for Cu, Mn, Cr, Ni [13], La, Y, Yb, Eu and Dy [14]. The adsorption capacities of nanometer TiO₂ were found as 0.108, 0.149, 0.039 and 0.034 mmol g⁻¹ for Cu, Cr,

* Corresponding author. Tel.: +86 373 3325971; fax: +86 373 3326336.
E-mail address: zhouqx@henannu.edu.cn (Q.-x. Zhou).

Mn and Ni and 7.0, 6.1, 9.8, 8.3 and 8.8 mg g⁻¹ for La, Y, Yb, Eu and Dy, respectively.

TiO₂ nanotubes has been used for the photodegradation as the photocatalyst. However, it should have much higher adsorption capacity than that of TiO₂ nanoparticle and much great potential for the trapping of compounds because it is proved to have larger surface area than the TiO₂ nanoparticles, the surface area of TiO₂ nanotubes synthesized from hydrothermal treatment can reach 400 m²/g. In our laboratory, the TiO₂ nanotubes have been firstly explored in the analysis of DDT and its metabolites and Cu²⁺. These preliminary experimental results showed that TiO₂ nanotubes earned outstanding property for the preconcentration of *p,p*-DDD, *p,p*-DDT, *o,p*-DDT and *p,p*-DDE and Cu²⁺ [15,16]. However, such reports have been found very few.

The main purpose of this work is to investigate the feasibility of TiO₂ nanotubes as SPE adsorbents for the extraction of heavy metal ions with nickel and cadmium as the model analytes for the sake of enlarging the application of TiO₂ nanotubes in the environmental field.

2. Experimental

2.1. Apparatus

A Z-5000 Polarized Zeeman Atomic Absorption Spectrophotometer (Hitachi Ltd., Tokyo, Japan) fitted with cadmium and nickel hollow cathode lamps were used. This apparatus was equipped with Zeeman Effect background correction. In these experiments, a modified cartridge used was prepared by modifying an Agilent ZORBAX SPE C18 (EC) cartridge. TiO₂ nanotubes of 200 mg were packed in the cartridge after the C18 packing was evacuated. The polypropylene upper frit and lower frit were remained at each end of the cartridge to hold the absorbent packing in place. A model SHZ-3 (III) vacuum pump (Yuhua Instrument Co. Ltd., Zhengzhou, China) was used in the preconcentration process. Ultrapure water was prepared in the laboratory using a water treatment device “Ultra-Clear” (SG Wasseraufbereitungsanlagen, Barsbüttel, Germany).

TiO₂ nanotubes were synthesized from hydrothermal treatment in our laboratory, the specific surface area was 291 m²/g and the medial aperture was 3.66 nm determined from the linear portion of the BET plots, and they were examined using JEM2011 scanning electron microscope (JEOL, Japan).

2.2. Standard solutions and reagents

National certified reference materials (GSB 07-1186-2000, Ni and GSB 07-1185-2000, Cd) were purchased from Yingtianyi Standard Sample Company (Beijing, China). All the other reagents and chemicals used are of analytical grade. Stock solutions of nickel and cadmium at a concentration of 1000 µg mL⁻¹ were prepared with nickelous chloride (NiCl₂) and cadmium chloride (CdCl₂·25H₂O). Working solutions were obtained by further diluting the stock solution to the required concentrations before use. 0.1 mol L⁻¹ 8-hydroxyquinoline solution was prepared with ethanol. Hydrochloric acid (5%, v/v) and sodium hydroxide (1%, v/v) were used to adjust pH values of the solution.

2.3. SPE procedure

Before the preconcentration, TiO₂ nanotubes (200 mg) were washed with 1.5 mol L⁻¹ HNO₃ and ultrapure water in order to remove the contaminants. The solid-phase extraction procedure for Cd²⁺ and Ni²⁺ was as follows: firstly, the cartridge equipped with

TiO₂ nanotubes was washed by 10 mL nitric acid/ethanol (1:9, v/v) and 10 mL ultrapure water. Then, the working solution containing 0.05 µg mL⁻¹ Cd²⁺ and Ni²⁺ ions chelated with 8-hydroxyquinoline was passed through the minicolumn under the vacuum condition. When the preconcentration was completed, 10 mL ultrapure water was used to clean the impurity. Further the target analytes were eluted with an optimum volume of nitric acid/ethanol (1:9, v/v). Finally, the concentration of the Cd²⁺ and Ni²⁺ was determined with FAAS. Between the extractions, the minicolumn was dried by passing the air through it for 30 min.

2.4. Water sample

In this investigation, four water samples were used for validating of the proposed method. They were collected from four different factories from Xinxiang City, Henan province and there were marked as samples 1, 2, 3, and 4, respectively. All of the water samples were immediately filtrated through the 0.45 µm membrane after collected and stored in brown reagent bottles at 4 °C.

3. Results and discussion

3.1. Optimization of the elution step

It was an important step to quantitatively recover the retained analytes from the SPE cartridge in the SPE procedure. In this experiment, a series of experiments were designed and performed to obtain a reasonable eluent to elute completely Cd²⁺ and Ni²⁺ ions after the enrichment of cadmium and nickel chelated with 8-hydroxyquinoline from 50 mL buffer solution. In general, inorganic acid may be effective to elute the heavy metal ions from the SPE column, hence, 4 mL of 1.5 mol L⁻¹ HNO₃, 1 mol L⁻¹ HCl, nitric acid/ethanol (1:9, v/v), and ethanol were investigated to obtain the optimal eluent for further experiments. The results showed that nitric acid/ethanol (1:9, v/v) could accomplish the quantitative elution of target analytes, Cd²⁺ and Ni²⁺ ions chelated with 8-hydroxyquinoline, from the cartridge. For the sake of achieving better enrichment, the volume of eluent was optimized in the range of 2–6 mL for obtaining the optimal volume, and the data is given in Fig. 1. It is obvious that 3 mL nitric acid/ethanol (1:9, v/v) is sufficient for quantitative elution of the retained target compound from the TiO₂ nanotubes. Thus 3 mL of nitric acid/ethanol (1:9, v/v) was used as an eluent for further studies. The amount of 8-hydroxyquinoline also had impact on the enrichment of metal ions

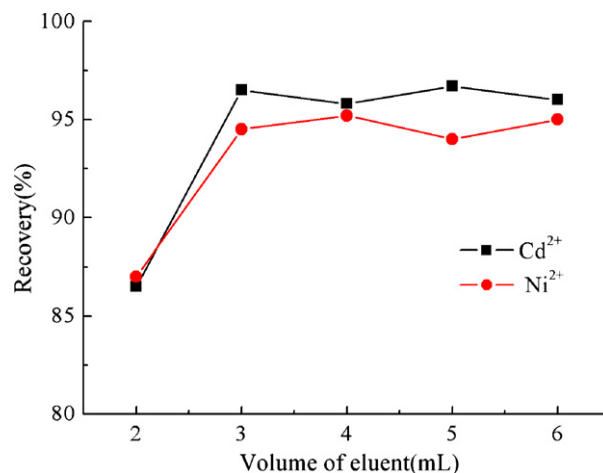


Fig. 1. Effect of eluent volume on the recovery of Cd²⁺ on TiO₂ nanotubes: Cd²⁺, 50 ng mL⁻¹; Ni²⁺, 50 ng mL⁻¹.

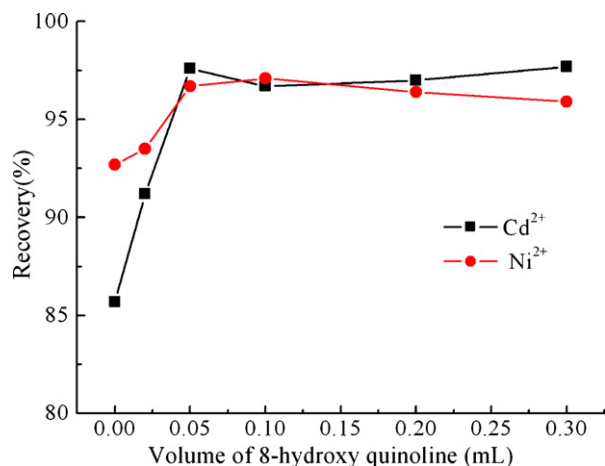


Fig. 2. Effect of 8-hydroxyquinoline on the recovery of Cd²⁺ and Ni²⁺ on TiO₂ nanotubes: Cd²⁺, 50 ng mL⁻¹; Ni²⁺, 50 ng mL⁻¹.

in the SPE process, preliminary experiments indicated that the best performance was achieved with 0.05 mL 8-hydroxyquinoline used (see Fig. 2). Therefore, 0.05 mL 8-hydroxyquinoline was used in the following experiments.

3.2. Effect of pH and flow rates

pH was an important parameter for the chelating reaction of metal ions. The generation of complexes determined whether it could be adsorbed onto the SPE adsorbent in most cases. To get excellent sensitivity, sample pH should be taken into account. In this experiment the effect of the pH on the retention of cadmium and nickel on the cartridge was studied in the range of 2.0–10.0, and its pH was adjusted by hydrochloric acid (5%, v/v) and sodium hydroxide (1%, v/v). Kept the other parameters being constant, the general procedure was applied and the concentration of cadmium and nickel was measured by FAAS. The results showed that the two metals were adsorbed much better at pH of 7–9 and the recoveries exceeded 90% at the pH 8.0. Hence, in the following experiments the sample pH was adjusted to pH 8.0.

Flow rate of sample is an important parameter for quantitative extraction and elution, and it controls the time of analysis and affected the retention of target analyte on the micro-column. So the optimum flow rate was investigated in the range of 0.2–1.25 mL min⁻¹. Before the beginning of the SPE procedure, Cd²⁺ ions and Ni²⁺ ions in the working solution were chelated with 8-hydroxyquinoline. The experimental results indicated that there was no significant impact to the recoveries of metal ion when the flow rate of sample was increased. So in the following study, the maximal flow rate was used.

3.3. Optimization of the sample volume

A series of experiments were performed to obtain a high enrichment factor. In general, a very simple method was to increase the volume of the sample. So the sample volume was investigated over the range of 50–200 mL. The results were exhibited in Fig. 3. From the figure, it could be seen that the recoveries of cadmium and nickel were in the range of 97.9–98.4% and 95.7–96.4%, respectively. There have no significant decrease when the volume of sample increased up to 200 mL. In order to save time, 200 mL was selected finally.

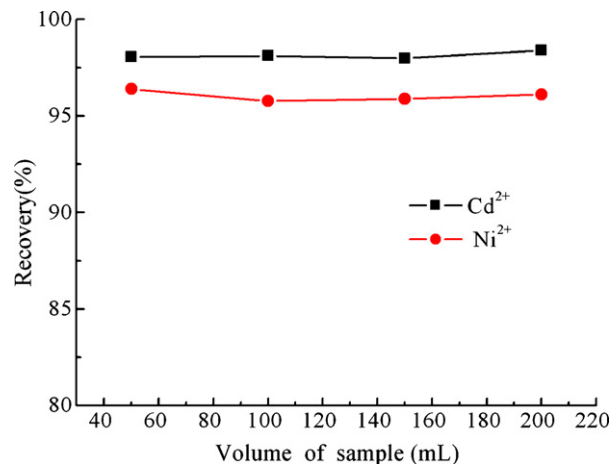


Fig. 3. Effect of sample volume on the recovery of Cd²⁺ and Ni²⁺ on TiO₂ nanotubes: Cd²⁺, 50 ng mL⁻¹; Ni²⁺, 50 ng mL⁻¹.

Table 1

The effect of coexisting ions (Cd²⁺ 50 ng mL⁻¹ and Ni²⁺ 50 ng mL⁻¹).

Coexisting ions	Concentration of coexisting ions (μg mL ⁻¹)	Recovery of cadmium (%)	Recovery of nickel (%)
Na ⁺	80	95.4	93.6
K ⁺	50	98.0	95.3
Mg ²⁺	20	91.5	93.2
Ca ²⁺	16	91.3	88.2
Cu ²⁺	1	97.5	92.6
Al ³⁺	1	95.0	93.0
Fe ³⁺	1	101.0	96.8
SO ₄ ²⁻	80	99.8	97.5
Cl ⁻	50	97.3	94.9

3.4. Effect of coexisting ions

In general, the matrix of real environment samples is much complex. The existence of coexistence ions would influence the preconcentration of nickel and cadmium by competitive adsorption. The presence of cations and anions in the environmental water samples would interfere the determining of nickel and cadmium. In order to validate the applicability of proposed method, several typical ions such as Ca²⁺, Mg²⁺, Na⁺, Cl⁻, SO₄²⁻ and other ions were investigated. The solutions contained different ions at different concentration were passed through the column at the optimum conditions. The results were given in Table 1. The results suggested that the presence of coexisting ions at a much higher level has no obvious influence on the preconcentration of cadmium and nickel.

3.5. Analytical performance

Some important parameters of the proposed method such as linear range, correlation coefficients and detection limits were also investigated under the optimal conditions for the quantitative analysis of Cd²⁺ and Ni²⁺ ions. The characteristics of the proposed method were shown in Table 2. In order to validate the applicability of the proposed method, certified reference materials were used and the results were listed in Table 3. From Table 3, it was

Table 2

Analytical parameters of proposed method.

Element	Linear range (ng mL ⁻¹)	R ²	LOD (ng mL ⁻¹)	Precision (R.S.D.) (%)	Enrichment factor
Cd	0.4–100	0.9998	0.25	2.2	66.7
Ni	1–150	0.9992	1	2.6	66.7

Table 3

Determination results of certified reference materials with proposed method.

Element	Certified concentration	Uncertainty	Detected concentration ($\mu\text{g mL}^{-1}$)	Recovery (%)	R.S.D. (% $n=3$)
Ni	0.158	± 0.006	0.152	96.2	1.2
Cd	0.402	± 0.018	0.386	95.9	1.6

Table 4

Results of blank and spiked recoveries of cadmium and nickel in real environmental samples.

Sample	Blank (ng mL^{-1})	Added (ng mL^{-1})	Spiked recoveries (%)	Element
1	7.3	10	91.9 ± 3.9	Cd^{2+}
	–		97.0 ± 3.5	Ni^{2+}
2	20.9	10	94.3 ± 4.1	Cd^{2+}
	15.4		94.4 ± 3.0	Ni^{2+}
3	19.5	10	90.2 ± 3.7	Cd^{2+}
	10.5		95.3 ± 4.5	Ni^{2+}
4	5.8	10	96.8 ± 4.0	Cd^{2+}
	–		99.2 ± 2.8	Ni^{2+}

easily found that the proposed method demonstrated excellent performance.

3.6. Analytical application

In order to evaluate the applicability of TiO_2 nanotubes as SPE adsorbents in the analysis of cadmium and nickel, four environmental water samples were collected from the region of Xinxiang City and used for the analysis. Firstly, blanks of all the samples were done to determine whether the target compounds were present or not. In the four samples, Cd^{2+} had been detected and their concentrations were 7.3, 20.9, 19.5 and 5.8 ng mL^{-1} , respectively. Nickel had been detected both in samples 2 and 3, and was not found in other samples. Further spiked recoveries with a spiked level of 10 ng mL^{-1} were investigated, and the data were listed in Table 4. All these results indicated that proposed method could be used to determine cadmium and nickel in real waters.

4. Conclusions

This paper proved that a novel nanomaterial, TiO_2 nanotubes had excellent enrichment ability for metal elements in environ-

mental samples and opened a new application prospect for TiO_2 nanotubes. The established method using TiO_2 nanotubes as SPE adsorbents for preconcentration of trace cadmium and nickel was satisfactory. The results obtained showed that the developed method was a rapid, simple, sensitive and effective analytical method for determination of cadmium and nickel at trace level, and it would be an alternative for the trace analysis of these two elements in water samples in the future.

Acknowledgements

This work was supported by High-Tech Research & Development Planning (863 Plan) of PR China (2006AA06Z424), the Natural Science Foundation of Henan Province (082102350022), the Personal Innovation Foundation of Universities in Henan Province ([2005]126), the fund of Henan Normal University (No. 2006PL06), and the funds from the Henan Key Laboratory for environmental pollution control.

References

- [1] A.M. Zou, M.L. Chen, X.W. Chen, J.H. Wang, Anal. Chim. Acta 598 (2007) 74.
- [2] Y. Wang, J.H. Wang, Z.L. Fang, Anal. Chem. 77 (2005) 5396.
- [3] M.L. Chen, Y. Tian, J.H. Wang, J. Anal. Atom. Spectrom. 23 (2008) 876.
- [4] A.M. Zou, M.L. Chen, Y. Shu, M. Yang, J.H. Wang, J. Anal. Atom. Spectrom. 22 (2007) 392.
- [5] A.M. Zou, X.W. Chen, M.L. Chen, J.H. Wang, J. Anal. Atom. Spectrom. 23 (2008) 412.
- [6] V. Vamvakaki, N.A. Chaniotakis, Sens. Actuators B 126 (2007) 193.
- [7] Y.Q. Wang, G.Q. Hu, X.F. Duan, H.L. Sun, Q.K. Xue, Chem. Phys. Lett. 365 (2002) 427.
- [8] G.S. Guo, C.N. He, Z.H. Wang, F.B. Gu, D.M. Han, Talanta 72 (2007) 1687.
- [9] M.K. Seery, R. George, P. Floris, S.C. Pillai, J. Photochem. Photobiol. A: Chem. 189 (2007) 258.
- [10] Z. Yuan, B. Su, Colloids Surf. A: Physicochem. Eng. Aspects 241 (2004) 173.
- [11] R. Liu, P. Liang, Anal. Chim. Acta 604 (2007) 114.
- [12] L. Zhang, Y. Morita, A. Sakuragawa, A. Isozaki, Talanta 72 (2007) 723.
- [13] P. Liang, Y. Qin, B. Hu, T. Peng, Z. Jiang, Anal. Chim. Acta 440 (2001) 207.
- [14] P. Liang, B. Hu, Z. Jiang, Y. Qin, T. Peng, J. Anal. Atom. Spectrom. 16 (2001) 863.
- [15] Q.X. Zhou, Y.J. Ding, J.P. Xiao, J. Chromatogr. A 1147 (2007) 10.
- [16] Q.X. Zhou, X.N. Zhao, G.H. Xie, J.P. Xiao, Atom. Spectrosc. 29 (2008) 145.



Excitation-emission-kinetic fluorescence coupled with third-order calibration for quantifying carbaryl and investigating the hydrolysis in effluent water

Shao-Hua Zhu, Hai-Long Wu*, A-Lin Xia, Jin-Fang Nie, Ying-Chao Bian, Chen-Bo Cai, Ru-Qin Yu

State Key Laboratory of Chemo/Biosensing and Chemometrics, College of Chemistry and Chemical Engineering, Hunan University, Changsha 410082, China

ARTICLE INFO

Article history:

Received 18 May 2008

Received in revised form

27 September 2008

Accepted 30 September 2008

Available online 14 October 2008

Keywords:

Carbaryl

Third-order calibration

Hydrolysis

Quadrilinear PARAFAC algorithm

ABSTRACT

A novel method for determination of carbaryl in effluent was proposed in this study. The kinetic evolution of excitation-emission matrix fluorescence (EEM) for the pesticide were recorded and come into being a four-way data array. The four-way fluorescence data were analyzed using the parallel factor analysis (PARAFAC). The methodology exploits the second-order advantage of three-order calibration based on quadrilinear parallel factor analysis, allowing analyte concentrations to be estimated even in the presence of an uncalibrated fluorescent background. It gave the satisfactory results for determination of the carbaryl in effluent samples. In addition, the kinetic study of degradation of carbaryl was performed according to the kinetic profile provided by the calibration.

© 2008 Elsevier B.V. All rights reserved.

1. Introduction

In recent years, multiway chemometrics techniques have been introduced to analyze the data involving high-dimensional structured information and have gained popularity [1–13]. The instruments that generate multidimensional data array are available to chemist, such as the high performance liquid chromatograph coupled with a diode array detector (HPLC-DAD) and the spectrofluorometer which can record excitation-emission matrices fluorescence signals. Furthermore, the advantage of the multiway methods is a higher stability towards instrument noise, interferences and matrix effects, in comparison with first-order methods and zero-order methods. The most appealing advantage is that they can separate directly the measured signals into the underlying contributions from individual analytes.

There are many second-order calibration algorithms in chemometrics to decompose second-order data array. The algorithms usually belong to three main groups: (i) the direct solution algorithms, including the generalized rank annihilation method (GRAM) [14] and the direct trilinear decomposition (DTLD) [15]; (ii) least-squares algorithms, such as bilinear least-squares (BLLS) [16,17]; (iii) the iterative algorithms, including the parallel factor analysis (PARAFAC) [18–20], alternating trilinear decomposition (ATLD) [21], the self-weighted alternating trilinear decompo-

sition (SWATLD) [22], multivariate curve resolution-alternating least-squares (MCR-ALS) [23], *N*-way partial least-squares (*N*-PLS) [24].

When the three-way array follows the so-called trilinear model, the decomposition based on the algorithms, such as PARAFAC and SWATLD, is unique, allowing spectral profiles and relative concentrations of individual sample components to be extracted directly in presence of uncalibrated interferences. This property was named as the second-order advantage. In the three groups the iterative algorithms, which based on PARAFAC model, ATLD, SWATLD, GRAM, MCR-ALS and bilinear least-squares/residual bilinearization (BLLS/RBL) [3–20] exhibit the second-order advantage too. This superiority has made the algorithms employed widely [9–13,25].

Calibration methods are not limited to the second-order calibration or the analysis of three-way data. Three-order calibration methods can also be used for the similar purpose and four-way data can be processed and interpreted in the similar way. In principle, the advantage of third-order calibration not only contains a similar second-order advantage that the components of interest can be determined even in the presence of uncalibrated interferences in complex samples, but also holds some additional advantage. It can provide more information about the analytes than second-order calibration for an additional dimension introduced. The intrinsic profiles in each mode can be determined uniquely for each species in the prediction samples [26]. Because four-way data array cannot be obtained conveniently nowadays, three-order calibration has scarcely been employed and only several works have been reported [2–8].

* Corresponding author. Tel.: +86 731 8821818; fax: +86 731 8821818.
E-mail address: hlwu@hnu.cn (H.-L. Wu).

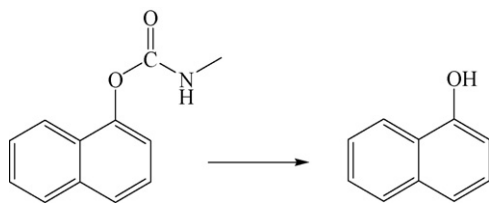


Fig. 1. The degradation of the carbaryl.

Carbaryl (1-naphthol *N*-methycarbamate), is the successful carbamate insecticide due to its broad-spectrum efficacy to control over 100 species of insects on citrus, fruit, cotton, forests, lawns, nuts, ornamentals, shade trees and other crops. The pesticide is used indiscriminately, so the toxicity has raised the public concern about the ecosystem and human health [27]. The carbaryl is rather stable in acidic condition, in basic conditions, however, hydrolyses readily in water (Fig. 1). The major degradation product is 1-naphthol. In present work, a novel method for determination of carbaryl in effluent was proposed by the means of excitation-emission-kinetic fluorescence data coupled with three-order calibration based on quadrilinear PARAFAC algorithm.

The hydrolysis reaction was monitored by measuring the evolution of EEM fluorescence signals and produced a four-way data array. Kinetic experiment introduces the temporal dimension into the measured data array. The three-order calibration based on the quadrilinear PARAFAC algorithm was applied to decompose the four-way data array. We can not only get the concentration of carbaryl in the samples, the profiles of excitation and emission fluorescence, but also obtain the kinetic profile of carbaryl hydrolysis. According to the kinetic profile and the kinetic model, the reaction rate constant can be determined.

2. Theory

2.1. Quadrilinear PARAFAC algorithm for three-order calibration

The trilinear decomposition model, the famous PARAFAC model, was proposed by Harshman [18] and Carroll and Chang [19]. The model has been widely accepted in chemistry since it follows the Lambert-Beer law. Fluorescence intensity measurements at several excitation and emission wavelengths can be described using the trilinear model. If an additional dimension is introduced, e.g. the temporal dimension, the quadrilinear PARAFAC model is required to describe the four-way data array.

For excitation-emission-kinetic fluorescence data measurements, a given sample produces a three-way data array with dimensions $I \times J \times K$. The quadrilinear PARAFAC model can be represented as following:

$$x_{ijkl} = \sum_{n=1}^N a_{in} b_{jn} c_{kn} d_{ln} + e_{ijkl} \quad (1)$$

where N is the total number of components, d_{ln} is the relative concentration of component n in the l th sample, and a_{in} , b_{jn} , and c_{kn} are the normalized intensities at the excitation wavelength i , emission wavelength j , and time channel k , respectively. e_{ijkl} which is the element of E_{ijkl} , collect the residual errors. The column vectors \mathbf{a}_n , \mathbf{b}_n , \mathbf{c}_n , and \mathbf{d}_n are collected into the corresponding profile matrixes \mathbf{A} , \mathbf{B} , \mathbf{C} , and \mathbf{D} .

The model can be respectively expressed in six fully equivalent slice-wise matrices and four fully equivalent stretched matrix representations owing to the symmetry of the model as [26]:

$$\mathbf{X}_{..kl} = \mathbf{A} \text{diag}(\mathbf{d}_{(l)}) \text{diag}(\mathbf{c}_{(k)}) \mathbf{B}^T + \mathbf{E}_{..kl}, \quad k = 1, 2, \dots, K, \quad l = 1, 2, \dots, L \quad (2)$$

$$\mathbf{X}_{i..l} = \mathbf{B} \text{diag}(\mathbf{a}_{(i)}) \text{diag}(\mathbf{d}_{(l)}) \mathbf{C}^T + \mathbf{E}_{i..l}, \quad i = 1, 2, \dots, I, \quad l = 1, 2, \dots, L \quad (3)$$

$$\mathbf{X}_{ij..} = \mathbf{C} \text{diag}(\mathbf{b}_{(j)}) \text{diag}(\mathbf{a}_{(i)}) \mathbf{D}^T + \mathbf{E}_{ij..}, \quad j = 1, 2, \dots, J, \quad i = 1, 2, \dots, I \quad (4)$$

$$\mathbf{X}_{.jk.} = \mathbf{D} \text{diag}(\mathbf{c}_{(k)}) \text{diag}(\mathbf{b}_{(j)}) \mathbf{A}^T + \mathbf{E}_{.jk.}, \quad k = 1, 2, \dots, K, \quad j = 1, 2, \dots, J \quad (5)$$

$$\text{And} \quad \mathbf{X}_{I \times J \times K L} = \mathbf{A}(\mathbf{D} \odot \mathbf{C} \odot \mathbf{B})^T + \mathbf{E}_{I \times J \times K L} \quad (6)$$

$$\mathbf{X}_{J \times K L I} = \mathbf{B}(\mathbf{A} \odot \mathbf{D} \odot \mathbf{C})^T + \mathbf{E}_{J \times K L I} \quad (7)$$

$$\mathbf{X}_{K \times L I J} = \mathbf{C}(\mathbf{B} \odot \mathbf{A} \odot \mathbf{D})^T + \mathbf{E}_{K \times L I J} \quad (8)$$

$$\mathbf{X}_{L \times I J K} = \mathbf{D}(\mathbf{C} \odot \mathbf{B} \odot \mathbf{A})^T + \mathbf{E}_{L \times I J K} \quad (9)$$

The quadrilinear PARAFAC algorithm is commonly carried out through an alternating least-squares minimization scheme. According to the Eqs. (6)–(9) one can obtain four equations as follows:

$$\mathbf{A} = \mathbf{X}_{I \times J \times K L} [(\mathbf{D} \odot \mathbf{C} \odot \mathbf{B})^T]^+ \quad (10)$$

$$\mathbf{B} = \mathbf{X}_{J \times K L I} [(\mathbf{A} \odot \mathbf{D} \odot \mathbf{C})^T]^+ \quad (11)$$

$$\mathbf{C} = \mathbf{X}_{K \times L I J} [(\mathbf{B} \odot \mathbf{A} \odot \mathbf{D})^T]^+ \quad (12)$$

$$\mathbf{D} = \mathbf{X}_{L \times I J K} [(\mathbf{C} \odot \mathbf{B} \odot \mathbf{A})^T]^+ \quad (13)$$

A typical iterative procedure for quadrilinear PARAFAC can be given as follows:

1. Estimate the number of factors, N .
2. Randomly initialize \mathbf{A} , \mathbf{B} , and \mathbf{C} .
3. Compute \mathbf{D} using Eq. (13).
4. Compute \mathbf{A} using Eq. (10) and scale \mathbf{A} to be columnwise normalized.
5. Compute \mathbf{B} using Eq. (11) and scale \mathbf{B} to be columnwise normalized.
6. Compute \mathbf{C} using Eq. (12) and scale \mathbf{C} to be columnwise normalized.
7. Compute \mathbf{D} using Eq. (13).
8. Repeat steps 4–7 until a stopping criterion is satisfied.

Because the four-way array decomposition only provides relative values, the analyte concentrations in the prediction samples are obtained after calibration step is performed, which is similar to a calibration curve for one component, or by regression of relative concentrations of each component of interest against its standard concentrations [21].

3. Experimental

3.1. Apparatus

The measurement of fluorescence was performed with a HITACHI F-4500 Fluorescence spectrophotometer with 10 mm quartz cells. A PINGFAN TGL-16A centrifuge and a BOXUN YXQ-LS-30 SII autoclave were employed to preprocess the effluent water.

The spectral data were imported to computer and analyzed in the Matlab environment. The programs of PARAFAC and linear regression algorithms were homemade. All programs were run on IBM compatible microcomputer.

3.2. Reagents

Carbaryl was purchased from FUTESI (Changsha, China). NaH_2PO_4 (analytical grade), H_3PO_4 (analytical grade), Na_2HPO_4 (analytical grade) and methanol (HPLC-grade) were purchased from YUFENG (Changsha, China). The effluent, which was sampled from a farm, was obtained from Environmental Protection Bureau of Changsha, China.

Stock solutions of $145 \mu\text{g ml}^{-1}$ carbaryl were prepared by dissolving appropriate amount in methanol. Working solutions were prepared by appropriate dilution of stock solution. All the solutions were stored in the refrigerator at 4°C .

Buffer solutions were obtained by mixing appropriate NaH_2PO_4 , H_3PO_4 and Na_2HPO_4 in doubly distilled water.

3.3. Procedure

The effluent was centrifuged to remove the particulate matter and then was sterilized in autoclave.

The external calibration method was employed in this work. Thereby the calibration set with six samples was constructed by the following way. Appropriate stock solutions of carbaryl and 2 ml phosphate buffer (pH 9.3) were added into 10 ml volumetric flask and mark in doubly distilled water. The concentration value is in the range of $17.2\text{--}93.6 \text{ ng ml}^{-1}$ for carbaryl. The prediction set included seven samples, and the concentration of carbaryl was limited to the range of calibration samples. The first three samples contain only the pesticide and 2 ml buffer, which were prepared in the same way as for calibration samples. The other four was prepared by adding 5 ml effluent, 2 ml buffer and the pesticide into 10 ml volumetric flask. Table 1 lists the concentration of carbaryl in calibration samples and prediction samples. When the buffer was mixed with the pesticide, the degradation reaction started. The kinetic evolutions of excitation-emission fluorescence matrices of these solutions were then recorded and the obtained data were subjected to four-way analysis, as described below.

All the samples were measured at excitation wavelength from 265 to 319 nm with 3 nm intervals and the emission wavelength from 319 to 487 nm with 8 nm intervals. The excitation and emission monochromator slit widths were 5 nm and the scanning rate was maintained at 2400 nm min^{-1} . For each sample EEM fluorescence signals at a series of specific moments (2 min, 9 min, 16 min,

..., 51 min, 58 min, 65 min) were scanned and an EEM data array with dimensions $22 \times 19 \times 10$ (excitation wavelength \times emission wavelength \times reaction time) was obtained. All the thirteen samples at the series of specific moments were measured and the four-way array ($22 \times 19 \times 10 \times 13$) was constructed.

4. Result and discussion

In the present paper, the hydrolysis of carbaryl in presence of alkaline buffer was described. We have tried the buffers with pH values (8.2, 9.3, 10.2 and 11.5) in the experiment, and the buffer (pH 9.3) was selected as it could provide a measurable reaction rate.

The effluent is a complex mixture which is composed of many different fluorescent chromophores of different compounds. So it is natural to exhibit strong and broad native fluorescence, and its fluorescence profile will overlap with that of carbaryl and 1-naphthol. Fig. 2 shows the fluorescence filled contour of the effluent.

When the samples were measured within the excitation wavelength range (230–350 nm) and the emission wavelength range (300–550 nm) at first, Rayleigh scattering was intense in this range. The scattering is not correlated with the target concentration of the analyte, therefore, for the calibration and prediction purposes, truncating the range that account for Rayleigh scattering signals, the EEM fluorescence were recorded by measuring the samples within the spectral excitation and emission ranges, 265–319 nm and 319–487 nm, respectively. The response data arrays were roughly compensated just by subtracting the average response matrix of three blank solutions to avoid and weaken the effects of Rayleigh scattering and Raman scattering.

The hydrolysis of carbaryl would start up in the presence of alkaline buffer, and a four-way data array of $22 \times 19 \times 10 \times 13$ was produced from the measurement of all the samples in all the specific moments. Fig. 3 shows the kinetic evolution contour plots of EEM for sample 5 within the selected range. In the figure the peak intensities of carbaryl were reduced and that of 1-naphthol were enhanced with the reaction time. This means the hydrolysis was running, and the concentration of carbaryl decreased and that of the 1-naphthol increased.

The four-way data array was processed using the quadrilinear PARAFAC. PARAFAC required the estimated factor number to analyze the data array. The factor number should be designated

Table 1

The concentration of carbaryl in calibration samples and prediction samples.

	Carbaryl (ng ml^{-1})	Buffer (ml)	Effluent (ml)
Calibration samples			
1	17.2	2	0
2	31.2	2	0
3	46.8	2	0
4	62.4	2	0
5	78.0	2	0
6	93.6	2	0
Prediction samples			
7	23.4	2	0
8	39.0	2	0
9	54.6	2	0
10	39.0	2	5
11	54.6	2	5
12	70.2	2	5
13	78.0	2	5

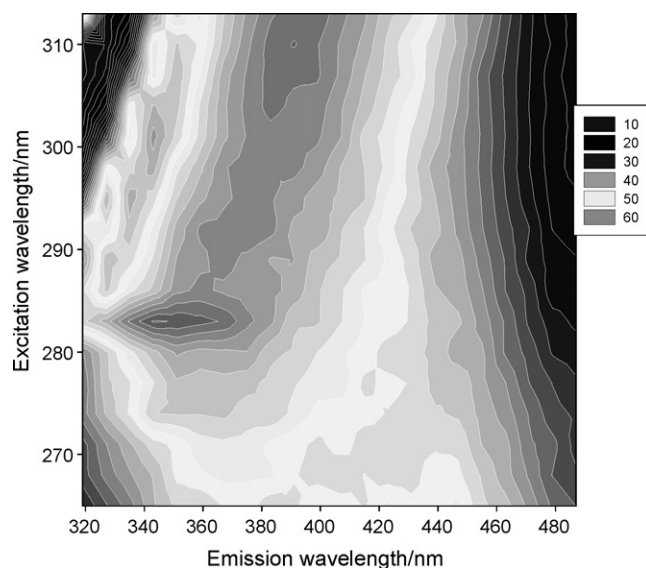


Fig. 2. The fluorescence filled contour of the effluent.

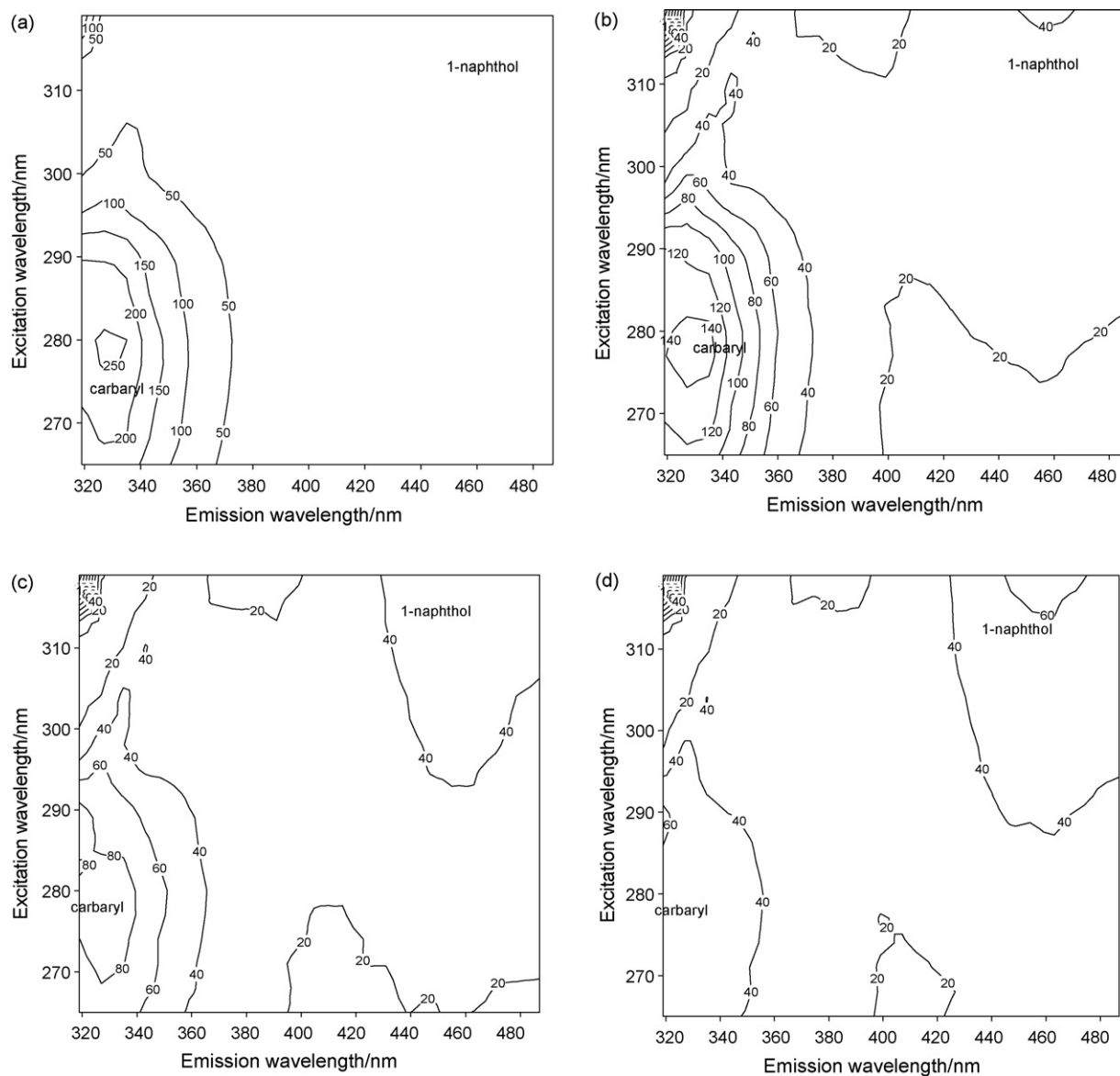


Fig. 3. The kinetic evolution contour plots of EEM for sample 5. Selected time: (a) 2 min; (b) 23 min; (c) 44 min; (d) 65 min.

in advance. To estimate the factor or component number for the decomposition of four-way data array, we tried the core consistency diagnostic at first. However, the core consistency diagnostic failed to give the appropriate factor number, and sometimes it cost several hours to give a wrong result. But factor indicator function (IND) suggested the appropriate factor number should be five. The factor number was tried from 1 to 10, and the corresponding function value of IND descended at first and then increased. The value reached the inflection point and returned minimum value when the number was selected to be five. The quadrilinear PARAFAC decomposed the four-way data array with the factor number of five and gave the satisfactory results.

The three-order calibration provided directly the excitation spectral profiles, emission spectral profiles and the kinetic profiles, which were shown in Fig. 4. Fig. 4(a) shows loadings related to the excitation spectral profiles, Fig. 4(b) shows loadings related to the emission spectral profiles and Fig. 4(c) shows loading related to the kinetic profiles. In the figure the lines A and D represent car-

baryl and 1-naphthol (the hydrolysate of carbaryl), *F* represents the actual profile of carbaryl, *C* and *E* represent the background profiles of the effluent and *B* represents Rayleigh scattering. The effluent is composed of many different fluorescent chromophores of different compounds, however the amount of the compounds is low or even trace. So it is natural that PARAFAC recognized the effluent as two factors. Although we have tried to eliminate the influence from Rayleigh scattering by the measures mentioned above, the residual still existed in the spectral range monitored. This is an unfavorable factor for the work, but it can be compensated by three-order calibration based on quadrilinear PARAFAC. The Rayleigh scattering can be regarded as a component or factor in the step of calibration model construction. It is similar with the description about removal the background drift in chromatographic analysis, which was proposed by Zhang et al. [28].

From the figure, it could be seen that the spectral profiles were overlapped each other. In such a situation, biased or wrong results might be obtained using conventional methods. However,

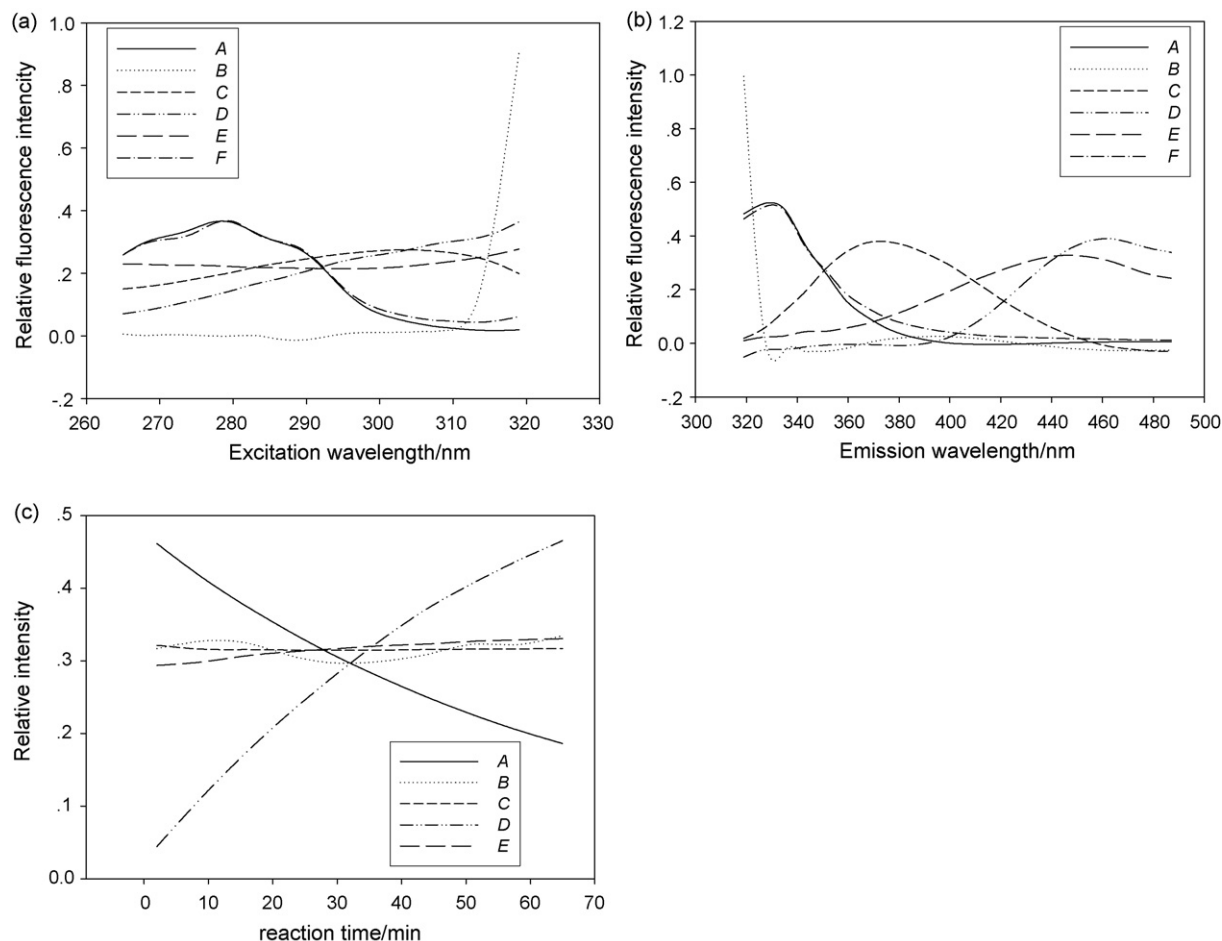


Fig. 4. Resolved the excitation profiles (a), emission profiles (b) and kinetic profiles (c), normalized to unit length, as obtained by PARAFAC when the chosen factor number was five, the loadings A and D represent carbaryl and 1-naphthol (the hydrolysate of carbaryl), F represents the actual profile of carbaryl, C and E represent the background profiles of effluent and B represents Rayleigh scattering.

good estimate concentrations were provided by the method of the three-order calibration based on quadrilinear PARAFAC. The results obtained by implementing the calibration and prediction steps were displayed in Table 2. The prediction concentration and recovery were satisfactory for prediction samples. The PARAFAC algorithm with five factors was capable to provide good estimate concentrations and spectral profiles despite the fact that the spectral profiles of the five components were heavily overlapped in the effluent samples as shown in Fig. 4.

The statistic parameter, the root mean square error of prediction (RMSEP), and figures of merit such as sensitivity, selectivity and limit of detection were displayed in Table 3. Although the second-order calibration has also the capacity to determine the analytes in presence of uncalibrated interferences, the three-order calibration has some superiority in resolving and quantifying analytes in

complex sample system. Four-way data array provide the opportunity of introducing an additional dimension to three-way data sets. In this work, the quadrilinear decomposition could provide simultaneously the excitation profiles, emission profiles, kinetic profiles and concentration for all the components. And this allows for providing more information about the complex sample and the analytes, and increasing predictive ability. Kim et al. compared and contrasted the selectivity based on trilinear PARAFAC and quadrilinear PARAFAC, and they considered that quadrilinear PARAFAC could give higher selectivity for each PAH than trilinear PARAFAC [29]. Olivieri considered that the use of third-order data leads to an increase in sensitivity [30].

In present work kinetic experiments introduce an additional temporal dimension in the measured data set. This not only

Table 2
Resolved concentrations of prediction samples.

	Added (ng/ml)	Found (ng/ml)	Recovery (%)
7	23.4	23.3	99.6
8	39.0	39.1	100.5
9	54.6	54.6	100.0
10	39.0	41.0	102.6
11	54.6	56.1	102.7
12	70.2	71.1	101.3
13	78.0	81.2	104.1

Table 3
The statistic parameters and figures of merit.

Parameter	^a RMSEP (ng ml ^{–1})	^b SEN (AFU ng ^{–1} ml)	^c SEL	^d LOD (ng ml ^{–1})
PARAFAC	2.64	24.41	0.915	3.58

^a The root mean square error of prediction (RMSEP) is determined as: $\text{RMSEP} = \left[\sum_{i=1}^M (c_i - \hat{c}_i)^2 / M \right]^{1/2}$, where M is the number of samples, c_i and \hat{c}_i are the actual and predicted concentrations, respectively.

^b The sensitivity is determined as: $\text{SEN}_n = k_n [(A^T A) \cdot (B^T B) \cdot (C^T C)]^{-1}_{nn}^{-1/2}$.

^c The selectivity can be simply obtained by dividing SEN by k_n ;

^d Limit of detection can be calculated as: $\text{LOD} = 3.3\text{S}_0$.

Table 4

Regression equation, rate constant and correlation coefficient of degradation reaction of carbaryl.

	Regression equation	Correlation coefficient	Rate constant (min^{-1})	Half life (min)
Carbaryl	$e^Y = 0.0142x + 0.7838$	0.9999	0.0142	48.8

^e Y represents the natural logarithm of relative concentration $1/C_t$, x represents time $t-t_1$ (min).

increases the selectivity and sensitivity of spectroscopic-based determination, but also provides more information about the analytes by the three-order calibration. Fig. 4(c), the kinetic profiles, displays the change of the fluorescence intensity of the five components with reaction time. In fact the intensity for carbaryl increased as a function of reaction time and the kinetic profile of carbaryl can be used to investigate the hydrolysis of carbaryl and provided more information about the reaction.

The conversion of carbaryl to 1-naphthol follows the first-order kinetic model. The concentration of carbaryl at t moment can be determined by the function:

$$-\frac{dC_{car}}{dt} = K \times C_{car} \quad (14)$$

According to the function one could get the function:

$$\ln(C_{car,t}) = \ln(C_{car,0}) - K \times t \quad (15)$$

where $\ln(*)$ denoted the natural logarithm of *, $C_{car,0}$ is the initial concentration of reactant, $C_{car,t}$ represented the concentration of reactant at the moment t since the reaction started. K indicated the reaction rate constant (min^{-1}). Then one could get:

$$\ln(1/C_{car,t}) = \ln(1/C_{car,1}) + K \times (t - t_1) \quad (16)$$

In this case, $C_{car,1}$ represented the concentration of carbaryl at the first specific moment $t_1 = 2$ min. According to the relative concentration displayed in Fig. 4(c), the natural logarithm of reciprocal of the relative concentrations at the 10 specific moments versus time $t-t_1$ was plotted in Fig. 5. It could be observed that all the points were almost in one line and the logarithm of reciprocal of concentrations linearly related to time. The regression equation and correlation coefficient of carbaryl were shown in Table 4. From the regression equation the half life of carbaryl could be obtained. The half life of carbaryl was 48.8 min in this condition. Fig. 4(c) implied that the half life was around 47 min which approximated the 48.8 min. All the results verified that the degradation

follows first-order kinetic model. So after decomposing the four-way data array using quadrilinear PARAFAC algorithm, three-order calibration provided the plentiful information, and according to the information the hidden knowledge, such as that about the hydrolysis of carbaryl in this work, could be found.

5. Conclusion

In present work excitation-emission-kinetic fluorescence data array were analyzed to determining carbaryl in effluent using three-order calibration based on quadrilinear PARAFAC algorithm. It exploited some superiority of three-order calibration. The second-order advantage makes it possible that determination of carbaryl can be performed even in the presence of unknown interferences. Since an additional temporal dimension was introduced, theoretically, three-order calibration could give a higher sensitivity and selectivity. Therefore, the carbaryl could be quantified accurately in the effluent samples. And due to introducing the temporal dimension we could research conveniently the hydrolysis of carbaryl according to the kinetic profile. The rate equation, rate constant and half life were obtained and the results revealed and verified that the degradation follows first-order kinetic model. The present paper provides not only a new and simple approach to study the kinetics but also a promising tool for exploring the kinetic behaviors of complex system.

Acknowledgements

The authors would like to acknowledge financial supports by the National Natural Science Foundation of China (Grant Nos. 20475014 and 20435010) and the National Basic Research Program (No. 2007CB216404).

References

- [1] E. Bezemer, S.C. Rutan, Chemom. Intell. Lab. Syst. 81 (2006) 82.
- [2] P.C. Damiani, I. Duran-Meras, A. Garcia-Reiriz, A. Jimenez-Giron, A.M. Pena, A.C. Olivieri, Anal. Chem. 79 (2007) 6949.
- [3] R.P.H. Nikolajsen, K.S. Booksh, A.M. Hansen, R. Bro, Anal. Chim. Acta 475 (2003) 137.
- [4] J.A. Arancibia, A.C. Olivieri, D.B. Gil, A.E. Mansilla, I. Duran-Meras, A.M. Pena, Chemom. Intell. Lab. Syst. 80 (2006) 77.
- [5] H.C. Goicoechea, S.J. Yu, A.C. Olivieri, A.D. Campiglia, Anal. Chem. 77 (2005) 2608.
- [6] A.M. Pena, I.D. Meras, A.J. Giron, H.C. Goicoechea, Talanta 72 (2007) 1261.
- [7] S.E.G. Porter, D.R. Stoll, S.C. Rutan, P.W. Carr, J.D. Cohen, Anal. Chem. 78 (2006) 5559.
- [8] A.C. Olivieri, J.A. Arancibia, A.M. Pena, I. Duran-Meras, A.E. Mansilla, Anal. Chem. 76 (2004) 5657.
- [9] I. Stanimirova, V. Simeonov, Chemom. Intell. Lab. Syst. 77 (2005) 115.
- [10] D. Arroyo, M. Cruz Ortiz, L.A. Sarabia, F. Palacios, J. Chromatogr. A 1187 (2008) 1.
- [11] Y. Zhang, H.L. Wu, A.L. Xia, Q.J. Han, H. Cui, R.-Q. Yu, Talanta 72 (2007) 926.
- [12] A. Espinosa-Mansilla, A.M. Peña, F. Cañada-Cañada, D.G. Gómez, Anal. Biochem. 347 (2005) 275.
- [13] G.M. Escandar, D.G. Gómez, A.E. Mansilla, A.M. Peña, H.C. Goicoechea, Anal. Chim. Acta 506 (2004) 161.
- [14] E. Sanchez, B.R. Kowalski, Anal. Chem. 58 (1986) 496.
- [15] E. Sanchez, B.R. Kowalski, J. Chemom. 2 (1988) 265.
- [16] M. Linder, R. Sundberg, Chemom. Intell. Lab. Syst. 42 (1998) 159.
- [17] M. Linder, R. Sundberg, J. Chemom. 16 (2002) 12.
- [18] R.A. Harshman, UCLA Working Papers in Phonetics 16 (1970) 1.
- [19] J.D. Carroll, J.J. Chang, Psychometrika 35 (1970) 283.

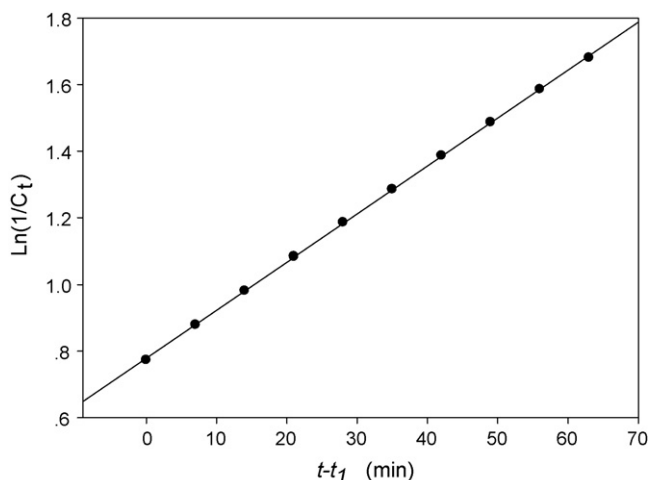


Fig. 5. The plot of the natural logarithm of reciprocal of relative concentration $\ln(1/C_t)$ versus time $t-t_1$.

- [20] R. Bro, *Chemom. Intell. Lab. Syst.* 38 (1997) 149.
- [21] H.L. Wu, M. Shibukawa, K.J. Oguma, J. *Chemom.* 12 (1998) 1.
- [22] Z.P. Chen, H.L. Wu, J.H. Jiang, Y. Li, R.Q. Yu, *Chemom. Intell. Lab. Syst.* 52 (2000) 75.
- [23] M. Esteban, C. Arino, J.N. Diaz-Cruz, M.S. Diaz-Cruz, R. Tauler, *Trends Anal. Chem.* 19 (2000) 49.
- [24] R. Bro, J. *Chemom.* 10 (1996) 47.
- [25] S.H. Zhu, H.L. Wu, A.L. Xia, Q.J. Han, Y. Zhang, *Anal. Sci.* 23 (2007) 1173.
- [26] L. Xia, H.L. Wu, S.F. Li, S.H. Zhu, L.Q. Hu, R.Q. Yu, J. *Chemom.* 20 (2007) 1.
- [27] Carbaryl (EHC 153, 1994), <http://www.inchem.org/documents/ehc/ehc/ehc153.htm>.
- [28] Y. Zhang, H.L. Wu, A.L. Xia, L.H. Hu, H.F. Zou, R.Q. Yu, J. *Chromatogr. A* 1167 (2007) 178.
- [29] Y.-C. Kim, J.A. Jordan, M.L. Nahorniak, K.S. Booksh, *Anal. Chem.* 77 (2005) 7679.
- [30] A.C. Olivieri, *Anal. Chem.* 77 (2005) 4936.